

# MICROWAVE MAGNETRONS

*Edited by*

GEORGE B. COLLINS

DEPARTMENT OF PHYSICS  
UNIVERSITY OF ROCHESTER

OFFICE OF SCIENTIFIC RESEARCH AND DEVELOPMENT  
NATIONAL DEFENSE RESEARCH COMMITTEE

FIRST EDITION



NEW YORK · TORONTO · LONDON  
MCGRAW-HILL BOOK COMPANY, INC.

1948







# MICROWAVE MAGNETRONS



62-77122

MASSACHUSETTS INSTITUTE OF TECHNOLOGY  
RADIATION LABORATORY SERIES

Board of Editors

LOUIS N. RIDENOUR, *Editor-in-Chief*  
GEORGE B. COLLINS, *Deputy Editor-in-Chief*

BRITTON CHANCE, S. A. GOUDSMIT, R. G. HERB, HUBERT M. JAMES, JULIAN K. KNIPP,  
JAMES L. LAWSON, LEON B. LINFORD, CAROL G. MONTGOMERY, C. NEWTON, ALBERT  
M. STONE, LOUIS A. TURNER, GEORGE E. VALLEY, JR., HERBERT H. WHEATON

---

1. RADAR SYSTEM ENGINEERING—*Ridenour*
  2. RADAR AIDS TO NAVIGATION—*Hall*
  3. RADAR BEACONS—*Roberts*
  4. LORAN—*Pierce, McKenzie, and Woodward*
  5. PULSE GENERATORS—*Glasoe and Lebacqz*
  6. MICROWAVE MAGNETRONS—*Collins*
  7. KLYSTRONS AND MICROWAVE TRIODES—*Hamilton, Knipp, and Kuper*
  8. PRINCIPLES OF MICROWAVE CIRCUITS—*Montgomery, Dicke, and Purcell*
  9. MICROWAVE TRANSMISSION CIRCUITS—*Ragan*
  10. WAVEGUIDE HANDBOOK—*Marcuvitz*
  11. TECHNIQUE OF MICROWAVE MEASUREMENTS—*Montgomery*
  12. MICROWAVE ANTENNA THEORY AND DESIGN—*Silver*
  13. PROPAGATION OF SHORT RADIO WAVES—*Kerr*
  14. MICROWAVE DUPLEXERS—*Smullin and Montgomery*
  15. CRYSTAL RECTIFIERS—*Torrey and Whitmer*
  16. MICROWAVE MIXERS—*Pound*
  17. COMPONENTS HANDBOOK—*Blackburn*
  18. VACUUM TUBE AMPLIFIERS—*Valley and Wallman*
  19. WAVEFORMS—*Chance, Hughes, MacNichol, Sayre, and Williams*
  20. ELECTRONIC TIME MEASUREMENTS—*Chance, Hulsizer, MacNichol, and Williams*
  21. ELECTRONIC INSTRUMENTS—*Greenwood, Holdam, and MacRae*
  22. CATHODE RAY TUBE DISPLAYS—*Soller, Starr, and Valley*
  23. MICROWAVE RECEIVERS—*Van Voorhis*
  24. THRESHOLD SIGNALS—*Lawson and Uhlenbeck*
  25. THEORY OF SERVOMECHANISMS—*James, Nichols, and Phillips*
  26. RADAR SCANNERS AND RADOMES—*Cady, Karelitz, and Turner*
  27. COMPUTING MECHANISMS AND LINKAGES—*Svoboda*
  28. INDEX—*Henney*
- 11



# MICROWAVE MAGNETRONS

*Edited by*

GEORGE B. COLLINS

DEPARTMENT OF PHYSICS  
UNIVERSITY OF ROCHESTER

OFFICE OF SCIENTIFIC RESEARCH AND DEVELOPMENT  
NATIONAL DEFENSE RESEARCH COMMITTEE

FIRST EDITION



NEW YORK · TORONTO · LONDON  
MCGRAW-HILL BOOK COMPANY, INC.

1948

✓



TK 6573

M 41

U. S.

C 3

## MICROWAVE MAGNETRONS

COPYRIGHT, 1948, BY THE  
MCGRAW-HILL BOOK COMPANY, INC.  
PRINTED IN THE UNITED STATES OF AMERICA

*All rights reserved. This book, or  
parts thereof, may not be reproduced  
in any form without permission of  
the publishers.*

SCIENCE LIBRARY



THE MAPLE PRESS COMPANY, YORK, PA.

# *MICROWAVE MAGNETRONS*

## *EDITORIAL STAFF*

GEORGE B. COLLINS  
A. FINEMAN  
JOYCE KINNEY

## *CONTRIBUTING AUTHORS*

J. G. BUCK  
A. M. CLOGSTON  
G. B. COLLINS  
J. R. FELDMEIER  
M. A. HERLIN  
N. M. KROLL  
S. MILLMAN  
F. F. RIEKE  
A. G. SMITH  
W. V. SMITH  
L. R. WALKER





## Foreword

---

THE tremendous research and development effort that went into the development of radar and related techniques during World War II resulted not only in hundreds of radar sets for military (and some for possible peacetime) use but also in a great body of information and new techniques in the electronics and high-frequency fields. Because this basic material may be of great value to science and engineering, it seemed most important to publish it as soon as security permitted.

The Radiation Laboratory of MIT, which operated under the supervision of the National Defense Research Committee, undertook the great task of preparing these volumes. The work described herein, however, is the collective result of work done at many laboratories, Army, Navy, university, and industrial, both in this country and in England, Canada, and other Dominions.

The Radiation Laboratory, once its proposals were approved and finances provided by the Office of Scientific Research and Development, chose Louis N. Ridenour as Editor-in-Chief to lead and direct the entire project. An editorial staff was then selected of those best qualified for this type of task. Finally the authors for the various volumes or chapters or sections were chosen from among those experts who were intimately familiar with the various fields, and who were able and willing to write the summaries of them. This entire staff agreed to remain at work at MIT for six months or more after the work of the Radiation Laboratory was complete. These volumes stand as a monument to this group.

These volumes serve as a memorial to the unnamed hundreds and thousands of other scientists, engineers, and others who actually carried on the research, development, and engineering work the results of which are herein described. There were so many involved in this work and they worked so closely together even though often in widely separated laboratories that it is impossible to name or even to know those who contributed to a particular idea or development. Only certain ones who wrote reports or articles have even been mentioned. But to all those who contributed in any way to this great cooperative development enterprise, both in this country and in England, these volumes are dedicated.

L. A. DuBRIDGE.





## *Preface*

---

THE pulsed 10-cm magnetron, perfected by the British in 1940, constituted the starting point for the development of microwave radar. From that time until the end of the war the magnetron proved to be one of the most important components in radar systems. As a consequence of this, the armed services, both in this country and in England, instigated extensive programs of research and development to produce new types and improve the characteristics of existing ones. The program soon became a major one for the electronic industry. At the Radiation Laboratory alone, over forty highly trained physicists and engineers spent more than four years studying magnetron performance and producing new designs. Comparable effort was expended by the many other industrial and research laboratories. The result was over twenty distinct types of magnetrons, producing powers in the tens to thousands of kilowatts at frequencies that were largely unexplored before 1940. What is more important, this program led to a better understanding of the principles of magnetron operation and to an increased appreciation of the importance of the field of electronics at high frequencies.

During the war very little attention could be given to evaluating, correlating, and recording these new developments, and what reports were written are disconnected and incomplete. Actually, much of the information existed only in the minds of the investigators and in their personal notebooks. The purpose of this book is to present in a usable form this large amount of theoretical and practical knowledge.

Conditions surrounding the preparation of the volume produced special problems. The time available was short, considering the amount and complexity of the material, and a division of labor among many authors was necessary. This permitted the selection of authors best qualified to present different subjects but resulted in a not too consistent style and level of presentation. Furthermore, it was appreciated that although microwave magnetrons were developed for use in radar systems, their importance to science and engineering was much broader; thus the material for the book was evaluated largely in terms of its possible future usefulness, and the uncertainty of this resulted in a tendency to include

too much rather than too little. More serious are the errors that may not have been eliminated because of insufficient time for adequate review.

The book contains a large fraction of what was known, as of January 1946, about the theory, design, and operation of magnetrons in the frequency range 1000 to 25,000 Mc/sec and the many modifications that extend the usefulness of these tubes. There is in this book, because of its radar background, a strong emphasis on magnetrons intended for pulsed operation, but the treatment is extended to c-w applications whenever possible.

The scope is dictated by the primary premise that all information necessary to "make a magnetron" be included. As a result, the character of the chapters ranges from a detailed theory of the various aspects of magnetron operation to the details of construction of production magnetrons. An introductory chapter reviews the early work on magnetrons, including the first 10-cm tube of the British, and presents the basic principles of magnetron operation in order to orient the reader unfamiliar with the subject.

Except for this introduction, the material is arranged so that theory precedes practical considerations. A final chapter gives operating data and important dimensions for a variety of magnetrons.

Although the authors of this volume were nearly all members of the MIT Radiation Laboratory or Columbia Radiation Laboratory, a great deal of the material included originated in the industrial concerns of this country and England. References to contributions by other laboratories is given whenever possible, but the free exchange of information existing during the war makes the origins of many of the ideas uncertain. In particular, the contributions of the Bell Telephone Laboratories and the Raytheon Manufacturing Company have been extensive and in many cases undistinguishable from those of the MIT and Columbia groups. The important contributions of these and the many other institutions are acknowledged.

The early work of the British deserves special recognition. All too few references to it are found in this volume, because soon after the original design was divulged to laboratories in this country, the development here proceeded along rather independent lines. The British magnetron, however, was the key to the production of high-power microwaves. A discussion of this tube and its important features is found in Chap. 1, based on material kindly furnished by Professor J. T. Randall and Dr. H. A. H. Boot who, more than any others, were responsible for its invention.

Acknowledgments are due to the many who reviewed chapters of the book. In particular, mention should be made of Dr. Lewi Tonks of the General Electric Company, Drs. W. B. Hebenstriet and H. D. Hagstrum

of the Bell Telephone Laboratories, Drs. A. Nordsieck and A. V. Hollenberg of Columbia University, Dr. Lloyd P. Smith of Cornell University, and Miss Helen Wieman for her assistance in preparing the manuscript for publication.

In conclusion, the editor wishes to emphasize that a book of this magnitude could not have been written without the wholehearted cooperation of all the authors, many of whom worked on the manuscript long after leaving the Radiation Laboratory.

GEORGE B. COLLINS.

CAMBRIDGE, MASS.,  
*July, 1946.*





# *Contents*

---

FOREWORD BY L. A. DuBRIDGE . . . . .	vii
PREFACE . . . . .	ix
CHAP. 1. INTRODUCTION . . . . .	1
1-1. Early Types of Magnetrons . . . . .	1
1-2. The British Cavity Magnetron . . . . .	8
1-3. Description of a Microwave Magnetron . . . . .	10
1-4. The Resonant System . . . . .	13
1-5. The Cathode . . . . .	23
1-6. The Space Charge . . . . .	24
1-7. D-c Voltage Magnetic-field Relationship . . . . .	29
1-8. Component Modes . . . . .	32
1-9. Efficiency and Frequency Stability . . . . .	35
1-10. Performance Charts and Rieke Diagrams . . . . .	37
1-11. Pulsed Magnetrons . . . . .	42
PART I. RESONANT SYSTEMS	
CHAP. 2. THE UNSTRAPPED RESONANT SYSTEM . . . . .	49
2-1. The Magnetron Cavity as a Circuit Problem . . . . .	49
2-2. Equivalent Network for the Side Resonators . . . . .	52
2-3. Equivalent Network for the Interaction Space . . . . .	52
2-4. Spectrum Predicted by the Equivalent Network . . . . .	54
2-5. Admittance of Side Resonators by Field Theory . . . . .	56
2-6. Admittance of the Interaction Space by Field Theory . . . . .	63
2-7. The Spectrum Predicted by Field Theory . . . . .	66
2-8. End-space Effects . . . . .	69
2-9. The Interaction Field . . . . .	74
2-10. Applications and Limitations . . . . .	76
2-11. The Computation of Admittances . . . . .	77
CHAP. 3. THE RISING-SUN SYSTEM . . . . .	83
3-1. The Spectrum . . . . .	83
3-2. The Interaction Field . . . . .	92
3-3. The Effect of the Mode Spectrum and Field Characteristics on $\pi$ -mode Operation . . . . .	98
3-4. The Effects of Various Parameters on the Mode Spectrum and the Interaction Field of a Rising-sun Magnetron . . . . .	101

3-5. Closed-end Rising-sun Systems . . . . .	110
3-6. The Unloaded $Q$ and $\sqrt{C/L}$ . . . . .	113
CHAP. 4. THE STRAPPED SYSTEM . . . . .	118
4-1. Introduction . . . . .	118
4-2. Analysis of Strapped Systems . . . . .	121
4-3. Rings of Networks. . . . .	123
SYMMETRICAL SYSTEMS . . . . .	131
4-4. Fixed-frequency Systems . . . . .	131
4-5. Effects of Various Parameters on the Mode Spectrum . . . . .	135
ASYMMETRICAL SYSTEMS . . . . .	140
4-6. Pattern Distortion and Mode-spectrum Effects Caused by Loading . . . . .	141
4-7. Effects of Strap Breaks. . . . .	147
4-8. Effects Caused by Various Types of Tuning. . . . .	157
CHAP. 5. OUTPUT CIRCUITS . . . . .	167
5-1. Introduction . . . . .	167
5-2. The 4-terminal Transducer . . . . .	171
5-3. The $Q$ -circle and the Rieke Diagram . . . . .	178
5-4. General Considerations Concerning the Output Circuit Problem . . . . .	187
5-5. Coaxial-output Circuits. . . . .	191
5-6. Waveguide-output Circuits . . . . .	194
PART II. ANALYSIS OF OPERATION	
CHAP. 6. THE INTERACTION OF THE ELECTRONS AND THE ELECTROMAGNETIC FIELD. . . . .	207
6-1. Introduction . . . . .	207
6-2. The Assumptions Underlying the Analysis . . . . .	209
6-3. The Field Equations. . . . .	217
6-4. The Equations of Motion. . . . .	222
6-5. Conditions Under Which Relativistic Effects May Be Eliminated . . . . .	228
6-6. The Nonrelativistic Equations. . . . .	231
6-7. Symmetrical States . . . . .	243
6-8. The Bunemann Small-amplitude Theory . . . . .	253
6-9. Analysis by the Method of Self-consistent Fields. . . . .	265
6-10. Qualitative Discussion of the Interaction . . . . .	274
6-11. Departures from the Rotating-wave Hypothesis. . . . .	282
CHAP. 7. THE SPACE CHARGE AS A CIRCUIT ELEMENT . . . . .	288
7-1. Introduction . . . . .	288
7-2. The Electron Stream as a Circuit Element . . . . .	291
7-3. Analysis of the Resonant System . . . . .	297
7-4. Interactions Between Space Charge and Resonator. . . . .	305
7-5. The Description of Magnetron Performance. . . . .	316
7-6. The Mismatched Transmission Line as a Resonant Load . . . . .	320
7-7. Experimental Data on the Space-charge Properties. . . . .	329

CHAP. 8. TRANSIENT BEHAVIOR . . . . .	339
8-1. Steady-state Properties of the Modes . . . . .	339
8-2. Steady-state Properties of the Pulser . . . . .	343
8-3. Types of Mode Changes . . . . .	345
8-4. Survey of the Process of Mode Selection . . . . .	348
8-5. The Mode Skip . . . . .	350
8-6. The Mode Shift . . . . .	351
8-7. Instability of the Power Supply: "Mode Jumps" . . . . .	355
8-8. Outline of a Theory of Starting . . . . .	357
8-9. Observations and Discussion of Starting . . . . .	367
8-10. Observations on R-f Buildup . . . . .	372
8-11. Effect of Design and Operation on Starting . . . . .	376
8-12. Interactions Between Modes . . . . .	380
CHAP. 9. NOISE . . . . .	388
9-1. Introduction . . . . .	388
9-2. Pre-oscillation Noise . . . . .	389
9-3. Signal-to-noise Ratio . . . . .	394
9-4. Origins of Noise . . . . .	395

### PART III. DESIGN

CHAP. 10. PRINCIPLES OF DESIGN . . . . .	401
10-1. The Primary Design Parameters . . . . .	401
10-2. The Method of Magnetron Design . . . . .	403
10-3. Conditions Imposed on the Resonant System . . . . .	406
10-4. Conditions Imposed on the Cathode . . . . .	411
10-5. Conditions Imposed on the Magnetic Circuit . . . . .	414
10-6. The Scaling Laws . . . . .	414
10-7. Reduced Operating Data on Various Types of Magnetrons . . . . .	419
10-8. Determination of the Secondary Design Parameters . . . . .	435
10-9. Comparison of the Reduced Performance Charts . . . . .	441
10-10. The Universal Performance Chart . . . . .	448
10-11. The General Design Formulas . . . . .	454
10-12. Numerical Example . . . . .	458
CHAP. 11. THE RESONANT SYSTEM . . . . .	460
11-1. Factors Influencing Choice of Resonant System . . . . .	460
STRAPPED RESONANT SYSTEMS . . . . .	461
11-2. Wavelength and Characteristic Admittance . . . . .	461
11-3. Unloaded $Q$ . . . . .	466
11-4. Mode Separation . . . . .	468
RIISING-SUN RESONANT SYSTEMS . . . . .	470
11-5. Limitations on Secondary Design Parameters . . . . .	472
11-6. Desirable Mode Spectrum . . . . .	474
11-7. Comparison Between Open-resonator and Closed-end Systems . . . . .	477
11-8. Ratio of Resonator Depths . . . . .	478
11-9. Wavelength Calculations for the $\pi$ -mode . . . . .	479



OUTPUT . . . . .	481
11-10. General Properties of Coaxial and Waveguide Outputs . . . . .	481
11-11. Coaxial Outputs . . . . .	482
11-12. Coaxial-to-waveguide Transitions . . . . .	485
11-13. Waveguide Outputs . . . . .	486
11-14. Waveguide Transformers . . . . .	491
11-15. Examples of Waveguide Output . . . . .	497
11-16. End-space Geometry . . . . .	498
CHAP. 12. THE CATHODE . . . . .	503
EMISSION PHENOMENA OF MAGNETRON CATHODES . . . . .	503
12-1. Characteristics of Cathodes under Pulsed Conditions . . . . .	503
12-2. Alkaline-earth Oxide Cathodes—Test Methods . . . . .	505
12-3. Alkaline-earth Oxide Cathodes—Life Tests and Sparking Phenomena . . . . .	508
12-4. Thorium Oxide Cathodes . . . . .	515
12-5. Secondary Electron-emission Properties of Magnetron Cathodes . . . . .	517
HEAT BALANCE IN THE CATHODE . . . . .	519
12-6. Thermal Behavior of a Pulsed Cathode . . . . .	520
12-7. Measurements of Back-bombardment Power . . . . .	525
12-8. Thermal Considerations in Cathode Design . . . . .	528
ESTABLISHMENT OF AN AXIAL BOUNDARY TO THE SPACE CHARGE . . . . .	537
12-9. Cathode End Shields . . . . .	537
CHAP. 13. THE MAGNETIC CIRCUIT . . . . .	540
13-1. Design of Permanent Magnets . . . . .	540
13-2. Magnet Charging . . . . .	548
13-3. Magnetic Stabilization . . . . .	550
13-4. Field Uniformity . . . . .	552
13-5. Testing and Measurements . . . . .	553
PART IV. TUNING AND STABILIZATION	
CHAP. 14. MECHANICAL TUNING . . . . .	561
14-1. General Considerations . . . . .	561
INDUCTIVE AND CAPACITIVE TUNING . . . . .	564
14-2. Symmetric Inductive Tuning: Sprocket Tuning . . . . .	565
14-3. Symmetric Capacitive Tuning: The Cookie Cutter . . . . .	570
14-4. Other Symmetric Inductive and Capacitive Methods of Tuning . . . . .	572
14-5. Unsymmetric Inductive Tuning . . . . .	575
COUPLED-CIRCUIT TUNING . . . . .	576
14-6. General Theory . . . . .	576
14-7. Double-output Tuning . . . . .	576
14-8. Symmetric Double-output Tuning . . . . .	582
14-9. Cavity Tuning . . . . .	583
14-10. Single-stub Tuning . . . . .	589

CHAP. 15. ELECTRONIC TUNING . . . . .	592
ELECTRON-BEAM TUNING . . . . .	592
15-1. General Considerations . . . . .	592
15-2. Fundamental Equations of Beam Tuning . . . . .	594
15-3. The Principles of Electron-beam Tuning in a Magnetic Field . . . . .	599
15-4. The Engineering Equations of Electron-beam Tuning . . . . .	604
15-5. Scaling . . . . .	610
15-6. Internal vs. External Cavity Tuning . . . . .	611
MAGNETRON DIODE TUNING . . . . .	615
15-7. Fundamental Principles . . . . .	615
15-8. Small-signal Theory . . . . .	616
15-9. Experimental Data on Large-signal Conditions . . . . .	619
15-10. Other Methods . . . . .	621
CHAP. 16. STABILIZATION OF FREQUENCY . . . . .	622
16-1. Introduction . . . . .	622
16-2. The Ideal Stabilizer . . . . .	624
16-3. Coupling Methods . . . . .	626
16-4. Means of Damping the Extraneous Modes . . . . .	633
16-5. The Design of Stabilizing Circuits . . . . .	639

## PART V. PRACTICE

CHAP. 17. CONSTRUCTION . . . . .	649
17-1. Fabrication of Anode Blocks . . . . .	649
17-2. Brazing and Soldering . . . . .	662
17-3. Selected Brazing Problems . . . . .	670
17-4. Chemical Processes . . . . .	674
17-5. Metal-to-glass Seals . . . . .	676
17-6. Cathode and Heater Construction . . . . .	685
17-7. Tube Evacuation and Processing . . . . .	693
17-8. Examination of Metals . . . . .	694
CHAP. 18. MEASUREMENTS . . . . .	698
MEASUREMENTS OF THE RESONANT SYSTEM . . . . .	698
18-1. Test Equipment Components . . . . .	698
18-2. Cavity-wavelength Measurements . . . . .	702
18-3. Measurement of Standing Waves . . . . .	705
18-4. Field-pattern Measurements . . . . .	710
18-5. Measurement of $Q$ . . . . .	713
18-6. The Stabilization Factor . . . . .	723
18-7. Magnetron-mode Identification . . . . .	726
18-8. Cathode-lead Loss . . . . .	728
18-9. Tube-model Techniques . . . . .	729
OPERATING MEASUREMENTS . . . . .	730
18-10. Measuring Techniques . . . . .	732
18-11. Operating Technique . . . . .	735

CHAP. 19. TYPICAL MAGNETRONS . . . . .	739
19-1. The LCW L-band C-w Magnetron . . . . .	740
19-2. The CM16B S-band C-w Magnetron . . . . .	744
19-3. 2J38-2J39 Low-voltage S-band Magnetrons . . . . .	747
19-4. Type 2J22-2J34 10-cm Pulsed Magnetrons . . . . .	751
19-5. 4J70-4J77 High-power S-band Tunable Magnetrons . . . . .	756
19-6. The HP10V High-power S-band Magnetron . . . . .	760
19-7. The BM50 Very Low Power X-band Magnetron . . . . .	764
19-8. 2J41 Low-power Stabilized X-band Magnetron . . . . .	766
19-9. The 2J42 Low-voltage X-band Magnetron . . . . .	770
19-10. The 725A Magnetron . . . . .	774
19-11. The 2J51 Magnetron . . . . .	778
19-12. 4J50 (4J52, 4578) High-power 3-cm Magnetron . . . . .	780
19-13. The AX9 Rising-sun Magnetron . . . . .	784
19-14. The 3J31 and 3J21 Rising-sun Magnetrons . . . . .	786
19-15. 22-cavity Rising-sun Magnetron . . . . .	790
19-16. The Closed-end 38-cavity Rising-sun Magnetron . . . . .	791
19-17. The XCR High-power 2.6-cm C-w Magnetron . . . . .	795
INDEX . . . . .	797

## CHAPTER 1

### INTRODUCTION

GEORGE B. COLLINS

A magnetron is a diode, usually cylindrical, with a magnetic field parallel to its axis. In modern usage, however, the word implies a diode that, with the aid of a magnetic field, produces short electromagnetic waves, and it is with this meaning that the term is used in this volume. Those magnetrons which produce radiation within the wavelength range 1 to 30 cm are here defined as microwave magnetrons. This class of tubes is sometimes called cavity magnetrons from the fact that, in the usual design, the resonant circuit is a number of closely coupled cavities contained within the evacuated portion of the tube.

**1.1. Early Types of Magnetrons.**—Microwave magnetrons and the theory of their operation have their origin in contributions made by a great many investigators extending back at least to 1921. A review of this development will be given here with the purpose of pointing out the significant steps that have led to the present highly efficient sources of microwaves. Editorial policy precludes the assignment of credit for origination of ideas or inventions, and this question will be purposely avoided as far as possible.

*Nonoscillating Diodes with Magnetic Fields.*—The basis for much of the theory of magnetron operation was laid by Hull<sup>1</sup> who investigated the behavior of electrons in a cylindrical diode in the presence of a magnetic field parallel to its axis. Such a diode is shown in Fig. 1.1*a*. A cylindrical anode surrounds a centrally placed cathode which is heated to provide a source of electrons. A nearly uniform magnetic field parallel to the axis of the tube is produced by a solenoid or external magnet not shown in the diagram. In the crossed electric and magnetic fields which exist between the cathode and anode an electron that is emitted by the cathode moves under the influence of a force  $\mathbf{F}_e = Ee$  and a force  $\mathbf{F}_m = e/c(\vec{v} \times \vec{B})$  (see Fig. 1.2), where  $E$  is the electric field,  $B$  the magnetic field,  $c$  the velocity of light,  $v$  the velocity of the electron, and  $e$  is its charge. The solution of the resulting equations of motion, which neglect space-charge effects, shows that the path of the electron is a quasi-cycloidal orbit with a frequency given approximately by

$$f_T = \frac{eB}{mc}. \quad (1)$$

<sup>1</sup> A. W. Hull, *Phys. Rev.*, **18**, 31 (1921).

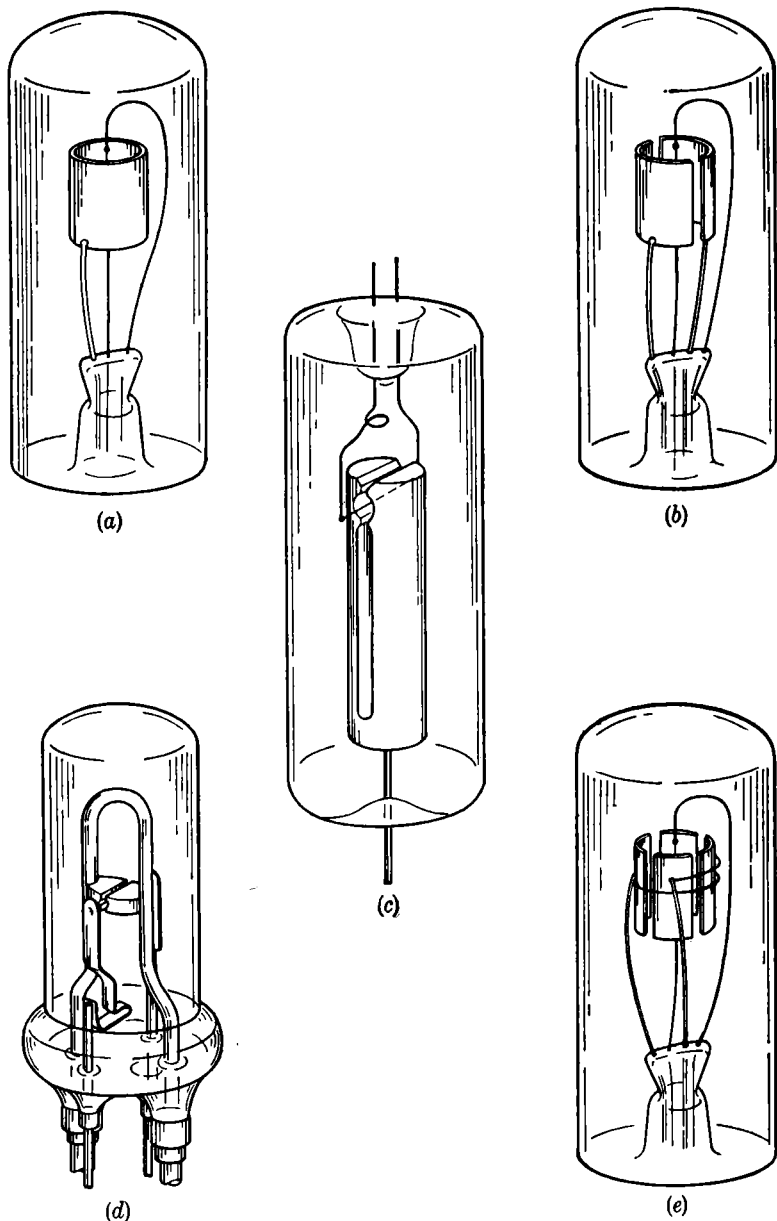


FIG. 1-1.—Early types of magnetrons: (a) Hull original diode; (b) split anode; (c) split anode with internal resonator; (d) improved split anode; (e) four-segment anode.



When this orbit touches the anode, a condition of cutoff is said to exist, and Eq. (2) holds

$$\frac{V}{B^2} = \frac{er_a^2}{8mc^2} \left[ 1 - \left( \frac{r_c}{r_a} \right)^2 \right]^2, \quad (2)$$

where  $V$  is the potential difference between the anode and the cathode and  $r_a$  and  $r_c$  are their radii. The relation is an important one from the standpoint of magnetron operation. It implies that for  $V/B^2$  less than the right side of Eq. (2), no current flows and, as  $V/B^2$  is increased through the cutoff condition, a rapid increase in current takes place. For obscure reasons the reduction of current at cutoff, which is observed experimentally, is not so abrupt as the theory outlined above would indicate.

**Cyclotron Frequency Oscillations.**—The type of diode shown in Fig. 1-1a can be made to oscillate at very high frequencies if the cathode and anode are made part of a resonant circuit with reasonably high impedance and low losses. Conditions for oscillation are that  $V/B^2$  must be adjusted close to the cutoff condition given by Eq. (2) and that the frequency of the resonant current be close to the transit frequency of the electrons. An explanation of these oscillations is given in terms of Fig. 1-3. The dashed circle represents the path of an electron in the interaction space and modifies the trajectories of such an electron. Curve (1) represents the trajectory of an electron emitted at an instant when the r-f field is in the same direction as the d-c field. Thus the effective  $V$  acting on the electron is increased, and from Eq. (2) it is seen that this increases the cutoff radius with the result that the electron strikes the anode.

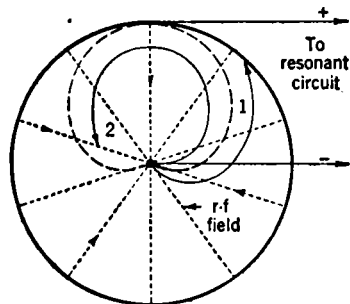


FIG. 1-3.—Trajectories of electrons: (1) phase with respect to the r-f field is unfavorable for the support of oscillations; (2) favorable.

Curve (2) is for an electron emitted one-half period later when the r-f fields are opposed to the d-c field. The electron now misses the anode and returns toward the cathode. Since the frequency of rotation as given by (1) is made close to the r-f frequency, electron (1) will return toward the cathode also retarded by the r-f field. This electron thus

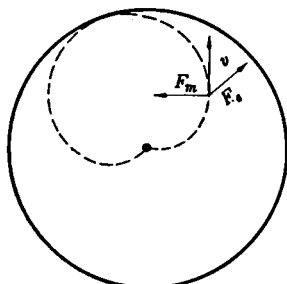


FIG. 1-2.—Forces on an electron moving in a diode with a magnetic field parallel to its axis.

contributes energy to the r-f oscillation, and the process will continue as long as the phase relationships with the r-f field persist or until the electron is removed by some process. As these phase relationships cannot be maintained indefinitely, provisions are usually made for removing the electrons before they fall out of phase. One method is to tilt the magnetic field slightly with respect to the axis of the tube. This causes the electrons to spiral out of the end of the anode before too many revolutions occur.

A characteristic of this type of magnetron, which is important to the operation of many magnetrons, is the quick removal from the r-f field of the electrons whose phase is unfavorable to the support of oscillations and the retention in the r-f field of the favorable ones.

Split-anode magnetrons such as shown in Fig. 1-1b will also oscillate when the frequency of the resonant circuit (now connected to the two segments) is close to the transit frequency of the electrons and the anode voltage adjusted close to cutoff conditions. No satisfactory analysis has been made that gives the trajectory of the electrons in this case, but it is probable that the unfavorable and favorable electrons are segregated by processes similar to that illustrated in Fig. 1-3.

No large number of cyclotron-type magnetrons have been made, but they have been used effectively as experimental sources of radio frequency.<sup>1,2,3</sup> At 50-cm wavelength output powers of 100 watts have been obtained; at 10-cm wavelength about 1 watt; and detectable radiation has been produced at 0.6 cm. The efficiency of the split-anode tubes is around 10 per cent for moderately long wavelengths as compared with 1 per cent for the diode variety.

The shortcomings of this class of magnetron are low efficiency, low power, and generally erratic behavior, but extremely high frequencies can be generated by these oscillators.

*Negative Resistance or Habann Type.*—If the magnetic field of a split-anode magnetron is greatly increased over what is required for the cyclotron-type oscillations, a new type can occur which has been called negative-resistance or Habann-type oscillations. The frequency is determined almost wholly by the resonant circuit, and the magnetic field is not critical as is the case with cyclotron oscillations. These oscillators have been investigated by Kilgore<sup>4</sup> who observed in a magnetron containing gas at low pressure, luminous paths corresponding to electron trajectories of the form shown in Fig. 1-4.

The form of the r-f field is shown, and this combined with the d-c

<sup>1</sup> A. Zarek, *Cos. Pro. Pest Math. a Frys.*, Prague, **53**, 578 (1924).

<sup>2</sup> H. Yagi, *Proc. IRE*, **16**, 715 (1928).

<sup>3</sup> C. E. Cleeton and N. H. Williams, *Phys. Rev.*, **50**, 1091 (1936).

<sup>4</sup> G. R. Kilgore, *Proc. IRE*, **24**, 1140 (1936).

field and the high magnetic field causes the electrons to spiral out to the anode segment that is at the lowest (most negative) potential. The magnetron thus has the characteristics of a negative resistance necessary to produce oscillations. It is observed that the efficiency of this type of oscillation is enhanced if the electron moves out to the anode making ten or more spirals. The frequency of the spiraling is determined by Eq. (1), and thus magnetic field strengths are needed that are ten times those required to produce the same frequency by cyclotron-type oscillations. Providing sufficiently high magnetic fields to satisfy this requirement for very high frequencies is one of the principal objections to this type of oscillation as a practical source of microwaves.

An important modification in the design of split-anode magnetrons was made when the resonant circuit was placed entirely within the vacuum system. This step was the result of efforts to increase both the frequency and power output. Figure 1-1c shows such a design. This type of tube has produced power outputs of 100 to 400 watts at 50 cm and 80 watts at 20 cm.

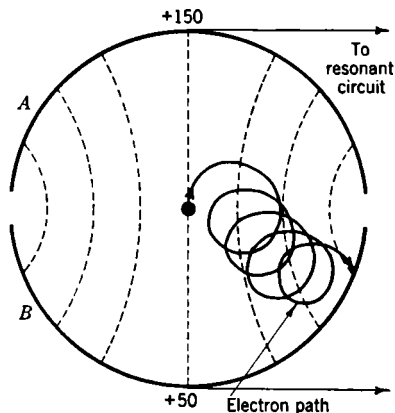


FIG. 1-4.—Trajectories of an electron in a split-anode magnetron when used as a Habann-type oscillator.

#### *Traveling-wave Oscillations.*—

This third type of oscillation also occurs in split-anode magnetrons and is related to the negative resistance type. The two differ only in the ratio of the angular frequency of the traveling wave to the cyclotron frequency. In the negative-resistance magnetron the magnetic field is so high that on the cyclotron time scale the traveling wave remains nearly stationary. There is no sharp dividing line between the two. For the same frequencies the magnetic field required is much lower than that needed to produce negative-resistance oscillations; and although the magnetic field may be close to the value necessary to produce cyclotron-type oscillation, its value is not critical and the anode potential is lower, so that oscillations occur below cutoff conditions.

Traveling-wave oscillations have also been observed<sup>1</sup> in four-segment and even eight-segment magnetrons. Figure 1-1d illustrates a four-segment magnetron and shows in particular the manner in which the alternate segments are connected together within the vacuum envelope.

<sup>1</sup> K. Posthumus, *Wireless Eng.*, **12**, 126 (1935).

A particularly important feature of this design is that for a given  $B$  and  $r_a$  the four-segment magnetron can be made to oscillate at twice the frequency of a two-segment one. Posthumus<sup>1</sup> developed a theory for oscillation of this type, which although space-charge effects are neglected, gives a reasonable explanation of the observed characteristics. This explanation can be made conveniently in terms of the four-segment tube. Figure 1-5 shows in an approximate manner the electric field distribution. These fields vary with time in a sinusoidal manner and may be considered as standing waves resulting from two sets of traveling waves rotating in opposite directions around the anode. For oscillations to occur the

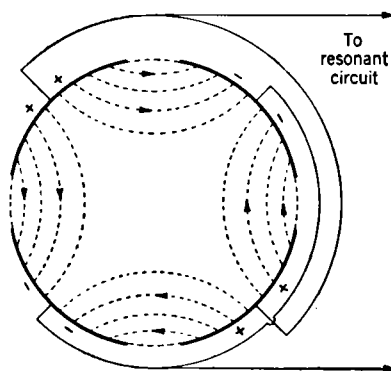


Fig. 1-5.—Electric fields in a four-segment magnetron.

angular velocity of the electrons must approximate that of one of the rotating waves so that the electrons retain for an appreciable length of time their phase relationship with the r-f field. Posthumus showed that this condition exists when

$$f = \frac{4\pi n V_a}{r_a^2 B}, \quad (3)$$

when  $f$  is the frequency,  $V_a$  and  $r_a$  the anode potential and radius,  $B$  the magnetic field, and  $n$  the number of pairs of segments.

The theory also shows that electrons which are retarded by the r-f field and thus contribute energy to it spiral outward and eventually strike the anode.

Equation (3) is consistent with the characteristics of these oscillations as observed by Posthumus. The upper-frequency limit for a given tube is inversely proportional to  $B$ , and for  $n = 2$  this limiting frequency is twice that for  $n = 1$ . The theory is also consistent with such facts, now well known, that the anode voltage is proportional to the square of  $r_a$  and that for oscillations to occur the ratio  $V/B$  must remain constant.

Of the three types of oscillations—cyclotron frequency, negative resistance, and traveling wave—the last has proved the most effective in magnetrons that are used as practical sources of microwaves. Some advantages of the traveling-wave type of oscillations are good efficiencies at high frequencies, moderate magnetic field requirements, and stability of operation over a wide range of input and output conditions.

For frequencies below 1000 Mc/sec it is convenient to have the resonant circuit external to the vacuum system, as the elements are rather bulky and because external circuits can be tuned more readily. This

<sup>1</sup> *Ibid.*

circumstance has led to the development of split-anode magnetrons in the 100 to 1000 Mc/sec region that has culminated in the design shown in Fig. 1-1d. An important feature of these tubes is the large-diameter conductors connecting the two sections of the anode to the external circuit. This reduces losses in the resonant circuit and increases the anode dissipation. Power outputs of 150 watts at frequencies between 15 and 1200 Mc/sec can be obtained reliably from this tube and similar ones.<sup>1</sup>

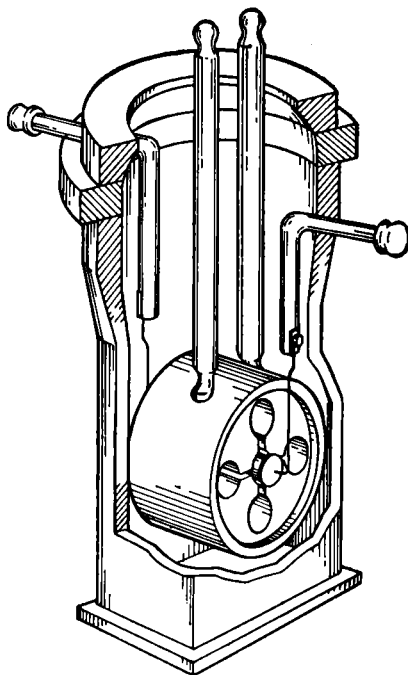


FIG. 1-6.—Early form of internal resonator magnetron.

In a search for magnetron sources of higher frequencies and higher powers certain modifications are suggested by the performance of the designs shown in Fig. 1-1. In particular the combination of the internal resonant circuit Fig. 1-1c with the multisegment feature of Fig. 1-1e seems desirable, as the internal resonant circuit is capable of handling high powers at high frequencies and the multisegment structure reduces the anode voltage and magnetic field. Figure 1-6 shows an arrangement of internal circuits that was investigated by Aleksereff and Malearoff.<sup>2</sup>

<sup>1</sup> This line of magnetron was developed by the General Electric Co.

<sup>2</sup> N. T. Aleksereff and D. E. Malearoff, *Jour. Tech. Phys. USSR*, **10**, 1297 (1940). Republished *Proc. IRE*, **32**, 136 (1944).

Similar arrangements have been suggested by many others.<sup>1,2,3</sup> Here the resonator system is made up of a number of internal resonators arranged around the axis of the cathode so that the capacitive portion of each resonator opens out into the cathode-anode space. The magnetron shown in Fig. 1-6 was tried with anode blocks having up to eight resonators and with various anode sizes. Powers of a few hundred watts at 9-cm wavelength are reported with efficiencies as high as 20 per cent, and a few watts were produced at 2.5-cm at very low efficiency. The power output was limited by overheating of the cathode which

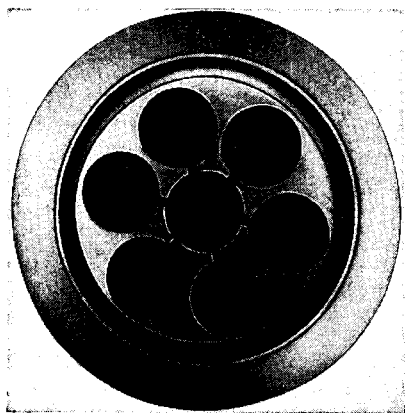


FIG. 1-7.—Anode block of first British 10-cm magnetron.

presumably resulted from back bombardment by electrons that received energy from the r-f field.

**1-2. The British Cavity Magnetron.**—The wartime need of radar for a transmitting tube capable of very high pulsed-power outputs at wavelengths of 10 cm or less led British investigators<sup>4</sup> to attempt late in 1939 the development of a magnetron with these characteristics. They invented and perfected a traveling-wave type magnetron with internal resonators that when pulsed produced microwave radiation with peak powers several orders of mag-

nitude greater than had been obtained before by any means. The fact that this magnetron was operated under pulsed input conditions is particularly significant. Duty ratios [(pulse duration)/(interval between pulses) + (pulse duration)] of about 0.001 were used so that heating of the cathode and anode was greatly reduced over that for c-w operation. Specifically, with a duty ratio of 0.001, pulse powers one thousand times the maximum c-w inputs are possible without producing overheating. After a comparatively short period of development 10-cm magnetrons were made that operated efficiently with peak power inputs of several hundred kilowatts and outputs in excess of 100 kw. Figure 1-7 shows the

<sup>1</sup> A. L. Samuel, U.S. Patent 2063341, 1936.

<sup>2</sup> British Patent 509104, Oct. 7, 1938.

<sup>3</sup> Reichspatent 663259, Aug. 3, 1938.

<sup>4</sup> Professor J. T. Randal and Dr. H. A. H. Boot, University of Birmingham, Birmingham, England. The work of these investigators was greatly aided as a result of cooperation with The General Electric Company, Ltd., Wembley, England, which made many contributions essential to the success of the production version of these early magnetrons.

first anode constructed by these investigators, and Fig. 1-8 the first experimental magnetron. This tube had an output of 400 watts c-w at a wavelength of 9.8 cm. Figure 1-9 shows the construction of this magnetron as it was produced for use in microwave radars.

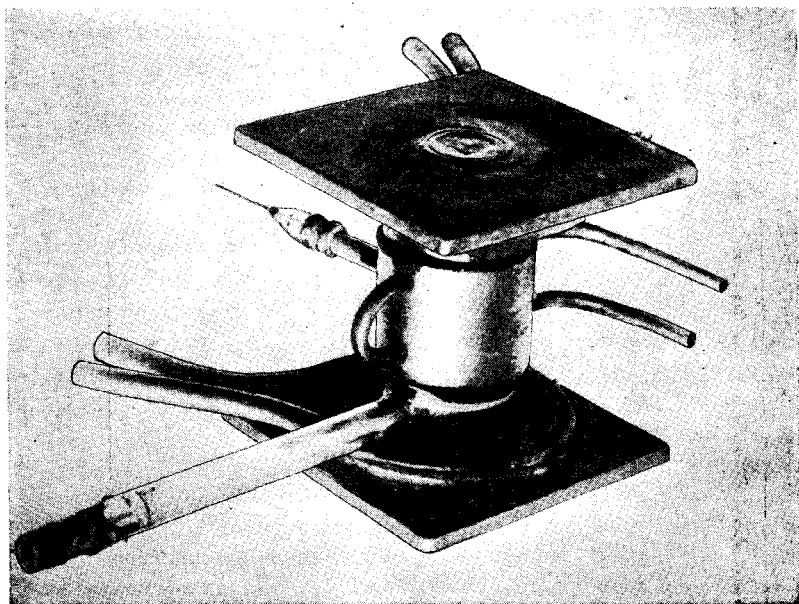


FIG. 1-8.—First British 10-cm magnetron.

The effectiveness of this magnetron is due especially to three important features of design:

1. A large-diameter oxide-coated cathode was used. The large diameter contributes appreciably to stable operation and provides a large emitting area. Under pulsed conditions the oxide coating was found to provide peak emission currents of 10 to 20 amp/cm<sup>2</sup>. This surprising performance of oxide coatings—the pulse emission is ten times the d-c value—is largely responsible for the magnetron's ability to accept high pulse-power inputs. Instabilities such as sparking might have been expected, as the magnetron operated with a plate

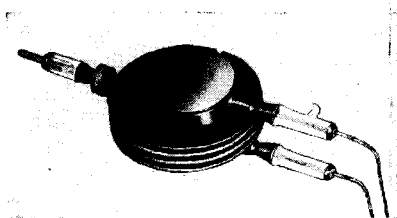


FIG. 1-9.—Production version of British 10-cm magnetron.

voltage of 10 kv, a figure considerably above the value considered safe for the use of oxide cathodes under normal conditions. Fortunately under pulsed conditions little trouble was experienced.

2. The anode block is part of the vacuum envelope. All the magnetrons shown in Figs. 1.1 and 1.6 have anode blocks suspended inside vacuum, and large anode dissipation is difficult to obtain; with the anode block a part of the vacuum envelope, a low-impedance thermal path from interior to exterior exists, and heat dissipation of several hundred watts of average power can be accomplished with air cooling alone.
3. The separate resonators are coupled by conducting elements or straps.<sup>1</sup> Without these the magnetron's several resonant frequencies are so close together that unstable operation results. With straps the efficiency is raised and stable operation may be obtained over a wide range of powers.

Other features and certain optimum dimensions, which in all contribute significantly to the operation of this magnetron, were incorporated as a result of experiment. Good examples of such features are the output construction and the critical cathode diameter and coupling loop size.

This early work also contributed greatly to the understanding of magnetron operation. The role of the electrons that return to the cathode in producing secondaries from the cathode was appreciated, and, in fact, magnetrons with secondary emitting cathodes and no primary emission were operated by Boot and Randall. In addition, a very useful technique for investigating the resonant modes of magnetrons by the use of signal generators (Chap. 18) was developed.

In spite of the spectacular performance of this early pulsed microwave magnetron its characteristics were not entirely satisfactory. Its performance was erratic, with regard both to the operation of individual tubes under varying conditions and to the operation of different but presumably identical tubes under the same conditions. In addition, any modification of the original design almost invariably resulted in unsatisfactory performance. For example, attempts at designing tubes to operate at wavelengths shorter than 10 cm or at lower anode voltages were not at first successful. The cause of most of these difficulties was the lack of a complete understanding of the principles of operation of the magnetron.

**1.3. Description of a Microwave Magnetron.**—The class of magnetron with which this book is concerned is distinguished by a resonant system

<sup>1</sup> The addition of straps to the resonant system of the magnetron was made by J. Sayers, of Birmingham University, about a year after the original magnetron was perfected.



within the tube envelope; this system is composed of a number of coupled resonators surrounding a relatively large cylindrical cathode. An example that will be used as a basis for discussion is shown in Figs. 1-10 and 1-11.

These magnetrons are self-excited oscillators, the purpose of which is to convert the d-c input power into r-f output power. This conversion takes place in the *interaction space I* which is between the cylindrical *cathode C* and the *anode block A*. A constant and nearly uniform magnetic field is maintained in this interaction space in a direction parallel to the axis of the tube. In operation, the cathode is maintained at a negative potential, while the anode block is usually at ground potential. The

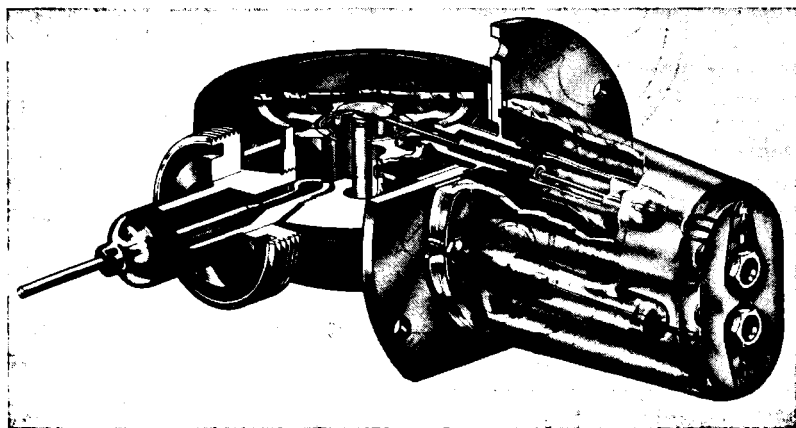


FIG. 1-10.—Cutaway of typical microwave magnetron showing construction.

anode block is pierced in a direction parallel to the axis by a number of *resonators R* which open into the interaction space so that the anode surface consists of alternate segments and gaps. The ends of the resonating cavities open into chambers that are called “end spaces” through which the lines of flux extending from one resonator to the next pass. The coupling between the resonators is increased by conducting bars called *straps S* which connect alternate segments. Power is extracted from one resonator, one method being a *coupling loop L* which forms a part of the *output circuit*. The combination of resonant cavities, end spaces, straps, and output circuit is called the *resonant system*.

In this design, the cathode *C* is oxide-coated and heated indirectly by an internal heating coil of tungsten or molybdenum. It is attached mechanically to two cathode stems supported by glass to provide anode-to-cathode insulation. Coaxial line chokes *K* are frequently placed on these stems to prevent the escape of any stray radiation that may be

picked up by the cathode structure. At each end of the cathode there is an *end shield* *H* whose purpose is to prevent electrons from leaving the cathode structure in a direction parallel to the axis of the magnetron. These end shields must be kept at a temperature too low to cause the emission of electrons.

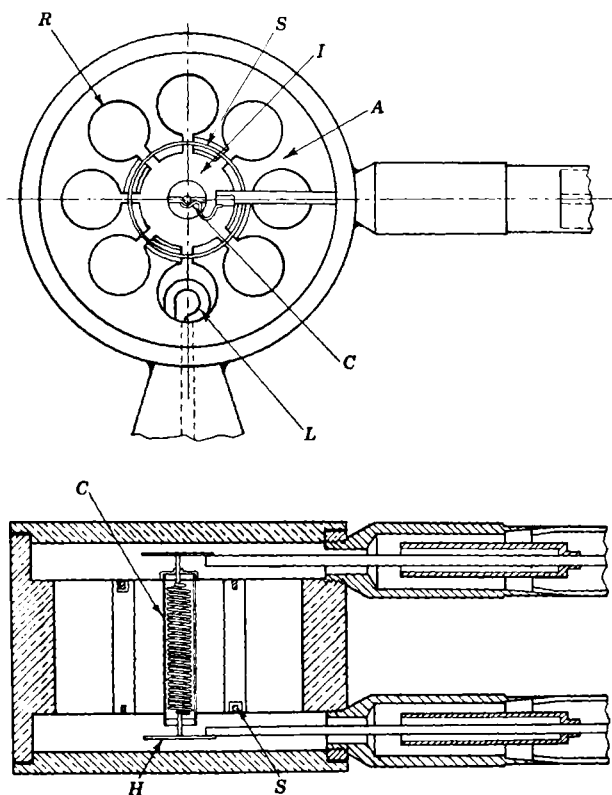


FIG. 1-11.—Cross-sectional views of typical magnetron shown in Fig. 1-10.

The radial dimensions of the interaction space depend upon the wavelength and voltage at which the magnetron is to operate and for any given type are proportional to the wavelength and to the square root of the anode voltage. For efficient operation, the ratio of cathode diameter to anode diameter must remain within narrow limits set by the number of resonators. In a 12-resonator magnetron, this ratio is about  $\frac{1}{2}$  the anode; for fewer oscillators, it is somewhat smaller, and for more than 12 oscillators, somewhat larger.

A magnetic field parallel to the axis of the cathode is required; it is

often produced by an electromagnet or permanent magnet with pole faces external to the magnetron. Figure 1.12a shows a typical permanent magnet and magnetron with radial cathode supports. Another type of magnetron construction, favored for the higher-frequency magnetrons where magnet weight is of importance, is shown in Fig. 1.12b. This magnetron-magnet combination is frequently called a "packaged magnetron." The cathode is usually supported axially through iron

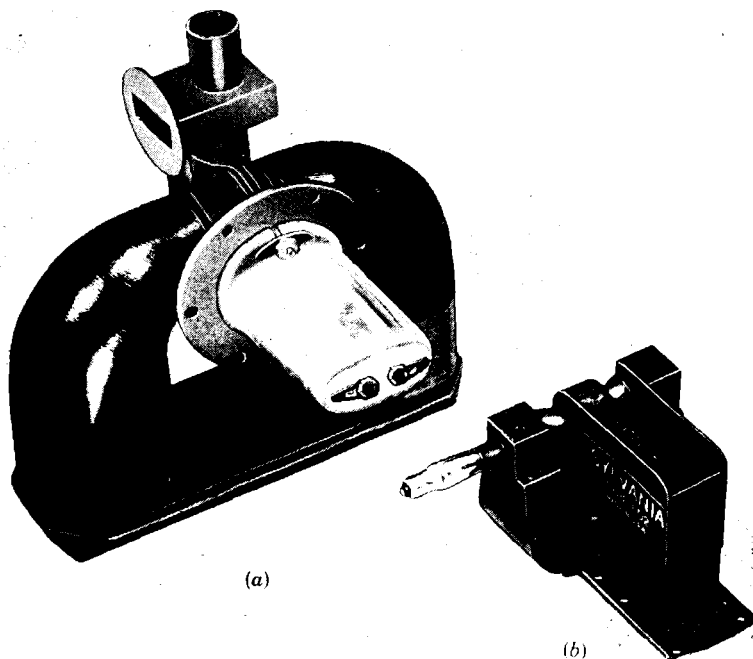


Fig. 1.12.—Two types of magnetron construction: (a) radial cathode supports with separate magnet; (b) axial cathode support with attached magnet.

pole pieces which extend quite close to the anode and thus reduce the magnetic field gap. Since the weight of a magnet that will produce a given magnetic field strength over a given iron-sectional area increases very rapidly with the length of the gap, considerable magnet weight can be saved in this manner. It is customary to supply this type of magnetron permanently attached to its magnet. The saving of size and weight resulting from this axial construction may be considerable.

**1.4. The Resonant System.**—The combination of the anode block, output circuit, end spaces, and other parts that contribute to the r-f

properties of the tube is defined as the resonant system. It is a most important part of the magnetron, for it determines the frequency and also plays a most important role in the electronic processes. This integration of the entire oscillating system into one tube complicates the problems of design and limits the versatility of single magnetrons as compared with low-frequency oscillators where the oscillator tube is distinct from the associated resonant circuits.

The function of the resonant system is to present to the space charge an r-f field of the desired frequency and with the proper configuration and magnitude to effect an efficient generation of radio frequency and further to transmit this power to an external load. The resonant system accomplishes this by storing a quantity of the energy to produce the r-f fields, at the same time releasing a portion to the external load.

A specific example will serve to fix the order of magnitude of the quantities involved in this process. For a pulse-power input of 100 kw, the 2J32 (see Fig. 1-11) delivers about 40 kw to its load, or about  $1.3 \times 10^{-5}$  joule per cycle, as the frequency is 3000 Mc/sec. Under these conditions, about  $10^{-2}$  joule is stored in the resonant system, and this energy results in an r-f voltage at the anode surface of about 10 kv. About 55 per cent (or 45 kw) of the input power is lost because of heating of the anode by the electrons, and 5 per cent (5 kw) is lost because of heating of the anode by the circulating r-f currents.

A good resonant system should have characteristics that make the operation of the magnetron as stable as possible. This includes stability against small changes in frequency and stability against discrete frequency jumps and constitutes one of the major problems of magnetron design.

The entire resonant system presents a problem too complicated for qualitative analysis, and it is usually assumed that only the anode block and output circuit affect the operation of the magnetron. Although this assumption is not always justified, as other parts of the magnetron may, indeed, affect its operation, it has usually been possible to isolate their effects and consider them as special problems. The discussion here of the resonant system as well as the more detailed treatments in Chaps. 2, 3, and 4 follow this procedure.

The so-called hole-and-slot anode block, shown in Fig. (1-10 and Fig. 1-11), will be used as a specific magnetron about which the following discussion will be centered. When operating in the desired manner, oscillations result in a disposition of charge and electric field, as is illustrated in Fig. 1-13. Figure 1-13a illustrates such a disposition at an instant when the concentration of charge on the ends of the anode segments is at maximum. One-quarter of a period later the electric field and charges have disappeared and currents are flowing around the inside

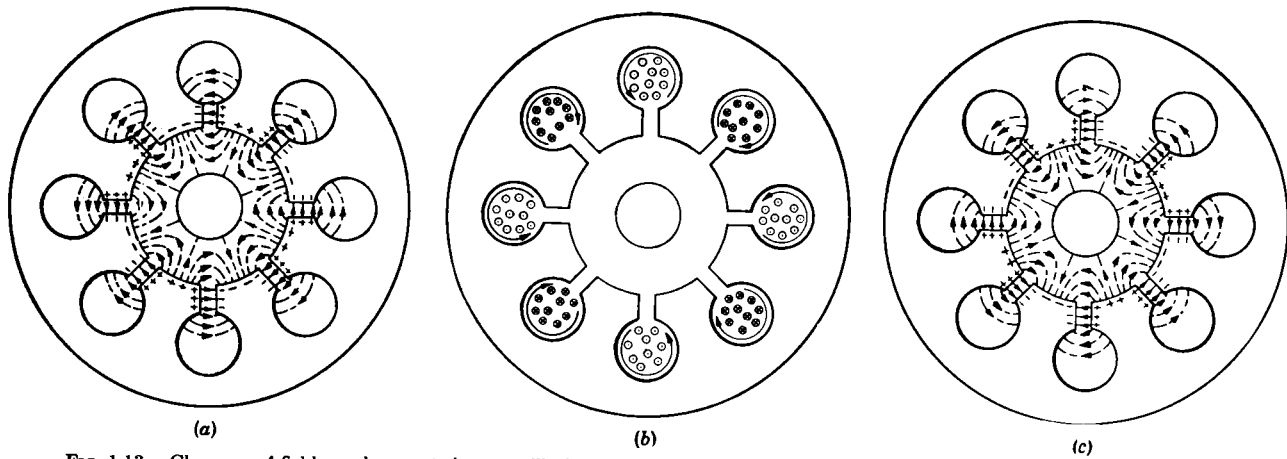


FIG. 1.13.—Charges, r-f fields, and currents in an oscillating magnetron. The phase of (a), (b), and (c) differs progressively by  $\pi/2$ .

of the cavities, producing a magnetic field along the hole portion of the cavities. Figure 1-13*b* depicts the currents and fields at this instant; Fig. 1-13*c* shows the disposition of charges and electric fields another quarter period later.

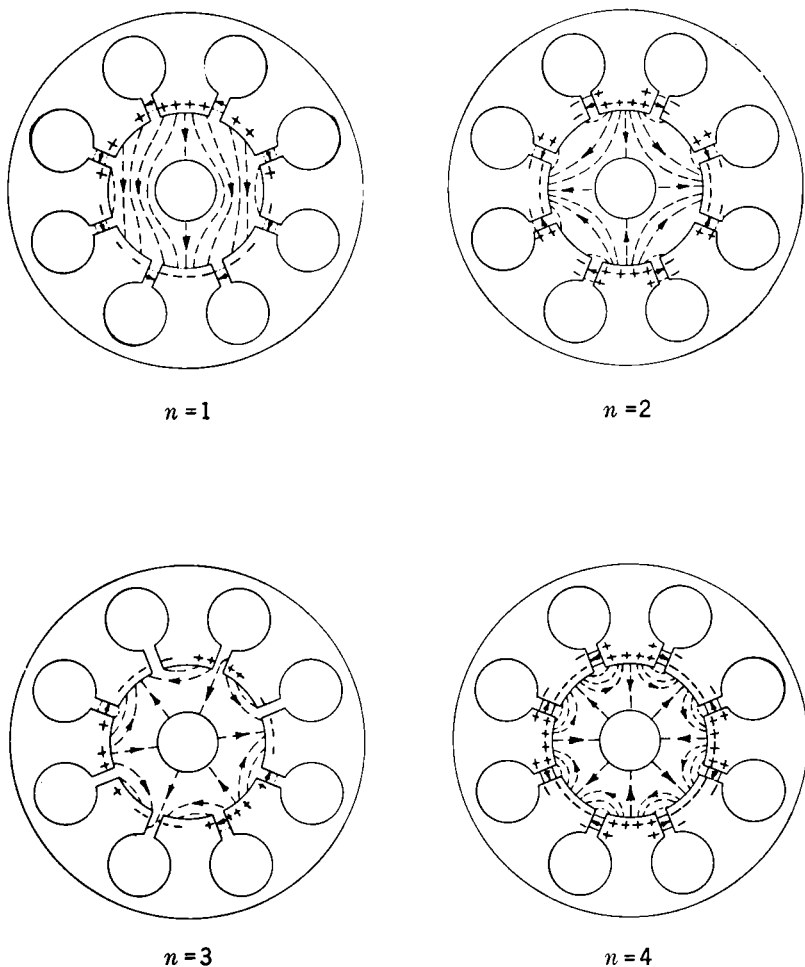


FIG. 1-14.—Field and charge distributions for the four principal modes of an eight-oscillator magnetron.

Oscillations of this character are called  $\pi$ -mode oscillations from the fact that the phase difference between adjacent resonators is  $\pi$ . Other modes are possible, however, and each is characterized by varying phase differences among the eight coupled resonators that comprise this

particular resonant system. The number of possible modes is reduced by the fact that the resonator system is a closed one and the total phase shift around the resonator system must be a multiple  $n$  of  $2\pi$ , where  $n$  is called the mode number. For an eight-resonator magnetron, the important modes are  $n = 1, 2, 3, 4$ . In general  $n = 1, 2, 3, \dots, N/2$  where  $N$  is the number of resonators. The phase differences between the resonators in the example chosen for  $n = 1, 2, 3, 4$  are  $\pi/4, \pi/2, 3\pi/4$ , and  $\pi$ . The charge and electric field distribution for these modes is illustrated in Fig. 1-14. In principle, one would also expect modes corresponding to  $n > N/2$  in which the phase difference between resonators is some multiple of  $\pi$  corresponding to harmonics of the individual resonators. These modes apparently are unimportant to the operation of magnetrons and have only rarely been observed. Figure 3-7c shows the charge distribution for this harmonic type of oscillation.

A more serious complication arises from the twofold degeneracy of some of the  $N/2$ -modes discussed above. The amplitudes of oscillation of the separate resonator segments may be considered as points on a closed standing-wave pattern containing a number of wavelengths equal to the mode number. The degenerate forms of each mode correspond to a rotation of this standing wave so that the positions of the nodes and antinodes are interchanged. Figure 1-15 shows views of a magnetron in a plane parallel to the cathode and at the same time opened out so that the anode faces lie in a plane. The closed lines surrounding the segments represent the magnetic flux, and the numbers on the faces of the segments indicate the maximum charge. The smoothed-out distribution of charge around the anode is shown below each. Eight such views are shown representing the four principal resonances or modes, each with their two degenerate forms. One of the degenerate forms of the ( $n = 4$ )-mode corresponds to a condition of zero charge on every segment and thus does not exist. This nondegenerate characteristic of the ( $n = N/2$ )-mode is an important feature of  $\pi$ -mode operation.

If all the resonators are identical, the frequencies of these degenerate modes are identical. In actual magnetrons, asymmetries usually exist and the degenerate forms have slightly different frequencies. As a general rule, then, it may be stated that the number of modes encountered is equal to  $N - 1$ . The question of the frequencies of these ( $N - 1$ )-modes can best be discussed by considering first an unstrapped anode block such as is shown in Fig. 1-13.

Each of these resonant cavities is similar to a simple oscillating circuit consisting of a lumped  $L$  and  $C$ . Although the inductance and capacitance of a magnetron cavity is not strictly lumped, the inductance of the oscillator resides mainly in the circular hole, and the capacitance mainly between the parallel plane surfaces of the slot. Since the fre-

quency is a function of the product  $LC$ , it is possible to represent one resonant cavity by a conventional parallel resonant circuit whose frequency is given by  $f = (1/2\pi)(1/\sqrt{LC})$ . Considering the frequency of

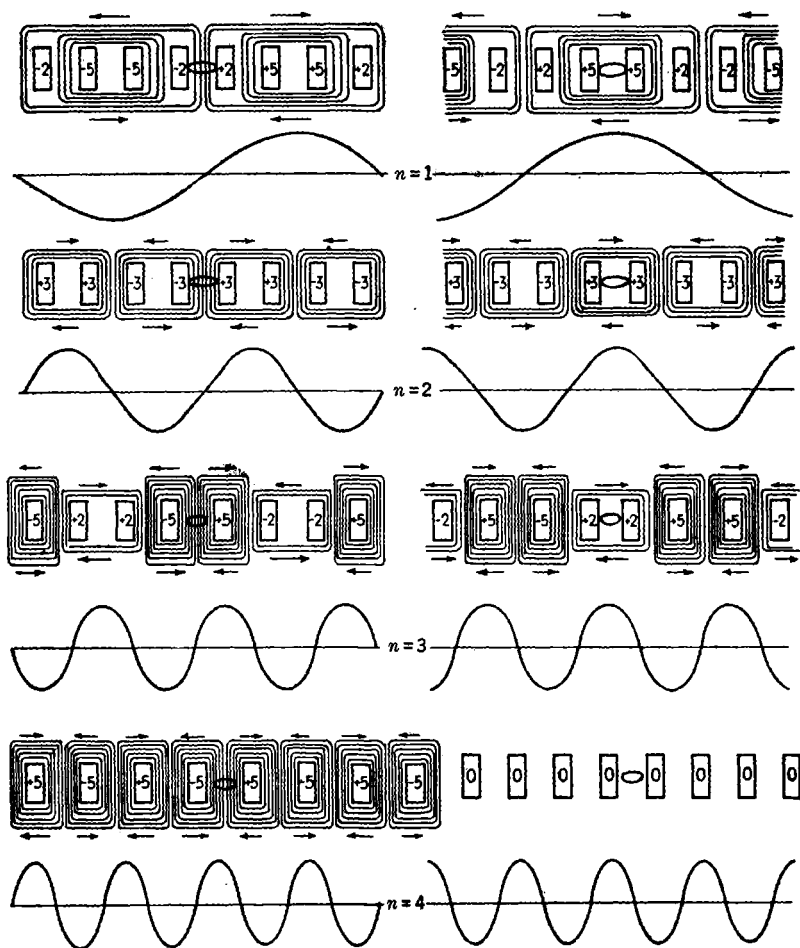


FIG. 1-15.—View from the cathode of an opened-out magnetron showing the magnetic fields and charge distribution for the four principal modes each with its two degenerate forms.

the resonant system as a whole, it should be noted that the arrangement of these cavities is such that for the desired or  $\pi$ -mode of operation, their individual  $C$ 's and  $L$ 's are all connected in parallel. Thus the effective capacitance for the whole magnetron oscillator is  $NC$  and the



effective inductance is  $L/N$ , where  $N$  is the number of resonators. The frequency of the magnetron is thus nearly that of an individual resonator.

The frequencies of the various modes will, in general, differ. This may be seen by referring to Fig. 1·14 and observing that the distribution of charge for the various modes is not the same and thus the effective capacitance for the various modes will be different. The same could be said with regard to the currents and effective inductances, so that different frequencies are to be expected. Unfortunately, the difference in frequencies of the modes, or mode separation as it is called, is not so great as is desirable. A separation of 5 to 20 per cent between the desired mode and the nearest one to it is needed.

Figure 1·16 shows the effect of strapping on the wavelengths of the modes of an eight-oscillator 10-cm magnetron. Wavelengths for an unstrapped tube are shown, and it is seen that the  $\pi$  or ( $n = 4$ )-mode has a separation of less than 2 per cent from the ( $n = 3$ )-mode. The frequencies of these modes depend upon the height of the end spaces, but for practical structures they are always quite close together. As a further complication,

each of these modes, except the  $\pi$ -mode, is a close doublet. Chapter 2 deals with the problem of the unstrapped resonant system in detail.

The effect of adding straps to an unstrapped resonant system is to increase the separation of the  $\pi$ - or ( $n = N/2$ )-mode from its nearest neighbor, usually the ( $N/2 - 1$ )-mode. In Fig. 1·16, the mode spectrum of a single-ringed strapped magnetron is shown. The  $\pi$ -mode separation is now seen to be over 10 per cent. Even greater mode separation is possible if larger or more straps are introduced. Several forms of strapping are shown in Fig. 4·1.

The explanation of the effect of strapping can be made in several ways. The simplest is to conceive of the strap as maintaining  $\pi$ -mode oscillations by tying together points that for this type of oscillation remain at the same potential. A more sophisticated explanation arises from a consideration of the effective capacitance and inductance of the straps for the various modes. For  $\pi$ -mode operation the concentration of charge on the strap is a maximum and the effective capacitance of the strap is relatively large. For any other mode the potential difference between adjacent segments will be less, resulting in less charge on the strap and thus decreasing the effective capacitance that it contributes to

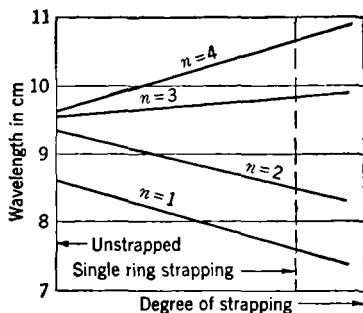


FIG. 1·16.—Effect of strapping on the mode separation of an eight-oscillator magnetron.

the resonant system. Also, for other modes, currents will flow along the entire strap, decreasing the effective inductance of the resonant cavity. Thus the straps present both a reduced capacitance and a reduced inductance for all non- $\pi$ -modes, and the frequency of these modes is increased with respect to the  $\pi$ -mode. A detailed quantitative analysis of strapped resonant systems is given in Chap. 4. Certain types of magnetrons, particularly low-frequency and low-power ones, have a good mode separation even without straps. In these cases strapping does not improve their performance, but in general the increase in stability and efficiency resulting from strapping is so great that straps are considered essential. The addi-

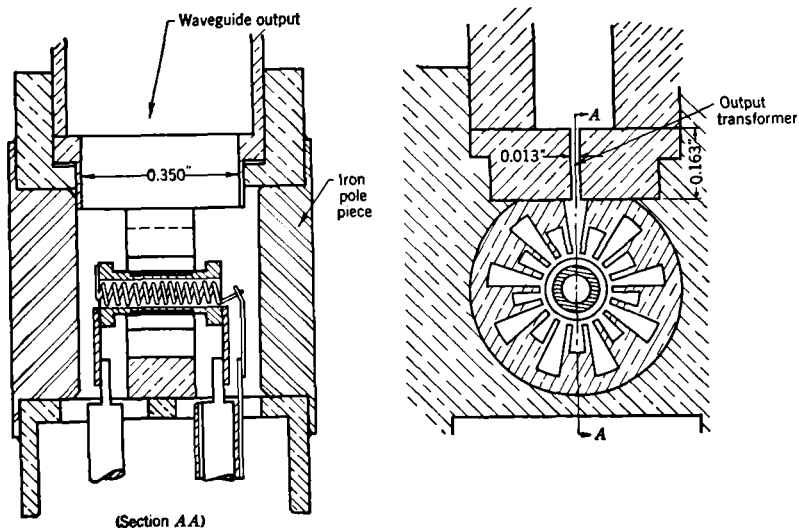


FIG. 1-17.—Cross-sectional views of rising-sun magnetron.

tion of straps to the original British magnetron resulted in a major improvement in performance. A great deal of the erratic changing of the mode of oscillation characteristic of the unstrapped tube was eliminated; the efficiency was improved; and operation at higher-power levels was possible. For example, the early British unstrapped magnetrons operated very unstably, had efficiencies ranging from 15 per cent to 40 per cent, and were prone to erratic mode shifting, while the strapped variety showed efficiencies consistently above 35 per cent and, over a considerable range of input conditions, rarely shifted modes.

At high frequencies (above 10,000 Mc/sec), straps become quite small and mechanically difficult to incorporate into the magnetrons. In addition, their small spacing results in large copper losses and thus lower magnetron efficiencies. Adequate mode separation in these high-

frequency tubes is still essential. The rising-sun magnetron is a most successful anode-block design for producing good mode separation at high frequencies that does not possess the disadvantages of strapping. Examples of this design are shown in Fig. 1-17. The essential features of the rising-sun design are the alternately large and small resonators. When oscillating in the desired mode the charge on the segment ends is alternating plus and minus, as shown in Fig. 3-7a, and the frequency is intermediate between that of a large and a small resonant cavity. The r-f voltage across the large cavities is larger than that across the small cavities, and as a result the r-f fields extending into the interaction space from the segments are not uniform, as shown in Fig. 1-13, but alternate between some large and small values. Fortunately this interaction-space field appears to be nearly as efficient as a uniform one. The peculiar mode spectrum of a typical rising-sun anode block is shown in Fig. 1-18. As an example an 18-resonator magnetron is chosen because one of the main advantages of the rising-sun design is its effectiveness when a large number of cavities is needed.

The difference between the mode spectrum of a strapped resonant system and a rising-sun system is conspicuous. The desirable operating mode in both cases is the  $N/2$ - or  $\pi$ -mode, but in the strapped system the  $\pi$ -mode is the longest wavelength, while in the rising-sun system the  $\pi$ -mode lies between groups of modes at a longer and shorter wavelength. Optimum separation between the  $\pi$ -mode and the long and short wavelength neighbors, which in general should not be the maximum possible, is obtained by adjusting the ratio of the frequencies of the large and small cavities or by other means such as closing off the ends of the anode block (Fig. 11-12).

The explanation of this mode spectrum is given in Chap. 3 in terms of an equivalent circuit and also by field theory methods. This mode spectrum can be visualized by considering the rising-sun anode block as consisting of two resonant systems, one comprising the small cavities and the other the large cavities. Each of these systems by itself would have the type of mode spectrum of an unstrapped anode block with  $N/2$  resonators. Some coupling exists, however, between the corresponding modes of these two systems, and the resulting frequencies differ from those of the isolated systems by an amount that depends on the degree of coupling. In Fig. 1-18 the modes numbered 1 to 4 correspond to the first four modes of the nine large resonators, and the modes numbered 8 to 5 correspond to the first four modes of the nine large resonators.

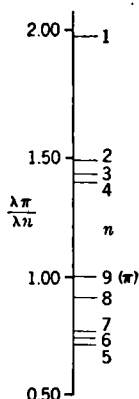


FIG. 1-18.—Wavelength distribution of the nine principal modes of an 18-oscillator rising-sun magnetron having a ratio of cavity depth  $\tau_1 = 1.9$ .

Weak coupling exists between 8 and 1, 2 and 7, etc., and their frequencies are thus only slightly altered. The coupling between the  $\pi$ -modes of the two systems is strong, however, and they combine to produce the operating or ( $n = 9$ )-mode intermediate between the two sets of modes and an ( $n = 0$ )-mode whose frequency is zero.

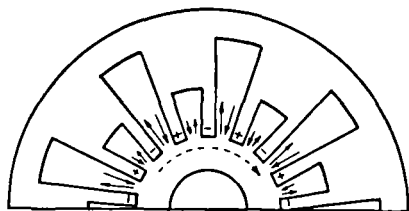


FIG. 1-19.—Currents in oscillators of rising-sun magnetron showing origin of circulating current.

The r-f currents in the large cavities exceed those in the small ones as is shown by the length of the arrows in each cavity; as the large cavity currents are always in the same direction around the anode, a net circulating current results. The direction of this at the moment chosen is shown by a dotted arrow.

This circulating current can reduce the efficiency of the magnetron if the magnetic field is such that the cyclotron frequency of the electrons, as given by Eq. (1), is close to that of the magnetron.

Finally mention should be made here of some of the various forms of resonant systems that have been investigated. By far the most usual and successful type is that exemplified by the original British design (see Fig. 1-11), and the related rising-sun design. Another type that has been the subject of considerable experimentation but is not generally used is shown in Fig. 1-20. The essential distinction between this and the more usual cavity type is that r-f currents flow axially along the segments instead of the predominantly radial currents of the conventional cavity type. Many variations of this basic design have been tried, but none has been found to possess any advantage over the cavity type.

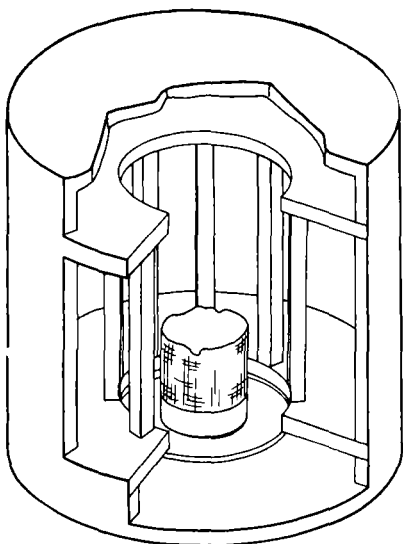


FIG. 1-20.—Magnetron anode block having large axial r-f currents.

Other forms of resonant systems have been investigated, but in most cases they were found unsatisfactory. Examples of such attempts are a linear resonator system and the so-called "inside out" magnetron in which the cathode surrounds the anode block. In both these designs, oscillations in the desired mode were not observed. The performance of all these various types of resonant systems has been poor in comparison with the cavity type. That this is due to some basic reason seems unlikely; it is more likely a consequence of the fact that the designs have not received the attention given to the cavity type. In any event, no further mention will be made of them.

**1.5. The Cathode.**—The cathode plays a much more important role in the operation of magnetrons than does the cathode of any other form of tube. In addition to being a source of electrons, a magnetron cathode must dissipate the relatively large amount of heat resulting from back-bombarding electrons. By means of so-called "end shields" it must prevent the axial escape of electrons from the interaction space, and these end shields should not emit electrons. The cathode is also part of the resonant system, as r-f currents are induced on its surface.

As a result of back bombardment, wide changes in the cathode temperature occur between starting and operations conditions which complicate the problem of emission. In pulsed tubes not only do these changes in temperature occur, but extremely high peak currents are extracted from the cathode. Current densities of from 10 to 100 amp per  $\text{cm}^2$  are obtained from oxide cathodes, depending on the pulse length and other conditions.

The size of the cathode must be held within close limits so that electrons are released to the space charge at a point where the r-f field conditions are proper for the efficient functioning of the space charge. Too small a radius results in mode instabilities; too large a radius results in inefficient operation. The optimum size in most cases is such that  $r_c/r_a$  equals or slightly exceeds  $(N - 4)/(N + 4)$ , where  $r_c$  and  $r_a$  are the cathode and anode radii and  $N$  is the number of resonators. The end shields may be small if they are located within the anode block and must increase in size as the distance above the anode is increased. No definite specifications are possible, as the curvature of the magnetic field at the ends of the anode also contributes to preventing the escape of the electrons.

It is not surprising in view of these manifold requirements that the cathode constitutes a major source of trouble and in nearly all cases is the single element that determines the life of the magnetron.

Oxide cathodes in one form or another have been used in nearly all pulsed and many c-w magnetrons. They are used in pulsed magnetrons because of their ability to emit very large currents under pulsed operation.

They are used in low-power c-w magnetrons because oxide cathodes are more efficient emitters and do not involve large heater currents that interact with the fixed magnetic field. The usual emission troubles are encountered, particularly in very high or very low power magnetrons where the back-bombarding electrons are not in the energy range for efficient production of secondary electrons.

In pulsed magnetrons sparking (the generation of bursts of gas) is a serious problem. The cathode is probably not wholly responsible for this phenomenon, but local vaporization of the oxide coating is observed, accompanied by the ejection of small pieces of the coating. The cathode is thus presumed to be a major source of trouble. The frequency and severity of the sparking is increased at high voltages and high-current densities, but extremely low current densities must be used to reduce the sparking rate essentially to zero. The emission and sparking of oxide cathodes is considered in detail in Part I of Chap. 12, together with an account of some preliminary investigations on thoriated cathodes. Part II of Chap. 12 deals with the problems of cathode design.

**1-6. The Space Charge.**—An electron in the interaction space of a magnetron is acted on by a constant magnetic field parallel to the axis of the cathode, a constant radial electric field resulting from the applied d-c potential, and the varying electric field extending into the interaction space from charges concentrated near the ends of the anode-block segments. Under these conditions the electron is part of a space charge with extreme variations in density, and the resulting problem is one of considerable complexity which is understood only in a qualitative way. No analytical expressions relating such quantities as current, d-c voltage, r-f voltage, and magnetic field have been obtained. The qualitative theory is presented here in outline. A more comprehensive review of the whole problem of magnetron electronics is found in Chap. 6.

Consider the simple case of a single electron in the interaction space of a magnetron in the absence of any perturbing r-f fields. In crossed magnetic and electric fields, there is a force  $-e\mathbf{E}$  due to the electric field and another,  $(e/c)\mathbf{v} \times \mathbf{B}$ , due to the magnetic field, where  $\mathbf{E}$  and  $\mathbf{B}$  are the electric and magnetic field strengths,  $e$  and  $v$  are the charge and velocity of the electron, and  $c$  is the velocity of light. The resulting motion shown in Fig. 1-21 is approximately represented by superposing a slow rotation around the cathode at nearly constant radius  $R_0$  (the  $R_0$  rotation) and a faster circular motion with a smaller radius  $r_0$  (the  $r_0$  rotation). The resultant of these two motions corresponds roughly to the motion of a point on the circumference of a wheel as it rolls around a circle somewhat smaller than the cathode in such a way that its center moves in a circle of radius  $R_0$ . The speed of the slow  $R_0$  rotation is given

approximately by the ratio  $E/B$ . The fast  $r_0$  rotation corresponds to the cyclotron frequency and is thus determined by  $B$  alone; its angular velocity is  $\omega_0 = eB/m$ . Although the angular velocity of this  $r_0$  rotation is constant, the magnitude of  $r_0$  depends on the initial kinetic energy of the electron and may vary for different electrons. The maximum distance that any electron can proceed toward the anode ( $R_0 + r_0$ ) in the absence of r-f oscillations is fixed by the ratio  $E/B$  and for good operating conditions is made to be about half of the way from cathode to anode.

This description of the path of a single electron is exact only for the case of small  $r_0$  and has little significance when normal space-charge conditions exist. It is given, as it assists in understanding the interaction of the electrons with the alternating electric fields.

In an oscillating magnetron, these electrons pass through the r-f fields, shown in Fig. 1-13, and a change in their velocity results. A somewhat surprising fact is that those electrons which are speeded up have their curvature increased and return to the cathode while those which are slowed down have their curvature reduced and move out toward the anode.

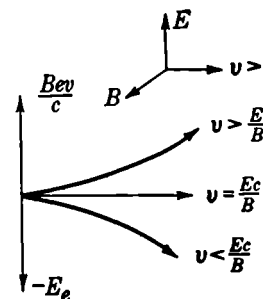


FIG. 1-22.—Paths of electrons in crossed electric and magnetic fields.

where  $R$  is the radius of the orbit of the electrons ( $R$  is positive for orbits curving down).

Where the path of the electrons is a straight line, the condition is obtained by letting  $R = \infty$ . Equation (4) then reduces to

$$v = \frac{Ec}{B} \quad (5)$$

Inspection of Eq. (4) also shows that for  $v < Ec/B$  the electromagnetic

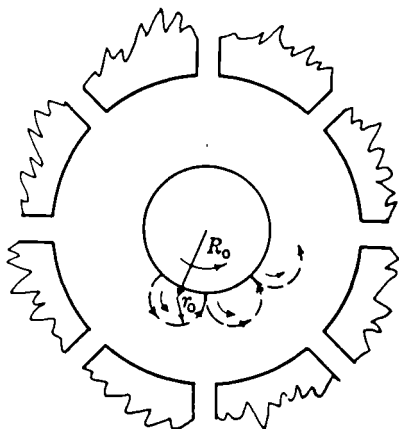


FIG. 1-21.—Path followed by a single electron in a nonoscillating magnetron.

To make this appear reasonable, consider the situation shown in Fig. 1-22. An electron moves through crossed, uniform electric and magnetic fields with a velocity  $v$  that is normal to  $E$  and  $B$ . The force equation under these conditions is

$$\frac{Bev}{c} = eE + \frac{mv^2}{R}, \quad (4)$$

force will be reduced and the electrons will be deflected in the direction of the electric force. For  $v > Ec/B$ , the deflection will be in the direction of the magnetic force. The deflection that an electron suffers in this example when speeded up or slowed down thus corresponds to what happens in a magnetron, and it is significant that the operating conditions are ones for which  $v \sim Ec/B$ .

The separation of the fast and slow electrons for an actual magnetron is shown in Fig. 1-23. Consider an electron at point *A* at the instant for which the fields are as shown. The r-f field at this point tends to

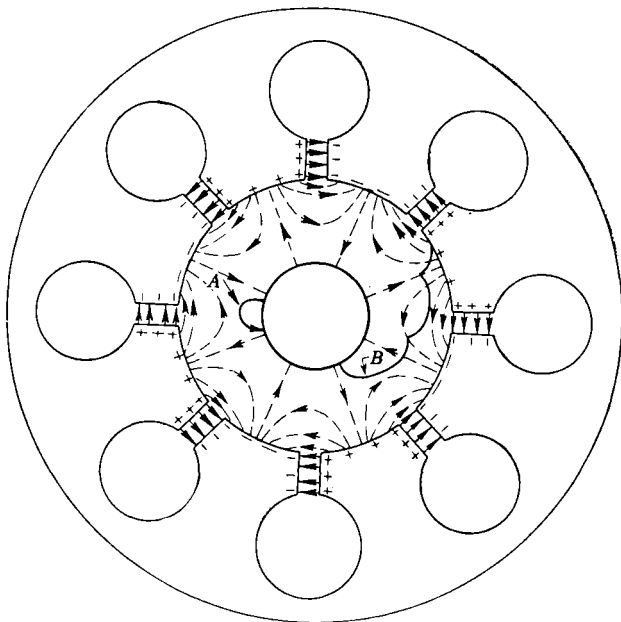


FIG. 1-23.—Paths followed by electrons in oscillating magnetron.

speed up the electron. As it speeds up, the curvature of its path is increased, and it will move along a path corresponding to the solid line and strike the cathode with appreciable energy. This electron is thus removed from the space charge and plays no further role in the process except perhaps to produce a few secondary electrons from the cathode. An electron at point *B*, however, is in a decelerating r-f electric field. As a result of the reduction in its velocity, the curvature is reduced. If the frequency of oscillation is appropriate, this electron will always be in a decelerating field as it passes before successive anode segments. The r-f phase shown in Fig. 1-23 is correct only when electrons *A* and *B* are at the points indicated. The result is that the electron eventually strikes



the anode following a path of the type shown. Because of retardation by the r-f field, this electron gives up to the r-f field a large part of the energy gained in its fall through the d-c field to the anode.

Since the electron moves from the cathode to the anode in a very small number of oscillations, the condition that the electron keep step with the variations of r-f oscillations, in its course around the cathode, need not be exactly satisfied. Electrons, once in step with the r-f field, remain in this state long enough to get to the anode even if their angular velocity is not exactly correct. This explains why the operating conditions of magnetrons are not very critical with respect to the magnetic field, input voltage, or other quantities that might affect the velocity of the electrons.

Appreciable energy is associated with the  $r_0$  rotation. This motion takes place, however, in a substantially constant r-f field, since the  $R_0$  rotation keeps the electron in step with the variations of the r-f field. As a result, the r-f field has little effect on the energy associated with the  $r_0$  rotation during the last part of the trajectory.

This qualitative picture shows how those electrons whose initial phase relationship is such that they absorb energy from the r-f field are eliminated at once from the space charge. This is the result of the fact that such electrons strike the cathode in the course of the first  $r_0$  period. On the other hand, electrons that leave the cathode at such a time and place that they transfer energy to the r-f field continue around the cathode in a cycloidal path which expands toward the anode, transferring to the r-f field the energy that they gain from the d-c field.

In addition to describing the paths taken by individual electrons in the interaction space, it is helpful to consider the behavior of the space charge as a whole. In the absence of r-f fields, the space charge forms a rotating cylindrical sheath around the cathode. Under the influence of the r-f fields, following the reasoning above, the electrons in this space charge that are in an accelerating r-f field travel back toward the cathode, while those in a decelerating r-f field travel toward the anode. As a result the rotating cylindrical sheath is distorted (for an eight-oscillator magnetron) into a smaller cylinder with four spokelike ridges running parallel to its axis. The configuration taken by the space charge is shown in Fig. 1-24. This space-charge configuration rotates with an angular velocity that keeps it in step with the alternating r-f charges on the anode segments, and the ends of these spokes may be thought of as brushing by the ends of the anode segments and thus transferring charge from the cathode to the anode.

These spokes of space charge are rather narrow and have fairly sharp boundaries. This is a consequence of the focusing action of the r-f fields, the nature of which may be seen by considering Fig. 1-25. Here one of

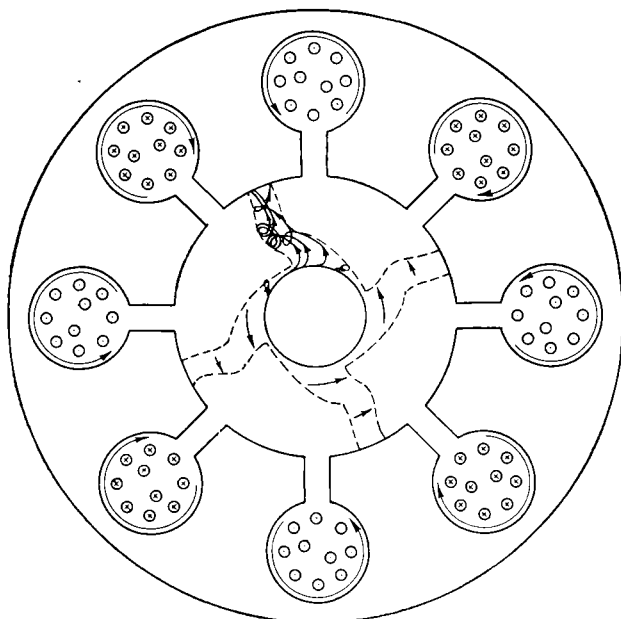


FIG. 1-24.—Space charge in oscillating magnetron.

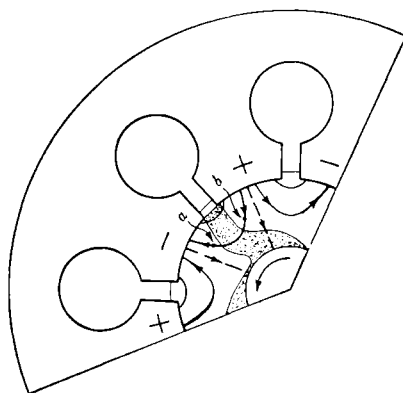


FIG. 1-25.—Diagram showing focusing action of r-f fields on space charge.

the space-charge spokes is shown in proper relation to the r-f fields extending in from the anode segments, and dashed lines show the direction of the d-c electric field. Any electron that, due to an excess in angular velocity, precedes this rotating spoke would be at a point such as *a*. Here the radial component of the r-f field and the d-c field are in opposition, and from the relation  $v = Ec/B$  its velocity will be reduced, even-

tually returning it to the space-charge spoke. The converse is true for an electron that lags corresponding to point *b*. When the space-charge spoke is opposite a segment, the direction of the r-f field is such that this focusing action would not take place, but at this moment the intensity of the fields is zero, and the net effect of the fields on the rotating space charge is to produce the focusing action mentioned.

The r-f current set up in the oscillators is principally a displacement current produced by this rotating space charge. As the spokes of space charge pass in front of an anode segment, a positive charge is induced on its surface. Half a period later, this positive charge has flowed around the back of the two adjacent oscillators to the two adjacent anode segments, and the spoke of the space charge has rotated to a position in front of the next anode segment.

In addition to these displacement currents, conduction currents are produced by the flow of electrons from space charge to the anode. These electrons, however, arrive at the anode at such a time as to constitute a conduction current 90° out of phase with the r-f voltage and thus do not contribute energy to the oscillations.

**1.7. D-c Voltage Magnetic-field Relationship.**—The concepts discussed in Secs. 1.4 and 1.6 lead to a simple expression relating the operating voltage *V*, the magnetic field *B*, the wavelength  $\lambda$ , and the anode and cathode radii, respectively  $r_a$  and  $r_c$ . Again as an example the magnetron shown in Fig. 1-10 is chosen. For efficient operation of the magnetron *V* and *B* must be such that the angular velocity of the electron keeps pace with the changes in phase of the resonators. Thus an electron must move from a point opposite any segment to a point opposite the next in one-half a period. Assuming that the electron is intermediate between the cathode and anode this distance is

$$\frac{2\pi}{N} \left( \frac{r_a + r_c}{2} \right),$$

where *N* is the number of resonators. The velocity must then be

$$v = \frac{\pi(r_a + r_c)}{N \frac{2}{f}},$$

where *f* is the frequency of the magnetron. Introducing the mode number

$$n = \frac{N}{2} \quad \text{and} \quad \lambda_0 = \frac{c}{f}$$

$$v = \frac{\pi c(r_a + r_c)}{n \lambda_0}. \quad (6)$$

From Eq. (5) the velocity of the electron is given by  $v = Ec/B$ ; and if one makes the simplifying assumption that the field  $E$  is given by the relation  $E = V/(r_a - r_c)$ ,

$$v = \frac{V_c}{B(r_a - r_c)}. \quad (7)$$

Equating (6) and (7) gives

$$V = \frac{\pi}{n\lambda_0} (r_a^2 - r_c^2)B. \quad (8)$$

If this problem is solved rigorously, Eq. (8) becomes

$$V = \frac{\pi}{n\lambda_0} (r_a^2 - r_c^2) \left( B - \frac{2\pi mc}{en\lambda_0} r_a^2 \right) \quad (9)$$

which is of the same form as Eq. (3), Sec. 1-1, developed by Posthumus. Equation (9) reduces to

$$V \text{ volts} = \frac{300\pi}{n_0} (r_a^2 - r_c^2) \left( B - \frac{10.600}{n_0} \right). \quad (10)$$

This voltage (which is a linear function of  $B$ ) is known as the Hartree voltage after Hartree<sup>1</sup> who developed this theory. This voltage is that at which oscillations should start provided at the same time that  $B$  is sufficiently large so that the undistorted space charge does not extend to the anode.

Figure 1-26, which is known as a Hartree diagram, explains the situation. This is a plot of Eq. (10) together with that of the Hull cutoff parabola given by Eq. (2). This diagram is based on the magnetron shown in Fig. 1-10. To the left of the cutoff parabola no oscillations occur as ordinary anode current is drawn. To the right of this parabola no current flows unless oscillations exist to distort the space charge until it touches the anode. This distortion is dependent on the existence of the proper electron velocities just discussed, and therefore current flows only when  $V$  and  $B$  correspond to a point near one of the straight lines representing the different values of  $n$ . Note that as  $n$  decreases, the electron must travel a greater distance around the cathode in one period and thus a larger  $E/B$  is required. This is evident from the  $(n = 3)$ - and  $(n = 2)$ -lines whose position was calculated assuming the same wavelengths as the  $(n = 4)$ -mode. Considerable departure from these lines is observed experimentally as a result of drawing large currents. The dotted lines above and parallel to the  $(n = 4)$ -line show the order of magnitude of this effect for different currents.

Important relationships among  $\lambda$ ,  $V$ ,  $B$ , and  $r_a$  can be obtained from the formula for the cutoff parabola Eq. (3) and the Hartree resonance formula Eq. (10). Assuming a constant ratio  $r_c/r_a$ , consider the effect

<sup>1</sup> Hartree, CVD Report.

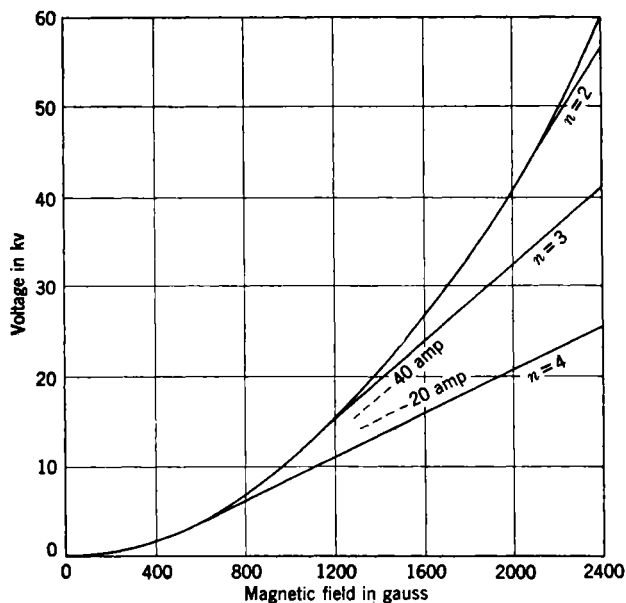


FIG. 1-26.—Hartree diagram.

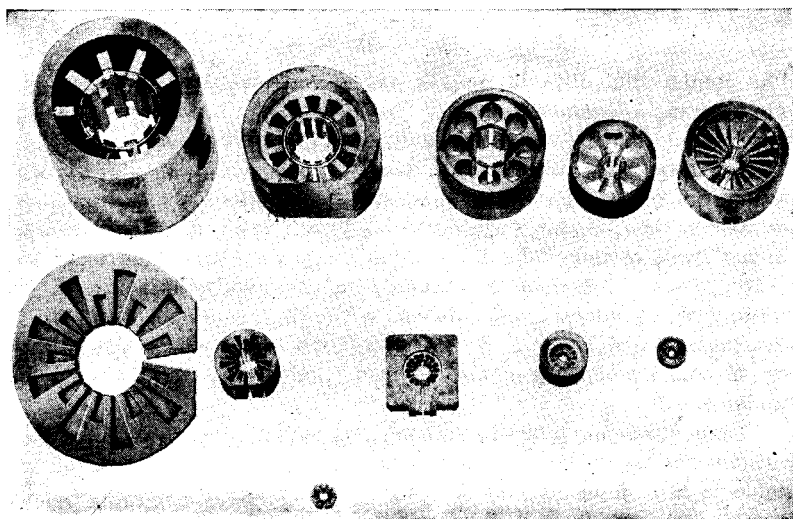


FIG. 1-27.—An array of anode blocks of different wavelength and power output. Top row: 10-cm, pulse power 2500 to 0.1 kw; second row: 3.2 cm, pulse power 600 to 0.025 kw; single block and insert 1.25 cm, 80 kw.

of keeping  $B$  and  $\lambda$  fixed and varying  $r_a$ . In Eq. (9),  $V$  is proportional to  $r_a^2$ , so that operating conditions remain unchanged if the operating voltage is increased proportional to the square of the anode radius. This relationship is illustrated in Fig. 1-27. The upper row are all 10-cm anode blocks which have operating voltages of 50, 25, 15, 5, and 1 kv, respectively. The reduction in anode diameter with voltage is evident, although the number of resonators is not the same for all of these blocks and some allowance must be made on this account. The second row shows a corresponding series of 3.2-cm anode blocks whose operations voltages are 30, 20, 5, and 2.5 kv.

It may be seen from the same equations that if  $V$  is kept constant,  $r_a$  must vary roughly as  $\lambda_0$  and  $B$  as  $1/\lambda_0$  in order to preserve equivalent operating conditions. A simplified proof of these relationships is possible, neglecting the final term in Eq. (10) which, in general, is small compared with  $B$  the product  $(r_a^2 - r_c^2)B \sim \lambda$ . Since  $r_a/r_c$  is assumed constant,  $r_a^2 B \sim \lambda$  and from Eq. (3) Sec. 1

$$r_a B = \text{const.}$$

Combining the two proportionalities gives the static proportionalities

$$r_a \sim \lambda$$

and

$$B \sim \frac{1}{\lambda}.$$

Two major difficulties in making very short wavelength magnetrons are inherent in these expressions: The cathode and anode become excessively small, and the requirements for magnetic fields excessively high.

**1-8. Component Modes.**—In Sec. 1-4 the modes of the resonant system are discussed; and if longitudinal oscillations are excluded, the number of these modes is stated to be  $N - 1$ , each of which is characterized by a certain field distribution and frequency. The most efficient process is based on the equality of the angular velocities of the rotating space charge and rotating r-f fields. Another possibility is the excitation of a mode by the interaction of the space charge with one of the components of the r-f field rotating less rapidly than the fundamental.

These components of the fundamental mode patterns are associated with the fact that the variation in intensity of the r-f field around the anode is not sinusoidal. The nonsinusoidal spatial variation can be represented by a sum of Fourier terms, each of which corresponds to a closed rotating wave containing a number of cycles, or complete periods, different from the fundamental and rotating with a different velocity.

These components are limited, according to Hartree,<sup>1</sup> to those which contain a number of complete periods around the circumference, given by the relationship

$$\gamma = n + mN, \tag{11}$$

where  $m$  is a whole number,  $n$  the mode number of the fundamental, and  $N$  the number of resonators. The angular velocity of these components is given by

$$\pm \omega_\gamma = \frac{2\pi f}{\gamma}, \tag{12}$$

where  $f$  is the frequency. Equation (11) applies only to the case of the symmetric anode block, whether it is strapped or not.

These components have a physical significance. If the electrons forming the undistorted space charge have angular velocities close to that of one of these components, the effect of the r-f field will be cumulative and the space charge will be distorted into the form shown in Fig. 1.24, but with a number of spokes equal to  $\gamma$ . The field of the components (or fundamental) that have a different angular velocity will not remain in phase with the electrons, and its effect will average out after a few cycles.

Table 1.1 shows the values of  $\gamma$  for the important components of the four modes of an eight-resonator magnetron. Negative values of  $\gamma$  mean that the component is rotating in a direction opposite to the fundamental and values of  $\gamma$  for  $m = 0$  correspond to the fundamental field pattern of the modes.

TABLE 1.1.—VALUES OF  $\gamma$  (NUMBER OF CYCLES) FOR CERTAIN COMPONENTS OF THE FOUR PRINCIPAL MODES OF AN EIGHT-RESONATOR MAGNETRON

$m$	$n$			
	1	2	3	4
0	1	2	3	4
-1	-7	-6	-5	-4
+1	+8	+10 +9	+11 +10	+12 +11
-2	-15	-14	-13	-12
+2	+17	+18	+19	+20
...	...	.....	.....	.....
...	...	.....	.....	.....

Since for every value of  $n$  there is a fundamental rotating in both directions, producing the familiar standing-wave pattern, there are two

<sup>1</sup> Hartree, CVD Report.

complete sets of components each rotating in opposite directions. This is implied by the  $\pm$  sign in Eq. (12).

Although the number of components is infinite, only values of  $\gamma$  for  $\pm m$  up to 2 are given, since higher values are of no practical importance. Actually, mode excitation in the case of symmetric resonant systems has been observed only for the ( $m = -1$ )-component. The unimportance of higher  $m$  values is probably due to the fact that they are necessarily associated with large values of  $|\gamma|$  and that the falling off in intensity of these components is proportional to  $(r/r_a)\gamma$ . Moreover large  $\gamma$  values give rise to values for the  $\gamma\lambda$  product considerably larger than that of the  $\pi$ -mode and require different operating conditions.

The nomenclature  $\gamma/n/N$  has been adopted to designate first the  $\gamma$  component responsible for the excitation of the mode number  $n$  in a magnetron having  $N$  oscillators. Thus the  $\pi$ -mode in an eight-oscillator magnetron, when excited through its fundamental, is represented by the symbol 4/4/8, and the ( $n = 3$ )-mode when excited by its fundamental by 3/3/8. If the ( $n = 3$ )-mode is excited through the ( $\gamma = -5$ )-component, it is designated by 5/3/8. The 3/3/8 and 3/5/8 modes have identical frequencies and r-f characteristics.

In unstrapped magnetrons and less frequently in strapped magnetrons component excitation of unwanted modes is a source of considerable trouble. Difficulties are most likely to arise when the product  $\gamma\lambda$  for the  $\pi$ -mode and an unwanted mode are nearly equal, as under these conditions both have the same angular velocity and may be excited by the same rotating space charge. The 2J32 (Fig. 1-10) is a good example. This tube has a tendency to oscillate during occasional pulses in the 5/3/8 mode. It is significant, however, that increased strapping of this tube, which decreases the wavelength of the ( $n = 3$ )-resonance with respect to the ( $n = 4$ )-resonance, resulted in mode changing by making the  $\gamma\lambda$ 's for the two modes more nearly equal. This problem is considered in detail in Chap. 8.

In rising-sun magnetrons an extension of these principles must be made due to the two sets of resonators. The mode spectrum (Fig. 1-18) shows that the coupling between these two sets of resonators is small except for the  $\pi$ -mode and (in considering the interaction of the field components of the modes with the space charge) that the modes associated with large and small sets can practically be treated separately as though each consisted of a resonant system consisting of  $N/2$  oscillators. Equation (1) then becomes

$$\gamma = n \pm m \frac{N}{2}. \quad (13)$$

When applying this relationship to the long- and short-wavelength



group shown in Fig. 1-18, the resonances marked  $n = 8, 7, 6, 5, 4$  should be assigned the values  $n' = 1, 2, 3, 4$ , respectively. Table 1-2 gives the values of  $\gamma$  for significant  $m$ 's for a typical rising-sun magnetron shown in Fig. 1-17 having 18 oscillators. Both long- and short-wave-

TABLE 1-2.—VALUES OF  $\gamma$  FROM EQ. 3 FOR RISING-SUN MAGNETRON WITH  $N = 18$ 

$m$	$n$ or $n'$			
	1	2	3	4
0	1	2	3	4
-1	-8	-7	-6	-5
+1	10	11	12	13
-2	-17	-16	-15	-14
+2	+19	+20	+21	+22
...	....	....	....	....
...	....	....	....	....

length resonances are observed to compete with ( $n = 9$ )- or  $\pi$ -mode operation.

Excitation of the long-wavelength resonances occurs through the ( $m = -1$ )-component, as these give  $\gamma$  values such that the  $\gamma\lambda$ 's may be close to the value of  $\gamma\lambda$  for the  $\pi$ -mode (the  $\lambda$ 's are larger, and the  $\gamma$  smaller). From Table 1-2 it is seen that components for values of  $m$  other than  $m = -1$  need not be considered, as the  $\gamma\lambda$  product will not be close to the  $\gamma\lambda$  for the  $\pi$ -mode for the longer-wavelength set.

Excitation of the short-wavelength resonances can, on  $\gamma\lambda$  product consideration, occur through the ( $m = \pm 1$ )-component. Here the  $\gamma\lambda$  product may approximate that of the  $\pi$ -mode, since the  $\lambda$ 's are shorter and the  $\gamma$ 's larger than the  $\pi$ -mode values. Actually only the components of ( $n' = 1$ )-mode have ever been observed to interfere with  $\pi$ -mode operation.

The theoretical basis for these results is found in Sec. 3-2, and its application to practical magnetron design is considered in Sec. 11-6.

**1-9. Efficiency and Frequency Stability.**—The uses to which a magnetron is put are usually such that it is desirable to attain both high efficiency and high-frequency stability against changes in load and changes in input conditions. These objectives are not consistent, and most magnetrons represent a compromise between efficiency and stability that depends on the particular application. The problem is a most important one in magnetron design.

For any given frequency, a variety of oscillator configurations is possible corresponding to different oscillator impedances of  $L/C$  ratios, and the efficiency and frequency stability desired determine the proper

oscillator impedance to use. Figure 1-28 shows three forms of oscillators arranged in order of increasing impedance.<sup>1</sup>

The efficiency  $\eta$  with which a magnetron converts the input power into r-f power at the output (cathode power is excluded) is given by  $\eta = (\text{power input} - \text{losses}) / \text{power input}$ . The losses arise from the

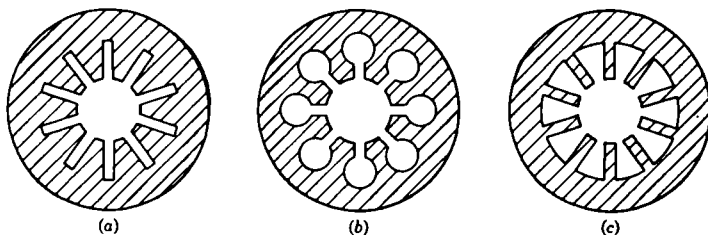


FIG. 1-28.—Three common types of magnetron cavities: (a) slot; (b) hole and slot; (c) vane.

bombardment of the anode by the electrons and from the circulating r-f currents producing  $I^2R$  losses in the copper and other materials. To distinguish these two sources of energy loss it is customary to express the over-all efficiency  $\eta$  of a magnetron as the product of the electronic efficiency  $\eta_e$  and circuit efficiency  $\eta_c$  or  $\eta = \eta_e \eta_c$ . The electronic efficiency

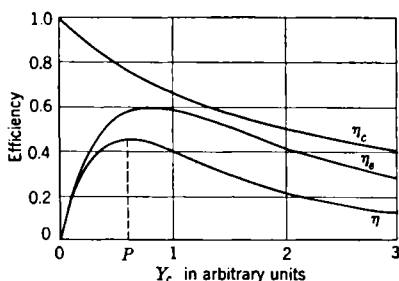


FIG. 1-29.—Efficiencies as a function of oscillator impedance  $Y_c$ .

is defined as the fraction of the input power that is converted into r-f power within the anode block, and the circuit efficiency is the fraction of this r-f power which is transmitted to the load. The problem of high efficiency may then be restated as one of making the product  $\eta_c \eta_e$  a maximum.

Both  $\eta_c$  and  $\eta_e$  are affected by the impedance of the oscillators, but in different ways. The circuit efficiency  $\eta_c$  is highest in high-impedance oscillators such as shown in Fig. 1-28c, since the circulating currents are less. In Chap. 4 it is seen that the electronic efficiency  $\eta_e$  depends on the r-f voltage across the oscillator gaps in such a way that maximum  $\eta_e$  occurs at a lower r-f voltage than can usually be obtained in actual operation, and the problem of increasing  $\eta_e$  is therefore one of reducing the r-f voltage for a given power output. The r-f voltage can be reduced either by decreasing the oscillator impedance (decreasing  $L/C$ ) or by coupling the system strongly to the load so as to reduce the amount

<sup>1</sup> It should be remarked that the straps of a magnetron also affect the oscillator impedance, but for the sake of brevity they are not considered here.

of stored energy. The most efficient oscillator configuration is that compromise between a high-impedance oscillator giving high  $\eta_c$  and a low-impedance oscillator giving high  $\eta_e$  which gives a maximum  $\eta_c\eta_e$ . In Fig. 1-29 two curves show the manner in which  $\eta_c$  and  $\eta_e$  vary with oscillator impedance. A third curve shows how  $\eta$  varies, and the optimum impedance is indicated by  $P$ .

Increasing the loading of the magnetron generally increases its efficiency. Only rarely can the loading be made so heavy that a decrease in efficiency results because the r-f voltage is reduced below the optimum value. It is usually necessary to place a lower limit on the frequency stability, and this requirement alters both the loading and resonator impedance values corresponding to maximum efficiency. Heavy loading means closer coupling between load and magnetron, and this makes the magnetron more sensitive to load changes; in other words, it reduces the frequency stability. A high-impedance oscillator also has less stability against load changes than a low-impedance one. The determination of the oscillator impedance and loading to satisfy given requirements for frequency stability and provide maximum efficiency is given in Chap. 10.

In addition to providing resonators with the proper frequency and impedance, the anode block should provide suitable mode separation, reasonably uniform r-f voltages across the different gaps, and adequate thermal conduction away from the anode surface and have a configuration that it is possible to construct.

Further interpretation of the Hartree diagram is made in the following section in connection with a discussion of performance charts.

**1-10. Performance Charts and Rieke Diagrams.**—For the interpretation of microwave magnetron performance it is necessary to make observations that are not usually made at lower frequencies with conventional types of tubes. The reasons for this are that at the frequencies considered the concept of lumped circuit constants breaks down and also because the magnetron is inseparable from its oscillating circuits. As a result of experience, particularly with pulsed magnetrons, it has been found convenient to present operational data by means of two charts discussed here.

Four parameters determine the operation of a magnetron: two associated with the input circuit and two with the output circuit. A typical set is the magnetic field  $B$ , current  $I$ , the conductance  $G$ , and susceptance  $H$  associated with the r-f load on the magnetron. The observed quantities are three in number, usually power  $P$ , wavelength  $\lambda$ , and voltage  $V$ . The problem of presenting these observed quantities in terms of the four parameters is greatly simplified by the fact that the input and output parameters operate nearly independently of each other. Thus, it is

possible to keep  $G$  and  $B$  (the load) fixed and study the effect of  $H$  and  $I$  on  $P$ ,  $\lambda$ , and  $V$  with the assurance that the nature of the results will not be greatly altered by changes in  $G$  and  $B$ . Conversely,  $H$  and  $I$  (the input) may be fixed, and the effect of  $G$  and  $B$  on  $P$ ,  $\lambda$ , and  $V$  observed. The "performance chart" shows the relationship among  $H$ ,  $I$ ,  $V$ ,  $P$ , and  $\lambda$  for constant load, and the "Rieke diagram" shows the relationships among  $G$ ,  $B$ ,  $P$ ,  $\lambda$ , and  $V$  for constant  $I$ .

*Performance Charts.*—Figure 1-30 is a performance chart for a typical pulsed magnetron (4J31) with a frequency of about 2800 Mc/sec.

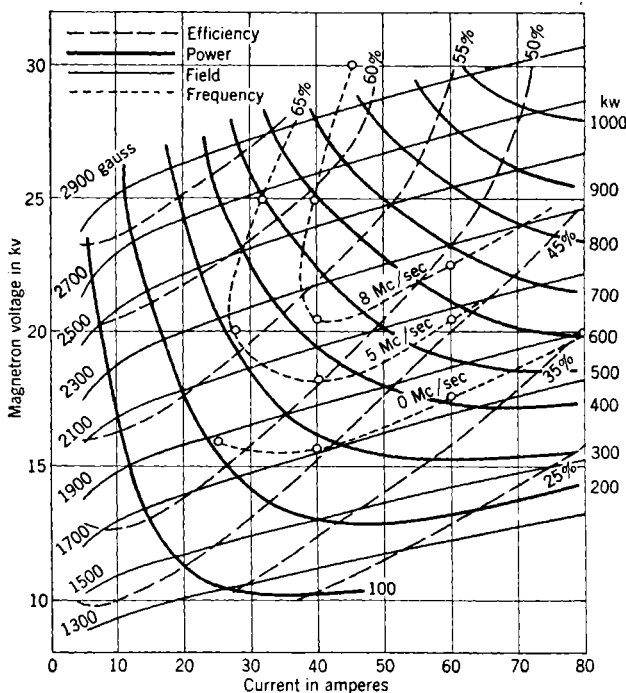


Fig. 1-30.—Typical performance chart of a magnetron (4J31).

It has been customary to plot  $V$  in kilovolts along the ordinate and current  $I$  in amperes along the abscissa. On such a graph the lines of constant  $H$  appear as more or less parallel lines which slope upward to the right. Thus (referring to Fig. 1-30) if the magnetron is operated at a constant magnetic field, say 2100 gauss, the relations of voltage and current are given by points on the  $H = 2100$  gauss line (at 20 kv, the current drawn will be 48 amp).

On the same chart are plotted the lines of constant power output. These are the solid lines the form of which suggests hyperbolas; they

show the pulse r-f power that is obtained under varying input conditions. Thus at 20 kv and 48 amp, the power output is 470 kw. This same power can also be obtained at 25 kv and 30 amp with a magnetic field a little less than 2700 gauss. Curves of constant efficiency, obtained directly from the above data, are added. These are the dotted lines looping up and to the right on the diagram.

It is possible to add to this chart lines of constant frequency, so that the variation of frequency with input parameters may be studied. This information is useful in establishing limits on the variation of current during a pulse. The dashed lines are contours of constant frequency. In this case, they are nearly parallel to the lines of constant magnetic field, an ideal condition, since changes in current produce no change in frequency.

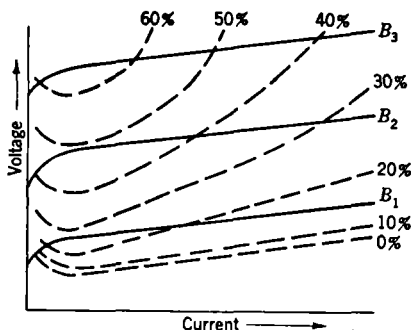


FIG. 1-31.—Idealized performance chart.

Many of the features of a performance chart can be interpreted in terms of the qualitative electronic theory (Sec. 1-7) and in terms of a Hartree diagram such as shown in Fig. 1-26. If the efficiency of a magnetron were independent of  $V$  and  $I$ , the contours would be hyperbolas asymptotic to the  $V$  and  $I$  axis. Inspection of Fig. 10-16 shows that to a first approximation this is the case. But it is the departure from this condition which is of interest and must be explained in terms of the variation in the efficiency as revealed by the performance chart. A simplified and somewhat idealized performance chart is shown in Fig. 1-31 which shows only contours of constant magnetic field and constant efficiency for a typical strapped magnetron. Performance charts for rising-sun magnetrons differ in having a distinct drop in efficiency at magnetic fields which by Eq. (1) result in a cyclotron frequency close to the operating frequency. This characteristic of rising-sun magnetrons is discussed in detail in Chap. 3.

Performance charts for different types of strapped magnetrons show considerable divergence, and Fig. 1-31 has been idealized to show only those features which are common to most performance charts.

1. Except for very low currents, increasing the current  $I$  while keeping  $B$  constant results in a decrease in efficiency. In Fig. 1-26 this corresponds to moving up from the  $n = 4$  Hartree line toward cutoff.
2. Decreasing the magnetic field at constant current results in a decrease in efficiency. In Fig. 1-26 this corresponds to moving along the  $n = 4$  Hartree line toward cutoff. From this it is clear that on the Hartree diagram electronic efficiency is increased if  $V$  and  $B$  correspond to points that are both near the Hartree line and far from cutoff. All magnetrons, the operation of which appears normal, support this conclusion. Accordingly, magnetrons are designed to operate at relatively high magnetic fields which correspond to points far from cutoff.
3. A drop in efficiency at very small currents which is indicated by a curving up of the line of constant efficiencies at the extreme left of Fig. 1-31. This is probably due to unproductive leakage current from the cathode. This falling off in efficiency is usually accompanied by a drooping of the lines of constant  $B$  as shown in Fig. 1-31.

These are the three most general features shown by performance charts. An inspection of those given in Chap. 19 will reveal many unusual configurations which are not capable of explanation.

*Rieke Diagram.*—The performance of a magnetron in terms of its output parameters, or r-f loading, is conveniently presented on a Rieke diagram. It would appear useful to express the r-f loading in terms of the resistance and reactance presented to the magnetron at the output loop. Since these quantities are difficult to determine experimentally, the Rieke diagram is in terms of quantities that can be obtained with ease experimentally. At microwave frequencies, it is customary to determine the constants of a load by observing the phase and magnitude of the standing waves set up by it, and the Rieke diagram is designed to use these experimental data directly. The desired range of r-f loading is obtained by adjusting a tuner until the desired phase and standing-wave ratio is indicated by a sliding pickup probe such as shown in Fig. 18-4. The standing-wave ratio is transformed into a reflection coefficient  $K$  by the relation  $K = (1 - \rho)/(1 + \rho)$  and  $K$  and  $\theta$  used as coordinates of a polar diagram. This is known as the Smith<sup>1</sup> chart, and the Rieke diagram is obtained by measuring the power output, frequency, and voltage at constant  $H$  and  $V$  for enough points on this chart to construct contours for these quantities. Such a diagram is shown in Fig. 1-32. Inspection of the Rieke diagrams given in Chap. 19 will show considerable

<sup>1</sup> P. H. Smith, *Electronics*, **12**, 29 (1939).

variation in their form; but as in the case of performance charts, certain features are exhibited by all of them.

Referring again to Fig. 1-32, it is seen that the power contours approximate one set of circles tangent at one point on the ( $K = 1$ )-circle, and it is significant that on a Smith chart the contours of constant load conductance are, indeed, such circles. The frequency contours are seen to approximate sections of a second set of circles which are everywhere perpendicular to the first set and are tangent at the same point. Again

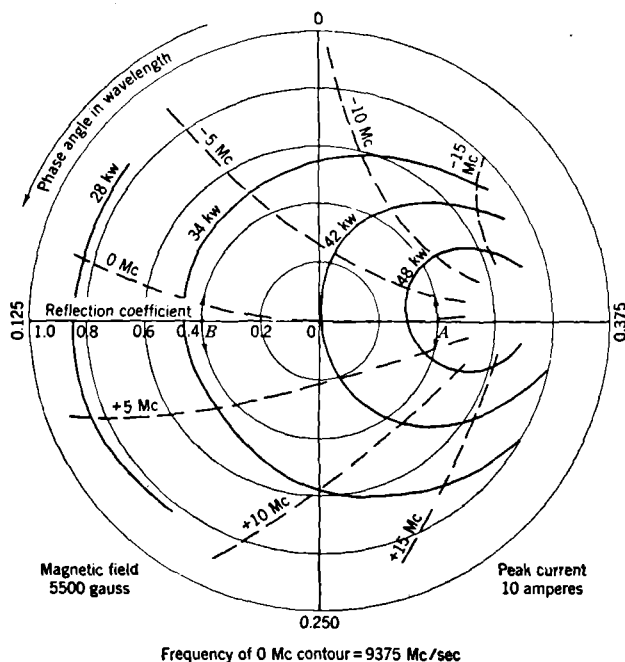


FIG. 1-32.—Typical Rieke diagram (725).

it is significant that on a Smith chart the contours of constant susceptance correspond to this second set of circles.

The comprehensive treatment of the Rieke diagram is found in Sec. 7-5.

Rieke diagrams provide information of considerable importance to magnetron designers and users. They are usually furnished as operating data, together with performance charts, by magnetron manufacturers for every type of tube.

As an example of their usefulness consider the effect of a mismatch in the magnetron's output. Assume that a reflection coefficient of 0.4 ( $\rho = 2.3$ ) exists, and suppose further that the phase of this mismatch

at the magnetron is such that the voltage minimum corresponds to point *A* (Fig. 1-32). The result will be a power output for the specified input conditions of about 50 kw. If the phase of the reflection is changed, say by increasing the line length between the magnetron and the mismatch until point *B* is reached, the power output falls to 33 kw. The efficiency of the magnetron at point *A* is thus 50 per cent greater, but operation at this loading may be unsatisfactory for reasons of stability. As representative of a general class of load instability, consider the effect of a change in phase angle about the loading *A* of  $\pm 7.5^\circ$  (arrows) that might result from the turning of an imperfect rotary joint. The power output will be essentially unaltered, but a maximum change in frequency of 10 Mc/sec occurs. At point *B*, however, corresponding to light loading, a phase shift of  $\pm 7.5^\circ$  results in only a 3-Mc/sec frequency shift. In radar systems or in other applications where frequency stability is required under conditions of changing load, a compromise must be made between efficiency and frequency stability on the basis of Rieke diagrams. Magnetrons are usually designed with an output coupling such that the center of the Rieke diagram, which corresponds to a matched load, represents a reasonable compromise between efficiency and frequency stability.

It is possible to adjust the loading on the magnetron to any reasonable value by the suitable use of r-f transformers in the output line. As an example, suppose that it is desirable to operate the magnetron represented by Fig. 1-32 at a point of high efficiency and low-frequency stability corresponding to point *A*. This can be accomplished by introducing a transformer that sets up a 2 to 1 VSWR and making its distance from the magnetron such that the phase of this VSWR corresponds to point *A*. By moving this transformer along the line in either direction one-quarter wavelength, operation corresponding to point *B* can be obtained.

**1.11. Pulsed Magnetrons.**—The most outstanding characteristic of microwave magnetrons is their extremely high pulse-power output which is over one thousand times the best c-w output at the same frequency. These high powers are due mainly to three factors.

1. The electronics of the magnetron are such that high efficiencies persist at very high levels of power.
2. The oxide cathode under pulsed conditions yields currents one hundred times that obtained under d-c conditions.
3. The procedure of pulsing at very small duty ratios has largely eliminated the problem of anode dissipation.

Because of these factors and intensive development as a result of the war effort magnetrons with frequencies up to 25,000 Mc/sec and pulse-power outputs from 0.02 to 2500 kw are available.



These high-pulsed powers together with the discovery of high-pulsed emission from oxide cathodes are examples of the many advances that have resulted from the introduction of pulsed techniques. From the standpoint of magnetron operation, however, pulsing also introduces certain problems. The most serious one is the buildup of oscillations from noise to full power that must occur reliably for every pulse in a time that may be as short as  $10^{-8}$  sec. Failure of the buildup to occur results in misfiring or mode changing, a phenomenon exhibited by essentially all magnetrons under certain conditions.

The explanation of mode changing is extremely involved, as the buildup of oscillations in a desired mode depends on a large number of factors, many of which are interrelated. The more important factors are

1. Rate of rise of voltage pulse.
2. Rate of buildup of oscillations in desired mode and undesired modes which involves the loading of the various modes and the noise level from which they start.
3. Voltage and current range over which oscillations in the desired mode and undesired modes may persist.
4. Impedance of the pulser.

As an example of the interrelation of these factors consider a particular kind of misfiring that results when the pulse voltage reaches and exceeds the limits within which oscillations can start before oscillations can build up. Misfiring or mode changing will then be more likely to occur when the rate of rise of the pulse is fast, when the voltage range over which oscillations can occur is small, and when the impedance of the pulser is high, since a high-impedance pulser means a higher no-load voltage for a given operating current and voltage. This example is a simple one, and in practice the solution of a particular problem of misfiring or mode changing will involve the transient characteristics of the pulser as well as the transient characteristics of the magnetron and the reactions of the pulser and magnetron on each other. The theory of transient behavior is given in Chap. 8, but the problem is such a complicated one that it can sometimes be used only as a guide to the experimental elimination of trouble.

The demands of microwave radar resulted in a rather extensive development of magnetrons the frequencies of which are concentrated more or less into four bands. Figure 1-33 shows on a logarithmic chart the frequency and peak power of magnetrons that have been produced in appreciable numbers and thus constitute well-tested designs. Production magnetrons are identified by their RMA type numbers, and experimental ones by the designation assigned to them in the laboratory where they were developed.

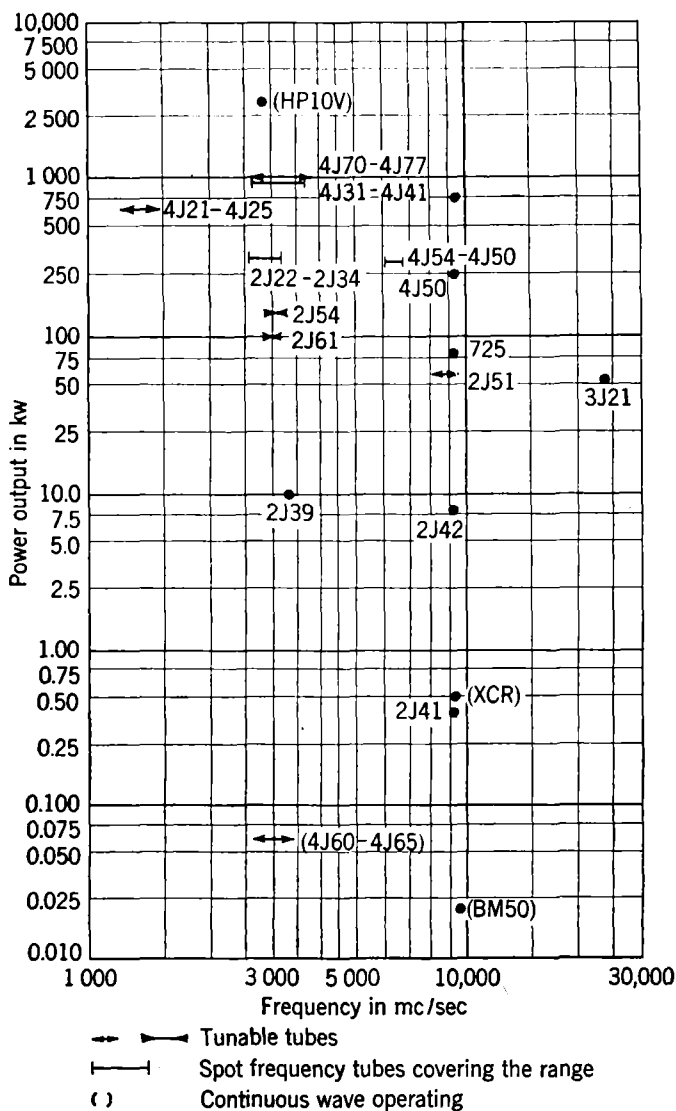


FIG. 1-33.—Diagram showing power and frequency distributions of representative microwave magnetrons developed up to 1946.

From this chart it is seen that the maximum pulse power increases with the wavelength.<sup>1</sup> If this power is limited by either cathode emission or voltage breakdown within the tube, the maximum pulsed power would vary as  $\lambda^2$  for comparable designs.

A summary of the more important characteristics of pulsed magnetrons in several wavelength bands is given in Table 1-3. These data refer to magnetrons in production and do not represent the limits reached

TABLE 1-3.—SUMMARY OF CHARACTERISTICS OF REPRESENTATIVE MAGNETRONS IN CERTAIN WAVELENGTH BANDS (1945)

Wave-length band, cm	Power level	RMA type	Average power output, watts	Pulse power output, kw	Input voltage, kv	Input impedance, ohms	Maximum pulse length, sec
30	.....	4J21	800	800	25.0	500	6.0
10	High	4J39	600	1000	30.0	400	2.5
	Low	2J39	100	10	5.0	1000	2.0
3.2	High	4J50	500	250	20.0	700	5.0
	Low	2J41	3	1000	2.5	1500	0.5
1.25	.....	3J21	50	50	15.0	1000	0.5

in experimental tubes. The figures for maximum pulse length should not be taken too literally, as the input power affects the maximum pulse length at which stable operation can be obtained.

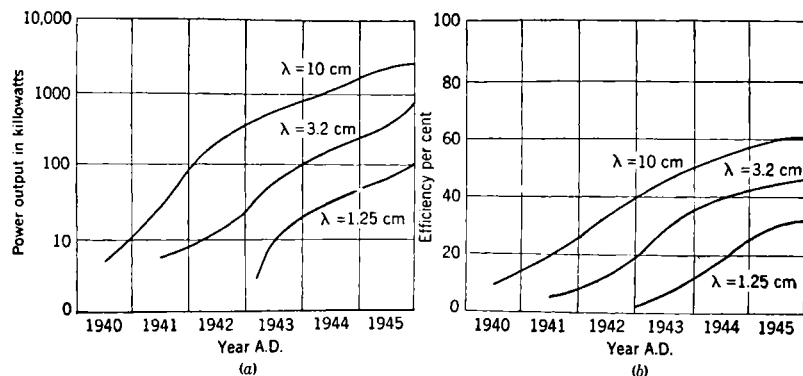


FIG. 1-34.—Maximum pulsed-power output and efficiency for magnetrons developed up to 1946.

Detailed information on the construction and operation of most of these tubes is given in Chap. 19.

<sup>1</sup> An exception to this are the magnetrons in the 1000- to 1500-Mc/sec range whose pulse power is not so high as might be expected. This situation results from a lack of need for very high powers in this wavelength range.

This information reflects the status of pulsed magnetrons only up to the year 1946, and it is interesting to speculate on future trends. Figure 1-34*a* shows the highest pulsed power obtained from experimental magnetrons at three wavelengths bands for the years 1940 to 1945, and Fig. 1-34*b* shows the efficiency of these tubes during the same period. From Fig. 1-34*a* it must be concluded that this design of high-frequency generator has not been fully exploited as far as maximum power output is concerned, since the curves show that the power obtained is roughly proportional to the integrated effort put into development. The leveling off of the 10-cm curve results from a cessation of work in this band, while the increase in the 3.2- and 1.20-cm curves reflects continued effort by the Columbia University Radiation Laboratory. Figure 1-34*b* indicates that the efficiency of magnetrons as they are now designed is reaching a limit, as the curves for all three bands have leveled off.

## PART I

# RESONANT SYSTEMS

The description of a microwave magnetron given in Chap. 1 has shown that the device may be naturally analyzed into three parts which differ in function. These are the electron stream, the resonant system, and the output circuit. The electron stream, flowing in crossed magnetic and electric fields, interacts with that part of the field of the resonators which penetrates the interaction space in such a way that energy is continually abstracted from the electrons to appear as electromagnetic energy in the resonant system. The principal function of the resonant system is to serve as a frequency-determining element. It accomplishes this by storing the energy received from the electrons over a large number of cycles. It may be thought of as a filter circuit with a narrow pass band which allows only the frequency component in the electron stream that is of interest to be transmitted. Finally the output circuit constitutes a coupling path between the electron stream and an external load. The properties of this transmission path are so arranged that the r-f voltages which the electron stream encounters are suitable for efficient power transfer.

The purpose of the four following chapters is to discuss some of the fundamental electromagnetic properties of the resonant system and of the output circuit. The simplest feature common to all resonant systems used in multisegment magnetrons is that they should be capable of being fed from a series of slots in a cylindrical anode, parallel to the axis of the cylinder. Systems filling this requirement may be devised in great variety; in practice, three such schemes have been used almost exclusively. These are the unstrapped system, the strapped system, and the alternating unstrapped, or rising-sun, system, in order of historical development.

The unstrapped system consists of a series of identical resonators between which the only coupling is that provided by the electromagnetic fields in the interaction space and in the end spaces. The alternating unstrapped system also utilizes these coupling paths, but alternate resonators are of two different kinds. The strapped resonator system, on the other hand, has a system of identical resonators, but a special coupling link is provided between each pair of neighboring resonators. The following discussion will deal exclusively with these three types of

resonant systems. In the practical design of magnetrons the unstrapped system has been superseded by the other types, although it was historically the first to be used. It may, however, be discussed theoretically rather completely, and in the analysis a number of concepts are brought out that are essential to the understanding of the rising-sun and strapped systems. It is possible to discuss unstrapped systems fairly rigorously by electromagnetic field theory, but the greater complexity of strapped structures requires the use of a more intuitive approach by the use of equivalent circuits.

The type of information sought in each case is essentially the same. The fields in the interactions space, the mode spectrum of the resonant system, and its dependence upon the dimensional parameters are found, and a number of circuit constants of interest in the electron-field interaction or in the oscillator-load coupling are derived for the three cases. The discussion does not take up specific problems in the design of resonator systems, a topic that is extensively discussed in Chaps. 10 and 11; instead, attention is concentrated on features of the three systems that are of importance in over-all design.

In the chapter devoted to the output circuit, the latter is considered primarily as a transducer the function of which is to convert the impedance of an external load to such a level within the magnetron that the electron stream encounters r-f voltages such that it delivers power efficiently. An account of transducer theory adequate for the needs of the problem is given, and various classes of output circuit are considered in some detail.

## CHAPTER 2

### THE UNSTRAPPED RESONANT SYSTEM

By N. KROLL

The unstrapped resonant system shown in Fig. 2-1*a* was one of the first systems developed for microwave multiresonator magnetrons. Figures 2-1*b* and *c* show variations of this early design. These anode blocks consist of an anode divided into a number of equal segments connected by identical resonators. These resonators are referred to as "side resonators" or "side cavities." Various shapes of side cavities are possible; those shown in Fig. 2-1 are the ones most commonly used. Although the unstrapped resonant system is now almost obsolete, a

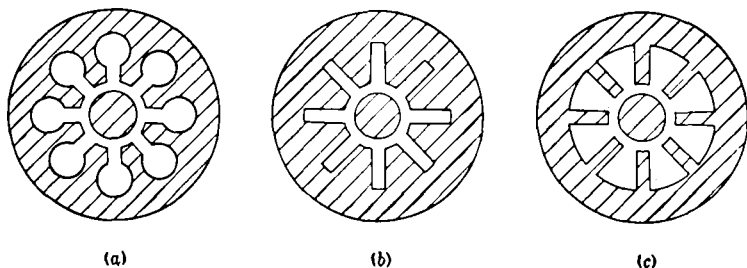


Fig. 2-1.—Examples of unstrapped resonant systems: (a) with hole-and-slot-type side resonators; (b) with slot-type side resonators; (c) with vane-type side resonators.

careful discussion of it is worth while for two reasons. (1) Many concepts that are used in the discussion of the more complicated systems are based on those developed for this system. (2) The problems that arise in the analysis of resonant systems and the possible methods for solving them are seen in their simplest form in the study of the unstrapped system.

**2.1. The Magnetron Cavity as a Circuit Problem.**—The interior of the magnetron (anode block, interaction space, and end spaces) can be thought of as constituting a cavity resonator of complicated geometry. It is a well-known fact that such a resonator has an infinite number of resonant frequencies and a particular field distribution associated with each one. The rigorous method of solving these problems is to find a solution of Maxwell's equations that behaves properly at the boundaries. However, because such a solution can ordinarily be found for only the

simplest geometries, it will be necessary to employ circuit analogies and approximate methods that use simplified geometry and simplified boundary conditions.

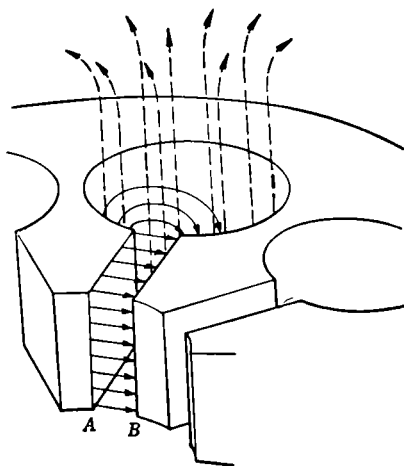


FIG. 2-2.—Typical orientation of electric and magnetic fields in the side resonator of a magnetron. Solid lines indicate electric field; dotted lines indicate magnetic field.

of field. Thus, the initial assumptions are that the electric field be transverse and that there be no axial variation of field. It then follows, as shown in Sec. 2-5, that the magnetic field is axial and has no axial variation (see Fig. 2-2).

On the basis of the preceding assumptions the equivalent circuit representation shown in Fig. 2-3 is possible. The circuit elements representing the side resonators are labeled  $Y_r$ ; A is a symmetric network with  $N$  pairs of terminals and represents the interaction space. Such a representation requires that an impedance or admittance at the various terminals be defined. Figure 2-2 shows the situation at a side resonator. The voltage at the terminals can be defined as  $\int_A^B \mathbf{E} \cdot d\mathbf{s}$ ; evidently the voltage so

defined will be dependent upon the path (assumed to be in a plane perpendicular to the axis) of integration. This ambiguity, however, will be of no significance if the path used for the computation of the

The problem will be simplified by making certain restrictive assumptions concerning the distributions of charge, current, and field. Consequently the solution will contain only those modes which approximately satisfy the assumed conditions and will not contain the complete set of resonances. In addition, of course, these assumptions introduce some error in the resonances found.

The most interesting modes are those with which the electrons can couple, according to the scheme described in Chap. 1. They require strong electric field lines going from anode segment to anode segment with little axial variation

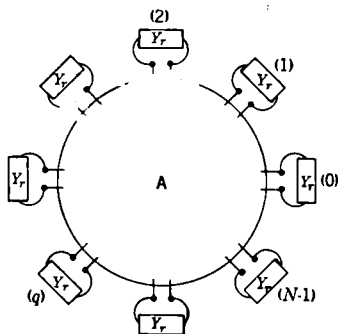


FIG. 2-3.—Circuit representation of the unstrapped resonant system.



admittance of a side resonator coincides with that used for the computation of the admittance of the interaction space.<sup>1</sup> The voltage so obtained has no axial variation. Inasmuch as the magnetic field is axial, the current is entirely transverse and is given by the magnetic field at the terminals  $A$  and  $B$  multiplied by the length of the anode  $h$ . Using current  $I$  and voltage  $V$  as defined above one might take for the admittance  $Y = I/V$ .

There are, however, other possibilities. One can write

$$Y = \frac{I}{V} \frac{V^*}{V^*} = \frac{2P^*}{V^2},$$

where  $P^*$  is the complex conjugate of the complex power (defined as  $\frac{1}{2}VI^*$ ).<sup>2</sup> The complex power can also be written in terms of the Poynting vector

$$P = \frac{1}{2} \int_s \mathbf{E} \times \mathbf{H}^* \cdot \mathbf{n} da,$$

which suggests for the admittance

$$Y = \frac{h \int_A^B \mathbf{E}^* \times \mathbf{H} \cdot \mathbf{n} ds}{\left| \int_A^B \mathbf{E} \cdot d\mathbf{s} \right|^2}, \quad (1)$$

where the path of integration is the same for the two integrals. The expression,  $\frac{1}{2} \int \mathbf{E} \times \mathbf{H}^* \cdot \mathbf{n} da$ , depends upon the surface over which the integration is performed and will, in general, differ from  $\frac{1}{2}VI^*$ . Consequently, the two expressions for admittance will differ; and for reasons to be given in Sec. 2-5, the latter expression is the one that will be used.

Because end-space effects are small in many applications, they have been completely ignored in the suggested equivalent circuit. There are, however, certain applications for which end-space effects are important. These will be discussed in Sec. 2-8.

The problem has now been reduced to the investigation of the circuit properties of the side cavities and of the interaction space. More specifically, it is necessary to calculate the admittance of the side resonators as a function of frequency. It is also necessary to calculate the admittance of the interaction space at any pair of terminals as a function of frequency, with proper restrictions on the admittances seen at the other  $(N - 1)$  pairs of terminals.

Two different approaches will be used. The first consists of representing each circuit element by a lumped-constant network. The magnitude

<sup>1</sup> In order to obtain manageable expressions one often finds it necessary to have the paths coincide only approximately.

<sup>2</sup>  $V$  and  $I$  are the peak rather than the rms values of voltage and current.

of the constants of the network must ordinarily be determined experimentally. The choice of network is at best an intelligent estimate so that the over-all results are ordinarily only semiquantitative. This method, however, has the advantage of simplicity and serves to introduce some important concepts. The second approach involves the calculation of the distribution of electric and magnetic field from which the admittance can be calculated. The main advantages are (1) more accurate results, with no need for guessing networks or for experimental evaluation of parameters, (2) the fact that the field distribution is part of the result.

**2.2. Equivalent Network for the Side Resonators.**—A simple parallel-resonant circuit (Fig. 2-4) will serve as an equivalent network for the side resonators. The admittance is given by the well-known formula

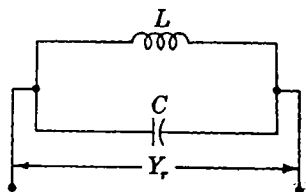


FIG. 2-4.—Equivalent network for a side resonator of an unstrapped resonant system.

$j[\omega C - (1/\omega L)]$ . The values for the inductance and capacitance can be chosen to give the correct value for the resonant frequency  $\omega_0 = 1/\sqrt{LC}$  and the correct admittance at one other frequency. If the range is limited, the intermediate values will be fairly accurate. It is to be noted that there is no resistance in the circuit. In all frequency and field calculations resistive losses will be neglected on the assumption that the

walls are of perfectly conducting material. Actually, the conductivity of materials used is so high as to make errors resulting from this assumption negligible in comparison with others already introduced.

**2.3. Equivalent Network for the Interaction Space.**—The interaction space is represented by the network in Fig. 2-5. This network takes into account capacitance between the anode segments and the cathode. It ignores all inductive effects and capacitive effects among anode segments. It should be most nearly correct when the anode circumference is small compared with the wavelength and the distance between cathode and anode is small compared with the width of the anode segments. (These conditions are rarely met by magnetrons.) It would be possible, but lengthy, to compute the admittance at a set of terminals assuming the admittances  $j[\omega C - (1/\omega L)]$  across the other  $(N - 1)$ -pairs. The problem can, however, be simplified considerably by making use of the symmetry present. Because all the side resonators are identical, the admittance looking into any one of them is the same. At resonance the admittance at the various terminals of the interaction space matches the resonator admittances; thus, at resonance, all of these admittances must be the same. It can also be assumed that the voltage and current distribution in one section differs from that in the adjacent section only

by a phase difference that is constant from section to section.<sup>1</sup> With the above information it is a simple matter to compute the admittance.

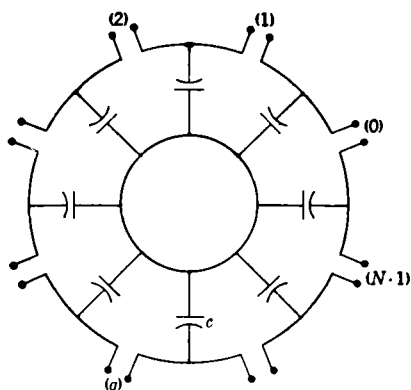


FIG. 2-5.—Equivalent network for the interaction space of an unstrapped resonant system.

The admittance looking into the network (see Fig. 2-6) is given by  $i_q/v_q$ . From Kirchhoff's laws

$$I_{q-1} = i_q - i_{q-1},$$

$$I_q = i_{q+1} - i_q,$$

$$V_{AB} = \frac{I_{q-1}}{j\omega c},$$

$$V_{CD} = \frac{I_q}{j\omega c},$$

and

$$v_q = V_{AB} - V_{CD}.$$

Thus

$$v_q = \frac{I_{q-1} - I_q}{j\omega c} = \frac{2i_q - (i_{q-1} + i_{q+1})}{j\omega c}.$$

From the assumption that corresponding currents in adjacent sections differ only by a constant phase factor it follows that

$$i_{q-1} = i_q e^{-j\gamma} \quad \text{and} \quad i_{q+1} = i_q e^{j\gamma};$$

therefore,

$$v_q = i_q \frac{2 - (e^{j\gamma} + e^{-j\gamma})}{j\omega c},$$

<sup>1</sup> It can be proved from the symmetry that the existence of any resonance for which the above is not true implies the existence of a partner resonance having the same resonant frequency and a distribution of amplitude as assumed. This means, of course, that a degeneracy of at least the second order must exist.

and the admittance  $Y$  is given by

$$Y = \frac{i_q}{v_q} = \frac{j\omega c}{2(1 - \cos \gamma)}.$$

Evidently the admittance of the network depends upon the phase angle  $\gamma$ . So far in this chapter this quantity has not been restricted. Because each section must be in phase with itself,  $e^{iN\gamma}$  must equal 1, and  $N\gamma = 2\pi n$ , where  $n$  is any positive or negative integer or zero. Thus,

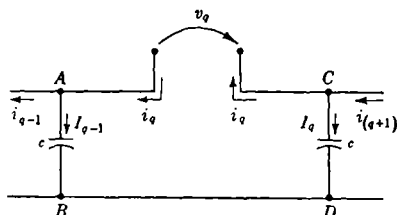


FIG. 2-6.—A single section of the equivalent network for the interaction space.

$$Y_n = \frac{j\omega c}{2 \left( 1 - \cos \frac{2\pi n}{N} \right)}.$$

**2-4. Spectrum Predicted by the Equivalent Network.**—Resonance occurs when the admittance looking out from the side resonators equals the admittance looking into the interaction space, that is, when

$$-j \left( \omega C - \frac{1}{\omega L} \right) = Y_n = \frac{j\omega c}{2 \left( 1 - \cos \frac{2\pi n}{N} \right)},$$

or

$$\frac{1}{\omega L} - \omega C = \frac{\omega c}{2 \left( 1 - \cos \frac{2\pi n}{N} \right)}.$$

By setting  $\omega_0 = 1/\sqrt{LC}$  and  $c/C = \rho$  it is found that

$$\frac{\omega_0^2}{\omega^2} - 1 = \frac{\rho}{2 \left( 1 - \cos \frac{2\pi n}{N} \right)},$$

or

$$\omega = \omega_0 \sqrt{\frac{1}{1 + \frac{\rho}{2 \left( 1 - \cos \frac{2\pi n}{N} \right)}}}. \quad (2)$$

A different resonant frequency is found for each value of  $n$  in the range 0 to  $N/2$  [or  $(N-1)/2$  if  $N$  is odd], after which the values begin to repeat. That is, replacing  $n$  by  $n + mN$  (where  $m$  is an integer) or by  $-n$  leaves  $\omega$  unchanged. A qualitative diagram for the spectrum is given in Fig. 2-7.

Each resonance, together with its associated fields (or voltages and currents), is called a "mode of oscillation" or, more simply, a "mode."

The number  $n$  is called the "mode number." If there are several linearly independent sets of field (or voltage) distributions with the same resonant frequency, the mode is said to be "degenerate," the order of the degeneracy being the same as the number of linearly independent distributions.

All of the modes have a second-order degeneracy excepting those for which  $n = 0$  or  $n = N/2$ . In other words, the same frequency is obtained by replacing  $n$  by  $-n$ , but a linearly independent set of amplitude coefficients  $e^{2\pi i n q/N}$  ( $q$  is the section number) is obtained by replacing  $n$  by  $-n$ , except for  $n = 0$  and  $n = N/2$ .<sup>1</sup>

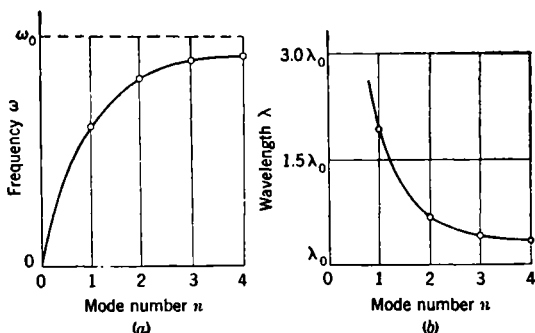


FIG. 2-7.—The spectrum predicted by Eq. (2) with  $\rho = 1$  for an eight-resonator unstrapped system.

The limitations of this equivalent circuit will become apparent after the admittances have been more correctly calculated. It suffices here to note that the circuit gives a good qualitative picture of the order and separation of the longest-wavelength group of magnetron modes. In order to apply the theory quantitatively it is, of course, necessary to evaluate experimentally the parameters  $\rho$  and  $\omega_0$ . The over-all quantitative agreement depends upon the particular way in which these parameters are evaluated. The previous discussion associates  $\omega_0$  with the side resonators alone and suggests that this parameter may be evaluated by means of an experiment involving only the side resonators. For example, one might measure the resonant frequency of the cavity formed by placing two side resonators facing each other. A value of  $\rho$  can then be chosen to give the correct resonant frequency for one of the modes. Under these conditions the predicted spectrum will differ considerably from the observed one. On the other hand, if one chooses  $\rho$  and  $\omega_0$  to give the correct values for the ( $n = 1$ )- and the  $N/2$ -modes, the

<sup>1</sup> While replacing  $n$  by  $n + mN$  leaves the frequency unchanged, it also leaves the amplitude coefficients  $e^{2\pi i n q/N}$  unchanged. The addition of  $mN$  corresponds to an increase in the phase difference between voltages and currents at adjacent sections by  $2\pi m$ , which, of course, has no physical significance.

frequencies of the intermediate modes may be given with reasonable accuracy.<sup>1</sup>

**2-5. Admittance of Side Resonators by Field Theory.**—Consider the side resonator shown in Fig. 2-8, which has an arbitrary cross section and an arbitrary boundary (dotted line) across which the admittance is to be measured. A distribution of the tangential electric field ( $E_t$ ) varying sinusoidally in time with arbitrary frequency  $\omega$  is assumed along this boundary. Because the tangential electric field is zero along the metal walls, it is possible in principle to apply Maxwell's equations and compute the electric field throughout the bounded region. A further application of Maxwell's equations yields the magnetic field throughout the bounded region, and the admittance can then be computed using the formula [from Eq. (1)]

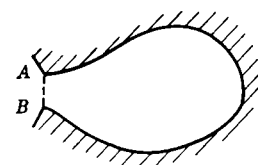


FIG. 2-8.—A side resonator of arbitrary cross section.

$$Y = \frac{h \int E_t^* H_z ds}{\left| \int E_t ds \right|^2},$$

where the integrals are evaluated along the dotted boundary. Evidently the value computed for the admittance depends upon two arbitrary choices: the choice of the boundary across which the admittance is measured and the distribution of tangential electric field assumed along this boundary. The choice of the boundary has no particular significance as long as the boundaries chosen for two adjoining elements (for example—at the junction between the interaction space and a side resonator) coincide. On the other hand, the values found for the resonant frequencies will to some extent depend upon the assumed electric field. Clearly, the proper distribution to use is that which actually obtains at resonance; but because this distribution is ordinarily not known, it is necessary to assume some arbitrary one. Equation (1) is used rather than  $I/V$  for the admittance because it can be shown<sup>2</sup> that resonant frequencies computed on the basis of this expression are considerably less sensitive to the assumed field distribution than are those computed on the basis of  $I/V$ . In the work that follows, the boundary will always

<sup>1</sup> This latter procedure can be justified by improving the equivalent network for the interaction space. That is, one can take into account the capacitance between adjacent anode segments by introducing a capacitance,  $c'$ , between each pair of terminals of the network in Fig. 2-5. In this case Eq. (2) still holds with  $\omega_0$  now given by  $1/\sqrt{L(\bar{C} + c')}$  and  $\rho$  by  $\frac{c}{\bar{C} + c'}$  and thus  $\omega_0$  depends upon the interaction space as well as the side resonators.

<sup>2</sup> N. Kroll and W. Lamb, "The Resonant Modes of the Rising Sun and Other Unstrapped Magnetron Anode Blocks," Appendix I. *J. of Applied Physics*, **19**, 183, (1948).

be chosen so that there is either exact or very near coincidence of boundaries when two elements are joined. The tangential electric field along the boundary will always be assumed constant.

*The Rectangular-slot Side Resonator.*—Differently shaped side resonators must be considered separately. The rectangular slot shown in Fig. 2-9 is considered first because it is the simplest. Maxwell's equations for free space are

$$\text{curl } \mathbf{E} + \frac{\partial \mathbf{B}}{\partial t} = 0, \quad (3)$$

$$\text{curl } \mathbf{H} - \frac{\partial \mathbf{D}}{\partial t} = 0, \quad (4)$$

$$\text{div } \mathbf{D} = 0 \quad (\mathbf{D} = \epsilon_0 \mathbf{E}), \quad (5)$$

and

$$\text{div } \mathbf{B} = 0 \quad (\mathbf{B} = \mu_0 \mathbf{H}). \quad (6)$$

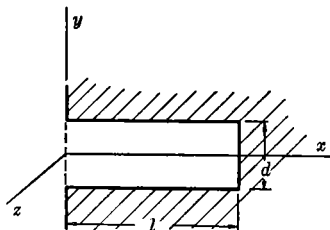


FIG. 2-9.—Rectangular-slot side resonator.

The time variation of all field components is given by  $e^{j\omega t}$  because for an impedance calculation one is concerned only with fields harmonic in time. The operator  $\partial/\partial t$  is then replaced by  $j\omega$ .

It has already been assumed that  $E_z = 0$  ( $E$  is transverse) and that  $\mathbf{E}$  has no axial variation. It follows directly from Eq. (3) that  $\mathbf{H}$  is axial and has no axial variation. That is,

$$H_z = H_z(x, y)e^{j\omega t}, \quad H_x = 0, \quad \text{and} \quad H_y = 0. \quad (7)$$

From Eq. (4) it follows that

$$E_x = -j \sqrt{\frac{\mu_0}{\epsilon_0}} \frac{\partial H_z}{\partial y}, \quad (8)$$

and

$$E_y = j \sqrt{\frac{\mu_0}{\epsilon_0}} \frac{\partial H_z}{\partial x}, \quad (9)$$

where  $\sqrt{\mu_0/\epsilon_0}$  = impedance of free space = 376.6 ohms and

$$k = \omega \sqrt{\mu_0 \epsilon_0} = \frac{2\pi}{\lambda}.$$

By combining Eqs. (3) and (4) it can be shown that  $H_z$ ,  $E_x$ , and  $E_y$  must satisfy the familiar wave equation

$$\nabla^2 F + k^2 F = 0. \quad (10)$$

A distribution of  $\mathbf{E}$  satisfying the following conditions must be found: (1) Its components  $E_x$  and  $E_y$  must satisfy Eq. (10); (2)  $E_y = 0$  at  $x = l$ , and  $E_x = 0$  at  $y = \pm d/2$ , (3)  $E_y$  must have the constant value  $E$  at  $x = 0$ ; and (4) all fields must be continuous. The rectangular-slot

resonator can be thought of as a parallel-plate transmission line or waveguide with planes located at  $y = \pm d/2$  and short-circuited with a plane at  $x = l$ . Assuming  $d < \lambda/2$  (as it always is) the complete fundamental set of fields for a parallel plane waveguide (omitting the time factor  $e^{j\omega t}$ ) is given by

$$\left. \begin{aligned} E_y^{(p)} &= \mp k_x \cos\left(\frac{2\pi p}{d} y\right) e^{\pm k_x x}, \\ E_z^{(p)} &= -\frac{2\pi p}{d} \sin\left(\frac{2\pi p}{d} y\right) e^{\pm k_x x}, \\ H_x^{(p)} &= \frac{jk}{\sqrt{\frac{\mu_0}{\epsilon_0}}} \cos\left(\frac{2\pi p}{d} y\right) e^{\pm k_x x}, \end{aligned} \right\} \quad (11)$$

and

where

$$k_x = \sqrt{\left(\frac{2\pi p}{d}\right)^2 - k^2} \quad (p = \text{any positive integer})$$

and by

$$\left. \begin{aligned} E_y^{(0)} &= \mp jk e^{\pm ikx}, \\ E_z^{(0)} &= 0, \\ H_x^{(0)} &= \frac{jk}{\sqrt{\frac{\mu_0}{\epsilon_0}}} e^{\pm ikx}. \end{aligned} \right\} \quad (12)$$

and

Any field configuration in a parallel-plate section, subject to the condition of no axial variation, must consist of a linear combination of the above fields.<sup>1</sup> Any field so formed satisfies the boundary condition  $E_x[x, \pm(d/2)] = 0$ . Application of the condition that  $E_y$  be constant at  $x = 0$  restricts the solution to a combination of the zero-order fields  $[E_z^{(0)}$  and  $H_x^{(0)}]$ . The requirements remaining are that  $E_y^{(0)} = 0$  at  $x = l$  and  $E_y^{(0)} = E$  at  $x = 0$ . Constants  $\alpha$  and  $\beta$  must be chosen such that

$$(E_y)_{x=l} = -jk(\alpha e^{ikl} - \beta e^{-ikl}) = 0 \quad (13)$$

and

$$(E_y)_{x=0} = -jk(\alpha - \beta) = E. \quad (14)$$

Thus,

$$\alpha = \frac{e^{-ikl}}{e^{-ikl} - e^{ikl}} \left( \frac{E}{-jk} \right); \quad \text{and} \quad \beta = \frac{e^{ikl}}{e^{-ikl} - e^{ikl}} \left( \frac{E}{-jk} \right),$$

which give

$$E_y = \frac{E}{e^{-ikl} - e^{ikl}} [e^{jk(x-l)} - e^{-jk(x-l)}] = E \frac{\sin k(l-x)}{\sin kl}, \quad (15)$$

<sup>1</sup> See, for example, R. I. Sarbacher and W. A. Edson, *Hyper and Ultra-high Frequency Engineering*, Wiley, New York, 1943, pp. 119-132.



and thus

$$H_z = \frac{-jE \cos k(l-x)}{\sqrt{\frac{\mu}{\epsilon}}}, \quad (16)$$

It is now possible to compute the admittance from

$$Y = \frac{h \int_{-\frac{d}{2}}^{\frac{d}{2}} H_z E_y^* dy}{\left| \int_{-\frac{d}{2}}^{\frac{d}{2}} E_y dy \right|^2},$$

to be evaluated at  $x = 0$ .

Because  $E_y$  and  $H_z$  are both independent of  $y$ , the integrations are trivial and

$$Y = \frac{-jh}{\sqrt{\frac{\mu_0}{\epsilon_0}} d} \cot kl, \quad (17)$$

which is the well-known form for the admittance of a short-circuited transmission line of length  $l$  and surge admittance  $\frac{h}{d \sqrt{\mu_0/\epsilon_0}}$ .

*The Cylindrical Side Resonator.*—In solving for the admittance of the cylindrical resonator shown in Fig. 2-10, the cylindrical coordinates  $\rho$ ,  $\phi$ , and  $z$  are preferable. Assuming as before that  $E_z = 0$  and that  $\mathbf{E}$  has no axial variation, it follows from Maxwell's equations that

$$H_z = H_z(\rho, \phi) e^{j\omega t}, \quad (18)$$

$$H_\rho = H_\phi = 0,$$

$$E_\rho = \frac{-j \sqrt{\frac{\mu_0}{\epsilon_0}}}{k\rho} \frac{\partial H_z}{\partial \phi}, \quad (19)$$

and

$$E_\phi = \frac{j \sqrt{\frac{\mu_0}{\epsilon_0}}}{k} \frac{\partial H_z}{\partial \rho}. \quad (20)$$

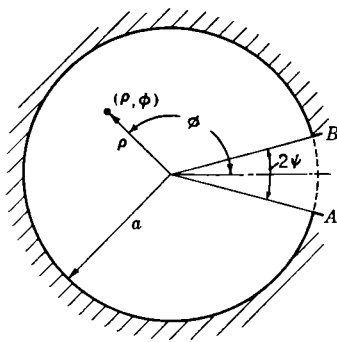


FIG. 2-10.—Cylindrical resonator.

The fundamental set of solutions for the wave equation in cylindrical coordinates are the functions

$$J_p(k\rho) e^{jp\phi}$$

and

$$N_p(k\rho) e^{jp\phi},$$

where  $p$  is zero or any positive or negative integer and  $J_p$  and  $N_p$  are the well-known Bessel and Neumann functions.<sup>1</sup> The functions  $J_p$  are regular at  $\rho = 0$ , whereas the functions  $N_p$  become infinite at the origin. For this problem only the functions  $J_p$  need to be considered, since the solution must be regular at the origin. Taking

$$H_z^{(p)} = J_p(k\rho)e^{ip\phi} \quad (21)$$

it follows from Eqs. (19) and (20) that

$$E_\rho^{(p)} = \frac{p\sqrt{\frac{\mu_0}{\epsilon_0}}}{k\rho} J_p(k\rho)e^{ip\phi}, \quad (22)$$

and

$$E_\phi^{(p)} = j\sqrt{\frac{\mu_0}{\epsilon_0}} J'_p(k\rho)e^{ip\phi}. \quad (23)$$

A linear combination of these functions is required such that  $E_\phi = 0$  at  $\rho = a$  when  $\psi \leq \phi \leq (2\pi - \psi)$  and  $E_\phi =$  the constant  $E$  at  $\rho = a$  when  $-\psi < \phi < \psi$ . Such a combination can be found by making a Fourier expansion for  $E_\phi$  in terms of the functions  $E_\phi^{(p)}$ . Thus

$$E_\phi = j\sqrt{\frac{\mu_0}{\epsilon_0}} \sum_{p=-\infty}^{\infty} C_p J'_p(k\rho)e^{ip\phi}, \quad (24)$$

where the constants  $C_p$  are to be determined.

$$(E_\phi)_{\rho=a} = j\sqrt{\frac{\mu_0}{\epsilon_0}} \sum_{p=-\infty}^{\infty} C_p J'_p(ka)e^{ip\phi} = f(\phi), \quad (25)$$

where

$$f(\phi) = 0 \quad \text{for } \psi \leq \phi \leq 2\pi - \psi,$$

and

$$f(\phi) = E \quad \text{for } -\psi < \phi < \psi.$$

The constants  $C_p$  will be given by

$$\begin{aligned} j\sqrt{\frac{\mu_0}{\epsilon_0}} C_p J'_p(ka) &= \frac{1}{2\pi} \int_0^{2\pi} e^{-ip\phi} f(\phi) d\phi = \frac{E}{2\pi} \int_{-\psi}^{\psi} e^{-ip\phi} d\phi \\ &= \frac{E\psi}{\pi} \left( \frac{\sin p\psi}{p\psi} \right) \quad \text{for } p \neq 0, \\ &= \frac{E\psi}{\pi} \quad \text{for } p = 0. \end{aligned}$$

<sup>1</sup> See, for example, J. A. Stratton, *Electromagnetic Theory*, McGraw-Hill, New York, 1941, pp. 351-360.

Thus

$$E_{\phi}(\rho, \phi) = \frac{E\psi}{\pi} \sum_{p=-\infty}^{\infty} \frac{J'_p(k\rho)}{J'_p(ka)} \left( \frac{\sin p\psi}{p\psi} \right) e^{ip\phi},$$

$$E_{\rho}(\rho, \phi) = \frac{-jE\psi}{\pi k\rho} \sum_{p=-\infty}^{\infty} p \frac{J_p(k\rho)}{J'_p(ka)} \left( \frac{\sin p\psi}{p\psi} \right) e^{ip\phi},$$

and

$$H_z(\rho, \phi) = -j\sqrt{\frac{\epsilon_0}{\mu_0}} \frac{E\psi}{\pi} \sum_{p=-\infty}^{\infty} \frac{J_p(k\rho)}{J'_p(ka)} \left( \frac{\sin p\psi}{p\psi} \right) e^{ip\phi}.$$

Because  $J_p = (-1)^p J_{-p}$ , the above relations can be rewritten as

$$E_{\phi}(\rho, \phi) = \frac{E\psi}{\pi} \left[ \frac{J'_0(k\rho)}{J'_0(ka)} + 2 \sum_{p=1}^{\infty} \left( \frac{\sin p\psi}{p\psi} \right) \frac{J'_p(k\rho)}{J'_p(ka)} \cos p\phi \right],$$

$$E_{\rho}(\rho, \phi) = \frac{2E\psi}{\pi k\rho} \sum_{p=1}^{\infty} p \left( \frac{\sin p\psi}{p\psi} \right) \frac{J_p(k\rho)}{J'_p(ka)} \sin p\phi, \quad (26)$$

and

$$H_z(\rho, \phi) = -j\sqrt{\frac{\mu_0}{\epsilon_0}} \frac{E\psi}{\pi} \left[ \frac{J_0(k\rho)}{J'_0(ka)} + 2 \sum_{p=1}^{\infty} \left( \frac{\sin p\psi}{p\psi} \right) \frac{J_p(k\rho)}{J'_p(ka)} \cos p\phi \right].$$

For a calculation of admittance,  $H_z(a, \phi)$  is required for  $-\psi < \phi < \psi$  and  $E_{\phi}(a, \phi)$  over the same range. Now

$$E_{\phi}(a, \phi) = E \quad \text{for } -\psi < \phi < \psi,$$

and

$$H_z(a, \phi) = -j\sqrt{\frac{\epsilon_0}{\mu_0}} \frac{E\psi}{\pi} \left[ \frac{J_0(ka)}{J'_0(ka)} + 2 \sum_{p=1}^{\infty} \left( \frac{\sin p\psi}{p\psi} \right) \frac{J_p(ka)}{J'_p(ka)} \cos p\phi \right]. \quad (27)$$

The admittance looking in across the boundary indicated in Fig. 2-10 is given by

$$Y = \frac{-h \int_{-\psi}^{\psi} a E_{\phi}^*(a, \phi) H_z(a, \phi) d\phi}{\left[ \int_{-\psi}^{\psi} a E_{\phi}(a, \phi) d\phi \right]^2},$$

which yields

$$Y = \frac{+hj\sqrt{\frac{\epsilon_0}{\mu_0}} \frac{E^2\psi a}{\pi} \left[ 2\psi \frac{J_0(ka)}{J'_0(ka)} + 2 \sum_{p=1}^{\infty} \left( \frac{\sin p\psi}{p\psi} \right) \frac{J_p(ka)}{J'_p(ka)} \left( \frac{2 \sin p\psi}{p} \right) \right]}{[2\psi a E]^2}$$

$$= j\sqrt{\frac{\epsilon_0}{\mu_0}} \frac{h}{2\pi a} \left[ \frac{J_0(ka)}{J'_0(ka)} + 2 \sum_{p=1}^{\infty} \left( \frac{\sin p\psi}{p\psi} \right)^2 \frac{J_p(ka)}{J'_p(ka)} \right]. \quad (28)$$

Although the admittance function looks complicated, it is not difficult to compute for low frequencies.<sup>1</sup> Like all admittances in lossless systems, this admittance has a slope that is always positive (neglecting the factor  $j$ ); and like that of the rectangular resonator, it has an infinite set of resonances which are alternately series and parallel. The series resonances occur at the roots of  $J'_p(ka)$ , and a parallel resonance occurs between each pair of series resonances.

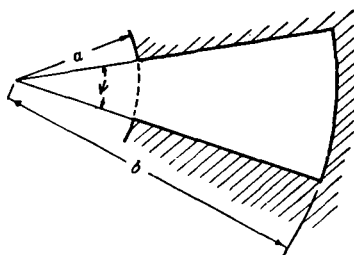


FIG. 2-11.—Annular-sector resonator.

*The Annular-sector Resonator.*—One of the most common resonator shapes is the annular-sector resonator shown in Fig. 2-11, which is often referred to as the “vane type” resonator. Application of the methods used in the preceding paragraphs leads to the following expression for the admittance.<sup>2</sup>

$$Y = j \sqrt{\frac{\epsilon_0}{\mu_0}} \frac{h}{\psi a} \frac{[J_0(ka)][N_1(kb)] - [J_1(kb)][N_0(ka)]}{[J_1(ka)][N_1(kb)] - [J_1(kb)][N_1(ka)]} \quad (29)$$

This function behaves very much like the other admittance functions. In fact  $Y$  approaches  $[-j \sqrt{(\epsilon_0/\mu_0)} (h/\psi a) \cot k(b-a)]$  as  $k$  becomes large.

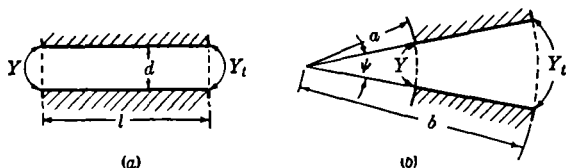


FIG. 2-12.—Arbitrary terminations: (a) for a rectangular-slot resonator; (b) for an annular-sector resonator.

*Transformation Formulas.*—Because many side resonators are of composite shape, for example, a rectangular slot or annular sector terminated by a hole, transformation formulas giving the admittance at the front of the resonator in terms of the admittance at the back are useful. For the rectangular slot (Fig. 2-12a)

$$Y = \frac{h}{d} j \sqrt{\frac{\epsilon_0}{\mu_0}} \frac{\sin kl + \frac{Y_t}{(jh/d) \sqrt{\epsilon_0/\mu_0}} \cos kl}{\cos kl - \frac{Y_t}{(jh/d) \sqrt{\epsilon_0/\mu_0}} \sin kl}; \quad (30)$$

<sup>1</sup> See Sec. 2-11.

<sup>2</sup> In practice the center of curvature of the rear surface often coincides with the center of the magnetron rather than with the center of curvature of the annular sector. The error in  $Y$ , however, is negligible if one takes for  $b$  the dimension indicated in Fig. 2-11.

for the annular sector (Fig. 2-12b)

$$Y = j \sqrt{\frac{\epsilon_0}{\mu_0}} \frac{h}{\psi a} \frac{J_0(ka) - \frac{J_1(kb)Y_t - j\sqrt{(\epsilon_0/\mu_0)}(h/\psi b)J_0(kb)}{N_1(kb)Y_t - j\sqrt{(\epsilon_0/\mu_0)}(h/\psi b)N_0(kb)} N_0(ka)}{J_1(ka) - \frac{J_1(kb)Y_t - j\sqrt{(\epsilon_0/\mu_0)}(h/\psi b)J_0(kb)}{N_1(kb)Y_t - j\sqrt{(\epsilon_0/\mu_0)}(h/\psi b)N_0(kb)} N_1(ka)} \quad (31)$$

Although these formulas allow for a change in height at the junction, they are considerably less dependable when such a change occurs.

**2-6. Admittance of the Interaction Space by Field Theory.**—The admittance of the interaction space (Fig. 2-13) is evaluated by applying the methods used for the circular resonator combined with those used for handling the lumped-constant equivalent of the interaction space. Again it is convenient to use cylindrical coordinates. In the following derivations  $N$  = the number of anode-block segments,  $r_a$  = the anode radius,  $r_c$  = the cathode radius, and  $2\theta$  = the angle subtended by the space between the segments of the anode block. It will be assumed that  $E_\phi$  across each gap is constant and further that the field at any gap differs from the field at an adjacent gap only by a constant phase factor. At the cathode and at the anode segments  $E_\phi$  must, of course, be zero. Explicitly, the boundary conditions for  $E_\phi$  are as follows:

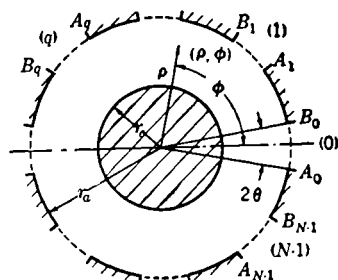


FIG. 2-13.—The interaction space of an unstrapped resonant system.

$$E_\phi(r_c, \phi) = 0, \\ E_\phi(r_a, \phi) = E e^{j2\pi n/Nq} \quad \text{for } \left(\frac{2\pi q}{N} - \theta\right) < \phi < \left(\frac{2\pi q}{N} + \theta\right), \quad (32)$$

and

$$E_\phi(r_a, \phi) = 0$$

for all other values of  $\phi$ . In Eqs. (32),  $q$  is the gap number and has the values 0 to  $N - 1$ , and  $n$  is an integer. As in the solution of the circular resonator, the solution for the interaction space is compounded out of the functions

$$J_\gamma(k\rho)e^{i\gamma\phi} \text{ and } N_\gamma(k\rho)e^{i\gamma\phi}.$$

In this problem it is necessary to use both functions to ensure  $E_\phi = 0$  at  $\rho = r_c$ . It is evident that the following set satisfies this condition.

$$\left. \begin{aligned} H_z^{(\gamma)}(\rho, \phi) &= Z_\gamma(k\rho) e^{i\gamma\phi} = \left[ J_\gamma(k\rho) - \frac{J'_\gamma(kr_c)}{N'_\gamma(kr_c)} N_\gamma(k\rho) \right] e^{i\gamma\phi}, \\ E_\rho^{(\gamma)}(\rho, \phi) &= \frac{\gamma \sqrt{\frac{\mu_0}{\epsilon_0}}}{k\rho} Z_\gamma(k\rho) e^{i\gamma\phi}, \\ E_\phi^{(\gamma)}(\rho, \phi) &= j \sqrt{\frac{\mu_0}{\epsilon_0}} Z'_\gamma(k\rho) e^{i\gamma\phi} = j \sqrt{\frac{\mu_0}{\epsilon_0}} \left[ J'_\gamma(k\rho) - \frac{J'_\gamma(kr_c)}{N'_\gamma(kr_c)} N'_\gamma(k\rho) \right] e^{i\gamma\phi}. \end{aligned} \right\} \quad (33)$$

A linear combination of the functions  $E_\phi^{(\gamma)}(\rho, \phi)$  that will satisfy the conditions stated at  $\rho = r_a$  can be found, as they were for the circular resonator, by making a Fourier expansion. Thus

$$E_\phi = j \sqrt{\frac{\mu_0}{\epsilon_0}} \sum_{\gamma=-\infty}^{\infty} C_\gamma Z'_\gamma(k\rho) e^{i\gamma\phi}. \quad (34)$$

The constants  $C_\gamma$  are determined by

$$E_\phi(r_a, \phi) = j \sqrt{\frac{\mu_0}{\epsilon_0}} \sum_{\gamma=-\infty}^{\infty} C_\gamma Z'_\gamma(kr_a) e^{i\gamma\phi} = f(\phi), \quad (35)$$

where

$$f(\phi) = E e^{i(2\pi n/N)\phi} \quad \text{for } \left( \frac{2\pi q}{N} - \theta \right) < \phi < \left( \frac{2\pi q}{N} + \theta \right)$$

and  $f(\phi) = 0$ , for all other values of  $\phi$ .

Then

$$\begin{aligned} j \sqrt{\frac{\mu_0}{\epsilon_0}} C_\gamma Z'_\gamma(kr_a) &= \frac{1}{2\pi} \int_0^{2\pi} e^{-i\gamma\phi} f(\phi) d\phi, \\ &= \frac{E}{2\pi} \sum_{q=0}^{N-1} e^{i(2\pi n/N)\phi} \int_{2\pi q/N - \theta}^{2\pi q/N + \theta} e^{-i\gamma\phi} d\phi, \\ &= \frac{E\theta}{\pi} \frac{\sin \gamma\theta}{\gamma\theta} \sum_{q=0}^{N-1} e^{i(2\pi n/N)\phi} e^{-i(2\pi q/N)\phi}, \\ &= E \frac{N\theta}{\pi} \frac{\sin \gamma\theta}{\gamma\theta} \quad \text{for } \gamma = n + mN, \end{aligned}$$

where  $m$  is any integer

= 0 otherwise.

Thus the fields are given by

$$\left. \begin{aligned}
 E_\theta(\rho, \phi) &= E \frac{N\theta}{\pi} \sum_{m=-\infty}^{\infty} \left( \frac{\sin \gamma\theta}{\gamma\theta} \right) \frac{Z'_\gamma(k\rho)}{Z'_\gamma(kr_a)} e^{i\gamma\phi}, \\
 E_\rho(\rho, \phi) &= -jE \frac{N\theta}{\pi k\rho} \sum_{m=-\infty}^{\infty} \gamma \left( \frac{\sin \gamma\theta}{\gamma\theta} \right) \frac{Z_\gamma(k\rho)}{Z'_\gamma(kr_a)} e^{i\gamma\phi}, \\
 \text{and} \\
 H_z(\rho, \phi) &= -j \sqrt{\frac{\epsilon_0}{\mu_0}} \frac{EN\theta}{\pi} \sum_{m=-\infty}^{\infty} \left( \frac{\sin \gamma\theta}{\gamma\theta} \right) \frac{Z_\gamma(k\rho)}{Z'_\gamma(kr_a)} e^{i\gamma\phi}.
 \end{aligned} \right\} \gamma = n + mN \quad (36)$$

The admittance looking in across the boundary indicated in Fig. 2-13 at the  $q$ th opening is given by

$$Y = \frac{-h \int_{(2\pi q/N) - \theta}^{(2\pi q/N) + \theta} r_a E_\phi^*(r_a, \phi) H_z(r_a, \phi) d\phi}{\left[ \int_{(2\pi q/N) - \theta}^{(2\pi q/N) + \theta} r_a E_\phi(r_a, \phi) d\phi \right]^2},$$

which yields

$$Y_n = j \sqrt{\frac{\epsilon_0}{\mu_0}} \frac{Nh}{2\pi r_a} \sum_{m=-\infty}^{\infty} \left( \frac{\sin \gamma\theta}{\gamma\theta} \right)^2 \frac{Z_\gamma(kr_a)}{Z'_\gamma(kr_a)}, \quad (37)$$

when  $\gamma = n + mN$ .

It is evident that as a result of the assumption concerning  $E_\phi$  at the anode radius, the admittance looking in at each gap is the same. This is a condition which is obviously necessary for resonance. The functions

$$\sum_{m=-\infty}^{\infty} \left( \frac{\sin \gamma\theta}{\gamma\theta} \right)^2 \frac{Z_\gamma(kr_a)}{Z'_\gamma(kr_a)}$$

will henceforth be designated by the symbol  $\sum_n (kr_a)$ . The dependence of the admittance on both frequency and  $n$  is contained in these functions. As in the solution for the equivalent circuit, only values of  $n$  from 0 to  $N/2$  or to  $(N-1)/2$  need to be considered because the functions are not changed when  $n$  is replaced by  $-n$  or by  $n + mN$ .

The low-frequency behavior of the admittances  $Y_n$  as predicted by the field theory (Fig. 2-14) is qualitatively similar to that predicted from the lumped-circuit network. As the frequency approaches zero, the values of  $Y_n$  for  $n \neq 0$  approach zero with finite positive slope in either case. Furthermore this slope decreases as  $n$  increases. On the other hand, the ratio of these slopes for different  $n$  as predicted by the field

theory is quite different from that predicted by the lumped-circuit network. For  $n = 0$  the behavior in the two cases is also somewhat similar, because  $Y_0$  is infinite according to the lumped-circuit network,

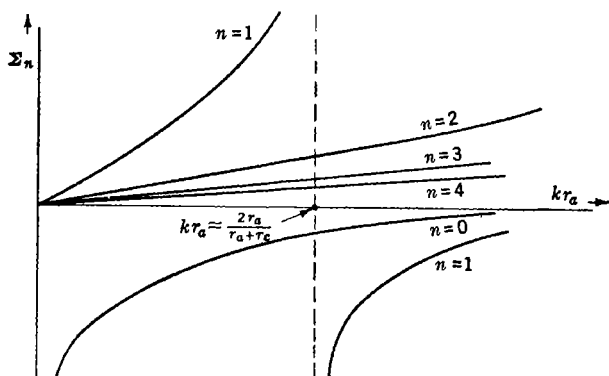


FIG. 2-14.—The qualitative behavior of the admittance functions for an interaction space with  $N = 8$  [see Eq. (37)].

whereas the field theory predicts that it will approach minus infinity as the frequency approaches zero. In addition the field theory predicts an infinite set of alternately series and parallel resonances (indicated by the infinities and zeros of the admittance functions) for each of the admittances, which have been omitted by the lumped-circuit network.

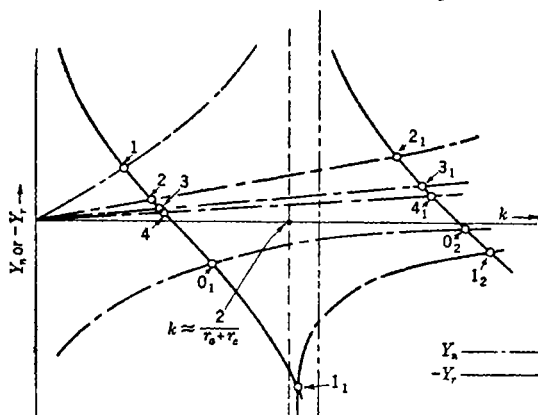


FIG. 2-15.—Graphical representation of the resonance equation  $Y_n = -Y_r$ . The first asymptote corresponds to the first series resonance of  $Y_1$ ; the second to the first series resonance of  $Y_r$ .

**2.7. The Spectrum Predicted by Field Theory.**—As in Sec. 2.4 the spectrum is found by setting the admittance looking out from a side resonator (the negative of the admittance looking in) equal to the



admittance looking into the interaction space. That is,  $Y_n + Y_r = 0$  at resonance, where  $Y_r$  is the admittance of a side resonator. Since both functions involve the frequency in a complicated way, it is best to solve the problem graphically by plotting both admittances as a function of  $k$  as shown in Fig. 2-15. The resonances are those values of  $k$  at which intersection occurs. A typical spectrum as predicted by the theory appears in Fig. 2-16. A comparison with the spectrum of the equivalent circuit shows a qualitative similarity for the resonances with wavelengths longer than that of the first parallel resonance of the side resonators. As are those of the equivalent circuit, each resonance predicted by field theory is a doublet (degeneracy of order 2) except those for which  $n = 0$  or  $N/2$  (these are nondegenerate). This result follows from the fact that although the same wavelength is obtained for  $-n$  as for  $n$  (except in the case of  $n = 0$  and  $n = N/2$ ), the electromagnetic field is different and the two fields are linearly independent. The equivalent-circuit theory

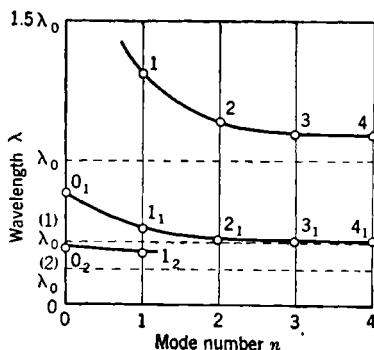


FIG. 2-16.—Typical spectrum predicted for an eight-resonator resonant system. Only the larger wavelength groups are shown. The  $\lambda_0^{(p)}$  are the parallel resonances ( $Y_r = 0$ ) of the side resonators,  $\lambda_0^{(p)}$  being the  $p + 1$  parallel resonance.

has missed all of the resonances that occur at frequencies higher than that of the first parallel resonance of the side resonators. The equivalent-circuit representation is considerably improved in this respect if the side resonators are represented by short-circuited transmission lines instead of by simple lumped LC-circuits.

Inasmuch as there are an infinite number of resonances associated with each value of  $n$ ,  $n$  is inadequate for designating a particular mode. Henceforth  $n$  will be used to designate a principal resonance,

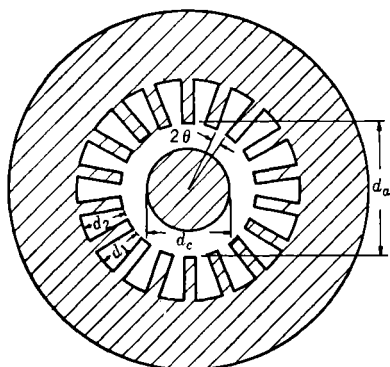


FIG. 2-17.—Cross section of an 18-resonator unstrapped resonant system.

that is, a resonance of the first group or the lowest-frequency root of the resonance equation. Resonances of the  $p$ th higher-order group [that is, members of the  $(p + 1)$ -group or the  $(p + 1)$ -root of the frequency equation] will be designated by  $n_p$ .

The most important features of the spectrum can be best described in terms of a specific example. The 18-resonator anode shown in Fig. 2-17 will be used. Only relative dimensions are significant, and accordingly all dimensions are given as fractions of the 9-mode wavelength. The dimensions and the wavelengths of the members of the first group are given in Table 2-1. The most significant feature of this

TABLE 2-1.—THE FIRST GROUP OF RESONANCES OF AN UNSTRAPPED RESONANT SYSTEM\*

$n$	$\frac{\lambda_n}{\lambda_9}$
1	1.840
2	1.226
3	1.104
4	1.055
5	1.030
6	1.016
7	1.007
8	1.003
9	1.000

\* Dimensions (see Fig. 2-17):

$$\begin{aligned} \frac{d}{\lambda_9} &= 0.170 & (d = d_1 = d_2) & \quad \frac{d_a}{\lambda_9} = 0.325 \\ \frac{d_e}{d_a} &= 0.595 & & \quad \theta = 0.068 \text{ radian} \end{aligned}$$

spectrum from the point of view of magnetron operation is the bunching together of the resonances for large  $n$ . Furthermore, as  $N$  increases, the separation between the  $(N/2)$ -mode and its neighboring modes decreases rapidly.<sup>1</sup> By a proper variation of parameters the separation of these modes can be somewhat increased. In general, the separation between modes is increased by increasing the cathode diameter, increasing the anode diameter, and increasing the width of the resonator openings as compared with the width of the anode segments. The separation is also increased by using a resonator shape that yields a slow variation of admittance with frequency.<sup>2</sup> There are, however, practical limitations that prevent any of these factors from being sufficiently altered to obtain a well-separated 9-mode.

The higher groups of resonances are similar in character to the first group, except, of course, that the frequencies are much higher. Ordinarily, the higher groups of resonances are of little interest in magnetron operation and, therefore, are not usually studied in detail. Attempts

<sup>1</sup> The separation between the  $(N/2)$ -mode and the  $(\frac{N}{2} - 1)$ -mode varies approximately as  $(1/N^2)(r_a/N\lambda)$ .

<sup>2</sup> It is interesting to observe that all of these variations can be interpreted physically as means of increasing the ratio of the capacitance between the cathode and the anode segments to the capacitance of the resonator. In the equivalent-circuit theory this parameter alone determines the mode separation.

have been made, however, to operate magnetrons in the ( $n = 0$ )-mode of the second group. This mode has the advantage of being well separated from other modes and of being nondegenerate.

**2.8. End-space Effects.**—Up to this point the problem of the end spaces has been completely ignored. In order to discuss their effects, it is necessary to abandon the circuit analogies of the preceding sections and reconsider the problem from the point of view of field theory.

The simplest kind of end-space problem, and one that can be solved exactly, is that of the closed-end anode block illustrated in Fig. 2-18. By considering the entire anode block as a section of waveguide of unusual cross section, the problem can be reduced to that of a section of waveguide with shorting plates at both ends. From this point of view the magnetron modes previously discussed are transverse electric or  $TE$ -modes because the electric field has no axial component. The resonances of the cavity will occur when the guide is an integral number of half wavelengths long, the wavelength being measured along the guide; that is, the resonance occurs when  $\lambda_{gn} = 2h/p$ , where  $p$  is an integer greater than or equal to 1. The guide wavelength  $\lambda_{gn}$  depends on the frequency and the mode according to the well-known formula

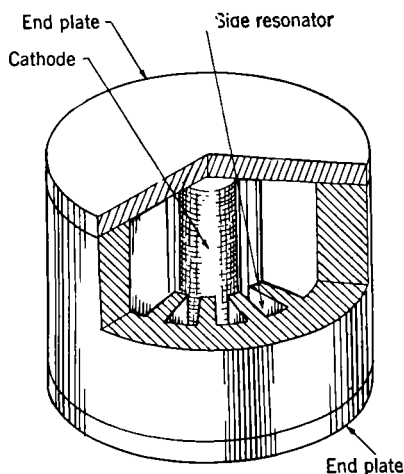


FIG. 2-18.—Cutaway view of closed-end resonant system.

$$\lambda_{gn} = \frac{\lambda}{\sqrt{1 - \left(\frac{\lambda}{\lambda_{cn}}\right)^2}}, \quad (38)$$

where  $\lambda_{cn}$  is the cutoff wavelength for the mode in question. Thus the problem of finding the resonant frequencies has been reduced to the problem of finding the cutoff wavelengths for the anode block considered as a section of waveguide. It will be shown that the resonances found in the preceding section correspond to these cutoff wavelengths.

The cutoff wavelengths of a  $TE$ -mode in a waveguide are determined by the condition that the equation

$$\nabla^2 H_z + \left(\frac{2\pi}{\lambda_c}\right)^2 H_z = 0 \quad (39)$$

have a continuous solution with continuous first derivatives and that it satisfy the boundary condition that the normal derivative of  $H_z$ ,  $\partial H_z / \partial n$ , be zero at the boundary. This condition is equivalent to the requirement that the tangential electric field be zero at the boundaries. The fields and their associated wavelengths found in the preceding section satisfy the differential Eq. (39) and the above boundary condition. Furthermore, the fields are continuous except perhaps at a junction between regions of different geometry.

The situation at a junction must be considered in detail. It simplifies matters to consider the specific case of the junction between a rectangular side resonator and the interaction space shown in Fig. 2-19. The fields in the two regions have been expressed in two different coordinate systems. It is assumed that the arc of the circle  $\rho = r_a$  and the straight

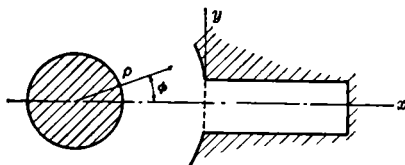


FIG. 2-19.—Junction of a side resonator with the interaction space.

line  $x = 0$  coincide across the resonator opening. As a corollary it follows that the  $y$  direction coincides with the  $\phi$  direction and the  $x$  direction with the  $\rho$  direction. If the voltage is considered to be continuous at the junction, it follows that  $E_\phi$  is equal to  $E_y$  at the junction because both are constant across the resonator opening, and the voltage is given by the electric fields  $E_\phi$  or  $E_y$  times the opening width. In Sec. 2-7 it was asserted that resonance occurs when the admittances at a junction match. Thus taking the voltage as continuous also ensures that the quantity  $\int E_y^* H_z dy$  is continuous at the junction. Because  $E_y^*$  is constant,  $\int H_z dy$  and, therefore, average values of the magnetic fields match at the junction. The magnetic field as given by the side-resonator function is constant along the junction, whereas that given by the interaction-space function  $H_z(a, \phi)$  is not. Therefore, the magnetic field cannot be continuous at the junction. If, however, the gap is narrow,  $H_z(a, \phi)$  will vary only a small amount and the discontinuity in the magnetic field will be small because the average values match. The electric-field component that is normal to the boundary,  $E_\rho$  or  $E_x$ , is also discontinuous across the junction boundary, for  $E_x$  is zero while  $E_\rho$  is not. However,  $E_\rho$  is small except very near the edges, where it becomes infinite. Therefore the fields are approximately continuous for a narrow opening.<sup>1</sup>

<sup>1</sup> The discontinuity, of course, is due to the fact that the tangential electric field has been assumed to be constant along the junction boundary. Had the correct

Thus, the resonant wavelengths computed in Sec. 2-7 should correspond closely to the required cutoff wavelengths, and from them the resonances of the closed-end anode can be computed. The experimental agreement is good; even with  $N\theta = 0.5$  and  $2\pi\tau_a/\lambda = 1.5$  the results are dependable within approximately 1 per cent.

The accuracy of the admittance matching method used in this chapter can be improved by finding a better approximation for the tangential electric field at the bounding surfaces. One can set up an integral equation for this field, and it should be possible to find approximate solutions. Such methods have been very useful in the treatment of problems involving waveguide junctions and obstacles in waveguides.<sup>1</sup> No attempt has yet been made, however, to apply these methods to the magnetron problem. As a matter of fact, the error involved in the treatment (or nontreatment) of the end spaces is such as to make more accurate values of the cutoff wavelengths of little use for most purposes.

There are other methods, based on field theory alone, for computing the cutoff wavelengths. One of these is the "relaxation method,"<sup>2</sup> which is essentially a method of successive approximations. While in principle one can achieve any desired degree of accuracy using this method, one finds in practice that a considerably longer computation time is required to achieve accuracy comparable to that achieved by the method outlined here, particularly when a large number of modes is involved. On the other hand the method of this chapter is limited to cases in which the resonant system can be split into regions of simple geometry, for which analytic solutions are possible. For resonant systems involving more complicated resonator shapes or resonant systems in which, for example, the anode segments are not all equidistant from the center of the magnetron, the relaxation method is very useful.

The problem discussed above is idealized; any magnetron must have its cathode insulated from its anode. However, an anode block with closed-end resonators that has an open interaction space approximates closely the anode block just discussed. All wavelengths, however, are somewhat higher than computed; for the large  $n$ -modes the change is about 1 to 2 per cent, but the ( $n = 1$ )-mode may be affected a great deal—as much as 25 per cent or more. It must also be remembered that the cathode is not usually a simple cylinder as assumed but may have end shields or other irregularities. This effect is usually small and can be accurately estimated after some experience.

---

distribution, which is unknown, been chosen for this field component, it would have been possible to find a frequency value for which all of the components would be continuous.

<sup>1</sup> See Vol. 10 of the Radiation Laboratory Series.

<sup>2</sup> D. N. de G. Allen, L. Fox, H. Motz, and R. V. Southwell, *Phil. Trans. Roy. Soc.*, Series C4, I, 85 (1942); H. Ashcroft and C. Hurst, CVD Report WR-1558.

The usual end-space problem is much more complicated than the one just discussed. Most magnetrons with symmetric unstrapped resonant systems have an open-end anode block with an empty region on either end. In previous sections it was assumed that end conditions were such that there was no axial variation of the fields in the side resonators or the interaction space. For many open-end anode blocks this is a fairly good approximation; when anodes are longer than  $0.4\lambda$  and have end-spaces deeper than  $0.2\lambda$ , the modes for which  $n$  is greater than 1 agree within 2 or 3 per cent with the computed values. The experimental values are lower than the computed values. The  $(n = 1)$ -mode is often depressed by more than 10 per cent. The general character of the spectrum and the relative separations, except for the  $(n = 1)$ -mode, are accurately given.

In the case of magnetrons operating at wavelengths greater than 10 cm, both the anode-block height and end-space height are usually small compared with the wavelength. (The anode height is usually less than  $\frac{1}{2}\lambda_N$ , and the end-space height less than  $\frac{1}{10}\lambda_N$ .) Under these conditions the observed spectrum is quite different from that computed in the preceding sections. One finds the order of modes reversed; that is, the wavelengths increase rather than decrease as the mode number increases.<sup>1</sup>

The most extensive discussion of this effect appears in a report by J. C. Slater,<sup>2</sup> which contains plots of the observed dependence of wavelength upon the heights of the block and the end spaces for an eight-resonator hole-and-slot anode block. One finds that the end-space height below which the order of modes is reversed decreases as the anode height is increased. From the point of view of application it is significant to note that the separation between the  $(N/2)$ - and  $\left(\frac{N}{2} - 1\right)$ -modes is small regardless of the order.

It is evident that an adequate theoretical treatment of the end spaces applicable to short end spaces and small anode height would be desirable. Flux plotting methods<sup>3</sup> have been developed which permit an accurate

<sup>1</sup> A good qualitative picture of the phenomena can be obtained by assuming the capacitances  $c$  in Fig. 2-5 shunted by inductances  $l$  and by assuming a particular dependence of  $c/C$  and  $L/l$  upon the height of the block and the end spaces. The required dependence upon the height of the block is, however, quite different from what one would expect physically. For further details see J. W. Dungey and R. Latham, "The Frequencies of the Resonant Modes of Magnetrons," CVD Report WR-1223, July 14, 1944.

<sup>2</sup> J. C. Slater, "Resonant Modes of the Magnetron," RL Report No. 43-9, Aug. 31, 1942, pp. 15-20.

<sup>3</sup> P. D. Crout, "The Determination of Fields Satisfying Laplace's, Poisson's, and

treatment of the end spaces. Calculations have been carried through for an unstrapped anode block with end spaces and anode height such that the modes occur in reverse order, and very good agreement with experiment has been obtained. In addition, both the previously mentioned relaxation method and the admittance matching method used in this chapter might in principle be extended to include the end spaces. The computations, however, become very laborious, and no such calculations have been carried through with satisfactory accuracy.

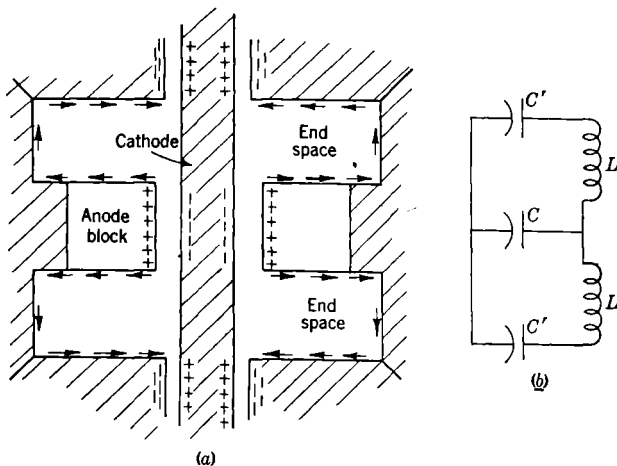


FIG. 2-20.—(a) Longitudinal cross section of a magnetron anode block showing the charge distribution and the direction of the impending current flow for a typical end-space resonance; (b) equivalent circuit for the end-space resonance.

As pointed out in Sec. 2-1, the assumptions made prevent the resultant spectrum from being complete. There are an infinity of resonances that do not even approximately satisfy the assumed conditions. Ordinarily these are short-wavelength resonances that do not interfere with operation and are rarely observed. There are, however, two types of resonances that may be troublesome. The first group is usually referred to as the “ $n'$ ” resonances.” These are similar in character to the ordinary magnetron resonances, except that there is axial variation of the fields. In fact, these resonances are characterized by an electric-field node at the median plane. The wavelengths of these resonances are of the same

---

Associated Equations by Flux Plotting,” RL Report No. 1047, Jan. 23, 1946.

P. D. Crout, “A Flux Plotting Method for Obtaining Fields Satisfying Maxwell’s Equations, with Applications to the Magnetron,” RL Report No. 1048, Jan. 16, 1946.

F. E. Bothwell and P. D. Crout, “A Method for Calculating Magnetron Resonant Frequencies and Modes,” RL Report No. 1039, Feb. 8, 1946.

order of magnitude as the first group of ordinary resonances only when the anode is abnormally long. The second group is referred to as "end-space resonances." These are characterized by strong fields in the end spaces and are most likely to be seen when the volume of the end spaces is large.<sup>1</sup> The field distribution, together with an approximate equivalent circuit of a typical end-space resonance, is shown in Fig. 2-20.

**2-9. The Interaction Field.**—The equations for the fields in the interaction space have been derived in Sec. 2-6. These are

$$\left. \begin{aligned} E_{\phi} &= \frac{N\theta E}{\pi} \sum_{m=-\infty}^{\infty} \left( \frac{\sin \gamma\theta}{\gamma\theta} \right) \frac{Z'_{\gamma}(k\rho)}{Z'_{\gamma}(kr_a)} e^{i\gamma\phi}, \\ E_{\rho} &= -\frac{j}{k\rho} \frac{N\theta E}{\pi} \sum_{m=-\infty}^{\infty} \gamma \left( \frac{\sin \gamma\theta}{\gamma\theta} \right) \frac{Z_{\gamma}(k\rho)}{Z'_{\gamma}(kr_a)} e^{i\gamma\phi}, \\ \text{and} \\ H_z &= -j\sqrt{\frac{\epsilon_0}{\mu_0}} \frac{N\theta E}{\pi} \sum_{m=-\infty}^{\infty} \left( \frac{\sin \gamma\theta}{\gamma\theta} \right) \frac{Z_{\gamma}(k\rho)}{Z'_{\gamma}(kr_a)} e^{i\gamma\phi}. \end{aligned} \right\} \gamma = n + mN \quad (36)$$

The special case  $n = N/2$  (wherein  $N$  must be an even number) will be discussed first. For this case the fields reduce to

$$\left. \begin{aligned} E_{\phi} &= \frac{2N\theta E}{\pi} \sum_{m=0}^{\infty} \left( \frac{\sin \gamma\theta}{\gamma\theta} \right) \frac{Z'_{\gamma}(k\rho)}{Z'_{\gamma}(kr_a)} \cos \gamma\phi, \\ E_{\rho} &= \frac{2N\theta E}{\pi k\rho} \sum_{m=0}^{\infty} \gamma \left( \frac{\sin \gamma\theta}{\gamma\theta} \right) \frac{Z_{\gamma}(k\rho)}{Z'_{\gamma}(kr_a)} \sin \gamma\phi, \quad \gamma = \left(m + \frac{1}{2}\right)N \\ \text{and} \end{aligned} \right\} \quad (40)$$

$$H_z = -j\sqrt{\frac{\epsilon_0}{\mu_0}} \frac{2N\theta E}{\pi} \sum_{m=0}^{\infty} \left( \frac{\sin \gamma\theta}{\gamma\theta} \right) \frac{Z_{\gamma}(k\rho)}{Z'_{\gamma}(kr_a)} \cos \gamma\phi.$$

These fields represent standing waves rather than rotating waves, a consequence of the fact that the ( $n = N/2$ )-mode is nondegenerate. Furthermore, there is a  $90^\circ$  phase difference between the electric and magnetic fields, as there always is in a standing-wave resonance. A qualitative picture of the electric field distribution is shown in Fig. 2-21.

At the electron velocities in the magnetron (usually less than one-tenth the velocity of light) the force due to the oscillating magnetic field is much less than that due to the electric field. Therefore a detailed discussion of the magnetic field is unnecessary. It is evident that the

<sup>1</sup> Certain of the end-space resonances can also be regarded as  $n$  resonances.



electric field consists of a sum of harmonic components the relative amplitudes of which depend upon  $\rho$  through the functions.

$$\frac{Z'_\gamma(k\rho)}{Z'_\gamma(kr_a)} \quad \text{for } E_\phi$$

and

$$\frac{\gamma}{k\rho} \frac{Z_\gamma(k\rho)}{Z'_\gamma(kr_a)} \quad \text{for } E_\rho.$$

For  $kr_a \ll \gamma$  these functions can be approximated by

$$\left(\frac{\rho}{r_a}\right)^{\gamma-1} \left[ \frac{1 - \left(\frac{r_c}{\rho}\right)^{2\gamma}}{1 - \left(\frac{r_c}{r_a}\right)^{2\gamma}} \right]$$

and

$$\left(\frac{\rho}{r_a}\right)^{\gamma-1} \left[ \frac{1 + \left(\frac{r_c}{\rho}\right)^{2\gamma}}{1 - \left(\frac{r_c}{r_a}\right)^{2\gamma}} \right]$$

respectively. These functions (except  $E_\rho$  for  $\gamma = 1$ ) all decrease as  $\rho$  approaches  $r_c$ , and the rate of decrease increases rapidly with  $\gamma$ . Thus, as  $\rho$  approaches  $r_c$ , the lower-order components become more prominent. The extent of the effect depends upon  $r_c/r_a$ , becoming less pronounced as  $r_c/r_a$  approaches one. However, at the values of  $r_c/r_a$  ordinarily used, the lowest component of the  $N/2$ -mode is the predominant one at the cathode, and the angular dependence near the cathode is given very nearly by  $\cos(N/2)\phi$ . In a discussion of the interaction between the field and the electrons (see Chap. 6), the analysis of the field into harmonic components is very useful because it is usually possible to ignore all but one of the components.

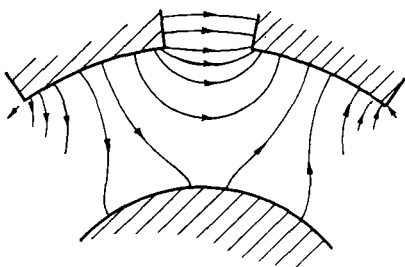


FIG. 2-21.—Distribution of electric field in the interaction space for the  $\pi$ -mode.

The  $(n = 0)$ -modes share with the  $\left(n = \frac{N}{2}\right)$ -modes the property of nondegeneracy.

*The Degenerate Modes.*—All other modes of the unstrapped resonant system have a degeneracy of the second order; that is, there is always a pair of linearly independent fields having the same resonant frequency.

In one of these the fundamental component [ $(m = 0)$ -component] rotates clockwise, whereas in the other it rotates counterclockwise.<sup>1</sup> The harmonic components all appear as waves that rotate at different angular velocities; that is, the velocity of rotation is proportional to  $1/\gamma$ , and thus waves of negative  $\gamma$  rotate in a direction opposite to those of positive  $\gamma$ . It is worth noting that the harmonic of the lowest  $\gamma$  (excluding the fundamental), given by  $m = -1$ , rotates in a direction opposite to that of the fundamental. The remarks that were made concerning the comparative rates of decrease of the harmonics with  $\rho$  for the nondegenerate modes apply here also. Ordinarily, however, the various harmonics are not integral multiples of the fundamental.

Degeneracy leads to certain practical difficulties in magnetron design. It is never possible to make a magnetron perfectly symmetric. The lack of symmetry tends to split the degenerate modes into two nondegenerate modes with slightly differing resonant frequencies. Ordinarily, both components are excited, but the relative degree of excitation depends upon the nature of the splitting and can be expected to vary considerably from tube to tube. This splitting leads to a certain lack of uniformity in tubes operating in degenerate modes.

**2-10. Applications and Limitations.**—It is evident from the preceding discussion that the unstrapped system has several resonant modes with which the electrons can couple (in the manner described in Chap. 1). The same is true of the other systems to be described later. Whether or not a magnetron can operate in a specific mode over a wide range of voltages, currents, and magnetic fields is determined for the most part by the wavelength and the field configuration of all the other modes relative to that specific one.<sup>2</sup> The symmetric unstrapped resonant system is satisfactory only for low values of  $N$ , because its modes crowd together for high values of  $n$  and  $N$ . It will be seen later that this effect restricts their application to comparatively long wavelengths.

The development of the unstrapped resonant system was abandoned when the strapped and rising-sun systems were discovered. Consequently, no extended attempt has been made to design the best possible unstrapped magnetron or to find what is the largest possible  $N$  that can be used. The largest  $N$  that has been used with full success<sup>3</sup> is 6. This

<sup>1</sup> There is a certain degree of arbitrariness with regard to which pair of fields is taken as fundamental. Thus it is possible to form other linearly independent pairs by taking linear combinations of the pair chosen above.

<sup>2</sup> The various factors that affect mode selection are discussed in Chap. 8.

<sup>3</sup> It is possible to increase the separation between the  $\pi$ -mode and the  $(\frac{N}{2} - 1)$ -mode by bringing a ring very close to the ends of the anode segments. Successful experimental magnetrons with  $N = 8$  have been constructed by making use of such a ring.

six-resonator magnetron<sup>1</sup> oscillates in the  $\pi$ -mode ( $n = \frac{N}{2}$ ) in the 700-Mc/sec band at an efficiency of 35 to 40 per cent. Thus, at a pulse current of 10 amp and 12,500 volts, the tube will produce 50-kw pulse power.

Another example of a  $\pi$ -mode unstrapped magnetron is the original British 10-cm tube. It has eight resonators, and the separation between the  $\pi$ -mode and the 3-mode is only 1 per cent. The maximum efficiency varies from 20 to 30 per cent so that at a pulse input of 15 amp and 12,000

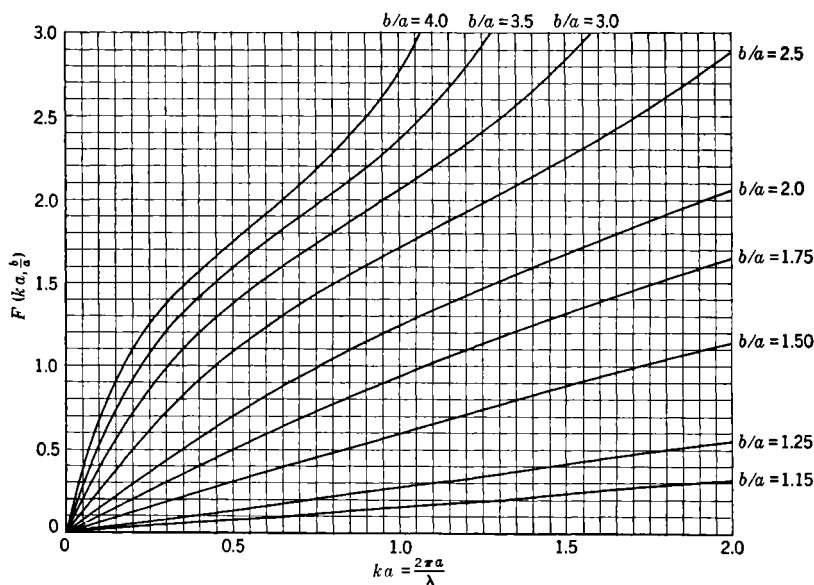


FIG. 2-22.— $F(ka, b/a)$  in radians plotted as a function of  $ka$  for  $b/a$  equal to 1.15 to 4.0.

volts an output of 45 kw might be obtained. At currents below 10 amp the tube oscillates in the 3-mode, and in general performance is erratic from tube to tube.

In both of the magnetrons described above, the anode length and end spaces are so short that the modes appear in reverse order (Sec. 2-8)—the  $\pi$ -mode is the longest-wavelength mode.

**2.11. The Computation of Admittances.**—In the various admittance formulas derived in previous sections, the dependence of admittance upon frequency and certain of the geometric parameters is contained in some rather complicated expressions involving Bessel and Neuman

<sup>1</sup> The 700 A (B, C, D) series.

functions. Tables, plots, and approximation formulas that are useful for the computation of these admittances appear below.

*The Annular Sector Resonator.*—The admittance of the annular sector shown in Fig. 2·11 is given by

$$Y = j \sqrt{\frac{\epsilon_0}{\mu_0}} \frac{h}{\psi a} \frac{J_0(ka)N_1(kb) - J_1(kb)N_0(ka)}{J_1(ka)N_1(kb) - J_1(kb)N_1(ka)}.$$

The functions

$$F\left(ka, \frac{b}{a}\right) = -\cot^{-1} \frac{J_0(ka)N_1(kb) - J_1(kb)N_0(ka)}{J_1(ka)N_1(kb) - J_1(kb)N_1(ka)}$$

are plotted in Figs. 2·22 and 2·23 as a function of  $ka$  for various values

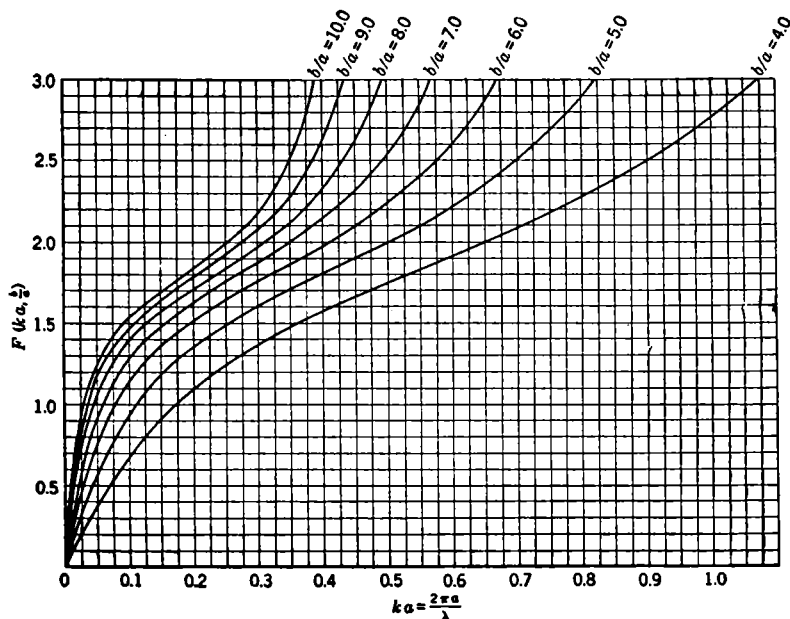


FIG. 2·23.— $F(ka, b/a)$  in radians plotted as a function of  $ka$  for  $b/a$  equal to 4 to 10.

of  $b/a$ . The function  $F(ka, b/a)$ , rather than  $\cot F$ , has been plotted in order to facilitate interpolation between the given values of  $b/a$ . The succession of poles in  $\cot F$  would make interpolation between curves very difficult.

*The Cylindrical Resonator.*—The admittance of the cylindrical resonator shown in Fig. 2·10 is given by

$$\begin{aligned}
 Y &= j \sqrt{\frac{\epsilon_0}{\mu_0}} \frac{h}{2\pi a} \left[ \frac{J_0(ka)}{J'_0(ka)} + 2 \sum_{p=1}^{\infty} \left( \frac{\sin p\psi}{p\psi} \right)^2 \frac{J_p(ka)}{J'_p(ka)} \right] \\
 &= j \sqrt{\frac{\epsilon_0}{\mu_0}} \frac{h}{2\pi a} G(\psi, ka).
 \end{aligned}$$

For  $ka \ll 1$  (which it usually is) one can take

$$\begin{aligned}
 \frac{J_0(ka)}{J'_0(ka)} &= -\frac{2}{ka} + \frac{ka}{4} - \frac{5}{96} (ka)^3, \\
 \frac{J_p(ka)}{J'_p(ka)} &= \frac{ka}{p} + \frac{(ka)^3}{2p^2(p+1)} \quad (p \neq 0),
 \end{aligned}$$

yielding

$$\begin{aligned}
 G(\psi, ka) &= -\frac{2}{ka} + \left[ \frac{1}{4} + 2 \sum_{p=1}^{\infty} \left( \frac{\sin p\psi}{p\psi} \right)^2 \frac{1}{p} \right] ka + (ka)^3 \left[ \frac{5}{96} \right. \\
 &\quad \left. + \sum_{p=1}^{\infty} \left( \frac{\sin p\psi}{p\psi} \right)^2 \frac{1}{p^2(p+1)} \right],
 \end{aligned}$$

which gives the frequency dependence comparatively simply. The series

$$\sum_{p=1}^{\infty} \left( \frac{\sin p\psi}{p\psi} \right)^2 \frac{1}{p}$$

converges rather slowly for small values of  $\psi$ . One can show, however, that

$$\sum_{p=1}^{\infty} \left( \frac{\sin p\psi}{p\psi} \right)^2 \frac{1}{p} = \frac{3}{2} - \ln 2\psi + \frac{\psi^2}{36} + \frac{\psi^4}{2700} + \dots$$

which converges quite rapidly for small values of  $\psi$  (including the usual range of values for  $\psi$ ). The series

$$\sum_{p=1}^{\infty} \left( \frac{\sin p\psi}{p\psi} \right)^2 \frac{1}{p^2(p+1)}$$

converges quite rapidly. Furthermore, one can usually omit the terms in  $(ka)^3$ .

For larger values of  $ka$  one can correct the above formula by using the exact values for  $[J_p(ka)]/[J'_p(ka)]$  for the low values of  $p$  and the series approximations for the larger values (larger values means those for which  $ka \ll p$ ).

TABLE 2-2.—VALUES OF  $[J_n(kr_a)]/[J'_n(kr_a)]$ 

$kr_a$	$n = 0$	$n = 1$	$n = 2$	$n = 3$	$n = 4$	$n = 5$	$n = 6$	$n = 7$	$n = 8$	$n = 9$
0.00	$\infty$	0.00000	0.00000	0.00000	0.00000	0.00000	0.00000	0.00000	0.00000	0.00000
0.04	-49.9899	0.04002	0.02000	0.01333	0.01000	0.00800	0.00666	0.00571	0.00500	0.00444
0.08	-24.9799	0.08013	0.04002	0.02667	0.02000	0.01600	0.01333	0.01142	0.01000	0.00889
0.12	-16.6367	0.12043	0.06007	0.04002	0.03001	0.02401	0.02000	0.01714	0.01500	0.01333
0.16	-12.4599	0.16103	0.08017	0.05339	0.04003	0.03201	0.02667	0.02286	0.02000	0.01778
0.20	-9.9500	0.20202	0.10033	0.06678	0.05005	0.04027	0.03335	0.02858	0.02501	0.02223
0.24	-8.27304	0.24352	0.12058	0.08019	0.06003	0.04805	0.04003	0.03430	0.03001	0.02668
0.28	-7.07265	0.28562	0.14092	0.09364	0.07014	0.05607	0.04670	0.04002	0.03502	0.03113
0.32	-6.16968	0.32844	0.16138	0.10712	0.08021	0.06411	0.05340	0.04575	0.04003	0.03558
0.36	-5.46508	0.37212	0.18197	0.12065	0.09029	0.07216	0.06009	0.05148	0.04504	0.04003
0.40	-4.89934	0.41678	0.20271	0.13423	0.10040	0.08021	0.06679	0.05722	0.05006	0.04449
0.44	-4.43457	0.46257	0.22362	0.14786	0.11054	0.08829	0.07350	0.06293	0.05507	0.04894
0.48	-4.04550	0.50964	0.24472	0.16156	0.12070	0.09637	0.08022	0.06870	0.06010	0.05339
0.52	-3.71467	0.55816	0.26603	0.17532	0.13089	0.10447	0.08694	0.07446	0.06512	0.05787
0.56	-3.42957	0.60833	0.28756	0.18915	0.14111	0.11259	0.09368	0.08022	0.07015	0.06234
0.60	-3.18103	0.66034	0.30935	0.20306	0.15137	0.12073	0.10043	0.08593	0.07519	0.06681
0.64	-2.96220	0.71444	0.33141	0.21706	0.16166	0.12888	0.10718	0.09176	0.08023	0.07128
0.68	-2.76780	0.77088	0.35377	0.23115	0.17200	0.13706	0.11396	0.09753	0.08527	0.07575
0.72	-2.59376	0.82996	0.37644	0.24533	0.18237	0.14526	0.12075	0.10333	0.09033	0.08023
0.76	-2.43684	0.89202	0.39946	0.25963	0.19280	0.15348	0.12754	0.10912	0.09538	0.08472
0.80	-2.29444	0.95745	0.42286	0.27403	0.20327	0.16173	0.13436	0.11494	0.10045	0.08920
0.84	-2.16449	1.02668	0.44666	0.28856	0.21379	0.17001	0.14119	0.12075	0.10552	0.09370
0.88	-2.04527	1.10023	0.47089	0.30322	0.22437	0.17831	0.14803	0.12658	0.11059	0.09820
0.92	-1.93535	1.17870	0.49559	0.31800	0.23501	0.18665	0.15490	0.13242	0.11568	0.10271
0.96	-1.83355	1.26281	0.52079	0.33293	0.24570	0.19501	0.16178	0.13827	0.12077	0.10722
1.00	-1.73889	1.35339	0.54652	0.34802	0.25647	0.20341	0.16868	0.14414	0.12588	0.11173

$kr_a$	$n = 0$	$n = 1$	$n = 2$	$n = 3$	$n = 4$	$n = 5$	$n = 6$	$n = 7$	$n = 8$	$n = 9$
1.04	- 1.65051	1.45144	0.57283	0.36326	0.26729	0.21184	0.17560	0.15001	0.13099	0.11626
1.08	- 1.56769	1.55820	0.59977	0.37868	0.27819	0.22031	0.18255	0.15590	0.13611	0.12078
1.12	- 1.48983	1.67512	0.62737	0.39427	0.28916	0.22882	0.18951	0.16181	0.14123	0.12532
1.16	- 1.41638	1.80405	0.65568	0.41006	0.30021	0.23737	0.19650	0.16772	0.14637	0.12986
1.20	- 1.34687	1.94727	0.68476	0.42604	0.31134	0.24595	0.20351	0.17366	0.15152	0.13441
1.24	- 1.28092	2.10764	0.71466	0.44223	0.32256	0.25458	0.21054	0.17961	0.15668	0.13897
1.28	- 1.21814	2.28889	0.74545	0.45864	0.33387	0.26326	0.21761	0.18557	0.16185	0.14353
1.32	- 1.15824	2.49585	0.77720	0.47530	0.34526	0.27198	0.22470	0.19156	0.16703	0.14811
1.36	- 1.10093	2.73495	0.80997	0.49217	0.35676	0.28075	0.23181	0.19755	0.17222	0.15269
1.40	- 1.04596	3.01501	0.84383	0.50933	0.36835	0.28957	0.23896	0.20358	0.17743	0.15728
1.44	- 0.99311	3.34828	0.87892	0.52676	0.38005	0.29844	0.24613	0.20961	0.18265	0.16187
1.48	- 0.94217	3.75249	0.91531	0.54445	0.39186	0.30737	0.25333	0.21566	0.18788	0.16648
1.52	- 0.89296	4.25414	0.95306	0.56245	0.40379	0.31635	0.26057	0.22174	0.19312	0.17110
1.56	- 0.84532	4.89489	0.99236	0.58078	0.41583	0.32539	0.26785	0.22783	0.19838	0.17572
1.60	- 0.79910	5.74391	1.03330	0.59944	0.42800	0.33449	0.27514	0.23396	0.20365	0.18036
1.64	- 0.75415	6.92565	1.07602	0.61845	0.44030	0.34366	0.28249	0.24009	0.20893	0.18500
1.68	- 0.71034	8.68769	1.12072	0.63783	0.45273	0.35289	0.28987	0.24625	0.21423	0.18966
1.72	- 0.66757	11.6048	1.16748	0.65761	0.46530	0.36218	0.29727	0.25244	0.21955	0.19433
1.76	- 0.62571	17.3841	1.21670	0.67778	0.47802	0.37155	0.30473	0.25864	0.22487	0.19900
1.80	- 0.58465	34.3675	1.26842	0.69838	0.49089	0.38098	0.31222	0.26488	0.23023	0.20369
1.84	- 0.54431	1199.48	1.32294	0.71946	0.50392	0.39049	0.31975	0.27113	0.23559	0.20839
1.88	- 0.50459	-36.5922	1.38057	0.74101	0.51711	0.40008	0.32733	0.27741	0.24097	0.21311
1.92	- 0.46539	-18.0348	1.44175	0.76306	0.53047	0.40975	0.33495	0.28373	0.24637	0.21783
1.96	- 0.42662	-11.9643	1.50674	0.78566	0.54402	0.41950	0.34261	0.29006	0.25179	0.22257
2.00	- 0.38821	8.9453	1.57590	0.80878	0.55775	0.42933	0.35032	0.29644	0.25722	0.22732

*The Interaction Space.*—The admittance is given by

$$Y_n = j \sqrt{\frac{\epsilon_0}{\mu_0}} \frac{Nh}{2\pi r_a} \sum_{m=-\infty}^{\infty} \left( \frac{\sin \gamma \theta}{\gamma \theta} \right)^2 \frac{Z_\gamma(kr_a)}{Z'_\gamma(kr_a)} = j \sqrt{\frac{\epsilon_0}{\mu_0}} \frac{Nh}{2\pi r_a} K_{n,N}(\theta, kr_a),$$

where  $\gamma = n + mN$ . For  $kr_a \ll \gamma$  one can use

$$\frac{Z'_\gamma(kr_a)}{Z_\gamma(kr_a)} = \frac{kr_a}{|\gamma|} (1 + \sigma^{2|\gamma|}) + \frac{(kr_a)^3}{2\gamma^2(|\gamma| + 1)},$$

where  $\sigma = r_c/r_a$ .

Since  $kr_a$  is not always less than  $n$ , one uses for  $K(\theta, ka)$

$$K(\theta, kr_a) = \left( \frac{\sin n\theta}{n\theta} \right)^2 \frac{Z_n(kr_a)}{Z'_n(kr_a)} + kr_a \sum_{m=-\infty}^{\infty}{}' \left( \frac{\sin \gamma \theta}{\gamma \theta} \right)^2 \frac{1 + \sigma^{2|\gamma|}}{|\gamma|} \\ + (kr_a)^3 \sum_{m=-\infty}^{\infty}{}' \left( \frac{\sin \gamma \theta}{\gamma \theta} \right)^2 \frac{1}{2\gamma^2(|\gamma| + 1)},$$

where the symbol  $\Sigma'$  indicates omission of the term for which  $m = 0$ . For  $\sigma = 0$ ,  $[Z_n(kr_a)]/[Z'_n(kr_a)] = [J'_n(kr_a)]/[J_n(kr_a)]$ . Values for these functions for  $n = 0$  through 9 appear in Table 2-2. For values of  $n \geq 2$ , the approximation  $Z_n/Z'_n = (J_n/J'_n)(1 + \sigma^{2n})$  is often satisfactory.



## CHAPTER 3

### THE RISING-SUN SYSTEM

By N. KROLL

The discussion of the unstrapped system has shown that a desirable resonant system would be one in which the  $N/2$ -mode is well separated from the neighboring modes and, further, remains well separated for values of  $N$  substantially larger than those usable in unstrapped systems. Two systems are commonly used to accomplish this objective. One is the rising-sun system in which alternate resonators are alike but adjacent resonators are not alike; the other is the strapped system,<sup>1</sup> discussed in Chap. 4. Two examples of the rising-sun structure are shown in Fig. 3-1. The design of Fig. 3-1*a* is obviously suggestive of the rather picturesque term by which this type of magnetron is known.

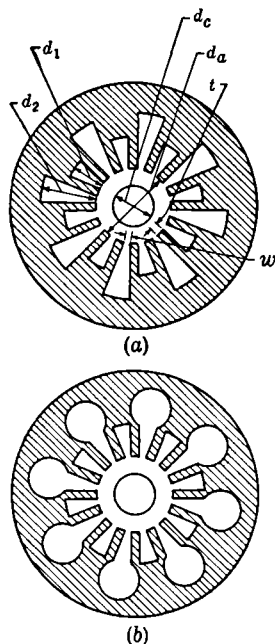


FIG. 3-1.—Two examples of rising-sun resonant systems: (a) vane type; (b) vane type with modified large resonators.

**3.1. The Spectrum.**—The electromagnetic-field problem for the rising-sun system can be reduced to a circuit problem by precisely the same means that were used for the unstrapped system (Sec. 2-1). That is, the magnetron can be represented by the circuit in Fig. 3-2, where the interaction space is represented by a network of  $N$  pairs of terminals and the resonators by admittances having a single pair of terminals. The assumptions leading to this representation are the same as those discussed in Sec. 2-1 and lead to the same restrictions upon the solutions.

In order to find the resonant frequencies, it will be necessary, as before, to investigate the circuit properties of the various elements.

<sup>1</sup> Arrangements of unlike resonators differing from that of the rising-sun system have been given some theoretical consideration. None of these has appeared to be promising, and none seems to offer any advantages over the rising-sun structure.

These properties have already been fully investigated for the resonators and can be summarized by the functions  $Y_{r_1}$  and  $Y_{r_2}$ . These functions are the admittances of the even- and odd-numbered resonators respectively (numbered as in Fig. 3-2) and are functions of the frequency. Formulas for computing these admittances for different resonator shapes are derived in Sec. 2-5.

On the other hand, the properties of the interaction space were not investigated fully enough to deal with the problem of this chapter. In Chap. 2, admittances for the unstrapped system were computed with the restriction that the electric field differed from gap to gap by only a constant phase factor; this resulted in the condition of equal admittances seen at any gap. This restriction is clearly invalid for the rising-sun

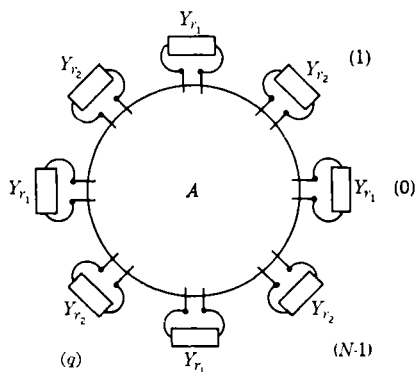


FIG. 3-2.—Circuit representation of the rising-sun system.

system, inasmuch as the admittances seen at adjacent gaps must, in general, be different. For the rising-sun system one assumes, as before, that the tangential electric field along the dotted boundaries (Fig. 2-13) is constant at each gap. Furthermore, one assumes that the field varies from even-numbered gap to even-numbered gap as  $e^{(2\pi j n/N)q}$  and from odd-numbered gap to odd-numbered gap also as  $e^{(2\pi j n/N)q}$ , with no restriction placed upon the ratio of the field at an even-numbered gap to that at an odd-numbered gap.<sup>1</sup> Thus the electric field at even-numbered gaps can be represented by  $E^{(e)}e^{(2\pi j n/N)q}$ , and at odd-numbered gaps by  $E^{(o)}e^{(2\pi j n/N)q}$ , where the ratio  $E^{(e)}/E^{(o)}$  is arbitrary and may be complex.

The required admittances can be readily computed by an application of the principle of superposition to previously obtained results. The field distribution described in the above paragraph can be obtained by superposing two "symmetric" distributions for which the tangential electric field

<sup>1</sup> As in Chap. 2,  $q$  is the gap number and has values of 0 to  $N - 1$ , and  $n$  is an integer.

at the  $q$ th gap is given by  $Ee^{j(2\pi n/N)q}$  and  $E'e^{j[2\pi(n-\frac{N}{2})/N]q}$  respectively. The electromagnetic fields associated with these distributions have been computed in Sec. 2.6 [Eq. (2.36)]. A superposition of these fields gives rise to the distribution  $Ee^{j(2\pi n/N)q} + E'e^{j[2\pi(n-\frac{N}{2})/N]q}$  which is equal to  $[E + (-1)^q E']e^{j2\pi nq/N}$ . It is evident that the field varies properly from even-numbered gap to even-numbered gap and from odd-numbered gap to odd-numbered gap. Thus  $E^{(e)} = E + E'$  and  $E^{(o)} = E - E'$ ; and inasmuch as  $E'/E$  is arbitrary, so is  $E^{(e)}/E^{(o)}$ .

The magnetic field at the various gaps will be given by

$$H_z(r_a, \phi) = H(r_a, \phi) + H'(r_a, \phi),$$

where  $H(r_a, \phi)$  is the magnetic-field distribution associated with  $Ee^{j(2\pi n/N)q}$ , and  $H'(r_a, \phi)$  is that associated with  $E'e^{j[2\pi(n-\frac{N}{2})/N]q}$ . According to the treatment following Eq. (2.36), Sec. 2.6, the admittance seen at the  $q$ th gap is given by

$$\begin{aligned} Y^{(q)} &= \frac{r_a h \int_{(2\pi q/N) - \theta}^{(2\pi q/N) + \theta} E_\phi(r_a, \phi) H_z(r_a, \phi) d\phi}{\left[ r_a \int_{(2\pi q/N) - \theta}^{(2\pi q/N) + \theta} E_\phi(r_a, \phi) d\phi \right]^2} \\ &= \frac{h}{4r_a \theta^2} \frac{\int_{(2\pi q/N) - \theta}^{(2\pi q/N) + \theta} H_z(r_a, \phi) d\phi}{(E + (-1)^q E')e^{j(2\pi n/N)q}}, \end{aligned} \quad (1)$$

since  $E_\phi = (E + (-1)^q E')e^{j(2\pi n/N)q}$  over the range of integration.

According to Eq. 2.36,  $H(r_a, \phi) = H\left(r_a, \phi - \frac{2\pi q}{N}\right)e^{j(2\pi n/N)q}$  and

$$\begin{aligned} H'(r_a, \phi) &= H'\left(r_a, \phi - \frac{2\pi q}{N}\right)e^{j[2\pi(n-\frac{N}{2})/N]q} \\ &= (-1)^q H'\left(r_a, \phi - \frac{2\pi q}{N}\right)e^{j(2\pi n/N)q}. \end{aligned}$$

Thus, taking  $\psi = \left(\phi - \frac{2\pi q}{N}\right)$ , Eq. (1) reduces to

$$\begin{aligned} Y^{(q)} &= \frac{h}{4r_a \theta^2} \frac{1}{1 + (E'/E)(-1)^q} \left( \frac{\int_{-\theta}^{\theta} H(r_a, \psi) d\psi}{E} \right. \\ &\quad \left. + (-1)^q \frac{E'}{E} \frac{\int_{-\theta}^{\theta} H'(r_a, \psi) d\psi}{E'} \right) \end{aligned} \quad (2)$$

The admittances  $Y_n$  computed in Sec. 2.6 can be written as

$$Y_n = \frac{h}{4r_a \theta^2} \frac{\int_{-\theta}^{\theta} H(r_a, \psi) d\psi}{E} \quad (3)$$

Similarly,

$$Y_{\left(\frac{N}{2}-n\right)} = Y_{\left(n-\frac{N}{2}\right)} = \frac{h}{4r_a\theta^2} \frac{\int_{-\theta}^{\theta} H'(\tau_a, \psi) d\psi}{E'} \quad (4)$$

Thus the expression for  $Y^{(q)}$  reduces to

$$Y^{(e)} = \frac{Y_n + RY_{\left(\frac{N}{2}-n\right)}}{1 + R} \quad (q \text{ even}) \quad (5a)$$

and

$$Y^{(o)} = \frac{Y_n - RY_{\left(\frac{N}{2}-n\right)}}{1 - R} \quad (q \text{ odd}), \quad (5b)$$

where  $R = E'/E$ . Therefore the admittances depend upon  $R$  as well as upon the frequency.

For resonance to occur it is necessary that the admittances match at both odd- and even-resonator openings. This condition yields

$$\frac{Y_n + RY_{\left(\frac{N}{2}-n\right)}}{1 + R} + Y_{r_1} = 0, \quad (6a)$$

$$\frac{Y_n - RY_{\left(\frac{N}{2}-n\right)}}{1 - R} + Y_{r_2} = 0, \quad (6b)$$

which on eliminating  $R$  yield, after some manipulation,

$$\begin{aligned} \left[ \frac{Y_n + Y_{\left(\frac{N}{2}-n\right)}}{2} + Y_{r_1} \right] \left[ \frac{Y_n + Y_{\left(\frac{N}{2}-n\right)}}{2} + Y_{r_2} \right] \\ = \left[ \frac{Y_n - Y_{\left(\frac{N}{2}-n\right)}}{2} \right]^2. \quad (7) \end{aligned}$$

The resonant frequency having been computed,  $R$  can be found from

$$R = - \frac{Y_n + Y_{r_1}}{Y_{\left(\frac{N}{2}-n\right)} + Y_{r_1}} = \frac{Y_n + Y_{r_2}}{Y_{\left(\frac{N}{2}-n\right)} + Y_{r_2}}. \quad (8)$$

As in the case of the unstrapped system, the resonance equation depends upon  $n$ . For the unstrapped system it was necessary to consider only the values 0 to  $N/2$  for  $n$ , as replacing  $n$  by  $-n$  or by  $(n + mN)$  where  $m$  is any integer, left the resonance equation unchanged. For the rising-sun system, however, the values 0 to  $N/4$  [or  $(N - 2)/4$ , whichever is an integer] are sufficient, as replacing  $n$  by  $\left(\frac{N}{2} - n\right)$ , as well as by  $(n + mN)$  or  $-n$ , leaves the resonance equation unchanged.

Each equation has an infinite number of roots, although only the lower-frequency roots are of practical interest (ordinarily only the first two are of interest). While it would be simplest to use a mode-numbering system analogous to that used for the unstrapped system, *i.e.*,  $n_p$  for the  $(p+1)$ -root of the frequency equation determined by  $n$ , this is not the system in common use. It has become customary to regard any magnetron resonant system having side resonators as a modification of the unstrapped system. That is, one considers the system as having been produced by a continuous perturbation of the unstrapped system. As the unstrapped system is modified, the resonant frequencies and their associated field distributions will also be modified and will change continuously if the perturbation is effected continuously. This implies that the modes of one system join continuously to the modes of the other and thus that there is a 1-to-1 correspondence between the modes of one system and the modes of the other. From this point of view it is convenient to give corresponding modes the same number. Unfortunately the correspondence is not unique (that is, it depends upon the intermediate steps of the perturbation), so that it is necessary to specify the way in which the perturbation is performed. For the rising-sun system one considers the perturbation as having been made by a continuous alteration of the side resonators, other dimensions being held fixed. In all practical cases this leads to the mode number  $n$  for the first root of Eq. (7) and the mode number  $\left(\frac{N}{2} - n\right)$  for the second root.

The higher roots always correspond to the higher-order  $n$ - or  $\left(\frac{N}{2} - n\right)$ -modes, with the particular correspondence depending upon the specific case.

Equation (7) contains the unstrapped system as a special case. For, setting  $Y_{r_1} = Y_{r_2} = Y_r$ , gives

$$\left[ \frac{Y_n + Y_{\left(\frac{N}{2} - n\right)}}{2} + Y_r \right]^2 = \left[ \frac{Y_n - Y_{\left(\frac{N}{2} - n\right)}}{2} \right]^2,$$

which yields the two equations

$$Y_r + Y_n = 0 \quad \text{and} \quad Y_r + Y_{\left(\frac{N}{2} - n\right)} = 0. \quad (9)$$

These are, of course, the previously derived equations for the  $n$ - and  $\left(\frac{N}{2} - n\right)$ -modes of the unstrapped system.

Although Eq. (7) appears to be complicated, it is subject to a simple physical interpretation. In order to illustrate this interpretation the

following specific example will be used. An 18-resonator anode block similar to that shown in Fig. 2-17 will be used; in this all dimensions are held fixed except the lengths of alternate resonators  $d_2$ , which are allowed to increase. In Fig. 3-3 the resultant resonant frequencies of

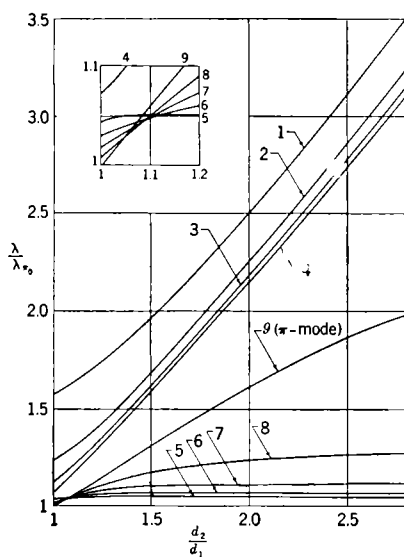


FIG. 3-3.—Mode spectrum of a rising-sun system as a function of the ratio of large resonator depth  $d_2$  to small resonator depth  $d_1$  held fixed.  $\lambda_{\pi 0}$  is the  $\pi$ -mode wavelength for  $d_2/d_1 = 1$ . Dimensions:  $d_1/\lambda_{\pi 0} = 0.172$ ;  $d_a/\lambda_{\pi 0} = 0.524$ ;  $d_c = 0$ ;  $\theta = 0.060$  radians.

the modes 1 to 9 are plotted as a function of the ratio of large to small resonator depths ( $r_1 = d_2/d_1$ ). Following the mode-numbering convention discussed above, the 9-mode is found as the second root of Eq. (7) with  $n = 0$  (the first root is the trivial  $\omega = 0$ ); the 1- and 8-modes are found as the first and second roots of Eq. (7) with  $n = 1$ ; and so forth for the other modes. It is evident that for sufficiently large values of  $r_1$ , the ( $n = N/2$ )-mode or the 9-mode becomes well separated from its neighbors, a requirement for operation in this mode. Furthermore, the other modes appear to break into two distinct groups, each of which bears a suggestive resemblance to the first group of modes of an unstrapped system having nine resonators. Table 3-1 shows the modes of the rising-sun system for

$d_2/d_1 = 2.1$  compared with the modes of an unstrapped system having the same dimensions as the rising-sun system except that in Case I the small

TABLE 3-1.<sup>1</sup>—THE RESONANCES OF AN 18-RESONATOR RISING-SUN SYSTEM COMPARED WITH THOSE OF TWO NINE-RESONATOR UNSTRAPPED SYSTEMS

Case I	Case II
$\lambda'_1/\lambda_1 = 0.987$	$\lambda''_1/\lambda_8 = 1.096$
$\lambda'_2/\lambda_2 = 0.9975$	$\lambda''_2/\lambda_7 = 1.015$
$\lambda'_3/\lambda_3 = 0.9994$	$\lambda''_3/\lambda_6 = 1.0034$
$\lambda'_4/\lambda_4 = 0.9997$	$\lambda''_4/\lambda_5 = 1.0006$
$\lambda'_{01}/\lambda_9 = 0.8816$	

resonators have been filled with metal leaving nine large resonators and in Case II the large resonators have been filled with metal leaving the

<sup>1</sup>The values of  $\lambda_n$  are the resonances of the rising-sun system of Fig. 3-3 at  $d_2/d_1 = 2.1$ . The  $\lambda'_n$  are the resonances of the nine-resonator unstrapped system formed by filling the small resonators with metal; the  $\lambda''_n$  are those of the nine-resonator symmetric system formed by filling the large resonators with metal.

nine small resonators. These results suggest that a rising-sun system of  $N$  resonators can be interpreted as two symmetric  $N/2$  resonator systems coupled together. A careful examination of Eq. (7) will corroborate this interpretation.

Consider first the expression  $[Y_n + Y_{(N/2-n)}]^{1/2}$ . Substituting the expression in Eq. 2.37 yields

$$\frac{Y_n + Y_{(N/2-n)}}{2} = j \sqrt{\frac{\epsilon_0}{\mu_0}} \frac{Nh}{4\pi r_a} \sum_{m=-\infty}^{\infty} \frac{Z_\gamma(kr_a)}{Z'_\gamma(kr_a)} \left( \frac{\sin \gamma \theta}{\gamma \theta} \right)^2, \quad (10)$$

where  $\gamma = n + m(N/2)$ .

This expression, however, corresponds precisely to  $Y_n$  for an interaction space having precisely the same dimensions but  $N/2$  openings instead of  $N$  openings. Then

$$\frac{Y_n + Y_{(N/2-n)}}{2} + Y_{r_1} = 0$$

is the equation for the resonant frequencies of an unstrapped system formed by the  $N/2$  resonators corresponding to one set of side resonators with the other set of side resonators filled with metal. A similar statement applies to the equation

$$\frac{Y_n + Y_{(N/2-n)}}{2} + Y_{r_2} = 0.$$

Thus the resonance equation for the rising-sun anode block,

$$\left[ \frac{Y_n + Y_{(N/2-n)}}{2} + Y_{r_1} \right] \left[ \frac{Y_n + Y_{(N/2-n)}}{2} + Y_{r_2} \right] = \left[ \frac{Y_n - Y_{(N/2-n)}}{2} \right]^2 \quad (11)$$

can be interpreted as a coupling equation for the corresponding modes of the two unstrapped systems with the term  $[(Y_n - Y_{N/2-n})/2]^2$  determining the strength of coupling. When this term is small, the coupling is weak and the resonances of the two systems are shifted only a very small amount. Except for the case  $n = 0$ ,  $[(Y_n - Y_{N/2-n})/2]^2$  is quite

small and becomes smaller as  $n$  and  $(\frac{N}{2} - n)$  become more nearly equal.

In the extreme case of  $n = N/4$ , the coupling term is identically zero and the resonance associated with one set of resonators is completely independent of the dimensions of the other set. Ordinarily (except for

$n = 0$ ), the coupling is quite weak,<sup>1</sup> although there is an important exception when the resonant frequencies of the two systems occur close together. Then both bracketed terms are small over the same frequency range, and the coupling term becomes important. This interpretation of the rising-sun resonances will be further supported in Sec. 3-2, where the field distribution will be examined.

Figure 3-3 shows the spectrum over the range of ratios in general use; the two groups shown correspond to the first group of resonances for both the large- and small-resonator systems. In the case shown,

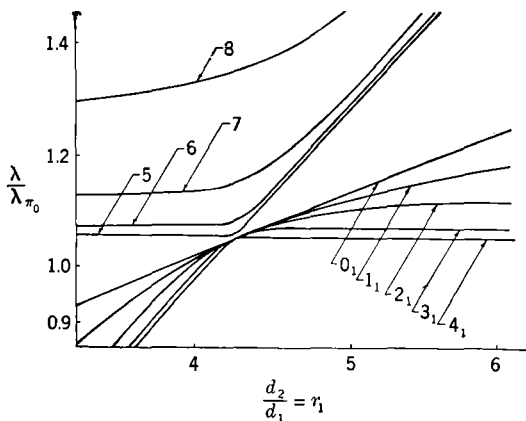


FIG. 3-4.—Mode spectrum, for large values of  $r_1$ , of the rising-sun system of Fig. 3-3. The two groups shown correspond to the first group of the small-resonator system and the second group of the large-resonator system.

the first group of resonances of the smaller-resonator unstrapped system happens to occur at a much higher wavelength range than that of the second group of resonances for the larger-resonator unstrapped system (not shown in the figure). For very large ratios this is no longer the case. Figure 3-4 shows the approximate behavior of the modes of the second group of the large-resonator system in relation to the first group of the small-resonator system, for  $r_1$  greater than 3.

Although the preceding discussion was to a large extent in reference to an  $N = 18$  resonant system, the discussion can easily be generalized. Thus, for a rising-sun system with  $N$  resonators and a ratio of resonator depths that is not too close to 1, the resonances of the first group of the spectrum can be divided into three subgroups. There is the set of modes numbered 1, 2,  $\dots$ ,  $(N - 2)/4$  (or  $N/4$ ). These correspond closely to

<sup>1</sup> This remark applies mainly to the case of small  $d_a/\lambda_\pi$ . As this quantity is increased, the coupling becomes stronger for  $n \neq 0$  and somewhat weaker for  $n = 0$ . For values of  $d_a/\lambda_\pi$  used in practice the coupling is always weak for  $n \geq 2$  but may be quite strong for  $n = 1$ .



the 1, 2,  $\dots$ ,  $(N-2)/4$  (or  $N/4$ ) of the unstrapped system of  $N/2$  resonators formed by filling the small resonators with metal. This set is frequently referred to as the upper multiplet. Second, there is the set of modes (the lower multiplet) numbered  $(N+2)/4$  or  $N/4, \dots$ ,  $(N/2) - 1$ . For moderate ratios of resonator sizes, these correspond closely to the  $(N-2)/4$ , (or  $N/4$ ),  $\dots$ , 2, 1, modes of the unstrapped system of  $N/2$  resonators formed by filling the large resonators with metal. [Note that the order is reversed. Thus the  $\left(\frac{N}{2} - 1\right)$ -mode of the rising-sun system corresponds to the 1-mode of the unstrapped system.] For very large ratios these modes correspond closely to the  $\left(\frac{N-2}{4}\right)_1$ ,  $\left[\text{or } \left(\frac{N}{4}\right)_1\right], \dots, 2_1, 1_1$ , modes of the large-resonator system (that is, the second group of resonances). This last correspondence occurs when the second group of resonances of the large-resonator system happens to occur at a longer wavelength than the first group of resonances for the small-resonator system. Third, there is the  $\pi$ - or  $N/2$ -mode, which occurs between the two subgroups mentioned above. The  $\pi$ -mode corresponds roughly to the  $0_1$ -mode of the large-resonator system, but its wavelength is as dependent upon the small-resonator dimensions as it is upon the large-resonator dimensions.<sup>1</sup>

As in the treatment of the unstrapped system, the preceding theory has entirely neglected the end spaces. The effects of the end spaces are somewhat similar for the two cases, in that all wavelengths turn out to be lower than the computed values. On the other hand, the general character of the spectrum and order of the modes remain the same. The reversal of order, mentioned for the unstrapped system, has never been observed in rising-sun systems, although one might expect it to occur

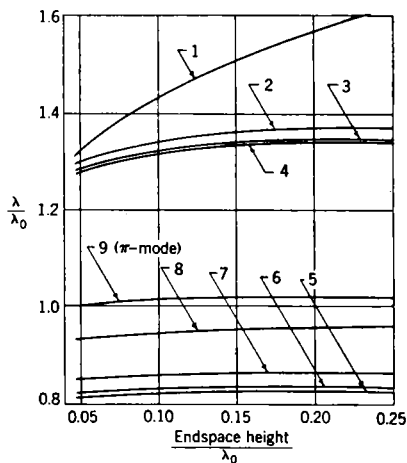


FIG. 3-5.—Typical example of the effect of end-space height on the mode spectrum of a rising-sun tube.  $\lambda_0$  is the initial value of the  $\pi$ -mode wavelength. Dimensions:  $d_a/\lambda_0 = 0.27$ ;  $h/\lambda_0 = 0.31$ ;  $r_1 = 1.75$ .

<sup>1</sup> The  $0_1$ -mode referred to above should not be confused with the  $0_1$ -mode in Fig. 3-4, which is the  $0_1$ -mode for the rising-sun system. The latter corresponds to the  $0_1$ -mode of the small-resonator system for small ratios and to the  $0_2$ -mode of the large-resonator system for large ratios.

for very short anodes with very short end spaces. The magnitude of the end-space effect depends upon the dimensions of the end space and the relative sizes of the side resonators. Experimentally it has been found that the  $\pi$ -mode may be depressed from 2 to 8 per cent; the lower-wavelength modes of the long-wavelength group are rarely depressed as much as 5 per cent, while the highest-wavelength mode, the 1-mode, may be depressed more than 20 per cent. The mode just below the  $\pi$ -mode, the  $\left(\frac{N}{2} - 1\right)$ -mode, is depressed about the same amount as the  $\pi$ -mode, although the separation between the two is usually changed somewhat. The other modes below the  $\pi$ -mode wavelength are depressed about 2 per cent. Figure 3-5 shows a typical example of the effect of end-space height on the mode spectrum.

**3-2. The Interaction Field.**—The tangential electric field at each gap was found in the last section to be given by

$$E \{ e^{i(2\pi n q/N)} + R e^{j[2\pi(n-\frac{N}{2})q]/N} \}.$$

This distribution was found by superposing the electromagnetic fields associated with  $E e^{j[2\pi(n-\frac{N}{2})q]/N}$  and the fields associated with

$$R E e^{j[2\pi(n-\frac{N}{2})q]/N}.$$

The various field components in the interaction space can then be found by simply superposing the fields associated with the above distributions. Thus

$$E_{\phi} = \frac{N\theta E}{\pi} \left\{ \sum_{m=-\infty}^{\infty} \left[ \left( \frac{\sin \gamma \theta}{\gamma \theta} \right) \frac{Z'_{\gamma}(k\rho)}{Z'_{\gamma}(kr_a)} e^{i\gamma\phi} + R \left( \frac{\sin \gamma' \theta}{\gamma' \theta} \right) \frac{Z'_{\gamma'}(k\rho)}{Z'_{\gamma'}(kr_a)} e^{i\gamma'\phi} \right] \right\}, \quad (12a)$$

$$E_{\rho} = -\frac{j}{k\rho} \frac{N\theta E}{\pi} \left\{ \sum_{m=-\infty}^{\infty} \left[ \gamma \left( \frac{\sin \gamma \theta}{\gamma \theta} \right) \frac{Z_{\gamma}(k\rho)}{Z'_{\gamma}(kr_a)} e^{i\gamma\phi} + R\gamma' \left( \frac{\sin \gamma' \theta}{\gamma' \theta} \right) \frac{Z_{\gamma'}(k\rho)}{Z'_{\gamma'}(kr_a)} e^{i\gamma'\phi} \right] \right\} \quad (12b)$$

$$H_z = -j \sqrt{\frac{\epsilon_0}{\mu_0}} \frac{N\theta E}{\pi} \left\{ \sum_{m=-\infty}^{\infty} \left[ \left( \frac{\sin \gamma \theta}{\gamma \theta} \right) \frac{Z_{\gamma}(k\rho)}{Z'_{\gamma}(kr_a)} e^{i\gamma\phi} + R \left( \frac{\sin \gamma' \theta}{\gamma' \theta} \right) \frac{Z_{\gamma'}(k\rho)}{Z'_{\gamma'}(kr_a)} e^{i\gamma'\phi} \right] \right\} \quad (12c)$$

where  $\gamma = n + mN$  and  $\gamma' = \left(n - \frac{N}{2}\right) + mN$ .

It is now possible to see which modes are degenerate and which are not. Substitution of  $-n$  does not change the resonant frequencies of the modes. However, except for  $n = 0$  or  $n = N/4$ , it does lead to a field distribution that is linearly independent of the  $+n$  field.<sup>1</sup> These modes then have a second-order degeneracy. When  $n = 0$ , no sign change is possible ( $-n = +n$ ), so that the  $\pi$ -mode is nondegenerate. To consider the case  $n = N/4$ , it is necessary to know the value of  $R$ . It can be shown that for the ( $n = N/4$ )-resonance associated with the even-numbered resonators  $R = 1$ , and for the  $N/4$ -resonance associated with the odd-numbered resonators  $R = -1$ . In either case, replacing  $n$  by  $-n$  does not lead to a linearly independent field so that modes with  $n = N/4$  are also nondegenerate. This is readily understandable if one observes what happens as the even- and odd-numbered resonators become alike. It is evident that the two roots of Eq. (7) for  $n = N/4$  are equal if  $Y_r = Y_n$ . It is also evident that both roots must be called

$N/4$ -modes because  $\left(\frac{N}{2} - n\right)$  is also equal to  $N/4$ . This corresponds to the fact that the  $N/4$ -mode has a second-order degeneracy in an unstrapped system. When the unstrapped system is perturbed into the rising-sun system, this  $N/4$  doublet splits, with one resonance following the odd-numbered resonator system and the other following the even-numbered resonator system. Thus, a rising-sun system in which  $N/4$  is an integer has two  $N/4$ -resonances. These two nondegenerate modes can be thought of as  $\pi$ -modes for the two unstrapped  $N/2$ -resonator systems.

It is apparent from the above expressions that a more detailed study of the fields requires further knowledge of  $R$ . It will be of interest to study some limiting cases first.

Case 1.— $Y_r = Y_n = Y$ . Here Eq. (7) can be factored yielding

$$Y_r + Y_n = 0,$$

which gives the  $n$ -mode frequencies, and

$$Y_r + Y_{\left(\frac{N}{2}-n\right)} = 0,$$

which gives the  $\left(\frac{N}{2} - n\right)$ -mode frequencies. Because

$$R = -\frac{Y_r + Y_n}{Y_r + Y_{\left(\frac{N}{2}-n\right)}},$$

it is clear that  $R = 0$  for an  $n$ -mode, and the fields are identical with

<sup>1</sup> Replacing  $n$  by  $\left(n + \frac{N}{2}\right)$  does not lead to linearly independent fields. [Note that  $R$  becomes inverted when  $m$  is odd (Eq. 8).]

those previously computed for an unstrapped system with  $N$  resonators oscillating in the  $n$ -mode. The ratio of the voltage<sup>1</sup> across an odd-numbered gap to that across the adjacent even-numbered gap in the clockwise direction is  $[(1 - R)/(1 + R)]e^{2\pi i n/N}$ . Thus if  $R = 0$ , the ratio is  $e^{2\pi i n/N}$ , which is appropriate to the  $n$ -mode of an unstrapped system rotating counterclockwise.

For the  $\left(\frac{N}{2} - n\right)$ -mode  $R = \infty$ . In order to have finite fields one must take  $RV$  finite and equal to  $V'$  with  $V = 0$ . Then the fields are identical with those previously computed for the  $\left(\frac{N}{2} - n\right)$ -mode. For the voltage ratio here is

$$\frac{(1 - R)}{(1 + R)e^{2\pi i n/N}} = -e^{2\pi i n/N} = e^{2\pi i (N - n)/N}$$

which is appropriate to the  $\left(\frac{N}{2} - n\right)$ -mode of an unstrapped system rotating clockwise.

Thus it can be seen that for  $R$  very near zero the voltages across odd and even gaps are approximately equal in magnitude. The fields are like those of a symmetric system with  $N$  resonators oscillating in the  $n$ -mode, with a small amount of  $\left(\frac{N}{2} - n\right)$ -mode mixed in. For  $R$  very large, the voltages across odd and even gaps are also approximately equal in magnitude. In this case the fields are like those of an unstrapped system with  $N$  resonators oscillating in the  $\left(\frac{N}{2} - n\right)$ -mode with a small amount of  $n$ -mode mixed in.

Case 2.— $Y_{r_2} \rightarrow \infty$ . This is the case for which the odd-numbered resonators are replaced by metal and the system reduces to an unstrapped system with  $N/2$ -resonators. The resonance equation becomes

$$\frac{Y_n + Y_{\frac{N}{2}-n}}{2} + Y_{r_1} = 0$$

and

$$R = -\frac{Y_{r_1} + Y_n}{Y_{r_1} + Y_{\frac{N}{2}-n}} = -\frac{Y_n - \frac{Y_n + Y_{\frac{N}{2}-n}}{2}}{Y_{\frac{N}{2}-n} - \frac{Y_n + Y_{\frac{N}{2}-n}}{2}} = 1.$$

Then  $[(1 - R)/(1 + R)]e^{2\pi i n/N} = 0$ , which is to be expected because the odd-numbered gaps are no longer present. The fields are those previously

<sup>1</sup> Here  $V = 2r_a\theta E$ , and  $V' = 2r_a\theta E'$ ; thus  $V'/V = E'/E = R$ .

computed for the  $n$ -mode of an unstrapped system with  $N/2$ -resonators. For example,  $E_\phi$  can be written as

$$E_\phi = \frac{N\theta E}{\pi} \sum_{m=-\infty}^{\infty} \left( \frac{\sin \gamma\theta}{\gamma\theta} \right) \frac{Z'_\gamma(k\rho)}{Z'_\gamma(kr_a)} e^{i\gamma\phi}, \quad (13)$$

where  $\gamma = n + mN/2$ .

Thus if  $R$  is near 1, the field is very much like that of an unstrapped system with  $N/2$ -resonators. The voltage across odd-numbered gaps is very small compared with that across even-numbered gaps. As a rule this means that the odd-numbered resonators are very weakly excited.

It can be shown similarly that  $R$  approaches  $-1$  as  $Y_r$  becomes very large. In this case the voltage across even-numbered gaps is small compared with that across odd-numbered gaps, and again the field is similar to that of an unstrapped system with  $N/2$ -resonators oscillating in the  $n$ -mode.<sup>1</sup>

It is evident that a good picture of the modification of the interaction field may be obtained by studying the variation of  $R$  as the shape of the odd or even set of resonators is changed. The behavior of  $R$  for the  $\pi$ -mode, although not typical of the usual behavior of  $R$ , is of fundamental

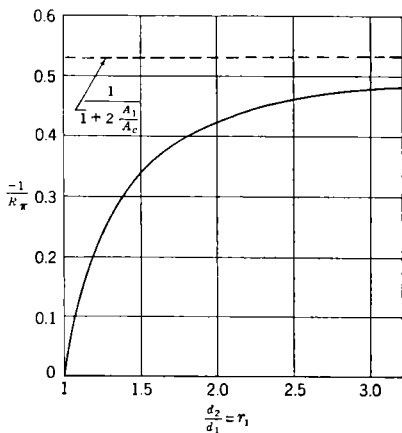


FIG. 3-6.— $-1/R_\pi$  as a function of  $r_1$  for the anode of Fig. 3-3.

importance in magnetron operation and will be discussed first. For a specific example consider the anode block used in Fig. 3-3 for which  $-1/R_\pi$  is plotted as a function of  $d_2/d_1$  in Fig. 3-6. As would be expected from the preceding discussion  $-1/R_\pi$  is zero for  $d_2/d_1 = 1$ . It is apparent that as  $d_2/d_1$  becomes large,  $-1/R_\pi$  approaches asymptotically a value that is less than 1. In fact, it can readily be shown that  $-1/R_\pi$  is always less than  $1/[1 + (2A_1/A_c)]$  where  $A_1$  is the total area of the small resonators and  $A_c$  is the area of the interaction space; this is the value which  $-1/R_\pi$  approaches in Fig. 3-6. In terms of voltages, this means that for  $d_2/d_1 = 1$ , the voltage across odd and even resonators is equal. As

<sup>1</sup> The expressions for the field components obtained by setting  $R = -1$  are formally different from those previously derived because of an effective shift of the polar axis through an angle  $2\pi/N$ . That is, since the even-numbered resonators are effectively absent, the polar axis goes between two resonators instead of through the center of a resonator.

$d_2/d_1$  increases, the voltage across the large resonators becomes larger than that across the small resonators, with the ratio approaching  $A_1/(A_c + A_1)$  as  $d_2/d_1$  becomes large. The fact that the voltages across the odd and even resonators are unequal implies that there is a net voltage around the anode circumference, a fact that is evident from an examination of  $E_\phi$ , for

$$E_\phi = \frac{N\theta E}{\pi} \left[ \frac{1}{R_\pi} \frac{Z'_0(k\rho)}{Z'_0(kr_a)} + 2 \sum_{m=1}^{\infty} \left( \frac{\sin \gamma'\theta}{\gamma'\theta} \right) \frac{Z'_\gamma(k\rho)}{Z'_\gamma(kr_a)} \cos \gamma'\theta \right. \\ \left. + \frac{1}{R_\pi} \left( \frac{\sin \gamma\theta}{\gamma\theta} \right) \frac{Z'_\gamma(k\rho)}{Z'_\gamma(kr_a)} \cos \gamma\phi \right], \quad (14)$$

and it is thus clear that for  $-1/R_\pi > 0$ ,  $E_\phi$  has a component that is independent of  $\phi$ . Thus  $r_a \int_0^{2\pi} E_\phi d\phi$  is not zero. A better understanding of the origin of this voltage can be had from an examination of the charge

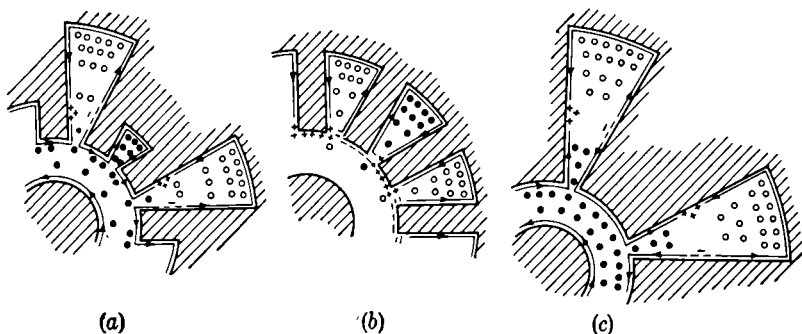


FIG. 3-7.—Qualitative distribution of magnetic field and current with impending charge distribution for (a) the  $\pi$ -mode of an  $N$ -resonator rising-sun system; (b) the  $\pi$ -mode of an  $N$ -resonator unstrapped system; and (c) the  $O_1$ -mode of an  $N/2$ -resonator unstrapped system. Magnetic lines into paper  $\bullet \bullet \bullet$ ; magnetic lines out from paper  $\circ \circ \circ$ .

and current distribution. Figure 3-7a shows the distribution of charge, current, and magnetic field in a rising-sun anode block. Whereas the voltages at odd- and even-resonator openings are opposite in direction, the magnetic fields are in the same direction. This would indicate that the magnetic field in the interaction space is unidirectional or that there is a net magnetic flux linking the anode circumference. This flux can be thought of as inducing the net voltage around the anode circumference. It is also apparent that the current across the anode segments is unidirectional. Figure 3-7b and c shows the charge and current distribution for the  $\pi$ -mode in an  $N$ -resonator unstrapped system and the  $O_1$ -mode in an  $(N/2)$ -resonator unstrapped system. The  $\pi$ -mode of the rising-sun

system evidently bears a certain resemblance to each and may be regarded as a perturbation of either.

As a measure of the distortion of the  $\pi$ -mode field in the rising-sun system, it is customary to use the ratio of the ( $\gamma = 0$ ) component to the ( $\gamma = N/2$ )-component of  $E_\phi$ . This ratio is given by

$$\bar{R}(\rho) = \frac{-Z'_0(k\rho)Z'_{N/2}(kr_a)\frac{N}{2}\theta}{2Z'_0(kr_a)Z'_{N/2}(k\rho)R_\pi\sin\frac{N}{2}\theta} \quad (15)$$

For rising-sun magnetrons in common use, this quantity is in the neighborhood of 0.1 at  $\rho = r_a$ . However, the  $N/2$ -component falls off much more rapidly than the zero component as  $\rho$  approaches  $r_c$ , and it is possible for  $R$  to exceed 1 in the vicinity of the cathode.

The behavior of  $R$  for modes other than the  $\pi$ -mode is quite different from that for the  $\pi$ -mode. As a specific example, consider the ( $n = 2$ )-mode and the ( $n = 7$ )- or  $\left(\frac{N}{2} - 2\right)$ -mode for the anode block used in Fig. 3-3. In Fig. 3-8,  $-R_2$  and  $1/R_7$  are plotted as functions of  $d_2/d_1$ . Although these quantities have the expected value of zero for  $d_2/d_1 = 1$ , they approach the value 1 quite rapidly, so that even for the rather moderate ratios used in practice the voltage across one set of resonators is small compared with that across the other set. In the case of the 2-mode the large resonators are the strongly excited ones, while for the 7-mode it is the small ones that are strongly excited.

$R_7$  differs from  $-R_2$  in that it does not approach 1 asymptotically. In fact, when the ratio  $d_2/d_1$  becomes so large that the lower-group resonances become associated with the large resonators,  $R_7$  changes rapidly from 1 and begins to approach  $-1$  asymptotically, which corresponds to the fact that the large resonators have come to be the strongly excited set. This behavior of  $R$  is typical of all modes except  $\pi$ -modes; that is, for the upper group  $R$  behaves like  $R_2$ , and for the lower group  $R$  behaves like  $R_7$ . Table 3-2 shows the values of  $R_n$  and also the ratio  $|V_L|/|V_s|$  of the magnitudes of voltages across the large and small resonators for  $d_2/d_1 = 2.1$ .

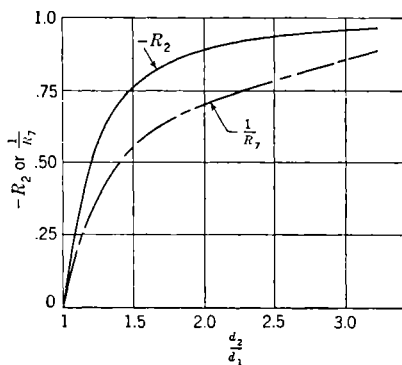


FIG. 3-8.— $-R_2$  and  $1/R_7$  as functions of  $d_2/d_1$  for the rising-sun system used in Fig. 3-3.

Further support for the interpretation of the rising-sun structure as two unstrapped systems coupled together is given by the field distributions. The coupling is quite weak for all the non- $\pi$ -modes except for the  $\left(\frac{N}{2} - 1\right)$ -mode and becomes increasingly weak as  $n$  or  $\left(\frac{N}{2} - n\right)$  approaches  $N/4$ . For the values of  $d_2/d_1$  used in practice and for the modes 1 through  $\left(\frac{N}{2} - 2\right)$ , an account of the spectrum and fields sufficiently accurate for many purposes can easily be obtained by ignoring the

TABLE 3.2.—VALUE OF  $R_n$  AND ALSO THE RATIO  $|V_L|/|V_S|$  OF THE MAGNITUDES OF THE VOLTAGES ACROSS THE LARGE AND SMALL RESONATORS FOR  $d_2/d_1 = 2.1$

$n$	$R_n$	$\frac{ V_L }{ V_S }$
1	-0.807	9.34
2	-0.908	19.2
3	-0.955	43.5
4	-0.986	114.
9	-2.290	2.55
8	2.680	0.457
7	1.370	0.157
6	1.140	0.067
5	1.050	0.024

set of resonators that are weakly excited and using the formulas for an unstrapped system of  $N/2$ -resonators. At the value of  $d_2/d_1$  and  $d_1/\lambda_\pi$  ordinarily used, the  $\left(\frac{N}{2} - 1\right)$ -mode retains a large measure of its  $\frac{N}{2} - 1$  character. The comparative excitation of the two sets of side resonators is of the same order as that for the  $\pi$ -mode.

**3.3. The Effect of the Mode Spectrum and Field Characteristics on  $\pi$ -mode Operation.** *The  $\gamma = 0$  Field Component.*—The interaction field of the  $\pi$ -mode in a rising-sun system differs from that of the  $\pi$ -mode in an unstrapped system (see Chap. 2) or a strapped system (see Chap. 4) in that the  $\phi$ -component of the electric field has a  $\gamma = 0$  field component. A detailed account of the effect of this component upon magnetron operation would require a discussion of magnetron electronics, a portion of magnetron theory that is very complicated and at present is incomplete. It will thus be possible to discuss the effects in a qualitative way only.

The most important effect of the zero component consists of a resonance phenomenon that occurs when  $\lambda B$  lies between 12,000 and 13,000 gauss cm or 0.012 and 0.013 weber per meter. From both theory and



experiment it would be expected that the electronic efficiency<sup>1</sup> at constant current would be a monotonic increasing function of the magnetic field; but in a rising-sun magnetron in the vicinity of  $\lambda B = 12,000$  gauss cm, there is a pronounced efficiency dip as shown in Fig. 3-9. Both the depth and breadth of this dip increase with increasing amounts of zero component. This effect is very important for magnetrons designed to operate below this dip (which at present includes all magnetrons for wavelengths less than 1.5 cm) because the amount of zero component determines the maximum efficiency obtainable for these magnetrons. The only magnetrons that have been successfully operated well above the dip have had only a small amount of zero component present (although enough to produce a pronounced dip). The zero component seemed to have very little effect on the high-field operation of these magnetrons, the electronic efficiency being fully as high as would be expected by comparison with strapped tubes.

This effect of the zero component has been explained in only the most qualitative manner. Ordinarily, the zero component

interacts with the electrons at random, so that there is no net exchange of energy between this component and the electrons. The electrons in a magnetron move in quasi-cycloidal orbits; at  $\lambda B \approx 12,000$  gauss cm, the transit time for each cycloidal arch is equal to the period of field oscillation, and it appears that under these conditions the effect of the zero component is cumulative rather than random. The loss of efficiency could be accounted for by either the transfer of energy from the zero component to the electrons or perhaps by the less efficient coupling with the  $\pi$ -component because of the distortion of the orbits.

There is another way in which the zero mode can interfere with the electron coupling. It was shown in the previous section, that proceeding from anode to cathode, the  $N/2$ - or  $\pi$ -component of  $E_\phi$  falls off much more rapidly than the zero component. Thus it is possible for the zero component to exceed the  $N/2$ -component near the cathode even though

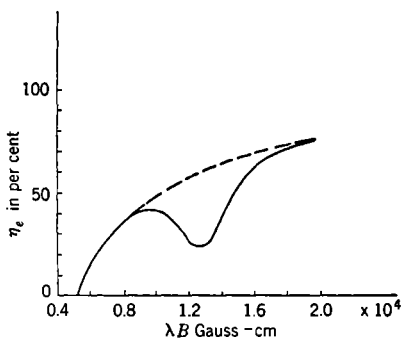


FIG. 3-9.—Approximate observed variation of electronic efficiency  $\eta_e$  with  $\lambda B$ .  
 - - - - a pure  $\pi$ -mode field ( $R(r_a) = 0$ );  
 ——— a  $\pi$ -mode field contaminated with the zero component ( $R(r_a) \approx .1$ ).

<sup>1</sup> Electronic efficiency is the power delivered into the electromagnetic field divided by the d-c power delivered to the magnetron. It differs from the over-all efficiency in that it neglects losses due to the r-f currents in the magnetron resonant system.

the  $N/2$ -component is much larger at the anode. This means that at any instant the field near the cathode is unidirectional. Such a phenomenon can interfere seriously with proper bunching of the electrons, and a loss of efficiency or a failure to operate in the  $\pi$ -mode may result. This effect may be most pronounced at high fields, because then the electrons are initially confined to regions near the cathode.

It should be mentioned that in spite of these difficulties, the amount of zero component is not a very critical parameter for operation below the efficiency dip, because the maximum efficiency obtainable falls off rather slowly as the zero to  $\pi$ -component ratio  $\bar{R}$  increases. No studies have been made of the effect of large amounts of the zero component for operation above the efficiency dip.

*Mode Competition.*—The  $\pi$ -mode operation of rising-sun magnetrons is subject to interference from certain of the other modes. The experimental results indicate that the interfering mode is always either a member of the long-wavelength group or the  $\left(\frac{N}{2} - 1\right)$ -mode<sup>1</sup> and, further, that it is possible to correlate the observed mode competition with the distribution of modes. The results of this correlation can be summarized as follows.

Interference from the  $\left(\frac{N}{2} - 1\right)$ -mode occurs when wavelength separation between the  $\pi$ -mode and the  $\left(\frac{N}{2} - 1\right)$ -mode is too small. Just what constitutes "too small" cannot be stated precisely because many factors besides the wavelength separation enter into mode competition. It has always been possible, however, to eliminate interference from the  $\left(\frac{N}{2} - 1\right)$ -mode by a proper increase in  $\lambda_\pi/\lambda_{\left(\frac{N}{2}-1\right)}$ . As a general rule  $\lambda_\pi/\lambda_{\left(\frac{N}{2}-1\right)} = 1.05$  may be considered a safe value.

Interference from members of the long-wavelength group occurs when the ratio of their wavelengths to  $\lambda_\pi$  becomes too large; the maximum allowable ratio decreases as  $N$  increases. Again it is not possible to give precise values, but the requirement that  $\frac{\lambda_4}{\lambda_\pi} < \frac{N}{2} / \left(\frac{N}{2} - 4\right)$  is an example of one rule that has proved useful. A more complete discussion and a physical interpretation of these results appear in Chap. 11.

It is apparent, then, that there are three major factors which govern the  $\pi$ -mode operation of a rising-sun system. These are (1)  $\bar{R}$  the ratio of the

<sup>1</sup> Interference is also observed from "nonmagnetron" modes, such as end-space resonances.

zero to the  $N/2$ -component in the  $\pi$ -mode field, (2) the ratio  $\lambda_r/\lambda_{(\frac{N}{2}-1)}$ , (3) the ratio of the upper-multiplet wavelengths to the  $\pi$ -mode wavelength. The system should be designed with  $\bar{R}$  as small as possible, with  $\lambda_r/\lambda_{(\frac{N}{2}-1)}$  sufficiently large,

and with the ratio of the upper multiplet wavelengths to the  $\pi$ -mode wavelength not too large. The next section will discuss the effect of the various parameters of the resonant system on these three factors.

**3.4. The Effects of Various Parameters on the Mode Spectrum and the Interaction Field of a Rising-sun Magnetron.**—Almost all of the experimental and developmental work on the rising-sun system has been done with the vane-type anode block illustrated in Fig. 3-1a. In these anode blocks, the side resonators consist of annular sectors whose sides are formed by radial rectangular vanes. The set of design parameters that has become associated with this design is (1) the ratio of the large-resonator depth to the small-resonator depth ( $d_2/d_1 = r_1$ ), (2) the ratio of the anode diameter to the  $\pi$ -mode wavelength ( $d_a/\lambda_r$ ), (3) the ratio of cathode diameter to anode diameter ( $d_c/d_a = \sigma$ ), (4) the number of resonators ( $N$ ), (5) the ratio of vane thickness to gap width

$$\left[ \frac{t}{w} = r_2 = \left( \frac{\pi}{N\theta} - 1 \right) \right].$$

Although some of these parameters apply to other types of anode blocks, the following discussion will refer exclusively to vane-type designs. The effects of these or corresponding parameters with respect to other type anodes can be deduced from a discussion to follow on the effect of variation of the side-resonator shape.

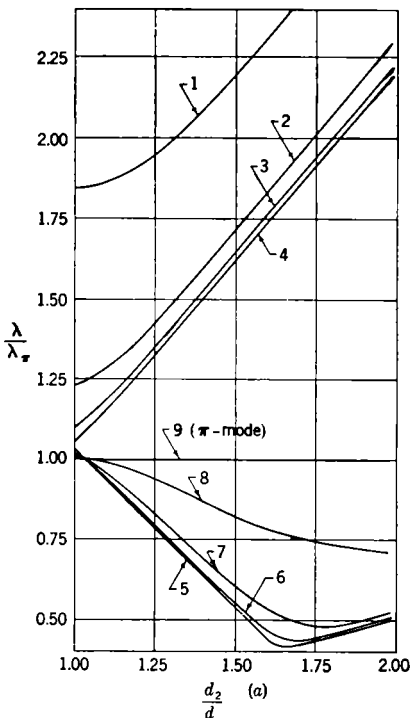


FIG. 3-10.—The effect of the ratio of resonator depths on the mode spectrum and the interaction field of a rising-sun magnetron. The dimensions are identical with those given in Table 2-1. (a) Mode spectrum as a function  $d_2/d$ . Both  $d_1$  and  $d_2$  are varied to maintain  $\lambda_r$  constant.  $d$  is the resonator depth for  $d_1 = d_2$ . (b) Values of  $1/r_1$  required to maintain  $\lambda_r$  constant, plotted as a function of  $d_2/d$ . (c)  $\bar{R}(r_a)$  the ratio of the zero component to the  $N/2$ -component of  $E_\phi$  at  $\rho = r_a$ , plotted as a function of  $d_2/d$ . (For parts (b) and (c) see page 102.)

*The Ratio of Resonator Depths.*—Figures 3-3 and 3-6 were used to illustrate the effect of  $r_1$  on the mode spectrum and on the interaction field of the  $\pi$ -mode, but the process is actually more complicated. Although all dimensions of the anode block other than resonator dimensions were held fixed, the  $\pi$ -mode wavelength changed, so that relative to  $\lambda_r$  these dimensions were not fixed (e.g.,  $d_a/\lambda_r$  changed). In order to examine the effect of  $r_1$  alone, it is therefore necessary to change the large- and small-resonator depths simultaneously, in such a manner that the  $\pi$ -mode wavelength is maintained constant, while all other anode block dimensions are kept fixed. (This is the sort of change in  $r_1$  that would probably

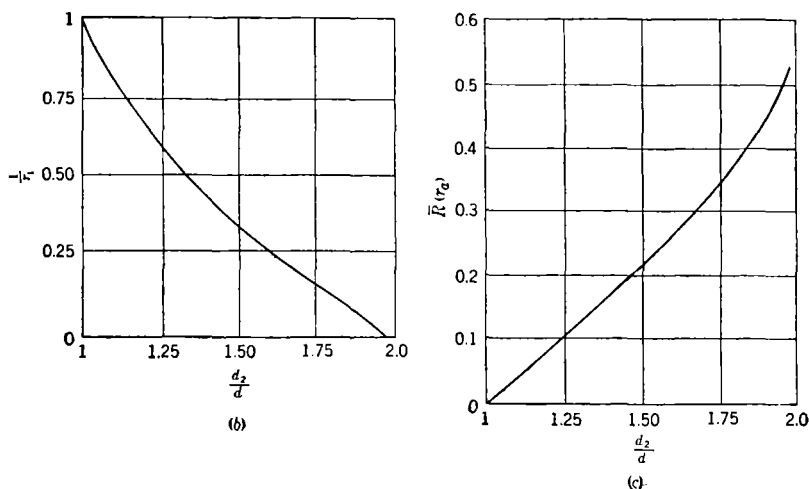


FIG. 3-10.—For descriptive legend see page 101.

be made in practice.) The effect of such a change in  $r_1$  is shown in Fig. 3-10a where the mode spectrum is plotted as a function of  $d_2/d$ ,  $d$  being the resonator depth when  $d_1 = d_2$ . Figure 3-10b shows the value of  $1/r_1$  required to keep  $\lambda_\pi$  constant as a function of  $d_2/d$ . The other dimensions of the anode block, all of which are held fixed, are given in Table 2-1. The effect of  $r_1$  upon the interaction field of the  $\pi$ -mode is shown in Fig. 3-10c, where  $\bar{R}(r_a)$ , the ratio of zero to  $N/2$ -component of  $E_\phi$  at  $\rho = r_a$ , is plotted as a function of  $d_2/d$ .

It is evident from Fig. 3-10a that a certain minimum value of  $r_1$  must be passed before the  $\pi$ - and 8-mode begin to separate and further that the amount of separation which can be obtained between these two modes is not unlimited. The bend in the curves of the short-wavelength modes which occurs as  $r_1$  becomes large is due to the fact that these modes have ceased to be associated with the small resonators and have come to correspond to the second group of resonances associated with the large

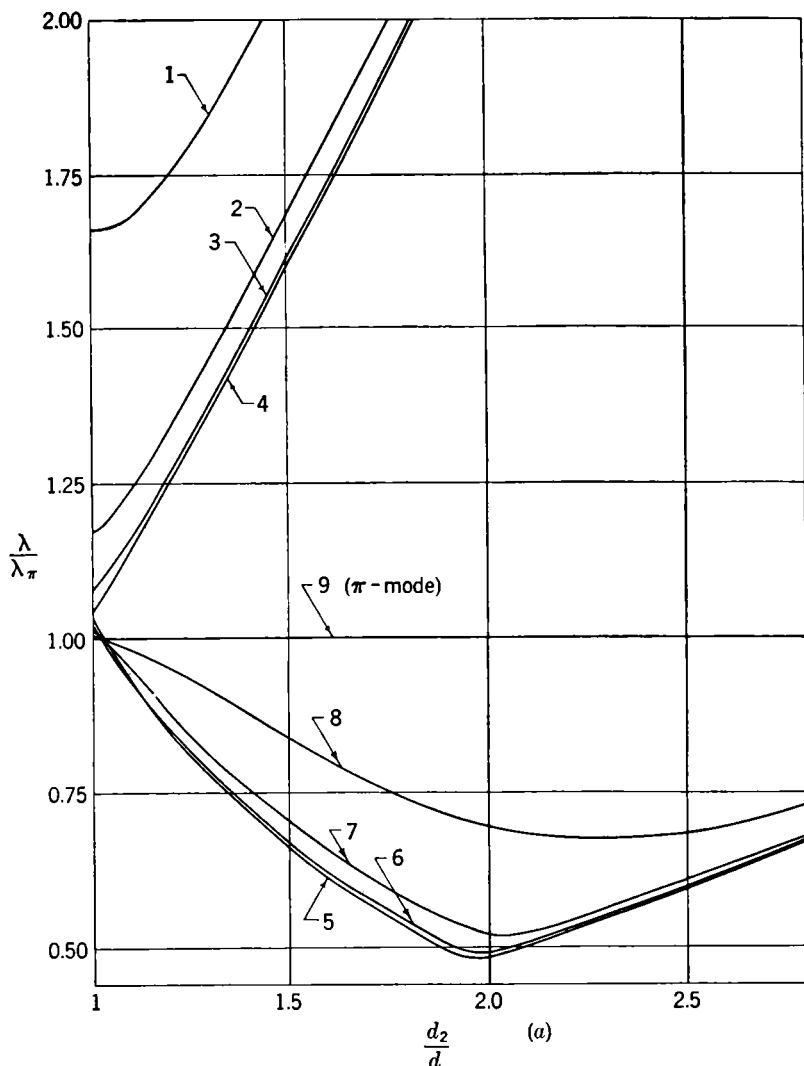


FIG. 3-11.—The effect of the ratio of resonator depths on the mode spectrum and the interaction field of a rising-sun magnetron. Dimensions are the same as those for Fig. 3-10 except that  $d_a/\lambda_\pi$  has been reduced from 0.325 to 0.217. (a) Mode spectrum as a function  $d_2/d$ . Both  $d_1$  and  $d_2$  are varied to maintain  $\lambda_\pi$  constant.  $d$  is the resonator depth for  $d_1 = d_2$ . (b) Values of  $1/r_1$  required to maintain  $\lambda_\pi$  constant, plotted as a function of  $d_2/d$ . (c)  $\bar{R}(r_a)$ , the ratio of the zero component to the  $N/2$ -component of  $E_\phi$  at  $\rho = r_a$ , plotted as a function of  $d_2/d$ . (For parts (b) and (c) see page 104.)

resonators. The fact that the 8-mode does not reverse is fortuitous; it is due to the particular values chosen for the other anode block dimensions.

An increase in  $r_1$  not only increases the separation between the  $\pi$ -mode and the  $\left(\frac{N}{2} - 1\right)$ -mode but also increases the separation between the  $\pi$ -mode and the long-wavelength group and increases the quantity  $\bar{R}(r_a)$ . The latter two effects are undesirable, so it is best to have  $r_1$  just large enough to give sufficient separation of the  $\pi$ -mode and the  $\left(\frac{N}{2} - 1\right)$ -mode. Just what value of  $r_1$  should be used depends upon the values

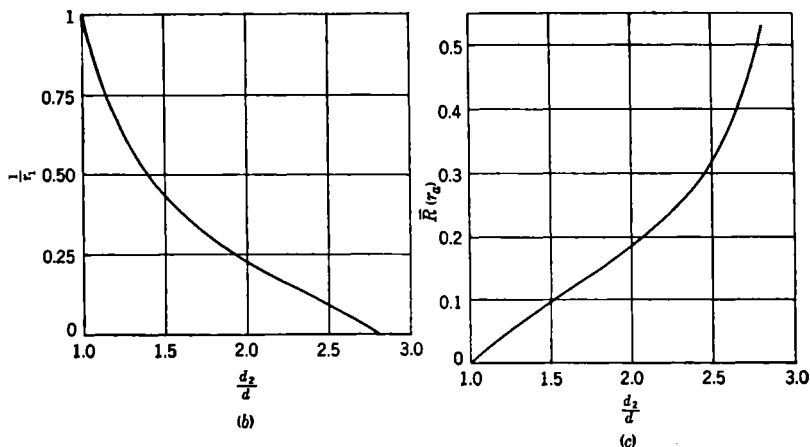


FIG. 3-11.—For descriptive legend see page 103.

of the other parameters, namely,  $d_a/\lambda_\pi$ ,  $\sigma$ ,  $N$ , and  $r_2$ . The specific numerical values for some designs that have been found satisfactory are listed in Chap. 11.

*The Ratio of Anode-block Diameter to  $\pi$ -mode Wavelength.*—The effect of the parameter  $d_a/\lambda_\pi$  can best be studied by comparing the curves of Fig. 3-10a, b, and c with a similar set of curves in Fig. 3-11a, b, and c computed for a different value of  $d_a/\lambda_\pi$ . The dimensions for this latter set are also those given in Table 2-1 with the exception that  $d_a/\lambda_\pi$  has been reduced from 0.325 to 0.217. Comparing the two spectra for the same value of  $r_1$ , while restricting  $r_1$  to small values, one finds that the separation between the  $\pi$ - and 8-modes is smaller and that  $\bar{R}(r_a)$  is larger for the block of larger  $d_a/\lambda_\pi$ . Figure 3-12a shows a direct comparison of  $\bar{R}(r_a)$  plotted as a function of  $\lambda_\pi/\lambda_8$  for the two values of  $d_a/\lambda_\pi$ , and Fig. 3-12b shows  $\lambda_4/\lambda_\pi$  as a function of  $\lambda_\pi/\lambda_8$  for the two cases. The effect of a further increase in  $d_a/\lambda_\pi$  is similar; that is, for equal values of  $\lambda_\pi/\lambda_{\left(\frac{N}{2}-1\right)}$ ,  $\bar{R}(r_a)$  increases while  $\lambda_4/\lambda_\pi$  does not change significantly.

Inasmuch as the effects of increasing  $d_a/\lambda_\pi$  are undesirable, it is best to have  $d_a/\lambda_\pi$  as small as is consistent with other design considerations. On the other hand, satisfactory operation is possible over a wide range of values of  $\bar{R}(r_a)$ , so that a correspondingly wide range of values is available for  $d_a/\lambda_\pi$ .

*The Ratio of Cathode Diameter to Anode Diameter.*—The general effect of  $\sigma$  on the spectrum is given in Table 3-3 which lists the computed wavelengths of the modes of an 18-resonator system with the cathode

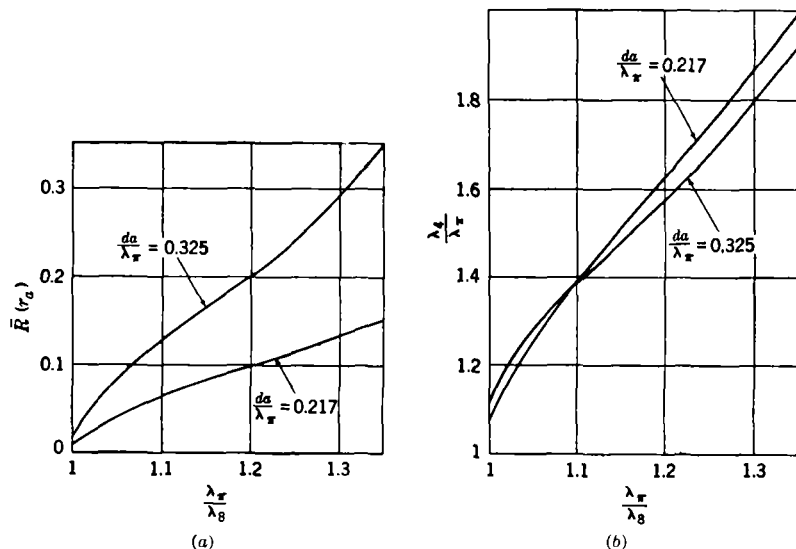


FIG. 3-12.—The effect of  $d_a/\lambda_\pi$  on the interaction field and the mode spectrum of the rising-sun systems of Figs. 3-10 and 3-11. (a)  $\bar{R}(r_a)$ , the ratio of the zero component to the  $N/2$ -component of  $E_\phi$  at  $\rho = r_a$  plotted as a function of  $\lambda_\pi/\lambda_8$  for two values of  $d_a/\lambda_\pi$ . (b) The quantity  $\lambda_4/\lambda_\pi$  is plotted as a function  $\lambda_\pi/\lambda_8$  for two values of  $d_a/\lambda_\pi$ .

present and with the cathode removed. It is seen that in this particular case an increase in  $\sigma$  reduces the  $\pi$ -mode wavelength but increases the wavelengths of all of the other modes.

The direction of the wavelength shift is determined by the sign of

$$\int_0^{2\pi} [\mu_0 H_z^2(r_c, \phi) - \epsilon_0 E_\rho^2(r_c, \phi)] d\phi, \quad (16)$$

an increase in  $\sigma$  decreasing or increasing the wavelength as the integral is positive or negative. For the values of  $r_1$  and  $\sigma$  used in practice, an increase in  $\sigma$  increases the wavelengths of all modes in the upper multiplet and decreases the  $\pi$ -mode wavelength, while the wavelengths of the lower-multiplet modes are raised or lowered as the cathode circumference is

less or greater than  $\left(\frac{N}{2} - n\right) \lambda_n$ . The rule for the lower multiplet is approximate and holds only when the contribution of the higher-order field components to the integral (16) is negligible as compared with the  $\left(\frac{N}{2} - n\right)$  field components.<sup>1</sup> The reversal in the direction of the wavelength shift actually occurs at a somewhat larger value of the cathode circumference than  $\left(\frac{N}{2} - n\right) \lambda_n$ .

TABLE 3-3.—THE EFFECT OF THE PRESENCE OF THE CATHODE ON THE SPECTRUM OF A TYPICAL RISING-SUN MAGNETRON

$n$	$\frac{\lambda_n}{\lambda_\pi}$ (cathode present)	$\frac{\lambda'_n}{\lambda_\pi}$ (cathode removed)	Dimensions
1	1.944	1.603	$\frac{d_n}{\lambda_\pi} = 0.307$
2	1.456	1.420	
3	1.381	1.375	$\frac{d_2}{d_1} = 1.780$
4	1.360	1.357	
9	1.000	1.030	$\frac{d_2}{\lambda_\pi} = 0.226$
8	0.920	0.853	$\theta = 0.068$ radian
7	0.800	0.786	$\frac{d_c}{d_a} = 0.59$ for $\lambda_n$
6	0.766	0.761	
5	0.754	0.752	$\frac{d_c}{d_a} = 0$ for $\lambda'_n$

As indicated in Table 3-3, the effect of the cathode becomes increasingly less for the lower-wavelength modes of both the long- and short-wavelength groups. In fact, for most purposes the effect of  $\sigma$  can be neglected for all modes except the 1-mode, the  $\left(\frac{N}{2} - 1\right)$ -mode, and the  $\pi$ -mode. Although the separation between the  $\pi$ -mode and the long-wavelength modes increases somewhat when  $\sigma$  increases, the most significant effect upon the spectrum is the loss of separation between the  $\pi$ -mode and  $\left(\frac{N}{2} - 1\right)$ -mode.

The zero-component contamination of the  $\pi$ -mode,  $\bar{R}(r_a)$ , decreases with increasing  $\sigma$ . For the magnetron in Table 3-3,  $\bar{R}(r_a)$  decreases from 0.161 to 0.106 when the cathode is introduced. There is an even greater decrease in  $\bar{R}(\rho)$  as  $\rho$  approaches  $r_c$  because the discrepancy in rate of

<sup>1</sup> This is always the case except when  $r_1$  or  $\sigma$  is nearly equal to 1.



decrease between the zero and  $N/2$ -components is less effective for a larger cathode. When the loss in mode separation is small, this effect may compensate for the loss in mode separation as far as mode competition is concerned.

Actually the above considerations have very little effect upon the choice of  $\sigma$ . The size of the cathode has a very strong effect on the relative strength of the various field components near the cathode because the higher  $n$ -modes and higher  $\gamma$  Fourier-components fall off much more rapidly, moving in from the anode, than those of lower  $n$  or  $\gamma$ . The character of fields near the cathode is very important in determining the amount of energy lost in the initial bunching process and in determining the mode in which the magnetron will start. In general, a reduction in cathode size increases the efficiency but also may lead to mode-competition difficulties (see Chap. 8). Ordinarily the smallest cathode diameter that gives stable  $\pi$ -mode operation is used. It has been found experimentally that the best value for  $\sigma$  depends almost entirely upon  $N$  and very little upon other parameters (Chap. 11). Evidently the effects of varying  $\sigma$  are largely dependent upon magnetron electronics.

*The Number of Resonators.*—If  $N$  is increased with fixed  $d_1$ ,  $d_2$ ,  $d_a$ ,  $r_2$ , and  $\sigma$ , the wavelengths of all of the original modes are virtually unchanged, but additional modes are added to the lower-wavelength end of both groups of resonances. Thus an increase in  $N$  in itself has no particular effect upon the significant characteristics of the resonant system. Difficulties with large  $N$  systems are due mainly to the fact that the maximum allowable ratio of the wavelengths of the upper multiplet modes to  $\lambda_\pi$  decreases as  $N$  increases (see Chap. 11).

*The Ratio of Anode-segment Width to Gap Width,  $r_2$ .*—An increase in  $r_2$ , with  $d_1$ ,  $d_2$ ,  $d_a$ , and  $\sigma$  fixed, increases the wavelengths of all of the modes. The comparative rates of increase for the various modes are such that the members of the upper-wavelength group move closer together, as do the members of the lower-wavelength group, while the  $\pi$ -mode moves away from the  $\left(\frac{N}{2} - 1\right)$ -mode and toward the upper-wavelength group. Furthermore,  $\bar{R}(r_a)$  increases.

A pertinent factor in magnetron design is the modification of the spectrum as  $r_2$  is changed, with  $d_1$  and  $d_2$  adjusted to keep the  $\pi$ -mode and  $\left(\frac{N}{2} - 1\right)$ -mode fixed. In this case, the upper-wavelength group descends while  $\bar{R}(r_a)$  increases. Thus an increase of  $r_2$  might avoid difficulty with the long-wavelength modes, but the increase in  $\bar{R}(r_a)$  would cause some loss in efficiency. No attempt has ever been made to avoid long-wavelength mode competition difficulties in this way, because the

range over which  $r_2$  can be varied is limited by mechanical considerations (see Chap. 11). Furthermore, it has always been possible to solve the problem of long-wavelength mode competition by closing the ends, as explained in Sec. 3-5.

*Variation of Resonator Shape.*—While the vane-type resonator is most commonly used, other types having different shapes may have mechanical or electrical advantages. One example is the hole-and-vane combination illustrated in Fig. 3-1*b*. Inasmuch as all of the anode-block parameters have been discussed for vane-type resonators, it is convenient to consider other resonator shapes as modifications of the vane-type and to define the “vane equivalent” of a resonator and an “equivalent ratio” of resonator depth. The vane equivalent of a resonator is defined as an annular sector resonator composed of vanes whose thickness is equal to the width of the anode segments and whose depth is such that its admittance at the  $\pi$ -mode wavelength is equal to that of the resonator in question. The admittance of a resonator and that of its vane equivalent will, in general, be different for wavelengths other than the  $\pi$ -mode wavelength. The equivalent ratio  $r_{eq}$  is defined simply as the ratio of the depths of the vane equivalents corresponding to the large and small resonators; it thus replaces the parameter  $r_1$  defined for vane-type resonators. Two rising-sun systems that are identical except for resonator shape and have the same  $\pi$ -mode wavelength and the same value for  $r_{eq}$  will have identical  $\pi$ -mode interaction fields; that is,  $\bar{R}$  is the same for both.

Inasmuch as the admittances of corresponding resonators are the same at the  $\pi$ -mode wavelengths, they will be nearly the same for wavelengths near that of the  $\pi$ -mode. Thus the modes with wavelengths near that of the  $\pi$ -mode will have nearly the same wavelength in the two anode blocks, and ordinarily the  $\pi$ - and  $\left(\frac{N}{2} - 1\right)$ -mode separations will be nearly the same. On the other hand, at wavelengths far from that of the  $\pi$ -mode, the admittance of corresponding resonators may be quite different, and the position of the long-wavelength group and the lower-wavelength members of the short-wavelength group may be considerably different for the two structures.

Aside from mechanical advantages, there are often electrical advantages to be gained by a wise choice of resonator shape. Two advantages relate to the circuit properties of anode blocks, the unloaded  $Q$  and the equivalent capacity, discussed in Sec. 3-6. A third advantage lies in the possibility of depressing the wavelengths of the long-wavelength group. As an example of the latter, consider the anode-block section in Fig. 3-13 which has the dimensions given in Table 2-1 except for the resonators and which has an  $r_{eq}$  equal to 2.71. Table 3-4 lists the result-

ant wavelengths of the spectrum in comparison with those of an equivalent vane-type anode block which has an  $r_1$  of 2.71. It is evident that the long wavelengths have been considerably depressed at a small cost in separation between the  $\pi$ - and 8-modes. Although a similar spectrum could be achieved with vane-type resonators having a larger value of  $r_2$ , the zero contamination of the  $\pi$ -mode would be worse. In general, large mode separation is obtained by using resonators whose admittances change slowly with frequency, and small mode separation by using resonators whose admittances change rapidly with frequency. In the particular case given in Table 3-4, the spread of the lower-wavelength resonances and the contraction of the higher-wavelength resonances is due to the fact that the two groups of resonators were designed on this basis.

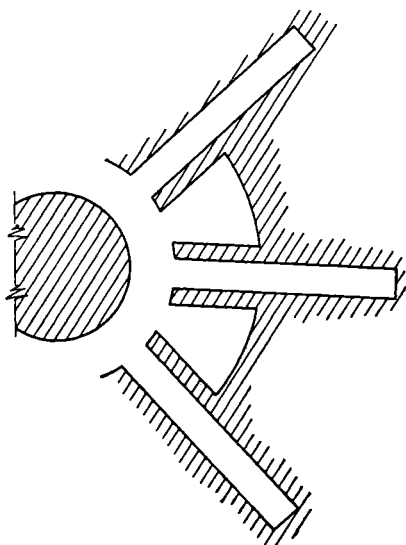


FIG. 3-13.—Rising-sun system with modified resonator shapes.

TABLE 3-4.—THE SPECTRUM OF THE SYSTEM IN FIG. 3-13 COMPARED WITH THAT OF ITS EQUIVALENT VANE-TYPE SYSTEM

$\lambda_n$  are the resonances of the vane-type system;  $\lambda'_n$  of the modified system

$n$	$\frac{\lambda_n}{\lambda_9}$	$\frac{\lambda'_n}{\lambda_9}$
1	2.183	1.604
2	1.697	1.279
3	1.621	1.241
4	1.602	1.231
9	1.000	1.000
8	0.828	0.864
7	0.616	0.607
6	0.570	0.544
5	0.555	0.525

In the development of magnetrons considerable attention was given to the possibility of modifying the symmetry of a resonant system in a

manner that would leave the  $\pi$ -mode practically unchanged but would have a marked effect on some of the other modes. The use of strap breaks in the strapped system (see Secs. 4-1 and 4-7) is the major example of such a modification. A somewhat analogous scheme for the rising-sun system would consist of replacing certain of the resonators (large or small) by resonators of a different shape but of the same vane equivalent as the other corresponding resonators. Inasmuch as the admittances of all of the large resonators (and those of all of the small resonators) appear to be alike at the  $\pi$ -mode wavelength, neither the resonant wavelength nor the interaction field of the  $\pi$ -mode is affected. On the other hand, for the non- $\pi$ -modes, and particularly for those with resonant wavelengths far from that of the  $\pi$ -mode, the various resonators no longer appear to be alike. Consequently, for these modes the wavelengths will be shifted, the doublets split (i.e., the degenerate modes split into two nondegenerate modes), the loading through the output modified, and the interaction field distorted. One might expect, then, that by a proper modification of resonators, interference from unwanted modes could be avoided. Neither this scheme nor the one described in the preceding paragraph has yet been tested on rising-sun magnetrons.

**3.5. Closed-end Rising-sun Systems.**—In the preceding sections it has been stated that one serious limitation of the rising-sun system is the competition which arises between the  $\pi$ -mode and the long-wavelength modes in systems of large  $N$  and large  $r_1$ . The difficulty is due to excessive separation between the  $\pi$ -mode and the long-wavelength modes, and so a means of reducing this separation is required. The closing of the ends of the resonators has been shown to be effective in this respect (see Fig. 11-9b).

It is a simple matter to compute the spectrum and interaction fields for a rising-sun system with totally closed ends. Similar to the treatment of the unstrapped system (Sec. 2-8), the anode block and cathode can be regarded as a section of waveguide. Then the resonant wavelengths computed for the open-ended system become the cutoff wavelengths of the corresponding  $TE$ -modes of this waveguide. The guide wavelengths for the various modes can be computed from these cutoff wavelengths, and the resonant wavelengths of the first group of modes can be found from the condition that  $\lambda_{gn} = 2h$ , where  $h$  is the anode height. Explicitly, the resonant wavelengths are given by

$$\lambda_n = \frac{\lambda_{cn}}{\sqrt{1 + \left(\frac{\lambda_{cn}}{2h}\right)^2}}, \quad (17)$$

where  $\lambda_{cn}$  is the wavelength of the  $n$ th mode in the open-ended system.

Figure 3-14 shows the spectrum as a function of  $d_2/d$  with  $r_1$  varied to keep the  $\pi$ -mode wavelength fixed. In this example the values for  $d_a/\lambda_\pi$ ,  $\sigma$ ,  $r_2$ , and  $N$  are the same as those in Table 2-1. The behaviors of  $1/r_1$  and  $R(r_a)$  as functions of  $d_2/d$  are the same as those shown in Fig. 3-11b and c.

In Fig. 3-15a and b the most significant features of this closed-end system are compared with those for an open-end system having the same value of  $d_a/\lambda_\pi$ . It can be seen that for the same values of  $\lambda_\pi/\lambda_s$ ,  $\bar{R}(r_a)$  is somewhat smaller for the closed-end system, while the ratios of the upper multiplet wavelengths to  $\lambda_\pi$  ( $\lambda_4/\lambda_\pi$  is typical) are considerably smaller for the closed-end system. This latter effect is, of course, due to the fact that all of the closed-end wavelengths must be less than  $2h$ . Thus, by making  $2h/\lambda_\pi$  small enough (note that  $2h/\lambda_\pi$  is always greater than 1) it should always be possible to have the upper group near enough to the  $\pi$ -mode to permit  $\pi$ -mode operation. There are, however, objections to making systems for which  $2h/\lambda_\pi$  is very close to 1 because as  $2h/\lambda_\pi$  approaches 1, the separation between the  $\pi$ - and  $\left(\frac{N}{2} - 1\right)$ -mode falls off to zero.<sup>1</sup> Furthermore, for values of  $2h/\lambda_\pi$  near 1 it is necessary that  $\lambda_{cs}/\lambda_\pi$  be very large, which means that the physical dimensions of the system must be large.

The electromagnetic fields for the closed-end system are similar to those of the open-end system except for the axial variation. That is,  $\mathbf{E}$  and  $H_z$  are unchanged as functions of  $\rho$  and  $\phi$ , but both are multiplied by  $\sin \pi z/h$  ( $z = 0$  and  $z = h$  correspond to the two ends of the system).  $H_\rho$  and  $H_\phi$  are no longer zero but are given by

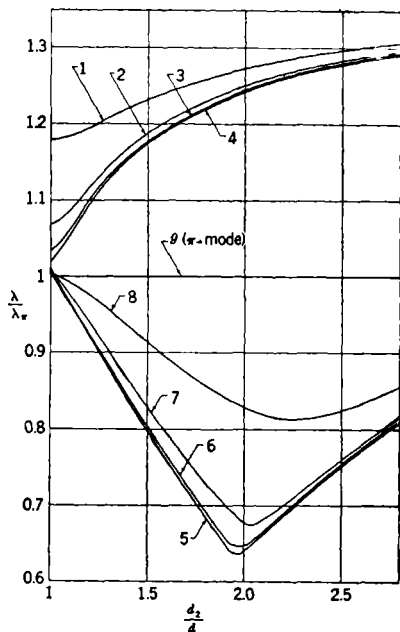


FIG. 3-14.—The spectrum of a closed-end rising-sun magnetron as a function of  $d_2/d$ , with  $r_1$  varied so that  $\lambda_\pi$  is kept constant.  $d$  is the resonator depth for  $d_1 = d_2$ . Dimensions:  $d/\lambda_\pi = 0.249$ ;  $h/\lambda_\pi = 0.680$ ; the rest from Table 2-1.

<sup>1</sup> There is an optimum height that gives the maximum separation between the  $\pi$ - and  $\left(\frac{N}{2} - 1\right)$ -modes for specific values of  $d_a/\lambda_\pi$ ,  $\sigma$ ,  $N$ ,  $r_2$ , and  $\bar{R}(r_a)$ .

$$H_\phi = \frac{\lambda_{c\pi}^2}{4\pi h\rho} \frac{\partial H_z(\rho, \phi)}{\partial \phi} \cos \frac{\pi z}{h}; \quad (18a)$$

$$H_\rho = \frac{\lambda_{c\pi}^2}{4\pi h} \frac{\partial H_z(\rho, \phi)}{\partial \rho} \cos \frac{\pi z}{h}. \quad (18b)$$

The computed frequencies for a closed-end magnetron usually agree within 1 per cent with the observed frequencies. Of course, no operating magnetron has its ends totally closed because the cathode must be insulated from the anode. Thus in practice "totally closed" means that the resonators are totally covered but that the interaction space remains uncovered. Under these conditions, the wavelengths are

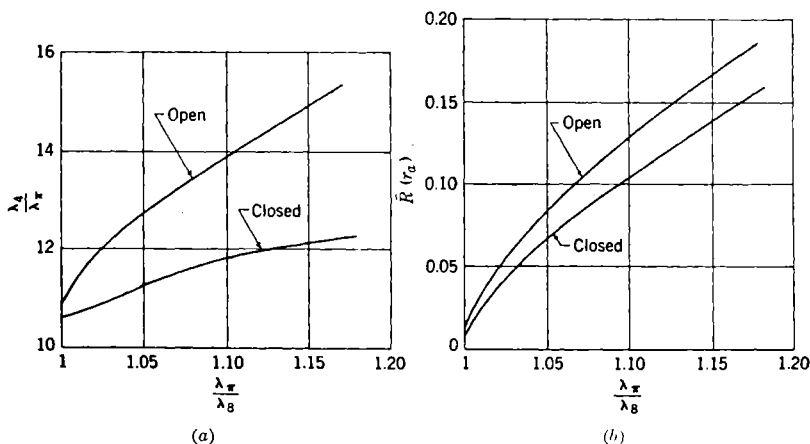


FIG. 3-15.—(a) A comparison of the separation between the upper-wavelength groups and the  $\pi$ -mode for closed-end and open-end rising-sun system. Wavelength  $\lambda_c$  is typical of the behavior of the upper-wavelength group. (b) A comparison of the zero-component contamination of the  $\pi$ -mode interaction field for closed-end and open-end rising-sun systems.

always higher than they would be if the ends were entirely closed. For the  $\pi$ -mode the increase is about 1 per cent. When  $d_a/\lambda_\pi$  is small, the effect on all modes except the 1-mode is from 1 to 2 per cent. The 1-mode may be increased 20 per cent or more, but ordinarily this is of no particular significance for magnetron operation. When  $d_a/\lambda_\pi$  is large, the  $\left(\frac{N}{2} - 1\right)$ -mode is also rather strongly affected (increases as great as 5 per cent have been observed), and consequently the separation between the  $\pi$ - and the  $\left(\frac{N}{2} - 1\right)$ -mode may become considerably less than the computed value.

In many cases, it is unnecessary to lower the long-wavelength group as much as results from fully closing the ends; the long-wavelength modes

can be lowered to a lesser extent by closing only the outer portion of the resonators. Such systems are called partially closed-end systems.

Semiempirical methods for computing resonances, based on computed frequencies, have been worked out for nearly closed blocks (see Chap. 11). Detailed information on the wavelength of non- $\pi$ -modes is not available. For systems that are less than half closed, an estimate of the wavelength can be made to within 5 or 10 per cent by treating the resonators as compound resonators. That is, the admittance of the closed portion is computed and then considered as the terminating admittance for the open portion (see Sec. 2-5). When the block is nearly open, this method should be more accurate than indicated above.

**3-6. The Unloaded  $Q$  and  $\sqrt{C/L}$ .**—In addition to the resonant frequency, there are two other circuit parameters that are of importance in magnetron design; these are the unloaded  $Q(Q_U)$  and the characteristic admittance  $\sqrt{C/L}$ .

Heretofore it has been assumed that the magnetron resonant system is lossless. Actually, however, some power is delivered to a load, and some energy is converted into heat by currents flowing in the metal walls. The unloaded  $Q$  is essentially a measure of the power dissipated in the metal and is defined by

$$Q_U = 2\pi \frac{\text{total stored energy}}{\text{energy per cycle dissipated in metal}}.$$

In a similar way one can define an external  $Q$  which takes into account only the energy delivered to the output and the total or loaded  $Q$  which takes into account both kinds of energy loss. These last two quantities will be discussed in connection with the output circuit in Chap. 5. The total stored energy is given by  $\mu_0/2 \int_V |H|^2 dv$ , where  $|H|$  is the amplitude of the magnetic field. The average rate of power dissipation is given by  $1/2\kappa\delta \int_S |H|^2 ds$  [where  $\delta = (\pi f \mu \kappa)^{-1/2}$  is the skin depth,  $f$  is the frequency,  $\mu$  is the permeability of the walls, and  $\kappa$  is the conductivity of the walls]. There then follows the well-known formula

$$Q_U = 2 \sqrt{\pi f \kappa \frac{\mu_0^2}{\mu}} \frac{\int_V |H|^2 dv}{\int_S |H|^2 ds}. \quad (19)$$

Inasmuch as  $H$  is known throughout the magnetron cavity,  $Q_U$  can be calculated directly. In performing the calculation it is helpful to consider the resonators and interaction space separately and to compute equivalent inductances and resistances for the various elements. Consider the circuit in Fig. 3-16 with an alternating voltage of frequency

$f = \omega/2\pi$  and amplitude  $V$  across the terminals. The maximum energy stored in the magnetic field is  $\frac{1}{2}Li_L^2$  or  $\frac{1}{2}L(V^2/\omega^2L^2)$ , where  $i_L$  is the maximum current through the inductance. Thus, one can write

$$L = \frac{V^2}{2\omega^2 E_m},$$

where  $E_m$  is the maximum energy stored in the magnetic field. Also, the power  $P$  dissipated in the resistance is  $\frac{1}{2}V^2/R$ , so that one can write

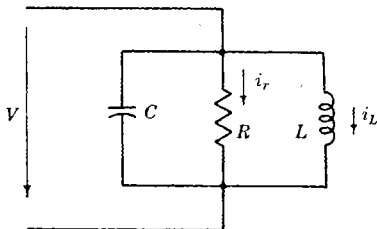


FIG. 3-16.—Parallel-resonant circuit for the computation of equivalent inductances and resistances.

$R = V^2/2P$ . These relations for  $L$  and  $R$  can be used to define an equivalent inductance and an equivalent resistance for the elements of the resonant system. The energy stored in the magnetic field can be computed from  $E_m = \mu_0/2 \int_V |H|^2 dv$ . Using this formula, the inductance for various resonator shapes can be computed.<sup>1</sup> For the rectangular slot (Fig. 2-9)

$$L = \frac{2ld \sin^2 kl}{h(kl)^2 \left(1 + \frac{\sin 2kl}{2kl}\right)} \mu_0 \quad (\text{notation as in Sec. 2-5}). \quad (20)$$

For the annular sector (Fig. 2-11)

$$L = \frac{2\psi\mu_0}{hk^2} \left\{ \frac{4}{\pi^2 k^2 a^2 [J_1(ka)N_1(kb) - J_1(kb)N_1(ka)]^2} - \left[ \frac{J_0(ka)N_1(kb) - N_0(ka)J_1(kb)}{J_1(ka)N_1(kb) - N_1(ka)J_1(kb)} \right]^2 - 1 \right\}^{-1}. \quad (21)$$

The previous formulas are for open-end resonators. For closed-end resonators the voltage varies axially so that it is necessary to specify the position at which the voltage is measured. Taking  $V$  as the maximum voltage amplitude, that is, the voltage amplitude at a median plane, yields for the rectangular slot

<sup>1</sup> The inductance defined as above means no more than is stated in the definition. Because of the distribution of parameters in the usual resonators, the equivalent inductance varies with frequency. However, for resonators such as the hole-and-slot, in which the inductance and capacitance are more or less lumped, the variation of the inductance with frequency is small.



$$L = \frac{4ld \sin^2 k_c l}{h(kl)^2 \left[ 1 + \frac{\sin 2k_c l}{2k_c l} \left( 1 - \frac{2\pi^2}{h^2 k^2} \right) \right]} \mu_0, \quad (22)$$

where

$$k_c = \frac{2\pi}{\lambda_c} \quad \lambda_c = \text{open-end wavelength,}$$

$$k = \frac{2\pi}{\lambda} \quad \lambda = \text{closed-end wavelength,}$$

and for the annular sector,

$$L = \frac{4\psi\mu_0}{hk^2} \left\{ \frac{4}{\pi^2 k_c^2 a^2 [J_1(k_c a) N_1(k_c b) - N_1(k_c a) J_1(k_c b)]} - \left[ \frac{J_0(k_c a) N_1(k_c b) - N_0(k_c a) J_1(k_c b)}{J_1(k_c a) N_1(k_c b) - N_1(k_c a) J_1(k_c b)} \right]^2 \right. \\ \left. + \frac{2\pi^2}{h^2 k^2 k_c a} \left[ \frac{J_0(k_c a) N_1(k_c b) - N_0(k_c a) J_1(k_c b)}{J_1(k_c a) N_1(k_c b) - N_1(k_c a) J_1(k_c b)} \right] - 1 \right\}^{-1}. \quad (23)$$

The equivalent resistance for the resonators is defined in an analogous manner as  $R = V^2/2P$ . The rate of power dissipation can be readily computed by use of the skin-depth theorem. The average power dissipated is given by  $P = 1/2\delta\kappa \int_S |H|^2 ds$ . Thus, the resistance is given by

$$R = \sqrt{\frac{\kappa}{\pi f \mu}} \frac{V^2}{\int_S |H|^2 ds}, \quad (24)$$

from which  $R$  can be computed for the various resonator shapes. For the rectangular slot,

$$R = \frac{\mu_0}{\epsilon_0} \sqrt{\frac{\kappa}{\pi f \mu}} \frac{d^2 \sin^2 kl}{hd + hl \left( 1 + \frac{\sin 2kl}{2kl} \right)} \quad \text{for open ends, and} \quad (25)$$

$$R = 2 \frac{\mu_0}{\epsilon_0} \sqrt{\frac{\kappa}{\pi f \mu}} \frac{d^2 \sin^2 k_c l}{hl \left[ 1 + \frac{\pi^2 (2d - h)}{h^3 k^2} + \frac{\sin 2k_c l}{2k_c l} \left( 1 - \frac{\pi^2 (h + 2d)}{h^3 k^2} \right) \right] + \left( \frac{k_c}{k} \right)^2 hd} \quad \text{for closed ends.} \quad (26)$$

The inductance and resistance of the interaction space will be defined for the  $\pi$ -mode only. For the non- $\pi$ -modes very little magnetic energy is stored in the interaction space and only a small fraction of the losses occur on the cathode or anode surfaces. Furthermore, accurate information concerning either the  $Q$  or the  $\sqrt{C/L}$  of the non- $\pi$ -modes is usually not desired, so the interaction space can be ignored in computing these

quantities. In the case of the  $\pi$ -mode, only the zero component of the field makes a significant contribution to the magnetic energy. The inductance is defined as before by  $L = V^2/2\omega^2 E_m$ . In this case the voltage  $V$  is taken as the line integral of  $E_\phi$  around the anode circumference or  $2\pi E_0(r_a)$  where  $E_0(r_a)$  is the zero component of  $E_\phi(r_a, \phi)$ . Then

$$L = \frac{4\pi\mu_0}{hk^2} \left\{ \left[ \frac{J_0(kr_a)N_1(kr_c) - N_0(kr_a)J_1(kr_c)}{J_1(kr_a)N_1(kr_c) - N_1(kr_a)J_1(kr_c)} \right]^2 + 1 - \frac{4}{\pi^2 k^2 r_a [J_1(kr_a)N_1(kr_c) - N_1(kr_a)J_1(kr_c)]^2} \right\}^{-1} \quad (27)$$

for open-end systems, and

$$L = \frac{8\pi\mu_0}{hk^2} \left\{ \left[ \frac{J_0(kr_a)N_1(kr_c) - N_0(kr_a)J_1(kr_c)}{J_1(kr_a)N_1(kr_c) - N_1(kr_a)J_1(kr_c)} \right]^2 + 1 - \frac{2\pi^2}{h^2 k^2 r_a} \left[ \frac{J_0(kr_a)N_1(kr_c) - N_0(kr_a)J_1(kr_c)}{J_1(kr_a)N_1(kr_c) - N_1(kr_a)J_1(kr_c)} \right] - \frac{4}{\pi^2 k^2 r_a^2 [J_1(kr_a)N_1(kr_c) - N_1(kr_a)J_1(kr_c)]^2} \right\}^{-1} \quad (28)$$

for closed-end systems. While the interaction space remains open even for closed-end systems, the fact that the wavelength is hardly affected indicates that the field distribution is similar to that which would be present if the ends were closed.

$$R = \frac{\mu_0}{\epsilon_0} \sqrt{\frac{\kappa}{\pi f \mu}} \frac{2\pi r_a}{h} \frac{[J_1(kr_a)N_1(kr_c) - N_1(kr_a)J_1(kr_c)]^2}{\frac{4}{\pi^2 k^2 r_c r_a} \sqrt{\frac{\kappa \mu'}{\mu \kappa'}} + \left(1 - \frac{N\theta}{\pi}\right) [J_0(kr_a)N_1(kr_c) - J_1(kr_c)N_0(kr_a)]^2} \quad (29)$$

for open-end systems. The quantities  $\kappa'$  and  $\mu'$  are the conductivity and permeability of the cathode surface.

It is a simple matter to compute  $Q_U$  in terms of the equivalent inductance and resistance previously defined. The total stored energy is given by

$$E = \frac{1}{2\omega^2} \left( \frac{N}{2} \frac{V_{r_1}^2}{L_{r_1}} + \frac{N}{2} \frac{V_{r_2}^2}{L_{r_2}} + \frac{V_c^2}{L_c} \right), \quad (30)$$

where the subscripts  $r_1$ ,  $r_2$ , and  $c$  refer to the two resonator types and the interaction space respectively. The energy dissipated per cycle is given by

$$\frac{1}{2f} \left( \frac{N}{2} \frac{V_{r_1}^2}{R_{r_1}} + \frac{N}{2} \frac{V_{r_2}^2}{R_{r_2}} + \frac{V_c^2}{R_c} \right), \quad (31)$$

yielding

$$Q_u = \frac{1}{\omega} \left[ \frac{\frac{1}{L_{r_1}} + \left( \frac{1-R}{1+R} \right)^2 \frac{1}{L_{r_1}} + \frac{N}{2} \left( \frac{2}{1+R} \right)^2 \frac{1}{L_c}}{\frac{1}{R_{r_1}} + \left( \frac{1-R}{1+R} \right)^2 \frac{1}{R_{r_1}} + \frac{N}{2} \left( \frac{2}{1+R} \right)^2 \frac{1}{R_c}} \right], \quad (32)$$

where  $(1-R)/(1+R)$  is the ratio  $V_{r_1}/V_{r_2}$ .

Computed values of  $Q_u$  are usually considerably higher than measured values, probably because the conditions at the metal are not as assumed. That is, with the very small skin depths associated with microwave frequencies, small surface irregularities and surface contamination have a large effect on the losses. The formula remains very useful, however, as a means of comparing the unloaded  $Q$ 's of different anode-block designs and in particular as a means of comparing different resonator shapes.

The characteristic admittance of the resonant system  $\sqrt{C/L}$  relates the power output of the magnetron to the r-f voltage between anode segments. Its importance will become apparent in Chap. 7. Referring to Fig. 3-16  $2\omega(\text{stored energy})/V^2$  at the resonant frequency of the circuit is given by  $\sqrt{C/L}$ . By analogy one defines  $\sqrt{C/L}$  for the magnetron cavity as  $2\omega(\text{stored energy})/V^2$ . As is always the case in defining admittances and allied quantities for resonant cavities, it is necessary to specify the path over which the voltage is to be measured. For the  $\pi$ -mode of the rising-sun system this voltage is taken to be the average of the voltage amplitudes at the large and small resonator openings; that is,  $(|V^{(e)}| + |V^{(o)}|)/2$ . At resonance the total stored energy is equal to the maximum energy stored in the magnetic fields so that  $\sqrt{C/L}$  can be found in terms of the previously defined inductance. The stored energy  $E$  is given by

$$E = \frac{[V_{r_1}]^2}{2\omega^2} \left[ \frac{N}{2} \frac{1}{L_{r_1}} + \frac{N}{2} \left( \frac{1-R}{1+R} \right)^2 \frac{1}{L_{r_2}} + N^2 \left( \frac{1}{1+R} \right)^2 \frac{1}{L_c} \right],$$

which gives

$$\sqrt{\frac{C}{L}} = \left( \frac{1+R}{R} \right)^2 \frac{N}{2\omega} \left[ \frac{1}{L_{r_1}} + \left( \frac{1-R}{1+R} \right)^2 \frac{1}{L_{r_2}} + 2N \left( \frac{1}{1+R} \right)^2 \frac{1}{L_c} \right]. \quad (33)$$

In the design of a resonant system it is ordinarily desirable to have both  $Q_u$  and  $\sqrt{C/L}$  large and the shapes of the resonators are the main factors in determining these quantities. Ordinarily resonator shapes leading to large  $Q_u$  lead to small values of  $\sqrt{C/L}$  and conversely, so that there is some conflict between these parameters. Resonators with a large volume-to-surface ratio usually (but not always) lead to higher values of  $Q_u$ . Narrow or "high capacitance" resonators usually favor high  $\sqrt{C/L}$ . It should be observed that  $\sqrt{C/L}$  is directly proportional to the block height  $h$  while  $Q_u$  is independent of the height, so there is at least one means of increasing  $\sqrt{C/L}$  without sacrificing  $Q_u$ .

## CHAPTER 4

### THE STRAPPED SYSTEM

BY L. R. WALKER

**4.1. Introduction.**—The first multisegment 10-cm magnetrons developed by the British were of the “symmetric unstrapped” type, described in Chap. 2. These early tubes operated at efficiencies of from 30 to 35 per cent, but their output power was severely limited by a change in the mode of oscillation as the current was increased. Assuming correctly that the  $\pi$ -mode would be the most efficient mode, Randall and Sayers at Birmingham used in 1941 what they referred to as “mode-locking straps.” These were a series of wire bridges which were attached to the high-voltage ends of the resonators in such a manner that they connected pairs of alternate segments and passed directly over the intervening segments. Because the paired segments would be at the same potential in the  $\pi$ -mode but in no other mode, it was thought that the  $\pi$ -mode would be but little disturbed, whereas other modes would be damped because of heavy currents flowing in the straps. The device was unexpectedly successful. The mode change was deferred to currents about three or four times as great as those observed before strapping, and the operating efficiency was increased to about 50 per cent. The presence of the latter effect indicated that strapping, while undoubtedly beneficial, hardly operated in the manner that had been anticipated.

An understanding of the function of strapping waited upon extensive measurements of mode spectra and r-f field patterns and upon a better insight into the relation between the electronic generator and the resonator system. As a result of these studies and of experience with operating tubes that exploited the practical merits of strapping, the strapped-resonator system underwent considerable evolution with increasing emphasis upon the strap itself as a circuit element. Figure 4.1 shows several stages in this process.

In this chapter the term “strap” refers to a circular (or, rarely, polygonal) conductor connected to alternate segments of the magnetron. Considerations of circuit requirements and of the method of fabrication determine the exact form. Frequently, the strap is made in the form of a flat strip bent into a circle with a series of feet for connection; it may, however, be a wire or a flat annulus. The strap may be continuous all around or “broken” at one point above a segment to which

it is not brazed. Generally, the strap is "recessed" or "shielded" by being set into an annular groove which is cut into the segments and is concentric with the interaction space. There may be one ring at each end of the tube (single ring) or two concentric rings at each end (double ring). In the double-ring design, the corresponding inner or outer straps at the two ends of the tube are staggered azimuthally by one segment, so that an individual segment is connected to only one of them. In the same manner, inner and outer rings at each end are staggered.

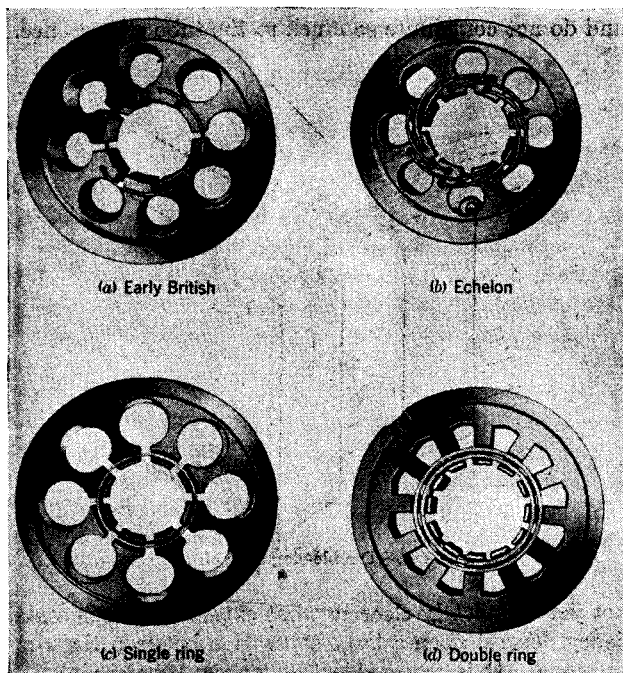


FIG. 4-1.—Four stages in the development of strapped magnetrons.

These relationships are indicated in the schematic drawing of Fig. 4-2. The expression "strap section" is used to refer to the part of the strap system between the midplanes of neighboring segments. The terms "weight of strapping," "heavy," and "light" strapping are in use to indicate roughly the dominance of the strapping in the resonant system. Thus, Fig. 4-1 shows a steady progress in time toward heavier strapping.

The two functions of the straps in a strapped-resonator system are (1) to establish a wide separation in wavelength between the  $\pi$ -mode and all other modes and (2) to affect the characteristic admittance of the resonant system. One of the most noticeable features of strapping,

marked at its first introduction, is that it increases the mode separation of the system by considerably increasing the wavelength of the  $\pi$ -mode while affecting the other modes to a lesser degree. Roughly, this effect may be thought of as arising in the following manner. In the  $\pi$ -mode, the midplane of each segment is a voltage loop, and current flows into the straps that are in parallel with the capacitance of the unstrapped resonator. The strap capacitance thus adds to the unstrapped-resonator capacitance, increasing the wavelength of the system. For the other modes, the individual strap capacitances are not all in phase with one another and do not contribute so much to the tube capacitance.

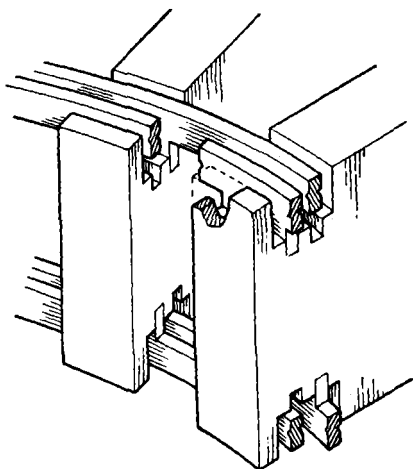


FIG. 4-2.—Double-ring strapping.

It is not yet completely clear to what extent the mode stability and high efficiency depend upon a large separation between the  $\pi$ -mode and its nearest mode. It is reasonable to suppose, however, that for good  $\pi$ -mode operation, undistorted r-f field patterns in the interaction space are necessary. If the fractional mode separation is approximately equal to the reciprocal of the loaded  $Q$  of the desired mode, there will be perceptible excitation of the next mode with consequent pattern distortion. This implies that a minimum mode separation of a few per cent is essential. The early unstrapped tubes ( $N = 8$ ) had an ( $n = 4$ )-to-( $n = 3$ ) separation of about 1 per cent, and both fields were severely distorted under operating circumstances. The light strapping initially used increased the separation to about 7 per cent with a considerable gain in efficiency. The weight of strapping plainly provides a means for varying the  $\pi$ -mode separation over a considerable range. When the

tube is tunable, there appears the further complication of maintaining the desired features of the mode spectrum over the whole tuning range.

Reference to Chap. 7 will indicate the great importance of the characteristic admittance  $Y_c$  for the operating behavior of the tube;  $Y_c$  is defined as  $\frac{1}{2}[\omega(\partial Y/\partial \omega)]_{Y=0}$ ,  $Y$  being the total admittance of the resonant system measured at a slot. Because the product of pulling figure and external  $Q$  (see Chap. 5) is constant at any wavelength, the practical limitations on the pulling figure mean that the loading cannot exceed a definite value. A relation exists, however, between the electronic conductance  $G_e$  and the loaded  $Q_L$  and  $Y_c$ , given by

$$Q_L G_e = Y_c.$$

The electronic efficiency is a function of  $G_e$ , apparently increasing monotonically with  $G_e$  up to a rather flat maximum (see Chap. 10). Thus, with limited loading, or  $Q_L$  greater than some fixed value, the value of  $G_e$  can be brought up to the level required for high efficiency only by making  $Y_c$  large enough. Because  $Y_c$  is roughly equal to  $\omega_0 C$ , where  $C$  is the capacitance of the resonant system,  $Y_c$  increases as strap capacitance is added (for the  $\pi$ -mode). The weight of strapping provides a flexible means, therefore, of adjusting the characteristic admittance to a preassigned value.

The following sections will discuss the mode spectra of strapped systems and their dependence upon various parameters, the effect of loading on the spectrum and on the r-f pattern, the asymmetries and mode shifts introduced by breaking the straps and the effect of tuning the system upon several of these properties.

**4.2. Analysis of Strapped Systems.**—As shown in Chaps. 2 and 3, the relative simplicity of the geometrical structure of unstrapped magnetrons permits considerable progress in their analysis by field theory. The addition of a strapped system, however, makes an exact calculation of the fields prohibitively difficult. Fortunately, in all practical cases, satisfactory working solutions can be obtained using equivalent circuits. In Chap. 2, where suitably equivalent circuits were used for the unstrapped system, it was shown that this artifice is possible when the higher modes of an individual resonator are short in wavelength compared with any wavelength of interest. The strap sections may be similarly replaced by simple equivalent circuits, essentially because their dimensions are short compared with a wavelength over the range of interest. The length of a strap is always its greatest dimension, and the condition that it be short compared with the wavelength  $\lambda$  is that

$$\frac{2\pi r_s}{N\lambda} < 1,$$

where  $r_s$  is an effective radius of the strap system.<sup>1</sup> The condition has been easily satisfied in all magnetrons built to date, and the strap system, having no resonances itself, except at frequencies far higher than that of the system as a whole, may then be represented by any convenient circuit having the appropriate low-frequency behavior.

It is important to state clearly the purposes and the limitations of the equivalent-circuit approach (see also Sec. 7.1). This method sets up a model of the resonant system that simulates its behavior over an appropriate frequency band and that correlates the information about the

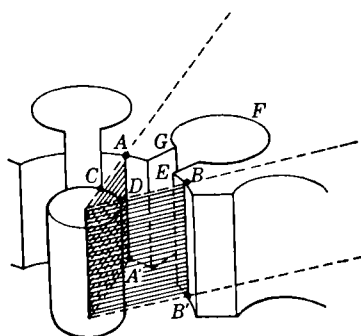


FIG. 4.3.—Location of the terminals of the network used to represent the unstrapped resonator.

system, permitting predictions to be made about the effects of various parameters. It is not, however, a method for calculating the system constants *ab initio*. Thus, the procedure always consists in using some experimentally measured quantities either to deduce others that might be measured or to calculate the effect of changes in the system. The equivalent-circuit model is changed from one case to another and is kept as simple as is consistent with the inclusion of all the factors considered relevant to a specific case.

The equivalent circuits for the basic elements of the strapped system may be considered here. The small mode separation of unstrapped systems suggests that the coupling between oscillators is not strong. In the analysis of strapped systems, then, the coupling through the interaction space and through the end spaces will be ignored. This is justifiable for the modes of highest  $n$ , because it has been observed that the height of the end spaces and the presence or absence of a cathode make little difference to the wavelength of these modes in strapped tubes. An unloaded strapped system may then be considered as consisting of a ring of  $N$  similar resonators that are coupled at their ends by the strapped system. The unstrapped resonator will be represented by a 4-terminal network with terminals  $A$ ,  $B$ , and  $A'$ ,  $B'$  located as shown in Fig. 4.3. Furthermore, this 4-terminal network may be supposed to consist of a length  $h$  of waveguide having a cutoff wavelength  $\lambda_{c0}$  and characteristic impedance  $K_{r0}/\sqrt{1 - \lambda^2/\lambda_{c0}^2}$ . The cross section of this guide is

<sup>1</sup> This inequality (slightly changed by the substitution of the anode radius  $r_a$  for  $r_s$ ) occurs also in the theory of the space charge in Chap. 6, where it is given as a condition for the neglect of the effect of r-f magnetic fields on the electrons and of relativistic effects.



*ACDBEFG*. The length  $h$  can be identified with the length of the anode; and to a good degree of approximation,  $\lambda_{r,0}$  can be identified with the  $\pi$ -mode wavelength of the unstrapped system. The term  $K_{r,0}$  is related to the characteristic admittance of the unstrapped system in the  $\pi$ -mode and may be calculated. A strap section may be similarly represented by a 4-terminal network, consisting of a length  $s$  of parallel-plate guide of impedance  $K_s$ . The length  $s$  is generally found to correspond to a strap radius somewhere within the strap system. No attempt is made to distinguish between the inner and outer straps in double-strapped tubes.

There is a measure of arbitrariness in the manner in which the connection of the strap and the resonant systems may be represented. For

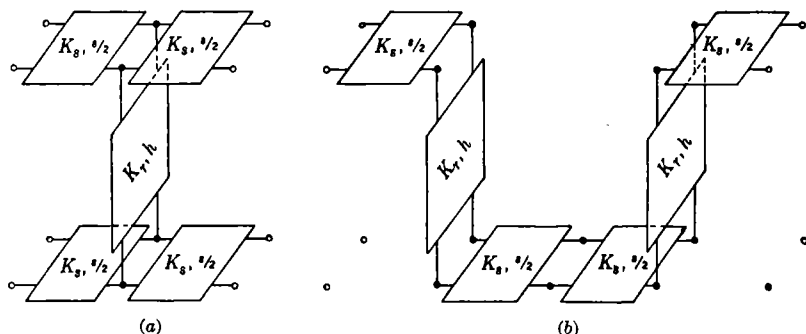


FIG. 4-4.—(a) A 4-terminal network representation for a single section of a double-strapped tube; (b) a 4-terminal network representation of two neighboring sections of a single-strapped tube.

double-ring strapping each section of the whole system has a left- and right-hand symmetry (horizontal); thus it seems reasonable to place half the length of each strap on either side of the unstrapped resonator as shown in the circuit of Fig. 4-4a. When there is only a single strap at each end, the circuit of Fig. 4-4b is suggested. If additional forms of coupling have to be considered, they could be included by additional 4-terminal linkages at the ends of the unstrapped resonator (end-space coupling) or at the midplane of the unstrapped resonator (interaction-space coupling). In every case the circuit for the whole tube is found by joining these networks. In general, there will be  $2P$  4-terminal coupling links with  $P$  networks on each side. Although the applications given in this chapter will involve only cases where  $P = 1$  or  $2$ , the general theory will be worked out for arbitrary  $P$ .

**4.3. Rings of Networks.**—Before developing the somewhat abstract analysis of the general case, a few facts may be recalled about the special case of chains of identical 4-terminal networks, which might, for example,

be filter sections. Supposing the networks to be symmetrical and lossless, the relations between the voltages  $V_1$  and  $V_2$  and the corresponding mesh currents  $I_1$  and  $I_2$  at the two ends of any given network are

$$\begin{aligned} I_1 &= jY_{11}V_1 + jY_{12}V_2, \\ I_2 &= -jY_{12}V_1 - jY_{11}V_2, \end{aligned}$$

or

$$\begin{aligned} V_2 &= -\frac{Y_{11}}{Y_{12}} V_1 - \frac{j}{Y_{12}} I_1, \\ I_2 &= j \left( \frac{Y_{11}^2}{Y_{12}} - Y_{12} \right) V_1 - \frac{Y_{11}}{Y_{12}} I_1. \end{aligned}$$

By writing  $-Y_{11}/Y_{12} = \cos \phi$  and  $-1/Y_{12} = Z_0 \sin \phi$ , where  $\phi$  is purely real or purely imaginary, one has in matrix notation

$$\begin{pmatrix} V_2 \\ I_2 \end{pmatrix} = \begin{pmatrix} \cos \phi & jZ_0 \sin \phi \\ jY_0 \sin \phi & \cos \phi \end{pmatrix} \begin{pmatrix} V_1 \\ I_1 \end{pmatrix} = \mathbf{M} \begin{pmatrix} V_1 \\ I_1 \end{pmatrix}.$$

The impedance  $Z_0$  is the iterative impedance of the section because if  $V_1 = Z_0 I_1$ , then  $V_2 = Z_0 I_2$ . The angle  $\phi$  is known as the transfer angle; for if  $V_1 = jZ_0 I_1 \tan \psi$ , then  $V_2 = jZ_0 I_2 \tan (\psi + \phi)$ . With respect to appropriate terminations, therefore, the network acts as a section of transmission line of characteristic impedance  $Z_0$  and electrical length  $\phi$ . The quantities  $Z_0$  and  $\phi$  are, of course, functions of the frequency.

If one now takes  $N$  identical sections in a chain and forms a ring by joining the corresponding terminals, there must be similar voltages and currents at the two ends of the ring. Thus,

$$\begin{pmatrix} V_{N+1} \\ I_{N+1} \end{pmatrix} = \mathbf{M}^N \begin{pmatrix} V_1 \\ I_1 \end{pmatrix} = \begin{pmatrix} V_1 \\ I_1 \end{pmatrix},$$

where  $V_{N+1}$  and  $I_{N+1}$  are the voltage and current at the end of the  $N$ th section. But this implies that

$$\text{Det} (\mathbf{M}^N - \mathbf{I}) = 0,$$

where  $\mathbf{I}$  is the unit matrix. However, because

$$\begin{aligned} \mathbf{M}^N &= \begin{pmatrix} \cos N\phi & jZ_0 \sin N\phi \\ jY_0 \sin N\phi & \cos N\phi \end{pmatrix}, \\ \text{Det} \begin{pmatrix} (\cos N\phi) - 1 & jZ_0 \sin N\phi \\ jY_0 \sin N\phi & (\cos N\phi) - 1 \end{pmatrix} &= 0, \end{aligned}$$

or

$$1 - \cos N\phi = 0$$

and

$$N\phi = 2s\pi,$$

where  $s = 0, 1 \dots N/2$  (assuming  $N$  is even) and

$$\phi = \frac{2s\pi}{N}.$$

Thus, a ring of  $N$  4-terminal networks will support a harmonic oscillation only for those frequencies which make  $\phi$  equal to one of the values  $2s\pi/N$ . These are the frequencies of the normal modes of the system. The modes will be widely spaced if  $\phi$  changes rapidly with frequency. As an example, suppose that each section consists of a shunt resonant circuit of inductance  $L$  and capacitance  $C$  with a mutual coupling  $M$

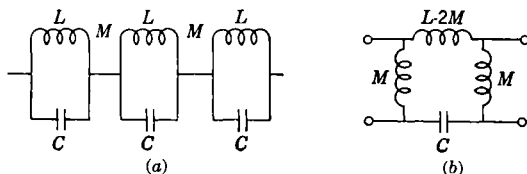


FIG. 4-5.—(a) Schematic circuit of a chain of 4-terminal networks; (b) equivalent circuit of Fig. 4-5a.

between each neighboring pair of inductances (see Fig. 4-5a and its equivalent circuit Fig. 4-5b). The matrix for this circuit is

$$\begin{pmatrix} 1 & 0 \\ \frac{1}{j\omega M} & 1 \end{pmatrix} \begin{pmatrix} 1 & \frac{1}{j\omega C} \\ 0 & 1 \end{pmatrix} \begin{pmatrix} 1 & j\omega(L-2M) \\ 0 & 1 \end{pmatrix} \begin{pmatrix} 1 & 0 \\ \frac{1}{j\omega M} & 1 \end{pmatrix} \\ = \begin{pmatrix} 1 & \frac{1}{j\omega C} \\ \frac{1}{j\omega M} & 1 - \frac{1}{\omega^2 MC} \end{pmatrix} \begin{pmatrix} 1 + \frac{L-2M}{M} & j\omega(L-2M) \\ \frac{1}{j\omega M} & 1 \end{pmatrix}$$

Thus,

$$\cos \phi = 1 + \frac{L-2M}{M} - \frac{1}{\omega^2 MC} = \frac{L-M}{M} - \frac{1}{\omega^2 MC}$$

$$2M \left( \cos^2 \frac{\phi}{2} \right) - L = -\frac{1}{\omega^2 C},$$

and

$$\frac{1}{\omega^2} = C \left( L - 2M \cos^2 \frac{\phi}{2} \right) = \left( \frac{\lambda}{2\pi c} \right)^2.$$

Thence if  $\phi_s = 2s\pi/N$ , the resonant frequencies are

$$\frac{1}{\omega_s^2} = C \left( L - 2M \cos^2 \frac{\phi_s}{2} \right).$$

The mode spectra in this and other cases are easily examined by plotting  $\cos \phi$  as a function of  $\omega$ , or  $\lambda$ , as in Fig. 4-6; the mode frequencies are then

found by locating the intersections of this curve with the lines  $\cos \phi = \cos 2\pi/N$ . It will be noted that in this simple example the network acts as a bandpass filter cutting off at  $\omega = 1/\sqrt{LC}$  and  $\omega = 1/\sqrt{C(L-2M)}$  and that the resonant frequencies lie within the pass band. As  $M$  increases, the separation of the modes and the width of the pass band both increase.

In taking up the more general case, in which the number of 4-terminal connections at each side of a unit network is unrestricted, methods similar

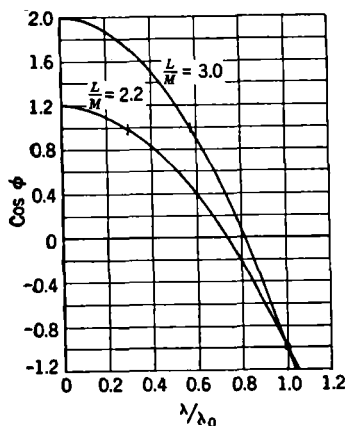


FIG. 4-6.— $\cos \phi$  as a function of  $\lambda/\lambda_0$  for a chain of shunt-resonant circuits with mutual coupling. Values of  $\cos \phi > 1$  correspond to  $\phi$  imaginary.  $\lambda_0$  is  $2\pi c\sqrt{LC}$ .

voltages and currents at the pairs of terminals on the left be  $\mathbf{v} = (V_1, V_2, \dots, V_p)$  and  $\mathbf{i} = (I_1, I_2, \dots, I_p)$  and those on the right be  $\mathbf{u} = (U_1, U_2, \dots, U_p)$  and  $\mathbf{j} = (J_1, J_2, \dots, J_p)$ , where  $\mathbf{v}$ ,  $\mathbf{i}$ ,  $\mathbf{u}$ , and  $\mathbf{j}$  are treated as vectors subject to matrix multiplication.

Let

$$\mathbf{i} = \mathbf{Y}_1 \mathbf{v} + \mathbf{Y}_2 \mathbf{u}, \quad (1a)$$

$$\mathbf{j} = \mathbf{Y}_3 \mathbf{v} + \mathbf{Y}_4 \mathbf{u}, \quad (1b)$$

where the  $\mathbf{Y}$  terms are square admittance matrices. The reciprocity theorem then gives

$$\mathbf{Y}_2 = -\mathbf{Y}_3 \quad (2)$$

(the minus sign is a consequence of the use of cyclic currents in the 4-terminal links), and also that  $\mathbf{Y}_1$  and  $\mathbf{Y}_4$  are symmetric matrices.

Thus,

$$\mathbf{i} = \mathbf{Y}_1 \mathbf{v} + \mathbf{Y}_2 \mathbf{u}, \quad (3a)$$

$$\mathbf{j} = -\mathbf{Y}_2 \mathbf{v} + \mathbf{Y}_4 \mathbf{u}. \quad (3b)$$

to those of the preceding paragraph will be used. Certain restrictions due to symmetry will be put on the individual networks and, hence, on their impedance matrices. The condition that the  $N$  networks be joined in a ring is then applied, and this is found to yield a determinantal equation for the possible frequencies. A few additional theorems are proved concerning the matrices of certain other structures, consideration of which arises in cases where asymmetries are introduced into the ring.

As each coupling is a 4-terminal network, the analysis can be made in terms of the voltages and mesh currents at the pairs of terminals corresponding to each link. The reciprocity theorem will hold for these voltages and currents. Let the

Consider the case in which the sections have horizontal symmetry. This implies that, simultaneously,

$$\begin{pmatrix} v \\ i \end{pmatrix} = T \begin{pmatrix} u \\ j \end{pmatrix} \quad \text{and} \quad \begin{pmatrix} u \\ -j \end{pmatrix} = T \begin{pmatrix} v \\ -i \end{pmatrix}; \quad (4)$$

but by substituting from Eq. (3),

$$\begin{pmatrix} v \\ i \end{pmatrix} = \begin{pmatrix} Y_2^{-1}Y_4 & -Y_2^{-1} \\ Y_1Y_2^{-1}Y_4 + Y_2 & -Y_1Y_2^{-1} \end{pmatrix} \begin{pmatrix} u \\ j \end{pmatrix}, \quad (5)$$

and

$$\begin{pmatrix} u \\ -j \end{pmatrix} = \begin{pmatrix} -Y_2^{-1}Y_1 & -Y_2^{-1} \\ Y_2 + Y_4Y_2^{-1}Y_1 & Y_4Y_2^{-1} \end{pmatrix} \begin{pmatrix} v \\ -i \end{pmatrix}; \quad (6)$$

hence,

$$Y_4 = -Y_1. \quad (7)$$

If there are  $N$  similar networks, the condition imposed by the ring connection is

$$\begin{pmatrix} v \\ i \end{pmatrix} = T^N \begin{pmatrix} v \\ i \end{pmatrix}, \quad (8)$$

where  $v$  and  $i$  refer to the terminals of any section. This implies that

$$\text{Det} (I - T^N) = 0 \quad (9)$$

where  $I$  is the unit matrix. Or, factoring the determinant, that

$$\text{Det} (\lambda_m I - T) = 0, \quad (10)$$

where  $\lambda_m^N = 1$ . Rewriting Eq. (3), taking Eq. (7) into account, gives

$$i = Y_1 v + Y_2 u \quad (11a)$$

and

$$j = -Y_1 v - Y_2 u. \quad (11b)$$

Now, if Eq. (10) is true,

$$\begin{pmatrix} v \\ i \end{pmatrix} = T \begin{pmatrix} u_m \\ j_m \end{pmatrix} = \lambda_m \begin{pmatrix} u_m \\ j_m \end{pmatrix}, \quad (12)$$

where  $\begin{pmatrix} u_m \\ j_m \end{pmatrix}$  is a characteristic vector for Eq. (10). Substituting in Eq. (11)

$$\begin{aligned} \lambda_m j_m &= Y_1 \lambda_m u_m + Y_2 u_m, \\ j_m &= -Y_2 \lambda_m u_m - Y_1 u_m, \end{aligned}$$

or

$$(\lambda_m^2 Y_2 + 2\lambda_m Y_1 + Y_2) u_m = 0. \quad (13)$$

Thus

$$\text{Det} \left( I \frac{\lambda_m^2 + 1}{2\lambda_m} + Y_2^{-1} Y_1 \right) = 0, \quad (14)$$

provided  $\text{Det } Y_2 \neq 0$ , where  $I$  is the unit matrix. If  $\lambda_m$  is written as  $\lambda_m = e^{i\psi_m}$ , where  $N\psi_m = 2\pi m$ , Eq. (14) takes the final form

$$\text{Det} (-Y_2^{-1}Y_1 - I \cos \psi_m) = 0. \quad (15)$$

Referring to Eq. (5) it is to be noted that  $-Y_2^{-1}Y_1$  is, in an obvious notation, the  $v$ - $u$  matrix of a unit section. The determinantal Eq. (15) now determines the possible resonances of the structure. There will be, in general,  $p$  roots or  $p$ -resonant frequencies for each value of  $m$ . The integer  $m$  will be used to describe the mode. It is related to the familiar mode number  $n$  by the relation  $m = (N/2) - n$ . The notation  $m_1, m_2, \dots, m_p$  may be used to denote the  $p$  modes for each  $m$  value. Since the frequencies depend upon  $\cos \psi_m$  only, two values of  $\psi_m$  leading to the same value of  $\cos \psi_m$  have the same frequency. Thus if  $\psi_m = 2\pi - \psi'_m$  or  $m' = N - m$ ,  $m'$  and  $m$  lead to the same frequency. There are evidently  $N$  values of  $m$ ; two of these, namely,  $m = 0$  and  $m = N/2$ , lead to a nondegenerate frequency; the other  $(N - 2)$ -values of  $m$  occur in pairs of the form  $(m, N - m)$  leading to degenerate frequencies. There are thus  $p \left( \frac{N}{2} + 1 \right)$  separate frequencies if the  $p$  different frequencies for a fixed  $m$  are not degenerate.

It is possible to write the section matrix  $T$  in a form that will be found useful later. Suppose that angles  $\phi_1, \phi_2, \dots, \phi_p$  are found such that  $\cos \phi_1, \cos \phi_2, \dots, \cos \phi_p$  are the latent roots of Eq. (15), and let the diagonalized form of  $-Y_2^{-1}Y_1$  be denoted by  $C_1$ . Then matrices  $D_{11}$  and  $D_{22}$  may be found such that

$$T = D^{-1}T_0D = \begin{pmatrix} D_{11}^{-1} & 0 \\ 0 & D_{22}^{-1} \end{pmatrix} \begin{pmatrix} C_1 & S_1 \\ -S_1 & C_1 \end{pmatrix} \begin{pmatrix} D_{11} & 0 \\ 0 & D_{22} \end{pmatrix}, \quad (16)$$

where  $S_1$  is also diagonal and has the diagonal elements  $\sin \phi_1, \sin \phi_2, \dots, \sin \phi_p$ . Between  $D_{11}$  and  $D_{12}$  the relation

$$S_1 D_{22} Y_2 + D_{11} = 0 \quad (17)$$

holds. It is easy to see that for  $r$  identical sections one has

$$T^r = D^{-1}T_0^r D = D^{-1} \begin{pmatrix} C_r & S_r \\ -S_r & C_r \end{pmatrix} D, \quad (18)$$

where  $C_r$  and  $S_r$  are again diagonal with elements  $\cos r\phi_1, \cos r\phi_2, \dots, \cos r\phi_p$  and  $\sin r\phi_1, \sin r\phi_2, \dots, \sin r\phi_p$ , respectively. It may be noted that if

$$u = jD_{11}^{-1}D_{22}i, \quad (19a)$$

then

$$v = jD_{11}^{-1}D_{22}j. \quad (19b)$$

From Eqs. (18) and (19) it is seen that the set of angles  $\phi_1, \phi_2, \dots, \phi_p$  forms a generalization of the usual transfer constant and  $jD_{11}^{-1}D_{22}$  is an extension of the usual iterative impedance; for if the network be terminated on the right with a network whose impedance matrix is  $jD_{11}^{-1}D_{22}$ , the impedance matrix at the left-hand terminals is again  $jD_{11}^{-1}D_{22}$ .

It may be observed that a chain of networks with 4-terminal connections is a structure which exhibits a series of velocities of propagation at any given frequency. With each angle  $\phi$ , there may be associated a velocity of phase propagation  $2\pi\phi/\omega$  at a frequency  $\omega$ ; and furthermore, for each  $\phi$ , there will be an individual  $\cos \phi$  vs.  $\omega$  (or  $\lambda$ ) curve, leading to a set of resonant frequencies.

In the event that the cell possesses end-for-end or vertical symmetry some further properties of the matrix may be deduced. If the various voltage and current vectors be written

$$\mathbf{v} = \begin{pmatrix} v_1 \\ v_2 \end{pmatrix}, \quad \mathbf{i} = \begin{pmatrix} i_1 \\ i_2 \end{pmatrix}, \text{ etc.,}$$

where the subscripts 1 and 2 refer to the two ends of the tube, then vertical symmetry means that the same relations hold between  $\mathbf{v}$ ,  $\mathbf{i}$ ,  $\mathbf{u}$ , and  $\mathbf{j}$  as between  $\mathbf{A}\mathbf{v}$ ,  $\mathbf{A}\mathbf{i}$ ,  $\mathbf{A}\mathbf{u}$ , and  $\mathbf{A}\mathbf{j}$ , where  $\mathbf{A}$  is a matrix that transforms the subscripts, or

$$\mathbf{A} = \begin{pmatrix} 0 & 1 \\ 1 & 0 \end{pmatrix}.$$

Applying this condition to Eq. (11) it is found that

$$\mathbf{A}\mathbf{Y}_1\mathbf{A} = \mathbf{Y}_1$$

and

$$\mathbf{A}\mathbf{Y}_2\mathbf{A} = \mathbf{Y}_2,$$

which means that  $\mathbf{Y}_1$  and  $\mathbf{Y}_2$  are of the form

$$\mathbf{Y}_{1,2} = \begin{pmatrix} \mathbf{P} & \mathbf{Q} \\ \mathbf{Q} & \mathbf{P} \end{pmatrix}. \quad (20)$$

The matrices  $\mathbf{D}_{11}$  and  $\mathbf{D}_{22}$  now have the form

$$\mathbf{D}_{11}, \mathbf{D}_{22} = \begin{pmatrix} \mathbf{R} & \mathbf{R} \\ \mathbf{S} & -\mathbf{S} \end{pmatrix}. \quad (21)$$

A further proposition on unsymmetrical matrices which is made use of in Sec. 4-7 will now be developed. Suppose that  $\mathbf{Y}_1$  and  $\mathbf{Y}_2$  are the matrices of networks which are mirror images (left and right hand) of each other. This is implied if

$$\begin{pmatrix} \mathbf{v} \\ \mathbf{i} \end{pmatrix} = \mathbf{Y}_1 \begin{pmatrix} \mathbf{u} \\ \mathbf{j} \end{pmatrix} \quad (22a)$$

and

$$\begin{pmatrix} u \\ -j \end{pmatrix} = Y_2 \begin{pmatrix} v \\ -i \end{pmatrix}; \quad (22b)$$

or if  $B = \begin{pmatrix} 1 & 0 \\ 0 & -1 \end{pmatrix}$ , then

$$B \begin{pmatrix} u \\ j \end{pmatrix} = Y_2 B \begin{pmatrix} v \\ i \end{pmatrix}$$

and

$$B = Y_2 B Y_1 \quad \text{or} \quad Y_1^{-1} = B^{-1} Y_2 B = B Y_2 B. \quad (22c)$$

Now consider a case in which

$$Y_1 Y_2 \begin{pmatrix} v \\ i \end{pmatrix} = \begin{pmatrix} v \\ i \end{pmatrix} \quad \text{or} \quad B Y_2 \begin{pmatrix} v \\ i \end{pmatrix} = Y_2 B \begin{pmatrix} v \\ i \end{pmatrix}; \quad (23a)$$

then

$$\left( B Y_2 - Y_2 B \right) \begin{pmatrix} v \\ i \end{pmatrix} = 0;$$

and if

$$Y_2 = \begin{pmatrix} A_{11} & A_{12} \\ A_{21} & A_{22} \end{pmatrix};$$

this leads to

$$\begin{pmatrix} 0 & 2A_{12} \\ -2A_{21} & 0 \end{pmatrix} \begin{pmatrix} v \\ i \end{pmatrix} = 0.$$

Thus

$$\text{Det } (A_{12}) = 0 \quad \text{and} \quad v = 0 \quad \text{or} \quad \text{Det } (A_{21}) = 0 \quad \text{and} \quad i = 0. \quad (23b)$$

A similar set of equations holds for  $Y_1$ .

The single-strapped structure does not come within the scope of the general analysis of this section because if the single sections are treated as 8-terminal networks, they have no horizontal symmetry and neighboring sections are mirror images rather than identical. The symmetry of the section is such that it is unchanged under a simultaneous exchange of ends and of left and right, and if this is taken into account, it is not difficult to show that the  $u$ - $v$  matrix for two neighboring sections is

$$Q = 2APAP - I,$$

where  $A$  has its previous significance and  $P$  is the  $u$ - $v$  matrix for one section. By substituting in Eq. (15), one has

$$\text{Det } (APAP - \cos^2 \psi_m) = 0. \quad (24)$$

It is probably simpler, however, to treat the single-strapped case as a 4-terminal network.



## SYMMETRICAL SYSTEMS

**4.4. Fixed-frequency Systems.**—In the most common case, that of double strapping, the circuit for a single section indicated in Fig. 4-4a may be dissected into three 8-terminal sections as in Fig. 4-7. The over-all matrix  $T$  is of the form

$$T = T_s T_r T_s \quad (25)$$

where  $T_s$  is the matrix of a half section of strap and  $T_r$  is the resonator matrix. The term  $T_s$  may be written by inspection as

$$T_s = \begin{pmatrix} \cos \theta_s & 0 & jK_s \sin \theta_s & 0 \\ 0 & \cos \theta_s & 0 & jK_s \sin \theta_s \\ jM_s \sin \theta_s & 0 & \cos \theta_s & 0 \\ 0 & jM_s \sin \theta_s & 0 & \cos \theta_s \end{pmatrix} \quad (26)$$

where  $2\theta_s = 2\pi s/\lambda$ , the electrical length of the strap, and  $M_s = 1/K_s$ . The matrix for the center section may be derived by supposing that the resonator is a symmetrical 4-terminal network with a matrix

$$\begin{pmatrix} a' & b' \\ c' & a' \end{pmatrix}$$

and that  $a'^2 - b'c' = I$ ; the mesh equations can be written and solved, yielding for the center matrix

$$\begin{pmatrix} 1 & 0 & 0 & 0 \\ 0 & 1 & 0 & 0 \\ -\frac{a'}{b'} & -\frac{1}{b'} & 1 & 0 \\ -\frac{1}{b'} & -\frac{a'}{b'} & 0 & 1 \end{pmatrix} \quad (27)$$

For the case considered,  $a' = \cos \theta_r$  and  $b' = jK_r \sin \theta_r$ , where  $\theta_r$  is the electrical length of the resonator and  $K_r = 1/M_r$  is its characteristic impedance. Thus

$$T_r = \begin{pmatrix} 1 & 0 & 0 & 0 \\ 0 & 1 & 0 & 0 \\ -jM_r \cot \theta_r & jM_r \csc \theta_r & 1 & 0 \\ jM_r \csc \theta_r & -jM_r \cot \theta_r & 0 & 1 \end{pmatrix} \quad (28)$$

Forming the product  $T_s T_r T_s$  and calculating only the u-v part, the latter is found to be

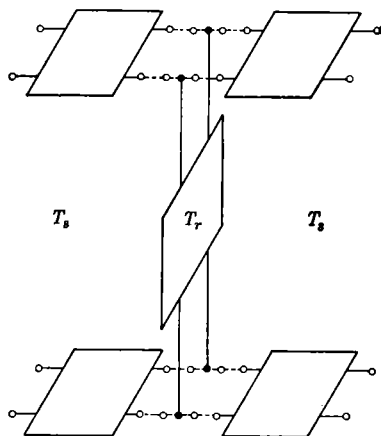


FIG. 4-7.—A single section of a double-strapped tube represented as three 8-terminal networks.

$$\begin{pmatrix} \cos 2\theta_s + \frac{1}{2}K_s M_r \sin 2\theta_s \cot \theta_r & -\frac{1}{2}K_s M_r \sin 2\theta_s \csc \theta_r \\ -\frac{1}{2}K_s M_r \sin 2\theta_s \csc \theta_r & \cos 2\theta_s + \frac{1}{2}K_s M_r \sin 2\theta_s \cot \theta_r \end{pmatrix} \quad (29)$$

The determinantal Eq. (15) now leads to

$$(\cos 2\theta_s + \frac{1}{2}K_s M_r \sin 2\theta_s \cot \theta_r - \cos \psi_m)^2 = (\frac{1}{2}K_s M_r \sin 2\theta_s \csc \theta_r)^2, \quad (30)$$

which factors into the two equations

$$\cos \psi_m = \cos 2\theta_s + \frac{1}{2}K_s M_r \sin 2\theta_s \tan \frac{\theta_r}{2} \quad (31a)$$

and

$$\cos \psi_m = \cos 2\theta_s + \frac{1}{2}K_s M_r \sin 2\theta_s \cot \frac{\theta_r}{2}. \quad (31b)$$

For future reference the matrix  $D$  which diagonalizes  $T$  according to Eq. (16) may be written here. If

$$D_{11} = \begin{pmatrix} 1 & 1 \\ 1 & -1 \end{pmatrix}, \quad (32a)$$

then

$$D_{22} = jK_s \tan \theta_s \begin{pmatrix} \cot \frac{\phi_1}{2} & \cot \frac{\phi_1}{2} \\ \cot \frac{\phi_2}{2} & \cot \frac{\phi_2}{2} \end{pmatrix}. \quad (32b)$$

Consideration of Eq. (12) and Fig. 4-4a shows that for the  $\pi$ -mode, where the voltage across the slots changes by  $180^\circ$  between each neighboring pair,  $\phi_m = 0$  or  $m = 0$ . In this case, Eq. (32) becomes

$$\frac{2}{K_s} \tan \theta_s + M_r \tan \frac{\theta_r}{2} = 0 \quad (33a)$$

and

$$\frac{2}{K_s} \tan \theta_s - M_r \cot \frac{\theta_r}{2} = 0. \quad (33b)$$

The interpretation of these equations shows that in the first case the two half-strap sections, open-circuited at the midplane of the segments, are resonating in parallel against half the unstrapped resonator, open-circuited at the median plane, and in the second case, against half the resonator short-circuited at the median plane. These may be referred to as symmetric and antisymmetric modes and designated as the ( $m = 0_1$ )- and ( $m = 0_2$ )-modes, respectively. A similar pair of modes exists for any other value of  $m$ , and the symbols  $m_1$  and  $m_2$  will be used to refer to them.

Returning to Eqs. (31) the following substitutions may be made:

$$2\theta_s = \frac{2\pi s}{\lambda}, \quad K_r = \frac{Z_{r0}}{\sqrt{1 - \lambda^2/\lambda_{r0}^2}}, \quad \text{and} \quad \theta_r = \frac{2\pi h}{\lambda} \sqrt{1 - \frac{\lambda^2}{\lambda_{r0}^2}}.$$

For the modes of greatest interest,  $\lambda > \lambda_{r_0}$ , with the result that hyperbolic functions replace the trigonometric ones pertaining to the resonator. Equations (31) then become

$$\cos \psi_m = \cos \frac{2\pi s}{\lambda} + \frac{K_s}{2Z_{r_0}} \sqrt{\frac{\lambda^2}{\lambda_{r_0}^2} - 1} \sin \frac{2\pi s}{\lambda} \tanh \frac{\pi h}{\lambda} \sqrt{\frac{\lambda^2}{\lambda_{r_0}^2} - 1} \quad (34a)$$

and

$$\cos \psi_m = \cos \frac{2\pi s}{\lambda} + \frac{K_s}{2Z_{r_0}} \sqrt{\frac{\lambda}{\lambda_{r_0}^2} - 1} \sin \frac{2\pi s}{\lambda} \operatorname{ctnh} \frac{\pi h}{\lambda} \sqrt{\frac{\lambda^2}{\lambda_{r_0}^2} - 1}. \quad (34b)$$

The nature of the mode spectrum and the effect of various parameters upon it may now be studied by plotting the right-hand sides of Eqs. (34) as functions of  $\lambda$ . Figure 4.8 shows the two expressions, which may be called  $\cos \phi_1$  and  $\cos \phi_2$ , as functions of  $\lambda/\lambda_{r_0}$ , for four values of  $k = K_s/2Z_{r_0}$ ; namely,  $k = 0.8, 0.4, 0.2$ , and the limiting case  $k = 0$ . The term  $k$  measures the weight of strapping, and it decreases as the strapping is made heavier. Representative values for  $2\pi s/\lambda_{r_0}$  and  $\pi h/\lambda_{r_0}$  are chosen; these are 0.55 and 0.80.

Over the interesting range of  $\lambda/\lambda_{r_0}$ ,  $\cos \phi_1$  and  $\cos \phi_2$  are monotonic increasing functions of this quantity; for sufficiently small values of  $\lambda/\lambda_{r_0}$ , however, the tangent and cotangent functions will give rise to a series of branches, but this region is generally not relevant. At such values of  $\lambda/\lambda_{r_0}$ , short waves are propagating up and down the resonator giving a series of modes. For the symmetric modes ( $\cos \phi_1$ ), all the curves pass through the point

( $\lambda/\lambda_{r_0} = 1$ ,  $\cos \phi_1 = \cos 2\pi s/\lambda_{r_0}$ ), and they lie above the limiting ( $k = 0$ )-curve for  $\lambda_{r_0} < \lambda$  and below it for  $\lambda_{r_0} > \lambda$ . As  $k$  is decreased, the ( $\cos \phi_1$ )-curves approach the limiting curve. The ( $\cos \phi_2$ )-curves, on the other hand, lie far to the left for large  $k$  and move steadily to the right, tending eventually to the limiting curve. Four horizontal lines are drawn on Fig. 4.8 corresponding to  $\cos \phi_1$  and  $\cos \phi_2$  equal to  $\cos 0^\circ$ ,  $\cos 22\frac{1}{2}^\circ$ ,  $\cos 30^\circ$ ,

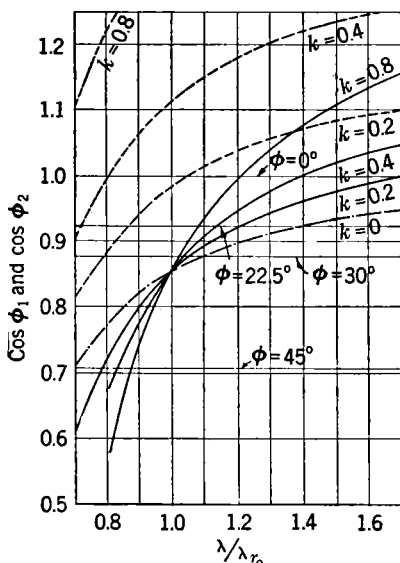


FIG. 4.8.—The dependence of  $\cos \phi_1$  and  $\cos \phi_2$  on  $\lambda/\lambda_{r_0}$  for various values of  $k$  in a double-strapped tube [see Eqs. (34)]. The solid lines are  $\cos \phi_1$  (symmetric modes); the broken lines are  $\cos \phi_2$  (antisymmetric modes). Values of  $\cos \phi > 1$  correspond to  $\phi$  imaginary. For  $k = 0$  the two sets of modes coincide.

and  $\cos 45^\circ$ . The intersections of these lines with the  $(\cos \phi_1)$ - and  $(\cos \phi_2)$ -curves give the wavelengths of modes for which  $\psi_m = 0^\circ, 22\frac{1}{2}^\circ, 30^\circ$ , and  $45^\circ$ . These represent, for example, the  $(m = 0)$ -,  $(m = 1)$ -, and  $(m = 2)$ -modes for  $N = 16$  ( $\psi = 0^\circ, 22\frac{1}{2}^\circ$ , and  $45^\circ$ ); the  $(m = 0)$ - and  $(m = 1)$ -modes for  $N = 12$  ( $0^\circ$  and  $30^\circ$ ); and the  $(m = 0)$ - and  $(m = 1)$ -modes for  $N = 8$  ( $0^\circ$  and  $45^\circ$ ).

It is clear from the form of the curves that for either the symmetric or antisymmetric set, the modes have the opposite order in wavelength from that in number. Also, as the weight of strapping increases ( $k \rightarrow 0$ ), the intersections move to the right for the antisymmetric modes; i.e.,

the wavelength increases. For the symmetric modes the intersections move to the right if  $\cos \phi_m > \cos 2\pi s/\lambda_{r_0}$  and to the left if

$$\cos \phi_m < \cos \frac{2\pi s}{\lambda_{r_0}}.$$

Thus, whether or not the wavelength of a mode is increased or decreased by strapping depends upon the mode number, the strap length, and the resonator wavelength. Figure 4-9, derived from Fig. 4-8, shows the wavelength of the modes as a function of  $k$ . For a given mode the intersections tend, as  $k \rightarrow 0$ , toward the points  $\cos \phi_m = \cos 2\pi s/\lambda$  or, because

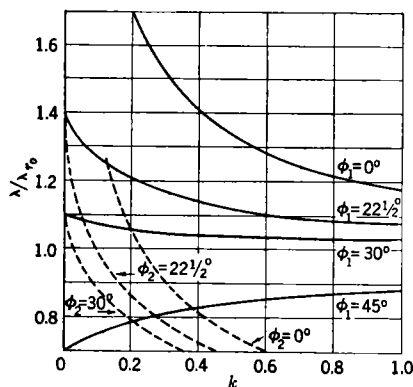


FIG. 4-9.—The dependence of  $\lambda/\lambda_{r_0}$  on  $k$  for various values of  $\phi_1$  and  $\phi_2$  in a double-strapped tube. The solid lines are the symmetric modes; the broken lines are the antisymmetric modes.

$\phi_m = 2\pi m/N$ , toward  $\lambda = Ns/m$ . Thus, the  $\pi$ -mode wavelength becomes indefinitely long, while all the others tend to a finite limit, dependent only upon the strap length, the mode number, and the number of oscillators. The limiting wavelengths, in fact, correspond to  $1/m$  times the strap circumference.

In practice, it is of interest to examine the mode spectrum as a function of weight of strapping, subject to the condition that the  $\pi$ -mode wavelength remain fixed. It is thus necessary to adjust the unstrapped wavelength  $\lambda_{r_0}$  in each case. Figure 4-10 shows  $\cos \phi_1$  and  $\cos \phi_2$  as functions of  $\lambda/\lambda_r$ , where  $\lambda_r$  is the wavelength of the  $\pi$ -mode, for  $k = 0.8, 0.4, 0.2$ , and  $0$ . The strap length and tube height used correspond to those of Fig. 4-8 with  $k = 0.4$ ; that is, the  $\pi$ -mode wavelength of the  $(k = 0.4)$ -case of Fig. 4-8 is used as the fixed  $\pi$ -mode wavelength of Fig. 4-10. Figure 4-11 derived from Fig. 4-10 shows the variation of the wavelengths of some of the modes as a function of  $k$ . The limiting

wavelengths in this case may be found by letting  $k \rightarrow 0$  with  $\lambda_r$  fixed in Eq. (34a). The equation then becomes

$$\cos \phi_1 = \cos \phi_2 = \cos \frac{2\pi s}{\lambda} + \frac{\lambda}{\lambda_r} \tanh \frac{\pi s}{\lambda_r} \sin \frac{2\pi s}{\lambda} \quad (35)$$

It is seen that in this case also, the symmetric and antisymmetric modes eventually tend for very heavy strapping to coincide in pairs of the same  $m$ -number and that all the modes now tend to a finite wavelength.

**4-5. Effects of Various Parameters on the Mode Spectrum.**—The general behavior of the modes is more easily examined if approximate forms are used for Eqs. (34a) and (35). Thus, if  $2\pi s/\lambda$  is sufficiently small to ignore terms of higher than the second order in  $2\pi s/\lambda$ , the sines and cosines in Eq. (35) may be expanded to give

$$\cos \phi = \cos \phi' = 1 - \frac{2\pi^2 s^2}{\lambda^2} + \frac{2\pi^2 s^2}{\lambda_r^2} \quad (36a)$$

or

$$\frac{1}{\lambda_{m_1}^2} = \frac{1}{\lambda_{m_2}^2} = \frac{1}{\lambda_r^2} + \frac{\sin^2 \frac{\pi m}{N}}{\pi^2 s^2} \quad (36b)$$

for the  $m$ th mode, where  $\psi_m = 2\pi m/N$ . With the same condition upon  $2\pi s/\lambda$  and the additional requirement that

$$\tanh \frac{\pi h}{\lambda} \sqrt{\frac{\lambda^2}{\lambda_{r_0}^2} - 1}$$

may be replaced by

$$\frac{\pi h}{\lambda} \sqrt{\frac{\lambda^2}{\lambda_{r_0}^2} - 1}$$

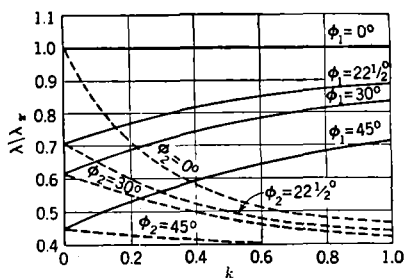


FIG. 4-11.—The dependence of  $\lambda/\lambda_r$  on  $k$  for various values of  $\phi_1$  and  $\phi_2$  in a double-strapped tube. The solid lines are  $\cos \phi_1$  (symmetric modes); the broken lines are  $\cos \phi_2$  (antisymmetric modes).

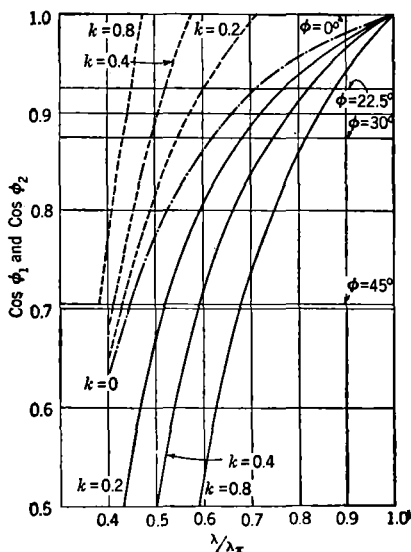


FIG. 4-10.—The dependence of  $\cos \phi_1$  and  $\cos \phi_2$  on  $\lambda/\lambda_r$  for various values of  $k$  in a double-strapped tube. The solid lines are  $\cos \phi_1$  (symmetric modes); the broken lines are  $\cos \phi_2$  (antisymmetric modes). For  $k = 0$  the two sets of modes coincide.

(a condition that requires either a very short tube or light strapping) Eq. (34a) for the symmetric modes becomes

$$\frac{1}{\lambda_{m1}^2} = \frac{1}{\lambda_r^2} + \frac{\sin^2 \frac{\pi m}{N}}{\pi^2 s^2 \left(1 + \frac{kh}{s}\right)}, \quad (37)$$

with

$$\lambda_r^2 = \lambda_{r_0}^2 \left(1 + \frac{s}{kh}\right), \quad (38)$$

and Eq. (34b) becomes

$$\lambda^2 = \frac{\pi^2 s^2}{\frac{ks}{h} + \sin^2 \frac{\pi m r}{N}}. \quad (39)$$

The close resemblance in form between Eqs. (36) and (37) is largely fortuitous; Eq. (36) is valid for  $k$  small; Eqs. (37) to (39) for  $k$  large. Taken together they reveal the main features of the spectrum. Equation (38), which holds when the variation of the fields along the strap sections and along the resonator can be ignored, may be written as

$$\lambda_r^2 = \lambda_{r_0}^2 \left(1 + \frac{C_s}{C_r}\right), \quad (40)$$

where  $C_s = 2s/\omega K_s$  and  $C_r = h/\omega Z_{r_0}$  are the strap capacitance and resonator capacitance, respectively. This shows that in the  $\pi$ -mode strap capacitance is in parallel with the resonator capacitance.

The effect of the number of oscillators on the mode spectrum may now be considered. From Eq. (37) it follows that if two systems are built with the same ratio of strap length to  $\pi$ -mode wavelength, the relative mode separations will be the same for light strapping if

$$1 + \frac{kh}{s} \approx \sin^2 \frac{\pi m}{N}.$$

For modes with small  $m$ ,  $\pi m/N$  is small and  $k$  is assumed large; thus one can write

$$k \sim \frac{1}{N^2}$$

for modes of the same  $m$  number. Thus, the weight of strapping required to produce a given mode separation varies as  $N^2$  for relatively light strapping. Again, according to Eq. (36), the limiting mode separation varies as

$$\left(\frac{\lambda_r \sin \frac{\pi m}{N}}{\pi s}\right)^2 \text{ or } \left(\frac{m \lambda_r}{Ns}\right)^2$$

when  $\pi m/N$  is sufficiently small. Now  $Ns$  is equal to  $2\pi r_s$ , or very nearly

$2\pi r_a$ . The mode separation is, thus, proportional to  $(m\lambda_r/2\pi r_a)^2$  and depends essentially upon the size of the tube in terms of its operating wavelength. Both Eqs. (36) and (37) indicate that the mode separation varies with  $1/s^2$  for a given number of oscillators, indicating the practical importance of keeping the straps short. The effective length of the straps depends somewhat upon the shape of the resonator because it affects the distribution of voltage at the places where the straps are connected. An illustration of this effect is given below.

The remaining variable whose effect is to be considered is the length  $h$ . Because Eqs. (34a) and (34b) differ only in that one contains a hyperbolic tangent, the other a hyperbolic cotangent, the  $m_1$ - and  $m_2$ -modes must approach each other when the argument of these functions becomes large. The condition for this is that

$$\frac{\pi h}{\lambda} \sqrt{\frac{\lambda^2}{\lambda_r^2} - 1} > 1, \text{ say.}$$

This may come about through heavy strapping ( $\lambda_r \ll \lambda$ ) or for long tubes ( $h$  large). As  $h$  is increased, the antisymmetric modes very rapidly increase in wavelength, finally reaching a state in which the ( $m_2 = 0$ )-mode is nearer to the ( $m_1 = 0$ )-mode than is the ( $m_1 = 1$ ). Since most output circuits do not couple out the antisymmetric modes, this represents an undesirable condition. As a solution for the difficulty center-strapping has been used. Essentially this means building a double-length tube by putting end-to-end two completely strapped systems each of single length. The mode spectrum of the whole system is then close to that of its component halves.

Some actual applications of the formulas of this section will give an indication of their reliability (see Fig. 4-12). In a scaled-up model

(Fig. 4-12a) of a 16-resonator hole-and-slot 3-cm magnetron (4J50) the measured wavelengths of the ( $m_1 = 0$ )-, ( $m_1 = 1$ )-, and ( $m_1 = 2$ )-modes and the unstrapped wavelength are 12.400, 10.152, 7.570, and 9.47 cm, respectively. Any three of these may be used to calculate  $k$  and  $2\pi s$  from Eq. (34a). With  $k = 0.46$  and  $2\pi s = 4.58$  cm, the calculated wavelengths are 12.35, 10.17, and 7.52 cm. The effective strap radius is 1.86 cm compared with the actual strap radii of 1.85 and 2.04 cm.  $k$ , tentatively estimated from the tube geometry, agrees well with the

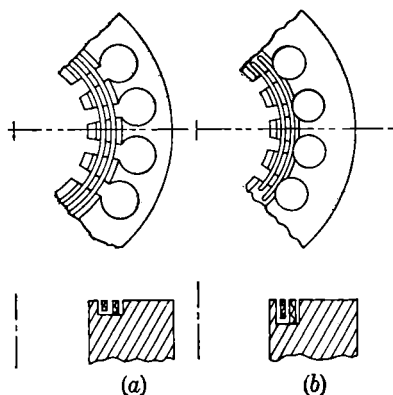


FIG. 4-12.—Two types of strapping used on 16-oscillator magnetrons.

above value. In a second 16-cavity tube (Fig. 4-12b) roughly twice the length of the above, the first two modes ( $m_1 = 0$ ) and ( $m_1 = 1$ ) were measured to be 10.53 and 8.45 cm, and the unstrapped wavelength 6.78 cm. With a value of 4.41 cm for  $2\pi s$  and 0.204 for  $k$  derived from these measurements and Eq. (34a), the antisymmetric modes ( $m_2 = 0$ ) and ( $m_2 = 1$ ) were found to be 9.51 and 7.59 cm. The measured wavelengths were 9.36 and 7.45 cm. In this case the effective strap radius is about 17 per cent greater than the actual mean strap radius. Presumably the lower effectiveness of the strap in Fig. 4-12b is due to the fact that the outer strap overhangs the hole and interacts with the flux through it and also to the shortness of the resonator, which puts the outer strap at a relatively low voltage point. Further evidence on this point is obtained from two 16-resonator vane-type magnetrons that had identical strapping but different vane depths. The wavelengths of the ( $m_1 = 0$ )- and ( $m_1 = 1$ )-modes were, for the first, 11.701 and 8.879 cm and, for the second, 9.545 and 7.852 cm. The unstrapped wavelengths can be calculated with some accuracy for vane tubes (see Sec. 11-2) and were computed to be 7.36 and 5.48 cm. With this information,  $2\pi s$  becomes 4.22 cm for the first tube and 4.37 cm for the second. Thus, the mechanically identical straps are electrically about 4 per cent shorter for the system with long resonators. The corresponding values of  $k$  are 0.263 and 0.230; the ratio of these is 1.14, whereas the calculated ratio of the resonator capacities is 1.19.

For single-strapped systems the separate sections may be treated as 4-terminal networks. By evaluating the single term of the ( $u-v$ )-matrix and using Eq. (15), the secular equation is found to be

$$\cos \psi_m = \cos \frac{2\pi s}{\lambda} \cosh \frac{2\pi h}{\lambda} \sqrt{\frac{\lambda^2}{\lambda_{r_0}} - 1} + \frac{1}{2} \left( \sin \frac{2\pi s}{\lambda} \sinh \frac{2\pi h}{\lambda} \sqrt{\frac{\lambda^2}{\lambda_{r_0}} - 1} \right) \left( \frac{K_s}{Z_{r_0}} \sqrt{\frac{\lambda^2}{\lambda_{r_0}} - 1} - \frac{Z_{r_0}}{K_s} \frac{1}{\sqrt{\frac{\lambda^2}{\lambda_{r_0}} - 1}} \right), \quad (41)$$

where the constants have the same significance as before, except  $s$ , which is the sum of the effective strap lengths at the two ends of the tube (per section).

Figure 4-13 shows  $\cos \phi$  as a function of  $\lambda/\lambda_{r_0}$  for values of  $k = 0.8$ , 0.4, and 0.2 for a single-strapped tube similar to Fig. 4-8 on double strapping, in which  $2\pi s/\lambda_{r_0} = 0.55$  and  $\pi h/\lambda_{r_0} = 0.80$ . The behavior of the mode spectrum under an increasing weight of strapping is considerably different in this case. The wavelength of all modes (in the range considered) increases with heavier strapping, and the mode order is the normal one for strapped tubes. However, the mode separation is only very slowly increased by increasing the weight of strapping, since



the slope of the curves of the  $\cos \phi$  vs.  $\lambda/\lambda_0$  changes quite slowly with decreasing  $k$ . Comparing the curves of Fig. 4-13 with those of Fig. 4-8, it is apparent that the mode separation for heavy single strapping is far less than for double strapping of the same impedance. The difference persists even when the two cases are compared on the basis of equal total strap capacity.

The reason for the very different behavior of single-strapped tubes may be found in the fact that the coupling path between oscillators now includes the oscillators themselves. Thus, if the resonant wavelength be increased beyond the unstrapped wavelength by adding straps, the coupling path of the resonator is now beyond cutoff. With sufficiently heavy strapping the coupling through the resonator becomes relatively weak, and mode separation is difficult to achieve. Actually, for sufficiently heavy strapping the model of Fig. 4-7 will break down because the impedance of the coupling path through the end cavities over unstrapped segments will become comparable to that through the resonator. It may be noted that the symmetry of the single-strapped tube is such that two sets, of symmetric and of antisymmetric modes, do not exist. Thus, long anodes lead to difficulties because of poor mode separation between ( $m = 0, 1, 2$ ), etc., rather than between ( $m = 0_1$ ) and ( $m = 0_2$ ).

Evidence for the correctness of this picture of the mode spectrum may be found in the data on the HP10V, a high-power 10-cm magnetron for which  $\pi h/\lambda_0 = 1.48$ ,  $2\pi s/\lambda_0 = 0.84$ , and  $N = 10$ . The ratio of  $\pi$ -mode wavelength to unstrapped wavelength is 1.245, but the mode separation between ( $m = 0$ ) and ( $m = 1$ ) is only 5 per cent.

The discussion of the mode spectrum of a strapped system has shown that the distribution of the modes in frequency depends upon the nature of the variation of the transfer angles  $\phi_m$  with frequency. The strapped system was discovered somewhat accidentally; and, so far, no resonant system has been developed synthetically, in the sense that the word

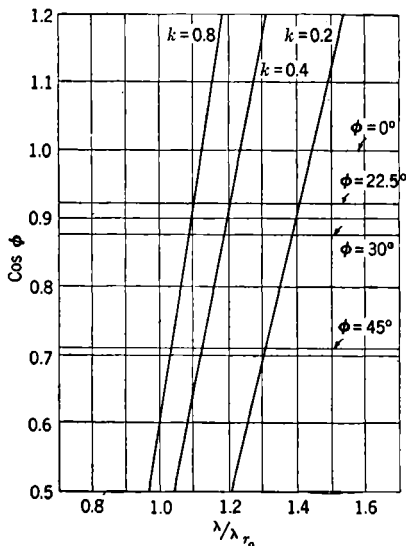


FIG. 4-13.—The dependence of  $\cos \phi$  on  $\lambda/\lambda_0$  for various values of  $k$  in a single-strapped tube. Values of  $\cos \phi > 1$  correspond to  $\phi$  imaginary.

is used in filter design. It seems probable that alternatives to the strapped or rising-sun systems with satisfactory mode spectra might be found by deliberately synthesizing a network with desired transfer characteristics, that is, with the required variation of the transfer angles with frequency.

It has been stressed that the equivalent lumped-circuit treatment of strapped resonant systems is not primarily a method for making wavelength calculations but is rather a model that correlates observed data. It is possible, however, to estimate wavelengths reasonably well by calculating  $\lambda_{r0}$ ,  $Z_{r0}$ ,  $s$ , and  $K_s$  and by making use of these values in the mode-spectrum formula. Methods of calculating  $\lambda_{r0}$ ,  $Z_{r0}$ ,  $s$ , and  $K_s$  are described at some length in Chap. 11 on the design of resonant systems. A value of  $\lambda_{r0}$  can usually be estimated for any resonator shape to about 3 to 4 per cent and  $Z_{r0}$  with perhaps half of this accuracy;  $s$ , the equivalent strap length, is the most difficult quantity to determine with certainty. As has already been pointed out, it will depend upon the location of the straps with respect to the resonator and upon the shape of the latter. Errors in its determination will not seriously affect the calculation of the  $\pi$ -mode wavelength, but they will cause considerable uncertainty in the value of the mode separation, because this quantity is so strongly dependent upon the effective strap length.

### ASYMMETRICAL SYSTEMS

The discussion of the strapped anode block has so far dealt with situations in which all the resonators were identical. Three departures from this condition are important. The first is the case in which power is coupled out from a single cavity. Here it is of interest to know how the wavelengths are affected and to what extent the field patterns in the interaction space are distorted. Experimentally, this distortion can be produced by heavy loading, and a correlation with lowered operating efficiency has been noted. The second case is the presence of strap breaks. In some tubes mode transition under certain conditions of operation can be prevented by breaking the straps at some point over a segment; in general, the effectiveness of this procedure depends upon the orientation of the breaks with respect to the output. Strap breaks give varied effects: they cause a shift in the frequency of the modes for  $m \neq 0$ , thereby affecting mode selection (see Chap. 8); they may influence the coupling to the output of the modes; finally, they cause distortion of the field patterns for  $m \neq 0$ , thereby making power transfer to those modes inefficient. The final case occurs in consideration of tuning schemes in which the frequency of the resonator system is varied by introducing reactance into a single cavity. This problem is an extension of that of loading; the questions of pattern distortion and

variation of mode separation are important. In principle, most of these questions can be answered; the complexity of some of the results may suggest recourse to a model, however.

**4.6. Pattern Distortion and Mode-spectrum Effects Caused by Loading.**—Pattern distortion due to loading or tuning may be adequately treated. Because most single-cavity tuners and output circuits do not couple the antisymmetric modes, the 8-terminal network used so far may be replaced by the 4-terminal one, which is obtained by considering only the upper or lower half of the tube open-circuited at the median plane. The resonator system will then be represented by a ring of 4-terminal networks, one of which is shown in Fig. 4-14a. The matrix for one section is then

$$\begin{aligned}\bar{T} &\equiv \begin{pmatrix} \cos \phi & jZ \sin \phi \\ jY \sin \phi & \cos \phi \end{pmatrix} \\ &= \begin{pmatrix} 1 & 0 \\ jY_{\text{res}} & 1 \end{pmatrix} \begin{pmatrix} \cos 2\theta_s & jK_s \sin 2\theta_s \\ jM_s \sin 2\theta_s & \cos 2\theta_s \end{pmatrix} \begin{pmatrix} 1 & 0 \\ jY_{\text{res}} & 1 \end{pmatrix}, \quad (42)\end{aligned}$$

where  $Y_{\text{res}} = M_s \tan \theta_s/2$  and all of the other symbols have their earlier significance. Thus,

$$\cos \phi = \cos 2\theta_s - \frac{K_s}{2} Y_{\text{res}} \sin 2\theta_s, \quad (43)$$

and

$$Z \sin \phi = K_s \sin 2\theta_s. \quad (44)$$

The  $\cos \phi$  is identical with the function  $\cos \phi_1$  used before. If one oscillator is loaded and the load is considered to be transformed to the upper (or lower) end of the oscillator slot, the ring of 4-terminal elements is changed by the addition of a shunt element,  $jY_{\text{load}}$ , say, and appears as in Fig. 4-14b. The condition for periodicity is now

$$\begin{pmatrix} 1 & 0 \\ jY_{\text{load}} & 1 \end{pmatrix} \bar{T}^N \begin{pmatrix} v_0 \\ i_0 \end{pmatrix} = \begin{pmatrix} v_0 \\ i_0 \end{pmatrix}. \quad (45)$$

Using the known expression for  $\bar{T}^N$  the determinantal equation is now

$$\begin{vmatrix} \cos N\phi - 1 & jZ \sin N\phi \\ jY \sin N\phi + jY_{\text{load}} \cos N\phi & \cos N\phi - 1 - ZY_{\text{load}} \sin N\phi \end{vmatrix} = 0 \quad (46a)$$

or

$$\sin \frac{N\phi}{2} \left( \sin \frac{N\phi}{2} - \frac{1}{2} ZY_{\text{load}} \cos \frac{N\phi}{2} \right) = 0, \quad (46b)$$

which leads to

$$\sin \frac{N\phi}{2} = 0, \quad \text{for } \phi = 0, \quad (47a)$$

otherwise,

$$\tan \frac{N\phi}{2} + \frac{1}{2}ZY_{\text{load}} = 0. \quad (47b)$$

These equations show that except for the  $\pi$ -mode each of the modes of the symmetrical tube is degenerate and consists of a doublet, one component of which will couple the output and one which will not. The ( $m = 0$ )- or ( $\phi = 0$ )-mode is nondegenerate because, as can be seen from Eq. (44),  $Z \sin \phi$  remains finite and, therefore, so does  $Z \sin N\phi/2$

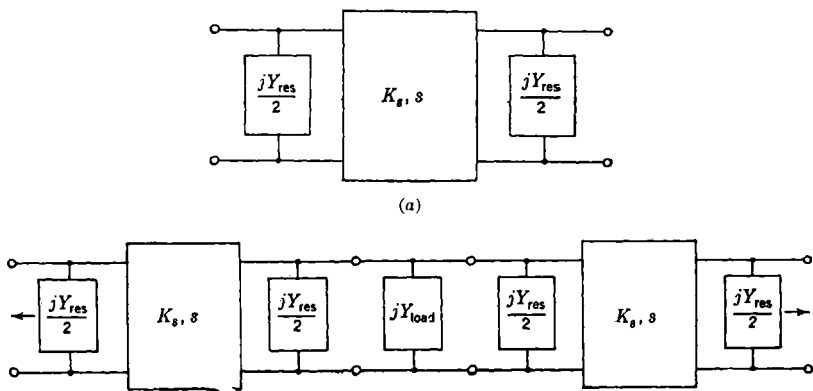


FIG. 4-14.—(a) The 4-terminal network for one section of the resonant system; (b) addition of a load to the ring of 4-terminal networks.

in Eq. (46). The degeneracy of the modes was also apparent from the fact that the terms of the form  $e^{\pm i\psi_m}$  that appeared in factoring  $T^N - 1$  [Eq. (9)], coalesced into  $\cos \psi_m$  in the determinantal equation when  $m \neq 0$ . Equation (47b) and the equations that define  $\cos \phi$  and  $Z$  determine the frequency shift. The variation of loading among the different modes may be examined if Eqs. (44) and (47b) are combined to give  $Y_s$ , the admittance looking into the tube at a slot,

$$-Y_{\text{load}} = Y_s = +2 \frac{\sin \phi \tan \frac{N\phi}{2}}{K_s \sin 2\theta_s}, \quad (48)$$

or, as it may be written by using Eq. (43),

$$Y_s = + \frac{\tan \frac{N\phi}{2}}{\tan \frac{\phi}{2}} \left( 2 \frac{\tan \theta_s}{K_s} + Y_{\text{res}} \right).$$

For the  $\pi$ -mode the bracketed term vanishes, and  $Y_s$ , the characteristic

admittance, is

$$Y_c = -\frac{1}{2} \left( \lambda \frac{\partial Y}{\partial \lambda} \right) = -\frac{N}{2} \lambda \frac{\partial}{\partial \lambda} \left( 2 \frac{\tan \theta_s}{K_s} + Y_{res} \right).$$

For  $m \neq 0$ , the unbracketed term vanishes, and

$$\begin{aligned} Y_c &= -\frac{1}{2} \left( 2 \frac{\tan \theta_s}{K_s} + Y_{res} \right) \lambda \frac{\partial}{\partial \lambda} \left( \frac{\tan \frac{N\phi}{2}}{\tan \frac{\phi}{2}} \right) & \phi &= \frac{2\pi m}{N} = \psi_m \\ &= -\frac{N}{4} \left( 2 \frac{\tan \theta_s}{K_s} + Y_{res} \right) \cotn \frac{\phi}{2} \left( \lambda \frac{\partial \phi}{\partial \lambda} \right) & \phi &= \psi_m. \end{aligned}$$

But

$$\lambda \frac{\partial \phi}{\partial \lambda} \sin \frac{\phi}{2} \cos \frac{\phi}{2} = \lambda \frac{\partial}{\partial \lambda} \left( \sin^2 \theta_s + \frac{1}{2} \frac{K_s Y_{res}}{2} \sin 2\theta_s \right)$$

from Eq. (43). Therefore,

$$\begin{aligned} \left( \frac{N}{2} \cotn \frac{\phi}{2} \right) \lambda \frac{\partial \phi}{\partial \lambda} &= -\frac{N}{2} \left[ \frac{K_s \sin \theta_s \cos \theta_s \lambda \frac{\partial}{\partial \lambda} \left( \frac{\tan \theta_s}{K_s} + \frac{Y_{res}}{2} \right)}{K_s \sin \theta_s \cos \theta_s \left( \frac{\tan \theta_s}{K_s} + \frac{Y_{res}}{2} \right)} \right] \\ &\quad + \left[ \frac{\left( \frac{\tan \theta_s}{K_s} + \frac{Y_{res}}{2} \right) \lambda \frac{\partial}{\partial \lambda} (K_s \sin \theta_s \cos \theta_s)}{K_s \sin \theta_s \cos \theta_s \left( \frac{\tan \theta_s}{K_s} + \frac{Y_{res}}{2} \right)} \right], \end{aligned}$$

and

$$\begin{aligned} -2Y_c &= \frac{N}{2} \lambda \frac{\partial}{\partial \lambda} \left( 2 \frac{\tan \theta_s}{K_s} + Y_{res} \right) + \frac{N}{2} \left( 2 \frac{\tan \theta_s}{K_s} + Y_{res} \right) \lambda \frac{\partial}{\partial \lambda} \log \sin 2\theta_s \\ &= \frac{N}{2} \lambda \frac{\partial}{\partial \lambda} \left( 2 \frac{\tan \theta_s}{K_s} + Y_{res} \right) + N \left( 2 \frac{\tan \theta_s}{K_s} + Y_{res} \right) \lambda \frac{\partial \theta_s}{\partial \lambda} \cotn 2\theta_s. \end{aligned}$$

Since we have considered only one-half of the tube, these values  $Y_c$  may be doubled to obtain the values for the whole tube.

For small values of  $\theta_s$ ,  $\lambda(\partial/\partial\lambda) \log \sin 2\theta_s = -1$ , which simplifies the second term. The characteristic admittance for the  $\pi$ -mode is  $N$  times that of a single section open-circuited at the midplanes of the segments. For the other modes, essentially because of the fact that they have an uncoupled component, only  $N/2$  times the characteristic admittance of the individual resonator appears, together with  $N$  times the actual admittance of the individual oscillator. It must be kept in mind that the values of  $Y_c$  found above are not actually those which enter into measurements of  $Q$ -values, because the admittance used here appears at the top or bottom of a *slot*. The individual oscillator containing the

output circuit acts as a transformer between the slot and the place at which the output circuit is supposed to begin. The effect of this transformer is discussed in Chap. 5.

The amount of pattern distortion caused by loading or tuning may be analyzed in terms of the field patterns of the undisturbed modes. Suppose that the actual voltages and currents across the resonators are  $V_0, V_1, \dots, V_{(n-1)}$  and  $I_0, I_1, \dots, I_{(n-1)}$ . Let the amplitude of the  $m$ th mode be  $a_m$ , where, if traveling waves are used,  $m$  has the values  $0, \pm 1, \pm 2, \dots, \pm(N/2 - 1), N/2$ . Then the voltage  $V_r$  on the  $r$ th resonator satisfies

$$V_r = \sum_m a_m e^{ir\psi_m}. \quad (49)$$

Multiplying Eq. (49) by  $e^{-ir\psi_m}$  and summing over  $r$ , one has, because  $N(\psi_m - \psi_n) = 2\pi(m - n)$ ,

$$Na_m = \sum_{r=0}^{N-1} e^{-ir\psi_m} V_r. \quad (50)$$

If a quantity  $b_m$  is defined such that

$$Nb_m = \sum_{r=0}^{N-1} e^{-ir\psi_m} I_r,$$

then

$$N \begin{pmatrix} a_m \\ b_m \end{pmatrix} = \begin{pmatrix} V_0 \\ I_0 \end{pmatrix} + e^{-i\psi_m} \begin{pmatrix} V_1 \\ I_1 \end{pmatrix} \dots + e^{-i(N-1)\psi_m} \begin{pmatrix} V_{N-1} \\ I_{N-1} \end{pmatrix} \quad (51)$$

and

$$Ne^{-i\psi_m} \bar{\Gamma} \begin{pmatrix} a_m \\ b_m \end{pmatrix} = e^{-i\psi_m} \begin{pmatrix} V_1 \\ I_1 \end{pmatrix} \dots + e^{-i(N-1)\psi_m} \begin{pmatrix} V_{N-1} \\ I_{N-1} \end{pmatrix} + e^{-iN\psi_m} \bar{\Gamma} \begin{pmatrix} V_{N-1} \\ I_{N-1} \end{pmatrix}. \quad (52)$$

But considering Eq. (45),

$$\bar{\Gamma} \begin{pmatrix} V_{N-1} \\ I_{N-1} \end{pmatrix} = \begin{pmatrix} 1 & 0 \\ -jY_{\text{load}} & 1 \end{pmatrix} \begin{pmatrix} V_0 \\ I_0 \end{pmatrix}. \quad (53)$$

The result of subtracting Eq. (52) from Eq. (51) and using Eq. (53) is

$$(1 - e^{-i\psi_m} \bar{\Gamma}) \begin{pmatrix} a_m \\ b_m \end{pmatrix} = \frac{1}{N} \begin{pmatrix} 0 & 0 \\ +jY_{\text{load}} & 0 \end{pmatrix} \begin{pmatrix} V_0 \\ I_0 \end{pmatrix} \quad (54)$$

or, by equating terms,

$$\begin{aligned} (1 - e^{-i\psi_m} \cos \phi) a_m - e^{-i\psi_m} Z b_m \sin \phi &= 0 \\ -e^{-i\psi_m} j Y a_m \sin \phi + (1 - e^{-i\psi_m} \cos \phi) b_m &= +j Y_{\text{load}} \frac{V_0}{N}. \end{aligned}$$

Eliminating  $b_m$ ,  $a_m$  satisfies the equation

$$a_m(\cos \psi_m - \cos \phi) = -\frac{1}{2} Z Y_{\text{load}} \frac{V_0}{N} \sin \phi;$$

or, using Eq. (47b)

$$a_m = \frac{-\sin \phi \tan \frac{N\phi}{2}}{N(\cos \phi - \cos \psi_m)}. \quad (55)$$

The term  $a_0$  gives directly the amplitude of the ( $m = 0$ )-mode;  $2a_m$  gives the amplitudes of the remaining standing-wave patterns. It is to be

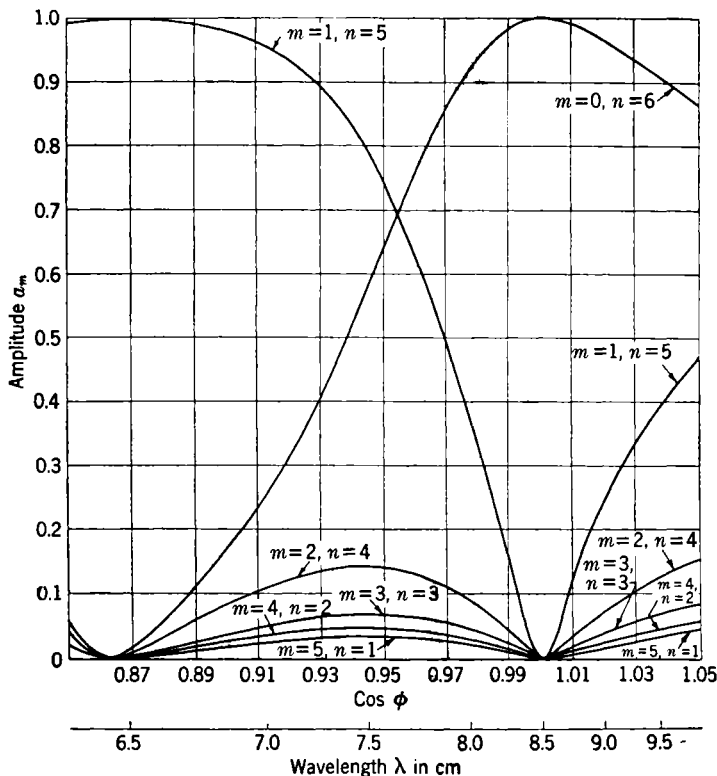


FIG. 4-15.—The amplitudes of various modes as functions of  $\lambda$ . Values of  $\cos \phi > 1$  correspond to  $\phi$  imaginary.

noted that  $a_m$  is expressed entirely in terms of the angle  $\phi$  which is presumably already known as a function of  $\lambda$ . As an example, Fig. 4-15 shows the relative intensities of the modes in a 12-resonator magnetron as a function of  $\phi$  and wavelength. If this magnetron were tuned by

introducing reactance into one cavity, Fig. 4.15 shows the relative intensities of the component modes when the system has any of its resonances at  $\phi$  and  $\lambda$ . For convenience the quantity  $-a_m/[(\sum a_m^2)^{1/2}]$  has been plotted. Equation (55) is, of course, also valid for the case of resistive loading when  $\phi$  is complex, but Fig. 4.15 applies to purely reactive loading ( $\cos \phi$  real). It is of some interest to note that with substantial mode separation, distortion sets in above and below the  $\pi$ -mode at about the same rate.

In the simple case of loading, the perturbations are relatively small. For the  $\pi$ -mode when  $Y_{\text{load}}$  is sufficiently small for terms in the expansions of  $\cos \phi$  and  $\sin \phi$  higher than  $\phi^2$  to be neglected, Eqs. (43), (44), and (47b) give

$$\phi^2 = -\frac{Y_{\text{load}}}{N} K_s \sin 2\theta_s; \quad (56)$$

Eq. (55) under similar circumstances becomes

$$2a_m = \frac{-\phi^2}{2 \sin^2 \frac{\pi m}{N}},$$

and using the value of  $\phi^2$ ,

$$2a_m = \frac{Y_{\text{load}} K_s \sin 2\theta_s}{2N \sin^2 \frac{\pi m}{N}}.$$

For large  $N$  and short straps this becomes

$$2a_m = -\frac{Y_{\text{load}} K_s}{\pi m^2} \left( \frac{sN}{\lambda_\pi} \right). \quad (57)$$

This is a result which might have been expected. It shows that distortion will be severe when the effective strap circumference  $sN$  is large relative to  $\lambda_\pi$ . It also shows that when the coupled admittance is comparable to the strap admittance, there will be distortion and, finally, that the other modes are excited in amounts varying as  $1/m^2$ . Because the tangential component of electric field for the  $m$ th mode falls off roughly as  $(r/r_a)^{(N/2)-m}$ , the pattern may become badly distorted at the anode because of a small amount of high- $m$  component.

A further source of pattern distortion is the longitudinal variation in field strength that arises from the influence of the straps at the ends. In the symmetric modes the fields have an axial variation of the form  $\cosh 2\pi z/\lambda \sqrt{(\lambda^2/\lambda_0^2) - 1}$ , measuring  $z$  from the median plane; in the antisymmetric modes, a hyperbolic sine is involved. This variation is considerable in heavily strapped tubes; thus in the long tube described at the end of Sec. 4.5 the fields at the end are twice as great as those at the



center; in the lighter strapped and shorter tube, also referred to in Sec. 4-5, the difference in fields is about 15 per cent. This source of pattern distortion may be removed by center-strapping.

**4-7. Effects of Strap Breaks.**—In double-strapped tubes the two straps at one end of the tube are customarily broken and each break is made over a segment; the straps at the other end of the tube are continuous rings. There will then be an odd number of sections between the breaks. The breaks may be represented in the equivalent circuit by a series reactance introduced at the discontinuities of the strap system as shown in Fig. 4-16. The same arrangement of the sections that was used in the loading analysis is used here, namely, two coupling sections in the

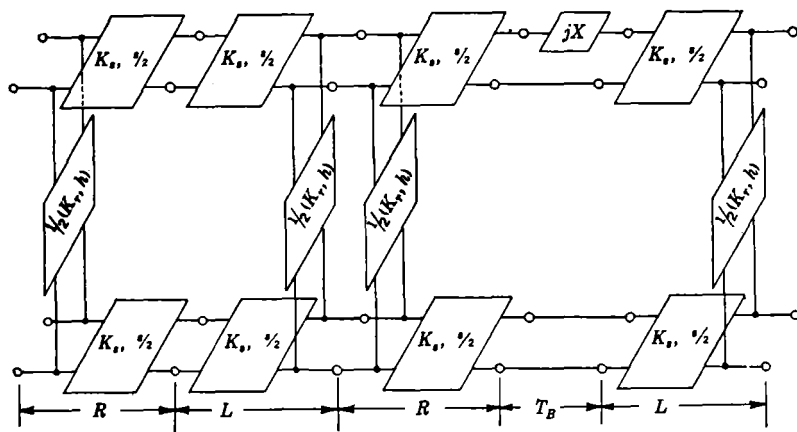


FIG. 4-16.—Equivalent circuit of two neighboring sections in a strapped tube; one section contains a strap break. The appropriate matrix is indicated for each part.

center and half the resonator section at each end. The matrix for a "break" section will be

$$T_B = \begin{pmatrix} 1 & 0 & jX & 0 \\ 0 & 1 & 0 & 0 \\ 0 & 0 & 1 & 0 \\ 0 & 0 & 0 & 1 \end{pmatrix} = \begin{pmatrix} 1 & jQ \\ 0 & 1 \end{pmatrix}. \quad (58)$$

If there were strap breaks at both tube ends on the same segments, then  $Q$  would be given by

$$Q = \begin{pmatrix} X & 0 \\ 0 & X \end{pmatrix}. \quad (59)$$

Referring to Fig. 4-16, let the matrices for the normally left- and right-hand sections be  $L$  and  $R$  respectively. Then

$$T = D^{-1}T_0D = LR. \quad \text{See Eq. (16).}$$

One may write

$$L = D^{-1}T_0^{1/2}DF \quad (60a)$$

and

$$R = F^{-1}D^{-1}T_0^{1/2}D. \quad (60b)$$

Then

$$\bar{T} = RL = F^{-1}D^{-1}T_0DF. \quad (61)$$

Thus,  $\bar{T}$  is the new section matrix and may be put into the same quasi-diagonal form  $T_0$  as  $T$ , while  $DF$  has replaced  $D$ . If the two diagonal submatrices of  $DF$  are  $(DF)_{11}$  and  $(DF)_{22}$ , these may be found and are

$$(DF)_{11} = \frac{1}{\cos \theta_s} \begin{pmatrix} \cos \frac{\phi_1}{2} & \cos \frac{\phi_1}{2} \\ \cos \frac{\phi_2}{2} & -\cos \frac{\phi_2}{2} \end{pmatrix} \quad (62)$$

and

$$(DF)_{22} = jK_s \sin \theta_s \begin{pmatrix} \csc \frac{\phi_1}{2} & \csc \frac{\phi_1}{2} \\ \csc \frac{\phi_2}{2} & -\csc \frac{\phi_2}{2} \end{pmatrix}. \quad (63)$$

Starting now from a point halfway between the strap breaks, supposed  $(2p+1)$  sections apart, where  $p$  is an integer, and using  $\bar{T}'$  for the temporary symbol of the matrix of a section containing a break, the periodic condition may be expressed as

$$[\bar{T}^{(N/2)-p}\bar{T}'\bar{T}_p][\bar{T}_p\bar{T}'\bar{T}^{(N/2)-p}] \begin{pmatrix} v_0 \\ i_0 \end{pmatrix} = \begin{pmatrix} v_0 \\ i_0 \end{pmatrix} \quad (64)$$

But  $\bar{T}'$  is given by

$$\bar{T}' = F^{-1}D^{-1}T_0^{1/2}DT_B D^{-1}T_0^{1/2}DF. \quad (65)$$

The two matrices in brackets in Eq. (64) correspond to sections that are mirror images, and they satisfy an equation such that the theorem proved in Eq. (23b) may be applied to either of them. The first of the matrices may be written as

$$F^{-1}D^{-1}T_0^{(N/2)-p-1/2}DT_B D^{-1}T_0^{(p+1/2)}DF;$$

and putting

$$\begin{pmatrix} v'_0 \\ i'_0 \end{pmatrix} = F^{-1}D^{-1}T_0^{(N/2)-p-1/2}DT_B D^{-1}T_0^{(p+1/2)}DF \begin{pmatrix} v_0 \\ i_0 \end{pmatrix}, \quad (66)$$

then, according to Eq. (23b)

$$i'_0 = i_0 = 0, \quad (67a)$$

or

$$v'_0 = v_0 = 0. \quad (67b)$$

Now

$$D T_B D^{-1} = \begin{pmatrix} D_{11} & 0 \\ 0 & D_{22} \end{pmatrix} \begin{pmatrix} 1 & jQ \\ 0 & 1 \end{pmatrix} \begin{pmatrix} D_{11}^{-1} & 0 \\ 0 & D_{22}^{-1} \end{pmatrix} = \begin{pmatrix} 1 & jD_{11}QD_{22}^{-1} \\ 0 & 1 \end{pmatrix}; \quad (68)$$

and using the forms for  $D_{11}$  and  $D_{22}$  given in Eq. (32), the result is

$$jD_{11}QD_{22}^{-1} = \frac{X \operatorname{ctn} \theta_s}{2K_s} \begin{pmatrix} \tan \frac{\phi_1}{2} & \tan \frac{\phi_2}{2} \\ \tan \frac{\phi_1}{2} & \tan \frac{\phi_2}{2} \end{pmatrix} \quad (69)$$

for breaks at only one end and

$$jD_{11}QD_{22}^{-1} = \frac{X \operatorname{ctn} \theta_s}{K_s} \begin{pmatrix} \tan \frac{\phi_1}{2} & 0 \\ 0 & \tan \frac{\phi_2}{2} \end{pmatrix} \quad (70)$$

for breaks at both ends. The conditions (67a) and (67b) lead then to

$$[-S_{N/2} + jS_{(N/2)-p-1/2}(D_{11}QD_{22}^{-1})S_{(p+1/2)}](DF)_{11}v_0 = 0 \quad (71)$$

or

$$[S_{N/2} + jC_{(N/2)-p-1/2}(D_{11}QD_{22}^{-1})C_{(p+1/2)}](DF)_{22}i_0 = 0 \quad (72)$$

Using Eqs. (69) and (67) and the fact that the determinants of the matrices between bars in Eqs. (71) and (72) must vanish, the following equations may be found:

$$\begin{aligned} \frac{2K_s}{X \operatorname{ctn} \theta} \sin \frac{N\phi_1}{2} \sin \frac{N\phi_2}{2} + \sin \frac{N\phi_2}{2} \left[ \sin \left( \frac{N}{2} - p - \frac{1}{2} \right) \phi_1 \right] \\ \left[ \sin \left( p + \frac{1}{2} \right) \phi_1 \right] \tan \frac{\phi_1}{2} + \sin \frac{N\phi_1}{2} \left[ \sin \left( \frac{N}{2} - p - \frac{1}{2} \right) \phi_2 \right] \\ \left[ \sin \left( p + \frac{1}{2} \right) \phi_2 \right] \tan \frac{\phi_2}{2} = 0 \end{aligned} \quad (73a)$$

and

$$\begin{aligned} \frac{2K_s}{X \operatorname{ctn} \theta_s} \sin \frac{N\phi_1}{2} \sin \frac{N\phi_2}{2} + \sin \frac{N\phi_2}{2} \left[ \cos \left( \frac{N}{2} - p - \frac{1}{2} \right) \phi_1 \right] \\ \left[ \cos \left( p + \frac{1}{2} \right) \phi_1 \right] \tan \frac{\phi_1}{2} + \sin \frac{N\phi_1}{2} \left[ \cos \left( \frac{N}{2} - p - \frac{1}{2} \right) \phi_2 \right] \\ \left[ \cos \left( p + \frac{1}{2} \right) \phi_2 \right] \tan \frac{\phi_2}{2} = 0 \end{aligned} \quad (73b)$$

for breaks at only one end. Because  $X \gg K_s \tan \theta_s$  for all normal strap breaks, the first term may be neglected and

$$\sin \frac{N\phi_2}{2} \left[ \sin \left( \frac{N}{2} - p - \frac{1}{2} \right) \phi_1 \right] \left[ \sin \left( p + \frac{1}{2} \right) \phi_1 \right] \tan \frac{\phi_1}{2} \\ + \sin \frac{N\phi_1}{2} \left[ \sin \left( \frac{N}{2} - p - \frac{1}{2} \right) \phi_2 \right] \left[ \sin \left( p + \frac{1}{2} \right) \phi_2 \right] \tan \frac{\phi_2}{2} = 0 \quad (74a)$$

and

$$\sin \frac{N\phi_2}{2} \left[ \cos \left( \frac{N}{2} - p - \frac{1}{2} \right) \phi_1 \right] \left[ \cos \left( p + \frac{1}{2} \right) \phi_1 \right] \tan \frac{\phi_1}{2} \\ + \sin \frac{N\phi_1}{2} \left[ \cos \left( \frac{N}{2} - p - \frac{1}{2} \right) \phi_2 \right] \left[ \cos \left( p + \frac{1}{2} \right) \phi_2 \right] \tan \frac{\phi_2}{2} = 0. \quad (74b)$$

For breaks at both ends there are four equations obtained by equating each of the bracketed terms to zero. The appearance of four equations in this case is a consequence of the fact that there still is end-for-end symmetry and a complete separation into symmetric and antisymmetric modes. When the break is at only one end, the two sets of modes are mixed and the only symmetry is that about the plane around which the breaks are symmetric. Thus, the modes for which  $i_0 = 0$  have a voltage loop in this plane, and those for which  $v_0 = 0$  have a voltage node. The  $\pi$ -mode is not affected by the strap breaks unless so much of the strap is removed that the capacitance of neighboring strap sections is affected.

The wavelengths of the ( $m_1 = 0$ )- and ( $m_1 = 1$ )-modes of the HK7 magnetron have been measured with unbroken straps and with strap breaks at one end,  $30^\circ$  and  $90^\circ$  apart ( $p = 0, 1$ ). For this tube  $N = 12$ . From the unstrapped, the ( $m_1 = 0$ ) and ( $m_1 = 1$ )-wavelengths in the unbroken case the values of  $k$  and  $s$  have been calculated and used with the aid of Eqs. (74) to evaluate the first three wavelengths in the broken

TABLE 4-1.—THE EFFECT OF STRAP BREAKS ON THE WAVELENGTH OF SEVERAL MODES OF THE HK7 MAGNETRON

Strap condition	$p$	No. of $m_1$ mode	Exper. $\lambda$ , cm	Calc. $\lambda$ , cm
Unbroken.....	..	0	10.645	10.645
		1	8.081	8.075
Broken at one end.....	}	0	10.645	10.645
		0	8.400	8.687
		0	8.900	8.783
		1	10.645	10.645
		1	9.165	9.086
		1	8.663	8.483
		2	.....	.....
		2	.....	9.248
		2	.....	8.190

strap cases for  $p = 0, 1$ , and  $2$ . The agreement with experiment may be seen from Table 4-1.

The  $1'$  modes are those having a voltage loop midway between the strap breaks; the  $1''$  modes, those having a voltage node. The experimental wavelengths are properly assigned according to pattern measurements. It may be seen that the order of the  $1'$  and  $1''$  modes depends upon the separation of the breaks; the order cannot be predicted without an examination of a specific case.

Some information on double breaks at each end is available from the ( $N = 16$ )-model 4J50 given in Sec. 4-5. Table 4-2 shows the agreement between measured and calculated values.

TABLE 4-2.—THE EFFECT OF STRAP BREAKS ON THE WAVELENGTH OF SEVERAL MODES OF A ( $N = 16$ ) MAGNETRON, THE 4J50

Strap condition	$p$	No. of $m_1$ mode	Exper. $\lambda$ , cm	Calc. $\lambda$ , cm
Unbroken.....	0	$\begin{cases} 0 \\ 1 \\ 2 \end{cases}$	$\begin{matrix} 12.400 \\ 10.152 \\ 7.570 \end{matrix}$	$\begin{matrix} 12.35 \\ 10.17 \\ 7.52 \end{matrix}$
Broken at both ends.....		$\begin{cases} 0 \\ 1 \\ 2 \end{cases}$	$\begin{matrix} 12.460 \\ 11.660 \\ 9.970 \end{matrix}$	$\begin{matrix} 12.35 \\ 11.57 \\ 9.99 \end{matrix}$

The pattern distortion caused by strap breaks may be calculated by a modification of the methods used earlier in this section. Since both symmetric and antisymmetric modes are excited, there will be two amplitudes,  $a_{m_1}$  and  $a_{m_2}$ , corresponding to these for each mode number  $m$ . In terms of these, the voltages  $V_{(m,A)}$  and  $V_{(m,B)}$ , say, at the two ends for the  $m$ th mode are given by

$$V_{(m,A)} = a_{m_1} + a_{m_2} \quad (75a)$$

and

$$V_{(m,B)} = a_{m_1} - a_{m_2}; \quad (75b)$$

or if

$$\begin{aligned} \mathbf{a}_m &= \begin{pmatrix} a_{m_1} \\ a_{m_2} \end{pmatrix}, \quad \text{and } V_{(m)} = \begin{pmatrix} V_{(m,A)} \\ V_{(m,B)} \end{pmatrix} \\ V_{(m)} &= \begin{pmatrix} 1 & 1 \\ 1 & -1 \end{pmatrix} \mathbf{a}_m = W \mathbf{a}_m. \end{aligned} \quad (75c)$$

As before, if  $v_r$  be the voltages at the two ends of the  $r$ th oscillator,

$$v_r = W \sum_m e^{ir\psi_m} \mathbf{a}_m$$

and

$$\mathbf{W}\mathbf{a}_m = \frac{1}{N} \sum_r e^{-jr\psi_m} \mathbf{v}_r.$$

If  $\mathbf{b}_m$  now be introduced as a similar generalization of the  $\mathbf{b}_m$  used before [see Eq. (51)];

$$N\mathbf{W} \begin{pmatrix} \mathbf{a}_m \\ \mathbf{b}_m \end{pmatrix} = \sum_r e^{-jr\psi_m} \begin{pmatrix} \mathbf{v}_r \\ \mathbf{i}_r \end{pmatrix}. \quad (76)$$

Then, for the case in hand,

$$Ne^{-j\psi_m} \bar{\mathbf{T}}\mathbf{W} \begin{pmatrix} \mathbf{a}_m \\ \mathbf{b}_m \end{pmatrix} = \sum_r e^{-j(r+1)\psi_m} \bar{\mathbf{T}} \begin{pmatrix} \mathbf{v}_r \\ \mathbf{i}_r \end{pmatrix},$$

and

$$N(1 - e^{-j\psi_m} \bar{\mathbf{T}})\mathbf{W} \begin{pmatrix} \mathbf{a}_m \\ \mathbf{b}_m \end{pmatrix} = e^{-j(p+1)\psi_m} \begin{pmatrix} \mathbf{v}_{p+1} \\ \mathbf{i}_{p+1} \end{pmatrix} - \bar{\mathbf{T}} \begin{pmatrix} \mathbf{v}_p \\ \mathbf{i}_p \end{pmatrix} \\ + e^{-j(N-p)\psi_m} \begin{pmatrix} \mathbf{v}_{(N-p)} \\ \mathbf{i}_{(N-p)} \end{pmatrix} - \bar{\mathbf{T}} \begin{pmatrix} \mathbf{v}_{(N-p-1)} \\ \mathbf{i}_{(N-p-1)} \end{pmatrix}. \quad (77)$$

But,

$$\begin{pmatrix} \mathbf{v}_{(p+1)} \\ \mathbf{i}_{(p+1)} \end{pmatrix} - \bar{\mathbf{T}} \begin{pmatrix} \mathbf{v}_p \\ \mathbf{i}_p \end{pmatrix} = \mathbf{F}^{-1}\mathbf{D}^{-1}\mathbf{T}_0^{1/2}\mathbf{D}(\mathbf{T}_B - \mathbf{I})\mathbf{D}^{-1}\mathbf{T}_0^{1/2}\mathbf{D}\mathbf{F} \begin{pmatrix} \mathbf{v}_p \\ \mathbf{i}_p \end{pmatrix} \\ = \mathbf{F}^{-1}\mathbf{D}^{-1}\mathbf{T}_0^{1/2}\mathbf{D}(\mathbf{T}_B - \mathbf{I})\mathbf{D}^{-1}\mathbf{T}_0^{(p+1/2)}\mathbf{D}\mathbf{F} \begin{pmatrix} \mathbf{v}_0 \\ \mathbf{i}_0 \end{pmatrix} \quad (78a)$$

and

$$\begin{pmatrix} \mathbf{v}_{(N-p)} \\ \mathbf{i}_{(N-p)} \end{pmatrix} - \bar{\mathbf{T}} \begin{pmatrix} \mathbf{v}_{(N-p-1)} \\ \mathbf{i}_{(N-p-1)} \end{pmatrix} = \mathbf{F}^{-1}\mathbf{D}^{-1}(\mathbf{I} - \mathbf{T}_0^{1/2}\mathbf{D}\mathbf{T}_B^{-1}\mathbf{D}^{-1}\mathbf{T}_0^{-1/2}) \\ \mathbf{T}_0^{-p}\mathbf{D}\mathbf{F} \begin{pmatrix} \mathbf{v}_0 \\ \mathbf{i}_0 \end{pmatrix} = \mathbf{F}^{-1}\mathbf{D}^{-1}\mathbf{T}_0^{1/2}\mathbf{D}(\mathbf{T}_B - \mathbf{I})\mathbf{D}^{-1}\mathbf{T}_0^{-(p+1/2)}\mathbf{D}\mathbf{F} \begin{pmatrix} \mathbf{v}_0 \\ \mathbf{i}_0 \end{pmatrix}. \quad (78b)$$

Now,

$$\mathbf{D}(\mathbf{T}_B - \mathbf{I})\mathbf{D}^{-1} = \begin{pmatrix} \mathbf{O} & j\mathbf{D}_{11}\mathbf{Q}\mathbf{D}_{22}^{-1} \\ \mathbf{O} & \mathbf{O} \end{pmatrix},$$

with the result that

$$\mathbf{D}(\mathbf{T}_B - \mathbf{I})\mathbf{D}^{-1}\mathbf{T}_0^{\pm(p+1/2)} = \begin{pmatrix} \mp j\mathbf{D}_{11}\mathbf{Q}\mathbf{D}_{22}^{-1}\mathbf{S}_{(p+1/2)} & j\mathbf{D}_{11}\mathbf{Q}\mathbf{D}_{22}^{-1}\mathbf{C}_{(p+1/2)} \\ \mathbf{O} & \mathbf{O} \end{pmatrix}$$

and

$$\mathbf{D}(\mathbf{T}_B - \mathbf{I})\mathbf{D}^{-1}\mathbf{T}_0^{\pm(p+1/2)}\mathbf{D}\mathbf{F} \begin{pmatrix} \mathbf{v}_0 \\ \mathbf{i}_0 \end{pmatrix} = [j\mathbf{D}_{11}\mathbf{Q}\mathbf{D}_{22}^{-1}(\mp \mathbf{S}_{(p+1/2)})(\mathbf{D}\mathbf{F})_{11}\mathbf{v}_0 \\ + \mathbf{C}_{(p+1/2)}(\mathbf{D}\mathbf{F})_{22}\mathbf{i}_0]. \quad (79)$$

Now, if Eqs. (71) and (72) are written out at length, it is easily verified that either

$$\mathbf{i}_0 = 0 \quad (j\mathbf{D}_{11}\mathbf{Q}\mathbf{D}_{22}^{-1})\mathbf{S}_{(p+\frac{1}{2})}(\mathbf{D}\mathbf{F})_{11}\mathbf{v}_0 = \begin{pmatrix} 1 \\ 1 \end{pmatrix} = \mathbf{E} \quad (80a)$$

$$\mathbf{v}_0 = 0 \quad (j\mathbf{D}_{11}\mathbf{Q}\mathbf{D}_{22}^{-1})\mathbf{C}_{(p+\frac{1}{2})}(\mathbf{D}\mathbf{F})_{22}\mathbf{i}_0 = \begin{pmatrix} 1 \\ 1 \end{pmatrix} = \mathbf{E}. \quad (80b)$$

Thus, the right-hand side of Eq. (77) may be written

$$e^{-j\frac{\psi_m}{2}}\mathbf{F}^{-1}\mathbf{D}^{-1}\mathbf{T}_0^{\frac{1}{2}} \begin{Bmatrix} [-e^{-j(p+\frac{1}{2})\psi_m} + e^{j(p+\frac{1}{2})\psi_m}] \mathbf{E} \\ \mathbf{O} \end{Bmatrix} \\ = [e^{-j\frac{\psi_m}{2}} 2j \sin(p + \frac{1}{2})\psi_m] \mathbf{F}^{-1}\mathbf{D}^{-1}\mathbf{T}_0^{\frac{1}{2}} \begin{pmatrix} \mathbf{E} \\ \mathbf{O} \end{pmatrix}$$

if  $\mathbf{i}_0 = 0$ , or

$$e^{-j\frac{\psi_m}{2}}\mathbf{F}^{-1}\mathbf{D}^{-1}\mathbf{T}_0^{\frac{1}{2}} \begin{Bmatrix} [e^{-j(p+\frac{1}{2})\psi_m} + e^{j(p+\frac{1}{2})\psi_m}] \mathbf{E} \\ \mathbf{O} \end{Bmatrix} \\ = e^{-j\frac{\psi_m}{2}} 2 \cos(p + \frac{1}{2})\psi_m \mathbf{F}^{-1}\mathbf{D}^{-1}\mathbf{T}_0^{\frac{1}{2}} \begin{pmatrix} \mathbf{E} \\ \mathbf{O} \end{pmatrix} \quad (81)$$

if  $\mathbf{v}_0 = 0$ .

Equation (77) thus becomes

$$N(\mathbf{I} - e^{-j\psi_m}\bar{\mathbf{T}})\mathbf{W} \begin{pmatrix} \mathbf{a}_m \\ \mathbf{b}_m \end{pmatrix} = \begin{bmatrix} 2e^{-j\frac{\psi_m}{2}} j \sin(p + \frac{1}{2})\psi_m \\ \cos \end{bmatrix} \begin{bmatrix} \mathbf{F}^{-1}\mathbf{D}^{-1}\mathbf{T}_0^{\frac{1}{2}} \begin{pmatrix} \mathbf{E} \\ \mathbf{O} \end{pmatrix} \end{bmatrix}, \quad (82)$$

where the alternative  $j \sin$  and  $\cos$  forms correspond to the cases for  $\mathbf{i}_0 = 0$  and  $\mathbf{v}_0 = 0$  respectively. Multiplying both sides by

$$e^{+j\psi_m}\bar{\mathbf{T}}^{-1} = \mathbf{F}^{-1}\mathbf{D}^{-1}(e^{j\psi_m}\mathbf{I} - \mathbf{T}_0^{-1})\mathbf{D}\mathbf{F}$$

gives

$$N\mathbf{F}^{-1}\mathbf{D}^{-1} \begin{bmatrix} (2 \cos \psi_m)\mathbf{I} - 2 \begin{pmatrix} \mathbf{C}_0 & \mathbf{O} \\ \mathbf{O} & \mathbf{C}_0 \end{pmatrix} \end{bmatrix} \mathbf{D}\mathbf{F}\mathbf{W} \begin{pmatrix} \mathbf{a}_m \\ \mathbf{b}_m \end{pmatrix} \\ = \begin{bmatrix} 2j \sin(p + \frac{1}{2})\psi_m \\ \cos \end{bmatrix} \mathbf{F}^{-1}\mathbf{D}^{-1}(e^{j\frac{\psi_m}{2}}\mathbf{T}_0^{\frac{1}{2}} - e^{-j\frac{\psi_m}{2}}\mathbf{T}_0^{\frac{1}{2}}) \begin{pmatrix} \mathbf{E} \\ \mathbf{O} \end{pmatrix}, \quad (83)$$

but

$$N \begin{pmatrix} (\cos \psi_m)\mathbf{I} - \mathbf{C}_0 & \mathbf{O} \\ \mathbf{O} & (\cos \psi_m)\mathbf{I} - \mathbf{C}_0 \end{pmatrix} \mathbf{D}\mathbf{F}\mathbf{W} \begin{pmatrix} \mathbf{a}_m \\ \mathbf{b}_m \end{pmatrix} \\ = \frac{j \sin(p + \frac{1}{2})\psi_m}{\cos} \begin{pmatrix} 2j\mathbf{C}_{\frac{1}{2}} \sin \frac{\psi_m}{2} & 2\mathbf{S}_{\frac{1}{2}} \cos \frac{\psi_m}{2} \\ -2\mathbf{S}_{\frac{1}{2}} \cos \frac{\psi_m}{2} & 2j\mathbf{C}_{\frac{1}{2}} \sin \frac{\psi_m}{2} \end{pmatrix} \begin{pmatrix} \mathbf{E} \\ \mathbf{O} \end{pmatrix};$$

hence

$$N[(\cos \psi_m)\mathbf{I} - \mathbf{C}_0](\mathbf{D}\mathbf{F})_{11}\mathbf{W}\mathbf{a}_m = \begin{bmatrix} j \sin(p + \frac{1}{2})\psi_m \\ \cos \end{bmatrix} 2j\mathbf{C}_{\frac{1}{2}} \sin \frac{\psi_m}{2} \mathbf{E}. \quad (84)$$

According to Eq. (62), however,

$$(DF)_{11} = \sec \theta_s \begin{pmatrix} \cos \frac{\phi_1}{2} & \cos \frac{\phi_1}{2} \\ \cos \frac{\phi_2}{2} & -\cos \frac{\phi_2}{2} \end{pmatrix};$$

therefore,

$$(DF)_{11}W = \sec \theta_s \begin{pmatrix} 2 \cos \frac{\phi_1}{2} & 0 \\ 0 & 2 \cos \frac{\phi_2}{2} \end{pmatrix}. \quad (85)$$

Substituting in Eq. (84) then,

$$\begin{aligned} N \sec \theta_s \begin{pmatrix} \cos \psi_m - \cos \phi_1 & 0 \\ 0 & \cos \psi_m - \cos \phi_2 \end{pmatrix} \begin{pmatrix} \cos \frac{\phi_1}{2} & 0 \\ 0 & \cos \frac{\phi_2}{2} \end{pmatrix} \begin{pmatrix} a_{m1} \\ a_{m2} \end{pmatrix} \\ = \frac{-\sin \left( p + \frac{1}{2} \right) \psi_m \sin \frac{\psi_m}{2}}{j \cos} \begin{pmatrix} \cos \frac{\phi_1}{2} & 0 \\ 0 & \cos \frac{\phi_2}{2} \end{pmatrix} \begin{pmatrix} 1 \\ 1 \end{pmatrix}, \quad (86) \end{aligned}$$

and finally,

$$a_{m1} = \frac{-\sin \left( p + \frac{1}{2} \right) \psi_m \sin \frac{\psi_m}{2} \cos \theta_s}{N(\cos \psi_m - \cos \phi_1)} \quad (87a)$$

and

$$a_{m2} = \frac{-\sin \left( p + \frac{1}{2} \right) \psi_m \sin \frac{\psi_m}{2} \cos \theta_s}{N(\cos \psi_m - \cos \phi_2)}. \quad (87b)$$

The relative loading of the modes when strap breaks are present can also be calculated. It will be sufficient here to outline the method of analysis and to quote the final results. Suppose again that the strap breaks are  $(2p + 1)$  sections apart and that between the output oscillator and one strap break there are  $q$  oscillators; between the output oscillator and the other break there are  $r$  sections in the opposite direction. The relation  $N = 2p + q + r + 4$  holds. The problem is most easily handled by using the  $T$  matrices rather than the  $\bar{T}$ . If the matrix for a loaded oscillator is written  $D^{-1}(T_0 + T_y)D$ , the condition of periodicity gives

$$D^{-1}T_0^q(T_0 + T_y)T_0^rT_BT_0^{2p+1}T_BD \begin{pmatrix} v_0 \\ i_0 \end{pmatrix} = \begin{pmatrix} v_0 \\ i_0 \end{pmatrix}. \quad (88a)$$



By rewriting this equation as

$$T_0^{p+\frac{1}{2}} D^{-1} T_B D T_0^q (T_0 + T_y) T_0^{-1} T_B D T_0^{(p+\frac{1}{2})} D \begin{pmatrix} v'_0 \\ i'_0 \end{pmatrix} = D \begin{pmatrix} v'_0 \\ i'_0 \end{pmatrix} \quad (88b)$$

and again as

$$T_0^{(p+\frac{1}{2})} D^{-1} T_B D T_0^{(N/2)-p-\frac{1}{2}} [1 + T_0^{(q-r-1)/2} T_y T_0^{(r-q-1)/2}] T_0^{(N/2)-p-\frac{1}{2}} D^{-1} T_B D T_0^{(p+\frac{1}{2})} D \begin{pmatrix} v'_0 \\ i'_0 \end{pmatrix} = D \begin{pmatrix} v'_0 \\ i'_0 \end{pmatrix} \quad (88c)$$

the problem assumes a more symmetrical form.

If it be assumed that the coupling does not link the antisymmetric modes and that the load admittance is shunted across the output resonator in the median plane, the form of  $T_y$  may be calculated. It is

$$T_y = \frac{\frac{1}{4} jY \sec^2 \frac{\theta_r}{2}}{1 - \frac{K_r Y}{2} \tan \frac{\theta_r}{2}} jK_s \sin 2\theta_s \begin{pmatrix} 1 & 0 & \tan \frac{\phi_1}{2} & 0 \\ 0 & 0 & 0 & 0 \\ \cot \frac{\phi_1}{2} & 0 & 1 & 0 \\ 0 & 0 & 0 & 0 \end{pmatrix}. \quad (89)$$

The problem is considerably simplified if the second and third rows and columns of all the matrices are both interchanged. This brings the  $T_0$  matrices to the form

$$T_0^* = \begin{pmatrix} \cos \phi_1 & \sin \phi_1 & 0 & 0 \\ -\sin \phi_1 & \cos \phi_1 & 0 & 0 \\ 0 & 0 & \cos \phi_2 & \sin \phi_2 \\ 0 & 0 & -\sin \phi_2 & \cos \phi_2 \end{pmatrix} = \begin{pmatrix} T_{01} & O \\ O & T_{02} \end{pmatrix}. \quad (90)$$

The load matrix  $T_y$  takes the form

$$T_y^* = -Y' K_s \sin 2\theta_s \begin{pmatrix} 1 & \tan \frac{\phi_1}{2} & 0 & 0 \\ \cot \frac{\phi_1}{2} & 1 & 0 & 0 \\ 0 & 0 & 0 & 0 \\ 0 & 0 & 0 & 0 \end{pmatrix} = \begin{pmatrix} L_1 & O \\ O & O \end{pmatrix}, \quad (91)$$

where

$$Y' = \frac{\frac{1}{4} Y \sec^2 \frac{\theta_r}{2}}{1 - \frac{K_r Y}{2} \tan \frac{\theta_r}{2}}.$$

The break matrix  $D^{-1} T_B D$  becomes

$$(\mathbf{D}^{-1}\mathbf{T}_s\mathbf{D})^* = \frac{X \operatorname{ctn} \theta_s}{2K_s} \begin{pmatrix} \tan \frac{\phi_1}{2} & 0 & \tan \frac{\phi_2}{2} & 0 \\ 0 & 0 & 0 & 0 \\ \tan \frac{\phi_1}{2} & 0 & -\tan \frac{\phi_2}{2} & 0 \\ 0 & 0 & 0 & 0 \end{pmatrix}. \quad (92)$$

The form of the load matrix shows that it does not couple the  $m_2$  set of modes; the strap-break matrix, on the other hand, has off-diagonal terms leading to a mixing of the  $m_1$ - and  $m_2$ -modes.

The final result for the perturbation of the modes when  $X \rightarrow \infty$  is contained in the equation

$$x_1 x_2 + \frac{2jYK_s \sin \theta_s}{\sin \phi_1} \left[ x_1 y_2 \cos^2 \left( \frac{r-q}{2} \right) \phi_1 - x_2 y_1 \sin^2 \left( \frac{r-q}{2} \right) \phi_1 \right] = 0, \quad (93)$$

where

$$\begin{aligned} x_1 &= \sin \frac{N\phi_1}{2} \cos \left( p + \frac{1}{2} \right) \phi_2 \cos \left( \frac{N}{2} - p - \frac{1}{2} \right) \phi_2 \tan \frac{\phi_2}{2} \\ &\quad + \sin \frac{N\phi_2}{2} \cos \left( p + \frac{1}{2} \right) \phi_1 \cos \left( \frac{N}{2} - p - \frac{1}{2} \right) \phi_1 \tan \frac{\phi_1}{2}, \\ x_2 &= -\sin \frac{N\phi_1}{2} \sin \left( p + \frac{1}{2} \right) \phi_2 \sin \left( \frac{N}{2} - p - \frac{1}{2} \right) \phi_2 \tan \frac{\phi_2}{2} \\ &\quad + \sin \frac{N\phi_2}{2} \sin \left( p + \frac{1}{2} \right) \phi_1 \sin \left( \frac{N}{2} - p - \frac{1}{2} \right) \phi_1 \tan \frac{\phi_1}{2}, \\ y_1 &= \cos \frac{N\phi_1}{2} \cos \left( p + \frac{1}{2} \right) \phi_2 \cos \left( \frac{N}{2} - p - \frac{1}{2} \right) \phi_2 \tan \frac{\phi_2}{2} \\ &\quad + \cos \frac{N\phi_2}{2} \cos \left( p + \frac{1}{2} \right) \phi_1 \cos \left( \frac{N}{2} - p - \frac{1}{2} \right) \phi_1 \tan \frac{\phi_1}{2}, \end{aligned}$$

and

$$\begin{aligned} y_2 &= \cos \frac{N\phi_1}{2} \sin \left( p + \frac{1}{2} \right) \phi_2 \sin \left( \frac{N}{2} - p - \frac{1}{2} \right) \phi_2 \tan \frac{\phi_2}{2} \\ &\quad + \cos \frac{N\phi_2}{2} \sin \left( p + \frac{1}{2} \right) \phi_1 \sin \left( \frac{N}{2} - p - \frac{1}{2} \right) \phi_1 \tan \frac{\phi_1}{2}. \end{aligned}$$

It may be noted that this is the equation which would determine the mode spectrum in a single-cavity, tunable tube with strap breaks.

The loading can now be found by forming  $\partial Y / \partial \omega$  from Eq. (93) and putting  $Y = 0$ . The result is

$$\frac{\partial Y}{\partial \omega} = \frac{1}{jK_s \sin \theta_s} \left[ \frac{\sin \phi_1 \cos \left( \frac{N}{2} - p - \frac{1}{2} \right) \phi_1}{\sin \frac{r-q}{2} \phi_1} \right]^2$$

$$\frac{\partial}{\partial \omega} \left\{ \text{ctn } \phi_1 \left[ \tan \left( p + \frac{1}{2} \right) \phi_1 + \tan \left( \frac{N}{2} - p - \frac{1}{2} \right) \phi_1 \right] \right.$$

$$\left. + \text{ctn } \phi_2 \left[ \tan \left( p + \frac{1}{2} \right) \phi_2 + \tan \left( \frac{N}{2} - p - \frac{1}{2} \right) \phi_2 \right] \right\} \quad (94a)$$

or

$$\frac{\partial Y}{\partial \omega} = \frac{1}{jK_s \sin \theta_s} \left[ \frac{\sin \phi_1 \sin \left( \frac{N}{2} - p - \frac{1}{2} \right) \phi_1}{\cos \frac{r-q}{2} \phi_1} \right]^2$$

$$\frac{\partial}{\partial \omega} \left\{ \text{ctn } \phi_1 \left[ \text{ctn} \left( p + \frac{1}{2} \right) \phi_1 + \text{ctn} \left( \frac{N}{2} - p - \frac{1}{2} \right) \phi_1 \right] \right.$$

$$\left. + \text{ctn } \phi_2 \left[ \text{ctn} \left( p + \frac{1}{2} \right) \phi_2 + \text{ctn} \left( \frac{N}{2} - p - \frac{1}{2} \right) \phi_2 \right] \right\}. \quad (94b)$$

The variation in the loading of the two sets of modes as the output position is changed is described by the terms  $1/[\sin^2(r-q/2)\phi_1]$  and  $1/[\cos^2(r-q/2)\phi_1]$  and is readily calculated, since  $\phi_1$  is known. It will be noted that the loading for each mode is the sum of terms pertaining to the symmetric and to the antisymmetric components.

**4.8. Effects Caused by Various Types of Tuning.**—The properties of tunable tubes discussed in this section are those directly connected with the resonant system. The general principles and methods of mechanical and electronic tuning are given in Chaps. 14 and 15.

*Single-cavity Tuner.*—In single-cavity tuning a variable reactive element is connected into a single resonator section, thereby changing the frequency of the whole system. The reactance is generally introduced in such a manner that the antisymmetric modes are not coupled, and they are, therefore, untuned. Similarly, the tuning element will not affect those components of the doublet modes ( $m \neq 0$ ) which do not couple with the perturbed cavity. The addition of strap breaks, however, will cause all modes to be coupled to some extent. For simplicity, this discussion will be limited to the case without strap breaks. The equations determining the new frequencies have been given in Sec. 4-6. They are

$$\cos \phi = \cos 2\theta_s - \frac{K_s Y_{\text{res}}}{2} \sin 2\theta_s, \quad (43)$$

$$Z \sin \phi = K_s \sin 2\theta_s, \quad (44)$$

and

$$\tan \frac{N\phi}{2} + \frac{1}{2} ZY_{\text{tuner}} = 0. \quad (47b)$$

Combining the last two equations gives

$$-Y_{\text{tuner}} = \frac{2 \sin \phi \tan \frac{N\phi}{2}}{K_s \sin 2\theta_s} = F(\lambda). \quad (95)$$

The tuner reactance transformed to the end of the resonator slots is represented, as before, by  $Y_{\text{tuner}}$ .  $\cos \phi$  is already known as a function of  $\lambda$ , so that the right-hand side of Eq. (95) may be plotted as a

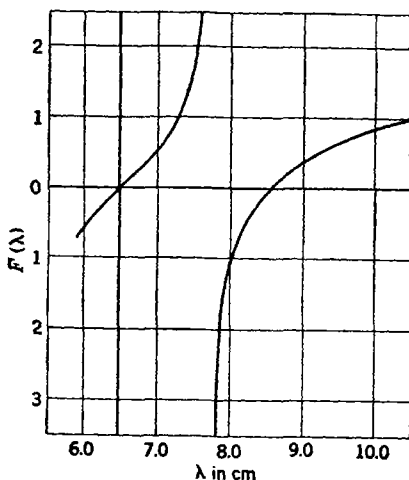


FIG. 4-17.—Single-cavity tuning curves [see Eq. (95)].

function of  $\lambda$ . Figure 4-17 shows the form of this function in a particular case. Because  $\sin 2\phi_s$  and  $\cos \phi$  are well-behaved functions of  $\lambda$  in the range considered, the function always consists of a series of branches running between the poles of  $\tan N\phi/2$  or  $\phi = [2\pi(m + \frac{1}{2})]/N$ . The dependence of  $Y_{\text{tuner}}$  upon  $\lambda$  cannot be specified, of course, until the form of the tuning reactance is known. In general,  $-Y_{\text{tuner}}$  will be an increasing function of  $\lambda$  with no poles in the tuning range. The intersections of  $-Y_{\text{tuner}}$  and  $F(\lambda)$  now give the new frequencies. As the curve for  $-Y_{\text{tuner}}$  moves up and down because of the variation in the tuning reactance, it can be seen that all the modes that are coupled change wavelength in the same sense. No matter how much susceptance is coupled in, the  $m$ th mode, originally at  $\phi = 2m\pi/N$ , cannot move beyond  $[(2m \pm 1)\pi]/N$ . There is, therefore, no crossing of the modes. The main

difficulties in the single-cavity tuning schemes arise from the pattern distortion in the  $\pi$ -mode. Equation (55) showed that the pattern distortion in a tube with a given number of oscillators is a function of  $\phi$  only. Distortion, then, is minimized by making the change in  $\phi$  over the tuning range as small as possible; this, it may be recalled, is the condition for large mode separation.

The loading of a single-cavity tunable tube can be treated as before by considering the insertion of a shunt element  $jY_{\text{load}}$  into the output oscillator. If the number of oscillators between the tuner and the output is  $(p - 1)$ , the periodicity condition is

$$\begin{pmatrix} 1 & 0 \\ jY_{\text{load}} & 1 \end{pmatrix} \bar{T}^{N-p} \begin{pmatrix} 1 & 0 \\ jY_T & 1 \end{pmatrix} \bar{T}^p \begin{pmatrix} v_0 \\ i_0 \end{pmatrix} = \begin{pmatrix} v_0 \\ i_0 \end{pmatrix}. \quad (96)$$

This is found to lead to

$$-Y_{\text{load}} = \frac{2 \sin N\phi \left( \frac{1}{Z} \tan \frac{N\phi}{2} + \frac{1}{2} Y_T \right)}{\sin N\phi - ZY_T \sin p\phi \sin q\phi}. \quad (97)$$

Thus, the characteristic admittance,  $Y_c = -\frac{1}{2}\lambda(\partial Y_{\text{load}}/\partial \lambda)$ ,

$$\begin{aligned} 2Y_c &= \frac{\cos^2 \frac{N\phi}{2}}{2 \cos^2 \left( \frac{N}{2} - p \right) \phi} \lambda \frac{\partial}{\partial \lambda} \left( \frac{\tan \frac{N\phi}{2}}{Z} + \frac{Y_T}{2} \right)_{Y_{\text{load}}=0} \\ &= \frac{\cos^2 \frac{N\phi}{2}}{2 \cos^2 \left( \frac{N}{2} - p \right) \phi} \lambda \frac{\partial}{\partial \lambda} \left[ \frac{\tan \frac{N\phi}{2}}{\tan \frac{\phi}{2}} \left( \frac{Y_{\text{res}}}{2} + \frac{\tan \phi_s}{K_s} \right) + \frac{Y_T}{2} \right]_{Y_{\text{load}}=0}. \end{aligned} \quad (98)$$

The value of  $Y_c$  thus varies with the relative position of the tuner and output as  $\sec^2 [(N/2) - p]\phi$ . The variation over the tuning range does not lend itself to expression in a simpler form. It should be noted that if the  $Y_c$  defined here were used to calculate  $Q$  values, the resistive loads would also have to be transformed to the top of the resonator slots.

To avoid the pattern distortion arising from tuning a single cavity, a number of schemes have been devised that act more or less symmetrically on all the cavities.

**Multicavity Strap Tuner.**—In this form of tuning a grooved ring, mounted at one end of the tube and having its axis coinciding with that of the tube, is moved up and down with respect to the strap system. The grooves are arranged so that the tuner can appreciably penetrate the strap system without directly contacting it (see Fig. 4-18). The other end of the tube is strapped conventionally. For the following mathematical treatment, it is supposed that there are no strap breaks,

although, in practice, they would be used. The model used differs from that of the ordinary double-strapped tube only in that the strap impedances are taken to be different and written  $K_{s1}$  and  $K_{s2}$ , where one impedance is fixed and the other variable. The effective strap lengths

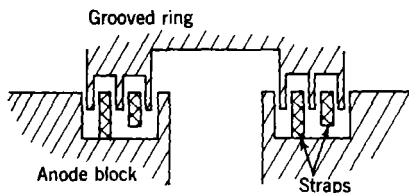


FIG. 4-18.—Cross section of strap tuner.

are assumed equal. The strap or coupling matrix is then

$$\begin{pmatrix} \cos \phi_s & 0 & jK_{s1} \sin \phi_s & 0 \\ 0 & \cos \phi_s & 0 & jK_{s2} \sin \phi_s \\ jM_{s1} \sin \phi_s & 0 & \cos \phi_s & 0 \\ 0 & jM_{s2} \sin \phi_s & 0 & \cos \phi_s \end{pmatrix}. \quad (99)$$

The (u-v)-matrix is now found to be

$$\begin{pmatrix} \cos 2\phi_s + \frac{K_{s1}M_r}{2} \cot \theta_r \sin 2\phi_s & -\frac{K_{s1}}{2} M_r \csc \theta_r \sin 2\phi_s \\ \frac{K_{s2}}{2} M_r \csc \theta_r \sin 2\phi_s & \cos 2\phi_s + \frac{K_{s2}M_r}{2} \cot \theta_r \sin 2\phi_s \end{pmatrix}, \quad (100)$$

and the secular equation

$$\left( \cos 2\phi_s + \frac{K_{s1}M_r}{2} \cot \theta_r \sin 2\phi_s - \cos \phi_m \right) \left( \cos 2\phi_s + \frac{K_{s2}M_r}{2} \cot \theta_r \sin 2\phi_s - \cos \phi_m \right) = K_{s1}K_{s2} \left( \frac{M_r}{2} \csc \theta_r \sin 2\phi_s \right)^2. \quad (101)$$

If  $K_{s1}/2Z_{r0} = k_1$  and  $K_{s2}/2Z_{r0} = k_2$  (using the same symbols as before),

$$\cos \phi_s = \cos \frac{2\pi s}{\lambda} - \sqrt{\frac{\lambda^2}{\lambda_{r0}^2} - 1} \sin \frac{2\pi s}{\lambda} \left[ \frac{k_1 + k_2}{2} \coth \frac{2\pi h}{\lambda} \sqrt{\frac{\lambda^2}{\lambda_{r0}^2} - 1} \right. \\ \left. \pm \sqrt{\left( \frac{k_1 + k_2}{2} \right)^2 \operatorname{csch}^2 \frac{2\pi h}{\lambda} + \sqrt{\frac{\lambda^2}{\lambda_{r0}^2} - 1} + \left( \frac{k_1 - k_2}{2} \right)^2} \right]. \quad (102)$$

There are, as before, two sets of modes corresponding to the ambivalent sign; when  $k_1 = k_2$ , they reduce to the earlier  $m_1$  and  $m_2$  sets of modes. If the tube is short or the strapping light, if, in fact,

$$\left( \frac{k_1 + k_2}{k_1 - k_2} \right)^2 \gg \sinh^2 \frac{2\pi h}{\lambda} \sqrt{\frac{\lambda^2}{\lambda_{r0}^2} - 1}, \quad (103)$$

the second term under the radical is negligible. The tube then behaves as a symmetrical tube with  $k = k_1 + k_2$ . The behavior of the modes will then be as indicated in Fig. 4-9. At the opposite extreme, with a very heavily strapped or very long tube,

$$\operatorname{ctnh} \frac{2\pi h}{\lambda} \sqrt{\frac{\lambda^2}{\lambda_{r_0}^2} - 1} \approx 1$$

and

$$\operatorname{csch} \left( \frac{2\pi h}{\lambda} \sqrt{\frac{\lambda^2}{\lambda_{r_0}^2} - 1} \right) \approx 0.$$

The term in brackets of Eq. (102) then becomes  $k_1$  or  $k_2$ ; the two ends of the tube are effectively out of touch with each other, and the spectrum consists of the untuned modes associated with one end and the tuned modes of the other end.

*Multicavity Segment Tuner.*—

It is also possible to tune by strapping the tube at only one end and then moving a flat ring up and down above the unstrapped ends of the segments. This arrangement, shown in Fig. 4-19a, introduces a new form of coupling. As represented in Fig. 4-19b, it may be seen that the ring coupling is effected by the capacitances of the segments to the ring and that the finite length of the ring section introduces some series inductance.

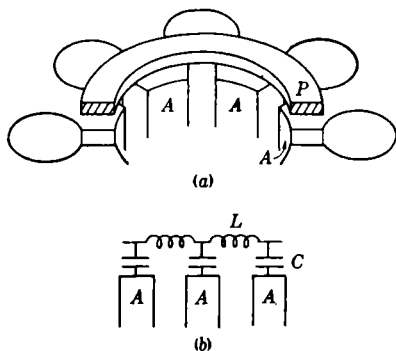


FIG. 4-19.—(a) Schematic view of segment tuner showing the tuning plate  $P$  over the anode block  $A$ ; (b) equivalent circuit of segment tuner.

It is assumed that the ring and the segments form a transmission line of impedance  $K_t$ . For simplicity the length of one section is assumed to be equal to the strap length. This is not unreasonable, because the ring and the strap system are usually the same size. The arrangement of the sections then assumes the form shown in Fig. 4-20 in which the resonator is in series with the coupling network at the unstrapped, tuned end and is in shunt with the straps at the strapped end. The matrix for the resonator section now has a new form. If the 4-terminal network representing the resonator has the matrix

$$\begin{pmatrix} a' & b' \\ c' & a' \end{pmatrix},$$

solution of the network equations gives

$$\begin{pmatrix} 1 & 0 & 0 & 0 \\ \frac{1}{\bar{a}'} & -1 & 0 & -\frac{b'}{\bar{a}'} \\ \frac{c'}{\bar{a}'} & 0 & 1 & \frac{1}{\bar{a}'} \\ 0 & 0 & 0 & -1 \end{pmatrix} \quad (104)$$

for the matrix of the center section. In this case

$$\mathbf{T}_{res} = \begin{pmatrix} 1 & 0 & 0 & 0 \\ \sec \theta_r & -1 & 0 & -jK_r \tan \theta_r \\ jM_r \tan \theta_r & 0 & 1 & \sec \theta_r \\ 0 & 0 & 0 & -1 \end{pmatrix}. \quad (105)$$

The coupling matrix is exactly like that for the strap-tunable tube with

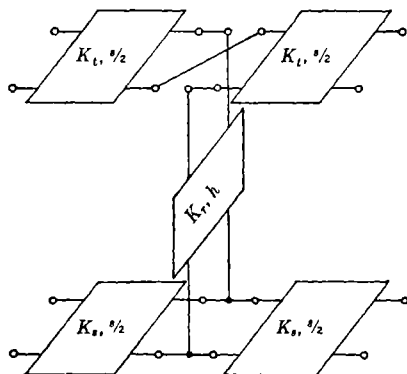


FIG. 4-20.—A 4-terminal network representation of one section of a segment-tuned magnetron.

impedances  $K_s$  and  $K_t$ . The (u-v)-matrix for the whole section is now

$$\begin{pmatrix} \cos 2\phi_s - \frac{1}{2}K_s M_r \sin 2\phi_s \tan \theta_r & -K_s M_t \sin^2 \phi_s \sec \theta_r \\ \cos^2 \phi_s \sec \theta_r & -\cos 2\phi_s + \frac{1}{2}K_r M_t \sin 2\phi_s \tan \theta_r \end{pmatrix}. \quad (106)$$

The determinantal equation [Eq. (15)] gives

$$(\cos \psi_m - \cos 2\phi_s + \frac{1}{2}K_s M_r \sin 2\phi_s \tan \theta_r)(\cos \psi_m + \cos 2\phi_s - \frac{1}{2}M_t K_r \sin 2\phi_s \tan \theta_r) + \frac{K_s M_t}{4} \sin^2 2\phi_s \sec^2 \theta_r = 0. \quad (107a)$$

Using the notation  $k_s = K_s/2Z_{r0}$  and  $k_t = K_t/2Z_{r0}$  and substituting the usual values for  $M_r$ ,  $\theta_r$ , and  $\phi_s$ , Eq. (107a) may be put in the form



$$\frac{1}{4k_t} = \left( \sqrt{\frac{\lambda^2}{\lambda_{r0}^2} - 1} \tanh \frac{2\pi h}{\lambda} \sqrt{\frac{\lambda^2}{\lambda_{r0}^2} - 1} \frac{\cos \psi_m + \cos \frac{2\pi s}{\lambda}}{\sin \frac{2\pi s}{\lambda}} \right) \left[ k_s + \frac{\operatorname{ctnh} \frac{2\pi h}{\lambda} \sqrt{\frac{\lambda^2}{\lambda_{r0}^2} - 1} \cos \psi_m - \cos \frac{2\pi s}{\lambda}}{\sqrt{\lambda^2/\lambda_{r0}^2} - 1} \frac{\sin \frac{2\pi s}{\lambda}}{\sin \frac{2\pi s}{\lambda}} \right] \cdot \quad (107b)$$

$$\left[ k_s + \frac{\tanh \frac{2\pi h}{\lambda} \sqrt{\frac{\lambda^2}{\lambda_{r0}^2} - 1} \cos \psi_m - \cos \frac{2\pi s}{\lambda}}{\sqrt{\frac{\lambda^2}{\lambda_{r0}^2} - 1}} \frac{\sin \frac{2\pi s}{\lambda}}{\sin \frac{2\pi s}{\lambda}} \right]$$

The behavior of this expression may be clarified in the following way: consider the case  $k_s = \infty$  when the tube is unstrapped. Then the term in brackets is unity; and for tubes that are not excessively long and that have short straps,

$$\frac{1}{4k_t} = \frac{h}{s} \left( \frac{\lambda^2}{\lambda_{r0}^2} - 1 \right) \left( \cos \psi_m + \cos \frac{2\pi s}{\lambda} \right). \quad (108)$$

The curves of  $1/4k_t$  against  $\lambda^2$  are thus very nearly straight lines through  $(\lambda_{r0}^2, 0)$ , and their slopes vary as  $\cos \phi_m + \cos 2\pi s/\lambda_{r0}$ . Furthermore, for  $\lambda$  very large the bracketed term tends to a constant value, and the values of  $1/4k_t$  become asymptotic to

$$\frac{h}{s} \left( \frac{\lambda^2}{\lambda_{r0}^2} - 1 \right) (\cos \psi_m + 1).$$

The wavelength  $\lambda_m$  of the modes varies, then, as  $1/\cos(\psi_m/2)$ . The  $\pi$ -mode has the smallest wavelength, and the wavelengths ascend in order of  $m$ . Thus, in the segment-tuned system the ring coupling is dominant and the mode order is that of an unstrapped system (see Chap. 2). This result is not surprising, because the end-space and interaction-space coupling in the unstrapped system are weak forms of the same type of coupling that is provided by the ring. Returning to Eq. (107b), the denominator of the bracketed term does not vary much for values of  $\lambda$  between  $\lambda_{r0}$  and  $2\lambda_{r0}$ , say, and the expression

$$\frac{\cos \psi_m + \cos \frac{2\pi s}{\lambda}}{\sin \frac{2\pi s}{\lambda}}$$

is usually not zero in that region. Thus, the behavior of  $1/4k_t$  for  $k_t$

very large is determined by the remaining factors or

$$-\frac{1}{\sin \frac{2\pi s}{\lambda}} \left( \cos \psi_m - \cos \frac{2\pi s}{\lambda} + k_s \sqrt{\frac{\lambda^2}{\lambda_{r_0}^2} - 1} \tanh \frac{2\pi h}{\lambda} \sqrt{\frac{\lambda^2}{\lambda_{r_0}^2} - 1} \sin \frac{2\pi s}{\lambda} \right). \quad (109)$$

The term in parentheses in Eq. (109) is of the form of the function  $\cos \psi_m - \cos \phi$  for a strapped tube of length  $2h$ , the resonances being determined by the points for which the function equals zero. Thus for

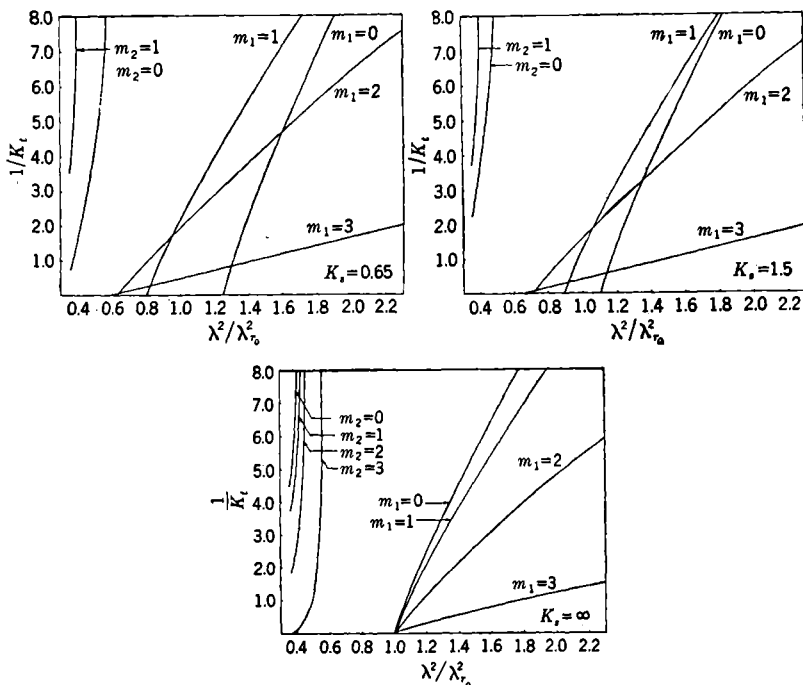


FIG. 4-21.—Values of  $1/k_t$  plotted against  $\lambda^2/\lambda_{r_0}^2$  for the cases  $k_s = \infty, 1.5$ , and  $0.65$ .

$k_t = \infty$ , the order of the modes is that of a strapped tube. In this type of tuner then, as  $k_t$  is made sufficiently small, the modes will cross over completely and shift from the strapped order to the unstrapped order.

A Bell Telephone Laboratories 30-cm magnetron uses this form of tuning. For this tube the values of  $2\pi s/\lambda_{r_0}$  and  $2\pi h/\lambda_{r_0}$  are 0.473 and 1.71. Figure 4-21 shows  $1/k_t$  plotted against  $\lambda^2/\lambda_{r_0}^2$  for the cases  $k_s = \infty, 1.5$ , and  $0.65$ . The inversion of mode order and consequent crossing is plainly in evidence. It is possible to compare the above analysis directly

with experiment, using the physical strap length for  $s$ , the wavelength of the  $\pi$ -mode with the tuner retracted, and the slope of one of the unstrapped tuning curves in order to calculate the tube constants. Figure 4-22a and b shows the observed and calculated tuning curves for the unstrapped tube and for the normal tube. The agreement is good except for the ( $m = 3$ )-mode, which lies at the border of the theory. Experimentally, ( $m = 1$ )-, ( $m = 2$ )-, and ( $m = 3$ )-doublets are resolved by various asymmetries such as the cathode leads and the notches cut in

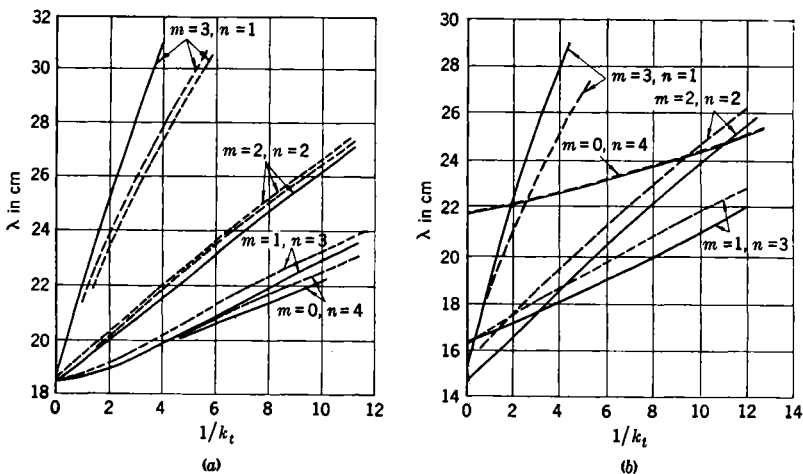


FIG. 4-22.—Calculated and observed tuning curves for an unstrapped, experimental 30-cm magnetron. The solid lines indicate calculated values; the broken lines, observed values. (a) The slope of the ( $m = 0$ )-curve is fitted to the experimental value at  $1/k_t = 0$ ; (b) ( $m = 0$ )-curve is fitted at  $1/k_t = 0$ . (Courtesy of W. B. Hebenstreit, Bell Telephone Laboratories.)

the tuner to clear them. These details were not included in the theoretical analysis given here.

**Multicavity Inductance Tuner.**—A third symmetrical tuning scheme is the “inductance” tuner which was developed by Columbia Radiation Laboratory for use in 3-cm tubes, because the use of strap and segment tuners was almost prohibited by difficulties with high voltages and small clearances. In the inductance tuner a series of pins is mounted at right angles to a movable plate, the up-and-down motion of which causes each of the pins to penetrate (without contact) into the holes of a hole-and-slot resonant system. The 2J51 tube to which this method has been applied is a double-ring strapped tube, and the representative network of Fig. 4-23 may be used to analyze its behavior. The effect of the pins has been represented by a division of the original unstrapped resonator into two lengths of line  $l$  and  $h - l$  having impedances  $K_l$  and  $K_r$ . The

electrical lengths will be called  $\theta_1$  and  $\theta_2$ . The matrix of the resonator section is now

$$\begin{pmatrix} \cos \theta_1 & jK_t \sin \theta_1 \\ jM_t \sin \theta_1 & \cos \theta_1 \end{pmatrix} \begin{pmatrix} \cos \theta_2 & jK_r \sin \theta_2 \\ jM_r \sin \theta_2 & \cos \theta_2 \end{pmatrix} \quad (110a)$$

or

$$\begin{pmatrix} \cos \theta_1 \cos \theta_2 - K_t M_r \sin \theta_1 \sin \theta_2 & jK_r \cos \theta_1 \sin \theta_2 + jK_t \sin \theta_1 \cos \theta_2 \\ jM_t \sin \theta_1 \cos \theta_2 + jM_r \cos \theta_1 \sin \theta_2 & \cos \theta_1 \cos \theta_2 - K_r M_t \sin \theta_1 \sin \theta_2 \end{pmatrix} = \begin{pmatrix} a & b \\ c & d \end{pmatrix}. \quad (110b)$$

Proceeding as before to evaluate the (u-v)-matrix for the section, this

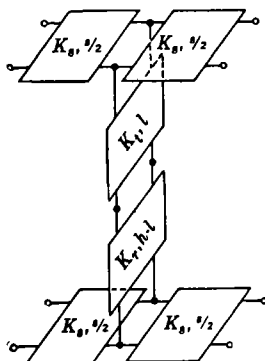


FIG. 4-23.—A 4-terminal network representation of one section of an inductance tuner.

matrix is now found to be

$$\begin{pmatrix} \cos 2\phi_s + \frac{1}{2} \frac{d}{b} K_s \sin 2\phi_s & -\frac{1}{2} \frac{K_s}{b} \sin 2\phi_s \\ -\frac{1}{2} \frac{K_s}{b} \sin 2\phi_s & \cos 2\phi_s + \frac{1}{2} \frac{a}{b} K_s \sin 2\phi_s \end{pmatrix}. \quad (111)$$

Writing the determinantal equation and rearranging it gives

$$\cos \psi_m = \cos 2\phi_s - \frac{jK_s}{2} \sin 2\phi_s \left[ \frac{a + d \pm \sqrt{(a-d)^2 + 1}}{2b} \right].$$

The mode spectrum when the tuner is retracted is that of a strapped tube with resonator impedance  $K_r$ ; when the tuner is inserted to the full length of the anode the spectrum is that of a strapped tube with resonator impedance  $K_t$ . The mode order will be the same at both extremities and there will thus be no mode crossing. The spectrum is transformed continuously as the tuner moves through the anode.

## CHAPTER 5

### OUTPUT CIRCUITS

BY L. R. WALKER

**5.1. Introduction.**—The preceding chapters have treated the resonant system of the magnetron in detail. It has been made clear that the electron stream interacts with the field of the resonant system and feeds power into it. This power is then utilized in two ways. One part, which is dissipated in the form of copper losses, serves to maintain high fields in the resonant system. As a consequence the resonant system stores considerable energy and acts as the main frequency-determining element in the magnetron. The residual power is fed to an external load, and the circuit coupling this power to the external load is referred to as the output circuit. Such a circuit may be considered as a 4-terminal transducer which transforms the load impedance to a new level within the tube. Broadly, the study of this transducer and its relationship to the resonant system forms the subject of this chapter.

It is clear that in microwave systems, in which the dimensions of the elements are comparable to a wavelength, the physical separation of the resonant system and the output circuit must be arbitrary. There is a similar difficulty in distinguishing between them on the basis of electrical function. In an ideal situation the output circuit would store an amount of energy negligible in comparison with that in the resonant system, and it would then be perfectly justifiable to consider the output circuit as frequency-insensitive in the neighborhood of any resonant frequency of the system. Magnetrons that have been developed thus far fall into two classes: (1) those with unstabilized outputs, in which the conditions of the ideal case are approximately met, and (2) those with stabilized outputs, in which the output circuit is deliberately designed to store energy and may, indeed, store more energy than the resonant system. The stabilized output is discussed extensively in Chap. 16 and will not be treated here. In unstabilized outputs, the degree of departure from ideal frequency-insensitivity varies greatly between various types of output circuits, but, in general, the output circuit stores less than about 25 per cent of the energy stored in the resonant system. It will thus be satisfactory to consider the properties of ideal frequency-insensitive output circuits as a guide to the behavior of real output circuits. Any specific case may then be examined for departure from ideal behavior.

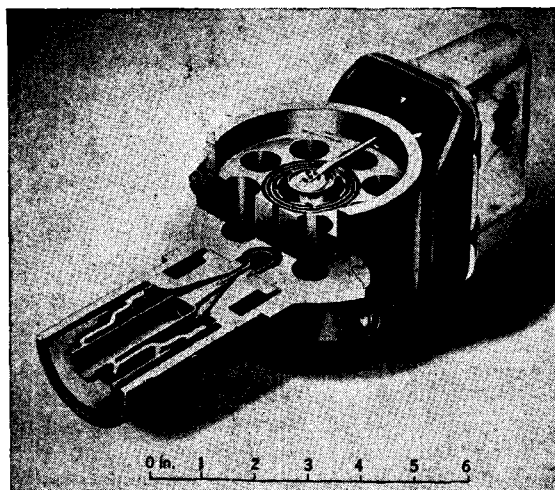


FIG. 5-1.—Center-loop coupling.



FIG. 5-2.—Halo-loop coupling.

In practice a number of considerations impose restrictions upon the output circuit. The wavelength and power level of the tube determine whether the external line will be waveguide or coaxial line. Constructional details of the anode block, such as its strapping and the geometry

of the resonators, influence the form of coupling used between the resonant system and the output line. It is also clear that the output

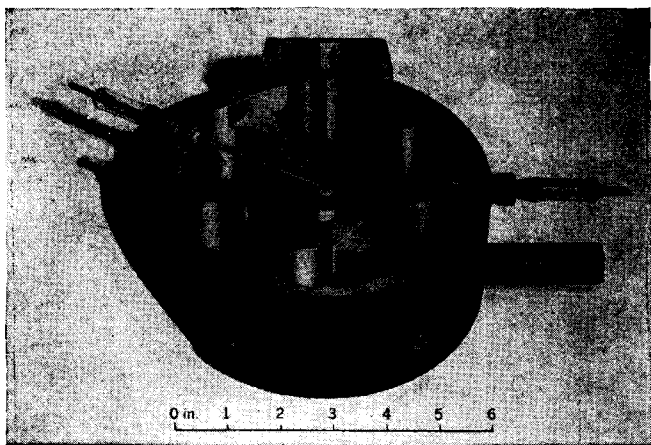


FIG. 5-3.—Segment-fed coupling.

circuit must contain a vacuum seal and that, because some of the output will be air-filled, it must be designed to avoid high-voltage breakdown.

Structurally, the main classification of output circuits is that into coaxial and waveguide types. The coaxial-output circuit consists of a length of coaxial line that varies in cross section, either through tapers or at discontinuities, and in which the central conductor is fed from the tube in a variety of ways. For example, in loop-coupling, the end of the central conductor is bent into a loop and attached to some point on the outer conductor. The loop is then placed where it will intercept the magnetic flux in one oscillator. Such loops have been introduced into the resonator in the median plane (center loop) as in Fig. 5-1 or have been placed immediately above the end of one resonator (halo loop) as in Fig. 5-2. In unstrapped tubes the center conductor has been run in above a segment and then attached to a point on one of the end faces of this

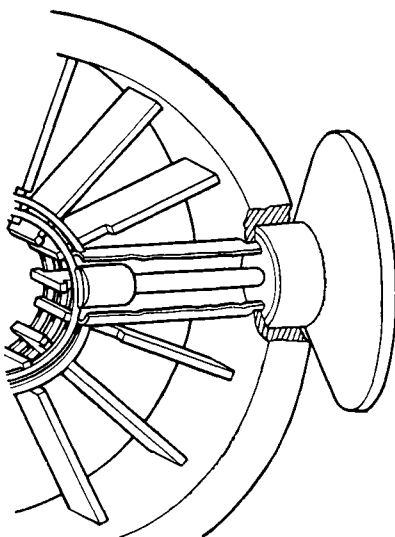


FIG. 5-4.—Strap-fed coupling.

segment (segment-fed coupling); in this case, the center conductor may be considered to intercept flux passing between neighboring oscillators or to be fed by the voltage along the segment (see Fig. 5-3). In a somewhat similar type of feed applicable to strapped tubes, the whole coaxial line runs above a segment, and the inner conductor then attaches directly to a floating strap section (strap-fed coupling) as in Fig. 5-4.

At the load side, the coaxial line output may feed either an external coaxial line or a waveguide. If the external line is coaxial, the connection may be directly mechanical or by means of choke joints. In the latter,

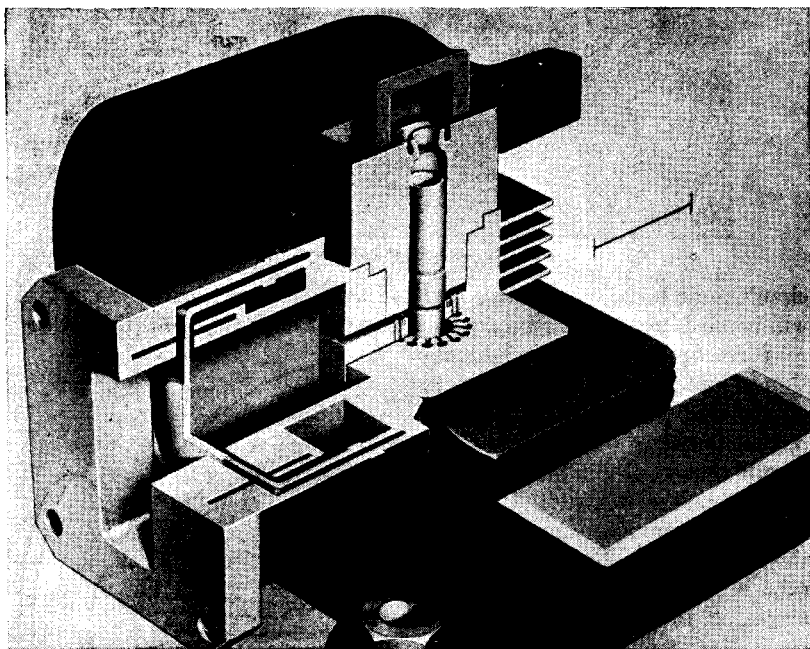


FIG. 5-5.—Waveguide output.

the output circuit must include a satisfactory junction from coaxial line to waveguide line. The vacuum seal is generally incorporated in the coaxial line or in the waveguide feed, and the glass serves as a support for the inner conductor.

Waveguide outputs consist of waveguide lines of variable cross section, which are fed either by opening directly into the back of one resonator or by communicating with it by means of an iris. The cross section of the output is generally modified until it is equal to that of the external waveguide, and the vacuum seal then consists of an iris window placed between choke joints in this guide (see Fig. 5-5).



In this chapter the discussion is confined mainly to an exposition of the role played by the output circuit in tube operation and of the concepts in terms of which its behavior is analyzed. The problems arising in the design of output circuits for specific purposes are treated extensively in Chap. 11. In general, the interesting properties of an output circuit cannot be accurately predicted by direct calculation, but some types of waveguide outputs, because of their geometrical simplicity, form an exception to this rule, and an outline of the methods available is given for this case. Many of the topics discussed are particular applications of more general material developed in other books, but the treatment in this chapter is adapted to the special needs of the magnetron problem.

**5-2. The 4-terminal Transducer.**—In Chap. 4, it is shown (explicitly for strapped magnetrons, but the argument is easily extended to cover other cases) that provided the tube is oscillating in the  $\pi$ -mode, the admittance of the resonator system measured at the junction of the resonator and the interaction space is the sum of the admittances of the  $N$  individual resonators. The latter admittances are also measured at the slot openings, and the planes bisecting each segment are assumed to be open-circuited. In this case, the resonator system, as far as its total admittance at any resonator opening is concerned, may evidently be replaced by  $N$  circuits in parallel, each having the characteristics of an individual, isolated resonator. Because such a representation is valid in the vicinity of the  $\pi$ -mode only, the individual resonators must be treated as single shunt-resonant circuits described completely by a characteristic admittance  $Y_r$  and a resonant frequency  $\omega_0$ . The admittance of a single resonator is then  $jY_r(\omega/\omega_0 - \omega_0/\omega)$ . For the  $\pi$ -mode, provided that the loading is not heavy enough to cause pattern distortion and a resultant variation among the slot voltages, the electronic loading will be the same at each resonator. The total electronic admittance will thus be  $N$  times that of an individual resonator. If the mode is other than a  $\pi$ -mode, an equivalent circuit admittance for the tube at any slot opening may still be defined, but it is no longer the sum of the individual values (see Chap. 4), and the variation among the slot voltages makes difficult the definition of an equivalent electronic admittance (see Chap. 7). For simplicity, it will be assumed in the following sections that a  $\pi$ -mode is being considered; the modifications necessary for other modes will be the replacement of  $NY_r$  by the appropriate equivalent characteristic admittance of the resonator system.

For the purposes of output-circuit analysis it will be convenient to make use of this representation of the resonator system and, simultaneously, to transform the load admittance to the opening of the resonator into which it is coupled. The admittance of the coupled oscillator

and its load are calculated, and then the load admittance is found by subtracting the admittance of an unperturbed oscillator. Thus the output circuit considered as a transmission path extends from the opening of the coupled resonator to some plane in the external line which is drawn to include all the discontinuities of the output circuit; the stored energy of the output circuit, however, does not include that of the coupled resonator. As an example, if a waveguide output couples directly into the back of a resonator, the load impedance  $Z$  at the junction is effectively in series with  $j\omega L$ , the inductance of the resonator, and appears at the slot as an admittance  $1/(j\omega L + Z)$ . By restoring to the resonant system the unperturbed admittance  $1/j\omega L$ , the load admittance becomes  $-Z/j\omega L(j\omega L + Z)$ ; this clearly involves the properties of the resonator.

It is now necessary to develop some properties of 4-terminal transducers that will be useful in analyzing output systems. One representation of a transducer is particularly helpful with the model being used. For any 4-terminal network

$$\text{and} \quad \left. \begin{aligned} V_2 &= Z_{22}I_2 + Z_{21}I_1 \\ V_1 &= Z_{21}I_2 + Z_{11}I_1 \end{aligned} \right\} \quad (1)$$

where  $V_2$ ,  $I_2$  and  $V_1$ ,  $I_1$  are the voltages and currents on the right- and left-hand<sup>1</sup> sides of the transducer respectively. Thus, if one writes

$$V_2 = \overleftarrow{Z}_2 I_2 \quad \text{and} \quad I_1 = \overrightarrow{Y}_1 V_1$$

where the arrow notation is used to denote the direction in which one is looking, there follows

$$\overleftarrow{Z}_2 I_2 = Z_{22}I_2 + Z_{21}\overrightarrow{Y}_1 V_1$$

and

$$V_1 = Z_{21}I_2 + Z_{11}\overrightarrow{Y}_1 V_1.$$

Eliminating  $V_1$  and  $I_2$ ,

$$(\overleftarrow{Z}_2 - Z_{22})(1 - Z_{11}\overrightarrow{Y}_1) = Z_{21}^2 \overrightarrow{Y}_1, \quad (2)$$

or, because  $\overrightarrow{Y}_1 = -\overleftarrow{Y}_1$ ,

$$\overleftarrow{Z}_2 = \left( Z_{22} - \frac{Z_{21}^2}{Z_{11}} \right) + \frac{\frac{Z_{21}^2}{Z_{11}}}{\overleftarrow{Y}_1 + \frac{1}{Z_{11}}},$$

<sup>1</sup> In the following sections the subscript 1 will be used to distinguish quantities measured on the left-hand side of a transducer, and it will further be assumed that this is the generator side. Similarly, the subscript 2 will distinguish quantities on the right-hand side, or load side, of the transducer.

which may be written

$$\vec{Z}_2 = Z_2 + \frac{n^2}{\vec{Y}_1 + Y_1}, \quad (3)$$

where  $Z_2$ ,  $Y_1$ , and  $n$  are independent of  $\vec{Z}_2$  and  $\vec{Y}_1$  and characterize completely the transformer properties of the network. Because

$$\begin{aligned} \vec{Z}_2 &= -\vec{Z}_2 & \text{and} & & \vec{Y}_1 &= -\vec{Y}_1, \\ \vec{Y}_1 &= Y_1 + \frac{n^2}{\vec{Z}_2 + Z_2}, \end{aligned} \quad (4)$$

the transducer may be represented by the network of Fig. 5-6 where  $Z_2$ ,  $Y_1$ , and  $n$  are complex; for lossless networks  $Z_2$  and  $Y_1$  will be imaginary and  $n$  real; for networks that are slightly lossy, the real parts of  $Z_2$  and  $Y_1$  and the complex part of  $n$  will be small. The three quantities are, in general, functions of frequency; the assumption of the "ideal" output is that they are frequency-independent.

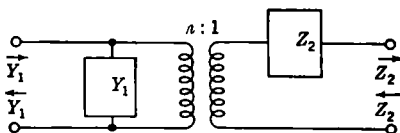


FIG. 5-6.—Schematic representation of a 4-terminal transducer.

It is also useful to have a representation that puts in evidence the relation between the reflection coefficients measured in transmission lines of characteristic impedances  $K_1$  and  $K_2$  attached to the left- and right-hand sides of the transducer (see Fig. 5-7). Such a representation forms the basis for most measurements on microwave transducer properties. By employing the usual definition of voltage reflection coefficient one may write

$$\vec{Z}_2 = K_2 \frac{1 + \vec{q}_2}{1 - \vec{q}_2}$$

and

$$\vec{Y}_1 = \frac{1}{K_1} \frac{1 - \vec{q}_1}{1 + \vec{q}_1}$$

where  $\vec{q}_1$  and  $\vec{q}_2$  are the reflection coefficients looking to the right along each line. Substituting in Eq. (2) and using  $\vec{Z}_2 = -\vec{Z}_2$ , one obtains, after division by  $K_1 K_2$ ,

$$\left( \frac{1 + \vec{q}_1}{1 - \vec{q}_1} - \frac{Z_{11}}{K_1} \right) \left( \frac{1 + \vec{q}_2}{1 - \vec{q}_2} + \frac{Z_{22}}{K_2} \right) + \frac{Z_{21}^2}{K_1 K_2} = 0. \quad (5)$$

Equation (5) implies a relation of the type

$$1 + \vec{c}_1 \vec{q}_1 + \vec{c}_2 \vec{q}_2 + \vec{d} \vec{q}_1 \vec{q}_2 = 0. \quad (6)$$

If we now write

$$c_2 = \frac{e^{a_2}}{b}, \quad c_1 = -\frac{e^{a_1}}{b}, \quad d = -e^{a_1+a_2},$$

as is always permissible, Eq. (6) becomes

$$\vec{q}_1 = e^{-a_1} \frac{b + e^{a_2} \vec{q}_2}{1 + b e^{a_2} \vec{q}_2}. \quad (7)$$

This representation is of particular value when the transformer is lossless. In this case,  $Z_{11}$ ,  $Z_{21}$ , and  $Z_{22}$  are all imaginary, and an examination of

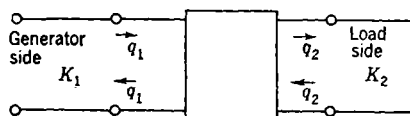


FIG. 5-7.—Schematic representation of a 4-terminal transducer in terms of reflection coefficients.

Eqs. (5) and (6) shows that  $a_1$ ,  $a_2$  are now imaginary and  $b$  is real.

This result might have been obtained in another way. Equation (5) indicates that the relation between  $q_1$  and  $q_2$  is a bilinear one.

Because  $|q| < 1$  for a passive load and  $|q| = 1$  for a purely reactive

load, a lossless transducer must transform the circle  $|q| = 1$  into itself and the interior  $|q| < 1$  also into itself. Bilinear transformations with this property are known to be of the form<sup>1</sup>

$$q_1 = e^{i\alpha_1} \frac{\beta + q_2 e^{i\alpha_2}}{1 + \beta q_2 e^{i\alpha_2}}, \quad (8)$$

where  $\alpha_1$ ,  $\alpha_2$ , and  $\beta$  are real.

Because of the frequent necessity for transforming through a given transducer in either direction it is useful to have the left-to-right analogue of Eq. (8). Using the system of notation shown in Fig. 5-7, one writes by analogy with Eq. (8)

$$\vec{q}_2 = e^{-i\alpha_2} \frac{\beta' + \vec{q}_1 e^{i\alpha_1}}{1 + \beta' \vec{q}_1 e^{i\alpha_1}}. \quad (9)$$

Using the relation that is inherent in the definition of  $q$

<sup>1</sup> A straightforward account of the bilinear or Möbius transformation, which is the simplest of all conformal transformations, is given in C. Carathéodory, *Conformal Representation*, Cambridge, London, 1932. Since all impedance and reflection transformations belong to this class, a knowledge of its properties is very illuminating. Equation (8) is derived from *ibid.*, p. 17, by multiplying his equation by  $e^{i(a_1-a_2)}$  and writing  $z_0 = -e^{-i\alpha_1}$ .

$$\overrightarrow{q} \overleftarrow{q} = 1, \quad (10)$$

one may show

$$\beta' = \beta, \quad (11a)$$

$$\overrightarrow{\alpha}_1 + \overleftarrow{\alpha}_1 = \pi, \quad (11b)$$

$$\overrightarrow{\alpha}_2 + \overleftarrow{\alpha}_2 = \pi. \quad (11c)$$

Because  $\beta = \beta'$ , the prime may be dropped. Equations (8) and (9), of course, embody the same physical properties. It should be noticed that  $\beta$ ,  $\alpha_1$ , and  $\alpha_2$  are dependent upon  $K_1$  and  $K_2$  as well as the internal properties of the transducer. A physical realization of Eq. (8) or (9) may be found by writing it as three equations. Thus,

$$\overrightarrow{q}_2' = e^{i\alpha_2} \overrightarrow{q}_2, \quad (12a)$$

and

$$\overrightarrow{q}_2'' = \frac{\beta + \overrightarrow{q}_2'}{1 + \beta \overrightarrow{q}_2'} \quad \text{or} \quad \frac{1 + \overrightarrow{q}_2''}{1 - \overrightarrow{q}_2''} = \left( \frac{1 + \beta}{1 - \beta} \right) \frac{1 + \overrightarrow{q}_2'}{1 - \overrightarrow{q}_2'}, \quad (12b)$$

and

$$\overrightarrow{q}_1 = \overrightarrow{q}_2'' e^{-i\alpha_1}. \quad (12c)$$

The transformation embodied in Eq. (12a) is that due to an electrical length  $\overrightarrow{\alpha}_2$  of line of characteristic impedance  $K_2$ . Equation (12b) repre-

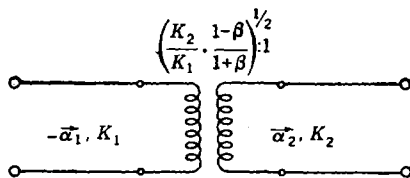


FIG. 5-8.—Equivalent circuit of a 4-terminal transducer.

sents passage through an ideal transformer, as may be seen by introducing  $\overrightarrow{Z}_2''$  and  $\overrightarrow{Z}_2'$ , the impedances corresponding to  $\overrightarrow{q}_2''$  and  $\overrightarrow{q}_2'$ . Then, from Eq. (12b)

$$\frac{\overrightarrow{Z}_2''}{K_1} = \left( \frac{1 + \beta}{1 - \beta} \right) \frac{\overrightarrow{Z}_2'}{K_2} = \Delta \frac{\overrightarrow{Z}_2'}{K_2}. \quad (12d)$$

The turns ratio of the ideal transformer is  $[\Delta(K_1/K_2)]^{1/2}$ . Finally Eq. (12c) indicates a further passage down a line of characteristic impedance  $K_1$  and electrical length  $-\overrightarrow{\alpha}_1$ . Thus, the circuit of Fig. 5-8 represents the whole transducer connected to lines of impedance  $K_1$  and  $K_2$ .

The geometrical significance of Eq. (8) is shown in Fig. 5-9, which

represents the motion of two given points in the  $\vec{q}_2$ -plane under the three stages of the transformation. The first and last transformations correspond to rotation through angles  $\vec{\alpha}_2$  and  $-\vec{\alpha}_1$  respectively. The passage through an ideal transformer is a transformation that leaves

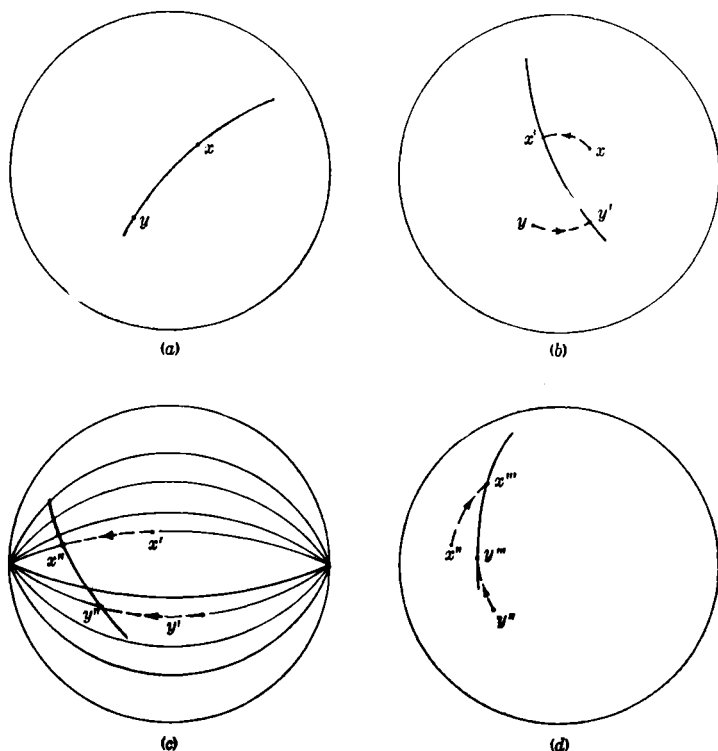


FIG. 5-9.—Analysis of the action of a general 4-terminal reflection-coefficient transducer into three elementary operations. Transformations (a) to (b) and (c) to (d) correspond to rotation through angles  $\vec{\alpha}_2$  and  $-\vec{\alpha}_1$  respectively. The transformation (b) to (c) may be termed a compression and refers to the transformation through the ideal transformer.

$\text{Arg}[(1 + \vec{q}_2'')/(1 - \vec{q}_2'')] = \text{Arg}[(1 + \vec{q}_2)/(1 - \vec{q}_2)]$  according to Eq. (12b).

But  $\text{Arg}[(1 + \vec{q})/(1 - \vec{q})] = \text{constant}$  is the equation of a circle through the points  $+1$  and  $-1$ ; such circles are thus transformed into themselves. Points lying on a common circle orthogonal to those which pass through  $+1$  and  $-1$  still lie on such a circle after transformation, since the transformation is conformal. This type of transformation may be referred to as a compression. It is important to note that it is only at

this stage that the size of figures and the magnitude of reflection coefficients are changed. The parameter  $\Delta = (1 + \beta)/(1 - \beta)$ , which may be called the principal transformer constant, mainly determines the properties of the transducer. One may note that  $\vec{q}_1(0) = \beta e^{-j\alpha_1}$  and  $\overleftarrow{q}_2(0) = \beta e^{-j\alpha_2}$  are the reflection coefficients looking into each side of the transducer when the remote side is matched. Since these points must fall within  $|q| = 1$ , then  $0 \leq \beta \leq 1$  and  $1 \leq \Delta$ .

The transducer constants could clearly be found by measuring  $\vec{q}_1(0)$  and  $\overleftarrow{q}_2(0)$ , but it is often difficult to match each of the lines, and another method is preferable. Suppose that  $\vec{q}_2$  is set up by a reactive load; then  $\vec{q}_2$  is of the form  $\vec{q}_2 = e^{j\phi_2}$ , where  $\phi_2$  is real. Since the transducer is lossless, one must have  $\vec{q}_1 = e^{j\phi_1}$ . Putting these values in Eq. (8) and reducing one finds

$$\tan \frac{\phi_1 + \alpha_1}{2} = \Delta \tan \frac{\phi_2 + \alpha_2}{2}. \quad (13)$$

Practically,  $\phi_1$  (or  $\phi_2$ ) may be found as a function of  $\phi_2$  (or  $\phi_1$ ) by moving a shorting plunger along one line and measuring the position of the associated short circuit in the other line. If  $\phi_1$  (or  $\phi_2$ ) be plotted against  $\phi_2$  (or  $\phi_1$ ), an S-shaped curve symmetrical about the line

$$\phi_1 + \alpha_1 = \phi_2 + \alpha_2$$

is obtained, repeating itself as both  $\phi_1$  and  $\phi_2$  increase by  $2\pi$  (see Fig. 5-10). From Eq. (13) one has

$$\sec^2 \frac{\phi_1 + \alpha_1}{2} \frac{d\phi_1}{d\phi_2} = \Delta \sec^2 \frac{\phi_2 + \alpha_2}{2}$$

or

$$\frac{d\phi_1}{d\phi_2} = \frac{\Delta \sec^2 \frac{\phi_2 + \alpha_2}{2}}{1 + \Delta^2 \tan^2 \frac{\phi_2 + \alpha_2}{2}} = \Delta - \frac{\Delta(\Delta^2 - 1)}{\Delta^2 + \cot^2 \frac{\phi_2 + \alpha_2}{2}}. \quad (14)$$

From Eq. (14) it follows that  $d\phi_1/d\phi_2 \leq \Delta$ , the equality occurring at  $\phi_2 + \alpha_2 = \phi_1 + \alpha_1 = 0$ . Similarly,  $d\phi_2/d\phi_1 \leq \Delta$ , and equality occurs at  $\phi_2 + \alpha_2 = \phi_1 + \alpha_1 = \pi$ . Thus, the transducer parameters may be found from the maximum slope of a  $\phi_1$  vs.  $\phi_2$  or  $\phi_2$  vs.  $\phi_1$  plot and the location of the point at which the maximum slope occurs.

**5-3. The  $Q$ -circle and the Rieke Diagram.**—This section will be concerned with the behavior of a resonant system that is connected to an external load by means of an ideal frequency-insensitive output circuit. The results that are derived may be applied to real output circuits provided the assumption of frequency-insensitivity is not seriously violated. It will not be assumed that the output circuit is lossless.

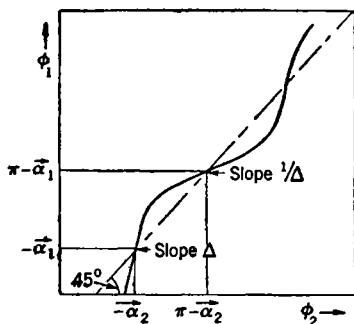


FIG. 5-10.—Representative  $S$ -curve for the computation of the transducer parameters.

5-11, where the  $\vec{Y}_1$  and  $\vec{Z}_2$  retain their previous meaning. As a consequence of the physical overlapping of the resonant system and the output circuit, it is not possible, in the absence of independent measurements of lead loss made on the isolable part of the output circuit, to separate the so-called “tube” and “lead” losses. Thus, the model uses a lossless shunt circuit for the resonant system and incorporates the losses of the latter with those of the shunt element  $Y_1$  of the output circuit.

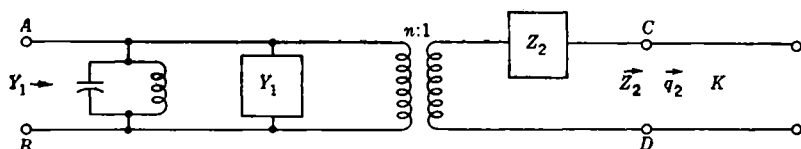


FIG. 5-11.—Representation of resonant system and output circuit.

It will be supposed that the load impedance  $\vec{Z}_2$  and its reflection coefficient  $\vec{q}_2$  are set up in a line of characteristic impedance  $K$ . A relation will first be derived between  $\vec{Y}_1(0)$ , the admittance looking into the resonant system in the direction of power flow, when the external line is matched, and  $\vec{q}_2$ , the reflection coefficient looking from the terminals  $CD$  of the transducer into the “cold” tube which contains no electrons. Writing  $jY_0 = jNY_r(\omega/\omega_0 - \omega_0/\omega)$  for the admittance of the resonant system, one has

$$\vec{Y}_1(0) = jY_0 + Y_1 + \frac{n^2}{K + \vec{Z}_2} \quad (15)$$



and

$$\overleftarrow{Z}_c = K \frac{1 + \overleftarrow{q}_c}{1 - \overleftarrow{q}_c} = Z_2 + \frac{n^2}{jY_0 + Y_1}. \quad (16)$$

Eliminating the frequency-dependent term  $jY_0 + Y_1$  between Eqs. (15) and (16) gives

$$\begin{aligned} K \frac{1 + \overleftarrow{q}_c}{1 - \overleftarrow{q}_c} &= Z_2 + \frac{n^2}{\overrightarrow{Y}_1(0) - \frac{n^2}{Z_2 + K}}, \\ \overleftarrow{q}_c &= \frac{\frac{Z_2}{K} - 1 + \frac{n^2/K}{\overrightarrow{Y}_1(0) - n^2/(Z_2 + K)}}{\frac{Z_2}{K} + 1 + \frac{n^2/K}{\overrightarrow{Y}_1(0) - n^2/(Z_2 + K)}} \\ &= \frac{\left(\frac{Z_2}{K} - 1\right) \overrightarrow{Y}_1(0) + \frac{n^2}{K} \left(1 - \frac{Z_2 - K}{Z_2 + K}\right)}{\left(\frac{Z_2}{K} + 1\right) \overrightarrow{Y}_1(0) + \frac{n^2}{K} \left(1 - \frac{Z_2 + K}{Z_2 + K}\right)} \\ &= \frac{Z_2 - K}{Z_2 + K} + \frac{2Kn^2}{(Z_2 + K)^2} \frac{1}{\overrightarrow{Y}_1(0)} \\ &= \overleftarrow{q}_0 + \frac{A}{\overrightarrow{Y}_1(0)}, \end{aligned} \quad (17)$$

where

$$\overleftarrow{q}_0 = \frac{Z_2 - K}{Z_2 + K} \quad (18a)$$

and

$$A = \frac{2Kn^2}{(Z_2 + K)^2}. \quad (18b)$$

But if the transformer be frequency insensitive,  $\overrightarrow{Y}_1(0)$  is of the form

$$\begin{aligned} \overrightarrow{Y}_1(0) &= \operatorname{Re} \left( Y_1 + \frac{n^2}{Z_2 + K} \right) + j \operatorname{Im} \left( Y_1 + \frac{n^2}{Z_2 + K} \right) + jNY_r \left( \frac{\omega}{\omega_0} - \frac{\omega_0}{\omega} \right) \\ \text{or}^1 \quad \overrightarrow{Y}_1(0) &= G_L + jB_L + j2NY_r \frac{\delta\omega}{\omega_0} \quad \text{where } \delta\omega = (\omega - \omega_0) \ll \omega_0. \end{aligned} \quad (19)$$

Thus,  $\overrightarrow{Y}_1(0)$  is represented in the complex plane by a straight line of the form  $G_L + jB(\omega)$ . It will be supposed that the assumptions of

<sup>1</sup> It may be noted that the frequency shift due to the load is given by

$$(\delta\omega)_L = - \left( \frac{B_L}{2NY_r} \right) \omega_0.$$

frequency-insensitivity and freedom from extra modes in the resonant system hold good over a frequency range sufficient to make  $B(\omega) \gg G_L$ .

Substantially then,  $B(\omega)$  runs from  $-\infty$  to  $+\infty$ . Then  $[\vec{Y}_1(0)]^{-1}$  is a circle of center  $1/2G_L$  and radius  $1/2G_L$ ; and from Eq. (17),  $\vec{q}_c$  is represented by a circle of center  $\vec{q}_0 + (A/2G_L)$  and radius  $|A|/2G_L$ . It has been proved, therefore, that the locus of input reflection coefficients for the "cold" tube, as a function of frequency, is a circle. This is known as the  $Q$ -circle.

From the definition of loaded  $Q$  as  $Q_L$  one has

$$Q_L = \frac{NY_r}{G_L} \quad (20)$$

Thus,

$$\begin{aligned} \vec{Y}_1(0) &= G_L + jB_L + jNY_r \frac{2\delta\omega}{\omega_0} \\ &= G_L \left( 1 + j \frac{B_L}{G_L} + jQ_L \frac{2\delta\omega}{\omega_0} \right) \\ &= G_L \left\{ 1 + jQ_L \frac{2}{\omega_0} [\delta\omega - (\delta\omega)_L] \right\} \end{aligned} \quad (21)$$

or

$$2Q_L \frac{\delta\omega - (\delta\omega)_L}{\omega_0} = \tan \text{Arg } \vec{Y}_1(0) \quad (22)$$

$$= \tan \text{Arg } \frac{A}{\vec{q} - \vec{q}_0}, \quad (23)$$

making use of Eq. (17). Considering Fig. 5-12 which shows a possible  $Q$ -circle and a series of observed points  $\vec{q}_1(\omega_1)$ ,  $\vec{q}_2(\omega_2)$ , etc., it is plain that  $\text{Arg } A/(\vec{q} - \vec{q}_0)$  is the angle between the line joining  $\vec{q}_0$  to a point  $\vec{q}$  on the circle and the diameter of the  $Q$ -circle passing through  $\vec{q}_0$ . Thus, if any line  $pp'$  is drawn normal to the diameter, the diameter and the line through  $\vec{q}$  and  $\vec{q}_0$  will intercept a segment on  $pp'$  proportional to  $\tan \text{Arg } A/(\vec{q} - \vec{q}_0)$ . From Eq. (23) the length of this segment varies linearly with  $\delta\omega$  and, hence, with  $\omega$ . In practice, then, if the reflection coefficient has been measured at a series of frequencies and a  $Q$ -circle drawn through the points, the diameter through  $\vec{q}_0$  may be drawn and the series of the segments on a normal to the diameter measured as above. If the segment length is then plotted against frequency, the slope of the resultant straight line leads, using Eq. (23), to a value for  $Q_L$ . Strictly speaking,

the value of  $\omega_0$  is not observed, but it is usually satisfactory to use a value of  $\omega$  in the neighborhood of that for which  $|q|$  is a minimum. As has been emphasized, this method of determining  $Q_L$  is idealized, presupposing frequency insensitivity of the output circuit and the absence of secondary resonances in the resonant system. It will be possible to locate  $\bar{q}_0$ , the off-resonance point, with a sufficient degree of accuracy provided that the assumed ideal conditions hold over a frequency range sufficient to make  $\delta\omega - (\delta\omega)_L \gg (\omega_0/2Q_L)$ . Provided that  $\bar{q}_0$  has been located correctly, the method is useful because it utilizes all the points measured and, by means of the linearity of the intercept-frequency plot, tests their internal consistency.

Once the  $Q$ -circle has been determined, it may be used to deduce a number of properties of the whole system. The circuit efficiency at match, defined as the ratio of power delivered to the load to that fed into the system at the resonator openings, may be shown to be given by the radius of the  $Q$ -circle. Thus in Fig. 5-11, if  $V_1$  is the voltage across  $AB$  and  $I_2$  the current through  $CD$ , then

$$|V_1| = \left| \frac{KI_2 + Z_2I_2}{n} \right| = \left| \frac{K + Z_2}{n} \right| |I_2|. \quad (24)$$

But the input power is  $G_L|V_1|^2$ , and the power to the load,  $K|I_2|^2$ , so that the circuit efficiency at match or  $\eta_c(0)$  is

$$\begin{aligned} \eta_c(0) &= \frac{K|I_2|^2}{G_L|V_1|^2} = \frac{K}{G_L} \left| \frac{n}{K + Z_2} \right|^2 \\ &= \frac{|A|}{2G_L}. \end{aligned} \quad (25)$$

It is customary to define a quantity  $Q_E$ , the external  $Q$ , which is  $2\pi$  times the ratio of the energy stored in the system to the energy dissipated in the external load per cycle. In accord with this definition, at match,

$$Q_E = \frac{Q_L(0)}{\eta_c(0)}, \quad (26)$$

where  $Q_L(0)$  has been written rather than  $Q_L$  to indicate a value measured at match. It is, of course, possible to define  $Q_L$  values for any value of  $\bar{q}_L$ , the load reflection coefficient. Provided that the system has not

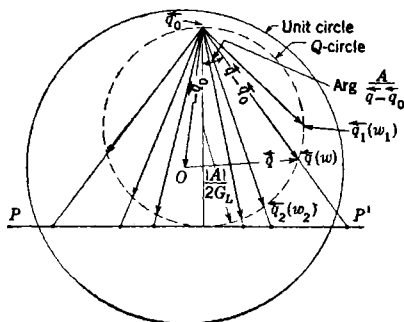


FIG. 5-12.—The  $Q$ -circle.

been pulled by the load from its unperturbed frequency, one has

$$\frac{Q_L(\vec{q}_L)}{Q_L(0)} = \frac{G_L}{G_L(\vec{q}_L)} = \frac{G_L(0)}{G_L(\vec{q}_L)}.$$

Similarly

$$Q_R(\vec{q}_L) = \frac{G_L(0)}{G_L(\vec{q}_L)} Q_L(0) \frac{1}{\eta_c(\vec{q}_L)}. \quad (27)$$

The behavior of  $Q_L(\vec{q}_L)$  and  $\eta_c(\vec{q}_L)$  as functions of  $\vec{q}_L$  are discussed below.

The pulling figure of the operating magnetron may be defined as the maximum change in frequency  $F(q_p)$  of the system when  $\vec{q}_L$  is varied over all phases with  $|\vec{q}_L| = q_p$ . Since the pulling figure will depend upon the susceptance of the electron stream, it is necessary to make a simplifying assumption about the behavior of the latter in order to deduce the pulling figure from the  $Q$ -circle. Suppose that the electron admittance is  $Y_e = G_e + jB_e$ , the load reflection coefficient is  $\vec{q}_L$ , and the load impedance consequently is  $K[(1 + \vec{q}_L)/(1 - \vec{q}_L)]$ ; then

$$0 = G_e + jB_e + j2NY_r \frac{\delta\omega}{\omega_0} + Y_1 + \frac{n^2}{Z_2 + K \frac{1 + \vec{q}_L}{1 - \vec{q}_L}}. \quad (28)$$

Making the substitutions

$$Z_2 = K \frac{1 + \vec{q}_0}{1 - \vec{q}_0}, \quad n^2 = \frac{(Z_2 + K)^2}{2K} A = \frac{2KA}{(1 - \vec{q}_0)^2},$$

Eq. (28) becomes

$$0 = G_e + jB_e + j2NY_r \frac{\delta\omega}{\omega_0} + Y_1 + \frac{A}{1 - \vec{q}_0} \frac{1 - \vec{q}_L}{1 - \vec{q}_L \vec{q}_0}. \quad (29)$$

Using the symbol  $D$  to denote the variation in a quantity as the phase of  $\vec{q}_L$  is varied, one has

$$0 = D(G_e + jB_e) + j2NY_r \frac{1}{\omega_0} D(\delta\omega) + D\left(\frac{A}{1 - \vec{q}_0} \frac{1 - \vec{q}_L}{1 - \vec{q}_L \vec{q}_0}\right). \quad (30)$$

The assumption to be made about the electron admittance is that, for small changes,  $D(B_e)/D(G_e) = \tan \alpha = \text{a constant}$ . Multiplying Eq.

(30) by  $e^{-i\alpha}$  gives

$$0 = \frac{D(G_c)}{\cos \alpha} + 2jN \frac{Y_r}{\omega_0} D(\delta\omega) e^{-i\alpha} + D \left( \frac{A e^{-i\alpha}}{1 - \overleftarrow{q_0}} \frac{1 - \overrightarrow{q_L}}{1 - \overleftarrow{q_L} \overleftarrow{q_0}} \right)$$

or

$$0 = 2N \frac{Y_r}{\omega_0} \cos \alpha D(\delta\omega) + DIm \left( \frac{A e^{-i\alpha}}{1 - \overleftarrow{q_0}} \frac{1 - \overrightarrow{q_L}}{1 - \overleftarrow{q_L} \overleftarrow{q_0}} \right). \quad (31)$$

Thus,

$$\begin{aligned} F(q_0) &= \frac{D_{\max}(\delta\omega)}{2\pi} = \frac{\omega_0}{2\pi} \frac{1}{Q_L} \sec \alpha D_{\max} Im \left( \frac{A e^{-i\alpha}}{1 - \overleftarrow{q_0}} \frac{1 - \overrightarrow{q_L}}{1 - \overleftarrow{q_L} \overleftarrow{q_0}} \right) \\ &= f_0 \frac{\sec \alpha}{Q_L} D_{\max} Im \left( \frac{A e^{-i\alpha}}{2G_L} \frac{\overrightarrow{q_L}}{1 - \overleftarrow{q_L} \overleftarrow{q_0}} \right) \\ &= \frac{f_0 \sec \alpha}{Q_L} D_{\max} Im \left( \frac{A e^{-i\alpha}}{2G_L} \frac{1}{\frac{\overrightarrow{q_L}}{\overleftarrow{q_L}} - \overleftarrow{q_0}} \right). \end{aligned} \quad (32)$$

The bracketed expression is  $A e^{-i\alpha}/2G_L$  times the inverse of a circle of center  $-\overleftarrow{q_0}$  and radius  $1/|\overleftarrow{q_L}| = 1/q_p$ . Considering the inversion of the two points on a diameter of this circle which passes through the origin, which two points, thus, still lie at the extremities of a diameter after inversion, the new diameter of the inverted circle is seen to be

$$\frac{1}{q_p^{-1} - |\overleftarrow{q_0}|} - \frac{1}{q_p^{-1} + |\overleftarrow{q_0}|} = \frac{2q_p^{-1}}{q_p^{-2} - |\overleftarrow{q_0}|^2} = \frac{2q_p}{1 - q_p^2 |\overleftarrow{q_0}|^2}.$$

Thus,

$$D_{\max} Im \left( \frac{A e^{-i\alpha}}{2G_L} \frac{1}{\frac{\overrightarrow{q_L}}{\overleftarrow{q_L}} - \overleftarrow{q_0}} \right) = \frac{|A|}{2G_L} \frac{2q_p}{1 - q_p^2 |\overleftarrow{q_0}|^2} = \frac{2\eta_c(0)q_p}{1 - q_p^2 |\overleftarrow{q_0}|^2} \quad (33)$$

and

$$\begin{aligned} F(q_p) &= \frac{f_0 \eta_c(0) \sec \alpha}{Q_L} \frac{2q_p}{1 - q_p^2 |\overleftarrow{q_0}|^2} \\ &= \frac{f_0 \sec \alpha}{Q_E} \frac{2q_p}{1 - q_p^2 |\overleftarrow{q_0}|^2}. \end{aligned} \quad (34)$$

The value of  $F(q_p)$  is seen to be determined from the  $Q$ -circle save for the term  $\sec \alpha$ , which is of electronic origin. The expression found by setting  $\alpha = 0$  is known as the "cold" pulling figure and represents the

effect of the oscillating and output circuits upon the total pulling figure. The pulling figure ordinarily used to describe magnetron performance specifies a value of  $q_p$  of 0.2.

The unloaded  $Q$ ,  $Q_u$  has not been mentioned thus far. In normal usage, this is a loose term intended to describe the tube losses. Because of the difficulty of separating the tube and lead losses there is some ambiguity in defining the unloaded  $Q$ . If the lead and tube losses are grouped together, then, with an obvious notation

$$G_L = G_s + G_u, \quad \frac{1}{Q_L} = \frac{1}{Q_s} + \frac{1}{Q_u} \quad \text{or} \quad Q_u = \frac{Q_L}{1 - \eta_c(0)}. \quad (35)$$

Alternatively, the lead losses may be separated as far as possible by defining  $Q_u$  as  $2\pi$  times the ratio of stored energy to the energy loss per cycle in the tube and lead when the latter is minimized with respect to variations in the external load. The result derived in this way is

$$\frac{1}{Q_L} = \frac{1}{Q_u} + \frac{1}{Q_s} \operatorname{Re} \left[ 2 \frac{1 - \overleftarrow{(q_0 A)}}{1 - |\overleftarrow{q_0}|^2} \right], \quad (36)$$

where  $\overleftarrow{(q_0 A)}$  is the scalar product of  $\overleftarrow{q_0}$  and  $A$ . The expression may be evaluated from the  $Q$ -circle if necessary.

*The Rieke Diagram.*—It has been explained in Chap. 1 that the Rieke diagram shows the power delivered to the load and the frequency of the system as functions of the load reflection coefficient  $\overrightarrow{q_L}$ . The complete theory of the diagram is given in Chap. 7. It is necessary here to discuss only the relations between the Rieke diagram and the  $Q$ -circle.

According to Eq. (29),

$$-G_e - jB_e = \overrightarrow{Y_1}(\overrightarrow{q_L}) = j2NY_r \frac{\delta\omega}{\omega_0} + Y_1 + \frac{A}{1 - \overleftarrow{q_0}} \frac{1 - \overrightarrow{q_L}}{1 - \overleftarrow{q_L} \overleftarrow{q_0}} \quad (29)$$

In Chap. 7 it is shown that the electronic efficiency is a function of  $G_e$  only, provided that the patterns are not distorted by loading. This being the case, the contours of constant electronic efficiency, of constant power transfer by the electrons, of constant  $G_e = -\operatorname{Re}[\overrightarrow{Y_1}(\overrightarrow{q_L})]$ , and of constant  $Q_L(\overrightarrow{q_L}) = NY_r/G_L(\overrightarrow{q_L})$  are identical. In the  $\overrightarrow{Y}$ -plane, these contours are straight lines of the form  $\operatorname{Re}(\overrightarrow{Y}) + jB = G + jB$ , where  $B$  is variable. These lines must transform into circles in the  $\overrightarrow{q_L}$  plane; and since each line contains the point at infinity, all the circles must

contain the transform of this point. From Eq. (29) the required transform is  $\vec{q}_L = 1/\vec{q}_0$ . Now, in determining the  $Q$ -circle,  $\vec{Y}_1 = -\vec{Y}_1 = 0$ , and thus  $G = 0$  for the  $Q$ -circle. But since  $\overleftarrow{qq} = 1$ , the circle in the  $\vec{q}$ -plane, corresponding to the  $Q$ -circle in the  $\overleftarrow{q}$ -plane, is the inverse of the former. Thus, the inverse of the  $Q$ -circle is one of the contours of constant  $Q_L$ ; namely,  $Q_L = 0$ . The whole family of contours of constant  $Q_L$  is evidently a family of nonintersecting circles passing through  $1/\vec{q}_0$  and tangent at that point to the inverse of the  $Q$ -circle. Figure 5-13 shows the disposition of these circles.

Without information from operating tubes about the variation of  $B_e$  with  $G_e$ , one cannot deduce the frequency contours. The assumption used in deducing the pulling figure cannot be used because it is true only for small variations of  $G_e$ . If it were universally valid, the frequency contours would be a set of circles also passing through  $1/\vec{q}_0$ , intersecting the  $Q_L$  set at a fixed angle  $\pi/2 - \alpha$ .

In order to deduce electronic efficiency as a function of load from the Rieke diagram, it is necessary to find out how the circuit efficiency varies. Suppose that the load reflection coefficient is  $\vec{q}_L$ ; this may be thought of as produced by a lossless transducer, and the presence of the latter will not affect the circuit efficiency. If  $\vec{q}_L = |\vec{q}_L|e^{j\theta}$ , such a transducer is represented from Eq. (8) by

$$\vec{q}_1 = e^{j\theta} \frac{|\vec{q}_L| + \vec{q}_2}{1 + |\vec{q}_L|\vec{q}_2} \quad (37)$$

or, from Eqs. (9) and (11),

$$\vec{q}_2 = \frac{\overleftarrow{q}_1 e^{j\theta} - |\vec{q}_L|}{1 - |\vec{q}_L|e^{j\theta}\overleftarrow{q}_1} = -\frac{1}{|\vec{q}_L|} + \frac{|\vec{q}_L|^{-1} - |\vec{q}_L|}{1 - |\vec{q}_L|e^{j\theta}\overleftarrow{q}_1} \quad (38)$$

The radius of the  $Q$ -circle measured on the load side of the transducer gives the new circuit efficiency,  $\eta_e(\vec{q}_L)$ ; but this  $Q$ -circle is the transform of the normal  $Q$ -circle by Eq. (38). If the  $Q$ -circle is written in the form,  $r_0 + \eta_e(\theta)e^{j\theta}$ , the diameter of the corresponding  $\vec{q}_2$  circle is

$$\eta_e(\vec{q}_L) = \frac{\eta_e(0)(1 - |\vec{q}_L|^2)}{|1 - r_0|\vec{q}_L|e^{j\theta}|^2 - \eta_e(0)^2|\vec{q}_L|^2}, \quad (39)$$

and this equation shows the variation of circuit efficiency with  $\vec{q}_L$ . The contours of constant  $\eta_e(\vec{q}_L)$  may be found by writing Eq. (39) in the form

$$\left[ \frac{\eta_c(0)}{\eta_c(\vec{q}_L)} + r_0^2 - \eta_c(0)^2 \right] |\vec{q}_L|^2 - 2r_0 \cos \theta |\vec{q}_L| + \left[ 1 - \frac{\eta_c(0)}{\eta_c(\vec{q}_L)} \right] = \Psi(|\vec{q}_L|, \theta) = 0. \quad (40)$$

It is always possible to find three real quantities  $q_1$ ,  $q_2$ , and  $\lambda$  where  $q_1$  and  $q_2$  are independent of  $\eta_c(\vec{q}_L)$  such that

$$|\vec{q}_L e^{i\theta} - q_1|^2 - \lambda^2 |\vec{q}_L e^{i\theta} - q_2|^2 = \Psi(|\vec{q}_L|, \theta) = 0. \quad (41)$$

Equation (41) is the equation of a set of coaxial circles having the points  $q_1$  and  $q_2$ , lying on the common diameter of the  $Q$ - and unit-circles, as

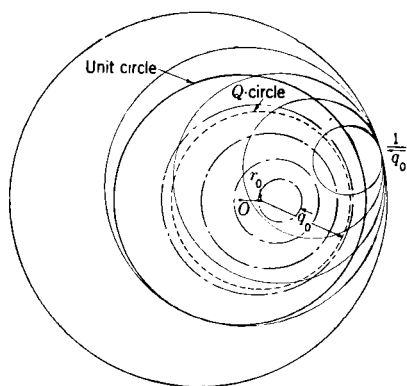


FIG. 5-13.—Contours of constant loaded  $Q$  and constant circuit efficiency. Solid lines represent  $Q_L$  and broken lines represent  $\eta_c$ .

limit points. The set may be determined in practice by identifying two of its members, namely, the unit circle and the inverse of the  $Q$ -circle. The former corresponds to  $\eta_c = 0$  (a reactive load), and the latter to  $\eta_c = -\infty$  (for in this case  $G_L = 0$  and power is being fed into the system). In Fig. 5-13 some members of the coaxial set are shown to indicate their relation with the  $Q$ -circle and constant  $Q_L$  contours. The presence of lead loss causes the sets of constant  $\eta_c$  and constant  $Q_L$  circles to have different common diameters.

Thus, when there is lead loss, the contours of constant over-all efficiency and the contours of constant load power in the Rieke diagram will not be circles nor will they lie symmetrically about a common axis. It can also be seen that the contours of constant  $Q_E(\vec{q}_L) = Q_L(\vec{q}_L)/\eta_c(\vec{q}_L)$  will not have a simple form.

Finally, it is of some practical interest to deduce from a given Rieke diagram the effect of inserting a lossless transducer between the tube and the load. The problem is to find the contour in the reflection plane into which the transducer converts the pulling circle  $|\vec{q}_L| = q_p$  and from the given Rieke diagram to find the frequency range spanned by the contour.

If the transducer is specified by the fact that it transforms  $\vec{q}_1 = 0$  into  $\vec{q}_2 = \vec{q}_L$ , the equations of the transformed circle are quite involved. However, if only an estimate of the new pulling figure is required, the problem is simpler. For since any transformation has been shown to



change the size of figures only in the "compression" stage, the size of the pulling figure can be altered only at this stage. But the compression transforms all circles through  $+1$  and  $-1$  into themselves, so that if two circles are drawn through  $+1$  and  $-1$  to touch the pulling circle

$|\vec{q}| = q_p$ , the transform of this circle will still touch the pair of circles after compression. Thus, the size of the new pulling circle is fixed as a function of its radial position (see Fig. 5-14). To a first approximation, it may be assumed that the transform of the center of the original

pulling circle ( $\vec{q} = 0$ ) is the center of the new pulling circle ( $\vec{q} = \vec{q}_L$ ) and, since  $\vec{q}_L$  is known, the size of the new pulling circle is known.

**5-4. General Considerations Concerning the Output Circuit Problem.**—In the last two sections the chief concepts used in describing output circuit behavior have been introduced, and the performance of a resonator system connected to a

load has been interpreted using the device of an ideal output circuit. It has been shown that most of the quantities involved in the relations between tube and load may be deduced from the  $Q$ -circle and the Rieke diagram. The quantity  $Y_r$ , which is needed for a complete analysis may be either calculated or obtained from  $Q$  measurements together with independent experiments on the output circuit. Thus, it is possible in some cases to measure directly the impedance level at the junction between output circuit and resonant system. As has been already indicated, the  $S$ -curve technique (see Fig. 5-10) is of great value in these measurements on isolated output circuits.

It is now desirable to discuss in a general way the functions of the output circuit in practice. The relationships among loaded  $Q$ ,  $Q_L$ , the pulling figure  $F(q_p)$ , the equivalent admittance of the resonant system  $NY_r$ , and the electronic efficiency  $\eta_e$ , which are mentioned in Chap. 7, form the foundation for determining output circuit requirements. One has the relations

$$Q_L = N \frac{Y_r}{G_L}, \quad (42a)$$

$$F(q_p) = \frac{f_0 \sec \alpha}{Q_r} \frac{2q_p}{1 - q_p^2/q_0^2}, \quad (42b)$$

$$Q_L = Q_r \eta_e(0), \quad (42c)$$

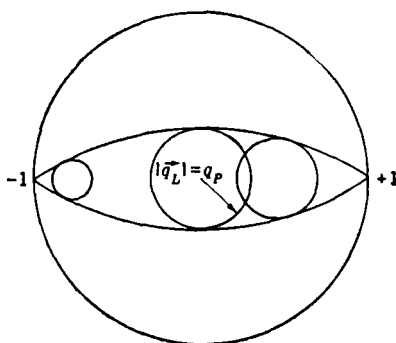


FIG. 5-14.—Transformation of the pulling circle.

together with the empirical information that electronic efficiency is almost invariably an increasing function of  $G_L$ . In almost any use of the magnetron, a definite degree of frequency stability is desired in the tube itself. This means that an upper limit is set upon the pulling figure. A compromise must always be effected between this requirement which, from Eqs. (42a) to (42c), sets an upper bound upon  $G_L$  for a given tube and that which demands a high electronic efficiency or a high  $G_L$ . To some extent this dilemma may be resolved by redesigning the resonant system to increase  $Y_r$ , which permits  $G_L$  to rise, while  $Q_L$  remains constant and  $Q_E$  and  $F(q_p)$  also remain approximately constant. However, this solution eventually breaks down because the additional capacitance introduced to increase  $Y_r$  lowers the circuit efficiency, and a point may be reached at which the over-all efficiency  $\eta_c\eta_e$  starts to decrease. It is clear also that the prescribed pulling figure will be affected by the operating wavelength. A constant pulling figure at all wavelengths would imply a  $Q_E$  proportional to frequency and thus a much smaller  $G_L$  at short wavelengths. The values of pulling figures that have been accepted as suitable compromises in unstabilized tubes are 10 Mc/sec at 3000 Mc/sec, 15 Mc/sec at 10,000 Mc/sec, and 30 Mc/sec at 30,000 Mc/sec. These figures correspond to  $Q_E$  values of about 125, 280, and 420 and, using typical values of  $\eta_c(0)$ , to  $Q_L$  values of 110, 200, and 300.

In different resonator systems, the admittance constant  $NY_r$  might be expected to vary considerably, since it is given by  $NY_r = N(hy_0 + Y_s)$ , where  $h$  is the anode height,  $y_0$  is the admittance of the unstrapped resonator per unit length, and  $Y_s$  is the strap admittance constant. The value of  $y_0$  is a function only of the shape of the oscillators. In practice the factors compensate to some extent. Rough ranges for the values of  $NY_r$  taken from Table 10-2 ( $NY_r = Y_c$ ) are 0.04 to 0.20 mho at 3000 Mc/sec, 0.15 to 0.60 mho at 10,000 Mc/sec, and about 0.3 mho at 30,000 Mc/sec. Using Eq. (42a), the resistance that must be shunted across the resonator opening to give the normal  $Q_L$  values is found to be 500 to 2500 ohms at 10 cm, 300 to 1300 ohms at 3 cm, and about 1000 ohms at 1.25 cm. It is plain that for the types of magnetron which have been designed thus far, this resistance falls generally within a range of 300 to 3000 ohms. It follows that the principal problem of output design is to supply this resistance by suitably connecting the resonant system to a matched load line whose impedance in the case of coaxial line is of the order of 50 to 100 ohms and 200 to 400 ohms for waveguide. The impedance  $K$  will be used for waveguides, defined such that the power flowing in a matched line will be given by  $V^2/K$ , where  $V$  is the line voltage.

The output circuit not only should produce the desired resistance at the assigned frequency but should do this without simultaneously

coupling in excessive reactance. The principal hazard attached to coupling in large amounts of reactance lies in the possibility of pattern deformation. The susceptibility of a strapped system to pattern distortion has been discussed in Chap. 4, where it is pointed out that to a first approximation distortion is produced to the same extent by either reactive or resistive loading. A criterion for pattern distortion is given by Eq. (57) of Chap. 4, in which it is shown that the amplitude  $\alpha_m$  of the  $m$ th mode excited when a  $\pi$ -mode is loaded is given by

$$|2\alpha_m| = \frac{Y_{\text{load}} K_s s N}{m^2 \pi \lambda_\pi} \quad m \geq 1, \quad (43)$$

where  $s$  is the strap length,  $\lambda_\pi$  the  $\pi$ -mode wavelength,  $K_s$  the strap impedance, and  $Y_{\text{load}}$  the load admittance at the slots. The symbol  $m$  is equal to  $(N/2) - n$ , where  $2n$  is the number of nodes in the r-f pattern around the interaction space. Equation (43) may be used to estimate the permissible value of  $Y_{\text{load}}$ . It will be noted that the latter depends upon the strength of coupling between oscillators and not uniquely upon  $Q_L$ . In most strapped systems it appears that distortion does not become serious until  $Q_L$  is perhaps about 30. The normal operating  $Q_L$  will be many times greater than this, and it is thus clear that the coupled reactance may be at least as large as the coupled resistance without causing difficulty.

It has already been emphasized that usually output circuits which are not deliberately stabilized store a relatively small amount of energy compared with that in the resonant system and that consequently they may be considered as frequency-insensitive over a frequency range of a few times  $\omega_0/Q_L$ , where  $\omega_0$  is the resonant frequency. It is generally considered desirable, even in fixed-frequency magnetrons, that the output circuit should exhibit considerable frequency insensitivity over a band of perhaps 20 to 30 per cent above the  $\pi$ -mode frequency. In this connection frequency insensitivity implies simply that the transformer properties of the output circuit should be slowly varying functions of frequency. This requirement of broadbandedness guarantees that the mode immediately below the  $\pi$ -mode in wavelength will be loaded to an extent comparable to the  $\pi$ -mode, and it is an insurance against the possibility of an undesired mode being favored in the starting process because its r-f amplitude exceeds that of the  $\pi$ -mode. In tunable magnetrons, the broadbanding of output circuits constitutes a special problem. In this instance the objective is usually to obtain a nearly constant pulling figure across the tuning band. From Eqs. (42a) to (42c) it is seen that this will, in general, require  $G_L$  to vary across the band which may perhaps have a width of 20 per cent. The required variation of  $G_L$  will be of the same order. The problem thus reduces to the empirical one of arranging

matters so the slow change of the output circuit transformer constants shall be in the right sense to keep  $G_L$  at an appropriate value. In this task the use of measurements on the isolable part of the output circuits is indicated.

One relation between the output system and resonator system which has been mentioned in Chap. 4 may be briefly referred to here. As the previous paragraph has indicated, it is of some importance to couple out all those modes which the electrons are likely to excite. For this reason, devices such as strap breaks have been introduced for the purpose of distorting the r-f patterns in such a way as to cause both components of an otherwise degenerate mode to couple to the output resonator. There is thus a problem, not specifically an output circuit problem, concerned with the relative disposition of discontinuities (strap breaks or tuners) and the output circuit.

The fundamental problem of coupling the load line into the resonant system may be solved in an indefinite number of ways. A useful distinction is that between high- and low-level impedance circuits. In the former the desired high impedance is introduced by the almost direct shunting of the load line across the opening of a resonator. This type of coupling is achieved in the "strap-fed" coupling shown in Fig. 5-4, in which the inner conductor of the coaxial line is tied directly to the floating section of one strap. Thus, except for a slight transformer effect due to the line length of the strap, the coaxial line is shunted across the resonator opening. In a high-level output circuit the impedance transformation is confined to the external line and may be relatively small. In general, the transformation required will be to a higher-impedance level. At the opposite extreme lie the various types of low-impedance level circuits which include most of the familiar designs. In such cases the external part of the output circuit is introduced in series with an oscillator at a high current point. If the output impedance at this point be  $Z$  and the resonator inductance  $L$ , the shunt impedance added by the output at the slot is roughly  $\omega_0^2 L^2 / Z$  (for  $\omega_0 L \gg Z$ ). Thus, the resonator acts as a transformer to raise the low impedance  $Z$  to the requisite high level. The impedance  $Z$  may be introduced in a number of ways. In a waveguide output it may be a direct series element if the output communicates with the resonator by means of a slot in the back of the resonator. In a coaxial line the impedance  $Z$  may appear as a result of the mutual coupling between a single resonator and a loop connected to the output circuit. For these low-level output circuits the external part of the circuit must effect a substantial impedance transformation downwards. For, as has been shown,  $\omega_0^2 L^2 / Z$  runs from 300 to 3000 ohms, while  $\omega_0 L$  is of the order of tens of ohms; thus  $Z$  must be of the order of 1 ohm. Between these extreme types of output circuit

it is possible to imagine intermediate forms which have been little explored. The output impedance of such forms is introduced as a series or as a shunt element at a position of intermediate voltage and current in the resonator.

**5-5. Coaxial-output Circuit.**—The purpose of this section and of Sec. 5-6 is to discuss some particular forms of output circuits in a general way. No attempt is made to give design formulas except in the case of one type of simple waveguide output. Methods of analysis for other types of circuits are indicated.

*Center- and Halo-loop Circuits.*—In these circuits, a loop intercepting the magnetic flux of one oscillator (see Figs. 5-1 and 5-2) feeds a coaxial line. The coaxial line contains a glass vacuum seal which also supports the inner conductor. To minimize breakdown across the glass, the glass usually takes the form of a length of tubing sealed to the inner conductor at one end and to the outer conductor at the other. The cross section of the line will usually have discontinuities at the seal, since the glass is butted against either a copper featheredge or a thin-walled Kovar cylinder. There is thus formed a section of line partially filled with coaxial dielectric. Con-

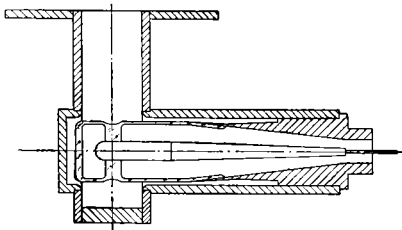


FIG. 5-15.—Example of coaxial output used as an antenna feed for a waveguide.

nection to the external line is made either directly by mechanical contact and choke joints as in Fig. 5-1 or as an antenna feed for waveguide as in Fig. 5-15. The circuit of Fig. 5-16 represents the electric behavior.

As has been already mentioned, this type of output circuit produces a low series impedance at  $CD$  in series with  $\omega_0 L$ , the inductance of one hole. The main part of the transformation is effected by the loop. The "external transformer"  $EFGH$  which contains the glass, seals, beads, choke joints, or coaxial-waveguide junctions performs a relatively small transformation. This condition is desirable because the standing wave in the relatively irregular, air-filled line is thus kept at a minimum. It is rarely possible to calculate the impedance transformations in such a line with confidence, but they are easily found by measurements either on output circuits from which the tube and loop have been removed or on smaller sections of the output circuit. By empirical means or by calculations on the regular portions of the circuit, the required properties may be obtained by a process of correction. Usually an effort is made to keep the principal transformer constant at all sections as well as the over-all constant close to unity; this gives a section with low-energy storage everywhere and hence a low-frequency sensitivity.

To a rough approximation the loop and the hole act as the primary and secondary of a transformer, but the representation is not particularly valuable, since the estimation of the turns ratio is far from simple. This arises from the difficulty of calculating the effective loop area. A crude approximation uses the mean diameter of the loop to give the area, and this may be used to obtain a rough idea of the transformation properties of the loop if the coupled impedance is calculated from  $\omega_0^2 M^2 / R$ , where  $M$  is the estimated mutual inductance of the loop and hole and  $R$  is the sum of the loop reactance and the impedance seen at  $AB$ . The transformer constant is clearly very dependent on the size of the loop and, in halo loops, also upon the height of the loop above the anode block, since the fields fall off rapidly in the end space. Experimentally it appears that the loop acts as a rather frequency-insensitive transformer.

In order to avoid coupling-in much reactance, it is desirable to arrange the properties of the external transformer so that the loop reactance is effectively canceled by a residual reactance at  $AB$ . The

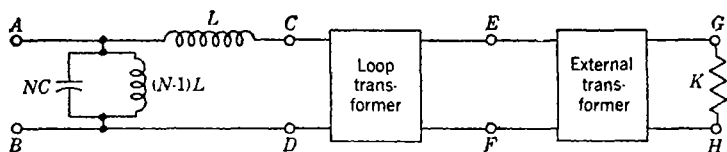


Fig. 5-16.—Schematic network of a loop-coupled output.

loop reactance may be considerable. It is accurate, in fair measure, to find the loop reactance for halo loops by assuming that the loop and its image in the anode block form a transmission line of length equal to the developed length of the loop. This length may approach a quarter wavelength for halo loops, leading to large reactances at  $AB$ . The estimation of reactive effects for center loops is difficult. However, if the loop transformer  $CDEF$  is represented by a network of the type of Fig. 5-6, the series element  $Z_2$  may be found by transforming the off-resonance point of the  $Q$ -circle taken on the complete tube, back through the transformer  $EFGH$ . Presumably  $Z_2$  represents mainly the loop reactance, and this may be balanced out by redesigning  $EFGH$  to produce the conjugate reactance at  $EF$ . The shunt element  $Y_1$  of the transducer can be found only by measuring the resonant frequency of the system with the output (including loop) removed and thus determining the pulling due to  $Y_1$  directly.<sup>1</sup>

<sup>1</sup> For an exhaustive discussion of a broadbanded halo-loop output having a waveguide junction, see J. C. Slater, "Properties of the Coaxial-waveguide Junction in the 725A and 2J51 Output," *BTL Tech. Memorandum* No. MM-44-180-4, Nov. 20, 1944; H. D. Hagstrum, "On the Output Circuit of the 2J51 (Tunable X-band Magnetron)," *BTL Tech. Memorandum* No. MM-44-140-55, Sept. 12, 1944.

An effect that may be important in halo loops is that arising from the electrostatic coupling of the loop to the neighboring strap. The orientation of the loop determines whether this coupling aids or opposes the magnetic coupling because the direction of current in the loop is reversed by rotating the loop through  $180^\circ$ , whereas the electrostatic coupling remains unaffected.

*Strap-fed Coupling Circuits.*—This type of output circuit, in which an external coaxial line is connected across the anode block and the center of a floating strap, may be represented schematically by the circuit of Fig. 5-17. The resonant system has been represented by a chain of  $N$  4-terminal networks each consisting of two strap sections and a resonator such as was used in Chap. 4. (Because the strap-fed coupling has longitudinal asymmetry, the length of the resonators actually has some effect. This, however, will be ignored.) Suppose the impedance of the output circuit looking out from  $CD$  to be  $Z$ . This may be transformed to a shunt element at  $AB$  provided that the strap length is sufficiently small for the squares and higher powers of  $2\pi s/\lambda_r$ , where  $s$  is the strap length, to be neglected. To the same approximation  $Z$  is not altered in this transformation. It has been shown experimentally that there is almost no residual reactance

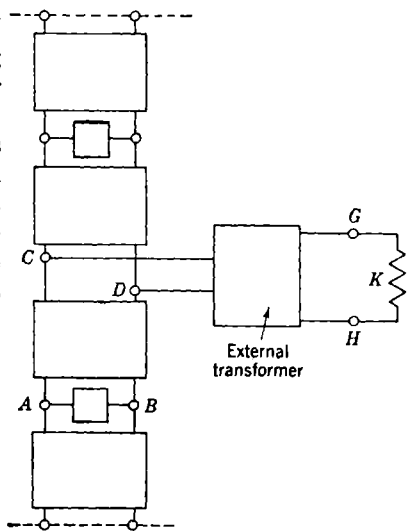


FIG. 5-17.—Schematic network of a strap-fed output.

added in making the junction between the strap and the coaxial line; hence  $Z$  will be the impedance at the start of the coaxial line. It has been remarked in the earlier discussion that  $Z$  will be a high impedance (300 to 3000 ohms, for example) and the function of the external transformer will be in all probability, with standard load lines, to transform the impedance level up somewhat. It is clearly possible to achieve a very heavy loading with this circuit by making  $Z$  small, and it has thus found more extensive application as a means of introducing reactance for tuning purposes. Tuning curves obtained by moving a shorting plunger in a uniform coaxial line connected directly to the strap have indicated that the circuit of Fig. 5-17 gives excellent qualitative agreement with the measurements. In one case, using a line of characteristic impedance of 63 ohms, the predicted and observed  $Q_L$  values were 10.9 and 11.2, respectively. In

another case, with a line of characteristic impedance of 40.7 ohms, the predicted and observed  $Q_L$  values were 7.1 and 7.6. The end effect at the junction was confirmed to be negligible. This type of output circuit is most valuable in long-wavelength magnetrons where the end spaces and straps are large enough to facilitate construction.

*Segment-fed Coupling.*—The center conductor may be brought over a segment for some distance and then bent down and connected to it (see Fig. 5-4). The analysis would follow the same lines as that for the center and halo loops, but it is somewhat more difficult to estimate the parameters of the loop transformer a priori, for one has an intimate mixture of electrostatic and magnetic coupling.

**5-6. Waveguide-output Circuits.**—All waveguide outputs used up to the present time have coupled into the resonant system at the point of highest current. As a consequence, they must present at this point a low impedance (perhaps a few ohms or a fraction of an ohm) which is transformed by the coupled resonator to a high level at the slot opening. There are two principal means of developing the low impedance in series with the resonator. In one, the waveguide line opens directly into the back of one resonator and the impedance is transformed down from that of the external line by suitable changes in the cross section of the waveguide. In the other, the waveguide communicates with the resonator by means of a nonresonant iris, which shunts part of the high guide

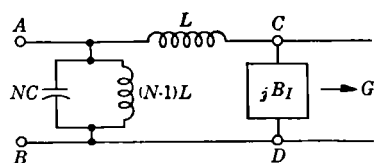


FIG. 5-18.—Schematic network of an iris-coupled output.

impedance. It is, of course, possible to combine the two arrangements. It may be noted that since the anode height and pole piece separation of most tubes is considerably less than a half wavelength and, hence, less than the cutoff dimension of rectangular guide, some artifice is almost

always necessary to effect a coupling between the short block and the wide guide.

*Iris Coupling.*—Iris coupling has not been extensively used because it has the inherent disadvantage of pulling the tube frequency. The circuit may be rather crudely represented by the arrangement shown in Fig. 5-18 in which the iris is represented simply as a shunt susceptance  $jB_I$ . It is likely that this is an oversimplification for an iris that is situated essentially between lines of unequal characteristic impedance. It will usually be the case that  $\omega_0 L \gg |1/B_I|$  and  $B_I \gg G$ , where  $G$  is the load admittance in shunt with the iris. If this is so, the combination of iris and load gives an impedance in series with  $\omega_0 L$  of value

$$\frac{1}{(jB_I + G)} \sim \left( \frac{1}{jB_I} \right) + \left( \frac{G}{B_I^2} \right).$$



Then, the additional shunt admittance at  $AB$  is

$$\frac{1}{j\omega_0 L + \frac{1}{jB_I} + \frac{G}{B_I^2}} - \frac{1}{j\omega_0 L} \sim \frac{1}{\omega_0^2 L^2} \left( \frac{1}{jB_I} + \frac{G}{B_I^2} \right) = \frac{1}{j\omega_0^2 L^2 B_I} + \frac{G}{\omega_0^2 L^2 B_I^2}.$$

Using the expressions already derived for  $Q_E$  and for the frequency shift  $\delta\omega$ , one finds

$$\frac{\delta\omega}{\omega_0} = \frac{1}{2Q_E} \cdot \frac{B_I}{G}. \quad (44)$$

Since  $B_I$  has been supposed substantially greater than  $G$ , the frequency shift may easily be excessive. It is possible to compensate for this coupled reactance in various ways. The coupled resonator may be made with a somewhat different inductance from the others, in such a way that the added reactance is balanced. Also by combining the iris coupling with suitable external transformers or with another iris from which the original iris is separated by a cavity, the frequency shift may be eliminated. These methods are of frequent application in stabilized output circuits and are discussed in Chaps. 11 and 16.

*Directly Coupled Waveguide Circuits.*—The most common method of coupling a waveguide to the resonant system is to allow it to open directly into the latter and to use external transformers to obtain the correct impedance. The two most familiar ways of effecting the transformation are by the use of a quarter-wavelength section of low-impedance guide or through tapered sections. The latter supplies a perfectly adequate means of arriving at a broadbanded transformer but is frequently mechanically difficult. The tapered section is designed to have its characteristic impedance change continuously and slowly (in terms of wavelengths) from the high level of the external guide to the required low level. Using well-known formulas for optimum frequency insensitivity in the taper excellent matches may be obtained. The process, however, entails the construction of a guide the cross section of which is varying in a rather involved way and, in addition, should be rather long for good results.<sup>1</sup>

The simplest transformer that can be used is a quarter-wavelength line the characteristic impedance of which lies between that of the external guide and the desired series impedance at the resonator. The transforming line may take a variety of forms, the choice being principally dictated by mechanical and dimensional considerations. In most cases it must be a so-called "lumped" line or one in which the capacitive and inductive parts of the guide are segregated to some extent. Such lines possess the property that their cutoff wavelength exceeds considerably

<sup>1</sup> See L. Tonks, GE Report No. 197, Mar. 23, 1943.

their "long" dimension, thus permitting access to a short tube. Another method of producing a high cutoff wavelength in a small space is to use a dielectric-filled guide. This technique has not been extensively used, but quartz-filled tapers have been utilized in one type of magnetron. When a guide of intermediate cross section is used, there will be transformer effects at the interfaces between this guide and the external line and between the guide and the tube. Generally, then, Fig. 5-19 will be needed to represent the whole output circuit. It will be supposed that the effect of any discontinuities (iris window) beyond the transformer are neglected and the external line terminated.

Suppose that the transformer constants of the three sections (proceeding from load to generator) are  $\vec{\alpha}_{22}, \vec{\beta}_2, \vec{\alpha}_{12}; 0, 0, \pi$ ; and  $\vec{\alpha}_{21}, \vec{\beta}_1, \vec{\alpha}_{11}$  respectively. They might also be written  $\vec{\alpha}_{22}, \vec{\beta}_2, 0; 0, 0, \vec{\alpha}_{12} + \pi - \vec{\alpha}_{21}$ ;

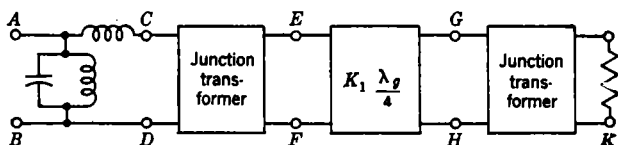


FIG. 5-19a.—Equivalent circuit for quarter-wavelength coupling.

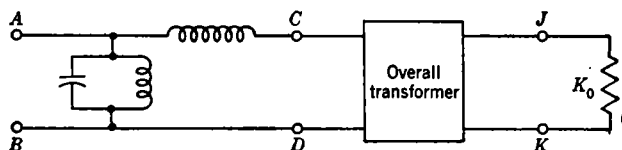


FIG. 5-19b.—Reduced equivalent circuit for quarter-wavelength coupling

and  $0, \vec{\beta}_1, 0$ , where  $\vec{\alpha}_{11}$  is ignored, since it is indistinguishable from the external line. Measurements on several such transformers have indicated that  $\vec{\alpha}_{22}$  and  $\vec{\alpha}_{12} - \vec{\alpha}_{21}$  are very small; this is equivalent to the statement that the end effects of the quarter-wavelength section are small. This observation has been made on output circuits in which the transformer cross section was such that the electric fields were largely confined to a region with a small dimension parallel to the  $E$ -vector. There was thus little interpenetration of the transformer and tube or external guide fields, with a consequent small end correction. Thus, ignoring  $\vec{\alpha}_{22}$ ,  $\vec{\alpha}_{12} - \vec{\alpha}_{21}$ , the transformer becomes simply  $0, \vec{\beta}_2, \pi$  or, in other words, a quarter-wavelength transformer whose apparent characteristic impedance is not that of the physical guide  $K_1$  but  $K_2$ , for example. The output circuit is thus modified as shown in Fig. 5-19b.

Let the load impedance be  $K_0$ , the equivalent characteristic impedance of the intermediate guide  $K_1$ , the operating wavelength  $\lambda$ , the intermediate guide wavelength  $\lambda_g$ , and its cutoff wavelength  $\lambda_{c0}$ . Further suppose, now, that  $\lambda$  is unrestricted, so that the intermediate guide is not necessarily exactly a quarter wavelength long. Suppose that its electrical length is  $\phi = 2\pi l/\lambda_g$ , where  $l$  is its physical length. One has

$$\frac{Z_1 - K_1}{Z_1 + K_1} = e^{i\phi} \frac{K_0 - K_1}{K_0 + K_1}, \quad (45)$$

where  $Z_1$  is the impedance seen at  $CD$ . For  $\phi = \pi$ ,  $Z_1 = K_1^2/K_0$ . Differentiating logarithmically and setting  $\lambda = \lambda_0$ , the wavelength at which  $l = \lambda_0/4$ ,

$$\begin{aligned} \frac{dZ_1}{d\lambda} \left( \frac{1}{Z_1 - K_1} - \frac{1}{Z_1 + K_1} \right) &= j \frac{\partial \phi}{\partial \lambda} = -j \cdot 2\pi l \frac{1}{\lambda_g^2} \frac{\partial \lambda_g}{\partial \lambda} \\ \frac{dZ_1}{d\lambda} &= -\frac{Z_1^2 - K_1^2}{2K_1} \cdot 2\pi l \cdot \frac{1}{\lambda_g^2} \cdot \frac{\lambda_g^2}{\lambda^3} = +j \frac{\pi}{2} \left( \sqrt{\frac{K_0}{Z_1}} - \sqrt{\frac{Z_1}{K_0}} \right) Z_1 \cdot \frac{\lambda_g^2}{\lambda^3}, \end{aligned} \quad (46)$$

where the relation  $d\lambda_g/\lambda_g^2 = d\lambda/\lambda^3$  has been used. Transforming the output impedance at the back of the resonator  $Z_1$  to the resonator opening, one has for the additional admittance at the slot,

$$Y_e = G_e + jB_e = Y_r^2 Z_1,$$

when  $Y_r \ll 1/Z_1$ . Explicitly

$$G_e = Y_r^2 \frac{K_1^2}{K_0} = Y_r^2 Z_1, \quad (47)$$

$$B_e = \frac{\pi}{2} Y_r^2 Z_1 \left( \sqrt{\frac{K_0}{Z_1}} - \sqrt{\frac{Z_1}{K_0}} \right) \left( \frac{\lambda_g}{\lambda_0} \right)^2 \left( \frac{\delta\omega_g}{\omega_0} \right);$$

or since  $K_0 \gg Z_1$ ,

$$= \frac{\pi}{2} Y_r^2 \sqrt{K_0 Z_1} \left( \frac{\lambda_g}{\lambda_0} \right)^2 \left( \frac{\delta\omega_g}{\omega_0} \right), \quad (48)$$

where  $\delta\omega_g$  is the departure of the frequency from the resonant frequency of the transformer. Using the relation  $Q_E = NY_r/G_e$ , one has

$$B_e = \frac{\pi}{2} Y_r^2 \sqrt{\frac{NK_0}{Q_E Y_r}} \left( \frac{\lambda_g}{\lambda_0} \right)^2 \left( \frac{\delta\omega_g}{\omega_0} \right). \quad (49)$$

This may be combined with the earlier expression  $\delta\omega_L/\omega_0 = -B_L/2NY_r$  for the frequency shift due to reactive loading to find the resonant frequency of the system when the transformer is not exactly a quarter wavelength long. It is important to note that up to changes of the first order in frequency, the resistive part of  $Z_1$  is constant. The changes in series reactance will produce some effect on  $G_e$  by varying the total reactance in series with  $Re(Z_1)$ . It is instructive to calculate the stored

energy in the output circuit. If, as has been tacitly assumed above, the junction transformers are frequency insensitive, the energy storage in the output may be compared with that of the resonant system by evaluating the ratio  $[\omega_0(\partial B_e/\partial \omega_0)]/NY_r = r$ . Using Eq. (49), there follows

$$r = \frac{\pi}{2} \sqrt{\frac{K_0 Y_r}{N Q_E}} \left( \frac{\lambda_g}{\lambda_0} \right)^2. \quad (50)$$

For a typical example with  $Q_E = 400$ ,  $K_0 = 400$ ,  $Y_r = 0.025$  mho,  $N = 10$ ,  $\lambda_g/\lambda_0 = 1.25$ , Eq. (50) gives  $r = 0.12$ . Equation (50) may easily be converted to other forms that put the dependence on other variables in evidence. The energy storage in this type of output circuit may be relatively high as Eq. (50) indicates.

The lines used for the quarter-wavelength section are generally "lumped," and some cross sections that have been used are shown in

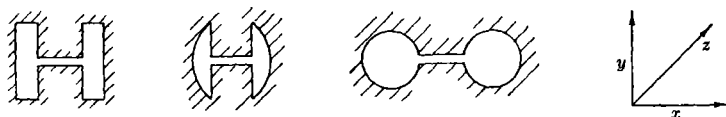


FIG. 5-20.—Example of "lumped" guides.

Fig. 5-20. In all cases the guide is essentially divided into two regions, one of which is capacitive with high electric fields in a narrow crossbar and the other inductive with high currents flowing in a more or less cylindrical section. The cutoff wavelength of such a guide may plainly be higher than that of a rectangular one of the same width, since the capacitance has been increased in the center and the inductance at the outside. The problem of calculating the cutoff in these sections is exactly analogous to that arising in calculating resonant frequencies of unstrapped oscillators. Thus, in order to find the fundamental transverse electric mode, one needs a solution of

$$\nabla^2 T + \chi^2 T = 0 \quad \text{with} \quad \frac{\partial T}{\partial n} = 0 \quad (51)$$

on the walls of the guide,<sup>1</sup> where  $\partial/\partial n$  denotes normal differentiation and  $\chi = 2\pi/\lambda$ . The fields are then given by  $E_x = -\partial T/\partial y$ ,  $E_y = \partial T/\partial x$ , and  $H_z = (\chi/jc\mu_0)T$ . Since the gap in the crossbar is usually small compared with the length of the latter, it is possible to put  $E_x = 0$  and to suppose  $E_y$  independent of  $y$  in the capacitive part (see Fig. 5-21). If the dimensions of the cylinder are small compared with  $\lambda/2\pi$ , one may solve Laplace's equation rather than Eq. (51) in this region and match the solutions at the junction by equating  $T$  and  $\partial T/\partial n$  there.

<sup>1</sup> See S. A. Schelkunoff, *Electromagnetic Waves*, Van Nostrand, New York, 1943, p. 380.

Calling  $T_0$  the solution of Laplace's equation in the cylinder with  $\partial T_0 / \partial n = 0$ , except at the junction, where  $\partial T_0 / \partial n = 1$ , one may obtain the equation for  $\chi_0 = 2\pi/\lambda_0$ , where  $\lambda_0$  is the cutoff wavelength

$$A \tan \chi_0 l = \frac{d}{\chi_0} + \chi_0 \int T_0 dS. \quad (52)$$

In Eq. (52),  $A$  is the area of the cylinder,  $l$  the length and  $d$  the width of the crossbar, and the integration is carried over the cylinder. If  $\chi_0 l$  is small, this gives

$$\chi_0^2 = \frac{d}{l - \frac{\int T_0 dS}{A}} \cdot \frac{1}{A}, \quad (53)$$

which is the result obtained by lumping the capacitance and inductance completely and taking account of an end correction  $-\int T_0 dS/A$  to

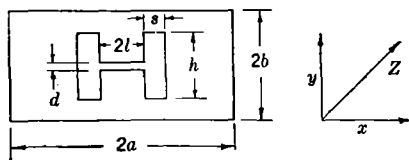


FIG. 5-21.—H-section guide.

the length of the condenser. The calculation of  $T_0$  is not difficult for simple geometrical shapes of the cylinder. For  $H$ -sections as shown in Fig. 5-21,  $\chi_H$  may be found from

$$\tan \chi_H l = \chi_H \frac{sd}{h} \left[ \frac{1}{\chi_H^2 s^2} - \frac{1}{3} - \frac{h}{\pi s} \left( 1 - \log_e \frac{\pi d}{h} \right) \right] \quad (54)$$

provided that  $2\pi s/h > 1$ .

The impedance of the lumped guide on the  $P - V^2$  basis may be found from the relation

$$K = \frac{2\omega\mu d}{\Gamma} \frac{\left( \frac{\partial T}{\partial x} \right)_{x=0}}{\left( \chi \frac{\partial T}{\partial \chi} \right)_{x=0}}. \quad (55)$$

For  $H$ -sections this becomes

$$K = \frac{377}{1 - \left( \frac{\lambda}{\lambda_H} \right)^2} \frac{\frac{d}{l}}{\left( 1 - \frac{\sin 2\chi_H l}{2\chi_H l} \right) + \frac{2d \cos^2 \chi_H l}{l s h \chi_H^2}} \quad (56a)$$

or

$$K \cong \frac{377 \frac{d}{2l}}{\sqrt{1 - \left(\frac{\lambda}{\lambda_H}\right)^2}} \quad \text{ohms.} \quad (56b)$$

The junction between the lumped guide and rectangular guide presents a problem that may be handled in a satisfactory manner provided the slot of the crossbar is narrow. The fields in the two guides may each be expanded in terms of the appropriate normal modes. The tangential field in the rectangular guide is then put equal to that in the lumped guide across the opening of the latter and zero elsewhere in the same plane. The tangential magnetic fields are equated across the opening. Using these relations and the orthogonality of the wave functions in each guide, a series of linear equations in the mode amplitudes may be obtained. So far the treatment is exact. One now neglects all but the principal modes or, in other words, supposes that there is no shunt reactance at the junction. Carrying out this procedure, the principal transformer constant  $\Delta$  for the junction is found to be

$$\Delta = \sqrt{\frac{1 - \lambda^2/\lambda_H^2}{1 - \lambda^2/\lambda_R^2}} \frac{1}{[\iint (\vec{E}_{OH} \cdot \vec{E}_{OR}) dS_H]^2}, \quad (57)$$

where  $\lambda_H$  and  $\lambda_R$  are the cutoff wavelengths in the H-section and the rectangular guide and  $\vec{E}_{OH}$  and  $\vec{E}_{OR}$  are the vector tangential electric fields in the fundamental modes, while the integral is carried over the common interface.  $\vec{E}_{OH}$  and  $\vec{E}_{OR}$  are normalized so that

$$\iint (\vec{E}_{OH} \cdot \vec{E}_{OH}) dS_H = \iint (\vec{E}_{OR} \cdot \vec{E}_{OR}) dS_R = 1. \quad (58)$$

For H-to-rectangular junctions,

$$\Delta = \left( \frac{1 - \frac{\lambda^2}{\lambda_H^2}}{1 - \frac{\lambda^2}{\lambda_R^2}} \right)^{1/2} \frac{abl}{8d} \left[ \frac{1 - \frac{\sin 2\chi_H l}{2\chi_H l} + \frac{2d \cos^2 \chi_H l}{lsh\chi_H^2}}{\left[ \frac{\chi_H}{\sin s\chi_H} \frac{\cos \chi_H l \cos \chi_R(l+s) - \cos \chi_R l \cos \chi_H(l+s)}{\chi_H^2 - \chi_R^2} \right]^2} \right], \quad (59)$$

where  $\chi_H = 2\pi/\lambda_H$  and  $\chi_R = 2\pi/\lambda_R$ . When all H-section dimensions are small compared with  $\lambda_H$  and  $\lambda_R$ , this may be written as

$$\Delta = \left( \frac{1 - \frac{\lambda^2}{\lambda_H^2}}{1 - \frac{\lambda^2}{\lambda_R^2}} \right)^{1/2} \frac{abl}{8d} \cdot \frac{2}{\left( l + \frac{s}{2} \right)^2} \quad (60)$$

Equation (59) gives excellent agreement with experiment when the assumptions of the analysis are fulfilled. The transformer constants were measured for an H-section junction at several wavelengths from 7.5 to 13.5 cm. The end corrections were found to be entirely negligible, while the values of

$$\Delta \sqrt{\frac{1 - \frac{\lambda^2}{\lambda_R^2}}{1 - \frac{\lambda^2}{\lambda_H^2}}}$$

which should, according to Eq. (59), be frequency independent, were found to be as indicated in Table 5-1. The dimensions in this case were such that the slot width was small compared with the guide width. It should be noted that the transformer effect at the junction is such as to raise the impedance level even above that of the rectangular guide. Using this value of  $\Delta$  one may now calculate  $E_y/H_z$  at the center of the crossbar at the junction with the tube and obtain

TABLE 5-1.—TRANSFORMER CONSTANTS OF AN H-SECTION JUNCTION

Dimensions of H-section:  $d = 0.191$  cm;  $l = 0.952$  cm;  $s = 0.495$  cm;  $h = 1.95$  cm  
 Dimensions of rectangular guide:  $b = 3.81$  cm;  $a = 8.58$  cm

$\lambda_0$ , cm	$\Delta \sqrt{\frac{1 - \frac{\lambda^2}{\lambda_R^2}}{1 - \frac{\lambda^2}{\lambda_H^2}}}$	$\rightarrow$ $\alpha_R$ , degrees	$\rightarrow$ $\alpha_H$ , degrees
7.16	36.3	+10.0	+9.5
8.46	34.6	+4.3	+5.0
9.51	39.9	-3.6	+2.2
10.58	32.6	-0.7	-2.2
11.51	36.0	-1.4	-3.0
12.57	36.7	+5.0	-6.5
	AVG 36.0 $\pm$ 2.2*		

\* The calculated value of  $\Delta \sqrt{1 - (\lambda^2/\lambda_R^2)/1 - (\lambda^2/\lambda_H^2)}$  was 36.3.

$$\frac{E_y}{H_z} = \eta_0 \frac{\sqrt{1 - \frac{\lambda^2}{\lambda_R^2}}}{\sqrt{1 - \frac{\lambda^2}{\lambda_H^2}}} \left[ \iint (\vec{E}_{oH} \cdot \vec{E}_{oR}) dS_H \right]^2, \quad (61)$$

where  $\eta_0 = 377$  ohms. To a first approximation the coupled resistance will be

$$R = \frac{d}{2l} \cdot \frac{E_y}{H_z}, \quad (62)$$

since it may be assumed that the magnetic field in the cylinders is very loosely coupled to the resonant system. For H-sections the result becomes

$$R = \frac{4d^2}{l^2 ab} \cdot \frac{\left(1 - \frac{\lambda^2}{\lambda_R^2}\right)^{1/2}}{1 - \frac{\lambda^2}{\lambda_H^2}} \cdot \frac{\left(\frac{\chi_H}{\sin s\chi_H} \cos l\chi_H \cos (l+s)\chi_R - \cos l\chi_R \cos (l+s)\chi_H\right)^2}{1 - \frac{\sin 2l\chi_H}{2l\chi_H} + \frac{2d \cos^2 l\chi_H}{lsh\chi_H^2}} \cdot 377 \text{ ohms.} \quad (63)$$

Using the approximation of Eq. (60) one has

$$R = \frac{2d^2}{ab} \left(1 + \frac{s}{2l}\right)^2 \frac{\left(1 - \frac{\lambda^2}{\lambda_R^2}\right)^{1/2}}{1 - \frac{\lambda^2}{\lambda_H^2}} \cdot 377 \text{ ohms.} \quad (64)$$

This equation indicates the critical dependence of the coupling upon the width of the crossbar  $d$ . In strapped magnetrons the fields in the resonant system vary along the length of the anode as  $\cosh \alpha x$ , where  $x$  is again measured from the median plane (see Chap. 4), while the fields in the crossbar vary as  $\cos \chi_H x$ . This fact will affect the coupling at the junction with the resonant system, and there will be some transformer effect. This may be taken into account by multiplying  $R$  by another factor  $[\int (\vec{E}_{oH} \cdot \vec{E}_{o, res})]^2$ , where  $\vec{E}_{o, res}$  is the normalized resonator field across the junction. This factor may be evaluated for an H-section and is

$$\frac{2}{l \left(1 - \frac{\sin 2l\chi_H}{2l\chi_H} + \frac{2d \cos^2 l\chi_H}{lsh\chi_H^2}\right)} \frac{\left(\int_0^l \cosh \alpha x \cos \chi_H x dx\right)^2}{\int_0^l \cosh^2 \alpha x dx} \quad (65)$$

The magnitude of this correction will be small unless the tube is heavily strapped. The formulas of Eqs. (63) and (64) appear to give very close agreement with experimental results. For example, when applied to the case of the 4J50, a 16 hole-and-slot 3-cm magnetron having a quarter-wavelength H-section transformer of this type, a cold pulling figure



of 9.3 Mc is calculated. This compares favorably with the experimental values which are distributed close to 10 Mc.

One sees that contrary to the assumption of an earlier paragraph, there is some frequency dependence of the transformer effect at the junction given by the term  $\left[ \frac{1 - (\lambda^2/\lambda_H^2)}{1 - (\lambda^2/\lambda_R^2)} \right]^{1/2}$ . This may be minimized by making  $\lambda_H = \lambda_R$ .

*Iris Windows.*—The vacuum seal in waveguide-output circuits is usually an iris window. This consists of a disk of low-loss dielectric,

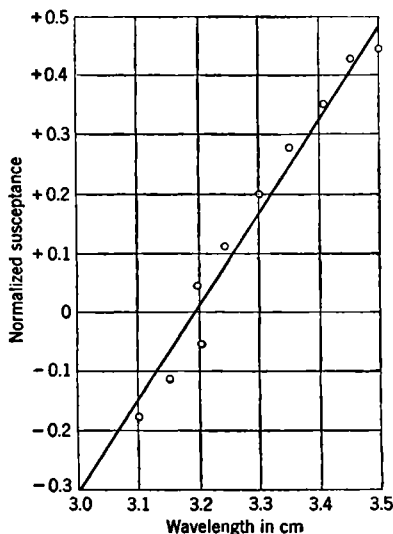


FIG. 5-22.—Variation of shunt susceptance with thickness of window.

usually glass, sealed across a metal iris opening. By a suitable choice of the glass thickness and iris diameter it is possible to obtain a window that, when placed between circular choke joints, produces a satisfactory match over a relatively broad band. Since the window is placed between guides of similar characteristic impedance, it behaves like a pure shunt susceptance. Figure 5-22 shows the variation of this shunt susceptance vs. wavelength for a particular window. The apparent external  $Q$  of the window loaded by the matched line is 2.6. Thus there is little energy stored in the window itself. By placing the window at a suitable distance from the junction with the intermediate guide, the variations in the resistive component of the reactance at the tube may be minimized.



**PART II**  
**ANALYSIS OF OPERATION**



## CHAPTER 6

### THE INTERACTION OF THE ELECTRONS AND THE ELECTROMAGNETIC FIELD

By L. R. WALKER

**6.1. Introduction.**—The central problem of the present chapter is to examine the interaction of the electron stream with the electromagnetic field of the resonator system in the annular region bounded by anode and cathode. At present the design of a magnetron of given characteristics, such as wavelength, magnetic field, operating voltage, power output, and pulling figure, is in principle a straightforward matter, the difficulties arising in practice being largely those of realizing the design mechanically. In view of this fact it is surprising to find that our understanding of the interaction processes is largely of a qualitative nature. That successful design should be possible may be ascribed to three facts: (1) A formula is at hand that has a sound theoretical basis and full support from experiment for estimating the voltage at which a magnetron of given dimensions will operate when a definite magnetic field is applied. (2) The behavior of the electron cloud may be shown to depend upon a small number of parameters derived from the tube dimensions and the operating variables (see Chap. 7). Thus, it is possible to say that any two magnetrons which may be run under conditions that make the values of these parameters the same will operate with equal efficiency. One magnetron design may, in this way, be derived from another that is known to be satisfactory. (3) Finally, experience has shown that the efficiency of magnetrons is remarkably insensitive to large changes in magnetic field and d-c current and, to a somewhat lesser extent, to changes in load. A performance chart for a 3-cm magnetron is shown in Fig. 6.1, which may be regarded as typical of present design. Figure 6.2 shows the effect of load upon the efficiency of the same tube. In this figure the electronic efficiency has been plotted as a function of the electronic (or load) conductance. As a result of this broad range of satisfactory operational conditions it is evidently possible to allow considerable leeway in the choice of design parameters and still be confident that a good magnetron will be obtained. Presumably, it is a consequence of this happy situation that it has not been thought essential during the wartime development of magnetrons to attack thoroughly the problem of understanding the processes whereby the electrons transfer energy to the oscillating field.

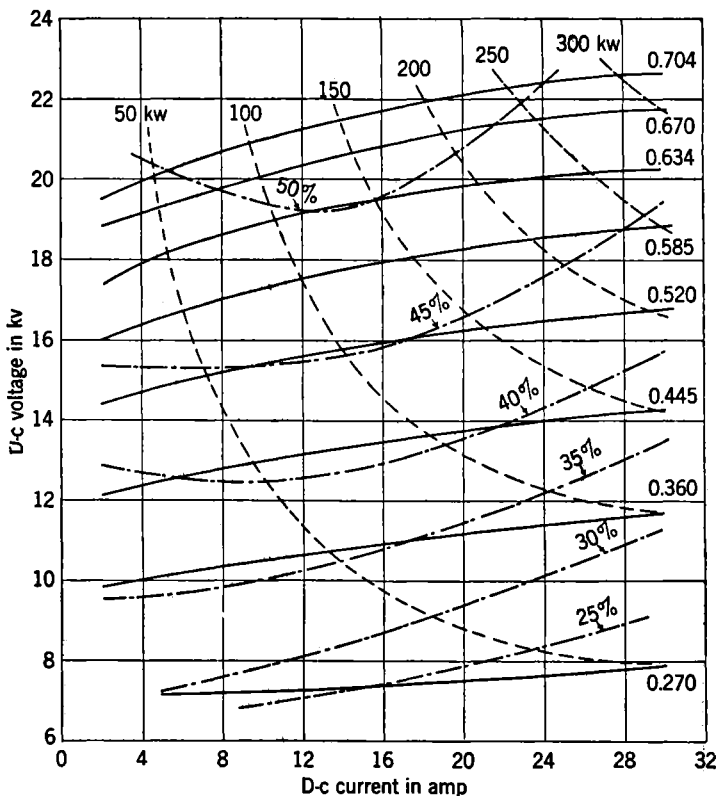


FIG. 6-1.—D-c voltage vs. d-c current for typical 3-cm magnetron ( $N = 16$ ) with — magnetic field in webers/sq meter, ---- power output in kw, and -.- efficiency in per cent.

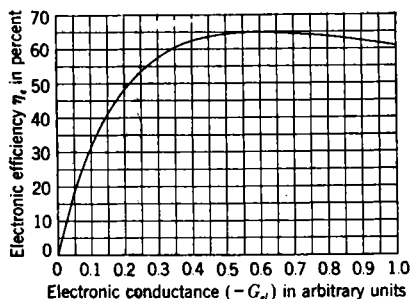


FIG. 6-2.—Electronic efficiency as a function of electronic conductance for a typical 3-cm magnetron ( $N = 16$ ).

There is little doubt that an acceptable qualitative description of the process may be given, and the picture that this offers has been adequately verified in those few instances for which numerical calculations have been undertaken. Quantitatively and analytically, however, the progress toward a solution has been meager. The steady-state problem may be formulated in the following way. From a given applied d-c voltage and r-f voltage at the anode and a uniform magnetic field in an interaction space of known dimensions, calculate the d-c and r-f currents that will flow to the anode. Then from these data, the input d-c power and the output r-f power may be calculated and, consequently, the efficiency. Knowing the in-phase and out-of-phase components of the r-f current and the r-f voltage, the admittance of the electron stream is calculable, and this will be the negative of the load admittance measured at suitably defined terminals on the anode surface. This problem has not been solved analytically under any set of operating conditions, even in an approximate fashion. Numerical solutions have been obtained for a few isolated cases but never for a range of values of the operating parameters in the same tube.

Turning from the steady-state problem to that of the initiation of oscillations, an equally unsatisfactory condition is revealed. No rigorous criterion has been established that will determine whether or not, under given conditions of magnetic field, voltage, and load, oscillations will build up from noise level. Similarly, there is no theory of starting time, which would require a solution of the problem with a constantly increasing d-c voltage.<sup>1</sup>

Although the inconclusive status of many of these problems may be attributed to the fact that emphasis has been laid on empirical development, they nevertheless present formidable analytical difficulties. In the account of the theory given in this chapter an attempt is made to formulate the problem in a straightforward way and thus to show where the difficulties arise that prevent a complete solution. An outline of various attempts to solve the main problem and certain simplified versions of it are given.

**6-2. The Assumptions Underlying the Analysis.**—Any discussion of the interaction problem must begin by making a number of assumptions, which are of varying degrees of plausibility. The more familiar of these will be discussed before setting up the equations of motion and the field equations. The justification and significance of some statements made here may not, however, appear until later. Reference to Fig. 6-3 will indicate the region in which the flow of electrons is to be investigated. The cylindrical cathode of radius  $r_c$  is held at zero potential; the concentric

<sup>1</sup> See, however, Chaps. 8 and 9 of this volume for an empirical approach to the analysis of transient behavior.

anode of radius  $r_a$  has applied to it a d-c potential  $V_0$ . In the annular region bounded by anode and cathode there exist r-f fields that form part of the total field of the resonant system and that must, therefore, satisfy certain boundary conditions at the anode. The applied magnetic field is supposed everywhere to be constant in magnitude and to be parallel to the axis of the cylinders, which axis is also taken as the  $z$ -axis of a system of polar coordinates.

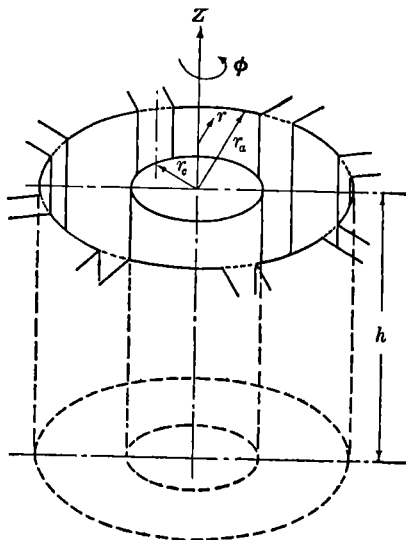


Fig. 6-3.—Interaction space and related coordinate system for ( $N = 8$ ) magnetron.

The first assumption is that the whole problem may be reduced to a two-dimensional one. In real magnetrons this can be a good approximation only for regions near to the median plane of the tube, since there will be appreciable end effects at the extremities of the interaction space. Here there will be, because of the discontinuity in the cross section of the anode block and the possible presence of straps and of hats on the cathode, a considerable modification of the tangential field, and furthermore  $z$ -components of the d-c and r-f electric fields will appear. In view of the extreme complexity of the field patterns in this region, however, it is desirable to ignore these end effects. Experimentally, no specific effects have been found that indicate critical conditions in the end regions, and it is roughly true that a magnetron of double length behaves like one of single length operating at half the current and power level if the effects of length in mode spectrum are compensated for. Thus, it is probably justifiable at present to treat the magnetron as part of an infinite cylindrical structure in which all the electric fields are tangential and



independent of the  $z$  coordinate and in which the magnetic fields are purely axial. Similarly it will be supposed that the motion of the electrons is wholly in the  $(r-\phi)$ -plane. Since the thermal velocity of emission in the  $z$  direction is small, this is a reasonable assumption in the absence of axial electric fields. It may be noted that the function of cathode hats, whether electric or magnetic, is to cause a deliberate distortion of the electric or magnetic fields at the ends of the interaction space, thus tending to keep electrons within the interaction space despite the effects of space-charge repulsion in an axial direction.

It is customary to assume that relativistic corrections and other effects that depend upon the finite velocity of propagation of light may be ignored. These include the relativistic variation of mass with velocity, the influence of the r-f magnetic field on the electron motion, the change in d-c magnetic field produced by the circulating currents, and the use of the wave equation rather than Laplace's equation. The conditions under which it is valid to make these approximations are discussed at some length in the succeeding section. It will be found that some of the simpler consequences of the equations of motion may be preserved in relativistic form.

Conditions of space-charge limitation are generally supposed to prevail at the cathode, and, in consequence, the potentials and radial components of all fields are supposed to vanish there. It is impossible to test the accuracy of this hypothesis, for there is no simple state of the space charge in a magnetic field the theory of which has been sufficiently worked out to provide an experimental test. At present one can merely assume the condition true until it is demonstrated that it leads to false results. It is true that the current densities drawn in magnetrons frequently exceed substantially those which can be drawn from identical cathodes in pulsed diodes under verifiably space-charge-limited conditions. However, the existence of excess cathode heating during magnetron operation indicates the presence of back bombardment by electrons, and the known secondary-emitting properties of oxide cathodes suggest that secondary emission is probably sufficient to yield the required current densities (see Chap. 12). The possibility of secondary emission from contaminated anode surfaces is a further complication which is ignored.

Associated closely with the assumption of space-charge limitation is the hypothesis of a zero velocity of emission of the electrons from the cathode. Plainly, the electrons have actually a thermal velocity distribution at the cathode, but it seems reasonable to suppose, since the mean thermal energy is so small compared with the energies acquired by the electrons in moving through the field, that the effect of the distribution is negligible in an operating magnetron. It will appear that

there are certain oversimplified conditions having critical solutions that might be affected by an energy distribution at the cathode, but these are far from simulating the conditions in a real tube. The experimental observation that, for many tubes, operation is independent of cathode temperature over a wide range may confirm the assumption that the initial velocity distribution of the electrons is not significant.

A most important simplification in the problem is effected by a further set of assumptions concerning the nature of the field with which the electrons interact. These simplifications may be combined into the definition of an anode voltage of the form  $V_0 + V_1 \cos(n\phi - \omega_0 t)$ , where  $n$  is the mode number and  $\omega_0$  is  $2\pi$  times the frequency of the resonant system. The principal point here is that the r-f voltage is represented by a traveling wave. This assumption will be discussed more fully in Sec. 6-3, but the argument may be summarized here. The electromagnetic field in the interaction space may always be expanded in a series of Fourier components, each of which represents a traveling or rotating wave in the interaction space. For a particle moving so that its angular velocity is close to that of the slowest of these waves, the other components (at least for the condition of  $\pi$ -mode operation) represent a high-frequency perturbation the effect of which can be ignored in general. A more complicated situation arises, however, for modes other than the  $\pi$ -mode. It will be shown that for a single rotating component it is always possible to define a "voltage" or potential in which the electrons move. The form used above for the anode voltage also assumes that the anode surface is a zero impedance sheet at the harmonic frequencies  $2\omega_0$ ,  $3\omega_0$ , etc., so that the harmonic components of current induce no corresponding voltage components on the anode.

The steady-state problem may now be formulated again for the sake of clarity. In the annular region between two coaxial cylinders there exists a constant, uniform magnetic field  $B_z$  parallel to the axis of the cylinders. The inner cylinder of radius  $r_c$  is held at zero potential, and the radial fields at its surface also vanish; electrons are emitted from this surface with zero velocity, and their  $z$ -component of velocity remains zero. The electromagnetic fields are transverse electric,<sup>1</sup> and a potential  $V_0 + V_1 \cos(n\phi - \omega_0 t)$  exists at the surface of the outer cylinder of radius  $r_a$ . It is desired to calculate the radial current density  $J_r$  at the anode in the form of a Fourier series

$$J_r = J_{r,0} + J_{r,1} \cos(n\phi - \omega_0 t) + J_{r,-1} \sin(n\phi - \omega_0 t) \\ + J_{r,2} \cos 2(n\phi - \omega_0 t) + J_{r,-2} \sin 2(n\phi - \omega_0 t) + \text{higher terms.}$$

Then the d-c power input is  $2\pi r_a h J_{r,0} V_0$  or  $I_0 V_0$ , and the r-f power output

<sup>1</sup> S. A. Schelkunoff, *Electromagnetic Waves*, Van Nostrand, New York, 1943, p. 154.

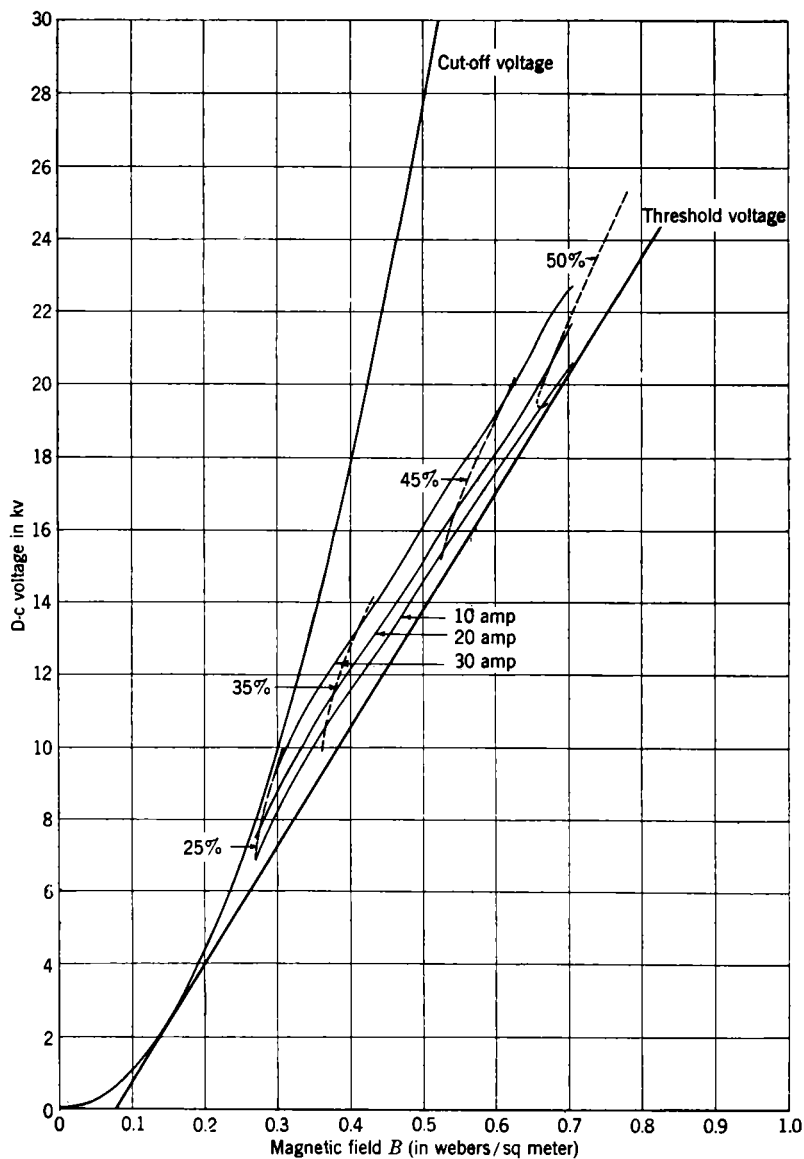


FIG. 6-4.—D-c voltage vs. magnetic field for typical 3-cm magnetron ( $N = 16$ ) with ——— current in amp, — — — efficiency in per cent.

is  $\pi r_a h J_{r,1} V_1$  or  $\frac{1}{2} I_1 V_1$ . The admittance of the electron stream is

$$2\pi r_a h \left( \frac{J_{r,1} + jJ_{r,-1}}{V_1} \right) = G_a + jB_a = \frac{I_1 + jI_{-1}}{V_1}.$$

The salient features of magnetron operation may be pointed out again by an examination of Figs. 6.1, 6.4, 6.5, and 6.6 which show the performance of strapped magnetrons in the alternative forms of  $V_0$  vs.  $I_0$  and  $V_0$

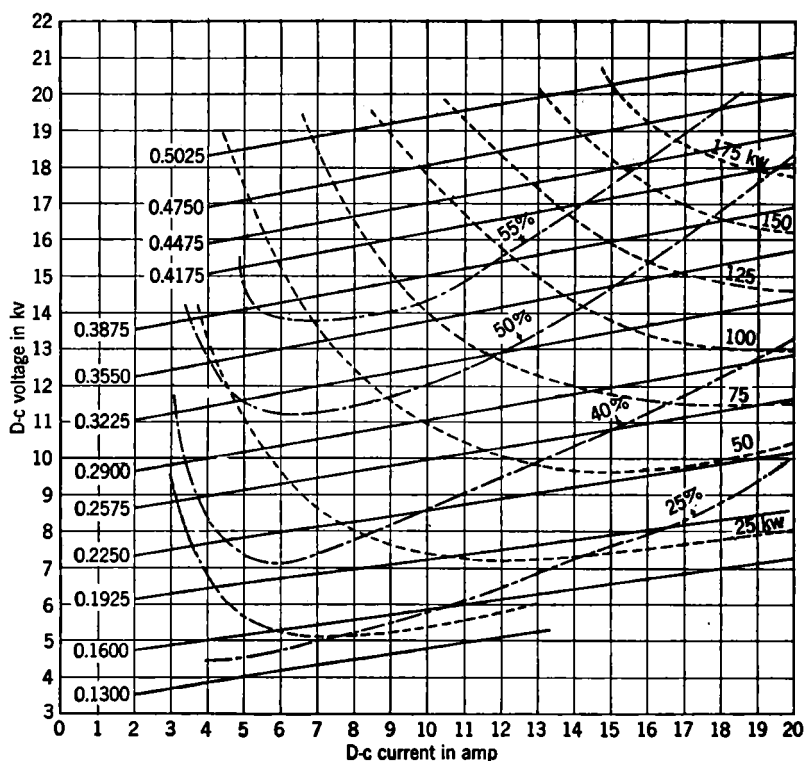


Fig. 6.5.—D-c voltage vs. d-c current for typical 9-cm strapped magnetron ( $N = 8$ ) with ——— magnetic field in webers/sq meter, - - - - power output in kw, - · - · efficiency in per cent.

vs.  $B_z$  plots. Similarly Fig. 6.7 shows the performance of a rising-sun magnetron on a  $V_0$  vs.  $I_0$  plot. Features that are typical of the normal performance of strapped magnetrons are the linearity of the operating lines in the  $V_0$  vs.  $I_0$  diagram and the linearity of the constant-current lines in the  $B_z$  vs.  $V_0$  diagram, the general tendency of efficiency to increase monotonically with magnetic field at fixed current, and the falling of the efficiency at very low and at high currents. The fall in

efficiency at low currents varies rather markedly among different types of tube. It is generally believed to be due to leakage current, a comprehensive term used to refer to electrons that reach the anode by means other than a direct interaction with the r-f field. The rising-sun magne-

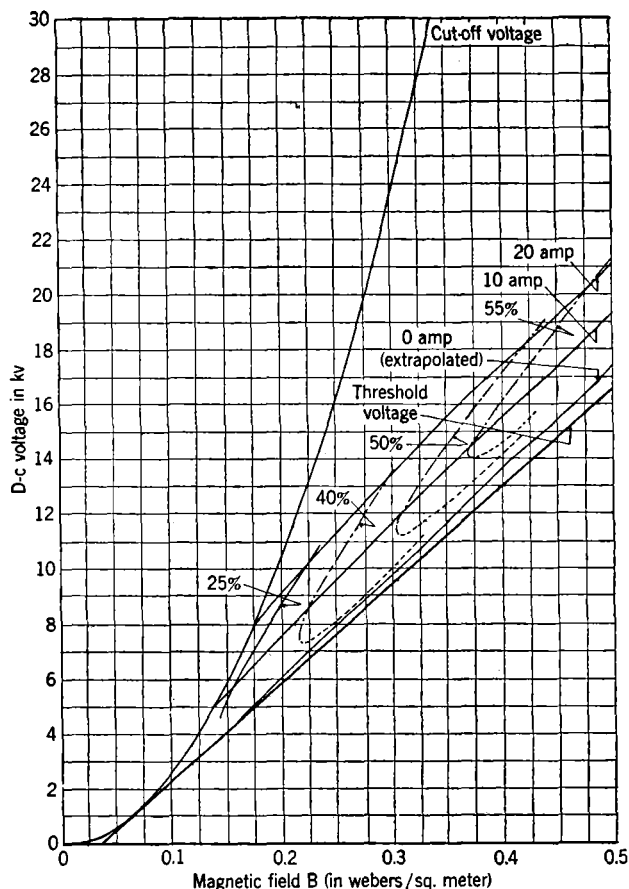


FIG. 6-6.—D-c voltage vs. magnetic field for typical 9-cm magnetron ( $N = 8$ ) with ——— current in amp, — — — efficiency in per cent.

tron is further complicated by having a region of magnetic field in which the efficiency temporarily falls off (see Chap. 3).

Figure 6-8 shows a series of operating lines on a  $(V_0, I_0)$ -plot for various values of the load conductance  $G_L = -G_a$ . The operating lines are now seen to be in general somewhat curved and to move toward higher voltages as  $G_L$  is increased. These data are derived from a 10-cm

magnetron, but the behavior is generally observed for all types. Finally Fig. 6-9 shows the variations<sup>1</sup> of  $I_1$  and  $I_{-1}$  as functions of  $V_0$  and  $V_1$ . Exhaustive data of this nature have rarely been taken, but general experience confirms the main features of Fig. 6-9.

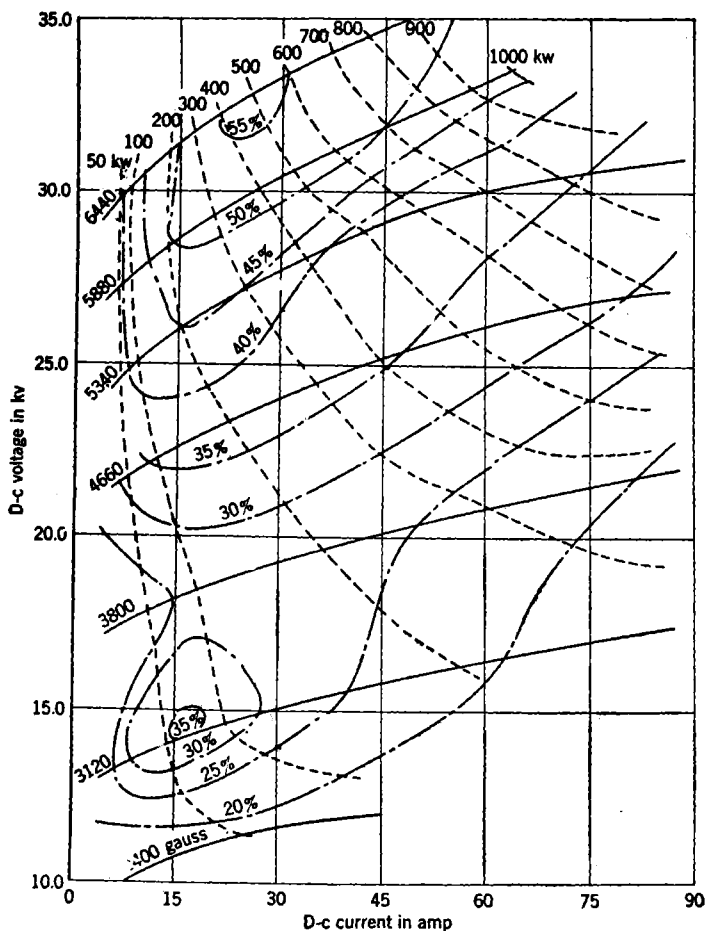


FIG. 6-7.—D-c voltage vs. d-c current for a typical 3-cm rising-sun magnetron with ——— magnetic field in gauss, - - - - power output in kw, - · - · efficiency in per cent.

All these curves lend support to the observation that the efficiency of operation of the magnetron is a slowly varying function of voltage, current, magnetic field, and load. It is also indicated experimentally

<sup>1</sup> The data from which this plot was obtained are given in the last section of Chap. 7.

that the properties of the space-charge cloud are singularly frequency independent and certainly negligibly so compared with the resonant system.

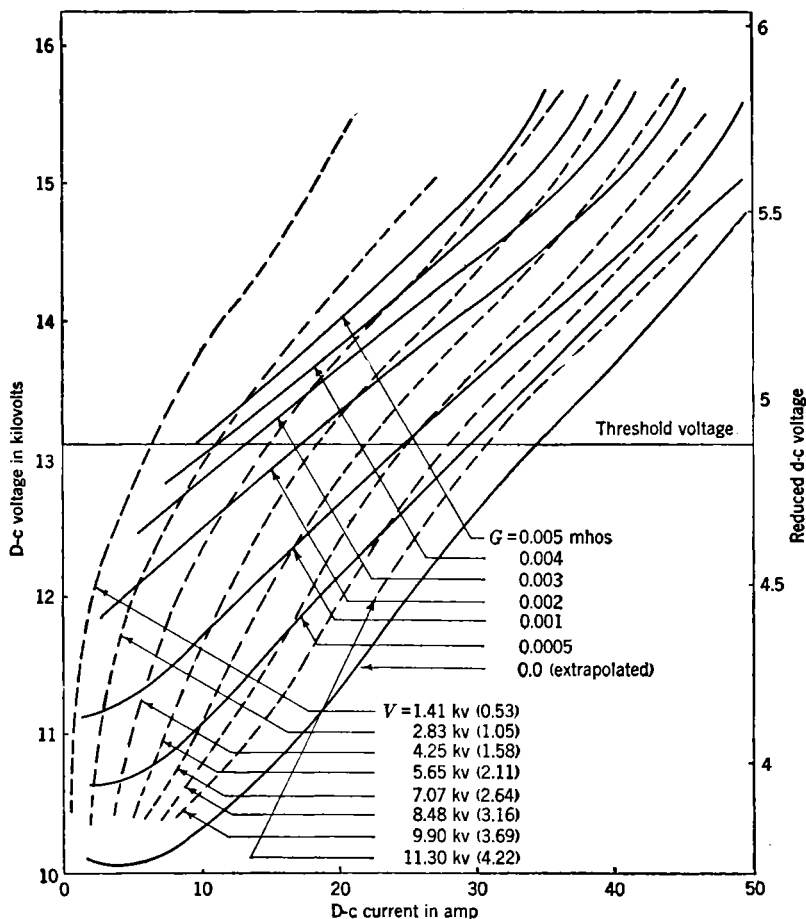


FIG. 6-8.—Operating lines for various values of electronic conductance and r-f voltage at a fixed magnetic field. 10-cm magnetron, 1371 gauss,  $N = 8$  with ——— electronic conductance in mhos, - - - - peak r-f voltage in kv. (Values in parentheses are reduced values.) Reduced linear current densities are given by  $I/36$ .

**6.3. The Field Equations.**—The Fourier analysis of the r-f fields existing in the interaction space was shown in Chap. 2 to lead to an indefinite number of components, the dependence of which upon time

and angle was governed by a term of the form  $\exp j(\omega t + p\phi)$ , where

$$p = \pm \left[ m - N \left( l + \frac{1}{2} \right) \right] = \pm [-n - lN].$$

Here  $N$  is the number of segments;  $l$  an arbitrary integer, positive or negative;  $m$  the mode number in the sense of Chap. 4; and  $n$  the usual mode number<sup>1</sup>  $= (N/2) - m$ . Waves for which  $p$  is negative travel

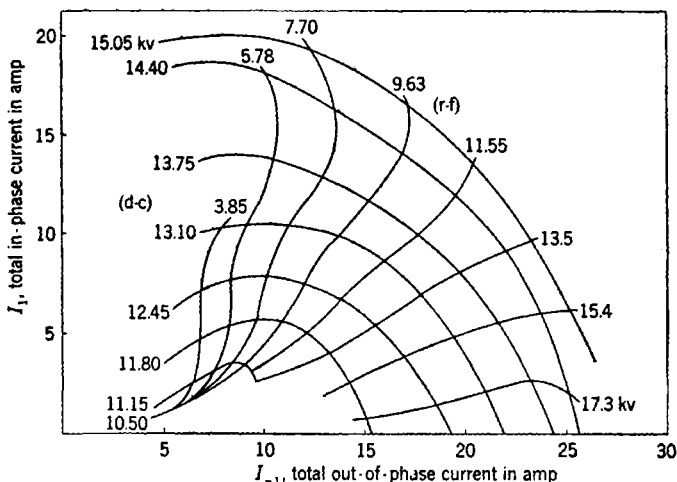


FIG. 6-9.—In-phase and out-of-phase r-f current amplitudes as a function of d-c and r-f voltages. Reduced linear current densities are given by  $I/36$ .

counterclockwise or in the same sense as an electron in a positive magnetic field. In the  $\pi$ -mode the slowest wave traveling in the same sense as the electrons has  $p = -N/2$  ( $m = 0, l = 0$ ). For an electron at rest with respect to such a wave or traveling so that on the average it is at rest with respect to it, another component,  $p'$  say, will appear to move with an angular velocity  $\omega_0(1/p' + 2/N)$  and thus produces a perturbation whose frequency is  $p'\omega_0(1/p' + 2/N)$  or

$$\omega_0 \left[ 1 + \left( \frac{2p'}{N} \right) \right] = \omega_0 [1 \mp (2l' + 1)].$$

<sup>1</sup> The appearance of this particular set of components is always to be expected if the fields satisfy the relation,  $V[\phi + (2\pi/N)] = e^{2\pi i/N} V(\phi)$ , regardless of the form of  $V(\phi)$ . For, if  $V(\phi) = \sum_{-\infty}^{+\infty} a_m e^{im\phi}$ , then  $V[\phi + (2\pi/N)] = \sum_{-\infty}^{+\infty} a_m e^{im\phi + j(2\pi m/N)}$  and one must have  $2n\pi/N = (2m\pi/N) + 2p\pi$  or  $m = n - pN$ , where  $p$  is arbitrary but integral.



Thus, the perturbations produced by the other components have the frequencies  $\pm 2\omega_0$ ,  $\pm 4\omega_0$ ,  $\pm 6\omega_0$ , etc. The situation is somewhat more complicated for the other modes. For the  $m$ th mode, the two slowest components in the counterclockwise direction have  $p = -[(N/2) \pm m]$ , and the frequencies of the perturbations due to other components are found to be given by  $\left[ \frac{N(l+1)}{(N/2) + m} \right] \omega_0$  and  $\left[ 2 - \frac{N(l+1)}{(N/2) + m} \right] \omega_0$  in the case corresponding to the  $+$  sign and  $-\left[ \frac{Nl}{(N/2) - m} \right] \omega_0$  and  $\left[ 2 + \frac{Nl}{(N/2) - m} \right] \omega_0$  for the case of the  $-$  sign. For the case  $m = 1$ , which is usually of most interest when  $m \neq 0$ , there are always low-frequency perturbations; the lowest frequencies are  $\left[ \frac{2}{(N/2) + 1} \right] \omega_0$  in the first case and  $\left[ \frac{-2}{(N/2) - 1} \right] \omega_0$  in the second. It follows that in  $\pi$ -mode operation the perturbations, produced by other components upon an electron that moves slowly on the average with respect to the slowest counterclockwise component, are all of high frequency, whereas for other modes this is certainly not the case. It appears, then, to be plausible, at least as an initial assumption, to ignore all the field components save the slowest counterclockwise one when the tube is running in the  $\pi$ -mode. To justify the assumption completely it would be necessary to show that in the field of such a single component electrons actually move so that they have on the average only a small angular momentum with respect to the wave and furthermore that the high-frequency waves do indeed have no secular effect. It will be found that this justification can be carried through in part and also that there are certain consequences of the rotating-wave hypothesis which are adequately confirmed by experiment. It is, in fact, found that even in cases of operation in modes for which  $m \neq 0$ , a single component determines certain features of the operation. The above considerations apply to strapped magnetrons without reservation, but in the rising-sun design there is always present, even in the  $\pi$ -mode, a component for which  $p = 0$  (see Chap. 3). The effects of this component have to be given special consideration (see Sec. 6-11).

A considerable simplification is introduced into the problem if only one component of the total field need be considered. For then in a system of axes that rotates with the angular velocity of this wave, all electromagnetic fields are independent of time. In addition, the electron distribution in velocity and position will be a stationary one. Thus, if the electromagnetic fields in the interaction space are described by a scalar potential  $A_0$  and a vector potential  $\mathbf{A} = A_r, A_\phi, A_z$ , these are functions of the variables  $r, \phi - \omega t, z$ , where  $\omega$  is the angular velocity of the rotating wave. One may write  $\psi = \phi - \omega t$ . As has been indicated

in the previous section it will be assumed that the fields are transverse electric and independent of  $z$ . The potentials are thus functions of  $r$  and  $\psi$  alone.

In writing down the field equations and the equations of motion, the relativistic form will be used for the latter and no terms dropped from the former. In this way, the approximations that involve the velocity of light may be made consistently. The MKS system of units will be adhered to throughout.

The field vectors  $\mathbf{E}$  and  $B_z$  which will be supposed to contain the applied fields are connected with the potentials through the equations

$$\mathbf{E} = -\text{grad } A_0 - \frac{\partial \mathbf{A}}{\partial t} \quad (1)$$

and

$$B_z = \text{curl}_z \mathbf{A}. \quad (2)$$

The potentials themselves satisfy

$$\nabla^2 A_0 - \mu_0 \epsilon_0 \frac{\partial^2 A_0}{\partial t^2} = \frac{\rho}{\epsilon_0} \quad (3)$$

with  $\rho$  positive for an electron cloud and

$$\text{div grad } \mathbf{A} - \mu_0 \epsilon_0 \frac{\partial^2 \mathbf{A}}{\partial t^2} = \mu_0 \mathbf{J}, \quad (4)$$

where  $\mu_0 = 1.257 \times 10^{-6}$  henry/meter,  $\epsilon_0 = 8.854 \times 10^{-12}$  farad/meter, and  $\rho$  and  $\mathbf{J}$  are the charge and current densities at any point. The subsidiary relation holds

$$\text{div } \mathbf{A} + \mu_0 \epsilon_0 \frac{\partial A_0}{\partial t} = 0. \quad (5)$$

Equations (1) to (5) may now be written out in the  $(r-\psi)$ -system. It should be noted that

$$\frac{\partial}{\partial \phi} = \frac{\partial}{\partial \psi} \quad \text{and} \quad \frac{\partial}{\partial t} = -\omega \frac{\partial}{\partial \psi}$$

from the definition of  $\psi$  and from the fact that  $\partial/\partial z = 0$ . Equations (1) and (2) give

$$E_r = -\frac{\partial A_0}{\partial r} + \omega \frac{\partial A_r}{\partial \psi}, \quad (6)$$

$$E_\phi = -\frac{1}{r} \frac{\partial A_0}{\partial \psi} + \omega \frac{\partial A_\phi}{\partial \psi} = -\frac{1}{r} \frac{\partial}{\partial \psi} (A_0 - \omega r A_\phi), \quad (7)$$

$$B_z = \frac{1}{r} \left[ \frac{\partial}{\partial r} (r A_\phi) - \frac{\partial A_r}{\partial \psi} \right]. \quad (8)$$

Equations (3) and (5) give

$$\frac{1}{r} \frac{\partial}{\partial r} \left( r \frac{\partial A_0}{\partial r} \right) + \left( \frac{1}{r^2} - \omega^2 \mu_0 \epsilon_0 \right) \frac{\partial^2 A_0}{\partial \psi^2} = \frac{\rho}{\epsilon_0} \quad (9)$$

and

$$\frac{1}{r} \frac{\partial}{\partial r} (r A_r) + \frac{1}{r} \frac{\partial A_\phi}{\partial \psi} - \mu_0 \epsilon_0 \omega \frac{\partial A_0}{\partial \psi} = 0. \quad (10)$$

Equation (4) requires a more extended treatment. One has the relations

$$A_x + j A_y = e^{-i\phi} (A_r + j A_\phi) \quad \text{and} \quad J_x + j J_y = e^{-i\phi} (J_r + j J_\phi).$$

Thus, Eq. (4) may be written in an obvious notation

$$\left( \nabla_{r,\phi}^2 - \mu_0 \epsilon_0 \frac{\partial^2}{\partial t^2} \right) [e^{-i\phi} (A_r + j A_\phi)] = \mu_0 e^{-i\phi} (J_r + j J_\phi) \quad (11)$$

or

$$\left( \nabla_{r,\phi}^2 - \mu_0 \epsilon_0 \frac{\partial^2}{\partial t^2} \right) (A_r + j A_\phi) + \left\{ e^{j\phi} \frac{\partial^2}{\partial \phi^2} [e^{-i\phi} (A_r + j A_\phi)] - \frac{\partial^2}{\partial \phi^2} (A_r + j A_\phi) \right\} \frac{1}{r^2} = \mu_0 (J_r + j J_\phi), \quad (12)$$

yielding the pair of equations

$$\left. \begin{aligned} \left( \nabla_{r,\phi}^2 - \mu_0 \epsilon_0 \frac{\partial^2}{\partial t^2} \right) A_r - \frac{1}{r^2} \left( 2 \frac{\partial A_\phi}{\partial \phi} + A_r \right) &= \mu_0 J_r, \\ \left( \nabla_{r,\phi}^2 - \mu_0 \epsilon_0 \frac{\partial^2}{\partial t^2} \right) A_\phi + \frac{1}{r^2} \left( 2 \frac{\partial A_r}{\partial \phi} - A_\phi \right) &= \mu_0 J_\phi, \end{aligned} \right\} \quad (13)$$

or

$$\frac{1}{r} \frac{\partial}{\partial r} \left( r \frac{\partial A_r}{\partial r} \right) + \left( \frac{1}{r^2} - \mu_0 \epsilon_0 \omega^2 \right) \frac{\partial^2 A_r}{\partial \psi^2} - \frac{A_r}{r^2} - \frac{2}{r^2} \frac{\partial A_\phi}{\partial \psi} = \mu_0 J_r, \quad (14a)$$

and

$$\frac{1}{r} \frac{\partial}{\partial r} \left( r \frac{\partial A_\phi}{\partial r} \right) + \left( \frac{1}{r^2} - \mu_0 \epsilon_0 \omega^2 \right) \frac{\partial^2 A_\phi}{\partial \psi^2} - \frac{A_\phi}{r^2} + \frac{2}{r^2} \frac{\partial A_r}{\partial \psi} = \mu_0 J_\phi. \quad (14b)$$

Equations (9), (10), (14a), and (14b) may be combined to give the two equations that imply the equation of continuity, namely,

$$\mu_0 r J_r = \frac{\partial}{\partial \psi} \left[ \mu_0 \epsilon_0 \omega r \frac{\partial A_0}{\partial r} - \frac{1}{r} \frac{\partial}{\partial r} (r A_\phi) + \left( \frac{1}{r} - \mu_0 \epsilon_0 \omega^2 r \right) \frac{\partial A_r}{\partial \psi} \right] \quad (15a)$$

and

$$\begin{aligned} \mu_0 J_\psi = \mu_0 (J_\phi - \omega r \rho) &= \frac{\partial}{\partial r} \left[ \mu_0 \epsilon_0 \omega r \frac{\partial A_0}{\partial r} - \frac{1}{r} \frac{\partial}{\partial r} (r A_\phi) \right. \\ &\quad \left. + \left( \frac{1}{r} - \mu_0 \epsilon_0 \omega^2 r \right) \frac{\partial A_r}{\partial \psi} \right]. \end{aligned} \quad (15b)$$

The bracketed function is essentially the stream function for electron flow in the rotating system.

It is to be noted that in writing down Eqs. (3) and (4), which imply that the fields are derivable from a continuous distribution of charge and current, a further assumption is being made which requires justification. Strictly speaking the charge distribution is not continuous, and

the expression  $\rho$  should be replaced by a summation over the individual electrons. In using the expression for the average charge density to calculate the field, one is ignoring the effects of what is usually referred to as "electron interaction," namely, the process whereby two electrons exchange energy directly as a result of a close encounter rather than through their average effect on the field. Some idea of the magnitude of this effect may be obtained in the following way. Consider a volume  $V$  containing  $nV$  electrons distributed at random. Then the force at any point fluctuates statistically about a mean value. The analogous problem of the gravitational field of a distribution of stars has been considered by Chandrasekhar,<sup>1</sup> and it is found that the natural measure of the force fluctuations is

$$F = \frac{2.6}{\epsilon_0} e \left( \frac{\rho}{e} \right)^{2/3} \quad \text{volts/meter} \quad (16)$$

in the notation of the present problem ( $\rho/e = n$ ). Assuming an emission of 50 amp/sq cm and a radial velocity of  $c/10$  one finds for  $F$  the value  $10^4$  volts/meter or 0.1 kv/cm. This is very small compared with the field strengths normally existing in the magnetron (20 to 50 kv/cm). The process of electron interaction, however, must be expected to play some role in the neighborhood of the cathode where electron densities are highest and the fields weakest.

**6.4. The Equations of Motion.**—The equations of motion may be derived in numerous ways. It is convenient here to make use of the Lagrangian function.<sup>2</sup> Two theorems concerning the Lagrangian equations of motion will be found useful in this connection. Suppose that  $L(x_1, x_2, \dots, x_n; \dot{x}_1, \dot{x}_2, \dots, \dot{x}_n; t)$  is the Lagrangian function of a particle, involving the time explicitly, but that by means of a change of variables  $x'_1 = x_1 + at$ ,  $x'_2 = x_2, \dots, x'_n = x_n$ , the time dependence may be eliminated. One has

$$\frac{\partial}{\partial x_q} = \frac{\partial}{\partial x'_q} \quad \text{and} \quad \frac{\partial}{\partial \dot{x}_q} = \frac{\partial}{\partial \dot{x}'_q}, \quad q = 1, 2, \dots, n,$$

and

$$\begin{aligned} \frac{d}{dt} &= \frac{\partial}{\partial t} + a \frac{\partial}{\partial x'_1} + \dot{x}_1 \frac{\partial}{\partial x'_1} + \dots + \dot{x}_q \frac{\partial}{\partial x'_q} + \dots + \dot{x}_1 \frac{\partial}{\partial \dot{x}'_1} + \dot{x}_q \frac{\partial}{\partial \dot{x}'_q} + \dots \\ &= \frac{\partial}{\partial t'} + \dot{x}'_1 \frac{\partial}{\partial x'_1} + \dots + \dot{x}'_q \frac{\partial}{\partial x'_q} + \dots + \dot{x}'_1 \frac{\partial}{\partial \dot{x}'_1} + \dots + \dot{x}'_q \frac{\partial}{\partial \dot{x}'_q} + \dots \\ &= \frac{d}{dt'}. \end{aligned}$$

<sup>1</sup> S. Chandrasekhar, "Stochastic Problems in Physics and Astronomy," *Rev. Mod. Phys.*, **15**, 1 (1943).

<sup>2</sup> A very lucid account of Lagrangian and Hamiltonian equations for high-speed (relativistic) particles is given by MacColl, *Bell System Tech. Jour.*, **22**, 153 (1943).

Thus, the Lagrangian equations of motion

$$\frac{d}{dt} \left( \frac{\partial L}{\partial \dot{x}_q} \right) = \frac{\partial L}{\partial x_q} \quad q = 1, 2, \dots, n \quad (17a)$$

become

$$\frac{d}{dt'} \left( \frac{\partial L'}{\partial \dot{x}'_q} \right) = \frac{\partial L'}{\partial x'_q} \quad (17b)$$

where

$$L'(x'_1, x'_2, \dots; \dot{x}'_1, \dot{x}'_2, \dots; t') = L(x_1, x_2; \dot{x}_1, \dot{x}_2, \dots; t). \quad (18)$$

The Eqs. (17a) and (17b) for a Lagrangian that does not involve the time directly are known to possess the integral

$$H' = -L' + \sum_q \dot{x}'_q \frac{\partial L'}{\partial \dot{x}'_q} \quad (19)$$

Thus, an integral may be found for the equations of motion although the fields in the original coordinates are time varying.

Now consider  $H'$  and  $L'$  as functions of the coordinates  $x_q$ , and denote derivatives with respect to the coordinates by  $\partial/\partial x_q$ . Then

$$\frac{\partial H'}{\partial x'_q} = -\frac{\partial L'}{\partial x'_q} - \sum \frac{\partial \dot{x}'_s}{\partial x'_q} \frac{\partial L'}{\partial \dot{x}'_s} + \sum \frac{\partial \dot{x}'_s}{\partial x'_q} \frac{\partial L'}{\partial \dot{x}'_s} + \sum \dot{x}'_s \frac{\partial}{\partial x'_q} \left( \frac{\partial L'}{\partial \dot{x}'_s} \right),$$

and using the equations of motion (17b) where  $s = 1, 2, \dots, n$

$$\frac{\partial H'}{\partial x'_q} = + \sum \dot{x}'_s \left[ \frac{\partial}{\partial x'_q} \left( \frac{\partial L'}{\partial \dot{x}'_s} \right) - \frac{\partial}{\partial \dot{x}'_s} \left( \frac{\partial L'}{\partial x'_q} \right) \right] = 0,$$

if all the particles have the same energy constant. Then in 3 dimensions, if one writes  $\frac{\partial L}{\partial \dot{\mathbf{x}}_s} = \mathbf{p}_s$ , one has  $\text{curl } \vec{\mathbf{p}} = \lambda \vec{\mathbf{x}}$ , with  $\lambda$  independent of position and time.

The Lagrangian function for an electron in a transverse electric field is in the relativistic case, with  $e$  a positive quantity,

$$L = -m_0 c^2 \left( 1 - \frac{\dot{r}^2 + r^2 \dot{\phi}^2}{c^2} \right)^{1/2} + e(A_0 - \dot{r}A_r - r\dot{\phi}A_\phi). \quad (21R)^1$$

Since it has been supposed that the transformation  $\phi = \psi + \omega t$  will eliminate the time dependence of the potentials, the lemmas of the

<sup>1</sup> Where the same equation is given in relativistic and nonrelativistic forms, the same number will be used with the affix  $R$  or  $N$  to distinguish the cases.

preceding paragraph may be used. One has

$$L' = -m_0 c^2 \left[ 1 - \frac{\dot{r}^2 + r^2(\dot{\psi} + \omega)^2}{c^2} \right]^{1/2} + e[A_0 - rA_r - r(\dot{\psi} + \omega)A_\phi], \quad (22R)$$

and the equations of motion are

$$\frac{d}{dt} \left[ \frac{m_0 \dot{r}}{(1 - \beta^2)^{1/2}} - eA_r \right] = \frac{m_0 r(\dot{\psi} + \omega)^2}{(1 - \beta^2)^{1/2}} + e \left[ \frac{\partial A_0}{\partial r} - \dot{r} \frac{\partial A_r}{\partial r} - (\dot{\psi} + \omega) \frac{\partial(rA_\phi)}{\partial r} \right] \quad (23R)$$

and

$$\frac{d}{dt} \left[ \frac{m_0 r^2(\dot{\psi} + \omega)}{(1 - \beta^2)^{1/2}} - erA_\phi \right] = e \left[ \frac{\partial A_0}{\partial \psi} - \dot{r} \frac{\partial A_r}{\partial \psi} - (\dot{\psi} + \omega) \frac{\partial(rA_\phi)}{\partial \psi} \right], \quad (24R)$$

where

$$\beta^2 = \frac{\dot{r}^2 + r^2(\dot{\psi} + \omega)^2}{c^2}.$$

Or, alternatively,

$$\frac{d}{dt} \left[ \frac{m_0 \dot{r}}{(1 - \beta^2)^{1/2}} \right] = \frac{m_0 r(\dot{\psi} + \omega)^2}{(1 - \beta^2)^{1/2}} + e \frac{\partial}{\partial r} [A_0 - \omega r A_\phi] - e\dot{\psi} \left[ \frac{\partial(rA_\phi)}{\partial r} - \frac{\partial A_r}{\partial \psi} \right], \quad (25R)$$

$$\frac{d}{dt} \left[ \frac{m_0 r^2(\dot{\psi} + \omega)}{(1 - \beta^2)^{1/2}} \right] = e \frac{\partial}{\partial \psi} [A_0 - \omega r A_\phi] + e\dot{r} \left[ \frac{\partial(rA_\phi)}{\partial r} - \frac{\partial A_r}{\partial \psi} \right]. \quad (26R)$$

The integral  $H'$  may be formed:

$$\begin{aligned} H' &= m_0 c^2 \left[ 1 - \frac{\dot{r}^2 + r^2(\dot{\psi} + \omega)^2}{c^2} \right]^{1/2} - e[A_0 - \dot{r}A_r - r(\dot{\psi} + \omega)A_\phi] \\ &\quad + \frac{m_0[\dot{r}^2 + r^2\dot{\psi}(\dot{\psi} + \omega)]}{(1 - \beta^2)^{1/2}} - e(\dot{r}A_r + r\dot{\psi}A_\phi) = \frac{m_0[c^2 - r^2\omega(\dot{\psi} + \omega)]}{(1 - \beta^2)^{1/2}} \\ &\quad - e(A_0 - \omega r A_\phi). \end{aligned} \quad (27R)$$

If the convention is introduced that  $A_0$ ,  $A_\phi$ , and  $A_r$  shall all vanish at the cathode and the assumption of vanishing velocities at the cathode in the stationary coordinate system be recalled, one has

$$H' = m_0 c^2. \quad (28R)$$

Since  $H$  is independent of the electron considered, the second lemma (20) holds with  $\lambda = 0$ , and one has

$$\frac{\partial}{\partial \dot{\psi}} \left[ \frac{m_0 \dot{r}}{(1 - \beta^2)^{1/2}} - eA_r \right] = \frac{\partial}{\partial r} \left[ \frac{m_0 r^2(\dot{\psi} + \omega)}{(1 - \beta^2)^{1/2}} - erA_\phi \right]. \quad (29R)$$

This equation may be written as a pair of equations

$$\frac{m_0 \dot{r}}{(1 - \beta^2)^{1/2}} = eA_r + \frac{\partial W}{\partial r}, \quad (30R)$$

$$\frac{m_0 r^2 (\dot{\psi} + \omega)}{(1 - \beta^2)^{1/2}} = erA_\phi + \frac{\partial W}{\partial \psi}, \quad (31R)$$

and (27R) becomes

$$m_0 c^2 + eA_0 - \omega \frac{\partial W}{\partial \psi} = c \sqrt{m_0^2 c^2 + \left( eA_r + \frac{\partial W}{\partial r} \right)^2 + \left( eA_\phi + \frac{1}{r} \frac{\partial W}{\partial \psi} \right)^2}. \quad (32R)$$

In the nonrelativistic case a similar set of equations is found. The Lagrangian is now

$$L' = \frac{m_0}{2} [\dot{r}^2 + r^2 (\dot{\psi} + \omega)^2] + e[A_0 - \dot{r}A_r - r(\dot{\psi} + \omega)A_\phi], \quad (21N)$$

and the equations of motion are

$$m_0 \ddot{r} = m_0 r (\dot{\psi} + \omega)^2 + e \frac{\partial}{\partial r} (A_0 - \omega r A_\phi) - e\dot{\psi} \left[ \frac{\partial(rA_\phi)}{\partial r} - \frac{\partial A_r}{\partial \psi} \right], \quad (25N)$$

$$\frac{d}{dt} [m_0 r^2 (\dot{\psi} + \omega)] = e \frac{\partial}{\partial \psi} (A_0 - \omega r A_\phi) + e\dot{r} \left[ \frac{\partial(rA_\phi)}{\partial r} - \frac{\partial A_r}{\partial \psi} \right]. \quad (26N)$$

In this case the equations may be further modified to read

$$m_0 \ddot{r} = m_0 r \dot{\psi}^2 + e \frac{\partial}{\partial r} \left( A_0 - \omega r A_\phi + \frac{m_0}{2e} \omega^2 r^2 \right) - e\dot{\psi} \left[ \frac{\partial(rA_\phi)}{\partial r} - \frac{\partial A_r}{\partial \psi} - \frac{2m_0 \omega r}{e} \right], \quad (33)$$

$$\frac{d}{dt} (m_0 r^2 \dot{\psi}) = e \frac{\partial}{\partial \psi} \left( A_0 - \omega r A_\phi + \frac{m_0}{2e} \omega^2 r^2 \right) + e\dot{r} \left[ \frac{\partial(rA_\phi)}{\partial r} - \frac{\partial A_r}{\partial \psi} - \frac{2m_0 \omega r}{e} \right]. \quad (34)$$

These equations have a simple interpretation. They are the equations of motion of a particle moving in a scalar potential

$$A_0 - \omega r A_\phi + \left( \frac{m_0}{2e} \right) \omega^2 r^2$$

and in a magnetic field

$$\frac{\partial}{\partial r} (rA_\phi) - \frac{\partial A_r}{\partial \psi} - \frac{2m_0 \omega}{e}.$$

The term  $(m_0/2e)\omega^2 r^2$  is related to the centrifugal force, and the term  $2m_0 \omega r/e$  to the Coriolis' force, appropriate to the rotating axes. Such a formulation of the equations was not possible in the relativistic case.

The integral  $H'$  is now

$$\begin{aligned} H' &= -\frac{m_0}{2} [\dot{r}^2 + r^2(\dot{\psi} + \omega)^2] - e[A_0 - \dot{r}A_r - r(\dot{\psi} + \omega)A_\phi] \\ &\quad + m_0[\dot{r}^2 + r^2\dot{\psi}(\dot{\psi} + \omega)] - e\dot{r}A_r - e\dot{\psi}rA_\phi \\ &= \frac{m_0}{2} (\dot{r}^2 + r^2\dot{\psi}^2) - e(A_0 - r\omega A_\phi) - \frac{m_0}{2} r^2\omega^2; \end{aligned} \quad (27N)$$

and with the usual conditions at  $r = r_c$ , one has  $H' = 0$ .

Thus,

$$\frac{\partial}{\partial \dot{\psi}} (m_0 \dot{r} - eA_r) = \frac{\partial}{\partial r} [m_0 r^2 (\dot{\psi} + \omega) - erA_\phi] \quad (29N)$$

and

$$m_0 \dot{r} = eA_r + \frac{\partial W}{\partial r}, \quad (30N)$$

$$m_0 r^2 (\dot{\psi} + \omega) = erA_\phi + \frac{\partial W}{\partial \dot{\psi}}, \quad (31N)$$

$$eA_0 + \omega \frac{\partial W}{\partial \dot{\psi}} = \frac{1}{2m_0} \left[ \left( eA_r + \frac{\partial W}{\partial r} \right)^2 + \left( eA_\phi + \frac{1}{r} \frac{\partial W}{\partial \dot{\psi}} \right)^2 \right]. \quad (32N)$$

It will be noted that Eqs. (32R) and (32N) are essentially the Hamilton-Jacobi equations of the system, since  $\partial W / \partial t' = -\omega (\partial W / \partial \dot{\psi})$ .  $W$  is thus the action function of the system.<sup>1</sup> The introduction of the action function in the magnetron problem does not appear to be so fruitful as one might expect. The reason for this lies in one of the most complicated characteristics of the electron motion, namely, that the motion is essentially of a multiple-stream type. Through any point in the interaction space, transformed into the rotating system, there will pass a number of electron orbits. This fact hardly requires proof, but it has been established empirically by computation of orbits. It follows as a consequence that the electron velocity is a multiple valued function of position and thus that  $W$  has similar properties.  $W$ , then, is a function having many branches, and these branches will meet along branch curves which will be the envelope of a series of electron trajectories. The character of these branch curves has been discussed by Cherry,<sup>2</sup> who has given expressions for the potential and velocities in the neighborhood of such curves.

The multiple-stream property of the electron flow gives rise to severe analytical difficulties in handling the field equations, for it is necessary to write an equation of continuity for each stream, where a stream is

<sup>1</sup> The function  $W$  has been used by Gabor, *Proc. IRE*, **33**, 792 (1945), in problems of electron dynamics.

<sup>2</sup> Cherry, "General Theory of Magnetron," Council for Scientific and Industrial Research, Sydney, Report No. MUM-1, 1943, has discussed the formulation of the magnetron equations in terms of  $W$ .



defined as a set of electron orbits leaving one branch curve and terminating on another. With each stream there is associated a charge density, and it is the sum of these charge densities and the sum of the currents that must be substituted in Eqs. (9), (14a), and (14b). So far there does not seem to have been developed any analytical method that will effectively handle all the streams together and automatically perform the required summations. It is always necessary to handle the individual streams separately and fit them together at the branch curves.

There are two important equations that may be deduced from the integrals (27R) and (27N). Thus, if a particle is to reach a given point in the interaction space at all, one must have  $\dot{r}$  and  $\dot{\psi}$  both real at that point. Putting  $\dot{r} = 0$  in Eq. (28R) and writing  $\psi + \omega = \phi$ , one has

$$m_0 c^2 + e(A_0 - \omega r A_\phi) = \frac{m_0(c^2 - r^2 \omega \phi)}{\sqrt{1 - \frac{r^2 \dot{\phi}^2}{c^2}}} = D,$$

$$c^4 - 2c^2 r^2 \omega \phi + r^4 \omega^2 \dot{\phi}^2 = \frac{D^2}{m_0^2} \left(1 - \frac{r^2 \dot{\phi}^2}{c^2}\right),$$

$$\left(r^4 \omega^2 + \frac{D^2 r^2}{m_0^2 c^2}\right) \dot{\phi}^2 - 2c^2 r^2 \omega \phi + \left(c^4 - \frac{D^2}{m_0^2}\right) = 0.$$

For the reality of  $\dot{\phi}$  one must have

$$\left(r^4 \omega^2 + \frac{D^2 r^2}{m_0^2 c^2}\right) \left(c^4 - \frac{D^2}{m_0^2}\right) < c^4 r^4 \omega^2$$

or

$$\frac{e}{m_0 c^2} (A_0 - \omega r A_\phi) \geq \sqrt{1 - \frac{r^2 \omega^2}{c^2}} - 1. \quad (33R)$$

The nonrelativistic analogue is easily deduced from (27N) or from (33R) by supposing  $r\omega \ll c$  and is

$$e(A_0 - r\omega A_\phi) \geq -\frac{m_0 r^2 \omega^2}{2}. \quad (33N)$$

Equations (33N) and (33R) play a very important role in the analysis of magnetron behavior, since they yield an inequality that the fields must satisfy in order that electrons shall reach a preassigned point in the interaction space. They will be discussed further at a later point in this section.

Another pair of significant formulas is obtained by rewriting (27N) and (27R) in terms of the stationary coordinates. In this way one finds

$$m_0 c^2 = \frac{m_0(c^2 - \omega r^2 \phi)}{\sqrt{1 - \beta^2}} - e(A_0 - \omega r A_\phi) \quad (34R)$$

and

$$0 = \frac{m_0}{2} (\dot{r}^2 + r^2 \dot{\phi}^2) - e(A_0 - r\omega A_\phi) - m_0 r^2 \dot{\phi} \omega. \quad (34N)$$

From (34R)

$$eA_0 - m_0 c^2 \left( \frac{1}{\sqrt{1 - \beta^2}} - 1 \right) = - \frac{m_0 \omega r^2 \dot{\phi}}{\sqrt{1 - \beta^2}} + e\omega r A_\phi = -\omega \frac{\partial W}{\partial \dot{\psi}}, \quad (35R)$$

and from (34N)

$$eA_0 - \frac{m_0}{2} (\dot{r}^2 + r^2 \dot{\phi}^2) = -m_0 r^2 \dot{\phi} \omega + e\omega r A_\phi = -\omega \frac{\partial W}{\partial \dot{\psi}}. \quad (35N)$$

The expression on the left of Eq. (35N) is the difference between the potential energy of an electron in the scalar field and the kinetic energy of the electron; it therefore represents the energy loss of the electron to the oscillating field.

### 6-5. Conditions under Which Relativistic Effects May Be Eliminated.

Before discussing more fully the equations of motion it is essential to find out under what conditions the relativistic and propagation effects can be eliminated. The field equations, Eqs. (9), (10), (14a), and (14b), and the equations of motion (25R) and (26R) describe exactly the conditions in the interaction space. When one proceeds from the relativistic Lagrangian to the nonrelativistic form, the procedure is equivalent to ignoring all terms in the relativistic expression of higher powers in  $v/c$  than the second, where  $v$  is the electron velocity. It is important then to ignore all terms of the same order occurring in the field equations. To be able to recognize such terms it is useful to introduce a set of characteristic variables for length, time, scalar and vector potentials, and charge density that will be appropriate to the relativistic regime. Thus, for a characteristic length one uses  $r_0 = c/\omega = n\lambda_0/2\pi$ , since the quantity  $\mu_0 \epsilon_0 \omega^2 = \omega^2/c^2$  is the only parameter occurring in the field equations. For a characteristic time,  $t_0 = 1/\omega$  is chosen; and for the scalar and vector potentials, the natural units are  $m_0 c^2/e$  and  $m_0 c/e$ . The characteristic charge density is  $e/m_0 \omega^2 \epsilon_0$ . Writing

$$r^* = \frac{r}{r_0} = \frac{\omega r}{c}, \quad t^* = \frac{t}{t_0} = \omega t, \quad A_0^* = \frac{e}{m_0 c^2} A_0, \\ A_{r,\phi}^* = \frac{e}{m_0 c} A_{r,\phi}, \quad \rho^* = \frac{m_0 \omega^2 \epsilon_0}{e} \rho,$$

Eqs. (9), (10), (14a), and (14b) become

$$\frac{1}{r^*} \frac{\partial}{\partial r^*} \left( r^* \frac{\partial A_0^*}{\partial r^*} \right) + \left( \frac{1}{r^{*2}} - 1 \right) \frac{\partial^2 A_0^*}{\partial r^{*2}} = *, \quad (36)$$

$$\frac{1}{r^*} \frac{\partial}{\partial r^*} (r^* A_r^*) + \frac{1}{r^*} \frac{\partial A_\phi^*}{\partial \psi} - \frac{\partial A_0}{\partial \psi} = 0, \quad (37)$$

$$\frac{\partial}{\partial \psi} \left[ r^* \frac{\partial A_0^*}{\partial r^*} - \frac{1}{r^*} \frac{\partial}{\partial r^*} (r^* A_\phi^*) + \left( \frac{1}{r^*} - r^* \right) \frac{\partial A_r^*}{\partial \psi} \right] = r^* \bar{r}^* \rho^*, \quad (38)$$

$$\frac{\partial}{\partial r^*} \left[ r^* \frac{\partial A_0^*}{\partial r^*} - \frac{1}{r^*} \frac{\partial}{\partial r^*} (r^* A_\phi^*) + \left( \frac{1}{r^*} - r^* \right) \frac{\partial A_r^*}{\partial \psi} \right] = r^* \bar{\psi} \rho^*, \quad (39)$$

where the bar denotes differentiation with respect to  $t^*$ . Similarly the integrals of the equation of motion are

$$1 + A_0^* - r^* A_\phi^* = \frac{1 - r^{*2}(\bar{\psi} + 1)}{\sqrt{1 - \bar{r}^{*2} - r^{*2}(\bar{\psi} + 1)^2}} \quad (40)$$

and

$$\frac{\partial}{\partial \psi} \left[ \frac{\bar{r}^*}{(1 - \beta^2)^{1/2}} - A_r^* \right] = \frac{\partial}{\partial r^*} \left[ \frac{r^{*2}(\bar{\psi} + 1)}{(1 - \beta^2)^{1/2}} - r^* A_\phi^* \right]. \quad (41)$$

In order to examine the conditions under which the above equations may be simplified, one calculates  $A_\phi$  for the applied magnetic field  $B_s$  in the absence of an electron stream. Since  $B_s = (1/r)(\partial/\partial r)(rA_\phi)$ , if  $A_\phi = 0$  at  $r = r_c$ , then

$$rA_\phi = \frac{B_0}{2} (r^2 - r_c^2), \quad (42)$$

or, in reduced variables,

$$r^* A_\phi^* = \frac{eB_0}{2m\omega} (r^{*2} - r_c^{*2}) = \frac{1}{\gamma} (r^{*2} - r_c^{*2}), \quad (43)$$

where

$$\gamma = \frac{2m\omega}{eB_0}.$$

The unperturbed magnitude of  $r^* A_\phi^*$  evidently depends upon two independent quantities:  $r^* = 2\pi r/n\lambda_0$ , which measures the size of interaction space in terms of  $n\lambda_0$ , and  $\gamma$ , which is the ratio of the Larmor frequency of the electron precession in a magnetic field  $B_0$  to the angular velocity of the rotating wave. Suppose that  $r^{*2} \ll 1$ , then the condition [Eq. (33R)] that an electron shall be able to reach a point in the interaction space becomes

$$1 + A_0^* - r^* A_\phi^* \geq \sqrt{1 - r^{*2}}$$

which may be written

$$A_0^* \geq r^* A_\phi^* - \frac{r^{*2}}{2}$$

or

$$A_0^* \geq (r^* \tilde{A}_\phi^*) + \frac{1}{\gamma} (r^{*2} - r_c^{*2}) - \frac{r^{*2}}{2}, \quad (44)$$

where  $(r^* \tilde{A}_\phi^*)$  is the contribution to  $r^* A_\phi^*$  coming from the r-f fields and from the circulating currents. It will now be assumed that  $A_0^*, r^* A_\phi^*$ ,

and  $A_r^*$  are all small compared with unity. This is equivalent to saying that all voltages are small compared with  $mc^2/e = 506$  kv; this is true for all magnetrons that have been built up to the present. For the inequality to be satisfied, it is to be noted that a lower limit is set upon the value of  $\gamma$  in a tube of given dimensions (fixed  $r_c^*$  and  $r_a^*$ ). Using Eq. (28R), limits may be set upon the values of  $\bar{r}^*$  and  $r^*(\psi + 1)$ ; thus,

$$|\bar{r}^*| \leq \sqrt{1 - \frac{1}{\beta^2 + r^{*2}}} \quad (45a)$$

and

$$\frac{r^* - \beta \sqrt{\beta^2 + r^{*2} - 1}}{\beta^2 + r^{*2}} \leq r^*(\psi + 1) \leq \frac{r^* + \beta \sqrt{\beta^2 + r^{*2} - 1}}{\beta^2 + r^{*2}}, \quad (45b)$$

where

$$\beta = 1 + A_0^* - r^* A_\phi^*.$$

Thus  $|\bar{r}^*|$  and  $r^*|\psi + 1|$  are of the order of  $(A_0^* - r^* A_\phi^*)^{1/2}$ . From Eq. (36),  $\rho^*$  is of the order of  $A_0$ ; and neglecting squares of  $r^{*2}$ ,  $A_0^*$  satisfies Poisson's equation. The right-hand sides of Eqs. (38) and (39) are of order  $r^* A_0^{*3/2}$  and  $A_0^* (A_0^{*1/2} - r^*)$ , and these equations may be written

$$\frac{\partial}{\partial \psi} \left\{ \frac{1}{r^*} \left[ \frac{\partial A_r^*}{\partial \psi} - \frac{\partial}{\partial r^*} (r^* A_\phi^*) \right] \right\} = r^* \left( \frac{\partial^2 A_r^*}{\partial \psi^2} + \frac{\partial^2 A_0^*}{\partial r^{*2} \partial \psi} \right) + \text{terms of the order of } (r^* A_0^{*3/2}), \quad (46a)$$

and

$$\frac{\partial}{\partial r^*} \left\{ \frac{1}{r^*} \left[ \frac{\partial A_r^*}{\partial \psi} - \frac{\partial}{\partial r^*} (r^* A_\phi^*) \right] \right\} = \frac{\partial}{\partial r^*} \left[ r^* \frac{\partial A_r^*}{\partial \psi} - r^* \frac{\partial A_0^*}{\partial r^*} \right] + \text{terms of the order of } (A_0^{*3/2} - r^* A_0^*). \quad (46b)$$

The right-hand sides of these equations are small compared with the left, and thus

$$\frac{\partial A_r^*}{\partial \psi} - \frac{\partial}{\partial r^*} (r^* A_\phi^*) = r^* \text{ times a constant} \quad (46c)$$

which for the particular boundary conditions  $= -B_0$ . Equation (37) leads, neglecting  $r^{*2} A_0$  in comparison with  $r^* A_\phi$ , to

$$\frac{\partial}{\partial r^*} (r^* A_r^*) + \frac{\partial A_\phi^*}{\partial \psi} = 0. \quad (46d)$$

Combining, the part of  $A_\phi^*$  depending upon the r-f fields and circulating current and  $A_r^*$  satisfy

$$r^* A_r^* = \frac{\partial T}{\partial \psi} \quad (47a)$$

and

$$\bar{A}_\phi^* = \frac{\partial T}{\partial r^*}, \quad (47b)$$

where

$$\frac{1}{r^*} \frac{\partial}{\partial r^*} \left( r^* \frac{\partial T}{\partial r^*} \right) + \frac{1}{r^{*2}} \frac{\partial^2 T}{\partial \psi^2} = 0. \quad (47c)$$

It may be noted that

$$\frac{1}{r^*} \frac{\partial}{\partial r^*} \left[ r^* \frac{\partial(r^* \tilde{A}_\phi^*)}{\partial r^*} \right] + \frac{1}{r^{*2}} \frac{\partial^2(r^* \tilde{A}_\phi^*)}{\partial \psi^2} = 0. \quad (47d)$$

Summing up the results of this section, it appears that for the neglect of relativistic effects and of propagation effects to be permissible it is necessary to have  $r^*$  small and also  $\gamma$  sufficiently small so that  $A_0^*$  is small compared with unity, while  $r^* A_\phi^*$  must also be small compared with unity. Physically, the dimensions of the tube must be small in units of  $\hbar\lambda/2\pi$ , and all voltages must be small when measured in a unit of 500 kv. Under these circumstances the scalar potential  $A_0$  satisfies Poisson's equation, while the potentials  $A_r$  and  $A_\phi$  are derived from a quantity  $T$  satisfying Laplace's equation. Furthermore, the term entering the equations of motion of the form  $[\partial(rA_\phi)/\partial r - \partial A_r/\partial \psi]$  is in a nonrelativistic approximation equal to  $B_0$ , the applied magnetic field; for if the second integral [Eq. (29R)] of the motion is written in reduced units,

$$\frac{\partial}{\partial \psi} \left[ \frac{\tilde{r}^*}{\sqrt{1 - \beta^2}} \right] - \frac{\partial}{\partial r^*} \left[ \frac{\tilde{\psi} + 1}{\sqrt{1 - \beta^2}} \right] = \frac{\partial A_r^*}{\partial \psi} - \frac{\partial(r^* A_\phi^*)}{\partial r^*} \quad (48)$$

and the right-hand side is  $-r^* B_0$  plus small terms.

**6-6. The Nonrelativistic Equations.**—The equations of motion in the normal, nonrelativistic case may now be put into a more convenient form. Substituting the expression  $\frac{1}{2}B_0(r - r_c^2/r)$  for the part of the vector potential  $A_\phi$  due to the applied magnetic field and dropping the term  $A_r$ , which contributes only to the r-f magnetic field just shown to be negligible, Eqs. (33) and (34) become, writing  $\tilde{A}_\phi$  for the r-f tangential component of vector potential,

$$m_0 \ddot{r} = m_0 r \dot{\psi}^2 + e \frac{\partial}{\partial r} \left[ A_0 - \omega r \tilde{A}_\phi - \frac{\omega B_0}{2} (r^2 - r_c^2) + \frac{m_0}{2e} \omega^2 r^2 \right] - e \dot{\psi} r \left( B_0 - \frac{2m_0 \omega}{e} \right), \quad (49a)$$

$$\frac{d}{dr} [m_0 r^2 \dot{\psi}] = e \frac{\partial}{\partial \psi} \left[ A_0 - \omega r \tilde{A}_\phi - \frac{\omega B_0}{2} (r^2 - r_c^2) + \frac{m_0}{2e} \omega^2 r^2 \right] + e \dot{r} r \left( B_0 - \frac{2m_0 \omega}{e} \right), \quad (49b)$$

or

$$m_0 \ddot{r} = m_0 r \dot{\psi}^2 + e \frac{\partial V_E}{\partial r} - e r \dot{\psi} B_1, \quad (50a)$$

$$\frac{d}{dt}(m_0 r^2 \dot{\psi}) = e \frac{\partial V_E}{\partial \dot{\psi}} + e r \dot{r} B_1, \quad (50b)$$

where

$$V_E = A_0 - \omega r \tilde{A}_\phi - \frac{\omega B_0}{2} (r^2 - r_c^2) + \frac{m_0}{2e} \omega^2 r^2 \quad (51a)$$

and

$$B_1 = B_0 - \frac{2m_0 \omega}{e}. \quad (51b)$$

The associated field equations will reduce to two by virtue of the neglect of  $A_r$  and the other small terms. Since, in the equations of motion,  $A_0$  and  $\tilde{A}_\phi$  appear only in the combination  $A_0 - \omega r \tilde{A}_\phi$ , it is useful to write down the equation that this new variable satisfies, and this is plainly

$$\frac{1}{r} \frac{\partial}{\partial r} \left[ r \frac{\partial (A_0 - \omega r \tilde{A}_\phi)}{\partial r} \right] + \frac{1}{r^2} \frac{\partial^2 (A_0 - \omega r \tilde{A}_\phi)}{\partial \psi^2} = \frac{\rho}{\epsilon_0}. \quad (52)$$

The two equations involving the currents are no longer of interest in so far as they affect the potentials, but the equation of continuity that they imply remains, and one has

$$\frac{\partial}{\partial r}(\rho r \dot{r}) + \frac{\partial}{\partial \psi}(\rho r \dot{\psi}) = 0, \quad (53)$$

where properly there is one such equation for each stream, and  $\rho$  in Eq. (52) is summed over all streams.

Equations (49a) (49b), (52), and (53) may be taken as the fundamental equations of the magnetron problem. It is convenient at this point to introduce a new system of reduced or dimensionless variables suitable for the nonrelativistic problem, by choosing an appropriate characteristic length, time, voltage, and so forth. The choice of such units is largely arbitrary. There are, for example, two natural frequencies appearing: (1) the angular velocity of the electromagnetic fields  $\omega/2\pi = \omega_0/2\pi n$  and (2) the frequency of precession of an electron in a constant magnetic field  $B_0$ , namely,  $(1/2\pi)(eB_0/2m)$ , in the absence of electric fields. Either one of these frequencies might be used to determine a characteristic time. The unit of length might be chosen to be one of the radial dimensions of the tube  $r_c$  or  $r_a$  or might again be associated with the free-space wavelength as was natural in studying propagation effects. Similarly, various unit voltages suggest themselves because any suitably defined energy or amount of work associated with an electron when divided by  $e$  gives a possible voltage. Thus, one could use the kinetic energy of an electron at rest in the moving system at some appropriate radius; the kinetic energy of an electron moving around a circle of given radius in a constant magnetic field  $B_0$ ; the work done in moving an electron at rest in the moving system against magnetic forces over a definite distance, and so on.

The system of characteristic quantities that will be used here is as follows: For length, the cathode radius is used,  $r_c$ ; for time, the reciprocal of  $2\pi$  times the Larmor frequency, or  $2m/eB_0$  (this has the advantage of enabling one to pass readily to the case where there is no traveling wave); for a unit voltage,  $\frac{1}{2}\omega B_0 r_c^2$  will be used. The latter is the work done against the magnetic field  $B_0$  in moving unit charge at rest in the rotating system from  $r = 0$  to  $r = r_c$ . It would be more natural, no doubt, to use  $\frac{1}{2}\omega B_0(r_a^2 - r_c^2)$  as a unit, since this would measure the work done between cathode and anode, but this choice leads to clumsy expressions in the reduced equations.

Thus, one writes

$$s = \frac{r}{r_c}, \quad \tau = \frac{eB_0}{2m_0} t, \quad a_0 = \frac{2A_0}{\omega B_0 r_c^2}, \quad \tilde{a}_\phi = \frac{2\tilde{A}_\phi}{B_0 r_c}, \quad \text{and} \quad \gamma = \frac{2m_0\omega}{eB_0},$$

as before. Then the equations (49a) and (49b) become

$$\bar{s} = s\bar{\psi}^2 + \gamma \frac{\partial V_E}{\partial s} - 2(1 - \gamma)s\bar{\psi}, \quad (54a)$$

$$\frac{d}{d\tau}(s^2\bar{\psi}) = \gamma \frac{\partial V_E}{\partial \psi} + 2(1 - \gamma)s\bar{s}, \quad (54b)$$

where the bar denotes differentiation with respect to  $\tau$  and

$$V_E = a_0 - s\tilde{a}_\phi - (s^2 - 1) + \frac{\gamma}{2}s^2. \quad (55)$$

The field equations [Eqs. (52) and (53)] become

$$\frac{1}{s} \frac{\partial}{\partial s} \left[ s \frac{\partial(a_0 - s\tilde{a}_\phi)}{\partial s} \right] + \frac{1}{s^2} \frac{\partial^2(a_0 - s\tilde{a}_\phi)}{\partial \psi^2} = \frac{2}{\omega B_0 r_c^2} \rho = \varrho \quad (56)$$

and

$$\frac{\partial}{\partial s}(\varrho s\bar{s}) + \frac{\partial}{\partial \psi}(\varrho s\bar{\psi}) = 0. \quad (57)$$

For future reference, the form assumed by Eqs. (54a), (54b), (56), and (57) for the case of a linear magnetron will be written down here. It will be assumed that  $n$  and  $r_c$  tend to infinity together in such a way that  $r_c/n = \lambda_0/2\pi$ , where  $\lambda_0$  will be the wavelength of the traveling wave in the linear tube. Measuring  $y$  outward from the cathode and  $x$  parallel to the cathode, then

$$s = 1 + \frac{y}{r_c} = 1 + \frac{\lambda_0}{r_c} \frac{y}{\lambda_0} = 1 + \frac{\lambda_0}{r_c} \zeta$$

and

$$r_c\psi = x = \lambda_0 \frac{x}{\lambda_0} = \lambda_0 \xi.$$

Equations (54a) and (54b) become

$$\bar{\xi} = \delta \frac{\partial V_{EP}}{\partial \xi} + 2\bar{\zeta}, \quad (58a)$$

$$\bar{\zeta} = \delta \frac{\partial V_{EP}}{\partial \zeta} - 2\bar{\xi}, \quad (58b)$$

where

$$\delta = \frac{\gamma r_c}{\lambda_0} = \frac{2m_0\omega}{eB} \frac{n}{2\pi} = \frac{m_0\omega_0}{\pi eB}$$

and

$$V_{EP} = \frac{r_c}{\lambda_0} (a_0 - \tilde{a}_x) - 2\zeta + \frac{\delta}{2}. \quad (59)$$

Equations (56) and (57) take the form

$$\left( \frac{\partial^2}{\partial \xi^2} + \frac{\partial^2}{\partial \zeta^2} \right) \left[ \frac{r_c}{\lambda_0} (a_0 - \tilde{a}_x) \right] = \frac{4\pi\rho}{\omega_0 B_0 \epsilon_0} = \varrho_p \quad (60)$$

and

$$\frac{\partial}{\partial \xi} (\varrho_p \bar{\xi}) + \frac{\partial}{\partial \zeta} (\varrho_p \bar{\zeta}) = 0. \quad (61)$$

The formulation of the magnetron problem is now completed by specifying the boundary conditions for the fields and velocities. Since the electrons are supposed to leave the cathode at rest in the stationary system, one has

$$\bar{s} = 0, \quad (62a)$$

$$\bar{\psi} = -\gamma \quad \text{at } s = 1, \quad (62b)$$

and

$$\bar{\xi} = 0, \quad (63a)$$

$$\bar{\xi} = -\delta \quad \text{at } \zeta = 0 \quad (63b)$$

in the linear system. At the cathode ( $s = 1$  or  $\zeta = 0$ ) the potentials  $a_0$  and  $s\tilde{a}_\phi$  (or  $\tilde{a}_x$ ) vanish; and if there is to be space-charge limitation, so must the radial field  $E_r$  (or  $E_y$ ). Since

$$\begin{aligned} E_r &= -\frac{\partial A_0}{\partial r} + \omega \frac{\partial A_r}{\partial \psi} \\ &= -\frac{\partial}{\partial r} (A_0 - \omega r A_\phi) - \omega r B_s \\ &= \frac{\partial}{\partial r} (A_0 - \omega r \tilde{A}_\phi), \\ &= 0 \end{aligned}$$

then

$$\frac{\partial}{\partial s} (a_0 - s\tilde{a}_\phi) = 0 \quad \text{at } s = 1 \quad (64a)$$



or

$$\frac{\partial}{\partial \xi} (a_0 - \tilde{a}_x) = 0 \quad \text{at } \xi = 0. \quad (64b)$$

The boundary conditions at the anode are set on the potentials and are assumed to be

$$a_0 = A_0, \quad (65a)$$

$$s\tilde{a}_\phi = A_1 \cos n\psi \quad \text{at } s = s_a = r_a/r_c, \quad (65b)$$

or

$$a_x = A_1 \cos 2\pi\xi \quad \text{at } \xi = \xi_a = y_a/\lambda_0. \quad (65c)$$

All potentials must be periodic then in  $\psi/n$  or  $\xi/2\pi$ . It will be recognized that in the preceding paragraphs, the assertion made in the first section that a potential could be defined on the anode whose value was said to be  $V_0 + V_1 \cos (n\phi - \omega_0 t)$  has been justified. For the combination of potentials  $a_0 - s\tilde{a}_\phi$  or  $a_0 - \tilde{a}_x$  is the only one entering the nonrelativistic equations of motion. It should be noted from Eq. (7) that this potential is  $-\int r E_\phi d\psi$  or the tangential integral of the tangential electric field.

The solution of the problem would consist of a determination of the electron velocities, the charge density, and the potential at any point of the interaction space. From these the radial current density  $\rho\dot{r}$  could be found in the form

$$\rho\dot{r} = J_r = J_{r,0} + \tilde{J}_{r,1} \cos n\psi + \tilde{J}_{r,-1} \sin n\psi + \dots \quad (66)$$

where

$$2\pi r J_{r,0} = \int_0^{2\pi} \rho r \dot{r} d\psi = \frac{I_0}{h}, \quad \pi r \tilde{J}_{r,1} = \int_0^{2\pi} \rho r \dot{r} \cos n\psi d\psi = \frac{I_1}{h},$$

$$\pi r \tilde{J}_{r,-1} = \int_0^{2\pi} \rho r \dot{r} \sin n\psi d\psi = \frac{I_{-1}}{h}, \text{ etc.}$$

Or, if  $2\pi e \omega B_0^2 r_c^2 \epsilon_0 / 4m$  is introduced as a characteristic current density per unit length, with the definition,  $i = \rho s \tilde{s}$ ,

$$2\pi i_{r,0} = \int_0^{2\pi} \rho s \tilde{s} d\psi, \quad \pi i_{r,1} = \int_0^{2\pi} \rho s \tilde{s} \cos n\psi d\psi,$$

$$\pi i_{r,-1} = \int_0^{2\pi} \rho s \tilde{s} \sin n\psi d\psi, \text{ etc.}$$

where  $i_{r,0}, \dots$  are reduced linear current densities per unit length.

The d-c power input is  $2\pi r_a h J_{r,0} V_0 = (\pi h / 4m) e \omega^2 B_0^2 r_c^2 \epsilon_0 (\tilde{i}_{r,0} A_0)$ , and the r-f power output is  $\pi r_a h J_{r,1} V_1 = (\pi h / 8m) e \omega^2 B_0^2 r_c^2 \epsilon_0 (\tilde{i}_{r,1} A_1)$ . The admittance of the electron stream per unit length is

$$2\pi r_a \frac{J_{r,1} + j J_{r,-1}}{V_1} \text{ or } 2\pi \frac{e B_0}{2m} \epsilon_0 \frac{\tilde{i}_{r,1} + j \tilde{i}_{r,-1}}{s \tilde{a}_{\phi,1}} = G_a + j B_a = y_a.$$

Under equilibrium conditions,  $G_{\text{al}} + jB_{\text{al}} = -Y_{\text{load}}$ . In principle, then, the potentials determine the currents, and, in turn, the load may be found. Practically, one sets the load, and the potentials and currents adjust themselves to suitable values for producing the correct admittance of the electron stream.

One may summarize the analysis by putting the result in functional form. Thus,

$$y_{\text{al}} = y(\gamma, s_a, a_0, \tilde{a}_\phi, n) \quad (67)$$

and

$$i_{r,0} = i_{r,0}(\gamma, s_a, a_0, \tilde{a}_\phi, n); \quad (68)$$

$\gamma$  is a parameter in the equations of motion;  $s_a$  governs the range of integration;  $a_0$  and  $\tilde{a}_\phi$  appear in the boundary conditions; and  $n$  in a condition of periodicity. The nonrelativistic Eqs. (54a), (54b), (56), and (57) and their solution in the form of Eqs. (67) and (68) provide the basis for the process of "scaling" magnetrons. Thus, if the linear dimensions of a magnetron are changed by a factor  $\alpha$ , the operating wavelength changed by a factor  $\alpha$ , and the magnetic field altered by a factor  $1/\alpha$ , it is clear that the variables  $\gamma$ ,  $s_a$ ,  $a_0$ , and  $\tilde{a}_{\phi,1}$  do not alter provided that the d-c and a-c voltages are unchanged. It follows from Eqs. (67) and (68) that  $y_{\text{al}}$  and  $i_{r,0}$  do not change. If the height  $h$  is also scaled by the factor  $\alpha$ , the characteristic admittances and currents for the tube will be unchanged, and thus the total current and admittance remain the same. Thus, two magnetrons related in this way will operate at the same d-c voltage and current with identical power output and loading (provided, one must add, that the circuit efficiencies are the same).

Similarly if the wavelength and magnetic field are left unchanged but the radial dimensions of the interaction space are multiplied by a factor  $\beta$ , the values of  $s_a$  and  $\gamma$  are unaltered. Now, an increase of a factor  $\beta^2$  in the d-c and r-f voltages leaves  $a_0$  and  $s\tilde{a}_\phi$  unchanged. One has, again, no change in  $i_{r,0}$  and  $y_{\text{al}}$ . The characteristic admittance for the whole tube is left the same, while the characteristic current is increased by  $\beta^2$ . Thus the loading is unchanged, while the total current increases by  $\beta^2$ . The power level increases by  $\beta^4$ . A scaling process of this nature is referred to usually as voltage scaling.

The process of scaling is extensively used in practice to design new magnetrons, and the systematics of the method are described fully in Chap. 10. The prediction of similar operation when the variables  $\gamma$ ,  $s_a$ ,  $n$ ,  $a_0$ , and  $s\tilde{a}_\phi$  are unchanged has been thoroughly confirmed by experimental results. The first scaling process will retain its validity in the relativistic range, since there will be no change in the additional parameter  $r = 2\pi r/n\lambda$  which appears in that case. However, voltage scaling will not be applicable because of the uncompensated change in  $r$ .

Attempts have been made to reduce the number of parameters upon which tube performance depends by introducing various combinations of  $\gamma$ ,  $s_a$ , and  $n$  into the definitions of the characteristic variables, thus obtaining new reduced variables. It is hoped that in such variables a fewer number than five may suffice to describe the behavior. One such a set is due to Slater<sup>1</sup> and has been extensively used by Clogston in Chap. 10. In this case a characteristic magnetic field given by  $B_0(1 - r_c^2/r_a^2)$  is used. The quantity is closely related to the vector potential of the magnetic field. The characteristic voltage is  $1/e$  times the kinetic energy of an electron moving around the cathode surface at rest in the rotating system. The characteristic current is chosen to be the current flowing at cutoff in the magnetron acting as a diode when a certain special voltage is applied to the anode.<sup>2</sup> It is not clear that this current has any intimate connection with the currents flowing in an operating magnetron, since the mechanism whereby electrons reach the anode in the operating magnetron is quite different from that involved in the magnetron without tangential fields. The characteristic voltages and currents may be used to define a characteristic admittance. In terms of these variables, reduced performance charts may be plotted for tubes with various values of  $n$ ; and if the variables had been expeditiously chosen, one might hope to find no dependence upon  $n$ . As pointed out in Chap. 10, this hope is not fulfilled.

*Analytical Deductions from the Equations of Motion.*—Returning now to the discussion of the equations of motion one may note that the expressions (27N) and (29N) now take the form

$$\frac{1}{2}(\dot{s}^2 + s^2\dot{\psi}^2) = \gamma V_E \quad (69)$$

and

$$\frac{\partial}{\partial s}(s^2\dot{\psi}) - \frac{\partial \dot{s}}{\partial \psi} = 2(1 - \gamma)s. \quad (70)$$

The condition that an electron be able to reach a point in the interaction space is simply that  $V_E > 0$  or  $a_0 - s\dot{a}_\phi > (1 - \gamma/2)s^2 - 1$ . This appears quite clearly as a consequence of the fact that the motion now takes place in a conservative potential field. So far as it has been possible to check this inequality experimentally it appears to be universally confirmed. In order to make the comparison it is necessary to know the r-f voltages within the tube, and this information is generally not available. If the data shown in Sec. 7-7 are examined, it will be found that under all circumstances the sum of the d-c voltage and the r-f voltage

<sup>1</sup> J. C. Slater, "Theory of Magnetron Operation," RL Report No. 43-28.

<sup>2</sup> This voltage is the threshold voltage defined in the next section. As Eq. (75) will show, there is only one magnetic field at which threshold and cutoff voltage can be equal.

exceeds  $(\pi c/n\lambda)r_a^2[(1 - 1/s_a^2)B_0 - (m\omega/e)]$  which is the form taken by the inequality when written in ordinary variables. The inequality provides information about the d-c voltage only when the r-f voltage is taken to be vanishingly small. Under such circumstances one has

$$a_0 \geq (1 - \gamma/2)s^2 - 1 \quad (71a)$$

or at the anode

$$V_0 \geq 9.42 \times 10^8 \frac{r_a^2}{n\lambda} \left[ \left(1 - \frac{1}{s_a^2}\right) B_0 - \frac{0.0107}{n\lambda} \right]. \quad (71b)$$

The voltage defined by the equality sign in Eqs. (71a) and (71b) is known as the threshold voltage. Its significance for the operation of magnetrons was first pointed out by Hartree;<sup>1</sup> essentially the same form had been found by Posthumus<sup>2</sup> for the case of vanishingly small cathode radius. It may be thought of as the minimum d-c voltage that will permit electrons to reach a point in the interaction space as the r-f voltage is made vanishingly small. It therefore plays a role for the multisegment (or tangential resonance) type of magnetron analogous to that of the Hull or cutoff voltage in a magnetron with cylindrical symmetry. The relation between the two formulas may be seen if Eq. (54b) is integrated in the form

$$\psi - 1 + \gamma = \frac{1}{s^2} \left( -1 + \gamma \int \frac{\partial V_E}{\partial \psi} d\tau \right) \quad (72)$$

and the result substituted in Eq. (69)

$$\begin{aligned} \bar{s}^2 + \left[ (1 - \gamma)s + \frac{1}{s} \left( -1 + \gamma \int \frac{\partial V_E}{\partial \psi} d\tau \right) \right]^2 \\ = 2\gamma(a_0 - s\bar{a}_\phi) - \gamma(2 - \gamma)s^2 + 2\gamma, \\ \bar{s}^2 + \left( s - \frac{1}{s} \right)^2 + \frac{2\gamma}{s} \left[ (1 - \gamma)s - \frac{1}{s} \right] \int \frac{\partial V_E}{\partial \psi} d\tau + \frac{\gamma^2}{s^2} \left( \int \frac{\partial V_E}{\partial \psi} d\tau \right)^2 \\ = 2\gamma(a_0 - s\bar{a}_\phi). \quad (73) \end{aligned}$$

Then in the absence of tangential fields ( $\partial V_E / \partial \psi = 0$ ) the condition satisfied by  $(a_0 - s\bar{a}_\phi)$  is simply

$$\gamma(a_0 - s\bar{a}_\phi) \geq \frac{1}{2} \left( s - \frac{1}{s} \right)^2. \quad (74)$$

This is the classical Hull formula giving the maximum radius that an electron can attain in a constant magnetic field under a given voltage. Using an obvious notation one has

<sup>1</sup> D. R. Hartree, CVD Report No. 1536, Mag. 17.

<sup>2</sup> K. Posthumus, *Wireless Eng. and Exp. Wireless*, **12**, 126 (1935).

$$\gamma(a_0 - s\tilde{a}_\phi)_{\text{Hull}} - \gamma(a_0 - s\tilde{a}_\phi)_{\text{threshold}}$$

$$\begin{aligned} &= \frac{1}{2} \left( s - \frac{1}{s} \right)^2 - \gamma \left( 1 - \frac{\gamma}{2} \right) s^2 + \gamma \\ &= \frac{1}{2} \left[ (\gamma - 1)s + \frac{1}{s} \right]^2 \\ &= \frac{1}{2} \left[ s\psi - \frac{\gamma}{s} \int \frac{\partial V_E}{\partial \psi} d\tau \right]^2 \\ &\geq 0. \end{aligned} \tag{75}$$

The threshold voltage thus lies below the Hull voltage save at the point  $(\gamma - 1)s = -1/s$  or  $\gamma = 1 - 1/s^2$ ; at this point the curves of threshold and Hull voltage as functions of  $\gamma$  have a point of common tangency.

It is found experimentally that if the threshold voltage given by Eq. (71b) be plotted against  $B_0$ , the straight line resulting is generally very nearly parallel to the constant-current lines in the  $V_0, B_0$  representation of magnetron performance. Depending upon the value of  $g_{\omega}$ , the threshold, or Hartree line as it is frequently known, lies above or below the  $V_0, B_0$  line for extrapolated zero current, by different amounts. Strictly speaking it should coincide with the zero-current line, and the data shown in Sec. 7-7 indicate that at very low currents the constant  $B_0$  lines in a normal  $V_0, I_0$  performance chart must be curved. This region of very low r-f voltage is almost unobservable experimentally because of the presence of leakage currents. Somewhat fortuitously, for most magnetrons operating with their normal loads and at normal currents, the constant-current lines in the  $B_0, V_0$  plane lie quite close to the Hartree line. The agreement is usually good to about one kilovolt. This fact has been of outstanding value in the design of magnetrons, since it permits the operating voltage at a given field to be estimated with sufficient accuracy in advance. At the same time the good agreement between the operating voltage and the threshold voltage over a very wide range of magnetic fields provides a confirmation of the supposition that the electrons interact with only one rotating component of the total field.

According to Eq. (35N) the energy that an electron contributes to the oscillating field measured by the difference between its potential energy in the scalar field  $A_0$  and its kinetic energy is

$$\begin{aligned} eV_{\text{loss}} &= e\omega r A_\phi - m_0 r^2 \omega (\psi + \omega) \\ &= e\omega r \tilde{A}_\phi + e\omega \frac{B_0}{2} (r^2 - r_c^2) - m_0 r^2 \omega (\psi + \omega). \end{aligned} \tag{6.35N}$$

Writing

$$V_{\text{loss}} = \frac{\omega B_0 r_c^2}{2} a_{\text{loss}},$$

then

$$a_{\text{loss}} = s^2(1 - \gamma - \bar{\psi}) - 1 + s\bar{a}_\phi \quad (76a)$$

$$= s\bar{a}_\phi - \gamma \int \frac{\partial(a_0 - s\bar{a}_\phi)}{\partial \psi} d\tau, \quad (76b)$$

and the efficiency of an individual electron  $\eta$  is given by

$$1 - \eta = \frac{a_0 - a_{\text{loss}}}{a_0} = \frac{(a_0 - s\bar{a}_\phi) + \gamma \int \frac{\partial(a_0 - s\bar{a}_\phi)}{\partial \psi} d\tau}{a_0}. \quad (77)$$

The efficiency for vanishingly small r-f voltage and a d-c voltage equal to the threshold voltage may be written down directly; then since  $\bar{\psi} = 0$  and  $s\bar{a}_\phi = 0$ , one finds

$$\eta = \frac{s^2(1 - \gamma) - 1}{s^2\left(1 - \frac{\gamma}{2}\right) - 1} = 1 - \frac{1}{\frac{2}{\gamma}\left(1 - \frac{1}{s^2}\right) - 1}. \quad (78)$$

Efficiencies calculated from this expression are substantially higher than those observed in practice (for example, for the 3-cm strapped magnetron whose performance chart appears in Fig. 6-1, the calculated efficiencies are greater by a factor of 1.2 to 1.5). This might have been expected from the highly idealized conditions under which Eq. (78) was derived. At the same time, the unavoidable presence of leakage current in operating tubes lowers the efficiency in the very region of low r-f amplitudes. Equation (78) indicates an identical efficiency per electron for magnetrons having the same value of  $\frac{1}{\gamma}\left(1 - \frac{1}{s_a^2}\right)$ . This will no longer be true if the accurate expression for energy loss is used, but it corresponds roughly to a fact of experience, namely, that a lower  $\gamma$  (higher magnetic field) is needed for the same efficiency when  $s_a$  is decreased. As a rough working rule the connection between  $\gamma$  and  $s_a$  may be assumed, indeed, to be  $1 - \left(\frac{1}{s_a^2}\right) = \text{constant} \times \gamma$  for the same efficiency.

The actual over-all efficiency of the magnetron will be given by

$$\eta = \frac{\int_0^{2\pi} \rho s \bar{s} [s^2(1 - \gamma) - 1 - s^2 \bar{\psi} + s\bar{a}_\phi] d\psi}{a_0 \int_0^{2\pi} \rho s \bar{s} d\psi}, \quad (79)$$

where the integrals are the sum of two integrals over anode and cathode

separately. Equation (79) may be written as

$$\eta = \frac{s^2(1 - \gamma) - 1}{a_0} + \frac{\int_0^{2\pi} \varrho s \bar{s} (s \bar{a}_\phi - s^2 \bar{\psi}) d\psi}{a_0 \int_0^{2\pi} \varrho s \bar{s} d\psi}, \quad (80)$$

the first term of which is the expression in Eq. (78), if  $a_0$  is the threshold voltage.

The behavior of the energy loss function [Eq. (76)] is indicated by Figs. 6-10 and 6-11 which show the energy loss as a function of magnetic field at fixed load for a 3-cm strapped magnetron and as a function of

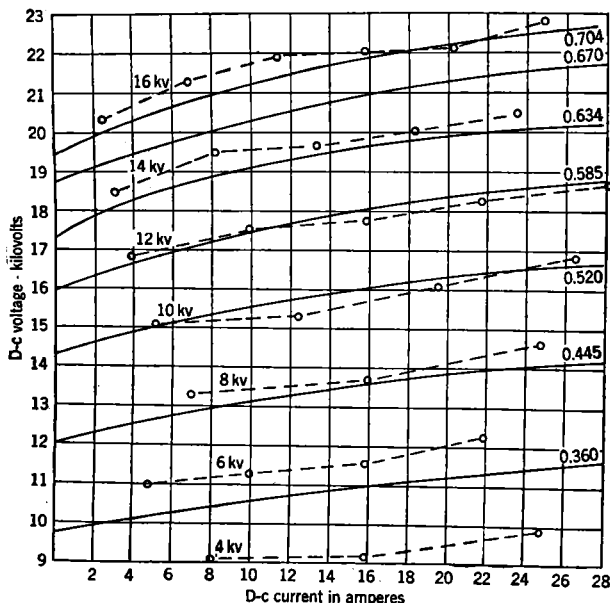


FIG. 6-10.—Average energy loss per electron in kilovolts at constant load for a typical 3-cm strapped magnetron with ——— magnetic field in webers/sq meter, - - - - electron loss in kv.

r-f and d-c voltages for a 10-cm strapped magnetron. It is of some interest to see that for the particular load of Fig. 6-10 the average energy loss per electron is remarkably independent of current, which indicates that the general behavior of the individual electrons is not much altered as the operating line is traversed but that the number of electrons increases. This may be accidental, since the evidence from Fig. 6-11 is that the average energy loss is largely a function of r-f voltage and relatively independent of d-c voltage. One cannot be certain that the apparent maximum in the energy loss as a function of r-f voltage is real

or whether or not the presence of leakage current at low levels is giving low values of energy loss. The maximum energy loss observed under the conditions of Fig. 6-11 is 2.33, which compares with the value of  $s_0^2(1 - \gamma) - 1$  of 3.5. It must be recalled that the average energy loss is diminished by inclusion of the energy gain due to electrons returning to the cathode.

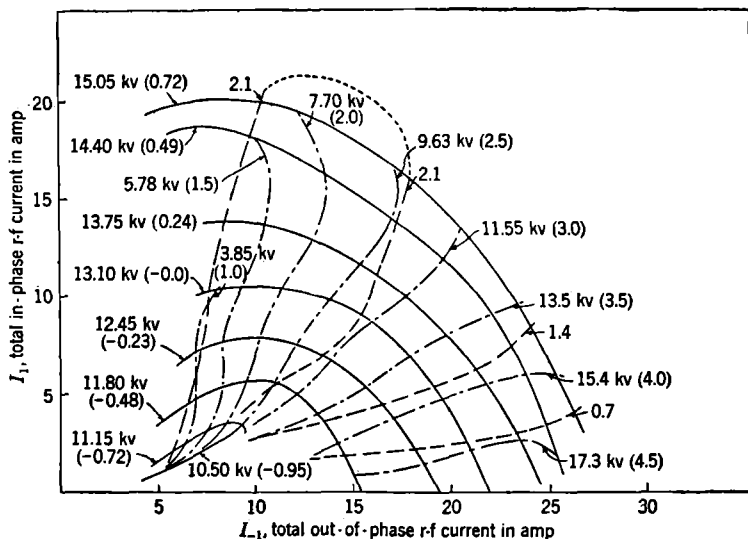


FIG. 6-11.—Average energy loss per electron (in reduced units) at constant magnetic field with ——— d-c voltage contours in kv, - - - r-f voltage contours in kv, - · - · - electron loss in kv. Figures in parentheses are reduced voltages; d-c values relative to threshold. Reduced linear current densities are given by  $I/36$ .

One further point may be noted in connection with Eq. (76b). Writing the radial conduction current density as  $j_{\text{cond}}$ , the r-f power must be

$$\int_0^{2\pi} j_{\text{cond}} s \tilde{a}_\phi s d\psi - \gamma \int_0^{2\pi} j_{\text{cond}} s d\psi \int_0^\tau \frac{\partial(a_0 - s \tilde{a}_\phi)}{\partial \psi} d\tau. \quad (81)$$

But the first term is simply the r-f power delivered by the conduction current, and hence the second term must be the r-f power supplied by the displacement current. It is worth while noting that the second term is the one from which the dominant contribution to the power arises while the first may and, in general, does represent a loss. This fact was pointed out by Slater.<sup>1</sup> Equation (76b) puts the energy loss in a form that shows clearly the contribution arising from the electron's moving in a time varying potential, when it is recalled that  $\partial/\partial t \equiv -\omega(\partial/\partial \psi)$ .

<sup>1</sup> J. C. Slater, "Theory of Magnetron Operation," RL Report No. 43-28.



The various forms of the expression for energy loss indicate that the latter will increase with  $s_a$ . This is seen from the leading term of Eq. (80) or the second term of Eq. (81) and arises from the fact that the larger  $s_a$  is the longer the time the electron spends in the interaction space. If  $\partial(a_0 - s\tilde{a}_\phi)/\partial\psi$  has the sign appropriate for a loss of energy over most of the path, the total loss will increase with transit time. Thus, from the standpoint of efficiency,  $s_a$  would naturally be made large. There is no series of carefully controlled experiments to confirm the expected increase of efficiency with  $s_a$ , but all the scattered data confirm it.

In practice, the choice of  $s_a$  is determined by considerations connected with mode shifting. It appears to be true that for any number of oscillators  $N$  there is a maximum value of  $s_a$  beyond which operation will not take place consistently in the  $\pi$ -mode. Since mode shifting is in at least one aspect a starting problem, the lack of a theory of starting prohibits a determination of the maximum  $s_a$ . It is probably true, however, that the essential factor is that as  $s_a$  is increased, the ratio of the intensity of the  $\pi$ -mode field to that of the field of any other mode decreases for equal amplitudes at the anode when the ratio is measured at some point within the initial nonoscillating cloud of space charge. Thus the building-up of some other mode than the  $\pi$ -mode is more probable.

**6-7. Symmetrical States.**—In this section the investigations that have been carried out on symmetrical states of the magnetron or those in which the potential has no angular variation will be considered. Despite the very different conditions that prevail in a normal magnetron, it might be expected that the symmetrical states would be of importance in the initiation of oscillations. Many of the difficulties that prevent exact integration of the equations of electron motion in the presence of a rotating potential wave persist in the symmetrical case, notably the difficulty of dealing with multistream states. In fact, the solutions of the symmetrical problem are sufficiently tentative so that it is difficult to make them the foundation of a theory of starting for the tangential-field type of magnetron. Because the problem is in some respects simpler than that which includes rotating waves, it has been the subject of considerable analytical and numerical work. It is proposed to outline some of this work mainly to bring out the difficulties involved and to indicate the relevance of the conclusions to the major problem. The discussion is based upon the work of Hartree, Allis, Brillouin, and Bloch<sup>1</sup> and follows most closely the work of Bloch.

The equations of motion in the absence of a rotating field may be formed from Eqs. (54a) and (54b) by letting  $\gamma$  tend to zero and writing

<sup>1</sup> D. R. Hartree, CVD Report, Mag. 23; Allis, RL Report No. 9S, Sec. V, 1941; L. Brillouin, AMP Report No. 129; F. Bloch, NDRC 15-411-175, 1945.

$\gamma V_z = V_z$ . This leads to

$$\bar{s} = s\bar{\psi}^2 - 2s\bar{\psi} + \frac{\partial V_z}{\partial s} \quad (82a)$$

and

$$\frac{d}{d\tau}(s^2\bar{\psi}) = 2s\bar{s}, \quad (82b)$$

where  $V_z$  is equal to  $(4m_0/eB_0^2r_0^2)A_0$  and is independent of angle but may, however, now be a function of time. The second equation may be integrated; and putting  $\bar{\psi} = 0$  at  $s = 1$ , there follows

$$\bar{\psi} = 1 - \frac{1}{s^2}. \quad (83)$$

Substituting this value in Eq. (82a) one finds

$$\begin{aligned} \bar{s} &= \frac{1}{s^3} - s + \frac{\partial V_z}{\partial s} \\ &= \frac{1}{s^3} - s - e_z. \end{aligned} \quad (84)$$

The other equations are

$$\frac{1}{s} \frac{\partial}{\partial s} \left( s \frac{\partial V_z}{\partial s} \right) = -\frac{1}{s} \frac{\partial}{\partial s} (s e_z) = \rho \gamma \quad (85)$$

and

$$\frac{1}{s} \frac{\partial}{\partial s} [s(\gamma \rho \bar{s} - \bar{e}_z)] = 0, \quad (86)$$

where the displacement current  $\bar{e}_z$  must be included in the current. Equation (86) leads to

$$s(\rho \bar{s} \gamma - \bar{e}_z) = \gamma i, \quad (87)$$

where  $i$  is the reduced current per unit length and is independent of  $s$ . Thus, using Eq. (85)

$$\begin{aligned} \frac{d(e_z s)}{d\tau} &= \bar{s} \frac{\partial(e_z s)}{\partial s} + s \bar{e}_z \\ &= -\gamma i \end{aligned}$$

or

$$-e_z = \frac{1}{s} \int_{\tau_0}^{\tau} \gamma i d\tau \quad (88)$$

and Eq. (84) takes its most compact form,

$$\bar{s} = \frac{1}{s^3} - s + \frac{1}{s} \int_{\tau_0}^{\tau} \gamma i d\tau. \quad (89)$$

Eqs. (87) and (89) have one very specialized solution which may be written down immediately. For suppose that  $\bar{s} = 0$  identically. Then

$$V_2 = \frac{1}{2} \left( s - \frac{1}{s} \right)^2, \quad (90)$$

and

$$\vartheta = \frac{2}{\gamma} \left( 1 + \frac{1}{s^4} \right). \quad (91)$$

The solution represents a single-stream state in which all the electrons move in circles about the cathode with angular velocities given by Eq. (83). The charge density is so disposed that the space-charge forces exactly balance the magnetic ones. The cloud of electrons extends out to some definite radius beyond which a logarithmic potential continues the solution to the anode when the voltage on the latter is less than  $\frac{1}{2}[s_a - (1/s_a)]^2$ . The potential at any point is exactly the Hull cutoff voltage, as one might expect, since  $\bar{s} = 0$ . There is no radial current, since the charge density is everywhere finite; this means that  $\tau$  has to be allowed to become indefinitely large in Eq. (89). This special solution was discovered by Blewett and Ramo<sup>1</sup> for the case of negligible cathode radius and again by Brillouin;<sup>2</sup> it is frequently referred to as the Brillouin steady state. It will be described here as a type *S* state, indicating that it is a single-stream state. It may be observed that an analogous state may be found when the exact relativistic equations of motion and field are used. It is necessary here to take into account the effect of the magnetic field of the circulating current.

Another conceivable steady state is one in which the electrons return to the cathode after turning back at some point. In this case there will be a double-stream or type *D* state. Since the voltage is to be considered constant, the current is constant and one may write

$$\bar{s} = \frac{1}{s^3} - s + \frac{\gamma i r}{s}, \quad (92)$$

since there will be equal and opposite currents through any point of the interaction space. Consider  $i\gamma$  as representing the ingoing or outgoing current. Explicitly

$$i\gamma = \frac{8m_0^2}{2\pi e^2 B_0^3 r^2 \epsilon_0} I$$

where  $I$  is the current per unit length. Evaluating one finds

$$i\gamma = 4.55 \times 10^{-12} \frac{I}{B_0^3 r^2}.$$

<sup>1</sup> J. P. Blewett and S. Ramo, *Phys. Rev.* **57**, 635 (1940).

<sup>2</sup> L. Brillouin, *Phys. Rev.* **60**, 385 (1941), and **65**, 166 (1942).

For the values of  $I$ ,  $r_c$ , and  $B$  common in operating magnetrons  $i\gamma$  will be quite small. Solutions of Eqs. (89) and (92) with  $s = 1$ ,  $\bar{s} = 0$  at  $\tau = 0$  have been investigated by Allis and others. It may be shown that for  $i\gamma$  tending to zero,  $\bar{s} > 0$  for all  $s < 2.271$  and, hence, that no type  $D$  state is possible for cloud radii less than 2.271. For  $i\gamma$  not zero, numerical integration must be resorted to, and Allis, Hartree, and Brillouin have shown in this way that a slightly lower critical cloud radius is found. The value of this radius appears to approach a limit close to 2 as  $i\gamma$  becomes large. Thus, in a tube for which  $s_a > 2.271$  it appears that as the anode voltage is raised, no type  $D$  state will be possible until the voltage exceeds a certain minimum value; such a state will exist over a certain range of voltages, after which current will be drawn to the anode.

A question that has been treated extensively by Bloch is that of the transient phenomena occurring in those cases where  $i$  is not constant in time. Writing Eq. (89) in the form

$$s\ddot{s} = \dot{s}^{-2} - s^2 + \phi(\tau, \tau_0), \quad (93a)$$

where

$$\phi(\tau, \tau_0) = \int_{\tau_0}^{\tau} \gamma i \, d\tau, \quad (93b)$$

it will be supposed that  $\gamma i \ll 1$  for all  $\tau$ , which, as was remarked above, will be true over the usual range of parameters. The linear case will be considered also because of its peculiar features. Putting

$s = 1 + \frac{y}{r_c}$  and allowing  $r_c \rightarrow \infty$ , Eq. (93a) becomes

$$\ddot{y} = -4y + r_c \phi(\tau, \tau_0). \quad (94a)$$

This is simply the equation of a harmonic oscillator subject to a driving force  $r_c \phi(\tau, \tau_0)$ . A solution is required with  $y = 0$ ,  $\dot{y} = 0$  at  $\tau = \tau_0$ . The problem admits of an exact solution. Considering a function  $y_0(\tau, \tau')$  such that

$$\frac{\partial^2 y_0}{\partial \tau^2} + 4y_0 = \frac{\partial^2 y_0}{\partial \tau'^2} + 4y_0 = 0 \quad (94b)$$

and

$$y_0(\tau', \tau') = 0 \quad \frac{\partial y_0}{\partial \tau}(\tau', \tau') = 1,$$

one may multiply Eq. (94a) by  $y_0$  and Eq. (94b) by  $-y$ . Then, adding the results and integrating from  $\tau_0$  to  $\tau'$ , one has

$$\left( y_0 \frac{dy}{d\tau} - y \frac{dy_0}{d\tau} \right)_{\tau_0}^{\tau'} = \int_{\tau_0}^{\tau'} r_c \phi(\tau, \tau_0) y_0(\tau, \tau') \, d\tau \quad (95)$$

and using the boundary conditions on  $y_0$

$$-y(\tau') = y_0(\tau_0, \tau') \frac{dy}{d\tau}(\tau_0) - y(\tau_0) \frac{dy_0}{d\tau}(\tau_0, \tau') + \int_{\tau_0}^{\tau'} r_c \phi(\tau, \tau_0) y_0(\tau, \tau') d\tau.$$

Observing the boundary conditions on  $y(\tau')$ ,

$$y(\tau') = - \int_{\tau_0}^{\tau'} r_c \phi(\tau, \tau_0) y_0(\tau, \tau') d\tau. \quad (96)$$

A suitable choice for the function  $y_0(\tau, \tau')$  is  $\frac{1}{2} \sin 2(\tau - \tau')$ , and thus Eq. (96) becomes

$$y(\tau) = - \frac{1}{2} \int_{\tau_0}^{\tau} r_c \phi(\tau', \tau_0) \sin 2(\tau' - \tau) d\tau'. \quad (97)$$

Consider, now,  $\partial y(\tau)/\partial \tau_0$ . From Eq. (97)

$$\begin{aligned} \frac{\partial y}{\partial \tau_0} &= - \frac{1}{2} \int_{\tau_0}^{\tau} \frac{\partial [r_c \phi(\tau', \tau_0)]}{\partial \tau_0} \sin 2(\tau' - \tau) d\tau' \quad \text{since } \phi(\tau_0, \tau_0) = 0 \\ &= \frac{1}{2} \int_{\tau_0}^{\tau} r_c \gamma i(\tau_0) \sin 2(\tau' - \tau) d\tau' \\ &= - \frac{1}{4} r_c \gamma i(\tau_0) [1 - \cos 2(\tau_0 - \tau)] \\ &\geq 0 \quad \text{since } i(\tau_0) \geq 0. \end{aligned} \quad (98)$$

This, however, is exactly the condition that electron orbits shall not cross, for it implies that at any given time an electron emitted later than another lies closer to the cathode than does the latter. The state is thus of type *S*. The result is independent of the variation of current and hence of that of the voltage. On the other hand, if the condition of space-charge limitation is relaxed, Brillouin has shown that the orbits do cross. Although the orbits do not actually cross in the case considered above, they may touch and, indeed, will do so when  $\tau_0 - \tau = (n + \frac{1}{2})\pi$ . There will then exist curves in space defined by this equation with which the orbits have tangential contact; the charge density on such curves will be indefinitely large. This appears to be an instance in which the inclusion of an initial velocity distribution for the electrons might be expected to modify the results very considerably, but this point has not been investigated.

The situation in the cylindrical case is considerably more complicated, and the nature of the results quite different. To make progress by analytical means it is necessary to suppose that  $(\gamma i) \ll 1$ . Then  $\phi(\tau, \tau_0)$  is a slowly varying function of  $\tau$ . If this be so, an approximate solution of Eq. (93a) is seen to be given by  $s_0$ , where

$$s_0^2 - s_0'^2 = \phi(\tau, \tau_0), \quad (99)$$

for  $s_0$  defined by Eq. (99) is a slowly varying function of  $\tau$ , and  $\bar{s}_0$  will be small.

Suppose then that

$$s = s_0 + x, \quad (100)$$

where  $x$  is capable of being written in the form

$$x = \lambda x_1 + \lambda^2 x_2 + \lambda^3 x_3 + \dots$$

in which  $\lambda$  is of the order of  $\partial\phi/\partial\tau$  and, hence,  $\lambda \ll 1$ . Substituting Eq. (100) in Eq. (93a) one has

$$\bar{x} + 2(1 + s_0^{-4})x = -\bar{s}_0 + (s_0^{-1} + 5s_0^{-5})x^2 - (s_0^{-2} + 9s_0^{-6})x^3 + (s_0^{-3} + 14s_0^{-7})x^4 - \dots \quad (101)$$

This is, once again, the equation of an oscillator driven by the forces represented by the right-hand side. There is, however, the important distinction that the frequency of the oscillator is slowly changing because of the dependence of  $s_0$  upon  $\tau$ . The total motion of the electron thus consists of a slow drift, monotonically away from the cathode, given by  $s_0(\tau, \tau_0)$ , superimposed upon which is an oscillatory term with adiabatically varying frequency. The secular motion becomes more sluggish as  $\partial\phi/\partial\tau$  or  $i \rightarrow 0$ . Equation (101) may be solved correctly to the first order in  $\partial\phi/\partial\tau$  by neglecting the terms in  $x^2$ ,  $x^3$ , etc., provided that solutions of

$$\bar{x} + 2(1 + s_0^{-4})x = \bar{x} + \omega_1^2(\tau, \tau_0)x = 0 \quad (102)$$

are available correct to the first order in  $\partial\phi/\partial\tau$ . To obtain these introduce  $\theta(\tau, \tau_0) = \int_{\tau_0}^{\tau} \omega_1(\tau', \tau_0) d\tau'$  and write  $x = \exp \int_0^{\theta} z d\theta'$ ; then in such variables Eq. (102) becomes

$$z^2 + \frac{\partial z}{\partial \theta} + \frac{\partial \log \omega_1}{\partial \theta} z + 1 = 0. \quad (103a)$$

Putting  $z = \pm i + p$ , where  $p$  is of the order of  $\partial\phi/\partial\tau$ , one has to the first-order

$$\frac{\partial p}{\partial \theta} = \mp 2ip \mp i \frac{\partial \log \omega_1}{\partial \theta} \quad (103b)$$

or, integrating,

$$p = \pm i \int_0^{\theta} \frac{\partial \log \omega_1}{\partial \theta'} \exp \mp 2i(\theta - \theta') d\theta' \quad (103c)$$

and

$$x = \exp \left[ \pm i\theta \pm i \int_0^{\theta} d\theta' \int_0^{\theta'} \frac{\partial \log \omega_1}{\partial \theta''} \exp \mp 2i(\theta - \theta'') d\theta'' \right]. \quad (103d)$$

Integrating by parts

$$x = \frac{\exp \pm i\theta}{\sqrt{\omega_1}} \exp \int_0^\theta \frac{\partial \log \sqrt{\omega_1}}{\partial \theta'} \exp \mp 2i(\theta - \theta') d\theta'. \quad (103e)$$

Provided that the variation of current is reasonably uniform, the last integral will be of the order of  $\partial\omega_1/\partial\theta$  or  $\partial\phi/\partial\tau$ . Thus, the zero-order solutions are of the form

$$y = \frac{A}{\sqrt{\omega_1}} \exp \pm i\phi. \quad (104)$$

The solution of Eq. (101), correct to first-order terms, may now be found as it was in the linear case, where for the function  $y_0(\tau, \tau')$  one uses

$$y_0(\tau, \tau') = \frac{\sin(\theta - \theta')}{\sqrt{\omega_1(\tau, \tau_0)\omega_1(\tau', \tau_0)}} \quad (105)$$

This satisfies the condition that  $\partial y_0(\tau', \tau')/\partial\tau = 1$ , since  $\partial\theta/\partial\tau = \omega_1(\tau, \tau_0)$  by definition. Making use of Eq. (95) and noting that the driving term is  $-\bar{s}_0$ , one has

$$y(\tau') = -y_0(\tau_0, \tau') \frac{\partial x}{\partial \tau}(\tau_0) + \frac{\partial y_0}{\partial \tau}(\tau_0, \tau') x(\tau_0) + \int_{\tau_0}^{\tau'} \bar{s}_0(\tau, \tau_0) y_0(\tau, \tau') d\tau. \quad (106)$$

Now,  $s_0 + x$  satisfies the boundary conditions  $s_0 + x = 1$  and  $\bar{s}_0 + \bar{x} = 0$  at  $\tau = \tau_0$ ; thus,  $x(\tau_0, \tau_0) = 0$  and  $\partial x(\tau_0, \tau_0)/\partial\tau = -\bar{s}_0(\tau_0, \tau_0)$ . Thus, Eq. (106) becomes, using Eq. (105),

$$y(\tau') = -\bar{s}_0(\tau_0, \tau_0) \frac{\sin \theta'}{\sqrt{\omega_1(\tau_0, \tau_0)\omega_1(\tau', \tau_0)}} + \int_{\tau_0}^{\tau'} \bar{s}_0(\tau, \tau_0) \frac{\sin(\theta - \theta')}{\sqrt{\omega_1(\tau, \tau_0)\omega_1(\tau', \tau_0)}} d\tau \quad (107)$$

Since  $\omega_1(\tau_0, \tau_0) = 2$  and because  $2\bar{s}_0(s_0 + s_0^{-3}) = \partial\phi(\tau, \tau_0)/\partial\tau$ , which implies  $\bar{s}_0(\tau_0, \tau_0) = \frac{1}{4}(\partial\phi(\tau_0, \tau_0)/\partial\tau)$ , the final result for the motion correct to first-order terms in  $\partial\phi/\partial\tau$  is

$$s(\tau, \tau_0) = s_0(\tau, \tau_0) - \frac{\sin \theta}{4\sqrt{2\omega_1(\tau, \tau_0)}} \frac{\partial \phi}{\partial \tau}(\tau_0, \tau_0) + \int_{\tau_0}^{\tau} \bar{s}_0(\tau', \tau_0) \frac{\sin(\theta' - \theta)}{\sqrt{\omega_1(\tau, \tau_0)\omega_1(\tau', \tau_0)}} d\tau'. \quad (108)$$

If this is to be a type *S* state,

$$\frac{\partial s}{\partial \tau_0} < 0 \quad \text{for all } \tau_0 \text{ and } \tau.$$

Differentiating with respect to  $\tau_0$  and retaining only terms of zero and first order,

$$\begin{aligned} \frac{\partial \mathbf{s}}{\partial \tau_0} = & \frac{\partial \mathbf{s}_0}{\partial \tau_0} - \frac{\bar{\phi}(\tau_0, \tau_0)}{4} \frac{\sin \theta}{\sqrt{2\omega_1(\tau, \tau_0)}} - \frac{\bar{\phi}(\tau_0, \tau_0)}{4} \frac{\cos \theta}{\sqrt{2\omega_1(\tau, \tau_0)}} \frac{\partial \theta}{\partial \tau_0} \\ & + \bar{\mathfrak{S}}_0(\tau_0, \tau_0) \frac{\sin \theta}{\sqrt{\omega_1(\tau, \tau_0)\omega_1(\tau_0, \tau_0)}} + \int_{\tau_0}^{\tau} \left[ \frac{\bar{\mathfrak{S}}_0(\tau_0, \tau_0)}{\sqrt{\omega_1(\tau, \tau_0)\omega_1(\tau', \tau_0)}} \right] \\ & \left[ \left( \frac{\partial \theta'}{\partial \tau_0} - \frac{\partial \theta}{\partial \tau_0} \right) \cos (\theta' - \theta) d\tau \right]. \quad (109) \end{aligned}$$

To the first order, the second and fourth terms cancel, leaving

$$\begin{aligned} \frac{\partial \mathbf{s}}{\partial \tau_0} = & \frac{\partial \mathbf{s}_0}{\partial \tau_0} - \frac{\bar{\phi}(\tau_0, \tau_0)}{4} \frac{\cos \theta}{\sqrt{2\omega_1(\tau, \tau_0)}} \frac{\partial \theta}{\partial \tau_0} \\ & + \int_{\tau_0}^{\tau} \left[ \frac{\bar{\mathfrak{S}}_0(\tau_0, \tau_0)}{\sqrt{\omega_1(\tau, \tau_0)\omega_1(\tau', \tau_0)}} \right] \left[ \left( \frac{\partial \theta'}{\partial \tau_0} - \frac{\partial \theta}{\partial \tau_0} \right) \cos (\theta' - \theta) d\tau \right]; \quad (110) \end{aligned}$$

furthermore,

$$\frac{\partial \mathbf{s}_0}{\partial \tau_0} = - \frac{\bar{\phi}(\tau_0, \tau_0)}{2(\mathbf{s}_0 + \mathbf{s}_0^{-3})},$$

and

$$\frac{\partial^2 \mathbf{s}_0}{\partial \tau_0^2} = \frac{+\bar{\phi}(\tau_0, \tau_0)}{2(\mathbf{s}_0 + \mathbf{s}_0^{-3})} - \frac{(1 - 3\mathbf{s}_0^{-4})}{4(\mathbf{s}_0 + \mathbf{s}_0^{-3})^3} \bar{\phi}(\tau_0, \tau_0)^2.$$

So one has

$$\begin{aligned} \frac{\partial \mathbf{s}}{\partial \tau_0} = & - \frac{\bar{\phi}(\tau_0, \tau_0)}{4} \left[ \frac{2}{\mathbf{s}_0 + \mathbf{s}_0^{-3}} + \frac{\cos \theta}{\sqrt{2\omega_1(\tau, \tau_0)}} \frac{\partial \theta}{\partial \tau_0} \right] \\ & + \int_{\tau_0}^{\tau} \frac{\bar{\phi}(\tau_0, \tau_0)}{2(\mathbf{s}_0 + \mathbf{s}_0^{-3})} \frac{\frac{\partial \theta'}{\partial \tau_0} - \frac{\partial \theta}{\partial \tau_0}}{\sqrt{\omega_1(\tau, \tau_0)\omega_1(\tau', \tau_0)}} \cos (\theta' - \theta) d\tau. \quad (111) \end{aligned}$$

This reduces, as it should, to Eq. (98) when  $\mathbf{s} = 1 + (y/r_e)$  and  $r_e \rightarrow \infty$  for then  $\mathbf{s}_0 = 1$ ,  $\theta' = 2(\tau' - \tau_0)$ , and  $\omega_1(\tau, \tau_0) = 2$ . The conditions for  $\partial \mathbf{s} / \partial \tau_0 < 0$  are now more complicated than they were in the linear case if  $\bar{\phi}(\tau_0, \tau_0)$ , or, in other words, the current, is allowed to vary in an unrestricted fashion. If the current is small enough and its rate of change is also small and regular, the integral term in Eq. (111) may be ignored and the condition for a type *S* solution becomes

$$\frac{2}{\mathbf{s}_0 + \mathbf{s}_0^{-3}} \geq \frac{1}{\sqrt{2\omega_1(\tau, \tau_0)}} \left| \frac{\partial \theta}{\partial \tau_0} \right|. \quad (112a)$$

By its definition

$$\begin{aligned} \frac{\partial}{\partial \tau} \left( - \frac{\partial \theta}{\partial \tau_0} \right) = & - \frac{\partial \omega_1(\tau, \tau_0)}{\partial \tau_0} = \frac{\partial \omega_1(\tau, \tau_0)}{\partial \tau} \frac{i(\tau_0)}{i(\tau)} \\ & - \frac{\partial \theta}{\partial \tau_0} = \omega_1(\tau_0, \tau_0) + \int_{\tau_0}^{\tau} \frac{\partial \omega_1(\tau', \tau_0)}{\partial \tau'} \frac{i(\tau_0)}{i(\tau')} d\tau'. \quad (112b) \end{aligned}$$



Thus, even for small currents, the form of  $\partial\theta/\partial\tau_0$  varies considerably according to the law of current. When  $i$  is constant,

$$\left| \frac{\partial\theta}{\partial\tau_0} \right| = \omega_1(\tau, \tau_0) = \sqrt{2(1 + s_0^{-4})} \quad (112c)$$

and the condition in Eq. (112a) becomes

$$1 < \frac{1}{s_0} \left( \frac{2}{1 + s_0^{-4}} \right)^{3/4} \quad (112d)$$

or

$$s_0 < 2.271.$$

Thus, a solution of type *S* exists as long as the cloud radius is less than 2.271; this is the same limiting radius found by Allis as the lower limit of cloud radii for which a type *D* state was possible. It may, indeed, be shown that for finite currents there always exists a critical radius separating type *S* and type *D* states.

Now suppose that  $i$  is no longer constant but increases or decreases monotonically, remaining at all times small, however. Since  $\omega_1$  steadily decreases with  $\tau$ ,  $\partial\omega_1/\partial\tau$  is negative; and then for positive currents, from Eq. (112b),  $-\partial\theta/\partial\tau_0$  must also decrease monotonically with  $\tau$ . If  $i$  increases monotonically,  $i(\tau_0)/i(\tau) < 1$  for all  $\tau$ ; and using Eq. (112b) again, one has

$$2 > \left| -\frac{\partial\theta}{\partial\tau_0} \right| > \omega_1(\tau, \tau_0). \quad (113)$$

Since the condition for breakdown of a type *S* state is Eq. (112a) or

$$\frac{2^{3/2} \sqrt{\omega_1(\tau, \tau_0)}}{s_0 + s_0^{-3}} = \left| -\frac{\partial\theta}{\partial\tau_0} \right|,$$

this may be combined with Eq. (113) to give an inequality for the critical radius

$$2 > \frac{2^{3/2} \sqrt{\omega_1(\tau, \tau_0)}}{s_0 + s_0^{-3}} > \omega_1$$

or

$$2 > \frac{2^{3/2} 2^{1/4} (1 + s_0^{-4})^{1/4}}{s_0 (1 + s_0^{-4})} > 2^{3/2} (1 + s_0^{-4})^{1/2}.$$

This yields

$$2.271 > s_0 > 1.434. \quad (114)$$

There is thus a critical cloud radius between these limits, the exact value of which hinges upon the law followed by the current at which a type *s* state becomes impossible. Since Allis' work shows that there is no type *D* state, it would appear that under a condition of increasing anode voltage, if a single-stream state is set up when  $s_{\text{cloud}} < 1.434$ , this must

break up into some transient state until the voltage is high enough to give a cloud radius greater than 2.271.

When the current decreases monotonically  $[i(\tau_0)/i(\tau)] > 1$ , the integral term from Eq. (112b) decreases faster than  $\omega_1(\tau, \tau_0)$  and furthermore  $-\partial\theta/\partial\tau_0 < \omega_1(\tau_0, \tau_0)$ . Two things may happen: If  $|\partial\theta/\partial\tau_0| < \omega_1(\tau_0, \tau_0)$ , the condition for the breakdown of the  $S$  state Eq. (112a) is altered to give a larger value of  $s_0$  and the  $S$  state may persist beyond  $s_0 = 2.271$ ; whereas if  $|\partial\theta/\partial\tau_0| > \omega_1(\tau_0, \tau_0)$ , as may happen if  $-\partial\theta/\partial\tau_0$  becomes sufficiently negative, the breakdown condition, as in the case of a monotonically increasing current, becomes more severe and the  $S$  state breaks down for cloud radii less than 2.271.

Finally suppose that a small current flows for a certain time  $T$ , after which it becomes zero. Then

$$\frac{\partial\omega_1(\tau, \tau_0)}{\partial\tau_0} = \frac{-8s_0^{-5}}{\omega_1(\tau, \tau_0)} \frac{\partial s_0}{\partial\tau_0} = -\frac{8s_0^{-5}}{\omega_1(\tau, \tau_0)} \frac{1}{2(s_0 + s_0^{-3})} \frac{\partial}{\partial\tau_0} \int_{\tau_0}^{\tau} \frac{i\gamma}{2\pi} d\tau. \quad (115)$$

For  $\tau > T$ , this expression becomes

$$\frac{\partial\omega_1(\tau, \tau_0)}{\partial\tau_0} = + \frac{4s_0^{-5}}{\omega_1(\tau, \tau_0)(s_0 + s_0^{-3})} \frac{\gamma i(\tau_0)}{2\pi} > 0, \quad (116)$$

and, from Eq. (112b),

$$\frac{\partial}{\partial\tau} \left( \frac{\partial\theta}{\partial\tau_0} \right) = \text{a positive constant}, \quad \tau > T.$$

It follows that  $\partial\theta/\partial\tau_0$  can become as large as one pleases after sufficiently long times. Thus the instability criterion Eq. (112a) shows that a cloud of any radius established during the flow of current becomes unstable after a sufficient length of time. The length of time required for the instability to appear will be of the order of  $1/\gamma i(\tau_0)$ .

This review of the work which has been carried out on the symmetric states of magnetrons has indicated the unsatisfactory status of the analysis. There are essentially no experimental data to confirm or to contradict any of the tentative conclusions reached; and in fact, it is not clear for those cases of greatest interest in which no anode current is drawn how experiment would distinguish among the various states of electron flow. Probe measurements would invalidate the assumption of azimuthal symmetry.

One or two points may be noted. One is the connection between the cylindrical and linear problems. The solution of the linear problem has a very artificial appearance. The appearance of a series of layers on which neighboring orbits touch, as indicated by Eq. (98), thus giving an infinite charge density, would probably be modified if an initial distribution of electron velocities was included. Furthermore the slightest

curvature of the cathode surface, in the concave sense, will give rise to a crossing of orbits, while in the convex sense, it will cause the orbits no longer to touch. If a linear flow of the type indicated by the solution (98) initially existed, a small curvature applied to the cathode would render it unstable, since the cloud radius would be less than  $2.271r_c$ . Presumably, however, it would be quasi-stable in the sense that a considerable time would elapse before the initial organization was destroyed. This raises the question whether or not there may not be states with cloud radius  $\leq 2.271$  times the cathode radius which are effectively stable, in the sense that over periods of time which are comparable to the starting time of the magnetron, they would maintain a potential distribution and a cloud radius closely comparable to that of the Brillouin steady state. In this connection it should be noted that in double-stream states, where they can exist, the potential distribution is always close to  $1/2\gamma[s - (1/s)]^2$  unless very large radial currents are flowing.

**6-8. The Bunemann Small-amplitude Theory.**—The only serious investigation of the conditions under which tangential resonance oscillations will build up in a magnetron has been made in an extensive report by O. Bunemann.<sup>1</sup> It cannot be claimed that Bunemann's results are conclusive or that the assumptions of his treatment are completely sound. However, the viewpoint taken in the paper is illuminating, and it will be discussed here rather fully.

Bunemann's approach is to assume an initial state of electronic motion that has azimuthal symmetry under conditions of constant d-c voltage and magnetic field. It is then supposed that a rotating r-f wave of very small amplitude, of frequency  $\omega_0$  and angular velocity  $\omega = \omega_0/n$ , is imposed on the anode. The small perturbations of the original steady state are then worked out, taking into account the equations of motion, the equation of continuity, and Poisson's equation. In this way the impedances of the electron cloud is calculated and the wave impedances within and without the cloud are matched. The variation with frequency of the impedance of the charge cloud is studied and is shown to be such as to lead, under some conditions of voltage, magnetic field, and frequency, to a state in which oscillations will build up spontaneously. The analysis is then extended in a more speculative manner to determine the rate of buildup of oscillations with various loads.

This formulation of the problem appears to simplify the true state of affairs, for it divides the process of initiation of oscillations into two stages: (1) the establishment of a steady azimuthally symmetric state which is supposed to persist while the anode voltage remains constant, (2) the breakup of this state under the angle-dependent rotating perturba-

<sup>1</sup> O. Bunemann, "A Small Amplitude Theory for Magnetrons," CVD Report, Mag. 37, 1944.

tion. In practice one has a d-c voltage that increases steadily during the process. If the time of rise of the voltage be taken to be  $0.04 \mu\text{sec}$ , which is fairly typical, this becomes, in terms of the unit of time  $2m/eB_0$ , equal to  $3.6 \times 10^2 B_0$  ( $B_0$  in kilogauss). A typical rate of rise in reduced units gives  $\partial a_0/\partial \tau \sim 5 \times 10^{-9} (n\lambda/r_c^2 B_0^2)$  (MKS). It is evident that the rate at which the voltage rises is indeed slow in terms of the natural units, occupying many Larmor periods. Thus it is probably satisfactory to consider the problem as a static one.

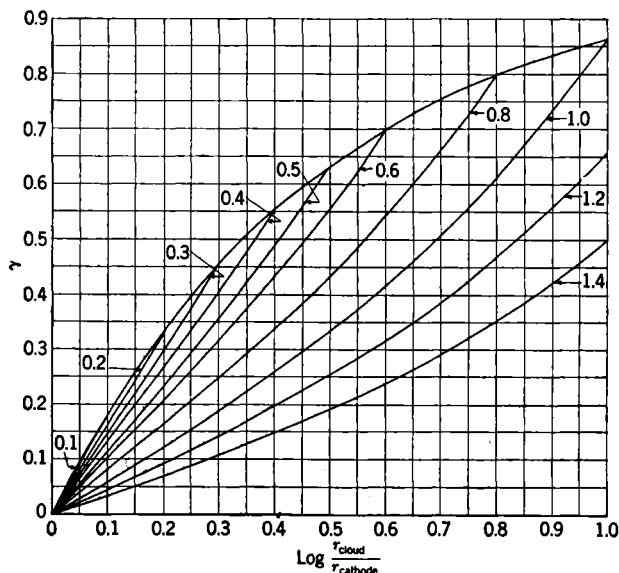


FIG. 6-12.—Radius of Brillouin steady-state  $r_{\text{cloud}}$  as a function of  $\gamma$ , for various anode radii  $r_a$ , when the anode voltage is equal to the threshold voltage.  $\text{Log } r_{\text{cloud}}/r_{\text{cathode}}$  is plotted against  $\gamma$  for various values of  $\text{log } r_{\text{anode}}/r_{\text{cathode}}$ . The boundary curve shows the radius of the stationary layer.

The state chosen by Bunemann as an initial state for the electrons is the Brillouin steady state in which the radial current is zero and the electrons move about the cathode on concentric circles. As has been shown in the previous section, if the cloud radius is less than 2.271, no stationary double-stream solution with zero radial current and constant anode voltage is possible. The only single-stream state for vanishing radial current is the Brillouin one. In Fig. 6-12 the radius of the Brillouin steady state is shown for various anode to cathode ratios and values of  $\gamma$  when it is assumed that the anode voltage is given by the threshold voltage. This assumption is a reasonable one, since the cloud radius does not vary rapidly with anode voltage and the magnetron certainly operates near the threshold voltage. It may be seen that for most practical cases

the cloud radius under these conditions is less than 2.271. While the result that only the Brillouin steady state is possible as a stationary condition for fixed anode voltage must be accepted, it must also be recalled that Bloch's analysis indicates that when the anode voltage is actually varying, the motion may be more complicated. It cannot then be said that the establishment of the Brillouin steady state under a slowly rising voltage has been unequivocally shown.

The conditions in the Brillouin state are described by the equations

$$\bar{s}_0 = 0, \quad (117a)$$

$$\bar{\psi}_0 = 1 - \gamma - \frac{1}{s^2}, \quad (117b)$$

$$a_0 = \frac{1}{2\gamma} \left( s - \frac{1}{s} \right)^2, \quad (117c)$$

$$g_0 = \frac{2}{\gamma} \left( 1 + \frac{1}{s^4} \right), \quad (117d)$$

where the zero subscript refers to unperturbed values. If the perturbed state be also a type *S* state, then one may introduce a single-valued "velocity potential," from which the velocities may be derived [see Eq. (30*N*, 31*N*)]. In the nonrelativistic case the velocity potential may be introduced directly from Eq. (70),

$$\bar{s} = \frac{\partial f}{\partial s}, \quad (118a)$$

$$s^2 \left( \bar{\psi} - 1 + \gamma + \frac{1}{s^2} \right) = \frac{\partial f}{\partial \psi}, \quad (118b)$$

where *f* is chosen so that  $\partial f / \partial s$  and  $\partial f / \partial \psi$  vanish at  $s = 1$ . For the unperturbed state, evidently  $f = 0$ . Equation (69) takes the form

$$\gamma \left[ a_0 - s \bar{a}_\phi - \left( 1 - \frac{\gamma}{2} \right) s^2 + 1 \right] = \frac{1}{2} \left\{ \left( \frac{\partial f}{\partial s} \right)^2 + \left[ \left( 1 - \gamma \right) s - \frac{1}{s} + \frac{1}{s} \frac{\partial f}{\partial \psi} \right]^2 \right\}. \quad (119)$$

Writing

$$a_0 - s \bar{a}_\phi = \frac{1}{2\gamma} \left( s - \frac{1}{s} \right)^2 + a_1 \quad (120)$$

and neglecting squares of  $\partial f / \partial s$  and  $\partial f / \partial \psi$ , one has

$$\gamma a_1 = \left( 1 - \gamma - \frac{1}{s^2} \right) \frac{\partial f}{\partial \psi}. \quad (121a)$$

If the perturbations are now such that their dependence on angle is given

by  $e^{-nj\psi}$ , then if  $f = |f|e^{-nj\psi}$  and  $a_1 = |a_1|e^{-nj\psi}$ ,

$$|a_1| = -\frac{jn}{\gamma} \left( 1 - \gamma - \frac{1}{s^2} \right) |f|. \quad (121b)$$

It is generally the case, as a study of Fig. 6-12 will show, that  $1 - \gamma - (1/s^2)$  passes through zero within the cloud and at that point the linear term in  $\partial f / \partial \psi$  will not be large compared with the quadratic ones. Equation (121b), however, gives correctly the term in the voltage perturbation that varies as  $e^{-nj\psi}$ . Physically, the vanishing of  $1 - \gamma - (1/s^2)$  corresponds to the presence of a layer of charge that is at rest in the rotating system. Shells of electrons within this layer have negative angular velocities; those without it, positive angular velocities.

Substituting  $a_0 + a_1$  in Poisson's equation

$$\frac{1}{s} \frac{\partial}{\partial s} \left( s \frac{\partial |a_1|}{\partial s} \right) - \frac{n^2}{s^2} |a_1| = |\varrho_1|, \quad (122)$$

where  $\varrho_1 = |\varrho_1|e^{-nj\psi}$  is the perturbation of the charge density. Finally, one has the equation of continuity

$$\begin{aligned} \frac{\partial}{\partial s} \left\{ \left[ \frac{2}{\gamma} \left( 1 + \frac{1}{s^4} \right) + \varrho_1 \right] s \frac{\partial |f|}{\partial s} \right\} + \frac{\partial}{\partial \psi} \left\{ \left[ \frac{2}{\gamma} \left( 1 + \frac{1}{s^4} \right) \right. \right. \\ \left. \left. + \varrho_1 \right] s \left[ 1 - \gamma - \frac{1}{s^2} - \frac{nj}{s^2} |f| \right] \right\} = 0, \quad (123a) \end{aligned}$$

or, correct to first-order terms,

$$\begin{aligned} \frac{2}{\gamma} \frac{\partial}{\partial s} \left[ \left( 1 + \frac{1}{s^4} \right) s \frac{\partial |f|}{\partial s} \right] - s \left( 1 - \gamma - \frac{1}{s^2} \right) nj |\varrho_1| \\ - \frac{2n^2}{\gamma s} \left( 1 + \frac{1}{s^4} \right) |f| = 0. \quad (123b) \end{aligned}$$

Eliminating  $|a_1|$  and  $|\varrho_1|$  between Eqs. (121b), (122), and (123b), one finds for  $|f|$  the second-order equation

$$\frac{\partial}{\partial t} \left[ A \frac{\partial |f|}{\partial t} \right] = (A + B) |f|, \quad (124)$$

where  $t$  is given by  $s = e^{t/n}$  and thus,

$$\frac{d}{dt} = \frac{s}{n} \frac{d}{ds},$$

and

$$A = -2 \left( 1 + \frac{1}{s^4} \right) + n^2 \left( 1 - \gamma - \frac{1}{s^2} \right)^2, \quad (125a)$$

$$B = \frac{4}{s^2} \left( 1 - \gamma - \frac{1}{s^2} \right). \quad (125b)$$

The value of  $t$  at the anode for practical magnetrons is very nearly constant. The form taken by Eq. (124) for large  $n$  may be found as before by writing  $s = e^{t'/n} = 1 + (\lambda_0/r_c)\zeta$  or  $t \sim 2\pi\zeta$ . It is

$$\frac{d}{dt'}(1 - t'^2) \frac{d|f|}{dt} = (1 - t'^2)|f|, \quad (126)$$

where

$$t' = 2\pi \left( \zeta - \frac{\delta}{2} \right).$$

Equation (124) forms the basis of Bunemann's analysis. Since it is a linear differential equation of the second order, it is impossible for  $|f|$  and  $d|f|/dt$  to vanish at the same point, without  $|f|$  vanishing identically. Equation (124), therefore, indicates that the perturbations of voltage and of radial field cannot vanish simultaneously; in particular, they cannot both vanish at the cathode. Thus, if the potential vanishes at the cathode, neither the radial field nor the radial velocity can vanish there. Bunemann endeavors to avoid the difficulty caused by this conclusion, which appears to be in conflict with the usual assumption of space-charge limitation and vanishing initial velocity, by asserting that these conditions properly apply to the total radial field and velocity, but not to any one Fourier component.

The nature of the difficulty may be brought out by considering more closely the behavior of  $f$  close to the cathode. Suppose that the case of radial symmetry be examined; the azimuthal variation does not affect the conclusions. Then if there is an outgoing current  $i$ ,

$$e s \frac{\partial f}{\partial s} = i, \quad (127)$$

$$\frac{1}{s} \frac{\partial}{\partial s} \left( s \frac{\partial v}{\partial s} \right) = e,$$

with

$$2\gamma v = \left( s - \frac{1}{s} \right)^2 + \left( \frac{\partial f}{\partial s} \right)^2. \quad (128)$$

Combining these into an equation for  $\partial f/\partial s$ , one has

$$\frac{\partial f}{\partial s} \frac{\partial}{\partial s} \left\{ s \frac{\partial}{\partial s} \left[ \left( s - \frac{1}{s} \right)^2 + \left( \frac{\partial f}{\partial s} \right)^2 \right] \right\} = 2\gamma i. \quad (129)$$

Near to the cathode ( $s = 1$ ),  $f$  behaves like  $\frac{2}{3}(9\gamma i/2)^{1/2}(s-1)^{3/2}$ . The thickness of the sheath close to the cathode in which  $f$  follows this law may be estimated by equating  $s - (1/s)$  and  $\partial f/\partial s$ . This gives,  $s_{\text{sheath}} \approx 1 + \frac{2}{18}\gamma i$ . The charge contained in the sheath varies as  $i$ , while the charge density varies as  $(s-1)^{-3/2}$ . It is also evident that

beyond the sheath one will have

$$\frac{\partial f}{\partial s} \approx \frac{i}{2\gamma} \frac{1}{\frac{\partial}{\partial s} \left[ s \frac{\partial}{\partial s} \left( s - \frac{1}{s} \right)^2 \right]}. \quad (130)$$

If the Brillouin steady state be imagined as derived from such a solution by allowing  $i$  to tend to zero, it is clear that conditions at the cathode will be somewhat peculiar, since for any finite  $i$  however small,  $f$  will behave like  $(s-1)^{3/2}$  through a sheath  $\frac{1}{18}\gamma i$  in thickness. Thus, in Bunemann's analysis, if the perturbation causes currents to flow at any part of the cathode,  $f$  will be of the order  $(s-1)^{3/2}$  and the term  $(\partial f/\partial s)^2$  in Eq. (130) will be of a lower order than  $f$  over a distance of the order of  $i$  from the cathode. Bunemann ignores this sheath and puts  $f = 0$  essentially at a distance  $i$  from the cathode, where, in fact,  $f$  is about

$$\frac{3}{5} \left( \frac{9\gamma i}{2} \right)^{1/2} (s-1)^{3/2} \approx \frac{3}{640} (9\gamma i)^2.$$

It would appear that this is justifiable.<sup>1</sup>

Accepting the validity of these arguments one may consider Eq. (124). This has certain features which are independent of  $n$ . It has always two singular points, which may be labeled  $s_+$  and  $s_-$ , given by

$$A(s) = -2 \left( 1 + \frac{1}{s^4} \right) + n^2 \left( 1 - \gamma - \frac{1}{s^2} \right)^2 = 0. \quad (131a)$$

This may be written as

$$\left( \frac{m\omega_0}{eB} \right) = \frac{n\gamma}{2} = \frac{n}{2} \left( 1 - \frac{1}{s_{\pm}^2} \right) \pm \sqrt{\frac{1}{2} \left( 1 + \frac{1}{s_{\pm}^4} \right)} = \pi b_{\pm} \pm \sqrt{1 - 2b_{\pm} + 2b_{\pm}^2}, \quad (131b)$$

where  $b = \frac{1}{2}(1 - 1/s^2)$  and runs from 1 to  $\frac{1}{2}(1 - s_-^2)$ . The radius at which the unperturbed velocity vanishes in the rotating system is given by

$$1 - \gamma_0 - \frac{1}{s_0^2} = 0 \quad \gamma = 2b_0, \quad \text{or} \quad \frac{m\omega_0}{eB} = nb_0 = \pi\delta. \quad (131c)$$

Figures 6.13a, b, and c show  $m\omega_0/eB$  or  $\pi\delta$  as a function of  $b_+$ ,  $b_-$ , and  $b_0$  for three values of  $n$ , ( $n = 4$ ), ( $n = 8$ ), and ( $n = \infty$ ).

The variable  $\pi\delta$  must be thought of as running from  $-\infty$  to  $-\infty$ , since one is interested in perturbing waves running in either direction. Considering a fixed  $\delta$ , or a fixed frequency and fixed magnetic field,

<sup>1</sup> See in this connection, W. E. Lamb and M. Phillips, *Jour. App. Phys.*, **18**, 230 (1947).



the cloud radius will increase as the applied voltage increases. Thus,  $b_{\text{cloud}}$  will increase steadily from zero, and the cloud will contain all values of  $b$  between 0 and  $b_{\text{cloud}}$ . From Figs. 6-13a, b and c, it may be seen

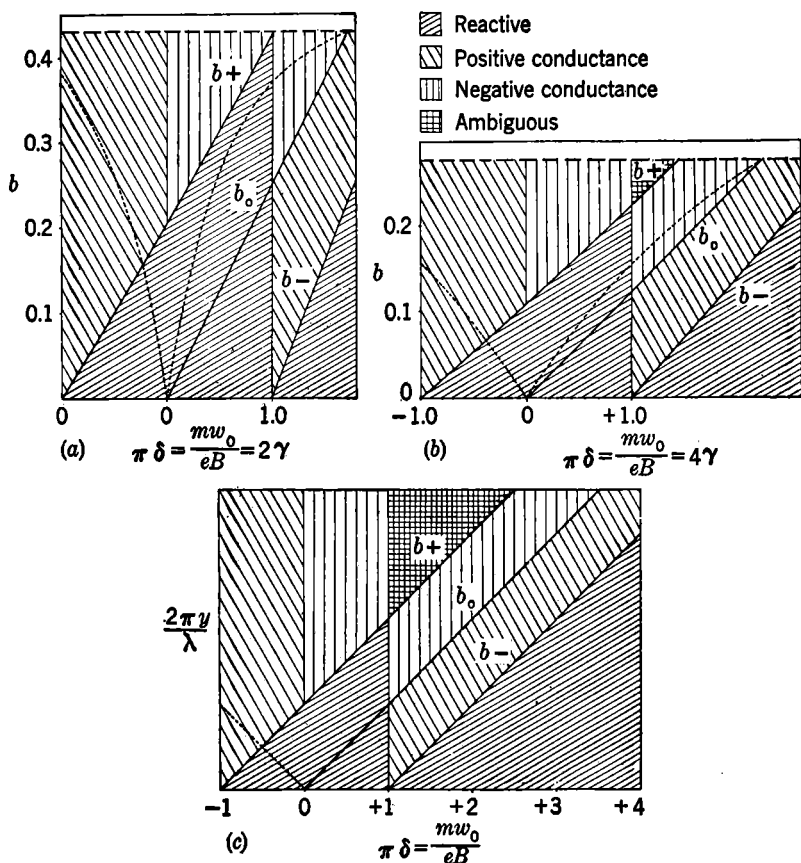


FIG. 6-13.—(a) Radii of the two singular streams and the stationary stream as a function of  $mw_0/eB$  for  $n=4$ . The function  $b = \frac{1}{2}(1 - r_{\text{cathode}}^2/r^2)$  is plotted. The broken line represents a typical value for the anode radius, and the dotted line indicates the cloud radius when the anode voltage is equal to the threshold voltage. (b) Same for  $n=8$ . (c) Location of the singular streams and stationary stream as a function of  $mw_0/eB$  for  $n=\infty$ . The variable  $2\pi(y/\lambda_0)$ , where  $\lambda_0$  is the wavelength of the field in the interaction space, is plotted. The cloud radius coincides with that of the stationary layer when the anode voltage is equal to the threshold voltage for each case.

that when  $\pi\delta < -1$ , none of  $s_+$ ,  $s_0$ , or  $s_-$  is within the cloud; for  $-1 < \pi\delta < 0$ ,  $s_+$  is included for a sufficiently high voltage; for  $0 < \pi\delta < 1$ ,  $s_0$  is first included, then  $s_+$ ; for  $1 < \pi\delta$ ,  $s_-$ ,  $s_0$ , and  $s_+$  are successively included as  $V$  increases. Not all cases may be realized, since  $b_{\text{cloud}} < b_{\text{anode}}$ .

The values of  $b$  corresponding to the threshold voltage as the anode have also been plotted; for  $n = \infty$  the stationary layer is exactly at the cloud boundary when the threshold voltage is on the anode. Clearly the presence or absence of the singularities depends upon voltage, magnetic field, and frequency. The singularities have some physical significance, for  $n[1 - \gamma - (1/s^2)]$  is the frequency with which the electrons encounter the variations in potential while, as was shown previously,  $\sqrt{2[1 + (1/s^4)]}$  is the local frequency of oscillation of the space charge in a cylindrically symmetric field. The two singularities correspond to resonance between these frequencies. The two roots appear from the two senses of rotation of the electrons; they are separated by the root for the stationary layer as they should be.

It is now necessary to derive an expression for the wave admittance  $H_z/E_\phi$  at the surface of the space-charge cloud. Some care is necessary, since a quasi-static approximation is being used. One has

$$\begin{aligned} H_z &= -\frac{r}{nj} \left( \epsilon_0 \frac{\partial E_r}{\partial t} + J_r \right) = -\frac{r}{nj} \left( J_r - \omega \epsilon_0 \frac{\partial E_r}{\partial \psi} \right) \\ &= -\omega \epsilon_0 r \left[ -\omega r \mu_0 H_z - \frac{\partial}{\partial r} (A_0 - \omega r A_\phi) \right] - \frac{r J_r}{nj} \\ H_z &\approx \omega \epsilon_0 r \frac{\partial V_1}{\partial r} - \frac{r}{nj} J_r \end{aligned} \quad (132)$$

neglecting  $\omega^2 \epsilon_0 \mu_0 r^2$  compared with 1 and putting  $V_1 = A_0 - \omega r A_\phi$ . Between the concentric circles that bound the perturbed layer of the space charge there is an r-f surface current of magnitude  $+\rho_0 \Delta r (\psi_0 + \omega)$ , where  $\Delta$  is the amplitude of the perturbation of the surface.  $\Delta$  may be found from the equation<sup>1</sup>

$$\frac{\partial \Delta}{\partial \psi} = \frac{\dot{r}}{\psi_0} \quad \text{or} \quad \Delta = -\frac{\frac{\partial f}{\partial r}}{nj \dot{\psi}_0} \quad (133)$$

Thus,

$$\begin{aligned} H_z &= H_z(\text{inside}) + H(\text{surface current}) \\ &= \omega \epsilon_0 r \frac{\partial V_1}{\partial r} - \frac{\rho_0 r}{nj} \frac{\partial f}{\partial r} + \frac{\rho_0 r}{nj} \frac{\partial f}{\partial r} \left( \frac{\psi_0 + \omega}{\dot{\psi}_0} \right) \\ &= \omega \epsilon_0 r \frac{\partial V_1}{\partial r} + \frac{\rho_0 r}{nj} \frac{\omega}{\dot{\psi}_0} \frac{\partial f}{\partial r}, \end{aligned} \quad (134a)$$

and

$$E_\phi = \frac{nj}{r} V_1. \quad (134b)$$

<sup>1</sup> An unreduced  $f$  is used at this point.

The cloud admittance is thus given by

$$\begin{aligned} Y_{cl} &= \frac{H_z}{E_\phi} = \frac{r}{njV_1} \left( \omega \epsilon_0 r \frac{\partial V_1}{\partial r} + \frac{\rho_0 r}{nj} \frac{\omega}{\psi_0} \frac{\partial f}{\partial r} \right) \\ &= \left( \frac{\omega \epsilon_0 r}{j} \right) \frac{1}{nV_1} \left( r \frac{\partial V_1}{\partial r} + \frac{\rho_0 r}{\epsilon_0 nj \psi_0} \frac{\partial f}{\partial r} \right) \\ &= -(jY_0) \frac{1}{nV_1} \left( r \frac{\partial V_1}{\partial r} + \frac{\rho_0 r}{\epsilon_0 nj_0 \psi} \frac{\partial f}{\partial r} \right). \end{aligned} \quad (135a)$$

where  $Y_0 = \omega \epsilon_0 r$

In reduced variables

$$\frac{Y_{cl}}{jY_0} = -\frac{1}{\gamma a_1} \left[ \frac{d(\gamma a_1)}{dt} + \frac{\varrho_0}{nj\psi_0} \frac{df}{dt} \right] = P. \quad (135b)$$

Since, according to Eq. (121a)  $\gamma a_1 = -[1 - \gamma - (1/s^2)]njf$

$$-P = \frac{g'}{g} + \frac{A}{n^2 g^2} \frac{f'}{f}, \quad (136)$$

where  $g = 1 - \gamma - (1/s^2)$

Substituting for  $Af'/f$  in Eq. (124), one obtains the equation for  $P$

$$\frac{dP}{dt} = -1 + P^2 + \frac{1}{\alpha^2} + \frac{\left(P + \frac{g'}{g}\right)^2}{\alpha^2 - 1}, \quad (137)$$

where

$$\alpha = \frac{ng}{\sqrt{\gamma \varrho_0}},$$

or, for  $Q = 1/P$ , the normalized impedance

$$\frac{dQ}{dt} = -1 + Q^2 \left( 1 - \frac{1}{\alpha^2} \right) - \frac{\left( 1 + \frac{g'}{g} Q \right)^2}{\alpha^2 - 1}. \quad (138a)$$

For  $n \rightarrow \infty$ , this becomes

$$\frac{dQ}{dt'} = Q^2 \left( 1 - \frac{1}{t'^2} \right) - \frac{\left( 1 + \frac{Q}{t'} \right)^2}{t'^2 - 1} - 1 \quad (138b)$$

where, as before,  $t' = 2\pi(\sigma - \delta/2)$ .

The Eq. (138a) has to be integrated up to the surface of the charge cloud with the condition that  $Q = 0$  at  $t = 0$ . It may be well to emphasize that these equations do not describe the variation of admittance or impedance as one moves through a cloud of fixed radius but rather represent the variation of these quantities at the surface of the cloud

as the radius of the latter is varied (say by increasing the voltage). Functionally  $P, Q = P, Q(s_e, n, \gamma)$ . The singularities of Eqs. (137) and (138a) are the same as those of Eq. (124). The zero value of  $\alpha$  does not lead to a singularity; for from Eq. (138a), if  $s_0$  or  $t_0$  marks the stationary layer,

$$Q \approx (s - s_0)^2 \quad \text{or} \quad (t - t_0)^2$$

near  $s_0$  or  $t_0$ . This is the result as given by Bunemann and is not strictly correct, since in the neighborhood of  $s_0$ , the definition of  $\Delta$  has to be modified in view of the vanishing of  $\psi$ . Examination shows that one has

$$Q \approx |s - s_0|.$$

Since  $s_0$  is a function of  $\omega$  (through  $\delta$ ), then, if  $\omega = \omega_0 + (\omega - \omega_0)$  where  $s_0(\omega_0) = s$ ,

$$\begin{aligned} Q \approx |s - s_0(\omega)| &= \left| s - s_0(\omega_0) - \frac{\partial s_0}{\partial \omega_0} (\omega - \omega_0) \right| \\ &= |\omega - \omega_0| \left| \frac{\partial s_0}{\partial \omega_0} \right|. \end{aligned} \quad (139)$$

Bunemann's discussion of stability depends upon the following considerations concerning admittance functions. Consider an admittance  $G + jB$  (or an impedance  $R + jX$ ) that is a function of the complex frequency  $\omega + j\sigma$ . Then for networks and for any system whereby the admittance is calculated as a function of frequency by analytical means,  $G + jB$  is an analytic function of  $\omega + j\sigma$ . Using the Cauchy-Riemann conditions,

$$\begin{aligned} \frac{\partial G}{\partial \omega} &= \frac{\partial B}{\partial \sigma}, \\ \frac{\partial G}{\partial \sigma} &= - \frac{\partial B}{\partial \omega}. \end{aligned}$$

For a circuit that is reactive for real frequencies ( $\sigma = 0$ ), one has when  $\sigma = \delta\sigma$

$$\delta G = - \frac{\partial B}{\partial \omega} \delta\sigma. \quad (140)$$

Thus if  $\delta\sigma$  is negative, corresponding to a slightly increasing amplitude of oscillation,  $\delta G$  is positive for normal networks, since  $\partial B/\partial \omega > 0$ , and the network behaves like a load. But if  $\partial B/\partial \omega$  were negative,  $\delta G$  would be negative and any transient that started to build up would be aided by the circuit which could act as a generator. Thus a network, purely reactive for real frequencies, will be unstable if  $\partial B/\partial \omega < 0$ ; similarly, when  $\partial X/\partial \omega < 0$ .

The behavior of  $Q$  (or  $P$ ) must then be studied as a function of fre-

quency. Consider  $f$  in the neighborhood of one of the singularities. Since the zero of  $A$  is simple, if it occurs at  $t = t_{\pm}$  corresponding to  $s = s_{\pm}$ , then  $f$  has the form  $C + \log(t_{\pm} - t)$  or  $C' + \log(s_{\pm} - s)$ . This may be inserted into the equation defining  $P$  which, noting that  $A(s_{\pm}) = 0$ , becomes

$$P_{\pm} = \mp \sqrt{s_{\pm}^4 + 1} \left[ 1 + \frac{2}{C' + \log(s_{\pm} - s)} \right] + \frac{4}{n(s_{\pm}^4 + 1)} \frac{1}{C' + \log(s_{\pm} - s)}. \quad (141)$$

The first logarithmic term dominates the second for  $n > 1$ . The plus sign refers to the left-hand (upper) hyperbola in Figs. (6-13); the minus sign to the right-hand (lower) one. As before,  $s_{\pm}$ , defined by  $A(s_{\pm}) = 0$ , is a function of  $\omega$ . Thus

$$\begin{aligned} C' + \log(s_{\pm} - s) &= C' + \log[s_{\pm}(\omega) - s] \\ &= C' + \log \left[ s_{\pm}(\omega_{\pm}) + (\omega - \omega_{\pm}) \frac{\partial s_{\pm}}{\partial \omega} - s \right] = C'' + \log(\omega - \omega_{\pm}), \end{aligned} \quad (142)$$

where

$$s_{\pm}(\omega_{\pm}) = s.$$

Thus, the dominant part of  $-Y_{\text{cloud}}$ , considered as a function of frequency for fixed cloud radius  $s$  in the neighborhood of a singular frequency  $\omega_{\pm}$ , is

$$\frac{j}{120\pi} \frac{\omega_0 r}{nc} \left[ \pm \sqrt{s^4 + 1} \left( 1 + \frac{2}{C'' + \log(\omega - \omega_{\pm})} \right) \right]. \quad (143)$$

The logarithmic character of the singularity indicates that  $f$  acquires an imaginary part in passing a singular point and  $P$  (or  $Q$ ) will acquire a real part. It is evident from this fact that in case the admittance gains a negative real part, the whole analysis has been extended into a region in which it is invalid. For if the space-charge cloud is to act as a generator [ $\text{Re}(P) < 0$ ] in a steady state, there must be a steady flow of energy into the resonant system. This, in turn, implies that electrons must flow to the anode, and this is incompatible with the earlier hypothesis of the small signal theory. Physically, then, one cannot safely carry the analysis beyond the singularities.

If in some region  $f$  is complex, say  $f = f_1 + jf_2$ , then the imaginary part of  $A(d \log f/ds)$  is  $A(f_1 f_2' - f_2 f_1')/f_1^2 + f_2^2$ , and the numerator is independent of  $t$ , since  $f_1$  and  $f_2$  individually satisfy Eq. (124). Substituting in Eq. (141) defining  $P$ , it is seen that the conductance can change sign only at  $t_+$  or  $t_-$ , where  $f_1$  and  $f_2$  are discontinuous. Starting from a cloud radius of unity, the admittance will be purely susceptive and  $c'$  real. As the first singularity is passed,  $\log(s_{\pm} - s)$  acquires an

imaginary part  $\pm j\pi$  whose sign depends upon the path by which the singularity is avoided. One is interested in a case where  $\omega_0 = \omega_0 + j\sigma$  and  $\sigma$  is slightly negative. Using the relation

$$\frac{m_0\omega_0}{eB} = \frac{n}{2} \left(1 - \frac{1}{s^2}\right) \pm \frac{1}{\sqrt{2}} \left(1 + \frac{1}{s^4}\right)^{1/2},$$

one has

$$\frac{m_0}{eB} \frac{\partial \omega_0}{\partial s} = \frac{2n}{s^3} \mp \frac{\sqrt{2}}{s^5 \left(1 + \frac{1}{s^4}\right)^{1/2}}; \quad (144)$$

and for  $n > 0$ ,  $\partial \omega_0 / \partial s > 0$ , so that if  $\delta \omega_0 = j\sigma$  where  $\sigma$  is negative, then  $\delta \text{Im}(s) < 0$  and the path of integration goes below the axis. This means that the logarithm increases by  $-j\pi$ . The term

$$[C' + \log(s_0 - s)]^{-1},$$

therefore, acquires a positive imaginary part. Examining Eq. (143) it is seen that the sign of the real part of  $Y$  is the same as that in front of the radical for  $\omega_0 < 0$  and opposite to it for  $\omega_0 > 0$ . The  $b, \pi\delta$  plane is now divided into reactive regions and regions of positive and negative conductance as shown in Fig. 6-13. The behavior in the region beyond the second singularity is ambiguous without special examination.

From Eq. (143) for the admittance in a susceptible region close to a singularity, i.e., immediately to the right of the singular curves in Fig. 6-11, it is found that the susceptance decreases with frequency to the right of the  $s_+$  curve and increases to the right of the  $s_-$  curve. Since in the neighborhood of the  $s_0$  curve the susceptance follows  $|\omega - \omega_0|$  and therefore its variation with frequency changes sign, it is reasonable to conjecture that throughout the susceptible region between the  $s_0$  and  $s_+$ , the susceptance decreases with frequency. This has been verified by Bunemann by numerical integration of Eq. (124) in several cases of different  $n$  values, and the behavior for the several  $n$  values turned out to be substantially alike. It thus appears that these regions will be unstable according to the criteria set up. Bunemann now pursues the analysis to obtain a match between the reactive part of the admittance and that of the load, leaving the real parts to adjust themselves. For sharply resonant circuits matching can be effected at a given  $\omega_0$  and  $B$  only for a narrow range of cloud radii. Thus, if  $s_a$  be also fixed, a nearly unique voltage is defined at which build-up can occur. This "instability" voltage<sup>1</sup> will differ from the threshold voltage; one may expect the start-

<sup>1</sup>This voltage has been calculated by Copley and Willshaw, G. E. C. Report 8490, August 1944, for several  $N$  and  $s_a$ . The application given there to oscillating states is questionable.

ing voltage of the tube to exceed either. The inevitable presence of leakage at low levels makes experimental check difficult.

**6-9. Analysis by the Method of Self-consistent Fields.**—In the first sections of this chapter the equations of the magnetron are set up and discussed. The analytical difficulties that arise in their solution have been pointed out, and it has been found that many of these difficulties are carried over into the symmetrical case. The case in which tangential fields are present has been the subject of considerable numerical investigation. This has not been carried so far as one might wish, but the results have given considerable insight into the operating conditions. The methods used are, in any event, of great importance.

The problem may be stated once again to emphasize the aspects of interest. One has a static field, satisfying certain boundary conditions at the anode and cathode. In this field the electrons move, satisfying the equations of motion and the equation of continuity. As a result of their motion, a charge density exists and the static field must be consistent with this density through Poisson's equation. Thus, in the terminology of atomic physics, the problem is a self-consistent field problem. That is, the electron motions are determined by the fields in which they move; the fields are determined by the distribution of electrons. In the atomic problem of many-electron energy levels, it may be recalled, the method of the self-consistent field assumes a potential; the Schrödinger equation is solved for the motion of individual electrons in this potential; an effective charge distribution is found from the wave functions so determined; and, finally, this charge distribution yields a new potential. A repetition of the calculations using the new potential will yield a second potential and so on. In general, the potentials and wave functions found in this way will converge to a set of values that satisfy all the equations of the problem.

Similarly, in the present method, a potential distribution is first assumed that satisfies the boundary conditions and in the selection of which may be reflected any knowledge of the probable behavior of the fields. In this potential the electron trajectories are calculated by numerical means. From a sufficient number of orbits a charge distribution may be calculated. From this charge distribution by virtue of a numerical solution of Poisson's equation a new potential distribution is found. If this potential field agrees with the original field, the problem would be solved; if not, new orbits may be found and so on through the cycle of operations. Intelligent correction of the field may be made at any point. It may be anticipated that if the initial choice of field were a good one, the successive calculated potentials would show convergence to some limit, and this potential distribution, with its accompanying orbits, would provide a solution of the original problem.

The method clearly has disadvantages in comparison with an approximate analytical solution, for it provides information about only one set of initial conditions. Thus if the d-c voltage, r-f voltage, magnetic field, or the interaction space dimensions are altered, the calculations must be started *ab initio*. If the new parameters are close to the old ones, it is probable that the assumption of the final field of one problem being the initial field of the next would lead to fairly rapid convergence. However, the labor involved is excessive with any except the more recent types of digital computers. On the other hand, a self-consistent field calculation carried through until the solution converges satisfactorily provides very definite information about the behavior of the magnetron under some assigned conditions. It thus enables one to see how the magnetron is actually working at some point. Combining this with the empirical fact that magnetron operation is not much affected by substantial changes in operating parameters, it may be felt to furnish information about typical conditions. Thus, its value lies not so much in the particular numerical values that it yields as in giving an accurate physical picture of processes in the interaction space and in suggesting new lines of attack upon the analytical solution.

The principal work in this direction has been carried out by Hartree and his coworkers at Manchester and by Stoner and his group at Leeds. The discussion given here will be based principally upon a report by Tibbs and Wright<sup>1</sup> which is typical of the methods developed. Actually, only three cases have been studied extensively by the self-consistent field method, and one of these cases showed a notable absence of convergence.

The magnetron studied by Tibbs and Wright was a British 10-cm tube, the CV76, which had been the subject of earlier work by Hartree<sup>2</sup> at low fields (1050 gauss,  $\gamma = .520$ ). The relevant parameters for their problem are

$N = 8$	$n = 4$	
Anode radius.....		$r_a = 0.8$ cm
Cathode radius.....		$r_c = 0.3$ cm
Wavelength.....		10.0 cm
D-c voltage.....		28.5 kv
R-f voltage.....		8.55 kv
Magnetic field.....		2300 gauss
Observed current.....		17.5 amps/cm

In reduced variables

$$\begin{aligned}
 s_a &= 2.67, \\
 a_0 &= 5.85, \\
 a_1 &= s_a \tilde{a}_\phi = 1.75, \\
 \gamma &= 0.233.
 \end{aligned}$$

<sup>1</sup> Tibbs and Wright, CVD Report, Mag. 41, 1945.

<sup>2</sup> D. R. Hartree, CVD Report, Mag. 36, 1944.



The anode potential may be written as

$$a = a_0 + a_1 \cos n\psi, \quad (145a)$$

and the potential in the interaction space as

$$a(s) = a_0(s) + a_1(s) \cos n\psi + a_{-1}(s) \sin n\psi \\ + a_2(s) \cos 2n\psi + \cdots \quad (145b)$$

while the cathode emission density is

$$j = j_0 + j_1 \cos n\psi + j_{-1} \sin n\psi + j_2 \cos 2n\psi + \cdots \quad (145c)$$

It is assumed that all but the first three terms of these series may be ignored. Then

$$-e_r = \frac{\partial a_0}{\partial s} + \frac{\partial a_1}{\partial s} \cos n\psi + \frac{\partial a_{-1}}{\partial s} \sin n\psi \\ = -e_0 - e_1 \cos n\psi - e_{-1} \sin n\psi, \quad (145d)$$

where  $e_r$  is the radial field. The initial procedure is to make estimates of  $e_0$ ,  $e_1$ , and  $e_{-1}$ , from which the potentials are found in the form

$$-a = \int_1^s e \, ds.$$

Experience indicates that the success of the self-consistent field method depends upon an intelligent choice of the initial fields. These fields are usually subject to two conditions. Since current is being drawn, if space-charge limitation is to be adhered to, each of the functions  $e_0$ ,  $e_1$  and  $e_{-1}$  must behave close to the cathode like  $(s-1)^{3/4}$ , as was shown in the preceding section. This ensures that the total radial field will behave correctly close to the cathode. In the second place,  $e_0$ ,  $e_1$ , and  $e_{-1}$  must satisfy the conditions

$$-a_0 = \int_1^{s_0} e_0 \, ds, \quad (146a)$$

$$-a_1 = \int_1^{s_0} e_1 \, ds, \quad (146b)$$

$$0 = \int_1^{s_0} e_{-1} \, ds. \quad (146c)$$

The choice of  $e_0$  is suggested by the fact that near the cathode where the r-f fields are relatively weak, the electron motion should, in its d-c component, resemble the motion in a magnetron without r-f and with the same d-c voltage on the anode. If the cloud radius exceeded 2.271, one could use the fields of the double-stream steady-state that have been found by numerical integration; for  $s_{\text{cloud}} < 2.271$  one can make use of the single-stream state up to the first radius at which the electrons

have a point of inflexion (or  $\ddot{r} = 0$ ). Thus, the computed diode field is used up to this radius and then fitted to a logarithmic potential beyond this point, corresponding to an absence of charge. In fitting, the peak in the diode field brought about by the large charge density at the junction must be drastically smoothed out.

Using known diode fields<sup>1</sup> the initial cloud radius is found to be 1.49 with the given conditions; this is only slightly different from the radius in the Brillouin state for this case, namely, 1.44. In smoothing out the field, regard has been paid to the fact that there is actually d-c current in the whole interaction space, and the field has been made constant rather than of the form  $1/s$  beyond the cloud radius.

If there were no space charge,  $e_1 \cos n\psi$  would be of the form

$$na_1 \frac{s^n + s^{-n} \cos n\psi}{s_a^n - s_a^{-n}} \frac{1}{s}, \quad (147)$$

and this expression is chosen to represent  $e_1$  in the region  $1.6 < s < 2.67$  outside the cloud. A constant multiplier is introduced to satisfy the boundary conditions. Close to the cathode the field is of the form  $A(s-1)^{1/2}$ , and this expression is used between  $s = 1$  and  $s = \frac{1}{15}$ . Between these two regions one has little guidance save from previous calculations, and these have indicated that the r-f fields vary very little with radius. Thus,  $e_1$  is put equal to the value of the Laplace field at  $s = 1.6$  and held constant between  $s = 1.6$  and  $s = \frac{1}{15}$ .  $A$  is adjusted for fit at  $s = \frac{1}{15}$ , and the constant multiplier in the other fields adjusted to give  $a_1$  correctly at the anode.

The selection of  $e_{-1}$  is very arbitrary. It is put equal to  $D'(s-1)^{1/2}$  from  $s = 1$  to  $s = \frac{1}{15}$ . It is again assumed to be independent of  $s$  from  $s = \frac{1}{15}$  to  $s = 1.6$  but of only half the value of  $e_1$ . This makes the phase angle of the rotating field  $\tan^{-1}(e_{-1}/e_1)$  equal to  $-26.5^\circ$ . Beyond  $s = 1.6$  it is made to fall off linearly in such a way that  $a_{-1}$  is zero at the anode.

In order to have some means of testing the choice of a trial field without the labor of calculating several orbits, Tibbs and Wright introduce the idea of "favorable regions" of the field. The idea here is that it is possible to say that in certain parts of the interaction space an electron will continually lose energy. Thus, if it stays in those regions, it will eventually reach the anode. If an electron situated in the favorable region (determined *a priori*) cannot reach the anode, the trial field may be rejected. Assuming for the moment that the phase of the r-f field does not change over the radial region of interest, one may write

$$-sa_\phi = f(s) \cos n\psi',$$

<sup>1</sup> Stoner, CVD Report, Mag. 8, 1941.

where  $\psi' = \psi + \text{phase angle of r-f.}$  Now considering one of the expressions for energy loss

$$a_{\text{loss}} = s a_\phi - \gamma \int \frac{\partial(a_0 - s a_\phi)}{\partial \psi} d\tau, \quad (148)$$

this is undoubtedly positive for  $\pi/2 < n\psi' < \pi$ ; thus, this may be considered a favorable region. Tibbs and Wright claim that  $0 < n\psi' < \pi/2$  is also a favorable region. Their argument depends upon combining Eqs. (54a) and (54b) in the form

$$s = \frac{1}{s^3} \left[ 1 - \gamma \int \frac{\partial(a_0 - s a_\phi)}{\partial \psi} d\tau \right]^2 - s + \gamma \frac{\partial(a_0 - s a_\phi)}{\partial s}. \quad (149)$$

They point out that for  $0 < n\psi' < \pi/2$ , if  $s_D(\gamma)$  is the radial coordinate in the absence of tangential forces,

$$\bar{s} > \bar{s}_D. \quad (150)$$

Then, since an electron returns exactly to the cathode at the end of its first loop, when tangential fields are absent, it is asserted that the inequality (150) implies that an electron moving wholly in  $0 < n\psi' < \pi/2$  will not return to the cathode. It is fairly clear that this does not follow from (150),<sup>1</sup> and there seems to be no reason for thinking that  $0 < n\psi' < \pi/2$  is actually a favorable region. The whole idea of "favorable regions" is rendered of somewhat doubtful value, as Tibbs and Wright themselves admit, by the fact that electrons leave the cathode with angular velocity  $-\gamma$  and may possibly cross from favorable to unfavorable regions and vice versa.

As a trial orbit the electron starting at  $n\psi = 90^\circ$ , which is in the region  $90^\circ < n\psi' < 180^\circ$ , both close to the cathode and in the diode region, is used. This orbit and another trial orbit are shown in Fig. 6-14. It appears that the orbit is going to run over into the unfavorable region; and according to Tibbs and Wright, it does not reach the anode. The reason given for the failure of this trial field is that it makes the average tangential velocities come out too high, so that electrons pass from the favorable to the unfavorable region. In the diode field the angular velocity is  $1 - \gamma - 1/s^2$ ; and if this is averaged to the edge of the cloud from the cathode, one has  $\bar{v}_{\text{avg}} = 1 - \gamma - 1/s_{\text{cloud}}$ . A possible choice of the diode field may now be made by making  $s_{\text{cloud}} = 1/(1 - \gamma)$ , which has the effect of making  $\bar{v}_{\text{avg}} = 0$ , and on the average an electron in a favorable region might be expected to stay there. This leads to a new choice of cloud radius of  $s_{\text{cloud}} = 1/(1 - 0.232)$ . Simultaneously

<sup>1</sup> Consider the functions  $s_1 = 1 - \cos \tau$  and  $s_2 = a - a \cos \tau$  where  $a < 1$ , then  $\bar{s}_1 = 1 - s_1$  and  $\bar{s}_2 = a - s_2$ ; therefore,  $\bar{s}_1 > \bar{s}_2$  at the same value of  $s$ , but both  $s_1$  and  $s_2$  start with  $s = \bar{s} = 0$  at  $\tau = 0$ , and both return to  $s = 0$ .

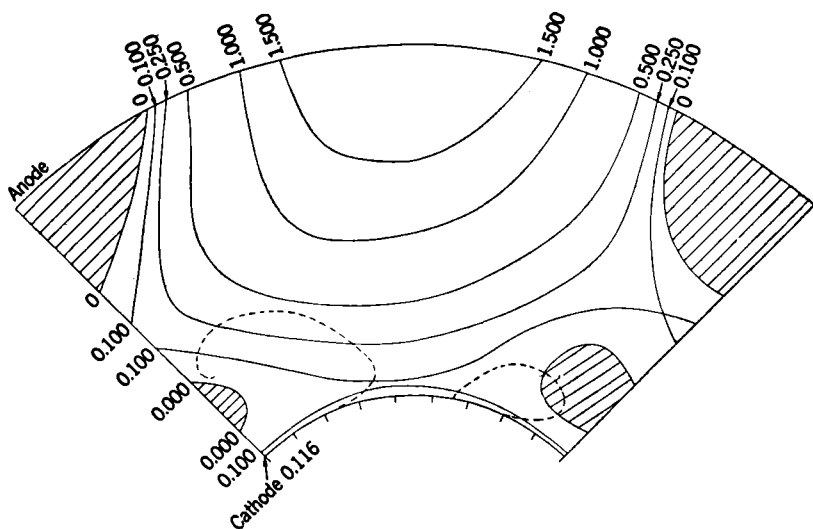


FIG. 6-14.—Equivalent potential for rejected trial field in Tibbs and Wright's self-consistent field calculation. Two orbits are shown. Shaded regions are inaccessible to the electrons

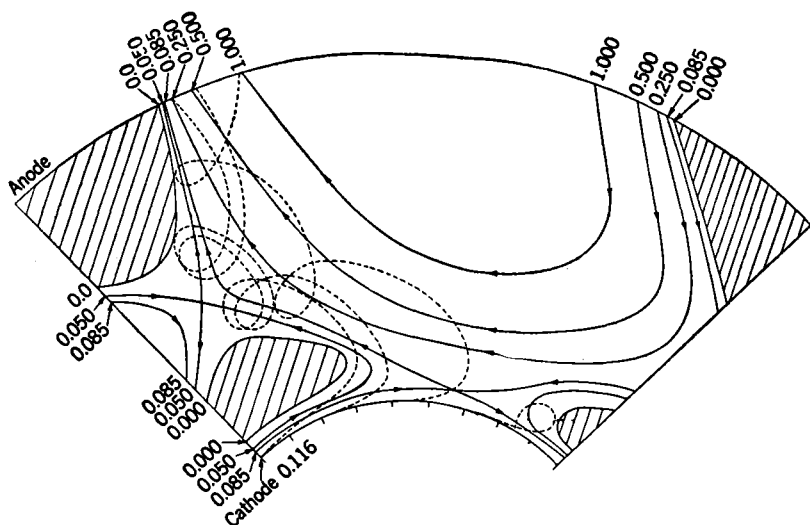


FIG. 6-15.—Equivalent potential for acceptable trial field in self-consistent field calculation. Four orbits are shown. Shaded regions are inaccessible to the electrons. Arrows indicate the direction of the secular motion of electrons.

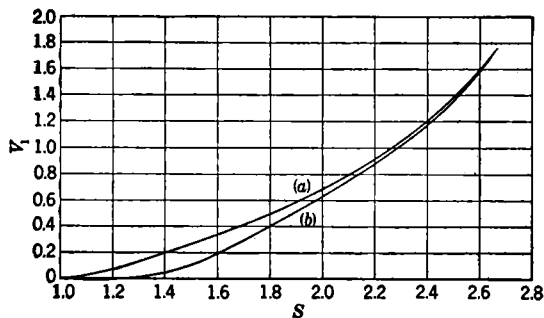


FIG. 6-16.—The in-phase potential  $a_1$  (in reduced units) as a function of radius. (a) Trial field; (b) derived field.

with this change in the radial field, a change is made in the field  $e_{-1}$ . This is now made equal to  $-e_{-1}$ . The trial orbit now reaches the anode, and the new field is made the basis for several orbit calculations. Some of these orbits are shown in Fig. 6-15. Figures 6-16 to 6-18 show the new choice of potentials  $a_0$ ,  $a_1$ ,  $a_{-1}$ .

The calculation of the charge density and the cathode emission depends upon a method introduced by Hartree.<sup>1</sup> In this method the orbits and the interaction space are subjected to a transformation. When an orbit has been calculated, it is implied that

one knows  $r = r(\tau, \psi_0)$  and  $\psi = \psi(\tau, \psi_0)$ , where  $\psi_0$  is the initial azimuth at the cathode and  $\tau$  is the transit time. It is thus possible to make a trans-

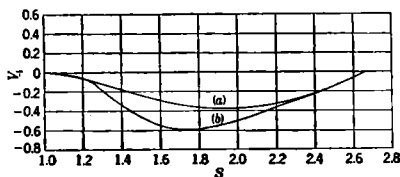


FIG. 6-17.—The out-of-phase potential  $a_{-1}$  (in reduced units) as a function of radius. (a) Trial field; (b) derived field.

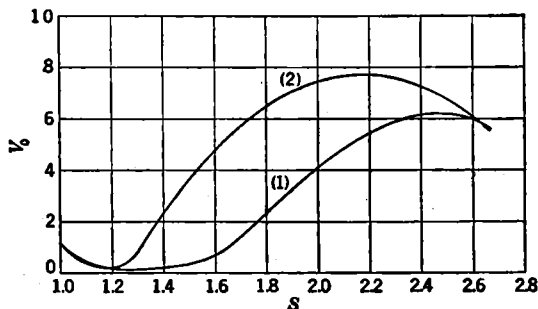


FIG. 6-18.—The effective radial potential  $a_0$  (in reduced units) as a function of radius. (a) Trial field; (b) derived field.

<sup>1</sup> Hartree, CVD Report, Mag. 36, 1944.

formation  $\tau = \tau(r, \psi)$  and  $\psi_0 = \psi_0(r, \psi)$ . The orbits appear as vertical lines in such a  $(\tau, \psi_0)$ -plot, and lines of constant  $r$  and  $\psi$  may be drawn in the diagram. The  $(\tau, \psi_0)$ -plot for the first set of orbits is shown in Fig. 6-19.

Poisson's equation is solved in the following way: A function  $q(n\psi, \log r/r_0) = q(\theta, l)$  is introduced, defined by

$$q(\theta, l) = n \int_{l_0}^l \int_0^{e/n} \frac{1}{\epsilon_0} \rho r \, dr \, d\phi; \quad (151)$$

Poisson's equation then reads

$$\frac{\partial^2 V}{\partial l^2} + n^2 \frac{\partial^2 V}{\partial \theta^2} = \frac{1}{\epsilon_0} \frac{\partial^2 q}{\partial l \partial \psi}. \quad (152)$$

If  $\partial q / \partial \psi$  is expanded in a Fourier series, one has

$$\frac{\partial^2 V_0}{\partial l^2} = \frac{1}{\epsilon_0} \frac{\partial}{\partial l} \left( \frac{\partial q}{\partial \psi} \right)_0 \quad (153a)$$

and

$$\frac{\partial^2 V_k}{\partial l^2} + n^2 V_k = \frac{1}{\epsilon_0} \frac{\partial}{\partial l} \left( \frac{\partial q}{\partial \psi} \right)_k \quad k = \pm 1, \quad (153b)$$

and  $V_0, V_k$  may be found analytically if  $q$  is known. But the latter may be found in the following way; if the cathode emission has the form

$$\begin{aligned} J &= J_0 + J_1 \cos n\psi + J_{-1} \sin n\psi \\ &= (J_0 - J_1 - J_{-1}) + J_1 (\cos n\psi + 1) + J_{-1} (\sin n\psi + 1), \end{aligned} \quad (154)$$

where a partition has been made that makes all the terms of the emission positive, the three cases 1,  $(1 + \cos n\psi)$ , and  $(1 + \sin n\psi)$  may be treated separately. For each case the appropriate  $q$  may be found, since each element of area in the  $(\tau, \psi_0)$ -plot has associated with it the charge that left an element of the cathode  $\psi_0, \psi_0 + d\psi_0$  between the times  $(\tau, \tau + d\tau)$ ; it thus contains a charge  $j(\psi_0) d\psi_0 d\tau$ . Thus, the charge in a region of the  $(l, \theta)$ -plot may be found giving  $q$ . The  $V$ 's calculated from the three  $q$ 's are multiplied respectively by  $J_0 - J_1 - J_{-1}, J_1$ , and  $J_{-1}$ . There are three boundary conditions, and these give three simultaneous equations to determine the  $J$ 's.

The fields derived from the charge distribution may now be compared with those originally assumed. If the agreement is good, the calculation may be considered complete; if not, a further repetition of the process is necessary. The convergence of the process is frequently poor. An earlier calculation by Tibbs and Wright<sup>1</sup> for a 3-cm magnetron showed very little convergence after several stages and was found to require exceedingly high cathode emissions at each stage. They were led to

<sup>1</sup> Tibbs and Wright, "Temperature and Space Charge Limited Emission in Magnetrons," CVD Report, Mag. 38.

conclude that the requirement of space-charge limited emission could not be met and to abandon this boundary condition. However, as they later pointed out, the trouble does not lie in the physical conditions of the problem but rather in the fact that if the successive solutions of

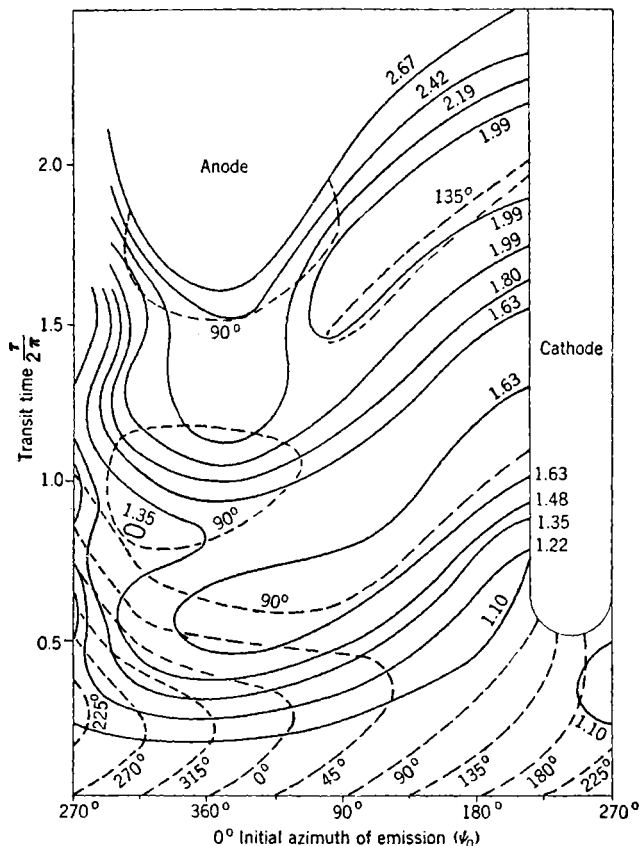


FIG. 6-19.— $\tau$  vs.  $\psi_0$  diagram for the self-consistent field analysis with - - - - contours of constant azimuth  $\psi$  and ——— contours of constant radius  $s$ . Orbits are lines parallel to the  $\tau$ -axis. Vertical scale represents  $\frac{\tau}{2\pi}$ .

the problem are to converge, it is apparently necessary to make a good initial estimate of the fields.

As may have been noted, the methods of choosing initial fields are rather arbitrary and entail a process of judicious extrapolation from earlier calculations. Furthermore, the estimation of the goodness of a solution by a simple visual comparison of the radial plots of the field components seems unsatisfactory. In the next section a possible method

of improving the self-consistent field technique will be referred to. Despite the lack of precision in the solution found by Tibbs and Wright, the efficiency and cathode emission that they derived are in reasonably good agreement with experiment.

**6-10. Qualitative Discussion of the Interaction.**—The analytical difficulties that prevent a solution of Eqs. (54a), (54b), (56), and (57) compel one to fall back upon a qualitative discussion in order to understand some of the salient features of magnetron operation. In this discussion one is helped to some extent by the self-consistent field calculations, but it appears that these have not been carried far enough or worked out for a sufficient variety of cases to be of great assistance.

The most important feature of the magnetron equations in determining the characteristic behavior of the tube is that they may be formulated as the equations of a static problem. It follows that the nature of the effective potential, given by Eq. (55), is of considerable significance and that an examination of this potential function should give considerable insight into the type of motion possible. Were the potential function known in its entirety, of course, it would imply that the whole problem had been solved, so that one is restricted to a qualitative knowledge of its variation. From experimental data on operating tubes it is known that the d-c voltage always lies within about 20 per cent of the threshold voltage. Thus at the anode

$$\left| a_0 - \left( 1 - \frac{\gamma}{2} \right) s^2 + 1 \right| < 0.2 \left[ \left( 1 - \frac{\gamma}{2} \right) s^2 - 1 \right]. \quad (155)$$

Furthermore, it appears from what little data are available that when the r-f voltage is equal to the d-c voltage, operation becomes very inefficient and the region of usual operation is at considerably lower r-f voltage. If this is the case, at the anode again,

$$|s a_0| < \left( 1 - \frac{\gamma}{2} \right) s^2 - 1.$$

If one treats  $\gamma V_E$  as the effective potential, then it appears that  $\gamma V_E$  is of the order of  $\gamma[(1 - \gamma/2)s^2 - 1]$  at the anode. At other points of the interaction space one cannot be precise, but a consideration of the potential distribution for the symmetrical diode or the Brillouin steady state, when the anode voltage is equal to the threshold voltage, indicates that the potential  $\gamma V_E$  will be everywhere of the order of  $\gamma$ . It is a consequence of this that the forces due to the potential will also be of the order of  $\gamma$ . ("Effective" and "equivalent" potential are used interchangeably.)

For the purpose of visualizing the motion in crossed electric and magnetic fields one needs an approximate solution of the equations of motion



in an arbitrary static potential and a constant magnetic field. Suppose that the equations of motion are written in Cartesian coordinates as

$$\ddot{x} = \omega\dot{y} + V_x(x, y), \quad (156a)$$

$$\ddot{y} = -\omega\dot{x} + V_y(x, y), \quad (156b)$$

where  $V_x = \partial V / \partial x$ ,  $V_y = \partial V / \partial y$ , and  $V$  is a function of position. Then, if  $x + jy = Z$ , one may write

$$\ddot{Z} + j\omega\dot{Z} = (V_x + jV_y) = F. \quad (156c)$$

Now if  $F$  were independent of position, this equation would have the solution with the initial conditions  $Z = Z_0$ ,  $\dot{Z} = \dot{Z}_0$ ,

$$Z = \frac{Ft}{j\omega} + Z_0 + \frac{F - j\omega Z_0}{\omega^2} (1 - e^{-j\omega t}). \quad (157)$$

This represents a combination of two independent motions: the first given by  $-j(Ft/\omega)$ , which is a motion at right angles to the field  $F$  of velocity  $|F|/\omega$ ; the second, a motion around a circle of radius  $|F - j\omega Z_0|/\omega^2$ , with frequency  $\omega/2\pi$ . If, now,  $F$  varies with position but sufficiently slowly so that it does not change greatly over the orbit during one cycle, it might be expected that the new solution could still be represented as a superposition of two motions. One motion should consist of a path everywhere at right angles to  $F$ , traversed with a velocity  $|F|/\omega$ . The other would consist of a circular motion centered about the instantaneous position of a point on the first path. The frequency of the circular motion might be expected then to be a slowly varying function of time or of position. If these conditions were fulfilled, the center of the circle would, since it moves always at right angles to  $F$ , be moving along an equipotential or line of constant  $V$ . Before examining this solution analytically it is useful to consider Fig. 6-15, in which has been plotted the effective potential corresponding to the fields used by Tibbs and Wright<sup>1</sup> and also the orbits that they calculated in this field. It may be seen that the orbits do actually consist of a series of loops, the centers of which travel rather closely along the equipotential lines. It will be shown below that this is not a particularly favorable case.

Writing  $D \equiv d/dt$ , one may solve Eq. (156c) formally in the form

$$\begin{aligned} Z &= re^{-j\omega t} + \frac{F}{j\omega} - \frac{DF}{(j\omega)^2} + \frac{D^2F}{(j\omega)^3} + \dots \\ &= re^{-j\omega t} + \frac{V_x + jV_y}{j\omega} - \frac{1}{(j\omega)^2} \left( \ddot{x} \frac{\partial}{\partial x} + \ddot{y} \frac{\partial}{\partial y} \right) (V_x + jV_y) \\ &\quad + \frac{1}{(j\omega)^3} \left( \ddot{x} \frac{\partial}{\partial x} + \ddot{y} \frac{\partial}{\partial y} \right)^2 (V_x + jV_y) + \dots \quad (158) \end{aligned}$$

<sup>1</sup> Tibbs and Wright, *loc. cit.*

The convergence of this expansion depends upon the smallness of  $(1/\omega^n)D^n F$ . Suppose that all terms beyond the second are ignored. Then

$$\mathbf{Z} = r e^{-j\omega t} + \frac{\mathbf{V}_x + j\mathbf{V}_y}{j\omega}, \quad (159a)$$

or

$$\mathbf{Z} = \left[ \frac{F(\mathbf{Z}_0)}{j\omega} - \mathbf{Z}_0 \right] e^{-j\omega t} + \frac{\mathbf{V}_x + j\mathbf{V}_y}{j\omega} = r e^{-j\omega t} + \frac{\mathbf{V}_x + j\mathbf{V}_y}{j\omega}, \quad (159b)$$

where  $\mathbf{Z}_0 = \mathbf{Z}$  and  $\mathbf{Z} = \mathbf{Z}_0$  at  $t = 0$ . This may be written

$$\bar{x} = r \cos \omega t + \frac{V_y}{\omega}, \quad (160a)$$

$$\bar{y} = -r \sin \omega t - \frac{V_x}{\omega}. \quad (160b)$$

The higher terms in the expansion become, using this approximation,

$$- \left( \frac{j}{\omega} \right)^n \left[ \left( r \cos \omega t + \frac{V_y}{\omega} \right) \frac{\partial}{\partial x} + \left( -r \sin \omega t - \frac{V_x}{\omega} \right) \frac{\partial}{\partial y} \right]^{n-1} (V_x + jV_y). \quad (161)$$

Considering only the first term, one has

$$- \frac{1}{(j\omega)^2} \left[ \left( r \cos \omega t + \frac{V_y}{\omega} \right) V_{xx} + \left( -r \sin \omega t - \frac{V_x}{\omega} \right) V_{xy} \right] \\ + j \left[ \left( r \cos \omega t + \frac{V_y}{\omega} \right) V_{xy} + \left( -r \sin \omega t - \frac{V_x}{\omega} \right) V_{yy} \right] \quad (162)$$

If this is to be small compared with the first term  $(V_x + jV_y)/j\omega$ , then

$$r V_{xx}, r V_{xy}, r V_{yy}, \frac{V_y V_{xx} - V_x V_{xy}}{\omega}, \frac{V_y V_{xy} - V_x V_{yy}}{\omega} \ll \omega |V_x + jV_y|, \quad (163)$$

where

$$r = \left| \frac{V_x(\mathbf{Z}_0) + jV_y(\mathbf{Z}_0)}{j\omega} - \mathbf{Z}_0 \right|.$$

In the magnetron problem

$$V_x = \gamma \left[ a_0 - s a_x - \left( 1 - \frac{\gamma}{2} \right) (x^2 + y^2) + 1 \right]. \quad (164)$$

A proof that the inequality (163) is satisfied cannot be given in rigorous form because of the lack of knowledge of the fields. One may argue in the following way, however. If  $\mathbf{Z}_0$  is taken to be a point on the cathode,  $V_x = V_y = 0$  and  $\mathbf{Z}_0 = \gamma$ ; thus  $r = \gamma$ . If, in addition, the earlier assumption is retained that  $V \approx \gamma$ ,  $V_x$ ,  $V_y$ ,  $V_{xx}$ ,  $V_{yy}$ , and  $V_{xy} \approx \gamma$ , then the inequality (163) is satisfied provided that  $\gamma \ll 1$  (for the field used by Tibbs and Wright,  $\gamma = 0.232$ , which is not very small compared

with unity). A similar argument would indicate the smallness of higher terms in the expansion, Eq. (158). It is quite evident that the above reasoning is tentative and that there may be regions of the interaction space, small in extent, over which the fields change more rapidly than will allow Eq. (163) to be satisfied. However, it is likely that in the main the considerations hold good. The most likely regions for difficulties to arise are in regions of large charge density and fairly rapid motion. The region very close to the cathode does not appear to be one in which Eq. (159) fails because in this case although the field derivatives are large, this is compensated for by the low velocities.

One may note that substitution of the first-order approximation (159b) into the next term of the expansion (158) leads to a second-order approximation

$$\bar{x} \approx r \left( 1 + \frac{V_{xx}}{\omega^2} \right) \cos \omega t - r \frac{V_{xy}}{\omega^2} \sin \omega t + \left[ \frac{V_y}{\omega} \left( 1 + \frac{V_{xx}}{\omega^2} \right) - \frac{V_x}{\omega} \frac{V_{xy}}{\omega^2} \right] \quad (165a)$$

$$\bar{y} \approx -r \left( 1 + \frac{V_{yy}}{\omega^2} \right) \sin \omega t + r \frac{V_{xy}}{\omega^2} \cos \omega t + \left[ -\frac{V_x}{\omega} \left( 1 + \frac{V_{yy}}{\omega^2} \right) + \frac{V_y}{\omega} \frac{V_{xy}}{\omega^2} \right]. \quad (165b)$$

One may consider first the starting process from the viewpoint of the effective potential diagram. Figure 6-20 represents the effective potential for a case related to that of Tibbs and Wright. As in Bunemann's analysis it has been assumed that a Brillouin steady state exists before oscillations are initiated. The anode d-c voltage is that of the problem of Tibbs and Wright, and a logarithmic potential is assumed between the anode and the cloud radius. The potential corresponding to the Brillouin steady state has been assumed right up to the cathode as was done by Bunemann. A r-f field, supposed to satisfy Laplace's equation with an amplitude equivalent to that used by Tibbs and Wright, has been added to the d-c field. The amplitude does not affect the argument, which is purely qualitative, but it is chosen large for convenience in drawing the potential diagram.

Two important features appear clearly in this diagram. These are the shaded regions in which the potential is negative and into which the electrons therefore cannot travel and the appearance of two saddle points in the equipotential surface. The appearance of a forbidden region near the anode is a consequence of a choice of d-c voltage in excess of the threshold voltage and a rather large r-f voltage. The forbidden region near the cathode will occur for any r-f voltage,

however small. The effective potential within the charge cloud is

$$\begin{aligned}\gamma V_E &= \gamma \left[ \frac{1}{2} \left( s - \frac{1}{s} \right)^2 - \left( 1 - \frac{\gamma}{2} \right) s^2 + 1 \right] \\ &= \frac{1}{2} \left[ (1 - \gamma) s - \frac{1}{s} \right]^2.\end{aligned}\quad (166)$$

The potential vanishes for  $s_0^2 = 1/(1 - \gamma)$ ; and if the cloud radius is greater than this, there will be created, when an r-f voltage is super-

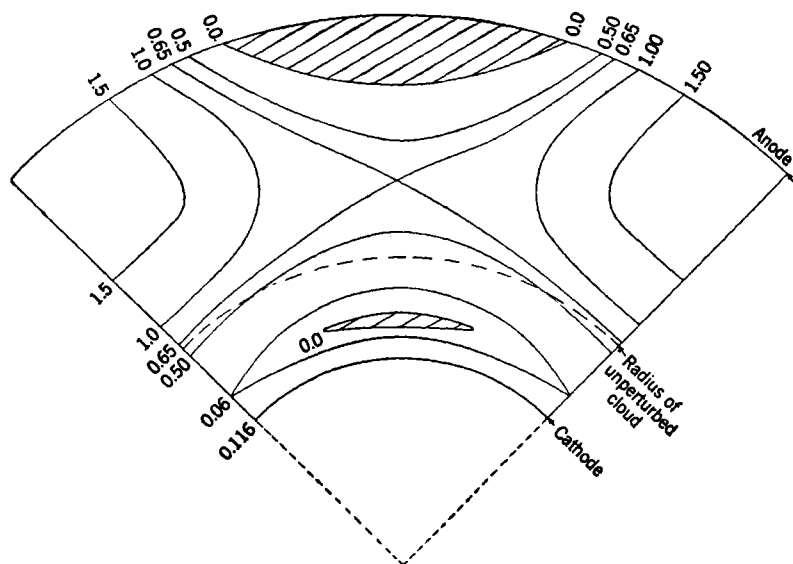


FIG. 6-20.—Equivalent potential for the starting problem in reduced units. The shaded regions cannot be traversed by electrons.

imposed that is negative in some places, a region of negative potential or a forbidden region. Now, according to Bunemann,

$$\bar{s} = \frac{\partial f}{\partial s},$$

where

$$\gamma V_E = \left( 1 - \gamma - \frac{1}{s^2} \right) \frac{\partial f}{\partial \psi}.$$

If  $\gamma V_E$  varies as  $\cos n\psi$ , then  $\bar{s}$  varies as  $\sin n\psi$  for  $s > s_0$  and as  $-\sin n\psi$  for  $s < s_0$ . Thus, the orbits are deformed in the same way as the equipotential lines in Fig. 6-20. One may now argue that the motion of the negative charge cloud toward the higher saddle point will make the potential in the neighborhood of the latter lower. In the new potential

thus derived the orbits will be still further distorted in the same sense. It is then possible, although not assured, that the distortion of the orbits will proceed further in this way. If this process continues until the saddle point lies within the electron stream, one can expect a radical change in the nature of the flow. For it is now the case that an equipotential originating inside the electron cloud travels over to the anode and it will be possible for an electron to follow this equipotential, precessing about it. Thus, a part of the stream of electrons may turn off toward the anode, setting up further instability in the original cloud. It is easily shown that if the cloud radius be less than  $s_0$ , the perturbation of the electron stream is away from the higher saddle point and toward the lower saddle point. This produces such a change of potential that the perturbation is opposed.

This picture seems to give a good physical representation of Bunemann's analysis. For as long as the orbits are lying symmetrically disposed about the position of maximum r-f voltage, the impedance of the charge cloud is purely reactive. This may be seen, since  $E_r$  will vary as  $\cos n\psi$ , and  $\partial E_r / \partial t = -\omega(\partial E_r / \partial \psi)$  will vary as  $\sin n\psi$ . The case for which  $s > s_0$  and in which the perturbation grows corresponds to Bunemann's instability given by  $(\partial Y_{\text{cloud}} / \partial \omega) < 0$ , while for  $s < s_0$ , he found  $(\partial Y_{\text{cloud}} / \partial \omega) > 0$  and the perturbation is self-damping. If the disturbance grows to the critical amplitude at which the saddle point enters the stream, the asymmetrical nature of the latter after splitting gives an in-phase component of current.

When current has actually begun to flow to the anode, the resultant asymmetry of the charge cloud with respect to the maximum of the r-f voltage on the anode means that the assumed r-f field must be modified to include an out-of-phase term. Furthermore, since there is now a nonuniform distribution of space charge producing r-f fields, the latter must not be expected to satisfy Laplace's equation but rather Poisson's. Thus, in the operating case one is led to the choice of such fields as was made in the self-consistent field calculations. Figure 6-15, previously referred to, shows the effective potential for the field chosen by Tibbs and Wright as the starting point of their calculations. It may be remarked that in its essentials this potential distribution has much in common with the naïve starting field of the previous paragraph. The outer saddle point is now at a much lower potential and, in fact, lies below the inner saddle point. This implies that equipotentials starting from quite close to the cathode may reach the anode. (Arrows have been drawn along the equipotentials to indicate the directions of motion of the center of the precessional circle.)

It would seem that the diagram of effective potential might be very useful in connection with self-consistent field calculations, since it gives

considerable insight into the possible flow patterns of the electrons. Figure 6-21 shows the effective potential for the field derived by Tibbs and Wright from the space-charge distribution set up by the orbits of Fig. 6-15. It may be seen that the space charge has lowered the potential sufficiently to eliminate the outer saddle point and the two forbidden regions have coalesced. Comparison of the orbits of Fig. 6-15 with the potential diagram of Fig. 6-21 reveals the unfortunate fact that most of the orbits lie over a considerable part of their length in the forbidden region. This indicates that self-consistency has not been achieved in a satisfactory manner, although the derived radial fields appeared to agree fairly well with the initial ones. The new field, though it differs

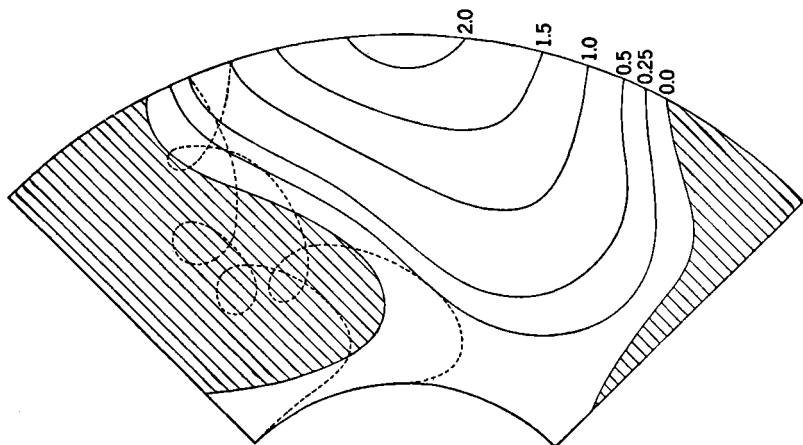


FIG. 6-21.—Equivalent potential for derived field in self-consistent field calculation. Two orbits calculated in the initial field are shown.

in detail from the starting field, retains some features in common. There are still equipotentials starting from close to the cathode that run up to the anode, and the orbits will presumably lie along these. However, the shape and orientation of the resultant arm of space charge cannot be predicted until a self-consistent field has been found. Inasmuch as a method with a self-consistent field procedure is largely an empirical one, proceeding by a series of estimates and approximations, it would appear that the use of the effective potential diagram would aid materially in visualizing the state of affairs in the interaction space. At the same time it provides a sensitive check on the approach to real self-consistency.

A comparison of the potential fields for the artificial starting problem shown in Fig. 6-20 and those assumed and derived in the self-consistent field calculation (Figs. 6-14 and 6-15) enables one to deduce some of the general properties of the field in an operating magnetron. There is a thin

layer surrounding the cathode in which the potentials vary radially as  $(s - 1)^{1/2}$ . Within this layer electric forces will originally predominate; but after a certain distance has been traversed, the magnetic forces will become comparable. In Sec. 6-8 it was estimated that the thickness of this layer was  $\frac{2}{\Gamma_0 \gamma} i$ , and the voltage drop across it is found to be  $\frac{2}{\Gamma_0 \gamma} \gamma i^2$ . Considering the case for which self-consistent fields have been calculated in Sec. 6-9, the thickness is 0.04 and  $\Delta a_0$  equal to 0.015; thus, the thickness is very small, and the potential drop under these circumstances small compared with the cathode potential of 0.116. At very high currents the cathode layer may become thick enough and the potential drop across it large enough to alter the initial stages of the motion.

Beyond the cathode layer there exists a region that might be called the "bunching" or "sorting" region. This may be thought of roughly as extending out to about the radius of the Brillouin steady state appropriate to the d-c anode voltage. Passing radially outward from the cathode through this region one always encounters a potential minimum at about the radius  $s_0 = 1/(1 - \gamma)$  at which the Brillouin steady state had a potential of zero. The effect of the r-f field is to depress an angular region around this minimum to a negative potential, thus producing a forbidden area; between each pair of forbidden regions there will be a saddle point. Electrons leaving the cathode from points opposite the forbidden region travel close to the cathode, held there essentially by a negative radial r-f field, until they pass the end of the excluded area, where they enter a region of tangential r-f field, so directed that they move outward. Electrons starting between the forbidden region and the saddle point move mostly in a positive (outward) radial r-f and d-c field once they have crossed the minimum; this causes them to move toward the left and brings them into step with the first set of electrons. Finally those electrons which start from beyond the saddle point may either cross the minimum and be sent toward the left like the second set or, if they approach close to the forbidden region, be sent back to the cathode by the tangential electric field. The over-all effect is that electrons which have started behind the forbidden region to the left of the saddle point are bunched together while electrons coming from the cathode between saddle point and forbidden region return to the cathode. The general features of this bunching mechanism will not be changed in their essentials provided that the potential field retains the characteristic features described earlier.

Beyond the bunching region, in which the electrons have been concentrated into a relatively narrow range of angles, lying in the region of maximum tangential field, the stream travels out to the anode. The stream, as it moves outward, will continue to lie in the region of maximum tangential field, following the equipotentials. It can be expected, then,

to arrive at the anode at some effective potential near zero but, of course, always positive. There will be a process of phase focusing in this region as may be seen by considering the equipotentials in Fig. 6-15. The equipotentials surrounding the zero equipotential converge toward the anode, and the various orbits centered on the equipotentials will also tend to converge. It is within this region that the process of energy conversion largely takes place, since the electrons have now been concentrated entirely into regions in which the tangential electric field has the proper sign for the electrons to lose energy. One sees that for low magnetic fields (slightly greater than  $1 - 1/s_0^2$ ) the efficiency will be low, for the initial cloud radius will extend out very close to the anode and the energy-exchange region will be small. As  $\gamma$  decreases, the radius of the bunching region will decrease and more of the interaction space will become available for energy loss.

The fact that the magnetron problem may be formulated in static terms seems to be fundamental for its behavior. That operation will be possible over a large range of values of  $\gamma$  with an efficiency steadily increasing with  $\gamma$  appears evident because changes in  $\gamma$  mean only changes in the initial velocities of the electrons and a consequent change in the effective potential. The frequency of precession of the electrons about the magnetic field in a field of constant effective potential is  $2(1 - \gamma)/2\pi$ ; the oscillatory motion to which this precession corresponds is not driven by any harmonically varying forces, and it thus exhibits no resonance effects for any  $\gamma$ . Variations of  $\gamma$  then mean merely variations in the boundary conditions and equations of a purely static problem.

Similarly by examining the definitions of the reduced variables it is seen that the dependence of the operation upon frequency is contained in the dependence upon  $a_0$  and  $\gamma$ , for this is the only place in which the frequency appears. Now  $a_0$  is essentially correlated with  $\gamma$  by the necessity of satisfying the threshold criterion everywhere; thus, the frequency dependence is principally contained in the  $\gamma$ -dependence. Since there is reason to suppose that the latter is small, one deduces that the frequency dependence is small. Once again, there are no resonance effects.

The dependence of the operation upon the r-f voltage as contained in Fig. 6-9 is very inadequately understood.

**6-11. Departures from the Rotating-wave Hypothesis.**—The foregoing discussion of magnetron operation has been based on the assumption that only the slowest rotating wave which moves with the electrons has any appreciable interaction with them. It now appears that many of the characteristic features of magnetron behavior are due to this mode of interaction. It is, therefore, of interest to consider cases in which



another Fourier component plays a part. One notable example of this occurs in the operation of the rising-sun type of magnetron. As has been shown in Chap. 3, the presence of two sets of resonators, alternately large and small, gives rise to a Fourier component that is not normally excited in unstrapped and strapped systems. This is a mode for which there is no angular dependence ( $n = 0$ ). Such a field will appear in any rotating system as a tangential electric field varying as  $e^{j\omega_0 t}$ , without angular dependence and falling off slowly toward the cathode. A method of estimating the effect of such a perturbation was indicated by Slater;<sup>1</sup> his treatment will be followed in a more general form.

Writing Eqs. (54a) and (54b) in Cartesian coordinates again, one has

$$\bar{\bar{x}} = 2(1 - \gamma)\bar{y} + \gamma \frac{\partial V_E}{\partial x}, \quad (167a)$$

$$\bar{\bar{y}} = -2(1 - \gamma)\bar{x} + \gamma \frac{\partial V_E}{\partial y}, \quad (167b)$$

where  $x$  and  $y$  are measured in units of  $r_c$  and

$$V_E = (a_0 - s\tilde{a}_\phi) - \left(1 - \frac{\gamma}{2}\right)(x^2 + y^2) + 1. \quad (167c)$$

Suppose now that  $x_0(t)$ ,  $y_0(t)$  are the equations of an orbit satisfying Eqs. (167a, b), and consider the perturbation of a single orbit. Let  $\mathbf{x} = \mathbf{x}_0 + \mathbf{n}$  and  $\mathbf{y} = \mathbf{y}_0 + \boldsymbol{\zeta}$ , and where  $\mathbf{n}$  and  $\boldsymbol{\zeta}$  are small. Then to terms linear in  $\mathbf{n}$  and  $\boldsymbol{\zeta}$ , one obtains

$$\bar{\bar{\mathbf{n}}} = 2(1 - \gamma)\bar{\boldsymbol{\zeta}} + \gamma \left( \mathbf{n} \frac{\partial^2 V_E}{\partial x^2} + \boldsymbol{\zeta} \frac{\partial^2 V_E}{\partial x \partial y} \right), \quad (168a)$$

$$\bar{\bar{\boldsymbol{\zeta}}} = -2(1 - \gamma)\bar{\mathbf{n}} + \gamma \left( \mathbf{n} \frac{\partial^2 V_E}{\partial x \partial y} + \boldsymbol{\zeta} \frac{\partial^2 V_E}{\partial y^2} \right) \quad (168b)$$

Writing  $d/d\tau \equiv D$ , then Eqs. (168a) and (168b) become

$$(D^2 - \gamma V_{xx})\mathbf{n} - [2(1 - \gamma)D + \gamma V_{xy}]\boldsymbol{\zeta} = 0, \quad (169a)$$

$$[2(1 - \gamma)D - \gamma V_{xy}]\mathbf{n} + (D^2 - \gamma V_{yy})\boldsymbol{\zeta} = 0. \quad (169b)$$

Thus,  $\eta$  and  $\zeta$  will have solutions dependent upon  $\tau$  as  $e^{G\tau}$  where

$$G^4 + [4(1 - \gamma)^2 - \gamma(V_{xx} + V_{yy})]G^2 + \gamma^2(V_{xx}V_{yy} - V_{xy}^2) = 0. \quad (170)$$

To a first approximation then,

$$\begin{aligned} G^2 &= -4(1 - \gamma)^2 + \gamma \nabla^2 V_E \\ &= -4 \left[ 1 - \gamma - \frac{\gamma}{4} \nabla^2 (a_0 - s\tilde{a}_\phi) \right], \\ G &= \pm j \left[ 2 - \gamma - \frac{\gamma}{4} \nabla^2 (a_0 - s\tilde{a}_\phi) \right]. \end{aligned} \quad (171)$$

Suppose, generally, that a perturbation of the form  $e^{i\alpha\omega t} = e^{i\alpha n\gamma\tau}$  be applied; then there will be resonance between the applied perturbation and the small oscillations about an equilibrium orbit if

$$n\alpha\gamma = 2 - \gamma - \frac{\gamma}{4}\nabla^2(a_0 - s\tilde{a}_\phi)$$

or

$$\gamma_{\text{res}}[n\alpha + 1 + \frac{1}{4}\nabla^2(a_0 - s\tilde{a}_\phi)] = 2, \quad (172)$$

where  $\gamma_{\text{res}} = 2m_0\omega_0/neB_{\text{res}}$  is the value of  $\gamma$  for which resonance takes place and, similarly,  $B_{\text{res}}$  is the magnetic field at which resonance occurs for a fixed  $\omega_0$ . Writing  $m_0\omega_0/e = B_{\text{cyc}}$ , where  $B_{\text{cyc}}$  is the so-called cyclotron field, Eq. (172) becomes

$$\begin{aligned} B_{\text{res}} &= B_{\text{cyc}} \left[ \alpha + \frac{1}{n} + \frac{1}{4n} \nabla^2(a_0 - s\tilde{a}_\phi) \right] \\ &= B_{\text{cyc}} \left[ \alpha + \frac{1}{n} + \frac{1}{4n} \varrho \right]. \end{aligned} \quad (173)$$

For the rising-sun case,  $\alpha = 1$  and

$$B = B_{\text{cyc}} \left[ 1 + \frac{1}{n} + \frac{1}{4n} \varrho \right]. \quad (174)$$

It is difficult to go further than this, since one's knowledge of  $\varrho$  is very inadequate. Roughly since

$$2\pi i_\varrho = \int_0^{2\pi} \varrho s \tilde{s} d\psi, \quad (175)$$

$$\varrho_{\text{avg}} \sim \frac{2\pi i_\varrho}{s_{\text{avg}}(s\Delta\psi)}, \quad (176)$$

where  $s\Delta\psi$  is the breadth of the outgoing electron stream. Furthermore since  $\varrho$  is not constant throughout the cloud, it is not clear where its value should be taken.

The performance chart for a rising-sun magnetron (Fig. 6-7) shows the characteristic behavior of these tubes. The efficiency instead of rising monotonically with magnetic field shows a minimum for a fairly definite magnetic field. The effect, in most cases that have been examined, is less pronounced at high currents. Using crude estimates of  $\tilde{s}_{\text{avg}}$  and  $(s\Delta\psi)$ , the formula Eq. (174) gives reasonable agreement with experiment.

Slater has given a result that has been frequently quoted in this connection. This expression is

$$\frac{B_{\text{res}}}{B_{\text{cyc}}} = 1 + \frac{3}{2n}. \quad (177)$$

It may be derived from Eq. (174) in the following way: Slater considers a special orbit in a cylindrically symmetric field, namely, one in which an electron moves on a circle about the cathode with an angular velocity equal to that of the traveling wave. In the rotating system then the orbit degenerates to a fixed point. From Eqs. (54a and b), if  $\psi = 0$  in a symmetric field,

$$1 - \gamma = \frac{1}{s^2}$$

and also

$$\begin{aligned} 0 = \bar{s} &= s(\psi - 1 + \gamma)^2 - s(1 - \gamma)^2 + \gamma \frac{\partial(a_0 - s\bar{a}_\phi)}{\partial s} - (2 - \gamma)s \\ &= \frac{1}{s^3} - s + \gamma \frac{\partial(a_0 - s\bar{a}_\phi)}{\partial s} \\ \frac{\partial(a_0 - s\bar{a}_\phi)}{\partial s} &= \frac{1}{\gamma} \left( s - \frac{1}{s^3} \right) \quad \text{at } \frac{1}{s^2} = 1 - \gamma. \end{aligned}$$

Now in Eq. (174) one has

$$\begin{aligned} \nabla^2(a_0 - s\bar{a}_\phi) &= \frac{1}{s} \frac{\partial}{\partial s} \left[ s \frac{\partial(a_0 - s\bar{a}_\phi)}{\partial s} \right] \\ &= \frac{\partial^2(a_0 - s\bar{a}_\phi)}{\partial s^2} + \frac{1}{s} \frac{\partial(a_0 - s\bar{a}_\phi)}{\partial s}, \end{aligned} \quad (178)$$

and neglecting the second derivative, as does Slater,

$$\nabla^2(a_0 - s\bar{a}_\phi) = \frac{1}{s} \frac{\partial(a_0 - s\bar{a}_\phi)}{\partial s} = \frac{1}{\gamma} \left( 1 - \frac{1}{s^4} \right) = 2 - \gamma \sim 2. \quad (179)$$

Substituting in Eq. (174) gives

$$\frac{B_{res}}{B_{cyc}} = 1 + \frac{3}{2n}. \quad (6-177)$$

The result, although agreeing quite well with experiment, cannot be considered as well founded.

A phenomenon that occurs in strapped magnetrons appears to be of the type considered in this section. Measurements of the energy transferred to the cathode by electrons that return after being accelerated in the r-f field have been made for a number of tubes. An example of the results obtained is shown in Fig. 6-22<sup>1</sup> where the contours of back-bombardment power are shown on a regular performance chart. It may be seen that the back bombardment shows a maximum at 1400 gauss for this magnetron which operates at 10.7 cm. It appears that at this field for which  $B/B_{cyc} = 1.41$ , there is some kind of resonance effect, since there is no obvious reason why any special back bombardment

<sup>1</sup> W. E. Danforth, C. C. Prater, and D. L. Goldwater, "Back-bombardment of Magnetron Cathodes," NDRC 14-309.

might be expected to take place if the electrons are moving in the quasi-static field. There is observed little or no effect upon the efficiency of the magnetron, so that the whole process is much less pronounced than that taking place in the rising-sun type. The fact that the critical field is substantially greater than  $B_{cye}$  indicates that the resonance effect is not confined to a layer near the cathode in which the electrons are at

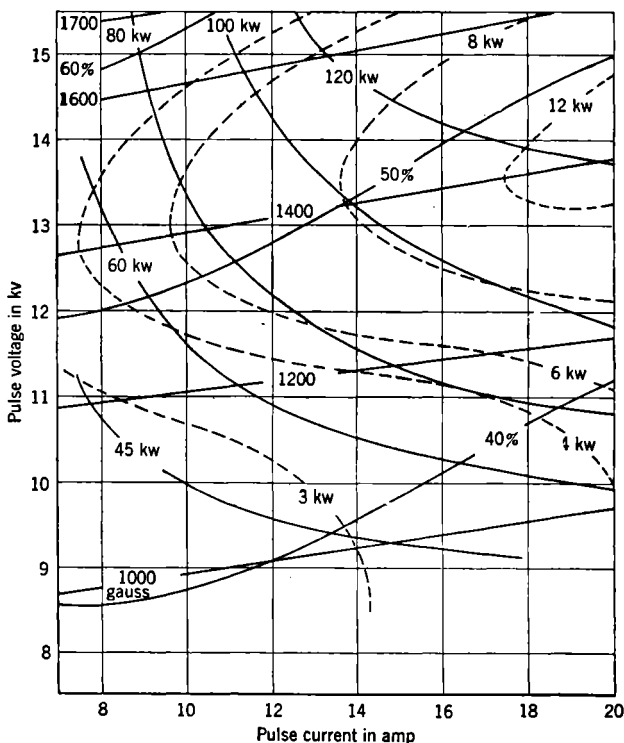


FIG. 6-22.—Performance chart showing pulse back-bombardment power with ----- pulse back-bombardment power in kilowatts.

rest in the laboratory system of coordinates, for in that case one would expect a field equal to  $B_{cye}$  to produce a disturbance. The most plausible explanation is that some ( $n = 0$ )-contamination is actually present. Actually it has been observed from data taken on field patterns in nonoperating magnetrons that there is indeed a certain amount of ( $n = 0$ )-mode present in strapped tubes. This is caused by the fact that one strap lies behind the other, and thus in the interaction space there will exist a net radial component of electric field having ( $n = 0$ )-symmetry, which will be strongest at the ends of the anode. It should

be noted that this is a radial electric field rather than a tangential one, as in the case of the rising-sun magnetron. A somewhat minor point in favor of this analysis is that the maximum of back bombardment was not observed for an unstrapped design on which measurements were made. The observed  $B_{res}$  for the data of Fig. 6-22 is in good agreement with that calculated from Eq. (174) making plausible estimates of  $\bar{s}_{avg}$  and  $(s\Delta\psi)$  from Hartree's calculations on a 10-cm. magnetron operating near 1400 gauss.

One related fact may be mentioned as indicative of the operation of fields not included in the rotating wave. From Eqs. (54a), (54b), and (55) for an electron at the cathode one has

$$\bar{s}^2 + \bar{\psi}^2 = \gamma^2$$

and for the energy loss from Eq. (76a)

$$a_{loss} = -\gamma - \bar{\psi}.$$

Thus

$$-2\gamma < a_{loss} < 0.$$

Therefore the maximum energy with which an electron can return to the cathode is  $2\gamma$  or in volts,  $2(m_0/e)(\omega r_c)^2 = 2(m_0 c^2/e)(2\pi r_c/n\lambda)^2$ , which gives  $4 \times 10^4 (r_c/n\lambda)^2$  kv. For  $r_c = 3 \times 10^{-3}$  meters and  $\lambda = 10^{-1}$  meters  $n = 4$ , the maximum energy is 2.25 kv. The evidence from the work of Danforth and his associates is that energies considerably higher than this are found, although these experiments are difficult to perform.

In discussing the perturbations produced by other Fourier components earlier in this chapter, it was found that for the  $\pi$ -mode the frequencies of the perturbations were  $\pm 2\omega_0$ ,  $\pm 4\omega_0$ , etc. Thus, it might be expected from Eq. (174) that the perturbations with frequency  $2\omega_0$  which is due to the ( $p = +N/2$ )-component would be in resonance with the electron orbit perturbations at a field  $B_{res}$  given by

$$B_{res} = B_{cyc} \left( 2 + \frac{1}{n} + \frac{1}{4n} \theta \right).$$

For any magnetrons that have been operated at fields as high as this value of  $B_{res}$ , no decline in efficiency has been found. No cathode back-bombardment data have been taken at these levels. The absence of such an effect upon the efficiency is probably due to the fact that the ( $p = +N/2$ )-field falls off rapidly toward the cathode as compared with a ( $p = 0$ )-field. It thus acts effectively only close to the anode, and the number of cycles that an electron spends in a significant field is not sufficiently great to affect its behavior. This is a possible clue to the action of the ( $p = 0$ )-field in lowering efficiency, for it suggests that it must act relatively close to the cathode and probably interferes with the sorting of the electrons into bunches.

## CHAPTER 7

### THE SPACE CHARGE AS A CIRCUIT ELEMENT

BY F. F. RIEKE

**7-1. Introduction.**—The characteristics of a magnetron as an oscillator can be described in terms of two quite distinct sets of properties. One set of properties belongs to the complex of resonant cavity, output coupler, and r-f load considered purely as passive circuit elements. The other set of properties is associated with the electron cloud, or space charge, as it exists in the configuration of electric and magnetic fields peculiar to the magnetron. The purpose of this chapter is to show how the over-all performance may be analyzed in terms of these two sets of properties and how an understanding of them may be used to predict the manner in which performance will be influenced by modifications in the design of the circuit or by peculiar conditions of operation.

To a large extent, the discussion concerns the various influences that the output load exerts on the performance of the magnetron. Actually, these effects in the magnetron have a general resemblance to the corresponding ones in many other types of self-excited oscillators, and it may be of some interest to examine the reasons for giving them here a much greater prominence than they ordinarily receive in discussions of vacuum-tube oscillators.

An intensive study of the effects of variations in the load was first taken up primarily out of practical considerations. Originally, the load was adjusted to secure maximum efficiency consistent with general stability. It then came to be realized that satisfactory performance of a radar system depended also upon the stability of the *frequency* of the magnetron. Inasmuch as there was some correlation between changes in frequency and changes in load, there immediately arose a need for an understanding of the relation between the two. Thus, the problem arose out of a combination of circumstances that are more or less peculiar to microwave pulse-radar, namely,

1. The primary, frequency-controlling oscillator is directly coupled to the load, since no suitable buffering amplifier is available.
2. The output system tends to have an unstable impedance, as it is large in terms of wavelengths, so that mismatches can give rise to a complicated spectrum of resonances.

3. The magnetron must operate in conjunction with a fairly selective receiver (at least in consideration of noise figure, if not of interference).

The experimental studies that grew out of the situation indicated above eventually resulted in the construction of "Rieke diagrams" for a large assortment of magnetrons operated under a wide range of conditions. It then occurred to many who became familiar with these diagrams that basic information about the inner workings of the magnetron could be obtained from them. In consequence, methods were developed<sup>1</sup> for analyzing the effects of the load in a more fundamental way. These methods, although generally applicable to self-excited oscillators of many types, are particularly useful in the study of microwave oscillators, of which the magnetron is but one example.

With conventional oscillators that generate ordinary radio frequencies, the interior conditions of the active oscillator—as represented by various voltages and currents—can usually be evaluated by direct measurements. In microwave generators, however, all the essential parts are contained within the vacuum envelope, and the only alternating-current measurements that are at all easy to make, even in principle, are those of impedance, power, and frequency. Consequently, to evaluate the internal conditions one either must be content with indirect methods or must undertake elaborate experiments on tubes designed for the express purpose of making the measurements possible.

In the special case of the oscillating magnetron, the only quantities that seem to be fundamental and that also can be measured conveniently are (1) magnetic field; (2) power, frequency, and load impedance at the output terminals; and (3) current and voltage at the input terminals. Accordingly, it becomes worth while to exploit fully the relations among these quantities so as to obtain information about the internal conditions of the oscillating system. The results will necessarily be expressed in a rather abstract form, since the detailed theory of the magnetron has so far not provided a sufficient framework of general relations to permit a complete analysis of the data.

To some readers, the profuse use of equivalent circuits in connection with the magnetron cavity may seem questionable, inasmuch as the dimensions of the cavity are not small compared with the free-space wavelength of the oscillations. Strictly speaking, the concepts of inductance, capacitance, and resistance imply a particular form of approximate solution to Maxwell's equations which is valid only for

<sup>1</sup>J. C. Slater, "Theory of Magnetron Operation," RL Report No. 200, Mar. 8, 1943; F. F. Rieke, "Analysis of Magnetron Performance, Part I," RL Report No. 229, Sept. 16, 1943. J. R. Pierce, "Oscillator Behavior," BTL Memorandum MM-43-140-19.

systems that are small compared with the free-space wavelength at the frequencies involved. Leaving aside the question of  $L$ ,  $C$ , and  $R$  for the moment, it can be said that the concept of *impedance* can be so generalized as to avoid this limitation by defining the impedance as the ratio of the orthogonal components of the electric and magnetic fields.<sup>1</sup> In special cases, the generalized impedance can be related to currents and voltages, particularly where a *TEM*-mode is involved (as in a coaxial line) or where the fields have approximately a *TEM*-mode character, as in the slot of a magnetron resonator.

The theory of cavity resonators, based directly on Maxwell's equations,<sup>2</sup> leads to the result that various impedances in such a cavity are related to each other in the same way as the impedances in *LRC*-networks, which means that between certain components of electric and magnetic fields there are linear relations of the type

$$\begin{aligned} E_1 &= z_{11}B_1 + z_{12}B_2, \\ E_2 &= z_{12}B_1 + z_{22}B_2 \end{aligned}$$

which correspond to the relations between currents and voltages in a network. Moreover, when the  $z_{jk}$  factors are expanded in terms of the frequency, the forms are of the same general type as those met with in network analysis. According to the theory of networks, given such an impedance function, it is always possible to "synthesize" *LRC*-networks which will have just that impedance function. (This statement is subject to the condition that the cavity can be adequately represented by a finite number of terms in the expansion.) Accordingly the cavity can be represented by an equivalent network, but this equivalent network need have no physical relation, part by part, with the cavity and is not even unique. Thus the equivalent circuit, in one extreme, may be regarded only as a special representation of a mathematical formula. However, between this viewpoint and the other extreme, that of literal interpretation of the elements in the equivalent circuit as inductances, capacitances, and resistances actually existing in the resonant system, there is a middle ground, because the *LRC* approximation to a solution of Maxwell's equations can be a quantitative rather than a qualitative matter.

In practice, one attempts (on the basis of intuition or experience) to derive a suitable equivalent circuit from the shape of the cavity and its observed behavior. From measurements, one then arrives at values of such quantities as  $\sqrt{C/L}$ ,  $\sqrt{LC}$ , and  $R\sqrt{C/L}$  that are meaningful, although the values of  $L$ ,  $R$ , and  $C$  derived from them may not be (or

<sup>1</sup> S. A. Schelkunoff, *Electromagnetic Waves*, Van Nostrand, New York, 1943.

<sup>2</sup> J. C. Slater, "Forced Oscillations in Cavity Resonators," RL Report No. 188, Dec. 31, 1942.



may be so only in a limited sense). The degree of complication of the equivalent circuit first assumed is dependent upon the particular situation and the degree of approximation required.

**7.2. The Electron Stream as a Circuit Element.**—The features of the magnetron cavity relevant to the following treatment are illustrated in Fig. 7.1; the nature of the electric fields is indicated by lines of force. In this discussion only the alternating component of the electric field  $E$  is considered; thus the field indicated by the lines of force contains a time factor  $\cos \omega t$ , or in the conventional complex-variable notation  $e^{j\omega t}$ . The instantaneous value of the integral  $\int E \cdot ds$  across any one of the slots is substantially independent of the path of integration, provided the path lies entirely within the interaction space, so the integral can be considered to represent an instantaneous voltage across the slot; it is

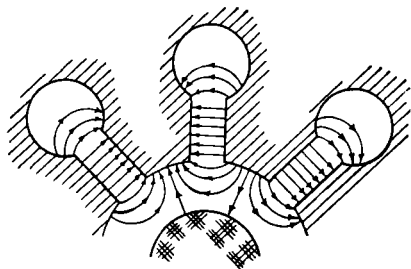


FIG. 7.1.—The electric fields in a magnetron cavity.

an alternating voltage  $\tilde{V}e^{j\omega t}$ . In the principal or  $\pi$ -mode of oscillation of magnetron cavity  $\tilde{V}$  alternates in sign from one slot to the next, but it has the same magnitude for all of the slots, and this magnitude can at present be considered to be the a-c voltage developed by the cavity.

A voltage amplitude  $\tilde{V}$  having been defined, a current amplitude  $\tilde{I}$  can also be defined, simply by making use of the fact that  $\frac{1}{2}(\tilde{I}\tilde{V})$  must equal the average power delivered by the electron stream to the resonant system. However, because there are also reactive effects connected with the electron stream, it is convenient to treat the current-amplitude  $\tilde{I}$  as a complex quantity in order to express the fact that it has a component in quadrature with the voltage. The power is then equal to one-half the real part of the product  $\tilde{V}\tilde{I}$ .

The physical meaning of the current  $\tilde{I}$  can be understood by considering the contributions of the individual electrons to the instantaneous  $VI$  product. An electron with vector velocity  $\vec{v}$  at a point where the vector electric field is  $\vec{E}$  makes an instantaneous contribution  $e\vec{E} \cdot \vec{v}$  to the  $VI$  product. The significant terms in  $\vec{E} \cdot \vec{v}$  can be calculated

by considering the interaction of the electron with the particular Fourier component of the electric field that rotates in unison with the predominant motion of the electron stream. However, partly because of the complications in the motion of the electron (see Fig. 7.2*a* and *b*),  $\vec{E} \cdot \vec{v}$  contains many higher harmonics that are not pertinent to this discussion. The electric field of the significant component is illustrated in Fig. 7.2*c*; the fields and the electron stream may be considered to rotate together, in a clockwise direction. An electron near the cathode, as at *A*, makes only a very small contribution to the  $VI$  product because

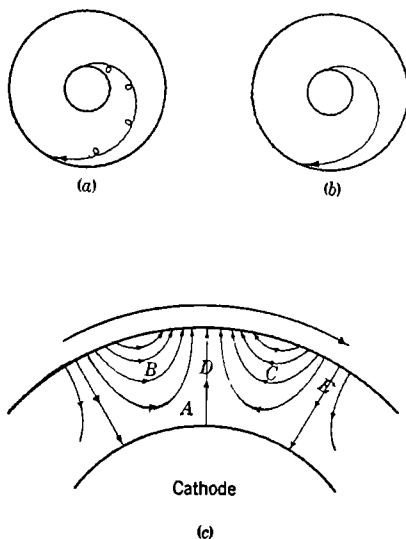


FIG. 7.2.—(a) Actual path of electrons; (b) simplified path assumed for calculations; (c) electric field configuration of the Fourier component that rotates in unison with the predominant motion of the electron stream.

$E$  is small near the cathode. Electrons at *B* absorb energy from the field and thus make a relatively large positive contribution to the real part of  $\tilde{I}$ , whereas those at *C* make a negative contribution. Electrons at *D* make a positive contribution to the imaginary part of  $\tilde{I}$ ; those at *E* a negative contribution. Because of the space modulation of the stream, there is a preponderance of electrons at positions like *C*, so the total current has a negative real component.

Having shown that the voltage  $\tilde{V}$  and the current  $\tilde{I}$  as applied to the electron stream have definite meanings, one can treat their ratio  $\tilde{I}/\tilde{V}$  as an admittance. Accordingly, the perimeter of the interaction space can be considered as a pair of terminals—in a generalized sense—at which the electron stream is connected to the resonant system, and the

complete assembly of resonant system and electron stream can be represented by the equivalent circuit drawn in Fig. 7.3. The terminals  $A$  represent the junction of the electronic current  $\tilde{I}_e = \tilde{I}_{e1} + j\tilde{I}_{e2}$  and the load current  $\tilde{I}_L$ . Because  $\tilde{I}_e$  and  $-\tilde{I}_L$  are identical, with the convention indicated in Fig. 7.3 for their positive directions, and  $\tilde{V}$  is common to the resonant system and electron stream, the relation

$$Y_e + Y_L = 0 \quad (1)$$

must always be satisfied (unless  $\tilde{V} = 0$ ).

The part of Fig. 7.3 to the right of  $A$  is composed of ordinary circuit elements—resistances, capacitances, and inductances—so its admittance has well-known properties.<sup>1</sup> In particular,  $Y_L$  is independent of the amplitude  $\tilde{V}$  and depends only on the frequency  $\nu$ ; that is

$$G_L = G_L(\nu) \quad \text{and} \quad B_L = B_L(\nu). \quad (2)$$

For the moment it is supposed that these functions are known. Consequently, if under particular conditions of operation it is observed that

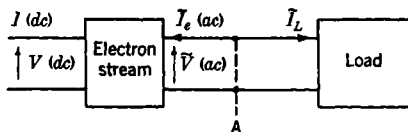


FIG. 7.3.—Equivalent circuit of the resonant system and the electric stream.

the magnetron oscillates at a frequency  $\omega'/2\pi$  and generates power  $\tilde{P}'$ , the conditions within the space charge can be computed by means of the following equalities:

$$-G'_e = G_L(\nu'), \quad (3)$$

$$-B'_e = B_L(\nu'), \quad (4)$$

$$\tilde{V}'_e = \left( \frac{2\tilde{P}'}{G'_L} \right)^{1/2}. \quad (5)$$

The components of the current can be found from the relation  $\tilde{I}_e = Y_e \tilde{V}$ . One thus has a procedure for evaluating experimentally the conditions within the space charge.

The inverse problem of predicting  $\nu$  and  $P$  when the operating conditions are specified may now be considered. The method consists essentially of solving a system of equations made up of Eq. (2) and additional

<sup>1</sup> An electronic admittance, on the other hand, has properties that are quite different from those of the admittance of a passive circuit (which is composed only of condensers, inductances, and resistances). A passive circuit is linear; in other words, its admittance is independent of the applied voltage and depends only on the frequency, whereas electronic devices are necessarily nonlinear except for applied voltages of small amplitude—at large amplitudes, saturation effects always set in.

equations that contain the properties of the electron stream. These additional equations relate  $Y_e$  to such quantities as the d-c voltage applied to the magnetron, the magnetic field, etc. The general nature of these relations will be taken up first.

In a typical experiment on a magnetron, one applies a magnetic field  $\mathcal{B}$ , a d-c voltage  $V$  at the input terminals, and an impedance  $Z = R + jX$  at the output terminals. In turn, one observes that the magnetron oscillates at a frequency  $\nu$ , generates power  $\tilde{P}$ , and draws a direct current  $I$  at the input terminals. The first four variables— $\mathcal{B}$ ,  $V$ ,  $R$ , and  $X$ —have been set arbitrarily and can be termed the *independent* variables of the system. The values of the last three variables— $\nu$ ,  $\tilde{P}$ , and  $I$ —are fixed by the choice of the independent variables and by the inherent properties of the magnetron;  $\nu$ ,  $\tilde{P}$ , and  $I$  are the *dependent* variables of the system. A somewhat different ordering of the original experiment would correspond to a different choice of independent variables—for instance, one might have decided to fix the input current  $I$  arbitrarily and let the input voltage  $V$  adjust itself accordingly. The essential fact is, however, that four independent variables and three dependent variables, or, generally, seven variables and three relations between them, are required to describe the fundamental properties of the magnetron.

A convenient form for expressing these properties is the following set of relations:

$$G_e = G_e(V, V, \nu, \mathcal{B}), \quad (6a)$$

$$B_e = B_e(V, V, \nu, \mathcal{B}), \quad (6b)$$

$$I = I(V, \tilde{V}, \nu, \mathcal{B}). \quad (7a)$$

An alternative form for Eqs. (6a) and (6b) is

$$\tilde{I}_e = (G_e + jB_e)V = \tilde{I}_e(V, \tilde{V}, \nu, \mathcal{B}). \quad (7b)$$

A direct physical interpretation can be attached to this set of relations by considering an ideal experiment. Suppose that under particular conditions of oscillation the quantities involved in Eqs. (7a) and (7b) have the values  $I'$ ,  $V'$ ,  $V'$ ,  $\nu'$ ,  $\mathcal{B}'$ , and  $I'_e$ . In principle, the part of the system to the right of the terminals  $A$  in Fig. 7-3 can be replaced by a generator that has an output voltage  $V'$  and frequency  $\nu'$ ; the conditions to the left of  $A$  remain unchanged, and all the variables listed above must retain their original values. By varying  $\mathcal{B}$ ,  $V$ ,  $\tilde{V}$ , and  $\nu$  and observing  $I$  and  $I_e$  all possible conditions of oscillation can be duplicated and the results expressed in the form of Eqs. (6a), (6b), and (7a) or alternatively Eqs. (7a) and (7b). In addition, the relations could be extended by means of such experiments to ranges of the variables that do not correspond to any stable state of oscillation. For example, it is plausible that for very large values of  $\tilde{V}$ , saturation effects of some sort

would set in, and the real component of  $I_e$  (and therefore  $G_e$ ) would become positive, which would entail the absorption rather than the generation of alternating-current power by the electron stream. Actually, information about the functions (6a) to (7b) has to be obtained principally from data on stable states of oscillation, but it is important to realize that the functions have meaning for extended ranges of the variables.

It so happens that in most of the applications of relations (6a) to (7b) only a small range of the frequency  $\nu$  is of interest. For example, if one is concerned with the effect of the external load on the performance of a fixed-tuned magnetron, one need consider frequencies that differ from the "normal" frequency of oscillation  $\nu_0$  by at most a few per cent. In handling such problems it is very convenient to make the approximation that the relations (6a) to (7b) do not involve the frequency at all—relations evaluated at  $\nu_0$  are used throughout the entire range of  $\nu$ . Evidence showing that this procedure is permissible will be discussed later. Inasmuch as there will be no ambiguity about  $\nu_0$  in problems of the type indicated, it will be convenient to have available for reference the relations (8a) to (9b) in the following approximate forms:

$$G_e = G_e(V, \tilde{V}, \mathfrak{B}), \quad (8a)$$

$$B_e = B_e(V, \tilde{V}, \mathfrak{B}), \quad (8b)$$

$$I = I(V, \tilde{V}, \mathfrak{B}), \quad (9a)$$

$$I_e = I_e(V, \tilde{V}, \mathfrak{B}). \quad (9b)$$

In practice, the functions (8a) to (9b) are known only in the form of tabulations of experimental data. It has not seemed feasible to fit analytical equations to the data, and the relations are actually used in the form of graphs; but since a function of three variables cannot be represented by a single two-dimensional curve, only partial relations can be expressed. For example, if in Eq. (8a)  $\tilde{V}$  and  $\mathfrak{B}$  are held at fixed values,  $G_e$  can be plotted against  $V$ . Such questions as which variables should be held fixed are matters that have to be adapted to the particular problem in hand. Therefore, any attempt to carry through the present discussion on the basis of a specialized form of the relations would involve much graphical solution of equations, replotting, etc., and it seems preferable to adopt a somewhat general viewpoint. For the present, it will be taken for granted that the necessary information about relations (8a) to (9b) is available and that it can always be put into a desired form by the appropriate computational procedures.

One may now consider the problem that initiated the discussion of relations (6a) to (9b), namely, that of predicting the frequency of oscillation  $\nu$  and the power output  $P$  from the known properties of  $Y_L$  and  $Y_e$  [the approximate forms (8a) to (9a) will be used]. If a magnetic field

$\mathfrak{B}'$  and a d-c voltage  $V'$  are applied to the magnetron, the real and imaginary parts of Eq. (1), with Eqs. (2), (8a), and (9a) substituted into it, become

$$G_L(\nu) + G_e(V', \tilde{V}, \mathfrak{B}') = 0, \quad (10)$$

$$B_L(\nu) + B_e(V', \tilde{V}, \mathfrak{B}') = 0. \quad (11)$$

These two equations may be solved for  $\tilde{V}$  and  $\nu$ ; the solution  $\tilde{V}'$ ,  $\nu'$  then substituted along with  $V'$  and  $\mathfrak{B}'$  into Eq. (9a) to obtain  $I'$ ; and the problem thus completed. A graphical solution would take the following form:

The pair of relations

$$G = G_L(\nu) \quad \text{and} \quad B = B_L(\nu) \quad (12)$$

are the parametric equations for a curve in the  $GB$  plane. Such a curve is illustrated schematically in Fig. 7.4, where the variation of the parameter  $\nu$  along the curve is represented by the small circles that mark off equal increments in  $\nu$ . (The fact that only a small range of  $\nu$  is represented has been indicated by marking off  $\Delta\nu$  rather than  $\nu$ .)

Similarly, the pair of relations

$$G = -G_e(V', \tilde{V}, \mathfrak{B}')$$

and

$$B = -B_e(V', \tilde{V}, \mathfrak{B}') \quad (13)$$

are the parametric equations for a second curve which is also illustrated in Fig. 7.4. The variation of the parameter  $\tilde{V}$  along this curve is indicated by a scale. According to Eq. (9a),  $I$  also varies in a perfectly definite manner along this curve [that is,  $I = I(V', \tilde{V}, \mathfrak{B}')$ ], and its variation is indicated

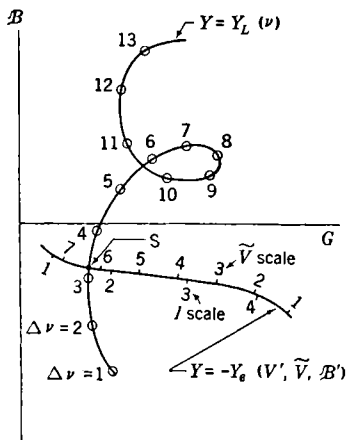


FIG. 7.4.—Admittance plots in the  $GB$  plane for a magnetron operated at constant  $\mathfrak{B}$  and  $V$ .

by a second scale. A curve of this type is sometimes termed an "operating curve"; other sorts of operating curves may be drawn, however, so when a distinction must be made, the present type may be referred to as "an operating curve at constant  $V$ ."

The intersection of the two curves indicated in Fig. 7.4 by the point  $S$  is a solution to Eqs. (10) and (11). At the intersection  $S$  the values of  $\tilde{V}'$ ,  $I'$ , and  $\nu'$  can be read from the scales attached to the curves.

It has thus been shown that the operating curve for  $\mathfrak{B} = \mathfrak{B}'$ ,  $V = V'$  is the curve defined by the simultaneous equations  $G = -G_e(V', \tilde{V}, \mathfrak{B}')$  and  $B = -B_e(V', \tilde{V}, \mathfrak{B}')$  and that the operating curve for  $\mathfrak{B} = \mathfrak{B}'$ ,

$I = I'$  is the curve defined by the system of equations  $G = -G_e(V, V, \mathcal{B}')$ ,  $B = -B_e(V, \tilde{V}, \mathcal{B}')$  and  $I' = I(V, \tilde{V}, \mathcal{B}')$ . If, however, one should wish to take into account the fact that the d-c power supply (or modulator) used to drive the magnetron has an internal voltage drop that varies with the current drawn, the appropriate operating curve can in principle be obtained as follows: Suppose that  $V$  and  $I$  are connected by a relation

$$V = f(I) \quad (14)$$

and that  $\mathcal{B} = \mathcal{B}'$ ; then the operating curve becomes simply a plot of the function (14) in the curvilinear coordinate system formed by the various constant- $V$  and constant- $I$  operating curves for  $\mathcal{B} = \mathcal{B}'$ .

Diagrams of the general type of Fig. 7.4 provide a means for the direct interpretation of many aspects of magnetron behavior. The curve  $Y = Y_L(\nu)$  has the important property of depending entirely on the system that lies to the right of the terminals  $A$  in Fig. 7.3. Thus any effect that accompanies a change in either the resonant system or the external load can be interpreted in terms of the corresponding shift of the  $Y_L$  curve. In the same way, the curve  $Y = -Y_e$  depends only on what is to the left of the terminals  $A$ , so that all effects which are connected with changes in the input conditions ( $V, I, \mathcal{B}$ ) can be interpreted in terms of shifts in the  $-Y_e$  or operating curve.

The loop in the curve  $Y = Y_L(\nu)$  of Fig. 7.4 strongly suggests the possibility that Eqs. (10) and (11) may sometimes have more than one solution. Since multiple solutions present a special set of problems, discussion of them will be postponed to Sec. 7.4. In addition, there is the possibility that a solution to the equations may represent an *unstable* state of oscillation; the question of stability will also be taken up in Sec. 7.4.

**7.3. Analysis of the Resonant System.**—In the foregoing discussion it was assumed that the properties of the part of the system to the right of terminals  $A$  in Fig. 7.3 were known in the form of the functions  $G_L(\nu)$  and  $B_L(\nu)$ . These functions, whose specialized forms are analyzed in this section, contain combined properties of the system (magnetron cavity + output coupler + lead + transmission line + termination). An example of such a system is illustrated schematically in Fig. 7.5a. The divisions between the various components is to some extent a matter of convention.

Oscillation of the magnetron in only the  $\pi$ -mode is considered, and it is assumed that the resonances of the other modes of the cavity are well enough separated from the  $\pi$ -mode resonance so that their presence may be ignored. That is, the frequency of oscillation is considered to be much closer to that of the  $\pi$ -mode resonance than to any other mode, and it is then possible to analyze the system in terms of the equivalent

circuit drawn in Fig. 7-5b. The parallel-resonant circuit has constants that are appropriate to the cavity alone (with the output loop completely removed from it); it thus contributes an admittance  $Y_v$  at the terminals  $A$ .

When the loop, with the remainder of the load system attached to it, is inserted into the cavity, the admittance at  $A$  is augmented by an admittance  $Y_e$ ; thus

$$Y_L = Y_v + Y_e. \quad (15)$$

The terminals  $S$  in Fig. 7-5b represent an arbitrary division between the magnetron proper—which will be treated as a fixed system—and what-

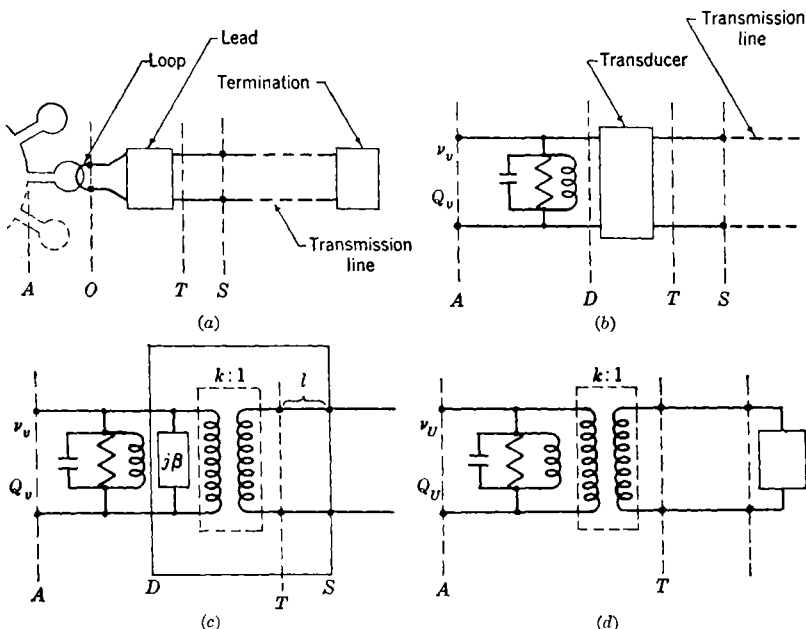


FIG. 7-5.—(a) The components of the resonant system; (b) representation of the resonant system of Fig. 7-5a; (c) equivalent circuit of Fig. 7-5b; (d) simplification of Fig. 7-5c.

ever power-absorbing equipment one chooses to attach to it. The admittance  $Y_s$  of that part of the system to the right of  $S$  will be treated for the present as a known function of the frequency inasmuch as its evaluation does not involve any properties of the magnetron. The transducer  $D$ - $S$  in Fig. 7-5b is a device introduced to express the fact that at any given frequency the currents and voltages at  $D$  and at  $S$  are connected by linear relationships. In terms of admittances these relationships take the form

$$Y_e = \frac{\alpha Y_s + \mathfrak{C}}{\beta Y_s + \mathfrak{D}}, \quad (16)$$



where  $\mathcal{A}$ ,  $\mathcal{B}$ ,  $\mathcal{C}$ , and  $\mathcal{D}$  are complex and are functions of the frequency. The general properties of relations of this type and methods for evaluating the quantities  $\mathcal{A}$ ,  $\mathcal{B}$ ,  $\mathcal{C}$ , and  $\mathcal{D}$  or their equivalents are described in Chap. 5. For some purposes it may be convenient to replace the transducer  $D$ - $S$  by an equivalent chain of transducers connected at intermediate pairs of terminals. For example, it may sometimes be desirable to bring the terminals  $O$  of Fig. 7-5a into evidence in the equivalent circuit.

In order to concentrate attention on the most interesting features of the resonant system, the approximations will be made

1. That the transducer  $D$ - $S$  is free of electrical losses.
2. That the coefficients of Eq. (16) can be treated as constants over frequency bands a few per cent in width.

The special effects associated with the quantities neglected in the first of the two approximations are treated in Chap. 5, and the effects that are connected with the frequency sensitivity of the transducer are discussed in Sec. 7-5.

As a result of the approximations introduced above, Eq. (16) can be written in the form

$$Y_e = \frac{dY_s + jc}{jbY_s + a}, \quad (17a)$$

where  $a$ ,  $b$ ,  $c$ , and  $d$  are *real* constants. It is possible to represent a relation of this type by an equivalent circuit composed of a shunt susceptance  $\beta$ , an ideal transformer of turns-ratio  $k$ , and a length  $l$  of transmission line of the same characteristic admittance  $M$  as the output transmission line. Accordingly, the circuit of Fig. 7-5b can be made exactly equivalent to that of Fig. 7-5b; and if the admittance of the output transmission line is evaluated at the reference plane  $T$  instead of at  $S$ , Eq. (17a) takes the form

$$Y_e = j\beta + \frac{1}{k^2} Y_T. \quad (17b)$$

The circuit of Fig. 7-5c can, in turn, be replaced by the simpler circuit of Fig. 7-5d in which the parallel-resonant circuit has a resonance frequency of  $\nu_U$  instead of  $\nu_o$ , where

$$\nu_U = \nu_o - \frac{\beta}{4\pi C}. \quad (18)$$

To make use of the circuit of Fig. 7-5d, the admittance in the output transmission line must be computed at the reference plane  $T$  instead of at  $S$ . The reference plane  $T$  can, of course, be translated any integral number of half wavelengths ( $\lambda_U$ ) toward or away from the magnetron, but by properly choosing  $T$  it is possible to compensate to

some extent for the errors introduced by the simplifying assumption originally made, namely, that the coefficients  $a$ ,  $b$ ,  $c$ , and  $d$  of Eq. (17a) are independent of frequency. The best choice of  $T$  can be determined for the particular magnetron from cold-test measurements or from a Rieke diagram.

It follows, then, that if the admittance in the output transmission line is computed with respect to an appropriately chosen reference plane, the resonant system of the magnetron viewed at the terminals  $A$  will behave approximately as a parallel-resonant circuit shunted by an admittance equal to  $(1/k^2)Y_T$ . The properties of a parallel-resonant circuit will thus be referred to frequently in the succeeding sections, and in order to provide a convenient summary of the notation and the various approximate formulas that will be used a review of the pertinent properties of this type of circuit is given below.

In the notation of Chap. 5, the admittances that have so far been introduced in this chapter are properly written

$$\vec{Y}_c, \vec{Y}_L, \vec{Y}_v, \vec{Y}_e, \vec{Y}_s, \text{ and } \vec{Y}_T.$$

Inasmuch as the direction of these admittances will remain consistent throughout this chapter, however, the arrows will be omitted in the following treatment.

Usually impedance and admittance formulas are developed on the basis of sinusoidal voltages and currents expressed as exponentials, viz.,

$$I = ie^{j\omega t} \quad \text{and} \quad V = ve^{j\omega t}.$$

It is equally feasible to develop the formulas for positively or negatively damped sinusoidal voltages and currents, also expressed as exponentials:

$$I = ie^{pt} \quad \text{and} \quad V = ve^{pt}$$

where  $p = \xi + j\omega$ . That is to say, impedances and admittances can be defined for a complex frequency  $p/2\pi j$  as well as for a real frequency  $\nu = \omega/2\pi$ . Later on, the complex frequency will be used in the treatment of transients by approximating a voltage of varying amplitude  $V = \tilde{V}(t)e^{j\omega t}$  as a pure exponential  $V = ve^{(\xi + j\omega)t}$ , where  $\xi = (d/dt) \ln \tilde{V}(t)$ .

A circuit composed of an inductance  $L$ , a capacitance  $C$ , and a resistance  $R = 1/G$ , all connected in parallel, is a convenient prototype. For this circuit, the condition for the conservation of charge can be written

$$C \frac{dV}{dt} + GV + \frac{1}{L} \int_0^t V dt = \text{const.} \quad (19)$$

The general solution to the equation is

$$V = C_1 e^{p_0 t} + C_2 e^{p_0^* t}, \quad (20)$$

where

$$p_0 = \xi_0 + j\sqrt{\omega_0^2 - \xi_0^2}, \quad p_0^* = \xi_0 - j\sqrt{\omega_0^2 - \xi_0^2},$$

$$\xi_0 = \frac{G}{2C}, \quad \omega_0 = \frac{1}{\sqrt{LC}}.$$

The  $Q$  of the circuit is defined by the relation  $1/2Q = -\xi_0/\omega_0$ . The two terms in the right-hand side of Eq. (20) represent the two natural oscillations, or modes, of the system.

For an impressed voltage of the type  $V = ve^{pt}$  the admittance and impedance of the circuit are given by the formulas

$$Y = G + jB = \frac{1}{Z} = C \frac{(p - p_0)(p - p_0^*)}{p} \quad (21)$$

or

$$Z = \frac{1}{C} \left( \frac{a}{p - p_0} + \frac{a^*}{p - p_0^*} \right), \quad (22)$$

where

$$a = \frac{p_0}{p_0 - p_0^*}.$$

If the usual convention of representing a sinusoidally applied voltage  $V = ve^{j\omega t}$  by a positive value of  $\omega$  is adopted, then for a real frequency  $\omega/2\pi$ , Eq. (21) can be written in the forms

$$Y = \frac{1}{Z} = G + jC\omega_0 \left( \frac{\omega}{\omega_0} - \frac{\omega_0}{\omega} \right) \quad (23a)$$

$$= \sqrt{\frac{C}{L}} \left[ \frac{1}{Q} + j \left( \frac{\omega}{\omega_0} - \frac{\omega_0}{\omega} \right) \right]. \quad (23b)$$

All of the foregoing formulas are exact, but it is generally more convenient to use approximate formulas that are accurate only to first-order terms in  $\xi/\omega_0$ ,  $\xi_0/\omega_0$  and  $(\omega - \omega_0)/\omega_0$ . Ordinarily there will be no loss of accuracy in using these approximations, because the use of a parallel-resonant circuit to represent the properties of a complicated cavity for frequencies near one of its resonances is usually in itself significant only with regard to first-order terms in these quantities. If Eq. (21) is expanded, then an approximate formula is obtained which can be written in any of the following ways:

$$Y = \frac{1}{Z} = Y_c \left( \frac{\xi}{\omega_0} - \frac{\xi_0}{\omega_0} + 2j \frac{\omega - \omega_0}{\omega_0} \right), \quad (24a)$$

where

$$Y_c = C\omega_0 = \sqrt{\frac{C}{L}},$$

$$Y = \frac{1}{Z} = 2C(p - p_0), \quad (24b)$$

and

$$Y = \frac{1}{Z} = Y_c \left( \frac{1}{Q_0} + \frac{\xi}{\omega_0} + 2j\delta \right), \quad (24c)$$

where

$$\delta = \frac{\omega - \omega_0}{\omega_0} = \frac{\nu - \nu_0}{\nu_0} \approx \frac{\lambda_0 - \lambda}{\lambda_0}.$$

When the constants of the equivalent circuit are derived from impedance measurements, the following relations are used:

$$\omega_0 = \omega|_{B=0} \quad \text{or} \quad \nu_0 = \nu|_{B=0}, \quad (25a)$$

$$Y_c = \frac{1}{2\omega_0} \frac{dB}{d\omega} \Big|_{B=0} = \frac{1}{2\nu_0} \frac{dB}{d\nu} \Big|_{B=0}, \quad (25b)$$

$$\frac{1}{Q_0} = \frac{1}{Y_c} G \Big|_{B=0}. \quad (25c)$$

It is sometimes convenient to represent the combination of a parallel-resonant circuit and a shunt admittance  $Y' = G' + jB'$  by an equivalent parallel-resonant circuit that has a resonance frequency different from that of the original one. Thus

$$Y_c \left( \frac{1}{Q_0} + j2 \frac{\omega - \omega_0}{\omega_0} \right) + G' + jB' \approx Y_c \left( \frac{1}{Q'_0} + j2 \frac{\omega - \omega'_0}{\omega'_0} \right), \quad (26)$$

where

$$\frac{1}{Q'_0} = \frac{1}{Q_0} + \frac{G'}{Y_c} \quad \text{and} \quad \frac{\omega'_0 - \omega_0}{\omega_0} = - \frac{2B'}{Y_c}.$$

Returning to the resonant system of the magnetron, Eq. (15) may be expressed in the form

$$Y_L = Y_U + Y_E, \quad (27)$$

where

$$Y_U = G_U + j4\pi C(\nu - \nu_0) + j\beta$$

and

$$Y_E = \frac{1}{k^2} Y_T.$$

It is frequently convenient to express  $Y_T$  in normalized form, that is, as  $y_T = Y_T/M$ , where  $M$  is the characteristic admittance of the output transmission line; this gives

$$Y_L = G_U + j4\pi C(\nu - \nu_0) + j\beta + \frac{M}{k^2} y_T. \quad (28)$$

Equation (28) is often used in either of the forms of Eq. (29) or (30) given below. The subscripts  $U$ ,  $E$ , and  $L$  that appear in these equations will be used consistently to denote the following:

$U$  = characteristic of the "unloaded" condition of the resonant system,

$E$  = contribution connected with  $y_T = g_T + jb_T$ ,

$L$  = characteristic of the "loaded" condition of the resonant system.

When the variation of  $y_T$  with frequency can be ignored, Eq. (28) can be written as

$$Y_L = G_L + j4\pi C(\nu - \nu_L). \quad (29)$$

Inasmuch as the difference between  $Y_c = C\omega_0$  and  $C\omega_L$  is small, Eq. (29) can also be written as

$$Y_L = Y_c \left( \frac{1}{Q_L} + 2j \frac{\nu - \nu_L}{\nu_L} \right), \quad (30)$$

where

$$\frac{1}{Q_L} = \frac{1}{Q_U} + \frac{1}{Q_E}, \quad (31a)$$

$$\frac{1}{Q_U} = \frac{G_U}{Y_c}, \quad (31b)$$

$$\frac{1}{Q_E} = \frac{M}{k^2} \frac{g_T}{Y_c}; \quad (31c)$$

$$\nu_L = \nu_U + \nu_E, \quad (32a)$$

$$\nu_U = \nu - \frac{\beta}{4\pi C}, \quad (32b)$$

$$\nu_E = -\frac{M}{k^2} \frac{b_T}{C}. \quad (32c)$$

The special case where the output transmission line is matched (i.e.,  $y_T = 1$ ) is of particular significance. For the present, the values of  $Q_L$ ,  $\nu_L$ , etc., for this case will be indicated by the subscript  $M$ , viz.,  $Q_{LM}$ ,  $Q_{EM}$ , etc. By making use of these quantities, Eq. (28) can be put into still another form:

$$Y_L = Y_c \left( \frac{1}{Q_U} + 2j \frac{\nu - \nu_{LM}}{\nu_{LM}} + \frac{1}{Q_{EM}} y_T \right). \quad (33)$$

Equation (33) is especially useful because  $Q_U$ ,  $\nu_{LM}$ , and  $Q_{EM}$  can be derived very simply from the "Q-circle" which is obtained by making impedance measurements looking into the terminals  $T$  from the output transmission line (see Chap. 5). By using for  $Q_U$  the value obtained in this way, one compensates *in part* for the electrical losses inherent in the output circuit.

With the derivation of Eq. (33) the properties of the resonant system and output circuit of the magnetron have been taken into account, but the term  $y_T$  in Eq. (33) still remains to be considered. In general,  $y_T$  is a function of the frequency, but the nature of this function depends very strongly on the particular type of system that is to the right of the terminals  $T$  in Fig. 7.5a.

In one extreme,  $y_T$  is essentially independent of frequency (as when the transmission line is perfectly terminated), and  $Y_L$  then has the frequency dependence of a parallel-resonant circuit as illustrated in

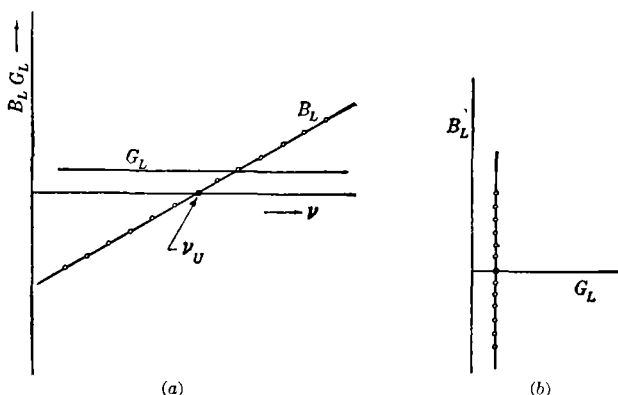


Fig. 7-6.—(a) Curves of  $G_L$  and  $B_L$  vs. frequency for a nonfrequency-sensitive load; (b) Fig. 7-6a replotted in terms of  $G_L$  vs.  $B_L$ .

Fig. 7-6a; the  $Y_L(\nu)$  curve is simply a straight vertical line with the frequency varying uniformly along it, as in Fig. 7-6b. In the other extreme, the load has a complicated spectrum of resonances (as when numerous reflections take place in the output transmission line), and

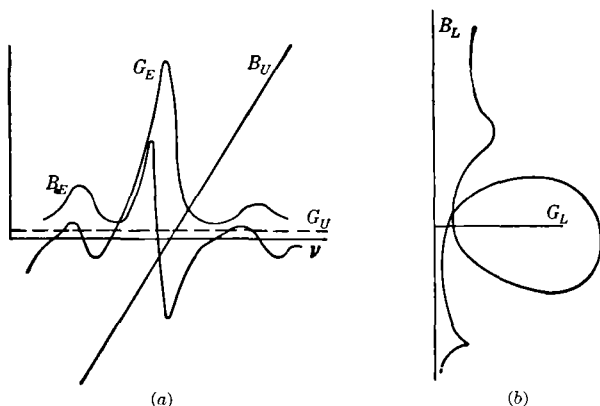


Fig. 7-7.—(a) Curves of  $G_U$ ,  $G_E$ ,  $B_U$ , and  $B_E$  vs. frequency for a frequency-sensitive load; (b) the load curve:  $B_L (= B_E \text{ and } B_U)$  plotted against  $G_L (= G_E \text{ and } G_U)$ .

the components of  $Y_F = G_E + jB_E$  vary with frequency in the general fashion indicated in Fig. 7-7a;  $G_U$  and  $B_U$  are also shown. Figure 7-7b shows  $B_L (= B_E + B_U)$  as a function of  $G_L (= G_E + G_U)$ .

**7-4. Interactions between Space Charge and Resonator.**—In the previous section it was shown that the state of oscillation of a magnetron could be obtained from the intersection of two curves in the  $GB$  plane such as those given in Fig. 7-4. It was also indicated how the operating curve  $Y = -Y_e(\tilde{V}, \alpha)$  could be derived from systematic observations on the performance of the magnetron and how the admittance curve  $Y = Y_L(\nu)$  could be computed from known properties of the magnetron cavity, output circuit, and load. The symbol  $\alpha$  stands for whatever input parameter is considered to be variable. For instance, one may wish to consider a set of operating

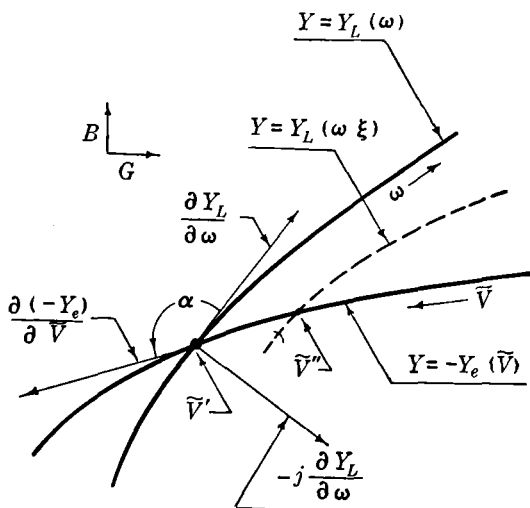


FIG. 7-8.—Stability diagram on the basis of the load and operating curves. The condition for stability is that the angle  $\alpha$ , between the vectors  $\partial Y_L / \partial \omega$  and  $\partial(-Y_e) / \partial V$ , measured in a counterclockwise direction, must lie between  $0^\circ$  and  $180^\circ$ .

curves for various constant values of  $I$ , of  $V$ , or of  $V_0$  where  $V_0 = V + RI$ . When the discussion does not concern changes in input conditions,  $\alpha$  will be omitted. The various types of phenomenon that are connected with the intersections of the curves and with displacements or distortions of one or the other of these curves are discussed below.

**General Considerations of Stability.**—It is evident that when the  $Y_L$  curve has loops, as illustrated in Fig. 7-7b, the operating curve can intersect it in several points. It has been stated previously that some of these intersections may correspond to unstable states of oscillation; the present discussion is concerned with a rule that may enable one to distinguish between the stable and the unstable states. A necessary condition for stability can be derived on the basis of Fig. 7-8 and the

following consideration: If by any means  $\tilde{V}$  is made to take on a value  $\tilde{V}''$  different from the value  $\tilde{V}'$  that it has at the intersection of the load and operating curves, the system can be stable only if there exists a natural tendency for  $\tilde{V}$  to return to the value  $\tilde{V}'$ ; it will be unstable if the anomaly in  $\tilde{V}$  tends to increase with time.

The condition of the space charge for  $\tilde{V} = \tilde{V}''$  will be represented by the point  $\tilde{V}''$  on the operating curve shown in Fig. 7-8. At first sight, this condition might seem to involve a contradiction, since the relation  $Y_L(\omega) + Y_e(\tilde{V}) = 0$  is not satisfied at  $\tilde{V}''$ . However, the curve

$$Y = Y_L(\omega)$$

holds only for steady-state conditions, that is to say, for  $\tilde{V} = \text{constant}$ . When  $\tilde{V} = \tilde{V}''$ , the amplitude  $\tilde{V}$  changes with time, or, in other words, the frequency is complex. Through the point  $\tilde{V}''$  there passes another admittance curve  $Y = Y_L(\omega, \xi')$ . If  $\xi'$  is negative, the amplitude  $\tilde{V}$  is decreasing with time; if positive, increasing. Thus if  $(\tilde{V}'' - \tilde{V}')$  and  $\xi$  have opposite signs at the point  $\tilde{V}''$ ,  $\tilde{V}$  must tend toward  $\tilde{V}'$ , and the system is stable at  $\tilde{V}'$ . The problem consists then of the determination of the sign of  $\xi'$ .

The problem can be solved by making use of the fact that  $Y_L$  is an *analytic* function of the complex variable  $p = \xi + j\omega$ . This circumstance enables one to derive the necessary information about the dependence of  $Y_L$  on  $\xi$  from its known dependence upon  $\omega$ . For values of  $\tilde{V}$  that are nearly equal to  $\tilde{V}'$ , the variation of  $\xi$  along the operating curve can be obtained from the relation

$$\frac{dY_L}{dp} dp + \frac{\partial Y_e}{\partial \tilde{V}} d\tilde{V} = 0, \quad (34)$$

where  $\partial Y_e / \partial \tilde{V}$  is taken along the operating curve. Since  $Y_L$  is an analytic function of  $p$ ,  $dY_L / dp = \partial Y_L / \partial(j\omega) = -j(\partial Y_L / \partial \omega)$ , so Eq. (34) can be written

$$\frac{\partial p}{\partial \tilde{V}} = \frac{\left( \frac{\partial(-Y_e)}{\partial \tilde{V}} \right)}{\left( -j \frac{\partial Y_L}{\partial \omega} \right)}. \quad (35)$$

[In Eq. (35)  $\partial p / \partial \tilde{V}$  and  $\partial(-Y_e) / \partial \tilde{V}$  are directional derivatives along the operating curve;  $\partial Y_L / \partial \omega$  is a directional derivative along the  $Y(\omega)$  curve.] Since  $\xi = 0$  at  $\tilde{V}'$ , it is necessary that the real part of  $\partial p / \partial \tilde{V}$  be negative at  $\tilde{V}'$  in order for  $\xi$  to be negative when  $\tilde{V} - \tilde{V}'$  is positive. The derivatives in the right-hand side of Eq. (35) can be expressed as vectors in the manner indicated in Fig. 7-8. In terms of these vectors, the condition for stability is that the angle  $\alpha$  measured between the



$\partial Y_L / \partial \omega$  and  $\partial(-Y_e) / \partial V$  vectors in a counterclockwise direction must lie between  $0$  and  $+180^\circ$ .

The various types of intersection that can occur between the load and operating curves are illustrated in Fig. 7-9. According to the criterion just derived, the intersections  $D$ ,  $E$ , and  $F$  in this figure represent states of oscillation that are inherently unstable, whereas at intersections

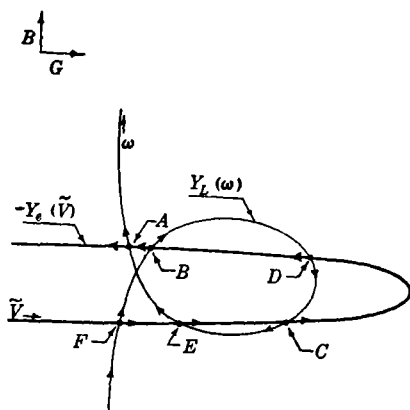


FIG. 7-9.—Types of intersection between the load and operating curves.

$A$ ,  $B$ , and  $C$  oscillations might be stable. With regard to these latter intersections two questions arise:

1. Can the system oscillate simultaneously in more than one of the possibly stable states?
2. If the system can oscillate in only one state, which of the possibly stable intersections represents the preferred state?

Inasmuch as these questions are of considerable practical importance, they will be discussed in some detail, even though a complete answer to them cannot be given.

As far as is known, a state of oscillation that corresponds to an intersection of type  $C$  in Fig. 7-9 has never been observed. This intersection represents a somewhat peculiar combination of conditions; namely, the negative of the electronic conductance  $-G_e$  increases with  $\tilde{V}$ , and the load-susceptance  $B_L$  decreases with frequency. The condition is necessarily connected with the presence of a loop in the  $Y_L$  curve, since in the absence of such a loop  $B_L$  increases with increasing frequency (see Fig. 7-6).

A second important general observation is that the magnetron does not oscillate at two frequencies simultaneously. This must mean either that there is involved some sort of selection process which operates in

favor of one or the other of the intersections or that simultaneous oscillation at two frequencies is an inherently unstable state. In discussing this matter further, it is necessary to make a distinction between pulsed magnetrons and c-w magnetrons. In the case of pulsed operation, one is interested primarily in "turn-on" phenomena, while in the case of c-w operation one is interested also in the way that the magnetron behaves when adjustments are made in the load or in other operating conditions without interrupting the applied voltage  $V$ .

Consider c-w operation with oscillation established at some intersection such as  $B$  in Fig. 7-9. If the voltage applied to the magnetron (or the magnetic field) is altered gradually, the  $-Y_c$  curve will move so that the intersection  $B$  travels along the  $Y_L$  curve. It can happen that the intersection  $B$  suddenly disappears, as when the operating curve first becomes tangent to the top of the loop and then moves completely beyond the loop. In that case the frequency becomes complex; and according to the argument applied in connection with Fig. 7-8,  $\xi$  is negative,<sup>1</sup> so the state of oscillation that involves this particular intersection becomes positively damped and thus dies out. It seems plausible that, in general, oscillations will start up again and the steady-state will then be established at an intersection such as  $A$ , although it is conceivable that oscillations might not be reestablished. Similar arguments can be applied to the case where the  $Y_L$  curve is altered by some adjustment of the resonant system. This adjustment might consist of a change in the external load or a change in the tuning adjustment of a tunable magnetron. In these cases the  $Y_L$  curve either will suffer a simple translation or will be made to go through some snakelike deformations, and pairs of intersections can coalesce and then be extinguished. While the above considerations must apply generally, it is also possible for an established state of oscillation to become unstable for reasons other than the vanishing of an intersection in an admittance diagram. It might happen that at some critical condition it becomes possible for oscillations at some other frequency to build up and make the initial state unstable. This possibility will be discussed later on in this section. In any case, it is understandable that in c-w operation a certain amount of hysteresis is observed in changing from one state of oscillation to another.

In pulsed magnetrons, one is concerned principally with erratic selection of the frequency of oscillation at successive pulses. (Hysteresis effects ordinarily do not occur; and when they do, they must be attributed to such secondary causes as thermal lags.) Considerable experience has been accumulated in two rather different types of situation. One concerns the performance of the magnetron when it feeds into a moderately

<sup>1</sup> This statement presupposes that with increasing frequency a loop is always traversed in a clockwise direction. From experience, this seems to be the case.

long, mismatched transmission line; the other concerns the use of auxiliary cavities coupled to the resonant system of the magnetron for the purpose either of tuning it or of stabilizing the frequency. In the case of the long line, it seems that the selection of frequencies is erratic when the two intersections (between the  $-Y_e$  and the  $Y_L$  curves) are close together. When the intersections are well separated, the one that occurs at the lower (or lowest) value of  $G_L$  is preferred. (The subject of long transmission lines is treated in detail in Sec. 7-6.) The general problem of an auxiliary cavity involves a much wider variety of  $Y_L$  curves than does the mismatched transmission line, and no simple rule for the selection of intersections is universally applicable. In some situations the "minimum conductance rule" just stated provides some correlation for the observed behavior, but the general case is not at all clear.

*Multiple Stable Intersections of the Load and Operating Curves.*—Considerations of stability that are based entirely on the intersections of the  $-Y_e$  and  $Y_L$  curves have an inherent flaw; they rest on the assumption that oscillations at more than one frequency are never present. While this assumption is justified by experience as far as steady states of oscillation are concerned, it is entirely unjustified with regard to transient states. To state the case more exactly, it has been assumed that the instantaneous a-c voltage  $\tilde{V}_i$  is of the form

$$\tilde{V}_i = a \exp (\xi + j\omega)t. \quad (36)$$

However, there is no reason why a voltage of the form

$$\tilde{V}_i = a_1 e^{p_1 t} + a_2 e^{p_2 t} + \cdots + \cdots \quad (37)$$

where  $p_k = \xi_k + j\omega_k$  cannot exist temporarily in the system, and the stability relations derived on the basis of Eq. (37) may be quite different from those derived on the basis of Eq. (36).

The  $Y_L(\nu)$  curve does not give any very direct indication of the response of the resonant system for a voltage of the form of Eq. (37), and there thus seems to be some advantage in approaching the problem from a somewhat different viewpoint, namely, the consideration that one is dealing with coupled circuits or with a system that has several natural modes of oscillation. It is to be noted that the word "mode" as it is used here has a context somewhat different from the one that it usually has in discussions of magnetrons. Usually the modes that are mentioned are the natural modes of the magnetron cavity either unloaded or with a nonresonant load coupled to it, each of these modes having its own peculiar configuration of electric fields in the interaction space of the magnetron. However, under conditions where there are irregularities in the load curve one is dealing with the natural modes that arise when the  $\pi$ - or  $N/2$ -mode of the cavity is coupled to a highly resonant external

system but where the fields in the interior of the magnetron are always those characteristic of the  $\pi$ -mode.

The occurrence of loops or other irregularities in the  $Y_L(\omega)$  curve is in itself evidence that more than one mode of oscillation of the resonant system is possible. According to a general result of circuit analysis the impedance of any passive circuit at a pair of terminals can be expressed in the form

$$Z = \frac{1}{Y} = \left( \frac{\frac{a_1}{p - p_1} + \frac{a_2}{p - p_2} + \dots}{\frac{a_1^*}{p - p_1^*} + \frac{a_2^*}{p - p_2^*} + \dots} \right) + b_0 + b_1 p, \quad (38)$$

where the  $p_k$ 's are the natural modes of the system when it is open-circuited at the terminals. In any physical passive system the  $p_k$ 's

are complex, and their real parts ( $\xi_k$ 's) must be negative, for in a passive system all resonances are necessarily positively damped. For high- $Q$  resonances, which are the sort that will generally be dealt with here, the  $\xi_k$ 's are relatively small; that is,

$$-\xi_k = \frac{\omega_k}{2Q_k} \ll \omega_k.$$

A term  $a_k/(p - p_k)$  becomes especially important when  $(p - p_k)$  is small, and if a particular  $p_k$ —say  $p_1$ —is quite different from any of the others, then for  $p$  nearly equal

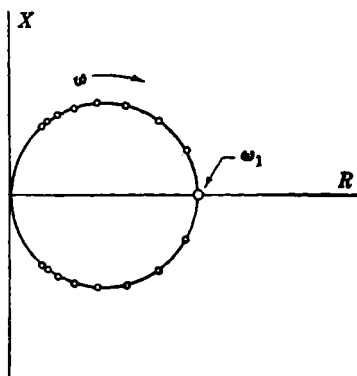
FIG. 7-10.—A plot of  $Z(\omega)$  of Eq. (39).

to  $p_1$  Eq. (37) can be approximated by just its first term. If  $\xi_1$  is small, then  $a_1$  necessarily has a small imaginary part that can be neglected (otherwise  $Z$  will have a negative real part for some values of  $\omega$ ) and

$$Y = \frac{1}{Z} \approx 2C_1(p - p_1) \quad \text{where } 2C_1 = \frac{1}{\text{Re}(a_1)}. \quad (39)$$

This is just the state of affairs which enables one to approximate a complicated circuit by a simple parallel-resonant circuit, because Eq. (39) is the same as Eq. (24b). The curve of  $Y(\omega)$  for Eq. (39) has the form shown in Fig. 7-6b, and the curve  $Z(\omega)$  in the  $RX$  plane has the form illustrated in Fig. 7-10.

When two or more of the  $p_k$ 's are nearly equal, things become more complicated. To keep the illustrations reasonably simple, it will be assumed that  $p_1$  and  $p_2$  are nearly equal in Eq. (38) but that they are very different from any of the remaining  $p_k$ 's. Then for  $p$  nearly equal



to  $p_1$  and  $p_2$  the first two terms are of comparable importance, and the simplest useful approximation to Eq. (38) is the sum of the first two terms. For simplicity, it will be assumed that  $a_1$  and  $a_2$  have negligible imaginary parts<sup>1</sup> so that, in analogy to Eq. (39), one may write

$$Z = \frac{1}{2C_1} \frac{1}{p - p_1} + \frac{1}{2C_2} \frac{1}{p - p_2} \quad (40)$$

or

$$Y = \frac{1}{Z} = 2C \frac{(p - p_1)(p - p_2)}{p - p_0}, \quad (41)$$

where

$$C = \frac{C_1 C_2}{C_1 + C_2}$$

and

$$p_0 = \frac{C_1 p_1 + C_2 p_2}{C_1 + C_2}.$$

It is evident that for a certain range of  $p$  the properties of the system can be represented by the equivalent circuit to the right of the terminals  $A$  in Fig. 7-11a. The  $Z(\omega)$  and  $Y(\omega)$  curves have the general forms illustrated in Fig. 7-11b and c. To a first approximation,  $|Z(\omega)|$  has a maximum and  $|Y(\omega)|$  has a minimum for  $\omega = \omega_1$  and  $\omega = \omega_2$ ;  $|Z(\omega)|$  has a minimum and  $|Y(\omega)|$  has a maximum for  $\omega = \omega_0$ . When the terminals  $A$  are open-circuited, the system has the natural modes  $p_1$  and  $p_2$ ; when the terminals  $A$  are short-circuited, the system has the natural mode  $p_0$ . When any admittance  $Y'$ , which varies only very slowly with frequency, is connected across the terminals  $A$ , the system has normal modes that are solutions of the quadratic equation

$$2C(p - p_1)(p - p_2) + Y'(p - p_0) = 0. \quad (42)$$

<sup>1</sup> In the general case this is not necessarily true, and the equivalent circuit in Fig. 11a may not be appropriate. This point is discussed, for instance, by Bode in *Network Analysis and Feedback Amplifier Design*, Van Nostrand, New York, 1945, p. 202. The general argument to be outlined can be applied equally well to any circuit, but for purposes of illustration a circuit has been chosen that brings the normal modes directly into view.

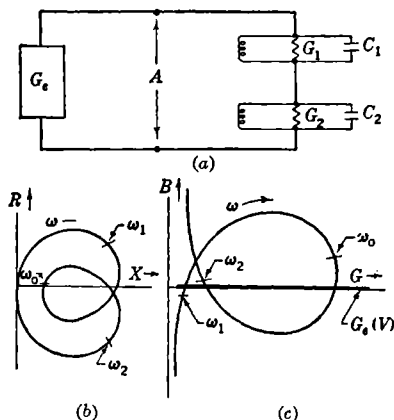


FIG. 7-11.—(a) Equivalent circuit representing the case of two possible transient modes of oscillation; (b) the  $Z(\omega)$  curve for the circuit of Fig. 11a; (c) the  $Y(\omega)$  curve for the circuit of Fig. 11a.

If  $Y'$  represents a passive circuit element, the solutions necessarily have negative real parts; but if  $Y'$  has a negative component of conductance, it is possible for one or more of the solutions to have positive real parts. In the latter case it is possible for one or more modes of oscillation in the circuit to build up from any slight disturbance of the system such as might arise from thermal excitation or any other source of *noise*.

For the present it will be taken for granted that it is sensible to substitute the electronic admittance  $Y_e$  for  $Y'$  in Eq. (42). Since the aim here is simply to illustrate the qualitative aspects of the problem,

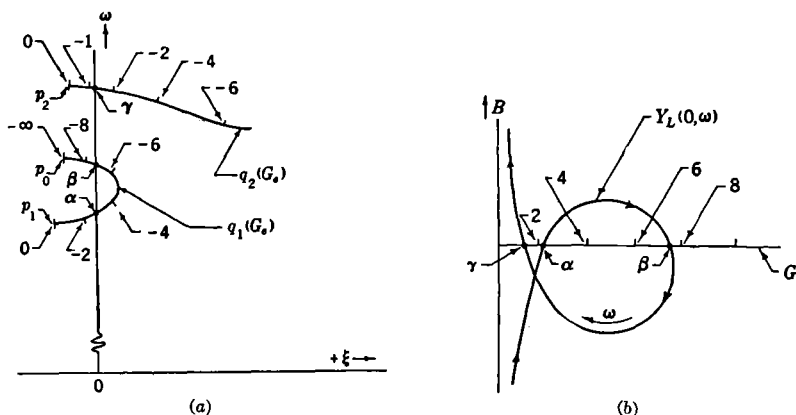


FIG. 7-12.—(a) The general behavior of the roots  $q_1G_e$  and  $q_2G_e$  plotted in the  $\omega - \xi$  plane for the indicated negative values of  $G_e$ ; (b) the related  $Y_L(0, \omega)$  curve. The  $G$ -axis coincides with the operating curve  $-G_e \tilde{V}$ .

it is also assumed that  $Y_e$  is a pure conductance. To proceed further, one must find how the roots of the equation

$$2C(p - p_1)(p - p_2) + G_e(p - p_0) = 0$$

vary when  $G_e$  takes on negative values. There are two roots,  $p = q_1(G_e)$  and  $p = q_2(G_e)$ ; these can be plotted in the  $p$  (or  $\xi$ ,  $\omega$ ) plane and will trace out a curve as  $G_e$  varies. When  $G_e = 0$ , the roots are, of course,  $p_1$  and  $p_2$ ; that is,  $q_1(0) = p_1$  and  $q_2(0) = p_2$ . When  $G_e \rightarrow -\infty$ , one of the two roots must approach  $p_0$  (which of the roots does this depends in a rather complicated way upon the values of  $p_1$ ,  $p_2$ , and  $p_0$ ), and the other root must approach  $(+\infty, 0)$ . The general behavior of the roots for negative values of  $G_e$  is illustrated in Fig. 7-12a. The related  $Y_L(0, \omega)$  curve is shown in Fig. 7-12b.

According to the simplifying assumption made above—that  $Y_e$  is a pure conductance—the operating curve in Fig. 7-12b lies along the  $G$ -axis. It intersects the  $Y_L(0, \omega)$  curve in the points  $\alpha$ ,  $\beta$ ,  $\gamma$  and these points correspond exactly to those similarly labelled in Fig. 7-12a, where either

$q_1$  or  $q_2$  is a pure imaginary. The criterion for stability based on Fig. 7-8 is fulfilled at  $\alpha$  and  $\gamma$  provided  $\delta G_e / \delta \tilde{V} > 0$  and at  $\beta$  provided  $\delta G_e / \delta \tilde{V} < 0$ . That criterion, however, is only a *necessary* condition for stability inasmuch as its fulfillment insures merely that a state of oscillation is stable against its own transients. We wish further to find out which of the states listed above are stable against transients of other modes of oscillation; this can be done by means of Fig. 7-12a.

The point  $\alpha$  is associated with a value of  $-2.8$  for  $G_e$  and  $\beta$  with a value of  $-7.2$ . For both of these values of  $G_e$  the real part of  $q_2$  is positive and this circumstance implies that a mode of oscillation associated with  $q_2$  will build up exponentially from any small disturbance. Consequently one may conclude that neither  $\alpha$  nor  $\beta$  represents a truly stable state of oscillation. At the point  $\gamma$ , on the other hand, the value of  $G_e$  is  $-1.2$  and for this value there is no  $q$  that has a positive real part; consequently  $\gamma$  represents the one completely stable state in the present example. The above conclusions, however, are based on the assumption that the space charge can be treated as a linear circuit element, which is obviously an oversimplification. If the conclusions were valid, it could happen only as the result of exceedingly improbable circumstances that either one of two modes could be stable alternatively under identical operating conditions, whereas such instances are commonly observed with c-w magnetrons. Therefore the next step is to inquire how the foregoing considerations can be modified so as to take into account the nonlinearity of the space charge, particularly when the voltage contains components of different frequencies.

A voltage of the type expressed by Eq. (37) can also be expressed as a sinusoidal voltage with superimposed amplitude and frequency (or phase) modulations; that is,

$$\tilde{V}_i = \tilde{V}(t) e^{j[\omega t + \phi(t)]}. \quad (43)$$

If, in Eq. (37), the  $\xi$ 's are relatively small and the differences between the  $\omega$ 's are also small,  $\tilde{V}$  and  $\phi$  in Eq. (43) are slowly varying functions of the time; thus the modulations are slow. Since no fundamental change in the symmetry of the electric fields in the interaction space of the magnetron is involved, the electron stream, or "space-charge wheel," can readily accommodate itself to the slow modulations. That is to say, the relation between  $\tilde{V}$  and  $\tilde{I}_e$  must be practically the same as for steady-state operation, although they both vary with time. Thus

$$\tilde{I}_{ei} = \tilde{I}_e(t) \exp [j\omega t + j\phi(t)], \quad (44)$$

where

$$\tilde{I}_e(t) = \tilde{I}_e[\tilde{V}(t)]. \quad (45)$$

For the present purposes it is sufficient to consider a case where Eq. (37) contains just two terms, one much larger than the other, and where

the frequencies are real, in which case Eq. (37) can be written as

$$\tilde{V}_i = \tilde{V}_1 e^{j\omega_1 t} + \tilde{V}_2 e^{j\omega_2 t} = \tilde{V}_1 e^{j\omega_1 t} (1 + \sigma e^{j\Omega t}), \quad (46)$$

where  $\sigma = \tilde{V}_2/\tilde{V}_1 \ll 1$  and  $\Omega = \omega_2 - \omega_1$ . For this case Eq. (43) takes the form

$$\tilde{V}_i = (\tilde{V}_1 \sqrt{1 + 2\sigma \cos \Omega t + \sigma^2}) \left[ \exp \left( j\omega t + j \tan^{-1} \frac{\sigma \sin \Omega t}{1 + \sigma \cos \Omega t} \right) \right] \quad (47)$$

which can be approximated by

$$\tilde{V}_i = [\tilde{V}_1 (1 + \sigma \cos \Omega t)] [(1 + j\sigma \sin \Omega t) \exp (j\omega_1 t)]. \quad (48)$$

Equation (45) can be approximated by

$$I_e = I_e(\tilde{V}_1) + \left[ \left( \frac{dI_e}{d\tilde{V}} \right)_{\tilde{V}=\tilde{V}_1} \right] \tilde{V}_2 \cos \Omega t = I_e(\tilde{V}_1) (1 + \delta \cos \Omega t), \quad (49)$$

where

$$\delta = \left( \frac{\tilde{V}_2}{I_e} \frac{dI_e}{d\tilde{V}} \right)_{\tilde{V}=\tilde{V}_1} \ll 1.$$

Thus Eq. (44) becomes

$$I_{ei} = I_e(\tilde{V}_1) (1 + \delta \cos \Omega t) (1 + j\sigma \sin \omega_1 t) e^{j\omega_1 t}. \quad (50)$$

If the term in  $\sigma\delta$  is neglected, Eq. (50) can also be written

$$I_{ei} = I_e(\tilde{V}_1) \left( 1 + \frac{\delta + \sigma}{2} e^{j\Omega t} + \frac{\delta - \sigma}{2} e^{-j\Omega t} \right) e^{j\omega_1 t}. \quad (51)$$

We assume that the cross term in  $\omega_1 - \Omega = 2\omega_1 - \omega_2$  can be ignored; then Eq. (51) can be written

$$I_{ei} = \tilde{V}_1 \left( \frac{I_e}{\tilde{V}} \right)_{\tilde{V}_1} e^{j\omega_1 t} + \tilde{V}_2 \left( \frac{1}{2} \frac{dI_e}{d\tilde{V}} + \frac{1}{2} \frac{I_e}{\tilde{V}} \right)_{\tilde{V}_1} e^{j\omega_2 t}. \quad (52)$$

The terms in parentheses evidently are the effective admittances for the respective voltage components in Eq. (46).

In what follows  $I_e$  will be treated as a real quantity, in accordance with the simplifying assumption made previously that the operating curve lies along the  $G$ -axis. (If  $I_e$  were considered to have an imaginary component, the real and imaginary parts could be treated independently in the way indicated above.) A plot of  $-I_e$  (actually, of the real component of  $-I_e$ ) against  $\tilde{V}$  is presumed to be of one or the other of the general types illustrated in Fig. 7.13a and c; corresponding operating curves are shown in Fig. 7.13b and d. The solid parts of these curves correspond to observations made on steady-state oscillations; the dotted parts are



based on indirect evidence discussed in Chap. 8. When the magnetron is oscillating steadily at frequency  $\omega_1$  at the point  $(\tilde{V}', I_e')$  in Fig. 7-13a, the space-charge conductance  $G_1$  for the steady-state oscillations is equal to  $I_e'/\tilde{V}'$ ; however, the space-charge conductance  $G_2$  for any superimposed transient of small amplitude at some frequency  $\omega_2$  distinct from  $\omega_1$  is equal to one-half the sum of  $I_e'/\tilde{V}'$  and the differential conductance  $dI_e/d\tilde{V}$  at that point. (For a superimposed transient at frequency  $\omega_1$  the conductance is just  $dI_e/d\tilde{V}$ .) Since, in general,  $G_2$  is considerably less negative than  $G_1$ , an established state of oscillation has the odds

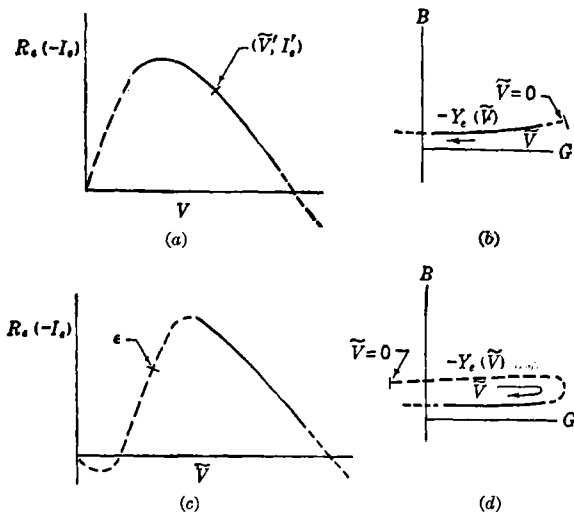


FIG. 7-13.—(a), (c) The real component of the electronic current  $I_e$  plotted vs. the a-c voltage  $\tilde{V}$ ; (b), (d) the operating curves corresponding to Fig. 7-13a and c.

weighted in its favor; thus hysteresis effects can be accounted for. Nonlinearities will not, however, serve to stabilize oscillations under the conditions represented by the intersection  $C$  in Fig. 7-9 and by  $\beta$  with  $\delta G_e/\delta \tilde{V} < 0$  in Fig. 7-12. Inasmuch as  $\delta I_e/\delta \tilde{V}$  is more negative than  $I_e/\tilde{V}$  in these cases, as at the point  $\epsilon$  in Fig. 7-13c, the electronic conductance is more negative for a transient than it is for the steady state.

As regards turn-on phenomena, the nonlinearity of the space charge tends to stabilize the mode of oscillation that builds up most rapidly. The initial buildup of oscillations can take place only along an operating curve such as is represented in Fig. 7-13a and b as distinguished from Fig. 7-13c and d. For such an operating curve the space charge is approximately linear for small values of  $\tilde{V}$ ; that is  $I_e$  is nearly directly proportional to  $\tilde{V}$ , and the earlier discussion based on Fig. 7-12 is directly applicable. Thus for the conditions represented by that figure it is

evident that Mode 2 will build up more rapidly than the other mode, inasmuch as  $G_1$  starts out by being strongly negative and  $\xi_2$  is then also strongly negative. It so happens that, in this situation, the most stable mode is also the one which starts most rapidly. It can happen, however, that the mode which starts most rapidly is not the most stable on the basis of a linear space charge but is nevertheless able to establish itself because it always has by far the greater amplitude when the nonlinearities first become important. In that case the preferred mode will not necessarily be the one of minimum steady-state  $G_L$ .

The above discussion of nonlinearities of the space charge is based on the assumption that only one of the amplitudes is large. The case where two amplitudes are large can be treated by the method outlined in Chap. 8.

The emphasis in this section has been principally on stability and transient behavior for one specific mode of the magnetron cavity as affected by loops in its  $Y_L(\omega)$  curve. For the most part, the input conditions have been assumed to remain fixed or to vary only slowly and to be contained implicitly in the operating curve. Related problems are treated in Chap. 8, but there the emphasis is placed on the effect of rapid variations in the input conditions, and the  $Y_L(\omega)$  curve is generally assumed to have the simple form illustrated in Fig. 7-6b. Because of the complexities that are involved, no adequate effort has been made either here or in Chap. 8 to take into account the reactances that may be present (and that physically are never entirely avoidable) in the input circuit of the magnetron. In principle the reactances can give rise to more possibilities for instability, since they introduce additional degrees of freedom into the complete system.

In magnetrons that are tuned by means of a very tightly coupled auxiliary cavity there exist modes of oscillation that are all associated with one definite mode of the magnetron cavity but have frequencies which differ by 10 per cent or even more. In such cases it is no longer justified to treat the space-charge properties as independent of frequency; selection among these modes involves some of the factors that enter into the selection of the various natural modes of the magnetron cavity.

**7-5. The Description of Magnetron Performance.**—It was shown in Sec. 7-2 that the performance of the magnetron can be expressed in terms of three functions of four independent variables and that by making use of the approximation that the space-charge properties are insensitive to the frequency, the number of independent variables can be reduced to three. If this approximation is adopted, one then has to deal with functions of the general type

$$u = F(x, y, z),$$

which are to be represented by means of graphs. If the possibility of interpolation is allowed,  $z$  can be held at some fixed value  $z'$  and the resulting function plotted as

$$u' = f(x, y) \equiv F(x, y, z')$$

in two dimensions by drawing contours of constant  $u'$  in the  $xy$ -plane. The contours are simply curves defined by the relation

$$u' = f(x, y)$$

when  $u'$  takes on a series of discrete constant values. If  $F$  is to be represented for all values of  $x, y, z$ , a set of contour diagrams, one diagram for each of a series of values of  $z$ , must be plotted. Any one diagram, regardless of type, is necessarily incomplete, since it alone can give no indication of how the performance of the magnetron is influenced by variations in  $z$ .

By following the scheme just outlined, Eqs. (8a), (8b), and (9a) can be represented in a great many different ways; there are 6 choices for the variable  $z$ , and for each choice of  $z$  there are 10 choices for the pair  $x, y$ , or 60 choices in all. Some of these systems of relations might be impractical because of multiple-valued functions, etc., but it is nevertheless surprising that only two types of diagram are very widely used.

These diagrams which are in general use fall into two classifications: those in which  $y_T$  is held constant and those in which the magnetic field  $\mathcal{B}$  is held constant. The former are of value in exhibiting those properties which are not extremely sensitive to the load, such as the useful range of operating conditions.

In many more specialized problems, however, the interesting phenomena occur at constant applied magnetic field; detailed information about dependencies on  $\mathcal{B}$  is therefore superfluous and can profitably be left out of the diagram in order to make room for the display of information about the dependencies on the load  $y_T$ .

Probably the most familiar diagram of magnetron performance is the *performance chart*. Ideally in this type of diagram the external load  $y_T$  is held fixed,  $I$  and  $V$  are the independent variables, and  $\tilde{V}$ ,  $\mathcal{B}$ , and  $B_e$  are represented by contours. Ordinarily the power  $\tilde{P}$  is plotted instead of  $\tilde{V}$  and the frequency  $\nu$  instead of  $B_e$ , but this does not alter the shapes of the contours. As the load is constant,  $G_E$  is also constant, and a curve of constant  $\tilde{P}_E = G_E \tilde{V}^2$  is also one of constant  $\tilde{V}$ . Furthermore as  $-B_e = B_L = B_E + 4\pi C(\nu - \nu_U)$  and  $B_E$  and  $\nu_U$  are constant with constant external load, contours of  $\nu$  and  $B_e$  are identical.

Another widely used type of diagram is the so-called *Rieke diagram* in which the magnetic field  $\mathcal{B}$  and the current  $I$  are held constant; the two components of the load are the independent variables that provide

the coordinate system in which contours of r-f voltage  $\tilde{V}$  (or power  $\tilde{P}$ ), electronic susceptance  $B_e$  (or frequency  $\nu$ ), and input voltage are plotted. Alternatively, the diagram may be taken at constant input voltage  $V$ , with the current  $I$  plotted as contours. The pair of variables that specify the load can be chosen in numerous ways: the conductance  $G_E$  and susceptance  $B_E$ , the normalized values  $g_T$  and  $b_T$ , or the absolute value and angle of the complex reflection coefficient  $q_T = (1 - y_T)/(1 + y_T)$ , etc. It is to be noted that in this type of diagram *two* variables are held constant. If the assumptions implicit in Eqs. (8a), (8b), and (9a) are valid, there must be some redundancy in the diagram for two independent variables are used where one should be sufficient. On the other hand, the diagram can represent the properties of the magnetron regardless of whether or not those assumptions are valid, that is, even when the space-charge properties and the transducer functions vary appreciably with the frequency.

In the ideal case the various Rieke diagrams take on very simple forms. The simplest form occurs when the components of the admittance  $Y_L$  are chosen as the independent variables. In that case all the constant- $\nu$  contours coincide and are identical with the operating curve discussed in Sec. 7-3, and the  $V$  and  $\tilde{V}$  (or  $\tilde{P}$ ) contours are just the scale marks that indicate the corresponding quantities along the operating curve. Other Rieke diagrams, which involve different independent variables, can be regarded as being generated by transformations of the operating curve. In general the frequency contours become separated because the transformation involves the frequency—each frequency contour is shifted by an amount that depends upon the frequency.

If the diagram is drawn in the  $Y_e$  plane, the transformation from the  $Y_L$  plane is

$$G_e = G_L - G_o, \quad B_e = B_L - 4\pi C(\nu - \nu_o).$$

The form of the diagram and its relation to the operating curve are illustrated in Fig. 7-14b. The diagram will have a similar appearance in the  $Y_E$  and  $y_T$  planes in so far as the transducer properties involved do not vary appreciably with the frequency;<sup>1</sup> and if this is so, then Fig. 7-14b can also represent the diagram in the  $y_T$  plane. If instead of rectangular coordinates the Smith chart is used for  $g_T$  and  $b_T$ , the diagram should have the appearance illustrated in Fig. 7-14c. Plotting the diagram in the Smith chart is equivalent to a transformation to the  $q_T$  plane where  $q_T$  is complex and is related to  $y_T$  by  $q_T = (1 - y_T)/(1 + y_T)$ .

<sup>1</sup> In the coordinate system  $G_E$ ,  $B_E$ , the diagram will be similar except for the frequency shift  $\nu_o - \nu_e$  connected with the susceptance  $\beta$  that is associated with the output coupler; if  $\beta$  varies non-uniformly with frequency, the frequency contours in the  $Y_E$  plane will not be uniformly spaced.

At some other pair of terminals such as  $S$  in Fig. 7-5c, the diagram differs from that at  $T$  principally by a rotation.

Figure 7-14c may be considered to be an ideal Rieke diagram. It is distinguished by the following features: the constant- $\tilde{V}$  (or  $\tilde{P}$ ) contours and constant- $V$  contours are a set of circles all tangent to the unit (or ( $y_r = \infty$ ) circle at a common point, and the constant- $\nu$  contours also

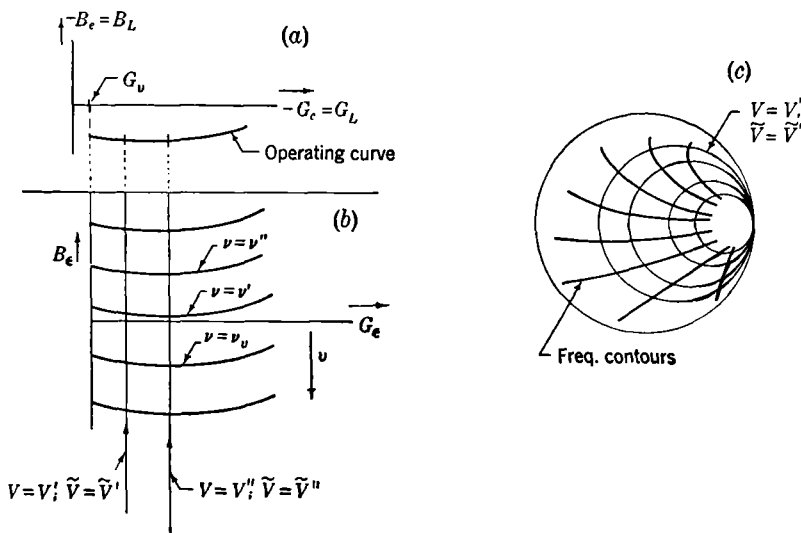


FIG. 7-14.—(a) Ideal Rieke diagram in the  $Y_L$ -plane; (b) ideal Rieke diagram in the  $Y_c$ -plane; (c) ideal Rieke diagram in the reflection coefficient plane.

converge at that point. Any diagram constructed from experimental data shows several departures from the ideal form, on account of one or more of the circumstances listed below.

1. The quantities  $a$ ,  $b$ ,  $c$ ,  $d$  of Eq. (17) are not constant but vary with the frequency. Each constant- $\nu$  contour is transformed differently from its neighbors, and the contours do not have a common point of convergence. The  $\tilde{P}$  and  $V$  contours have similar shapes but are not circles.
2. The transducer is not dissipationless. The  $\tilde{P}$  and  $V$  contours do not have exactly identical shapes; the  $\tilde{P}$  contours may become kidney-shaped. Furthermore the  $\nu$ -contours (extrapolated) may converge at a point outside the unit circle.
3. The space-charge properties are not independent of frequency. Some dependence is to be expected, merely on the basis of the scaling relations; however, at constant current one should expect the relative change in the voltage to be a little smaller than the rela-

tive change in the frequency. It is also possible that "detuning" of the cavity by means of reactance coupled into just one oscillator may affect the space-charge properties by distorting the pattern of the electric fields in the interaction space, and these effects might be expected to give rise to kidney-shaped power contours.

4. The measurement of the power is likely to be affected by a systematic error which increases with the standing-wave ratio in the transmission line, particularly when the power is measured calorimetrically and no account is taken of losses in the standing-wave introducer.
5. The diagram may be incomplete because the load actually used in the experiments is resonant. When the external load varies rapidly with the frequency, the stability relations are such that some regions of the Rieke diagram become inaccessible. This effect is discussed in considerable detail in the following section.

**7-6. The Mismatched Transmission Line as a Resonant Load.**—The effects caused by mismatches, or standing waves, in the output transmission line of a magnetron are important both in practical applications and in laboratory experiments. Probably the best illustration of the nature of these effects is provided by the behavior of a tunable magnetron operating into a moderately long, mismatched line. Figure 7-15*a* and *b* illustrates the tuning curves that are observed with pulsed magnetrons under those conditions, Fig. 7-15*a* with a small mismatch, and Fig. 7-15*b* with a fairly large mismatch. In these figures,  $x$  represents the position of the tuning mechanism; the light straight line is the tuning curve observed when the line is perfectly terminated, and the heavy curve is that observed when there is a mismatch.

Under conditions that correspond to Fig. 7-15*a*, the magnetron is observed to have an abnormally broad spectrum over those parts of the tuning curve which are nearly vertical. In addition, the frequency varies rapidly if either the input current to the magnetron or the output load is changed.

Under conditions that correspond to Fig. 7-15*b*, the operation of the magnetron is generally satisfactory except for tuning adjustments that are near the breaks in the curve; at such points two frequencies are excited randomly at successive pulses. However, since the tuning curve is discontinuous, it is not possible to adjust the frequency to any arbitrary value, some values being inaccessible.

Figure 7-15*c* has been added to illustrate the sort of behavior that might be expected of a c-w magnetron under the conditions of Fig. 7-15*b*. In the neighborhood of a break two frequencies are possible; the adjustment at which the break occurs depends upon the direction from which

the break is approached. Although the discontinuities in frequency are not so large as in Fig. 7-15*b*, there are nevertheless some frequencies that are inaccessible.

The spacing  $\Delta\nu$  between the breaks or anomalies in the tuning curve depends upon the length of the transmission line measured in wavelengths; the width of the breaks  $W\Delta\nu$  depends upon the degree of mismatch. The location of the breaks varies uniformly with the phase of the reflection; and if the tuning adjustment is held fixed and the phase is varied, the frequency may change rapidly or discontinuously at some particular phase. Thus a mismatched transmission line can also lead to unsatisfactory operation of a fixed-tuned magnetron if the reflection in the line is variable.

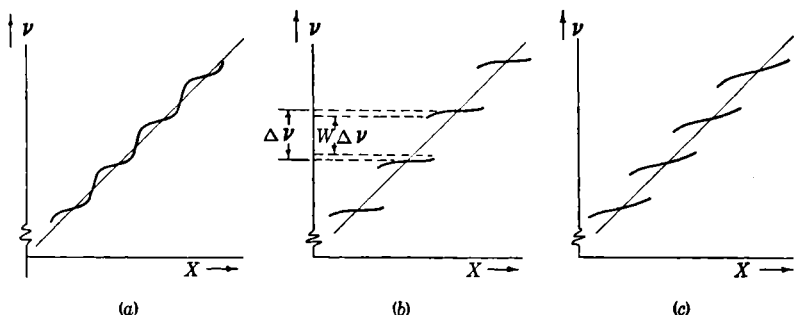


FIG. 7-15.—Tuning curves: (a) Pulsed magnetron, slightly mismatched line; (b) pulsed magnetron, greatly mismatched line; (c) c-w magnetron, greatly mismatched line.

Many variations of the effects just described are possible. For example, the mismatch may arise not only from an imperfect termination of the transmission line but also entirely or in part from reflections that occur at intermediate points because of imperfect joints and bends. In the latter case the reflections may reinforce each other at some frequencies and tend to cancel at others. The general result will be that the breaks or anomalies in the tuning curve are irregularly spaced and the widths of the breaks are unequal. Inasmuch as the more complicated cases involve the same general considerations as the simpler ones, the subsequent discussion will be confined to the somewhat ideal case where the mismatch arises entirely from an imperfect termination.

In the ideal case, the phenomena described above can result only from the influence of waves that have traveled to the end of the transmission line, been reflected there, and returned to the magnetron. The phenomena cannot occur when the two-way transit time of the transmission line exceeds the length of the pulse generated by the magnetron and must therefore disappear when the line is made very long. In view of this fact, the phenomena have sometimes been referred to as

"short-line effects," although the term "long-line effect" has been more generally used in the United States. Most of the following considerations are based upon steady-state formulas for the admittance of a mismatched transmission line, and it is therefore implied that the transit time of the line is small compared with the length of the pulse. In practice, the results derived seem to apply fairly well when the transit time is only a few times smaller than the pulse length.

The tuning curves illustrated in Fig. 7-15 are closely related to the admittance curves  $Y(\nu)$ . The latter might be calculated by substituting in Eq. (33) the appropriate values of  $y_T$  obtained from transmission-line charts or formulas. The possible variety of  $Y(\nu)$  curves is very great, since many parameters are involved, but it will be shown that all of the curves can be derived from a two-parameter family of curves. The two parameters can in a certain sense be thought of as (1) the degree of mismatch in the line and (2) the ratio ( $Q$  of the line)/( $Q$  of the magnetron).

In computing the admittance  $y_T$  it is assumed that the transmission line is terminated in a load with a reflection coefficient  $q = |a| \exp(j\phi)$  which is independent of  $\nu$ . At the terminals  $T$  of Fig. 7-5c the reflection coefficient  $q_T$  is given by

$$q_T = [|q| \exp(2\alpha l)] [\exp j(\phi - 2\beta l)] = a \exp(j\theta), \quad (53)$$

where  $\alpha - j\beta$  is the propagation function of the transmission line;  $\alpha$  may be treated as a constant, but  $\beta$  varies with  $\nu$ .

In terms of the standing-wave ratio  $\rho$  at the magnetron

$$a = \frac{(\rho - 1)}{(\rho + 1)}$$

where  $\rho$  is the SWVR. Since  $\beta = 2\pi/\lambda_g$  where  $\lambda_g$  is the "wavelength in guide" for the transmission line,

$$\theta = \phi - \frac{4\pi l}{\lambda_g}. \quad (54)$$

For some frequency  $\nu_0$ ,  $\theta$  is just equal to  $-(2n + 1)\pi$ , and for frequencies not too different from  $\nu_0$  one may use for  $\theta$  the approximate expression

$$\begin{aligned} \theta &= -\pi \left[ 2n + 1 + 4l \left( \frac{d}{d\nu} \frac{1}{\lambda_g} \right)_{\nu_0} (\nu - \nu_0) \right] \\ &= -2\pi \left( n + \frac{1}{2} + \varepsilon \right), \end{aligned} \quad (55a)$$

where

$$\varepsilon = 2l \left( \frac{d}{d\nu} \frac{1}{\lambda_g} \right)_{\nu_0} (\nu - \nu_0) = 2 \frac{l}{\lambda_0} \frac{\lambda_{g0}}{\lambda_0} \frac{\nu - \nu_0}{\nu_0}. \quad (55b)$$



The admittance  $y_T$  is given by the formula

$$y_T = \frac{1 - a^2 - j2a \sin \theta}{1 + a^2 + 2a \cos \theta} \quad (56a)$$

or, in terms of  $\varepsilon$ ,

$$g_T = \frac{1 - a^2}{1 + a^2 - 2a \cos 2\pi\varepsilon} = g(\varepsilon, a) \quad (56b)$$

and

$$b_T = \frac{-2a \sin 2\pi\varepsilon}{1 + a^2 - 2a \cos 2\pi\varepsilon} = b(\varepsilon, a). \quad (56c)$$

For the calculation of  $Y_E$  it is convenient to write Eq. (33) in the form

$$\begin{aligned} \frac{Q_{EM}}{Y_c} Y_L &= \frac{Q_{EM}}{Q_U} + j2Q_{EM} \frac{\nu_0 - \nu_U}{\nu_L} + j2Q_{EM} \frac{\nu_0}{\nu_L} \frac{\nu - \nu_0}{\nu_0} + y_T \\ &= g_0 + jb_0 + \left[ \frac{j\varepsilon}{A} + g(\varepsilon, a) + jb(\varepsilon, a) \right], \end{aligned} \quad (57)$$

where

$$g_0 = \frac{Q_{EM}}{Q_U}, \quad b_0 = 2Q_{EM} \frac{\nu_0 - \nu_U}{\nu_L}$$

and

$$A = \frac{\nu_L}{\nu_0} \frac{1}{Q_{EM}} \frac{l}{\lambda_0} \frac{\lambda_{g0}}{\lambda_0}.$$

If the transmission line is fairly long, the possible values of  $\nu_0$  are close together and  $\nu_0$  can be chosen nearly equal to  $\nu_U$ . In that case

$$A \approx \frac{l}{\lambda_0} \frac{\lambda_{g0}}{\lambda_0} \frac{1}{Q_{EM}} \approx \frac{l}{\lambda_U} \frac{\lambda_{gU}}{\lambda_U} \frac{1}{Q_{EM}}. \quad (58)$$

The general shape of the  $Y_L(\nu)$  curve depends upon the terms in the square bracket, since they alone depend upon  $\nu$ ; the parameters that fix the shape of the curve are  $A$  and  $a$ .

For convenience, the square bracket of Eq. (57) will be represented by the quantity  $w = u + jv$ , where

$$u = g(\varepsilon, a) \quad \text{and} \quad v = \frac{\varepsilon}{A} + b(\varepsilon, a). \quad (59)$$

The  $Y_L(\nu)$  curve has the same shape as the  $w(\varepsilon)$  curve; it differs from it by scale factors  $Y_c/Q_{EM} = \Delta Y_L/\Delta w$  and  $(c\lambda_0)/(2\lambda_{g0}) = \Delta \nu/\Delta \varepsilon$  and by a translation  $g_0 + jb_0$ . Tuning the magnetron, which amounts to changing  $\nu_U$ , translates the curve vertically, since  $b_0$  varies almost linearly with  $\nu_U$ .

The shape of the  $w(\varepsilon)$  curve is governed by the parameters  $A$  and  $a$ . Three general forms are possible; the separate components of  $w(\varepsilon)$  are illustrated in Fig. 7-16, and the function  $w(\varepsilon)$  in Fig. 7-17. If the quantity

$$s = \left( \frac{dv}{d\varepsilon} \right)_{\varepsilon=0} = \frac{1}{A} - \frac{4\pi a}{1 - a^2} = \frac{1}{A} - \pi(\rho^2 - 1) \quad (60)$$

is less than zero, the  $w(\epsilon)$  curve has loops, as in Fig. 7-17c. If  $s = 0$ , the curve has cusps as in Fig. 7-17b; if  $s > 0$ , the curve has merely undulations as is Fig. 7-17a.

When the operating curve cuts across a loop in the  $Y(\nu)$  curve, there are two intersections and therefore two distinct frequencies at which oscillation might be stable. In case the loops are so large or so closely spaced that they overlap, there may be four or more such intersections.

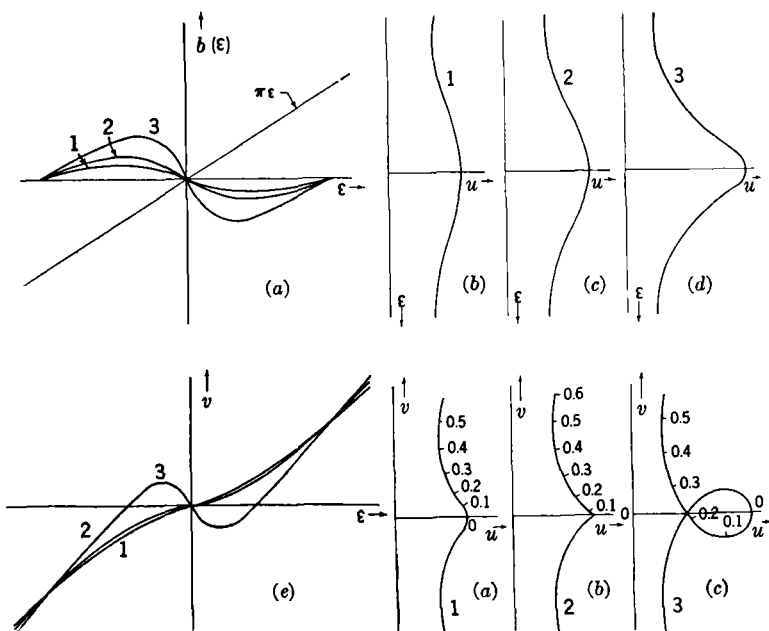


FIG. 7-16.

FIG. 7-17.

FIG. 7-16.—Plots of the terms of Eq. 59. (a) Values of  $b(\epsilon, a)$  and  $\epsilon/A$  as functions of  $\epsilon$  for three values of  $a$ ; (b), (c), (d) values of  $g(\epsilon, a)$  as functions of  $\epsilon$  for the same three values of  $a$ ; (e) the function  $v = \epsilon/A + b(\epsilon, a)$  plotted against  $\epsilon$  for the same three values of  $a$ . The parameter  $A$  is kept constant at  $1/\pi$ .

FIG. 7-17.—(a), (b), (c) The function  $w = u + jv$  of Eq. (59) for the three conditions shown in Fig. 7-16. Values of  $\epsilon$  are indicated.

An extensive series of experiments was performed in the MIT Radiation Laboratory with a pulsed 3-cm tunable magnetron and various values of  $l$ , the line length, and of  $a$ , the degree of mismatch. From these experiments it was concluded that oscillation is ordinarily established at that intersection which has the lowest value of  $G_L$ ; only in cases where the two lowest values of  $G_L$  are nearly equal are two frequencies excited randomly at successive pulses.

In other words, the tuning curve of Fig. 7-15b can be interpreted in the following way. As the magnetron is tuned, the  $w(\epsilon)$  curve of Fig.

7-17c is moved across the operating curve and the frequency of oscillation corresponds to the intersection of minimum  $G_L$ . At the stage where there are substantially two such intersections, the frequency alternates randomly between two well-separated values; otherwise the frequency changes discontinuously as that stage is passed. The width of the break in the tuning curve  $W\Delta\nu$  is exactly equal to the frequency interval that carries the  $Y_L(\nu)$  curve completely around a loop.

The irregularities in the tuning curve in Fig. 7-15a can be interpreted in a similar manner. The steep parts of the tuning curve correspond to those parts of the  $w(\epsilon)$  curve where  $\nu(\epsilon)$  varies very slowly with  $\epsilon$ . When conditions are such that the  $Y(\nu)$  curve and the operating curve intersect at a very small angle, one should expect the frequency of oscillation to vary rapidly not only with the tuning adjustment but also with the input conditions of the magnetron, as a small shift in the operating curve must lead to an appreciable change in  $\nu$ . Consequently it is understandable that the spectrum, or Fourier analysis of the pulse, should be abnormally broad in such cases. To a fair approximation, the development of a cusp in the  $w(\epsilon)$  curve represents the transition from an uneven tuning curve to a broken one, although if the operating curve has an appreciable slope, the transition occurs at a somewhat lower value of  $a$  than that which leads to a cusp. In practice, however, the transition is gradual, since it is difficult to distinguish between one broad spectrum and two broad spectra with nearly equal center frequencies.

The spacings  $\Delta\nu$  of the breaks or irregularities in the tuning curves correspond to the period of the functions  $g(\epsilon, a)$  and  $b(\epsilon, a)$ , which is 1 in  $\epsilon$  or  $\frac{1}{2}(c/l)(\lambda/\lambda_0)$  in  $\nu$ . If  $l$  is expressed in meters,  $\nu$  in megacycles per second, and the value 300 meters/ $\mu$ sec is used for  $c$ , then the spacing is equal to

$$\Delta\nu = \frac{150}{l} \frac{\lambda}{\lambda_0} \frac{\text{meters} \times \text{megacycles}}{\text{second}} \quad (61)$$

and is actually just the spacing between the resonances of the transmission line. The width  $W\Delta\nu$  of the breaks can be computed on the basis of the loop that occurs near  $\epsilon = 0$  (Fig. 7-17c). The values of  $\epsilon$  where the  $w(\epsilon)$  curve intersects itself and the  $u$ -axis are the solutions (other than  $\epsilon = 0$ ) of

$$\frac{\epsilon}{A} + b(\epsilon, a) = 0.$$

It is simpler, however, to compute the value  $A'$  that will give rise to such intersection at  $\epsilon'$  from the relation

$$\frac{1}{A'} = - \frac{b(\epsilon', a)}{\epsilon'} \quad (62)$$

The width  $W\Delta\nu$  of the breaks is equal to  $2\epsilon'\Delta\nu$ .

For practical purposes it is convenient to express  $A$  in a form that involves the pulling figure  $F$  of the magnetron rather than  $Q_{EM}$ , as ordinarily  $F$  is given in the specifications. From the relation

$$F = \frac{0.42\nu U}{Q_{EM}} \sec \alpha, \quad (63a)$$

where  $\tan \alpha$  is the slope of the operating curve of  $-B_s$  vs.  $-G_s$ , it follows that

$$A = l \frac{\lambda_g}{\lambda} \frac{F}{0.42c \sec \alpha}. \quad (63b)$$

In Fig. 7-18, Eq. (62) is presented graphically by plotting  $a$  against the quantity  $l(\lambda_g/\lambda)F$  for various values of  $W = 2\epsilon'$ . In constructing the

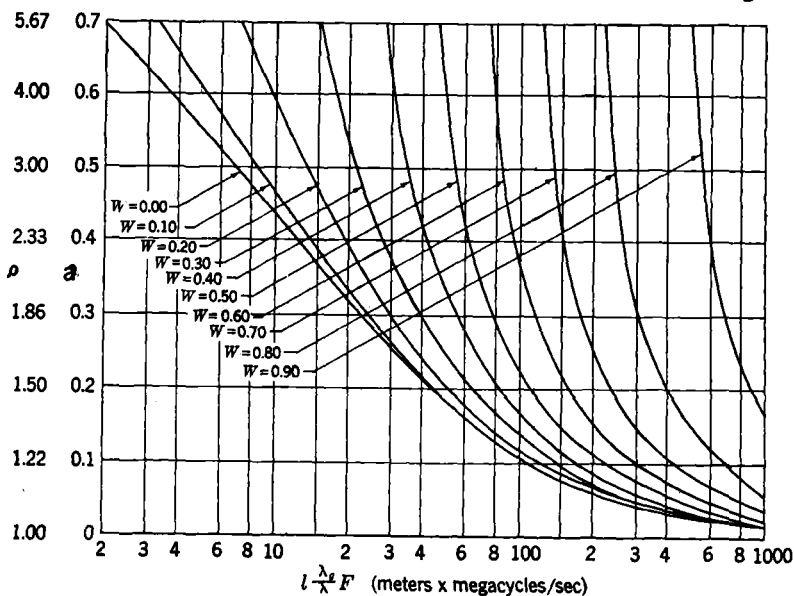


Fig. 7-18.—The effect of mismatch on the tuning curves. The width of the break is  $W\Delta\nu$  where  $\Delta\nu = (150/l)(\lambda/\lambda_g)$  meters Mc/sec.

figure a value of 1.05 has been assumed for  $\sec \alpha$ , so that the coordinate  $l(\lambda_g/\lambda)F$  is numerically equal to  $131A$ .

The uses of Fig. 7-18 are illustrated by the following example. It is proposed to use a waveguide transmission line 10 meters long with a pulsed 3-cm tunable magnetron. The pulling figure  $F$  of the magnetron is 15 Mc/sec;  $\lambda_g/\lambda$  for the waveguide  $\approx 1.3$ ; and the attenuation is 0.20 db per meter. The following information is then required: (1) the permissible mismatch of the termination if the operation of the magnetron is to be satisfactory at all frequencies within its tuning range

and (2) the effect on the performance if the standing-wave ratio of the termination reaches 2.0. In this example,  $L\lambda_g/\lambda = 13$ , so that the spacing  $\Delta\nu$  of the irregularities in the tuning curve is  $\frac{1}{13} \frac{5.0}{\lambda} = 11.5$  Mc/sec. The quantity  $L\lambda_g/\lambda$  is equal to 195. The attenuation factor of the guide is  $\text{antilog}_{10} 2.0 = 1.6$ .

The following considerations then apply:

1. The value of  $a$  that corresponds to  $L\lambda_g/\lambda = 195$  and  $W = 0$  is found from Fig. 7-18 to be 0.06; multiplying by the attenuation factor gives the value  $|q| = 0.096$ , which corresponds to a standing-wave ratio  $\rho = 1.2$  for the termination. For perfectly satisfactory performance at all frequencies a SWVR somewhat lower than 1.2 will be required.
2. The value  $\rho = 2.0$  corresponds to  $|q| = 0.33$  and

$$a = \frac{0.33}{1.6} = 0.208.$$

From Fig. 7-18 the value  $W = 0.65$  is obtained, and the width of the breaks in the tuning curve is thus equal to

$$11.5 \times 0.65 = 7.5 \text{ Mc/sec.}$$

Thus with a termination of SWVR 2 one cannot be sure that the transmitter can be adjusted to any arbitrarily chosen frequency more closely than within  $\pm 4$  Mc/sec.

The considerations that apply to tunable magnetrons apply also, of course, to fixed-frequency magnetrons. However, in the case of the latter the effects connected with long transmission lines can be examined in greater detail by making use of Rieke diagrams. Consider first an ideal Rieke diagram appropriate to the terminals  $T$  of Fig. 7-5c, such as is illustrated in Fig. 7-19a. The ideal diagram appropriate to terminals at a distance  $s$  to the right of  $T$  can be obtained by rotating each contour of Fig. 7-19a through an angle equal to  $4\pi s/\lambda_g$ ; since  $\lambda_g$  depends upon  $\nu$ , each contour is rotated differently. The appearance of the new diagram will be determined by the relative rotations of the various contours. Let the value of  $\nu$  for the contour that passes through the center of the diagram be denoted by  $\nu_0$  and the rotation of the other contours, relative to the  $\nu_0$  contour, be denoted by  $\psi(\nu)$ . By analogy with Eq. (55b) one may write

$$\psi(\nu) = 4\pi \frac{s}{\lambda_0} \frac{\lambda_{g0} \nu - \nu_0}{\nu_0}. \quad (64)$$

As the result of this transformation, the ideal diagram appropriate to the extreme end of the transmission line will take on a form such as is illustrated in Fig. 7-19b.

According to this figure,  $\nu$  is a multiple-valued function of the load in some regions of the diagram; these regions represent just those values of the load which give rise to loops in the  $Y_L(\nu)$  curve. When the stability

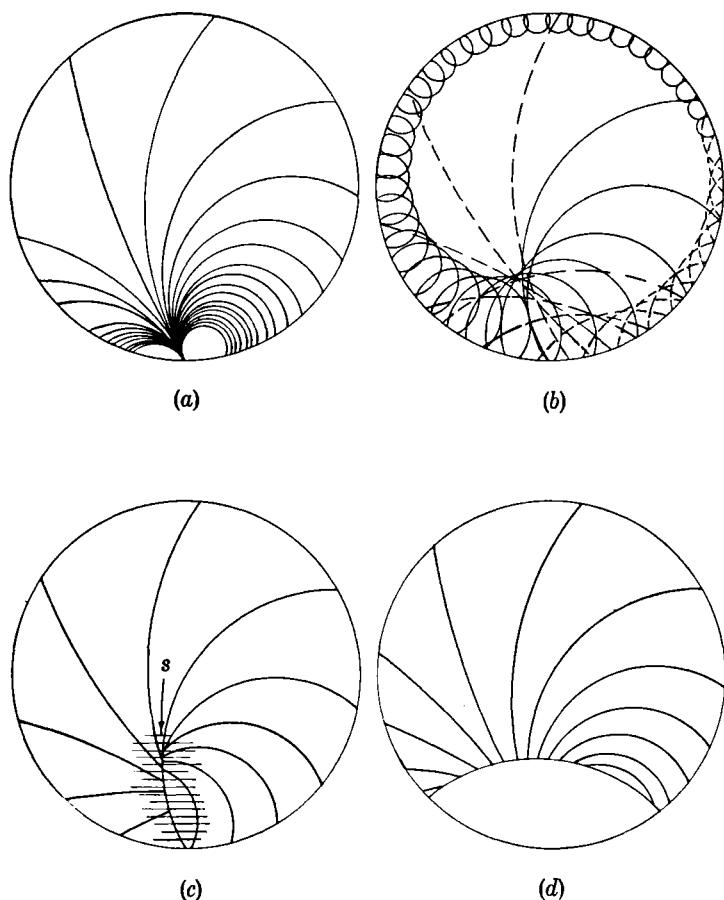


FIG. 7-19.—Transformations of the Rieke diagram. (a) The ideal Rieke diagram at the output terminals; (b) at the extreme end of the transmission line; (c) actual contours observed for condition (b); (d) result of transforming diagram (c) back to the output terminals referred to in diagram (a).

relations are taken into account, it turns out that the contours which might actually be observed are those illustrated in Fig. 7-19c. The point  $S$  of this diagram has sometimes been referred to as the "frequency sink."<sup>1</sup>

<sup>1</sup> It is only for loads which fall within the shaded region of the figure that there is an uncertainty in the frequency of oscillation.

When the diagram of Fig. 7-19c is transformed back to the terminals  $T$ , it takes on the form shown in Fig. 7-19d. The last figure illustrates the fact that a long transmission line makes a part of the ideal Rieke diagram inaccessible for measurements; the size of the region increases with the length of the line and with the pulling-figure of the magnetron. In experimental setups, the effective length of the transmission line is that which is included between the magnetron and the standing-wave introducer. Although this distance is relatively small—perhaps six wavelengths or so if a slotted section is placed next to the magnetron for standing-wave measurements—it makes it very difficult to study the performance of pulsed magnetrons at the larger values of  $G_L$ . This difficulty can be surmounted by using magnetrons with very small values of  $Q_{EM}$ , for if  $Q_{EM}$  is small, large values of  $G_L$  are brought across the center of the diagram into the region where operation is always stable. With c-w magnetrons, these difficulties might be surmounted by taking advantage of hysteresis, although it may happen that the phenomena discussed in Sec. 7-4 will prove to limit the usefulness of this procedure.

**7-7. Experimental Data on the Space-charge Properties.**—This section consists principally of a summary of the results of a long series of experiments that were performed on a particular 2J32 magnetron (see Fig. 19-18); all the data included in Figs. 7-21 to 7-30 were taken on this magnetron.

The first set of experiments<sup>1</sup> to be described were performed principally to test the validity of the equivalent circuit analyses of the preceding sections and to find out if a Rieke diagram could actually be reduced to an operating curve.

The properties of the output lead (actually a duplicate provided by the manufacturer) were measured in the manner described in Chap. 5. Measurements were made at several different frequencies, and in all the subsequent calculations the variation of the transducer coefficients with frequency was taken into account. By means of these coefficients and appropriate formulas, all measurements of impedances both on the "cold magnetron" and on the load in cases where the magnetron was oscillating were reduced to impedances at the terminals of the coupling loop.

The analysis of the data has been carried out on the basis of the equivalent circuit shown in Fig. 7-20. An elementary calculation leads to the result that the "cold impedance"  $\bar{Z}$ —observed by "looking into" the loop, with the terminals  $A$  open-circuited—should be of the form

<sup>1</sup> R. Platzman, J. E. Evans, and F. F. Rieke, "Analysis of Magnetron Performance, Part II," RL Report No. 451, Mar. 3, 1944.

$$\bar{Z}(\nu) = j2\pi\nu L_0 + \frac{m^2}{Y_c \left( \frac{1}{Q_v} + j2 \frac{\nu - \nu_v}{\nu_v} \right)}, \quad (65)$$

where

$$\begin{aligned} L_0 &= L_1 \left( 1 - \frac{M^2}{L_1 L_2} \right), \\ m &= \frac{M}{L_2}, \\ Y_c &= \sqrt{\frac{C}{L_2}}, \\ 2\pi\nu_v &= \frac{1}{\sqrt{CL_2}}. \end{aligned}$$

The term in  $L_0$  may be regarded as being the "leakage reactance" of the loop. The measured values of  $Z(\nu)$  proved to be consistent with

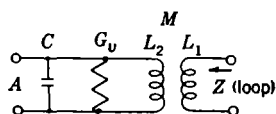


FIG. 7-20.—Equivalent circuit for a loop-coupled magnetron.

Eq. (65), and from them, by curve-fitting, values of the constants  $L_0$ ,  $m^2/Y_c$ ,  $Q_v$ , and  $\nu_v$  were obtained. As will be shown presently, the computation of the admittance  $Y_L$  in absolute units (mhos) requires that  $Y_c$  be known, whereas the cold-impedance measurements yield a value only for  $m^2/Y_c$ . A numerical

value for  $Y_c$  was computed from the value  $L_2 = 5.1 \times 10^{-10}$  henry, given by A. G. Smith.<sup>1</sup>

Smith's measurement is based on the following considerations. If a capacitance  $\Delta C$  is connected at the terminals A of Fig. 7-20, the square of the resonant wavelength should vary linearly with  $\Delta C$ , and from the relation

$$\Delta(\lambda_0^2) = (2\pi c)^2 L_2 \Delta C \quad (66)$$

$L_2$  can be obtained. In the experiments  $\Delta C$  was the increment in the capacitance of the slots caused by filling the slots with material of a known dielectric constant. (Smith's value of  $L_2$  is consistent with one obtained theoretically on the basis of a very elaborate lumped-circuit model of the cavity.) The incremental capacitance  $\Delta C$  in Smith's experiments may be regarded as the "standard impedance" upon which all the absolute values of r-f voltages and currents quoted in this section are based.

From the cold-impedance measurements and the adopted value of  $L_2$ , all of the constants that appear in Eq. (65) can be given numerical

<sup>1</sup> A. G. Smith, "Establishment of Tolerances for the Eight-oscillator Magnetron," B.S. Thesis, Massachusetts Institute of Technology, 1943.



values. To illustrate the magnitudes of these quantities, the values are given in the following list:

$$\begin{aligned} L_1 &= 6.3 \times 10^{-9} && \text{henry,} \\ L_2 &= 5.1 \times 10^{-10} && \text{henry,} \\ M &= 2.4 \times 10^{-10} && \text{henry,} \\ C &= 6.3 \times 10^{-12} && \text{farad,} \\ Y_c &= 0.111 && \text{mho,} \\ Q_v &= 1610, \\ \frac{1}{G_v} &= 1.4 \times 10^4 && \text{ohms.} \end{aligned}$$

The admittance  $Y_L$  at terminals  $A$  as a function of  $\nu$  and the load impedance  $\vec{Z}$  at the loop is given by  $10^{-3} \times 2$

$$Y_L = Y_v + Y_e,$$

where

$$Y_v = Y_c \left( \frac{1}{Q_v} + j2\pi \frac{\nu - \nu_v}{\nu_v} \right)$$

$$Y_e = \frac{m^2}{\vec{Z} + j2\pi\nu L_0}$$

Data for three Rieke diagrams, all at approximately the same magnetic fields (1300 gauss), were taken at input currents of 12.5, 17, and 26 amp, respectively. Inasmuch as the diagrams are qualitatively similar, only the one at 12.5 amp will be shown in detail. Constant-power and constant- $V$  contours, plotted in the  $G_e, B_e$ -plane are shown in Fig. 7-21 to illustrate the departure from the ideal forms of the Rieke diagram which would simply be straight vertical lines. In the cold-impedance measure-

ments at frequencies far removed from resonance, the magnetron had a SWVR of about 90, or a reflection coefficient of 0.98. In the most unfavorable part of Fig. 7-21 the loss of power in the lead could thus not amount to more than 6 per cent. The admittances  $Y_L$  for all of the experimental points are plotted in Fig. 7-22. This figure demon-

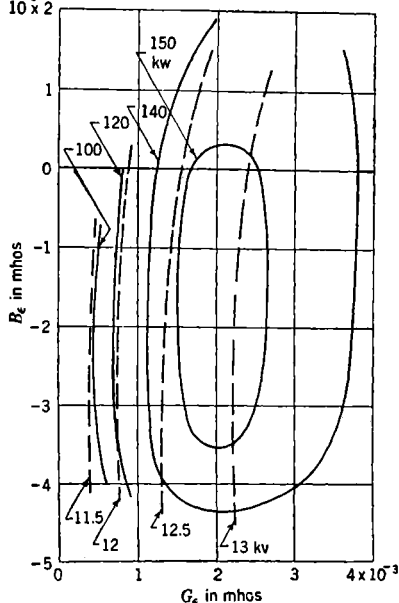


FIG. 7-21.—Constant output a-c power and constant input d-c voltage contours in the  $G_e B_e$ -plane for a 2J32 magnetron operating at 1270 gauss and 12.5 amp.

strates that within experimental error, all of the constant-frequency contours actually do coalesce into an operating curve when they are plotted in the  $Y_L$ -plane.

The input voltage  $V$  and the power output  $\bar{P}_e$  are plotted against

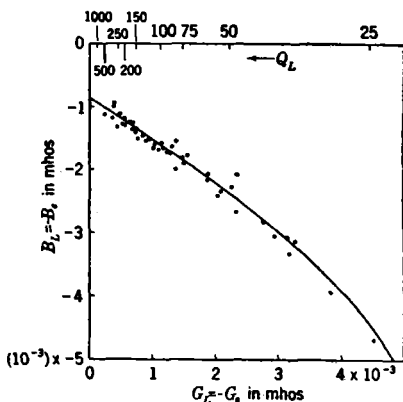


FIG. 7-22.—Operating curve in the  $G_L$ ,  $B_L$ -plane for input current of 12.5 amp and magnetic field of 1270 gauss.

most favorable choice of load for a magnetron is more or less independent of operating conditions.

In addition to the Rieke diagrams, performance charts were also taken at several different values of  $G_L$ . In principle, this series of performance charts should constitute an exhaustive description of the performance of the magnetron. Actually, the data were accumulated over a considerable period of time, during which appreciable changes in the calibrations of the apparatus and perhaps also in the magnetron itself took place. The uncertainties thus introduced obscure many of the cross relations that involve relatively small differences between observed quantities. (This experience is mentioned to illustrate some of the difficulties encountered in attempting to secure self-consistent data on magnetron operation.) Consequently only one of the performance charts is reproduced as Fig. 7-25.

When efforts were later made to extend the concepts and methods developed in this chapter to the transient behavior of magnetrons, the need arose for a better understanding of the relations among  $G_e$ ,  $\bar{V}$ ,  $V$ , and  $I$  at constant  $\mathcal{B}$ , and it was decided to work out these relations as completely as possible. Actually they were worked out for just one value of  $\mathcal{B}$ . The necessary data were taken in the following way. The frequency was kept at a constant value  $\nu'$  throughout, and the contour  $\nu = \nu'$  was traced out in a Rieke diagram for nine different fixed values

$G_L$  in Fig. 7-23. The dotted curve in Fig. 7-23b represents  $\bar{P}_e G_L / G_e$ , the total r-f power delivered by the electron stream. In Fig. 7-24 the electronic efficiency  $\eta_e = \bar{P}_e / VI$  is plotted against  $G_L$ . These curves are an important consideration in the design and application of magnetrons, because they provide the means of relating the efficiency to the unloaded and external  $Q$ 's of the cavity. Fortunately, the general shape and the location of the maximum in these curves do not depend strongly on either the magnetic field  $\mathcal{B}$  or the current  $I$ , so the

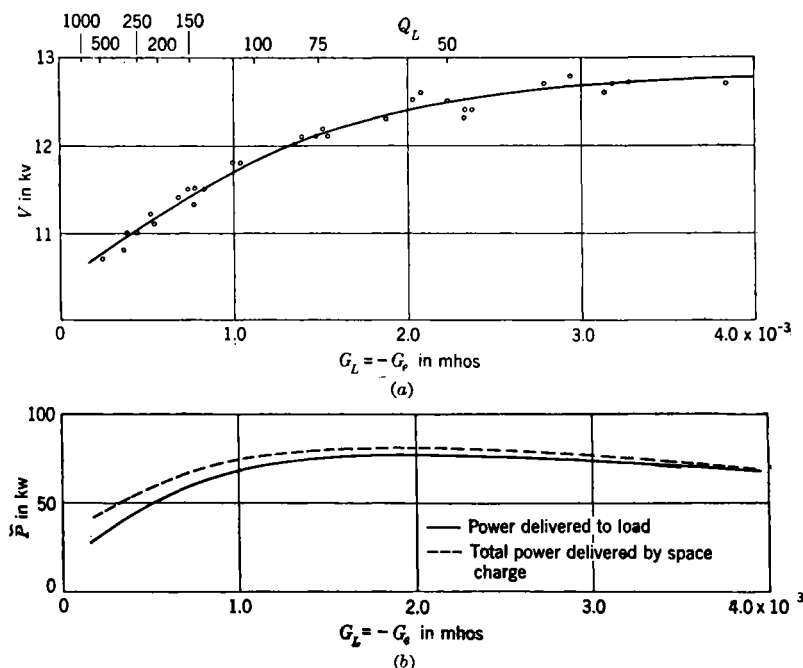


FIG. 7.23.—(a) Input d-c voltage vs.  $G_L$ ; operating conditions 1270 gauss and 12.5-amp input; (b) a-c power output vs.  $G_L$  for same operating conditions.

of  $V$ ; for each observation  $q$ ,  $P$ , and  $I$  were measured. In all, about 140 observations of this kind were made. By taking all the data at one frequency, the computation of the  $Y_L$ 's was greatly facilitated. To avoid fluctuations in the magnetic field, a permanent magnet was used. The combination of a very strong air blast for cooling and a low duty-cycle (1/2000) served to keep the temperature of the tube low at all times and thereby minimize changes in the resonant frequency that would enter as errors in  $B_L$  in the final results.

As has been mentioned previously, there are many possible systems for representing the data graphi-

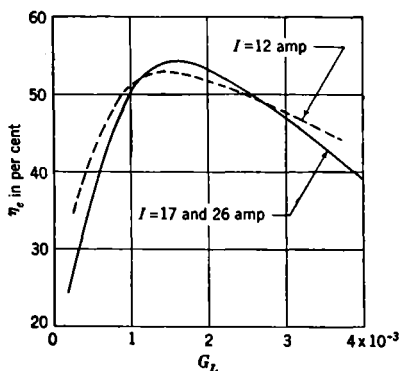


FIG. 7.24.—Electronic efficiency  $\eta_e$  as function of  $G_L$  for three values of input current.

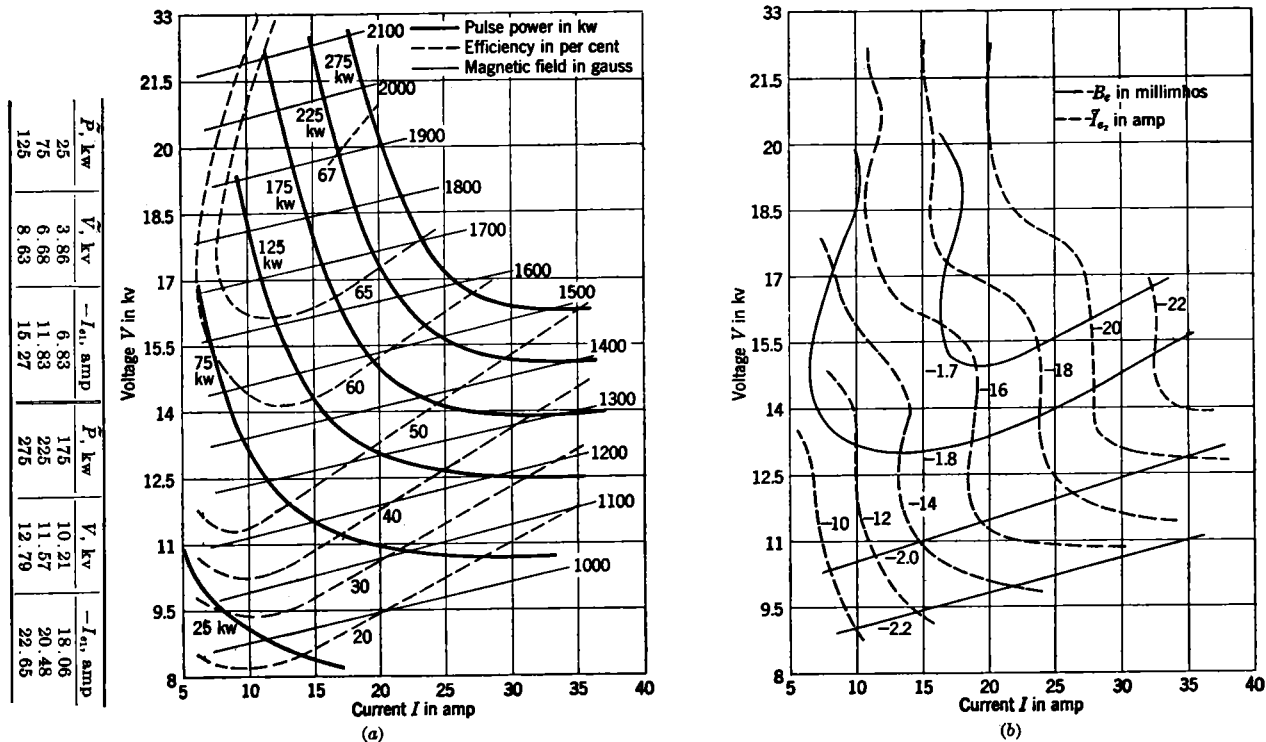


FIG. 7-25.—(a), (b) Performance charts. Operating conditions: 1120 PRF;  $1.04 \mu\text{sec} - G_e = G_L = 1.77 \times 10^{-9}$  mho (mean value). Power contours are also contours of  $\bar{V}$  and  $I_{cs}$ .

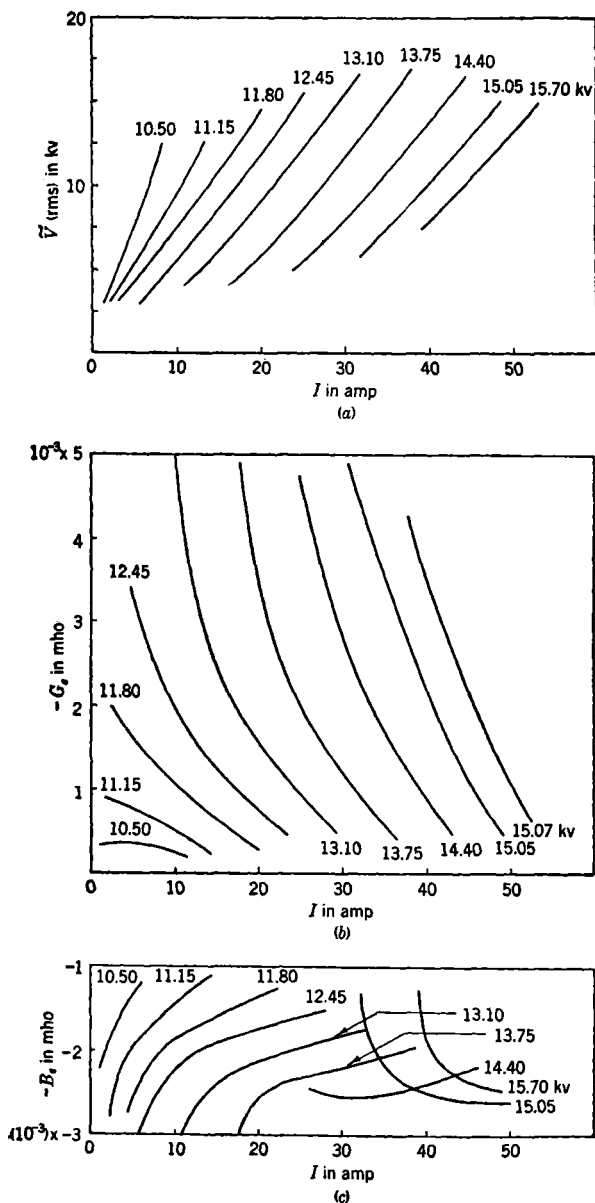


FIG. 7-26.—Plots of (a) rms a-c voltage  $\tilde{V}$ , (b) electronic conductance  $G_e$ , and (c) electronic susceptance  $B_e$ , as functions of the input d-c current  $I$ , with the input d-c voltage  $V$  as parameter.

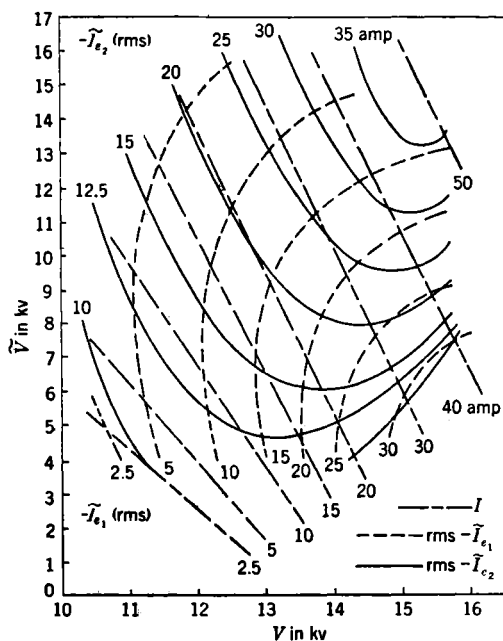


FIG. 7.27.—Plots of d-c current  $\bar{I}$  and a-c currents  $\bar{I}_{a1}$  and  $\bar{I}_{a2}$  in the  $\tilde{V}$ - $V$ -plane.

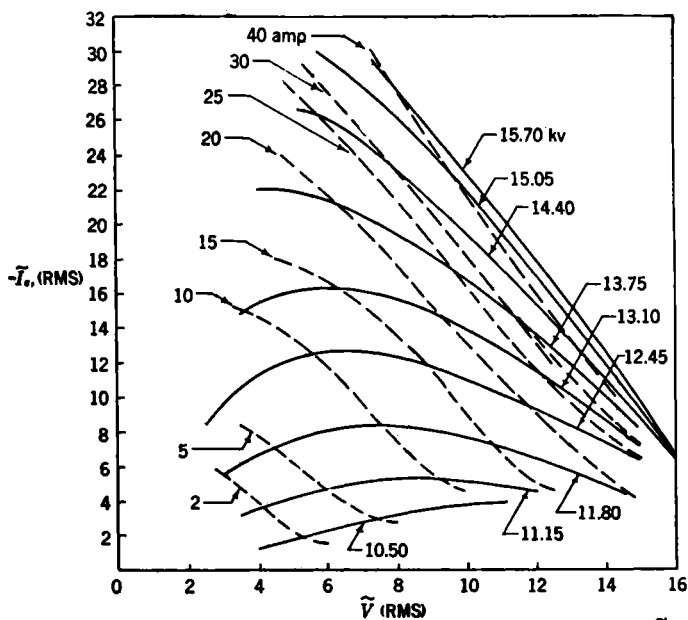


FIG. 7.28.—Plots of  $\bar{I}_{a1}$ , the real component of the a-c current vs. a-c voltage  $\tilde{V}$  with the d-c current  $\bar{I}$  and d-c voltage  $V$  as parameters.

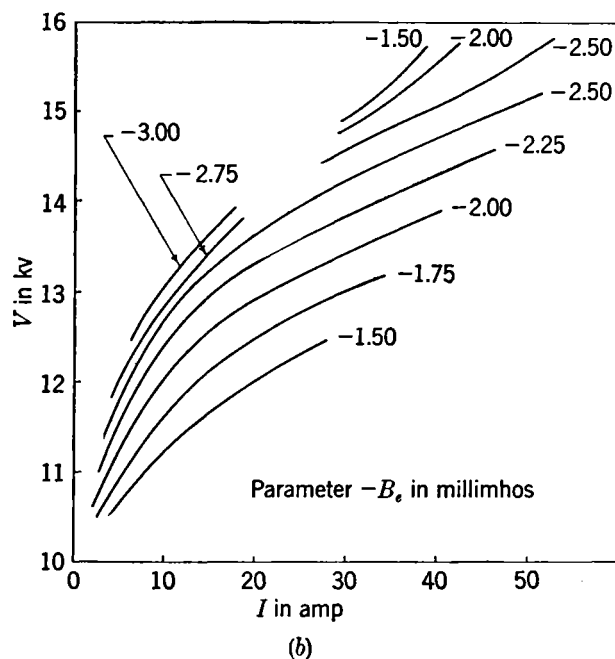
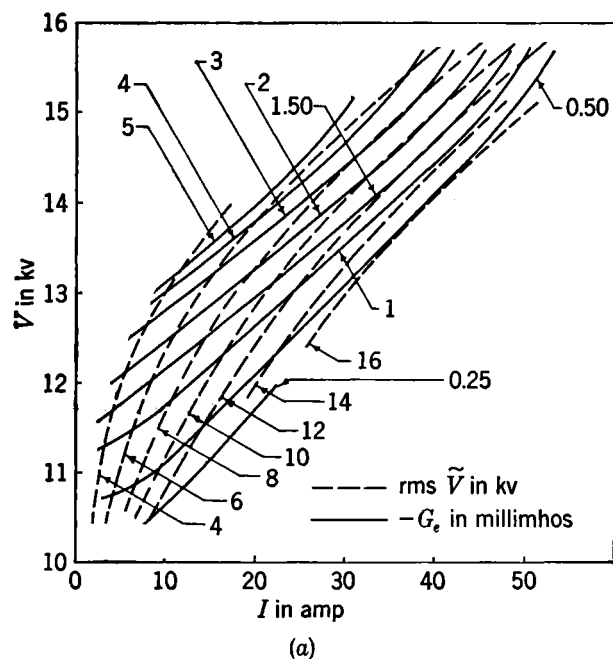


FIG. 7.29.—(a) Electronic conductance  $G_e$  and rms a-c voltage  $\tilde{V}$  in the  $(V, I)$ -plane; (b) electronic susceptance  $B_e$  in the  $(V, I)$ -plane.

cally. A few systems are illustrated (some only partially) in the following series of figures. Some of the figures are given because of their relation to topics discussed in various places in this book; others are given because they seem likely to be significant theoretically.

In principle, the various sets of curves ought to be mutually consistent where cross relationships exist, but actually they are not entirely so. Generally, the curves have been drawn to fit plotted points that represent pairs of values based on the original, individual observations. The drawing of smoothed curves is partly a matter of judgment, inasmuch as theoretical relationships are nonexistent. It has not seemed worth while to go through the elaborate process of adjustment that would be required to make all of the curves strictly consistent with one another,

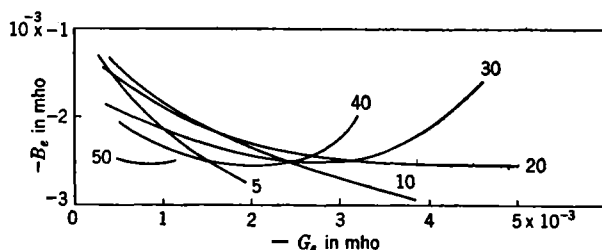


FIG. 7-30.—Operating curves with d-c input current  $I$  as parameter.

to keep the curves plausibly simple, and at the same time to secure a good fit for all the data.

Figure 7-26a, b, and c are straightforward plots of the original data.

Figure 7-27 illustrates the functions that appear in Eqs. (9a) and (9b), represented by means of contours in the  $V$ ,  $\bar{V}$ -plane.

Figure 7-28 is a plot of  $\bar{I}_{e1}$  against  $\bar{V}$  for various constant values of  $V$  and  $I$ .

Figure 7-29a is the "conductance map" used in Chap. 8 as the basis for the discussion of the transient behavior of the magnetron. The associated susceptance map is illustrated in Fig. 7-29b.

Figure 7-30 contains operating curves for various constant values of  $I$ . Inasmuch as the frequency varies linearly with  $B_e$  when the external load is held fixed, these curves show how the conductance  $G_L$  influences the degree to which the frequency depends upon the input current  $I$ .



## CHAPTER 8

### TRANSIENT BEHAVIOR

BY F. F. RIEKE

It is inevitable that a magnetron cavity with many resonators should have several natural modes of oscillation, and it is generally possible for self-excited oscillations to occur in more than one of the modes. Inasmuch as the modes have different frequencies and the operation in some of them is very inefficient, it is highly desirable that oscillations should occur consistently in the proper mode. The problem of securing such correct properties of mode selection has actually been one of the major obstacles encountered in the development of new magnetrons.

Ideas concerning mode selection tended for some time to center about the concept of interaction and competition between modes, and a great amount of effort was expended on devising and trying out features designed to handicap oscillation in undesired modes. As experience accumulated and techniques of observation improved, it became evident that any such simple approach could at best be only sporadically successful. Actually, mode-selection processes are diverse in nature and are influenced in varying degrees by many factors that have to do not only with the magnetron itself but also with the auxiliary equipment with which it is operated.

Some essential parts of the present subject are treated in preceding chapters—the natural modes of the cavity in Chaps. 2, 3, 4, and 6 and resonance relations in Chap. 7. According to the resonance relations, self-sustaining oscillations in a particular mode can occur only if certain conditions are fulfilled by the magnetic field and applied voltage.

In this chapter it will be shown that the resonance relations do not, in general, restrict oscillations to one mode but merely limit the possibilities. The deciding factors under these circumstances are (1) the noise levels existing in the various modes just prior to the starting of oscillations, (2) the transient phenomena that occur at the onset of oscillation, (3) the stabilities of the states of oscillation. An evaluation of these factors is largely dependent upon the detailed observation of mode-selection phenomena.

**8-1. Steady-state Properties of the Modes.**—The  $(N - 1)$ -modes of an  $N$ -oscillator cavity, such as the magnetron cavity described in Chap. 2, are frequently spoken of as “the modes.” This chapter is concerned with

these modes of oscillation only, although it is possible that some magnetron phenomena involve modes of other types. Throughout the discussion only cases in which  $N$  is even are considered.

It has been shown by Hartree<sup>1</sup> that when a Fourier analysis is made of the electric field in the interaction space, the only components associated with a mode of number  $n$  and frequency  $f$  are those which have angular velocities of  $\pm 2\pi f/\gamma$ , where  $\gamma = n + mN$  and  $m$  is an integer, positive or negative. If the mode is to be excited by the space charge, it is necessary that something like a condition of resonance be established between the angular velocity of the electrons and some one of the Fourier components mentioned above. Hartree's condition<sup>2</sup> is

$$V - V_\gamma = \frac{2V_\gamma}{B_\gamma} (B - B_\gamma),$$

where

$$V_\gamma = 2 \frac{m}{e} (\pi c r_a)^2 \frac{1}{(\gamma \lambda)^2}$$

and

$$B_\gamma = \frac{4\pi c}{r_a^2 - r_c^2} \left( \frac{m r_a}{e} \right)^2 \frac{1}{\gamma \lambda}.$$

The value of  $V$  given by this formula is, theoretically, the minimum d-c voltage, at magnetic field  $B$ , at which electrons can reach the anode when an alternating field of infinitesimal amplitude is applied; it should therefore represent a condition for the starting of oscillations in the  $\gamma$ -component. At magnetic fields less than  $B_\gamma$ , oscillations in the  $\gamma$ -component should not start at all. So far, excitation has been observed only through components for which  $m = 0$  or  $-1$ . The symbol  $(\gamma/n/N)$  is adopted here to indicate, in order, the component number, the mode number, and the number of oscillators; thus  $(5/3/8)$  indicates the  $(\gamma = 5)$ -component exciting the  $(n = 3)$ -mode in an eight-oscillator tube. In common practice, this condition is sometimes referred to as the "5-mode." It should be emphasized that the  $(5/3/8)$ - and  $(3/3/8)$ -modes are identical in so far as wavelength and r-f field configurations in the cavity are concerned. They differ only as regards the conditions within the space charge. The above equation may be represented graphically as in Fig. 8-1, which shows the Hull cutoff parabola and the Hartree lines for the modes commonly observed in eight-oscillator strapped magnetrons. On the basis of this diagram it should be expected that at a magnetic field equal to  $B'$ , excitation of the  $(n = 3)$ -mode should start at voltages  $V'$  and  $V'''$  and of the  $(n = 4)$ -mode at  $V''$ ; at  $V''''$  the tube should draw current without oscillating.

<sup>1</sup> D. R. Hartree, CVD Report No. 1536, Mag. 17.

<sup>2</sup> *Ibid.*

In the actual operation of a magnetron it is found that at constant magnetic field the voltage at which a tube runs in a given mode increases with the direct current drawn and with the degree of loading of the r-f circuit. The d-c voltage relations for the (4/4/8)-mode of a typical eight-oscillator magnetron (the 2J32) for several different values of load at one fixed value of magnetic field are shown in Fig. 8-2. It may be observed that oscillation (at finite amplitude) is possible at a voltage somewhat below the value given by the Hartree formula. At constant current and load the voltage increases linearly with the magnetic field. Similar relations between  $B$ ,  $V$ ,  $I$ , and load are observed for components

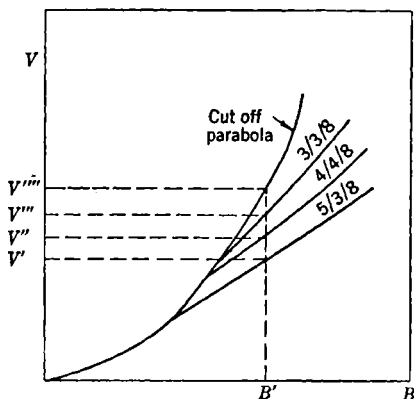


FIG. 8-1.—Schematic Hartree diagram for an eight-oscillator magnetron.

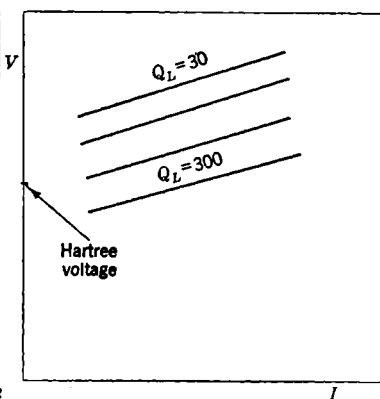


FIG. 8-2.—Current-voltage relations of the (4/4/8)-mode of an eight-oscillator magnetron at constant  $B$  with various values of load (schematic).

of other modes, although they cannot be followed over so great a range. It sometimes happens that some of the modes for which  $n \neq N/2$  are so weakly coupled to the output load that it is impossible to exert any appreciable influence on them by varying the external load. In such cases the output power may be so low that the wavelength can be measured only with difficulty, even though the mode is strongly excited.

For questions having to do with mode selection, one is frequently interested simultaneously in the  $(V, I)$ -relations of several components, all at the same magnetic field and at a fixed setting of some matching device in the output transmission line. The relations may be represented by  $(V, I)$ -diagrams, such as those shown in Fig. 8-3. The voltage of each component is, to a first approximation, equal to its Hartree voltage. The difference between the actual voltage and this approximation depends upon the load and the current, as is illustrated for a (4/4/8)-component in Fig. 8-2. However, it is important to remember that a

fixed setting of the matching device implies a different degree of loading for each mode, both because of the differences in coupling and because of the frequency sensitivity of the matching device. Thus, adjustments of the device may affect two modes oppositely and may interchange the relative positions, in a  $(V, I)$ -plot, of the curves for two components with nearly equal values of  $\gamma\lambda$ . As the magnetic field is changed, the  $(V, I)$ -diagram changes in accordance with the curves shown in Fig. 8-1.

The cutoff curve of Fig. 8-3 is drawn as it is observed in magnetrons of the type under discussion. It has sometimes been confused with a noncoupled mode of oscillation. The fact that the current increases continuously rather than discontinuously at the cutoff voltage is a well-known discrepancy between magnetron theory and experiment. The

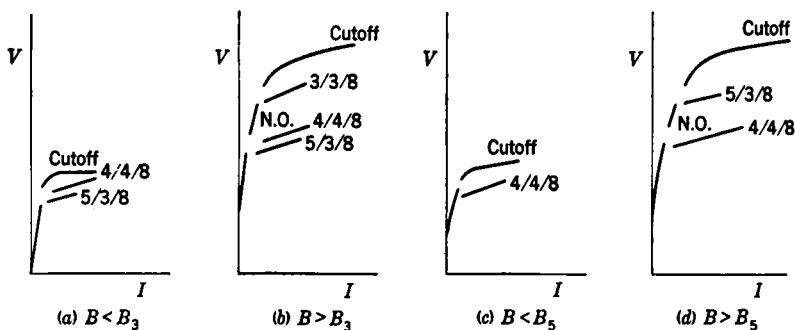


FIG. 8-3.—Schematic  $(V, I)$ -relations for an eight-oscillator magnetron: (a) and (b) with small wavelength difference between modes and (c) and (d) with large wavelength difference between modes. N.O. indicates a nonoscillating state.

curve has been identified with cutoff because the bend occurs at approximately the correct voltage, because the voltage varies quadratically with the magnetic field rather than linearly as do the modes, and because the current follows the application of voltage instantaneously (as far as can be observed) rather than with the delay of a few hundredths of a microsecond which is associated with the oscillating states.

The nonoscillating state just above the  $(4/4/8)$  component indicated in Fig. 8-3b and d generally escapes observation because with many tubes it can be observed only if the pulser has special characteristics. However, such nonoscillating states seem to occur whenever adjacent components are widely separated in voltage.

Apparently, oscillations can persist in just one mode at a time. At least the author is unaware of any instance in which a magnetron has been observed to oscillate in two modes simultaneously and continuously for as long as a very small fraction of a microsecond. However, it is very common for oscillations to change from one mode to

another. Changes of mode may take place in either of two ways: One or the other of two modes may be excited at successive turn-ons or pulses, or oscillation may suddenly shift from one mode to another during the continuous application of voltage. In either case operation in each of the modes appears to be normal; that is to say, when the respective instantaneous currents and voltages are plotted in a  $(V, I)$ -diagram, the resulting lines for each mode appear as in Fig. 8-3, and the data join on continuously with (or may even overlap) those taken with the tube operating entirely in one mode or the other.

**8-2. Steady-state Properties of the Pulser.**—The effect of the current-voltage characteristics of the pulser in determining the voltages and currents at which a tube may operate in any one of the various modes is now considered. For the present, the discussion is restricted to steady-state operation, thereby excluding the very rapid transients that occur at the beginning of oscillation or within an intrapulse transition from one mode to another. (Experimental details of the measurements will be discussed later.)

If instantaneous currents and voltages for each mode are observed when a tube is changing from one mode to another, then for each setting of the pulser-supply voltage one obtains a pair of voltage and current values, which, when plotted, are found to lie as shown in Fig. 8-4a. The solid lines represent the  $(V, I)$ -characteristics of the respective modes. The dotted lines which may be interpreted as  $(V, I)$ -characteristics of the pulser are drawn through pairs of points (one point for each mode) that are observed with the same value of input voltage to the modulator. This interpretation is confirmed by repeating the experiment with a resistor connected in series with the cathode lead of the magnetron to increase the internal resistance of the pulser. The  $(V, I)$ -points are then found to lie as illustrated in Fig. 8-4b, and the change in the slope of the dotted lines is equal to the negative of the value of the added resistance.

The  $(V, I)$ -characteristic of a hard-tube pulser may be related directly to the  $(I_p, E_p)$ -curves of the tubes in the final stage. If the characteristic of the tube (or parallel arrangement of tubes) is such as that shown in

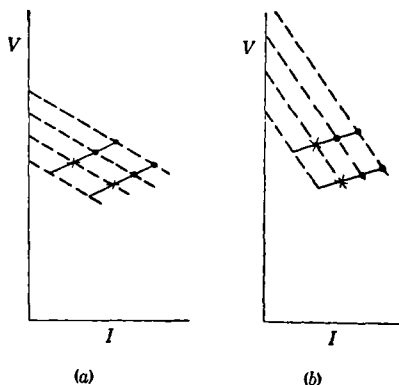


FIG. 8-4.— $(V, I)$ -relations for a magnetron that is changing modes. In (b) the internal resistance of the pulser has been increased over that of (a).

Fig. 8-5a when the control-grid voltage is equal to that delivered by the driver, then the  $(V, I)$ -characteristic of the pulser is like that shown in Fig. 8-5b, where the supply voltage is represented by  $V'$ .

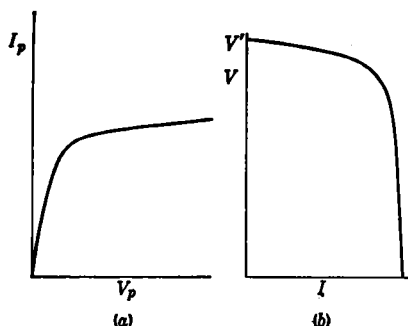


FIG. 8-5.—(a)  $(I_p, V_p)$ -characteristic of tubes in output stage of hard-tube pulser; (b)  $(V, I)$ -characteristic of the pulser of (a).

as an ideal transformer. Thus the characteristic of such a pulser is a straight line, as shown in Fig. 8-6. Usually the pulse-forming network is matched to the magnetron at the operating current and voltage, as at  $P$

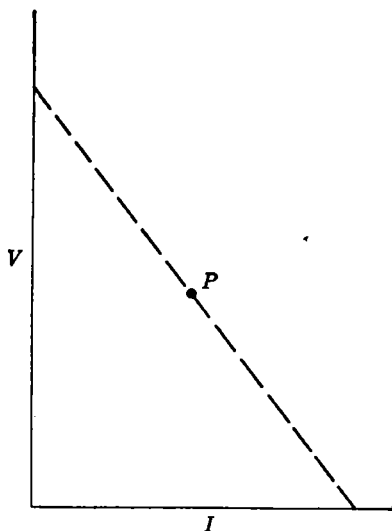


FIG. 8-6.— $(V, I)$ -characteristic of a line-type pulser.

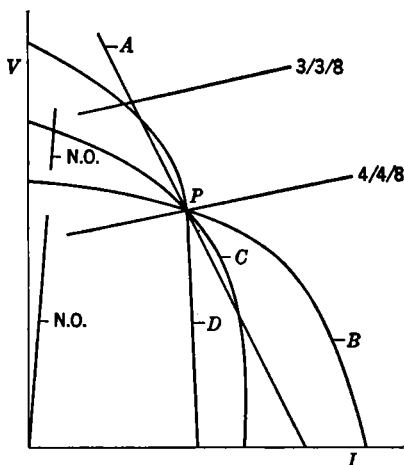


FIG. 8-7.—Comparison of  $(V, I)$ -characteristics for different pulsers.

in Fig. 8-6, so the open-circuit voltage is just twice the normal operating voltage of the magnetron.

Although the  $(V, I)$ -relationships of the pulser and magnetron together result only in necessary conditions which must be satisfied by

the steady-state currents and voltages of whatever modes are excited (the actual selection of modes being influenced by still other factors), they provide an explanation of many of the variations that are observed when tubes are tested on different pulsers. As an illustration, consider the ideal case represented by Fig. 8-7. A magnetron having the characteristics shown is to be operated in the  $(4/4/8)$ -mode at the point  $P$ . Only selection among the  $(4/4/8)$ - and  $(3/3/8)$ -modes and the non-oscillating states is discussed; it is assumed, as is commonly the case, that there is no interference from the  $(5/3/8)$ -mode. Curve  $A$  represents a line-type pulser, which obviously will permit operation in either the  $(4/4/8)$ - or the  $(3/3/8)$ -mode. Curve  $B$  represents a hard-tube pulser with a large reserve of current-carrying capacity which permits operation only in the desired mode. Curve  $C$  is typical of a hard-tube pulser operated near the upper limit of its capacity; it offers the choice between the  $(4/4/8)$ -mode and the nonoscillating state. Curve  $D$  illustrates a hard-tube pulser at plate-current saturation, which will permit operation in the  $(4/4/8)$ - and  $(3/3/8)$ -modes, just as does the line-type pulser.

**8.3. Types of Mode Changes.**—As has been mentioned in Sec. 8-1, changes of mode may take either of two forms. One form consists of a

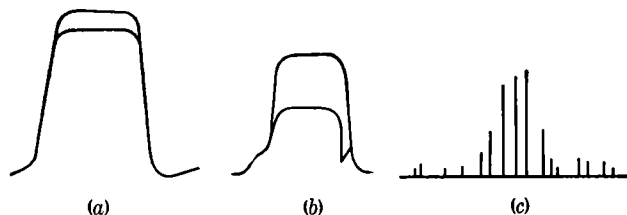


FIG. 8-8.—Symptoms of a mode skip. (a) The voltage pulses, (b) the current pulses, and (c) the spectrum.

random alternation between two modes at successive turn-ons or pulses; this type will be referred to as a “mode skip.” The other form is a transition from one mode to another during the continuous application of voltage; this type will be designated as a “mode shift.” Sometimes the two forms appear in combination.

The mode skip is the more common form in pulsed magnetrons. Its symptoms are double voltage and current pulses such as are shown in Fig. 8-8a and b and a spectrum that, with the conventional analyzer, appears to have lines missing as in Fig. 8-8c. The proportion of the numbers of pulses in the respective modes changes with power-supply voltage, usually continuously as indicated in Fig. 8-9; but because of a sort of instability connected with the regulation of the power supply, a sudden transition from *all pulses in one mode* to *all pulses in the other* may take place when the power-supply control is changed gradually.

(This instability is discussed at greater length in Sec. 8-7.) Mode skips are generally attributable to failures to start, or "misfiring," in the lower-voltage mode and in many cases can be eliminated by sufficiently reducing the rate at which voltage is applied to the magnetron.

A mode shift in a pulsed magnetron results in current and voltage pulses such as those illustrated in Fig. 8-10. (This figure represents a

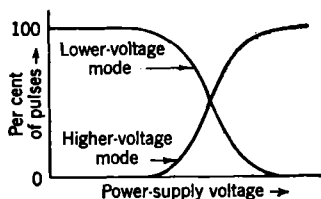


FIG. 8.9.—Effect of power-supply voltage on the distribution of pulses in a mode skip.



FIG. 8.10.—The pulses of (a) voltage and (b) current that are associated with a mode shift.

shift from a lower- to a higher-voltage mode, but shifts in the opposite direction also occur.) The spectra of the respective modes have no "missing lines" but are somewhat broadened because of the shortened effective pulse in each mode. Mode shifts may be considered to result from the loss of stability in the initial mode of oscillation. The condition of instability may be reached as the result of a change (however gradual) in the operating conditions or, conceivably, as the result of changes within the magnetron. In many cases it is quite sensitive to the load on the r-f circuit. Mode shifts can be especially troublesome in c-w magnetrons that are amplitude-modulated.

*Methods of Observation.*—Information about the dynamics of the types of phenomenon just mentioned has been derived principally from

observations on pulsed magnetrons. Measurements with a peak voltmeter and average-current meter are entirely inadequate for such studies. It is possible to construct diagrams such as Fig. 8-3 point by point from measurements of instantaneous current and voltage made with a synchroscope, but a more convenient and satisfactory method is to connect

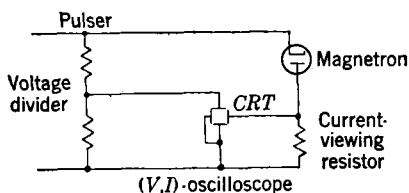


FIG. 8-11.—Schematic diagram of an oscilloscope used for automatic plotting of voltage against current.

the cathode-ray tube as shown in Fig. 8-11 so that the tube itself plots voltage against current automatically. As a first approximation, for each setting of power-supply voltage this arrangement yields one point in a  $(V,I)$ -plot corresponding to the flat portions of the pulses or two points in



case the tube changes modes. This limitation can be overcome, however, by modulating the power supply at a low frequency—say 60 cps—so that the successive pulses, during one complete sweep of the power supply, trace out a complete diagram. To make the arrangement practical, the cathode-ray tube must be intensity modulated, somewhat as in the synchroscope, so that the beam is on only during pulses.

Actually, since both current and voltage vary continuously throughout a pulse, the beam of the  $(V, I)$ -scope traces out a closed curve for each pulse, and the form of the curve is related to the transients. Figure 8-12 represents schematically a typical  $(V, I)$ -trace, correlated with the corresponding parts of the voltage and current pulses.

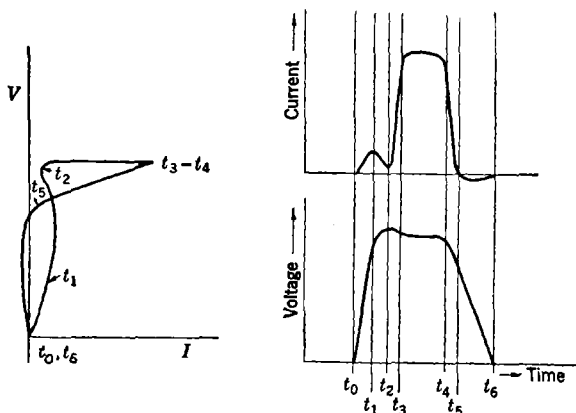


FIG. 8-12.—A  $(V, I)$ -trace with corresponding current and voltage pulses.

magnetron input circuit. The buildup of oscillation occurs between  $t_2$  and  $t_3$ . From  $t_3$  to  $t_4$  the magnetron oscillates steadily. As the voltage starts to fall at the end of the pulse, the oscillations die out between  $t_4$  and  $t_5$ , but the rate of fall of voltage is usually slow enough that the current-voltage relation is the same as for steady-state conditions. The discharging current  $t_5$  to  $t_6$  is much smaller than the charging current  $t_1$  because of the smaller magnitude of  $dV/dt$  at the trailing end as compared with the leading edge of the pulse.

There are thus two ways in which the  $(V, I)$ -scope may be used. To view the steady-state characteristic, the intensity modulation is set to bring out the flat part of the pulse ( $t_3$  to  $t_4$  in Fig. 8-12) and the power supply is modulated. To view the transients, the intensity modulation is set to bring out the appropriate portion of the pulse—the leading edge, for instance—and the power-supply voltage is held fixed. When the apparatus is arranged so that the change from one type of observation

to another can be made quickly and so that the various controls can be manipulated without interrupting the observations, it is possible to survey the behavior of a magnetron very quickly.

**8-4. Survey of the Process of Mode Selection.**—As a preface to the detailed discussion of the observations on mode selection, the pattern into which they fall is summarized here, and it is shown how the  $(V,I)$ -traces provide a convenient basis for discriminating between the various types of mode-selection processes.

The characteristic feature of the  $(V,I)$ -trace in a mode skip is the branching illustrated in Fig. 8-13, where the heavy arrowed curves represent the two alternative paths of the  $(V,I)$ -point, one to Mode A

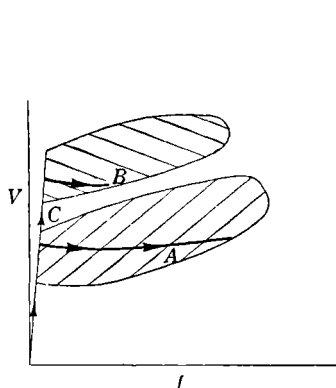


FIG. 8.13.—Mode skip determined by speed of starting in the lower mode.

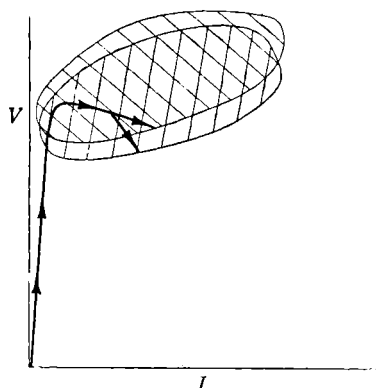


FIG. 8.14.—Mode skip governed by competition between two modes.

and one to Mode B. As will be shown later, modes widely separated in voltage have associated with them distinct regions of the  $(V,I)$ -plane within which oscillations in one, and only one, of the modes can build up and sustain themselves; these regions are indicated by shading in Fig. 8-13. When voltage is applied, as at the beginning of the pulse, the  $(V,I)$ -point rises to within the starting region of the lower mode where oscillation and consequently d-c current build up. If the buildup is sufficiently rapid, the  $(V,I)$ -point may be held within this region because of internal drop in the pulser, even though the open-circuit voltage of the pulser lies above this region. However, if the buildup is less rapid (relative to the rise of open-circuit voltage of the pulser), the current and voltage point may pass outside the region of the lower mode—whereupon oscillations in Mode A quickly die out—and thence into the oscillation region of Mode B. Depending upon circumstances, the  $(V,I)$ -point might eventually come to rest on the steady-state characteristic of B or on the cutoff curve somewhere above B; it might also fall

short of entering the region of the higher-voltage mode and come to rest at a nonoscillating state—say at  $C$ —between the two regions, as shown in Fig. 8-13. All the above possibilities are, of course, subject to the relations discussed in Secs. 8-1 and 8-2. It is clear that in this type of mode selection the controlling factors are the speed with which oscillations start in the lower mode and the characteristics of the pulser, particularly the rate of rise of voltage; there enters no element of competition between the two modes directly concerned.

A variation of the mode skip is illustrated by Fig. 8-14 in which two modes are so close together in voltage that their oscillation regions overlap extensively. Here it may be supposed that oscillations start in both modes simultaneously but that during the later stages of buildup the nonlinearities in the space charge enter in such a way that one of the modes gains predominance and eventually suppresses the other. If the competition were very evenly balanced, the outcome might be determined by random fluctuations; hence a mode skip would result that, contrasted with the type described earlier, would be very little influenced by the rate of rise of the applied voltage. Direct interaction between modes might be suspected of being an important factor whenever two modes have components with nearly equal values of  $\gamma\lambda$ . However, as will be discussed in more detail later, the above condition alone does not appear to be a very good index of the importance of interactions.

The mode shift is an entirely different sort of selection process and is characterized by a  $(V, I)$ -trace such as is illustrated in Fig. 8-15. This drawing corresponds to a case in which the rise of voltage is relatively slow, so that after the initial stages of buildup, the  $(V, I)$ -point proceeds toward higher currents along the steady-state characteristic of Mode A. Eventually a point of instability is reached; the oscillations in A cease to be self-sustaining; and as they die out, the  $(V, I)$ -point moves upward quickly, more or less along the pulser characteristic. Figure 8-15 represents a case in which the  $(V, I)$ -point then enters the oscillating region of Mode B and eventually comes to rest on the steady-state characteristic of that mode. In case the modes are widely separated and the pulser has a low impedance, the  $(V, I)$ -point may arrive at a nonoscillating state between Modes A and B. If the magnetic field is too low to permit oscillation in Mode B, the  $(V, I)$ -point will end on the cutoff curve.

In addition to the sort of shift that has a  $(V, I)$ -trace of the type

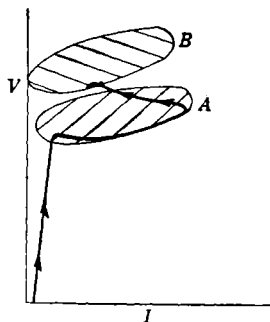


FIG. 8-15.—Mode shift caused by instability of the lower mode at high current.

illustrated in Fig. 8-15, there are sometimes observed shifts with  $(V, I)$ -traces like those illustrated in Fig. 8-16. These transitions can arise only from an interaction between modes; for if the primary event were simply the cessation of oscillations in the initial Mode  $A$ , the current (which can flow only because of the oscillations, since the voltage remains well below cutoff throughout) should tend to decrease and the voltage to rise *during the transition*—which is opposite to what is observed. Evidently, while the tube is in Mode  $A$ , a condition is reached that permits  $B$  to build up, and eventually the oscillations in  $B$  reach a great enough amplitude to suppress  $A$ .

The mode instabilities that have been investigated most thoroughly are the mode skip of Fig. 8-13 and the mode shift of Fig. 8-15. These

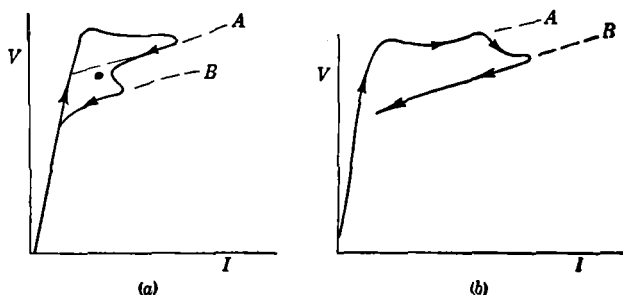


FIG. 8-16.—Mode shifts caused by competition between modes.

are discussed separately in detail in Secs. 8-5 and 8-6. The more complicated phenomena, in which interactions between modes play an important part, have so far been studied only more or less incidentally and are considered in Sec. 8-12.

**8-5. The Mode Skip.**—As a rule, mode skips are encountered when attempts are made to operate pulsed magnetrons at high currents, and in many such cases the mode skip can be attributed to misfiring in the desired mode of oscillation; that is, the mode-selection process is of the type illustrated by Fig. 8-13.

The manner in which a mode skip caused by misfiring usually develops when increasing voltages are applied to a magnetron (at constant magnetic field) is illustrated by the series of  $(V, I)$ -traces reproduced in Fig. 8-17a to f.

A complete steady-state characteristic taken at the same magnetic field is shown in Fig. 8-18. In Fig. 8-17a, the voltage is just below that at which oscillations start; in Fig. 8-17b and c, oscillations start at every pulse, and the steady-state current increases as the voltage is raised. At higher voltages, oscillations start in the lower mode only during some

of the pulses, but in such pulses the steady-state current continues to increase with applied voltage. In Fig. 8-17*d* and *e*, failure to start in the lower mode results in a transition into a nonoscillating state, but

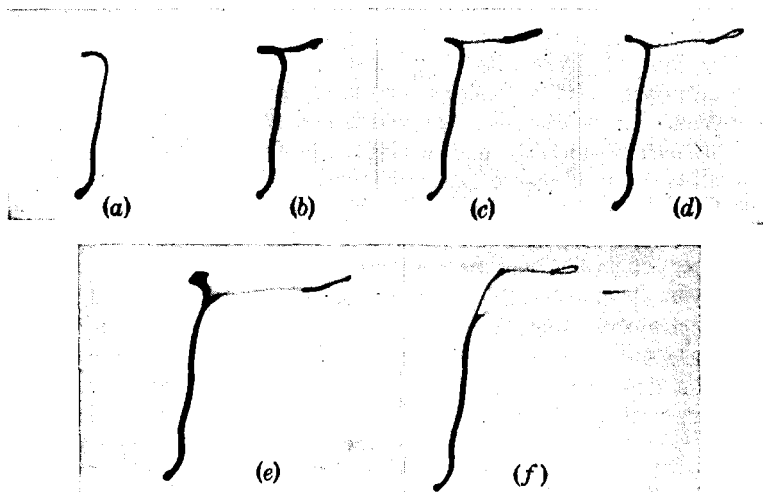


FIG. 8-17.— $(V, I)$ -traces of a mode skip arranged in order of increasing voltage. Only the trace corresponding to the rising edge of the pulse is shown. (a) Below oscillations; (b) beginning of oscillations; (c) middle of oscillation region; (d) beginning of misfiring; (e) misfiring into the nonoscillating state; (f) misfiring into a higher-voltage mode.

with a still greater applied voltage (Fig. 8-17*f*) the  $(V, I)$ -point continues upward through the nonoscillating state and into the higher-voltage mode.

Additional evidence that misfiring in the lower-voltage mode is the primary cause of the mode skip when the modes are widely separated in voltage is provided by the fact that the proportion of pulses in the higher-voltage mode (or alternatively, the nonoscillating state) can be decreased by reducing the rate at which the voltage rises at the leading edge of the pulse. With a sufficiently slow rise of voltage, the upper mode is suppressed completely. This behavior is readily understood on the basis of the discussion of Fig. 8-13. (The possibility that a mode *shift* may occur when the rise of voltage is made very slow does not affect the validity of the argument.) The effect is further discussed in Sec. 8-9.

**8-6. The Mode Shift.**—The type of mode shift that seems to occur most commonly and about which most is known is that illustrated in

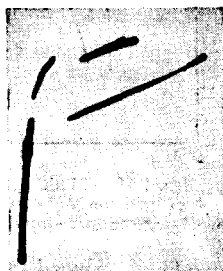


FIG. 8-18.—Steady-state characteristic of the mode skip illustrated in Fig. 8-17.

Fig. 8-15, in which the transition is caused by simple instability in the initial mode of oscillation. In many cases the instability at high currents appears to result from an inherent property of the space charge in the oscillating magnetron, although in others it is definitely attributable to a deficiency in the electron emission from the cathode.

The inherent instability shows up most prominently in magnetrons scaled to operate at low voltages, particularly in tubes designed for c-w operation. Its outstanding characteristic is a strong dependence of the limiting current upon the r-f load; lighter loads (large loaded  $Q$ 's) permit oscillation to continue to higher currents. The effect was recognized first by R. N. Hall and L. Tonks of the General Electric Company, Schenectady, N.Y., who encountered it in the course of developing c-w magnetrons for radar countermeasures.

The conclusion that this limitation on current is an inherent property of the magnetron such as can occur even when the emission from the cathode is limited by space charge is based on the facts that the observed limitation does depend strongly on the load and that the effects observed in a wide variety of magnetrons show a qualitative consistency. However,

the impossibility of ascertaining to what degree the emission is actually limited by space charge in an oscillating magnetron precludes any precise analysis of the data available.

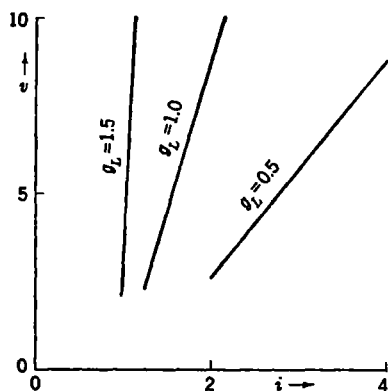


FIG. 8-19.—Limiting current as a function of load conductance. The parameters are expressed in reduced variables.

Figure 8-19 shows the limiting current that may be expected for various values of load. The plot is presented in the form of reduced variables (see Chap. 10). Operation at a given load is possible only to the left of the load line. In addition to the uncertainties mentioned, there is some question as to how exactly effects in dissimilar magnetrons can be correlated by

means of reduced variables, so that predictions based on Fig. 8-19 may well prove to be in error by a factor of 2 in special cases.

In most of the magnetrons designed for pulsed operation the inherent limit on current cannot be demonstrated, because these tubes run at high current densities, so that other limitations, such as low emission or sparking from the cathode, appear first. It has been observed, however, in low-voltage pulsed tubes (for example, the experimental LL3 magnetron described in Sec. 8-9) by the application of a heavy load and a slowly rising pulse.

Another type of limitation on current shows up in some tubes when the cathode is abnormally poor or when it is run at a subnormal temperature, and this limitation is thus attributable to inadequate emission. Usually when the current is limited by cathode emission (including

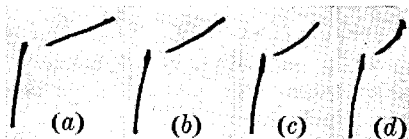


FIG. 8-20.—Steady-state characteristics showing from (a) to (d) the effect of decreasing heater power. A 500- $\mu$ f condenser was connected in parallel to eliminate misfiring.

secondary electrons, of course), the  $(V, I)$ -characteristic bends upward at high currents—sometimes a kilovolt or so above the extrapolated straight part of the characteristic—before instability sets in. The location of the bend usually can be altered by varying the temperature of

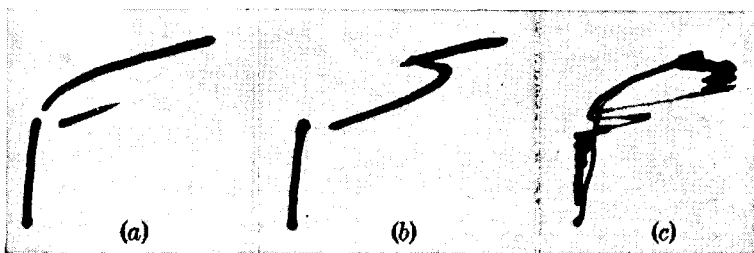


FIG. 8-21a.—Steady-state characteristic showing misfiring into the cutoff curve.

FIG. 8-21b.—Steady-state characteristic for the same conditions as Fig. 8-21a, but with a 500- $\mu$ f condenser in parallel with the magnetron. There appears an upper limit to the amount of current that can be drawn in the main mode.

FIG. 8-21c.—A  $(V, I)$ -trace for a voltage setting on the cutoff curve of Fig. 8-21b. (Note that oscillations which build up in the main mode become unstable at high current.)

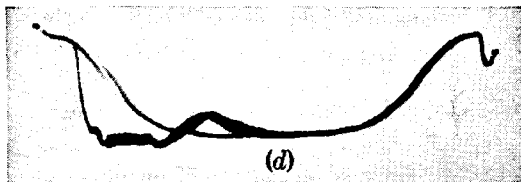


FIG. 8-21d.—The current pulse of Fig. 8-21c indicating the relative lengths of time involved in this transition. (Note also that sometimes the tube misfires directly into the cutoff curve.)

the cathode. The four parts of Fig. 8-20 demonstrate this behavior in the LL3.

A good example of how a poor cathode can cause a tube to behave abnormally because of a mode shift is provided by some 725 magnetrons that had received very severe treatment. Normal 725 tubes operate

with no evidence of mode instabilities; but in testing these tubes on a hard-tube pulser which had a very slowly rising pulse, it was observed that oscillations started with each pulse but ceased as soon as the current rose to about 30 amp. Examination then showed that the pulsed primary emission was hardly detectable.

Pulsed tubes normally do not exhibit a mode shift unless they do have very poor cathodes and the rate of rise of the voltage pulse is sufficiently slow, because misfiring takes place instead, when the voltage is raised in the attempt to increase the current. As an example, Fig. 8-21a shows a steady-state ( $V, I$ )-diagram of the LL3 taken at a low magnetic field. (The upper "mode" in this case is the cutoff curve.) When a 500- $\mu\text{f}$  condenser is shunted across the modulator, the misfiring is eliminated,

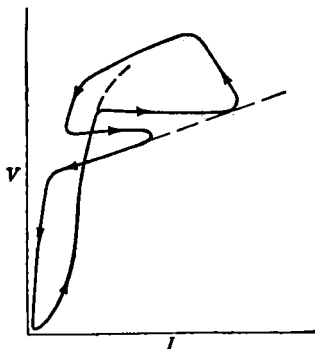


FIG. 8-22.—Schematic diagram of the trace shown in Fig. 8-21c of a mode instability.

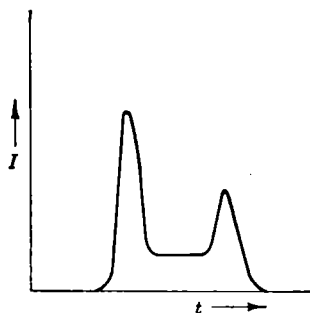


FIG. 8-23.—A current pulse showing excitation of a low-voltage mode at the beginning and end of the pulse.

and a mode shift occurs. The steady-state characteristic for this case is shown in Fig. 8-21b, and the corresponding ( $V, I$ )-trace and current pulse for a high-voltage pulse are shown in Fig. 8-21c and d. These figures show that the misfiring has not been completely eliminated. The ( $V, I$ )-trace of Fig. 8-21c is copied schematically in Fig. 8-22; the arrows show the direction of motion of the ( $V, I$ )-point.

Sometimes a mode shift occurs very early in the pulse, so that the lower mode is excited for only a brief interval at the beginning of the pulse and for another brief interval at the end of the pulse when the voltage falls again within the starting range. The current pulse then has the shape indicated in Fig. 8-23. The suddenness of the transition from a normal current pulse to one of this type may be accentuated by an instability of the combination of magnetron, pulser, and power supply, which will be discussed in Sec. 8-7. If, as is usual in such cases, the limiting current is a function of cathode temperature, peculiar time



lags may be observed, since the heating by back bombardment may be very different in the two conditions of operation.

Shifts in which the second mode has a *lower* voltage than the initial mode have been observed to occur in two ways, corresponding to Fig. 8-16*a* and *b*. Type *a*, in which the instability sets a lower limit to the current in a higher-voltage mode, requires special conditions for its observation—namely, that a higher-voltage mode be reached initially (as a result of misfiring or high-current instability in the lower mode) and that the voltage then fall so that the lower current limit of the higher-voltage mode is approached from the high-current side. This sort of transition has been observed only between closely spaced modes; it is exhibited well in some unstrapped X-band tubes (specifically, the 2J21). Practically, it does not seem to be of much importance.

Type *b*, as shown in Fig. 8-16*b*, was observed in an experimental tube (the LM2 produced by the Raytheon Manufacturing Company) in which the 2J39 anode block is strapped to a wavelength of 12.3 cm. When run on a hard-tube pulser, this tube has a steady-state characteristic for certain loads such as is indicated by the heavy curve in Fig. 8-24. Here, misfiring in the (4/4/8)-mode on a medium-voltage pulse leads to the non-oscillating state N.O.; but a higher-voltage pulse, which rises to where the (5/3/8)-mode should start, results instead in the excitation of the (4/4/8)-mode. Close observation of the current pulse shows, however, that the (5/3/8)-mode is actually excited for a brief interval at the beginning of the pulse.

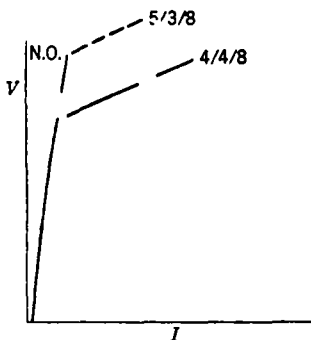


FIG. 8-24.—A steady-state characteristic of the LM2. At high voltages the  $\frac{5}{3}$ -component is excited at the start of each pulse.

**8-7. Instability of the Power Supply: "Mode Jumps."**—When a mode change takes place in such a way that an increase in applied voltage results in a decrease in magnetron current, complicating phenomena may occur. For instance, pulsed magnetrons sometimes exhibit a very sudden change from one mode to another, apparently with no perceptible transition range. This phenomenon—occasionally referred to as a "mode jump"—has sometimes been interpreted as a distinct type of change different from those which have been described in preceding sections. Actually, such behavior is a result of instability of the combination of power supply, pulser, and magnetron rather than a special characteristic of the magnetron.

A power supply that consists of a rectifier and filter will, in general,

have a time constant that is large compared with the repetition period of the pulser, and its output voltage (as affected by internal regulation) will be dependent upon the average current drawn by the magnetron rather than the pulse current. If the power supply has a condenser output, the condition for stability is that

$$\frac{1}{R} + \frac{dI}{dV} > 0,$$

where  $R$  is the internal resistance of the power supply,  $I$  is the average current, and  $V$  is the input voltage to the pulser (considered to be equal to the open-circuit output voltage of the pulser).

In the case of a mode skip, the average current as a function of power-

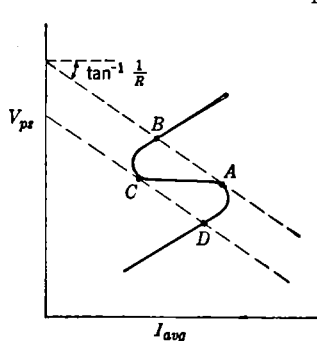


FIG. 8-25.—A negative resistance region offered to the power supply of the pulser because of a mode change in the magnetron.

supply voltage can be computed on the basis of curves such as are illustrated in Figs. 8-4 and 8-9. In general, an S-shaped curve such as is shown in Fig. 8-25 will result. With a power supply that has a characteristic like that shown by the broken lines, there will be a region of instability. As the supply voltage is increased, there will be a jump from A to B—the mode skip is observed as a “jump.” On the other hand, if the voltage is decreased, the jump will be from C to D; thus hysteresis occurs. This hysteresis effect seems to be present in all “mode jumps,” and a close examination

of the current pulse just prior to the jump usually indicates the beginning of either a mode skip or a mode shift.

Conditions that tend to make  $dI/dV$  have a large negative value are that the transition (Fig. 8-9) occurs in a narrow range of voltage and that the currents in the two modes be widely different for a fixed supply voltage. Both conditions are most likely to be fulfilled with a hard-tube pulser inasmuch as a rapid rise of voltage at the beginning of the pulse will tend to make the transition region narrow and a low pulser impedance will tend to make the difference in currents large.

Under special conditions a *mode shift* in a pulsed magnetron can also be influenced by instability of the power supply. For instance, if the shift is like that illustrated in Fig. 8-15 and the voltage rises throughout the pulse, a small increase in supply voltage can cause the shift to a lower current to take place earlier in the pulse and thus result in decreased average current.

It is obvious that conditions of instability can also arise with c-w magnetrons and may lead to oscillations in the input circuit.

**8-8. Outline of a Theory of Starting.**—It has been indicated in Chap. 7 that the type of analysis there applied to steady-state operation can be extended to apply to transients, and this section is essentially an elaboration of that idea. Many of the general principles involved are derived from a report by J. R. Pierce.<sup>1</sup> This treatment may be termed an “adiabatic theory” of starting, because it is based on the assumption that the transient takes place so slowly that it may be approximated as a continuous succession of steady states. Even under conditions where the approximation is rather poor, the theory should give some insight into the nature of the phenomena that take place. Of course, it is possible to conceive of conditions in which an adiabatic approach is entirely inadequate, but it is not evident that such conditions are commonly realized in current practice.

The analysis of the steady-state operation has been based on the fundamental relation

$$Y_e + Y_c = 0, \quad (1)$$

where  $Y_e$  is the admittance of the space charge and  $Y_c$  is the admittance of the circuit. In so far as admittances can be defined for transients, the same relation must apply because it is simply an expression of the continuity of current. The discussion of Chap. 7 has indicated that the admittance of a circuit has a definite meaning, and that it can be computed from the usual formulas by substituting the “complex frequency” instead of the purely real frequencies, for oscillations that increase or decrease exponentially with time. The admittance  $Y_e$  of the electrons is assumed to depend only on the instantaneous values of the applied voltage  $V$  and the r-f voltage  $\tilde{V}$ , not on their time derivatives—this assumption constitutes the hypothesis that the buildup is adiabatic.

A detailed discussion will be given only for the case in which the resonant system may be represented as a simple parallel-resonant circuit (Fig. 8-26) with admittance given by

$$\begin{aligned} Y_c &= 2C(p - p_L) \\ &= G_L + 2C \left[ \frac{1}{\tilde{V}} \frac{d\tilde{V}}{dt} + j(\omega - \omega_L) \right], \end{aligned} \quad (2)$$

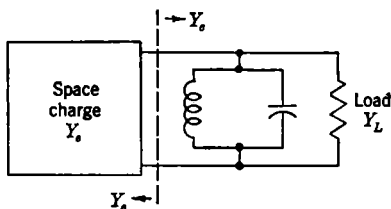


FIG. 8-26.—Equivalent circuit of a magnetron.

<sup>1</sup> J. R. Pierce, “Oscillator Behavior,” *BTL Memorandum* MM-42-140-60, Sept. 8, 1942.

where  $-jp_L$  is the loaded, complex, resonant frequency equal to  $\omega_L - j\xi_L$  (see Chap. 7). In so far as one is interested in the amplitude of the r-f voltage, but not the frequency, as a function of time, only the real part of Eq. (2) need be considered; with the value of  $Y_e$  substituted from Eq. (1), it is

$$\frac{1}{\tilde{V}} \frac{d\tilde{V}}{dt} = \frac{d}{dt} \ln \tilde{V} = - \frac{G_e + G_L}{2C}, \quad (3)$$

where  $G_e$  is the electronic conductance and  $G_L$  is the steady-state conductance of the loaded circuit. Equation (3) has to be solved in conjunction with relations that describe the dependence of  $G_e$  upon  $\tilde{V}$  and the input conditions. The solution will contain a constant of integration that is related to the noise level from which oscillations begin.

Equation (3) is now to be developed in such a way as to make direct connection with the  $(V, I)$ -traces which constitute the greater part of the observational material on the starting of oscillations. That is to say, the behavior of the system will be followed by tracing its course in the  $(V, I)$ -plane.

As shown in Chap. 7, the properties of the space charge, at some fixed value of magnetic field, may be expressed in the form

$$\tilde{V} = \tilde{V}(V, I) \quad (4)$$

and

$$G_e = G_e(V, I). \quad (5)$$

(Because the magnetic field is ordinarily constant during any transient, it enters only as a parameter and will not be included explicitly.) It is convenient to represent the functions  $\tilde{V}$  and  $G_e$  by means of a "conductance map," which is constructed by drawing contours of constant  $\tilde{V}$  and constant  $G_e$  in the  $(V, I)$ -plane, as illustrated in Fig. 8-29. For the present, it is assumed that the functions are known.

In the interest of simplicity, the reactances in the pulser and in the input circuit of the pulser will be ignored, so that the pulser can be described by a relation of the form<sup>1</sup>

$$V = V(I, t). \quad (6)$$

At every instant Eq. (6) defines a curve—the instantaneous pulser characteristic—on which must lie the point  $(V, I)$  which describes the state of the system. It is convenient to make the following substitutions:

<sup>1</sup> With reactances, Eq. (6) must be replaced by relations that contain derivatives and integrals. An attempt to take reactances into account in a general way would involve one in the theory of the transient response of networks, with the added complication of the magnetron as a peculiar circuit element.

$$\xi(V, I) = -\frac{G_s + G_L}{2C}, \quad (7)$$

and

$$\psi(V, I) = \ln \frac{\tilde{V}}{\tilde{V}_0} \quad (\tilde{V}_0 = \text{reference level.})$$

(In the conductance map, contours of constant  $\psi$  are identical, except for labeling, with those of constant  $\tilde{V}$  and the gradients of  $\psi$  and  $\tilde{V}$  are in the same direction; similarly for  $\xi$  and  $-G_s$ .) In terms of  $\xi$  and  $\psi$ , Eq. (3) takes the form

$$\frac{d}{dt} \psi(V, I) = \xi(V, I). \quad (8)$$

From Eqs. (6) to (8) the following relations may be derived by differentiation:

$$\frac{dI}{dt} = \frac{-\left(\frac{\partial \psi}{\partial \tilde{V}}\right)_I \left(\frac{\partial \tilde{V}}{\partial t}\right)_I + \xi}{\left(\frac{\partial \psi}{\partial \tilde{V}}\right)_I \left(\frac{\partial \tilde{V}}{\partial I}\right)_I + \left(\frac{\partial \psi}{\partial I}\right)_V}, \quad (9)$$

and

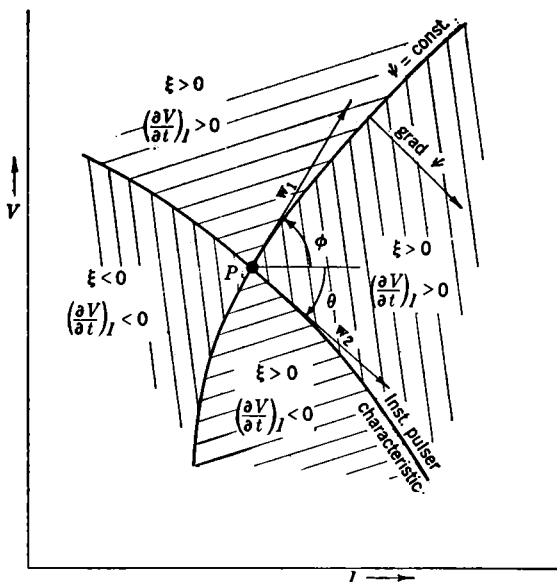
$$\frac{dV}{dt} = \frac{\left(\frac{\partial \psi}{\partial I}\right)_V \left(\frac{\partial \tilde{V}}{\partial t}\right)_I + \left(\frac{\partial \tilde{V}}{\partial I}\right)_I \xi}{\left(\frac{\partial \psi}{\partial \tilde{V}}\right)_I \left(\frac{\partial \tilde{V}}{\partial I}\right)_I + \left(\frac{\partial \psi}{\partial I}\right)_V}. \quad (10)$$

These two equations give the velocity in the  $(I, V)$ -plane of the point  $P$  which describes the system, in terms of known functions of the coordinates of  $P$  and of the time  $t$ . The result can be put into a form that can be interpreted more directly, for inspection of the equations shows that the velocity of  $P$  is the sum of two vectors, one tangent to the instantaneous pulser characteristic at  $P$  and of magnitude proportional to  $\xi$ , the other tangent to the constant- $\psi$  contour through  $P$  and of magnitude proportional to  $(\partial V / \partial t)_I$ . If two unit vectors  $\mathbf{w}_1$  and  $\mathbf{w}_2$  are chosen as shown in Fig. 8-27, the velocity of  $P$  may be expressed as a vector  $\mathbf{W}$  where

$$\mathbf{W} = \mathbf{w}_1 \frac{\cos \theta}{\sin(\phi - \theta)} \left(\frac{\partial V}{\partial t}\right)_I + \mathbf{w}_2 \left[ \frac{1}{\sin(\phi - \theta)} \frac{\xi}{\text{grad } \psi} \right]. \quad (11)$$

The direction of  $\mathbf{W}$  for various combinations of the signs of  $(\partial V / \partial t)_I$  and  $\xi$  is indicated by sectors in Fig. 8-27.

The quantitative calculation of a transient would presumably have to be carried out by numerical integration of some sort. The way in which the process might be performed graphically is illustrated in Fig. 8-28, which is based on a simplified conductance map. The instantaneous

FIG. 8-27.—The unit vectors  $w_1$  and  $w_2$  of Eq. (11).

pulser characteristic is drawn in for successive times separated by some constant interval  $\Delta t$  (equal to unity in the drawing). The point  $P$

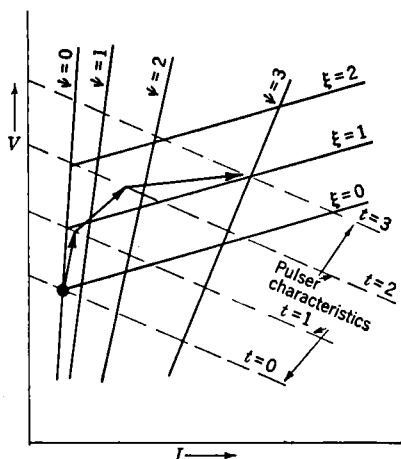


FIG. 8-28.—Graphical calculation of a transient.

approaches the ( $\xi = 0$ )-contour along the constant- $\psi$  contour which represents the noise level in the resonant circuit indicated by  $\psi = 0$  in Fig. 8-28. The vector that represents the displacement of  $P$  in each of the time intervals is so drawn that the increment in  $\psi$  is equal to  $\Delta t$  times the value of  $\xi$  averaged over the length of the vector.

In order to trace out the complete transient, the functions  $G_e(V, I)$  and  $\tilde{V}(V, I)$  have to be known along the entire path. In Chap. 7 it is shown how these functions can be derived from steady-state measurements, but

such measurements are confined to regions of *stable* operation, whereas during a transient, region are accessible in which the system is

inherently unstable. Consequently the functions must in part be deduced from observations of transients. Inasmuch as existing measurements of transients are very crude, as judged by the present requirements, it is possible to make only qualitative deductions about the behavior of  $G_e$  and  $\tilde{V}$  in the regions not covered by steady-state measurements.

From consideration of all the information available, it seems that the conductance map derived from steady-state measurements (see Fig.

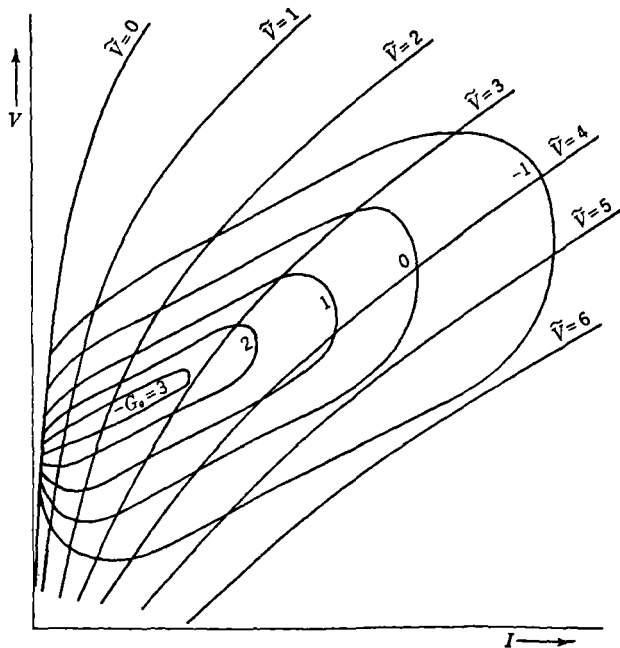


FIG. 8-29.—Schematic graph of  $\tilde{V}$  and  $G_e$  as functions of  $V$  and  $I$ .

7-29a) should be extended in the general fashion indicated in Fig. 8-29 in order to explain the transient phenomena observed. In Fig. 8-29 the constant- $\tilde{V}$  contours are simply extrapolated from Fig. 7-29a and are consistent with the premise that  $I$  should increase monotonically with both  $\tilde{V}$  and  $V$ . The ( $\tilde{V} = 0$ )-contour resembles the current-voltage characteristic of a magnetron without oscillators, as it is actually observed. The curving of the  $G_e$  contours in the lower left part of the diagram is introduced to explain the starting voltage and related phenomena, which are described in Sec. 8-9. (With regard to this feature there is some uncertainty. As drawn, the contours are entirely consistent with the observed behavior of pulsed magnetrons, but they are

not precisely consistent with the characteristics of c-w magnetrons at low currents, which are discussed in Sec. 9-2.)

The doubling back of the  $G_e$  contours at high currents is designed to account for the observed instability at high currents and for the fact that the limiting current decreases as  $G_L$  is made larger. This phenomenon is described in Sec. 8-6. The  $G_e$  contours are made to return to the ( $\tilde{V} = 0$ )-curve at higher values of  $V$  (upper left part of the diagram) in order to restrict the range of  $V$  in which oscillations can start and thus to explain the *nonoscillating states* indicated in Fig. 8-3 and further described in Sec. 8-9.

The question of stability will be taken up first, and the types of transient behavior that are connected with Fig. 8-29 will be considered later. When the modulator characteristic is stationary,  $(\partial V/\partial t)_I = 0$ , and, according to Eq. (11), the intersections of the ( $\xi = 0$ )- or  $(-G_e = G_L)$ -contour with the pulser characteristic should represent stationary states. Such an intersection will constitute a state of stable operation, however, only in case small displacements from it tend to diminish rather than increase with time. Since the input circuit is considered to be free of reactances, any displacement from an intersection  $P'$  must occur along the pulser characteristic and can be represented by a distance  $s$ . In the neighborhood of  $P'$ , the change in  $\xi$  can be approximated by  $(\partial \xi/\partial s)s$  and Eq. (11) can be written as

$$\frac{1}{s} \frac{ds}{dt} = \frac{\frac{\partial \xi}{\partial s}}{\frac{\partial \psi}{\partial s}} \quad (12)$$

Thus, the condition for stability is that the right-hand side of Eq. (12) be negative; that is,  $\xi$  (or  $-G_e$ ) and  $\psi$  must increase in opposite directions along the pulser characteristic.

However, it is doubtful if the condition just mentioned is stringent enough to ensure stability in an actual case, for this condition is based on the assumption that reactances are entirely absent from the input circuit, although they can never be eliminated completely in practice. If reactances are included,  $P$  is not constrained to move along the steady-state pulser characteristic, and additional possibilities arise. According to the condition that has been derived, stable operation could be achieved in the upper portion of Fig. 8-29 by the somewhat artificial but not altogether impossible expedient of using a pulser with the proper *negative* internal resistance, but it seems implausible that this would actually work. Very probably oscillations of one sort or another would take place in the input circuit. If reactances are taken into account, the input circuit will, in general, have a multiplicity of normal modes (in the



conventional network-theory sense), and for stability it is required that all of these modes shall be positively damped.

It seems reasonable to conclude that with a normal pulser (with *positive* internal resistance) stable operation is limited to the lower part of Fig. 8-29, where  $-G_e$  increases with  $V$ . At low currents, operation can be stable only if the internal resistance of the pulser is large,

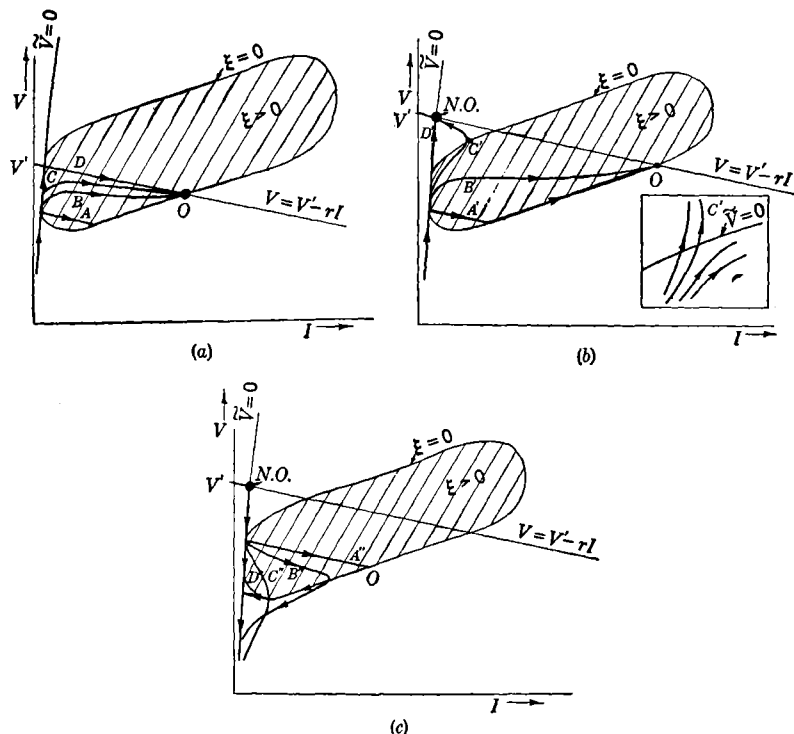


FIG. 8-30.—Examples of transient behavior. It is to be noted that the coordinates are input current and voltage; the *time* enters only as a parameter, which increases along each of the paths in the direction indicated by the arrows, but the exact time dependence of  $V$  and  $I$  is not shown.

and even then there is some possibility that oscillations will occur in the input circuit.

As has been stated, some of the features of the conductance map as drawn in Fig. 8-29 are justified principally by the observations to be described in Sec. 8-9. However, the relation between the map and observation may best be illustrated by proceeding as though the former were known independently and showing the types of transient behavior that can be predicted on the basis of it. The results, which are illus-

trated in Fig. 8-30, have been arrived at by qualitative considerations based on Eq. (11) and Fig. 8-27, but there can be little doubt that the procedure illustrated by Fig. 8-28 would lead to substantially the same curves.

The shaded area of Fig. 8-30 (where  $\xi$  is positive) is the region in which oscillations always increase with time; outside the shaded area, oscillations always decrease with time. It is assumed that the pulser is simply

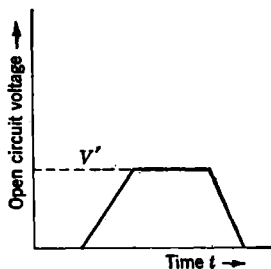


FIG. 8-31.—The open-circuit pulser voltage as a function of time.

a voltage source with internal resistance  $r$ , and the applied open-circuit voltage is in the form of the pulse illustrated<sup>1</sup> in Fig. 8-31.

In Fig. 8-30a and b, which applies to the first half of the pulse shown in Fig. 8-31, the open-circuit voltage rises at a uniform rate to a final value  $V'$  as indicated and then remains fixed. In Fig. 8-30c, which applies to the second half of the pulse, the open-circuit voltage, having remained at the value  $V'$  throughout the period of steady-state operation, falls to zero at a uniform rate. In Fig. 8-30a,  $V'$  lies within the starting range; that is, the line  $V = V' - rI$  (the steady-state pulser characteristic) cuts the  $(\bar{V} = 0)$ -curve in the region in which  $\xi$  is positive.

One steady-state condition, represented by the point 0, is reached invariably, regardless of how rapidly or slowly the voltage is applied at the beginning of the pulse. The series A to D illustrates the variation in path as the rate of rise of voltage is increased.

In Fig. 8-30b,  $V'$  lies outside the starting range, and therefore two steady states are possible: the oscillating state 0 reached by paths A' and B' and the nonoscillating state N.O. reached by paths C' and D'. In cases where this nonoscillating state is reached, the phenomena illustrated by Fig. 8-30c occur during the falling edge of the pulse. In Fig. 8-30c path A'' represents the limiting case in which the rate of fall of voltage is sufficiently slow that the final decay of oscillations occurs along the steady-state characteristic of the magnetron. Path D'' represents the opposite extreme where no oscillations at all occur, and C'' and B'' are intermediate.

The nature of the  $(V, I)$ -curves is greatly influenced by the fact that the gradient of  $\psi$  is very large in the neighborhood of the  $(\bar{V} = 0)$ -contour. The point P enters the positive- $\xi$  region closely alongside this contour, because the noise excitation of the resonant circuit is relatively small,

<sup>1</sup> Figure 8-31 does not represent the voltage across the magnetron output terminals; it simply represents the voltage that would exist there if the magnetron did not draw current.

and departs from it only very slowly at first. It is just this circumstance—that oscillations must build up for some time before the current  $I$  is affected appreciably—which gives rise to the possibility of misfiring when the voltage is applied very rapidly.

The noise in the resonant circuit has been treated, so far, as a constant, which it actually is not. If fluctuations in the noise are taken into account, each of the three cases represented by a single path in Fig. 8-30 should be shown as a bundle of paths. Ordinarily the bundle will be narrow; but if conditions are critical, so that the fluctuations determine which of two widely different general courses will be followed, the bundle will spread out. Thus a path such as  $C'$  may become fuzzy, as illustrated in the insert of Fig. 8-30b. For some purposes it may be necessary to consider the dependence of the noise on time, for the noise excitation depends on the input conditions, and the amplitude of the noise voltage in the circuit will have its own law of buildup.

The time relations along any given  $(V, I)$ -path may be computed by means of the line integral

$$t'' - t' = \int_{\psi'}^{\psi''} \frac{d\psi}{\xi} = \int_{\tilde{V}'}^{\tilde{V}''} \frac{2C}{G_L + G_e} \frac{d\tilde{V}}{\tilde{V}} \quad (13)$$

taken along the path. The speed of starting is sometimes expressed in terms of the starting time, which is the interval required for oscillation to build up to the point where the r-f output and the increase in input current are easily perceptible on instruments generally used to measure the final or steady-state values of these quantities. The starting time will be least when the early stages of buildup—in which the greater part of the increment in  $\ln \tilde{V}$  has to be covered—take place where  $\xi$  has its maximum value, which is somewhere near the middle of the starting range.

It is informative to express the starting time  $\Delta t$  in terms of an “effective  $Q$  for buildup”  $Q_B$  according to the relation

$$\Delta t = -\frac{1}{\omega} Q_B \Delta \ln \tilde{V}^2 = -1.22 \times 10^{-11} \lambda Q_B \Delta \log_{10} \tilde{V}^2. \quad (14)$$

The orders of magnitude that seem to be generally involved, for 10-cm pulsed magnetrons, are  $\Delta t = 10^{-8}$  sec,  $Q_B = -20$ , and  $\Delta \log_{10} \tilde{V}^2 = 4$ .

It is interesting to inquire into the implications, as related to transient behavior, of the same scaling relations that are used to systematize the steady-state properties of magnetrons. This may be done by expressing the various quantities that enter into Eq. (3) in terms of the “reduced variables” introduced by Slater.<sup>1</sup> According to the ideas of dimen-

<sup>1</sup> J. C. Slater, “Theory of Magnetron Operation,” RL Report No. 200, Mar. 8, 1943.

sional analysis, there exists for each mode of each magnetron a set of "characteristic parameters"  $\mathfrak{R}$ ,  $\mathfrak{V}$ , and  $\mathfrak{g}$ , such that Eqs. (4) and (5) have a universal form when expressed in terms of the dimensionless "reduced variables"  $v = V/\mathfrak{V}$ ,  $\bar{v} = \bar{V}/\mathfrak{V}$ ,  $b = B/\mathfrak{R}$ , etc. It is convenient to introduce also the "characteristic conductance"  $\mathfrak{g} = g/\mathfrak{V}$ .

In what follows, the discussion will be restricted to the  $\left(\frac{N}{2} / \frac{N}{2} / N\right)$  component, and it is assumed that the cathode-anode ratio is chosen according to the widely used formula  $r_c/r_a = (N - 4)/(N + 4)$ . Subject to these restrictions, the expressions given by Slater for the characteristic parameters can be written in the forms

$$\left. \begin{aligned} \mathfrak{R} &= \frac{\pi c}{2} \frac{m}{e} \frac{1}{\lambda} \left(1 + \frac{4}{N}\right), \\ \mathfrak{V} &= 2c^2 \frac{m}{e} \left(\frac{2\pi r_a}{N\lambda}\right)^2, \\ \mathfrak{g} &= \frac{\pi^2}{16} c^3 \frac{m}{e} \epsilon_0 \left(\frac{2\pi r_a}{N\lambda}\right)^2 \frac{h}{\lambda} N A_N, \\ \mathfrak{G} &= \frac{1}{32} \pi^2 c \epsilon_0 \frac{h}{\lambda} N A_N, \end{aligned} \right\} \quad (15)$$

where  $A_N = 1.24 + (9.6/N)$ . The formulas have been put in the above forms to clarify the dependence upon the number of oscillators  $N$ . The expression for  $\mathfrak{g}$  agrees within 5 per cent with the more complicated one given by Slater as long as  $N$  is not less than 8.

When written in reduced variables, Eq. (3) can be put in the dimensionless form

$$\frac{d}{dt} \ln \bar{v}(v, \bar{t}) = -g_s(v, \bar{t}) - g_L, \quad (16)$$

where

$$t_s = \frac{2C}{\mathfrak{G}}.$$

The parameter  $t_s$  may be treated as the "characteristic time interval for transients." From Eq. (15) it is evident that the transient behaviors of two magnetrons should be compared on the basis of their respective reduced times  $t/t_s$ . However, even on this basis Eq. (15) will not have identical types of solutions for the two magnetrons unless the pulsers are appropriately scaled, that is to say, unless Eq. (6), when written for each of the pulsers in the reduced variables appropriate to the magnetron with which the pulser is associated, takes on one identical form

$$v = v\left(\bar{t}, \frac{t}{t_s}\right).$$

If it is assumed that the last condition is fulfilled—which is never the case in practice—there still remains the question of the initial conditions that represent the noise. Here it appears that the principle of similitude breaks down, for it would require that the charge on the electron be scaled to the magnetron. It seems not too unreasonable to suppose that the noise has some relation to the shot effect, which involves  $e$  rather than the quantity  $e/m$ , which appears in the scaling relations. Thus, where noise is involved, the scaling relations can be applied only with some degree of reservation.

In so far as noise is not involved, the speed of transients should vary inversely as  $t_s$ . According to Eq. (15)

$$t_s \propto \frac{C\lambda}{hN} \frac{1}{A_N} \propto \left( \frac{1}{hN} \sqrt{\frac{C}{L}} \right) \lambda \frac{1}{A_N}. \quad (17)$$

The factor in parentheses depends only on the shape of the resonant system.

**8-9. Observations and Discussion of Starting.**—The observations described in the first part of this section were made on a magnetron designed especially to demonstrate the starting of oscillations under the simplest possible conditions. (This magnetron will be referred to as the "LL3.") It has a very large mode separation, so that the principal mode is excited at voltages far below those at which the various components of the other modes might occur; thus, the operation in the principal mode should be, *a priori*, free of interactions with those modes. In addition, the LL3 operates in a convenient range of voltages (3 to 10 kv) and is thus readily adaptable to a variety of demonstrations; consequently it has been used for most of the illustrations of this chapter. It is convenient to consider the LL3 as the "standard case" and to discuss other tubes in terms of their deviations from the standard.

The LL3 is an eight-oscillator tube with anode dimensions identical with those of the 2J39 (LVS); namely,  $r_a = 0.4$  cm,  $r_c = 0.15$  cm, and  $h = 1.20$  cm. It differs from the 2J39 in having double unbroken ring straps (instead of single broken rings) and in having no internal pole pieces. Its (4/4/8)-mode is at 11.3 cm; cold tests down to 7 cm failed to reveal any other mode. The tube can be made to oscillate at 5.5 cm, and the voltage of this mode is consistent with that of the (5/3/8)-mode. The ( $V, I$ )-relations thus correspond to Fig. 8-3c and *d*. Observed steady-state ( $V, I$ )-diagrams are reproduced in Figs. 8-18 and 8-21a.

The observations described first are those which demonstrate the existence of nonoscillating states between widely separated modes and which show that for a given mode there is a definite range of voltage, quite sharply defined both above and below, within which it is possible for oscillations to start. The nonoscillating state between modes is

shown clearly in the steady-state ( $V, I$ )-diagram reproduced in Fig. 8-18. Figure 8-21a demonstrates that when the magnetic field is too low to permit the excitation of the upper mode, the nonoscillating state joins continuously with the cutoff curve.

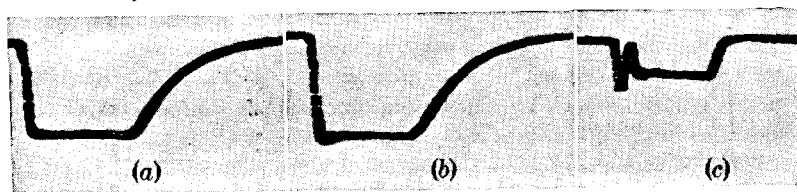


FIG. 8-32.—Voltage and current pulses taken with  $\frac{1}{4}$ - $\mu$ sec pulser having a rapid voltage rise. (a) Voltage below oscillating region; (b) voltage pulse in oscillating region; (c) current pulse in oscillating region.

Figures 8-32 and 8-33 illustrate the starting behavior observed when the voltage pulse has a very steep rise and a flat top, that is, under conditions that approach those assumed in drawing paths  $D$  and  $D'$

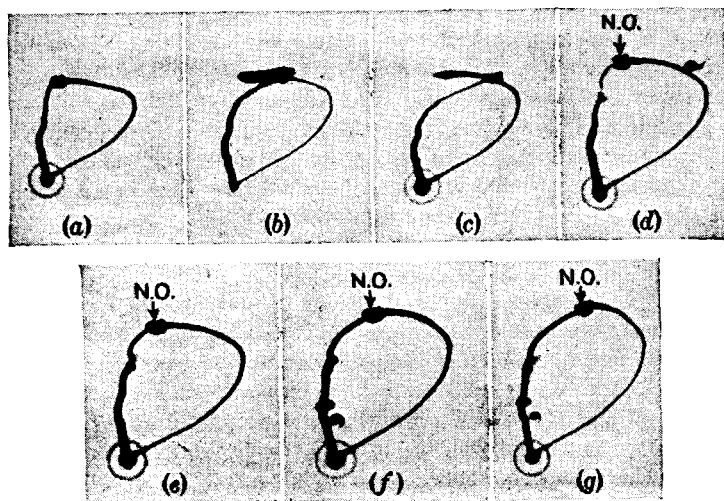


FIG. 8-33.—Complete ( $V, I$ )-traces for rapidly rising applied voltage, for a series of voltages increasing through the oscillating range. Note the gap in the descending part of the traces in (d), (e), (f), and (g), where the tube makes an "attempt" to start. (a) Below oscillations; (b) beginning of oscillations; (c) end of oscillations; (d) alternately oscillating and misfiring; (e) misfiring; (f) misfiring into cutoff (note that there is no delay in current); (g) misfiring into cutoff at higher voltages. There is still no delay in current.

in Fig. 8-30a and b. This series demonstrates that with such a pulse, starting occurs only in case the voltage *comes to rest* within the starting range. If the final open-circuit voltage of the pulse is above the starting range, the voltage remains within the range for so short a time that buildup does not make appreciable headway. The pictures were taken

with a  $\frac{1}{8}$ - $\mu$ sec pulser, and Fig. 8-32*a*, a voltage pulse below the starting range, shows that the entire rise occurs in about 0.02  $\mu$ sec. Figure 8-32*b* shows a voltage pulse within the starting range, and Fig. 8-32*c* shows the corresponding current pulse. The "spike" at the leading edge of the current pulse represents the current required to charge<sup>1</sup> the input capacitance of the cathode circuit as the voltage rises and is especially large in this case because of the magnitude of  $dV/dt$  at the leading edge of the pulse; the corresponding deviation in the  $(V,I)$ -trace serves to distinguish the leading edge from the trailing edge of the pulse. Because the charging current drops almost to zero and then rises again, it may be seen that the space-charge current does not start to build up until the voltage has practically ceased rising. Figure 8-32*b* shows a small hump on the beginning of the voltage pulse which is absent in Fig. 8-32*a*; this hump results from the voltage drop that occurs, because of pulser impedance, when the magnetron starts to draw current.

Figure 8-33 shows  $(V,I)$ -traces taken with pulser voltage increasing from just below the starting range (Fig. 8-33*a*) to well above it (Fig. 8-33*g*). The steady state corresponding to this series is approximately like that illustrated in Fig. 8-21*a*. These traces were taken with the magnetic field just too low to permit excitation of the upper mode. For Fig. 8-33*d* the voltage was just at the top of the starting range; during a few pulses oscillations start, but during the majority they do not, and the  $(V,I)$ -point remains at the nonoscillating state, which lies on the cutoff curve. At a slightly higher voltage (Fig. 8-33*e*), oscillations invariably fail to start during the pulse, and at still higher voltages (Fig. 8-33*f* and *g*), the  $(V,I)$ -point proceeds directly to the cutoff curve. It should be noticed that when the voltage reaches the cutoff curve, current is drawn immediately—there is no indication of the delay in current that is evident when oscillations must start before the current can build up. The current pulses (not reproduced) show that within the oscillation range, the delay in current is subject to appreciable variations; it is greatest at the extremes of the starting range, where it is equal to the pulse length and decreases fairly continuously toward the midrange where it is about 0.015  $\mu$ sec.

Further indication of the extent of the starting range is given by the behavior observed when the voltage, having passed by a mode at the beginning of a pulse, falls again into the starting range of that mode at the end of the pulse, as has been assumed in drawing Fig. 8-30*c*. If the voltage does not fall too rapidly, the  $(V,I)$ -point reaches the steady-state characteristic and follows it to lower voltages. (Usually the slope of the voltage pulse has a much smaller magnitude at the trailing edge of a pulse than it does at the leading edge.) This sort of path is shown

<sup>1</sup> This charging current has not been taken into account in Fig. 8-30*a* and *b*.

very clearly in Fig. 8-34. If the voltage falls rapidly, only a slight deviation in the  $(V,I)$ -trace occurs. Evidence of starting at the trailing edge of the pulse may be seen in Fig. 8-33 even with the faster falling

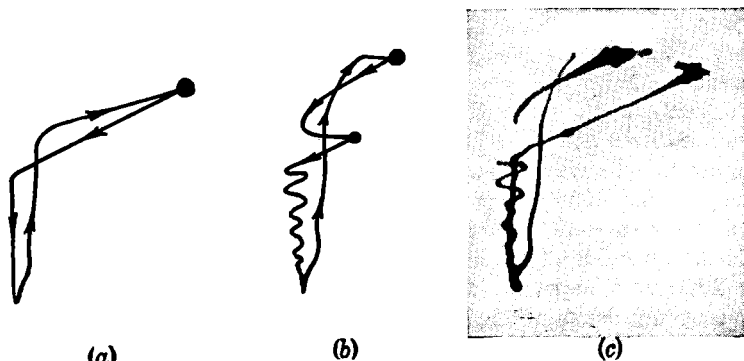


FIG. 8-34.—A complete  $(V,I)$ -trace of a mode skip in a magnetron operating from a hard-tube pulser. Note the gap in the descending part of the trace for the higher-voltage mode, where the lower-voltage mode builds up. (The oscillations are due to a natural resonance in the pulser.) The actual photograph (c) is a result of the superposition of two  $(V,I)$ -paths represented by the tracings (a) and (b).

voltage, but in most of these photographs the deviation is evidenced by only a gap, since an exposure time adapted to the slower parts of the trace is not long enough to register the deviation, which is swept out rapidly and therefore appears only faintly on the oscilloscope screen.

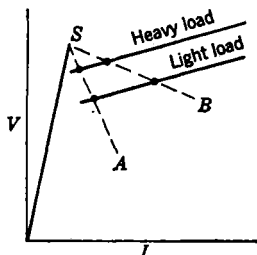


FIG. 8-35.—Effect of the r-f load and pulser impedance on minimum steady-state current. *A* is for high pulser impedance; *B* is for low pulser impedance; and *S* is the starting voltage.

The lower limit of the starting range will be referred to as the “starting voltage”; for the LL3, as for most magnetrons, it is somewhat greater than the minimum voltage for steady-state oscillation. Consequently, if the open-circuit voltage of the pulser is brought up just to the starting voltage, the steady-state current increases discontinuously, as is shown by the gap at the low-current end of the steady-state characteristic of each mode in Fig. 8-18. The minimum current for steady-state operation is influenced by the impedance of the pulser and by the r-f load on the magnetron as illustrated in Fig. 8-35. In drawing this figure, it has been assumed that the starting voltage is independent of the r-f load; while this may not be exactly true, visual observations of the  $(V,I)$ -traces have shown that it is a moderately good approximation. Figure 8-36, a series of photographed  $(V,I)$ -traces taken with various resistors



in series with the modulator, shows how the minimum steady-state current decreases when the internal resistance of the pulser is increased.

In terms of the conductance map, the general behavior just described has been interpreted to mean that the constant- $G_c$  contours bend upward toward low currents, as in the lower left part of Fig. 8-29. It might

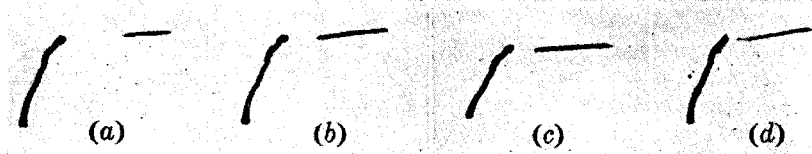


FIG. 8-36.—Steady-state characteristics showing the effect of changing the pulser impedance on the minimum current that can be drawn. (a) No series resistor; (b) 200 ohms in series; (c) 500 ohms in series; (d) 1000 ohms in series.

be expected that the curvature could be made to show up in the steady-state characteristic of the magnetron by putting a very large resistance in the input circuit, but attempts to do this were unsuccessful, possibly because of instability. On one occasion, when a magnetron quite similar to the LL3 was operated with a condenser shunted across it and with a resistance in series with the pulser, relaxation oscillations were observed to be superimposed on the voltage pulse. However, some

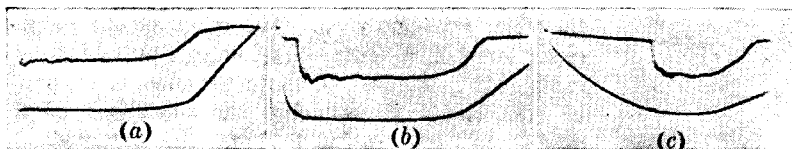


FIG. 8-37.—The effect of parallel capacitance on the shapes of the current and voltage pulses. (a) Voltage and current pulses with no condenser. The first part of the voltage pulse does not show because the sweep of the oscilloscope is triggered by the driver pulse of the pulse generator. (b) Voltage and current pulses with 250  $\mu\text{f}$  in parallel with the magnetron. (c) Voltage and current pulses with 1000  $\mu\text{f}$  in parallel.

further indication that the magnetron characteristics do not fall uniformly toward very low currents may be seen in  $(V, I)$ -traces that show the trailing edge of the pulse, particularly Fig. 8-38a and b. There it appears that at a certain minimum current the  $(V, I)$ -point suddenly changes its direction of motion and—as judged by the density of the trace—also its speed.

Observations that indicate how starting behavior is influenced by the speed with which voltage is applied to the magnetron are illustrated<sup>1</sup>

<sup>1</sup> Unfortunately, this series of traces does not correspond to the sequence of Curves A' to D' of Fig. 8-30b, which have been discussed theoretically. For those curves, it was assumed that the reactance in the input circuit of the magnetron was negligible, but in the present series of traces the effects have been produced entirely by adding reactance to that circuit. The demonstration would be more pertinent if the rate of rise of voltage had been controlled entirely by modifications in the driver of the pulser.

by Figs. 8-37 and 8-38. For this experiment a Raytheon Laboratory pulser was used, with shunting condensers to vary the rate of rise. Even

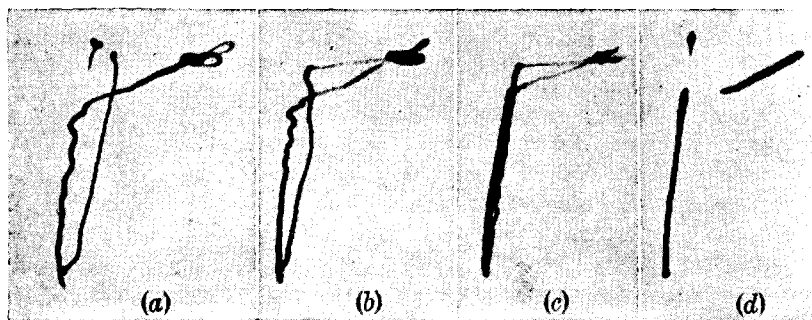


FIG. 8-38.—The effect of parallel capacitance on the overshoot of the starting voltage. (a) The  $(V,I)$ -trace with no condenser. The voltage rises high enough on the rising edge to cause misfiring in some pulses. (b) The  $(V,I)$ -trace with  $250\ \mu\text{f}$  in parallel with the magnetron. The voltage does not rise so high as in (a), and misfiring is eliminated. (c) The  $(V,I)$ -trace with  $1000\ \mu\text{f}$  in parallel. The overshoot is decreased still more. (Note that the slight decrease in steady-state voltage from (a) to (c) is due to an error in setting and is not associated with the phenomena being discussed.) (d) The steady-state  $(V,I)$ -characteristic corresponding to (a).

with no shunting condenser, the voltage rise on this pulser was considerably slower than that of the  $\frac{1}{2}$ - $\mu\text{sec}$  pulser used for Figs. 8-32 and 8-33. The effect of the parallel capacitance on the current and voltage pulses is shown in Fig. 8-37. Figure 8-38 shows the effect of the parallel capacitance in reducing the overshoot of the applied voltage. In Fig. 8-38c the rate of rise of voltage is slow and the current builds up suddenly when the voltage reaches the starting value; but when the voltage rises more rapidly (as in Fig. 8-38a), there is an increasing tendency to overshoot the starting voltage before the buildup of current sets in. Figure 8-38d shows a steady-state characteristic corresponding to Fig. 8-38a.

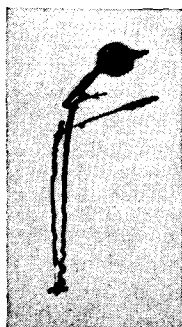


FIG. 8-39.—A  $(V,I)$ -trace from a 2J42 magnetron, showing the "attempt" to start made by the lower-voltage mode even when the tube eventually oscillates in the higher-voltage mode. (Photograph courtesy of J. V. Lebacqz.)

A  $(V,I)$ -trace of the exact type of Curve  $C'$  in Fig. 8-30b was not observed with the LL3 magnetron, although some attempt was made to produce conditions in which it might appear. However, such a curve has been observed with a different magnetron. Figure 8-39 is a reproduction of a  $(V,I)$ -trace for a 2J42 (LVX) magnetron that gives unmistakable evidence that a false start is made on the rising part of the trace.

**8-10. Observations on R-f Buildup.**—The results just described, along with the theoretical considerations contained in Sec. 8-8, give a fairly

general qualitative understanding of the way oscillations start in a magnetron. However, the speed of the transients in microwave magnetrons is so great that a rather complete revision of the measuring techniques is essential if the subject is to be put on a quantitative footing. The following experiments, which were interrupted by the end of the war, represent a start in that direction.<sup>1</sup> They were made possible by

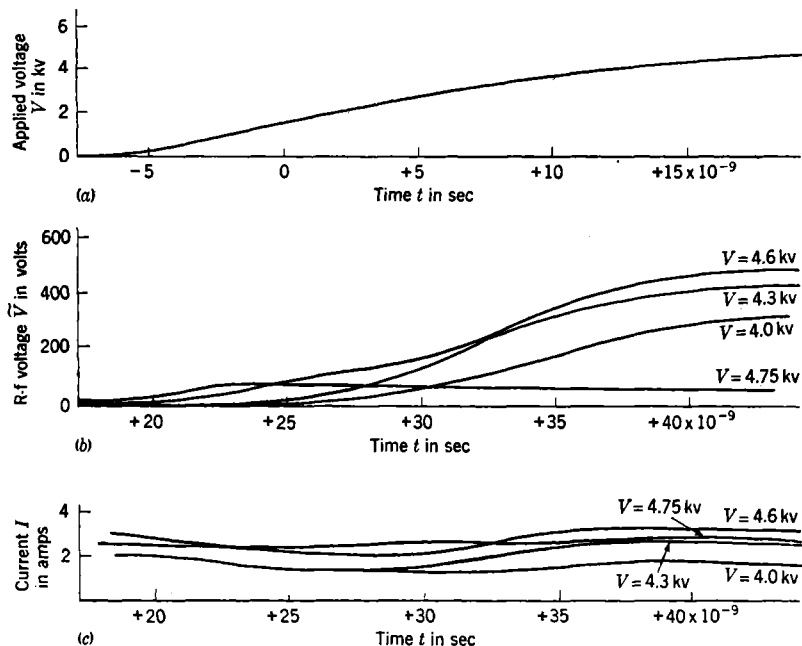


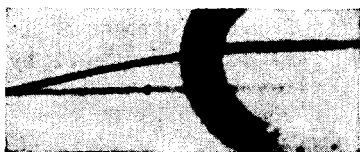
FIG. 8-40.—The buildup of magnetron current and r-f voltage through the operating range of applied voltage. (a) Typical applied voltage; (b) envelopes of r-f oscillations for different voltages; (c) tube currents for different applied voltages. (The ordinate is the voltage developed at the oscillograph, and is *proportional* to the r-f voltage within the magnetron.)

the development<sup>2</sup> of an oscillograph with a "resolving time" smaller than  $10^{-10}$  sec. The instrument actually consists of three oscillograph systems that record on the same photographic plate simultaneously. Thus it is possible to record, for a single isolated pulse, the r-f output and the input current and voltage as functions of time.

<sup>1</sup> For a more complete report of the experiments, see R. C. Fletcher and G. M. Lee, NDRC 14-543, November 1945.

<sup>2</sup> By G. M. Lee, in the Insulation Research Laboratory of Massachusetts Institute of Technology.

The aim of these experiments was to investigate the speed of buildup as a function of the applied voltage. This was to be done by applying a rapidly rising voltage pulse, so that the buildup would occur at essentially constant voltage, as along path *D* in Fig. 8-30a. From such results, it would be possible to derive  $G_e$  as a function of  $V$  in the neighborhood of the ( $\tilde{V} = 0$ )-curve.



(a)



(b)



(c)

FIG. 8-41.—Typical oscillograms of the high-speed oscillograph. (a) Applied voltage; (b) r-f oscillations; (c) tube current.

One series of experiments was performed with the  $\frac{1}{8}$ - $\mu$ sec pulser that had been used for Figs. 8-32 and 8-33. Figure 8-40 shows typical voltage, r-f and current pulses as obtained from measurements of oscillograms like those in Fig. 8-41. (The r-f and current pulses for 4.75 kv are peculiar and will be explained later.) It is evident that the pulser is rather slow for the present purpose, for, as is shown by the overlapping of the charging current and the buildup current in Fig. 8-40c, the buildup of oscillations has proceeded quite far before the applied voltage stops rising.

The rate of buildup can be represented conveniently by plotting the

logarithm of the amplitude of successive oscillations against the ordinal number of the cycle, as is done in Fig. 8-42 for the same traces as were used for Fig. 8-40. Within the limits of experimental error, the curves (except that for 4.75 kv) approach a straight line at low r-f voltages, which indicates that the oscillations build up exponentially at first, that is, according to the law  $\tilde{V} \propto e^{at}$ , where  $a$  is positive.<sup>1</sup> From the slope of the straight-line portion of the curve the "buildup  $Q$ "  $Q_B$  may be computed according to the relation

$$\frac{1}{Q_B} = \frac{-2.30 \Delta \log_{10} \tilde{V}^2}{2\pi \Delta N} \quad (18)$$

Values of  $Q_B$  so obtained, from Fig. 8-42 and from additional data of the same sort, are plotted against  $V$  in Fig. 8-43. (Here  $V$  is taken equal to the maximum value reached by the applied voltage.)

<sup>1</sup> It should be emphasized that this law of buildup is entirely different from that for a parallel-resonant circuit suddenly connected to a constant-current source, in which  $\tilde{V} \propto (1 - e^{-at})$ .

Above 4.6 kv the curves were peculiar, somewhat like the 4.75-kv curve of Fig. 8-40, and it was not possible to derive values of  $Q_B$  from them. The horizontal portion of the 4.75-kv curve in Fig. 8-40b does not represent a true stable state of oscillation, for it is common at the higher applied voltages for the curves to stop rising and then start in

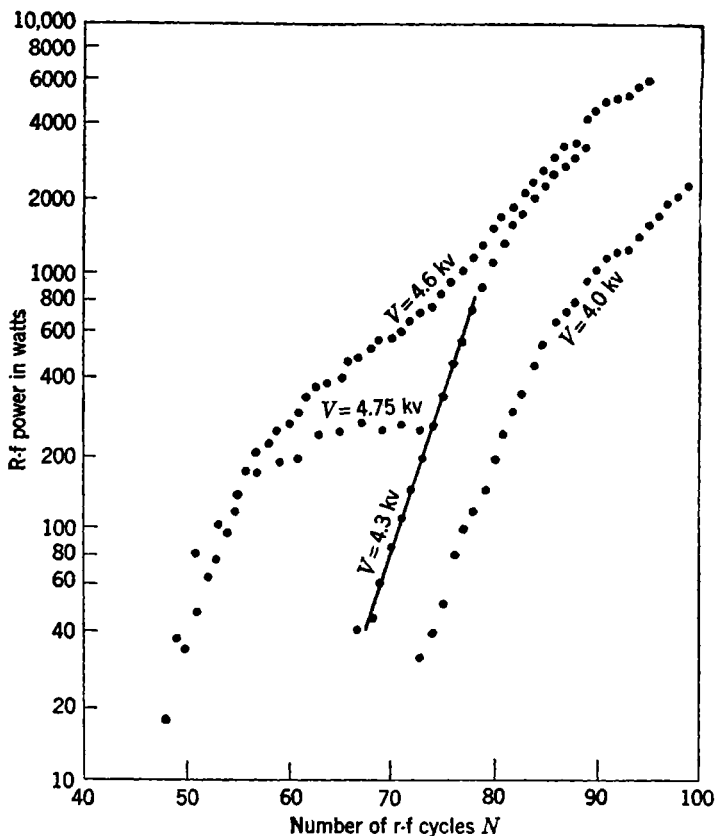


FIG. 8-42.—Logarithmic plots of the r-f envelopes shown in Fig. 8-40b.

again. This behavior may be interpreted to mean that the  $(V, I)$ -point follows a path that is very nearly tangent to the upper boundary of the positive- $\xi$  region.

From the results one can conclude that the buildup is exponential in its early stages, that  $-Q_B$  is about 25 in the middle of the starting range, and that  $-Q_B$  tends to decrease at lower applied voltages. A more complete analysis would be difficult, because the applied voltage

varies considerably during buildup and its variation would have to be measured very precisely.

**8-11. Effect of Design and Operation on Starting.**—In succeeding paragraphs an attempt is made to enumerate the various factors entering

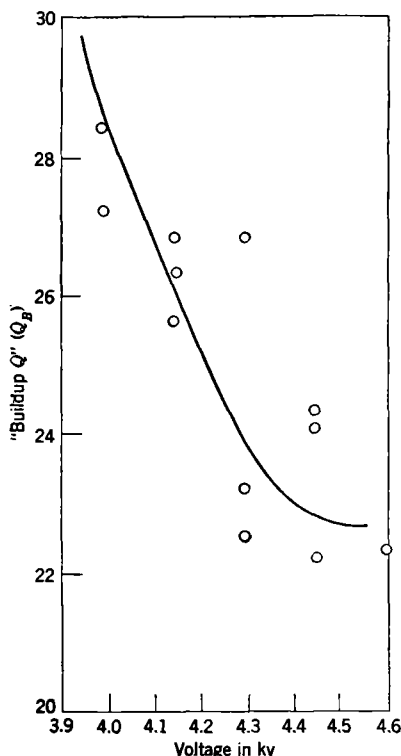


Fig. 8-43.—The "buildup  $Q$ " as a function of applied voltage.

into the design and operation of magnetrons that are related to starting and misfiring. The discussion applies only to cases in which interactions between modes are not important. According to the considerations of Sec. 8-8, it should be possible to reduce the tendency toward misfiring by (1) increasing the amplitude of the noise, (2) increasing the rate of buildup as measured by  $-1/Q_B$ , and (3) increasing the time interval during which the applied voltage remains within the starting range. Whatever information there is has to be obtained from over-all effects such as the location of the current boundary on the performance chart where mode changes occur. Because detailed observations are lacking, it is not always possible to form a very clear picture of how the primary factors mentioned above are involved.

Some caution should be exercised in drawing conclusions from observations on mode changes.

For instance, it has been rather common practice to describe this aspect of magnetron performance by drawing a "mode boundary" on a performance chart. The results already presented show that this boundary is not a property of the magnetron alone but rather of a specific combination of magnetron and pulser. Also, it must be remembered that misfiring is a threshold phenomenon and that just at the threshold small influences can lead to large effects. Magnetrons that are prone to skip modes are obviously those which have at best a narrow margin of starting speed, so it should not be surprising if such tubes prove sensitive in some degree to almost any sort of variation in construction and operating conditions.

*The R-f Load.*—Heavy loads, according to general observations, result in a reduction of the current at which misfiring takes place. This behavior is not at all surprising, but the primary factors listed above seem to enter in a rather obscure fashion. There is perhaps some reason to believe that the load should not have a strong effect on the noise level. At least, if the noise does behave like the shot effect, the voltage amplitude of the noise should depend on the effective capacitance of the circuit and not on its  $Q$ . Furthermore,  $Q_B$  should not be strongly affected by such changes in load as are ordinarily met. For instance, if it is assumed that  $Q_B$  is equal to  $-25$  when the loaded  $Q$  is equal to  $150$ , the relation between  $Q_B$  and  $Q_L$  is as indicated in Table 8-1.

TABLE 8-1.—RELATION BETWEEN  $Q_L$  AND  $Q_B$ 

$Q_L$	300	150	100	75	50	30
$Q_B$	-23	-25	-27	-30	-37	-75

Ordinarily, such extreme loads as are represented by the last two columns in Table 8-1 are not applied in practice. Thus it appears that the more important direct effects of heavy loads are to restrict somewhat the starting range and, more important, to raise the steady-state characteristic, so that a higher voltage must be applied to the tube in order to obtain a given current.

It is common in experimental work and in testing to vary the load by means of transformers in the output transmission line. When rapid transients are involved, the effect of the transformer can be expected to depend quite appreciably on the distance between the transformer and the coupling loop. If the reflection coefficient at the magnetron is equal to  $q$  for steady-state oscillations, then for oscillation increasing in amplitude as  $\exp(-\omega t/2Q_B)$ , the reflection coefficient is equal to  $q \exp(\omega l/v_g Q_B)$ , where  $v_g$  is the group velocity in the transmission line and  $l$  is the distance from the magnetron to the transformer. In coaxial line,  $v_g = \lambda\omega/2\pi$ , and the factor is  $\exp(2\pi l/\lambda Q_B)$ ; for  $l/\lambda = 1$ , which might apply to a fixed transformer put as close as possible to the magnetron, the reflection coefficient is reduced in the ratio of 0.78; and for  $l/\lambda = 5$ , which might apply to a test bench with a standing-wave detector between the magnetron and a variable transformer, the factor is 0.28 if  $Q_B$  is assumed to be  $-25$ .

*The Effective Capacitance of the Resonant Circuit.*—Other things being equal, the speed of buildup is inversely proportional to the capacitance  $C$ . In addition it seems likely that the capacitance influences the amplitude of the noise voltage; for in so far as one can judge by the behavior of the shot effect, the amplitude of the noise voltage should be inversely proportional to  $C$ . Thus, from the standpoint of starting, it is desirable

that  $C$  be made small. On the other hand, if  $C$  is made small and at the same time the loading is adjusted for high efficiency, the frequency becomes unstable against changes in load, so that some compromise has to be made.

At first thought it might be expected that highly stabilized magnetrons—for instance, those which have an external stabilizing cavity—would tend to start very slowly, since the effective capacitance is increased in proportion to the stabilization factor. Actually the “stabilizing resistor” that is used in such arrangements to damp out extraneous resonances must to some extent isolate the magnetron from the high- $Q$

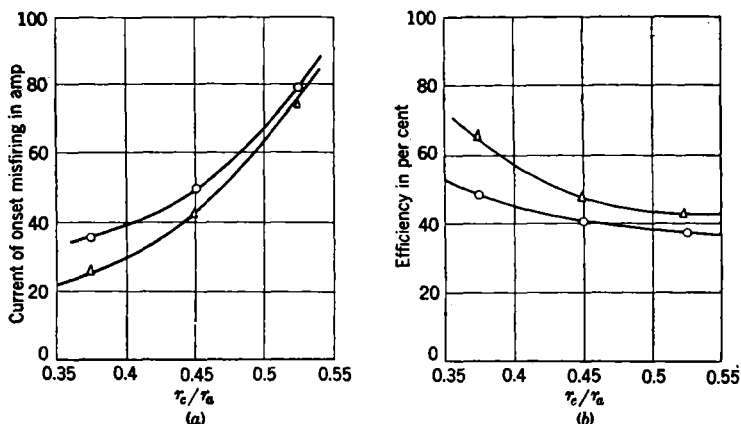


FIG. 8-44.—Effect of cathode diameter on (a) misfiring and (b) efficiency. Circles are for 45 per cent loop; triangles for 60 per cent loop.

cavity as far as rapid transients are concerned. There should be some tendency for the magnetron to build up at nearly its normal rate and for equilibrium between the magnetron and the cavity to be established more slowly.

**Diameter of the Cathode.**—It has been observed with several types of magnetrons that increasing the diameter of the cathode reduces the tendency toward misfiring. This effect is illustrated by Fig. 8-44a, which represents data obtained at the Bell Telephone Laboratories<sup>1</sup> for an eight-oscillator 25-cm magnetron. The curves of Fig. 8-45b show the effect of the cathode diameter on the efficiency and demonstrate, in accord with general observation, that enlarging the cathode tends also to reduce the efficiency of the magnetron, so that again the design must be based on a compromise.

<sup>1</sup> H. D. Hagstrum, W. B. Hebenstreit, and A. E. Whitcomb, “On the Maximum Current Limitation Encountered in L-band Magnetrons,” Case 24375-2, *BTL Memorandum* MM-45-2940-2, June 25, 1945.



**Cathode-end Structures.**—Some experiments by Forsberg<sup>1</sup> indicate that the details of the structures at the ends of the cathode—put there for the purpose of confining the electrons to the interaction space—exert a considerable influence on the tendency to misfire. The experiments started from the observation that a partial correlation could be made between current at onset of misfiring and “leakage current”; some of the tubes that had the least tendency to misfire were those which had a steady-state characteristic that fell off gradually at low currents, more or less as illustrated by Curve A in Fig. 8-45, rather than ones with a sharp break such as is indicated by Curve B. Attention was then directed toward inventing end structures that would accentuate the leakage but would not reduce the efficiency in the range of currents where the tube normally operated. It was found that a slight enlargement of the cathode for a small distance at the ends served the purpose. The leakage was effective only if it occurred within the interaction space. Larger end disks were retained to confine the space charge; details of the structures are described in Chap. 12. Forsberg further found some indication that the tubes which showed the least inclination to misfire also had the greatest noise levels; his curves indicated differences as great as 20 db. However, the observations were not sufficiently detailed to warrant the conclusion that this is the only effect which is involved.

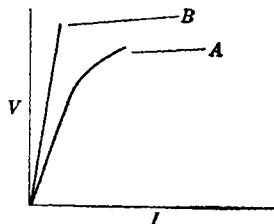


FIG. 8-45.—A study of misfiring based on steady-state characteristics. Tubes of Type A show more tendency to misfire than tubes of Type B.

**Cathode Emission.**—With some magnetrons, the tendency to misfire is correlated to some extent with low primary emission of electrons from the cathode. However, it is difficult to understand why the tendency to misfire should be very much affected by the condition of the cathode unless the condition is very poor, for the observations with the ( $V, I$ )-scope indicate that the conditions leading to either misfiring or complete buildup are established before the current has built up very far. (Of course, a correlation should be expected if what is occurring is a mode *shift* early in the pulse.) Otherwise it may be a secondary effect—for instance, if inadequate emission raises the steady-state characteristic (as in Fig. 8-20), it will also result in the application of a higher voltage when comparison is made on the basis of constant steady-state current. Magnetrons that do not ordinarily skip modes (presumably those which start very rapidly) seem generally to function satisfactorily even when the primary emission of the cathode is very low.

<sup>1</sup> According to private communication from P. W. Forsberg.

*Uniformity of the Magnetic Field.*—Nonhomogeneities in the magnetic field can have a pronounced effect on the tendency to misfire. For instance, the 2J39 was improved to a marked degree by making a slight change in the magnet poles that reduced the excess of magnetic field at the ends of the interaction space. The original inhomogeneity presumably caused a strong concentration of the space charge at the middle of the interaction space. Effects of nonuniform and nonaxial fields on starting have been observed on many occasions.

*The Pulser.*—The principal means available for correcting misfiring in any completed magnetron is control of the input conditions. If it can be so arranged that the open-circuit voltage of the pulser falls within the starting range, no difficulty with misfiring should be experienced; but when the magnetron has to be operated at a relatively high current, or when the use of a high-impedance pulser is dictated by other considerations, there exists some possibility that misfiring may occur. To eliminate the misfiring, one must, in essence, reduce the rate at which voltage is applied to the magnetron, but this is only a qualitative statement of the requirements. A precise statement of the conditions just sufficient to ensure reliable starting could be made only on the basis of a thorough understanding of the effects of the reactances in the input circuit. An analysis of these effects could be made by extending the methods developed in Sec. 8-8, but such a program would undoubtedly involve very extensive calculations. For further discussion of pulsers, the reader is referred to Vol. 5 of the Radiation Laboratory Series.

**8-12. Interactions between Modes.**—The preceding sections have dealt with a more or less ideal magnetron—one purposely designed to have so great a mode separation that as far as operation in the principal mode was concerned, the existence of other modes could be ignored completely. In practice, magnetrons have to be designed to meet other specifications, and it may be impossible, with existing techniques, to meet those specifications and at the same time make the mode separation great enough to fulfill the condition mentioned above. Therefore it is important to inquire how, in such cases, the transient behavior and the stability of the principal mode can be affected by interactions with other modes, even though this inquiry must be largely speculative.

It seems obvious that an interaction between modes must introduce a considerable additional degree of complexity into the phenomena treated in Secs. 8-8 and 8-9, so perhaps it should not be surprising that reliable experimental data are exceedingly scarce. In most of the early work on mode selection, it seems that it was taken for granted that any mode change could be interpreted exclusively in terms of an interaction between the two modes. Since it is now known that misfiring and instability can occur entirely independently of such causes, all conclusions

about interaction which are based on the mere observation that a mode change does or does not take place should be regarded with skepticism.

If one excludes from consideration purely electromagnetic interactions which can be investigated by cold-resonance methods, an interaction between modes can take place under normal operating conditions (i.e., no *external* source of r-f power) only if two modes are excited simultaneously by the space charge. The simultaneous excitation of two modes occurs only as a transient, for as had been mentioned previously in this chapter, it is never observed under steady-state conditions.<sup>1</sup> Evidently the nonlinearities of the space charge are of such a nature that oscillation in two modes represents an unstable condition when the amplitudes of oscillation become large.

Ways in which an instability of this sort may come about can be illustrated by extending the analysis outlined in Sec. 8-8 to include simultaneous oscillation in two modes. It is assumed that one has to deal with two modes that have different values of  $n$  and that no interaction other than that which enters through the space charge need be considered. Because the modes have different frequencies and their electromagnetic fields are of distinct types, the excitation of each mode can be characterized by an r-f voltage and an electronic admittance. The admittance for frequencies in the neighborhood of the resonance of a mode behaves like that of a parallel-resonant circuit; thus the complete system can be represented by the equivalent circuit shown in Fig. 8-46.

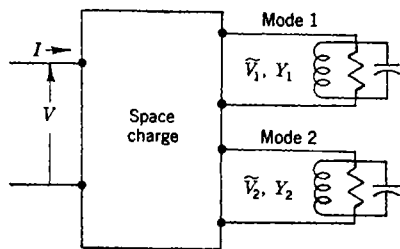


FIG. 8-46.—Equivalent circuit for the simultaneous excitation of two modes.

The nonlinearity of the space charge, which for one mode is expressed by the dependence of the admittance on the r-f voltage, is for two modes expressed by a dependence of each of the admittances on both r-f voltages as well as upon the input voltage  $V$ . In addition, the input current is dependent on both r-f voltages as well as upon the input voltage  $V$ . The magnetic field enters as a parameter that need not be expressed, and the electronic susceptance may be ignored, because small shifts in frequency are not of interest. Thus the space charge can be described by the relations

$$G_{e1} = G_{e1}(V, \tilde{V}_1, V_2), \quad (19)$$

$$G_{e2} = G_{e2}(V, \tilde{V}_1, \tilde{V}_2), \quad (20)$$

$$I = I(V, \tilde{V}_1, \tilde{V}_2). \quad (21)$$

<sup>1</sup> The observation of a relatively weak noise spectrum at the frequency of a second mode is not considered to indicate excitation in the present sense.

The transient behavior is governed by the relations

$$\frac{d}{dt} \ln \tilde{V}_1 = - \frac{(G_{e1} + G_{L1})}{2C_1}, \quad (22)$$

$$\frac{d}{dt} \ln \tilde{V}_2 = - \frac{(G_{e2} + G_{L2})}{2C_2}, \quad (23)$$

$$V = V(I, t), \quad (24)$$

where Eq. (24) describes the properties of the pulser.

Some idea of the nature of the solutions of the above set of equations can be obtained by following through a somewhat idealized special case which can be treated by graphical methods. It is assumed that the open-circuit voltage of the pulser rises so rapidly that it can be approximated by a step function, with the result that the entire buildup takes place along a fixed curve—the steady-state pulser characteristic—in the  $(V, I)$ -plane, and Eq. (24) can be replaced by

$$V = V' - f(I). \quad (25)$$

(This is the analogue of the case represented by Curve *D* of Fig. 8-30a.) By combining Eqs. (21) and (25),  $I$  can be eliminated and  $V$  can be expressed as a function of  $\tilde{V}_1$  and  $\tilde{V}_2$ ; consequently  $G_{e1}$  and  $G_{e2}$  can be expressed as functions of  $\tilde{V}_1$  and  $\tilde{V}_2$  only. Thus when substitutions corresponding to Eq. (7) are made, Eqs. (22) and (23) take the forms

$$\frac{d}{dt} \psi_1 = \xi_1(\psi_1, \psi_2), \quad (26)$$

$$\frac{d}{dt} \psi_2 = \xi_2(\psi_1, \psi_2). \quad (27)$$

The course of the transient can be followed by tracing the path of the point  $(\psi_1, \psi_2)$  in the  $(\psi_1, \psi_2)$ -plane; the differential equation for the path is

$$\frac{d\psi_1}{d\psi_2} = \frac{\xi_1(\psi_1, \psi_2)}{\xi_2(\psi_1, \psi_2)}. \quad (28)$$

The solution of Eq. (28) will contain the initial values of  $\psi_1$  and  $\psi_2$  which represent the noise voltages that exist in the respective modes at the time buildup starts.

If the functions  $\xi_1$  and  $\xi_2$  are represented by a contour map, the solutions can be traced out as illustrated<sup>1</sup> in Fig. 8-47. The initial noise voltages in the respective modes can be represented by a density distribution of points  $(\psi_1, \psi_2)_0$  (which presumably are concentrated somewhere

<sup>1</sup> Equation (28) and diagrams of the general type of Fig. 8-47 were originally applied to the present problem by Arnold Nordsieck in some informal lectures at the Radiation Laboratory.

in the lower left region of Fig. 8-47). The probability that the system will follow some path that lies between any two given paths is directly proportional to the number of points  $(\psi_1, \psi_2)_0$  that are contained between those two paths; this is the form of the final result.

The contours of  $\xi_1$  and  $\xi_2$  in Fig. 8-47 have been drawn on the basis of the following considerations. It seems entirely reasonable to suppose that when either r-f voltage is small, the space charge should be linear

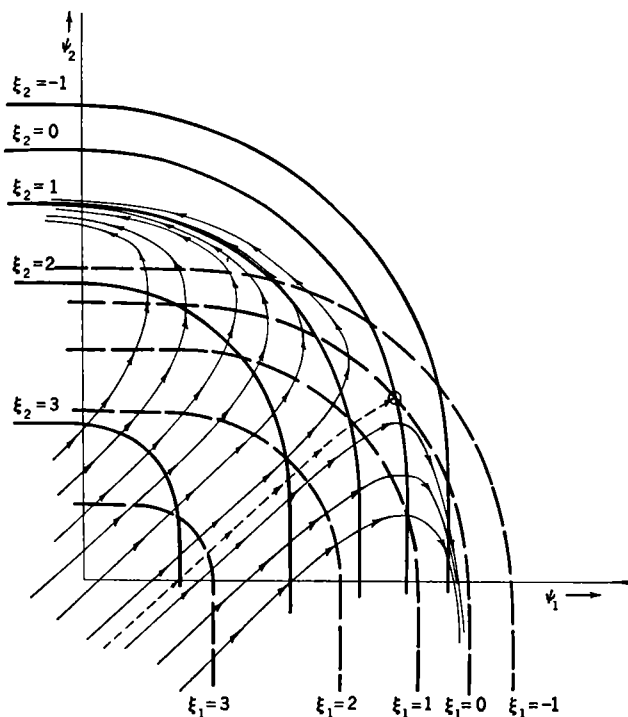


FIG. 8-47.—Contours of  $\xi_1$  and  $\xi_2$  in the  $(\psi_1, \psi_2)$ -plane.

with respect to that voltage. Thus, when  $\psi_1$  is small, both  $\xi_1$  and  $\xi_2$  are independent of  $\psi_1$ , and the dependence of  $\xi_2$  on  $\psi_2$  is the same as if Mode 1 did not exist. It is further assumed—and this is open to question—that when  $\xi_1$  and  $\xi_2$  are both large so that nonlinear effects become important, the dependence of  $\xi_2$  on  $\psi_1$  is stronger than its dependence on  $\psi_2$ ; similarly with the subscripts interchanged. Figure 8-47 is supposed to represent a case in which the two modes would have nearly coincident conductance maps if interactions were not present and in which the pulser characteristic passes near the centers of the starting ranges.

According to Fig. 8-47 the system has zero probability of arriving at the intersection of the ( $\xi = 0$ )-contours—which conceivably might represent a stable state of simultaneous oscillation in two modes—because out of the infinity of orbits leaving the lower left part of the diagram, only one orbit proceeds to the intersection. This result is a consequence of the fact that the contours have been drawn in such a way that certain requirements for stability are not fulfilled at the intersection. By making approximations similar to those made in deriving Eq. (12), it can be shown that operation at the intersection can be stable only if the following conditions are fulfilled at that point:

$$\begin{aligned} \frac{\partial \xi_1}{\partial \psi_1} + \frac{\partial \xi_2}{\partial \psi_2} &< 0 \\ \frac{\partial \xi_1}{\partial \psi_1} \frac{\partial \xi_2}{\partial \psi_2} - \frac{\partial \xi_1}{\partial \psi_2} \frac{\partial \xi_2}{\partial \psi_1} &> 0. \end{aligned} \quad (29)$$

If these conditions are fulfilled, orbits that pass within the neighborhood of the intersection will also reach the intersection. In so far as simultaneous steady oscillation in two modes is not observed, it would appear that relations (29) are in contradiction to some inherent property of the space charge. A more rigorous treatment of the input circuit would undoubtedly lead to additional requirements for stability.

A further development would consist in finding how the mode selection is influenced by operating conditions such as the magnetic field, the r-f loads on the respective modes, the open-circuit voltage and the internal resistance of the pulser. All of these variables enter into the values of  $\xi$  as parameters; in addition, some of them may influence the noise distribution. Still other problems arise in connection with the design of magnetrons, and one might inquire how the values of  $\xi$  and thus the mode selection are influenced by the separation of the modes and the character of their field patterns in the interaction space.

So far, the discussion has been based on an idealization, namely, that the buildup occurs along a stationary pulser characteristic. As shown in the closing paragraphs of Sec. 8-9, this approximation is rather poor. With an applied voltage that rises during buildup, the values of  $\xi$  depend explicitly on the time, and the contours of Fig. 8-47 have to be thought of as moving about during the transient. An important problem that arises in this connection is that of the effect of mode interactions on starting time. For instance, as between two modes that interact, the undesired mode may never win out, but the interaction may have the effect of slowing down the buildup to such an extent that there is an abnormally great tendency toward misfiring. Or the interaction might conceivably produce the opposite effect.

Inasmuch as the strapping of magnetrons has received much promi-

nence as a device for controlling mode selection, it seems worth while to consider how the functions of the straps are related to the considerations advanced above. The primary function of the straps undoubtedly is to tighten the coupling between the individual oscillators of the cavity; this effect naturally results also in increased separations between the frequencies of the modes. In addition, the straps afford the possibility of exercising some measure of control over the loading of the various modes and over their patterns in the interaction space. Symmetrical straps, such as unbroken rings, regularize the patterns of all the modes. Asymmetrical straps, such as broken rings, separate the members of the doublet modes from each other in frequency and tend to deteriorate the patterns of all the modes; however, the asymmetries can be so designed as to distort the  $(N/2)$ -mode much less than the other modes. The orientation of the asymmetries, relative to the coupling loop, determines whether only one or both of the members of a separated doublet will be coupled to the external load.

In so far as there may be present some interaction between the  $(N/2)$ -mode and an undesired mode, it would seem advantageous to distort the pattern of the unwanted mode and thus "handicap" that mode. In addition it would seem desirable that the unwanted mode should be damped to some extent by being coupled to the external load. On the basis of these arguments, strap breaks have been incorporated into many magnetrons. In most cases, the introduction of the breaks definitely affects the behavior of the magnetron, but there are not available sufficient data to show whether the effects are attributable to the patterns, the loading, the removal of the degeneracy, or simply the quite appreciable change in mode separation that occurs when the straps are broken. Certainly strap breaks should not be considered at all as a remedy for misfiring in the type of situation presented by the LL3.

The mode that usually gives trouble of the sort that might be attributed to an interaction is the  $\left(\frac{N}{2} + 1/\frac{N}{2} - 1/N\right)$ -mode, for it so happens that in many magnetrons this mode and the  $\left(\frac{N}{2}/\frac{N}{2}/N\right)$ -mode have nearly equal values of  $\gamma\lambda$ , and thus have overlapping starting ranges. The values of  $\gamma\lambda$  are exactly equal when the wavelength of the  $\left(\frac{N}{2} + 1/\frac{N}{2} - 1/N\right)$ -mode is just  $N/(N+2)$  times that of the  $\left(\frac{N}{2}/\frac{N}{2}/N\right)$ -mode—for instance, 0.8 for eight oscillators, 0.86 for twelve—and it so happens that in high-voltage magnetrons it is difficult to

make the mode separation very different from this value. Moreover, the  $\left(\frac{N}{2} + 1/\frac{N}{2} - 1/N\right)$ -mode frequently seems to have considerable vitality.

One type of behavior is common to the following magnetrons: 2J38, 2J39, 4J33, and 720. In all these magnetrons the  $\left(\frac{N}{2} + 1/\frac{N}{2} - 1/N\right)$ -mode has a slightly larger  $\gamma\lambda$  (lower voltage) than the  $\left(\frac{N}{2}/\frac{N}{2}/N\right)$ -mode, and the straps have breaks. All of the tubes exhibit mode changes at low currents; that is to say, the  $\left(\frac{N}{2} + 1/\frac{N}{2} - 1/N\right)$ -mode is excited if attempts are made to run the tube at too low a current in the  $\left(\frac{N}{2}/\frac{N}{2}/N\right)$ -mode. To some extent, the behavior can be interpreted on the basis of the starting voltages. If the applied voltage is above the starting voltage of the  $\left(\frac{N}{2} + 1/\frac{N}{2} - 1/N\right)$ -mode but below that of the  $\left(\frac{N}{2}/\frac{N}{2}/N\right)$ , the former is excited; if the applied voltage enters the starting range of the  $\left(\frac{N}{2}/\frac{N}{2}/N\right)$ -mode, that mode takes control. From this argument one should expect that with a very slow rise of voltage, operation in the  $\left(\frac{N}{2} + 1/\frac{N}{2} - 1/N\right)$ -mode could be pushed to higher currents. Examination of the  $(V, I)$ -traces of a 2J32 magnetron, however, showed that very complicated intrapulse transitions occurred. With a more rapid rate of rise of voltage, the starting behavior of these magnetrons in the normal operating range is like that of the LL3.

The 725 and 2J42 magnetrons have mode separations similar to those of the tubes listed above and have broken straps, but these tubes show no tendency at all to oscillate in the  $\left(\frac{N}{2} + 1/\frac{N}{2} - 1/N\right)$ -mode. Omission of the strap breaks in the 2J42 was found to have no effect on its behavior. Qualitatively, the starting in these tubes is entirely similar to that of the LL3, although the 725 starts so rapidly that it is exceedingly difficult to make it misfire.

A third type of behavior was observed in two experimental 4J33 magnetrons from which strap breaks had been omitted. The  $\left(\frac{N}{2}/\frac{N}{2}/N\right)$ - and  $\left(\frac{N}{2} + 1/\frac{N}{2} - 1/N\right)$ -modes had voltages so nearly



equal that they could just be distinguished in the  $(V, I)$ -scope. There was a skip between these two modes, quite independently of whether a rapidly or slowly rising pulse was applied, and both modes persisted to very high currents. Apparently this is a case in which two modes overlap so perfectly that the interaction diagram (Fig. 8-47) preserves its general symmetry for all possible positions of the pulser characteristic.

The first and last sets of examples give some indication of how the effect of interaction depends upon the mode separation, although the difference between the first and second set of examples remains unexplained. It would not seem too difficult to invent interaction diagrams that would account for the peculiar phenomena illustrated in Fig. 8-16.

## CHAPTER 9

### NOISE

BY F. F. RIEKE

**9-1. Introduction.**—The problems that involve the noise-generating properties of the magnetron appear to be of two rather distinct types. In one sort of problem the noise is of interest as the starting point for the buildup of coherent oscillations. In the other type of problem the noise is of concern as one of the factors in the signal-to-noise ratio of the steady-state oscillations of the magnetron.

It is emphasized in Chap. 8 that the "starting time" of a magnetron bears a close relation to the maximum rate at which the input voltage can be applied without causing the magnetron to misfire. The starting time, in turn, is determined by two factors, each equally important, namely, the noise-level from which the buildup of oscillations starts and the rate of buildup. Thus the matter of noise generation enters into the problem of mode selection, and it was primarily in this connection that studies of noise in magnetrons was taken up in the Radiation Laboratory. A rather special problem, closely related to the more general one just mentioned, is concerned with the practicability of establishing phase coherence between successive pulses by "priming" the pulsed magnetron with power derived from a stable source of c-w oscillations. An important consideration in any application of this device is the amount of c-w power required to ensure a specified degree of coherence. It seems reasonable to suppose that the voltage from which buildup starts is the vector sum of the c-w voltage (of constant phase) and the noise voltage (of random phase). On this basis the c-w power required to ensure a given degree of coherence between the pulses can be related to the noise-power normally present in the magnetron.

The second type of problem—that of signal-to-noise ratio—was encountered (in the RCA Laboratories) in developing a c-w magnetron for a special sort of radar that required part of the transmitted signal to be fed into the receiver as local-oscillator power. In this case the over-all signal-to-noise ratio of the system is strongly dependent upon that of the *transmitter*, a circumstance quite different from the one met with in the more conventional pulse radars. Although the case just mentioned is a rather specialized one, similar problems very likely will be encountered in any attempt to adapt magnetrons for use as local oscillators, and it is

not unlikely that the magnetron will be given serious consideration for that purpose for frequencies somewhat above 30,000 Mc/sec. In addition, there is already some indication that signal-to-noise ratio in magnetron transmitters will be an important consideration in the adaptation of these tubes to wideband communication systems.

Considered from a more theoretical standpoint, studies of noise may provide an additional means of investigating conditions within the electron stream in the magnetron, a matter far from settled by existing theoretical treatments. This possibility has been pointed out previously in a paper by Linder<sup>1</sup> on the evaluation of the electron temperature in single-anode magnetrons. Linder found that probe measurements and also the results of an analysis of the cutoff curves in single-anode magnetrons indicated electron temperatures of the order of  $10^{50}$ , and he suggested that so high a degree of disorder in the electron stream should also manifest itself in the noise-generating properties of the magnetron.

The actual investigation of noise in magnetrons has been taken up only recently, however, and it is not possible to discuss the subject with very much assurance. It is hoped, nevertheless, that the present chapter may be of value in giving some indication of the present status of the subject.

**9-2. Preoscillation Noise.**—The noise that occurs in magnetrons before coherent oscillations start is of practical interest in connection with pulsed magnetrons. Because of experimental difficulties, however, it was possible to make only crude measurements of the noise in pulsed magnetrons. Conditions for measurement are much better in the case of c-w tubes; and as there is no fundamental difference between the two kinds of magnetron, the c-w measurements will be described in greater detail.

The measurements were made on a series of tubes that had similar oscillator structures<sup>2</sup> but varied considerably in the construction of the "hats," or end disks, placed at the ends of the cathode to confine the electron stream to the interaction space. (It was not apparent that these modifications caused any significant differences in the behavior of the noise.) The magnetron was pumped continuously. A spectrum analyzer, with a pass band of 0.1 Mc/sec, was used to measure both the power and the bandwidth (between half-power points) of the noise. In computing the noise power, the power per unit frequency interval observed at the center of the spectrum was multiplied by  $\pi/2 \times W$ , where  $W$  is the width of the spectrum in megacycles per second between half-power points.

<sup>1</sup> Linder, E. G., *Jour. Applied Phys.*, **9**, 331 (1938).

<sup>2</sup> The magnetron was a 9.8-cm, 20-oscillator tube, with  $V_0 = 175$  volts,  $B_0 = 399$  gauss,  $I_0 = 0.31$  amp.

The results of a representative experiment are shown in Fig. 9-1, where bandwidth, power, and input current are plotted against the

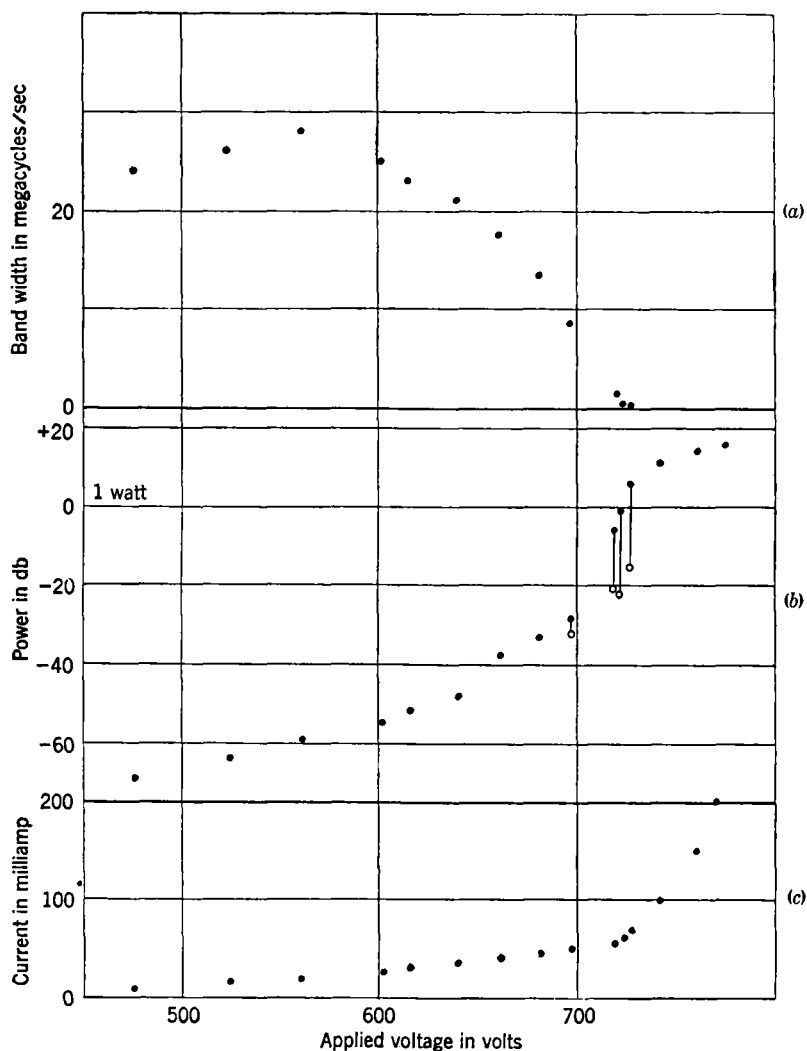


Fig. 9-1.—(a) Bandwidth, (b) noise power, and (c) input current as a function of applied voltage for a magnetic field of 960 gauss.

applied voltage for a magnetic field of 960 gauss. For voltages below 600 the bandwidth is about 27 Mc/sec—roughly consistent with the loaded  $Q$  of the magnetron ( $Q_L = 160$ ,  $\Delta\nu = \nu_L/Q_L = 19$  Mc/sec).

As the applied voltage approaches 722, the power rises rapidly and the bandwidth goes sharply to zero. (Actually, of course, it is not possible to measure the half-value width when it becomes less than the pass band of the analyzer.) At 722 volts the input current also starts to increase rapidly, and this point may be considered to be the critical voltage where self-sustained oscillations begin.

Observations on pulsed magnetrons indicate crudely the same sort of behavior as that described above. In one respect the pulsed tubes differ—the current increases discontinuously at the critical voltage, as is illustrated in Fig. 8-36. This discontinuity shows up in some c-w magnetrons and not in others, for reasons so far not understood.

The phenomena just described can be interpreted in the following way. The space charge generates a (noise current)<sup>2</sup> per unit frequency interval (denoted by  $di_n^2/d\nu$ ), that is a slowly varying function of the frequency. Inasmuch as the noise current is substantially constant over the frequency interval  $\nu/Q$ , the observed noise spectrum is simply the constant-current response of the resonant system of the magnetron expressed in terms of power. The variations in the bandwidth are attributed to the changes in the  $Q$  of the system caused by electron loading, which can be described in terms of the electronic conductance  $G_e$  discussed in Chaps. 7 and 8. The  $Q$  of the system is given by the relation

$$Q = \frac{Q_L G_L}{G_L + G_e}.$$

The narrowing of the spectrum just below the critical voltage, according to this interpretation, means that  $G_e$  is negative in this range. To check this hypothesis, impedance measurements were made “looking into” the magnetron while voltages below the critical value were applied to it.<sup>1</sup>

The normalized conductance  $g_0$  of the magnetron at resonance is given by the expression

$$g_0 = \frac{G_U + G_e}{G_E} = \frac{G_U + G_e}{G_L - G_U}.$$

As  $G_e$  becomes increasingly negative, starting from zero,  $g_0$  decreases from the value  $G_U/G_E = Q_E/Q_U$  to zero, then changes sign and becomes increasingly negative. (It is to be expected that when  $g_0$  becomes equal

<sup>1</sup> Except for the fact that the electron stream is present in the magnetron, these measurements are similar to “cold-impedance measurements.” Since the signal used in the measurements falls entirely within the pass band of the analyzer, the deflection produced by the signal greatly exceeds that produced by the noise even though the signal power is of the same order of magnitude as the noise power generated by the magnetron.

to  $-1$ , the system will break into sustained oscillations, and from then on the nonlinearity of the space charge will be the controlling factor.) From the impedance measurements one obtains  $\rho_0$ , the standing-wave ratio at resonance, and

$$\frac{1}{\rho_0} = |g_0|$$

provided  $|g_0| < 1$ , as was always the case in this experiment. Thus there is in principle an ambiguity in the sign of  $g_0$  as determined by the standing-wave measurements.

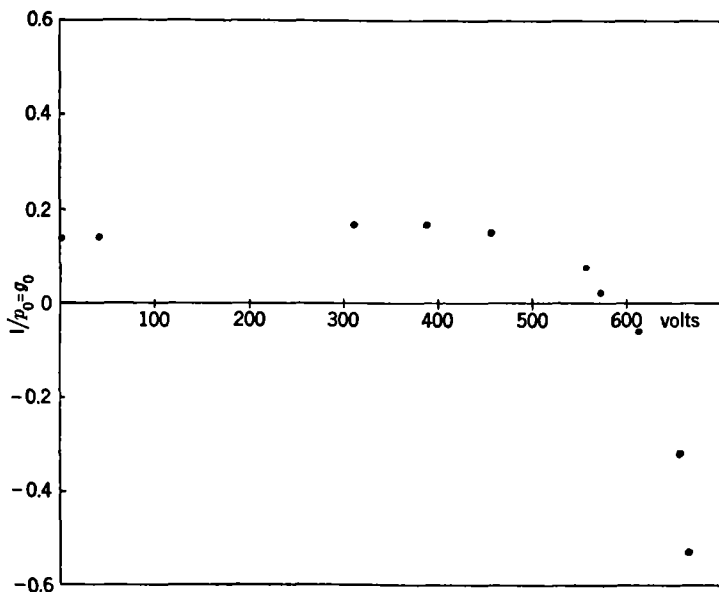


FIG. 9.2.—The standing-wave ratio at resonance  $\rho_0$  as a function of the applied voltage.

The values of  $\rho_0$  obtained in a series of measurements are plotted against  $V$  in Fig. 9.2. In plotting the points it has been assumed that  $g_0$  does change sign at zero, and the shape of the curve indicates that this assumption is justified. Because of the interference caused by the noise at higher applied voltages, it was not possible to carry the impedance measurements further. The data given in the figure, however, seem to justify the interpretation that has been given for the narrowing of the noise spectrum near the critical voltage.

From the foregoing analysis it follows that when the bandwidth of the noise is narrowed, part of the observed noise power is generated by the noise current and part of it by the negative conductance of the space

charge. To obtain the power generated by the noise current the observed powers must be multiplied by

$$\frac{G_L + G_e}{G_L} = \frac{\text{observed bandwidth}}{\nu/Q_L}.$$

The points of Fig. 9-1 for which the correction is appreciable are indicated by open circles connected to the corresponding uncorrected points.

In another experiment the noise power was measured over a wide range of magnetic fields. The results of this experiment are shown in Fig. 9-3; the noise powers plotted in this figure have been multiplied by the correction factor given above.

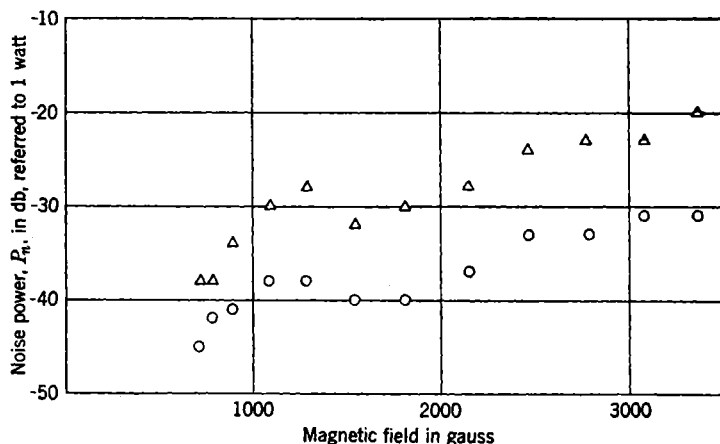


FIG. 9-3.—Noise power as a function of magnetic field.  $\Delta$  Bandwidth, 3 Mc/sec;  $\circ$  Bandwidth, 6 Mc/sec.

The significance of the order of magnitude of the observed noise can be illustrated by computing a noise temperature by means of the formula

$$P_n = kT \Delta\nu = \frac{kT\nu}{Q_L}.$$

With the values  $P_n = 10^{-4}$  watt and  $Q_L = 150$ , a temperature of  $4 \times 10^{11}^\circ\text{C}$ . is obtained, which is numerically equivalent to a mean electron energy of  $2 \times 10^7$  electron volts.

Surprisingly large noise powers for the nonoscillating magnetron were also derived from experiments on the phasing of pulsed magnetrons.<sup>1</sup> Experiments were performed on two magnetrons. One of them delivered pulse powers of 2 to 25 kw; the other 20 to 150 kw. To obtain a moderate degree of coherence between pulses, 0.05 to 1.0 watt of priming power

<sup>1</sup> J. E. Evans, R. C. Fletcher, and F. F. Rieke, "R-f Phasing of Pulsed Magnetrons," RL Report No. 1051, Feb. 6, 1946.

had to be *absorbed* by the smaller magnetron; 0.5 to 2.0 watts were required in the larger one. A crude theoretical analysis led to the conclusion that the noise powers generated in the magnetrons might well be larger by at least a factor of 10 than the powers required for phasing. Direct measurements of the noise in the smaller magnetron, pulsed just below the critical voltage, yielded values of the order of 10 watts.

**9-3. Signal-to-noise Ratio.**<sup>1</sup>—The work to be described was done in connection with the development of a 4000-Mc/sec c-w magnetron designed to operate at about 900 volts, with a power output of 20 watts. Many of these magnetrons generated excess noise; the noise rose precipitously at a threshold voltage  $V_{a0}$  that varied somewhat from tube to tube. Usually  $V_{a0}$  was below or dangerously close to the specified operating voltage of the tube. (An electronic tuner built into this magnetron determines the magnetic field and therefore the voltage at which the tube must be operated.) The primary problem was to eliminate the excess noise or to raise  $V_{a0}$  well outside the operating range. In the course of the attempts to do this, noise measurements were made on many magnetrons that differed from each other in one or more details of their construction.

The measurements of noise were carried out in the following way. The output of the magnetron was fed through an attenuator into a crystal; by varying the attenuation, the crystal current was adjusted to a standard value of 0.5 ma. The high-frequency components of the crystal current were fed into a radio receiver, and the output of the second detector of the receiver was registered on a microammeter. This system functions essentially as follows. The coherent component of the magnetron output provides local-oscillator power for the crystal, which operates as a mixer. The "signal" is made up of those frequency components—the noise—in the magnetron output which fall within the ranges  $(\nu_M - \nu_R - \delta\nu)$  to  $(\nu_M - \nu_R + \delta\nu)$  and  $(\nu_M + \nu_R - \delta\nu)$  to  $(\nu_M + \nu_R + \delta\nu)$ , where  $\nu_M$  is the magnetron frequency,  $\nu_R$  is the receiver frequency, and  $2\delta\nu$  is the bandwidth of the receiver.

In the experiments,  $\nu_R$  was usually 1.5 Mc/sec and  $2\delta\nu$  was 4 kc/sec. In general, the excess noise decreased with larger values of  $\nu_R$  and was quite small for  $\nu_R = 30$  Mc/sec—as is to be expected, for the loaded  $Q$  of the magnetron could hardly have been less than 100. Within the limits indicated above, the excess noise observed did not depend strongly upon the tuning of the receiver.

Diverse correlations suggested the working hypothesis that the excess noise was related to ionization within the magnetron. Residual gas in the tubes, however, does not provide a consistent explanation for the

<sup>1</sup> The material for this section has been taken from an RCA report: R. L. Sproull, "Noise in Magnetrons," Report No. 29, Navy Contract NXsa 35042.



noise; rather, as is shown by observations to be described presently, it is barium and strontium from the oxide-coated cathode that are involved. One of the observations consisted simply of detecting the spectra of Ba and Sr in the interaction space of the magnetron. Following this observation, apparatus was constructed especially for the purpose of measuring the ionization in the neighborhood of a hot, oxide-coated cathode bombarded by electrons. From the results obtained with this apparatus it was concluded that the equivalent pressure of Ba and Sr near a hot magnetron cathode is of the order of  $10^{-2}$  mm.

In other experiments, the relation between noise and residual gas was studied. In magnetrons with conventional oxide-coated cathodes, the introduction of neon had no influence on the noise as long as the pressure was less than about  $5 \times 10^{-3}$  mm; at  $10^{-2}$  mm a glow discharge began to set in. Other magnetrons were constructed with tungsten spirals for cathodes. In these tubes, varying the pressure of neon between  $10^{-3}$  and  $5 \times 10^{-3}$  mm did influence the noise. (Apparently the oxide-coated cathodes provided so many ions that the introduction of neon produced little additional effect.)

The magnetrons with tungsten cathodes had also been operated sealed off; under these conditions the threshold voltage  $V_{ao}$  was about 1000 volts when the heating current through the tungsten spiral was just sufficient to permit normal oscillation, but  $V_{ao}$  dropped to 700 volts when the heating current was increased by 10 per cent. It seems not quite certain whether this result is to be attributed entirely to residual gas released as a result of the increased temperature of the cathode (and also of the other parts of the magnetron) or some obscure additional effect is involved.

The preponderance of evidence supported the hypothesis that the excess noise in magnetrons with oxide cathodes was caused by electron bombardment of the oxide coating. Consequently a special form of cathode was devised to minimize the bombardment of the coated surface. The sleeve had longitudinal V's cut in its surface, so that it resembled a long pinion gear; only the sides of the teeth facing in one direction were coated. Since the electrons that return to the cathode have predominantly an azimuthal motion and the direction of the motion is determined by that of the magnetic field, it was possible to arrange matters so that either the coated or the uncoated sides of the teeth were the more heavily bombarded. Magnetrons constructed with these cathodes had decidedly better signal-to-noise ratios with the magnetic field in the "correct" direction.

**9-4. Origins of Noise.**—The observations reviewed in the preceding section demonstrate quite conclusively that ions in the interaction space of an *oscillating* magnetron can give rise to strong sidebands of noise

in the magnetron output. Presumably the noise gets into the output of the magnetron as the result of modulation effects, for it is hardly conceivable that the motions of the ions contain the frequency components present in the noise spectrum. The ions move much more slowly than the electrons, and for the electrons the transit times across the gaps of the resonators are just small enough to permit the electrons to deliver power at the resonance frequency of the magnetron. It seems likely that the effect of the ions is to be explained somewhat as follows: The ions, by neutralizing space-charge, cause momentary variations in the electron current, and thus there results an irregularity or noise modulation of the magnetron output.

The noise generated in the absence of oscillations (described in Sec. 9-2) might also be termed "excess noise," since, as will be shown presently, it is orders of magnitude larger than can be accounted for by elementary considerations. To what extent this type of noise is influenced by ions is entirely unknown, but to dismiss the results summarily as a manifestation of "gas" would appear to beg the question because of the difficulty with transit times mentioned above. Modulation effects could hardly be invoked, for in this case there is no carrier to be modulated.

One source of noise must be present under all circumstances, namely, shot effect, and it may be of interest to calculate an upper limit of the noise power to be expected from it. This calculation can be carried through quite simply for the nonoscillating magnetron operated at magnetic fields below cutoff on the basis of the single-stream solution to the space-charge equations (see Chap. 6). This solution has been used quite widely as the starting point for theoretical investigations of magnetron phenomena. Mathematically, the d-c current to the anode is zero under the conditions assumed; in practice the current is relatively small. There is, however, a large azimuthal component of current that flows across the faces of the resonators, and it seems reasonable to suppose that the shot effect arises primarily from this component of the electron current.

Inasmuch as only a rough calculation is to be made, equations for a plane magnetron will be used. If the distance between oscillators is  $s$ , the formula  $r_c/r_a = (N - 4)/(N + 4)$  yields for the cathode-to-anode distance in a plane magnetron the value  $4s/\pi$ , and the characteristic parameters (see Chap. 10) of the magnetron are

$$\mathfrak{B} = \frac{\pi}{2} \frac{m}{e} \nu_0,$$

$$\mathfrak{V} = 2 \frac{m}{e} \nu_0^2 s^2,$$

$$g = \frac{\pi^2}{24} \frac{m}{e} \epsilon_0 \nu_0^3 s^2 N L,$$

where  $\nu_0$  is the frequency of the  $\pi$ -mode,  $N$  the number of oscillators, and  $L$  the length of the anode. (A numerical factor of 1.24 is omitted from  $\mathcal{G}$ .) The solutions to the space-charge equations are

$$\frac{v}{2s} = \nu_0 \frac{B}{\mathfrak{B}} \frac{\pi}{4} \frac{y}{s},$$

$$\rho = \frac{4}{NLs^2} \frac{\mathcal{G}}{\nu} \left( \frac{B}{\mathfrak{B}} \right)^2,$$

for

$$y < \frac{4s}{\pi} \left( 1 - \sqrt{1 - \frac{V}{\mathfrak{U}} \left( \frac{B}{\mathfrak{B}} \right)^2} \right),$$

where  $v$  is the velocity of an electron at the distance  $y$  from the cathode and  $\rho$  is the charge density.

The current due to a single electron is computed as follows. With an r-f voltage  $\tilde{V}$  on the resonant system, the alternating electric field has an  $x$ -component  $E_x$  given by  $E_x = (2\tilde{V}/s)f(y)(\cos \pi x/s) \cos 2\pi \nu t$  + higher components, where  $f(y)$  is approximately 1 at the anode and falls to zero at the cathode. Since only an upper limit is to be computed for the current,  $f(y)$  is taken as equal to 1 throughout. The higher components are small and will be neglected; the error thus introduced will be discussed later. The component wave that travels along with the electrons has an amplitude  $E_x = \tilde{V}/s$ , and an electron traveling with the wave ( $v = 2s\nu$ ) does work at the rate  $e v \tilde{V}/s$ . Thus the current  $i_e$  induced by a single electron is given by

$$i_e = \frac{ev}{s} = 2\nu e.$$

The (noise current)<sup>2</sup>/unit frequency interval  $di_n^2/d\nu$  is equal to  $i_e^2$  summed over all electrons with velocities between  $2s\nu$  and  $2s(\nu + d\nu)$ . Thus

$$\begin{aligned} \frac{di_n^2}{d\nu} &= (2\nu e)^2 \frac{\rho}{e} NLs \frac{dy}{d\nu} d\nu \\ &= \frac{2^6}{\pi} e \left( \frac{\nu}{\nu_0} \right)^2 \mathcal{G} \frac{B}{\mathfrak{B}}; \quad \nu > \nu_m \\ \frac{di_n^2}{d\nu} &= 0; \quad \nu < \nu_m, \end{aligned} \quad (1)$$

where

$$\nu_m = \nu_0 \left[ \frac{B}{\mathfrak{B}} - \sqrt{\left( \frac{B}{\mathfrak{B}} \right)^2 - \frac{V}{\mathfrak{U}}} \right].$$

Taking the result at its face value,  $di_n^2/d\nu$  should vary as  $\nu^2$  up to  $\nu_m$  and then fall suddenly to zero. Had the higher components of the electric field been included in the calculation of the noise current, how-

ever, there would be a weak extension of the spectrum toward higher frequencies. The maximum in the noise spectrum at  $\nu_m$  occurs at the resonance frequency of the magnetron when the applied voltage is just equal to the Hartree voltage  $V = \mathfrak{U}[2(B/\mathfrak{R}) - 1]$ . Because the tube would break into oscillation with so high an applied voltage, the noise measurements described in Sec. 9-3 were all made at lower applied voltages. Thus a noise current computed on the basis of Eq. (1) must surely represent an upper limit.

For the magnetron used in the measurements of noise,  $\mathcal{I} = 0.3$  amp. With  $B = 4\mathfrak{R}$ , Eq. (1) yields the value

$$\nu \frac{di_m^2}{d\nu} = 1.2 \times 10^{-8} (\text{amp})^2.$$

The noise power integrated over the resonance curve of the magnetron is given by

$$P_n = \frac{\pi}{2Y_c} \nu \frac{di_m^2}{d\nu}.$$

The value of  $Y_c$  for the magnetron is estimated to be 0.5 mho and leads to the numerical value for the noise  $P_n = 4 \times 10^{-8}$  watt, or 74 db below 1 w. Since this value is roughly 40 db lower than the noise powers observed, it is evident that the observed noise cannot be accounted for on the basis of shot effect in a single-stream space charge.

## PART III

# DESIGN

This part of the book is devoted to magnetron design. The available theoretical and experimental knowledge of the electronics of magnetrons and of their resonant systems and magnetic circuits will be used to develop procedures by which a tube can be designed to meet specific requirements. The general principles that are needed have been discussed in Part I and Part II of the book, and to this will be added a great deal of experimental information gathered at the Radiation Laboratory and from industrial laboratories.

The design of a magnetron must consider four principal components: the cathode, the interaction space of the fields and electrons, the resonant system, and the magnetic circuit. Chapter 10 will discuss the rather complex interrelations of these components; it will also analyze in detail the problem of designing the interaction space to meet given conditions of operation. Subsequent chapters will consider the resonant system, the cathode, and the magnetic circuit.



## CHAPTER 10

### PRINCIPLES OF DESIGN

By A. M. CLOGSTON

**10-1. The Primary Design Parameters.**—When a need arises for the design of a new magnetron to meet operating conditions not fulfilled by existing types, experience has shown that the requirements of the situation can be set forth by the specification of certain primary design parameters. These parameters express the relationship of the magnetron to the other components of the equipment in which it is to be used and indicate the requirements set for the tube by the over-all equipment specifications. The primary design parameters to be considered are

1. Frequency.
2. Pulse-power output.
3. Voltage.
4. Efficiency.
5. Pulse duration and average power input.
6. Heater power.
7. Tuning requirements.
8. Frequency stability.
9. Weight.

The emphasis on the various parameters will not, of course, be similarly distributed in all cases.

It may happen that the requirements made upon the design will be impossible to meet through existing techniques, but the analysis to be carried out will indicate the compromises that may best be made to arrive at a usable design.

The outstanding characteristics of any oscillator are its frequency and power output. Magnetrons ranging in frequency from 30 to 30,000 Mc/sec and in power output from 30 to 3,000,000 watts have been developed. Generally, from 30 to 1000 watts c-w operation has been feasible, while pulsed oscillators capable of delivering from 1 to 3000 kw have been developed. The working voltage range covered by existing types of magnetrons extends from about 500 to 50,000 volts, indicating by comparison with the power range a rather narrow spread of static input impedance.

Magnetrons have been built in which the electrons generate r-f power at efficiencies up to 80 per cent. Usually much of this efficiency

is sacrificed to gain other ends, and a certain amount is inevitably lost in the resonant system. The over-all efficiencies of most existing magnetrons fall in the range of 30 to 60 per cent at the nominal operating point.

Magnetrons have been required to operate under a variety of duty ratios. Pulse durations from 0.1 to 10  $\mu$ sec have been used, and a number of applications have required continuous-wave operation. The corresponding average power outputs have covered a much more restricted range than the pulse powers, extending only from 1.5 to 1500 watts, or from about 3 to 3000 watts average power input.

Occasionally an upper limit is placed upon the cathode heater-power consumption by considerations of equipment weight. Tubes designed for airborne service have had a cathode drain as small as 1.5 watts, while very high power magnetrons have required as much as 150 to 300 watts heater power.

It is desirable in many applications that a magnetron be tunable over a particular band of frequencies. Tunable magnetrons exist that achieve, by complex mechanisms, tuning ranges varying from 5 to 40 per cent. In some cases in order to permit precise frequency settings a tuning range of only 1 per cent or less has been obtained by very simple methods. Recently several methods of electronically varying the frequency of a magnetron have been developed. For the f-m transmission of video data or very precise stabilization of frequency, it is now feasible to build magnetrons with an electronic tuning range of several megacycles per second. Tubes have been built at 1000, 3000, and 4000 Mc/sec with a deviation range of about 10 Mc/sec. For electronic tuning, the ratio of megacycles per second of tuning to volt of signal is of considerable design importance, as is also the required bandwidth.

Magnetron tuning is closely allied with the problem of frequency stabilization. In a number of applications it is necessary that the frequency of a tube over a wide range of operating conditions remain within very narrow limits, set perhaps by the pass band of a receiver. This must be accomplished without constant manual attention, and the fluctuations are indeed often too rapid to be compensated by mechanical means. An example of such stringent conditions is given by the 2J32, a magnetron used in 10-cm beacons. This tube must not vary from its center frequency by more than  $\pm \frac{1}{2}$  Mc/sec as its temperature varies  $\pm 10^\circ\text{C}$ , its plate current varies from 8 to 12 amp, and its load varies over all phases with an SWVR equal to 2.0. The problem has been met by the development of a technique of tightly coupling high- $Q$  resonant cavities to the magnetron, achieving thereby stabilizing factors up to 10.

Because a magnetron requires a strong magnetic field for its operation,



the combined weight of tube and magnet is considerably greater than that of the more conventional electron tube. The weight of the magnet required is therefore a factor of considerable importance in design. Very severe requirements have had to be met in tubes planned for use in airborne equipment or in sets designed for extreme ease of transportation. Magnets have ranged in weight from several ounces to 100 lb.

**10-2. The Method of Magnetron Design.**—There is one very simple approach to magnetron design. In the past a great variety of tubes has been constructed, and their performance examined. If one of these tubes comes close to meeting the requirements of the situation, small variations may be made in its design with good hope of success in meeting the new conditions. The relations among the components of a magnetron are so complex, however, that it may not always be possible to arrive easily at a new design simply by variation of an existing type. A more analytical approach is necessary to formulate a procedure that is applicable in all cases and to bring out most clearly the processes involved.

The four parts of a magnetron are so interdependent that no one of them can be designed independently of the rest. Each component is affected not only by the primary parameters but also by the design of the other three parts. It is necessary, therefore, to arrive at a solution to the design problem in which each part of the tube, besides meeting the requirements set by the primary design parameters, is consistent with the design adopted for the other components. The most convenient way to do this is to settle upon a trial design of the interaction space. A complete set of specifications is thereby established for the other components, and it is a straightforward matter to decide whether or not each component can be designed to meet these conditions.

Figure 10-1 is a block diagram setting forth an analysis of magnetron design conceived in the above manner. At the left are the 10 primary design parameters discussed in the previous section; the four tube components are shown in heavy outline.

As indicated in this figure, the design of the interaction space depends directly upon the required current, voltage, and wavelength. These quantities alone, however, are insufficient to determine the size and shape of the interaction space and its state of oscillation. It will be seen in Sec. 10-8 that, in addition, it is necessary to specify three quantities,  $N$ ,  $\sigma$ , and  $\mu$ , called the "shape factors," and three other quantities,  $b$ ,  $i$ , and  $g$ , which constitute what will be called the "relative operating point." The shape factors determine the cross-sectional shape of the interaction space but not its size, while the relative operating point can be considered as determining the nature of the electronic orbits.

The choice of the shape factors and the relative operating point determine the trial design of the interaction space mentioned above.

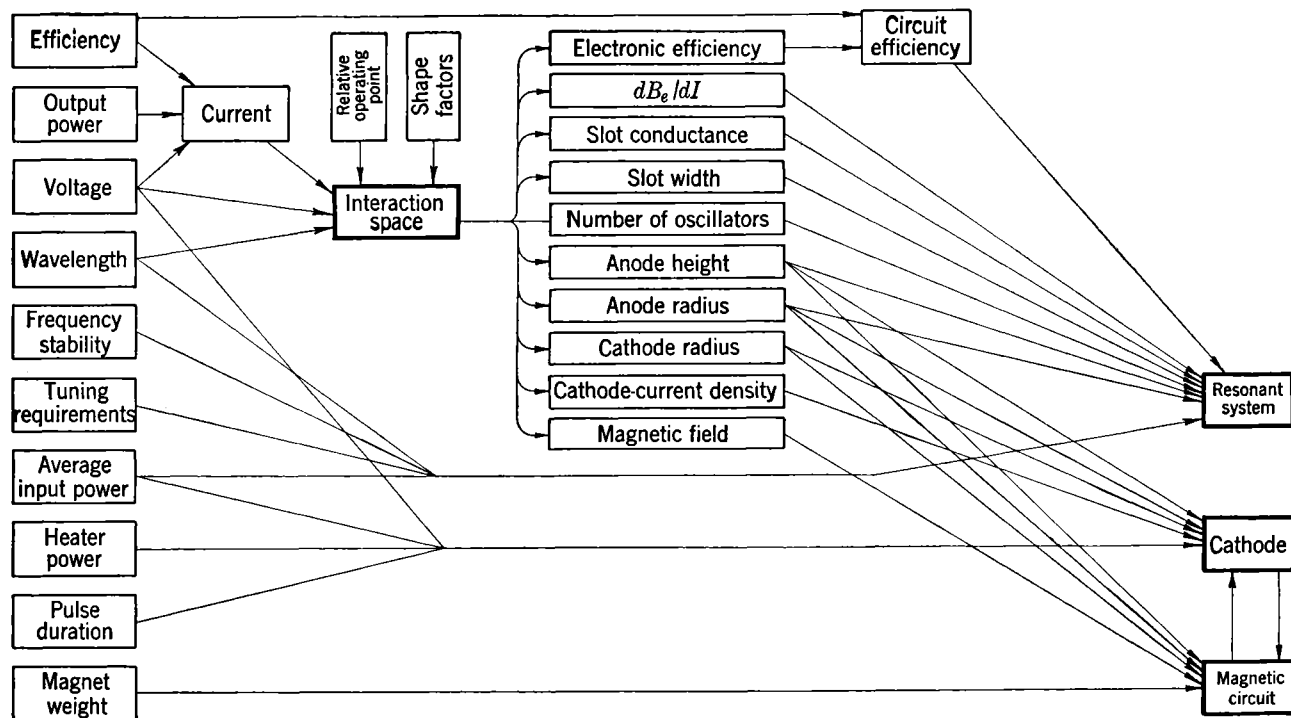


FIG. 10-1.—Analysis of magnetron design.

In principle, this choice can be made without previous information and, if proper, will lead to a consistent solution of the design problem, if such exists. If the choice is inept, on the other hand, it can be discarded and replaced by a more suitable one. In practice, experience with other tubes should reduce the choice of  $N$ ,  $\sigma$ , and  $\mu$  and  $b$ ,  $i$ , and  $g$  to well-defined limits. The data that have been gathered in Chap. 19 summarize a considerable amount of previous experience that may be found useful.

In Sec. 10.8 it will be shown that the determination of the interaction space leads to the specification of 10 quantities which will be called the "secondary design parameters." These include four dimensions—the anode radius  $r_a$ , the cathode radius  $r_c$ , the anode height  $h$ , the slot width  $w$ , and the number of oscillators  $N$ —and five operating constants including the electronic efficiency  $\eta_e$ , the change of electronic susceptance with current  $dB_e/dI$ , the slot conductance  $G_L$  arising from internal losses and external loading, the cathode-current density  $J_c$ , and the magnetic field  $B$ .

By referring to Fig. 10.1, it is seen that a number of conditions are placed in this way upon the design of the resonant system, the cathode, and the magnetic circuit. These conditions are indicated by arrows leading from the various design parameters to the appropriate components. In order to proceed with the problem, it must be decided whether or not each part of the tube can be designed to meet the conditions imposed upon it. If this is possible, the choice of interaction space has been a good one, and a satisfactory solution can be achieved. If, on the other hand, it is impossible to arrive at a design for a particular component, or if the design would be very extreme or inconvenient, it becomes necessary to make a new choice for the interaction space or to make a compromise with the primary design parameters. It is necessary to rely in each case upon the particular circumstances to indicate the proper direction to take.

In arriving at the design of the interaction space, theory and the available data are not always competent to specify closely the magnetic field  $B$  and the electronic efficiency  $\eta_e$ , and very little data are available for determining the quantity  $dB_e/dI$ . The tentative solution, however, specifies the dimensions required to build trial magnetrons if necessary and to measure the questionable quantities. Other factors not considered in this analysis, such as noise level, can be similarly determined.

In the design of each component of the magnetron, there must constantly be considered whether or not an unduly difficult mechanical problem is presented. A design may often be unfeasible because it requires impossibly small parts or unreasonably close machining tolerances.

**10-3. Conditions Imposed on the Resonant System.**—The analysis of the preceding section yields a set of 11 conditions upon which the resonant system is simultaneously dependent, namely,

1. Tuning range.
  2. Frequency stability.
  3. Number of oscillators  $N$ .
  4. Anode radius  $r_a$ .
  5. Anode height  $h$ .
  6. Slot width  $w$ .
  7. Wavelength  $\lambda$ .
  8. Circuit efficiency  $\eta_c$ .
  9. Slot conductance  $G_L$ .
  10. Average power input.
  11. The change of electronic susceptance with current,  $dB_e/dI$ .
- In addition, the resonant system must extend to the electrons a reasonably pure  $\pi$ -mode under all conditions of tuning, stabilization, and loading.

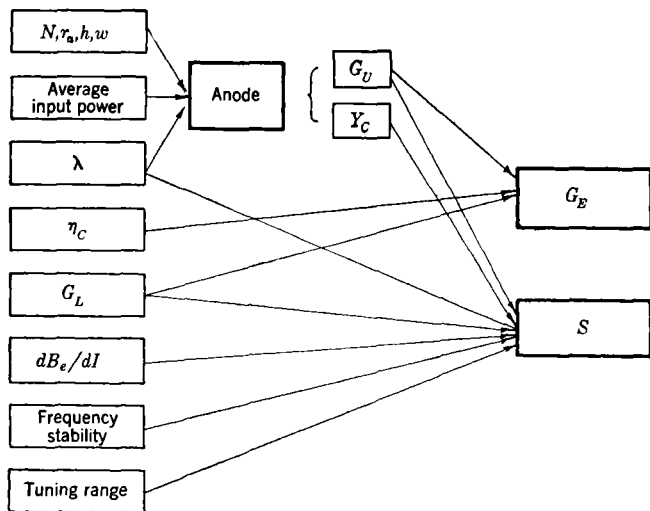


FIG. 10-2.—Analysis of resonant-circuit design.

In this section, the relation of these conditions to the design of the resonant system will be considered.

There are essentially three independent components of the resonant system: the anode block proper, the stabilization circuit, and the load. The anode block is characterized by its characteristic admittance  $Y_c$  and a conductance  $G_v$  presented at the slots by its internal losses. The effect of the stabilizer is expressed through the stabilization factor  $S$ ,

and the load through a conductance  $G_E$ , also presented at the slots. The interrelations of these four quantities and the 11 conditions listed above are set forth in Fig. 10-2.

The quantities  $N$ ,  $r_a$ ,  $h$ , and  $w$  determine that portion of the anode shown in Fig. 10-3. The rest of the structure must be constructed so that the proper wavelength and mode separation is obtained and the desired average power can be dissipated without an excessive temperature gradient. A variety of structures may be possible, each with a characteristic  $G_U$  and  $Y_c$ . If one of these is chosen, a number of conditions are placed upon  $G_E$  and  $S$ .

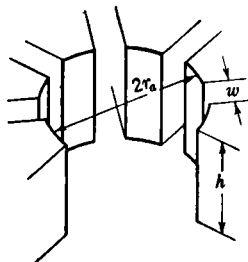


FIG. 10-3.—Anode interaction-space interface.

The slot conductance  $G_L$  and the circuit efficiency  $\eta_c$  are related to  $G_U$  and  $G_E$  by the expressions

$$G_L = G_E + G_U, \quad (1)$$

$$\eta_c = \frac{G_E}{G_E + G_U}. \quad (2)$$

The shift of wavelength  $\Delta\lambda$  with a change in current  $\Delta I$ , a change of temperature  $\Delta T$ , and a change of normalized load reactance  $\Delta b = \Delta B/Y_0$  are given approximately by

$$\Delta\lambda = \frac{1}{SY_c} \frac{\lambda}{2} \left( \frac{dB_c}{dI} \right) \Delta I, \quad (3)$$

$$\Delta\lambda = \frac{1}{S} \lambda \alpha \Delta T, \quad (4)$$

and

$$\Delta\lambda = \frac{G_E}{SY_c} \frac{\lambda}{2} \Delta b, \quad (5)$$

where  $\alpha$  is the linear thermal expansion coefficient and it is assumed that the stabilizer is unaffected by changes in temperature. These relations will be established in Chap. 16.

The change in wavelength of the tube with a small change in the parameters of the resonant circuit can be taken as roughly representative of the available tuning range. For a change  $\Delta C$  in the capacitance of the anode block one has

$$\Delta\lambda = (\pi c) \frac{1}{SY_c} \Delta C. \quad (6)$$

A change  $\Delta L$  in the inductance of the anode block causes a shift

$$\Delta\lambda = (\pi c) \frac{Y_c}{S} \Delta L, \quad (7)$$

and a change  $\Delta\lambda$ , in the wavelength of the stabilizer gives

$$\Delta\lambda = \frac{S-1}{S} \Delta\lambda_s. \quad (8)$$

Equations (1) and (2) impose two conditions on  $G_E$ :

$$G_E = G_L - G_U, \quad (9)$$

and

$$G_E > G_U \frac{\eta_c}{1 - \eta_c}, \quad (10)$$

where the inequality sign is inserted because there can certainly be no objection to a circuit efficiency greater than the required value of  $\eta_c$ . The anode block must be designed so that Eqs. (9) and (10) are simultaneously satisfied.

If the bracket  $( )_m$  means in each case the maximum tolerable ratio allowed by the primary design conditions of frequency stability and tuning range, one obtains from Eqs. (3) to (8) and Eq. (1) the following relations which set upper and lower limits to the stabilization that must be incorporated into the design:

$$S > \frac{\lambda}{2 \left( \frac{\Delta\lambda}{\Delta I} \right)_m} \frac{1}{Y_c} \left( \frac{dB_s}{dI} \right), \quad (11)$$

$$S > \frac{\lambda}{\left( \frac{\Delta\lambda}{\Delta T} \right)_m} \alpha, \quad (12)$$

$$S > \frac{\lambda}{2 \left( \frac{\Delta\lambda}{\Delta b} \right)_m} \frac{G_L - G_U}{Y_c}, \quad (13)$$

$$S > \frac{\left( \frac{\Delta\lambda_s}{\Delta\lambda} \right)_m}{\left( \frac{\Delta\lambda_s}{\Delta\lambda} \right)_m - 1}, \quad (14)$$

$$S < (\pi c) \frac{1}{Y_c} \left( \frac{\Delta C}{\Delta\lambda} \right)_m, \quad (15)$$

and

$$S < (\pi c) Y_c \left( \frac{\Delta L}{\Delta\lambda} \right)_m. \quad (16)$$

One of the Eqs. (11) to (13) will set a lower limit to  $S$ . If tuning of the resonators is employed, Eq. (15) or (16) will set an upper limit to  $S$ . Tuning by means of the stabilizer, on the other hand, will set a lower

limit to  $S$  according to Eq. (14). In order to have a possible design, these various limits must not overlap.

Equations (9) through (16) depend on three primary design parameters: the wavelength; the frequency stability expressed by  $(\Delta\lambda/\Delta T)_m$ ,

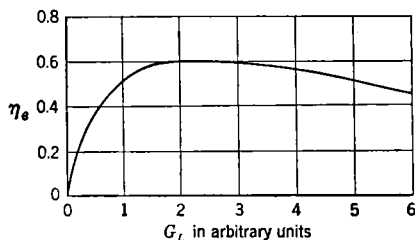


FIG. 10-4.—Electronic efficiency as a function of slot conductance.

$(\Delta\lambda/\Delta I)_m$ , and  $(\Delta\lambda/\Delta b)_m$ ; and the tuning range entering through  $(\Delta L/\Delta\lambda)_m$ ,  $(\Delta C/\Delta\lambda)_m$ , or  $(\Delta\lambda_s/\Delta\lambda)_m$ . In addition, three secondary design parameters  $(dB_e/dI)$ ,  $G_L$ , and  $\eta_e$  are involved, as are also the quantities  $G_U$  and  $Y_c$ . If the various conditions (9) to (16) set for  $G_E$  and  $S$  are inconsistent, changes must be made in  $G_U$  and  $Y_c$  (that is, the anode block), in the secondary design parameters (that is, the interaction space), or in the primary design parameters. This situation is expressed most clearly by Fig. 10-2.

Equations (1), (2), (11), and (13) form a basis for discussing the relations between the over-all efficiency of operation  $\eta$  and the conditions of frequency stability. As has been discussed in Chap. 7, the electronic efficiency  $\eta_e$  of a magnetron is a function of slot conductance  $G_L$  of the form shown in Fig. 10-4. Also, it will be seen in Chap. 11 that for a group of similar anode blocks the internal losses  $G_U$  increase with increasing  $Y_c$  as indicated in Fig. 10-5. Suppose it is desired to keep the stabilization against changes in load required by

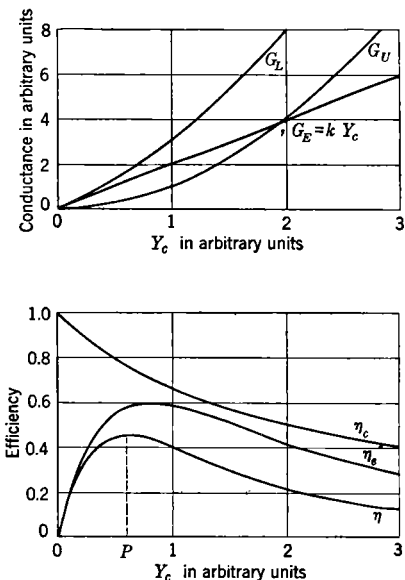


FIG. 10-5.—Conductance and efficiency as a function of  $Y_c$ .

Eq. (13) constant. In that case it is necessary that

$$\frac{G_E}{Y_c} = k, \quad (17)$$

where  $k$  is some constant. Using Eq. (17), there is obtained from Eqs. (1) and (2)

$$G_L = kY_c + G_U \quad (18)$$

and

$$\eta_c = \frac{kY_c}{kY_c + G_U}. \quad (19)$$

Equations (18) and (19) allow the curves for  $G_L$  and  $\eta_c$  to be drawn in Fig. 10-5. Furthermore, with  $\eta_c$  known as a function of  $G_L$  and  $G_L$

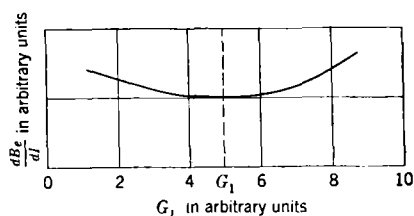


FIG. 10-6.— $(dB_e/dI)$  as a function of  $G_L$ .

as a function of  $Y_c$ , a plot of  $\eta_c$  against  $Y_c$  can be made in Fig. 10-5. Then using the relation  $\eta = \eta_c \eta_e$  the total efficiency can also be plotted against  $Y_c$ . It is observed that  $\eta$  must obtain a maximum value at some point  $P$  to the left of the point at which  $\eta_c$  obtains its maximum value. A

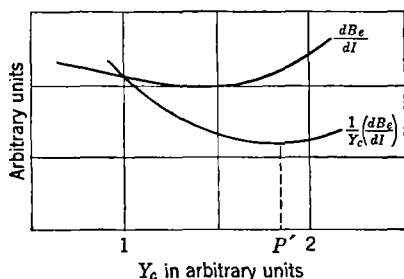


FIG. 10-7.— $(dB_e/dI)$  and  $1/Y_c(dB_e/dI)$  as functions of  $Y_c$ .

magnetron that has been inadvertently designed with  $Y_c$  not at  $P$  can be redesigned for a higher efficiency without sacrifice of stability against changes in load by changing the  $Y_c$  of the resonant system.

When other operating conditions are held constant, the rate of change of electronic susceptance with current  $dB_e/dI$  is a function of total slot conductance as illus-

trated in Fig. 10-6. It obtains a minimum value at some value of conductance  $G_1$ . From Eq. (3), it is observed that the shift of wavelength with current, at constant  $S$ , is proportional to  $1/Y_c(dB_e/dI)$ . Maintaining the stability against changes in load constant as before,  $dB_e/dI$  and  $1/Y_c(dB_e/dI)$  can be plotted as functions of  $Y_c$  in Fig. 10-7. At some point  $P'$ ,  $1/Y_c(dB_e/dI)$  will have a minimum value. In general,  $P'$  will not be coincident with  $P$  in Fig. 10-5.



The following situation, then, exists in the choice of  $Y_c$ . By always maintaining the stability against load constant, a maximum value of  $\eta$  is obtained at one value of  $Y_c$  and a minimum value of  $1/Y_c(dB_c/dI)$  at another point. Frequency stability against changes in current can therefore be achieved at the expense of efficiency.

**10-4. Conditions Imposed on the Cathode.**—In Sec. 10-2 it was pointed out that the cathode design is subject to the following eight conditions:

1. Anode height  $h$ .
2. Anode radius  $r_a$ .
3. Cathode radius  $r_c$ .
4. Plate voltage  $V$ .
5. Cathode-current density  $J_c$ .
6. Average power input.
7. Heater power.
8. Pulse duration.

The cathode that is to meet these conditions performs two important functions in the magnetron. It must supply the stipulated cathode-current density under conditions of complete or very nearly complete space-charge limitation, and it must dissipate the energy of the back-bombarding electrons without harm to itself.

The design of the cathode structure may at present draw upon experience with three types of electron emitters: (1) low-temperature oxide cathodes; (2) high-temperature cathodes such as thoriated tungsten, tantalum, or thorium oxide; and (3) cold cathodes that operate by secondary emission, such as beryllium or silver-magnesium alloy. The properties of these cathodes are so disparate that each finds its particular field of usefulness.

A second property of the cathode at the disposal of the design is the supporting structure. It is necessary to distinguish two methods of support because of the very different effect that they have on the magnetic circuit. The end-mounted cathode is accompanied by built-in, hollow pole pieces and, in practice, attached magnets; the radial-mounted cathode requires a wider magnetic gap and is usually accompanied by an external magnet. This interdependence is indicated in Fig. 10-1.

The back-bombardment power on the cathode of a magnetron is not far from a fixed percentage of the average input power in all cases and is determined, therefore, by Condition 6. For handling very large back-bombardment powers, water-cooled secondary-emission cathodes have been used successfully; but because of several disadvantages, these cathodes have not yet seen extensive application.

With heated cathodes, there is an intimate relation between the back-bombardment power and the heater power. Suppose that the bombardment power is  $P_B$  and the heater power is  $P_H$ . Furthermore,

to simplify the argument, suppose that the distribution of heater power is thermally equivalent to the distribution of  $P_B$ . Suppose that it is considered permissible to initiate operation of the tube with a cathode temperature  $T_1$  and to operate with a temperature  $T_2 > T_1$ . The power dissipated in the cathode to maintain the temperature  $T_1$  will be  $P_B$ , while a higher power  $\beta P_H$  will be required to maintain a temperature  $T_2$ . Finally, suppose that the heater power can be reduced to an amount  $\chi P_H$  during operation. During operation, the heat balance of the cathode will therefore be expressed by

$$P_B + \chi P_H = \beta P_H. \quad (20)$$

Solving Eq. (20) for  $P_H$  then gives

$$P_H = \frac{P_B}{(\beta - \chi)}. \quad (21)$$

In Fig. 10-8  $P_H$  is plotted as a function of  $\chi$  for  $\beta = 1.4$  and  $\beta = 1.0$ .

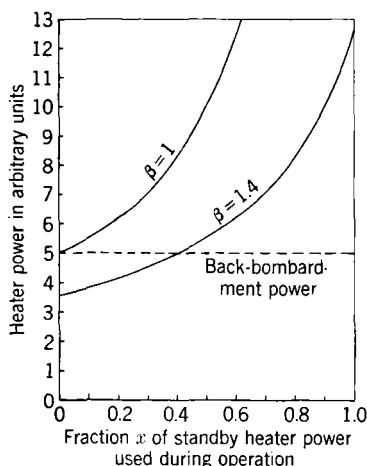


Fig. 10-8.— $P_H$  as a function of  $\chi$  for two values of  $\beta$ .

A large  $P_B$  requires  $P_H$  to be large also, and a great reduction is brought about in  $P_H$  by tolerating a certain range in cathode temperature. Furthermore, arranging to reduce the heater power in operation allows a still further decrease in these quantities. A requirement for very low heater power can be met in a design that calls for small average power input (low  $P_B$ ), tolerates wide temperature limits, and permits reduction of the heater power in operation.

In general, the high-temperature cathodes can dissipate more power than the low-temperature ones, and it is usually easier to design an end-mounted cathode for large dissipation than a radial-mounted one. The

length and diameter are important factors in settling on the proper cathode and supporting structure.

A magnetron normally operates under conditions of space-charge limitation at the cathode. This situation results in the familiar, nearly linear contours of constant magnetic field in the  $(V, I)$ -plane. If the total emission of the cathode is insufficient to maintain space-charge limitation beyond a certain current, a potential gradient appears at the cathode, and the magnetic-field line deviates from its normal position

toward higher voltage. This shift of the  $(V, I)$ -characteristic results in an increased tendency to mode-skip in pulsed magnetrons (see Chap. 8) and is sometimes accompanied by a poor spectrum. Continuous-wave magnetrons will tolerate a somewhat larger deviation from space-charge limitation but will cease oscillating if the deviation becomes great enough.

To maintain normal operation, Condition 5 requires that the cathode be capable of furnishing a space-charge-limited current density at least equal to  $J_c$ . In the operating magnetron, because of the back-bombardment electrons,  $J_c$  may be composed partially of primary electrons and partially of secondary electrons, and only a portion  $J_p$  of the required current density need be primary emission. The secondary emission current, at a given operating point, depends upon the nature and state of the cathode, its temperature, and the distribution of energy in number of the returning electrons. If these factors are all known,  $J_p$  can be calculated and constitutes a requirement on the cathode. Actually, very little information is available on the energy distribution of back-bombardment electrons because of the difficulty in making the necessary measurements.

For oxide cathodes, therefore, it is usually impossible to specify  $J_p$ . Instead, the practice has been to see that  $J_c$  does not exceed a limit  $J_m$  set by cathode sparking. Because of the high secondary emission of the oxide cathodes under the conditions present in most magnetrons during oscillation,  $J_p$  is usually a small fraction of  $J_c$ . Moreover, the primary emission normally to be expected from such a cathode is a larger fraction of  $J_m$ , and it is therefore sufficient for space-charge-limited operation. On the other hand, if the secondary emission ratio is about unity, the primary current density must be nearly equal to  $J_c$ . Such a case obtains with the high-temperature metallic emitters such as thoriated tungsten or tantalum and with very low voltage magnetrons in which the returning electrons have low energies.

A limit  $J_m$  exists to the total current density, both primary and secondary, that can be furnished by the low-temperature oxide cathodes without sparking. This limit depends considerably on the structure of the emitting material and increases as the pulse duration decreases. The current density  $J_c$  required by Condition 5 must therefore be considered for consistency with the pulse duration set by Condition 8. No corresponding limits are usually encountered with the high-temperature metallic emitters.

The distance between the anode and the cathode set by Conditions 2 and 3 is of some importance. The potential gradient that appears at the cathode surface upon failure of space-charge limitation is roughly inversely proportional to this distance, and a smaller separation may therefore lead to increased sparking.

**10-5. Conditions Imposed on the Magnetic Circuit.**—The function of the magnetic circuit is to produce a fairly uniform magnetic field of the desired value over the extent of the interaction space, and this must be done within the specified limits of magnet weight. There are therefore five conditions set for the magnetic circuit:

1. Anode height  $h$ .
2. Anode radius  $r_a$ .
3. Cathode radius  $r_c$ .
4. Magnetic field  $B$ .
5. Magnet weight.

The magnet weight is essentially proportional to the square of the field strength, to the distance between the magnet poles, and to the area of the uniform field. The distance between poles is determined by  $h$  and by the decision to end-mount or radial-mount the cathode. In principle, the area of the magnetic field need be only the cross-sectional area of the interaction space, but it may be impossible in practice to confine it to this region.

Magnetic material is occasionally included in a magnetron cathode to decrease the effective pole separation, improve the shape of the field, or produce a focusing field at the ends of the interaction space. A further interdependence of the cathode design and the magnetic circuit is introduced if this is done.

**10-6. The Scaling Laws.**—It has been seen in Chap. 7 that the operation of a magnetron is determined by the external magnetic field  $B$ , the plate current  $I$ , and the r-f impedance presented by the load to the output circuit of the tube,  $Z(\lambda)$ . In this case, the plate voltage  $V$ , the operating wavelength  $\lambda$ , and the power output  $P$  are determined. In order to eliminate direct consideration of the resonant system, the specification of  $Z(\lambda)$  may be replaced by a description of the anode-block interaction-space interface and the specification of  $G_r(\lambda)$  and  $B_r(\lambda)$ , the conductance and susceptance respectively for each resonator opening. In the following considerations  $G_r(\lambda)$  and  $B_r(\lambda)$  will be taken as identical for each resonator opening, and the values of  $G_r$  will be taken as independent of  $\lambda$ . In this case the operation of the tube may be specified by the magnetic field  $B$ , the plate current  $I$ , the total slot conductance  $G_L$ , and the wavelength  $\lambda$ ;  $V$  and  $P$  are thereby determined. Such a specification is possible for magnetrons with resonant systems made up of equivalent resonators. For rising-sun magnetrons,  $B_r(\lambda)$  has a different value for alternate resonators, but this fact may be ignored except in the vicinity of the critical field (see Chap. 3).

One further piece of information is needed before the operation of any magnetron is completely specified, namely, the boundary conditions satisfied by the electric fields at the cathode. Normally all cathodes

impose the boundary conditions that the field be zero at the surface, and the question can be ignored. A cathode with an unduly heavy current drain, however, may present a different boundary condition to the fields with a correspondingly altered behavior of the magnetron.

It has been shown in Chap. 6 that provided the interaction space is such that  $(\lambda/2\pi r_a)$  may be considered a small quantity and provided that the interaction of the electrons and the r-f magnetic field may be neglected, the basic equations of a magnetron may be expressed in terms of a set of dimensionless variables

$$\frac{1}{2} \left( \frac{e}{m} \right) \left( \frac{\lambda}{2\pi c} \right) B, \quad (22a)$$

$$2 \left( \frac{e}{m} \right) \left( \frac{\lambda}{2\pi c} \right)^2 \frac{1}{r_a} E, \quad (22b)$$

$$\frac{1}{2\pi} \left( \frac{e}{m} \right) \left( \frac{\lambda}{2\pi c} \right)^3 \frac{1}{r_a} \frac{1}{\epsilon_0} J, \quad (22c)$$

$$\frac{r_c}{r_a}, \quad (22d)$$

and

$$\left( \frac{2\pi c}{\lambda} \right) t. \quad (22e)$$

Consequently, on the basis of the various assumptions that have been made, it follows that the specification of the quantities

$$\frac{1}{2} \left( \frac{e}{m} \right) \left( \frac{\lambda}{2\pi c} \right) B, \quad (23a)$$

$$\frac{1}{2\pi} \left( \frac{e}{m} \right) \left( \frac{\lambda}{2\pi c} \right)^3 \frac{1}{r_a^2 \epsilon_0 h} I, \quad (23b)$$

and

$$\frac{1}{4\pi} \left( \frac{\lambda}{2\pi c} \right) \frac{1}{\epsilon_0 h} G_L \quad (23c)$$

determine the additional quantities

$$2 \left( \frac{e}{m} \right) \left( \frac{\lambda}{2\pi c} \right)^2 \frac{1}{r_a^2} V \quad (24a)$$

and

$$\frac{1}{\pi} \left( \frac{e}{m} \right)^2 \left( \frac{\lambda}{2\pi c} \right)^3 \frac{1}{r_a^4 \epsilon_0 h} P \quad (24b)$$

for a group of magnetrons with geometrically similar interaction-space cross sections, possessing resonant systems made up of equivalent resonators and with cathodes imposing a zero-value boundary condition

on the electric fields. A group of magnetrons answering this description is said to form a "family" of magnetrons.

Henceforth the dimensionless variables corresponding to  $B$ ,  $V$ ,  $I$ ,  $G_L$ , and  $P$  will be called "reduced variables" and will be designated by  $b$ ,  $v$ ,  $i$ ,  $g$ , and  $p$ , the corresponding quantities being related by the expressions

$$b = \frac{B}{\mathfrak{B}}, \quad (25a)$$

$$v = \frac{V}{\mathfrak{V}}, \quad (25b)$$

$$i = \frac{I}{\mathfrak{I}}, \quad (25c)$$

$$g = \frac{G_L}{\mathfrak{G}}, \quad (25d)$$

$$p = \frac{P}{\mathfrak{P}}. \quad (25e)$$

$\mathfrak{B}$ ,  $\mathfrak{V}$ ,  $\mathfrak{I}$ ,  $\mathfrak{G}$ , and  $\mathfrak{P}$  are characteristic scale factors for a given magnetron and will be termed the "characteristic" magnetic field, voltage, current, conductance, and power. They are given by the expressions

$$\mathfrak{B} = 2 \left( \frac{m}{e} \right) \left( \frac{2\pi c}{n\lambda} \right) \frac{1}{\left[ 1 - \left( \frac{r_c}{r_a} \right)^2 \right]} = \frac{21,200}{(n\lambda) \left[ 1 - \left( \frac{r_c}{r_a} \right)^2 \right]} \text{ gauss}, \quad (26a)$$

$$\mathfrak{V} = \frac{1}{2} \left( \frac{m}{e} \right) \left( \frac{2\pi c}{n\lambda} \right)^2 r_a^2 = 253,000 \left( \frac{2\pi r_a}{n\lambda} \right)^2 \text{ volts}, \quad (26b)$$

$$\mathfrak{I} = \frac{2\pi a_1}{\left[ 1 - \left( \frac{r_c}{r_a} \right)^2 \right]^2 \left( \frac{r_a}{r_c} + 1 \right)} \left( \frac{m}{e} \right) \left( \frac{2\pi c}{n\lambda} \right)^3 r_a^2 \epsilon_0 h$$

$$= \frac{8440 a_1}{\left[ 1 - \left( \frac{r_c}{r_a} \right)^2 \right]^2 \left( \frac{r_a}{r_c} + 1 \right)} \left( \frac{2\pi r_a}{n\lambda} \right)^3 \frac{h}{r_a} \text{ amp}, \quad (26c)$$

$$\mathfrak{G} = \frac{g}{\mathfrak{V}}, \quad (26d)$$

and

$$\mathfrak{P} = g\mathfrak{V}. \quad (26e)$$

These characteristic scale factors were brought to their present form by J. C. Slater<sup>1</sup> who introduced the expression for  $g$ . The quantity  $a_1$  is a function of  $r_a/r_c$  and is shown in Fig. 10-9 taken from Slater's report. It is seen that  $b$ ,  $v$ ,  $i$ ,  $g$ , and  $p$  are identical with the dimensionless variables given in Eqs. (23) and (24) except for factors involving the mode number

<sup>1</sup> J. C. Slater, "Theory of Magnetron Operation," RL Report No. 200, Mar. 8, 1943.

$n$  and the anode-cathode ratio  $\sigma = r_c/r_a$ . For magnetrons with geometrically similar interaction spaces these factors are constant and have no effect on the situation. They are included in the expressions for  $b$ ,  $v$ ,  $i$ ,  $g$ , and  $p$  to facilitate a comparison made later of magnetrons with different values of  $n$  and  $r_c/r_a$ .

For the purposes of this chapter,  $n$  will always be equal to  $N/2$ , where  $N$  is the number of oscillating segments of the magnetron.

The performance charts for any magnetron, presented in reduced variables, express the behavior of a whole family of magnetrons. To predict the behavior of a new member of the family, it is necessary merely to

calculate the characteristic magnetic field, voltage, current, power, and conductance of this new member. Performance charts for the new tube can then be drawn up using the relations

$$B = b\mathfrak{B}, \quad (27a)$$

$$V = v\mathfrak{V}, \quad (27b)$$

$$I = i\mathfrak{I}, \quad (27c)$$

$$G = g\mathfrak{G}, \quad (27d)$$

and

$$P = p\mathfrak{P}. \quad (27e)$$

This process has come to be known as the "scaling" of one magnetron to another. It is obvious that for scaling one must always use the power generated by the electrons, correcting for the power lost in the resonant system.

To specify the family of magnetrons represented by a reduced performance chart, it is necessary to indicate the shape of the interaction space. Referring to Fig. 10-10, it is seen that the shape of the interaction space can be specified by the number of oscillators  $N$  and by the ratios  $\sigma = r_c/r_a$  and  $\mu = w/d$ . A reduced performance chart should therefore be accompanied by values of  $N$ ,  $\sigma$ , and  $\mu$ . The load for which the data were taken should moreover be indicated by a value of  $g = G/\mathfrak{G}$ .

The accuracy with which a reduced performance chart of an actual magnetron represents the ideal behavior of a family of magnetrons is limited by several factors discussed below.

The equations that are used to characterize the magnetron represent by a potential function the field presented to a single electron by all the other electrons. This procedure does not consider the small effects due

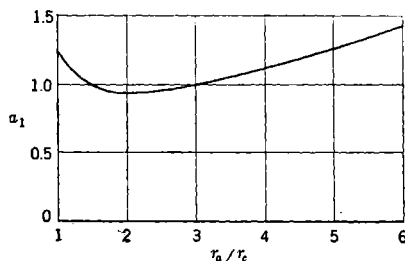


FIG. 10-9.— $a_1$  as a function of  $r_a/r_c$ .

to near electron encounters which produce noise fluctuations of the space-charge cloud. The noise currents generated will not scale precisely like the normal currents. Wherever the noise currents can be important, as, for instance, in the low d-c current region, the reduced performance chart will cease to be representative.

End-space effects are of considerable importance in actual magnetrons. Direct currents flow at the ends of a tube by leakage from the interaction space and by emission from the end shields. These currents considerably

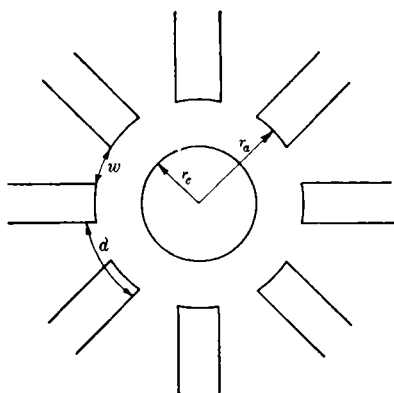


FIG. 10-10.—Cross section of interaction space.

affect the behavior of some magnetrons in the low-current region and naturally do not scale from tube to tube. The low-current behavior may also be affected by spurious oscillations in the end spaces of a tube. In some cases, the r-f fields are not uniform along the length of the anode, and the behavior of the magnetron is affected in a way difficult to assess. A magnetron with small mode separation may have irregular r-f patterns that cause its operating characteristics to depart widely from the ideal behavior of its family. In

particular, the electronic efficiency is likely to be lower than normal. These sources of inaccuracy will be systematic in a number of identical samples of a magnetron design.

In addition, data taken on a particular tube may be nonrepresentative for some further reasons. Normally a magnetron operates space-charge limited. As already mentioned, under conditions of heavy cathode drain, space-charge limitation may fail, and the boundary conditions on the electric fields at the cathode become dependent on the nature and state of the emitting surface. The operation of a magnetron under such conditions cannot accurately represent the space-charge-limited behavior of other members of its family. Data taken near the extremes of operation of a tube are likely to be inaccurate and may be less reliable for some samples than for others. Sparking and misfiring of a magnetron are greatest in these regions and affect the average values of power and current. This effect tends to close the efficiency contours about the region of operation. Finally, a particular tube may be poorly constructed. The anode, for example, may be irregular in shape, causing a reduction in electronic efficiency, or a cathode may be off-center with a resultant decrease in efficiency and a reduction of d-c voltage. The



nonsystematic errors of this sort may be largely eliminated by averaging data over a number of tubes or by using data taken on a tube of known average behavior. The latter method is often to be preferred for realizing self-consistency of the information.

### 10-7. Reduced Operating Data on Various Types of Magnetrons.—

For design purposes, the data that one would like to have on a particular

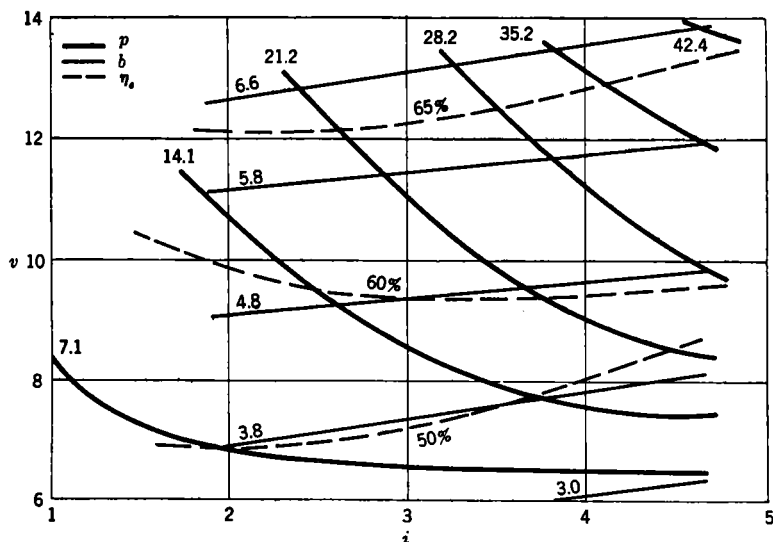


FIG. 10-11a.—Reduced performance chart of ZP676.  $N = 4$ ;  $\sigma = 0.15$ ;  $\mu = 0.35$ ;  $g = 0.28$ .

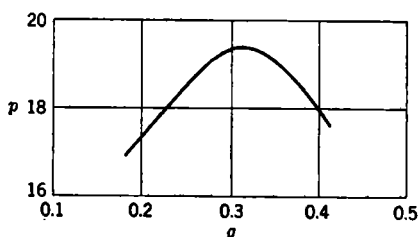


FIG. 10-11b.

FIG. 10-11b.—Load curve of ZP676 for  $b = 5.5$  and  $i = 2.8$ .

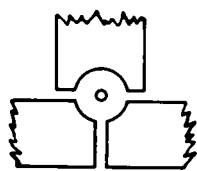


FIG. 10-11c

FIG. 10-11c.—Cross section of interaction space of ZP676.

magnetron of interest are a set of wide-range performance charts taken at a variety of loads. Usually, however, there are available only a performance chart taken at one load and a Rieke diagram presenting, as a function of load, the operation at a particular magnetic field and current. The Rieke diagram can substitute in some measure for having

several performance charts if it is assumed that a magnetron's performance varies fairly uniformly with load over its range of operation. Very often, the diagram contains data only on power and frequency, omitting information about voltage. In other cases there is available only a performance chart.

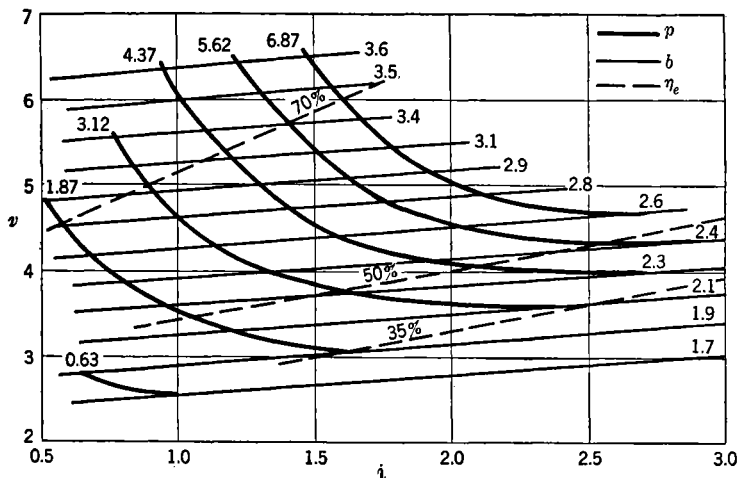


Fig. 10-12a.—Reduced performance chart of 2J32.  $N = 8$ ;  $\sigma = 0.38$ ;  $\mu = 0.37$ ;  $g = 0.51$ .

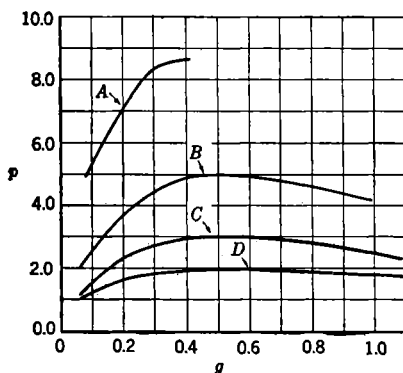


Fig. 10-12b.—Load curves of 2J32 for various values of  $b$  and  $i$ . For A,  $b = 3.6$ ,  $i = 2.1$ ; B,  $b = 2.4$ ,  $i = 2.2$ ; C,  $b = 2.4$ ,  $i = 1.4$ ; D,  $b = 2.0$ ,  $i = 1.0$ .

Accordingly, the data set forth in this chapter for a variety of magnetrons will be presented by a reduced performance chart at fixed  $g$  and, if the information is available, by a reduced load curve showing  $p$  as a function of  $g$ , for a particular value of  $b$  and of  $i$ .

When the dimensions of a magnetron are known, it is easy to calculate  $\mathfrak{B}$ ,  $\mathfrak{U}$ ,  $\mathfrak{J}$ , and  $\mathfrak{P}$  from Eqs. (26) and to construct a reduced performance

chart from measured data. The measured power output of the magnetron, however, must be corrected for the circuit efficiency of the resonant system and output circuit. The losses in the output circuit usually represent only a 2 to 3 per cent correction to the power lost in

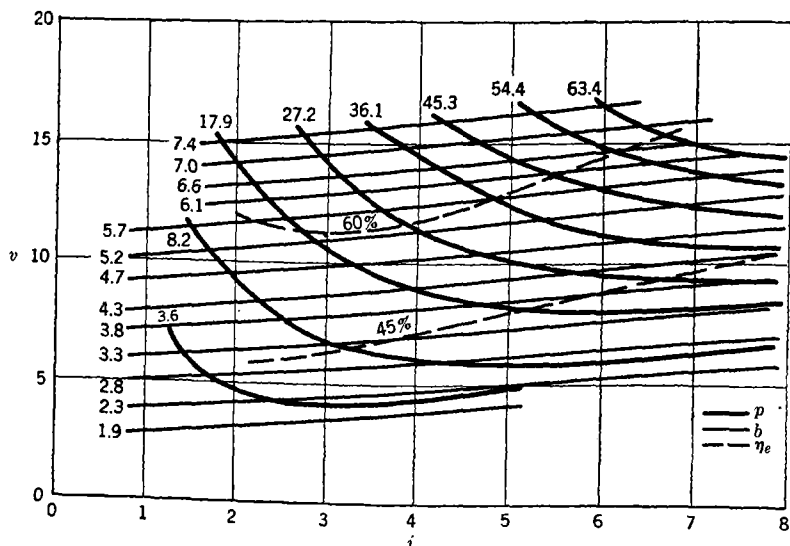


FIG. 10-13a.—Reduced performance chart of 2J39.  $N = 8$ ;  $\sigma = 0.38$ ;  $\mu = 0.52$ ;  $g = 0.17$ .

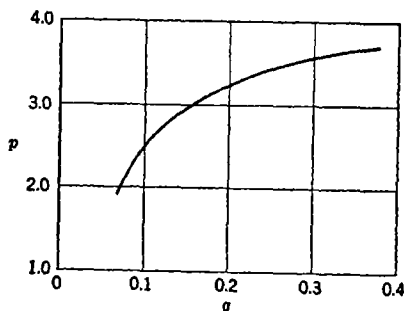


FIG. 10-13b.—Load curve for 2J39 for  $b = 2.4$  and  $i = 2.0$ .

the resonant system and have been neglected in what follows, because the data for making this correction are not generally available. In this approximation, one can write for the circuit efficiency

$$\eta_c = \frac{1}{1 + \frac{1}{\alpha_L} \frac{Q_E}{Q_U}}, \quad (28)$$

where  $Q_E$  and  $Q_U$  are derived from impedance measurements on the nonoscillating tube. The quantity  $\alpha_L$  is the ratio between the conductance presented to the tube by the load and the characteristic admittance of the line. The conductance  $G_L$  at the slots can be calculated if

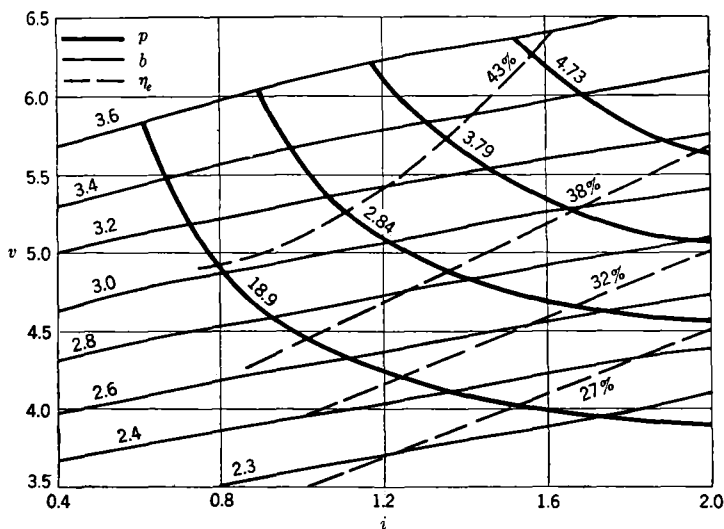


FIG. 10-14a.—Reduced performance chart of HP10V.  $N = 10$ ;  $\sigma = 0.50$ ;  $\mu = 0.36$ ;  $g = 0.22$ .

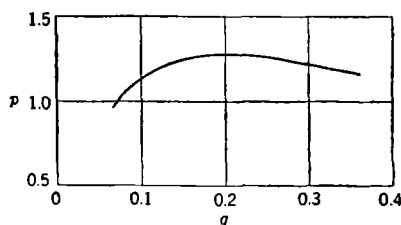


FIG. 10-14b.—Load curve for HP10V for  $b = 2.44$  and  $i = 0.79$ .

the characteristic admittance  $Y_c$  of the resonant system is known. In that case,

$$G_L = Y_c \left( \frac{1}{Q_U} + \frac{\alpha_L}{Q_E} \right), \quad (29)$$

$$g = \frac{Y_c}{S} \left( \frac{1}{Q_U} + \frac{\alpha_L}{Q_E} \right). \quad (30)$$

Unfortunately,  $Y_c$ , can at present be measured only with great difficulty, and only approximate methods exist for its calculation. This difficulty

introduces a considerable degree of uncertainty into the general design procedure, in the sense that the value of  $G_L$  for which a certain performance is to be expected may not be accurately predicted. In the data presented below, the best available methods have been used to calculate  $Y_c$ ; if better methods are found, a recalculation can be made from the information given in Chap. 20.

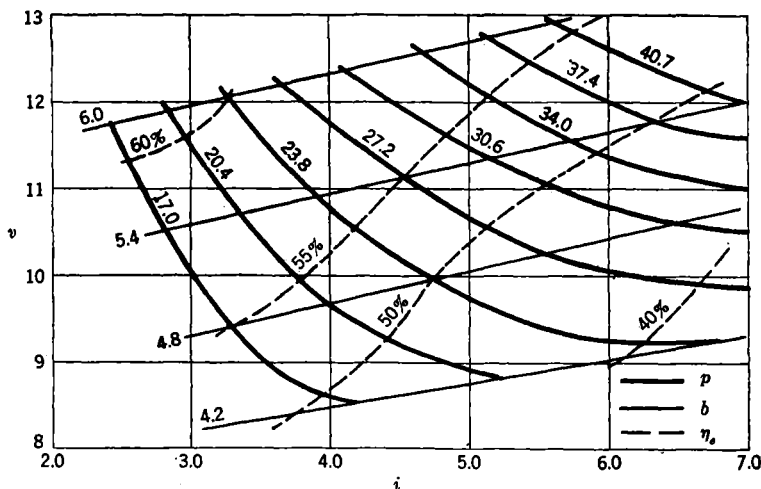


FIG. 10-15a.—Reduced performance chart of 4J33.  $N = 12$ ;  $\sigma = 0.59$ ;  $\mu = 0.33$ ;  $g = 0.46$ .

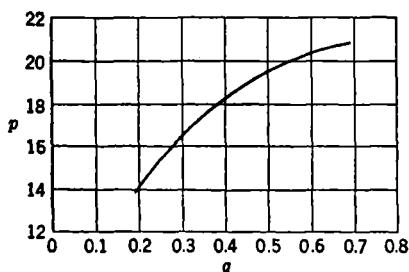


FIG. 10-15b.—Load curve of 4J33 for  $b = 4.8$  and  $i = 3.9$ .

Figures 10-11 to 10-26 contain the data used in this chapter. The factors employed in reducing the performance charts and load curves from the original data are listed in Tables 10-1 and 10-2. Some particular points in connection with the charts should be discussed.

The charts of Fig. 10-11 are for the ZP676, sometimes known as the "neutrode." A sketch of the anode cross section is shown in Fig. 10-11c. Technically, these charts can be used only in scaling to similar cross

TABLE 10-1.—CHARACTERISTIC SCALE FACTORS AND PARAMETERS EMPLOYED IN COMPUTING THE REDUCED PERFORMANCE CHARTS

Tube type	$\Phi$ , gauss	$V$ , volts	$I$ , amp	$P$ , watts	$G$ , mhos	$\sigma$	$\mu$	$N$	$\lambda$ , cm	$Q_U$	$Q_E$	$\eta$ , %	$\frac{1000}{Q_L}$	$Y_c$ , mhos	$\frac{Y_c}{S}$	$g$
ZP676	271	102	0.107	10.9	$1.05 \times 10^{-2}$	0.15	0.35	4	40.0	240	127	0.65	12.0	0.024	22.9	0.28
2J32	577	3470	12.0	41,600	3.46	0.38	0.37	8	10.7	1600	66	0.96	15.9	0.111	32.1	0.51
2J39	682	1220	2.52	3,070	2.07	0.38	0.52	8	9.06	1500	136	0.90	8.02	0.045	21.7	0.17
HP10V	533	8030	79.8	568,000	8.82	0.50	0.36	10	10.6	1500	119	0.93	9.07	0.183	24.5	0.22
4J33	502	2420	12.8	31,000	5.29	0.59	0.33	12	10.7	1500	85	0.95	12.6	0.194	36.7	0.46
4J39	633	3840	25.4	97,600	6.61	0.59	0.33	12	8.50	1100	193	0.85	6.10	0.271	41.0	0.25
725A*	1480	1820	7.05	12,800	3.87	0.50	0.39	12	3.20	650	221	0.75	6.06	0.327	84.5	0.51
725A†	1480	1820	7.05	12,800	3.87	0.50	0.43	12	3.20	1000	220	0.82	5.55	0.162	41.8	0.23
4J50	1470	2500	15.6	39,000	6.25	0.66	0.53	16	3.20	840	305	0.73	4.48	0.341	54.6	0.25
LCT	125	423	0.761	322	1.80	0.61	0.44	16	33.5	1050	95	0.92	11.5	0.109	60.6	0.70
QK61	437	149	0.362	53.9	2.43	0.60	0.48	16	9.42	770	308	0.72	4.55	0.173	71.2	0.32
AX93	1210	3440	49.6	171,000	14.4	0.62	0.41	18	3.16	1070	350	0.75	3.80	0.608	42.2	0.16
3J31	2940	3260	20.3	66,200	6.23	0.60	0.39	18	1.25	1010	480	0.68	3.07	0.298	47.8	0.15
SCWC	331	167	0.346	57.8	2.07	0.60	0.50	20	10.0	1000	200	0.83	6.00	0.291	141.	0.85
BM50	1045	160	0.227	36.3	1.42	0.61	0.50	20	3.20	556	230	0.71	6.16	0.216	152.	0.94
RD11-2	2610	4010	48.7	195,000	12.1	0.71	0.53	26	1.25	920	668	0.58	2.58	.....	.....	.....
GK13-1	2060	3040	47.1	143,000	15.5	0.77	0.49	38	1.30	1000	805	0.55	2.24	.....	.....	.....

\* Western Electric model.

† Raytheon model.

TABLE 10.2.—FACTORS INVOLVING  $N$  AND  $\sigma$ 

Tube	$N$	$\sigma$	$1 - \sigma^2$	$(1 - \sigma^2)^2$	$\frac{1}{\sigma}$	$a_1$	$1 + \frac{1}{\sigma}$	$A^*$	$\frac{1}{N(1 - \sigma^2)}$	$\frac{N}{A}$	$N\sigma$	$\frac{A}{N^2\sigma}$	$\frac{A}{\sigma}$
ZP676	4	0.152	0.977	0.955	6.57	1.52	7.57	0.210	0.256	19.0	0.608	0.0865	1.38
2J32	8	0.375	0.859	0.738	2.67	0.963	3.67	0.356	0.145	22.5	3.00	0.0148	0.952
2J39	8	0.375	0.859	0.738	2.67	0.963	3.67	0.356	0.145	22.5	3.00	0.0148	0.952
HP10V	10	0.500	0.750	0.562	2.00	0.937	3.00	0.557	0.133	17.9	5.00	0.0112	1.110
4J33	12	0.585	0.658	0.433	1.71	0.950	2.71	0.809	0.126	14.9	7.03	0.00954	1.37
4J39	12	0.585	0.658	0.433	1.71	0.950	2.71	0.809	0.126	14.9	7.03	0.00954	1.37
725A	12	0.500	0.750	0.562	2.00	0.937	3.00	0.557	0.111	21.5	6.00	0.00775	1.11
4J50	16	0.660	0.565	0.319	1.51	0.988	2.51	1.24	0.110	13.0	10.60	0.00731	1.87
LCT	16	0.605	0.634	0.401	1.65	0.960	2.65	0.903	0.0986	17.7	9.69	0.00583	1.49
QK61	16	0.596	0.644	0.414	1.68	0.953	2.68	0.859	0.0970	18.6	9.55	0.00562	1.44
AX93	18	0.619	0.617	0.381	1.61	0.963	2.61	0.967	0.0900	18.5	11.1	0.00487	1.55
3J31	18	0.600	0.640	0.410	1.67	0.955	2.67	0.872	0.0867	20.7	10.8	0.00447	1.45
SCWC	20	0.600	0.640	0.410	1.67	0.955	2.67	0.872	0.0781	22.9	12.0	0.00364	1.45
BM50	20	0.605	0.634	0.401	1.65	0.960	2.65	0.903	0.0788	22.2	12.1	0.00372	1.49
RD11-2	26	0.707	0.500	0.250	1.41	1.017	2.41	1.69	0.0769	15.4	18.4	0.00352	2.39
GK13-1	38	0.765	0.416	0.173	1.31	1.060	2.31	2.65	0.0632	14.3	28.7	0.00243	3.47

$$* A = \frac{a_1}{(1 - \sigma^2)^2 \left(1 + \frac{1}{\sigma}\right)}$$

sections. The assumption has been that the tube operates as though the missing gap were present, but it should not be considered an accurate representative of a family of magnetrons with  $N = 4$ . The data were taken on a single tube not known to be an average sample.

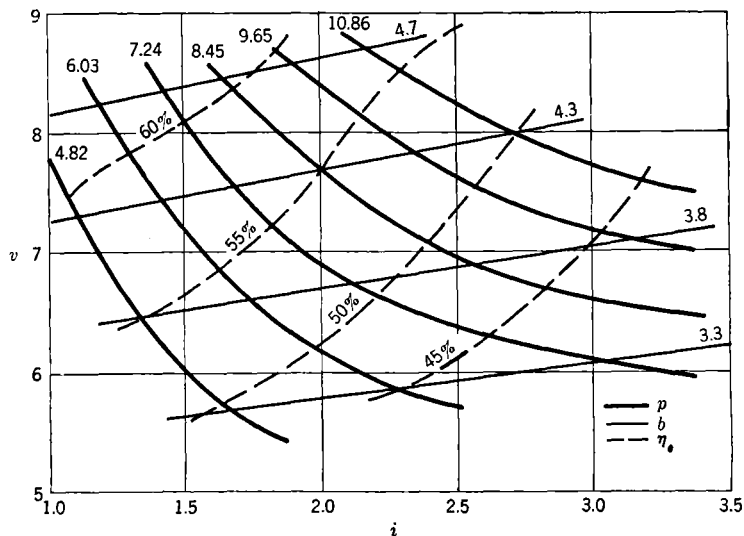


FIG. 10-16a.—Reduced performance chart of 4J39.  $N = 12$ ;  $\sigma = 0.59$ ;  $\mu = 0.33$ ;  $g = 0.25$ .

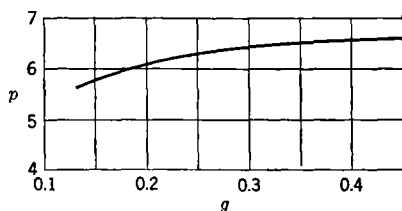


FIG. 10-16b.—Load curve of 4J39 for  $b = 4.0$  and  $i = 1.6$ .

The data plotted for the 2J32 in Fig. 10-12 are the most complete known to have been taken on a single tube. The tube was an average sample, and the data were very carefully compiled.

The performance chart of Fig. 10-13 is plotted from data on a single average 2J39 and covers a wider range of reduced variables than any of the other charts. The load curve represents average data for the 2J39 tubes.

The performance chart and load curve of Fig. 10-14 are derived from average data on production HP10V magnetrons. This tube is known



to have an irregular  $Q$ -curve and an anode block long enough that variations of r-f voltage and magnetic field along its length are appreciable. The data may therefore not be representative of this family of 10-oscillator magnetrons.

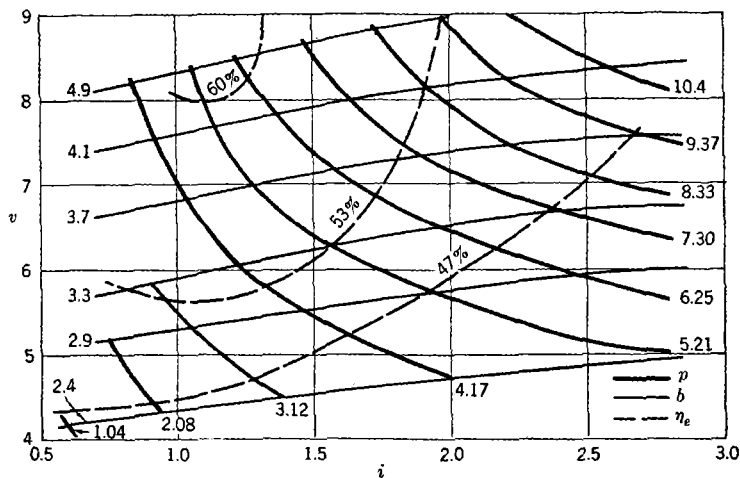


FIG. 10-17a.—Reduced performance chart of 725A.  $N = 12$ ;  $\sigma = 0.50$ ;  $\mu = 0.43$ ;  $g = 0.51$ . (Bell Telephone Laboratories.)

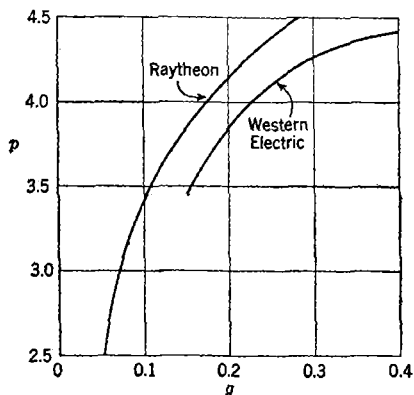


FIG. 10-17b.—Load curve of 725A for  $b = 3.7$  and  $i = 1.1$ . (Courtesy of Raytheon and Bell Telephone Laboratories.)

The performance chart and load curve shown in Fig. 10-15 are average data for production 4J33 magnetrons.

The performance chart and load curve of Fig. 10-16 are average data for production 4J39 magnetrons.

The performance chart (Fig. 10-17) is plotted from data on an average Western Electric 725A. Load curves are given for the Raytheon 725A and the Western Electric 725A, each curve being an average of data on three normal tubes. Because of their different oscillator construction, the tubes have very different characteristic admittances and operate at different load points. The agreement between the two curves is satis-

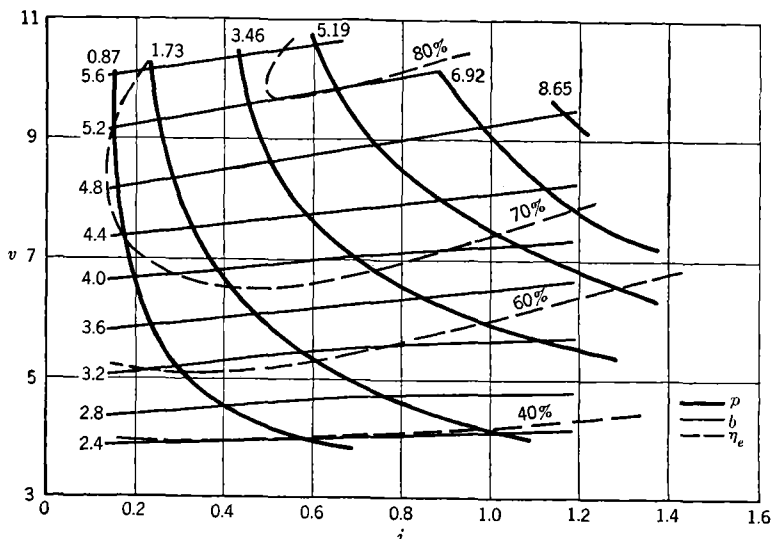


FIG. 10-18a.—Reduced performance chart of LCW.  $N = 16$ ;  $\sigma = 0.61$ ;  $\mu = 0.44$ ;  $g = 0.70$ .

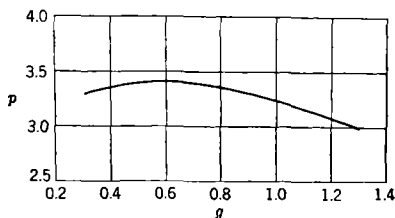


FIG. 10-18b.—Load curve of LCW for  $b = 4.0$  and  $i = 0.66$ .

factory. The slightly higher curve of the Raytheon tube may be due to less electron leakage or to an error in one of the values of  $Y_c$ .

Figure 10-18 shows data for a single LCW magnetron not known to be an average sample.

The data of Fig. 10-19 were obtained on a single average 4J50 magnetron.

Figure 10-20 was plotted from data on a single average QK61 magnetron.

The performance chart of Fig. 10-21 was taken on a single AX9 magnetron not known to be an average tube. The performance chart shows the efficiency valley that is characteristic of the rising-sun resonant system. This region of anomalously low efficiency is not representative

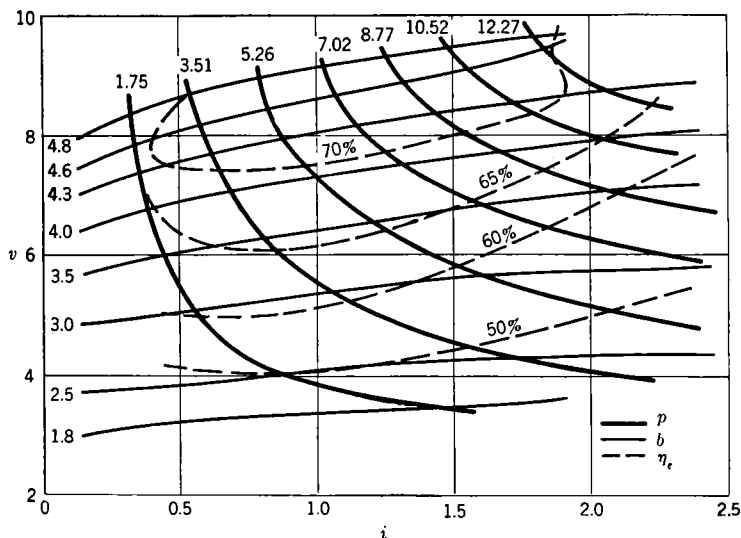


FIG. 10-19a.—Reduced performance chart of 4J50.  $N = 16$ ;  $\sigma = 0.66$ ;  $\mu = 0.53$ ;  $g = 0.25$ .

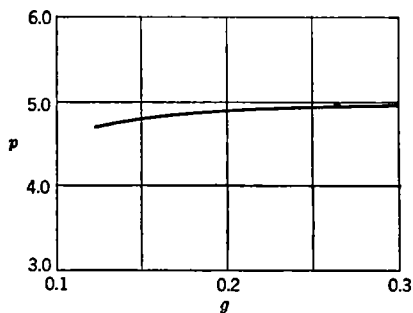


FIG. 10-19b.—Load curve of 4J50 for  $b = 4.1$  and  $i = 1.0$ .

of this family of magnetrons but is caused by the zero-component content of the  $\pi$ -mode which occurs in the rising-sun type of magnetron (see Chap. 3).

The data of Fig. 10-22 were obtained on a single average 3J31 magnetron.

The performance chart and load curve given in Fig. 10-23 were derived from a single BM50 magnetron which was chosen from several

samples because its data appeared most normal. For this reason it cannot be considered very reliable.

The performance chart and load curve of Fig. 10-24 were obtained on a single SCWC magnetron not known to be an average sample.

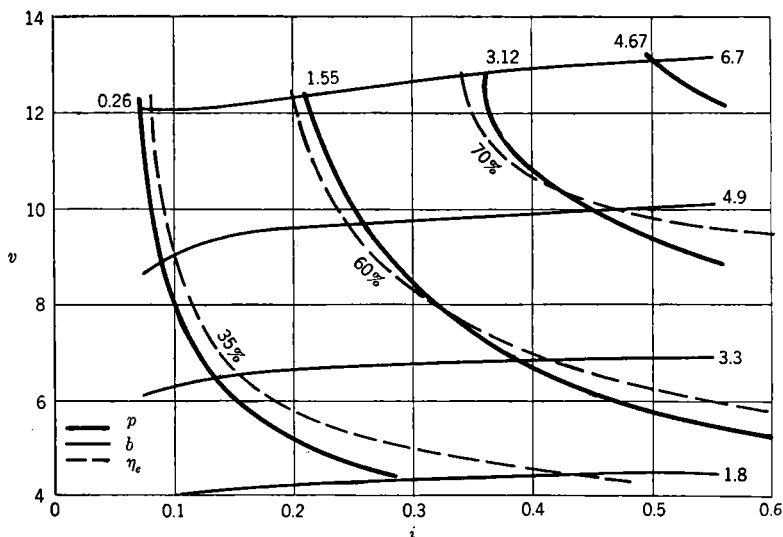


FIG. 10-20a.—Reduced performance chart of QK61.  $N = 16$ ;  $\sigma = 0.60$ ;  $\mu = 0.48$ ;  $g = 0.32$ . (Raytheon.)

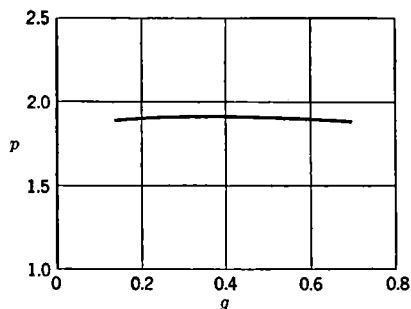
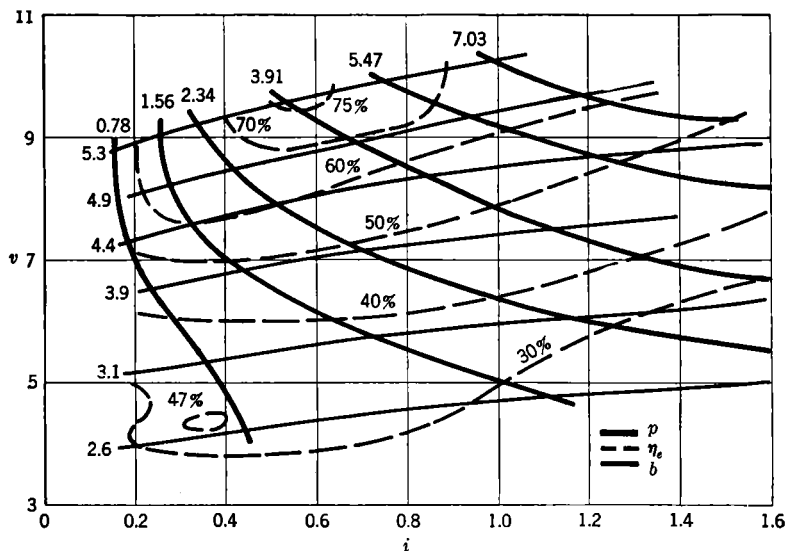
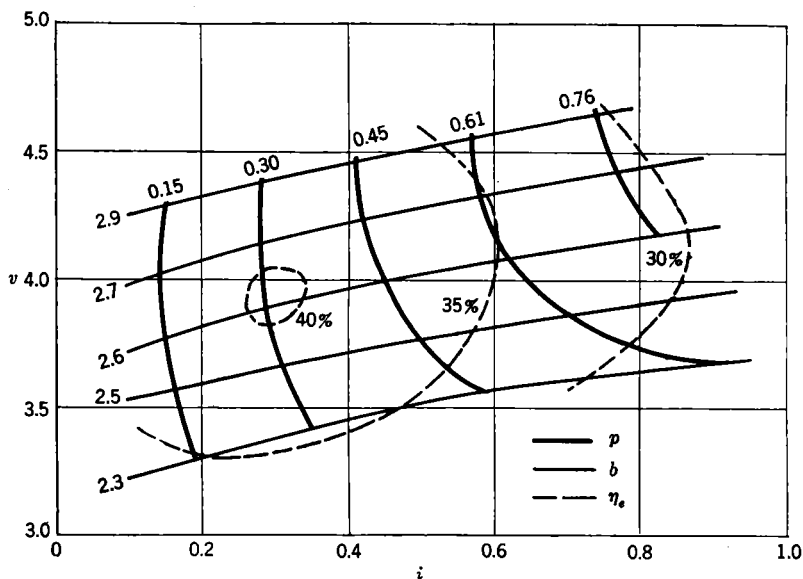
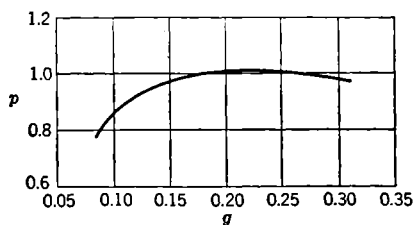
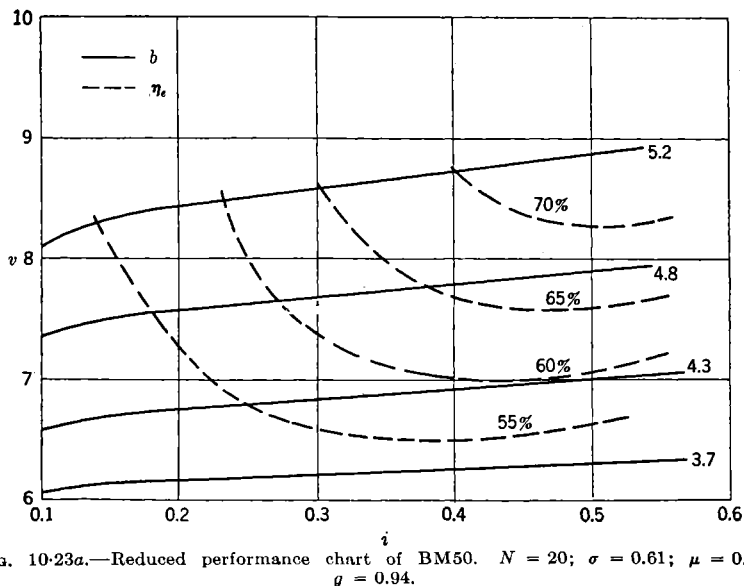
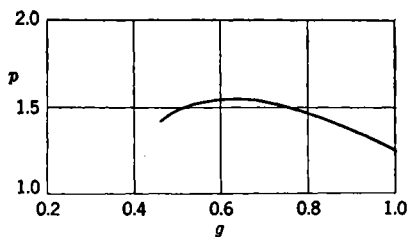


FIG. 10-20b.—Load curve of QK61 for  $b = 4.1$  and  $i = 0.35$ .

The performance charts shown in Figs. 10-25 and 10-26 were obtained on single samples of RD11-2 and GK13-1 magnetrons that are not known to be average tubes. These tubes are closed-end rising-sun magnetrons and have a sinusoidal variation of r-f voltage along the anode. Consequently, neither is really representative of its family, and the data are


 FIG. 10-21.—Reduced performance chart of AX9.  $N = 18$ ;  $\sigma = 0.62$ ;  $\mu = 0.41$ ;  $g = 0.16$ 

 FIG. 10-22a.—Reduced performance chart of 3J31.  $N = 18$ ;  $\sigma = 0.60$ ;  $\mu = 0.39$ ;  $g = 0.15$

FIG. 10-22b.—Load curve of 3J31 for  $b = 2.6$  and  $i = 0.69$ .FIG. 10-23a.—Reduced performance chart of BM50.  $N = 20$ ;  $\sigma = 0.61$ ;  $\mu = 0.50$ ;  $g = 0.94$ .FIG. 10-23b.—Load curve of BM50 for  $b = 4.1$  and  $i = 0.37$ .

included as the only available information on 26- and 38-oscillator magnetrons. No load curves are included because of the ambiguity introduced in  $Y_c$  by the lengthwise variation of r-f voltage.

It will be noted that many of the load curves show a definite maximum, the existence of which may be regarded with considerable suspicion.

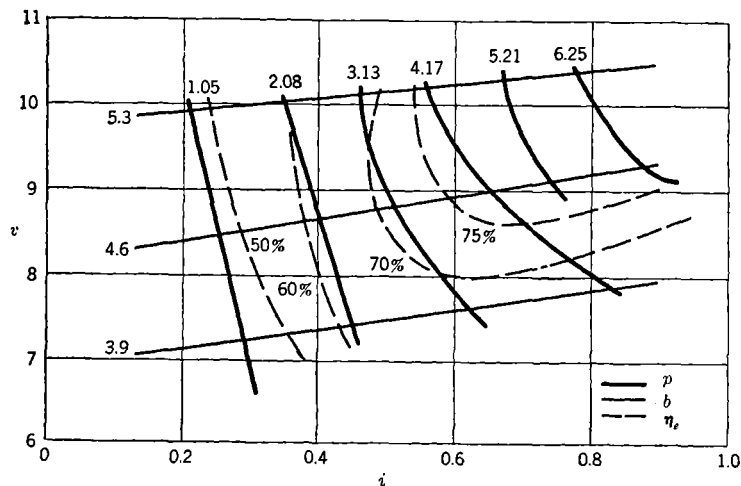


FIG. 10-24a.—Reduced performance chart of SCWC.  $N \approx 20$ ;  $\sigma = 0.60$ ;  $\mu = 0.50$ ;  $q = 0.85$ .

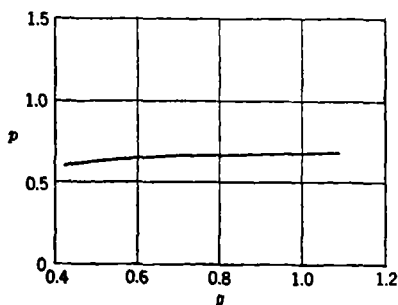


FIG. 10-24b.—Load curve of SCWC for  $b = 3.3$  and  $i = 0.29$ .

In a region of heavy loading (large  $g$ ), a number of factors tend to affect the power output unfavorably. The output-circuit loss is most important at large  $g$ , as is the loss in any external tuning device, and these losses have not been considered. Furthermore, in this region any mode instability of a tube is enhanced, and the r-f patterns become the most irregular.

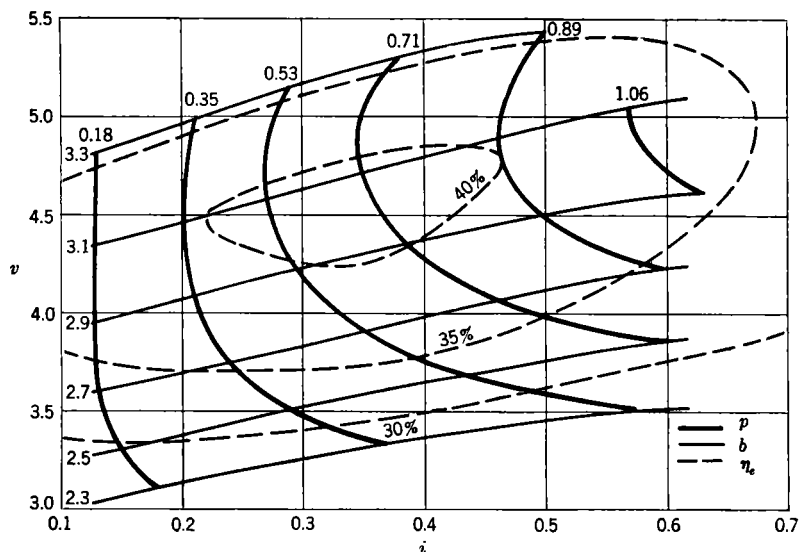


FIG. 10-25.—Reduced performance chart of RD11-2.  $N = 26$ ;  $\sigma = 0.71$ ;  $\mu = 0.53$ ;  
 $1/Q_L = 2.58 \times 10^{-3}$ .

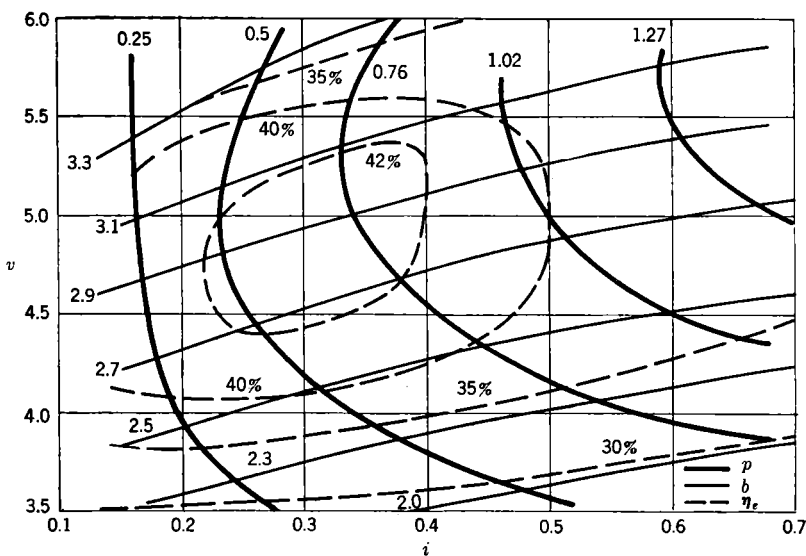


FIG. 10-26.—Reduced performance chart of GK13-1.  $N = 38$ ;  $\sigma = 0.77$ ;  $\mu = 0.49$ ;  
 $1/Q_L = 2.24 \times 10^{-3}$ .



**10-8. Determination of the Secondary Design Parameters.**—As described in Sec. 10-2, the primary parameters affecting the design of the interaction space are the voltage  $V$ , the current  $I$ , and the wavelength  $\lambda$ . These are not sufficient, however, completely to determine the interaction space and permit the calculation of the secondary design parameters. In addition, it is necessary to choose a set of shape factors,  $N$ ,  $\sigma$ , and  $\mu$ , and settle upon a relative operating point expressed by  $b$ ,  $i$ , and  $g$ . The nine quantities  $V$ ,  $I$ , and  $\lambda$ ;  $N$ ,  $\sigma$  and  $\mu$ ; and  $b$ ,  $i$ , and  $g$  can then be used to calculate the secondary parameters  $r_a$ ,  $r_c$ ,  $h$ ,  $w$ ,  $\eta_e$ ,  $G_L$ ,  $J$ , and  $B$ .

In the present formulation, the choice of the shape factors and relative operating point has been considered essentially a guess that provides a trial solution to the design problem that may or may not turn out to be self-consistent. Actually, in many cases, past experience will serve as a guide. Furthermore, the expressions that are to be calculated for the secondary design parameters will readily indicate how an inadequate choice of the shape factors or operating point must be amended.

In fixing  $N$ ,  $\sigma$ , and  $\mu$ , a choice is made of a particular family of magnetrons represented by one of the reduced performance charts. A choice of  $b$  and  $i$  then determines where, relative to this chart, the new magnetron is to operate. If now a value of  $g$  is selected that is the same as that for which the chart was measured, values of  $v$  and of  $p$  can be read off directly. If a different value of  $g$  is desired, an approximation must be made to the proper performance chart in a way to be considered shortly.

The magnetic field  $B$  can be found directly from Eqs. (25a) and (26a) and may be written

$$B = b \frac{42,400}{\lambda N(1 - \sigma^2)}. \quad (31)$$

The anode radius is determined from Eqs. (25b) and (26b) to be

$$r_a = \lambda \frac{N}{6320} \sqrt{\frac{V}{v}}. \quad (32)$$

Similarly the anode height  $h$  is found from Eqs. (25c) and (26c) to be

$$h = 2.39\lambda \left(\frac{v}{V}\right) \left(\frac{I}{i}\right) N \frac{(1 - \sigma^2)^2 \left(1 + \frac{1}{\sigma}\right)}{a_1}. \quad (33)$$

By using Eqs. (25d) and (26d), the load  $G_L$  is given by

$$G_L = g \left(\frac{v}{V}\right) \left(\frac{I}{i}\right). \quad (34)$$

Because the cathode radius is given by  $r_c = \sigma r_a$ , one has from Eq. (32)

$$r_c = \frac{\lambda \sqrt{\frac{V}{v}} N \sigma}{6320}. \quad (35)$$

Similarly, the slot opening is determined by  $w = \mu(2\pi r_a/N)$ , which becomes

$$w = \mu \frac{\sqrt{\frac{V}{v}}}{1010}. \quad (36)$$

The cathode-current density  $J$  is found from Eqs. 25c and 26c to be

$$J = 420 \frac{i}{\lambda^2} \sqrt{\frac{V}{v}} \frac{1}{N^2 \sigma} \frac{a_1}{(1 - \sigma^2)^2 \left(1 + \frac{1}{\sigma}\right)}. \quad (37)$$

Finally, the electronic efficiency is read from the performance chart or calculated from

$$\eta_e = \frac{p}{vi}. \quad (38)$$

Equations (31) to (38) express the secondary design parameters in terms of the voltage, current, and wavelength; the shape factors  $N$ ,  $\sigma$ , and  $\mu$ ; and the relative operating point given by  $b$ ,  $i$ , and  $g$ .

In Sec. 10-9 a comparison will be made of the reduced performance charts presented in this section.

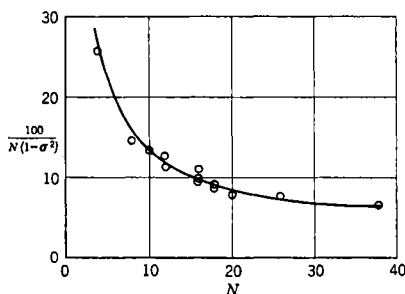


FIG. 10-27.— $100/[N(1 - \sigma^2)]$ , as a function of  $N$ .

It will be found, after a load correction is applied, that they are very similar except for a moderate decrease in electronic efficiency with larger values of  $\sigma$ . To a first approximation, therefore, the effect of the shape factors and relative operating point upon the secondary design parameters can be considered independent.

It is of interest to consider in detail the effect of the shape factors, the relative operating point, and the primary design parameters upon the magnetic field, the anode height, the cathode radius, and the cathode-current density.

**Magnetic Field.**—From Eq. (31) it is seen that the magnetic field is proportional to  $b$ ,  $1/\lambda$ , and  $1/N(1 - \sigma^2)$ . An attempt to operate high on the reduced performance chart, in search of high efficiency, for

example, requires a high field. Furthermore, the shorter the wavelength the greater the magnetic field must be. In Fig. 10-27, the quantity  $1/[N(1 - \sigma^2)]$  has been plotted against  $N$  for the tubes considered in this section. A steady decrease with increasing  $N$  is observed, indicating that a smaller field is required for larger values of  $N$ .

It is necessary to discuss at this point a limitation that is placed upon the choice of  $b$  when an anode block of the rising-sun type is used. It has been shown in Chap. 3 that the  $\pi$ -mode of a rising-sun anode block contains a certain amount of the zero component and that this contamination particularly disturbs the electron orbits and therefore decreases the electronic efficiency at magnetic fields for which the frequency of the cycloidal motion of the electrons is close to the oscillating frequency. For a plane magnetron, this critical field should be given by

$$B_c = \frac{10,600}{\lambda}; \quad (39)$$

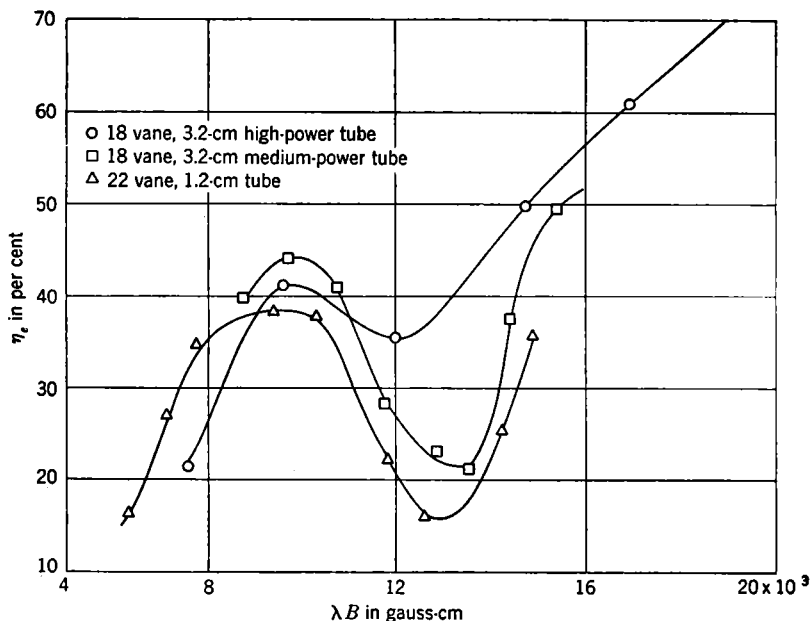
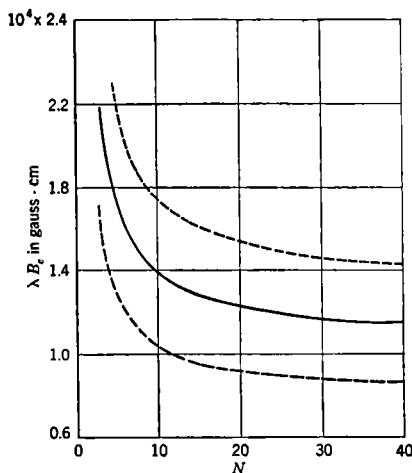
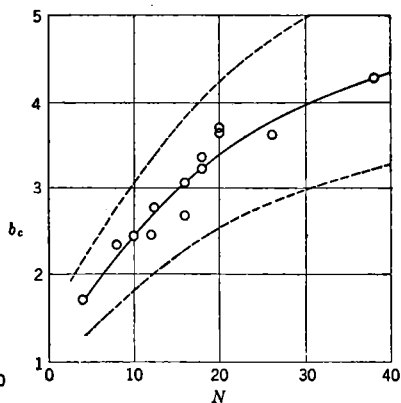
but for cylindrical magnetrons, a very qualitative argument by Slater<sup>1</sup> indicates that a correction term should be added so that the field becomes

$$B_c = \frac{10,600}{\lambda} \left( 1 + \frac{3}{N} \right). \quad (40)$$

In Fig. 10-28 the electronic efficiency at constant current is plotted against  $\lambda B$  from data obtained with two 18-vane 3-cm magnetrons and with one 22-vane 1-cm magnetron. An efficiency minimum is exhibited by the curves that checks surprisingly well with Eq. (40). Unfortunately, no rising-sun magnetrons have been made with  $N$  smaller than 18, so that Eq. (40) cannot be experimentally checked for low values of  $N$ . An interesting fact will be found in Sec. 12-6, however, which may have bearing on this subject. It will be seen that the back-bombardment power on the cathode of a 2J32 magnetron expressed in percentage of input power reaches a maximum value in the neighborhood of 1400 gauss. By placing  $\lambda = 10.7$  and  $N = 8$  in Eq. (40), a value of  $B_c$  is obtained equal to 1360 gauss. If the increased back-bombardment power could be ascribed to the same type of interaction that produces the efficiency valley of a rising-sun magnetron, the agreement of these fields would be additional evidence for the validity of Eq. (40). The identification of the two phenomena, however, cannot be made with certainty with the present knowledge of magnetron electronics.

No particular significance should be attached to the values of efficiency at the minimum point because they depend primarily upon the amount of zero component present, and that in turn depends mainly on the ratio of cavity sizes and on the anode diameter.

<sup>1</sup> J. C. Slater, RL Report No. V-5S, August 1941.

FIG. 10-28.—Dependence of electronic efficiency on  $\lambda B$  in rising-sun magnetrons.FIG. 10-29.— $\lambda B_c$  as a function of  $N$ .FIG. 10-30.—Critical reduced magnetic field  $b_c$  as a function of  $N$ .

It is clear from Fig. 10-28 that a range of about  $\pm 25$  per cent around the critical value of magnetic field  $B_c$  is excluded in designing a rising-sun magnetron. By using Eq. (40) a plot is made in Fig. 10-29 of  $\lambda B_c$  against  $N$ . The region to be avoided is delineated by two dashed lines spaced plus and minus 25 per cent from the full curve. For magnetrons of 1-cm or shorter wavelength that have a large number of oscillators, the difficulty of getting strong fields at moderate magnet weight may serve to limit the field to values for which  $\lambda B$  is less than  $0.9 \times 10^4$  gauss-cm. For longer-wavelength tubes, fields corresponding to  $\lambda B$  values greater than  $1.7 \times 10^4$  are easier to obtain, and operation above the critical region becomes feasible.

From Eqs. (31) and (40), the critical reduced field is found to be

$$b_c = (1 - \sigma^2) \frac{N + 3}{4}. \quad (41)$$

By using the values of  $\sigma$  given in Table 10-2, a plot of this quantity is made in Fig. 10-30, showing how  $b_c$  increases with increasing  $N$ . An average curve is drawn through the points, and two dashed lines spaced plus and minus 25 per cent from the average curve indicate approximately the region to be avoided.

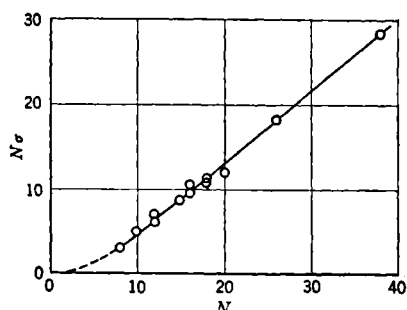


FIG. 10-32.— $N\sigma$  as a function of  $N$ .  $N\sigma = 0.85N - 3.83$ .

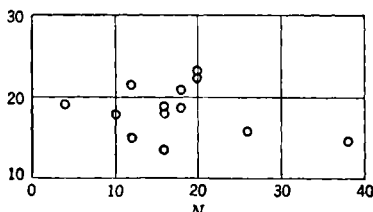


FIG. 10-31.— $N/A$  as a function of  $N$ .

**Anode Height.**—In Eq. (33), the anode height is found to be proportional to  $I/V$ ,  $v/i$ , and  $N[(1 - \sigma^2)^2(1 + 1/\sigma)]/a_1$ . A low-impedance magnetron therefore requires a long anode. In addition, a long anode is required for operation in the upper left of the reduced performance chart (in

general, a region of high efficiency), although a short anode is obtained in the lower right portion of the chart (a region of low efficiency). In Fig. 10-31  $a_1/[(1 - \sigma^2)^2(1 + 1/\sigma)]$  has been set equal to  $A$ , and the quantity  $N/A$  plotted against  $N$ . It is observed that there exists no definite trend of  $N/A$  with increasing  $N$ . This slow variation of  $N/A$  with  $N$  has an interesting implication. From Eqs. (26b) to (26d) it

may be computed that

$$\frac{G}{h} = \frac{0.420}{\lambda} \frac{A}{N}. \quad (42)$$

Hence, normalized to the same wavelength, the tubes thus far designed have had values of  $\sigma$  such that the characteristic conductances per unit length have varied over a relatively small range. Referring now to

Eq. (34), it is clear that in general  $G_L$  will be proportional to  $h/\lambda$  almost independently of  $N$ .

*Cathode Radius.*—In Eq. (35), the cathode radius is observed to be proportional to  $\sqrt{V/v}$  and  $N\sigma$ . The product of  $N\sigma$  is plotted against  $N$  in Fig. 10-32 and is observed to be nearly a linearly increasing function of  $N$ . For a low-voltage magnetron with small  $V$ , therefore, the cathode can be kept at a reasonable size by increasing  $N$  instead of by using a very small value of  $v$  and accepting a consequently low efficiency.

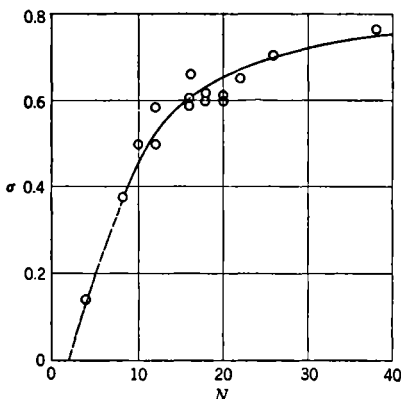


FIG. 10-33.— $\sigma$  as a function of  $N$ .

The straight line in Fig. 10-32 has the equation

$$N\sigma = 0.85N - 3.83 \quad (43)$$

or

$$\sigma = 0.85 - \frac{3.83}{N}. \quad (44)$$

Equation (44) has been used to draw the solid curve shown in Fig. 10-33, where  $\sigma$  is plotted against  $N$ .

*Cathode-current Density.*—The cathode-current density  $J$  expressed by Eq. (37) is proportional to  $i$ ,  $1/\lambda^2$ ,  $\sqrt{V/v}$ , and  $A/N^2\sigma$ . It is interesting to observe that  $J$  has no explicit dependence on  $I$ . Other things being equal, a low-current density is obtained only by operating at the far left of the reduced performance chart. This fact is illustrated by the charts for the various c-w magnetrons that, although operating at very low plate currents compared with pulsed tubes, obtain the low-current density appropriate to a c-w cathode only by operating at small reduced currents. The dependence of  $J$  on  $\lambda$  illustrates the well-known law that the current density required of a cathode varies inversely as the square of the wavelength. The dependence on  $V/v$  indicates that a smaller current density is required of low-voltage magnetrons and of

magnetrons operating high on the reduced performance chart. The quantity  $A/N^2\sigma$  has been plotted against  $N$  in Fig. 10-34. It decreases steadily with increasing  $N$  and indicates that a lower  $J$  can be achieved for a larger number of oscillators.

If a value of  $g$  is taken different from the value indicated on the chosen performance chart, the values of  $v$  and  $p$  will be correspondingly altered. To correct  $p$ , it must be assumed that it varies in the same manner as the curve in the corresponding chart of  $p$  vs.  $g$ , even though different relative operating points may be involved. The assumption of a generally uniform variation of the performance chart with load is the only justification of this procedure.

The value of  $v$ , for a given  $b$  and  $i$ , may vary from 10 to 15 per cent over the ordinary range of  $g$ , being lower for small values of  $g$ . The data for making this correction are not usually available. If the correction is ignored and a value of  $v$  is used larger than the correct value the tube will be found to require a magnetic field somewhat larger than the calculated value in order to operate at the voltage  $V$  and current  $I$ .

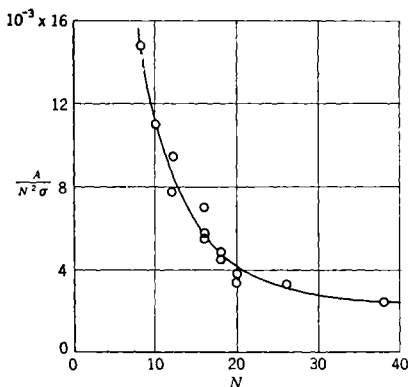


FIG. 10-34.— $A/N^2\sigma$  as a function of  $N$ .

**10-9. Comparison of the Reduced Performance Charts.**—The usefulness of the scaling principle naturally suggests an attempt to correlate the performance of magnetrons of different families. The quantities defined in Eqs. (26) have been suggested as being characteristic scale factors sufficient to reduce to a common basis the performance of magnetrons not only of different size and wavelength but also of different  $N$  and  $\sigma$ . If this is correct, all performance charts with the same  $g$  and  $\mu$  should be similar when reduced in this manner.

The characteristic factors defined in Eqs. (26) have been obtained only by arguments of plausibility. The quantities  $\mathcal{V}$  and  $\mathcal{B}$  are the voltage and field at the point of intersection of the cutoff curve and Hartree resonance line in a diagram of voltage against field, and  $\mathcal{J}$  is the corresponding current. Because this is a very characteristic point in such a diagram, it is thought possible that the performance of a tube expressed in units of  $\mathcal{B}$ ,  $\mathcal{V}$ , and  $\mathcal{J}$  should be nearly independent of its size, shape, and frequency. The reduced performance charts of this chapter have been expressed in terms of  $\mathcal{B}$ ,  $\mathcal{V}$ , and  $\mathcal{J}$  and will be used to examine this supposition.

The factor  $\mu$  determining the relative slot width should have little effect on operation over the range of values listed in Table 10-1. For unit voltage across the slots of a magnetron, the tangential electric field in the interaction space for the  $\pi$ -mode is given by

$$E_{\phi} = \sum_{m=0}^{\infty} \alpha_m \sin m\phi \frac{J'_m\left(\frac{2\pi r}{\lambda}\right)}{J'_m\left(\frac{2\pi r_a}{\lambda}\right)}, \quad (45)$$

where  $\phi$  is the angular coordinate. The coefficients  $\alpha_m$  exist for  $m = N/2, 3N/2, 5N/2, \dots$ , and are given by

$$\alpha_m = \left(\frac{N}{\pi r_a}\right) \frac{\sin \frac{m}{N} \pi \mu}{\frac{m}{N} \pi \mu}. \quad (46)$$

In Table 10-3 the values of  $\left(\sin \frac{m}{N} \pi \mu\right) / \frac{m}{N} \pi \mu$  are given for  $m = N/2, 3N/2$ , and  $5N/2$  and various values of  $\mu$ . It is seen that the fundamental

TABLE 10-3.—VALUES OF  $\sin \frac{m}{N} \pi \mu / \frac{m}{N} \pi \mu$  FOR SELECTED VALUES OF  $m$  AND  $\mu$

$\mu$	$\frac{\sin \frac{\pi \mu}{2}}{\frac{\pi \mu}{2}}$	$\frac{\sin \frac{3\pi \mu}{2}}{\frac{3\pi \mu}{2}}$	$\frac{\sin \frac{5\pi \mu}{2}}{\frac{5\pi \mu}{2}}$
0.30	0.963	0.699	0.300
0.35	0.950	0.605	0.139
0.40	0.936	0.505	0.000
0.45	0.919	0.402	0.108
0.50	0.900	0.300	0.180

component  $a_{N/2}$  varies only about 6 per cent as  $\mu$  goes from 0.30 to 0.50. The successive components vary more but are much smaller contributors to  $E_{\phi}$  within the interaction space because of the factor

$$\frac{[J'_m(2\pi r/\lambda)]}{[J'_m(2\pi r_a/\lambda)]}$$

which varies essentially as  $(r/r_a)^{m-1}$ . Successive components are multiplied by  $(r/r_a)^N$ , which for  $N$  as small as 4 and  $r/r_a$  as large as  $\frac{3}{2}$  is only 0.316. Experimentally it has been observed that only very slight changes are made in the performance of a magnetron when  $\mu$  is varied within the range 0.30 to 0.50. Measurements illustrating this fact are included



in a report by M. Healea.<sup>1</sup> Consequently, a difference in  $\mu$  will not be considered a source of serious disagreement between the reduced data of various magnetrons.

Although the factor  $\mu$  may be disregarded in comparing the various reduced performance charts, this comparison should still be made for charts with the same reduced load  $g$ . The charts of this chapter vary widely in load; they cannot, therefore, be directly compared but must be first corrected to a common  $g$ .

Two difficulties present themselves: (1) The value computed for  $g$  in any case is directly proportional to  $Y_e$ , a quantity whose value calculated by present methods is always dubious. The amount of correction to a particular case to bring it to a chosen value of  $g$  is therefore uncertain. (2) Even if  $g$  were accurately known, the load curves give very incomplete information about the variation in a performance chart as its  $g$  is changed. In meeting these difficulties, the reduced magnetic field lines and power contours will be considered separately.

It is much more convenient to compare efficiency contours than contours of constant reduced power. It will be seen that the efficiency contours can be represented with sufficient accuracy by straight lines, and this fact simplifies the extrapolation and interpolation of the data. It will be necessary to assume that power and efficiency vary proportionally as the load is changed at a point on a performance chart, and an approximation is thereby introduced that is illustrated in Fig. 10-35. The load curve gives the relation between the reduced powers  $p$  and  $p'$  corresponding to  $g$  and  $g'$  at constant  $b$  and  $i$ . Because the voltage increases slightly as  $g$  is increased,  $v'$  will be larger than  $v$ , and the efficiencies will be related by

$$\frac{\eta'_e}{\eta_e} = \left(\frac{v}{v'}\right) \frac{p'}{p}. \quad (47)$$

The efficiency  $\eta''_e$  at  $v$  and  $i$  with load  $g'$  will be again slightly smaller than  $\eta'_e$ . Because  $(v' - v)$  is small, the error in placing

$$\eta''_e = \eta_e \left(\frac{p'}{p}\right) \quad (48)$$

<sup>1</sup> M. Healea, RL Report No. 586, Aug. 1, 1944.

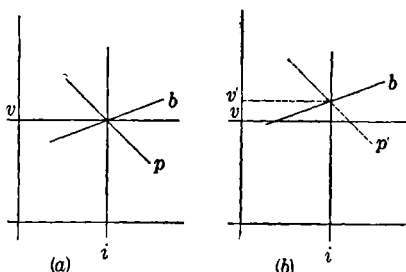


FIG. 10-35.—Variation of performance chart with load. (a) Load  $g$ ; (b) load  $g' > g$ .

is unimportant compared with the other sources of error mentioned earlier.

Instead of trying to correct all the performance charts to a common value of  $g$ , each set of efficiency contours will be adjusted by multiplying them by the ratio of the power at the maximum of the appropriate load curve to the power at the load point of the performance chart. It will develop that the efficiencies corrected in this way show certain correlations, so that the procedure is useful even if arbitrary. If it is assumed that the efficiencies of all magnetrons at all operating points are the same function of  $g$ , and if  $\mathfrak{G}$  operates as a proper scale factor, a group of ideal load curves should appear as the full lines in Fig. 10-36

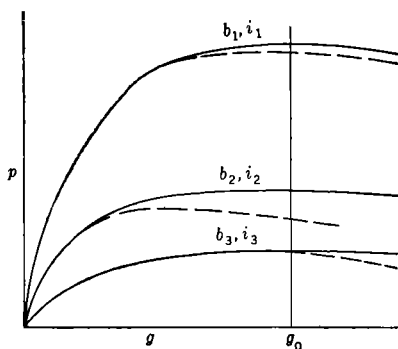


Fig. 10-36.—Expected appearance of a group at load curves.

with their ordinates everywhere proportional. Experimental load curves appear to change very slowly after reaching a maximum point, and Fig. 10-36 has been drawn accordingly. Because lead losses and pattern distortion may cause the power to increase less rapidly than expected for increasing  $g$  and in a different way for each tube, the load curves should actually be expected to appear, under the above assumptions, as the dotted lines in Fig. 10-36, where small changes in power have caused

the maximum points to scatter widely. With load curves of this shape, the adjustment of the efficiency contours to maximum power results in an approximate correction to a common load  $g_0$  located somewhere in the flat region of the curves.

An assembly of the actual load curves up to  $N = 16$  is given in Fig. 10-37. These curves seem to depart further from proportionality than the assumptions made above would lead one to expect. This behavior can be due to (1) inaccurate values of  $Y_c$ , (2) inaccurate data, (3) unsuccessful scaling by  $\mathfrak{G}$ , or (4) nonadherence to the assumption of completely uniform variation of the performance charts with load. The source of the difficulty is not evident at present.

The data beyond  $N = 16$  are not considered reliable enough to contribute to the comparisons that will be made, while the data for ZP676 and HP10V are to be excluded for reasons given in Sec. 10-5. Data concerning the QK61 will be found to have poor agreement with the other data used and have also been omitted from Fig. 10-37. The

load curve for the 725A in Fig. 10-37 is an average of the curves for the Raytheon and Western Electric tubes.

As a first step, the adjusted efficiency contours for all tubes of a given  $N$  have been collected on a single plot. These plots are shown for  $N = 8$ ,  $N = 12$ , and  $N = 16$  in Figs. 10-38 to 10-40. On these plots, it has been possible to draw a set of straight lines representing the data

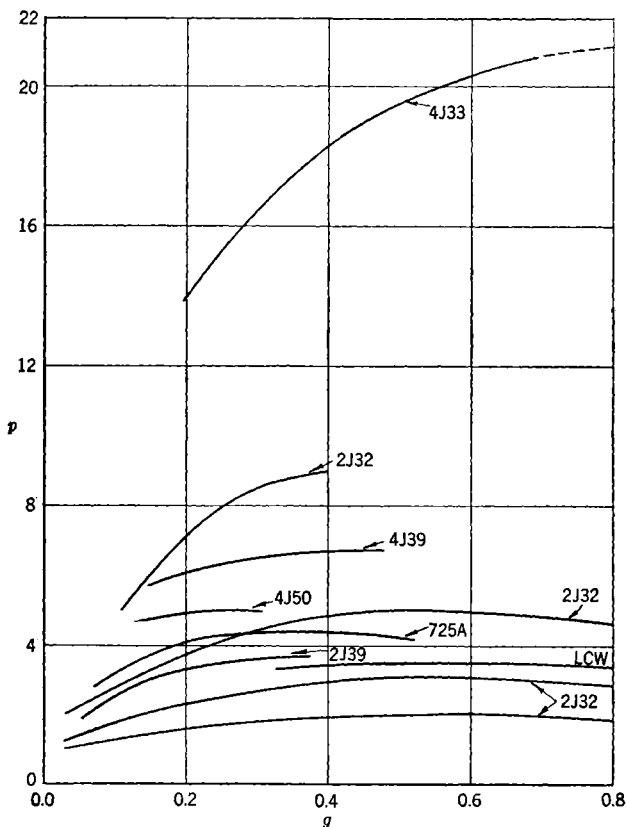


FIG. 10-37.—Assembly of the reduced load curves.

within 15 per cent except at one or two points. A number of reasons have been given previously that indicate why efficiencies should be lower than normal at the extremes of operation of a tube, thus tending to close the efficiency contours about the operating region. This effect should be considered in evaluating how well the straight lines represent the data. In Fig. 10-40, there is observed the very unusual behavior of the efficiency

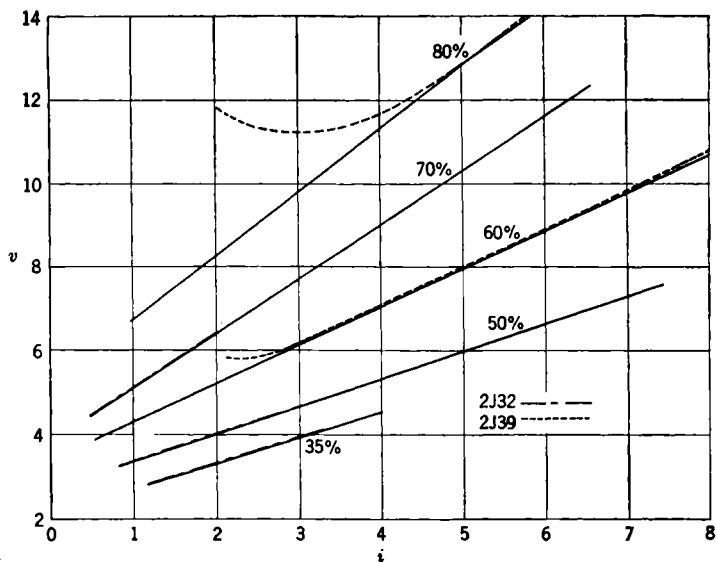


FIG. 10-38.—Collected efficiency contours for  $N = 8$ .  $\sigma = 0.38$ .

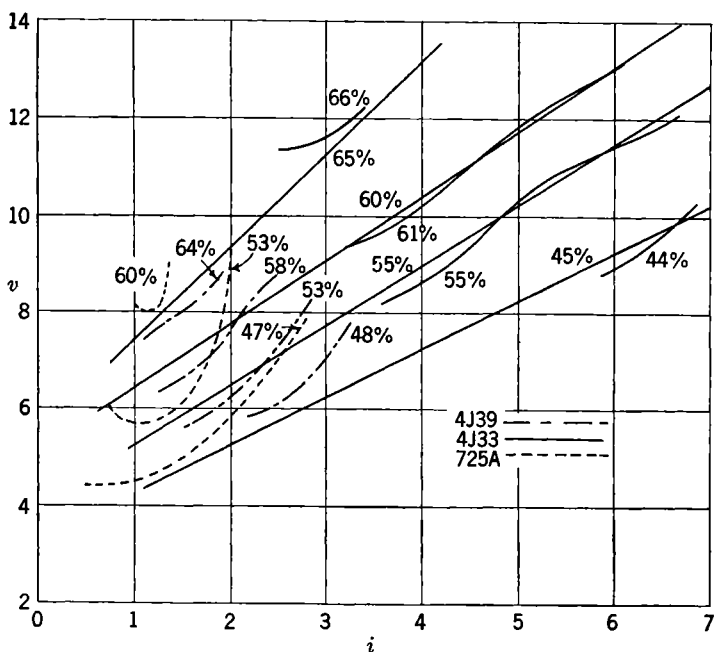


FIG. 10-39.—Collected efficiency contours for  $N = 12$ .  $\sigma = 0.50$  to  $\sigma = 0.59$ .

lines for the QK61. It is not certain whether this shape is due to some disturbing effect, such as leakage current, or represents the real behavior of the contours below  $i = 0.5$ . The straight lines have not been extended into this region.

The general good consistency of the efficiencies in the plots for  $N = 8$ ,  $N = 12$ , and  $N = 16$  confirms the reasonableness of the adjustments made in the contours and indicates that the small differences in  $\sigma$  for the tubes of the same  $N$  either have been taken into account by the scale factors or cause negligible effects. Consequently, each chart has been indicated as valid over the range of  $\sigma$  shown.

In Fig. 10-41 the efficiency lines for the various values of  $N$  have been drawn on a single chart. Two important points emerge: (1) The various lines show a remarkable family resemblance; and (2) although the contours for  $N = 12$  and  $N = 16$  show reasonable numerical agreement, the efficiencies for  $N = 8$  are everywhere much higher. From the first point, support is given to  $\bar{v}$  and  $\bar{s}$  as proper scale factors. From the second point, however, it is clear that the scaling process used has not resulted in a complete coincidence of the efficiency contours and in that sense has failed.

Before considering this matter further, a comparison will be made of the contours of constant  $b$ . Again, this comparison cannot be strictly made unless the reduced charts are first reduced to a common value of  $g$ ; but because the data to make this correction are unavailable, it will be disregarded. A direct comparison will nevertheless be of value, because the correction would result only in a small, roughly parallel displacement of the field lines. In Fig. 10-42 the contours of almost all of the tubes have been superimposed for  $b$  equal to 2.50, 3.50, 4.50, 5.50, and 6.50. These particular contours have been obtained by a linear interpolation of the lines of  $b$  on the individual performance charts. The data for the QK61 have been excluded because of extreme disagreement of unknown origin. Included on the chart are a set of straight heavy lines

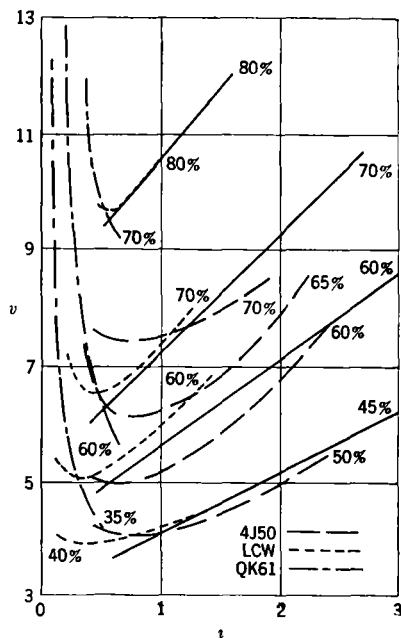


FIG. 10-40.—Collected efficiency contours for  $N = 16$ .  $\sigma = 0.60$  to  $0.66$ .

identified by a value of  $b$ , passing through the corresponding Hartree voltage at  $i = 0$  and giving, in each case, the best average agreement with the corresponding experimental contours. The intermediate lines are interpolated. The vertical spacing of these lines corresponds well with the spacing of the experimental contours. Thus, by inspection of Fig. 10-42, it is seen that there is a maximum spread in each set of field contours of 20 per cent and a maximum deviation from the straight lines of 10 per cent. The correction for load would increase or decrease the deviation by a small amount. To this extent, therefore, the field lines

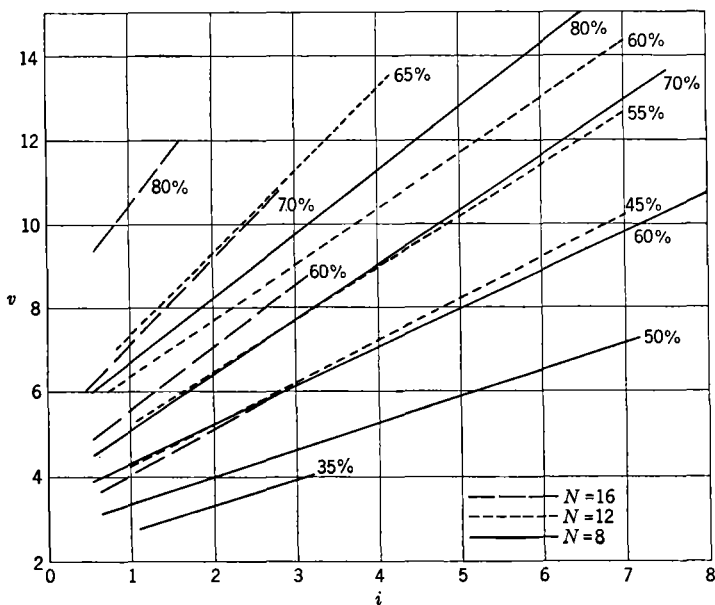


FIG. 10-41.—Assembly of efficiency contours for  $N = 8$ ,  $N = 12$ , and  $N = 16$ .

have been brought into coincidence. There appear to be some systematic changes in shape of the contours as  $N$  increases, but this question cannot be adequately discussed without data sufficient to reduce the charts accurately to a common  $g$ .

**10-10. The Universal Performance Chart.**—The comparisons that have been made above indicate that the scale factors  $\mathfrak{B}$ ,  $\mathfrak{U}$ ,  $\mathfrak{J}$ , and  $\mathfrak{G}$  are sufficient over the range considered to produce at least a rough coincidence of the magnetic field lines and to demonstrate a similarity between the efficiency contours of tubes with different  $N$ . An efficiency contour passing through a particular point of the  $(v, i)$ -plane appears to have a particular direction independent of the value of  $N$ . However, the

numerical value that this contour possesses does seem to depend on  $N$ . The use of these scale factors, therefore, results in what may be called a "pseudo scaling" of a magnetron.

The inability of the scale factors to produce a true scaling is confirmed by measurements taken by M. Healea.<sup>1</sup> The efficiency of an eight-oscillator magnetron was measured at constant magnetic field, current, and load for three different values of  $\sigma$ . These three points appear in Fig. 10-43, together with efficiency lines from Fig. 10-38, which correspond to a value of  $\sigma = 0.38$ . The value of  $g$  for Healea's data is not the same as that appropriate to Fig. 10-38 so that her efficiency for  $\sigma = .37$  does not agree with the values indicated on the efficiency lines.

Nevertheless, it is observed that there is a spread of 25 per cent in the three efficiencies, although the spacing of the lines would predict a spread of not more than 7 per cent.

That the scaling introduced by  $\mathfrak{B}$ ,  $\mathfrak{V}$ ,  $\mathfrak{g}$ , and  $\mathfrak{g}$  should behave in this way has been suggested in a report by Allis.<sup>2</sup> He calculates that the efficiency of a magnetron should be constant along a line given by

$$D = \frac{b}{\sqrt{v}} = \text{const.}, \quad (49)$$

and that the efficiency to be associated with each such line is a function of  $\sigma$ . This theory, however, is uncertain in many ways, and in particular, as will be seen shortly, the efficiency contours predicted by Eq. (49) do not agree completely with Fig. 10-41. Therefore, Allis' results cannot be called upon to indicate a theoretical method of associating efficiencies for each case with the various contours.

In establishing a universal performance chart, one can proceed with the present data only to the following extent. A set of  $(v, i)$ -characteristics can be drawn that represent the data of this chapter within 10 per cent but that do not reproduce well the shape of the experimental characteristics in all cases. These lines are drawn with no dependence on load because there is insufficient data to introduce such a correction. A set of straight lines are added that when assigned the proper values in

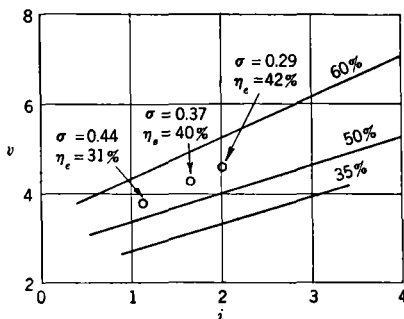


FIG. 10-43.—Variation in efficiency with  $\sigma$  for  $N = 8$ .

<sup>1</sup> M. Healea, RL Report No. 586, Aug. 1, 1944.

<sup>2</sup> W. P. Allis, "Theory of Space Charge in an Oscillating Magnetron," RL Report No. 176, July 1, 1942.

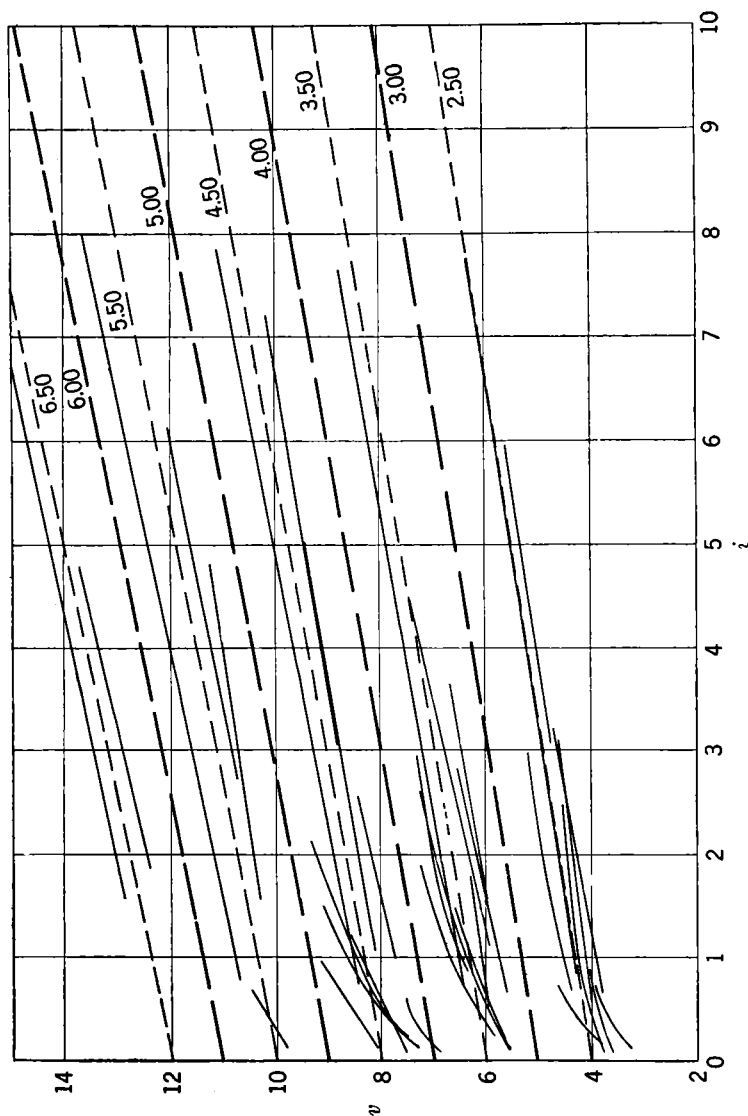


FIG. 10-42.—A comparison of  $(v, i)$ -characteristics for various values of  $b$ .

each of three cases represented by different values of  $N$  and  $\sigma$ , reproduce the experimental efficiencies within 15 per cent when these are corrected to a loading that gives maximum power.



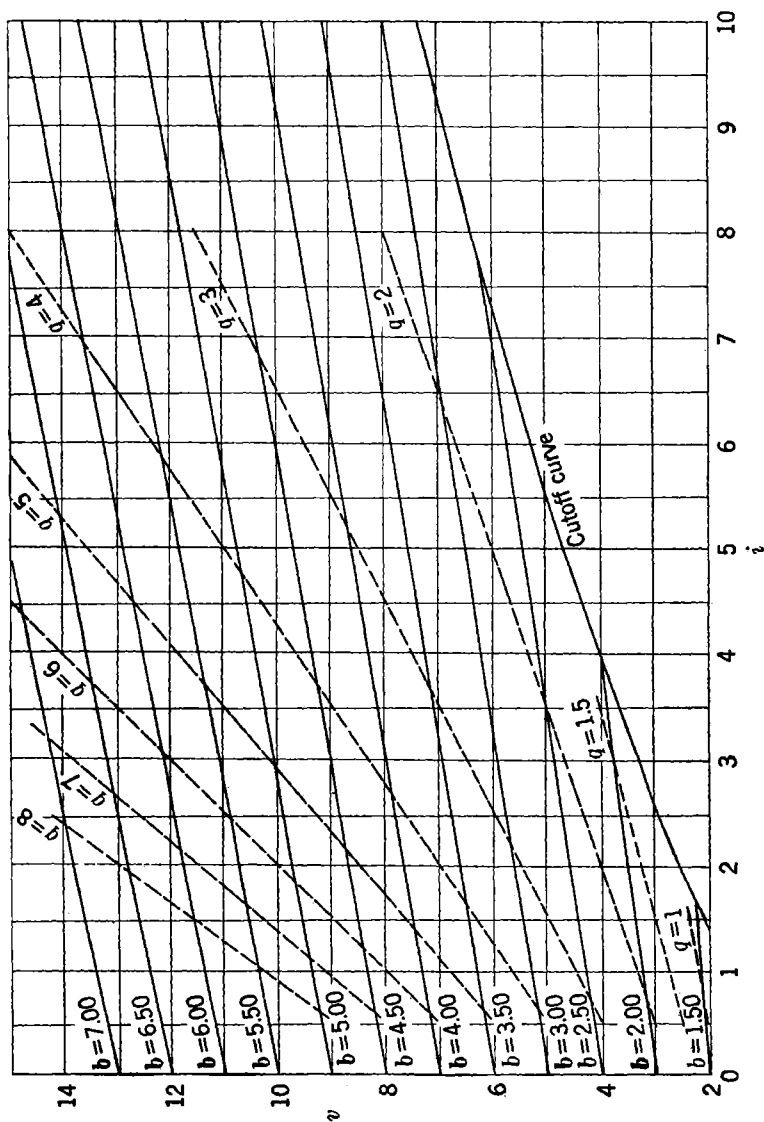


FIG. 10-44.—Universal performance chart. The solid lines are  $(v, i)$ -characteristics for which  $v = (2b - 1) + (9 + b)(i/40)$  when  $b \geq 2.50$ , and  $v = (2b - 1) + [2(b + 1)/b^2] i$  when  $b < 2.50$ . The dashed lines are efficiency for  $v = (5q + b)/6 + (q/3)i$ .

A universal performance chart constructed in this way is shown in Fig. 10-44. Above  $b = 2.50$ , the  $(v, i)$ -characteristics are the same as those drawn in Fig. 10-42 and can be represented by the linear equation

$$v = (2b - 1) + \frac{9 + b}{40} i. \quad (50)$$

The contour for  $b = 1.00$  must be a horizontal line passing through  $v = 1$ , a condition not satisfied by Eq. (50). Consequently, it is assumed that below  $b = 2.50$  the characteristics have the slope suggested by Slater<sup>1</sup> and given by

$$v = (2b - 1) + \frac{2(b - 1)^2}{b^3} i. \quad (51)$$

The characteristics defined by Eqs. (50) and (51) coincide closely for  $b = 2.50$ . Having defined the  $(V, I)$ -characteristics, it is possible to draw in the cutoff curve that must satisfy the relation  $v = b^2$ . All efficiencies must become zero on this curve to be consistent with the  $(V, I)$ -lines.

The efficiency contours of Fig. 10-41 have been matched closely with a family of straight lines given by

$$v = \frac{5q + 6}{6} + \frac{q}{3} i. \quad (52)$$

The quantity  $q$  is a parameter designating a member of the family, and its value is indicated on each efficiency line drawn in Fig. 10-44. The efficiencies to be associated with these lines will be called  $\eta_0(q, \sigma, N)$  and are indicated in Table 10-4, to the extent of the present data. There are

TABLE 10-4.—TABLE OF EFFICIENCY  $\eta_0$  AS A FUNCTION OF  $q$ ,  $\sigma$ , AND  $N$

$q$	$N = 8,$ $\sigma = 0.38$	$N = 12,$ $\sigma = 0.50 \text{ to } 0.59$	$N = 16,$ $\sigma = 0.60 \text{ to } 0.66$	SCWC, $N = 20,$ $\sigma = 0.60$
1.5	0.30	....	....	....
2.0	0.50	....	....	....
3.0	0.62	0.46	0.48	....
4.0	0.73	0.57	0.59	....
5.0	0.82	0.62	0.67	....
6.0	....	0.67	0.72	0.68
7.0	....	....	0.76	0.74
8.0	....	....	0.79	....

included values obtained from comparison with the performance chart for the SCWC.

<sup>1</sup>J. C. Slater, "Theory of Magnetron Operation," RL Report No. 200, Mar. 8, 1943.

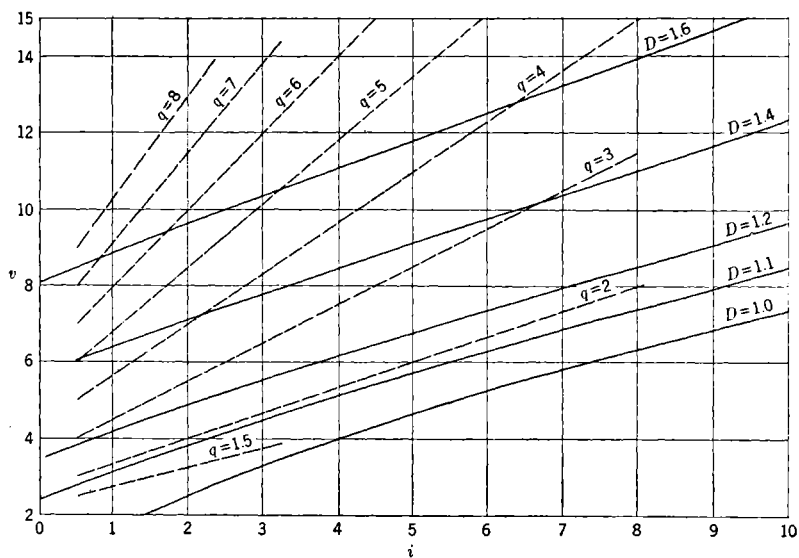
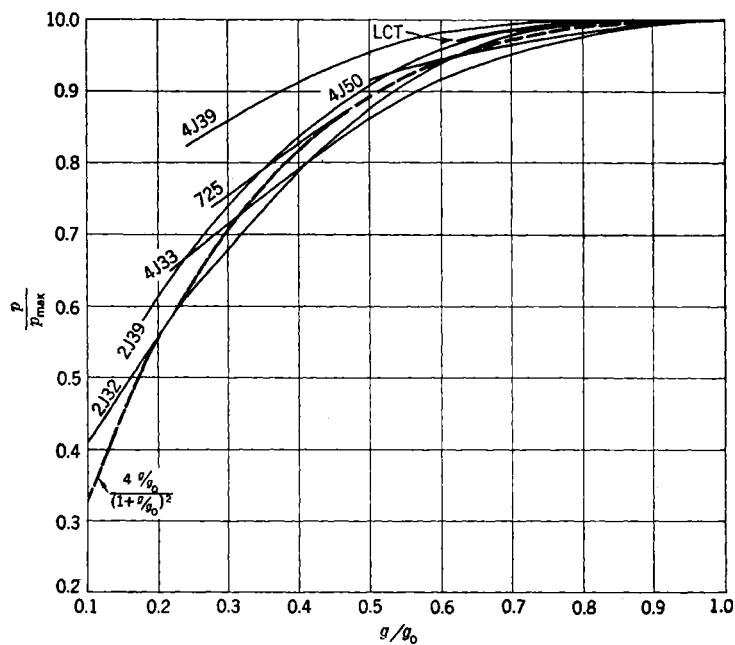
FIG. 10-45.—Comparison of efficiency lines and lines of constant  $D$ .

FIG. 10-46.—Normalized load curves.

Using the  $(v,i)$ -characteristics defined in Eqs. (50) and (51), the lines of constant  $D$  defined in Eq. (49) can be constructed. These lines are compared in Fig. 10-45 with the efficiency contours defined by Eq. (52); the lines disagree badly in slope except close to the cutoff curve. The experimental efficiencies therefore decrease more rapidly with increasing current than Allis' theory would predict, except for small values of  $b$ . This observed fact is consistent with the careful data taken by Rieke,<sup>1</sup> Platzman, and Evans in which the efficiencies are found to follow very closely lines of constant  $D$  because their data do not extend above  $v = 6$ .

It would be very desirable at this point to be able to exhibit a single curve giving the variation of the efficiencies of the universal performance chart with load. As has been said, the unsystematic appearance of the load curves in Fig. 10-37 makes it impossible to state a single value of  $g$  for which the efficiencies that have been given are valid. A certain amount of progress can be made, however, by normalizing the load curves to the maximum value of  $p$  and the corresponding value of  $g$ . These curves are shown in Fig. 10-46 where  $p/p_{\max}$  has been plotted against  $g/g_0$  for the cases considered. Except for one case the curves now show a reasonably similar variation with  $g/g_0$  and can be represented by an equation of the form

$$\frac{p}{p_{\max}} = \frac{4 \frac{g}{g_0}}{\left(1 + \frac{g}{g_0}\right)^2}. \quad (53)$$

Therefore, using an approximation introduced in Eq. (48), one can write

$$\frac{\eta_e}{\eta_0(q, \sigma, N)} = \frac{4 \frac{g}{g_0}}{\left(1 + \frac{g}{g_0}\right)^2}, \quad (54)$$

or

$$\eta_e = \eta_0(q, \sigma, N) \frac{4g_0g}{(g_0 + g)^2}. \quad (55)$$

The difficulty that has been encountered can now be expressed by saying that the data do not indicate if a single value of  $g_0$  exists. The average value of  $g_0$  is 0.5, but the range is from 0.25 to 0.80, or almost a factor of 2 each way.

**10-11. The General Design Formulas.**—The analysis that has been made of the general scaling laws opens the way for more comprehensive design procedures. The 10 equations that have been formulated are

<sup>1</sup> F. F. Rieke *et al.*, "Analysis of Magnetron Performance, Part II," RL Report No. 451, Mar. 3, 1944.

$$B = b \frac{42,400}{N\lambda(1 - \sigma^2)}, \quad (56)$$

$$r_a = \frac{N\lambda}{6320} \sqrt{\frac{V}{v}}, \quad (57)$$

$$h = 2.39\lambda \frac{N}{A} \left(\frac{I}{i}\right) \left(\frac{v}{V}\right), \quad (58)$$

$$r_c = \lambda \frac{N\sigma}{6320} \sqrt{\frac{V}{v}}, \quad (59)$$

$$J = 420 \frac{i}{\lambda^2} \sqrt{\frac{V}{v}} \frac{A}{N^2\sigma}, \quad (60)$$

$$w = \frac{\mu\lambda}{1010} \sqrt{\frac{V}{v}}, \quad (61)$$

$$G_L = g_0\gamma \left(\frac{I}{V}\right) \left(\frac{v}{i}\right), \quad (62)$$

$$\eta_e = \eta_0(q, \sigma, N) \frac{4\gamma}{(1 + \gamma)^2}, \quad (63)$$

$$v = (2b - 1) + (9 + b) \frac{i}{40} \quad b \geq 2.50, \quad (64a)$$

$$v = (2b - 1) + \frac{2(b - 1)^2}{b^3} i \quad b < 2.50, \quad (64b)$$

$$v = \frac{5q + 6}{6} + \frac{q}{3} i. \quad (65)$$

The accuracy of this set of design formulas is limited by Eqs. (62), (64a), (64b), and (65). In Eqs. (62) and (63),  $g$  has been replaced by  $\gamma g_0$  in such a way that all the uncertainty about  $g_0$  appears in the equation for  $G_L$ . The quantity  $\gamma = g/g_0$ , indicating at what fraction of the load for maximum power a magnetron operates, replaces  $g$  as a variable. The precision with which Eqs. (64a), (64b), and (65) represent the magnetic field lines and efficiency contours has already been discussed.

The scope of the design formulas is limited by the factor  $\eta_0(q, \sigma, N)$  in Eq. (65) which is known with the present data only to the extent of Table 10.4.

The 10 equations listed above contain 19 quantities; any design procedure must fix in some way 9 of these quantities. In Secs. 10-5 through 10-8 a process has been discussed at length in which the primary design parameters  $\lambda$ ,  $V$ , and  $I$  are fixed; the shape factors  $N$ ,  $\sigma$ , and  $\mu$  and the relative operating point  $b$ ,  $i$ , and  $\gamma$  are assumed; and the quantities  $\eta_e$ ,  $G_L$ ,  $B$ ,  $J$ ,  $r_a$ ,  $r_c$ ,  $h$ , and  $w$  are computed and then examined for consistency with other aspects of the design. Some alternative procedures are to be discussed below which again fix the values of  $\lambda$ ,  $V$ , and  $I$  and result in trial values of the remaining quantities. These alternatives

vary by assuming the values for different groups of six parameters. Table 10-5 illustrates the choice made in three such alternatives.

TABLE 10-5.—THE FIXED PARAMETERS IN ALTERNATIVE DESIGN PROCEDURES

Parameter	Those used in Chap. 10	Alternative		
		I	II	III
$N$	✓	✓	..	✓
$\sigma$	✓	..	..	✓
$\mu$	✓	✓	✓	✓
$b$	✓	..	✓	..
$i$	✓	✓	✓	..
$\gamma$	✓	..	✓	✓
$\eta_e$	..	✓	✓	✓
$G_L$	..	✓	..	..
$B$	..	..	..	..
$J$	..	..	✓	✓
$r_a$	..	..	..	..
$r_c$	..	..	..	..
$h$	..	✓	..	..
$w$	..	..	..	..

*Alternative I.*—This case recognizes an attack made on the general design problem by Hagstrum, Hebenstreit, and Whitcomb of Bell Telephone Laboratories. The choice of assumed parameters used here assures that the design will meet certain fixed requirements laid on the circuit efficiency, the magnetic field, and the anode height. One relation between  $v$  and  $\sigma$  can be obtained from Eqs. (56) and (64), and a second relation is provided by Eq. (58). When these expressions are combined,  $\sigma$  becomes

$$\sigma = \left[ \left( \frac{i}{I} \right) \frac{hV}{2.39N\lambda} \right] A - \left[ \frac{N\lambda B}{42,400} \left( 2 + \frac{i}{40} \right) \right] (1 - \sigma^2) + \left( 1 - \frac{9i}{40} \right) = 0. \quad (66)$$

This equation is not precisely that obtained by Hagstrum, Hebenstreit, and Whitcomb because, instead of Eqs. (64), they use an expression more closely fitting their particular case and neglecting any change in slope of the  $(v, i)$ -characteristic with increasing  $b$ .

Equation (66) does not necessarily provide a reasonable value of  $\sigma$ . The parameters entering the equation, therefore, have the restriction that  $\sigma$  must lie within some accepted range. The remaining undetermined quantities can now be found by using the value of  $\sigma$  given by Eq. (66).

*Alternative II.*—This procedure fixes the cathode current density  $J$ , the electronic efficiency  $\eta_e$ , and the relative operating point. From

Eqs. (64) and (65)  $v$  and  $q$  can be determined immediately; Eqs. (60) and (55) then provide two relations between  $N$  and  $\sigma$  as follows:

$$\frac{A}{\sigma} = N^2 \frac{\lambda^2 J}{420 \sqrt{V}} \frac{\sqrt{v}}{i}, \quad (67)$$

and

$$\eta_0(q, \sigma, N) = \eta_e \frac{(1 + \gamma)^2}{4\gamma}. \quad (68)$$

By choosing a value of  $N$ ,  $A/\sigma$  is determined and therefore  $\sigma$  can be found from Fig. 10-47. The value of  $\eta_0$  corresponding to these values of  $N$  and  $\sigma$  can then be estimated from Table 10-4 if they are within the known

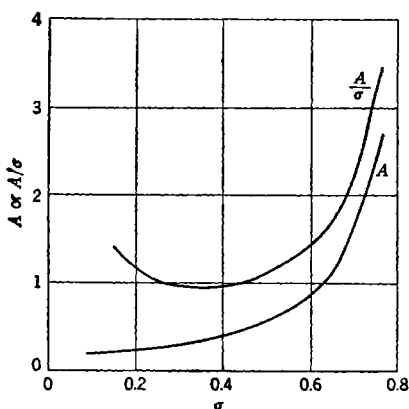


FIG. 10-47.— $A$  and  $A/\sigma$  as functions of  $N$ .  $A = a_1/[(1 - \sigma^2)^2(1 + 1/\sigma)]$ .

range and examined for consistency with Eq. (68). A certain slack has to be permitted at this point, because  $N$  is not a continuous variable. Equations (67) and (68) restrict somewhat the choice of the fixed quantities. In particular,  $A/\sigma$  has a minimum value of about 0.94 at  $\sigma \approx 0.35$ . The values of  $\sigma$  and  $N$  determined from Eqs. (67) and (68) allow the calculation of the remaining unknowns.

*Alternative III.*—This case is presented as one corresponding rather closely to the way in which many magnetrons have been designed in practice. The shape factors  $N$ ,  $\sigma$ , and  $\mu$  are assumed fixed, as are the circuit efficiency and the cathode-current density. It is also assumed that the tube will operate at a fraction  $\gamma$  of the load for maximum power. From Eq. (55), a value can be obtained for  $\eta_0(q, \sigma, N)$  and then a value for  $q$  by using Table 10-4. Equations (37) may be written

$$\frac{\sqrt{v}}{i} = \frac{420 \sqrt{V}}{\lambda^2 J} \left( \frac{A}{N^2 \sigma} \right). \quad (69)$$

The quantities on the right of Eq. (69) are fixed and therefore determine  $\sqrt{v}/i$ . The values of  $N$  and  $\sigma$  employed will approximately satisfy Eq. (44) in order to correspond to Table 7-6, and a graph of  $A/N^2\sigma$  as a function of  $N$  can therefore be given in Fig. 10-48.

In Fig. 10-49, contours of constant  $b$  have been drawn in the  $(\sqrt{v}/i, q)$ -plane and serve to determine  $b$ . With  $q$  and  $b$  known,  $v$  and  $i$  can be found

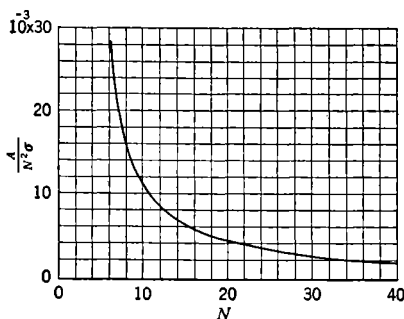


FIG. 10-48.— $A/N^2\sigma$  as a function of  $N$  for  $\sigma = 0.85 - 3.83/N$ .

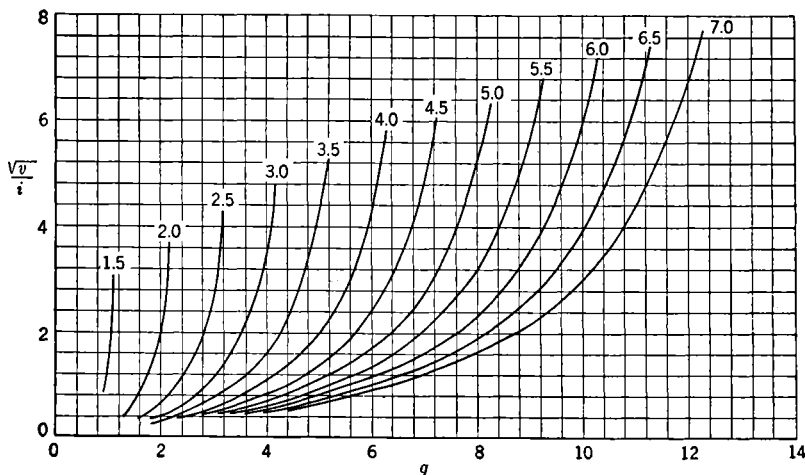


FIG. 10-49.— $\sqrt{v}/i$  as a function of  $q$  for various values of  $b$ .

from Fig. 10-44 or computed from Eqs. (64) and (65). The remaining parameters can then be found without difficulty.

**10-12. Numerical Example.**—In order to illustrate most clearly the methods discussed in this section, a numerical example will be considered. Suppose that it is desired to build a c-w magnetron that operates with  $\lambda = 10$  cm,  $V = 1000$  volts, and  $I = 0.15$  amp. Suppose further that an electronic efficiency of about 0.70 is desired for  $\gamma = 1.00$



and that it is required that  $J$  equal  $0.15 \text{ amp/cm}^2$  in order to remain well below an arbitrary limit of  $0.20 \text{ amp/cm}^2$ .

Consider first the procedure established by Alternative III. Suppose, on the basis of previous experience, it is believed that  $N = 16$  may be a suitable number of oscillators for the tube. From Eq. (44) the corresponding value of  $\sigma$  is found to be 0.61. Since it is assumed that  $\gamma = 1.0$ , it is necessary that  $\eta_0(q, \sigma, N) \cong 0.70$ . The corresponding value of  $q$  is found by reference to Table 10-4 to be equal to 6. By the use of Eq. (69) and Fig. 10-48, it is next found that  $\sqrt{v}/i = 4.9$ . With this value of  $\sqrt{v}/i$  and the value  $q = 6$ , a reference to Fig. 10-49 determines the value of  $b$  as 3.9. The value of  $v$  is found to be 7.0 from Fig. 10-44, and the corresponding value of  $i$  is  $(i/\sqrt{v}) \sqrt{v} = 0.54$ .

From Eqs. (56) to (59)  $B = 1600$  gauss,  $h = 0.87 \text{ cm}$ ,  $r_a = 0.30 \text{ cm}$ , and  $r_e = 0.19 \text{ cm}$ . The tube the main features of which are thus established corresponds roughly to the QK61 c-w magnetron discussed in Chap. 19.

Alternative II can now be illustrated by supposing in the same example that  $b$  and  $i$  have the values already calculated but that  $N$  and  $\sigma$  are undecided. The quantities  $v$  and  $q$  can be considered as determined by  $b$  and  $i$ . From Eq. (67) it is now found that

$$\frac{A}{\sigma} = 5.5 \times 10^{-3} N^2. \quad (70)$$

By use of Eq. (70) and Fig. 10-47, one can now construct Table 10-6.

TABLE 10-6.—POSSIBLE VALUES OF  $N$  IN AN EXAMPLE OF MAGNETRON DESIGN

$N$	$\frac{A}{\sigma}$	$\sigma$	$0.85 - \frac{3.83}{N}$
10	0.55	....	0.47
12	0.79	....	0.53
14	1.08	0.50	0.58
16	1.41	0.59	0.61
18	1.78	0.66	0.64
20	2.20	0.69	0.66

It is observed that the conditions imposed on the design cannot possibly be met with  $N$  less than 14. At  $N = 14$  the calculated value of  $\sigma$  is considerably less than the value given by Eq. (44), but at  $N = 20$  the calculated value becomes larger than the value given by Eq. (44). The best match is given by  $N = 16$  or 18. For  $N = 16$ , reference can now be made to Table 10-4, where it is found that  $\eta_0(q, \sigma, N)$  for  $q = 6$  and  $N = 16$  is consistent with the desired value.

## CHAPTER 11

### THE RESONANT SYSTEM

BY S. MILLMAN AND W. V. SMITH

**11.1. Factors Influencing Choice of Resonant System.**—Chapter 10 analyzed the problem of designing an anode block based on trial values of the parameters  $N$ ,  $d_a/\lambda$ ,  $\mu = w/d$ , and  $h/\lambda$ . The present chapter will give specific solutions to the problem and indicate modifications necessary in the trial solution. The specific types of blocks to be considered are the rising-sun block and the strapped block, which are

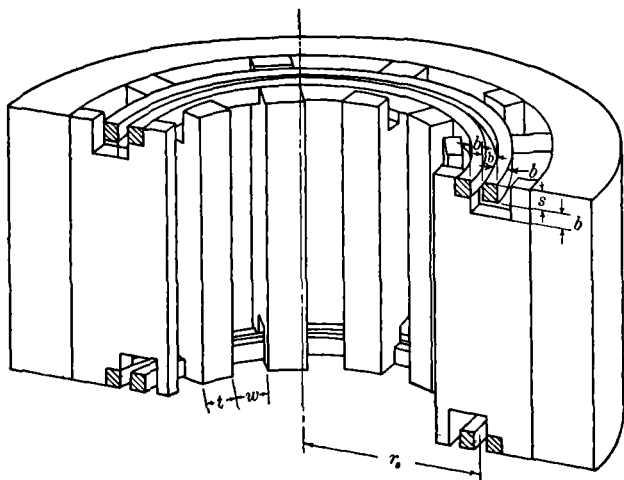


FIG. 11-1.—Double-ring-strapped anode block.

discussed from a theoretical viewpoint in Chaps. 3 and 4 and which are illustrated in Figs. 11-1 and 3-1. For wavelengths above 3 cm strapped resonant systems become increasingly preferable to rising-sun resonant systems, while for wavelengths below 3 cm the situation is reversed. The three major factors influencing the choice between these two designs are size and ease of construction, unloaded  $Q$  and circuit efficiency, and mode separation as functions of  $d_a/\lambda$  and  $h/\lambda$ .

At 1 cm the prime design criterion is that dimensions be as large as possible compared with a wavelength. The rising-sun construction with

its elimination of straps and accompanying increase in resonator dimensions fulfills this criterion. At 10 cm the prime size criterion is to make the complete anode block as small as possible, hence favoring strapped blocks.

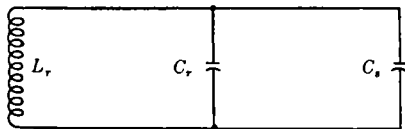
The unloaded  $Q(Q_u)$  for a strapped block is about half that for a comparable rising-sun block. Furthermore, because  $Q_u$  decreases and the external  $Q(Q_E)$  increases at short wavelengths and large  $N$ , the circuit efficiency in a strapped tube becomes quite low at 1 cm. A comparison of rising-sun and strapped-block values at this wavelength, for  $V = 3$  kv and  $N = 18$ , is as follows: (1) In the rising sun,  $Q_u = 900$ ,  $Q_E = 500$ , and  $\eta_c = 64$  per cent. (2) In the strapped,  $Q_u = 550$ ,  $Q_E = 500$ , and  $\eta_c = 52$  per cent. By contrast, at 10 cm, typical values for rising sun are  $Q_u = 2500$ ,  $Q_E = 150$ ,  $\eta_c = 94$  per cent; and for strapped,  $Q_u = 1500$ ,  $Q_E = 150$ ,  $\eta_c = 90$  per cent. Thus at 10 cm, the difference in  $\eta_c$  between strapped and rising-sun blocks is negligible. Conservative strapped anode-block designs have values of  $d_a/\lambda$  and  $h/\lambda$  less than 0.3, with resulting mode separations in excess of 15 per cent for the double-ring strapping illustrated in Fig. 11-1. Successful magnetron operation has been attained, however, with rising-sun blocks having values of  $d_a/\lambda$  and  $h/\lambda$  of about 0.6 and mode separations as low as 2 per cent. Thus mode separation appears to be incidental to the choice between strapped and rising-sun blocks. One consequence of the small mode separations accompanying large values of  $d_a/\lambda$  and  $h/\lambda$  is the difficulty encountered in tuning the resonant system.

### STRAPPED RESONANT SYSTEMS

By W. V. SMITH

**11-2. Wavelength and Characteristic Admittance.**—This section is concerned only with  $\pi$ -mode wavelengths, because this is usually the operating mode in strapped resonant systems. The accuracy of prediction is  $\pm 3$  per cent, so that as a rule it is necessary to build a model, measure its wavelength, and make minor corrections for the final tube.

The analysis of Chap. 4 shows that for certain conditions, usually equivalent to keeping  $d_a/\lambda$  and  $h/\lambda$  less than 0.3, the  $\pi$ -mode wavelength  $\lambda_r$  and the characteristic admittance of the entire block  $Y_c$  can generally be computed with sufficient accuracy by the aid of the simple



$L_r$  = Resonator inductance.

$C_r$  = Resonator capacity + fringing capacity.

$C_s$  = Strap capacity.

FIG. 11-2.—Equivalent circuit of a single resonator in a strapped magnetron operating in the  $\pi$ -mode, seen from the interaction space.

parallel-resonant circuit of Fig. 11-2, where  $L_r$  and  $C_r$  are the inductance and capacitance of a single unstrapped resonator and  $C_s$  is the capacitance of the straps associated with one resonator. The total block capacitance is  $N(C_r + C_s)$ .  $C_s$  may be computed from the d-c approximation because pertinent dimensions are small as compared with a wavelength. No simple formulas can cover the multiplicity of possible strap designs, but

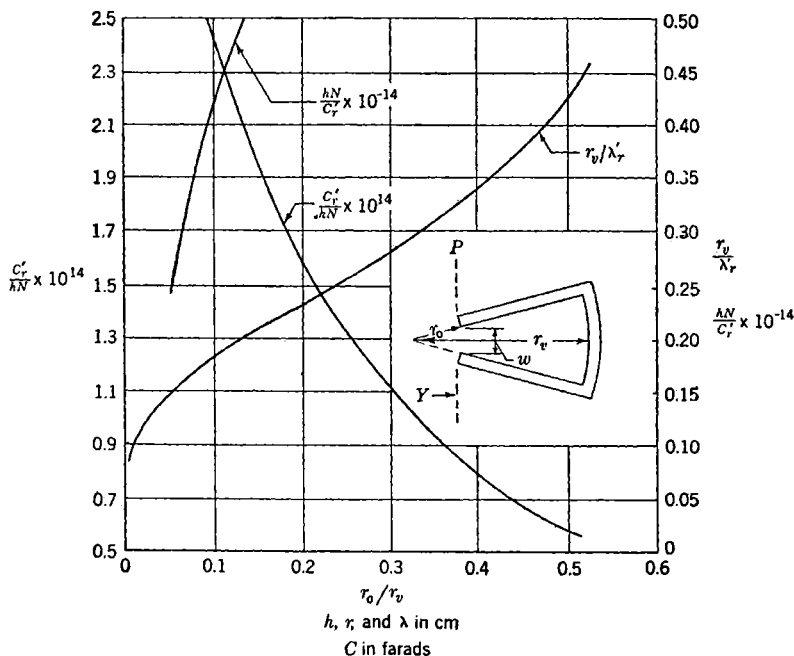


FIG. 11-3.—Circuit parameters of vane-type resonator.

the formulas given in Eq. (1) for the strapping of Fig. 11-1 are typical of the approximate relations that are most useful. Greater accuracy is not consistent with the approximations made in the rest of the problem.

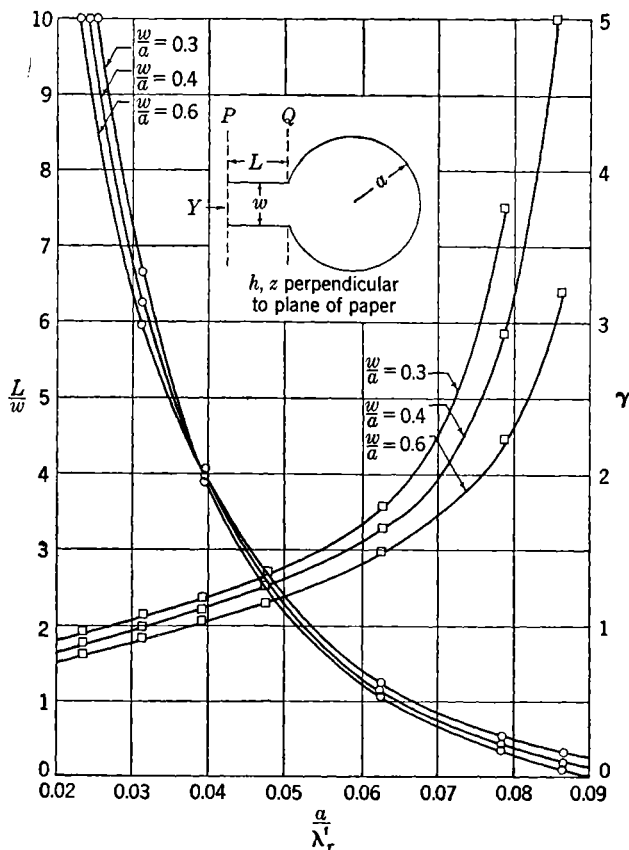
$$C_s = \epsilon_0 \left( t f_A + \frac{2\pi r_s}{N} f_B \right), \quad (1a)$$

where

$$f_A = \frac{2s + t}{b}, \quad \text{and} \quad f_B = \frac{2s + 2t + 2b}{b}. \quad (1b)$$

The circuit constants of the unstrapped resonator are best computed from field theory following the methods discussed in Chap. 2. Because these methods yield resonant wavelength  $\lambda$ , and capacitance  $C_r$ , as the fundamental circuit constants, it is not necessary to evaluate the inductance

explicitly. In this development the resonator is assumed to be a section of an infinitely long cylinder, thus neglecting the fringing fields at each end of the resonators. The constants are determined in two steps



$L, w$  and  $h$  in cm  
 $C$  in farads

$\square = \gamma$   
 $\circ = \frac{L}{w}$

$$\frac{1}{\gamma} = \frac{1}{C_r'} \left[ 0.885 \times 10^{-13} \frac{Lh}{w} \right]$$

FIG. 11-4.—Circuit parameters of a hole-and-slot resonator.

In the first step (primed symbols) the fringing fields in the interaction space are neglected. In the second step, the effects of the fringing capacitance  $C_f$  are added to this result to give

$$C_r = C'_r + C_f = \frac{\text{total unstrapped capacitance}}{N}, \quad (2a)$$

$$C_T = C_r + C_s = \frac{\text{total capacitance}}{N}, \quad (2b)$$

$$\lambda_r = \lambda'_r \sqrt{1 + \frac{C_f}{C'_r}} = \text{unstrapped wavelength}, \quad (2c)$$

$$\lambda_\pi = \lambda_r \sqrt{1 + \frac{C_T}{C'_r}}. \quad (2d)$$

A resonator of the vane type is illustrated in the cross-sectional sketch of Fig. 11-3. Also plotted in this figure are curves showing  $C'_r$  evaluated at the plane  $P$  and  $\lambda'_r$  as functions of the parameters  $r_0$ ,  $r_v$ ,  $h$ , and  $N$ . The resonant wavelength is computed by solving Maxwell's equations for the resonator, subject to the boundary condition  $H = 0$  along the plane  $P$ . The admittance  $Y' = (h/w)(H_z/E_\theta)$  is evaluated at

$P$  as a function of  $\omega$ , and the characteristic admittance  $Y'_r$  per resonator from the relation

$$Y'_r = \frac{\omega'_r}{2j} \left( \frac{\partial Y'}{\partial \omega} \right)_{\omega=\omega'_r} = \omega'_r C'_r, \quad (3)$$

where  $\omega'_r$  is  $2\pi$  times the resonant frequency of a single oscillator neglecting the fringing fields.

A hole-and-slot resonator is illustrated in Fig. 11-4. In this type of geometry the resonant wavelength may be found from the plot of  $L/w$  as a function of  $a/\lambda'_r$  and  $w/a$ , where  $L$ ,  $a$ , and  $w$  are shown on the cross-sectional sketch. The capacitance  $C'_r$  is given by the d-c approximation  $\epsilon_0(Lh/w)$  multiplied by a dimensionless constant  $\gamma$  also plotted in

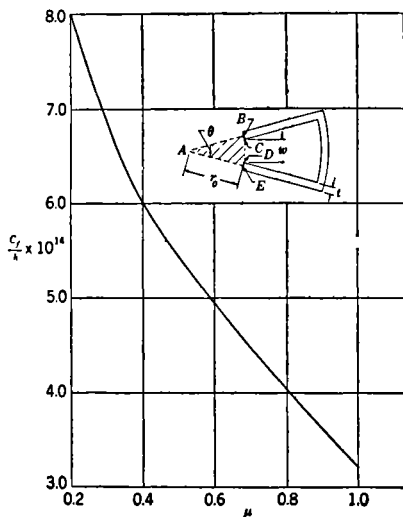


Fig. 11-5.—Fringing capacitance per resonator as a function of  $\mu$ .

the figure. In the simplest lumped-constant approximation,  $\gamma$  would be 1. It is seen that  $\gamma$  is nearly 1 for  $0.03 < a/\lambda'_r < 0.04$ , where all dimensions are small as compared with a wavelength.

In deriving the above results for the hole-and-slot resonator, it was necessary to match admittances appropriate to the two geometrical shapes involved at the boundary  $Q$  in Fig. 11-4. A list of appropriate transformation formulas is given in Chap. 2. Because dimensions are small as compared with a wavelength, the fringing capacitance per

resonator  $C_f$  may be computed by solving Laplace's equation in the section of the interaction space shown as the shaded area of the insert in Fig. 11-5. The boundary conditions are that  $H_z = 0$  on the boundaries  $AB$ ,  $CD$ , and  $EA$  and that  $E_\theta = 0$  on the boundaries  $BC$  and  $DE$  of the vane tips. The resulting approximate formula, plotted in Fig. 11-5, is

$$C_f = \frac{h\epsilon_0}{\pi} \left( 1 + \log_e \frac{4}{\pi\mu} \right). \quad (4)$$

This formula is independent of the shape of the resonator, as it depends only on  $h$  and  $\mu$ .

Observed and computed circuit constants for a number of tubes are listed in Table 11-1. Not all of the geometrical solutions included in the table correspond exactly to those of Figs. 11-1, 11-3a, and 11-4, but the calculation methods used are similar to those described. In all cases the block height has been assumed uniform along the vane length, and no allowance has been made for the notches in which the strapping system is set. Tubes are listed in order of increasing  $\mathcal{U}$ . The average deviation of observed and computed wavelengths is seen to be about  $\pm 3$  per cent.

For some purposes, it is useful to conceive of the equivalent circuit looking in at the back of a resonator, as shown in Fig. 11-6. The fundamental constants are the inductance  $L_b$  and resonant wavelength  $\lambda_r$ . The inductance  $L_b$  is only slightly affected by the fring-

TABLE 11-1.—CIRCUIT CONSTANTS OF THE  $\pi$ -MODE FOR STRAPPED ANODES  
Dimensions are in centimeters; capacitance is in micromicrofarads

Tube	$N$	$h$	$D_A$	$W$	$\mu$	$r_0$	$r_v$	$L$	$a$	$b$	$t$	$s$	$f_A$	$f_B$	$r_s$	$C_s$	$\lambda_r'$	$C_f'$	$C_f$	$C_T$	$\lambda_r$ computed	$\lambda_r$ observed
CM16B	16	1.020	0.590	0.061	0.47	0.141	1.536	.....	.....	0.051	0.051	0.102	5.0	8.00	0.487	0.1170	8.740	0.4150	0.0570	0.4720	0.5890	9.320
BM50*	20	0.241	0.289	.....	0.50	.....	.....	.....	.....	.....	.....	.....	0.0	8.00	0.229	0.0270	2.350	0.0984	0.0745	0.1730	0.2000	3.120
2J42	12	0.523	0.394	0.052	0.49	0.100	0.509	.....	.....	0.051	0.051	0.051	3.0	6.00	0.362	0.0772	2.290	0.1005	0.0309	0.1314	0.2066	2.605
725BTL	12	0.635	0.519	0.081	0.43	.....	.....	0.137	1.000	0.031	0.025	0.089	6.7	8.20	0.368	0.1730	2.000	0.1730	0.0388	0.2120	0.3850	2.310
725Ray	12	0.635	0.519	0.076	0.40	0.117	0.526	.....	.....	0.043	0.034	0.039	2.6	5.80	0.368	0.0836	2.230	0.1120	0.0372	0.1462	0.2330	2.560
4J33	12	2.000	2.000	0.351	0.33	0.342	1.562	.....	.....	0.089	0.051	0.127	3.6	6.15	1.240	0.3960	6.650	0.3550	0.320	0.4870	0.8830	7.50
4J50M	16	0.635	0.612	0.065	0.40	.....	.....	0.122	0.094	0.025	0.025	0.102	9.0	11.00	0.508	0.2910	1.740	0.1350	0.0392	0.1740	0.4650	10.50
4J50M <sub>6</sub>	16	0.635	0.612	0.075	0.53	.....	.....	0.168	0.111	0.025	0.025	0.051	5.0	7.00	0.508	0.1600	2.065	0.1350	0.0339	0.1690	0.3290	3.24
HP10V†	10	4.000	3.000	0.600	0.36	0.578	1.943	.....	.....	0.152	0.152	0.254	0.0	3.67	1.805	0.3690	7.010	0.4560	0.2520	0.7080	1.0760	3.23
																					8.50	10.75

\* Geometry not covered in derivations (see Chap. 18).

† Single-ring strap;  $f_A = 0$ .

ing fields at the interaction space, and therefore the symbols used will be unprimed. Referring to the vane resonator illustrated in Fig. 11-7, the characteristic impedance  $Z_b$  looking to the left from the plane  $R$  is computed from Eq. (3), replacing  $Y_r'$  by  $Z_b$  and  $C_r'$  by  $L_r$ . The resulting value of  $L_b$  is plotted against  $r_0/r_v$ .

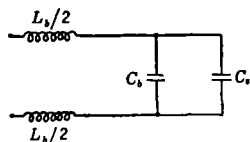


FIG. 11-6.—Equivalent circuit of a single resonator in a strapped magnetron operating in the  $\pi$ -mode, seen from the back of the resonator.

In practical tube design many geometries other than the ones computed may be useful. For instance, a vane tube may be constructed with the back half of each vane reduced in height. This design increases

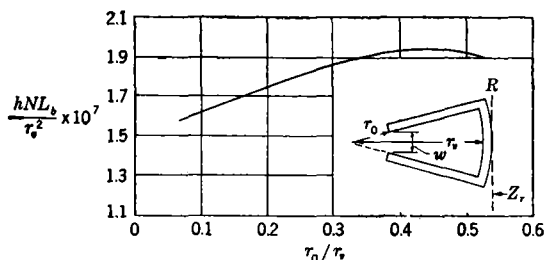


FIG. 11-7.—Inductive circuit parameter of a vane-type resonator. All dimensions in centimeters;  $L_b$  in henrys.

the tube inductance, thus increasing the wavelength, without any change in vane length.

**11-3. Unloaded  $Q$ .**—For estimating  $Q_u$  of the magnetron, the equivalent circuit of Fig. 11-2 must be expanded to that of Fig. 11-8. The internal losses of the resonator represented by  $G_r$  can be computed from the unstrapped unloaded  $Q = Q_r$  given by

$$Q_r = \frac{\omega_r C_r}{G_r} = 2 \frac{A}{\delta P} \quad (5)$$

where  $C_r$  is given in Eq. (2a).  $A$  is the cross-sectional area of the resonator;  $P$  is the perimeter of the resonator; and  $\delta$  is the skin depth. The strap losses can be computed by representing the double-ring straps as having spacing  $b$ , an open-circuited parallel-plate transmission line

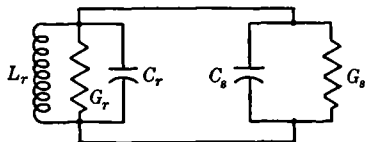


FIG. 11-8.—Equivalent circuit, including losses, of a single resonator in a strapped magnetron operating in the  $\pi$ -mode, seen from the interaction space.



of length  $l/2$ , characteristic admittance  $Y_0$ , and attenuation constant<sup>1</sup>  $\alpha = (\delta/b)(\beta/2)$ , where  $\beta = 2\pi/\lambda$ . If  $Y_s$  is the admittance of this section of the straps, then

$$Y_s = Y_0 \tanh (\alpha + j\beta) \frac{l}{2}, \quad (6)$$

whence, for  $l/2 \ll \lambda$ ,

$$Y_s = Y_0 \frac{l}{2} (\alpha + j\beta) = G_s + j\omega_r C_s$$

and

$$Q_s = \frac{\omega_r C_s}{2G_s} = \frac{\beta}{2\alpha} = \frac{b}{\delta}. \quad (7)$$

Analyzing the circuit of Fig. 11-8 in terms of  $Q_r$  and  $Q_s$ ,

$$\frac{1}{Q_u} = \frac{G_r + G_s}{\omega_r (C_r + C_s)} = \frac{1}{Q_r} \sqrt{\frac{C_r}{C_s}} + \frac{1}{2Q_s} \left( \frac{C_s}{C_r} \right). \quad (8)$$

The unloaded Q values calculated by means of Eqs. (5), (7), and (8) are too high, as the computed and observed values of Table 11-2 demonstrate. This is probably owing in part to the lower conductivity of the soldered portions of the anode block as compared with that of the solid copper structure assumed in the computations.

TABLE 11-2.—THE  $\pi$ -MODE UNLOADED Q VALUES OF STRAPPED ANODE BLOCK  
Material = OFHC copper

Tube	$\lambda_r$	$\frac{C_s}{C_r}$	$Q_r$	$Q_s$	$Q_u^*$ computed	$Q_u$ observed
CM16B	9.90	0.198	2370	444	1590	1200
BM50	3.10	0.135	1010	198	785	550
2J42	3.20	0.369	1850	783	1500	900
725 <sub>BTL</sub>	3.20	0.450	1545	477	1040	680
725 <sub>RAY</sub>	3.20	0.481	1940	666	1470	920
4J33	10.70	0.448	3150	750	1860	1500
4J50M	3.20	0.626	1450	390	818	735
4J50M <sub>0</sub>	3.20	0.486	1700	390	957	928
HP10V	10.70	0.342	3690	1280	2830	....

\* Although individual discrepancies between observed and computed values of  $Q_u$  are fairly large, the average  $Q_u$  values for 3-cm tubes are 800 observed and 1100 computed; for the two 10-cm tubes, 1350 observed and 1725 computed. Using these average values, the ratio of the observed  $Q_u$  for 10 cm to that for 3 cm is 1.7; the theoretical value computed for wavelength scaled structures is 1.8.

Equations (5) and (7) for copper anode blocks with dimensions in mils and wavelengths in centimeters take the form

<sup>1</sup> J. C. Slater, *Microwave Transmission*, McGraw-Hill, New York, 1942, pp. 140-145.

$$Q_r \text{ hole-and-slot} = 70 \frac{a}{\sqrt{\lambda_r}}, \quad (9a)$$

$$Q_r \text{ vane} = \left( \frac{70}{\sqrt{\lambda_r}} \right) \left( \frac{r_v + r_0}{\frac{r_v}{r_0} + \frac{N}{\pi}} \right), \quad (9b)$$

and

$$Q_s = \frac{70b}{\sqrt{\lambda_r}}. \quad (9c)$$

Equation (9b) shows the approximate inverse proportionality of  $Q_r$  to  $N$ .

**11.4. Mode Separation.**—The analysis of Chap. 4 shows that for double-ring-strapped tubes with  $d_a/\lambda$  and  $h/\lambda$  less than about 0.3, the mode separation<sup>1</sup> is given by Eq. (4.37). This equation may be rewritten as

$$\frac{\lambda_{\left(\frac{N-1}{2}\right)}}{\lambda_\pi} = \sqrt{\frac{1}{1+\alpha}}, \quad (10a)$$

where

$$\alpha = \frac{C_s}{C_T} \left( \frac{\lambda_\pi}{2\pi r_s} \right)^2. \quad (10b)$$

Table 11-3 lists separations between the  $\pi$ -mode and the next lower mode  $\left(\frac{N}{2} - 1\right)$  as computed by Eqs. (10), together with observed values.

Agreement is seen to be good for double-ring strapping. It does not apply to single-ring strapping and if used will yield wrong results, as shown in the table. Mode separation for single-ring strapping is less than that for double-ring strapping at the same  $C_s/C_T$ . The two columns labeled "quantities that should be  $\ll 1$ " are quantities that, according to the analysis of Chap. 4, should be small compared with unity in order for Eq. (10) to be valid. From the agreement between theory and experiment, it appears that the criterion "small compared with unity" may be interpreted as  $\leq 0.5$ . This is not surprising because it is shown in Chap. 4 that Eqs. (10a) and (10b) are also valid for  $C_s/C_T \gg 1$ . It is not correct, however, to assume universal validity of Eqs. (10) simply because they agree with more rigorous equations in two different limiting cases.

Table 11-3 and Eqs. (10) show that large mode separations are easily attained in low-voltage tubes, where  $\lambda_\pi/2\pi r_s$  is large. For high-voltage tubes, the decrease in  $\lambda_\pi/2\pi r_s$  must be compensated for by an increase in  $C_s/C_T$ . Large values of  $C_s/C_T$  may, however, introduce other difficulties, such as excessive variations in r-f field patterns along the block length

<sup>1</sup> For more exact restrictions, see Chap. 4.

TABLE 11-3.—THE RATIO  $\lambda_{(\frac{N}{2}-1)}/\lambda_\pi$  FOR STRAPPED ANODE BLOCKS

Tube	Type of strapping	$\lambda_\pi$	$\frac{C_S}{C_T}$	$\frac{\lambda_\pi}{2\pi r_s}$	$\alpha$	Quantities that should be $\ll 1$		$\lambda_{(\frac{N}{2}-1)}$	$\lambda_{(\frac{N}{2}-1)}$
						$\left(\frac{8\pi^2 r_s}{N\lambda_\pi}\right)^3$	$\left(\frac{\pi h}{\lambda_\pi} \sqrt{\frac{C_S}{C_T}}\right)^2$		
CM16B	Double-ring strap	9.90	0.198	3.370	2.220	0.013	0.004200	0.551	0.57
BM50	Single-ring strap	3.10	0.135	2.150	0.626	0.025	0.000029	0.783	0.89
2J42	Double-ring strap	3.20	0.369	1.410	0.732	0.420	0.069000	0.760	....
725 <sub>BTL</sub>	Double-ring strap	3.20	0.450	1.390	0.863	0.420	0.180000	0.733	0.77
725 <sub>RAY</sub>	Double-ring strap	3.20	0.481	1.390	0.690	0.420	0.101000	0.768	....
4J33	Double-ring strap	10.70	0.448	1.415	0.898	0.420	0.147000	0.725	0.75
4J50M	Double-ring strap	3.20	0.626	1.005	0.635	0.480	0.518000	0.783	0.81
4J50M <sub>0</sub>	Double-ring strap	3.20	0.486	1.005	0.547	0.480	0.223000	0.803	0.83
HP10V	Single-ring strap	10.70	0.342	0.942	0.304	2.400	0.608000	0.875	0.95

or displacement of other modes toward the  $\pi$ -mode wavelength. Thus for long, heavily strapped anode blocks, the mode nearest in wavelength to the  $\pi$ -mode may be one with  $\pi$ -mode azimuthal symmetry but with a node at the center of the block longitudinally. Denoting this mode as  $\pi'$ , Eq. (4-34) yields

$$1 = \frac{C_r}{C_s} \sqrt{\frac{\lambda_\pi^2}{\lambda_r^2} - 1} \tanh \frac{\pi h}{\lambda_\pi} \sqrt{\frac{\lambda_\pi^2}{\lambda_r^2} - 1} \sin \frac{8\pi^2 r_s}{N\lambda_\pi} + \cos \frac{8\pi^2 r_s}{N\lambda_\pi}, \quad (11a)$$

and

$$1 = \frac{C_r}{C_s} \sqrt{\frac{\lambda_\pi^2}{\lambda_r^2} - 1} \coth \frac{\pi h}{\lambda_{\pi'}} \sqrt{\frac{\lambda_\pi^2}{\lambda_r^2} - 1} \sin \frac{8\pi^2 r_s}{N\lambda_{\pi'}} + \cos \frac{8\pi^2 r_s}{N\lambda_{\pi'}}. \quad (11b)$$

Computed values of  $\lambda_{\pi'}/\lambda_{\pi}$  are listed<sup>1</sup> in Table 11-4.

TABLE 11-4.—THE RATIO  $\lambda_{\pi'}/\lambda_{\pi}$  FOR STRAPPED ANODES

Tube	$\lambda_{\pi}$ observed	$\frac{C_r}{C_s}$	$\frac{8\pi^2 r_s}{N}$	$\lambda_{\pi}$	$\lambda_{\pi'}$	$\frac{\lambda_{\pi'}}{\lambda_{\pi}}$
4J50M	3.2	0.60	2.51	3.02	2.15	0.713
HP10V*	10.7	1.88	14.25	10.46	8.89	0.850

\* The HP10V computations are for double-ring strapping, although the actual strapping used is single ring. For double-ring strapping both the  $\left(\frac{N}{2} - 1\right)$ -mode and the  $\pi'$ -mode are almost equally removed from the  $\pi$ -mode for  $C_s/C_r = 0.34$ . Increasing  $C_s$  decreases the separation from the  $\pi'$ -mode; decreasing  $C_s$  decreases the separation from the  $\left(\frac{N}{2} - 1\right)$ -mode. The actual use of single-ring strapping on the HP10V anode block satisfactorily displaces the  $\pi'$ -mode but leaves the  $\left(\frac{N}{2} - 1\right)$ -mode uncomfortably close.

With long anode blocks the lowest modes, such as  $N = 1$  or  $N = 2$ , can also approach the main mode wavelength and do so for the HP10V. The general features of the mode spectrum of various structures are discussed in detail in Chap. 4.

The preceding analysis has been found applicable to designs where one or more straps are broken over one of the vanes to which the strap is not attached. The function of the break is to distort the r-f patterns of one of the lower modes by interrupting the current flow at the strap break. The r-f patterns for the  $\pi$ -mode, however, are undisturbed, because in the  $\pi$ -mode no current normally flows through the location of the strap break. Although the strap break does function in the above manner (see Chap. 4), correlation of the effects of strap breaks on tube performance is poor. Existing information indicates that in many cases the primary effect on tube performance is caused by the shift in wavelength of the  $\left(\frac{N}{2} - 1\right)$ -mode resulting from the strap break. The subject of strap breaks will be dismissed with the remainder that the break removes the degeneracy of the lower modes, changing each into a doublet. Both components are then displaced in wavelength nearer to the  $\pi$ -mode.

### RIISING-SUN RESONANT SYSTEM

By S. MILLMAN

The general design principles of Chap. 10 apply equally well to the rising-sun and strapped-block resonant systems. Because of the difference in structure of these two types, however, the emphasis in the design

<sup>1</sup> For experimental verification of Eqs. (11) using data from other anode blocks, see Chap. 4.

parameters is not the same. In the rising-sun magnetron, the strap design is entirely omitted, and in its place the ratio of resonator depths  $r_1$  appears as a new parameter. The quantity  $C/L$ , which is so important in strapped-tube design, has played a relatively minor role in the design of rising-sun magnetrons. Similarly the quantity  $Q_u$ , representing the internal losses, is rarely regarded as an independent design parameter. The losses of the rising-sun tubes are less than in strapped tubes and are not appreciably affected by changes in other parameters that are likely to be made in ordinary block design. The concept of mode separation

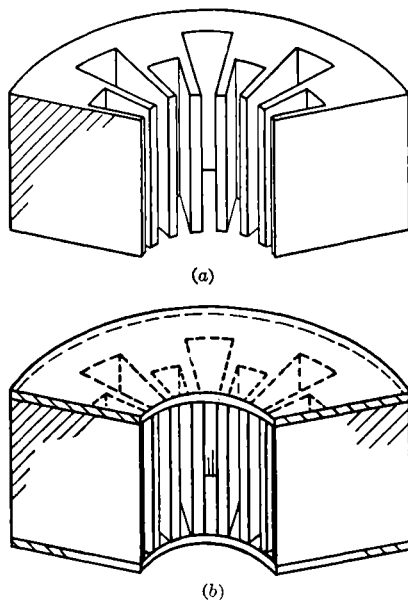


FIG. 11.9.—Rising-sun blocks. (a) Open-resonator anode block; (b) closed-end design.

does not have quite the same significance in the two types of structures. The choice of magnetic field for a rising-sun magnetron is more limited than for a strapped tube, but on the other hand there is considerably more latitude in the choice of the block length.

The discussion of rising-sun anode-block design will include two different types of systems. One is the conventional open-resonator anode block, which gives rise in the interaction space to r-f fields that are approximately independent of axial position in the block. The other, which is used principally with blocks containing large numbers of resonators, is the closed-end type<sup>1</sup> in which the r-f fields vary sinusoidally

<sup>1</sup> W. E. Lamb, Jr., "Closed End Magnetrons," *RL Coordination Minutes*, **8**, No. 7, 206, Jan. 24, 1945.

along the axis. Perspective sketches of these resonator types are shown in Fig. 11-9a and b.

**11-5. Limitations on Secondary Design Parameters.**—In this section a brief account is given of the available information on the range of useful values for some of the secondary anode-block parameters of rising-sun magnetrons, i.e., the anode diameter  $d_a$ , the number of resonators  $N$ , the ratio of resonator depths  $r_1$ , the block height  $h$ , and  $t/w$ , the ratio of vane thickness to the space between vanes.

**Anode Diameter.**—The limitations on the size of the anode diameter in the rising-sun resonant systems are somewhat similar to those in strapped tubes. For a given number of resonators and for a fixed value of the wavelength, an increase in the anode diameter decreases the wavelength separation between the  $\pi$ -mode and the  $\left(\frac{N}{2} - 1\right)$ -mode and increases the fraction of zero contamination in the  $\pi$ -mode if the ratio of resonator depths is held constant (see Chap. 3). Either of these results is, in general, undesirable. If the increase in diameter is accomplished with no change in mode separation, as can be done by increasing the resonator depth ratio, the zero-mode content is increased even more. The theory as presented in Chap. 3 is capable of predicting the magnitude of these changes but cannot, of course, predict in any quantitative way the effect on magnetron operation. A summary of the largest values of anode diameters used successfully in various rising-sun magnetrons is presented in Table 11-5.

TABLE 11-5.—LARGEST ANODE DIAMETERS USED IN RISING-SUN MAGNETRONS

Type of anode block	$\frac{d_a^*}{\lambda}$
18 vane-open.....	0.37
22 vane-open.....	0.38
26 vane-open.....	0.44
26 vane-closed.....	0.52
38 vane-closed.....	0.68

\* The value of  $d_a/\lambda$  is not to be regarded as the maximum that can be used for a given  $N$  but rather as one below which good magnetron design is certainly feasible. The upper limit for  $d_a/\lambda$  is not known.

**Number of Resonators.**—Rising-sun magnetrons have been constructed mainly with anode blocks of 18 or more resonators because these tubes were first designed for the 1-cm region where a large number of resonators is particularly advantageous. However, from the theory of the rising-sun structure and from the comparison of the behavior of tubes having 18 resonators with those of a larger number, one can safely predict that systems having less than 18 resonators should make good magnetrons. It is the use of a number of resonators substantially greater than 18 that becomes troublesome.

As the number of resonators increases, the ranges of useful values for other parameters decrease. In the case of 18-cavity anode blocks there is considerable latitude regarding the other parameters. Good magnetrons can be built in the high-voltage region ( $V = 3.0$  kv) with a considerable range of values for the ratio of cavity depths  $r_1$ . Moreover, the performance does not critically depend on the value of  $\sigma$  (the ratio of cathode-to-anode radius). For 22-vane magnetrons the indications are that the useful ranges for  $r_1$ ,  $d_a$ , and  $\sigma$  are not likely to be restrictive in anode-block design. In the case of 26-vane tubes, however, there is practically no latitude in the choice of  $r_1$  for high-voltage blocks, while for 38-vane magnetrons no combination of values has been found for  $r_1$  and  $\sigma$  that would produce even moderately fair operation at high voltages. In the lower-voltage region ( $V \sim 450$  volts), the indications are that good magnetron design can be obtained with 34-vane anode blocks.

In the closed-end resonant system a considerably greater number of resonators is possible than in the open-resonator system. Good magnetrons in the high-voltage region have been built with 26 and with 38 resonators and in the low-voltage region with 34 resonators. The upper limit of the useful value of  $N$  for closed-end anode blocks is not known at present.

*Anode-block Height.*—For the open-cavity rising-sun magnetrons, the block height does not in a first approximation affect the  $\pi$ -mode wavelength, the mode separations, or zero-mode contamination of the  $\pi$ -mode. This block parameter can therefore be chosen independently. No mode instabilities have been encountered for block heights up to  $0.8\lambda$ .

For magnetrons having closed-end resonators the practical block height falls within a rather narrow range, because the  $\pi$ -mode wavelength is necessarily less than twice the block height and therefore the lower limit of the length is  $0.5\lambda$ . In order to keep the resonator sizes from getting unduly large, one would probably not design a magnetron with a block height of less than  $0.55\lambda$ . The block should not be too long, perhaps no longer than  $0.7\lambda$ , if one intends to produce a substantial decrease of the wavelengths of the resonances associated with the large resonators. The lengths of practically all of the closed-end blocks fall in the range of  $0.58\lambda$  to  $0.72\lambda$ .

*Ratio of Vane Thickness to Space between Vanes.*—The ratio of copper to space at the anode circumference does not enter critically into the operation of the magnetron. An increase in the thickness of the vanes for a fixed value of the anode and resonator diameters increases the mode separation, the zero-component content of the  $\pi$ -mode, the wavelength of the  $\pi$ -mode, and the  $C/L$  ratio. The changes are not very great and do not affect the magnetron operation in the same sense; thus an increase

in mode separation may be desirable, while an increase in zero contamination is not.

Experiments with 1-cm 18-vane magnetrons to determine some optimum value for this ratio have not yielded any conclusive results, because there was no marked variation in magnetron performance for values in the range of 1.0 to 2.0. The value used in the standard 1-cm tubes is 1.5, and that in the high-power 3-cm magnetron is 1.4. Values in the range of 1.0 to 1.3 have been used in experimental tubes, particularly in those of shorter wavelengths.

**11-6. Desirable Mode Spectrum.**—The theory of the rising-sun anode block has been fully presented in Chap. 3, but a brief review of the essential characteristics of the theory as it affects the anode-block design

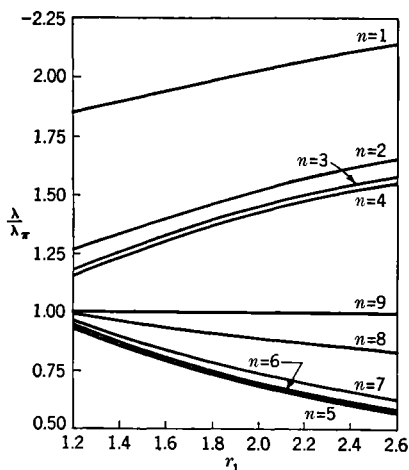


FIG. 11-10.—Mode spectrum of an 18-vane open-resonator rising-sun anode block as a function of the cavity ratio  $r_1$ .

will be given here. A typical mode spectrum for an 18-vane open-resonator rising-sun system is exhibited in Fig. 11-10. The variation in wavelength of the various resonances is plotted in terms of the  $\pi$ -mode wavelength as a function of the ratio of the resonator depths  $r_1$  for fixed values of the  $\pi$ -mode wavelength, the anode and cathode diameters, and the vane thickness. For sufficiently large values of  $r_1$  the mode spectrum can be regarded as consisting of three distinct parts. There is a long-wavelength multiplet ( $n = 1, 2, 3, 4$ ) which is characteristic of a symmetric anode block having nine resonators of about the same size as the large

resonators of the rising-sun design; a short wavelength multiplet ( $n = 8, 7, 6, 5$ ) which is associated with the nine small resonators and corresponds to modes 1, 2, 3, 4 respectively for a symmetric anode block having only such resonators; and the  $\pi$ -mode somewhere between the two multiplets but nearer to the short-wavelength resonances. For a rising-sun system with more than 18 cavities, the mode spectrum is very similar to the one shown except that additional resonances appear below and very close to each of the two multiplets.

The most important factor that determines the type of spectrum that will here be considered desirable is the absence of mode competition of  $\pi$ -mode operation. This design consideration is of particular significance



in rising-sun resonant systems because a greater number of modes are generally involved than in strapped systems, and it is almost always possible to find a harmonic of some mode the oscillating region of which overlaps that of the  $\pi$ -mode, i.e., in which the value  $\gamma\lambda$  for the competing mode is close to  $(N/2)\lambda_r$  (see Chap. 8). As far as the lower multiplet is concerned, one need consider only the  $\left(\frac{N}{2} - 1\right)$ -mode, as it is the only one that has ever been observed to compete with  $\pi$ -mode operation. It was shown in Chap. 3 that the  $\left(\frac{N}{2} - 1\right)$ -mode has a considerable admixture of an  $(n = 1)$ -component, which increases with increasing value of  $r_1$  and which renders operation in the  $\left(\frac{N}{2} - 1\right)$ -mode less efficient and more difficult to build up. An increase in  $r_1$  is thus likely to favor  $\pi$ -mode operation, not only by increasing the wavelength separation between the  $(N/2)$ - and  $\left(\frac{N}{2} - 1\right)$ -modes but also by increasing the contamination of the latter with the  $(n = 1)$ -component. The fact that disturbance from this source appears generally at low magnetic fields and recedes to lower fields with increasing  $r_1$  may be owing to the circumstance that the radius of the charge closed is larger at lower fields. The electrons find themselves in a region where the fraction of  $(n = 1)$ -component is less, and they can thus more readily support the  $\left(\frac{N}{2} - 1\right)$ -mode.

As far as the long-wavelength multiplet is concerned, the requirements of a good mode spectrum favor small-wavelength separation between this multiplet and the  $\pi$ -mode, a condition that is generally in line with low values of  $r_1$ . Before discussing possible explanations for this requirement, the available information bearing on this subject will be summarized:

1. For the range of  $r_1$  values that are of interest in the design of rising-sun systems, the  $n\lambda$  values for any of the fundamentals of the long-wavelength multiplet are sufficiently less than  $(N/2)\lambda_r$  so that they do not form a source of mode competition with  $\pi$ -mode operation. The components  $\gamma = (N/2) - n$  of some of the modes in this multiplet do constitute sources of mode competition.
2. Serious interference with  $\pi$ -mode operation results if  $\left(\frac{N}{2} - n\right)\lambda_r$  for  $n \leq 4$  is close to  $(N/2)\lambda_r$ .

<sup>1</sup> See Sec. 3-3.

3. Mode competition from the component  $\left(\frac{N}{2} - 3\right)$ , has been observed, but it is likely that such disturbances can be eliminated even if  $\left(\frac{N}{2} - 3\right)\lambda_3$  is near  $(N/2)\lambda_\pi$ , by a suitable choice of  $\sigma$ , the ratio of cathode-anode diameters.
4. No interference has ever been observed from components of the  $(n = 2)$ - and  $(n = 1)$ -modes.
5. Interference from the long-wavelength resonances can in general be eliminated if the following empirical relationship is satisfied for the wavelength of the mode of the upper multiplet that has the highest  $n$  value

$$\lambda < \lambda_\pi \frac{N}{N - 6}.$$

A qualitative explanation for the experimental results listed above can be given. In the long-wavelength multiplet,  $\gamma$  for the competing mode is less than  $N/2$ , so the r-f field falls off less rapidly in the direction toward the cathode for the competing mode than for the  $\pi$ -mode. At the start of oscillations the electrons are relatively close to the cathode, and thus the coupling of the electrons to the component field is favored. The effect becomes worse as  $(N/2) - \gamma$  increases, i.e., as  $n$  increases. This explains why mode competition from a long-wavelength resonance of smaller  $n$  value is less probable than from one of larger  $n$  (smaller  $\gamma$ ). In addition, component operation is handicapped by the domination (shielding effect) of the r-f field of the fundamental associated with the resonance, since the fundamental content of the r-f field impairs the efficiency of the component operation and raises its buildup time. The domination increases with increasing value of the difference

$$(\gamma - n) = \left(\frac{N}{2}\right) - 2n.$$

This again renders competition to  $\pi$ -mode operation less probable from modes of low  $n$  value.

A good mode spectrum for a rising-sun system requires, then, sufficient mode separation between the  $(N/2)$ - and  $\left(\frac{N}{2} - 1\right)$ -resonances, and low values for the wavelengths of the long-wavelength resonances. The first condition favors large values of  $r_1$ , while the second condition is more easily met with small  $r_1$  values. For open-resonance blocks the two conflicting requirements become increasingly restrictive in anode-block design as the number of resonators increases and lead to the neces-

sity of modifications in the oscillating circuit, such as the use of closed-end resonators.

The dependence on  $N$  of the required mode separation between the  $(N/2)$ - and  $\left(\frac{N}{2} - 1\right)$ -resonances is not well established. Evidently it is not necessary to have as much mode separation for a resonant system of large  $N$  as for one of smaller  $N$ . Thus in the case of the high-voltage region,  $V \sim 3.0$  kv, 38-vane magnetrons with a mode separation of only about 1 per cent operate satisfactorily at low magnetic fields, whereas for similar operating conditions 18-cavity magnetrons require a mode separation of 5 per cent. In the high magnetic-field region, the high-power 18-cavity, 3-cm magnetron is relatively free from mode interference even though the wavelength separation between the  $\pi$ - and 8-mode is less than 4 per cent.

### 11.7. Comparison between Open-resonator and Closed-end Systems.

As the number of resonators in a rising-sun anode block increases, the conflicting requirements of a desirable mode spectrum discussed in Sec. 11-6 become very restrictive. On the one hand, large  $r_1$  values are required to overcome the decrease in mode separation between the  $(N/2)$ - and  $\left(\frac{N}{2} - 1\right)$ -resonances, caused by the increasing anode and cathode diameters, and on the other hand smaller  $r_1$  values are needed in order to avoid mode competition from the long-wavelength multiplet. As demonstrated in Chap. 3, however, both requirements can be met for large  $N$  values with the use of closed-end resonators. In this type of design, large  $r_1$  values are used to obtain the proper mode separation on the low-wavelength side of the  $\pi$ -mode, and at the same time the wavelengths of the upper multiplet are kept low enough to avoid mode competition from that source.

The probability of exciting a component of an upper-multiplet resonance as compared with that for starting the  $\pi$ -mode decreases as the value of  $\gamma$  for that component approaches  $N/2$ . The difference  $(N/2) - \gamma$  may thus be taken as an indication of the likelihood of competition from that source. As the number of resonators increases, the value of  $(N/2) - \gamma$  will increase if  $\gamma\lambda$  is to be approximately equal to  $(N/2)\lambda_\pi$  and the wavelength ratio  $\lambda/\lambda_\pi$  is to be constant. For example, if in an 18-resonator rising-sun system the competing component is the  $\frac{5}{3}$ , with a wavelength of  $1.5\lambda_\pi$ , the disturbing component of wavelength  $1.5\lambda_\pi$  for a 30-resonator system will be the  $\frac{1}{2}$ . The increase in  $(N/2) - \gamma$  from 3 to 5 is believed to aid the probability of competition with  $\pi$ -mode operation. This effect is further aggravated if  $r_1$  is increased and the wavelengths of the upper-multiplet resonances are thereby also increased.

As a closed-end block is more difficult to build than an open-resonator type, it should probably not be undertaken unless it is believed that a system with the required number of open resonators will not be a safe design. One electrical disadvantage of closed-end design is that the block height is rather restricted, whereas in the open-resonator type, the height can be chosen practically at will. For high-voltage magnetrons,  $\mathcal{V} \approx 3.0$  kv. The closed-end construction should be used if the number of resonators required is 26 or more. In the low-voltage region ( $\mathcal{V} \approx 450$  volts), the use of the simpler open-resonator construction can be extended to a system of 30 or more resonators.

**11-8. Ratio of Resonator Depths.**—In designing a rising-sun magnetron, it is best to plan to use as small a value of  $r_1$  as possible, consistent with noninterference from the  $\left(\frac{N}{2} - 1\right)$ -mode. The available information on the proper value for the resonator depth ratio for various values of  $N$  is based mainly on experience with magnetrons that were designed for operation in the low-field region ( $\lambda H$  from 6000 to 10,000 gauss cm). The optimum value of  $r_1$  for the high-field region is not necessarily the same as that for low fields. The study of the performance of 18-vane open-resonator magnetrons designed for  $\mathcal{V}$  close to 3.0 kv but with  $r_1$  values varying in the range of 1.4 to 2.5 showed that in the low magnetic-field region, values of  $r_1$  less than 1.6 are too low because of competition from the ( $n = 8$ )-mode while  $r_1$  values greater than 2.0 are objectionable because of competition from the resonances associated with the large-resonator systems. In the high-field region, however, an  $r_1$  value of 1.6 was found quite satisfactory for magnetrons in the same range of voltage. A summary of the range of probably useful values of  $r_1$  for various values of  $N$  is given in Table 11-6 for open-resonator mag-

TABLE 11-6.—USEFUL VALUES OF  $r_1$ , THE RATIO OF RESONATOR DEPTHS, FOR  $\lambda H$  BETWEEN 6000 AND 10,000 GAUSS/CM

$N$	$\mathcal{V}$ , kv	Range of $r_1$
18	3.0	1.7-2.0
22	3.0	1.7-1.9
26	3.0	1.75
34	0.4	1.8-2.0

netrons designed for operation in the low-field region. The lack of any definite range in  $r_1$  for the case of  $N = 26$  demonstrates the difficulty of building large  $N$ , open-resonator magnetrons in the high-voltage region.

For the closed-end system the values of  $r_1$  are higher than in the open-resonator type. This trend is consistent with theoretical expectations,

because for a given value of  $r_1$  both the mode separations and zero-mode contamination of the  $\pi$ -mode are less for the closed-end than for the open-resonator type. In the closed-end system these electromagnetic properties depend, of course, on the block height as well as on  $r_1$ . One would expect to find smaller values of  $r_1$  with longer blocks. In closed-end resonant systems containing 26 cavities, values of  $r_1$  from 2.1 to 2.7, for block heights of  $0.63\lambda$ , and  $\mathcal{V}$  values of about 3.5 kv have been found satisfactory. The optimum value of  $r_1$  is probably in the region of 2.2 to 2.4 for this block height. Good closed-end 38-vane magnetrons have been built with  $r_1$  close to 2.7 for a block height of  $0.7\lambda$  and  $\mathcal{V}$  of 3.3 kv.

**11.9. Wavelength Calculations for the  $\pi$ -mode.**—For a vane-type, open-resonator, rising-sun magnetron, the wavelength of the  $\pi$ -mode can be calculated to within 2 or 3 per cent by means of a simple empirical formula involving principally the perimeters of the two different resonators. Thus, if  $P$  represents the perimeter of the total path for two adjacent resonators in a block cross section, as shown by the solid lines in Fig. 11-11, then with certain restrictions the wavelength is given by

$$\lambda = P[1.03 - 0.06(r_1 - 1.8) + 0.05(r_2 - 1.5)], \quad (12)$$

where  $r_1$  is the ratio of the radial depth of the large resonator to that of the smaller resonator,  $(r_L - r_a)/(r_s - r_a)$ , and  $r_2$  is the ratio of copper to space,  $t/w$ .

This formula, which is consistent with the data on 18-, 22-, and 26-vane open-resonator magnetrons, will apply only if the end-space geometry is not appreciably different from that shown in the open-resonator rising-sun magnetrons in Chap. 19, if the anode diameter corresponds to a  $\mathcal{V}$  near the range of 2.5 to 3.5 kv, and if the other block parameters are consistent with good tube design. For example, despite the fact that the decrease of the  $\pi$ -mode wavelength with increasing cathode diameter is appreciable, the cathode diameter does not appear in the wavelength formula, because this effect is small if one is confined to the range of  $\sigma$  values that is likely to be used. A decrease in anode diameter, however, brought about by decreasing  $\mathcal{V}$  from 3000 to 500 volts with  $P$ ,  $r_1$ ,  $r_2$ , and  $\sigma$  held constant increases the  $\pi$ -mode wavelength about 10 per cent.

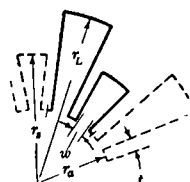


FIG. 11-11.—Geometrical quantities used in the calculation of the  $\pi$ -mode wavelength.

Equation (12) should enable the magnetron designer to select the proper resonator diameters with sufficient accuracy for a first model. Subsequent small changes in the anode-block geometry, within the precision of tube construction, may then be made to correct for an initial error in the wavelength obtained. When more accurate wave-

length predictions are needed, the formulas given in Chap. 3 should be used. These are based on the field theory calculations and include the parameters  $P$ ,  $r_1$ ,  $r_2$ ,  $\sigma$ , and  $d_a$  but omit effects of the geometry of the end spaces and the cathode end shields. The theoretical formulas may also be used for calculating resonances of the mode spectrum other than that of the  $\pi$ -mode.

The wavelength calculations for a closed-end system are somewhat more complicated, particularly when the resonators depart from the sector-shaped cross section. The procedure for wavelength calculation of the  $\pi$ -mode is outlined below for two different types which represent most of the closed-end anode blocks that have been used.

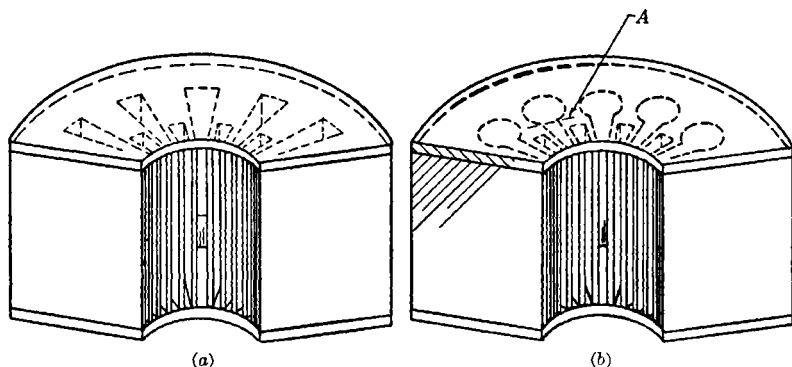


Fig. 11-12.—Closed-end rising-sun anode blocks. (a) Vane-type; (b) with circular cylinders at the backs of the large resonators.

CASE I.—Completely closed vane-type anode block (see Fig. 11-12a).

1. Calculate  $\lambda_\infty$  (block of infinite length with no variation in properties along the Z-axis) with the aid of the formulas given in Chap. 3 or from Eq. (12), adding about 7 per cent for end-effect corrections.
2. Compute the  $\pi$ -mode wavelength from the expression

$$\frac{1}{\lambda^2} = \frac{1}{\lambda_\infty^2} + \frac{1}{4h^2}, \quad (13)$$

where  $h$  is the block height. In the design of an anode block the procedure will very likely be reversed. The desired  $\lambda$  will be known, and the block height will be decided on before determining the cross-sectional geometry of the resonators. In that case apply Eq. (13) to compute the required value for  $\lambda_\infty$ . The perimeter of the resonators is then determined by either of the two procedures given in Step 1. From this value and from the predetermined values of the anode diameter and of the resonator-depth ratio the diameters of the two resonators are determined.

CASE II.—Case II differs from Case I in that the backs of the large resonators are circular in cross section (see Fig. 11-12b).

1. Follow the procedure outlined in Case I to determine the proper sector-shaped geometry to produce the desired wavelength for the chosen values of  $h$ ,  $r_1$ , and  $d_a$ .
2. Using the formulas or curves given in Chap. 3 for the admittance of circular- and of sector-shaped cavities, design the proper hole geometry to give the same admittance at plane  $A$  (see Fig. 11-12b) as that obtained with the section of replaced sector-shaped cavities. If the circular section is designed to give the same cross-sectional area as the replaced sector section, the wavelength generally turns out to be too low, because that region is not completely inductive, whereas if the substitution is based on preserving the perimeters, the resulting wavelength is too high. The procedure of determining equivalent admittances may also be followed where the substituted portions of the resonators have other than circular geometries.

## OUTPUT

BY W. V. SMITH AND S. MILLMAN

**11-10. General Properties of Coaxial and Waveguide Outputs.**—The function of the output of a magnetron is to couple the r-f energy generated in the tube to a useful load. To accomplish this end, the output must have the following properties: (1) As a circuit element, it must transform the load impedance to some desired level inside the tube. (2) As a physical element joining the evacuated tube to a transmission line, it must contain a vacuum seal. (3) As a section of transmission line, it must be capable of transmitting the high average and pulse powers generated by the magnetron.

The circuit properties of the output are treated in Chap. 5. For magnetrons that do not differ radically from the examples shown in Chap. 19, the analyses of Secs. 5-4, 5-5, 5-6, and 11-2 may be used to estimate the suitability of a given output design for the particular block geometry and loading requirements involved. The type of output is determined by requirements of mechanical strength, constructability, size, pulse or average power transmission, and frequency sensitivity.

At 1 cm, waveguide outputs are the logical choice, because at this wavelength the construction of waveguide outputs is simpler and more reproducible than coaxial outputs, and coaxial lines will withstand only about 20 kw of 1-cm pulse power. At 3 cm, where the ultimate transmission line is also waveguide, waveguide outputs are generally used, although coaxial outputs embodying coax-to-waveguide transitions are

satisfactory for pulse powers under 50 kw. The ultimate transmission line for 10-cm radiation is generally coaxial for pulse powers less than 200 kw and waveguide for pulse powers in excess of this amount; waveguide is also used to transmit average powers greater than 400 watts. Consequently, 10-cm magnetrons that deliver less than 200-kw pulse or 400 watts average are equipped with coaxial outputs, while more powerful tubes are designed with either waveguide outputs or coax-to-waveguide transitions. The large size of waveguide equipment at 10-cm makes it uneconomical to use this type of construction for operation at low-power levels.

For linear scaling to different wavelengths, the percentage frequency sensitivity is unchanged, whereas the change in size affects the breakdown power which scales as the square of the wavelength. In coaxial line, at a fixed wavelength, the breakdown power scales as the square of the diameter of the line, assuming that the characteristic impedance is maintained constant and the lead construction is similar. Both of these conclusions are dependent upon the assumption that at atmospheric pressure, breakdown will occur above a maximum field strength  $E_{\max}$  that is independent of wavelength. The breakdown voltage decreases as the duty ratio increases, and for c-w operation it is considerably below the pulsed values.

**11-11. Coaxial Outputs.**—The observations in this section are concerned with outputs designed for wavelengths in the vicinity of 10 cm. However, the data specific to a given wavelength may be scaled at least qualitatively. Figures 11-13 to 11-15 illustrate coaxial leads designed for loop couplings. As shown in Chap. 5, other types of coupling may be used, however, depending on the external  $Q$  desired and the type of magnetron under consideration. Whenever possible, the coupling is designed to give the desired loading at a minimum shift in tube wavelength and with a minimum frequency sensitivity, the rest of the lead being kept as well matched as possible. This technique generally improves the breakdown properties and minimizes the complexity of construction. In special cases, however, it is possible to cancel one reflection with another and one frequency sensitivity with another by use of the method given in Sec. 11-12 for coaxial-to-waveguide transitions.

**Frequency Sensitivity.**—A typical medium-power coaxial output for  $\frac{7}{8}$ -in. line is shown in Fig. 11-13. The lead consists of a section of line  $A$  of characteristic impedance  $Z_A$ , a taper  $B$ , a section of line  $C$  of characteristic impedance  $Z_C$ , a glass seal  $D$ , a choke joint  $E$ , a section of line  $F$  of characteristic impedance  $Z_F$ , a connecting "bullet"  $G$  of the same characteristic impedance  $Z_G$  as the final coaxial line, and a quarter-wave transformer  $H$  of characteristic impedance  $Z_H$ . The lead is terminated by the final matched transmission line of characteristic impedance  $Z_o$ .



A more simplified design is shown in Fig. 11-14 in which the elements *A*, *B*, *C*, and *D* are essentially similar to those of Fig. 11-13 but in which the single series impedance *J* in the outer conductor replaces elements *E*, *F*, and *G*. The elimination of the transformer is made possible by setting the size and penetration of the loop to give the desired external *Q*. The design of Fig. 11-14 is mechanically sturdier than that of Fig.

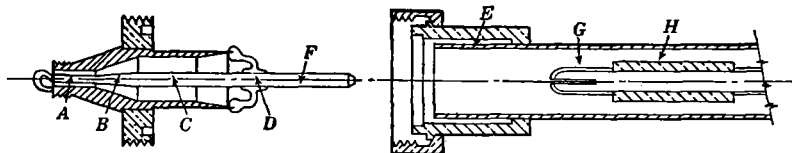


Fig. 11-13.—200-kw pulse-power coaxial output and coupling section with choke joint.

11-13 and is also less frequency sensitive, because it contains no large discontinuities of characteristic impedance.

The improvement in the design is primarily due to the use of the Kovar-to-glass sealing technique.<sup>1</sup> The use of a Kovar cup rather than a small tungsten lead for the inner conductor allows a construction that fits into a standard r-f coupling, and the short length of *J* eliminates the necessity for the choke joint.

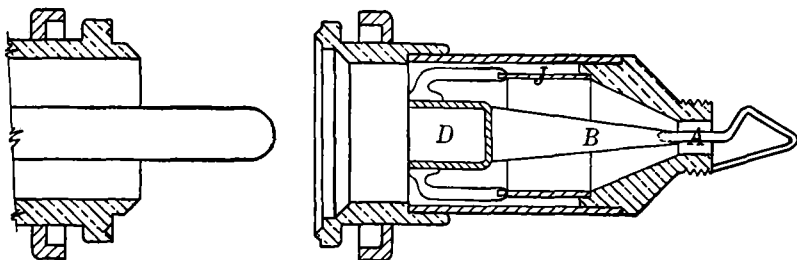


Fig. 11-14.—300-kw pulse-power coaxial output and coupling section without choke joint.

A calculation of the series impedance introduced by section *J* shows that it is negligible. Thus, with  $J \frac{7}{16}$  in. long, the outside diameter  $\frac{13}{8}$  in., and the inside  $\frac{11}{8}$  in., the series impedance is given by

$$Z_J = 60 \log_e \frac{13}{11} \tan \frac{2\pi(\frac{7}{16}) \text{ in.}}{\lambda} = 8 \quad \text{ohms.}$$

As the line characteristic impedance is 48 ohms and the loop impedance usually of the same order of magnitude,  $Z_J$  can be neglected.

The glass seal approximately halves the characteristic impedance of the line in the region of the bead but leaves the impedance practically unaltered where the glass is thin and near the outer conductor. Assum-

<sup>1</sup> It should be noted, however, that the No. 704 glass which is used in making Kovar seals is more lossy than the No. 707 glass used in the tungsten seal of Fig. 11-13.

ing the bead length to vary up to a maximum length of  $\frac{1}{4}$  in. or  $\lambda_g/8$  (allowing for the short wavelength in glass), the resulting impedance transformation represents an effect comparable in magnitude to the loop impedance. As a rule no attempt is made to balance out these two impedances.

A modification of Fig. 11-14 is illustrated in Fig. 11-15 which shows a drawing of a lead for a  $1\frac{5}{8}$ -in. line. The design of Fig. 11-15 differs qualitatively from that of Fig. 11-14 because, in the larger size, a longer length of Kovar is necessary for a satisfactory metal-to-glass seal and a half-wave choke must be included. From the dimensions shown it may be calculated that the frequency sensitivity of the choke joint is negligible. In conformity with standard choke-joint design, the frequency sensitivity

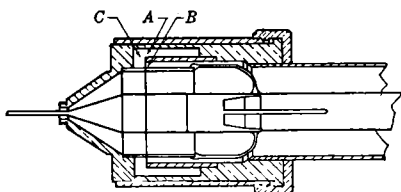


FIG. 11-15.—800-kw pulse-power coaxial output and coupling section with choke joint.

of the choke joint is minimized by making section A of relatively high characteristic impedance and section B of low characteristic impedance. Section B is thus terminated at its junction to A by a high impedance that, transformed down a quarter wavelength of low-impedance line, becomes a very low impedance.

The junction C between the output lead and the connecting section appears in series with the high impedance terminating B, and its nature is therefore not important.

Occasionally leads exhibit sharp resonances that markedly affect the tube loading, the efficiency, and the lead-breakdown power. These resonances result from weakly coupled resonant circuits such as that of a choke joint operating in a mode where the circumference of the choke is equivalent to one guide wavelength. For large circumferences these modes occur near the principal coaxial mode, particularly if a section of the choke joint is capacitance loaded by the glass of the seal. Inside metal-to-glass seals eliminate this difficulty but are usually less rugged mechanically.

*Voltage Breakdown and Average Power Transmission.*—For a given output power  $P$  into a matched line of inner and outer diameters  $a$  and  $b$  the mean squared electric field  $\bar{E}_a^2$  at the center conductor is

$$\bar{E}_a^2 = \frac{60P}{a^2 \log \frac{b}{a}} \quad (14)$$

The relative values of  $\bar{E}_a^2$ , for  $b/a = 6.5$  as in the design of Fig. 11-13, for  $b/a = 2.17$  as in the design of Fig. 11-14, and the optimum value of

$b/a = 1.65$  are 4.0, 1.2, and 1.0 respectively. A further increase in the diameter of the center conductor over that given in the design of Fig. 11-14 would therefore have small value.

To minimize surface breakdown, the glass seal should present a long path to the electric field, and the component of the electric field parallel to the glass surface should be made as small as possible. Re-entrant glass surfaces with crevasses between the glass and the outer conductor should be avoided because localized high-frequency discharges take place in the crevasses and the glass is eventually ruptured.

Safe pulsed ratings for all phases of a 1.5 SWVR are 200 kw<sup>1</sup> for the design of Fig. 11-13 and 300 kw for the design of Fig. 11-14; average power ratings are 250 and 450 watts respectively.

On the basis of the scaling laws, the breakdown power of the high-power lead of Fig. 11-15 is computed to be 1000 kw. This design may be conservatively rated at 800 kw, although it will usually pass 1500 kw into a well-matched line. On average power transmission, it will safely pass 1.5 to 2 kw and with forced-air cooling has transmitted 3 kw experimentally.

**11-12. Coaxial-to-waveguide Transitions.**—Coaxial-line-to-waveguide transition sections<sup>2</sup> are illustrated by the “doorknob” transition type of Fig. 11-16 and the “probe” type of Fig. 11-17.

The breakdown characteristics of the doorknob transition are similar to those of a lead terminated in a coaxial line. The probe type, however,

<sup>1</sup> The breakdown data given in this section refer to pulsed operation at 1  $\mu$ sec, 1000 PRF, and remain valid as the pulse duration and repetition frequency are varied by a factor of 2.

<sup>2</sup> See Vol. 9, Chap. 6, Radiation Laboratory Series, for a detailed treatment of this subject.

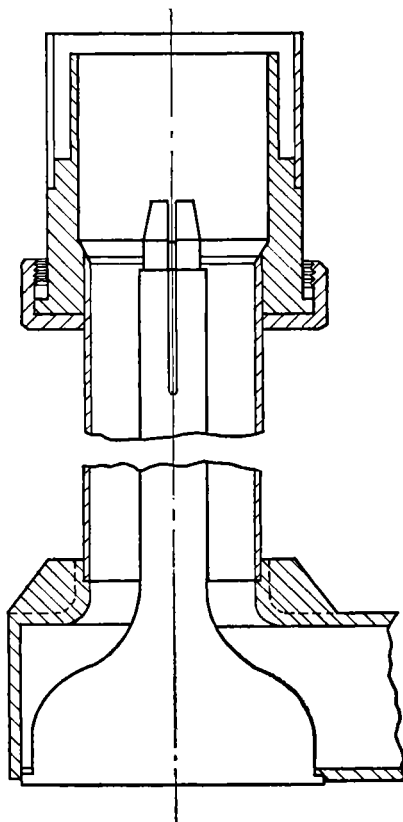


FIG. 11-16.—10-cm, 800-kw pulse-power “doorknob” transition for  $1\frac{1}{2}$ -in. coaxial line to  $1\frac{1}{2}$ - by 3-in. waveguide.

has been improved in this respect by the location of the glass seal in a region of low electric field. At 8.5 cm the probe transition is rated at 800 kw as compared with 500 kw for the doorknob type. The frequency sensitivity of the probe design is also superior to that of the doorknob. A set of data showing the frequency sensitivity of the probe transition of Fig. 11-17 is given in Fig. 11-18 in which the standing-wave ratio in the coaxial line is plotted as a function of wavelength, the waveguide being terminated in a matched load. To attain the low-frequency sensitivity shown in Fig. 11-18 it is necessary deliberately to mismatch

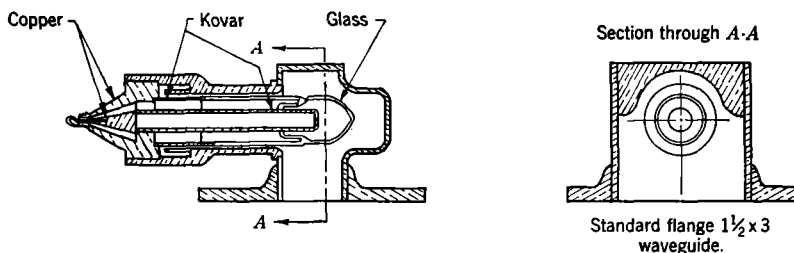


FIG. 11-17.—8.5-cm, 800-kw pulse-power "probe" transition for coaxial line to  $1\frac{1}{2}$ -by 3-in. waveguide.

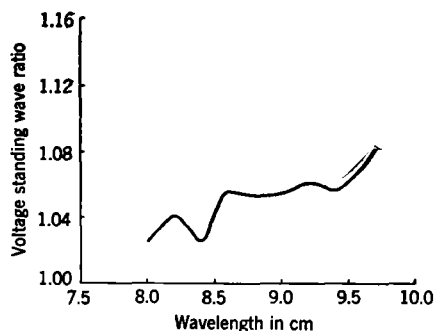


FIG. 11-18.—Frequency characteristics of a "probe" transition shown in Fig. 11-17.

the junction of probe to waveguide and then to cancel out the resultant reflection by an inductive iris in the waveguide. This procedure sets up standing waves in the transition section and may reduce its breakdown power, but the sacrifice is unavoidable if broadbanded transition is desired. The theory of this type of broadbanding is given in Vol. 9, Chap. 6.

**11-13. Waveguide Outputs.**—The two important components of a direct waveguide output for magnetrons are the window and the transformer. The window functions as a vacuum seal and an r-f connection between the internal and external guides, and the transformer transforms the load impedance to a value proper for magnetron operation. The

design information presented in the following sections is restricted to component types that have been widely applied. The discussion of windows is limited to those of the circular cross sections, because this type of window is easily manufactured in a reproducible way and has been used in almost all of the magnetrons with direct waveguide output. Similarly, most of the discussion on transformers is devoted to the quarter-wave type, a design for which considerable information is available. A description of the circular iris output, used with a half-wavelength stabilized cavity, is included in Secs. 11-14 and 11-15.

*The Window.*—A good window should be almost lossless and almost reflectionless. A practical approach to a lossless window for 1.25-cm magnetrons is shown in Fig. 11-19. The design embodies a low-loss glass (Corning No. 707) sealed in the base of a Kovar cup. Electrical

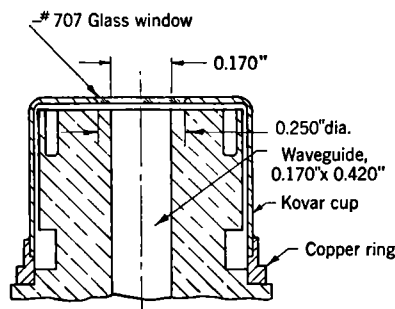


Fig. 11-19.—Window for the waveguide output of a 1.25-cm magnetron.

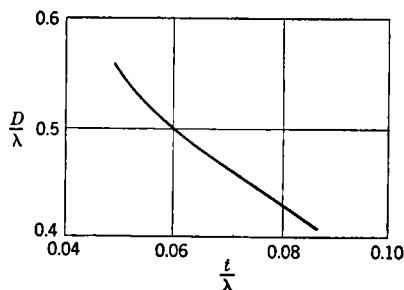


Fig. 11-20.—Waveguide-window diameter  $d$  required for match as a function of glass thickness  $t$ .

contact between the window and the guide is effected on each side by means of standard r-f chokes, one of which is shown in the figure.

The nonreflecting property of the glass window is achieved by the choice of the proper diameter and thickness for the glass. A nonreflecting window may be looked upon as a short circular waveguide of the same characteristic impedance as the rectangular guides between which the window is inserted. The characteristic impedance of circular guide increases with decreasing diameter, and a rectangular guide of high characteristic impedance therefore requires a window of small diameter. The comparison should not be used for quantitative calculations, however, because the window thickness is only a small fraction of a wavelength and also because the end effects play an important part in the matching of the window to the guide. This is verified by the fact that the proper window diameter for nonreflection is not independent of thickness. Figure 11-20 shows a plot of the observed window diameter required for match as a function of window thickness for one fixed set of guide dimen-

sions. A procedure that is commonly followed in designing a window is to choose the thickness on the basis of mechanical considerations and then to determine the diameter by testing for nonreflection. The thickness

of windows in common use ranges from  $0.02\lambda$  to  $0.04\lambda$ , and the diameters from  $0.4\lambda$  to  $0.8\lambda$ . It is not difficult to make windows with reflection coefficients of 0.05 or less for guides transmitting r-f power at 1-cm or longer wavelengths.

Although the breakdown strength of the window design in Fig. 11-19 is considerably better than that of a coaxial output, it is inadequate for high-power magnets. Arcing at the window may occur at about one-quarter the power required to break down the guide itself because of the sharp physical discontinuities between the circular window and the rectangular guide, particularly at the center of the guide where the electric field is strongest. Initial attempts at "rounding the corners" of the guides have led to a systematic and reproducible method of chamfering the guide to obtain a physical match be-

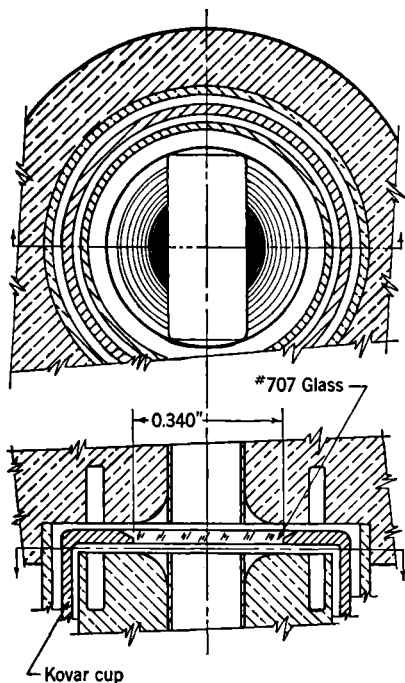


FIG. 11-21.—Waveguide window for chamfered guide.

tween the guide and the window (see Fig. 11-21).

When the guide is chamfered at the window boundary, there is a twofold improvement of the breakdown strength. Not only are the sharp discontinuities removed, but also there is an increase in the diameter of the window required for match. This increase in diameter may be regarded as resulting from the fact that the chamfering has served to introduce shunt inductances on both sides of the window and that this is balanced by the equivalent shunt-capacitance effect of a large window. As the nonreflecting properties are achieved by a balance of shunt susceptances, the spacing between the window and the guide should be the same on both sides of the window. For the chamfer design shown in Fig. 11-21, the diameter of the window is about 35 per cent larger than for ordinary guide and the power-handling capacity of the guide is almost doubled. With this type of window geometry a pulsed

power of over 700 kw has been transmitted without arcing at atmospheric pressure for a 3-cm magnetron operating with a pulse duration of 0.5  $\mu$ sec and terminated with a matched guide.

The available data on the broadband properties of the combination of window and r-f chokes for the two types of window geometries discussed above do not permit a good evaluation of the advantage or disadvantage of chamfering the guide from the standpoint of frequency sensitivity. The range of wavelengths for which a given window will introduce a reflection coefficient of 0.1 or less is of the order of 20 per cent for either type and can probably be improved if the broadband property of the window is taken into account when the window geometry is designed. A typical plot of the standing wave introduced by the window and chokes as a function of wavelength is given in Fig. 11-22 for a window design that includes chamfered guides. The details in the curve are not always reproduced, but the general appearance of the curve is similar for windows of presumably identical construction.

The low-loss No. 707 glass that is used in windows is adequate for ordinary magnetrons but is inadequate for outputs transmitting high average power. Thus with 3-cm radiation, 500 watts of average power is close to the upper limit that can be transmitted through the window without the use of special cooling devices. As the losses in glass increase with temperature, a "blow-in" of the window becomes a serious limitation in the high-power tubes. The substitution of mica for glass seems to offer a good solution to the high-power problem because the loss in mica is about 15 per cent of that in No. 707 glass. The technique of constructing mica windows for waveguide outputs is given in Sec. 17-4.

*The Transformer.*—The transformer in a waveguide-output design serves as an impedance-matching device that reduces the high impedance of the waveguide used in power transmission to a value sufficiently low (about one-hundredth of the guide impedance) to effect the proper loading for the magnetron. A simple form of such a transformer is a quarter-wave section of waveguide of rectangular or other cross section which connects one of magnetron resonators to the short section of standard waveguide used in the output. At the transformer-resonator boundary the current is continuous, so that the axial current in the transformer is equal to the r-f current in the back of the resonator.

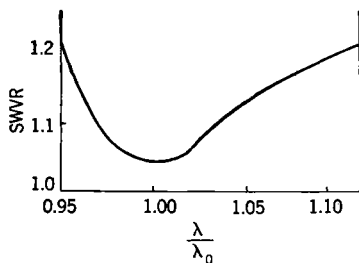


FIG. 11-22.—Standing-wave voltage ratio introduced by window and chokes, as a function of wavelength, for a window design that includes chamfered guides.

The impedance required at the resonator depends on the block geometry and the desired stability of the magnetron; i.e., on the external  $Q$ . This quantity may be written in the form

$$Q_E = \frac{\omega \sum_{k=1}^N \frac{1}{2} l_k I_k^2}{\frac{1}{2} R I^2}, \quad (15)$$

where  $l_k$  is the equivalent inductance of a resonator,  $I_k$  is the current amplitude in that resonator,  $I$  is the current amplitude at the transformer-resonator boundary,  $R$  is the real part of the impedance presented by the load at the resonator, and the summation extends over all the resonators.

For a strapped anode block the values of  $l_k$  are the same for all resonators. Furthermore, if the loading is assumed to be sufficiently light, the current amplitudes will be nearly the same in all resonators and the quantity  $Q_E$  will assume the simpler form

$$Q_E = \frac{\omega N l}{R}. \quad (16)$$

Thus when the effective inductance of a resonator of a strapped block is known, and when  $Q_E$  is specified, the required load is determined.

Equation (16) is not valid for open-resonator rising-sun blocks because the equivalent inductance of a small resonator is less than that of a large one and because the current amplitude in the back of a small resonator is greater than that in a large one. For this type of magnetron design, then, Eq. (15) will take the form

$$Q_E = \frac{\omega N (l_1 I_1^2 + l_2 I_2^2)}{2 R I^2}, \quad (17)$$

where  $l_1$  and  $I_1$  refer to the small resonators,  $l_2$  and  $I_2$  refer to the large ones, and light loading is assumed as before. It follows from this expression that the required load will depend on whether the output is taken from a large or from a small resonator. When the output is taken from a large resonator, as has been the case in all rising-sun systems, Eq. (17) becomes

$$Q_E = \frac{\omega N \left( l_2 + l_1 \frac{I_1^2}{I_2^2} \right)}{2 R}; \quad (18)$$

and as  $I_1$  is greater than  $I_2$ ,  $Q_E$  is greater than  $\omega N (l_1 + l_2) / (2R)$ . When the output is taken from the small resonator, however,  $Q_E$  is less than  $\omega N (l_1 + l_2) / (2R)$ . It follows, therefore, that in the rising-sun system the required load is not uniquely determined by the block geometry



and the specified  $Q_E$ . Thus when  $Q_E$  is defined for a rising-sun magnetron in terms of an equivalent inductance of a simple series resonant circuit  $Q_E = \omega L/R$ , it is implied that the equivalent value of  $L$  depends upon the resonator that is used for the output. This simply emphasizes the fact that the definition of an equivalent inductance for a resonator is, in general, not unique and depends on the current distribution in it.

Closed-end rising-sun systems require a considerably greater load resistance for a given  $Q_E$  than do the open-resonator systems, because the closed-end resonators contain two different kinds of oscillating currents. One is the usual radial-circumferential current which is associated with an axially oscillating magnetic field; the other current is transverse and is associated with radially oscillating fields. The transverse current does not couple to the transformer, because its amplitude vanishes near the output. However, a considerable amount of stored energy is associated with the transverse current, particularly when the block height is close to a half wavelength, and this increase in the total stored energy of the block requires an increase in  $R$  to maintain the same  $Q_E$ . The actual value of  $R$  depends on the block height; for some closed-end designs a value six times as large as that needed for the open-resonator type has been found necessary.

**11-14. Waveguide Transformers.** *The Rectangular Transformer.*—A simple type of quarter-wave transformer consists of a section of angular waveguide. With this type of transformer, neglecting end effects and assuming that the window does not reflect and that the waveguide used for the power transmission is terminated with a matched load, the impedance presented to the output resonator of the magnetron will be real and given by the expression

$$Z = \frac{Z_0'^2}{Z_0}, \quad (19)$$

where  $Z_0$  is the characteristic impedance of the guides on each side of the window and  $Z_0'$  is that of the transformer guide. From the  $V^2/w$  definition of impedance of a guide, the expression for  $Z_0$  and  $Z_0'$  in terms of the respective guide dimensions  $a, b$  and  $a', b'$  are, in units of 377 ohms,

$$Z_0 = \frac{2b}{a} \left[ 1 - \left( \frac{\lambda}{2a} \right)^2 \right]^{-1/2} \quad \text{and} \quad Z_0' = \frac{2b'}{a'} \left[ 1 - \left( \frac{\lambda}{2a'} \right)^2 \right]^{-1/2}. \quad (20)$$

Substituting Eq. (20) in Eq. (19) the expression for  $Z$  becomes, in units of 377 ohms,

$$Z = \frac{2b'^2}{b} \frac{a}{a'^2} \left[ 1 - \left( \frac{\lambda}{2a'} \right)^2 \right]^{-1} \left[ 1 - \left( \frac{\lambda}{2a} \right)^2 \right]^{1/2}. \quad (21)$$

If  $a, a'$ , and  $b$  are kept constant, as is usually the case when one is determining the proper loading for a given magnetron, the impedance is

directly proportional to the square of the narrow dimension of the transformer. Having measured  $Q_E$  for a block with a given transformer geometry, it is simple to determine the proper value of  $b'$  for any desired loading.

To ensure that the load presented to the magnetron resonator is one of pure resistance, it is necessary to take into consideration the end effects that were neglected in the preceding discussion. It is relatively simple to determine the equivalent shunt reactances associated with the physical discontinuities at the ends of the transformer and allow for them by a small departure of the transformer length from the value  $\lambda_g/4$ . An experimental procedure for determining the proper transformer length has been described.<sup>1</sup>

The broadband characteristics of the rectangular waveguide transformer are satisfactory for ordinary magnetron operation. The variation of the magnetron load with frequency can be seen in the expression for the impedance presented at the transformer-resonator boundary for arbitrary lengths of the transformer; namely

$$Z = Z'_0 \frac{\frac{Z_0}{Z'_0} + j \tan 2\pi \frac{l}{\lambda_g}}{1 + j \frac{Z_0}{Z'_0} \tan 2\pi \frac{l}{\lambda_g}},$$

where it is assumed that the impedance at the window end of the transformer is  $Z_0$  and that  $l$  is the effective length of the transformer, where end effects have already been taken into account. For values of  $l$  close to  $\lambda_g/4$  one may write

$$Z = R + jX = Z'_0 \left( \frac{Z'_0}{Z_0} \right) \csc^2 \frac{2\pi l}{\lambda_g} - jZ'_0 \cot \frac{2\pi l}{\lambda_g}. \quad (22)$$

The broadband characteristics of the output will be determined by the dependence of the real part of  $Z$  on wavelength and by the effect on the r-f current in the output cavity produced by the imaginary part of  $Z$ .

The dependence of  $R$  in Eq. (22) on wavelength is not very marked. The factor  $Z'_0/Z_0$  can be made independent of  $\lambda$  by making  $a' = a$ , and for a well-chosen guide a change in wavelength of 10 per cent will effect  $Z'_0$  by only about 5 per cent and  $\csc^2 (2\pi l/\lambda_g)$  by less than that. The frequency dependence of  $R$  can be further improved by making  $a'$  somewhat greater than  $a$ , as shown in Fig. 11-23, where  $R/R_0$  is plotted as a function of  $\lambda/\lambda_0$  for various values of  $a'$  and  $a$ , the large dimension of the transformer and output guide, respectively. The transformer dimension  $b'$  is chosen to give the desired  $R$  value ( $R_0$ ) at midband ( $\lambda_0$ ).

<sup>1</sup> S. Millman, "Waveguide Output for 1.25-cm Magnetrons," NDRC 14-245, Feb. 1, 1944.

The effect of the imaginary part of  $Z$ , aside from the small change in the magnetron wavelength and the almost negligible distortion in the mode pattern, is to alter the r-f current in the output cavity. Assuming a fixed r-f voltage across the mouth of the output resonator, the change in current will be given

$$\frac{I}{I_0} = \frac{\sqrt{(\omega L)^2 + R_0^2}}{\sqrt{(\omega L + x)^2 + R^2}},$$

where  $I_0$  is the current amplitude at midband and  $L$  is the equivalent inductance associated with the output resonator. The effect of this

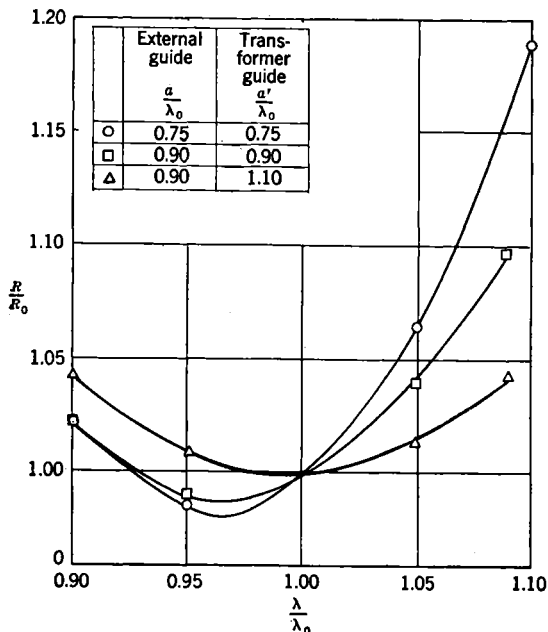


FIG. 11-23.—Resistive component of magnetron load vs. wavelength for various combinations of the dimension  $a$  of the transformer guide and the external guide.

current change on  $Q_E$  is, according to the definition of  $Q_E$  as given in Eq. (15), to multiply  $Q_E$  by a factor that is to a first-order approximation  $[1 + (X/\omega L)]^2$ , wherein the effect of  $X$  on the total stored energy of the magnetron has been neglected. This factor is easily evaluated from the definition of  $X$  as given in Eq. (22) when the value of  $L$  for the output resonator is known.

*The Transformer of H-shaped Cross Section.*—For magnetrons with short block heights, the large size of the dimension  $a'$  of the rectangular waveguide transformer may prove mechanically inconvenient. With

the H-type waveguide, however, an effectively large  $a'$  can be achieved with small physical sizes. A transformer of this guide shape has been used in the output design of the 4J50 magnetron described in Chap. 19. The relative dimensions of this H-type cross section and the output waveguide are shown in a drawing of the transformer-guide boundary (Fig. 11-24).

The proper transformer length is obtained by determining  $\lambda_g$  in this type of guide and by evaluating the end corrections at the boundaries.

The value of  $\lambda_g$  can be either measured experimentally or calculated as shown in Sec. 5-6. The end corrections can be determined in the same way as those for the rectangular guide transformer.<sup>1</sup>

The required transformer width depends on the load to be presented to the magnetron at the output resonator. However, in this type of transformer the effective resistance at the output resonator depends not only on the characteristic impedance of the H-section and of the output waveguide but also on the transformer action at the boundary between the waveguide and transformer. This is a result of the fact that the coupling between the transformer and waveguide extends over only a fraction of the total height of the guide. The calculations for this effect are given in Sec. 5-6. The effect of the difference in height between the transformer and waveguide is to require an increase in the transformer width. The dependence of the resistance on the square of the transformer width holds for the H-section as well as for the rectangular waveguide type and can be used for correcting initial errors in the design.

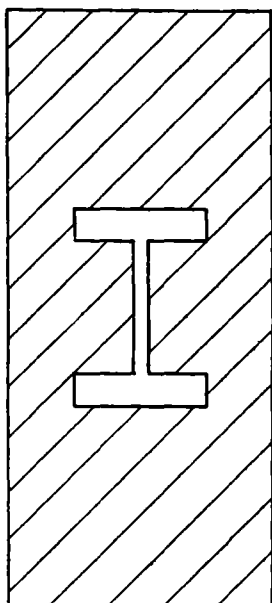


FIG. 11-24.—Relative sizes of H-section transformer and output waveguide in the 4J50 output.

The frequency dependence of the H-section transformer is very similar to that of the rectangular waveguide type. When good broadband characteristics are required, the dimensions of the H-section should be chosen in such a way as to yield a cutoff wavelength in the transformer that is at least as long as that in the output waveguide.

*The Iris Transformer.*—A method has been developed for controlling the magnetron loading by means of an iris-type transformer in conjunction with a stabilized cavity.<sup>2</sup> The stabilizer is in the form of a half-

<sup>1</sup> *Ibid.*

<sup>2</sup> A. Nordsieck, "New R-f Output Transformer for K-band Magnetron," *RL Coordination Minutes*, 7, 45, Sept. 13, 1944.

wavelength section of rectangular waveguide inserted between the output guide and one of the magnetron resonators. The strong coupling required between the cavity and the resonator is achieved by means of a rectangular resonant iris, while the comparatively weak coupling between the cavity and the output guide is obtained with a circular iris in the thin wall separating the cavity from the output guide. The diameter of this iris determines the magnetron load. The stabilizing properties of the half-wavelength cavity will be further discussed in Chap. 16. The discussion in this section will be concerned with the proper cavity length for a pure resistive load, the dependence of  $Q_s$  on the diameter of the iris, and the frequency sensitivity of the iris-type transformer.

The proper length for the stabilizing cavity is that length which does not change the resonant wavelength of the anode block. The departure of this length from  $\lambda_0/2$  is due to end effects. At the resonator end of the cavity, a resonant iris gives maximum coupling between the cavity and the resonator and also eliminates any shunt susceptance at that junction. An experimental setup for determining the proper iris length is shown in Fig. 11-25. A rectangular iris of arbitrary width and thickness  $h$  is soldered to a short section of waveguide having the same cross-sectional dimensions as the stabilizing cavity. The source of r-f power and the standing-wave detector are attached to the other end of the guide. Two sections of parallel-plate transmission line having the same cross-sectional dimensions as the back of the output resonator of the anode block are alternately butted up against the iris. The length  $L$  of one of these sections is  $\lambda_0/4$ , and that of the other is  $\lambda_0/2$ . The experiment consists of varying the length of the iris  $h$  and recording for each value the minimum position of the standing wave  $X_m$  for each of the two parallel plate sections used. The criterion for resonance is that iris length which yields

$$X_m\left(\frac{\lambda_0}{2}\right) - X_m\left(\frac{\lambda_0}{4}\right) = \frac{\lambda_0}{4}.$$

This method of determining the length of the resonant iris avoids the need of making assumptions concerning the proper geometrical plane,

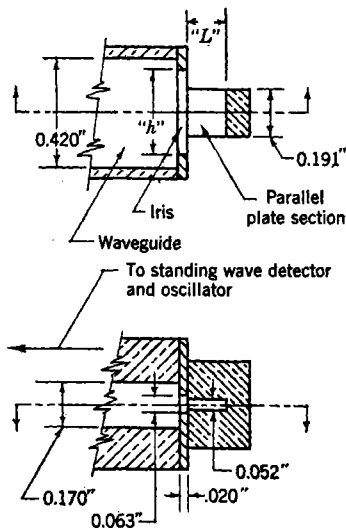


FIG. 11-25.—Experimental setup for the determination of the proper length  $h$  of a resonant iris.

in an iris of finite thickness, that would represent the electrical location of the junction between the cavity and the resonator.

At the guide end of the cavity a correction to the cavity length is required because of the equivalent shunt susceptance of the circular iris. In Vol. 10 is given the value of this susceptance for circular iris diaphragms of infinitesimal thickness. It can also be deduced for an iris of finite thickness from the measurement of the external  $Q$  of a half-wave cavity coupled to waveguide by such an iris. However, because of the ambiguity in the electrical reference plane, the knowledge of the shunt

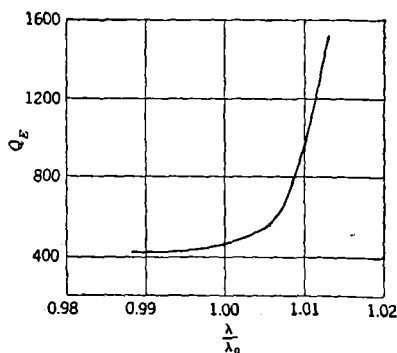


FIG. 11-26.—The observed dependence of the external  $Q$  on the resonant wavelength of the combination of anode block and stabilizing resonator.

susceptance is not quite sufficient to determine the end correction. The proper cavity length can be obtained experimentally by attaching the whole coupling unit, including the resonant iris, to an anode block of known resonant wavelength and observing the resonant wavelength of the entire combination as a function of cavity length.

The loading of the magnetron is controlled by the diameter of the circular iris, and the external  $Q$  is approximately proportional to the sixth power of the diameter. It is still easier to control the external  $Q$

with this type of coupling device, however, than it is with a quarter-wave transformer, particularly at short wavelengths.

The major disadvantage of the iris-type transformer is its frequency sensitivity. The observed dependence of  $Q_e$  on the resonant wavelength of the combination of anode block and stabilizing cavity is shown in Fig. 11-26 where the change in wavelength was obtained by changing the length of the cavity and keeping the anode-block resonance and dimensions of the two irises fixed. This curve indicates one reason why it is necessary to match the resonant frequency of the cavity to that of the block. The electronic efficiency of the magnetron is also affected by an appreciable mismatch of the resonant frequencies. This type of transformer is therefore not suited for use in a magnetron in which a tuning range of more than a few per cent is required. Neither is it advisable to use this coupling device with experimental magnetrons, because it may aggravate the problem of mode competition from resonances having wavelengths appreciably different from that of the  $\pi$ -mode. It should be introduced into a block design only after all disturbances to the proper magnetron operation due to other modes have been eliminated.

**11-15. Examples of Waveguide Output.**—A brief description of the important features of waveguide-output design will be given in this section for three output types that have found wide application in short-wavelength magnetrons.

*Output Design for High-power 1-cm Magnetrons.*—Figure 11-27 shows a waveguide output that is essentially the one used for the 1.25-cm 3J31 magnetron and for other tubes in this wavelength region. The

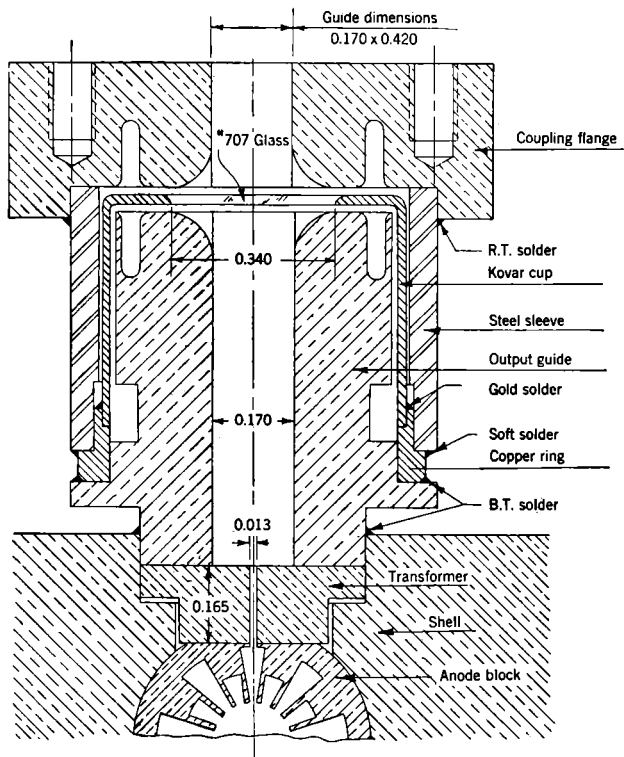


FIG. 11-27.—A typical waveguide output for 1.25-cm magnetrons.

chamfering of the guides at the window permits the transmission of pulsed powers up to 130 kw at atmospheric pressure. The transformer dimensions shown in the figure give an external  $Q$  of about 400 for the 3J31 tube. The required transformer dimensions for open-resonator anode blocks having more than 18 resonators are not appreciably different. Scaled versions of this design have been used in the high-power 3-cm rising-sun magnetron and in tubes of wavelengths less than 1.0 cm.

*Output with H-section Transformer.*—This output, shown in Fig. 11-28, has been used in the 16-resonator, strapped, high-power 3-cm magnetron,

the 4J50. The dimensions given in the drawing are appropriate for an external  $Q$  of about 350. The window design is similar to that of Fig. 11-27, except that the guides have not been chamfered.

**Stabilized Iris Output.**—Figure 11-29 shows the important dimensions of the half-wavelength stabilized cavity and the two irises for the stabilized iris output used in the 1.25-cm, 18-vane, rising-sun 3J21 magnetron. The window end of the output guide is almost identical with that of Fig. 11-27. The dimensions of the circular iris are appropriate to an external  $Q$  of about 550. As a result of the stabilizing cavity the  $Q_0$  value of this tube is about 1.6 as great as that of a magnetron having the same anode block but a simple rectangular-guide transformer.

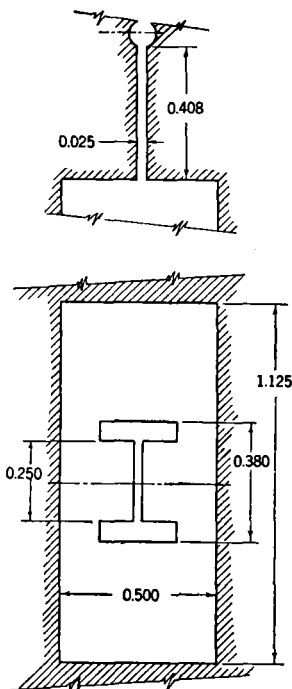


FIG. 11-28.—The H-section transformer used in the 3.2-cm 4J50 magnetron.

#### 11-16. End-space Geometry. *Disturbances Produced by End-space Resonances.*—

In designing a magnetron anode block attention may have to be given to the end regions surrounding the resonators. The dimensions of the end spaces have not been taken into account in the design of the essential resonator dimensions, partly because of the general difficulty of handling end effects and partly because in most cases the magnetron mode spectrum is not appreciably affected in a manner that would interfere with  $\pi$ -mode operation. The effects on the wavelength and on the mode separation that are produced by changes in the end spaces can usually be compensated for by relatively small changes in

some parameter of the resonant system. The end regions are frequently not “designed,” therefore, but simply assume a geometry that is dictated mainly by mechanical considerations after the requirements of the more essential tube parameters such as block height, pole gap, and output transformer have been satisfied. Such a procedure does not always lead to a good magnetron design. Tube resonances other than those associated with the normal magnetron modes may couple to the electrons in the interaction space at the same voltage and field values as the  $\pi$ -mode, thus offering considerable disturbance to the operation of the magnetron. For such oscillations, the end spaces store a considerable fraction of the r-f energy and therefore determine the wavelength of the disturbing



resonances and the conditions for maximum interference with normal magnetron behavior.

Although the following discussion on the need of end-space design is based principally on the experience gained with rising-sun magnetrons, it is not to be inferred that magnetrons having strapped blocks are necessarily free from end-space disturbances. The difference in size between the large resonators of the rising-sun block and the small

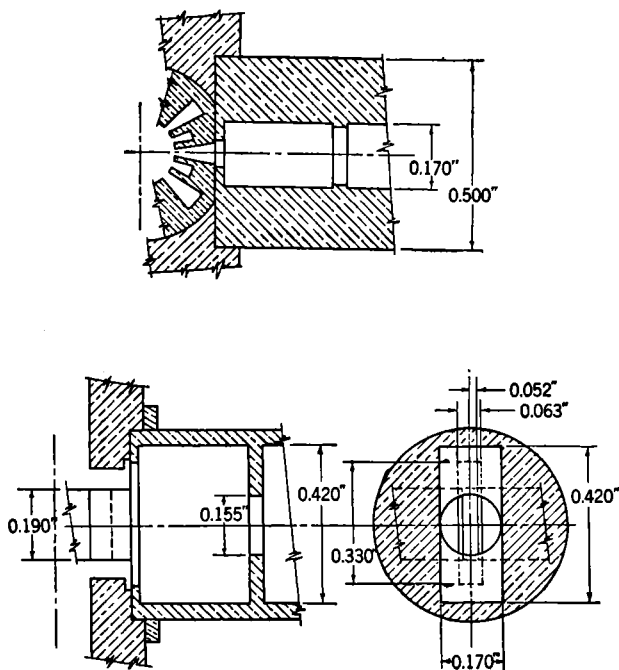


FIG. 11-29.—The stabilized iris output of the 1.25-cm, 18-vane, rising-sun 3J31 magnetron.

resonators associated with strapped blocks of the same wavelength makes it more probable that smaller end spaces will be found in strapped tubes. It is this circumstance, as well as the fact that the wavelengths of the competing end-space resonances are large, which makes end-space disturbance less likely for strapped tubes than for rising-sun magnetrons.

A good example of the effect of end-space geometry on magnetron performance can be found by comparing the performance at a given magnetic field for two 18-vane open-resonator rising-sun magnetrons differing only in the geometry of the end-spaces. Longitudinal sections of the blocks and end regions of these tubes are shown in Fig. 11-30a and b. Voltage-current plots at 7900 gauss are given for these tubes

in Fig. 11-31*a* and *b*; the operating efficiencies at the same field are plotted as a function of anode current. It is shown that the dynamic impedance  $dV/dI$  is much greater in the low-current region for the tube

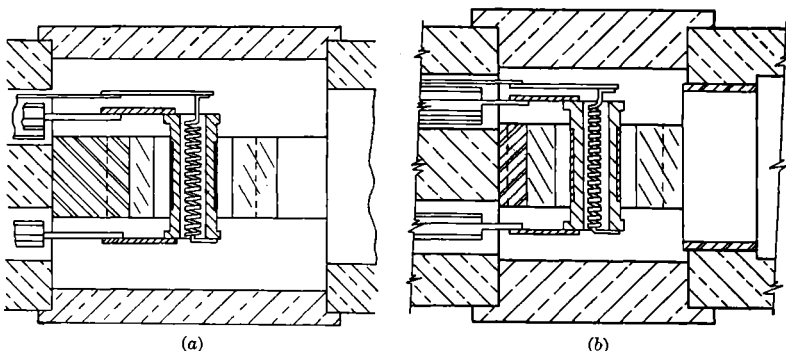


FIG. 11-30*a*.—Rising-sun magnetron with large end spaces.  
FIG. 11-30*b*.—Rising-sun magnetron with small end races.

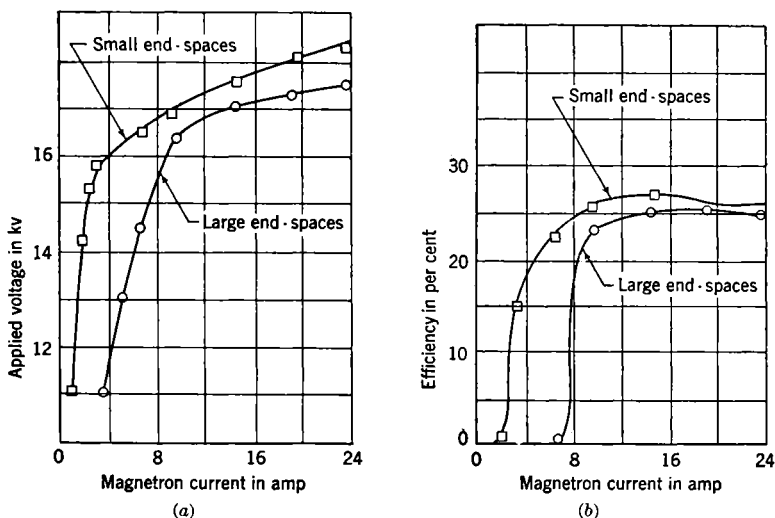


FIG. 11-31.—A comparison of the operating characteristics at 7900 gauss of the magnetrons of Fig. 11-30*a* and *b*. (a) Voltage-current characteristics; (b) efficiency as a function of anode current.

with the larger end spaces. Moreover, the operating efficiencies measured at the output guide are practically zero for this tube up to 7 amp. This is in marked contrast to the performance of the tube with the smaller end-spaces. From a study<sup>1</sup> of the long-wavelength resonances that are

<sup>1</sup> A. Ashkin and S. Millman, "Dynamic Impedance of A-type Magnetrons," NDRC 14-266, Mar. 1944, p. 1.

observed at low currents near the cathode leads and are accompanied by abnormal overheating of the cathode, it was conclusively established that these differences in performance were not due to leakage or emission from the cathode end shields but rather were consistent with the assumption that the end-space oscillations could be characterized by a predominantly radial electric field in the interaction space and r-f currents in the end-space regions, as sketched in Fig. 11-32. The low-current disturbances to magnetron operation that arise from end-space resonances can be eliminated by decreasing the diameter of the end-space cylinder. No end-space disturbances are observed with open-resonator rising-sun blocks when the difference between the diameter of the shell and that of the large resonators is kept small ( $< 0.16\lambda$ ). For closed-end systems the end-space problem is automatically solved when an axial mount is

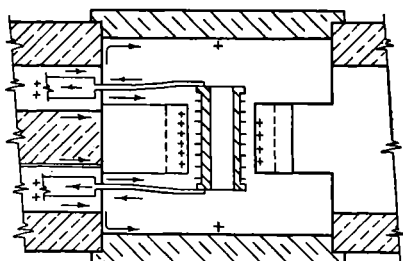


FIG. 11-32.—Possible charge and current distributions for end-space oscillations.

used for the cathode and when the pole pieces are in contact with the block covers.

*Leakage of  $\pi$ -mode Radiation at End Regions.*—The end spaces may further affect magnetron operation adversely either by absorbing  $\pi$ -mode r-f power or by transmitting it to the exterior of the magnetron. Both of these effects are characterized by abnormally low  $Q_0$  values for the anode block; and if the r-f power is transmitted to the exterior, a considerable amount of r-f power will be observed at the cathode supports. These energy "sinks" are objectionable not only because they decrease the output efficiency but also because the extraneous losses are likely to be variable, particularly for short-wavelength experimental tubes in which the end spaces are not always readily reproducible.

The manner in which the r-f energy couples to the end spaces is different for strapped and rising-sun magnetrons. In the former case the coupling arises from the fact that the two inside straps are usually connected to alternate fins and are therefore oppositely charged. As the induced charges on the cathode produced by these straps are greater than those arising from the more distant outer straps, a net induced dipole on the cathode results. A radial electric field with a voltage node

in the central plane is then produced in the interaction space. The power that is radiated through the cathode in this manner will depend, of course, on other parts of the transmitting circuit, which may include the end spaces, and transmission by means of the lowest coaxial mode through the cathode leads is possible. In the rising-sun design there is no comparable coupling action between anode block and cathode. When the cathode is accurately centered in the tube, the only coupling mechanism is by means of the zero component of a  $TE_{01}$ -mode in which the electric field possesses only an  $E_z$  component, and large holes in the pole pieces or in the pipes surrounding the cathode supports would therefore be required to transmit the radiation. When the cathode is off center, the zero mode at the cathode may have an admixture of a  $TE_{11}$ -mode, and the transmission of power in this mode requires considerably smaller holes in the pole pieces. The conditions under which r-f leakage has been observed at the cathode supports in rising-sun magnetrons corroborate this analysis; practically no r-f leakage is observed when the hole sizes are small enough to cut off all but the principal coaxial mode of transmission.

When the cause of the r-f leakage has been determined, it is generally not difficult to eliminate the spurious losses. In general, it is preferable to decrease the volume of the end spaces. If the geometry of the end spaces provides a resonating chamber for the  $\pi$ -mode, a small change will shift their resonant wavelength to a harmless region. If the losses are a result of transmission through the cathode leads, however, the leakage may be greatly reduced by introducing an r-f choke in the coaxial line in which the inner conductor forms the cathode support.

## CHAPTER 12

### THE CATHODE

By J. G. BUCK AND A. M. CLOGSTON

#### EMISSION PHENOMENA OF MAGNETRON CATHODES

By J. G. BUCK

**12-1. Characteristics of Cathodes under Pulsed Conditions.**—The electronics of the magnetron involves considerations not only of the space charge but also of the complex orbits of electrons moving under the influence of static and oscillating electric and magnetic fields. In the oscillating magnetron the cathode is back-bombarded with a considerable number of high-energy electrons, and consequently secondary electrons are ejected from the cathode into the interaction space. By such repeated interactions of electrons with the cathode surface it has been possible, in some cases, to obtain many times more total anode current from a cathode than could be supplied by the primary thermionic emission alone.

In the past, oxide cathodes operated normally at direct currents of approximately  $0.1 \text{ amp/cm}^2$ . At present, however, for duty ratios up to several tenths of 1 per cent, cathodes of pulsed microwave magnetrons are required to supply pulse currents of magnitudes varying from about  $10 \text{ amp/cm}^2$  at 10-cm wavelengths to  $100 \text{ amp-cm}^2$  for 1-cm tubes. Cathodes that can fulfill these requirements might be classified as (1) efficient pulsed thermionic emitters, (2) inefficient thermionic emitters that can be run hot enough to give the required pulsed currents, or (3) good secondary emitters that will give enough electrons to build up the required current density under back bombardment. The ideal cathode would be of Class 1 because it would impose fewer restrictions on tube design and the associated electrical equipment; the cathodes that can now be made in production magnetrons are not ideal, however, and are workable only because they have desirable features from Classes 2 and 3. For instance, investigations at the Bartol Research Foundation have shown that even a relatively inactive alkaline-earth oxide cathode will give at least five secondary electrons per primary electron at operating temperatures.<sup>1</sup>

Prominent limitations that depend upon cathode emission properties

<sup>1</sup> M. A. Pomerantz and D. L. Goldwater, "Secondary Electron Emission from Oxide-coated Magnetron Cathodes," NDRC-14310.

exist in magnetron performance even after the geometrical design problems on a tube have been finished. These limitations may be classified as two types of instabilities in performance: (1) frequency instabilities, such as mode changes and poor spectra, and (2) sparking. In some cases the limitations in magnetron performance, which under fixed testing conditions are manifested by high-current mode changes, current limits for a good spectra, or other types of frequency instability, are dependent upon the primary thermionic emission that is available from the cathode during the buildup of oscillations. The magnitude of this primary emission is essentially that value of current which is available from the cathode with zero electric-field gradient at its outer surface. For a given magnetron under fixed oscillation conditions, there is evidence that a minimum value of primary thermionic emission exists below which stable operation cannot be expected at the chosen operating point. For tube types having alkaline-earth oxide cathodes, this primary-emission minimum need be only a small fraction of the pulse current required for operation. This may be shown by comparing the primary current available without magnetic field with the current available during oscillation. For example, in the low-voltage 10-cm 2J39 magnetron the fraction may be as high as one-sixth at an operating point of 5 kv, 5 amp, at 0.1 per cent duty ratio and may be as low as one-hundredth in the medium-power 3-cm 725A magnetron at an operating point of 11 kv, 15 amp, at 0.1 per cent duty ratio. Presumably, this fraction is influenced by (1) the secondary-electron-emission properties of the cathode, (2) the operating voltage, (3) the effective rate of rise of the voltage pulse, and (4) the details of the design and loading of the tube.

Current instabilities in magnetrons, i.e., sparking, arcing, or flashing, have appeared as limitations in the performance of nearly every design of pulsed microwave magnetrons. Although considerable progress has been made in the elimination of these instabilities, they still remain a major problem in magnetrons operating at high power levels, long pulse durations, or continuous wave. Because most pulsed microwave magnetrons have used alkaline-earth oxide cathodes, the majority of the investigations on cathode sparking was devoted to this type of emitter. A detailed discussion of the fundamental sparking properties of alkaline-earth oxide cathodes is given in the next section. It is probable that sparking in high-vacuum tubes is caused by more than one abrupt breakdown mechanism; for although the role of the cathode in sparking was the first source of trouble to be located, attention has recently been directed to processes occurring at the anode and other parts of the tube.<sup>1</sup>

<sup>1</sup> W. E. Ramsey, "A General Survey of Sparking Phenomena in High Vacuum Thermionic Tubes," NDRC 14-516.

The choice of the type of electron emitter suitable for the conditions existing in a given magnetron depends on many factors besides the primary and secondary electron-emission of the cathode, but an appreciation of these fundamental emission properties is essential. The following sections will describe some of the properties of alkaline-earth oxides, thorium oxide, and such secondary-emission surfaces as silver magnesium and Dowmetal.

**12-2. Alkaline-earth Oxide Cathodes.** *Test Methods.*—From the standpoint of physical-chemical theory the oxide-cathode emitter is a very complex system, and it is, therefore, doubtful that the optimum preparation and processing have ever been achieved. However, a cathode that emits satisfactorily according to usual expectations may be obtained by many variations in preparation techniques. The oxide cathode is commonly prepared by coating a base-metal structure with a definite weight of alkaline-earth carbonates.<sup>1</sup> The cathode is heated in vacuum to convert the carbonate coating to oxide and then is activated by passing current through it.

Several forms of the alkaline-earth oxide cathode have been used in pulsed magnetrons: plain uncombined oxide, uncombined screen, metalized, "overwound," nickel "mesh," and sintered nickel.<sup>2</sup> Because the basic structure is the plain, uncombined oxide cathode, the discussion of fundamental properties will be restricted to this type. The procedure for testing the thermionic activity of cathodes in diode structures consists fundamentally in obtaining characteristics of plate current  $I$  vs. plate voltage  $V$  at a fixed temperature and interpreting these data by the use of the Langmuir-Child's law which may be written in the form

$$I^{3/2} = K^{3/2}V; \quad (1)$$

this equation expresses the current  $I$  and voltage  $V$  relation in a diode when the current is limited by space charge.

Pulse methods of testing cathodes have been developed. These tests are taken with pulses of short duration and low recurrence frequency, in order to eliminate the rise in temperature that occurs when cathodes are pulsed at high-duty ratios and to reduce the chances of destroying the cathode surface by sparking.

For the measurement of the  $(V, I)$ -curves of both simple cylindrical test diodes and magnetrons without magnetic field, the voltage is applied to the anode as a series of negative pulses (see Fig. 12-1). The fundamental emission tests are taken at 1  $\mu$ sec 60 PRF, but pulses of  $\frac{1}{2}$  to

<sup>1</sup> In this chapter "double carbonates" will refer to a 50-50 molar solid solution of barium and strontium carbonates.

<sup>2</sup> E. A. Coomes, J. G. Buck, A. S. Eisenstein, and A. Fineman, RL Report No. 933, June 1946.

10- $\mu$ sec duration at pulse recurrence frequencies from 60 to 4000 have also been found useful. The voltage pulses are obtained from a hard-tube laboratory pulser that has been provided with a special 60-PRF trigger circuit.<sup>1</sup> The pulse voltage is measured with a noninductive resistance divider or capacity divider and viewed on a synchroscope. The pulse current, also viewed on the synchroscope, is observed as the voltage drop across a noninductive resistance in series with the tube under measurement. The cathode is set at the desired temperature, and the pulse voltage across the tube is increased until the cathode just begins to "spark." The term "sparking" refers to that cathode limitation which is characterized by

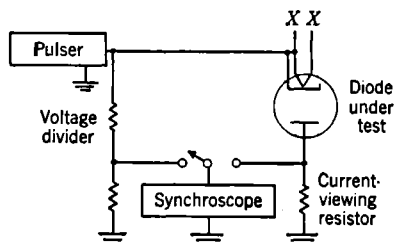


FIG. 12-1.—Arrangement of test equipment for the measurement of pulse current and voltage.

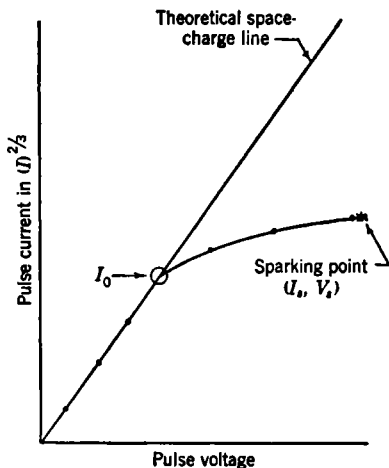


FIG. 12-2.—Diode curve of an oxide cathode showing the normal Schottky emission effect.

the physical transfer of incandescent particles of oxide coating from the cathode sleeve to the anode.

The most convenient manner to present pulse-emission data in diodes is by plotting of  $I^{2/3}$  vs.  $V$ . A computation of  $K^{2/3}$  can be made from tube geometry, and a theoretical space-charge line drawn to satisfy the Langmuir-Child's equation. A cathode can then be classified by the manner in which emission data follow or deviate from the theoretical space-charge line.

The results of testing a considerable number of diodes in the manner outlined above indicate that the cathode-emission curves are characterized by several different types of behavior. Two of these may be considered prime types.

1. The normal Schottky effect is shown in Fig. 12-2. The experimental points follow the theoretical Langmuir line up to a current value represented by  $I_0$  (corresponding to the maximum space-

<sup>1</sup> See Vol. 5 of the Radiation Laboratory Series for a discussion of pulse equipment and pulse test methods.



charge-limited emission). Experimental points from  $I_0$  up to the sparking point ( $I_s, V_s$ ) can be plotted to the form of the Schottky emission equation, but the slope is usually described as corresponding to a fictitious temperature considerably different from the true cathode temperature.

2. The anomalous Schottky effect is shown in Fig. 12-3. This type of emission curve exhibits the same characteristics as Fig. 12-2 at the beginning of the curve but has an inflection point followed by a region in which the emission increases rapidly with voltage. From correlations between nonoscillating- and oscillating-magnetron characteristics it appears that the location of the inflection point and the slope of the anomalous Schottky characteristic are of considerable importance in cathode sparking in microwave magnetrons. No completely satisfactory theory exists for fitting the curve in this region; however, it is possible that the anomalous Schottky effect may be associated with properties of the interface between the oxide coating and the base metal. This type of behavior is generally to be expected at some time in the life of the double carbonate oxide cathode.

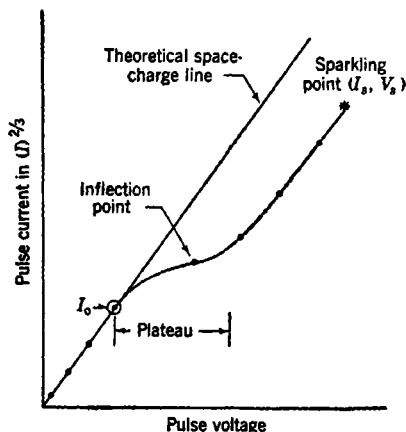


FIG. 12-3.—Diode curve of an oxide cathode showing the anomalous Schottky emission effect.

Other types of deviations from the space-charge line have been observed and will be considered in connection with applications. Small amounts of gas are often evidenced by large and random fluctuations in experimental curves, and larger amounts generally produce systematically increasing deviations above the space-charge line. Cathodes that have been poisoned during preparation have had, in a number of instances, emission curves that indicated that the current was not limited by space charge at any voltage but showed slight deviations below the theoretical space-charge line even down to zero voltage. Figure 12-4 is an example of this phenomenon.

The useful terms defined in Figs. 12-2 and 12-3 may be summarized as follows:

1. The maximum space-charge-limited emission  $I_0$  which is taken as the point on the plot of  $I^{2/3}$  vs.  $V$  at which the experimental points first deviate from the theoretical space-charge line.
2. The type of behavior above  $I_0$  (the Schottky region) corresponding to one of two types: (a) the normal Schottky effect, in which

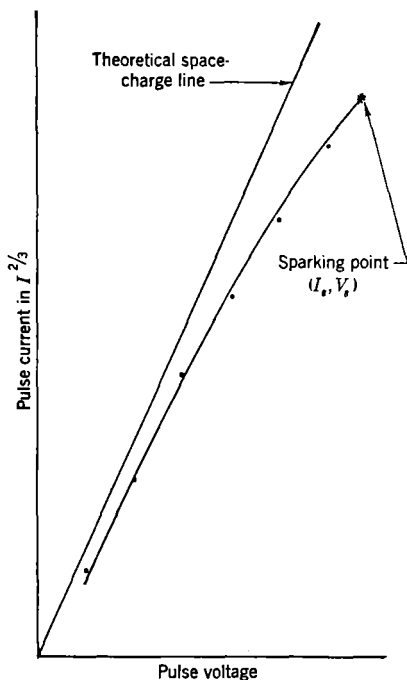


FIG. 12-4.—Diode curve of an oxide cathode showing gradual deviations of the pulsed emission from the space-charge line.

the experimental points follow the form of the Schottky emission law, and (b) the anomalous Schottky effect in which the  $(I^{2/3}, V)$ -curve has an inflection point in the Schottky region.

3. The sparking current and voltage ( $I_s, V_s$ ) which are the diode values at which cathode emission is limited by sparking.

**12-3. Alkaline-earth Oxide Cathodes.** *Life Tests and Sparking Phenomena.*—Diode life tests at 800°, 875°, and 950°C have shown that in this temperature region the expected life at fixed operating conditions is markedly dependent on temperature; the higher the temperature the lower the pulse life. The expected life of a double-carbonate coating on Grade A nickel under the test condition of 1  $\mu$ sec, 400 PRF, and 10 amp/cm<sup>2</sup> is illustrated in Fig. 12-5.

In Fig. 12-6 the sparking current is plotted against life for electrolytic-nickel base metal and compared with that for Grade A nickel base metal; standard double-carbonate coating was used in both cases. It is seen that the same general pattern is followed in both cases but that the pure nickel curve lies above that of the Grade A.

It has been recognized previously<sup>1</sup> that there are probably two types of sparking encountered when high pulse currents are demanded from oxide cathodes. Differentiation between these two types of sparking may be made in the following manner:

<sup>1</sup> O. H. Shade, *Proc. IRE*, **7**, 341 (1943).

1. Space-charge-limited sparking, in which the sparking current has a value  $I_s = I_{s0}$  on the space-charge line. The value of  $I_{s0}$

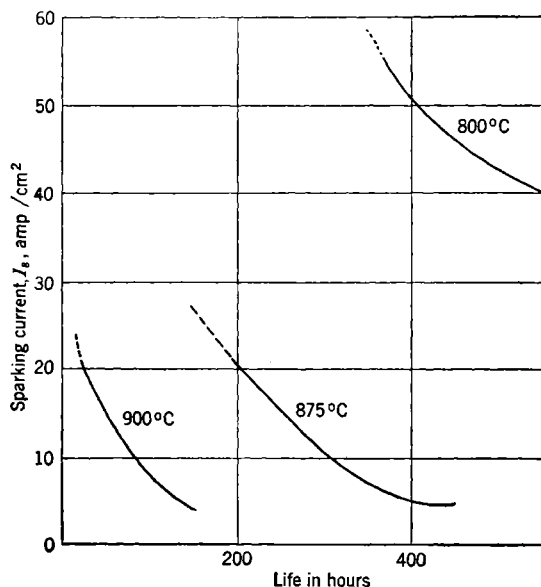


FIG. 12-5.—The expected life, at three different temperatures, of a double-carbonate coating on Grade A nickel. Test conditions: 1  $\mu$ sec; 400 PRF; 10 amp/cm².

measured at 1  $\mu$ sec and 60 PRF is about 50 amp/cm² at 800°C for double-carbonate coating on Grade A nickel and is about 100 amp/cm² for double carbonate on pure nickel. Substitution of triple carbonate containing 4 or 11 per cent of  $\text{CaCO}_3$  does not appreciably change these values.

2. Field-limited sparking that occurs late in the life of an oxide cathode, in which the sparking is limited by a critical value of field corresponding to  $V_s = F_{sf}$ . The value of  $F_{sf}$  has been found experimentally to depend in a fundamental manner

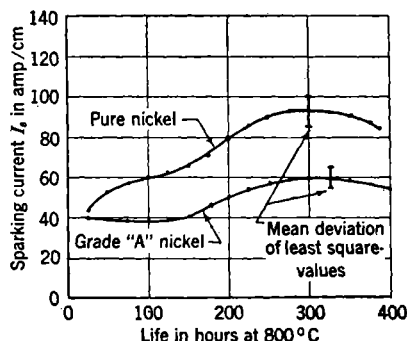


FIG. 12-6.—Sparking currents under pulse conditions as functions of life for pure nickel and Grade A nickel cathodes.

upon the nature of the oxide at the cathode surface. Its experimental value lies between 40 to 60 kv/cm for cathodes prepared

with  $\text{SrCO}_3$  or  $\text{BaSr}(\text{CO}_3)_2$  and in the range 100 to 125 kv/cm for single  $\text{BaCO}_3$  cathodes.

The transition from Type 1 to Type 2, as life progresses, is shown in Fig. 12-7 for double-carbonate coating on Grade A nickel.

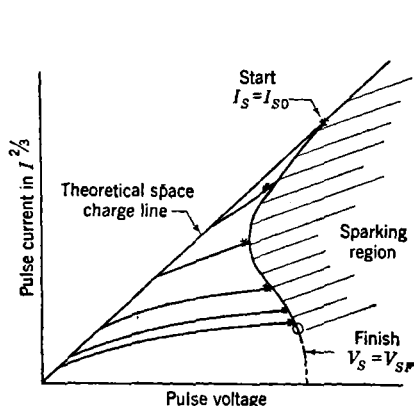


FIG. 12-7.—Transition from space-charge-limited sparking to field-limited sparking during the life of oxide-coated cathodes.

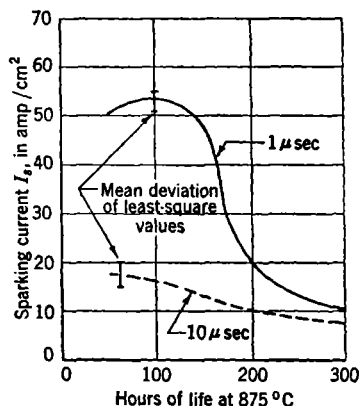


FIG. 12-8.—Dependence of sparking current on the pulse length during the life of an oxide-coated cathode.

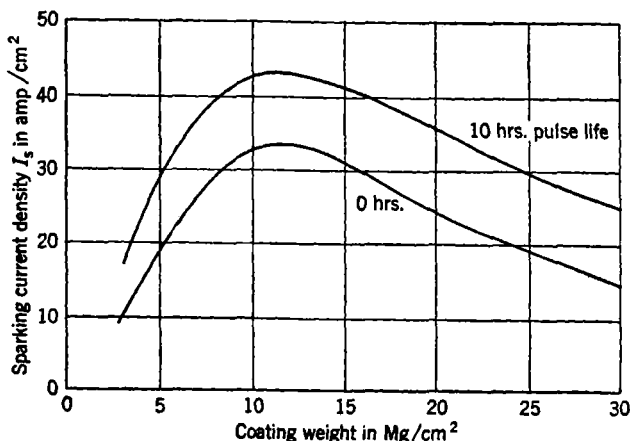


FIG. 12-9.—Sparking-current density under pulsed conditions as a function of coating weight on Grade A nickel at 875°C.

The dependence of sparking current on pulse length, which is marked early in the life of a cathode before the field-limited state sets in, disappears when the cathode sparking becomes entirely field limited. This condition is shown by Fig. 12-8, which gives a comparison of the sparking current at 1 and at 10  $\mu\text{sec}$  as a function of life. The cathodes consisted of double-carbonate coating on Grade A nickel.

*Emission Dependence on Cathode Coating.*—Proper choice of coating weight and density is important in obtaining the optimum pulse emission to which an oxide cathode can be activated. Figure 12-9 shows the pulsed sparking current in amperes per square centimeter as a function of coating weight available for plain oxide cathodes of density about  $\text{gm/cm}^3$ , prepared with double carbonates on Grade A nickel for fixed processing conditions. These curves display a range of optimum weights of approximately 9 to 13  $\text{mg/cm}^2$ . Experience has also indicated that cathodes prepared with higher-density coatings are better pulse emitters when processed to optimum.

Published reports of correlations between carbonate particle size and emission<sup>1</sup> have suggested the advisability of maintaining rigid controls of the particle-size distribution of the cathode coating. It has been shown by Eisenstein,<sup>2</sup> however, that no correlation exists between the size of the carbonate particles and crystals and the size of the oxide crystals because

1. Both the crystal and particle sizes of the carbonates begin to increase at about 500°C and approach an equilibrium of values that depend primarily on the time and temperature of treatment.
2. A similar crystal growth in the oxide occurs rapidly about 950°C, dependent primarily on the maximum temperature and bearing no relationship to the crystal or particle size of the carbonate from which it was formed. It therefore appears that the correlation between carbonate particle size and emission is not due to a direct interrelation of these two factors. The cathode-coating texture may be affected by the carbonate-particle-size distribution under a fixed set of spraying conditions. This resultant texture coupled with a fixed processing schedule could then influence the final emission obtainable from the cathode.

*Emission Dependence on Cathode Base Metal.*—The following base metals were studied for pulse emission:

1. The purest available nickel.
2. Grade A nickel.
3. Nickels alloyed with large amounts of the elements commonly found in Grade A nickel.

Well-activated cathodes with base metals of the purest nickels, such as the electrolytic nickel obtainable from the International Nickel Company

<sup>1</sup> M. Benjamin, R. J. Huck, and R. O. Jenkins, *Proc. Phys. Soc.*, **50**, 345 (1938); R. C. Chirnside and H. P. Rooksby, General Electric Limited Report No. 8355, December 1943; A. S. Eisenstein, "A Study of Oxide Cathodes by X-ray Diffraction Methods, Part I," *Jour. Applied Phys.*, June 1946.

<sup>2</sup> Eisenstein, *op. cit.*

or Driver Harris No. 499, give sparking currents of  $90 \pm 10$  amp/cm<sup>2</sup> for periods of several hundred hours when operated at 800°C. The corresponding figure for electronic Grade A nickel was  $50 \pm 10$  amp/cm<sup>2</sup>. The emission efficiency in terms of pulse amperes per watt was 18 for the pure nickel cathodes as compared with about 10 for the Grade A nickel cathodes.

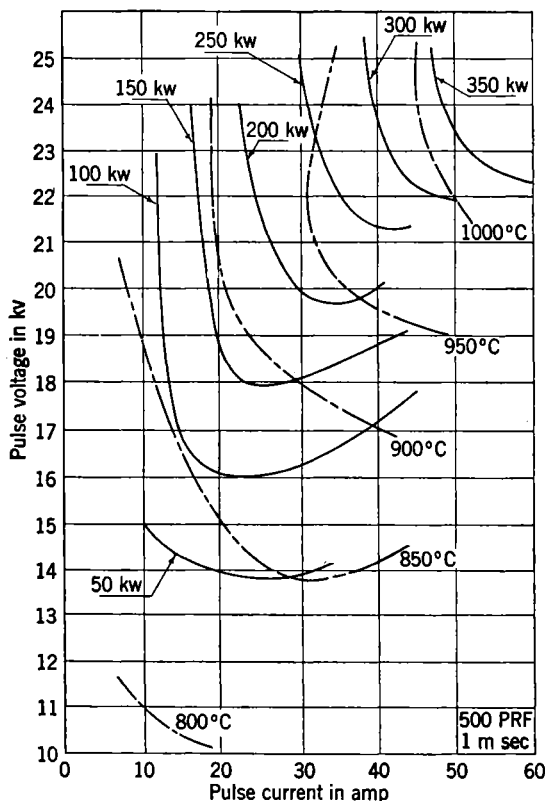


FIG. 12-10.—The variation of cathode temperature over the performance chart of a 10.7-cm magnetron operating at constant load. (Courtesy of C. S. Robinson, Jr.)

Cathodes composed of double carbonates on nickel alloys containing 5 per cent of Al, Si, Mn, or Ti had pulsed lives and sparking currents less than those obtained for Grade A nickel at an operating temperature of 875°C. A 5 per cent Cr alloy, however, showed an improvement over Grade A nickel and produced results equal to the high values obtained from the pure nickels.

*Pulse Temperature Rise and Coating Resistance.*—When the temperature of an oxide cathode is measured in a magnetron oscillating at

constant load over its  $(V, I)$ -performance chart, it is found that the temperature may increase several hundred degrees above its value at zero cur-

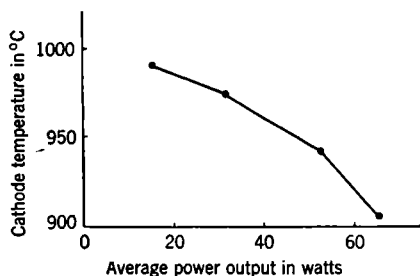


FIG. 12-11.—The effect of loading on the cathode temperature. The data were taken on a 9.1-cm strapped magnetron at 1000 PRF and 1- $\mu$ -sec pulse duration. (Courtesy of C. S. Robinson, Jr.)

rent.<sup>1</sup> Figure 12-10 illustrates the order of magnitude of the effect. The cathode temperature is also changed with varying values of magnetron load as shown in Fig. 12-11.

Part of this temperature increase is caused by an increase in back bombardment. However, the cathode temperature will increase with pulse current even if the magnetron is operated as a diode. The magnitude of this increase in temperature, the pulse temperature rise (PTR), is a function of the pulse current, the duty ratio, the initial quiescent operating temperature, and the physical state of the cathode. The PTR varies with the cathode construction and from cathode to cathode of the same type; it also varies throughout the life of a given cathode. The average PTR measured in diodes for a number of double-carbonate cathodes of the plain uncombined oxide, the uncombined screen, and the metallized, screen cathode types are given as a function of life in Fig. 12-12.

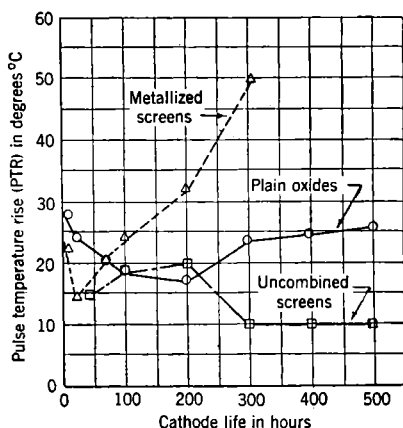


FIG. 12-12.—Pulse temperature rise (PTR) as a function of cathode life. The PTR was measured at 10 amp/cm<sup>2</sup>, 1- $\mu$ -sec pulse duration, and 1000 PRF from a quiescent temperature of 850°C. During life testing, the tube was operated at 10 amp/cm<sup>2</sup>, 1- $\mu$ -sec pulse duration, and 400 PRF and 875°C.

The PTR of a cathode in a diode is apparently due to the  $I^2R$  dissipation within the cathode when the pulse current  $I$  flows through the oxide

<sup>1</sup> C. S. Robinson Jr., "Cathode Temperatures in Magnetrons," RL Report No. 11-5S. Mar. 31, 1942.

coating. Values for the total coating resistance  $R$ , measured either by a calorimetric method<sup>1</sup> or by probes embedded in the cathode coating,<sup>2</sup> have been found to be a function of the pulse current and to have characteristics typical of a blocking-layer rectifier system.

*Screen Cathodes.*—The need for cathodes of longer life in the strapped 3-cm medium-power magnetrons resulted in the development of the screen cathode. This cathode is made by firmly bonding nickel mesh to a supporting nickel sleeve and impregnating the interstices of the mesh with the cathode coating. Experience has shown that in order to obtain a good cathode of high primary emission with normal Schottky emission characteristics, it is necessary first to bond the nickel mesh to the underlying metal at as many points of contact as possible. This contact is important for obtaining good thermal and electrical conductivity and is accomplished either by welding the mesh at close intervals or by sintering in a hydrogen furnace. Second, it is important that the carbonate coating make good contact with all the exposed area of the nickel mesh and the substrate nickel and that it be firmly packed to prevent all voids (see Sec. 17-7). In the 3-cm 725A and the 10-cm 4J32 and HP10V the screen cathode showed decided advantages over the plain oxide cathode in extending tube life, improving the stability of operation, and increasing output power.

Early life test studies on screen cathodes in magnetrons were made with mesh sizes up to 60 by 60, and the longest lives were obtained with the finest mesh. Further life tests on screen cathodes with 150-by-150 mesh showed that the normal Schottky emission characteristic extended to higher sparking voltages and that the sparking currents for 10- $\mu$ sec pulses were higher. The use of this fine-mesh cathode in low-voltage 3-cm magnetrons resulted in increased mode stability, less sparking, and longer tube life.

*Direct-current Emission Values.*—At a temperature of 800°C, cathodes made of double carbonates on Grade A nickel have operated at 1 amp/cm<sup>2</sup> direct current for over 1000 hr under space-charge-limited conditions. Preliminary tests have shown d-c emissions of 10 amp/cm<sup>2</sup> under space-charge-limited conditions at 850°C for several hours. These results indicated that cathode poisoning by structures external to the cathode may be an important factor in limiting the d-c emission from oxide cathodes.

It is difficult, if at all possible, to correlate the pulsed and d-c emission properties of oxide cathodes. About all that can be stated at the present time is that good pulsed cathodes are usually good d-c cathodes but that the reverse is by no means true.

<sup>1</sup> E. A. Coomes, *Jour. Applied Phys.*, July 1946.

<sup>2</sup> A. Fineman and A. S. Eisenstein, *Jour. Applied Phys.*, July 1946.



**12-4. Thorium Oxide Cathodes.**—A type of thorium oxide cathode suitable for use in magnetrons has been developed by the Bartol Research Foundation.<sup>1</sup> The cathode, which consists of a shell of sintered thorium oxide, is prepared by compressing thoria powder in a die and heating to a high temperature in a specially prepared furnace; a coil of fine heater wire is embedded in the thoria. Cathode shapes of any desired form may be made in this manner. The fundamental problems concerned with thorium oxide cathodes are still incompletely solved, but this progress has excited considerable interest in the possibilities of applications in magnetrons for high-pulse powers, long-pulse durations, and high-duty ratios.

Studies of thoria cathodes in test diodes have indicated that the elaborate activation schedules which are generally used with alkaline-earth oxides can be dispensed with. Thoria cathodes of small area are simply raised to their emitting temperatures for a few minutes and then operated immediately. The activation of large-area cathodes (about 7 cm<sup>2</sup>) in high-power magnetrons may be somewhat more difficult to accomplish (as is also the case with alkaline-earth oxide cathodes); there are, however, good indications that the thorium oxide cathode is much less sensitive to those conditions existing in a tube which ordinarily cause deactivation of emission surfaces. Cathode sparking of the type discussed in Sec. 12-2 for alkaline-earth oxides appears to be completely absent in thoria cathodes.<sup>2</sup> The thoria cathode would thus be of considerable importance for magnetrons operated at high-pulse powers or long-pulse durations.

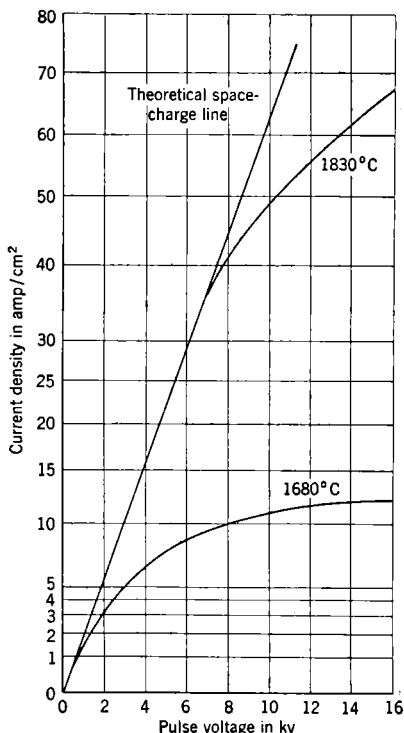


FIG. 12-13.—Pulsed thermionic emission of a sintered thorium oxide. Test conditions: 1  $\mu$ sec and 1000 PRF. (Courtesy of M. A. Pomerantz.)

<sup>1</sup> M. A. Pomerantz, "Sintered Thoria Cathodes," NDRC 14-517.

<sup>2</sup> W. E. Ramsey, "A General Survey of Sparking Phenomena in High Vacuum Thermionic Tubes," NDRC 14-516.

Typical diode ( $V, I$ )-curves obtained for thorium oxide are given in Fig. 12-13. The cathode temperatures given on the figure are brightness temperatures obtained by an optical pyrometer. The emission efficiencies of thorium cathodes in terms of amperes per watt are about 0.4 at 1580°C and 0.7 at 1740°C.

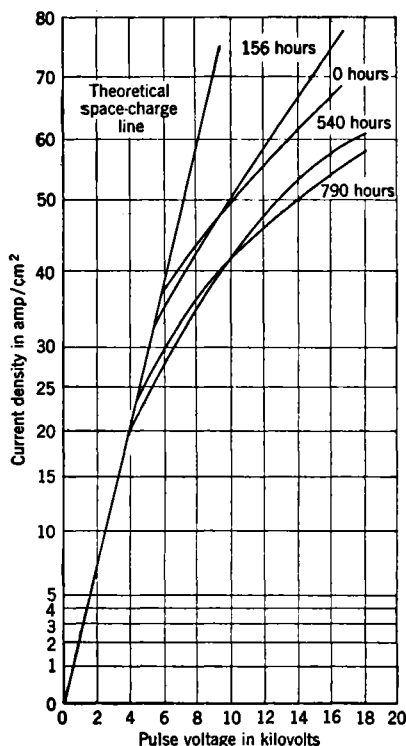


FIG. 12-14.—Pulsed-thermionic emission of a sintered thorium oxide cathode at different intervals of life. (Courtesy of M. A. Pomerantz.)

Test conditions	Life test conditions
1 $\mu$ sec	0.9 $\mu$ sec
1000 PRF	400 PRF
1800°C	1650°C
	15 amp/cm <sup>2</sup>

The thermionic emission from sintered thorium oxide cathodes was observed with pulses varying from less than a microsecond to several milliseconds. At a current level of 30 amp/cm<sup>2</sup> no decay in the pulse emission was found during this interval. Furthermore, in the temperature range in which it was possible to measure both the pulsed and d-c emission, the diode ( $I, V$ )-characteristics obtained for pulse and d-c operation agreed quite closely. From these data it would appear that the emission in respect to time effects differs fundamentally from that observed in alkaline-earth oxide cathodes.<sup>1</sup>

Figure 12-14 illustrates the type of diode ( $I, V$ )-curves that have been obtained with sintered thorium oxide cathodes at different intervals of life. It is seen that at the end of 800 hr, the maximum space-charge-limited emission has decreased to approximately a third of its initial value but that the total emission has decreased only slightly.

Figure 12-14 illustrates the type of diode ( $I, V$ )-curves that have been obtained with sintered thorium oxide cathodes at different intervals of life. It is seen that at the end of 800 hr, the maximum space-charge-limited emission has decreased to approximately a third of its initial value but that the total emission has decreased only slightly.

Cathodes have also been operated at 1.5 and 2 amp/cm<sup>2</sup> direct current for periods of 400 hr. Emission densities exceeding 5 amp/cm<sup>2</sup> direct current were obtained for short intervals of time and in the experiments performed were limited by factors involving the allowable anode dissipation rather than the emission capabilities of the cathode.

<sup>1</sup> E. A. Coomes, *Jour. Applied Phys.*, July 1946; R. L. Sproull, *Phys. Rev.*, **67**, 166, (1945).

**12-5. Secondary Electron-emission Properties of Magnetron Cathodes.**—A magnetron will operate stably in certain regions of the performance diagram even when only a small primary thermionic current is available from the cathode. The remainder of the pulse current required by the tube is supplied by secondary electron emission. The nature of the back-bombarding electrons has been investigated both experimentally and theoretically, but theory and experimental data can at present give little aid to the designer of new types of magnetron. Nevertheless, the possibility of using metallic cathodes having suitable secondary electron-emission characteristics to furnish the pulse currents required and capable of dissipating large powers and operating at long pulse durations has instigated considerable interest. Several working models have been developed.<sup>1</sup>

An example of this type of cathode design is the c-w 30-cm 10-kv split-anode tube, the VC-303W. The cathode of this tube is made from Dowmetal J1 alloy (93 per cent Mg, 6 per cent Al, 1 per cent Mn) and has an average life of only about 200 hr, probably because of the removal of the Dowmetal surface during operation.

Pulsed multicavity magnetrons using silver magnesium alloys have been operated at 1-, 3-, and 10-cm wavelengths for short periods of time. At 1-cm, densities of about 100 amp/cm<sup>2</sup> were obtained. At 10-cm, several cathodes were run with a maximum life of about 400 hr, at an initial operating point of 14 kv and 30 amp and a duty ratio of 0.2 per cent. The output power of these tubes fell off rapidly by about 25 per cent within a few hours and then remained almost constant.

A study of the secondary emission properties of cathodes in magnetrons has been made by McNall<sup>2</sup> by incorporating an electron gun in one of the cavities of a multioscillator magnetron. A magnetron with a given cathode is run over its performance chart at a constant load in order to determine the range of stable operation for a given set of operating conditions. The secondary emission characteristics are then determined. By suitable treatment the secondary emission properties of the cathode surface are changed and the region of stable operation of the magnetron is again determined. Figure 12-15 shows the secondary yield  $\delta$  as a function of primary energy for a Ag-Mg cathode in several states of activation. From these data it has been possible to draw contours of the minimum value of the secondary electron-emission yield that is required for a given magnetron tested under fixed operating conditions. Such a performance chart is given in Fig. 12-16 for an Ag-Mg cathode in a 2J30 anode block. It is possible to operate stably at all

<sup>1</sup> J. W. McNall, H. L. Steele, and C. L. Shackelford, Westinghouse Electric Co. Research Report No. BL-R-929-76-1.

<sup>2</sup> *Ibid.*

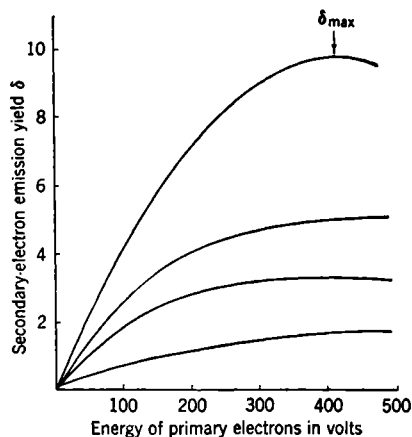


FIG. 12-15.—Secondary-electron-emission yield  $\delta$  of an Ag-Mg cathode surface under four different states of activation. (Courtesy of J. W. McNall.)

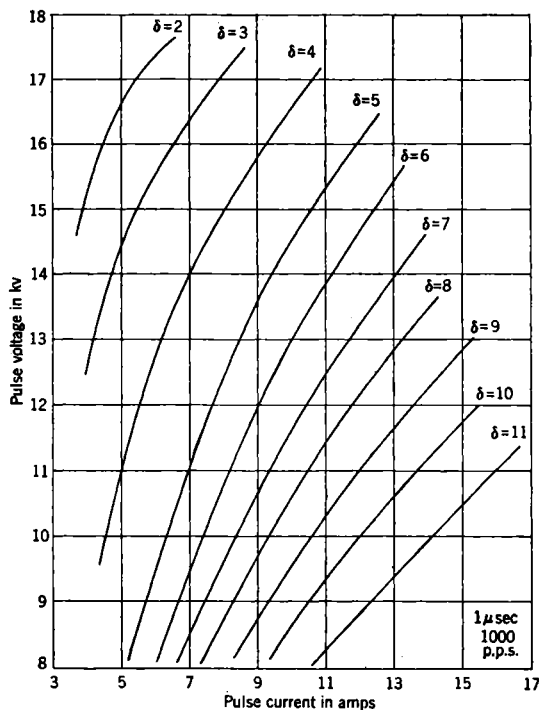


FIG. 12-16.—Estimated correlation of magnetron current with the secondary-emission yield of an Ag-Mg cathode in a 2J30 anode block. (Courtesy of J. W. McNall.)

values of voltage and current to the left of the contour corresponding to the chosen value of  $\delta$ .

Many secondary emission surfaces have been tried in pulsed and c-w magnetrons with varied success. These attempts have included silver-magnesium alloys, Dowmetal-metal alloys, beryllium, aluminum, nickel, a nickel-barium alloy, thorium, a beryllium-copper alloy, beryllium-plated copper, and evaporated magnesium on copper. Silver magnesium, Dowmetal-metal alloys, and possibly beryllium appear to be the most promising of the surfaces studied. Almost invariably the alloys are oxidized before assembly or at some time during the processing in order to obtain surfaces with high secondary yields. Many of these surfaces studied have not been satisfactory under the conditions chosen for operation in the magnetron or have been unstable in varying degrees during prolonged testing. Deactivation caused by arcing, gas, or other contaminations has been encountered in most of the studies made; there have been encouraging signs, however, that satisfactory solutions can be obtained for particular tube applications.

It was pointed out in Sec. 12-1 that most magnetrons using alkaline-earth oxide cathodes have operated satisfactorily only because the secondary electron-emission properties are capable of compensating for the thermionic emission deficiencies. The secondary electron-emission yields of alkaline-earth oxide cathodes are high,<sup>1,2</sup> and they have been reported to increase rapidly with temperature over a considerable range of operation. Figure 12-17 shows the secondary yield  $\delta$  for an oxide cathode as a function of primary energy and of temperature.

#### HEAT BALANCE IN THE CATHODE

By A. M. CLOGSTON

The next three sections of this chapter discuss the problem of heat balance in a magnetron cathode. The amount of back-bombardment

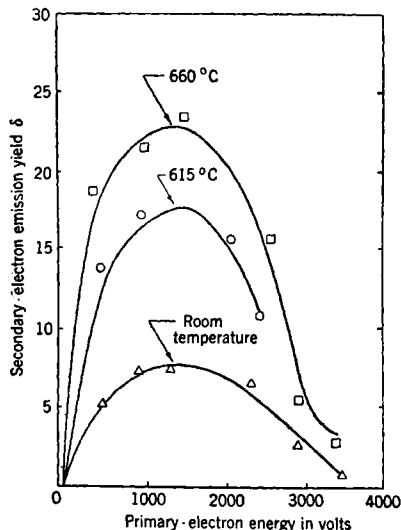


FIG. 12-17.—Secondary-electron-emission yield  $\delta$  of an alkaline-earth oxide cathode as a function of primary energy and of temperature. (Courtesy of M. A. Pomerantz.)

<sup>1</sup> M. A. Pomerantz and D. L. Goldwater, "Secondary Electron Emission from Oxide-coated Magnetron Cathodes," NDRC 14-310.

<sup>2</sup> J. B. Johnson, "Enhanced Thermionic Emission," *Phys. Rev.*, **66**, 352 (1944).

power delivered to the cathode of an operating magnetron will be discussed in Sec. 12-7, while Sec. 12-8 will consider how a cathode may be designed to dissipate this power.

**12-6. Thermal Behavior of a Pulsed Cathode.**—Because the best data available on back-bombardment power have been measured on pulsed magnetrons, and because applications of these sections may be made to pulsed tubes, consideration must be given to the differences in behavior between a cathode receiving pulses of back-bombardment power and one receiving the same average power continuously.

To study this question, the following simplified problem will be solved and used as a basis for qualitative conclusions about the behavior of real cathodes. Consider an outer cylindrical layer of a cathode unwrapped to form a rectangular sheet as in Fig. 12-18. Suppose that a back-bombardment power of  $P_B$  watts is delivered uniformly over

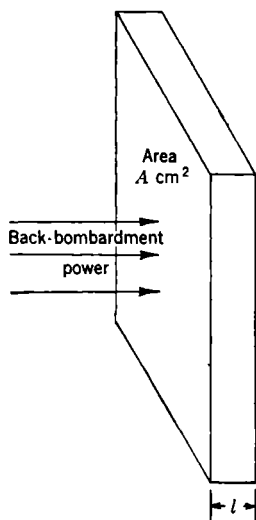


FIG. 12-18.—Cathode surface developed into a plane.

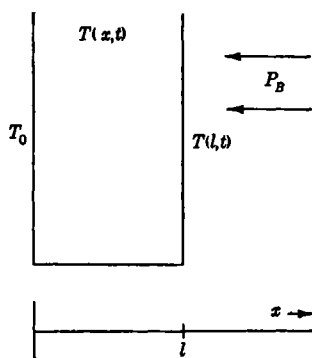


FIG. 12-19.—Cathode surface and coordinate system.

this surface during a pulse of duration  $\tau$  repeated at a frequency  $f$  times per second.

The developed area of the surface will be  $A$  cm<sup>2</sup>, and it will have a depth of  $l$  cm. Let it be supposed, tentatively, that it has been possible to choose this depth so that the back surface can be considered to remain at a fixed temperature  $T_0$ .

Suppose that the cathode surface is arranged relative to a coordinate system ( $x$ ) as indicated in Fig. 12-19. The temperature distribution within the layer will then be indicated by  $T(x, t)$ . It will be supposed that the area  $A$  is large enough that transverse variations of the temperature are unimportant. Furthermore, suppose the origin of time is chosen so that a pulse of power is applied to the cathode from  $t = 0$  to  $t = \tau$ .

During the pulse, a power of  $P_B/A$  watts/cm<sup>2</sup> or  $0.239 P_B/A$  cal/sec/cm<sup>2</sup> is fed to the surface at  $x = l$ . Therefore, if

$$q = \left(\frac{1}{K}\right) (0.239) \frac{P_B}{A},$$

where  $K$  is the thermal conductivity of the material in calories per centimeter per second per degrees centigrade, one has at the surface  $x = l$

$$\left. \begin{aligned} \left(\frac{\partial T}{\partial x}\right)_{x=l} &= q & \text{for } 0 \leq t \leq \tau, \\ \left(\frac{\partial T}{\partial x}\right)_{x=l} &= 0 & \text{for } \tau < t < \frac{1}{f}. \end{aligned} \right\} \quad (2)$$

The partial differential equation governing nonsteady-state heat flow in one dimension may be written

$$\frac{\partial^2 T}{\partial x^2} = \frac{1}{a^2} \frac{\partial T}{\partial t}, \quad (3)$$

where  $a^2 = K/c\rho$ . The thermal capacity per unit mass is indicated by  $c$ , and the density by  $\rho$ . A table of values of  $a^2$  may be found in Strong.<sup>1</sup> The solution of Eq. (3) appropriate to the present problem may be written<sup>2</sup>

$$T(x, t) = \sum_{n=-\infty}^{\infty} A_n e^{-in2\pi f t} \ln \sqrt{i \frac{n2\pi f}{a^2}} x + T_0. \quad (4)$$

If the constants  $A_n$  are now arranged so as to satisfy the boundary conditions set by Eqs. (2), Eq. (4) becomes

$$T(x, t) = \frac{qf}{a^2} \sum_{n=-\infty}^{\infty} \frac{(e^{in2\pi f \tau} - 1) \sin \sqrt{i \frac{n2\pi f}{a^2}} x}{\left(i \frac{n2\pi f}{a^2}\right)^{3/2} \cos \sqrt{i \frac{n2\pi f}{a^2}} l} e^{in2\pi f t} + T_0. \quad (5)$$

The quantity that will be of interest is the difference in temperature of the front face of the layer just before a pulse starts and just after it ends. This fluctuation in temperature will be called  $\Delta T$  and is defined by

$$\Delta T = T(l, \tau) - T(l, 0). \quad (6)$$

<sup>1</sup> J. Strong, *Procedures in Experimental Physics*, Prentice-Hall, New York, 1945, p. 494.

<sup>2</sup> H. Bateman, *Partial Differential Equations of Mathematical Physics*, Dover, New York, 1944, p. 214.

From Eq. (5)

$$\Delta T = \frac{2qf}{a^2} \sum_{n=1}^{\infty} \frac{(1 - \cos n2\pi f\tau)}{\left(\frac{n2\pi f}{a^2}\right)^{3/2}} \left[ i^{-3/2} \tan \sqrt{i \frac{n2\pi f}{a^2}} l + (-i)^{-3/2} \tan \sqrt{-i \frac{n2\pi f}{a^2}} l \right], \quad (7)$$

or

$$\Delta T = \frac{2qf}{a^2} \sum_{n=1}^{\infty} \frac{\sin^2 n\pi f\tau}{\left(\frac{n\pi f}{a^2}\right)^{3/2}} \frac{\sinh 2 \sqrt{\frac{n\pi f}{a^2}} l - \sin 2 \sqrt{\frac{n\pi f}{a^2}} l}{\cosh 2 \sqrt{\frac{n\pi f}{a^2}} l + \cos 2 \sqrt{\frac{n\pi f}{a^2}} l}. \quad (8)$$

Equation (8) is the solution to the problem. An interesting observation can now be made about Eq. (8). If  $l^2 > a^2/f$ , then  $2l \sqrt{n\pi f/a^2} > \sqrt{4\pi n}$ . Because  $n$  is never smaller than unity,  $2l \sqrt{n\pi f/a^2} > 3.54$ . Under this condition the second fraction in the series is very nearly unity for all  $n$  and may be disregarded. Therefore,  $\Delta T$  does not depend upon  $l$ . This result can mean only that the fluctuations in temperature experienced by the front face of the layer become insensible at a depth  $a/\sqrt{f}$  behind the front face. In the most unfavorable case that will be considered,  $a$  will have the value 0.5 cm/sec<sup>1/2</sup> for nickel, whereas if pulsing rates no slower than  $f = 400$  are considered,  $a/\sqrt{f}$  can at most be 0.025 cm or approximately 0.010 in. This example provides the justification for assuming that the problem which has been solved will represent the behavior of real cathodes. It is consistent to assume that a cathode receiving periodic bursts of energy will fluctuate in temperature only in a very thin outer layer and that there will be a cylindrical surface at some depth greater than  $a/\sqrt{f}$  which may be considered to remain at constant temperature.

Assuming from now on that  $l > a/\sqrt{f}$ , Eq. (8) may be written

$$\Delta T = \frac{2qa}{\sqrt{\pi^3 f}} \sum_{n=1}^{\infty} \frac{\sin^2 n\pi f\tau}{n^{3/2}}. \quad (9)$$

By the use of Poisson's summation formula,<sup>1</sup> the series may be written

$$\sum_{n=1}^{\infty} \frac{\sin^2 n\pi f\tau}{n^{3/2}} = \int_0^{\infty} \frac{\sin^2 \pi f\tau \chi}{\chi^{3/2}} d\chi + 2 \sum_{n=1}^{\infty} \int_0^{\infty} \frac{\sin^2 \pi f\tau \chi}{\chi^{3/2}} \cos 2n\pi \chi d\chi. \quad (10)$$

<sup>1</sup> Courant and Hilbert, *Methoden der Mathematische Physik*, Vol. I, Springer, Berlin, 1924, p. 59.



The integrals in Eq. (10) can be evaluated with the result

$$\sum_{n=1}^{\infty} \frac{\sin^2 n\pi f\tau}{n^{3/2}} = \sqrt{\pi^2 f\tau} + \sqrt{\frac{\pi}{2}} \sum_{n=1}^{\infty} \sqrt{2n\pi} \left( \sqrt{1 + \frac{f\tau}{n}} + \sqrt{1 - \frac{f\tau}{n}} - 2 \right) \quad (11)$$

provided that  $f\tau < 2$ , which is always true. If now  $f\tau \ll 1$ , Eq. (11) becomes approximately

$$\sum_{n=1}^{\infty} \frac{\sin^2 n\pi f\tau}{n^{3/2}} = \sqrt{\pi^2 f\tau} - 2.612 \frac{\pi}{4} (f\tau)^2. \quad (12)$$

By neglecting even the term in  $(f\tau)^2$ , Eq. (9) becomes

$$\Delta T = 2qa \sqrt{\frac{\tau}{\pi}}, \quad (13)$$

with the two conditions of validity

$$\left. \begin{array}{l} l > \frac{a}{\sqrt{f}} \\ f\tau \ll 1 \end{array} \right\} \quad (14)$$

and

The magnitude of the fluctuations in temperature of a cathode caused by periodic pulses of back-bombardment power will now be calculated. In data presented<sup>1</sup> in Sec. 12-7 one has  $\tau = 10^{-6}$  sec and  $f = 500$  per second. The surface layer of the cathode is a mixture of barium and strontium oxides. Approximate values for the constants of this oxide mixture at 900°C are  $K = 0.013$  and  $a = 0.11$ . With these values, the condition of validity noted in Eq. (14) requires that

$$l > 0.005 \text{ cm} = 0.002 \text{ in.},$$

which is certainly true. Furthermore,  $f\tau = 0.5 \times 10^{-3}$ , which is much less than unity. Suppose now that 10 kw of power is delivered to the cathode while the tube is operating. The surface area of the cathode under consideration is 3.8 cm<sup>2</sup>. It is easily found that  $q = 49,000^\circ\text{C}/\text{cm}$ . A fluctuation of 17°C is obtained by substitution in Eq. (13).

If the cathode surface presented to the back-bombardment energy were nickel instead of an oxide mixture, the constants would be  $K = 0.22$  and  $a = 0.50$ . With the same back-bombardment power,

$$q = 3000^\circ\text{C}/\text{cm}$$

and  $\Delta T = 5^\circ\text{C}$  for nickel.

<sup>1</sup> W. E. Danforth, C. D. Prater, and D. L. Goldwater, "Back Bombardment of Magnetron Cathodes," Bartol Research Foundation, NDRC 14-309, Aug. 25, 1944.

It is thus observed that if the assumptions made in these calculations are allowed, the fluctuations of cathode temperature caused by periodic pulses of back-bombardment power are rather small.

It must now be mentioned that the problem just solved does not contemplate cooling by radiation of the cathode surface drawn in Fig. 12-18. Suppose that the surface shown in Fig. 12-18 were radiating between pulses from its front surface. Suppose also that it is considered to be so thin that no temperature differences exist inside the material, and suppose that it is thermally isolated from its surroundings. These last two assumptions are artificial but will permit a calculation of the importance of the radiation effect. If the emissivity of the surface is taken as unity, the energy lost in time  $dt$  from the surface is  $A\sigma T^4 dt$  watt-seconds, where  $\sigma$  is Boltzman's constant. If  $c$  is the heat capacity per unit mass and  $\rho$  the density, one must have for the temperature change in time  $dT$

$$A\sigma T^4 dt = -c\rho Al dT. \quad (15)$$

If  $T_1$  is the temperature at time  $t = 0$ , Eq. (15) can be integrated to give

$$\frac{1}{T^3} = \frac{1}{T_1^3} + \frac{3\sigma t}{c\rho l} \quad (16)$$

for the temperature at time  $t$ . If the material being considered is nickel,  $c = 0.59$  joule/gm per  $^{\circ}\text{C}$  and  $\rho = 8.4$  gm/cm $^3$ . The value of  $\sigma$  is  $5.74 \times 10^{-12}$  watt/cm $^2$  per  $^{\circ}\text{C}$ . Let  $t = 0.002$  sec be the time between pulses at a 500 cps repetition rate, and let  $l$  be 0.02 cm, or approximately the depth indicated by Eq. (14). With these values it is found that

$$T^3 = \frac{T_1^3}{1 + (3.5 \times 10^{-13})T_1^3}. \quad (17)$$

Suppose now that  $T_1 = 1200^{\circ}\text{A}$ . From Eq. (17) it is found that  $T$  is less than  $T_1$  by only 0.02 per cent.

On the basis of this example, it is concluded that radiation has a negligible effect upon the fluctuations in temperature of a pulsed cathode. Consequently, fluctuations in cathode temperature due to periodic back bombardment may be disregarded under the conditions assumed in this section.

A source of periodic cathode heating during pulsing not considered here is the ohmic loss in the cathode coating due to passage of electrons. In the Bartol data that will be considered, this effect has been taken into account by operating the magnetron under consideration as a diode and measuring the temperature rise due solely to ohmic loss. In applications of the results of these sections, the two effects should be considered separately.

**12-7. Measurements of Back-bombardment Power.**—It is generally understood that a certain fraction of the electrons which leave the cathode of an operating magnetron return to the cathode with an increased energy gained at the expense of the oscillating fields. This increment of energy is expended in heating the cathode structure. Experience has led to general acceptance of the fact that about 3 to 10 per cent of the input power of a magnetron will appear as back-bombard-

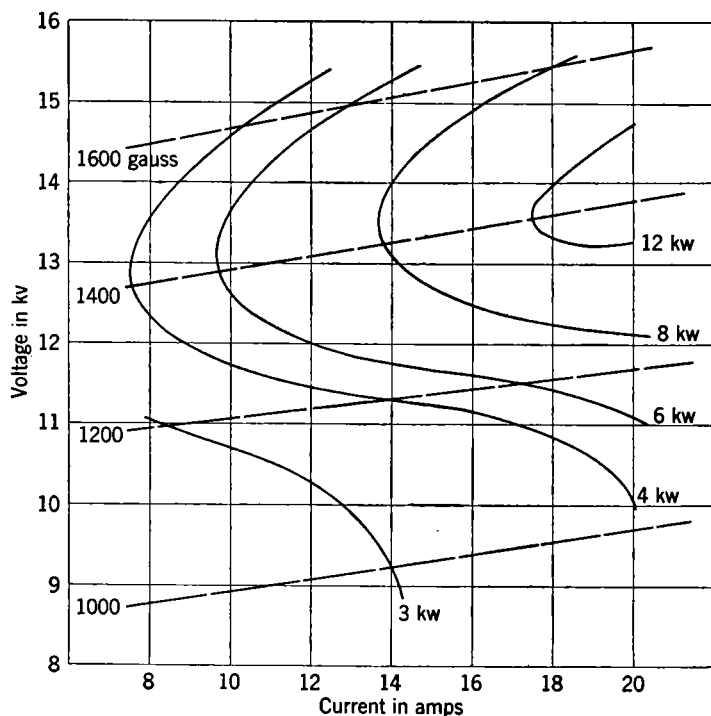


Fig. 12-20.—Contours of equal back-bombardment power.  $Q_L = 56$ .

ment power at its cathode. Very few serious attempts have been made, however, to measure back-bombardment power accurately.

The best data on this subject have been measured on a 2J32 magnetron at the Bartol Research Foundation.<sup>1</sup> Under a variety of operating conditions, these investigators measured the rise in temperature of the cathode of this tube above that maintained by the heating element during nonoscillating conditions. Furthermore, similar increments of

<sup>1</sup> W. E. Danforth, C. D. Prater, and D. L. Goldwater, "Back Bombardment of Magnetron Cathodes," Bartol Research Foundation, NDRC 14-309, Aug. 25, 1944.

temperature were achieved by increasing the heater power. In their case, the distribution of these two sources of heat can be considered equivalent, and it has just been shown in Sec. 12-6 that effects due to periodic back bombardment can be neglected. The temperature rise during oscillation can be correlated with an average back-bombardment power and, knowing the duty ratio, with a pulse back-bombardment power.

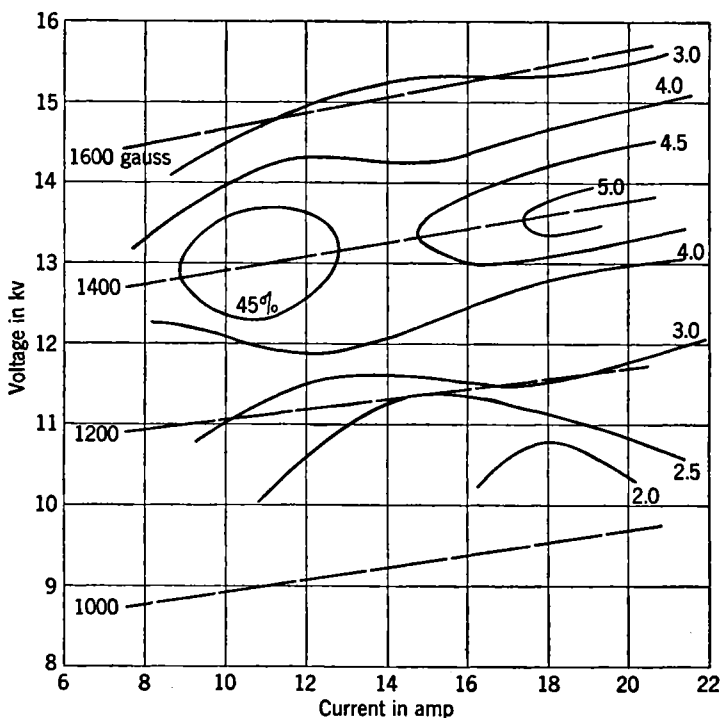


Fig. 12-21.—Back-bombardment power in percentage of input power for the 2J32 magnetron.  $Q_L = 56$ .

In Fig. 12-20 a chart is shown of contours of equal back-bombardment power in the  $(V, I)$ -plane for a 2J32 magnetron operated at a loaded  $Q$  of 56. The magnetic field lines are also shown. This chart is typical of a number of such plots given in the Bartol report. In Fig. 12-21, the same data are presented in terms of percentage of input power. It will be observed on this chart that from 2 to 5 per cent of the input power appears at the cathode at this loaded  $Q$ .

Furthermore, it will be observed that a very definite maximum in the percentage of input power returned to the cathode occurs in the

neighborhood of 1400 gauss. Mention of this fact has already been made in Sec. 10.8. It was stated there that this field value was empirically predicted by the formula

$$B_c = \frac{10,600}{\lambda} \left( 1 + \frac{3}{N} \right). \quad (18)$$

Until more information is available, it will be impossible to say whether or not a maximum in the percentage of input power returned to the cathode can generally be expected in the neighborhood of the field predicted by Eq. (18).

In Fig. 12.22 a plot is shown of the back-bombardment power of the same 2J32 as a function of total slot conductance  $G$ , for a field of 1200 gauss and a current of 12 amp. A curve of power  $P_s$  delivered by the electrons to the resonant system is included for comparison purposes. It will be seen that the back-bombardment power nearly doubles as the load is decreased, while over the same range, the output power is decreasing by nearly a factor of 2.

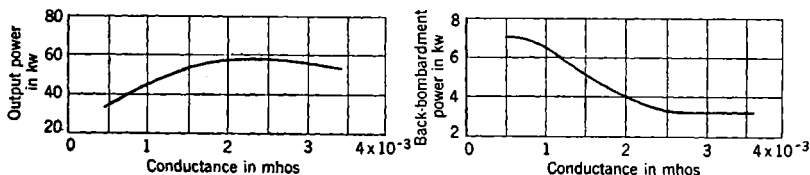


FIG. 12.22.—The dependence on load of (a) output power and (b) back-bombardment power for  $B = 1200$  gauss,  $I = 12$  amp, and  $G_L = 0.11/Q_L$ .

The data presented in Figs. 12.21 and 12.22 indicate that the back-bombardment power delivered to the cathode of a 2J32 magnetron may vary from 2 to 10 per cent of the input power over the known ranges of operation.

Consideration can now be given to the usefulness of the Bartol Research Foundation data in predicting the behavior of other magnetrons. If the 2J32 magnetron satisfies the requirements for exact scaling expressed in Sec. 10.6, the data can certainly be used to predict the back-bombardment power of other tubes in this family. Furthermore, in this case, the data should scale to magnetrons of different  $N$  at least as well as the output power. Consideration of the structure of the 2J32 indicates that it should scale properly, and performance charts for the tube given in Chap. 10 do, indeed, fit into the general scaling scheme. It has been shown in Chap. 10, however, that a rising-sun magnetron does not really satisfy the requirements for exact scaling. The coincidence that Eq. (18) predicts the critical field for a rising-sun

tube and also the field of maximum back-bombardment shown in Fig. 12-21 raises a possible suspicion that the 2J32 magnetron used here possesses in a slight degree some of the properties of a rising-sun magnetron. If this is true, the back-bombardment power might be very strongly affected while the output power and other properties of the tube are only negligibly influenced. The possibility exists, therefore, that the data presented may not be scalable to other magnetrons.

Other data have been taken, less extensive and reliable than that presented in the Bartol report. C. S. Robinson, Jr.<sup>1</sup> has taken data on an early model of the 2J32 that substantially confirms the Bartol data. In Fig. 12-23, cathode-temperature characteristics are given for a 2J42 low-voltage, 3-cm magnetron. Curves are given showing cathode temperature as a function of heater power for various average input powers. The data always refer to the same operating point because the average input power has been changed by varying the duty ratio. By reading across at a constant temperature of 900°C, the following table can be constructed. At this operating point, therefore, about 8 per cent of the input power to a 2J42 magnetron is delivered to the cathode.

TABLE 12-1.—COMPUTATIONAL TABLE

Input power, watts	Heater power, watts	Power supplied by back bombardment, watts	Ratio at back-bombardment power to input power, %
53.2	0.93	4.22	7.9
27.2	2.91	2.24	8.3
13.6	4.05	1.10	8.1
0.0	5.15	0.00	...

**12-8. Thermal Considerations in Cathode Design.**—A cathode with a length and diameter of active surface fixed by other considerations must be constructed to fulfill the following conditions:

1. Under stand-by conditions with the magnetron in a nonoscillatory state, a certain rated heater power must maintain the cathode above a minimum temperature that will permit oscillations to be initiated when plate voltage is applied at the required rate and without damage to the active surface. The temperature must furthermore be kept below a maximum value set by considerations of life.

<sup>1</sup> C. S. Robinson, Jr., "Cathode Temperatures in Magnetrons," RL Report No. 90, Mar. 31, 1942.

2. With the magnetron oscillating and the cathode receiving a certain back-bombardment power and with the rated heater power reduced by a prescribed amount, the cathode temperature must be maintained in a range ensuring proper operation of the tube and an adequate life.
3. The rated heater power must not be greater than some limit set by operational requirements.
4. For barium-strontium oxide cathodes it must be possible to dissipate sufficient power in the heating element to bring the cathode to breakdown temperature.

The design problem presented by these requirements is so complex and so different for each case that no attempt will be made to describe specific methods of procedure. Certain general features of the problem will be considered, but there will be no close discussion of questions of heat flow and radiation. Various degrees of calculation and experiment will be appropriate in each case to arrive at a satisfactory design. To summarize the existing art of cathode design and to serve as a point of departure in designing new cathodes, data will be presented on the construction and thermal properties of a number of cathodes that have already been built to meet a variety of operating conditions.

An increased understanding of the problem of cathode design can be gained by considering a class of cathodes for which certain general relations can be derived. This class includes cathodes answering the following description:

1. Their heater construction is such that the heater power and back-bombardment power may be considered thermally equivalent.
2. Heat is lost from the cathode almost entirely by radiation.
3. The whole cathode structure is at a nearly uniform temperature.

Radial-mounted cathodes that lose only a small proportion of heat through their supporting leads roughly satisfy this description.

Suppose that  $P_H$  is the rated heater power corresponding to a minimum tolerable temperature  $T_1$  for starting and that  $\beta P_H$  is the power corresponding to a maximum tolerable temperature  $T_2$  during operation. It has already been shown in Chap. 10 that  $P_H$  must satisfy the equation

$$P_H = \frac{P_B}{\beta - \chi} \quad (19)$$

where  $\chi$  is the fractional reduction in  $P_H$  during operation. For the cathodes under consideration,

$$P_H = C(T_1^4 - T_0^4), \quad (20)$$

and

$$\beta P_H = C(T_1^4 - T_0^4), \quad (21)$$

where  $C$  is some constant depending on the cathode shape and  $T_0$  is the temperature of the surroundings of the cathode and is assumed to remain constant. From Eqs. (20) and (21)

$$\beta = \frac{T_2^4 - T_0^4}{T_1^4 - T_0^4}. \quad (22)$$

Suppose, for example, that safe temperature limits for a barium strontium oxide cathode are  $750^\circ$  and  $950^\circ$ . If  $T_0$  is considered negligible compared with  $T_1$ , Eq. (22) yields, for this case,  $\beta = 2.1$ .

With  $P_H$  determined from Eqs. (19) and (22) the design problem for this class of cathodes is reduced to arranging that the cathode structure maintain a temperature  $T_1$  when  $P_H$  watts are dissipated in the heater. For a radial-mounted cathode with fixed length and diameter of active surface, this essentially involves proper design of the end shields.

If the heater power required by Eqs. (19) and (22) is more than a radial-mounted cathode with an active surface of the specified dimensions can be designed to dissipate at the temperature  $T_1$ , the use of an end-mounted cathode is indicated. On the other hand, Eqs. (19) and (22) may specify a heater power so small that the dissipation of the cathode structure cannot be sufficiently reduced to enable the temperature  $T_1$  to be attained at  $P_H$  watts in the heater. In this case, it is clear that the temperature range  $T_1$  to  $T_2$  may be decreased with a consequent decrease in  $\beta$  and increase in  $P_H$ .

The cathode data to be presented will include several examples of radial-mounted structures. It will not be possible, however, to correlate these data with Eqs. (19) and (22) because insufficient information exists on the temperatures  $T_1$  and  $T_2$  that have been considered practicable.

The cooling of an end-mounted cathode or of a radial-mounted cathode with heavy supporting leads is a mixture of radiative and conductive heat loss. The construction of end-mounted cathodes, furthermore, is often such that the distribution of heater power and back-bombardment power are far from equivalent. Consequently, general relations such as Eqs. (19) and (22) cannot be established for end-mounted cathodes, and the design problem is more complicated.

A considerable simplification is made in the problem if the heater power can be decreased to zero during operation ( $\chi = 0$ ). Then the cathode structure can first be designed to dissipate the back-bombardment power  $P_b$  at the temperature  $T_2$ , and  $P_H$  can be separately arranged so as to maintain a cathode temperature  $T_1$  in the nonoperating tube.



TABLE 12-2

Tube	Cathode type	Active area of cathode, cm <sup>2</sup>	Stand-by heater rating			Maximum average power input, watts
			volts	amp	watts	
Radial mounts:						
2J32	Plain oxide	3.77	6.3	1.5	9.5	600
4J70	Metallized screen	7.36	16	3.1	50.0	1200
4J70	Thorium oxide	7.36	12.6	25.5	320.0	<u>1500</u>
HP10V	Oxide screen	18.84	13.0	8.5	110.0	3000
725A	Metallized screen	0.52	6.3	1.0	6.3	180
End mounts:						
2J42	Oxide screen	0.36	6.3	3.0	3.0	83
BM50	Oxide screen	0.12	6.3	0.30	1.9	<u>0.19</u>
QK61	Oxide screen	1.12	6.3	3.5	22.0	350
4J50	Oxide matrix	1.07	12.6	2.2	28.0	700
3J21	Oxide matrix	.....	12.6	1.6	20.0	110
A-131	Tantalum	0.11	3.0	50.0	150.0	<u>500</u>

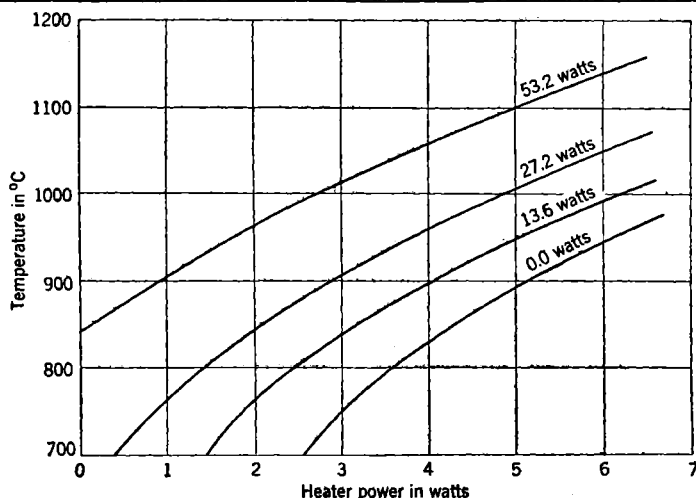


FIG. 12-23.—Cathode temperature vs. heater power characteristics of the 2J42 for various values of average input power to the magnetron. The curves were obtained by varying the duty ratio at a constant operating point of 5.5 kv, 4.5 amp, pulling figure of 12 Mc/sec, and loaded  $Q$  of 240.

A structure arrived at in this way can furthermore serve as a starting point in designing a cathode for which  $\chi$  is not to be equal to zero. If the radiative or conductive heat loss of this first approximation is successively increased, both  $P_H$  and  $\chi P_H$  must also increase. The increments

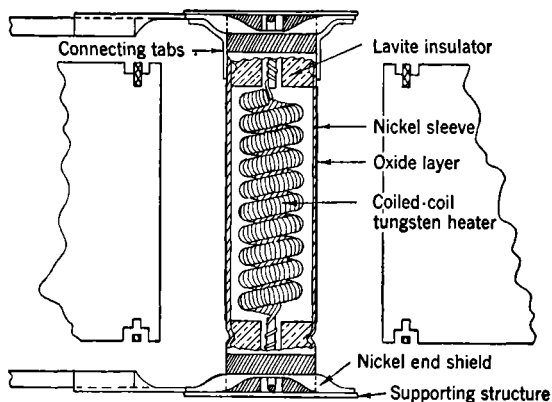


FIG. 12-24.—Plain oxide cathode of the 2J32. (2×.)

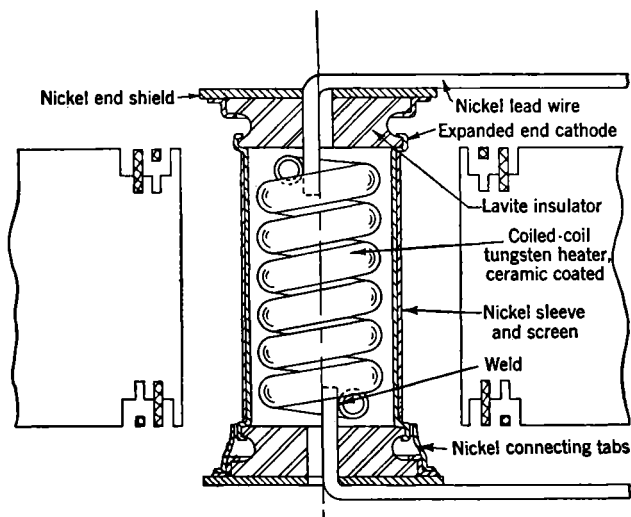


FIG. 12-25.—Metallized screen cathode of the 4J70. (2×.)

in  $\chi P_H$  will be greater than those in  $P_H$ , however, because  $T_2 > T_1$ . Therefore, by sufficiently increasing the heat loss,  $\chi$  can be brought to the desired value.

Figures 12-24 through 12-34 are 11 enlarged-scale cross-section views of cathodes that have been used in various production and experimental

magnetrons. Five of these cathodes are radial- and six are end-mounted designs. These tubes are listed in Table 12-2 with data on the type of emitting surface, the emitting area, the stand-by heater ratings, and the

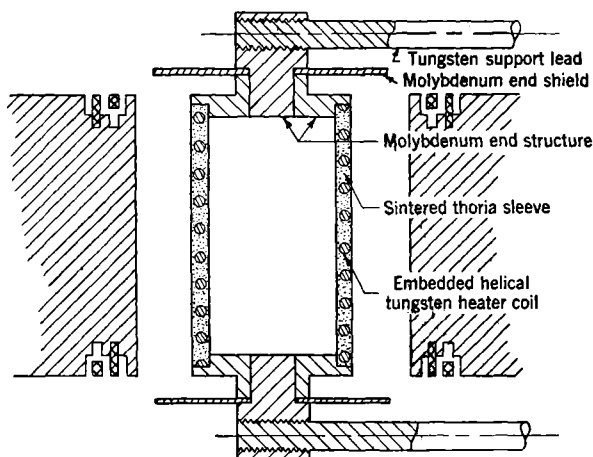


FIG. 12-26.—Thorium oxide cathode of the 4J70. (2×.)

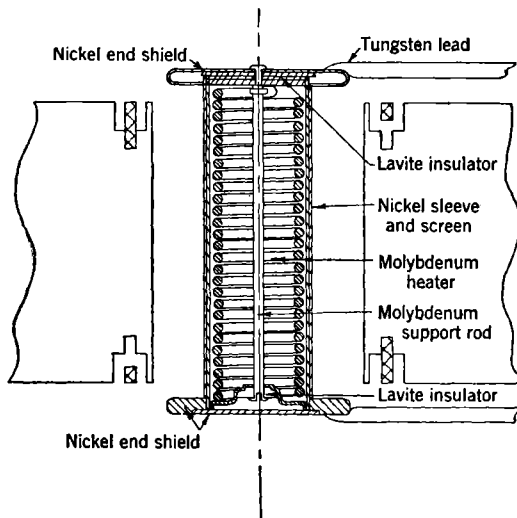


FIG. 12-27.—Oxide screen cathode of the HP10V. (Actual size.)

maximum average input power that the tube is rated to accept at any operating point. Except for the 2J32, which is discussed in Sec. 12-7, there is insufficient information to translate this input power into terms of back-bombardment power. Consequently these figures can be taken

only as a rough indication of the power-handling capabilities of the various cathodes. For three of the tubes, the average power entered in the table is underlined to indicate that the tube has accepted that power successfully but that it has not been determined to be a maximum value.

The characteristics of most of the tubes listed in Table 12-2 are discussed in Chap. 19. One exception is the A-131, a 3-cm c-w magnetron developed at RCA.<sup>1</sup> This tube has operated with an input power of

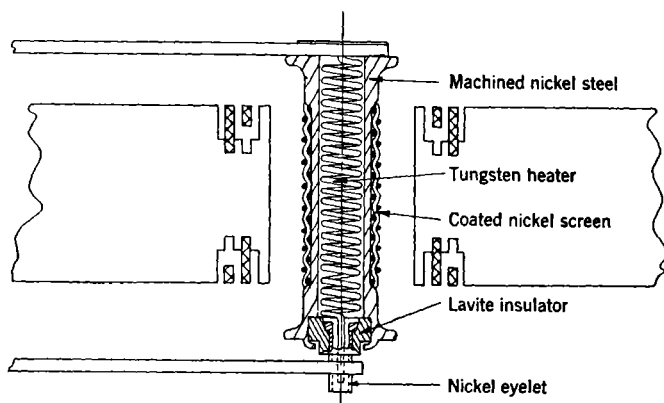


FIG. 12-28.—Metallized screen cathode of the 725A. (4×.)

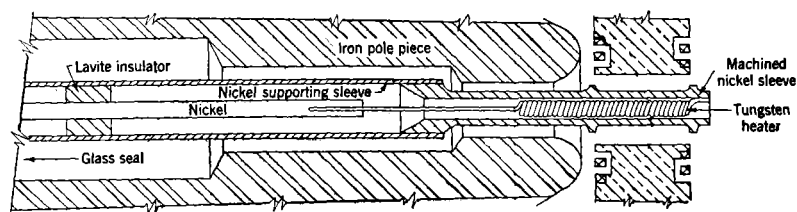


FIG. 12-29.—Oxide screen cathode of the 2J42. (2½×.)

500 watts at an efficiency of 40 per cent. Under these conditions the cathode was maintained at  $2600^{\circ}\text{K}$  by reducing the heater power to 80 watts.

Two cathode structures are shown for the 4J70 magnetron. One of these is the conventional oxide cathode used in production tubes; the second is an experimental thorium oxide cathode developed at the Bartol Research Foundation.<sup>2</sup> This cathode was developed to permit the use of higher input powers and longer pulse durations with the 4J70 and represents an experimental stage of development.

<sup>1</sup> NDRC 15-RP430C, 1946.

<sup>2</sup> M. A. Pomerantz, "Sintered Thoria Cathodes," Bartol Research Foundation of the Franklin Institute, NDRC 14-517, Oct. 31, 1945.

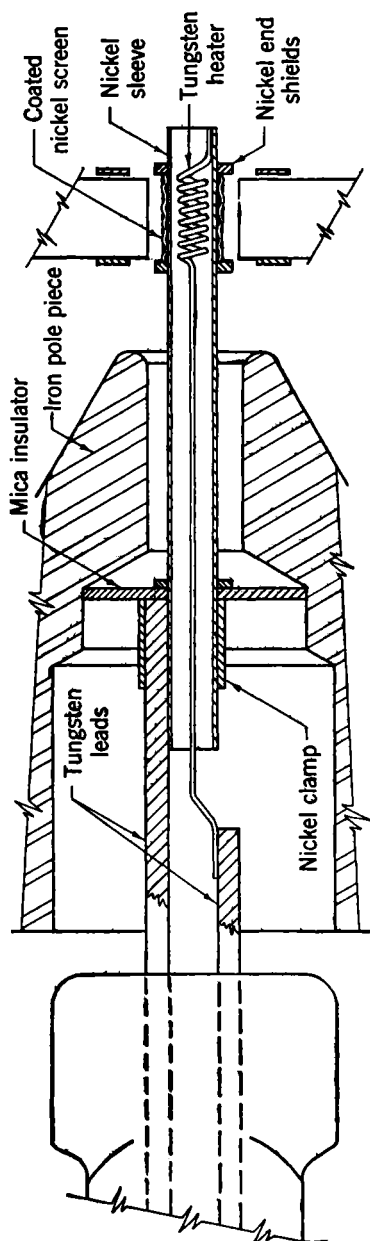


FIG. 12-30.—Oxide screen cathode of the BM50. (5 $\times$ .)

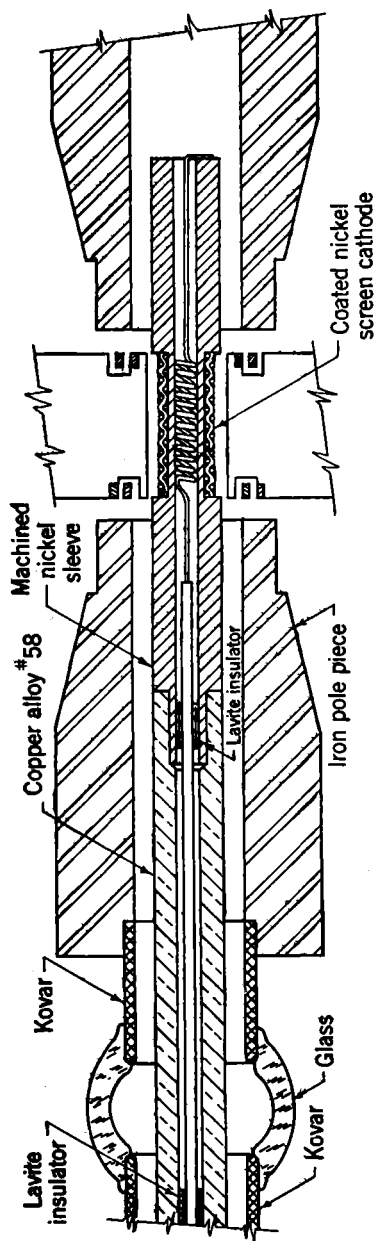


FIG. 12-31.—Oxide screen cathode of the CM16B. (2 $\times$ .)

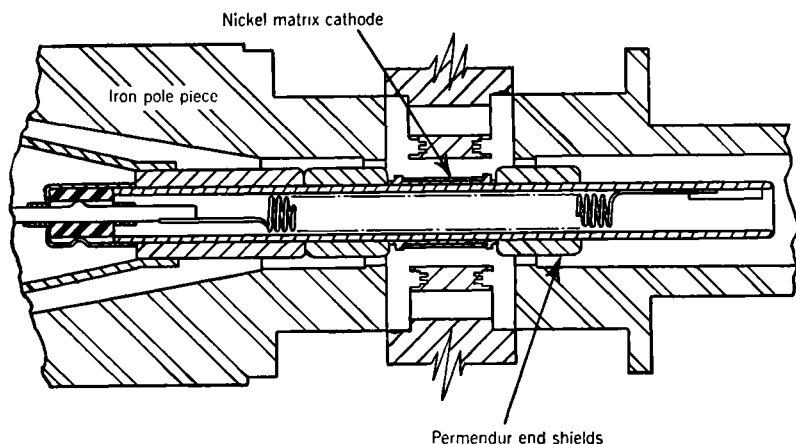


FIG. 12-32.—Oxide matrix cathode of the 4J50. (2×)

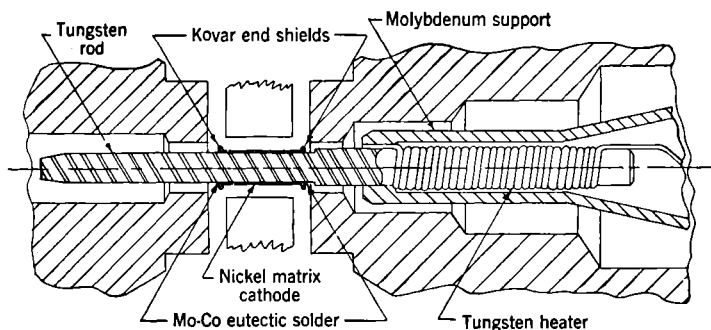


FIG. 12-33.—Oxide matrix cathode of the 3J21. (2×.)

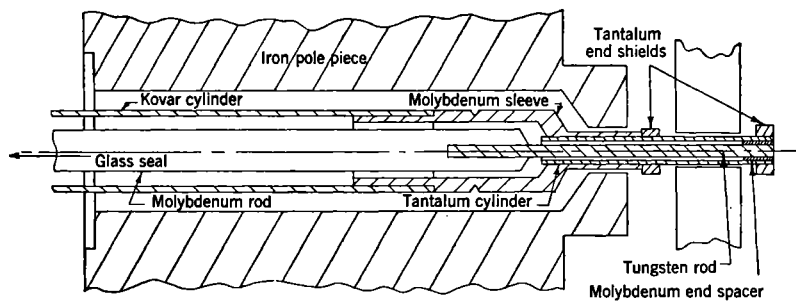


FIG. 12-34.—Tantalum cathode of the A131.

Rather complete data are available on the characteristics of the 2J42 cathode. These data are presented in Fig. 12-23 as an example of the thermal behavior of an end-mounted cathode.

### ESTABLISHMENT OF AN AXIAL BOUNDARY TO THE SPACE CHARGE

By A. M. CLOGSTON

**12.9. Cathode End Shields.**—Cathode end shields are short sections of enlarged diameter at the ends of a magnetron cathode. Numerous examples of these structures may be seen by referring to Figs. 12-24 through 12-34. The end shields may be relatively close to or far from the top of the anode block. The diameter of the shields may vary from only slightly greater than the cathode diameter to even larger than the anode diameter. The temperature of the end shields may be equal to the cathode temperature or may be sometimes so constructed as to maintain a temperature several hundred degrees cooler than the cathode. Mechanically, the shields may be an integral part of the cathode sleeve or may sometimes be separately mounted from the cathode supports. The potential of the end shields, however, is always kept the same as that of the cathode.

End shields are a necessary part of a magnetron cathode, required to prevent electron leakage from the interaction space. If the end shields are omitted from the cathode, the volt-ampere characteristic at a fixed field will be as shown by the solid curve in Fig. 12-35, whereas the characteristic of a normal tube is as shown by the dashed curve. It has been demonstrated that this current flowing to the anode in the absence of end shields is collected almost entirely on the end plates of the magnetron as long as the applied voltage is below cutoff. For example, currents up to 60 or 70 amp may thus flow out of the interaction space of a 4J70 magnetron built without end shields. Under these conditions a magnetron cannot oscillate.

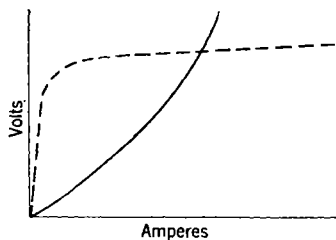


FIG. 12-35.— $(v, i)$  = characteristic of a magnetron without end shields.

There are two possible explanations of these large leakage currents that are not encountered in ordinary electron tubes, and both are connected with the presence of the magnetic field. (1) A magnetron is usually operated at a voltage several times greater than would normally be applied to a similar nonmagnetic diode. Consequently, the space-charge densities necessary to give a zero gradient of electric field at the cathode are also several times larger. The repulsive force exerted on electrons near the ends of the interaction space by this large space

charge may therefore account in part for the large leakage currents. (2) If the magnetic field near the ends of the cathode decreases in a direction away from the center plane of the anode block, the electrons in this region will feel an additional force directing them out of the interaction space. This effect can sometimes be counteracted by constructing the end shields of magnetic material in such a way that the fields increase away from the center plane. The 4J50 cathode illustrated in Fig. 12-31 has Permendur end shields for this purpose. A discussion of this effect will be found in Chap. 13.

Cathode end shields prevent electron leakage from the interaction space by distorting the equipotential lines near the ends of the interaction space in such a way as to inflict an inwardly directed component of force upon the electrons. This component of force, being essentially parallel to the magnetic field, simply urges the electrons toward the center plane of the anode block.

The presence of the end shields, unfortunately, is not always felt solely through their electrostatic effects. Under certain conditions, the shields may emit electrons that, originating closer to the anode than do those emitted from the cathode surface, respond differently to the electric fields. Such electrons may contribute to an observed leakage current, and they may sometimes act to increase or decrease the mode stability of a pulsed magnetron. A further discussion of this matter is to be found in Chap. 8 and in a report by P. Forsberg.<sup>1</sup>

Under various circumstances, the electrons emitted by an end shield may be either primary or secondary. Primary emission is promoted by a high end-shield temperature and by the accumulation of active material on the shield by evaporation or surface diffusion. Secondary emission apparently can arise from bombardment of the shields by the longitudinal movement of electrons in the interaction space as already discussed. Evidence for this effect will be found in the report by Forsberg.

For all practical purposes, the design of end shields is completely empirical. A good procedure for a new case would be to start with a design that resembles mechanically and electrostatically one of the examples in Sec. 12-8. If behavior of the magnetron is then satisfactory, the end-shield design can be considered adequate. On the other hand, the tube may present large leakage currents or poor mode behavior. In order to determine whether or not these effects are a matter of end-shield design, tests should be made to discover (1) if current is escaping from the interaction space and (2) if electrons are being emitted from the end shields. Point 1 may be tested directly by inserting insulated end plates or pole pieces in the tube and measuring the current collected upon

<sup>1</sup> P. Forsberg, "Some Relations between End Effects and Mode Stability in the 4J31-35 Magnetrons," RL Group Report No. 52, Nov. 2, 1945.



them. The point may also be studied by redesigning the end shields to decrease electron leakage from the interaction space and then observing the change in tube behavior. This redesign should increase the diameter of the shields or bring them closer to the top of the anode block.

Point 2 is difficult to test directly and can be best studied by making changes in design that tend to decrease any end emission present. The most effective course is to redesign the shields so that they operate at a lower temperature. The end-shield temperature can be directly observed if a window is incorporated into the tube. In making this redesign, it must be remembered that the shields may receive energy from electron bombardment as well as by conduction and radiation from the cathode. If improvement in the tube characteristics results from a decrease in the end-shield temperature, indicating that emission from the shields is present and important, further improvement in behavior may possibly be obtained as follows: (1) by designing a trap to prevent surface diffusion of active material to the shields, (2) by constructing the shields from or coating them with a very poor emitter, and (3) by decreasing the diameter of the shields so that any electrons which are emitted will have a less deleterious effect upon the operation of the tube.

## CHAPTER 13

### THE MAGNETIC CIRCUIT

BY J. R. FELDMEIER

The essential features of the magnetic circuit for microwave magnetrons are (1) minimum weight, particularly for airborne radar; (2) constant magnetic field under operating conditions; and (3) a proper field shape for efficient magnetron operation. The most convenient source of magnetic flux satisfying (1) and (2) is a permanent magnet, for an electromagnet requires a constant-current power supply. Electromagnets are, however, more convenient than permanent magnets for testing experimental tubes, as it is usually necessary to cover a considerable portion of the performance chart by varying the magnetic field. Thus both electromagnet and permanent-magnet designs are of concern. The principles of electromagnet design are generally understood and covered in most texts on electricity and magnetism; the principles of design of permanent magnets are less well known and so will be reviewed here with special emphasis on those features which are important in the design of lightweight permanent magnets for microwave magnetrons.<sup>1</sup>

**13-1. Design of Permanent Magnets.**—The general type of magnetic circuit used with microwave magnetrons is shown in Fig. 13-1. The following symbols are used to define the geometry of the magnet and air gap:

- $l_g$  = length of air gap,
- $d_g$  = diameter of air gap,
- $A_g$  = area of air gap,
- $l_m$  = length of magnet,
- $A_m$  = area of magnet (neutral section).

To arrive at a relationship of these geometrical variables with the flux densities and field strengths associated with the magnet and the air gap, one applies the equations of continuity and conservation of energy to the magnetic circuit;

$$\int B \, dA = \text{const.}, \text{ for any cross section of the circuit,} \quad (1)$$

<sup>1</sup> See R. L. Sanford, "Permanent Magnets," *Bur. Standards Circ. C448*, for a more general discussion and for a bibliography of the subject.

and

$$\int \bar{H} d\bar{l} = 0, \text{ for any closed path around the circuit,} \quad (2)$$

where  $B$  is the flux density and  $H$  is field intensity or magnetizing force.

Equations (1) and (2) are difficult to integrate because of the flux leakage along the circuit and the uncertainty of the path of a given line of force. For this reason it is customary among magnet designers to define  $B_m$  and  $H_m$  as average values in the neutral section of the magnet and  $B_g$  and  $H_g$  as average values within the geometrical gap area. Approximations to the integral equations are then obtained by the use of leakage factors defined as

$$f, f' \quad B_m A_m = B_g A_g F, \quad (3)$$

$$H_m l_m = H_g l_g f. \quad (4)$$

Combining Eqs. (3) and (4) gives  $A_m l_m = (Ff/B_m H_m) B_g H_g A_g l_g$ . Using  $\rho$  as the density of the magnet material, one obtains an equation for magnet weight.

$$\text{Weight of magnet} = \frac{Ff\rho}{B_m H_m} B_g^2 A_g l_g, \quad (5)$$

where  $H_g$  and  $B_g$  are considered numerically equal in the gap.

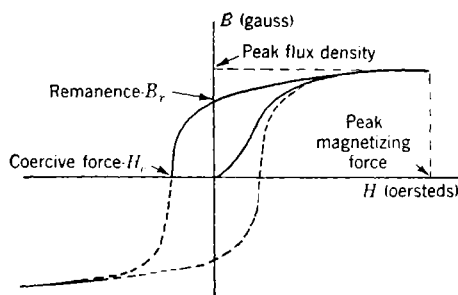


FIG. 13-2.—Typical hysteresis cycle of magnetic material.

This equation shows that the magnet weight is proportional to the leakage factors and to the volume of the air gap. The weight is also least for the maximum value of the product  $B_m H_m$ , which is known as the "energy product" because it is proportional to the energy per unit volume of magnetic material available for maintaining a magnetic field

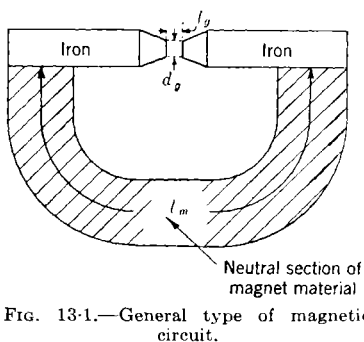


FIG. 13-1.—General type of magnetic circuit.

in a gap. Questions such as how to maximize the energy product and what values can be expected can be answered by studying the hysteresis cycle of the magnetic material. A typical hysteresis cycle is shown in Fig. 13-2. The solid line in the first quadrant is the path followed by the magnet material when the magnet is charged by applying the indicated peak magnetizing force and then reducing the magnetizing force to zero. For the present consideration the second quadrant of the cycle, resulting from a demagnetizing force due to the introduction of an air gap, is the important one because it is the region occupied by a working magnet. This second quadrant contains the so-called "demagnetization curve."

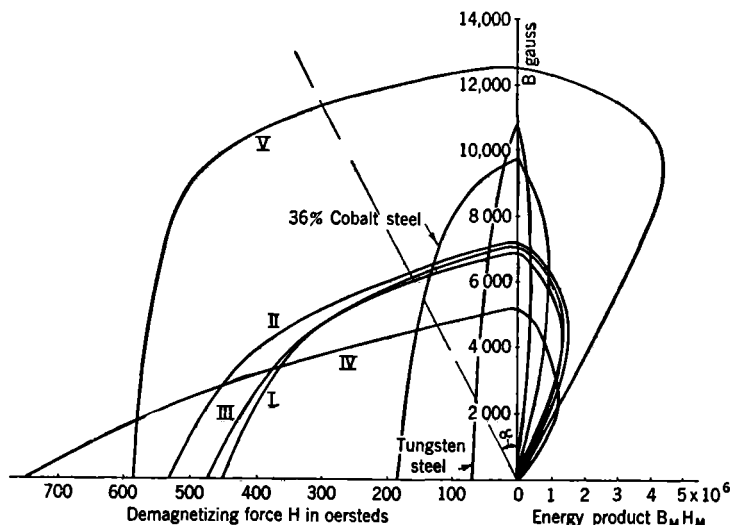


FIG. 13-3.—Demagnetization and energy product curves of Alnico alloys. (From the Arnold Engineering Co. Bulletin, "Permanent Magnets for Industry," and from the Indiana Steel Products Co., Permanent Magnets Manual No. 3.)

Such curves for several magnet materials are shown separately in Fig. 13-3, along with their corresponding  $(B_m H_m)$ -curves. The advantage of Alnico V from the point of view of weight conservation is patent, for its energy product is three times greater than the next best magnet material, Alnico II. In order to realize the maximum  $B_m H_m$  value of Alnico V of  $4.5 \times 10^6$ , the magnet must be operated at the point on the demagnetization curve of 9500 gauss flux density and 475 oersteds field strength. The point on the demagnetization curve at which a magnetic circuit will come to equilibrium upon the introduction of a gap may be expressed in terms of the angle  $\alpha$  shown in Fig. 13-3, which results from Eqs. (3) and (4).

$$\alpha = \tan^{-1} \frac{f l_g H_g A_m}{F l_m B_g A_g} \quad (6)$$

Thus for a magnetic circuit with an air gap ( $\mu = 1$ ) of given dimensions and for fixed leakage factors, the ratio of the area to the length of the magnet material should be adjusted for maximum  $B_m H_m$ . Figure 13-3 and Eq. (6) indicate that if the operating value of magnetic flux density is below 9500 gauss, the magnet must be decreased in cross-sectional area and increased in length (for the same magnet weight) in order to increase the magnet efficiency. Roughly, this adjustment is an increase in the magnetomotive force at constant reluctance with a corresponding increase

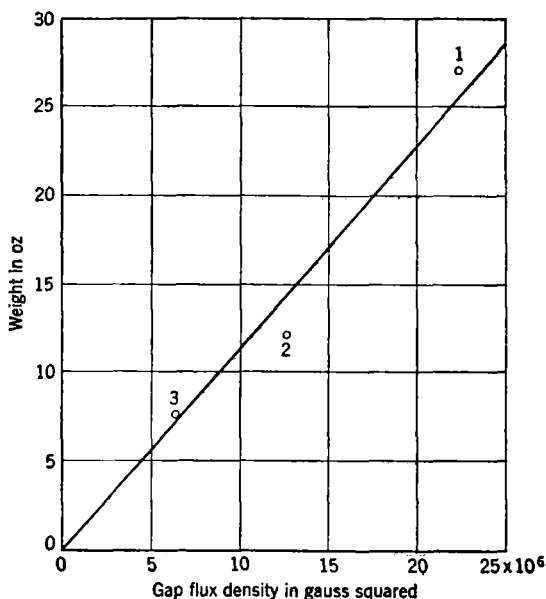


FIG. 13-4.—Variation of weight with the square of the gap flux density for a gap length of 0.312 in. For magnet 1:  $B_m = 7730$  gauss;  $H_m = 525$  oersteds;  $B_m H_m = 4.1 \times 10^6$ ;  $F = 28$ ; and  $f = 1.8$ .

in flux density. This balancing of magnetic reluctance and magnetomotive force is analogous to the case of a battery working into a resistance that is a nonlinear function of the current.<sup>1</sup>

Although Eq. (5) is only an approximate solution to the exact integral equations and the factors  $F$ ,  $f$ ,  $B_m H_m$ , and  $l_g$  are not independent, the equation does afford a convenient means of scaling from one set of conditions to another, particularly for small scaling factors. The equation predicts that the magnet weight should vary as  $B_g^2$  when the other quantities are assumed constant. This relationship is supported by experi-

<sup>1</sup> For a detailed discussion of the analogy between electric and magnetic circuits, see E. E. Staff of Massachusetts Institute of Technology, *Magnetic Circuits and Transformers*, Wiley, New York, 1944.

ence. The variation of  $B_g$  with the gap length  $l_g$  for a given form of magnet material as predicted by Eq. (5) is not obtained in actual practice because  $F$ ,  $f$ , and  $B_m H_m$  are strongly dependent on  $l_g$ . The data plotted in Figs. 13-4 and 13-5 exemplify these two cases; these data were taken using the iron pole tips described by Fig. 13-6. These curves are numbered to correspond to (1) the 27-oz 2J42 magnet, (2) the 12-oz 2J39 magnet, and (3) a 7.5-oz magnet similar in contour to the 2J39 magnet. The relationship between  $l_g$  and  $B_g$  is determined by the log plot of Fig. 13-5. The slopes of the lines for all three magnets are nearly the same and have a value of 1.06 rather than 2, the value predicted by Eq. (5).

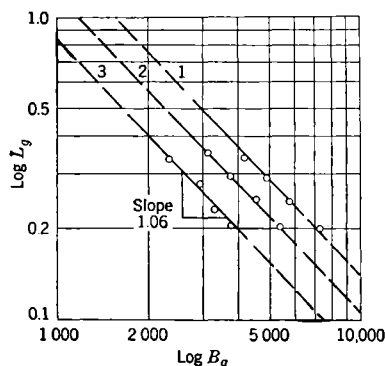


FIG. 13-5.—Log plot of gap length against flux density for three magnet designs.

Fig. 13-4 is in much better agreement with Eq. (5).

The usefulness of Eq. (5) is limited by the difficulty of calculating the leakage factors  $F$  and  $f$ . Methods for estimating these factors<sup>1</sup> have

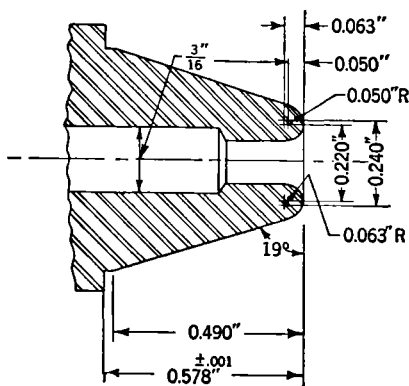


FIG. 13-6.—The 2J42 pole tip.

been devised, but none of them claim any great accuracy; hence greater reliance should be placed on experience obtained from similar circuits.

<sup>1</sup> E. M. Underhill, "Permanent Magnet Design," *Electronics*, **16**, 126 (1943); Sanford, *op. cit.*, p. 31; Staff, *op. cit.*, p. 105.

Flux leakage can be reduced if the following rules are followed:

1. The permanent magnet material should be located as near the gap as possible. Magnets 1 through 8 of Fig. 13-7 demonstrate this rule; the magnetic material is next to the air gap, and the iron yoke serves as a base.
2. The magnet material at all points should be worked at the optimum flux density  $B_m H_m$ . This is accomplished usually by increasing the

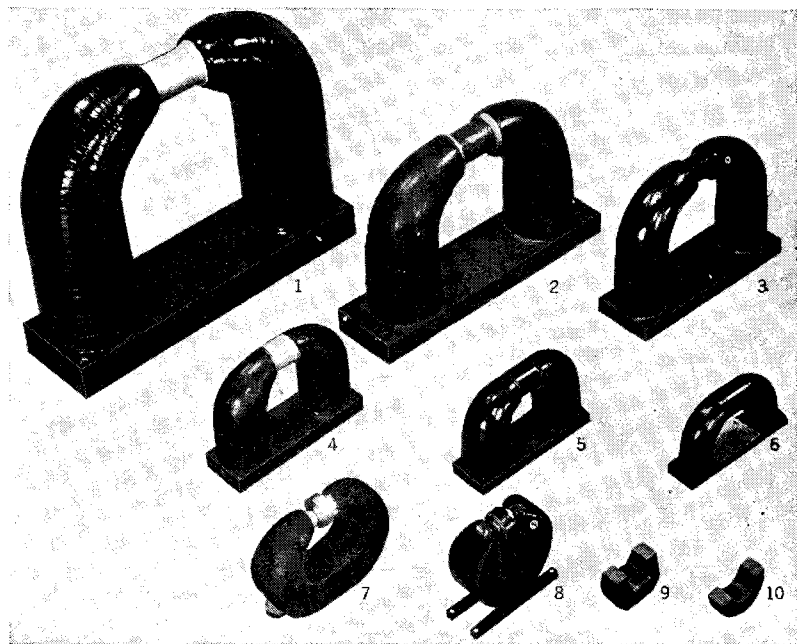


FIG. 13-7.—Magnetron magnets varying in weight from 250 lb to  $\frac{1}{4}$  lb.

cross section of the magnetic material as the distance from the air gap is increased.

3. In arrangements similar to that shown in Fig. 13-1 (except for the ends nearest the gap) the magnetic material should be kept separated as much as possible to prevent leakage across the enclosed region.
4. The angle of taper on iron pole tips should be the maximum that is consistent with saturation of the iron.

The latter is explained by reference to Fig. 13-8. For cylindrical pole tips as shown in Fig. 13-8a there will be less flux leakage across the space from one cylindrical surface to the other than in the case of the tapered tips

(truncated cones) shown in Fig. 13-8b. The flux leakage results in an increase of total flux in the iron with distance from the gap. Under the condition of constant cross-sectional area the flux density away from the gap will increase and the permeability decrease,<sup>1</sup> resulting in an increase in the reluctance of the iron. By tapering the iron to increase the cross-sectional area with distance from the gap, the reluctance can be maintained constant so that the iron will saturate uniformly along its length. This is done at the cost of increasing the flux leakage. If, in addition, the reluctance of the iron is maintained negligible compared with the reluctance of the gap, then the maximum magnetomotive force will appear across the gap.

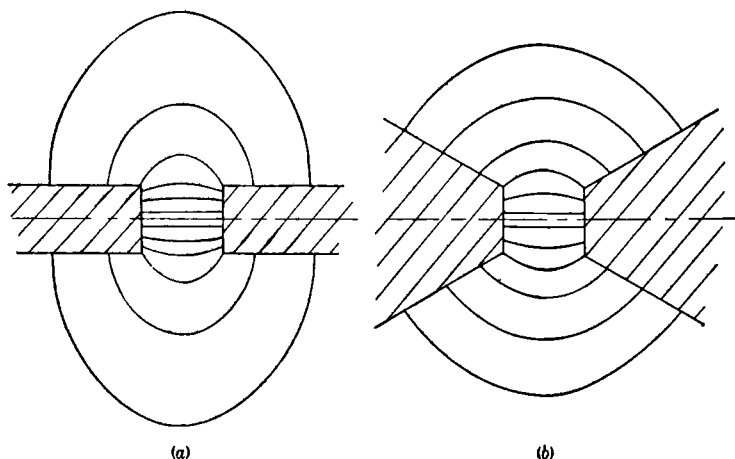


FIG. 13-8.—Plots of magnetic field.

If the field uniformity in the gap is to be determined by methods (see Sec. 13-5) where the contour of the iron is taken to be an equipotential surface, no parts of the iron in the neighborhood of the gap should be allowed to saturate below the working gap flux density. For this reason it is necessary to round off all corners to prevent saturation. Figure 13-6 shows the result of applying these principles to a pole-tip design. For a 0.312-in. separation of such tips no saturation occurs below 6000 gauss gap flux density. In cases where it is not important to know the exact field shape, the corners on the tips need not be removed.

Rules 1 to 4 are not always mutually consistent, and a compromise is usually necessary; the nature of the compromise depends on the particular application.

<sup>1</sup> See Staff, *op. cit.*, p. 23, for the magnetic properties of iron.



Figure 13-7 shows a variety of magnets that may serve as a basis for new designs; Table 13-1 gives the weight, field, and gap dimensions of these magnets.

TABLE 13-1.—PERTINENT DATA ON THE MAGNETS SHOWN IN FIG. 13-7

Magnet No.*	Weight, lb.	Approximate $B_o$ , gauss (stabilized 5%)	Gap length $l_o$ , in.	Gap diam. $d_o$ , in.	Remarks
1	250	3000	2.70	2.50	Iron base
2	100	2400	2.75	2.00	Iron base
3	42	3400	1.50	1.62	Iron base
4	14½	2500	1.40	1.62	Iron base
5	13½	2500	1.30	1.62	Iron base
6	6¾	1350	1.50	1.62	Iron base
7	13¾	4800	0.69	0.75	Alnico "C's" bolted together with iron spacer
8	8	4850	0.63	0.75	Alnico "C's" bolted together by aluminum base (no iron)
9	1¾	5000	0.28	→	Using iron pole pieces (5 oz) described in Fig. 13-6.
10	¾	3800	0.28		

\* Additional data on magnet weight and flux density are given in Chap. 19.

*Physical Properties of Alnico V.*—One of the most important physical properties of Alnico V for magnet design is the directional property of flux conductivity. This property is a result of the heat-treatment process to which Alnico V is subjected during manufacture. In the heat treatment the magnet material is cooled in the presence of a magnetic field, the direction of which is the same as the field to be generated by the working magnet. The shape of the Alnico V should conform as closely as possible to the magnetic field in which it is processed, and the difficulty of producing a processing field of any desired shape places a limitation on the possible shapes of the magnetic material. The bar magnet is the easiest to heat-treat because the necessary field can be produced between flat poles of an electromagnet. A C-shaped magnet like that of the 2J39 is not much more difficult to heat-treat because it can be treated in the fringing field of flat pole pieces. If one must deviate from these simple shapes, care should be taken to arrive at a shape consistent with the field shapes that can be obtained for heat treatment. Nevertheless, magnets of unusual shapes have been successfully made by locating ferromagnetic material in such a way as to distort a normally uniform field or a fringing field into the desired form.

In addition to the alignment of the magnetic field during heat treatment, a rapid quench is important. For this reason the volume of a

single piece of Alnico V must not be too great. To obtain a rapid quench for very large magnets it may be advantageous to make the magnet in several sections which finally are combined and held together with iron yokes to form a completed circuit.

Alnico V must be cast, and in this form it is coarse-grained, brittle, extremely hard, and nonforgeable. Because holes cannot be drilled economically, mounting holes are cored in the casting. Soft-iron inserts are cast into the magnet during the pouring process and later drilled and tapped; but because of the large shrinkage during cooling (2.6 per cent), this is successful only when the dimensions of the Alnico are large compared with the hole.

Flat surfaces can be ground to close tolerances, but cast tolerances are usually set by the magnet manufacturers at not less than  $\pm 0.015$  in. Arc welding of Alnico with stainless steel or phosphor bronze rods is only partially successful; soft soldering can be done if the surfaces are carefully prepared with an acid. The magnetic properties of Alnico V are impaired if it is raised to a temperature over  $1100^{\circ}\text{F}$  after the heat treatment.

Table 13-2 gives some additional properties<sup>1</sup> of Alnico V useful for design purposes.

TABLE 13-2.—PROPERTIES OF ALNICO V\*

Specific gravity.....	7.3
Electrical resistance at $25^{\circ}\text{C}$ .....	$47 \times 10^{-6} \Omega\text{cm/cm}^2$
Tensile strength.....	5450 lb/in. <sup>2</sup>
Transverse modulus of rupture.....	10,200 lb/in. <sup>2</sup>
Hardness, "Rockwell C".....	45-55
Coefficient of thermal expansion.....	$11.3 \times 10^{-6}/^{\circ}\text{C}$

\* Courtesy of E. M. Underhill.

**13-2. Magnet Charging.**—The magnet material is magnetized by taking it through the first quadrant of its hysteresis cycle as discussed in Sec. 13-1. In order to reach the maximum value of magnetic flux density, every part of the Alnico V must be magnetized to the point of practical saturation, and for this a magnetizing field of about 3000 oersteds applied to the Alnico in the direction of the working field is necessary. If the magnetic material is properly heat-treated and the above value of field strength is applied to the Alnico V, a remanence value of magnetic flux density of 12,600 gauss should be realized as shown in Fig. 13-3.

An electromagnet that can supply the required field provides a convenient means of charging bar magnets, as they require only straight fields. Magnetron magnets, however, are usually of such contour that

<sup>1</sup> E. M. Underhill, "Mechanical Problems of Permanent Magnet Design," *Electronics*, 17, 126 (1944).

it is simpler to charge them by surrounding the material with one or more solenoids. In this arrangement soft-iron bars are placed across the ends of the magnetic material so that a closed magnetic circuit results. The solenoid may be excited by connecting it across a d-c source with high current capacity, but a better method is to employ a high-current impulse. Condenser discharge and half-cycle<sup>1</sup> impulse chargers have been employed. A typical circuit for the condenser discharge method is shown in Fig. 13-9. The storage condenser consists of a bank of 100 40- $\mu$ f dry electrolytic condensers connected in parallel by heavy leads. The condensers, which have a rating of 500 working volts, are charged to 400 volts by a small 200-ma d-c power supply and discharged through

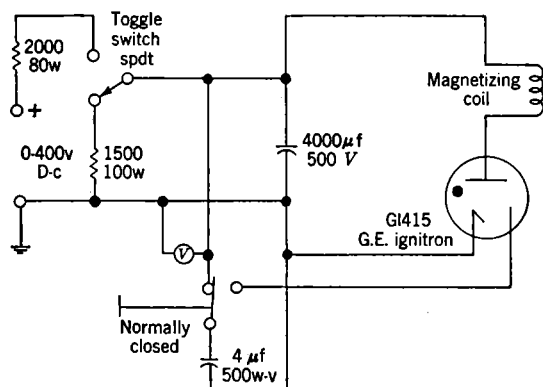


FIG. 13-9.—Circuit of condenser-discharge method for charging magnets.

an ignitron (GL415) in series with the magnetizing coils. Peak currents of 1000 amp can be obtained in this way. Care must be exercised when a condenser discharge is used for charging to prevent oscillations in the circuit and the resulting reversed magnetic fields. In this circuit the ignitron serves this purpose.

The magnetizing coil must be constructed so that for the pulse current obtainable a field of 3000 oersteds in air is produced. If the length of the coil is short compared with the magnet length, the coil should be moved along the magnet to apply the maximum magnetizing field to each portion of the Alnico V. Care should be taken not to cross-magnetize the magnetic material.

If the magnetron is the "packaged type," that is, with the magnet permanently attached to the tube, the magnet can be charged separately, stored with an iron "keeper," and then slid onto the magnetron so that

<sup>1</sup> See H. W. Lord, "A Half-cycle Magnetizer with Thyatron Control," *Gen. Elec. Rev.*, 40, 418 (1937).

the magnet is never made to operate into a gap greater than the working gap.

**13-3. Magnetic Stabilization.**—Inspection of a performance chart shows that the characteristics of a magnetron are such that constancy of magnetic field is extremely important if constant power input, power output, and magnetron frequency are to be maintained. This section will discuss qualitatively the phenomena of magnet stability and give some quantitative information on the effect of various demagnetizing forces.

*Stability against Change in Air Gap or against Stray Demagnetizing Fields.*—Figure 13-3 is useful in obtaining a qualitative understanding of

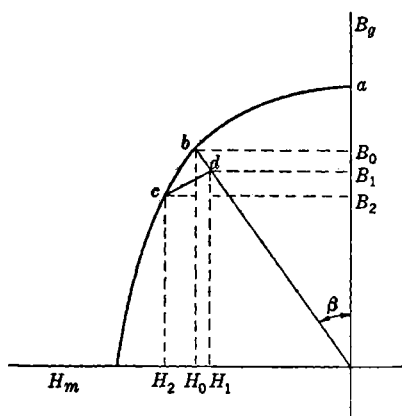


FIG. 13-10.—Variation of gap flux density with demagnetizing force.

magnet stability. It is preferable for this purpose, however, to plot the flux density in the air gap  $B_g$  along the vertical axis instead of the flux density in the magnet  $B_m$ , because  $B_g$  is the variable of direct concern. According to Eq. (3), this amounts to multiplying the vertical axis of Fig. 13-3 by the factor  $A_m/A_g F$ . Referring now to Fig. 13-10,  $a$  is the point at which a gapless magnetic circuit will come to equilibrium after the charging field is applied and then reduced to zero. If the keeper is removed, introducing an air gap of length  $l_g$ , the circuit will be in

equilibrium at point  $b$ , where  $b$  is defined according to Eq. (4), and may be expressed in terms of the angle  $\beta$  thus:

$$\tan \beta = \frac{fl_g}{\mu l_m} \quad (7)$$

The flux density  $B_0$  corresponding to the point  $b$  has become known as the "saturation value" of flux density. If a further demagnetizing force  $H_2 - H_0$  is applied and then removed, the circuit will first follow the major hysteresis curve  $b$  to  $c$  and then the minor hysteresis loop  $c$  to  $d$ . The result of the demagnetizing force is a decrease in magnetic flux density of  $B_0 - B_1$ . If the same demagnetizing force is applied and removed a second time, the magnet will follow very closely the same minor hysteresis loop and return to the point  $d$  with a negligibly small change in  $B$ . Hence  $B_1$  has become known as the "stabilized value" of flux density, stabilized for a demagnetizing force smaller than  $H_2 - H_1$ .

The previous discussion is valid for demagnetization effects due to the introduction of air gaps into the magnetic circuit or to the presence of neighboring a-c or d-c magnetic fields. Quantitatively the resistance of magnetic materials to these demagnetizing forces is a function of the coercive force of the material. As seen in Fig. 13-3, Alnico IV is better than Alnico V in this respect. [A recently reported new Alnico, Alnico IX, has an even higher coercive force (approximately 950 oersteds), but like Alnico IV its energy product is low— $1.8 \times 10^6$ .] Figure 13-11 shows the effect of stray demagnetizing fields on Alnico V compared with tungsten- and cobalt-alloy steels. The coercive forces for the tungsten and cobalt steels are 65 and 230 oersteds, respectively. It has been arbitrarily established that for magnetron magnets, the operating flux density  $B_1$  (see Fig. 13-10) is set from 3 to 5 per cent below the saturation value  $B_0$ . This controlled demagnetization is most conveniently accomplished by subjecting the Alnico to an a-c magnetic field. For magnetron magnets separate from the tubes, this can be done by alternately applying an a-c field and measuring the resultant flux density (see Sec. 10-5). It is also customary to "keeper stabilize" the magnet. This is done by inserting and removing the magnet keeper three or four times. On the  $BH$  curve of Fig. 13-10 this amounts to running up and down the minor hysteresis loop  $c-d$ , reducing the effects of the actual nonlinearity and nonreversibility of the path  $c-d$ .

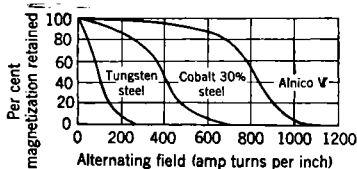


FIG. 13-11.—Resistance of magnetic materials to stray demagnetizing fields. (From the Arnold Engineering Co. Bulletin "Permanent Magnets for Industry.")

**Temperature Stability.**—The effect of temperature changes on the

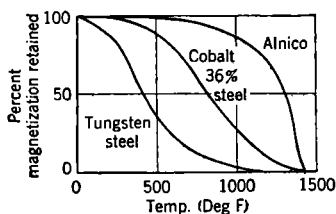


FIG. 13-12.—Resistance of magnetic materials to temperature changes. (From the Arnold Engineering Co. Bulletin "Permanent Magnets for Industry.")

magnetic properties of Alnico V is of a different nature from the effects discussed previously. This effect from  $-180^{\circ}$  to  $+500^{\circ}\text{C}$  is reversible, so that any temperature cycle between these values results in no permanent change in field strength. A typical value for this change is  $-0.25$  per cent in field per degree centigrade. This change in magnetic field with temperature produces a change in magnetron current that depends on the dynamic impedance and

rate of change of voltage with magnetic field of the particular magnetron. Figure 13-12 shows the behavior of Alnico over a wide range of temperature, along with a comparison of Alnico with some alloy steels.

*Effects of Neighboring Ferromagnetic Material.*—Neighboring ferromagnetic material has two effects on a magnetic circuit. The first is shunting of magnetic flux by the material, which has the same effect on the flux density in the magnet as a decrease of gap length; and hence, if the magnet has been stabilized to a great enough degree, no residual change in field strength remains after the material is removed. The second effect is a rearrangement of the magnetic dipoles in the magnetic material. This does leave a permanent effect unless the magnet is recharged. The magnitude of degaussing, produced by the proximity of ferromagnetic material, depends upon many factors, such as the size of the magnet and ferromagnetic object and the location of the point at which contact is made. An idea of the order of magnitude of this effect can be had from the fact that magnet 5 in Fig. 13-7 is degaussed by 5 per cent from the saturation value if an iron bar  $\frac{3}{4}$  in. in diameter and 6 in. in

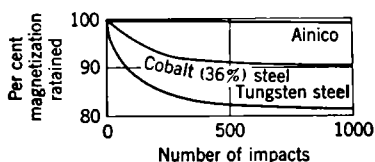


FIG. 13-13.—Resistance of magnetic materials to vibration effects. (From the Arnold Engineering Co. Bulletin, "Permanent Magnets for Industry.")

length is touched directly on the Alnico V near a magnet pole. This degaussing effect drops off rapidly with distance of approach of the iron bar, so that the degaussing is only 0.8 per cent if the bar is brought within  $\frac{7}{8}$  in. of the same spot as above. For this reason magnetron magnets are always covered with a

protecting material to prevent direct contact with magnetic material, particularly in the neighborhood of the magnet poles.

*Vibration Effects.*—Even though the effect of vibration on Alnico V does not appear important for any practical conditions associated with magnetron magnets, data are presented in Fig. 13-13 showing the resistance of Alnico and some alloy steels to vibration.

**13-4. Field Uniformity.**—The efficiency of a magnetron depends upon the magnetic-field uniformity within the interaction space. Except at the very ends of the interaction space (see Sec. 12-11), a uniform field is desirable.

The need for uniformity arises from the large changes in current that result from small changes in magnetic fields. The performance chart of a typical magnetron is shown in Fig. 19-44, and from this it may be seen that a change in field from 5100 to 5330 gauss results in a 2 to 1 change in current. Thus, a variation of this amount in magnetic field along the height of the anode will result in operation over the low-field regions at twice the current density of the high-field regions. Damage to the cathode at these low-field high-current points has frequently been observed. Axial uniformity to better than 5 per cent is a safe rule to follow.

For magnetrons having separate magnets with flat pole pieces, this condition is satisfied if the gap length is equal to or less than the gap diameter, provided the anode diameter of the magnetron is less than half the gap diameter. When tubes have attached magnets, often the pole tips have holes in them to admit the cathode structure. Up to a certain ratio of hole diameter to anode diameter, the holes tend to increase the field uniformity in the center of the region between the tips. Very large holes must be drilled in magnetrons with a large number of resonators, as the ratio of cathode to anode diameters becomes large, and undesirable field configurations are likely to occur. With 16 or more resonators it has been found that this hole becomes so large and the magnetic field so distorted that very low efficiencies result. To correct this, magnetic material is attached to the cathode structure, thereby effecting a concentration of flux toward the axis of the magnetron near the ends of the anode, and approximating the desired form as discussed in Sec. 12-11. The material attached to the cathode structure must not saturate below the working flux density, and, furthermore, the Curie point of the material must be above the cathode temperature. The magnetic material Permendur (50 per cent Fe, 50 per cent Co) meets these requirements satisfactorily. This material was used in the 4J52 (see Chap. 19), where it replaces the usual nickel electrostatic shields to prevent electron leakage at the anode ends. In addition to producing the desired field shape, it also reduces the effective gap between the poles.

**13-5. Testing and Measurements.**—The testing of permanent magnet materials to determine the shape of the hysteresis cycle<sup>1</sup> as well as methods for determining flux density<sup>2,3</sup> in the gap or neutral section of a finished magnet are well standardized and will not be discussed here. It should be emphasized, however, that the fields in the gaps of magnetron magnets are rarely uniform, and hence the measurement of the average flux density in one of these gaps depends largely upon the size and shape of the test coil employed. For this reason the Signal Corps and Bureau of Ships have established a set of standard test coils for measuring the average flux density over a volume corresponding to that of the interaction space.<sup>4</sup> The expression “flux density” as used in this chapter means the average flux density over the area occupied by the appropriate test coil.

<sup>1</sup> R. L. Sanford, “Magnetic Testing,” *Bur. Standards Circ.* C415, 1937.

<sup>2</sup> F. A. Laws, *Electrical Measurements*, McGraw-Hill, New York, 1938.

<sup>3</sup> Attention is drawn to a novel fluxmeter developed by the Marion Electrical Instrument Co., Manchester, N.H., which is extremely useful for making quick checks on flux density. *Rev. Sci. Instruments*, 17, 41 (1946).

<sup>4</sup> The details of the standard “200” coil suitable for gaps and magnetic fields encountered in 3-cm magnetrons may be obtained by writing to the U.S. Bureau of Standards.

**Field Shape.**—The shape of the magnetic field in the interaction space is of considerable importance, and it is often necessary to determine the field shape for a new tube design. If the volume of the air gap is large compared with the volume of the field-measuring device, the field pattern can be obtained by direct measurement of the field intensity at several points over the gap. For the air gaps associated with magnetrons at 5-cm wavelengths or longer, field plots can be made with a magnetometer developed by the General Electric Research Laboratories having a sensitive element only  $\frac{1}{8}$  in. long and  $\frac{1}{8}$  in. in diameter.

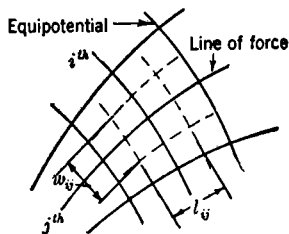


FIG. 13-14.—Two-dimensional field plot.

Equipotential plots of the electrostatic fields between model pole tips immersed in water give the shape of the magnetic field directly if three dimensional models are used.<sup>1</sup>

A geometrical method of obtaining flux plots satisfying Laplace's equation has been developed by Crout.<sup>2</sup> This method is useful in a wide variety of applications and will be considered in detail.

For simplicity the method will be described by considering the case of a static two-dimensional magnetic field. Suppose a number of lines of force and equipotentials be drawn as in Fig. 13-14 and the tubes of flux and the strips between adjacent equipotentials be numbered according to the following definitions:

- $u$  = potential at any point,
- $v$  = flux between a reference line of force and that point,
- $\Delta u_1, \Delta u_2, \dots$  = potential difference across the various strips formed by the equipotential lines,
- $[i, j]$  = curvilinear rectangle comprising the region common to the  $i$ th strip and  $j$ th tube of flux,
- $\Delta v_1, \Delta v_2, \dots$  = fluxes in the flux tubes of unit depths seen as  $[i, j]$  from above,
- $R_{ij}$  = reluctance of the volume of unit depth seen as  $[i, j]$  from above,
- $E_{ij}$  = energy in the volume of unit depth seen as  $[i, j]$  from above,
- $\mu$  = permeability of the medium containing the field (assumed constant throughout the field).

<sup>1</sup> V. K. Zworkin and G. A. Morton, *Television*, Wiley, New York, 1940, p. 73; L. M. Myers, *Electron Optics*, Van Nostrand, New York, 1939, p. 129; A. Kolin, "Mercury Jet Magnetometer," *Rev. Sci. Instruments*, **18**, 209 (1945).

<sup>2</sup> Prescott D. Crout, "The Determination of Fields Satisfying Laplace's, Poisson's, and Associated Equations by Flux Plotting," RL Report No. 1047, Jan. 23, 1946.



Accordingly,

$$R_{ij} = \frac{\Delta u_i}{\Delta v_j} \approx \frac{l_{ij}}{\mu w_{ij}}, \quad (8)$$

and

$$E_{ij} = \frac{\Delta u_i \Delta v_j}{8\pi}. \quad (9)$$

Now if the  $\Delta u_i$ 's are all equal and if the  $\Delta v_j$ 's are all equal, the curvilinear rectangles will all be similar and have the same reluctance and contain the same field energy. Furthermore, the field will consist of curvilinear squares if the spacings of the lines are such that  $\mu(\Delta u/\Delta v) = 1$ . Therefore, a map of the field can be obtained by sketching in a network of curvilinear squares by trial and error. The accuracy of the plot may be improved in any region by further subdividing the initial squares. When the field is known to have definite symmetry, this fact should be used to reduce the size of the required map.

To prove that the "square" flux plot is a possible field, one resorts to the definition of a gradient to obtain

$$\frac{|\Delta u|}{|\Delta v|} = \frac{l_{ij}}{w_{ij}} \quad (10)$$

and to Eq. (8) to show that

$$\frac{|\nabla u|}{|\nabla v|} = \frac{1}{\mu} = K = \text{const. for all points.} \quad (11)$$

Hence the gradients and the partial derivatives of  $u$  and  $v$  are related as in Fig. 13-15, from which it follows that

$$\frac{\partial u}{\partial x} = K \frac{\partial v}{\partial y} \quad (12)$$

and

$$\frac{\partial u}{\partial y} = -K \frac{\partial v}{\partial x}. \quad (13)$$

By differentiating Eq. (12) with respect to  $x$  and Eq. (13) with respect to  $y$  and adding, one obtains Laplace's equation:

$$\frac{\partial^2 u}{\partial x^2} + \frac{\partial^2 u}{\partial y^2} = 0, \quad (14)$$

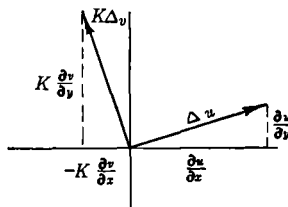


FIG. 13-15.—Relation between gradients and partial derivatives of  $u$  and  $V$ .

and similarly,

$$\frac{\partial^2 v}{\partial x^2} + \frac{\partial^2 v}{\partial y^2} = 0. \quad (15)$$

By similar arguments one can arrive at the conditions for the case of an axially-symmetrical three-dimensional field, which is the case

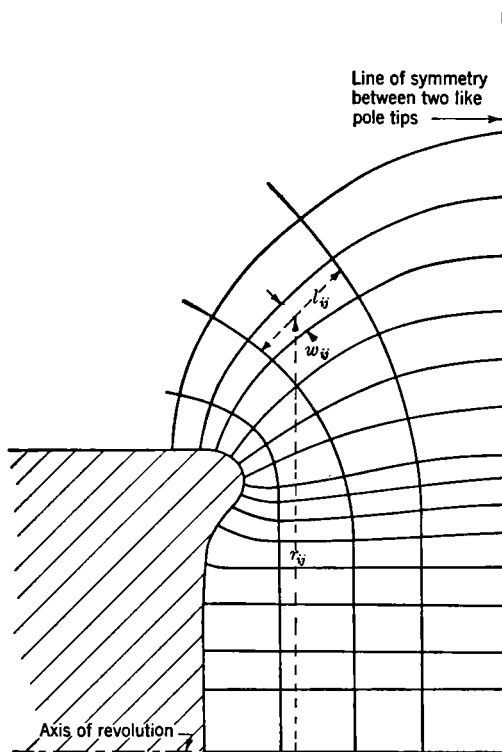


FIG. 13-16.—Flux plot of magnetron pole tip.

usually met in magnetron-magnet design. Using the same notation as before but rotating  $[i, j]$  through an angular depth of 1 radian to form the element of volume rather than taking a linear depth of 1 cm, one can say

$$R_{ij} = \frac{\Delta u_i}{\Delta v_j} \approx \frac{lij}{\mu r_{ij} w_{ij}} \quad (16)$$

and

$$E_{ij} = \frac{\Delta u_i \Delta v_j}{8\pi}, \quad (17)$$

where  $r_{ij}$  is the radius of the center of  $[i, j]$ . Rather than a network of curvilinear squares, the plot must be constructed to meet the condition

$$\frac{l_{ij}}{w_{ij}} = Kr_{ij},$$

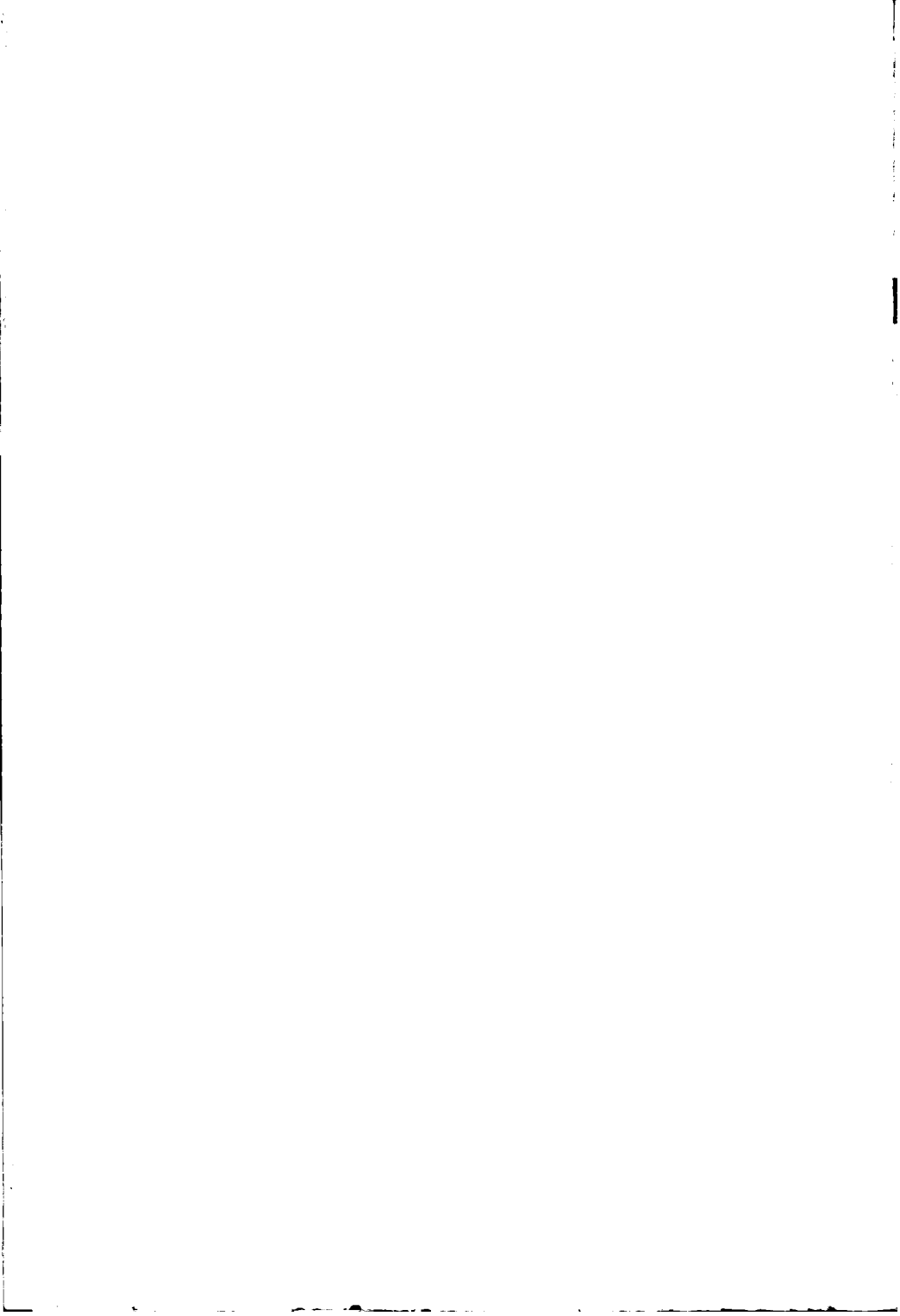
where

$$K = \frac{\mu \Delta u_i}{\Delta v_j} = \text{const.} \quad (18)$$

Figure 13.16 shows the result of the application of this method to the problem of magnetron pole-tip design.

In addition to being a quick method for obtaining a plot of any desired accuracy, this has the advantages of being applicable to peculiar boundary conditions, of giving a complete picture of the field, and of conveying an idea of the relative importance of the various factors that determine the field.<sup>1</sup>

<sup>1</sup> For application of the method to several additional cases, see the original report by Crout.



## PART IV

# TUNING AND STABILIZATION

One of the most inconvenient features of microwave magnetrons is the difficulty of making them tunable. Because the resonant circuits are within the vacuum envelope, they are rather inaccessible, and changing either their capacitance or inductance presents a mechanical problem of some intricacy. The problem is complicated further by the general limitations on space and the requirement that the tuning mechanism leave the normal resonances relatively undisturbed.

Considerable effort was expended in making magnetrons tunable, as this feature adds greatly to their usefulness. Not only does tunability permit a single magnetron to operate on a number of frequencies, but also it is essential if operation at a precise frequency is required.

Two distinct kinds of tuning exist. In one, the variation in frequency is accomplished by mechanical means. Here the rate at which tuning can be accomplished is slow, but the range of tuning is large. This topic is the subject of Chap. 14. The second kind is the so-called "electronic tuning," in which the frequency is varied by injecting a beam of electrons into a region containing r-f fields. Electronic tuning (Chap. 15) provides only a small tuning range, but the rate of tuning can be very rapid. It is thus well suited to applications requiring frequency modulation.

Stabilization of frequency is closely relative to the problem of tuning, and for this reason it is included in this part of the book. Both tuning and stabilization are aspects of the problem of control of frequency and must be considered together because high stabilization and large tuning range are incompatible. The question of stabilization also arises in other chapters. It appears in Chap. 6, "Interactions of the Electrons and the Electromagnetic Fields," because the frequency of oscillation is affected by space-charge conditions; it appears in Chap. 8, "Transient Behavior," because stabilization affects mode changing; and it appears in Chap. 10 "Design," because the design of a magnetron is influenced by the degree of stabilization required.



## CHAPTER 14

### MECHANICAL TUNING

BY W. V. SMITH

**14-1. General Considerations.**—A mechanically tunable magnetron is one whose resonant frequency is changed by moving some element in the resonant circuit associated with the magnetron. In general, the motion must take place in vacuum, although in low-power magnetrons the moving parts may be in air, separated by a dielectric vacuum seal (usually glass) from the high-vacuum portion of the tube. A tuning method is classed as “mechanical” whenever the frequency change is the result of a motion—whether the primary driving force is mechanical, thermal, magnetic, or any other. The term “electronic tuning” (Chap. 15) is reserved for frequency changes resulting from the injection of electrons into the resonant system.

From a consideration of circuits, two classes of tuning may be distinguished: symmetrical and unsymmetrical. In symmetrical tuning, the circuit elements are changed in a manner that preserves the angular symmetry of the operating mode which, unless otherwise specified, will be taken as the  $\pi$ -mode. In unsymmetrical tuning, this angular symmetry is not preserved; as a rule, only one side resonator is tuned, generally by means of a coupled circuit. The lack of symmetry results in alteration of the r-f mode patterns over the tuning range (Sec. 4-5) with consequent lowering of electronic efficiency at wavelengths removed from the unperturbed tube wavelength. Symmetrical tuning avoids this difficulty, often, however, by the loss of other advantages.

The three main subdivisions of symmetrical tuning are inductive tuning, capacitive tuning, and tuning by a coupled circuit. In inductive tuning, the inductance of the resonant circuit is varied by changing the surface-to-volume ratio in a high-current region of the oscillator (see Element *A* in Fig. 14-1). The unloaded  $Q$  is also changed—an important consideration at short wavelengths. In capacitive tuning, the capacitance of a gap is changed. Because this capacitance (see Element *B* in Fig. 14-1) is connected across adjacent, oppositely charged vanes, the voltage across the gap remains constant whereas the breakdown voltage varies with the gap width. This consideration is important at high-voltage levels. Some conduction current flows in the capacitive regions of short-wavelength tubes where only displacement current would exist

at long wavelengths. This conduction current results in skin losses that will somewhat lower the unloaded  $Q$  of the tube because of the small surface-to-volume ratio of these capacitive regions. The principles of coupled-circuit tuning are more involved and will be discussed later.

From the standpoint of operation, the extent of the tuning range is determined by mechanical limitations, by sparking across high-field regions in the tuner, by the falling off of efficiency, by mode-shifting, and, in special cases, by variation of some other of the many magnetron properties that can alter over the tuning range.

Most of these properties are independent of whether the tube operation is pulsed or c-w. Two properties, however, are not independent; in a pulsed tube a spark is extinguished between pulses, whereas in a c-w tube a spark, once initiated, is maintained. If the spark is an r-f spark (becoming an arc) in the tuning mechanism, it may persist without destroying the tube, but it will alter the tube wavelength, often drastically. The nature of the mode-shifting also differs between pulsed and c-w magnetrons. If the tuning range of a pulsed tube is extended to a point where mode-shifting occurs, the percentage of pulses firing in the wrong mode increases, finally becoming intolerably high.

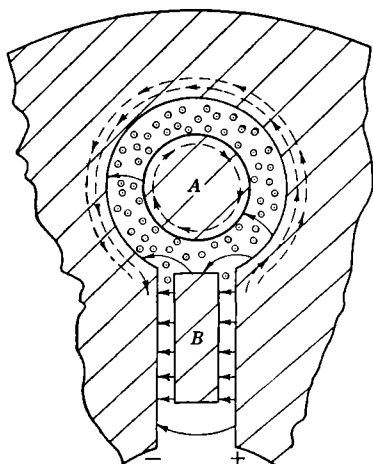


FIG. 14-1.—Cross section of a hole-and-slot side resonator in a magnetron tuned by the inductive element  $A$  and the capacitive element  $B$ .  $\odot$  is the r-f magnetic field directed into the page;  $\rightarrow$  is the r-f electric field; and  $-\cdot-\cdot-$  is the r-f current.

When the tube operation is c-w, however, the tube may be tuned to this range and sometimes considerably beyond without jumping modes. If the tube is turned off and restarted in this region, however, it will start in the wrong mode. Thus there is a "hysteresis" effect present in c-w tunable tubes that is not present in pulsed tubes.

One property of magnetrons that is common to all tunable tubes is the variation in the scale point (see Chap. 10) with a fixed operating point caused by the fact that the normalized parameters are functions of  $\lambda$ . By using the scaling laws developed in Sec. 10-6, this variation may be evaluated for a magnetron operating at constant  $B$  and  $I$  but with varying  $\lambda$ . The physical dimensions of the cathode-anode region are assumed constant. If  $I_1$ ,  $B_1$ , and  $V_1$  are defined as the operating parameters at  $\lambda_1$ ;  $I_1/g_1$ ,  $B_1/\mathfrak{G}_1$ , and  $V_1/v_1$  as the normalized parameters at  $\lambda_1$ ; and



$I_2$ ,  $B_2$ ,  $V_2$ ,  $I_2/g_2$ ,  $B_2/\mathfrak{B}_2$ , and  $V_2/\mathfrak{V}_2$  as the corresponding quantities at  $\lambda_2$ ; then, from the conditions that

$$I_1 = I_2 \quad \text{and} \quad B_1 = B_2 \quad (1)$$

and from the scaling laws

$$\frac{I_1}{\frac{g_1}{g_2}} = \left(\frac{\lambda_1}{\lambda_2}\right)^3 \quad \text{and} \quad \frac{B_1}{\frac{\mathfrak{B}_1}{\mathfrak{B}_2}} = \frac{\lambda_1}{\lambda_2} \quad (2)$$

and from Eq. (10-32), where it is shown that

$$\frac{V}{\mathfrak{V}} = 2 \frac{B}{\mathfrak{B}} - 1 + \frac{2 \left(\frac{B}{\mathfrak{B}} - 1\right)^2}{\left(\frac{B}{\mathfrak{B}}\right)^3} \frac{I}{g}, \quad (3)$$

the value of  $(V_1/\mathfrak{V}_1)/(V_2/\mathfrak{V}_2)$  may be found. Its wavelength dependence is complicated. For low-scale currents and high-scale magnetic fields, however,  $V/\mathfrak{V}$  is proportional to  $\lambda$ . Hence, because

$$\frac{\mathfrak{V}_1}{\mathfrak{V}_2} = \left(\frac{\lambda_2}{\lambda_1}\right)^2$$

(from Sec. 10-6),

$$\frac{V_1}{V_2} \approx \frac{\lambda_2}{\lambda_1} \left[ \frac{\frac{B}{\mathfrak{B}} \gg 1}{\frac{I}{g} \ll \left(\frac{B}{\mathfrak{B}}\right)^2} \right]. \quad (4)$$

Because the qualifying conditions on Eq. (4) hold in the operating region of most tubes, it is necessary to vary the tube voltage approximately inversely with the wavelength in order to maintain constant current at a constant magnetic field.

The above variations in scale point and voltage will result in a variation in efficiency, in output power, and in the current at which the tube changes modes. In view of the wide range of scale points at which tubes have been operated successfully, however (see Sec. 10-9), these variations do not, in general, limit the tuning range. It is to be noted that the optimum loading of a magnetron also varies over the tuning range and that for tuning ranges with ratios of the extreme wavelengths from 1 to 1.5, a deliberate variation in the loading can partly compensate for the change in scale point.<sup>1</sup> The loading is made lightest at the long-wavelength limit where the high-scale currents approach the region where mode changes occur.

<sup>1</sup> An intentional variation of load over the tuning range has been incorporated in some General Electric designs of wide tuning range.

Attainable tuning ranges for multiresonator magnetrons vary widely with resonant-system designs. The widest ranges (extreme-wavelength ratios of 1 to 1.5) have been obtained with symmetrical tuning on resonant systems having wide mode separation and dimensions small compared with a wavelength. These resonant-system properties are consistent with c-w designs at the longer wavelengths of from 20 to 50 cm or longer, that is, short, low-voltage (1 to 5 kv) resonant systems with a small number of side resonators (6 to 12). The difficulties of shorter wavelengths and higher voltages are reflected in the 10 per cent tuning range attainable at 3-cm radiation for a 12-kv resonant system with 12 resonators (the 2J51 magnetron of Chap. 20).

#### INDUCTIVE AND CAPACITIVE TUNING

In practice, inductive- and capacitive-tuning methods are generally symmetric. A case of unsymmetric tuning of this type is mentioned in Sec. 14-5.

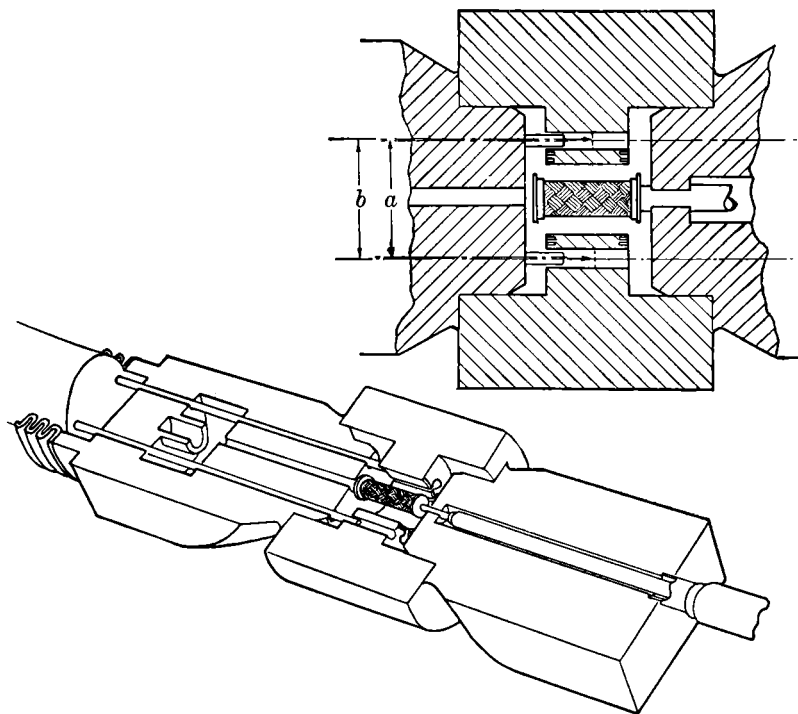


FIG. 14-2.—The sprocket-tunable magnetron 2J51 developed at Columbia University and Bell Telephone Laboratories. (a) Pitch diameter of the pins; (b) the pitch diameter of the resonator holes.

**14.2. Symmetric Inductive Tuning.**—The name “sprocket tuning” has been applied to a form of symmetric inductive tuning illustrated by the 2J51 magnetron shown in Fig. 14-2. This tube was developed at the Columbia and Bell Telephone Laboratories; its resonant system is a symmetric, strapped, 12-oscillator anode block of the hole-and-slot type. A round pin is inserted through the pole piece into each hole of the anode block; the pins are moved by means of a diaphragm or bellows. The effect of the pins is to decrease the inductance of each side resonator and hence to lower the resonant wavelength of the tube. The complete theory of the mode spectrum of this type of tube as a function of pin penetration, etc., is given in Sec. 4-6. The features of this theory that are useful for design purposes will be summarized briefly.

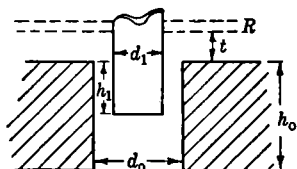


FIG. 14-3.—Cross section of the pin-to-hole region of one side resonator in a sprocket-tunable magnetron.

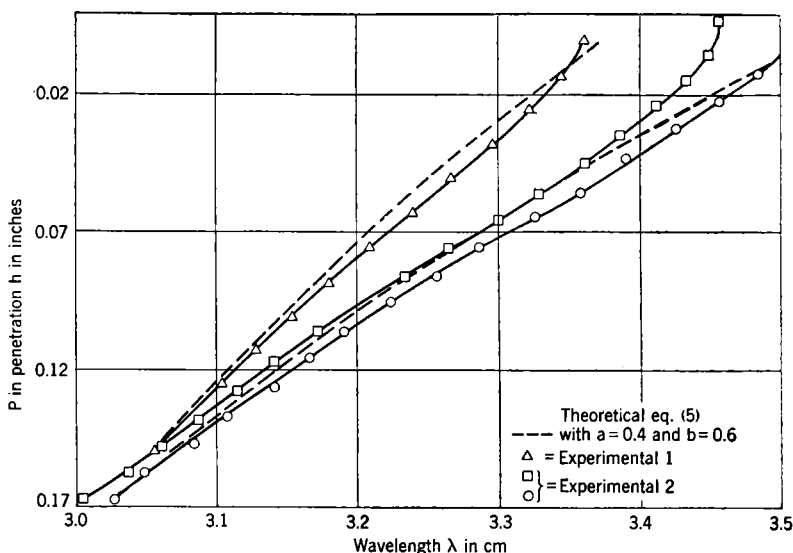


FIG. 14-4.—Observed and computed tuning curves for the sprocket-tunable magnetron. The dimensions given in Table 14-1 were used for the experimental tubes and the calculations.

The wavelength separations of the conventional modes do not vary greatly over the tuning range, and the wavelength of the main mode is given by the following simple formula:<sup>1</sup>

<sup>1</sup> P. Kusch and A. Nordsieck, “The Tuning Properties of Tunable Magnetrons in the 3-cm Band,” NDRC 14-234, p. 2, Jan. 11, 1944.

$$\frac{\lambda_0}{\lambda_1} = a + b \sqrt{1 + \frac{h_1 d_1^2}{h_0 (d_0^2 - d_1^2)}} \quad (5)$$

The dimensions entering Eq. (5) are shown in Fig. 14-3;  $\lambda_0$  is the wavelength at zero pin penetration;  $\lambda_1$  is the wavelength at penetration  $h_1$  (measured from the top of the anode block);  $h_0$  is the anode length;  $d_0$  the hole diameter;  $d_1$  the pin diameter; and  $a + b = 1$ . It is seen that for  $a = 0$  and  $b = 1$ , Eq. (5) may be derived from the simplest lumped-constant analogy in which the inductance is assumed localized in the holes, proportional to the area, and inversely proportional to the length of the hole. The current flow in this lumped-constant picture is circumferential around the pins, as shown in Fig. 14-1. Thus, because there is no longitudinal current flow, the nature of the contacts made by the pins with the pole piece is unimportant.

For the 725 anode block,  $a = 0.4$  and  $b = 0.6$  when

$$0.6 < \frac{d_1}{d_0} < 0.75.$$

Typical tuning data are shown in Fig. 14-4. The check with the semi-empirical Eq. (5) is seen to be excellent except in the fringing-field region of small pin penetrations.

TABLE 14-1.—TUBE DIMENSIONS\* FOR THE SPROCKET-TUNABLE MAGNETRONS OF FIG. 14-4

Experimental tube type	$d_0$	$d_1$	Pitch diam. of resonator holes†	Pitch diam. of pins†	Pin-to-strap clearance	Pin-to-back-wall clearance
1	0.082	0.0515	0.394	0.4040	0.015	0.010
2	0.085	0.0590	0.405	0.4135	0.016	0.009

\* Dimensions are in inches.

† See Fig. 14-2. The pitch diameter is defined as the diameter of the locus of hole centers or pin centers.

The problems of mechanical design with 0.010- to 0.015-in. clearances between the pins and the oscillator walls have not proved to be serious; the limitations on tuning range have been set by other considerations. The most troublesome problem is the elimination of extra resonances introduced by the tuning mechanism. Typical of these resonances is that in which the lumped capacitance between the pin and the hole wall of Fig. 14-3 resonates with the lumped inductance of the end cavity. In this mode, current circulates up the back wall, through the lid, and down the pins. The effect of these extra resonances is both to distort the tuning curve and to introduce loss. The loss is most pronounced when the r-f contacts generally present in the current path are poor; but loss

may also be troublesome even if the contacts are good, because excessive currents may flow near resonance. These extra resonances are most troublesome for long anodes and large end spaces (that is, wherever dimensions become large compared with a wavelength). They are most easily removed by reducing the size of the end space.

There is a fundamental limit to the use of tuning of this type in the shorter wavelengths because the unloaded  $Q$  decreases with  $\lambda$  and sprocket tuning further decreases  $Q_u$ . A rough estimate of the magnitude of this effect may be made by assuming that all the circulating current in the resonator is located in the region of the holes, yielding the approximate formula<sup>1</sup>

$$Q_r \frac{\delta}{\lambda} = \frac{2 \int B^2 d\tau}{\lambda \int B^2 d\sigma} \cong \frac{2}{\lambda} \frac{V_A B_A^2 + V_B B_B^2}{S_A B_A^2 + S_B B_B^2}, \quad (6)$$

where  $B$  = magnetic flux density,

$\int d\tau$  = integral over volume of resonator,

$\int d\sigma$  = integral over surface area of resonator,

$$S_A = h_1 \pi (d_0 + d_1),$$

$$S_B = (h_0 - h_1) \pi d_0 + \frac{\pi d_1^2}{4},$$

$$V_A = h_1 \frac{\pi}{4} (d_0^2 - d_1^2),$$

$$V_B = (h_0 - h_1) \frac{\pi}{4} d_0^2,$$

$\delta$  = skin depth, proportional to  $\sqrt{\lambda}$ ,

and

$$\frac{B_A}{B_B} = \frac{d_0^2}{d_0^2 - d_1^2}.$$

Equation (6) yields the unloaded  $Q$  of the resonator proper. This must be combined with the strap unloaded  $Q$ , that is,  $Q_s$ , as follows:

$$\frac{1}{Q_u} = \frac{1}{Q_r} \sqrt{\frac{C_r}{C_s}} + \frac{1}{2Q_s} \frac{C_s}{C_r}, \quad (11.10)$$

where  $C_r$  = resonator capacitance,

$C_s$  = strap capacitance,

$$C_T = C_r + C_s.$$

<sup>1</sup> E. U. Condon, *Rev. Mod. Phys.*, **14**, 364 (1942). The factor of 2 given in Eq. (6) comes from the approximate uniformity of  $B$  over the cross section.

Using the values of  $Q_u$ ,  $C_r$ , and  $C_s$  listed in Table 11.2 for the 725 anode block, the theoretical  $Q_u$  curve of Fig. 14.5 is obtained for the constants there listed. The theoretical and observed unloaded  $Q$  values are in fair agreement except for the region of greatest pin penetration, where the particularly low observed  $Q_u$  ( $=144$ ) is believed to be caused by a pin-to-end-space resonance.

It is desirable to maintain an external  $Q$  of about 400 with the 2J51 magnetron because low circuit efficiencies (less than 50 per cent) result

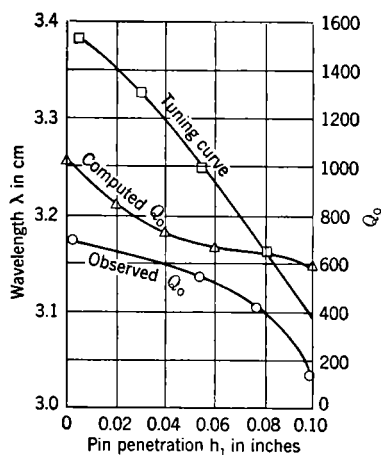


FIG. 14.5.—Cold-resonance data for the sprocket-tunable magnetron.  $h_0 = 0.250$  in.;  $d_0 = 0.086$  in.;  $d_1 = 0.0623$  in.;  $\delta/\lambda = 2.1 \times 10^{-6}$  for copper at 3.2 cm;  $Q_0$  was computed from Eq. (11.10).

in those regions of the tuning curve where the unloaded  $Q$  is less than 400.

Typical performance data on the 2J51 magnetron are shown in Fig. 14.6 and in Sec. 20.12. The pulling-figure variations shown in Fig. 14.6 indicate both the necessity for and the difficulty of adequately broad-banding the output circuit (Secs. 11.11 to 11.13). The average efficiency of 32 per cent at 14 amp and 15 kv may be compared with 35 to 40 per cent for the non-tunable version. The sacrifice in efficiency is to be ascribed primarily to the low unloaded  $Q$  of the tunable tubes.

Sprocket tuning has been tried on other magnetrons. An 18-vane 1.25-cm rising-sun magnetron (the 3J31 discussed in Sec. 20.17) has been tuned 3 per cent by inserting relatively small pins in the large oscillators only, thus maintaining a fairly high unloaded  $Q$  and reasonable ease of construction.

In applying sprocket tuning to rising-sun magnetrons, it should be noted that tuning only the large side resonators results in a change of the ratio of resonant wavelengths of the large to the small resonators and therefore a change in the mode spectrum and in the amount of zero-mode contamination of the main mode (Sec. 3.4). Because satisfactory operation of rising-sun tubes depends in part on the proper choice of resonator-to-wavelength ratio, it may be desirable to tune all resonators so that this ratio is maintained constant. This illustration of zero-mode variation is essentially a change in the r-f pattern resulting from imperfect symmetry in the tuning method.

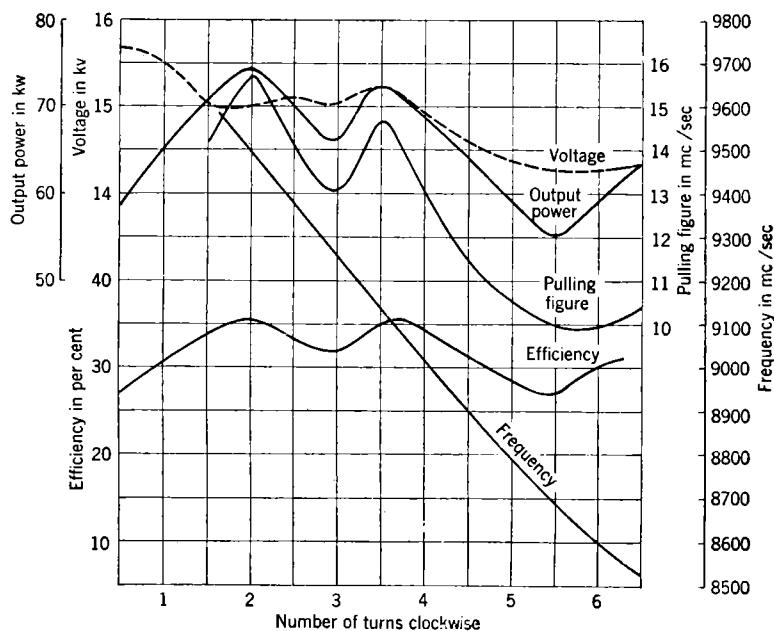


FIG. 14-6.—Typical performance data of type 2J51 magnetron. The operating current is 14 amp.

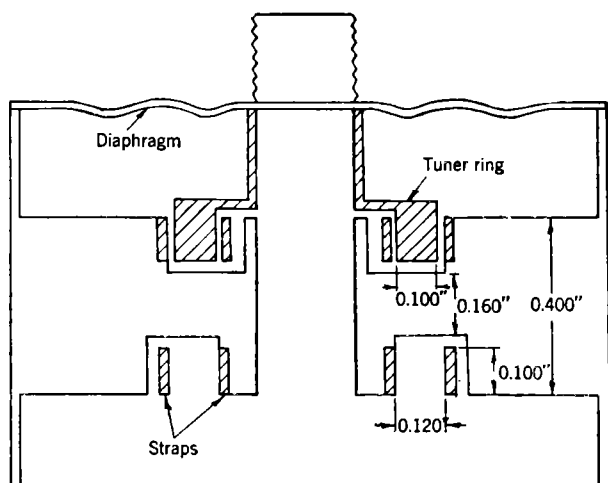


FIG. 14-7.—Cross section of the QK59, a cookie-cutter-tunable magnetron.

**14-3. Symmetric Capacitive Tuning. The Cookie Cutter.**—The term “cookie cutter” is applied to the capacitive method of tuning illustrated by the QK59 magnetron in Fig. 14-7. In this method a metal cylinder is inserted between the two rings of a double-ring-strapped magnetron, so that the strap capacitance and hence the wavelength are increased. Since the general theory of cookie-cutter tuning has been presented in Sec. 4-6, only the salient features will be repeated here. The main-mode wavelength may be calculated by assuming that the increased strap capacitance is in parallel with the tube capacitance. The mode separation from the next lower longitudinally symmetric mode increases as the main-mode wavelength is increased, whereas the longitudinally antisymmetric  $\pi$ -mode approaches the  $\pi$ -mode most closely at that point in the tuning range where the capacitances at each end are equal. For long, heavily strapped tubes this mode may cause some difficulty, but the main difficulties are with end-space resonances as in the sprocket-tunable magnetron; that is, a resonant circuit exists that is composed of the tuner-to-strap capacitance and the end-space inductance. It is usually possible to displace the resonance from the desired tuning region by varying the end-space geometry.

The anode block for the cookie-cutter-tunable magnetron (QK59) is described in Sec. 20-3. The unstrapped capacitance of the QK59 is taken as  $NC_r = 6 \mu\text{mf}$  (see Chap. 11). The strapping consists of a cylindrical condenser 0.100 in. high, with 0.348 in. ID and 0.588 in. OD. Ignoring fringing fields, its capacitance is  $C_A = 0.3 \mu\text{mf}$ . The strap-to-vane capacitance may be estimated as approximately  $0.55 \mu\text{mf}$ .

When the plunger is inserted between the straps, the sum of the gaps between straps is 0.020 in. instead of 0.120 in. and the interstrap capacity is multiplied six times. When the total capacitance  $C_1$  of the untuned tube is compared with that ( $C_2$ ) for the tuned tube, and when the fact that only one of the two strap cylinders is tuned is taken into consideration,

$$\left. \begin{aligned} \text{and} \quad \frac{C_1}{C_2} &= \frac{6 + 0.85 + 0.85}{6 + 0.85 + 0.55 + 6 \times 0.30} = \frac{7.7}{9.2} \\ \frac{\lambda_1}{\lambda_2} &= \sqrt{\frac{C_2}{C_1}} = 0.915. \end{aligned} \right\} \quad (7)$$

Because the added capacity is linear with plunger penetration, the change in wavelength is also linear for a small tuning range. The effects of the fringing fields will be to extend the tuning somewhat beyond the 0.100-in. tuner motion. They should also increase the over-all tuning, but, to a first approximation, this correction is canceled by the fact that the straps are not connected to the highest-voltage points of the vanes (the tips) but are of necessity located some distance back along the vanes. The



observed tuning curve is plotted in Fig. 14-8. In view of the approximations made in the computations, the 30 per cent discrepancy between the computed tuning range given by Eq. (7) and the experimental data is reasonable.

Operating data for a slightly modified version of Fig. 14-8, in which clearances are reduced to about 0.007 in. and the strapping is removed from the untuned end of the tube, are shown in Fig. 14-9. Theoretical unloaded- $Q$  values for the extremes of the tuning range are 2370 and 866. The agreement with observations is good only at the long wavelength end of the tuning curve.

In comparing cookie-cutter tuning with sprocket tuning, it may be noted that because cookie-cutter tuning requires smaller clearances and smaller motions at a given wavelength, it is more appropriate for the longer wavelengths.

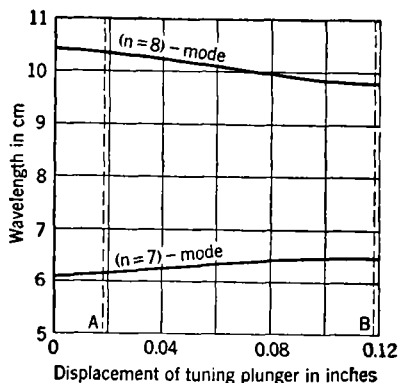


FIG. 14-8.—Tuning characteristics of the cookie-cutter-tunable magnetron. At A the plunger is flush with the bottom of the straps; at B it is flush with the top of the straps.

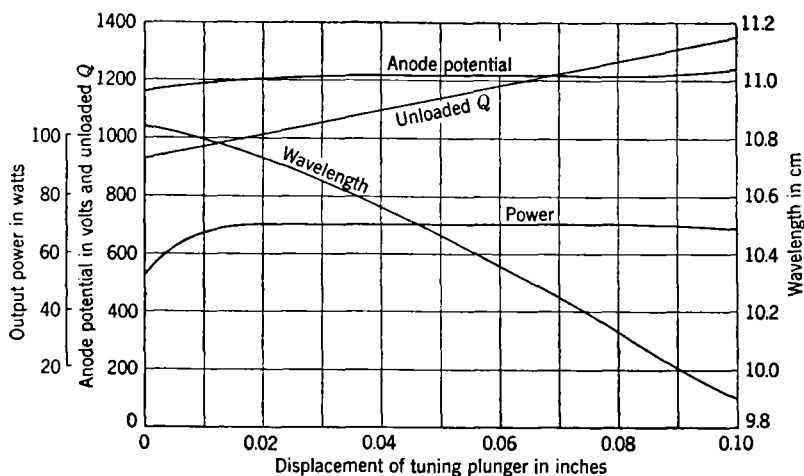


FIG. 14-9.—Data for cookie-cutter-tunable magnetron operating at 125-ma plate current. The pulling figure is 6 Mc/sec.

high voltage appearing across the tuner-to-strap gap restricts the application of cookie-cutter tuning to relatively low-voltage tubes, particularly

at the shorter wavelengths where small clearances increase the possibility of voltage breakdown.

#### 14-4. Other Symmetric Inductive and Capacitive Methods of Tuning.

The preceding examples of sprocket and cookie-cutter tuning illustrate the general limitations involved in inductive and capacitive tuning, namely, the high voltages appearing across the tuning element and the consequent danger of voltage breakdown for capacitive tuning, and variation in the unloaded  $Q$  for both capacitive and inductive tuning. Other examples of these types of tuning will be briefly discussed to illustrate the kinds of modification that may be required by specific tube problems.

For some purposes, particularly at the longer wavelengths, the motion required in sprocket tuning may be excessive. Examination of Eqs. (5) and (6) shows that this motion, corresponding to the plunger penetration  $h_1$ , can be decreased for the same percentage tuning by increasing  $d_1$  (at the expense, however, of a decrease in unloaded  $Q$ ). Because the increase in  $\lambda\delta$  makes the unloaded- $Q$  problem less serious at the longer wavelengths, a relative shortening of  $h_1$  becomes feasible. The pins, instead of penetrating the pole piece as in Fig. 14-2, may be suspended above the resonator holes from an annular metallic ring (dotted lines  $R$  in Fig. 14-3) which moves with the pins. Then provided the clearance  $t$  between the ring and the top of the vanes is large compared with that between the pin and the hole wall, there is no change in the tuning curves because the current flow in the pins is circumferential (Fig. 14-1). When  $t$  is small, however, radial currents are induced in the ring by the magnetic field in the end spaces, and the ring contributes to the tuning. All degrees of compromise between complete sprocket tuning and pure ring tuning ( $h_1 = 0$ ) are possible. Motions are smallest in pure ring tuning because in the  $\pi$ -mode the magnetic flux is strongly concentrated very near the vane tops, and consequently the ring is effective only when  $t$  is small. As  $t$  is decreased, the mode separation is increased because the magnetic flux for the lower modes fringes farther out into the end spaces and is more effectively tuned by the ring.

Similar gradual variations in capacitive tuning methods are possible starting from the cookie-cutter tuner. Instead of varying the strap capacitance, the tube capacitance may be varied in the manner shown in Fig. 14-1, and any combination of tube and strap capacitances can be varied. Because increasing the tube capacitance decreases the ratio of the strap capacitance to the tube capacitance, the mode separation of the untuned resonant system is decreased by this method of tuning, and the modes may even cross each other (Sec. 4-6). Although this decrease in mode separation is an objection to varying the tube capacitance, it is sometimes possible to incorporate larger clearances in a design by varying tube capacitance rather than strap capacitance and hence to obtain

higher r-f voltages without breakdown. The capacitive-tuning element operating between the vanes (Fig. 14-1) can be supported from an annular ring similar to the modification of sprocket tuning previously mentioned. Also, this ring alone can be used for capacitive tuning over the vane tops, just as a ring alone over the resonator holes can be used

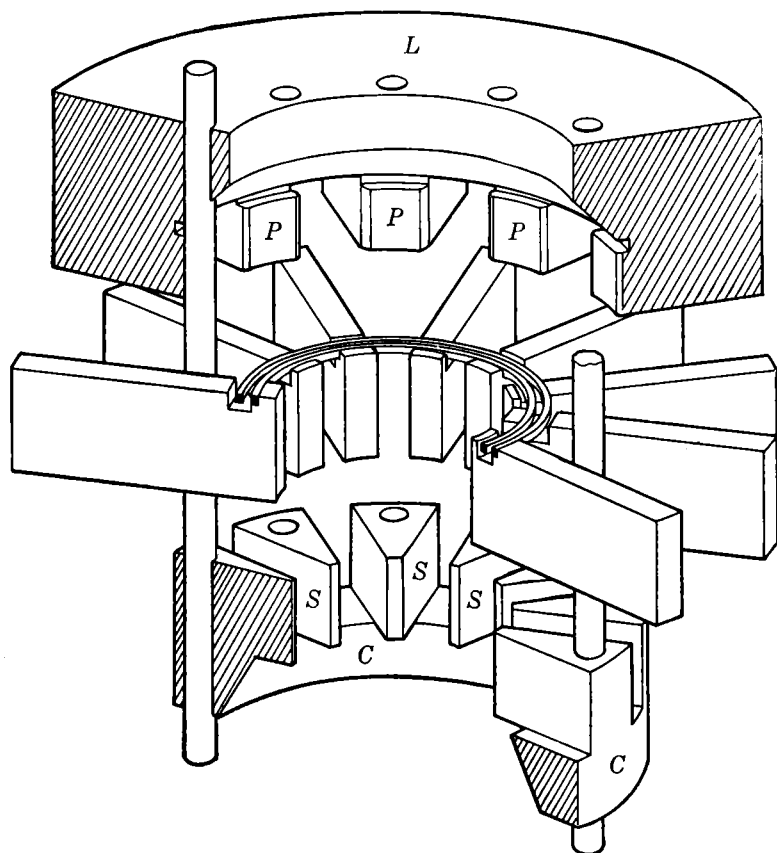


FIG. 14-10.—Cutaway view of the ZP639. This tube is tuned by the inductive tuning ring  $L$  with inserts  $P$  and by the capacitive tuning ring  $C$  with segments  $S$ . (Courtesy of General Electric Co.)

for inductive tuning. One of the most difficult engineering problems of this tuning method, as of sprocket tuning and cookie-cutter tuning, is the elimination of extra end-space resonances.

The widest tuning range attained on a multioscillator magnetron has been obtained by an ingenious design incorporating in a single tube several of the tuning methods mentioned above. This type of tuning

is illustrated in Fig. 14.10, which shows a portion of the 12-oscillator ZP639. A capacitive ring  $C$  with tuning segments  $S$  is connected by pins extending through the oscillator cavities to an inductive ring  $L$

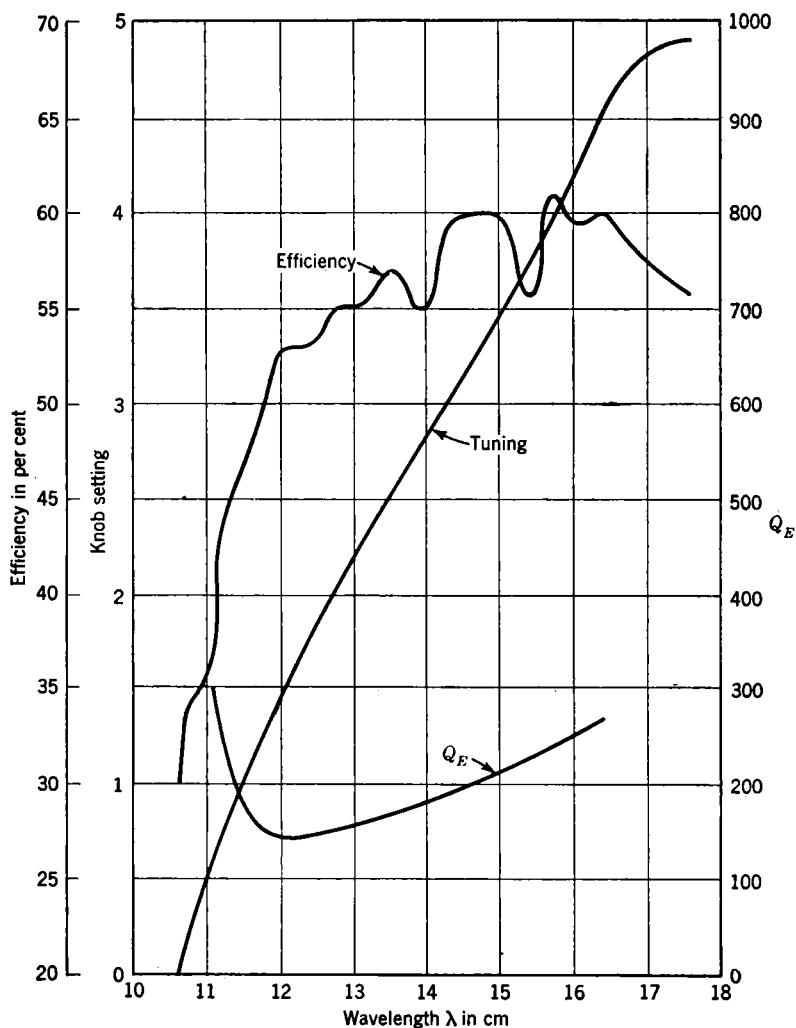


FIG. 14.11.—Tuning curve of inductive-capacitive-tunable magnetron ZP639. The input power is 1.0 kw at 5.0 kv. (Courtesy of General Electric Co.)

that supports a set of inductive tuning inserts  $P$ . Vertical motion of this two-ring combination simultaneously increases or decreases both inductance and capacitance together. Operating data for this tube are

shown in Fig. 14-11. For an input power of 1 kw at 0.200 amp, the efficiency remains above 50 per cent over a range of 1 to 1.5 in resonant wavelength.

In two examples that were given of inductive and capacitive tuning—the sprocket-tunable and the cookie-cutter-tunable magnetrons—there is very little tendency for the normal tube modes to cross each other, even over an extended tuning range and even if the initial mode separation is small. Nevertheless it seems significant that the widest tuning range (about 50 per cent) was observed on a tube with wide mode separation (40 per cent), that this tube had its anode length and radius small compared with a wavelength, and that the wavelength in question was long (15 cm). It is therefore important to summarize the factors independent of the r-f output power and other than normal mode crossing that limit the tuning range. These are

1. Extra resonances, associated with the end space or the tuning element or both. These resonances are favored by having tube dimensions large compared with a wavelength, a condition that also produces small normal mode separation.
2. Mode selection. Considerations of Chap. 8 show that it is difficult to establish general rules indicating what mode spectrum is most favorable to  $\pi$ -mode operation; in specific cases, however, variations in the mode spectrum over the tuning range may cause unfavorable mode selections.
3. Unloaded  $Q$ . This is a function of wavelength and tuning range, not of mode separation. In general,  $Q_u$  decreases as the wavelength is decreased and as the tuning range is increased. For a 10 per cent tuning range at 3 cm,  $Q_u$ , becomes about 500, a barely acceptable figure.

It is empirically observed that the operating tuning range seldom exceeds the mode separation of the original untuned anode.

**14-5. Unsymmetric Inductive Tuning.**—For the purpose of fixing a magnetron frequency within the normal scatter band of untuned magnetrons it is sometimes desirable to incorporate in the tube a small and simple tuning element capable of a restricted tuning range of about 1 per cent. Such a device usually is limited to tuning one resonator, for example, by means of a screw inserted in the side of the resonator hole. For mode separations greater than 5 per cent, deterioration of the r-f pattern from this unsymmetrical tuning is negligible (Sec. 4-5). The problem therefore is purely an engineering one of obtaining an adequately compact diaphragm and control mechanism, of eliminating extra resonances in the vacuum envelope associated with the diaphragm and tuning screw, and of maintaining adequate clearance between the screw and the oscillator walls to keep the unloaded  $Q$  high.

## COUPLED-CIRCUIT TUNING

In coupled-circuit tuning, the coupling is usually introduced through one resonator and therefore produces asymmetrical r-f patterns.

**14.6. General Theory.**—Tuning methods based on varying the magnetron frequency indirectly by a second resonant circuit coupled to the magnetron are free from some of the geometrical limitations imposed by anode-block dimensions. Furthermore, these coupled-circuit-tunable magnetrons can often, but not always, be made with higher unloaded  $Q$ 's than the inductive and capacitive tunable magnetrons discussed in Secs. 14.2 and 14.3. In some cases the mechanical motion of the tuning element may take place outside the vacuum envelope, but to date such magnetrons have generally proved less satisfactory than inductive or capacitive tunable magnetrons.

There are two general properties of coupled-circuit-tunable magnetrons. (1) The added resonant circuits increase the stabilization of the magnetron by storing r-f energy; (2) they introduce new modes to the spectrum. The added modes are often harmless, but they are never an advantage, and the increased stabilization usually increases the tendency of the magnetron to operate in undesired modes. When this tendency can be overcome, however, the added stabilization represents an advantage, as shown in Chap. 16. Most coupled-circuit-tunable magnetrons are unsymmetric; hence distortion of the r-f pattern occurs over the tuning range. The resulting decrease in electronic efficiency and the increased tendency to shift modes at wavelengths removed from the untuned resonant frequency (Chap. 8) generally limit the useful tuning range of a coupled-circuit-tunable tube to from one-third to one-half of the mode separation of the untuned tube. As a corollary of this pattern distortion, the coupling to the output circuit, hence the external  $Q$ , may change over the tuning range. This effect is distinct from the variation in external  $Q$  caused by change in stabilization over the tuning range, although it is not distinguishable by  $Q$ -measurements alone.

**14.7. Double-output Tuning.**—The term "double-output" tuning is applied to the coupled-circuit type of tuning illustrated in Fig. 14.12. A magnetron is provided with two output terminals; the first is actually used as a power-output terminal, while the second is used to couple into the resonant system a reactance that changes the resonant frequency of the magnetron. The variable reactance is provided by a short-circuited transmission line of variable length  $l$ . These circuits may be described with the aid of the equivalent circuits shown in Fig. 14.13. In these circuits

$L$  = the resonant-system inductance,

$C$  = the resonant-system capacitance,

$G = \sqrt{(C/L)}/Q_{u1}$ , where  $Q_{u1}$  = the unloaded  $Q$  of the resonant system,

$l$  = the distance to the short-circuiting plunger,

$Y_2$  = the characteristic admittance of the coaxial line of the tuner,

$G_2/Y_2$  = the VSWR in the tuner line,

$Y_1$  = the characteristic admittance of the coaxial line of the power output as seen across the slots (that is, transformed through the power-output coupling).

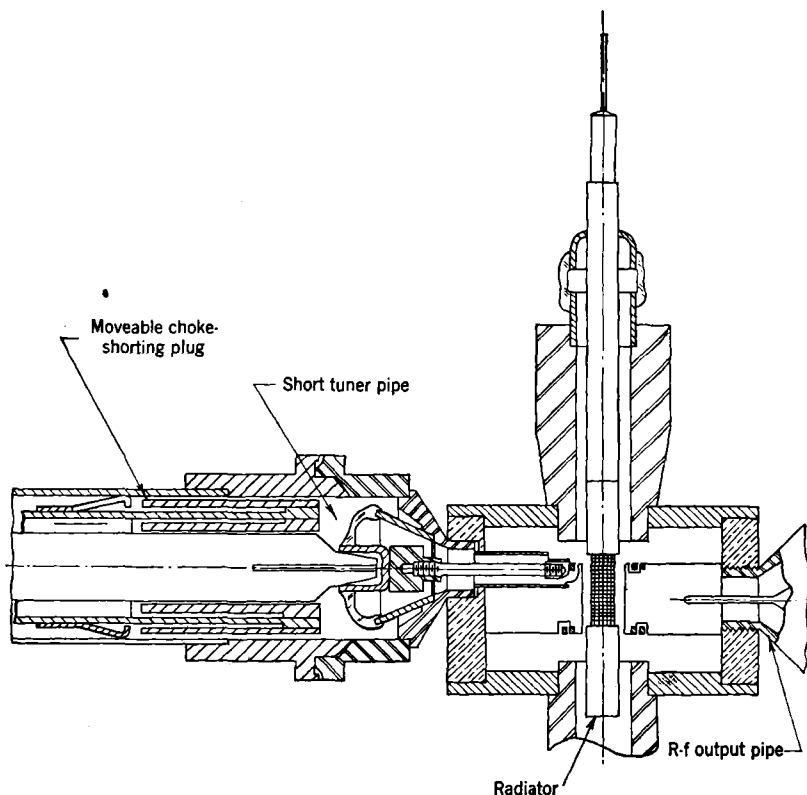


FIG. 14-12.—An example of double-output tuning.

The part of the equivalent circuit shown in Fig. 14-13a for the coupled reactance corresponds to the low external  $Q$  pin-to-strap type of coupling discussed in Sec. 5-2. It will be proved later that this low  $Q$  (here,  $Q_{E2}$ ) is a prerequisite for a wide mode-free tuning range; for example,  $Q_{E2} = 10$  corresponds to a 10 per cent tuning range. In the circuit of Fig. 14-13a the magnetron is connected directly across the tuner line at Terminals 2,

and the small junction effects are neglected. The power-output circuit is represented by the admittance  $Y_1 = \sqrt{(C/L)}/Q_{E1}$  at Terminals 1, where  $Q_{E1}$  is the external  $Q$  of the power-output circuit (with the tuning reactance removed). The frequency pulling by the power-output circuit is assumed negligible compared with the tuning introduced by the short-circuited tuner line.

It may be deduced from the analysis of Chap. 5 that a low external  $Q$  is possible, without the introduction of extra resonant elements into the circuit, only for coaxial-line outputs. Consequently, the analysis of Fig. 14-13a is here restricted to a tuner consisting of a coaxial stub.

Although it is possible to devise double-output-tuning methods incorporating an evacuated tuning line, the primary purpose of the method of tuning shown in Fig. 14-12 is to allow the mechanical motion to take place outside the vacuum envelope. This type of tuning is thus applicable only to magnetrons with low pulse-power outputs because

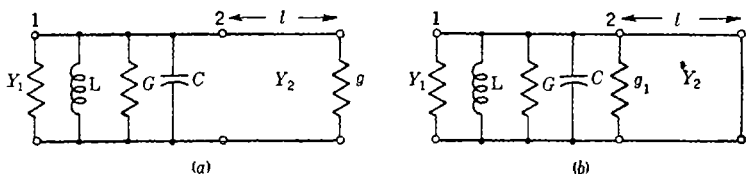


FIG. 14-13.—Equivalent circuits for double-output tuning.

breakdown would be encountered in the tuner line or across the tuner vacuum seal at high pulse powers. The nature of the tuner vacuum seal also limits the average output power of the magnetron because the high r-f fields that generally exist in the glass for at least a portion of the tuning range may heat the glass to its melting point. Coaxial-line tuners, having center diameters of  $\frac{3}{8}$  in. and inside diameters of their outer conductors equal to  $\frac{1}{16}$  in., have been attached to double-output magnetrons. These tubes, with seals of No. 704 glass, have been tested at pulse powers up to 10 kw and average powers up to 200 watts. A final limitation on this method of tuning is the circuit efficiency, which may be appreciably lowered from that of an untuned tube even if the plunger in the tuning line sets up a standing-wave ratio of 40 db or more.

As a result of these limitations, double-output tuning has not proved to be very successful. However, the low- $Q$  coupling devices developed for this type of tuning have been useful as means of coupling electronically controlled reactances into a magnetron and thus are an important part of some of the methods of frequency modulation discussed in Chap. 15. For this reason and also to illustrate the type of analysis that may be useful in other related problems, the various circuit properties



of double-output tuning will be derived from the equivalent circuits (Fig. 14-13) and compared with experiments.

The parameters to be evaluated in terms of this circuit are the tuning curves, the variation of stabilization, the circuit efficiency, and the total resistive loading over the tuning range for different values of the variables in Fig. 14-13a. The large mode separation in the untuned tube (the QK44, see Table 11-3) minimizes pattern distortion, which is therefore neglected in the computations.

By evaluating the admittance seen looking to the right at Terminals 2 of Fig. 14-13a, the simpler equivalent circuit Fig. 14-13b is justified for  $(G_2/Y_2 \tan 2\pi l/\lambda)^2 \gg 1$  (for a perfect short circuit,  $G_2 = \infty$ ). In this figure

$$G_l = \frac{Y_2}{G_2} \csc^2 \frac{2\pi l}{\lambda}. \quad (8)$$

Letting  $B_1$  be the admittance seen looking to the right at Terminals 1 of Fig. 14-13b and defining  $Q_{E2} = (\sqrt{(C/L)}/Y_2)$ , the tuning curve is given by

$$l = \frac{\lambda}{2\pi} \cot^{-1} Q_{E2} \left( \frac{\lambda_0}{\lambda} - \frac{\lambda}{\lambda_0} \right), \quad (9)$$

where  $\lambda_0$  is the resonant wavelength of the anode block. The stabilization  $S$  is then given by

$$S = \frac{\frac{dB_1}{d\omega}}{\frac{dB_1}{d\omega} \text{ Terminals 2 open-circuited}} = 1 + \frac{\pi l}{\lambda_0} \frac{1}{Q_{E2}} \csc^2 \frac{2\pi l}{\lambda}. \quad (10)$$

If the magnetron, tuned to some wavelength  $\lambda$ , is force-oscillated through the power output, it will yield a  $Q$ -curve similar to that for a nontunable magnetron, and the resulting parameters (unloaded  $Q = Q_U$  and external  $Q = Q_E$ ) have the usual relation to the operating behavior of the magnetron. These quantities are given by the relations

$$\left. \begin{aligned} \frac{1}{Q_U} &= \frac{1}{S} \frac{\lambda}{\lambda_0} \left[ \frac{1}{Q_{U1}} + \frac{1}{Q_{E2}} \left( \frac{G_e}{Y_2} \right) \right], \\ Q_E &= S \frac{\lambda_0}{\lambda} Q_{E1}, \end{aligned} \right\} \quad (11)$$

whence the circuit efficiency  $\eta_c$  is

$$\left. \begin{aligned} \eta_c &= \frac{Q_L}{Q_E} \\ \text{and} \quad \frac{1}{Q_L} &= \frac{1}{Q_U} + \frac{1}{Q_E} \end{aligned} \right\} \quad (12)$$

The total resistive loading  $G_{\text{TOT}}$  appearing across Terminals 1 or 2 may be expressed as

$$\frac{G_{\text{TOT}}}{\sqrt{C}} = \frac{1}{Q_{u1}} + \frac{1}{Q_{E2}} \left( \frac{G_e}{Y_2} \right) + \frac{1}{Q_{E1}} \quad (13)$$

The r-f voltage in the tuner is also readily derivable. When the value  $\tilde{V}_2$  at Terminals 2 is evaluated, the entire pattern in the tuner is easily deduced.

$$Q_E = \frac{2\pi\nu (\text{energy stored})}{P_o} = \frac{\tilde{V}_2^2 \sqrt{C}}{2P_o} = \frac{\tilde{V}_2^2 Y_2 Q_{E2}}{2P_o}, \quad (14)$$

whence

$$\tilde{V}_2 = \left( \frac{2P_o Q_E}{Y_2 Q_{E2}} \right)^{1/2},$$

where  $P_o$  = output power.

As a check on the validity of these derivations, a comparison of the theoretical Eqs. (9), (11), and (12) with experimental data is shown in Figs. 14·14 and 14·15. The experimental tube used in these measurements was a variant of the CM16B described in Sec. 20·3.

These two figures contain the calculated curves of  $\lambda$ ,  $Q_E$ ,  $Q_U$ , and  $\eta_e$ , which are fitted to correspond to the observed points by theoretical calculations based on the above equations and the five arbitrary constants  $Q_{E2}$ ,  $Q_{E1}$ ,  $Q_{u1}$ ,  $G_2/Y_2$ , and the branch  $m$  of the tuning curve, that is, the number of voltage nodes in the tuner line, counting the plunger position as one node. Thus the trial values  $Q_{E2} = 30$  and  $m = 4$  give good agreement with the data of Fig. 14·14, and the additional trial values of  $Q_{u1} = 950$ ,  $Q_{E1} = 110$ , and  $G_2/Y_2 = 42$  db give good agreement with the data of Fig. 14·15. Independent measurements determine three of these constants as  $Q_{u1} = 1200$ ,  $\pm 30$  per cent,  $G_2/Y_2 = 40$  to 45 db, and  $m = 3$ , in good agreement with the trial values except for the value of  $m$ . It is reasonable, however, to expect the best fit of Eq. (9) to occur for a larger value of  $m$  (for example, 4) than that given by the physical length of the lead (namely,  $m = 3$ ) because the frequency sensitivity of the lead (the taper, the glass seal, and the series inductance in the outer conductor) is equivalent to an extra length added to the tuner line.

The most noticeable feature of the curves in Fig. 14·14 is the multiple-valued dependence of wavelength on tuner position. Thus, for a 70-mm plunger position, two resonant wavelengths, 9.7 and 10.48 cm, are possible because of the multiple-valued properties of the cotangent in Eq. (9).

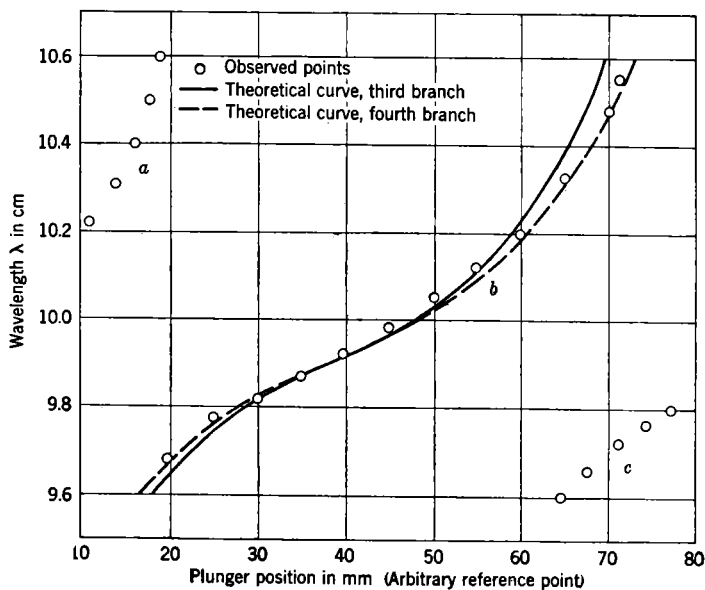


FIG. 14-14.—Observed and theoretical tuning curves for double-output tuning. The theoretical curves from Eq. (9) (with  $Q_{E2} = 30$ ) are fitted in position and slope to the experimental curve at  $\lambda_0 = 9.9$  cm. (a), (b), and (c) represent different branches of the tuning curve.

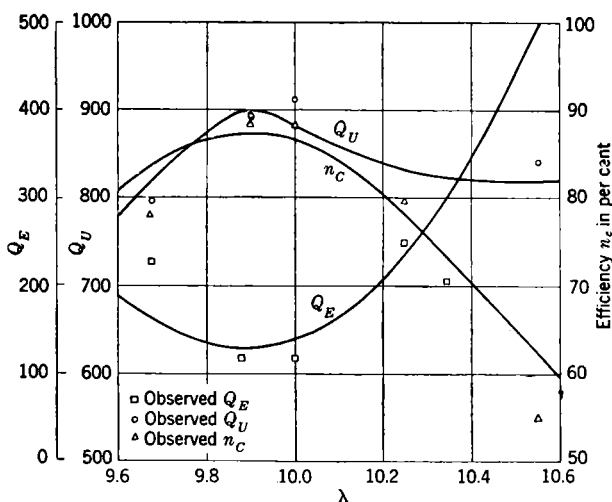


FIG. 14-15.—Theoretical curves and experimental points of  $Q_E$ ,  $Q_U$ , and  $\eta_c$  for double-output tuning. The  $Q_E$  curve was calculated with  $m = 4$ ,  $Q_{E2} = 30$ , and  $Q_{E1} = 110$ . The  $Q_U$  curve was calculated for  $m = 4$ ,  $Q_{E2} = 30$ ,  $G_2/Y_2 = 126$  (42 db), and  $Q_{u1} = 950$ .

The separation in wavelength of the tuning branches  $a$ ,  $b$ , and  $c$  is also seen from Eq. (9) to be greatest for low  $Q_{E2}$  and for low  $m$ .

The important feature of the curves in Fig. 14-15 is the frequency sensitivity of  $\eta_c$  and  $Q_E$  (which is proportional to the stabilization  $S$ ). Consideration of Eqs. (10) to (12) shows that the frequency sensitivity of  $\eta_c$  is diminished by low  $Q_{E2}$  and that of  $Q_E$  is diminished by low  $Q_{E2}$  and by small  $m$  (that is, short  $l$ ). A lower limit, however, is placed on  $Q_{E2}$  at the center of the tuning range by the circuit efficiency, which varies inversely to  $Q_{E2}$ , and by stabilization, which varies directly with  $Q_{E2}$ . Chapter 8 shows that both  $\eta_c$  and  $S$  decrease the current at which operation in the  $\pi$ -mode is stable by their effect on  $\sqrt{C/L_{TOT}}$  (here,  $S\sqrt{C/L}$ ) and  $G$  (here,  $G_{TOT}$ ). Furthermore, for  $Q_{E2} \ll 10$ , the equivalent circuit (Fig. 14-13a) breaks down because the frequency sensitivity of the lead becomes appreciable. Even in the example chosen, for  $Q_{E2} = 30$ , this frequency sensitivity required an increase in the effective branch of the tuning curve. Less frequency-sensitive leads than the one used for the data in Figs. 14-14 and 14-15 are available, leads furthermore that are physically shorter and allow operation on the ( $m = 2$ )-branch of the tuning curve. Such a tuner lead is illustrated in Fig. 14-12. Although the performance of this type of tunable magnetron has been

poor, tuning ranges of 10 to 20 per cent have been obtained at c-w output powers of 30 to 60 watts with an input power of 150 watts.

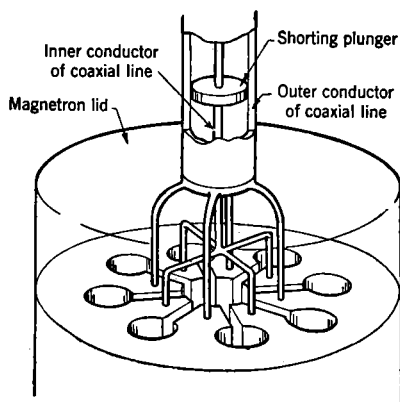


FIG. 14-16.—Schematic drawing of symmetric double-output-tunable magnetron.

**14-8. Symmetric Double-output Tuning.**—A method<sup>1</sup> of coupling a coaxial line to a magnetron so that the main-mode symmetry is preserved is illustrated in Fig. 14-16. The resulting tuning curves are shown in Fig. 14-17, where the position of the tuning plunger is plotted as abscissa and the wavelength as ordinate. For the main mode, the equivalent circuits of Fig. 14-13 are applicable. The validity of these circuits

is shown by the fair agreement between the magnetron characteristic impedance computed by Slater from the observed tuning curves (7.25 ohms) and that computed by James from the tube dimensions (10 ohms).<sup>2</sup>

<sup>1</sup> J. B. Fisk and P. L. Hartman, "The Development of Tunable Magnetrons," BTL-141, June 26, 1942.

<sup>2</sup> Both Slater's and James' computations can be found in J. C. Slater, "Input Impedance and Tuning of Magnetron Cavities," RL Report No. 43-18, Feb. 3, 1943.

The resulting close coupling of the magnetron to the line is shown by the large slope of the tuning curves at the unperturbed main-mode resonant wavelength of 10 cm. By contrast, the extremely small slope of the tuning curves at the lower modes shows that these are very loosely coupled to the line, as is to be expected from the symmetry of the coupling method. This small slope of the lower modes results in wider mode separation than would be found in an unsymmetric method of coupling. The combination of relatively wide mode separation and lack of pattern distortion thus favors the possibility of a wide tuning range if one starts with an anode of initially small mode separation. Because this tuning method was tried before the techniques of testing magnetrons were well developed, it is not possible to judge from the available data whether or not the anticipated advantages in symmetric tuning are actually realizable.

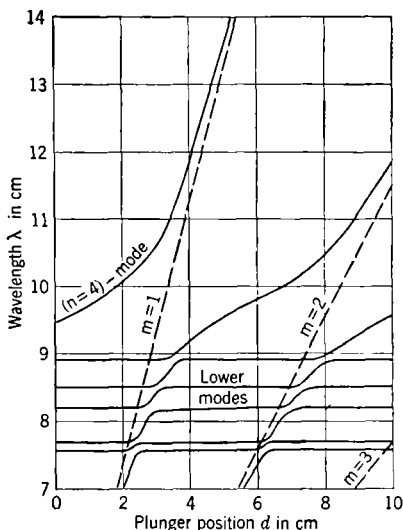


FIG. 14-17.—Tuning curves for symmetric double-output magnetron. The asymptotes for the different branching of the tuning curves are shown by dashed lines.

**14-9. Cavity Tuning.** *Iris-coupled Tuning.*—Figure 14-18 illustrates a method of coupling a magnetron (I) by means of an iris (II) to a cavity (III). The resonant frequency of the combined system—I, II, and III—is changed when the frequency of the cavity is changed by some mechanical motion. All three elements are frequency-sensitive and may be represented by simple series- or parallel-resonant circuits that are resonant at or near the resonant wavelength  $\lambda_0$  of the untuned anode block. It will be shown that the net result of these three resonant circuits is to introduce two new modes into the mode spectrum of the magnetron, one above and one below  $\lambda_0$ . The stabilization of all three modes is a function of the circuit parameters and varies over the tuning range. As a result, careful analysis is necessary to determine in which mode the magnetron will operate. Successful application of this analysis, however, leads to a design capable to a 5 to 10 per cent tuning range and capable of withstanding the highest r-f voltages generated in high-power magnetrons. This design simultaneously increases the unloaded  $Q$  of the magnetron as a result of the energy stored in the cavity, although the total skin losses are also increased. If the external  $Q$  is adjusted to be equal to that of the nontunable version of the magnetron (no cavity),

a gain in circuit efficiency results in the tunable tube. The attendant disadvantages are characteristic of unsymmetric tuning—variation over

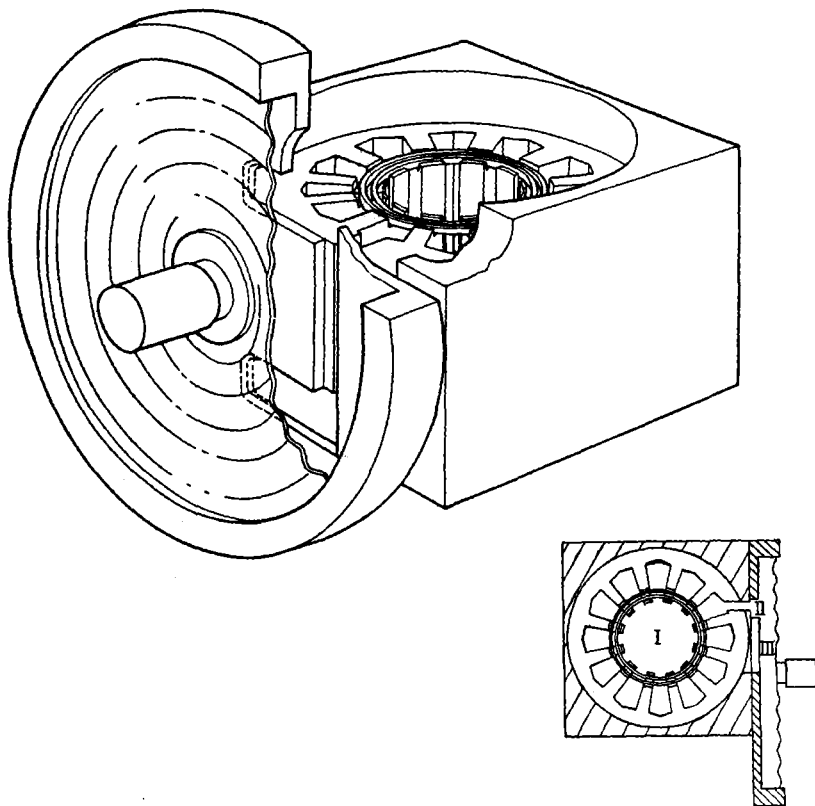


FIG. 14-18.—Iris-coupled cavity-tunable magnetron type 4J75.

the tuning range in the r-f patterns and in the electronic efficiency. Of designs giving equal mode separations, consideration of unloaded  $Q$  and methods of construction favor use of the cavity tuning illustrated by Fig. 14-18 for the shorter wavelengths.

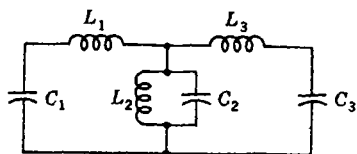


FIG. 14-19.—Equivalent circuit for iris-coupled cavity-tunable magnetron type 4J75.  $Z_n = \sqrt{(L_n/C_n)}$ .

Figure 14-19 shows the equivalent circuit of the 4J75 magnetron shown in Fig. 14-18. The magnetron I, opened at the back of one of the oscillators,

is represented as a series-resonant circuit  $L_1C_1$ . The resonant-iris coupling device II is represented as a parallel-resonant circuit  $L_2C_2$ ,

and the cavity III as a series-resonant circuit  $L_3C_3$  because it, like the magnetron, is opened at a high-current point.

If the mode separation in the untuned tube is large compared with that of the two extra modes introduced by the cavity and coupling, these extra modes may be considered as multiplets of the  $\pi$ -mode (see Fig. 14.20). Empirical observations and qualitative analysis of more complicated circuits show that when this condition does not hold, there is only a minor effect on the central  $\pi$ -mode and the long-wavelength  $\pi$ -mode but the short-wavelength  $\pi$ -mode cannot cross the next normal-mode wavelength. Solution of Kirchhoff's laws for the three networks of Fig. 14.19 is straightforward when

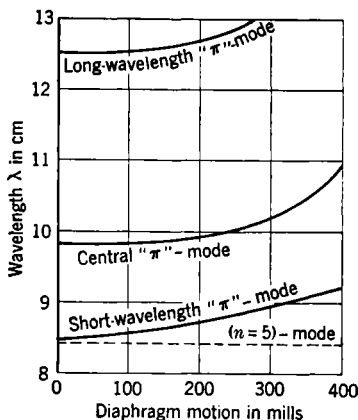


FIG. 14.20.—Tuning curves of 4J75 magnetron.

$$\omega_1 = \omega_2 = \omega_3 = \omega_0. \quad (15)$$

Denoting  $2\pi$  times the resonant frequency of the combined system as  $\omega$  and letting

$$\alpha = \frac{\omega}{\omega_0}$$

and

$$\gamma = \alpha - \frac{1}{\alpha}, \quad (16)$$

Kirchhoff's laws for the two networks (I + II and II + III) are, for the condition of Eq. (15),

$$\tilde{I}_1 \left( Z_1 \gamma - \frac{Z_2}{\gamma} \right) + \tilde{I}_2 \frac{Z_2}{\gamma} = 0$$

and

$$\frac{\tilde{I}_1 Z_2}{\gamma} + \tilde{I}_2 \left( Z_3 \gamma - \frac{Z_2}{\gamma} \right) = 0. \quad (17)$$

Hence, for resonance,

$$\gamma = 0 \text{ or } \pm \left( \frac{Z_2}{Z_1} + \frac{Z_2}{Z_3} \right)^{1/2}$$

and

$$\alpha^2 = 1 \text{ or } \frac{1}{2} \left[ \frac{Z_2}{Z_1} + \frac{Z_2}{Z_3} + 2 \pm \sqrt{\left( \frac{Z_2}{Z_1} + \frac{Z_2}{Z_3} + 2 \right)^2 - 4} \right]. \quad (18)$$

The energy storage in the three circuits can be computed from

$$\left. \begin{aligned} 2\omega E_I &= \tilde{I}_1^2 Z_1 \left( \alpha + \frac{1}{\alpha} \right), \\ 2\omega E_{II} &= (\tilde{I}_1 - \tilde{I}_2)^2 \frac{Z_2}{\gamma^2} \left( \alpha + \frac{1}{\alpha} \right), \\ \text{and} \\ 2\omega E_{III} &= \tilde{I}_2^2 Z_3 \left( \alpha + \frac{1}{\alpha} \right). \end{aligned} \right\} \quad (19)$$

The stabilization for the three modes of Eq. (18) can be computed from Eq. (19) and from the additional relation

$$\frac{\tilde{I}_2}{\tilde{I}_1} = 1 - \frac{Z_1}{Z_2} \gamma^2, \quad (20)$$

from Eq. (17). The result is that

$$S = \frac{E_I + E_{II} + E_{III}}{E_I} = 1 + \frac{Z_1}{Z_2} \gamma^2 + \frac{Z_3}{Z_1} \left( 1 - \frac{Z_1}{Z_2} \gamma^2 \right)^2, \quad (21)$$

whence

$$\left. \begin{aligned} S &= 1 + \frac{Z_3}{Z_1} \quad \text{for } \gamma = 0 \\ \text{and} \\ S &= 2 \left( 1 + \frac{Z_1}{Z_3} \right) \quad \text{for } \gamma^2 = \frac{Z_2}{Z_1} + \frac{Z_2}{Z_3}. \end{aligned} \right\} \quad (22)$$

Equation (18) shows that the separation between the unperturbed or  $[(\gamma = 0), (\alpha^2 = 1)]$ -mode and the extraneous modes introduced by the coupled circuits is greatest when  $Z_2$  is greatest. Thus, it is desirable to make the iris of high characteristic impedance; that is, the inductive areas of the iris should be as large as possible.

Equation (22) shows that when the stabilization of the unperturbed  $\pi$ -mode exceeds 3, the extra  $\pi$ -modes are less highly stabilized than the central mode. The analysis of mode selection in Chap. 8 and the analysis of stabilization in Chap. 16 show that for competition among several  $\pi$ -modes, the tube will usually oscillate in the mode of lowest stabilization unless special precautions are taken to ensure operation in the high-stabilization mode. Because these precautions increase the complexity of design and decrease the output power, cavity-tunable magnetrons are designed with lower stabilization of the desired operating mode than of the undesired modes unless high stabilization is also required in the design. The attainable tuning for high stabilizations will be discussed in Chap. 16.



Several considerations combine to favor the selection of the central mode as the operating mode. If this mode is stabilized less than 3, both competing modes will be stabilized greater than 3 and the magnetron will run in the central mode. Furthermore, the distortion of the r-f pattern is least in this mode. Finally, an analysis for  $\omega_3 \neq \omega_0$  shows that the tuning range for a given change in  $\omega_3$  is largest for the central mode. Criteria for satisfactory cavity-tunable design, therefore, are that the operating mode be the center mode and that its stabilization be kept less than 3. For design purposes, it is satisfactory to assume that  $S = 1.7$  is an optimum value.

The rate of tuning near  $\omega_3 = \omega_0$  is obtained from a modification of Eq. (10), which becomes

$$\frac{\Delta\omega}{\Delta\omega_3} = \frac{S-1}{S}. \quad (23)$$

For  $S = 2$ ,  $\Delta\omega/\Delta\omega_3 = \frac{1}{2}$ , whereas the maximum possible value is 1 when  $S = \infty$ .

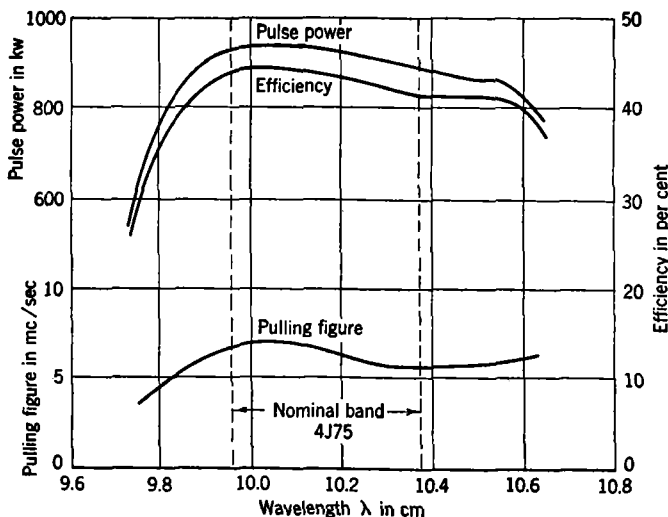


FIG. 14-21.—Operating data of typical 4J75 magnetron. Magnetic field = 2700 gauss; pulse plate current = 73.5 amp; pulse plate voltage = 28.1 to 29.1 kv; heater voltage = 8 volts.

Although it is possible to estimate  $Z_1$ ,  $Z_2$ , and  $Z_3$  from the magnetron dimensions, it is more useful to regard the ratios of the impedances  $Z_1$ ,  $Z_2$ , and  $Z_3$  as determined by appropriate measurements of tuning curves and stabilizations. A qualitative analysis of the variation of the impedances with physical dimensions then suggests appropriate changes to obtain more desirable tuning curves and stabilizations.

Figure 14-20 shows the observed mode spectrum for the Westinghouse cavity-tuned 4J75 magnetron. It is seen that the wavelength of the short-wavelength  $\pi$ -mode is as low as possible, because it cannot be lower than the ( $n = 5$ )-mode. Over the tuning range shown, the unloaded  $Q$  of the tunable magnetron is 2000, compared with 1500 for the untuned tube.

Operating data<sup>1</sup> for the 4J75 tube are shown in Fig. 14-21 where it is seen that the efficiency variation is small over the tuning range where no mode changes occur.

Brief mention should be made of the fact that because the diaphragm is part of the resonant circuit of the 4J75 tube and because it is stretched

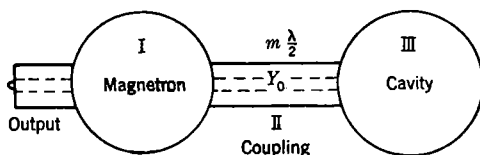


FIG. 14-22.—Schematic drawing of the coaxial-line-coupled cavity-tunable magnetron.

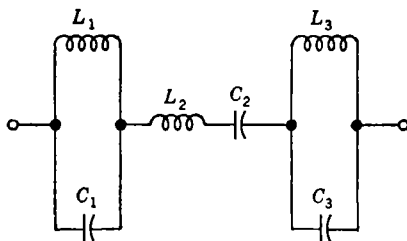


FIG. 14-23.—Equivalent circuit of coaxial-line-coupled cavity-tunable magnetron.  
 $Y_n = \sqrt{(C_n/L_n)}$ ;  $Y_1 = Q_{E1}Y_0$ ;  $Y_2 = (m/\pi)Y_0$ ; and  $Y_3 = Q_{E2}Y_0$ .

beyond its elastic limit, there is a hysteresis of a few megacycles per second in the tuning curve, and the resonant frequency for a given setting of the tuning mechanism depends on the direction of the tuner motion. This is not a fundamental property of cavity-tunable magnetrons.

*Coaxial-line-coupled Tuning.*—Figure 14-22 illustrates a method of tuning that is electrically similar to iris-coupled cavity tuning. A coaxial line replaces the iris shown in Fig. 14-18, and the equivalent circuit of Fig. 14-23 replaces that of Fig. 14-19. In Fig. 14-23 the magnetron is a parallel-resonant circuit; the cavity, as seen through its coupling connection, may be taken as a parallel-resonant circuit by suitable choice of terminals along the coupling line, and the length of line  $l_1$  between the magnetron and the cavity (necessarily  $m\lambda/2$  long, with each end a

<sup>1</sup> A. G. Smith, "The 4J70-77 Series of Tunable Magnetrons," RL Report No. 1006, Feb. 4, 1946.

voltage maximum) may be taken as a series-resonant circuit over a small-wavelength range. The preceding analysis for iris coupling will then also hold for coaxial-line coupling if  $Z_n = \sqrt{L_n/C_n}$  is replaced by  $Y_n = \sqrt{C_n/L_n}$  throughout. If the resulting mode separation is so great that the connecting coaxial line is not adequately represented by a series-resonant circuit over the wavelength range involved, the circuit of Fig. 14-23 becomes inadequate and an analysis similar to that for double-output tunable magnetrons is necessary. Then, for example, the tuning curves are given by

$$l_1 = \frac{\lambda}{2\pi} \cot^{-1} Q_{s2} \left( \frac{\lambda_1}{\lambda} - \frac{\lambda}{\lambda_1} \right) + \frac{\lambda}{2\pi} \cot^{-1} Q_{s2} \left( \frac{\lambda_2}{\lambda} - \frac{\lambda}{\lambda_2} \right), \quad (24)$$

by analogy with Eq. (9). The resulting mode separations will always be less than those predicted by the circuit in Fig. 14-23.

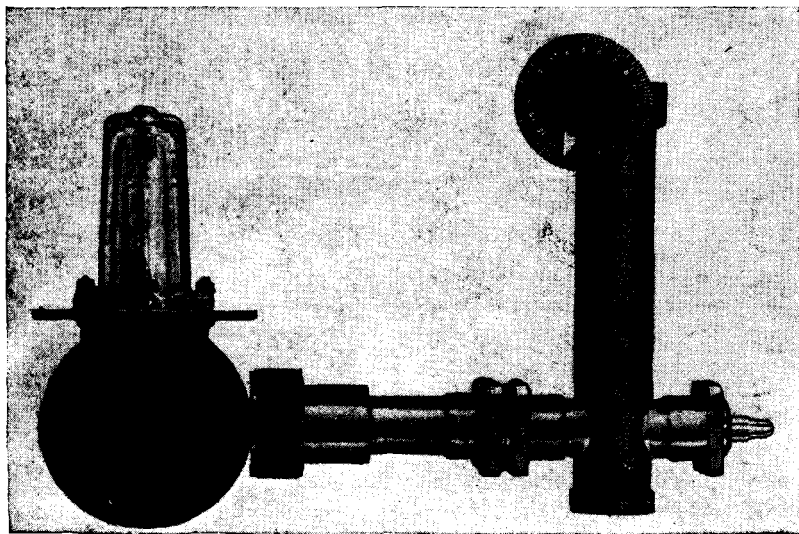


Fig. 14-24.—A magnetron coupled to a variable tuning stub.

**14-10. Single-stub Tuning.**—For applications requiring small tuning, of 1 per cent or less, at pulse-power outputs of a few kilowatts, it is possible to convert an ordinary fixed-frequency magnetron into a tunable one by a single tuning stub correctly positioned on the output line. Such an arrangement<sup>1</sup> is shown in Fig. 14-24. An equivalent circuit for Fig. 14-24 can be drawn by analogy with the equivalent circuit of Fig. 14-23 for coaxial-coupled cavity tuning by representing the tuning stub

<sup>1</sup> F. F. Rieke, "Adjustment of Magnetron Frequency by an External Tuner," RL Report No. 412, Sept. 6, 1943.

as a parallel-resonant circuit, at the center of the tuning range. Because it is desirable to keep the maximum voltage in the tuning stub low to avoid voltage breakdown, the useful tuning range is generally limited to that obtained by moving the plunger  $\pm 0.175\lambda_0$  about the central length,  $l = (m\lambda_0/2) + (\lambda_0/4)$ . Over this tuning range, the frequency sensitivity of a short length  $l_1$  between the magnetron and the stub is unimportant, the only necessary criterion being that it be electrically  $m\lambda_0/2$  long. Under the above condition then, the equivalent circuit of Fig. 14-13 for double-output tuning is appropriate if the length  $l$  in Fig. 14-13 is

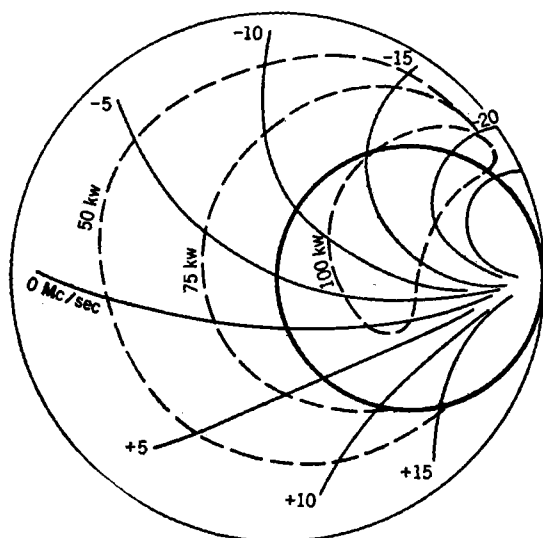


FIG. 14-25.—Rieke diagram of a magnetron tuned by a single-stub tuner. The heavy circle is the locus of the tuning curve.

identified with the plunger length. Equation (9) is then valid if  $Q_{E2}$  is now understood to mean normal magnetron external  $Q$ ; for the extreme values of  $l = \lambda_0/4 \pm 0.175\lambda_0$ , the useful tuning range is

$$\frac{\Delta\lambda}{\lambda} = \frac{2}{Q_{E2}} \quad (25)$$

A useful alternate way of describing single-stub tuning is shown in the typical Rieke diagram<sup>1</sup> of Fig. 14-25. The tuning stub is connected at that point ( $\pm m\lambda/2$ ) along the output line toward which the frequency contours converge, this condition being equivalent to making  $l_1$  electrically  $m\lambda/2$  long. The impedance presented to the magnetron by the

<sup>1</sup> *Ibid.*

variable stub and the matched line are represented by points on the heavy circle in this diagram. Location of the frequency sink within rather than at the edge of the circle is the effect of the finite length  $l_1$ . Restricting the useful tuning range to  $l = \lambda_0/4 \pm 0.175\lambda_0$  corresponds to operating on that semicircle of the heavy circle centered at the match point of the diagram.

## CHAPTER 15

### ELECTRONIC TUNING

By W. V. SMITH

The development of microwave magnetrons has until recently been concerned only with on-off pulse modulation as a means of transmitting intelligence. Because the magnetron is a self-excited oscillator, not an amplifier, it is impossible to modulate at low power levels and then amplify to the desired output as in conventional amplitude- and frequency-modulation systems; it is necessary instead for the impressed signal to modulate the full output of the tube in one stage. As a consequence, the power consumption in the modulator must increase as the output power is increased. Although this qualitative observation applies to both amplitude modulation and frequency modulation, the modulating power requirements for amplitude modulation may be deduced in a straightforward fashion from the static characteristics of magnetrons and will not be discussed further. It will be seen from the same static characteristics that a frequency modulation of several megacycles per second accompanies any straightforward amplitude modulation of microwave magnetrons. Although it would seem from Chap. 16, "Stabilization of Frequency," that there may be ways to overcome this difficulty, neither the theory nor the experiments with amplitude modulation of frequency-stabilized magnetrons have been pursued far enough to demonstrate completely the practicality of amplitude modulation. Frequency modulation, which is the subject of this chapter, has been demonstrated to be practical and rests on a sound theoretical basis. Present f-m magnetron designs are of two classes: electron-beam tuning and magnetron-diode tuning. Both are dependent on variation of the space charge to produce the frequency modulation, but they differ in the means employed to control the space charge.

#### ELECTRON-BEAM TUNING

**15-1. General Considerations.**—The physical sizes involved in microwave resonant-cavity oscillators suggest a direct method of electronically varying the cavity frequency that is not feasible for longer wavelength oscillators. This method consists of injecting an electron beam of variable intensity into a region of high r-f electric fields in the cavity. These r-f fields induce r-f components of electron motion, that is, r-f

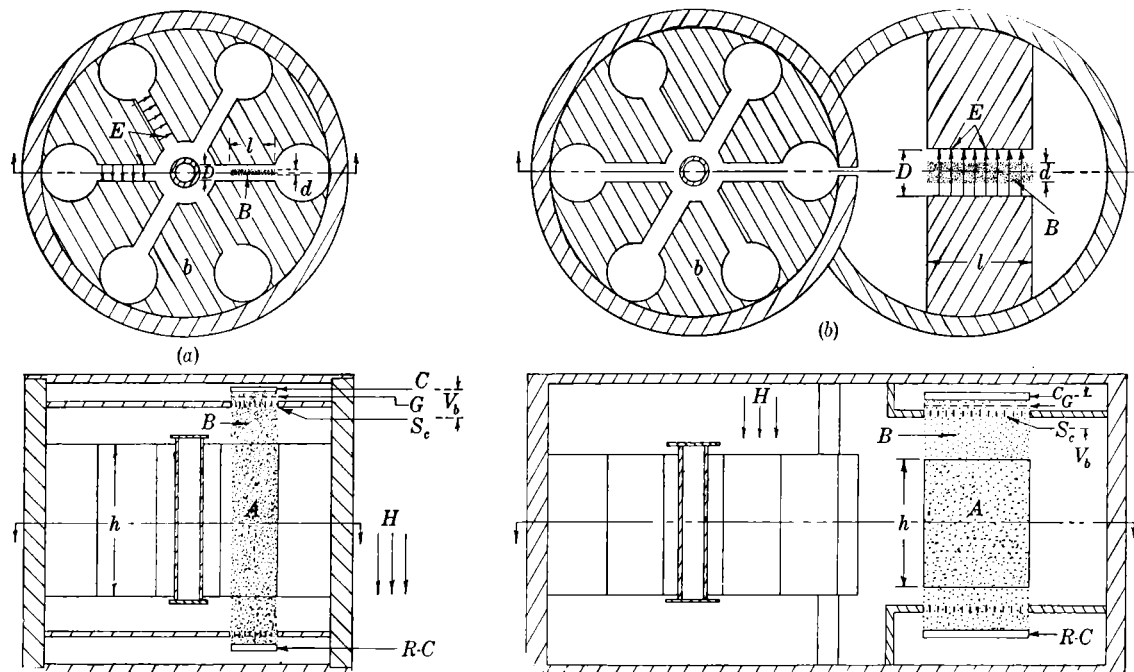


FIG. 15-1.—Examples of electronic tuning of magnetrons. (a) Internal tuning.  $H$  is the d-c magnetic field;  $B$  is the electron beam;  $l$  is the beam length;  $d$  is the beam width;  $\tilde{E}$  is the r-f electric field;  $D$  is the gap width;  $\tilde{E}D$  is the r-f voltage  $\tilde{V}_{RF}$ ;  $h$  is the condenser plate height;  $A$  is the condenser area  $lh$  traversed by the beam;  $AD$  is the gap region traversed by the beam;  $Ad$  is the beam region;  $C$  is the cathode for the electron beam;  $G$  is the control grid;  $S_e$  is the screen grid;  $R-C$  is the reflector or collector;  $V_b$  is the cathode-to-screen-grid voltage, which equals the cathode-to-condenser plate voltage; and  $b$  is the copper block. (b) External tuning, showing the magnetron and reactance tube.

currents that for simple cases may be considered to be analogous to the displacement currents in a dielectric. In this simplified picture, the variable intensity of the electron stream is analogous to a variable dielectric constant in the cavity, hence a variable resonant frequency of the cavity oscillator. As a numerical example, the frequency of a 4000-Mc/sec c-w magnetron with an output power of 25 watts can be modulated  $\pm 5$  Mc/sec by a  $\pm 10$ -ma modulation of a 100-volt, 10-ma electron beam. The incident amplitude modulation in this illustration is negligible. Typical examples of magnetrons that are tuned by electron beams are shown in Fig. 15-1a and b.

In Fig. 15-1a the electron beam is shot through a portion of the slot of a hole-and-slot magnetron, whereas in Fig. 15-1b the beam is shot through the capacitive region of a cavity coupled to the magnetron (see Chap. 14 for a general discussion of cavity-tuned magnetrons). The same nomenclature and derivations will be applicable to both Fig. 15-1a and b if in Fig. 15-1b the term "cavity" is understood to apply to the combination of the magnetron and the reactance tube. In Fig. 15-1a the electron beam traverses a region of high r-f electric field which is perpendicular to the d-c motion of the electrons. The electron beam is accelerated by the screen-grid potential  $V_s$  and passes between the segments of the anode block, which is at screen-grid potential. A magnetic field  $H$ , parallel to the axis of the tube, keeps the beam focused. The beam intensity is varied by the control grid  $G$ , and in the simplest case the beam is collected by the collector  $R - C$ , which may or may not be at the copper-block potential  $V_0$ .

**15-2. Fundamental Equations of Beam Tuning. General Case.**—The important circuit parameters of a resonant cavity are its unloaded  $Q = Q_u$  and its resonant frequency  $\nu_0$ . If this cavity is traversed by an electron beam, it may be shown by perturbation methods that, providing the r-f energy stored in the electron stream is small compared with that in the cavity and providing the cavity resonances are spaced far apart compared with the frequency shift induced by the electrons, the only effects of the electron stream are to change the  $Q$  of the cavity from  $Q_u$  to  $Q_L$  and to change its resonant frequency from  $\nu_0$  to  $\nu$ . The derivation of  $Q_L$  and  $\Delta\nu$  follows.<sup>1</sup>

If there is no electron beam, Maxwell's equations for the fields in the cavity are

$$\nabla \times \vec{E}_0 = i\omega_0\mu_0\vec{H}_0 \quad (1a)$$

and

$$\nabla \times \vec{H}_0 = -i\omega_0\epsilon_0\vec{E}_0, \quad (1b)$$

<sup>1</sup> A. Baños, Jr., and D. S. Saxon, "An Electronic Modulator for C-w Magnetrons," RL Report No. 748, June 26, 1945.



where  $\tilde{E}_0$  and  $\tilde{H}_0$  represent the complex vector amplitudes of the  $e^{-i\omega_0 t}$  components of electric and magnetic fields, which are denoted by the subscript 0 when no electrons are present. The electric field satisfies the boundary condition that its tangential component vanish on the metallic walls of the cavity. Thus, on these walls that are assumed to be perfectly conducting

$$n \times \tilde{E}_0 = 0, \quad (2)$$

where  $n$  is a unit vector normal to the surface.

When electrons are present, Maxwell's equations are

$$\nabla \times \tilde{E} = i\omega\mu_0\tilde{H} \quad (3a)$$

and

$$\nabla \times \tilde{H} = -i\omega\epsilon_0\tilde{E} + \tilde{J}, \quad (3b)$$

where  $\tilde{J}$  is the complex vector amplitude of the  $e^{-i\omega t}$  component of the current density. In this case  $\omega$  may be a complex number (see Chap. 7) the real part of which represents frequency and the imaginary part, a damping term contributed by the electrons. The boundary conditions are unchanged by the presence of electrons, and again

$$n \times \tilde{E} = 0 \quad (4)$$

on the walls of the cavity.

In order to find the shift in resonant frequency produced by the electrons, the scalar product of  $\tilde{E}$  times the conjugate of Eq. (1b) is subtracted from the scalar product of  $\tilde{H}$  times the conjugate of Eq. (1a), yielding

$$\tilde{H} \cdot \nabla \times \tilde{E}_0^* - \tilde{E} \cdot \nabla \times \tilde{H}_0^* = -i\omega_0(\mu_0\tilde{H} \cdot \tilde{H}_0^* + \epsilon_0\tilde{E} \cdot \tilde{E}_0^*). \quad (5)$$

Similarly, the difference of the scalar products of  $\tilde{H}_0^*$  times Eq. (3a) and  $\tilde{E}_0^*$  times Eq. (3b) yields

$$\tilde{H}_0^* \cdot \nabla \times \tilde{E} - \tilde{E}_0^* \cdot \nabla \times \tilde{H} = i\omega(\mu_0\tilde{H} \cdot \tilde{H}_0^* + \epsilon_0\tilde{E} \cdot \tilde{E}_0^*) - \tilde{J} \cdot \tilde{E}_0^*. \quad (6)$$

By adding Eqs. (5) and (6) and integrating the result over the entire volume  $V$  of the cavity,

$$\begin{aligned} \int_V \nabla \cdot (\tilde{E}_0^* \times \tilde{H} + \tilde{E} \times \tilde{H}_0^*) dV &= i(\omega - \omega_0) \int_V (\mu_0\tilde{H} \cdot \tilde{H}_0^* \\ &+ \epsilon_0\tilde{E} \cdot \tilde{E}_0^*) dV - \int_V \tilde{J} \cdot \tilde{E}_0^* dV. \end{aligned} \quad (7)$$

In writing the left-hand side of Eq. (7), use has been made of the vector identity

$$\nabla(A \times B) = B \cdot (\nabla \times A) - A \cdot (\nabla \times B).$$

By the divergence theorem, the left side of Eq. (7) can be rewritten as a surface integral over the bounding surface of the cavity. If  $n$  is the

outward normal,

$$\int_V \nabla \cdot (\tilde{E}_0^* \times \tilde{H} + \tilde{E} \times \tilde{H}_0^*) dV = \int_S n \cdot (\tilde{E}_0^* \times \tilde{H} + \tilde{E} \times \tilde{H}_0^*) dS = 0 \quad (8)$$

because the tangential components of both  $\tilde{E}_0$  and  $\tilde{E}$  vanish on the metallic boundary of the cavity. Hence Eq. (7) reduces to

$$i(\omega - \omega_0) = \frac{\int_V \tilde{J} \cdot \tilde{E}_0^* dV}{\int_V (\mu_0 \tilde{H} \cdot \tilde{H}_0^* + \epsilon_0 \tilde{E} \cdot \tilde{E}_0^*) dV}. \quad (9)$$

Thus far the calculation has been rigorous, but Eq. (9) can be simplified if analysis is restricted to the condition where  $\tilde{E}$  and  $\tilde{H}$  differ only slightly from  $\tilde{E}_0$  and  $\tilde{H}_0$ . Then

$$\omega - \omega_0 = \frac{1}{4iW} \int_V \tilde{J} \cdot \tilde{E}^* dV, \quad (10)$$

where  $W$  is the average energy stored in the unperturbed cavity and is equal to

$$W = \frac{1}{4} \int_V (\mu_0 |\tilde{H}_0|^2 + \epsilon_0 |\tilde{E}_0|^2) dV.$$

The electronic damping is best shown by rewriting Eq. (10) in the form

$$\frac{\Delta\nu}{\nu_0} - i \frac{1}{2Q_{el}} = \frac{1}{8\pi i \nu_0 W} \int_V \tilde{J} \cdot \tilde{E}^* dV, \quad (11)$$

where  $\Delta\nu$  is the frequency shift and  $Q_{el}$  is the electronic  $Q$ , which equals  $2\pi$  times the energy stored divided by the energy lost per cycle to the electrons. If the cavity walls are not perfectly conducting,  $Q_{el}$  can be combined with  $Q_u$  of the cavity in the usual manner, that is,

$$\frac{1}{Q_{el}} + \frac{1}{Q_u} = \frac{1}{Q_L}.$$

The plausibility of Eq. (11) may be seen by realizing that  $\int_V \tilde{J} \cdot \tilde{E}^* dV$  is the analogue of  $\tilde{V}^* \cdot \tilde{I}$  in ordinary circuit theory. Therefore, the real part of  $\int_V \tilde{J} \cdot \tilde{E}^* dV$  is twice the work done per second on the electrons by the cavity fields, and, by definition, division by  $8\pi\nu_0 W$  yields  $1/2Q_{el}$ , which is the result given in Eq. (11). Furthermore, in conventional circuit theory, the addition of a simple capacitive or inductive element to the circuit in such a way that only a small proportion of the stored energy is associated with the added element results in a relative shift

in resonant frequency equal to one-half the ratio of this energy in the added element to the total energy. Thus, because the imaginary part of  $1/2\pi\nu_0\int\tilde{J}\tilde{E}^*dV$  is twice the energy stored in the electron beam that passes through a magnetron cavity, division by  $4W$  gives the relative frequency shift. It is to be noted that Eq. (11) is valid in all electronic tuning schemes of practical interest because the energy stored in the beam is small compared with the total energy stored.

In an oscillator the electrons do work on the r-f fields; that is,  $Q_{el}$  is negative. In discussing electronic tuning, although the final aim is to modulate the frequency of an oscillating magnetron, it is convenient to discuss first the changes in the resonant frequency and  $Q$  that are produced in a nonoscillating magnetron by an electron beam that passes through the same high r-f fields that would exist in an oscillating magnetron. If the  $Q$  is not lowered greatly, the relative frequency shift for the oscillating magnetron will then be equal to that for the nonoscillating magnetron. Also, although the final aim is to modulate the magnetron frequency by modulating the electron beam at some modulation frequency  $\nu_m$ , future derivations will be restricted to computing the frequency shift produced by a steady electron beam. Because  $\tilde{J}$  remains essentially unchanged over many cycles of r-f fields when  $\nu_m \ll \nu_0$ , the modulation may then be treated as a succession of quasi-steady states, and the ensuing spectrum may be computed from conventional f-m analysis. Ratios of  $\nu_m$  to  $\nu_0$  less than  $1/100$  are, in general, satisfactory.<sup>1</sup>

Two methods of frequency modulation that involve changes in  $\tilde{J}$  are possible. In one the magnitude of  $\tilde{J}$  is changed, and in the other the phase  $\phi$  of  $\tilde{J}$  is changed relative to  $\tilde{E}$ . Any change in the phase changes the value of  $Q_{el}$ , whereas a change in the magnitude of  $\tilde{J}$  maintains  $1/Q_{el}$  equal to zero if  $\phi$  is kept constant at a value such that  $\int_V \tilde{J}\tilde{E}_{dv}^*$  is imaginary. The reflex klystron in the middle of one of its modes is a good example of frequency modulation by means of phase modulation; the phase is controlled by the reflector. The klystron illustrates the typical variation of  $Q_{el}$  (here negative) with frequency and the consequent variation in efficiency with frequency.

*Uniform Electron Gas.*—The application of Eq. (11) may be illustrated by the simple example of a cavity filled with a uniform electron gas of  $N$  electrons per cubic meter. At frequencies high enough so that the motion of the electrons takes place in a region so small that the spatial variation of the r-f field can be neglected,  $\tilde{J}$  may be simply evaluated from the equations of motion, neglecting Lorentz forces.<sup>2</sup> Thus, where

<sup>1</sup> See L. P. Smith and C. Shulman, Princeton Technical Report No. 22C, for an analysis applicable to the type of tuning shown in Fig. 15-1.

<sup>2</sup> A. Baños, Jr., and D. S. Saxon, *op. cit.*

$v$  is the electron velocity and  $r$  is the vector displacement of the electron,

$$m \left( \frac{dv}{dt} \right) = -e\tilde{E}e^{-i\omega t}, \quad (12)$$

$$v = \frac{e}{mi\omega} \tilde{E}e^{-i\omega t} \quad (13)$$

and

$$r = \frac{e}{m\omega^2} \tilde{E}e^{-i\omega t}. \quad (14)$$

The magnitude of the current density  $\tilde{J}$  may be calculated from Eq. (13). Thus,

$$\tilde{J}e^{-i\omega t} = -Nev = \frac{iNe^2}{m\omega} \tilde{E}e^{-i\omega t}, \quad (15)$$

where  $N$  is the number of electrons per cubic meter. Substitution of Eq. (15) in Eq. (11), remembering that

$$W = \frac{1}{2}\epsilon_0 \int_V |\tilde{E}|^2 dV, \quad (16)$$

yields the well-known dispersion formula for an electron gas of low density,<sup>1</sup>

$$\frac{\Delta\nu}{\nu_0} = \frac{1}{\epsilon_0} \frac{Ne^2}{2m\omega^2} = \frac{\rho e}{2m\omega^2\epsilon_0}, \quad (17)$$

where  $\rho$  is the charge density. Because collisions with the cavity walls are ignored and the electron velocity is a periodic function of time about a fixed point, there is no way for the electrons to abstract energy from the r-f fields, and it follows that  $Q_{el}$  is infinite. Equation (17) is the fractional change of the resonant frequency of a cavity from its empty-space value to its value when the cavity is filled with matter having a dielectric constant

$$K = 1 - \frac{Ne^2}{\epsilon_0 m\omega^2}. \quad (18)$$

For high beam-current densities (0.2 amp/cm<sup>2</sup> at 100 volts for a high-vacuum tube)  $N = 2.1 \times 10^{15}$ . Substitution in Eq. (17) shows that even for this value of  $N$ , at 10,000 Mc/sec, the total frequency shift due to the electrons is only 8.5 Mc/sec. Although a value of  $N$  substantially higher than  $10^{15}$  could be obtained by an arc discharge, no control of the density would be possible in the high r-f fields present.

It is possible to increase the tuning considerably by increasing  $\tilde{J}$  for fixed  $\tilde{E}$  and fixed d-c cathode emission using either of two methods. Referring to the first half of Eq. (15) these methods may be distinguished

<sup>1</sup> J. A. Stratton, *Electromagnetic Theory*, McGraw-Hill, 1941, pp. 325-327.

as increasing either the number of electrons  $N$  or the velocity of the electrons  $v$ . In the klystron, an example of the first method, an initially small velocity modulation superposed on a beam of electrons is changed by means of a drift space into a density modulation. By the use of a reflector the region of high-density modulation is made to coincide with the region of high  $\tilde{E}$  that produced the original velocity modulation. Thus  $N$  is increased locally with no added drain on the d-c emission from the cathode. An example of the second method is a cavity containing electrons in a magnetic field of flux density  $B$  with associated cyclotron frequency

$$\nu_c = \frac{eB}{2\pi m}. \quad (19)$$

In those regions where  $\tilde{E}$  is perpendicular to  $B$ , the resonance effects near  $\nu = \nu_c$  can be shown to increase greatly the amplitude of the displacement vector  $r$  for fixed  $\tilde{E}$ . As a consequence  $v$  is increased proportionally because an electron must now cover a greater distance in one cycle.

The present discussion is limited to the method of varying the electron velocity  $v$ , which so far appears to be the only practical way of handling the high output power of magnetrons.

### 15-3. The Principles of Electron-beam Tuning in a Magnetic Field.—

Figure 15-1 will be taken as the starting point for a quantitative analysis of electron-beam tuning. The cavity contains a region of high and fairly uniform electric field. A beam of electrons can readily be injected into this high-field region and can be kept focused by an aligning magnetic field that, being perpendicular to the electric field, also serves to determine the amplitude  $|r|$  of the electronic oscillations and hence the amount of tuning attainable.

The problem may be divided into an r-f problem and a d-c problem. In the r-f problem the tuning, the amplitude  $|r|$ , and the electronic  $Q$  are evaluated in terms of the d-c current density  $J_0$ , the d-c electron velocity  $v_0$ , the magnetic field  $B$ , and the physical dimensions. In the d-c problem,  $J_0$  and  $v_0$  are evaluated in terms of the cathode-to-block potential  $V_0$  and the physical dimensions. In both problems the effects of the fringing fields above and below the gap region are neglected. The effective lumping of the capacitance in Fig. 15-1 concentrates the r-f electric field in the gap region and leaves the r-f fringing fields small. The location of the beam in a plane of r-f symmetry further minimizes the fringing, which is estimated by Saxon and Baños<sup>1</sup> to affect tuning and electronic  $Q$  by less than 1 per cent. The somewhat more important

<sup>1</sup> A. Baños, Jr., and D. S. Saxon, "An Electronic Modulator for C-w Magnetrons," RL Report No. 748, June 26, 1945.

effects of the fringing fields for the d-c problem are shown<sup>1</sup> always to increase the current necessary to effect a given amount of tuning. If the fringing fields are neglected, the derivations that follow represent a lower limit on  $J_0$ .

Figure 15.2 illustrates the spiral path of an electron in the beam as it travels through the cavity. The electrons begin at zero amplitude, rise to a maximum radius  $|r_{\max}|$ , and fall again to zero; this process repeats itself to first approximation with a frequency  $\nu - \nu_c$  as long as the electrons remain between the plates. The frequency  $\nu - \nu_c$  is a beat between the operating frequency and the cyclotron frequency  $\nu_c$  associated with the magnetic field  $B$  [Eq. (19)]. The electrons enter the gap region with a kinetic energy  $mv_0^2/2$ . The kinetic energy that the electrons gain while in the gap region contributes to the stored r-f energy and hence changes the cavity frequency. The extra kinetic energy possessed by the electrons when they leave the gap (energy that has been acquired from the r-f fields of the cavity) is ultimately dissipated at the collector and hence represents a loss or resistance in the circuit.

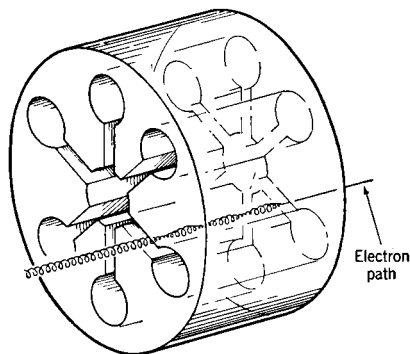


FIG. 15.2.—Path of an electron in beam tuning.

In the r-f problem, the analogous relations to Eqs. (14) and (17) of the electron gas treatment have been derived by Saxon and Baños.<sup>1</sup> Essentially they are

$$r_{\max} = \frac{2eE}{m\omega^2} \frac{1}{|\beta^2 - 1|}, \quad (20)$$

$$\frac{\Delta\nu}{\nu_0} = \frac{\rho e}{2m\omega^2\epsilon_0} \frac{q}{1 - \beta^2} F, \quad (21a)$$

and

$$\frac{1}{2Q_{el}} = \frac{\rho e}{2m\omega^2\epsilon_0} \frac{q}{1 - \beta^2} G, \quad (21b)$$

where

$$\beta = \frac{\nu_c}{\nu}. \quad (22)$$

In Eqs. (21)

$$q = \frac{\text{stored electric field energy in beam region}}{\text{total stored electric field energy}} = \frac{d}{D} p,$$

<sup>1</sup> *Ibid.*

where

$d$  = beamwidth,

$D$  = gap width,

$$p = \frac{\text{energy of the electric field stored in the gap region}}{\text{total stored electric field energy}}, \quad (23)$$

$$\rho = \text{charge density} = \frac{J_0}{v_0}. \quad (24)$$

$F$  and  $G$  are functions of the phase of the spiral path at which the electron leaves the gap region. Their values, generally less than unity, are

$$F = 1 - \frac{\beta + 1}{2} \frac{\sin \alpha}{\alpha}, \quad (25a)$$

and

$$G = \frac{\beta + 1}{2} \frac{(1 - \cos \alpha)}{\alpha}, \quad (25b)$$

where

$$\alpha = (\omega - \omega_c) \frac{h}{v_0} = (\omega - \omega_c)t \quad (26)$$

and

$t$  = transit time through the gap.

Thus,  $\alpha$  is the phase angle of the beat frequency between  $\nu$  and  $\nu_c$  over the length  $h$  of the gap. The approximations that have been made render Eqs. (20) and (25) invalid near  $\beta = 0$  and also in the immediate vicinity of  $\beta = 1$ .

The interpretation of Eq. (25b) in terms of the spiral path of Fig. 15-2 is clear for the case of  $G = 0$ ; that is,

$$\alpha = 2\pi n, \quad \text{where } n \text{ is an integer} \neq 0, \quad (27)$$

because this is the condition in which the electrons leave the gap region at a node in their r-f motion, thus abstracting no r-f energy from the field. The quantities  $F$  and  $G$  are plotted in Fig. 15-3. Separate evaluations of Eqs. (26) and (21) lead to an indeterminate answer at  $\beta = 1$ ,  $\alpha = 0$ ; but the proper limiting process shows that the tuning is zero and the loss finite for this practically unimportant case. It is important to note that the change of sign of  $(1 - \beta^2)$  in Eq. (21b) at  $\beta = 1$  considered in conjunction with Fig. 15-3 means that  $1/2Q_{el}$  is always positive or zero whereas the tuning changes sign near  $\beta = 1$  because  $\Delta\nu$  is positive for  $\beta < 1$  and negative for  $\beta > 1$ .

Considering now the d-c problem, the maximum current density  $J_{0\max}$  that can be sent between the two plates at a d-c potential  $V_b$ , in the absence of r-f fields, is<sup>1</sup>

<sup>1</sup> A. V. Haefl, *Proc. IRE*, **27**, 586, September 1939.

$$J_{0\max} = \frac{\epsilon_0}{Dd} \frac{16}{9} \sqrt{\frac{2e}{m}} V_b^{3/2} \Gamma_{\max} = \frac{9.35 \times 10^{-6}}{Dd} V_b^{3/2} \Gamma_{\max}, \quad (28)$$

where  $\Gamma_{\max}$  is a slowly varying function of  $d/D$  plotted in Fig. 15-4. It is assumed that the superposed r-f field does not greatly modify Eq. (28). The space-charge effect that limits the current also reduces the electron velocity, thus affecting  $\rho$ ,  $F$ , and  $G$  in Eqs. (21). An effective beam velocity  $v_e$ , determined by an effective beam voltage  $V_0$ , must

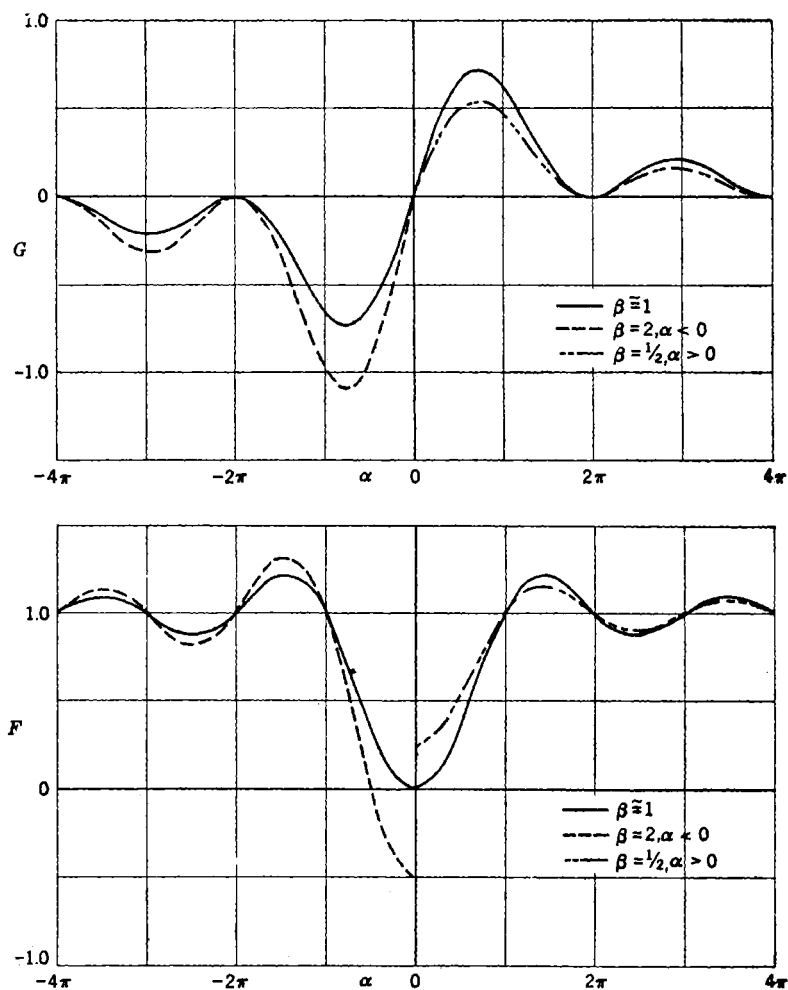


FIG. 15-3.— $F$  and  $G$  as functions of  $\alpha$  and  $\beta$ .



therefore be used in these equations. Because  $\Delta\nu/\nu_0$  varies as  $(1/\nu_0)_{\text{avg}}$  to a first approximation,  $1/\nu_e$  will be defined as  $(1/\nu_0)_{\text{avg}}$  and

$$eV_0 = \frac{m\nu_e^2}{2}. \quad (29)$$

The ratio  $V_0/V_b$  is related to  $d/D$  and  $J_0/J_{0\text{max}}$  as shown in Fig. 15-5.

If Eq. (27) is to be satisfied over the whole f-m band of the tube,  $\alpha$  and therefore  $V_b$  must be maintained constant; therefore the frequency modulation must be attained by varying  $J_0$  by the grid control while maintaining  $V_b$  constant. Under these conditions the frequency modulation will be linear with  $J_0$  except where  $J_0$  is near the space-charge-limited value  $J_{0\text{max}}$ , in which case the rapid variation in  $V_0$  will destroy the linearity (Fig. 15-5). There is usually some maximum value of  $r$  permissible before an excessive number of elec-

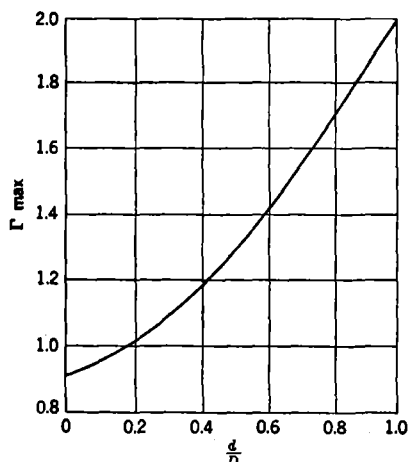


FIG. 15-4.—Parameter  $\Gamma_{\text{max}}$  as a function of  $d/D$ .

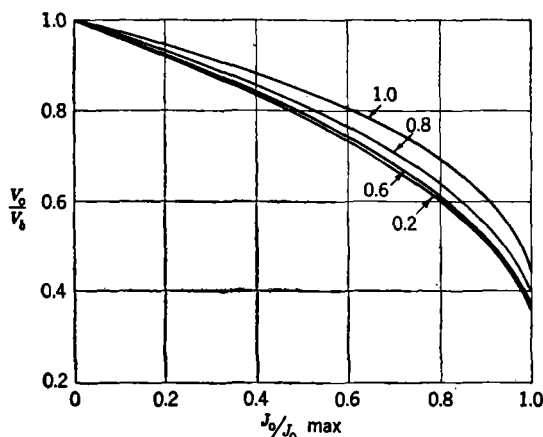


FIG. 15-5.— $V_0/V_b$  as a function of  $J_0/J_{0\text{max}}$  for several values of  $d/D$ .

trons hits a part of the tube. In Fig. 15-1, for instance, this value might be

$$r_{\text{max}} = \frac{D - d}{2} \quad (30)$$

and represents the distance between the electron beam and the cavity walls in the absence of an r-f electric field. If the number of electrons per cubic meter  $N$  is maintained constant, then  $r_{\max}$  limits the power that can be handled for a given amount of tuning because, at a fixed r-f voltage, changing the magnetic field to increase the tuning increases the orbit size and an increase in the r-f field at fixed tuning likewise increases the orbit.

**15.4. The Engineering Equations of Electron-beam Tuning.**—Equations (20) through (30) may be used either to analyze the electronic tuning that will be available with a given anode-block design or to synthesize an optimum anode-block design for a given amount of electronic tuning and output power. The first problem is by far the simpler. By starting with the magnetron output power, the r-f voltage across the gap through which the electrons are to travel may be computed by the methods discussed in previous chapters. Equations (20) and (30) then determine how closely one may approach the cyclotron frequency before electrons strike the walls of the gap. The tuning and the loss may then be computed from Eqs. (21), where the maximum value of  $\rho$  is limited by the cathode emission or by the space-charge limit [Eq. (28)].

In the synthesis of an optimum anode-block design, however, a convenient procedure is to start with the desired magnetron output power  $P_o$ , the external  $Q = Q_E$ , the frequency  $\nu_0$ , the desired tuning  $\Delta\nu$ , and the maximum safe peak current density  $J_0$ , which is determined by cathode quality, as the independent variables. These will then determine the values of the dependent variables  $V_b$ ,  $p$ ,  $\beta$ ,  $D$ ,  $d$ ,  $l$ , and  $h$ . The procedure is as follows. First, through  $\tilde{V}_{RF}$ , the r-f voltage appearing across the gap  $P_o$  and  $Q_E$  may be related to  $|r_{\max}|$  and  $D$ , subject to certain restrictions. It will then follow that the product  $\tilde{V}_{RF}(\Delta\nu/\nu_0)$  determines  $pV_b$ , subject to certain other restrictions, one of which is that the space-charge limit  $J_{0\max}$  is made equal to the cathode-emission limit  $J_{0p}$ . From  $V_b$ ,  $J_{0p}$ ,  $\tilde{V}_{RF}$ , and  $\Delta\nu/\nu_0$ , it is then possible to determine  $D$  and  $\beta$  for fixed  $d/D$  and  $p$ . Construction considerations limit the choice of  $p$ , and other considerations fix  $d/D$  near the value of  $\frac{1}{2}$ . The no-loss condition of Eq. (27) determines  $h$  when  $\beta$  is known. If the subsidiary restrictions—which are less important interrelations of the dependent variables—can be satisfied, the design is then complete.

The first step is to relate  $P_o$  to  $\tilde{V}_{RF} = \tilde{E}D$  (see Fig. 15.1a). To do this a characteristic admittance  $Y_c$  is ascribed to the gap region according to the relation

$$Y_c = 2 \left( \frac{\text{energy stored in gap region}}{\tilde{V}_{RF}^2} \right) = \frac{1}{60} \frac{lh}{D\lambda}, \quad (31)$$

using only the d-c capacitance of the gap region as a first approximation

to its actual value. This d-c approximation to  $Y_c$  will be used throughout this chapter. If the magnetron is coupled to the useful load by some lead (not shown in Fig. 15-1) having an external  $Q = Q_E$  as defined in Chap. 5, Eqs. (23) and (31) together with the definition of  $Q_E$  yield

$$\bar{V}_{RF} = \left( \frac{2pP_0Q_E}{Y_c} \right)^{1/2}. \quad (32)$$

It will be seen that in addition to  $P_0$ , Eq. (32) contains the new dependent variable  $Y_c$ , which is a function of three of the six dependent variables previously listed. Although their variation in subsequent equations is more important,  $p$ ,  $P_0$ , and  $Q_E$  enter Eq. (32) in an insensitive fashion, appearing as fractional powers. It is convenient, therefore, to make a trial guess at  $D$ ,  $l$ , and  $h$ , to use these estimates in subsequent calculations, and then to revise the estimates as is required by the final computation. The quantity  $p$  [Eq. (23)], which depends on  $l$ , is easily estimated. For a tube like that shown in Fig. 15-1a  $p$  would be approximately  $\frac{1}{10}$  because one of six oscillators is tuned and over half of the electric energy stored by the oscillator and its associated strap resides in the gap region. More accurate estimates of  $p$  can be made from the circuit analyses of the resonant cavity given in Chaps. 2 and 8. The external  $Q$  will be determined by conditions not affecting the electronic tuning problem, such as pulling figure, mode spectrum, and the electronic efficiency of the magnetron itself. Subject to these conditions,  $Q_E$  should be kept as low as possible to minimize  $V_{RF}$ .

A second relation involving  $V_{RF}$  may be derived from Eqs. (20) and (30).

$$\begin{aligned} V_{RF\max} &= \frac{m\omega^2|(\beta^2 - 1)|}{4e} \left( 1 - \frac{d}{D} \right) D^2 \\ &= 5 \times 10^6 |(\beta^2 - 1)| \left( 1 - \frac{d}{D} \right) \left( \frac{D}{\lambda} \right)^2. \end{aligned} \quad (33)$$

Equation (33) represents the maximum permissible r-f voltage at which the electrons do not hit the plates. Equations (32) and (33) set an upper limit to the output power  $P_0$  that can be handled by the beam.

By combining Eqs. (21a), (24), (27), and (29), the fractional tuning becomes

$$\frac{\Delta\nu}{\nu_0} = \frac{1}{4\epsilon_0\omega^2} \left( \frac{2e}{m} \right)^{1/2} \left( \frac{J_0}{V_b^{1/2}} \right) \left( \frac{V_b}{V_0} \right)^{1/2} p \frac{d}{D} \frac{1}{1 - \beta^2}, \quad (34)$$

or, in more practical units,

$$\nu_0 \Delta\nu = 4.24 \times 10^6 p \frac{d}{D} \frac{1}{1 - \beta^2} \left( \frac{J_0}{V_b^{1/2}} \right) \left( \frac{V_b}{V_0} \right)^{1/2}, \quad (35)$$

where  $\nu$  is in megacycles per second,  $J_0$  in amperes per square centimeter, and  $V$  in volts. Equation (35) is plotted in Fig. 15-6 with the restriction that  $J_0 = J_{0\max}$ , under which condition the average value of  $(V_b/V_0)^{1/2}$  is 1.58. To maximize the fractional tuning  $\Delta\nu/\nu_0$  while holding  $V_{RF\max}$  constant, only the quantity  $J_0/V_b^{1/2}$ , which is proportional to the charge density  $\rho$ , must be maximized, since the small variation of

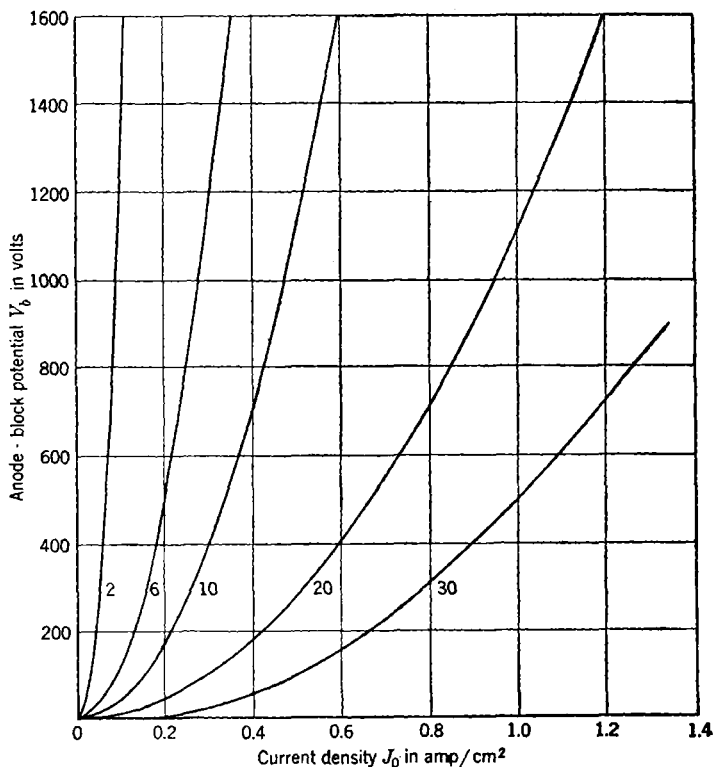


Fig. 15-6.—Anode-block potential  $V_b$  as a function of current density  $J_0$  for various values of  $(D/d)(1 - \beta^2)/p(\nu\Delta\nu/10^4)$  with  $(V_b/V_0)^{1/2} = 1.58$ .

$(V_b/V_0)^{1/2}$  may be ignored (see Fig. 15-5). In the space-charge-limited region,  $J_0$  may be made equal to  $J_{0\max}$ , whence, from the proportionality of  $J_{0\max}$  to  $V_b^{3/2}$  in Eq. (28),  $\Delta\nu/\nu_0$  is proportional to  $V_b$ . To increase  $V_b$  beyond the point at which  $J_{0\max}$  equals the emission limit  $J_{0p}$  decreases the tuning, however, because the increase in electron velocity decreases the space-charge density. Thus Eq. (34) is maximized by equating  $J_0$  to both  $J_{0p}$  and  $J_{0\max}$ . Eliminating  $J_0 = J_{0\max}$  from Eq. (34) by means of Eq. (28) and multiplying the resultant equation by Eq. (33)

yield

$$\left( V_{RF} \frac{\Delta\nu}{\nu_0} \right)_{\max} = p \left( 1 - \frac{d}{D} \right) \frac{2}{9} V_b \left( \frac{V_b}{V_0} \right)^{1/2} \Gamma_{\max} = p\phi V_b, \quad (36)$$

where  $\phi$  is plotted in Fig. 15-7, assuming  $(V_b/V_0)^{1/2} = 1.58$ .

It is to be noted that the product  $p\phi V_b$  is independent of magnetic field, again emphasizing that  $\beta$  can affect orbit size only for a given r-f voltage. The tuning is directly proportional to the relative orbit size, and the permissible r-f voltage is inversely proportional to it. Equation (36) for constant  $d/D$  is independent of  $D$  as a consequence of the space-charge limit set by Eq. (28).

Equation (36) determines the cathode-to-block potential  $V_b$  as a function of  $d/D$ . Maximizing both  $\Delta\nu/\nu_0$  and  $\tilde{V}_{RF}(\Delta\nu/\nu_0)$  in Eqs. (34) and (36) with respect to  $d/D$  represents a compromise best satisfied when  $d/D$  is approximately equal to  $\frac{1}{2}$ , as the plot of  $(d/D)\phi$  in Fig. 15-7 demonstrates. The value of  $V_b$  [Eq. (35)] is an important criterion of the practicality of the design. If  $V_b$  is too high, the tuner power will be great; if it is too low, close grid spacings are necessary to attain the requisite current density. It is always possible in the latter case to increase  $V_b$ , and thus to increase either tuning or power-handling ability of the design.

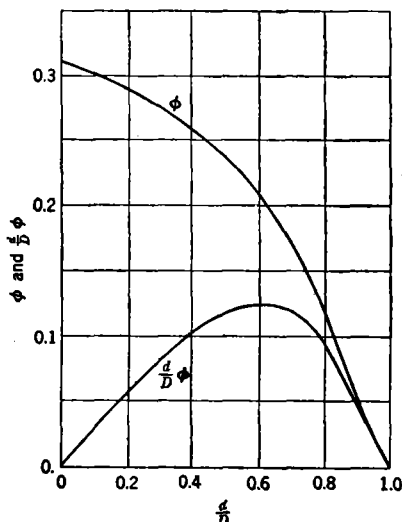


FIG. 15-7.—Parameter  $\phi$  as a function of  $d/D$ .

To summarize the engineering procedure to this point then,  $\tilde{V}$  has been determined by Eq. (32) from  $P_0$  and  $Q_E$  as independent variables and from trial values of  $Y_c$  and  $p$ . From  $\tilde{V}_{RF}$ ,  $\Delta\nu/\nu_0$  and  $p$ , together with a choice of  $d/D$  near  $\frac{1}{2}$ , and the assumed value of  $(V_b/V_0)^{1/2} = 1.58$ ,  $V_b$  is determined by Eq. (36) and Figs. 15-4 and 15-7. The assumption equating  $J_{op}$  to  $J_{0\max}$  in deriving Eq. (36) allows determination of  $D$  by Eq. (28). With  $D$  known,  $\beta$  can be determined from Eq. (33). It is to be noted that a trial value of  $D$  had been assumed in computing  $Y_c$  by Eq. (31), but it is, in general, not appropriate to make a new estimate of  $Y_c$  at this point, because  $l$  and  $h$  are still arbitrary.

The next step in the design is to determine if the requisite value of  $\beta$  is consistent with other demands of the problem. In the first place,

$\beta$  determines the cavity height  $h$  necessary to satisfy Eq. (27). This condition may be rewritten

$$\left( \begin{array}{c} n \\ \text{or} \\ K \gg 1 \end{array} \right) = \frac{\alpha}{2\pi} = \frac{(1 - \beta)\nu h}{v_e} = \frac{505(1 - \beta)}{V_b^{1/2}} \left( \frac{V_b}{V_0} \right)^{1/2} \frac{h}{\lambda}, \quad (37)$$

where  $v_e$  is defined by Eq. (29).

Equation (37) represents the no-loss condition or, strictly, the minimum-loss condition, since there is a velocity distribution across the beam. Because  $V_0$  varies with the current as shown in Fig. 15.5, some compromise value of  $V_0/V_b$  must be chosen, depending on the ratio of  $J_0$  to  $J_{0\max}$ , at which the loss is to be minimized. A reasonable value for ( $V_0/V_b$ ) is 0.7, in which case

$$\frac{h}{\lambda} = \frac{nV_b^{1/2}}{600(1 - \beta)}. \quad (38)$$

Although there are two adjustable parameters in Eq. (38),  $n$  and  $h$ , it cannot always be satisfied, because both parameters have further restrictions. Thus  $n$  must be an integer greater than or equal to 1, and the value of  $h$  must be consistent with considerations of size, cavity admittance  $Y_c$  effective lumping of capacitance ( $h < \lambda/4$ ), and magnet weight. Furthermore, if internal tuning of the tube is intended,  $h$  may already be determined by other considerations such as magnetron output power. For tuning of approximately one-tenth of 1 per cent it is not necessary to satisfy Eq. (37), although, as may be seen from Fig. 15.3 and Eq. (21a), it is still desirable to keep  $\alpha$  [see Eq. (26)] greater than  $\pi$  so that  $F$  will remain near unity.

An additional restriction on  $\beta$  is that it cannot be chosen too near 1 for reasons of magnet stability and of tunability. If the magnetron is to be mechanically tunable over a 10 per cent range, the extreme values of  $(\beta - 1)$  are 0.05 and 0.15 for a center value of  $(\beta - 1) = 0.09$ . This corresponds to a 300 per cent change in  $(\beta - 1)$  and would probably result in an intolerable variation in loss and ranges of frequency modulation. It is always possible to vary the magnetic field in a way that keeps  $\beta$  constant over the mechanical tuning range. Even if the approach of  $\beta$  to 1 is not limited by the above considerations, a fundamental limit is set by the inherent frequency sensitivity of Eq. (21a), the right-hand member of which is actually a function of  $\omega$  rather than  $\omega_0$  as has been tacitly assumed wherever  $\beta = v_e/\nu$  has been treated as a constant. This limitation, usually not very serious, has been discussed by Smith and Shulman,<sup>1</sup> who show that at maximum tuning the approximation of  $\omega$

<sup>1</sup> L. P. Smith and C. Shulman, Princeton Technical Report No. 22C.

by  $\omega_0$  is still valid providing that a quantity  $a_{\min}$  defined in Eq. (39), exceeds 1.

$$a_{\min} = \frac{9}{2\Gamma_{\max}} \left( \frac{nD}{h} \right)^2 \left( \frac{d}{D} \right) \frac{1}{p}. \quad (39)$$

Furthermore, if  $a_{\min}$  is less than  $\frac{1}{8}$ , more than one resonant frequency is possible.

When  $\beta$  is found to be satisfactory, the total input power required for the tuner can be determined. To find the total current the cathode length  $l$  must be known. This quantity is closely related to  $p$ , the ratio of stored energy in the gap to total stored energy in the cavity. It is also related to the cavity admittance  $Y_c$  in such a way that to maximize  $p$  and  $Y_c$ ,  $l$  must be as large as possible up to the approximate limit  $l = \lambda/4$ , where the lumped-constant approximation of  $Y_c$  becomes poor.

With the choice of  $l$  determined by a compromise between minimum current input to the tuner and maximum  $p$  and  $Y_c$ , all the variables have been determined. A new estimate of  $Y_c$  can then be made, and the process repeated if necessary. In general, the third approximation will be satisfactory.

As is evident from Fig. 15-1a, the current need not be collected at the potential  $V_b$  but can be collected at some lower potential near  $V_0$ . Alternately, the beam can be made to traverse the gap twice if the electrode  $R - C$  is made negative. In this case the space-charge equation [Eq. (28)] still limits  $J_{0\max}$ , but now  $J_{0\max}$  refers to the sum of the absolute values of the two current streams. Thus  $J_{0\max}$  here equals twice  $J_{0p}$ , the peak emission limit of the current stream leaving the cathode. Uncertainties as to where the return current is collected, whether or not more than two transits are possible, etc., complicate the use of a reflector at present.

Use of the equations derived above is best illustrated by a specific example. Let the independent variables be  $P_o = 3000$  watts,  $\nu_0 = 3000$  Mc/sec,  $\Delta\nu = 10$  Mc/sec,  $J_{0p} = 0.2$  amp/cm<sup>2</sup>, and  $Q_E = 200$ . No reflector will be used. The fractions  $p$  and  $d/D$  will be assumed equal to  $\frac{1}{2}$  and  $\frac{1}{2}$  respectively. As a first trial, the choice  $D = 0.5$  cm,  $l = 2$  cm, and  $h = 2$  cm yields  $Y_c = 0.0133$  mho, whence, from Eq. (28),  $D = 0.85$  cm. Next, from Eq. (33)  $\beta = 1.11$ , and from Eq. (37)  $h/n = 2.63$  cm. A choice of  $n = 1$ ,  $h = 2.63$  cm, and  $l = 2$  cm gives  $Y_c = 0.0103$  as a second approximation. Repeating the above process gives the convergence shown in Table 15-1. For simplicity  $l$  is maintained equal to 2 cm. The convergence is rapid despite the almost twofold change in  $D$  from the first guess. Experimental data on a tube similar to the above example are included in Table 15-5.

TABLE 15-1.—AN EXAMPLE OF CALCULATIONS FOR THE DESIGN  
OF AN ELECTRONICALLY TUNED MAGNETRON

Independent variables:  $P_o = 3000$  watts,  $\nu_o = 3000$  Mc/sec,  
 $\Delta\nu = 10$  Mc/sec,  $J_{op} = 0.2$  amp/cm<sup>2</sup>,  
 $Q_E = 200$ .

Arbitrary dependent variables:  $P = \frac{1}{2}$ ,  $d/D = \frac{1}{2}$ ,  $l = 2$ .

Trial	$D$ , cm	$h$ , cm	$Y_c$ , mhos	$\bar{V}_{RF}$ , volts	$V_b$ , volts	$\beta$	$n$
1	0.50	2.00	0.0133	4230	300	1.110	1
2	0.85	2.63	0.0103	4800	341	1.125	1
3	0.90	2.45	0.0091	5120	363	1.130	1
4	0.90	2.44	0.0090	5200	370	1.130	1

**15-5. Scaling.**—The usefulness of scaling laws in magnetron design has been amply demonstrated in Chap. 10. Anticipating a similar usefulness in electronic tuning, several scaling laws will be listed here without derivation, because they come from a straightforward application of the previously developed engineering equations.

The simplest type of scaling is that in which the percentage of tuning and the output power are kept constant. In this case, linear scaling of all dimensions, keeping  $V_b$ ,  $\beta$ , and  $Q_E$  constant and increasing  $J_o$  proportionally to the square of the frequency, solves the problem, thereby keeping the total current  $I$  constant. The total input power remains constant, and the high-frequency limit is set by excessive demands on cathode emission and close grid spacing.

A more practical scaling problem is that involved in keeping  $J_{op}$ ,  $p$ ,  $Y_c$ , and  $d/D$  constant and varying one or more of the quantities  $\Delta\nu$ ,  $\nu_o$ , or  $P_o$ . Denoting the two scaling points by the subscripts 1 and 2, and letting  $P_{DC} = V_b J_o p d$  be the d-c input power to the tuner, the resulting scaling laws are

$$\frac{V_{b1}}{V_{b2}} = \left( \frac{\nu_2}{\nu_1} \right) \left( \frac{\Delta\nu_1}{\Delta\nu_2} \right) \left( \frac{P_{o1}}{P_{o2}} \right)^{\frac{1}{2}}, \quad (40)$$

$$\frac{(1 - \beta_1^2)}{(1 - \beta_2^2)} = \left( \frac{\nu_2}{\nu_1} \right)^{\frac{1}{2}} \left( \frac{\Delta\nu_2}{\Delta\nu_1} \right)^{\frac{3}{2}} \left( \frac{P_{o1}}{P_{o2}} \right)^{\frac{1}{2}}, \quad (41)$$

$$\frac{D_1}{D_2} = \left( \frac{\nu_2}{\nu_1} \right)^{\frac{3}{4}} \left( \frac{\Delta\nu_1}{\Delta\nu_2} \right)^{\frac{3}{4}} \left( \frac{P_{o1}}{P_{o2}} \right)^{\frac{3}{4}}, \quad (42)$$

$$\frac{n_2(1 + \beta_2)h_1}{n_1(1 + \beta_1)h_2} = \left( \frac{\nu_2}{\nu_1} \right) \left( \frac{\Delta\nu_1}{\Delta\nu_2} \right)^2 \left( \frac{P_{o1}}{P_{o2}} \right)^{\frac{1}{2}}, \quad (43)$$

$$\frac{n_1(1 + \beta_1)l_1}{n_2(1 + \beta_2)l_2} = \left( \frac{\nu_2}{\nu_1} \right)^{\frac{3}{4}} \left( \frac{\Delta\nu_2}{\Delta\nu_1} \right)^{\frac{3}{4}} \left( \frac{P_{o1}}{P_{o2}} \right)^{\frac{1}{4}}, \quad (44)$$

and

$$\frac{n_1(1 + \beta_1)P_{DC1}}{n_2(1 + \beta_2)P_{DC2}} = \left( \frac{\nu_2}{\nu_1} \right)^{\frac{3}{2}} \left( \frac{\Delta\nu_1}{\Delta\nu_2} \right)^{\frac{1}{2}} \left( \frac{P_{o1}}{P_{o2}} \right)^{\frac{3}{4}}. \quad (45)$$



As an illustration of the use of these laws, the example of Table 15-1 will be scaled from 3000 Mc/sec to 1000 Mc/sec and 10,000 Mc/sec, keeping  $\Delta\nu$ ,  $P_o$ ,  $J_{op}$ ,  $p$ ,  $Y_c$ , and  $d/D$  constant. The results are shown

TABLE 15-2.—FREQUENCY SCALING OF THE EXAMPLE IN TABLE 15-1

Quantities held constant:  $P_o = 3000$  watts,  $\Delta\nu = 10$  Mc/sec,

$J_{op} = 0.2$  amp/cm<sup>2</sup>,  $Q_E = 200$ ,

$p = \frac{1}{2}$ ,  $d/D = \frac{1}{2}$ ,  $n = 1$ ,  $Y_c = 0.0090$ .

$\nu$ , Mc/sec	$V_b$ , volts	$\beta$	$D$ , cm	$h$ , cm	$l$ , cm	$P_{DC}$ , watts
1,000	1210	1.390	3.00	6.60	5.650	58.50
3,000	363	1.130	0.90	2.44	2.000	6.50
10,000	121	1.045	0.53	0.88	0.725	0.64

in Table 15-2. The most striking effect is the rapid increase of input power as the frequency is decreased. The approach of  $\beta$  to 1 at high frequencies makes the combination of mechanical and electronic tuning more difficult there.

**15-6. Internal vs. External Cavity Tuning.**—The two principal methods of utilizing electron-beam tuning have been shown in Fig. 15-1*a* and *b*. The beam is shot either through a portion of one or more of the side cavities of the magnetron or through a separate cavity appropriately coupled to the magnetron. At long wavelengths, where compactness is desirable, there is a distinct advantage to the internal tuner *a*; at short wavelengths, where the goal frequently is maximum size of parts, the external tuner *b* is preferred. It is important to compare the electrical properties of the two methods in order to be able to choose between them in specific cases.

Neither design can be made so that  $p = 1$ , the optimum condition for Eq. (36). In the internal tuner *a*, if  $N$  is the number of oscillators,  $m$  the number of side resonators through which a beam is shot,  $r_0$  the ratio of stored energy in the gap area to stored energy in one complete oscillator (including its associated straps), then

$$p_a = \frac{m}{N} r_0. \quad (46)$$

Vane tubes, because of their nonuniform gap width, require a modification (which will not be developed here) of some of the formulas. For slot or hole-and-slot anode blocks, to which the present formulas apply directly,  $r_0$  is generally about  $\frac{1}{2}$  when the anode blocks are strapped.

The general restrictions of cavity tuning covered in Sec. 14-3 apply to the external tuner. In particular, mode troubles appear if the stabilization  $S$  exceeds 2. Furthermore, if here  $r_c$  is the ratio of stored energy in the gap area to stored energy in the external cavity, it is difficult to

design cavities with  $r_c$  greater than  $\frac{1}{2}$ . Thus, a relation similar to Eq. (46) is

$$p_b = \frac{S-1}{S} r_c. \quad (47)$$

In comparing the methods of Fig. 15-1*a* and *b* as applied to identical anode blocks, it is appropriate to make  $Q_{E(b)}/S = Q_{E(a)}$  so that for the same output power the same r-f voltage  $\tilde{V}_a$  appears across the slots in both magnetrons. Under these conditions in *b*, the r-f voltage  $\tilde{V}_b$  appearing across the gap of the cavity may be related to  $\tilde{V}_a$  and to the characteristic admittances  $Y_c$  of the cavity and  $Y_M$  of the magnetron as follows:

$$\frac{\text{Energy in cavity}}{\text{Energy in magnetron}} = \frac{\tilde{V}_b^2 Y_c}{\tilde{V}_a^2 Y_M} = \frac{S-1}{1}. \quad (48)$$

For equal output powers and the same ratio of  $d/D$ , Eqs. (35), (45), (47), and (48) can be combined to relate the beam voltages necessary (at the space-charge limit) for internal tuning *a* as compared with external tuning *b*. The relation is

$$\frac{V_{b(a)}}{V_{b(b)}} = \frac{\tilde{V}_a P_a \frac{\Delta\nu}{\nu_{0(a)}}}{\tilde{V}_b P_b \frac{\Delta\nu}{\nu_{0(b)}}} = \sqrt{\frac{Y_c}{Y_M}} \frac{\sqrt{S-1}}{S} \frac{N}{m} \frac{r_c}{r_0} \left( \frac{\Delta\nu}{\nu_0} \right)_a. \quad (49)$$

If the current densities are maintained equal in the two cases, the voltages at the space-charge limit are proportional to the  $\frac{4}{3}$  power of the gap  $D$ . Furthermore, the anode dimension  $h$  can generally be made equal for internal and external tuning, whereas the beam dimension  $l$  (see Fig. 15-1) for a cavity tuner is approximately twice that for a single oscillator in the internal tuner. Thus one has

$$\text{and} \quad \left. \begin{aligned} \frac{V_{b(a)}}{V_{b(b)}} &= \left( \frac{D_a}{D_b} \right)^{4/3} \\ \frac{Y_c}{Y_M} &= \frac{2}{N} \frac{D_a}{D_b} \end{aligned} \right\} \quad (50)$$

Solving Eq. (49) for  $\Delta\nu/\nu_0$  and assuming  $r_0 = r_c$ ,

$$\left( \frac{\Delta\nu}{\nu_0} \right)_a = \frac{S}{\sqrt{S-1}} \frac{m}{\sqrt{2N}} \left( \frac{D_a}{D_b} \right). \quad (51)$$

In this derivation no attempt has been made to satisfy the no-loss condition.

The meaning of Eq. (51) can be illustrated by a specific example of an external cavity that would be required to give the same tuning as would be obtained by internally tuning six oscillators of a 12-oscillator tube. If  $S$  is 2, Eq. (51) then gives

$$\frac{D_b}{D_a} = 2.9$$

and

$$\frac{P_{DC(b)}}{P_{DC(a)}} = 4. \quad (52)$$

Thus, the complexity of six guns is to be balanced against the fourfold increase in power necessary with external-cavity tuning. Note that since the power requirements are low, approximating receiving-tube powers, the d-c input power to the tuner may not be an important consideration.

It might appear that external-cavity tuning would be more flexible in magnetron operating point because different magnetic fields can be used for the magnetron than for the tuner. However, practice reveals that the magnetic fields necessary for internal tuning are usually not different from those used in normal magnetron operation.

*Examples.*—Typical of the internal beam-modulated tubes are two RCA designs, Tube 1 at 4000 Mc/sec and Tube 2 at 800 Mc/sec. Operating characteristics of these tubes are given in Table 15-3. Both tubes are operated with single transit at  $\alpha = 2\pi$ . The smaller electronic tuning of the 800-Mc/sec tube reflects the combined effect of higher output power and longer wavelength, as discussed in Sec. 15-5. The tube

TABLE 15-3.—OPERATING CHARACTERISTICS OF INTERNALLY TUNED C-W MAGNETRONS

	Tube 1	Tube 2, mechanically tunable		
Frequency $\nu$ , Mc/sec.....	4000.00	720.00	780.00	840.00
Output power $P_o$ , watts.....	25.00	460.00	500.00	540.00
Maximum electronic tuning $\Delta\nu$ , Mc/sec..	10.00	2.50	3.80	4.70
Modulating-beam current $J_{op}$ , ma.....	20.00	500.00	500.00	500.00
Number of guns $m$ .....	2.00	5.00	5.00	5.00
Modulating-beam voltage $V_b$ , volts.....	100.00	300.00	300.00	300.00
Magnetron plate voltage $V_{RF}$ , volts.....	800.00	1950.00	2230.00	2520.00
Magnetron plate current $I$ , ma.....	80.00	400.00	400.00	400.00
Magnetic field $H$ , gauss.....	1600.00	330.00	353.00	377.00
Cyclotron frequency/r-f frequency, $\beta$ ....	1.15	1.26	1.25	1.24

parameters for the 800-Mc/sec tube<sup>1</sup> are listed in Table 15-4. From the dimensions and the operating data given in Table 15-3 the computed tuning is approximately 0.6 Mc/sec per gun, or a total of 3 Mc/sec; this figure agrees well with the observed values.

TABLE 15-4.—DESIGN PARAMETERS OF AN 800-Mc/SEC RCA TUBE

Number of oscillators $n$ .....	12
Vane thickness $t$ .....	0.187 in.
Anode length $h$ .....	2.000 in.
Anode diameter $d_a$ .....	1.250 in.
Electron-beam thickness $d$ .....	0.125 in.
Average plate separation $D_{avg}$ .....	0.500 in.
Minimum plate separation $D_{min}$ .....	0.375 in.
Beam-cathode length $l$ .....	0.500 in.

TABLE 15-5.—OPERATING CHARACTERISTICS OF A 2700-Mc/SEC EXTERNALLY TUNED MAGNETRON

The tube dimensions are  $D = 0.400$  in.,  $d = 0.200$  in.,  
 $l = 0.900$  in.,  $h = 0.900$  in.

$\frac{\text{Cyclotron frequency } \beta}{\text{r-f frequency}}$	1.05		1.15		1.1	
	Theoretical*	Observed	Theoretical*	Observed	Observed	Observed
Output power $P_o$ , watts.....	125.00	ca 100	1100.00	.....	.....	.....
Maximum electronic tuning $\Delta\nu$ , Mc/sec.....	.....	.....	6.50	6.0	10.00	16.0
Modulating-beam current $I_0$ , ma.....	.....	.....	.....	100.0	100.00	150.0
Modulating-beam voltage $V_b$ , volts.....	.....	.....	.....	300.0	400.00	500.0
Stabilization $S$ .....	.....	2.1	.....	2.1	.....	2.1
Ratio of energy stored in gap to energy stored in external cavity $\tau_c$ .....	0.47	.....	0.47	.....	0.47	.....
Magnetron plate voltage $V$ , volts.....	.....	1100.0	.....	.....	.....	.....
Magnetron plate current $I$ , ma.....	.....	300.0	.....	.....	.....	.....
External $Q$ , $Q_E$ .....	.....	300.0	.....	300.0	.....	300.0

\* Theoretical results are based on an accurate field-theory value for  $Y_c$ .

A typical external-cavity reactance tube is shown in Fig. 15-8. The reactance tube is designed for 15-Mc/sec frequency modulation of a 2700-Mc/sec magnetron with an output power of 400 watts. The magnetron and the reactance tube are coupled together by a coaxial line. Calculated and observed characteristics of this tube are listed in

<sup>1</sup> A. L. Vitter, Jr., *et al.*, "LCT, 900 Mc/sec FM C-w Magnetron," RL Group Report No. 52, Feb. 28, 1946.

Table 15-5, together with pertinent dimensions. The figures for  $\beta = 1.15$  correspond to single transit,  $\alpha = 2\pi$ . The figures for  $\beta = 1.1$  correspond to double transit,  $\alpha > 2\pi$ . The agreement between theory and observation is fortuitously good because the approximations involved in estimating  $r_c$ , properly evaluating space-charge effects, etc., introduce uncertainties in the calculations of about 20 per cent.

### MAGNETRON DIODE TUNING

**15-7. Fundamental Principles.**—It has been shown in Sec. 15-2 that the attainable electronic tuning of a side cavity traversed by a beam of electrons is proportional to the r-f current  $J e^{-i\omega t} = -Nev = -\rho v$  [Eqs. (11) and (15)]. In Sec. 15-3, attention was focused on means of maximizing  $v$ , the component of electron velocity parallel to the r-f field. The conditions under which  $v$  was there maximized required that the charge density be introduced by means of an electron beam of potential  $V_0$  and current density  $J_{0\max}$ . The electron-beam analyses undertaken in Sec. 15-3 showed that it is difficult to attain large values of  $\rho$  in this manner and that the available tuning range was thus limited.

In the present section emphasis is laid on a means of increasing  $\rho$  by utilizing the high space-charge density of a magnetron operated in the cutoff condition. The problem to be considered may be illustrated by a modification of Fig. 15-1, in which the electron beam is replaced by a filamentary cathode extending along the length  $h$  between the plates  $A$  and radially located at the center of the electron beam. The potential  $V_b$  is now applied between the filamentary cathode and plates  $A$ , and the aligning magnetic field is retained. As a result of the crossed electric and magnetic fields, the cathode will be surrounded by a rotating space-charge sheath of density  $\rho$ , the approximate magnitude of which may be most easily calculated by considering the simpler problem in which the two plates with separation  $D$  of Fig. 15-1a are replaced by a cylinder of diameter  $D$  concentric with the filamentary cathode. This is the conventional magnetron-diode problem solved by Hull<sup>1</sup> as

$$\rho = \epsilon_0 \frac{m}{2e} \omega_c^2, \quad (53)$$

<sup>1</sup> A. W. Hull, *Phys. Rev.*, **23**, 112 (1924).



FIG. 15-8.—Typical external-cavity reactance tube.

where  $\omega_c = 2\pi\nu_c$  and  $\nu_c$  is the cyclotron frequency [Eq. (19)]. For a magnetic field of 1070 gauss [ $\omega_c = 2\pi(3 \times 10^9)$ ], Eq. (53) yields  $\rho = 8.95 \times 10^{-3}$  coulomb/meter<sup>3</sup>, whereas the charge density of a 100-volt electron beam at 0.2-amp/cm<sup>2</sup> current density is  $3.35 \times 10^{-4}$  coulomb/meter<sup>3</sup>. Clearly the 27-fold increase in charge density in the magnetron diode is an attractive factor to attempt to utilize for electronic tuning.

Maximizing  $\rho$ , however, is only one aspect of the problem; it is also necessary to maximize  $v$ . This has been done effectively in electron-beam tuning by using the aligning magnetic field to increase the amplitude of electronic oscillations when the r-f frequency  $\nu$  is near the cyclotron frequency  $\nu_c$ . Although a similar resonance effect is to be anticipated when the filamentary cathode is used, an analysis is necessary to establish the exact relation. Furthermore, the power-handling abilities of the two types of tuning must be compared. For a given tuning the increased charge density surrounding the filamentary cathode allows a smaller amplitude of electronic oscillations, but there is no obvious way to determine a maximum tolerable amplitude analogous to  $|r_{\max}|$  of Sec. 15-3 because some electrons will return to the cathode for all finite oscillation amplitudes. Finally, there is no obvious means of including a grid control around a filamentary cathode because any grid would be located in a region of high r-f fields and currents. However, because for magnetron diodes with sharp cutoff characteristics the radius of the space-charge cloud surrounding the cathode can be varied by varying  $V_b$  though practically no current is drawn to the plate, it is possible to dispense with the negative grid control by modulating the plate voltage and still have a low a-c power drain on the modulator.

The similarity between the filamentary cylindrical diode just discussed and a conventional microwave multioscillator magnetron has led to theoretical analysis and experimentation with reactance tubes based on multioscillator magnetron design. The magnitudes involved are best illustrated by observing that a magnetron which, when oscillating, has an output power of 1 kw, may, when used as a reactance tube, be expected to handle an output power of 1 kw and that the difference between oscillating and nonoscillating resonant frequencies of multioscillator magnetrons is about 1 per cent, which corresponds to the anticipated electronic tuning.

**15-8. Small-signal Theory.**—The shift in resonant frequency of a nonoscillating magnetron, when its plate voltage is raised from zero to the cutoff condition, is a measure of the electronic tuning that could be accomplished with such a magnetron used as a reactance tube to tune another magnetron, providing the r-f energy level in the reactance tube is kept vanishingly small. In Chap. 6 it has been shown that the

electronics of a magnetron are exceedingly complex, even for the limit of small-signal strength. A brief discussion will be given<sup>1</sup> here of the reactive behavior of the space charge because the emphasis in Chap. 6 is on the negative-resistance region of the space charge.

Lamb and Phillips consider the shift in resonant frequency of a conventional multioscillator magnetron, operated in a condition of perfect cutoff, as a function of the anode voltage and hence of the radius  $r_e$  of the rotating electron cloud surrounding the cathode of radius  $r_c$ . The analysis is restricted to thicknesses  $y$  of the electron sheath, which are small compared with  $r_c$ .

The method used in computing the resonant frequency of the magnetron anode block in the presence of a space charge is an extension of the impedance-matching techniques used in Chap. 2 to compute the frequency of the anode block without space charge. In Chap. 2 the anode is divided into two regions (Fig. 2.13) that join at the anode radius  $r_a$ . Solutions of Maxwell's equations appropriate to the two regions are joined at  $r_a$  by matching the impedance  $Z = E_\theta/H_z$  at the boundary, and the resulting solution yields the resonant frequency. For each mode number  $m$ ,  $E_\theta$  in the cathode-anode space consists of a sum of functions of angular and time dependence  $e^{i(n\theta - \omega t)}$  and radial dependence

$$J_n(\beta r) + \delta_n N_n(\beta r), \quad (54a)$$

where

$$\delta_n = - \frac{J'_n(\beta r_c)}{N'_n(\beta r_c)}, \quad (54b)$$

$\beta = 2\pi/\lambda$ , and  $J_n$  and  $N_n$  are Bessel's functions of the first and second kind, respectively, their derivatives being  $J'_n$  and  $N'_n$ . The most important member of the sum is the term  $n = m$ . The condition of Eq. (54b) on  $\delta_n$  is determined by making the tangential electric field  $E_\theta$  vanish at the cathode. When the effect of the space-charge cloud is included in the calculations, the cathode-anode region is subdivided into two regions meeting at  $r = r_e$ , the boundary of the space-charge sheath. The impedance  $Z_{el}$  of the sheath is evaluated at this boundary, looking in toward the cathode, and this impedance is matched to the free-space solution in the region between  $r_e$  and  $r_a$ . Thus the boundary condition  $Z = 0$  at  $r = r_c$  of Eq. (54b) for the problem without space charge is replaced by  $Z = Z_{el}$  at  $r = r_c$  for the problem with space charge. The result can be expressed as replacing  $\delta_n$  in Eq. (54a) by a quantity  $\delta'_n$ , to be evaluated shortly. It will be recognized that the above approach differs from that of Secs. 15.2 and 15.3. It is more appropriate to a complex problem such as the present one, since, for one thing, no integrals need be evaluated.

<sup>1</sup> W. E. Lamb and M. Phillips, *J. Appl. Phys.*, **18**, 230 (1947).

In computing  $Z_{el}$ , the starting point is the Brillouin single-stream solution for the steady-state electron flow in the space-charge sheath and Bunemann's small-signal theory for the r-f perturbations imposed on this steady state by electromagnetic waves of the form  $e^{i(n\theta - \omega t)}$  (see Chap. 6). The result<sup>1</sup> is

$$Z_{el} = \sqrt{\frac{\mu_0}{\epsilon_0}} \frac{in^2 y}{r_c k} \frac{\omega^2}{r_c \omega_c^2 - \omega^2}, \quad (55)$$

where

$$\frac{ny}{r_c} < \frac{\omega_c^2 - \omega^2}{\omega^2}, \quad \text{and} \quad n \neq 0.$$

This result is not what would be obtained if the electrons in the space-charge sheath were treated as free electrons satisfying Eqs. (12) to (17) but having a charge density determined by Eq. (53). Thus the modification in electron velocities from the free electron picture, so important in the beam-tuning of Sec. 15-3, also plays a role in the present problem.

The expressions for  $\delta'_n$  resulting from Eq. (55) are

$$\delta'_n = \frac{(\beta r_c)^{2n}}{2^{2n}} \frac{\pi}{n!(n-1)!} \left( 1 + \frac{2ny}{r_c} \frac{\omega_c^2}{\omega_c^2 - \omega^2} \right), \quad (56a)$$

where  $n \neq 0$ ; and

$$\delta'_0 = \omega \left( \frac{\beta r_c}{2} \right)^2 \left[ 1 - \frac{2y}{r_c} \left( 1 + \frac{2}{3} \beta_c^2 y^2 \frac{\omega_c^2}{\omega_c^2 - \omega^2} \right) \right], \quad (56b)$$

where

$$\beta_c = \frac{\omega_c}{\omega} \beta.$$

In each expression the terms containing  $y$  represent the correction to  $\delta'_n$ . In Eq. (56a) the sign of the correction term changes at  $\omega = \omega_c$ , whereas the sign is always negative in Eq. (56b).

By letting  $r'$  be an effective cathode radius equal to

$$r_c \left( 1 + \frac{2ny}{r_c} \frac{\omega_c^2}{\omega_c^2 - \omega^2} \right)^{1/2n}$$

from Eq. (56a) or equal to

$$r_c \left[ 1 - \frac{2y}{r_c} \left( 1 + \frac{2}{3} \beta_c^2 y^2 \frac{\omega_c^2}{\omega_c^2 - \omega^2} \right) \right]^{1/2}$$

from Eq. (56b), the resonant wavelength may be computed from Table 3-2 (that gives wavelength vs. cathode size). When this is done, a qualitative agreement is found with the experimental curves of Fig.

<sup>1</sup> W. Lamb and M. Phillips, *op. cit.*



15-9. These curves<sup>1</sup> show the resonant frequency of the  $\pi$ -mode of an 18-vane rising-sun anode block (the 3J31 tube of Sec. 19-14) as a function of plate voltage (which is proportional to the electron-sheath thickness  $y$  for small  $y$ ) and magnetic field (which is proportional to  $\omega_c$ ). The enhanced tuning and change of sign at  $\omega = \omega_c$  (with  $H = 8800$  gauss) are ascribed to the ( $n = 9$ )-component, and the asymmetry of the curves above and below  $\omega_c$  to the ( $n = 0$ )-component. In normal operation this tube would run at over 10 kv, but for the data of Fig. 15-9 it was operated at nearly the same magnetic field but under 1 kv, corresponding to a condition of small  $y$ .

Since  $\beta r_c$  in Eq. (56a) is always designed to be less than 1, it is observed that  $\delta'_n$  decreases rapidly with increase in  $n$ . This corresponds to the rapid decrease in the r-f field strength from the anode to the cathode for large  $n$ . It also means a small ratio  $q$  of stored r-f energy in the space-charge region to total stored r-f energy [Eq. (23)]. By analogy with the beam-tuning analysis, specifically Eq. (36), in which the quantity  $p$  is proportional to  $q$ , it is to be expected that this small value of  $q$  will decrease the product of tuning and tolerable r-f voltage for large  $n$ .

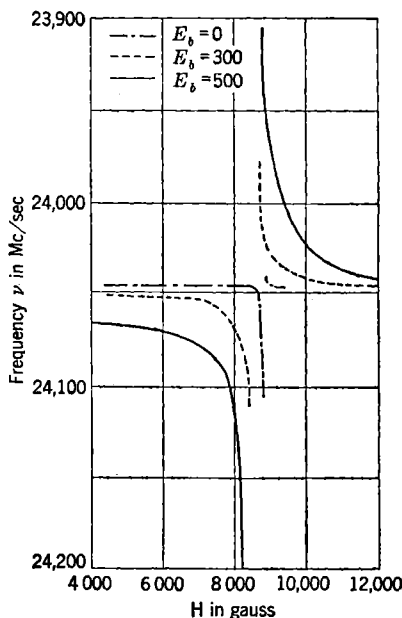


FIG. 15-9.—Space-charge tuning at low power levels.

**15-9. Experimental Data on Large-signal Conditions.**—When multi-oscillator magnetrons are used as reactance tubes to modulate high powers, the tuning characteristics depart from the low-level behavior of Fig. 15-9. The larger electronic orbits result in more collisions with the cathode, hence higher r-f loss and lower tuning.

The 10-cm, c-w magnetron described in Table 11-1 (the CM16B tube) has been used as a starting point of several electronically tuned magnetrons intended to operate at power levels of 10 to 100 watts, consistent with the reliable magnetron operating point of 1000 volts and 150 ma (see performance chart in Chap. 19). In the first modification illustrated in Fig. 14-17, oscillating magnetron I is connected to reactance tube

<sup>1</sup> *Ibid.*

magnetron III (indicated in Fig. 14-17 as "cavity") by a section of coaxial line of such length that both tubes appear as parallel-resonant circuits at the same point on the line, as is shown in the equivalent circuit of Fig. 14-23, and the coupling to each tube is so adjusted that there is equal r-f energy storage in magnetron and tuner ( $S = 2$ , see Sec. 14-3). In this case the tuning was observed to have a flat maximum at  $\omega_c/\omega$  near 2, with less than 10 per cent loss in output power. Loss was greatest at  $\omega_c/\omega = 1$ . Tuner tubes with  $r_c/r_a = 0.58, 0.75$ , and  $0.85$ , operated at similar points, showed tuning of 3, 9, and 20 Mc/sec respectively,<sup>1</sup> confirming the theoretical increase in tuning with cathode size [Eq. (56)]. For 15 watts r-f output and tuning of 20 Mc/sec, the d-c input to the reactance tube was 100 ma at 500 volts. This power was excessive for frequency modulation and was due to the poor cutoff characteristics of the tube. The tuning furthermore is distinctly nonlinear.

In a second tuning method starting with this c-w magnetron, the magnetron and the tuner were combined in a single tube. Two cathodes were inserted into the anode from opposite ends of the tube, one to drive the magnetron and the other to provide tuning.<sup>2</sup> The experimental arrangement is shown in Fig. 15-10.

The end shield provided for the magnetron cathode was found necessary to minimize leakage to the tuner cathode, which was always positive with respect to the magnetron cathode. The ratio of the cathode diameter to the anode diameter for the tuner was chosen as 77 per cent, corresponding approximately to the middle cathode-anode ratio tried by Everhart.<sup>3</sup> Operational data for this tube taken at 1700 gauss show 4-Mc/sec tuning at 420 volts, 20-ma d-c tuner input for an r-f output of 17 watts, whereas the tuner input is 40 ma at 440 volts for an r-f output of 35 watts and the same tuning. Thus the tuning characteristics are strongly dependent on the r-f output level, and again comparatively high modulator power is required. In this tube the r-f output power drops by 20 per cent at the 4-Mc/sec tuning point. Simplicity of construction and adaptability for combination with wide-range mechanical tuning are, however, important features of the above design.

Another modification is shown in Fig. 15-11. Here a portion of the vanes is cut away to provide space for a cylindrical tuner cathode that is concentric with the regular cathode. The tuner cathode is located in a region of comparatively low r-f fields, where the back bombardment is low. Furthermore, there is no leakage between the two cathodes. At 1500 gauss, a tuner d-c input of 15 ma at 600 volts tuned 4 Mc/sec

<sup>1</sup> E. Everhart, "The Magnetron as an Electronic Reactance Tube," RL Group Report No. 52, Mar. 15, 1945.

<sup>2</sup> Minutes of the Magnetron Modulation Coordinating Committee, Vacuum Tube Development Committee, May 25, 1945.

<sup>3</sup> Everhart, *op. cit.*

with an r-f output power of 30 watts. This tuning was strongly dependent on both r-f output power and magnetic field, the variation with magnetic field being complicated. For example, at 600 volts on the tuner the electronic tuning increased to 6.5 Mc/sec at 800 gauss, whereas for 300 volts the electronic tuning reversed sign. This behavior is seen to be quite inconsistent with the low-level behavior of Fig. 15-11.<sup>1</sup>

It is clear from the above illustrations that the attempts to utilize the high-electron density of a rotating space charge surrounding a cylindrical cathode have as yet met with only partial success.

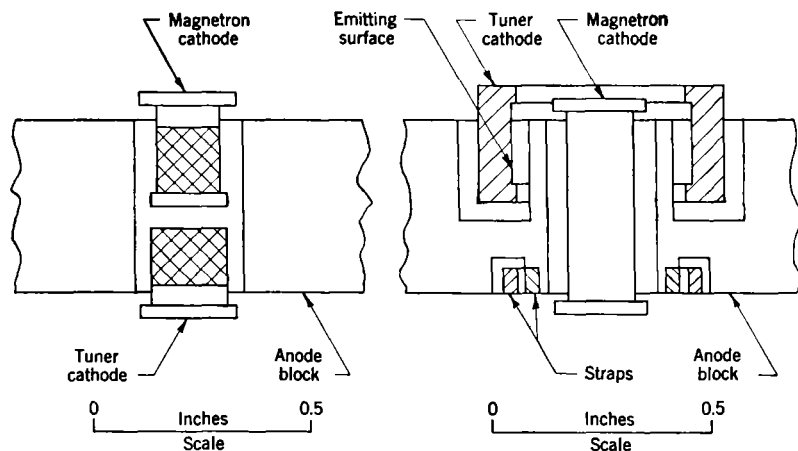


FIG. 15-10.—Cross section of a double-cathode magnetron.

FIG. 15-11.—Cross section of magnetron with two concentric cathodes.

**15-10. Other Methods.**—Two further methods of electronic tuning have been investigated with indifferent success. In the first method, an electron stream is used to change the conductance instead of the susceptance of a portion of the resonant system. By transmission down a  $\lambda/8$  length of line this variable conductance is made to appear primarily as a variable susceptance at the magnetron. Such tubes as have been tested have been capable of powers up to only 20 watts. The method furthermore inherently includes amplitude modulation and, in the particular designs tried, was sensitive to the power level of the magnetron.

A second method has been to introduce an electrode that is designed to modulate the electron stream already present in the magnetron, thus eliminating the use of an auxiliary cathode. The resulting frequency modulation is found to be small.

<sup>1</sup> Although the above illustrations have been for multioscillator tubes, much work has been done at the General Electric Co. with this method of tuning on split-anode magnetrons. Some of this work is summarized in the Minutes of the Magnetron Modulation Coordinating Committee, May 25, 1945.

## CHAPTER 16

### STABILIZATION OF FREQUENCY

BY F. F. RIEKE

**16-1. Introduction.**—This chapter is concerned primarily with the problem of minimizing the changes of frequency that occur as a result of accidental variations in the operating conditions of the magnetron and, more particularly, with methods of using an auxiliary resonant cavity for that purpose. It is not the aim of this chapter to give detailed instructions for building a magnetron stabilizer but rather to indicate the basic considerations that enter into its design. When it has been decided what properties the stabilizing circuit is to have, the realization of the circuit is a straightforward problem in microwave circuitry and as such is outside the scope of this book.

By usage, the term “stability of the frequency” has come to mean quite generally some quantity proportional to  $1/(d\nu/d\alpha)$ , where  $\alpha$  represents the temperature, the output load, or the input current (or perhaps still another parameter that enters into the conditions of operation). It would have been more appropriate to apply some such term as “stiffness” of the frequency in the above context, particularly since one has occasion to use the term “stability” in a more literal sense, namely, in connection with discontinuous changes in frequency that result from the instability of a normal mode of oscillation.

Applications that require the frequency of the magnetron to be very constant often require also that the frequency be set to a preassigned value; consequently the possibility of tuning must also be considered along with that of stabilization.

It has been shown in Chap. 7 that the frequency of oscillation of a magnetron can be related to the intersection of the curves  $-Y_e(\tilde{V})$  and  $Y_L(\nu)$  in the  $G, B$  plane. Changes in operating conditions cause shifts in one or the other of these curves; in principle one can relate changes in frequency to the shifts of the curves and to the variation of the parameter  $\nu$  along the  $Y_L(\nu)$  curve. Quantitatively the computation is somewhat complicated, since it involves the angle with which the curves intersect, etc. Qualitatively, the  $-Y_e(\tilde{V})$  curve may be considered to be simply a horizontal line; in that case the shifts of frequency will be inversely proportional to the derivative  $\partial B_L/\partial \nu$  along the  $Y_L$  curve. To “stiffen” the frequency one must make this derivative large; in other

words, one must, in effect, make the characteristic admittance  $Y_c$  of the resonant system large. Generally speaking, this requirement implies that the "stored energy" of the system be increased. Perhaps it should be pointed out, however, that while it is necessary to increase the stored energy, it is not sufficient, for the energy must be stored in the proper way in order to be effective.

To some extent one can increase the stored energy by modifying the shape of the conventional resonant system of the magnetron; but unless some new principle of design is invented, the possibilities in this direction are rather limited. In meeting the requirements imposed upon the interaction space, one seems necessarily to end up with a structure with small clearances between the high-voltage parts and thus a compact resonant system with a large surface/volume ratio. Such a resonator necessarily has a relatively small unloaded  $Q$ , so that the storage of a large amount of energy is impossible (always computed, of course, on the basis of a constant available power) and even moderate energy storage is expensive. Consequently it is advantageous to couple to the magnetron an auxiliary cavity designed to store the energy more economically, and it is this method of stabilizing (or stiffening) this frequency which is to be treated in detail here.

It should be mentioned that the principle of *automatic-frequency control* can also be applied to the problem of maintaining a magnetron at a preassigned frequency.<sup>1</sup> In an AFC system a frequency discriminator generates an error signal whenever the frequency departs from its proper value. The error signal is amplified and then used to actuate a tuning mechanism that eliminates the departure. In principle, the AFC system has one inherent advantage over the stabilizing cavity in that it acts to eliminate completely the errors in frequency rather than merely to reduce them in some constant proportion. If the AFC control depends upon mechanical tuning, however, it cannot respond to extremely rapid fluctuations. In any case, it is a rather complicated affair. In itself it cannot overcome the difficulties connected with instabilities that arise from a resonant load, although the auxiliary cavity can do so to a considerable extent, since in effect it increases the external  $Q$  of the magnetron. It is possible to combine the advantages of both systems by using a stabilizing cavity as the tuning element in an AFC system.

**16-2. The Ideal Stabilizer.**—In coupling the stabilizing cavity to the magnetron one attempts to approximate as nearly as possible the state of affairs represented by the equivalent circuit shown in Fig. 16-1, where the cavity (3) is coupled to the magnetron (1) by an ideal transformer. The terminals  $A$  and  $T$  correspond to those similarly labeled in Fig. 7-5

<sup>1</sup> A technical discussion of AFC systems as applied to magnetron transmitters is contained in Vol. 3, Chap. 13, Radiation Laboratory Series, Secs. 13-11 to 13-13.

of Chap. 7. Although in practice the ideal circuit can be approximated only over a rather narrow range of frequency, Fig. 16-1 provides a convenient basis for the discussion of some of the fundamental relations involved in stabilization. Except for that part added to the left of the

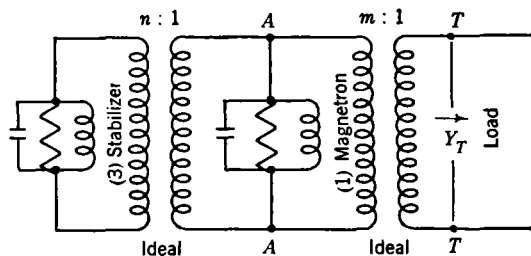


FIG. 16-1.—Equivalent circuit of an ideal stabilized magnetron.

terminals  $A$ , the circuit of Fig. 16-1 corresponds to that of Fig. 7-5*d*. The admittance  $Y_L$  is given by the relation

$$Y_L = n^2 Y_{c3} \left( \frac{1}{Q_{U3}} + j2 \frac{\nu - \nu_{U3}}{\nu_{U3}} \right) + Y_{c1} \left( \frac{1}{Q_{U1}} + j2 \frac{\nu - \nu_{U1}}{\nu_{U1}} \right) + \frac{M}{m^2} y_T. \quad (1)$$

By introducing the external  $Q$ 's (with respect to a matched output transmission line of characteristic admittance  $M$ )  $Q_{E1} = Y_{c1} m^2 / M$  and  $Q_{E3} = Y_{c3} n^2 m^2 / M$ , Eq. (1) can be written in the form

$$\frac{Q_{E1}}{Y_{c1}} Y_L = \frac{Q_{E1}}{Q_{U1}} + \frac{Q_{E3}}{Q_{U3}} + j2 \left( Q_{E1} \frac{\nu - \nu_{U1}}{\nu_{U1}} + Q_{E3} \frac{\nu - \nu_{U3}}{\nu_{U3}} \right) + y_T. \quad (2)$$

Provided that  $\nu_{U1}$ ,  $\nu_{U3}$ , and  $\nu$  are not very different from each other, Eq. (2) can be approximated by

$$Y_L = \frac{Y_c}{Q_U} \left( \frac{Q_E}{Q_U} + j2Q_E \frac{\nu - \nu_U}{\nu_U} + y_T \right), \quad (3a)$$

where

$$Q_E = Q_{E1} + Q_{E3}, \quad (3b)$$

$$\nu_U = \frac{Q_{E1} \nu_{U1} + Q_{E3} \nu_{U3}}{Q_{E1} + Q_{E3}}, \quad (3c)$$

$$\frac{Q_E}{Q_U} = \frac{Q_{E1}}{Q_{U1}} + \frac{Q_{E3}}{Q_{U3}}. \quad (3d)$$

The tuning properties of the combined system can be analyzed on the basis of Eq. (3c). From Eq. (3d) it follows that

$$\frac{\partial \nu_U}{\partial \nu_{U1}} = \frac{1}{S} \quad (4a)$$

and

$$\frac{\partial \nu_U}{\partial \nu_{U3}} = \frac{S-1}{S}, \quad (4b)$$

where

$$S = \frac{Q_{E1} + Q_{E3}}{Q_{E1}}. \quad (4c)$$

The quantity  $S$  will be referred to as the "stabilization factor." When  $S$  is large, the resonant frequency of the system follows closely the resonant frequency of the stabilizer and varies only slowly with that of the magnetron.

The effectiveness of the stabilizer in reducing the changes of frequency connected with temperature variations can be estimated on the basis of Eq. (4). In this respect the stabilizer can be effective only in so far as the stabilizer itself is better thermostated or better compensated against temperature changes than is the magnetron. If the thermal changes in the stabilizer resonance  $\nu_{U3}$  are negligible, the changes in  $\nu_U$  (and therefore in the frequency of oscillation) resulting from changes in the temperature of the magnetron are reduced by the factor  $1/S$ . Actually, the stabilizer does lend itself more readily to thermostating and compensation than does the magnetron, partly because less energy is dissipated in it and partly because it is a larger and simpler structure and generally more accessible. While stabilizing cavities have been constructed of invar, it has not been practicable to use this material for the magnetron proper.

The variation of frequency with current is inversely proportional to the value of  $\partial B_L / \partial \nu$ . From Eq. (3) it follows that, other things being equal, stabilization will reduce the derivative  $\partial \nu / \partial I$  in the ratio  $1/S$ .

The degree of dependence of the frequency (expressed in terms of  $\Delta \nu / \nu$ ) upon the external load  $y_T$  is inversely proportional to  $Q_E$ .<sup>1</sup> (The pulling figure  $F$  is given by the relation  $F/\nu = 0.42 \text{ sec } \alpha / Q_E$ .) Consequently, if  $Q_{E1}$  is held fixed, the stability of the frequency against changes in load is directly proportional to the stabilization factor  $S$ . The assessment of the possible advantages of stabilization in this respect, however, involves much more than this simple relation, inasmuch as it is possible without stabilization to increase  $Q_E$  simply by decreasing the coupling  $1/m^2$  to the external load. By this procedure the stability would be achieved at a considerable cost of circuit efficiency and, ordinarily, electronic efficiency. Consequently it is necessary to consider stability in relation to over-all efficiency.

The electronic efficiency  $\eta_e$  varies with  $G_L$  in the fashion illustrated in Fig. 7-24. In the interest of making  $Q_E$  large,  $G_L$  is usually made somewhat less than its value where  $\eta_e$  is a maximum, but  $G_L$  cannot be reduced

<sup>1</sup> The relation is a very general one. For convenience in expression, "increasing  $Q_E$ " will be used synonymously with "increasing the stability of the frequency against variation in the external load."

indefinitely, for  $\eta_e$  falls off very rapidly at the lower values of  $G_L$ . To some degree, stabilization affords the possibility of choosing  $G_L$  and  $Q_E$  independently, as is shown by the relation

$$(G_L)_{\nu r=1} = Y_{c1} \left[ \frac{1}{Q_{U1}} - \frac{1}{Q_{U3}} + S \left( \frac{1}{Q_E} + \frac{1}{Q_{U3}} \right) \right]. \quad (5)$$

Furthermore, the circuit efficiency at a given value of  $Q_E$  increases with the stabilization factor  $S$ , as is shown by the relation

$$\left( \frac{1}{\eta_e} \right)_{\nu r=1} = 1 + Q_E \left[ \frac{1}{Q_{U3}} + \frac{1}{S} \left( \frac{1}{Q_{U1}} - \frac{1}{Q_{U3}} \right) \right]. \quad (6)$$

It is assumed, of course, that  $Q_{U3}$  is many times larger than  $Q_{U1}$ ; in practice ratios of 5 or 10 can be achieved easily, and ratios of 20 or more are usually possible.

In applications to radar it generally comes about that stabilization is particularly worth while at the higher frequencies—say above 5000 Mc/sec. This circumstance arises from the fact that it is the *absolute* bandwidth  $\Delta\nu$  rather than the relative bandwidth  $\Delta\nu/\nu$  that controls the design of a receiving system. Although greater bandwidths are used at the higher frequencies, it has not been general practice to increase the bandwidth proportionally with  $\nu$ . As far as the magnetron is concerned, it is the relative bandwidth that counts, and the circumstance just mentioned requires that the magnetron have a greater  $Q_E$  at the higher frequencies. Inasmuch as the unloaded  $Q$  tends to decrease as  $\nu^{-1/2}$  with increasing frequency and the circuit efficiency decreases with increasing ratio  $Q_E/Q_U$ , the circuit efficiency becomes a very important consideration at the high frequencies.

Stabilized magnetrons have proved particularly useful in radar beacons, where the frequency must be held at an *assigned* value within rather small tolerances.

**16-3. Coupling Methods.**—The preceding discussion has been premised on the assumption that the circuit of Fig. 16-1 can be realized physically. If this circuit is taken literally, one arrives at the conclusion that it is always desirable to make the stabilization factor very large; that is, to arrive at a required value of  $Q_E$ , one should make  $S$  large and  $Y_{c1}$  proportionally small. This conclusion is rather obvious, for, other things being equal, it is advantageous to store a greater fraction of the energy in the most efficient element of the system, which is assumed to be the stabilizer rather than the magnetron proper. When physical limitations are taken into account—as will be done presently—it will be found that the advantages of stabilization, especially stabilization by large factors, have to be weighed against several disadvantages, among them increased



complexity and decreased flexibility of the system and perhaps more stringent limitations on manufacturing tolerances.

The basic problem that has to be met consists of coupling a low-impedance resonator (the magnetron) to a high-impedance resonator (the stabilizer) in such a way that the larger fraction of the energy is stored in the latter. The situation may be thought of in terms of the two circuits illustrated in Fig. 16-2a. One might couple the circuits by means of mutual inductance between the coils or by means of a tap as indicated by the dotted line in the figure, but in any case physical limitations make it impossible to secure a coupling coefficient of unity. In consequence, the system will have two modes of oscillation; if the coupling is weak, the separation of the modes  $\Delta\nu/\nu$  is just equal to the coefficient of coupling. The arrangements actually used in stabilization have the properties of the circuit shown in Fig. 16-2b, which has three modes of oscillation, and the difficulties encountered arise principally from these extra modes.

There are a considerable variety of arrangements that can be used to couple the stabilizer to the magnetron if details are taken into account. As far as essentials are concerned, however, the systems fall more or less into two classifications, depending mostly on whether the stabilizer is an integral part of the magnetron with a vacuum envelope common to both or is an attachment added after the magnetron has been otherwise completed and evacuated. In the former case the two resonant cavities are constructed tangent to each other, and the coupling effected by a common iris or resonant window. In the latter case the cavities are coupled to opposite ends of a transmission line whose length is an appreciable fraction of a wavelength or even a few wavelengths. Even between these two cases there is no difference in principle. Consequently the problem will be discussed in terms of transmission-line coupling, because the greater amount of experience by far has been accumulated with this type coupling.

A magnetron and stabilizer coupled through a transmission line

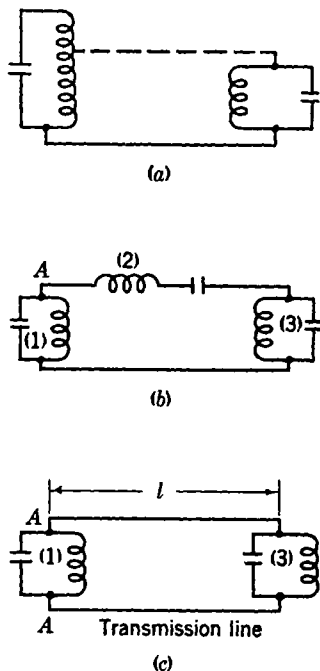


FIG. 16-2a,b,c.—Equivalent circuits of a magnetron coupled to a stabilizing cavity.

have, to a first approximation, an equivalent circuit like that shown in Fig. 16·2c. It turns out that the exact placement of the external load in the circuit has an appreciable influence on the characteristics of the circuit and also that it is necessary, when high stabilization is sought, to add an auxiliary load to damp extraneous modes of oscillation (see Sec. 16·4). Either of the loads can be connected in a variety of ways, and their inclusion in a general way would greatly complicate the equations to be dealt with. Therefore in outlining the general problem, purely reactive circuits will be used and the effects of the resistive elements will be treated qualitatively.

In computing the admittance of the system it is convenient to normalize the terms with respect to the characteristic admittance of the transmission line as was done in deriving Eq. (2). If  $y_1$  is the normalized admittance of the magnetron proper,  $y_3$  that of the stabilizer, and  $l$  the length of the transmission line between them, the admittance  $Y_U$  at the terminals  $A$  of Fig. 16·2c is given by

$$Y_U = \frac{Y_{c1}}{Q_{E1}} \left( y_1 + \frac{y_3 + j \tan \theta}{y_3 j \tan \theta + 1} \right), \quad (7)$$

where  $\theta = 2\pi l/\lambda_g$  and  $\lambda_g$  is the guide wavelength for the transmission line. At a particular frequency  $\nu_2$ ,  $\theta$  will be exactly equal to  $n\pi$ ; and for frequencies not very different from  $\nu_2$ ,  $\theta$  is given approximately (exactly if  $\lambda_g/\lambda$  is independent of  $\nu$ ) by

$$\theta = n\pi + 2Q_{E2} \frac{\nu - \nu_2}{\nu_2}, \quad (8)$$

where  $Q_{E2} = \pi l \lambda_g / \lambda_2^2$ . The frequency  $\nu_2$  can be considered to be the resonant frequency of the transmission line.

Inasmuch as one is concerned only with values of  $\nu$  for which  $(\nu - \nu_2)/\nu_2$  is small,  $\tan \theta$  can be approximated by  $2Q_{E2}(\nu - \nu_2)/\nu_2$ . For  $y_1$  and  $y_3$  the usual approximations for a parallel-resonant circuit will be used:  $y_L = Q_{E1}2j(\nu - \nu_1)/\nu_1$  and  $y_3 = Q_{E3}2j(\nu - \nu_3)/\nu_3$ . For the present it will be assumed that  $\nu_1 = \nu_2 = \nu_3 = \nu_0$ ; if the variable  $\delta = (\nu - \nu_0)/\nu_0$  is introduced, Eq. (7) can then be written

$$Y_U = \frac{Y_{c1}}{Q_{E1}} j \left( 2Q_{E1}\delta + \frac{2Q_{E2}\delta + 2Q_{E3}\delta}{1 - 4Q_{E2}Q_{E3}\delta^2} \right) \quad (9a)$$

or

$$Y_U = jB_U = Y_{c1}2j \left[ \frac{(\delta + \delta')\delta(\delta - \delta')}{(\delta + \delta'')(\delta - \delta'')} \right], \quad (9b)$$

where

$$\delta' = \frac{1}{2} \sqrt{\frac{Q_{E1} + Q_{E2} + Q_{E3}}{Q_{E1}Q_{E2}Q_{E3}}} \quad (9c)$$

and

$$\delta'' = \frac{1}{2} \sqrt{\frac{1}{Q_{E2} Q_{E3}}}. \quad (9d)$$

The values  $-\delta'$ , 0,  $+\delta'$  represent the resonances of the system. At the resonances, the rates of change of susceptance  $dB_U/d\delta$  are

$$\left(\frac{dB_U}{d\delta}\right)_{\delta=0} = 2Y_{c1} \frac{Q_{E1} + Q_{E2} + Q_{E3}}{Q_{E1}}, \quad (10a)$$

$$\left(\frac{dB_U}{d\delta}\right)_{\delta=\pm\delta'} = 2Y_{c1} 2 \frac{Q_{E1} + Q_{E2} + Q_{E3}}{Q_{E2} + Q_{E3}}. \quad (10b)$$

To illustrate the implications of the relations just derived, a numerical example will be given. It will be supposed that the magnetron has an

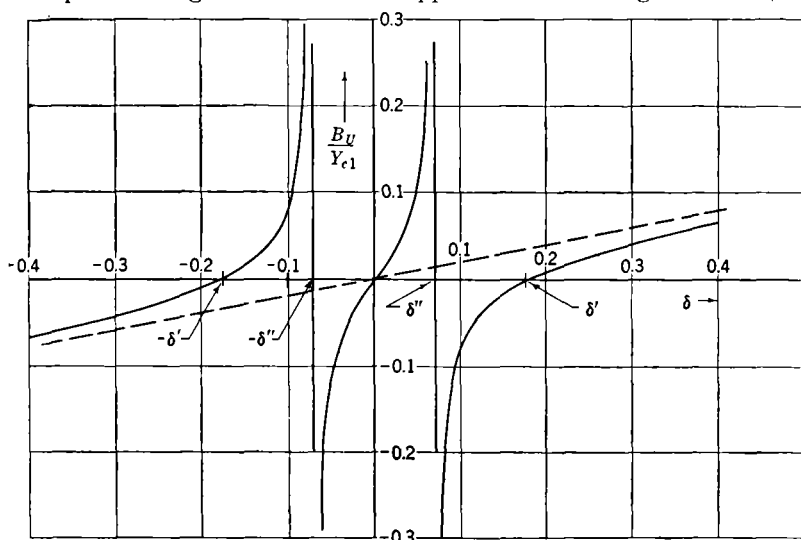


Fig. 16-3.—Susceptance curves.

output lead which is so coupled that  $Q_{E1}$ , the external  $Q$  with respect to it, is equal to 100—a typical value for normal output coupling. A stabilization factor  $S = 6$  is to be sought; thus Eq. (4c) gives  $Q_{E3} = 500$ . The transmission line has a length of  $3\lambda$ ; but instead of the value  $3\pi$  for  $Q_{E2}$ , the round number 10 will be used. On the basis of the values  $Q_{E1} = 100$ ,  $Q_{E2} = 10$ , and  $Q_{E3} = 500$ , one obtains the result

$$\delta' = 0.0175,$$

$$\delta'' = 0.0071,$$

$$\frac{1}{Y_{c1}} \left(\frac{dB_U}{d\delta}\right)_{\delta=0} = 12.2,$$

$$\frac{1}{Y_{c1}} \left(\frac{dB_U}{d\delta}\right)_{\delta=\delta'} = 4.8.$$

(Without the stabilizer,  $1/Y_{c1}(dB_U/d\delta) = 2.0$ .) The curve of susceptance plotted against  $\delta$  is shown in Fig. 16-3, where the dotted line indicates the corresponding quantity for the magnetron alone. With a typical value of  $Y_{c1} = 10^{-1}$  mho, it is roughly the range

$$-0.03 < \frac{B_U}{Y_{c1}} < +0.03$$

that is significant in magnetron operation.

Two ways of adding the external load to the system will be considered. The relations are simplest if (Case I) the magnetron is a specially constructed one with two output leads, one for the load and the other for the stabilizer. If the magnetron has only one output lead, the load must be tapped onto the transmission line of Fig. 16-2c, and it will be assumed to be connected in parallel with the stabilizer (Case II).

For Case I, the external load  $Y_E$  is simply added to  $Y_U$  of Eq. (9a). It will be assumed that  $Y_E$  is a pure conductance and has the value that it would have if the magnetron were not stabilized and were loaded with a  $Q_E$  of 100; then in the numerical example,  $Y_E/Y_{c1} = 1/Q_{E1} = 0.01$ . The  $Y_L(\nu)$  curve, conveniently treated as the  $(Y_L/Y_{c1})(\delta)$  curve, then has three coincident vertical branches through the point  $Y_L/Y_{c1} = 0.01$ .

To compute  $Y_L(\delta)$  for Case II, one must replace  $y_3$  by  $y_3 + y_E$  in Eq. (7). For the value of load assumed above, this amounts to replacing  $j2Q_{E3}\delta$  by  $(1 + j2Q_{E3}\delta)$  in Eq. (9a). The  $Y_L(\delta)$  curve then takes on the form indicated schematically in Fig. 16-4. The significant

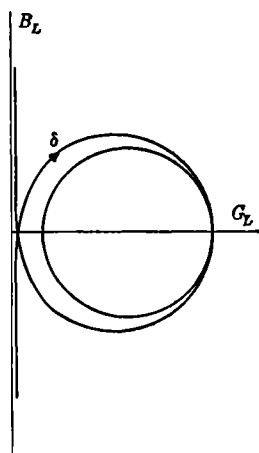


FIG. 16-4.—Admittance curve.

parts of the  $Y_L(\delta)$  curves for both cases are plotted to scale in Fig. 16-5; to avoid confusion, only the halves of the curve for  $\delta$  positive are shown; the other halves are obtained by reflection on the real axis. The only essential difference between the two arrangements is that for Case I the load is effective for all three modes of oscillation (although the stabilization is not fully effective for two of the modes); in Case II the load is effective only for the  $(\delta = 0)$ -mode; for the other two it is "shorted out" by the stabilizer.

It is to be noticed that for a small range of  $\delta$  centered about  $\delta = 0$ , either of the arrangements analyzed above duplicates the properties of the ideal system illustrated in Fig. 16-1. The mode of oscillation in this range will be referred to as the "principal mode." Two extra

modes of oscillation are introduced, however, and from experience it can be predicted that with the constants assumed in the above example, the system would fail to perform satisfactorily because of improper or uncertain selection of the mode of oscillation. The control of the extraneous modes is, therefore, the central problem. In the endeavor to prevent oscillations in the extraneous modes, three rather distinct principles have been tried.

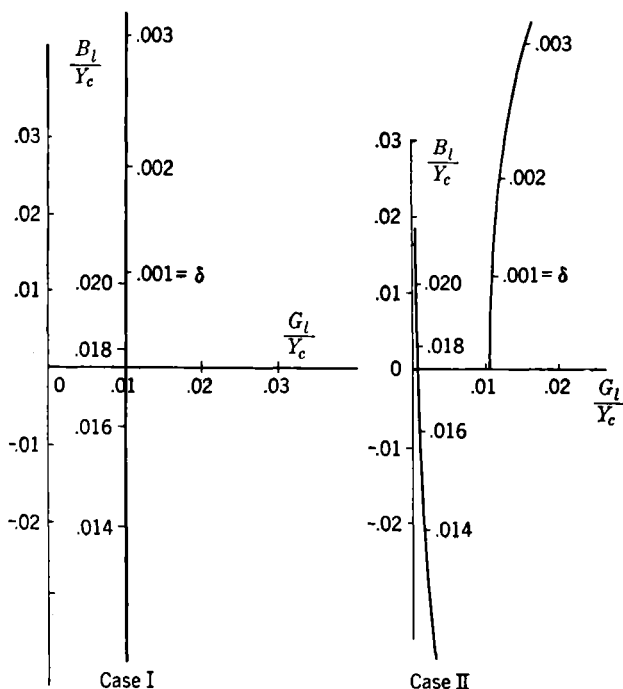


FIG. 16-5.—Admittance curves.

At one time it was expected that a very great separation of the extraneous modes from the principal mode would serve to discourage oscillation in the extraneous modes. As far as the magnetron is concerned, the extra modes arise from a very large reactive effect—in *just one elementary resonator*—the one to which the stabilizer is directly coupled. It seems very probable that if the extraneous modes differed from the principal mode (the principal mode has a frequency equal or very close to the normal  $\pi$ -mode of the magnetron) by 10 per cent or even more, these reactive effects would so distort the configuration of the electric fields in the interaction space that the interaction with the electron stream would be impaired considerably.

By coupling the stabilizer to the magnetron through an iris it is possible to separate the extraneous modes from the central one by as much as 20 per cent. This possibility was taken advantage of in "stabilized" magnetrons designed by Herlin<sup>1</sup> and Smith<sup>2</sup> (Sec. 19-5). These magnetrons had auxiliary cavities so coupled as to yield a stabilization factor of about 5 for the principal mode; the extraneous modes were about 20 per cent above and below the central mode. These magnetrons were complete failures in the sense that they could not be made to oscillate reliably in the principal, highly stable mode. They did, however, perform quite satisfactorily in the low-frequency mode, but without appreciable benefit from the auxiliary cavity in stabilizing the frequency. This experience was more or less duplicated by experiments at the Bell Telephone Laboratories. Thus it appears that the separation between the modes is of little consequence in determining whether or not the magnetron will oscillate in the "stabilized" mode.

From their initial failure, Herlin and Smith arrived at a second principle. They interpreted their result in the following way: The "speed of starting" of a mode of oscillation should vary inversely with the degree of "stabilization" of the mode. To express the same thing in a different way, the speed of starting should vary inversely with the "effective capacitance" of the mode. When the  $Y_L(\nu)$  curve is vertical and  $B_L$  varies fairly uniformly with  $\nu$  over an appreciable range of  $\nu$ , the system can be approximated by a parallel-resonant circuit of effective capacity  $C = \frac{1}{2}(dB_L/d\nu)$ . It is shown in Chap. 8 that, other things being equal, the speed of starting should vary inversely with  $C$ . As to the modes of the magnetron-stabilizer system, it can be deduced from Eqs. (10a) and (10b) that

$$\frac{\left(\frac{dB_L}{d\delta}\right)_{\delta=0}}{\left(\frac{dB_L}{d\delta}\right)_{\delta=\pm\delta'}} = \frac{Q_{E2} + Q_{E3}}{2Q_{E1}} = \frac{S - 1}{2}, \quad (11)$$

where  $S$  is the stabilization factor for the principal mode. It follows that if  $S$  is not greater than 3, the principal mode should get there first.

Experience has borne out the above line of reasoning in so far as it has been found that the extraneous modes give no trouble if the stabilization factor  $S$  is about 3 or less. It should be pointed out that relation

<sup>1</sup> M. A. Herlin, "Resonance Theory of the Waveguide Tunable Magnetron," RL Report No. 445, Oct. 15, 1943.

<sup>2</sup> W. V. Smith, "Magnetron Tuning and Stabilization," RL Report No. 567, July 13, 1944.

(11) holds only when  $\nu_{U1} = \nu_{U2}$ ; if the resonant frequencies of the magnetron and auxiliary cavity are not equal, the ratio is less favorable. Consequently if stabilization is the primary consideration, so that  $S$  is made nearly equal to 3, and the system is tuned by varying only one of the components, the useful tuning range is only a small fraction of the separation between the modes. The application of the foregoing considerations to the wide-range tuning of magnetrons is treated in Chap. 14.

**16-4. Means of Damping the Extraneous Modes.**—The third principle, and the only one so far discovered that enables one to take advantage of a high degree of stabilization, consists in introducing an auxiliary load into the system in such a way as to damp the extraneous modes preferentially. The placement of the auxiliary load represented by the resistance  $R$  is illustrated in Fig. 16-6. Inasmuch as the system is now to be analyzed in somewhat greater detail, the conductance  $G_3$  has been added to the equivalent circuit. If the external, or useful, load is to be connected directly to the magnetron as in Case I above,  $g_3$ , the normalized value of  $G_3$ , is equal to  $Q_{E3}/Q_{U3}$ , where  $Q_{U3}$  is the unloaded  $Q$  of the stabilizer cavity.

(It can be shown that the cases where the external load is connected between the terminals  $a$ - $c$  or  $a$ - $b$  of Fig. 16-6 can be reduced to the same equivalent circuit.)

The effect of adding the resistance  $R$  can be interpreted qualitatively in the following way. It will be shown that the presence of  $R$  has little damping effect on the principal mode  $\delta \approx 0$  and a large effect on the extraneous modes. At  $\delta = 0$  the impedance of the stabilizing cavity is equal to  $1/G_3$ —a rather large quantity. Thus the currents into the cavity are very small, and negligible power is dissipated in  $R$ . On the other hand, at the frequencies  $\pm \delta'$  of the extraneous modes, the stabilizer has a relatively small impedance, the currents into it are large, and the maintenance of either of those modes must entail a relatively large dissipation of power in  $R$ ; consequently those modes are strongly damped. From this argument one can conclude that the extraneous modes will be discouraged by the introduction of  $R$  into the system, but neither the stabilization nor the circuit efficiency of the system for the principal mode will be impaired appreciably.

The damping of the extraneous modes can be accomplished by adding dissipation to the system in any one of many ways—for instance, by

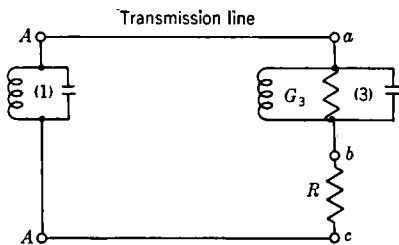


FIG. 16-6.—Stabilizer with damping resistor.

using a transmission line of appreciable attenuation for the connecting link between the two resonant systems—but the preferred methods are those which have a minimum of influence on the principal mode. When the latter consideration is taken into account, one seems to arrive always at a circuit substantially equivalent to Fig. 16-6. It is natural to inquire whether or not the extraneous modes could be damped by coupling them to the useful load, so that an auxiliary load would be unnecessary. This possibility has not been overlooked, but there seems to be no satisfactory way of accomplishing the desired result.

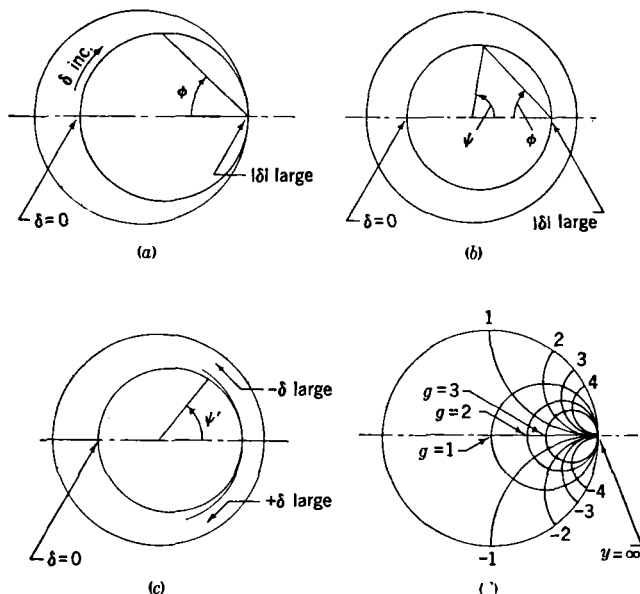


FIG. 16-7.—(a, b, c)  $Q$ -circles; (a) measured at terminals  $ab$  of Fig. 16-6; (b) at terminals  $ac$ ; (c) at opposite ends of transmission line; (d) Smith chart.

Some of the less fortunate consequences of adding the damping resistor to the system will now be discussed. In general, the larger the value of  $R$  the more effective it is for its intended purpose. It also happens that as  $R$  is made larger, the more restricted becomes the range through which the system can be tuned without undue loss of stabilization and circuit efficiency. More or less equivalently, the ranges of the fluctuations in temperature, load, etc., against which the stabilization is effective are similarly reduced. The question of the minimum tolerable value of  $R$  is thus an important one in the design of stabilizing systems.

The effect of the damping resistor in suppressing the extraneous modes can be partly analyzed by means of the  $Y_L(\nu)$  or  $Y_L(\delta)$  curves for



the system. The way in which the various parameters enter into these curves can be understood qualitatively by considering the admittance curves of isolated parts of the system; inasmuch as a transmission line is involved, it is convenient to draw the curves in a reflection-coefficient diagram (Smith chart). The  $Q$ -circle of the auxiliary cavity, as measured at terminals  $a$ - $b$  of Fig. 16-6, has the form indicated in Fig. 16-7*a*. As measured between the terminals  $a$ - $c$ , it has the form illustrated in Fig. 16-7*b*. In both cases, the tangent of the angle  $\phi$  varies linearly with the frequency. The value of the resistance  $R$  is always made less than the characteristic impedance of the transmission line, and the primary effect of the resistance is seen to be a lowering of the reflection coefficient (or SWVR) for frequencies far from resonance.

The  $Q$ -curve for this part of the system, as measured at the opposite end of the transmission line, is obtained simply by diminishing the angle  $\psi$  for each point by *twice* the angle  $\theta$  given by Eq. (8). When this is done, the curve is no longer a perfect circle but has the shape indicated in Fig. 16-7*c*. The behavior of the admittance can be estimated by comparing Fig. 16-7*c* with the Smith chart shown in Fig. 16-7*d*. Since the curve now passes completely through the region where the admittance varies rapidly with the angle  $\psi'$ , it can be inferred that the admittance of the system will contain violent fluctuations. These fluctuations occur for  $\delta$ 's in the neighborhood of the ( $\delta''$ )'s given by Eq. (9*d*) and, of course, are directly related to the infinities in the susceptance function illustrated in Fig. 16-3, becoming identical with them when  $R = 0$ .

The violence of the fluctuations becomes less as  $R$  is made larger (assuming always that the value of  $R$  is smaller than the characteristic impedance of the transmission line), as is evident from the nature of the Smith diagram.

The admittance curve for the complete system is obtained by adding to the admittance just discussed the term  $y_1$  of Eq. (7), which is the admittance of the magnetron proper. Whether or not the final admittance curve will contain loops depends upon the values of both  $Q_{E1}$  and  $R$ ; the relations are exactly the same as those discussed in connection with the mismatched transmission line in Chap. 7. A numerical example of the way in which the presence or absence of loops is influenced by the value of  $R$  is contained in Fig. 16-8*a*, *b*, and *c* computed with  $Q_{E1} = 20$ ,  $Q_{E2} = 3\pi/2$ ,  $Q_{E3} = 100$ ; the external load is assumed to be coupled directly to the magnetron so as to load the magnetron, unstabilized, to a  $Q_L$  of 100.

So far, only cases where the resonance frequencies of the magnetron, transmission line, and auxiliary cavity are exactly equal have been discussed. An increase in  $\nu_1$ , the resonance frequency of the magnetron, results simply in a downward displacement of the curve and vice versa.

The shape of the curve is determined entirely by the ratio  $\nu_3/\nu_2$ ; thus the curve becomes unsymmetrical when the cavity is tuned or when the transmission line is constructed with an incorrect length. These effects are perhaps more easily deduced directly from figures such as Fig. 16-7c and d than from a verbal explanation. Concrete examples of the changes in the curve caused by tuning the cavity are given in Fig. 16-8b, d, and e,

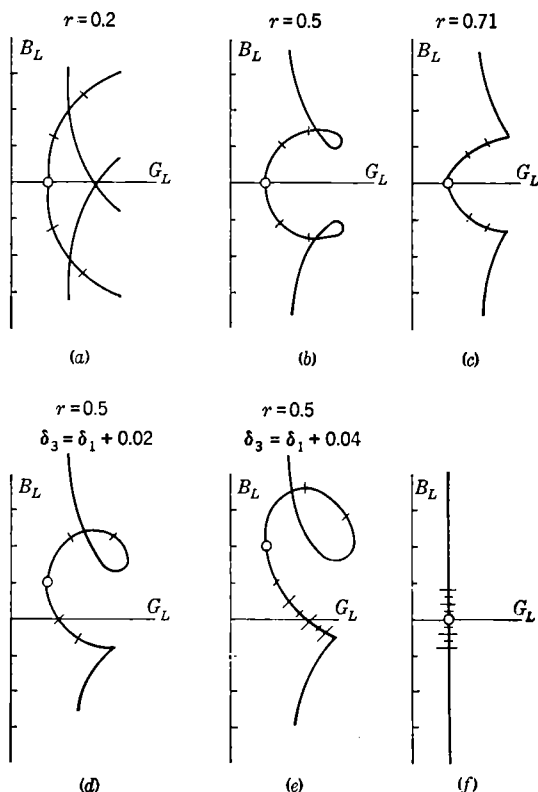


FIG. 16-8.—(a,b,c) Admittance curves of stabilized magnetron as affected by  $R$ ; (b,d,e) as affected by tuning the cavity; (f) unstabilized magnetron.

where  $\delta_3 = (\nu_3 - \nu_1)/\nu_1$ . The point of each curve marked by a circle represents the condition  $\delta = \delta_3$ .

In designing a stabilizer, it is advantageous to make  $\nu_2$  and  $\nu_3$  equal to the normal transmitting frequency of the magnetron rather than equal to its "cold resonance" frequency  $\nu_1$ ; in that way the  $Y_L(\nu)$  curve for the system is made roughly symmetrical about the operating curve.

The general problem of selection among the modes that results from coupling a second resonant system to that of the magnetron proper is

discussed in Chap. 7. Unfortunately, there seems to be no straightforward rule that applies to the present case, although one result is certain, namely, that the extraneous modes will not be excited if there does not exist a corresponding intersection between the  $Y_L(\nu)$  curve and the operating curve of the magnetron. Thus, from the standpoint of mode selection, a  $Y_L(\nu)$  like that of Fig. 16-8c is desirable, for with such a curve, a second intersection is possible only if the operating curve has an abnormally great slope.

On the other hand, from the standpoint of other properties of the system, it is desirable to make  $R$  as small as possible. For the case represented by Fig. 16-8a through  $e$  the circuit efficiency is inversely proportional to  $G_L$ . If losses in the cavity are taken into account, and also if the load is connected across the terminals  $a-c$  of Fig. 16-6, the circuit efficiency is given by a more complicated expression but the behavior is qualitatively the same. Figure 16-8a,  $b$ , and  $c$  illustrates that when  $R$  is large, the circuit efficiency falls off more rapidly with departures from normal conditions. It can also be judged from a comparison of the figures that the range of conditions—load, temperature, current, etc.—in which the stabilization is fully effective is reduced materially by values of  $R$  great enough to suppress the loops completely.

If these latter considerations are vital, it becomes worth while to find out whether or not loops in the  $Y_L$  curve can be tolerated, and this question will have to be settled by cut-and-try methods; otherwise the safe thing to do is to make  $R$  large enough to suppress the loops. It can be shown that the required value, normalized, is given approximately by the expression

$$r = \left( \frac{2Q_{F2}}{Q_{E1}} \right)^{\frac{1}{2}}.$$

(This expression holds more exactly when the useful load is coupled directly to the magnetron and when the losses in the auxiliary cavity are negligible.) The presence or absence of loops can be checked by computing the curve or by making cold-test measurements. If the magnetron has a second output lead, the  $Q$ -curve observed looking into this lead will reproduce the  $Y_U$  curve of the system.

Perhaps it should not be surprising that the practical problem of mode selection should involve a good deal of empiricism. The argument given in Chap. 7 indicates that the true normal modes of the system—especially when the electronic admittance is taken into account—have a somewhat complicated relation to the  $Y(\nu)$  curve. (It would be somewhat of a chore to investigate the normal modes in the present case, for the presence of three modes entails a cubic equation. Furthermore, in a quantitative treatment the electronic susceptance would have to be taken

into account, since changes in the susceptance alone can determine whether a particular normal mode is positively or negatively damped.) It seems likely that the pulse shape may have some influence, but it has not been studied enough in connection with stabilized magnetrons to warrant any conclusions.

In the case of pulsed magnetrons, it is important to inquire whether or not stabilization will greatly increase the tendency of the magnetron to misfire. It is indicated in Chap. 8 that misfiring results from too slow a buildup of oscillations, relative to the rate of increase of the applied voltage. In so far as stabilization increases the effective capacity of the

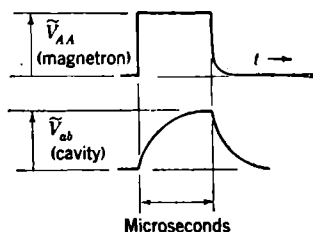


FIG. 16-9.—Buildup of oscillations in a 10-cm magnetron-stabilizer system.  $S \approx 60$ .

resonant system, it perhaps might be expected that the rate of buildup should be proportional to  $1/S$  and that a high degree of stabilization would increase the tendency toward misfiring unless the rate of rise of the applied voltage were reduced by the factor  $1/S$ . That this is not necessarily true is proved by the results of some experiments which were concerned<sup>1</sup> with the problem of producing very high electric fields within a resonant cavity by exciting it with a pulsed magnetron. The

method of coupling employed can be represented by the equivalent circuit of Fig. 16-6 with roughly the following constants:

$$Q_{\pi 1} = 100, \quad Q_{\pi 2} = 20, \quad Q_{\pi 3} = 16,000, \quad \frac{1}{g_3} = Q_{U3}/Q_{\pi 3} = 1, \\ r = \frac{2}{3}.$$

The system can be considered to be a magnetron stabilized by a factor  $S$  of about 60. The terms involving  $G_3$  are not negligible in this case, and the stabilization factor is given approximately by

$$S = 1 + \frac{I}{(1 + rg_3)^2} \frac{Q_{\pi 3}}{Q_{\pi 1}}.$$

The modulator employed to drive the magnetron was of the high-impedance type, and no particular effort was made to reduce the rate-of-rise of its output voltage; thus, according to the argument given in the preceding paragraph, conditions were favorable for the magnetron to misfire. Nevertheless, no abnormally great tendency of this sort was observed. Observations were made which, in terms of Fig. 16-6, were equivalent to measuring the a-c voltage at terminals AA and at terminals

<sup>1</sup> J. Halpern, A. E. Whitford, and E. Everhart; Research Group of Electronics, Massachusetts Institute of Technology, private communication.

*ab.* The types of r-f pulses observed are indicated schematically in Fig. 16-9. Evidently oscillations build up within the magnetron itself at something like the normal rate, while the amplitude builds up within the cavity at a rate that is roughly consistent with its  $Q$ . That this can happen is due essentially to the buffering action of the resistance  $R$ . (The fallacy in the argument that introduced this discussion lies in not considering the properties of the system throughout a range of frequencies great enough to encompass the bandwidth of the transient.)

**16-5. The Design of Stabilizing Circuits.**—Primary emphasis will be given to systems that use a transmission line to couple the auxiliary cavity to the magnetron because the construction of built-in stabilizers for large stabilization factors has not progressed beyond the experimental stage. The coupling of the transmission line to the magnetron is treated elsewhere in this volume and will be taken for granted here. The problem then is reduced to approximating as closely as possible the equivalent circuit of Fig. 16-6 and becomes largely an exercise in microwave plumbing. It is feasible here merely to indicate some of the structures that have been found to be practicable.

An iris has usually been used to couple the transmission line to the cavity. The coupling results from the interaction of magnetic fields across the iris; and since fairly tight coupling is required, the iris is cut into a region of the cavity where the magnetic field is large. The cutaway in Fig. 16-14 illustrates this type of coupling to a coaxial line. A cavity similarly coupled to the broad side of a rectangular waveguide has similar electrical properties. The cavity acts as a parallel-resonant circuit in series with one side of the transmission line at the location of the iris.

A complete system, employing coaxial line, is illustrated schematically in Fig. 16-10*a*. If the useful load is to be coupled directly to the magnetron, the  $T$ -junction is omitted. Except for the half-wavelength of transmission line between the  $T$ -junction and the cavity and for the imperfections of the  $\lambda/4$  transformers—neither of which are actually of great importance—this arrangement is a good realization of the required circuit. A complete system employing rectangular guide is illustrated schematically in Fig. 16-10*b*. Because of the fact that an  $E$ -plane junction is used, the distances of cavity to junction and of junction to magnetron differ by a quarter wavelength from the coaxial cases; if an  $H$ -plane junction is used, these distances are the same as for the coaxial case.

It must be emphasized that in the large-scale application of stabilizing cavities a most important consideration is the control of the electrical distance between the magnetron and the stabilizing cavity. This distance appears as a length  $l$  in the equivalent circuits and the equations. Actually it has to be measured from the reference plane  $T$  introduced in Fig. 7-5; this plane has no simple relation to the mechanical features

of the magnetron, but it can be determined by cold-impedance measurements. The location of the plane of reference varies from one magnetron to another because of inequalities in the construction and installation of the output leads. The permissible tolerance in the placement of the stabilizing cavity is of the order of  $0.01\lambda$ —very much less than the

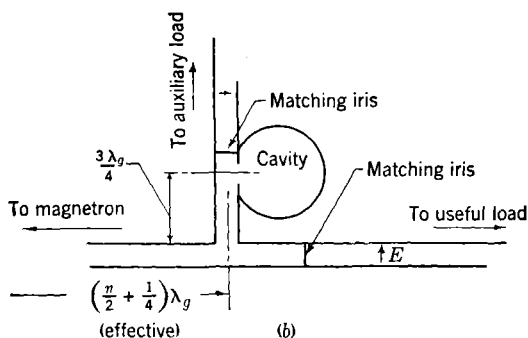
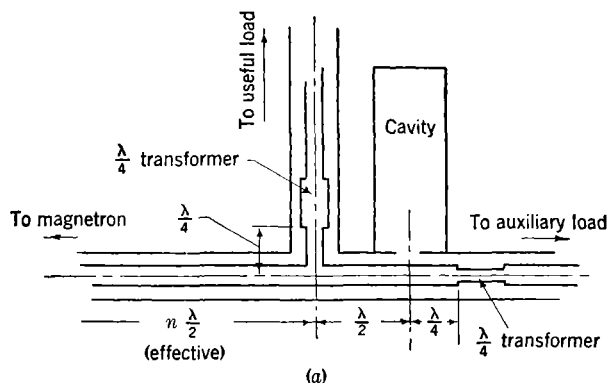


FIG. 16-10.—(a) Complete stabilizing system employing coaxial line; (b) complete stabilizing system employing rectangular guide.

uncertainty in the plane of reference for practically all commercial magnetrons.

In the case of the 2J59 magnetron (Fig. 16-11) the difficulty is solved by controlling the output lead of the magnetron—the manufacturer tests the leads in advance and uses only those which have the proper “electrical length.” In the stabilizer designed for the 2J48 magnetron<sup>1,2</sup>

<sup>1</sup> W. M. Preston and J. B. Platt, RL Group Report No. 473.

<sup>2</sup> W. M. Preston, RL Group—5/31/44 Report No. 71, May 31, 1944.

(Fig. 16-12) the distance is made adjustable by incorporating a sliding T-junction into the stabilizer. In the 2J41 magnetron (Fig. 16-13)<sup>1</sup> a tuning screw is placed in the transmission line in such a way as to allow

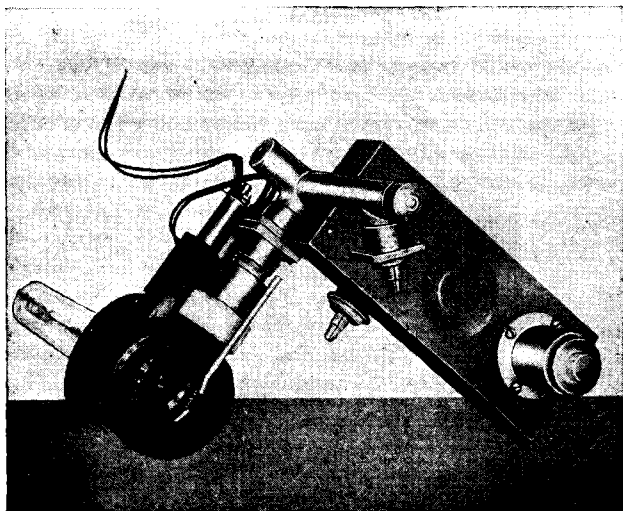


FIG. 16-11.—Type 2J59 magnetron and stabilizing cavity.

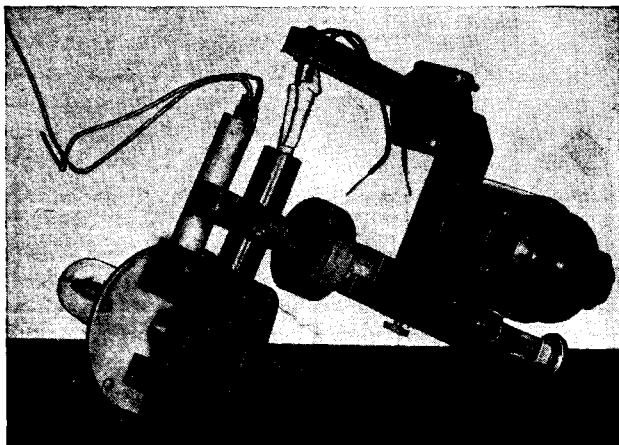


FIG. 16-12.—Type 2J48 magnetron with stabilizing cavity.

some degree of correction; in this case the magnetron and stabilizer are permanently assembled and adjusted at the factory.

Electrical breakdown within the cavity is a second important consideration. By using the rule that the external  $Q$  of a system is equal to

<sup>1</sup> M. A. Herlin Group Report 52—6/10/45.

$[2\pi\nu$  (energy stored)]/power, one can derive for a rectangular cavity the relation

$$\frac{Q\lambda P}{E^2 v} = \frac{\pi\epsilon_0 C}{2} \quad (\text{MKS units}),$$

where  $E$  is the electric field and  $v$  the volume of the cavity. Expressed in the units  $\lambda$  cm,  $E$  volts/cm,  $v$  cm<sup>3</sup>,  $P$  watts, the relation is

$$\frac{Q\lambda P}{E^2 v} = 2.1 \times 10^{-3}.$$

The relation will give the order of magnitude of the volume required in cavities of other simple shapes. The above relation yields, for the condi-

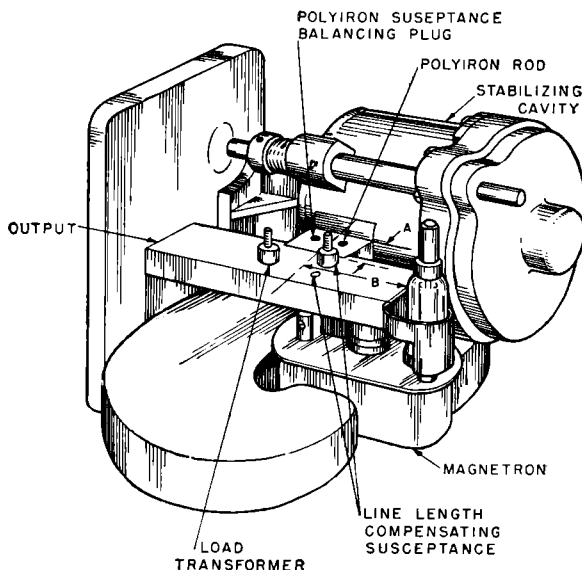


FIG. 16-13.—Type 2J41 stabilized magnetron.

tions  $Q = 500$ ,  $E = 30,000$ ,  $\lambda = 10$ ,  $P = 50,000$ , a required volume of 132 cm<sup>3</sup>, and experience shows that this is too small by a factor of about 4. Of course, care must be taken with the tuning mechanism; or because of localized intense fields, it will greatly reduce the power-handling capability of the system.

Ordinarily a stabilizer must be designed for a given tuning range and degree of stabilization. The tuning range throughout which the efficiency and stabilization will not fall below something like 75 per cent of their maximum values will amount to about one-third of the value of



$\delta''$  given by Eq. (9d); that is,

$$\text{Tuning range} \approx \frac{1}{8}(Q_{E2}Q_{E3})^{-1/2}$$

or

$$\text{Tuning range} \approx \frac{1}{8}[(S - 1)Q_{E1}Q_{E2}]^{-1/2}.$$

(To compute the tuning range accurately, one would have to take into account many of the details of the circuit.) Generally it will be found that the tuning range is all too small, and one will make  $Q_{E2}$  as small as is practicable by shortening the transmission line, but this possibility is soon exhausted. To increase the tuning range further,  $Q_{E1}$  must be made smaller; that is, the magnetron must be more tightly coupled to the transmission line. This will require a special magnetron with an abnormally large pulling figure.

When a special magnetron is required, it would seem sensible to have one constructed with two output leads—one normally coupled lead for the useful load and one tightly coupled lead for the stabilizer. In that way the  $T$ -junction can be eliminated and the line made shorter. The plumbing problem is considerably simplified also, and the system is made generally neater. An experimental c-w magnetron stabilized in this way is shown in Fig. 16-14; this combination was constructed by attaching a stabilizer to the "tuning lead" of the magnetron illustrated in Fig. 14-12. With pulsed magnetrons, however, one has to consider the circumstance that the voltages developed in the transmission line will increase with the coupling.

When the stabilized magnetron is required to run at a preassigned frequency, the stabilizer can be used with a fixed-tuned magnetron provided the combination has a great enough tuning range to compensate for the scatter that is unavoidable in manufacture as well as for aging effects in the magnetron and for the fluctuations in operating conditions. A higher degree of stabilization is feasible, however, if the magnetron itself is tunable, so that tuning range of the stabilized combination can be sacrificed in the interest of a higher stabilization factor. By taking advantage of this possibility, it has been possible to attain a stabilization factor of about 10 in the combinations shown in Figs. 16-11 and 16-13; these magnetrons were designed for use in beacon transmitters and therefore must operate at an assigned frequency.

*Built-in Stabilizers.*—A moderate degree of stabilization has been built into two commercial magnetrons in order to improve the efficiency at the pulling figure required of them in their applications. The stabilization factor  $S$  is less than 3, so no damping resistor is required. The cavities are incorporated into the output leads of the magnetrons.

When the auxiliary cavity is essentially tangent to the magnetron, so that the coupling can be effected by simply an iris, with no trans-

mission line, it is possible to secure very tight coupling and wide mode separations. Thus the essential requirements of a wide tuning range can be met. However, no entirely satisfactory way of introducing the

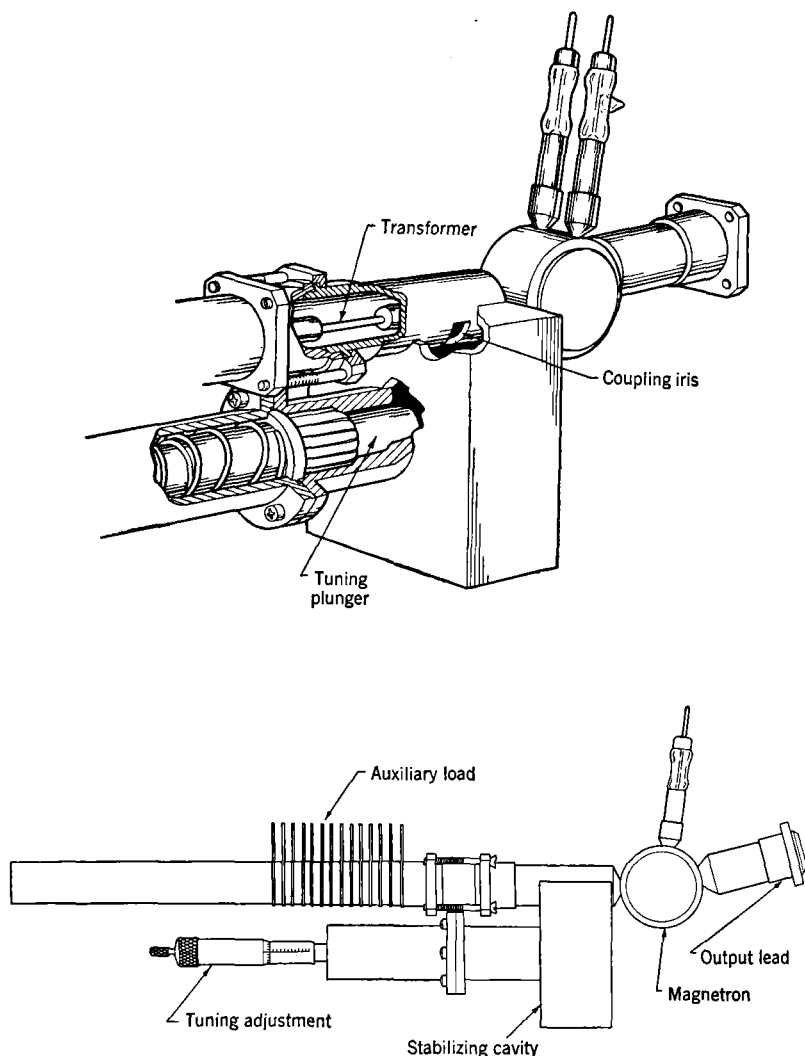
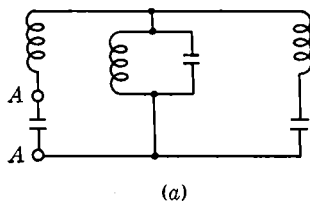


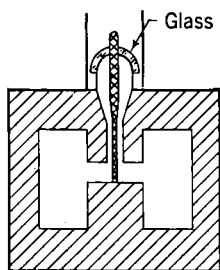
FIG. 16-14.—A stabilized c-w magnetron.

damping resistor has been discovered, so the potential benefits to be derived from the close coupling have not been realized in a tube with a high stabilization factor. Experimental tubes were constructed with a

circuit similar to that used in the tunable magnetrons described in Chap. 14, except that the constants of the system were chosen for high stabilization. An equivalent circuit that is closely related to the physical structure is that shown in Fig. 16-15a; this circuit has the same properties as that of Fig. 16-2b as far as the admittance at the terminals *A* is concerned. In the circuit of Fig. 16-15a the damping resistor must be



(a)



(b)

FIG. 16-15.—(a) Equivalent circuit of cavity and magnetron coupled by an iris; (b) iris with damping resistor.

shunted across the parallel-resonant circuit, which corresponds to the gap in the iris.

In the experimental magnetrons, the gap of the iris was loaded by connecting a coaxial line across it, as is illustrated by a sectional view in Fig. 16-15b. The coaxial line passes through a vacuum seal as in a coaxial output lead, so the power-dissipating element can be placed outside the vacuum envelope. For the damping resistor to fulfill its function, it is, of course, necessary that it have the proper value and also that it be "broadband"; otherwise it will introduce extra resonances into the system. It appears that it is rather difficult to satisfy this condition.



## PART V

# PRACTICE

It has been the experience of the Radiation Laboratory that one of the major tasks in producing a satisfactory magnetron design is the elimination of minor undesirable characteristics. Every new design involved the construction of a large number of good experimental tubes and a thorough testing of them. In the process, a large amount of practical knowledge was acquired and Chaps. 17 to 19 contain the part of this "know how" that will be helpful to those confronted with the problem of constructing a workable magnetron.

The construction of experimental magnetrons free of imperfections that would interfere with the interpretation of experimental data is a major problem, and those who are unfamiliar with this practice may find it difficult to understand the importance given to it here. The techniques and processes described in Chap. 17 have been chosen not only for their particular importance in the construction of magnetrons but for their broader applications as well.

Rarely, if ever, does the first experimental model of a proposed magnetron meet all the requirements contemplated, and data must be taken on the first experimental tube to determine the modifications to be incorporated in the next attempt. Two kinds of data may be taken: the so-called "cold resonance" measurements, made on the anode block and output circuit of a nonoscillating tube, and the measurements on the operating magnetron. The first kind, which is discussed in the first part of Chap. 18, is useful in that it isolates the r-f circuit problems from the over-all operating characteristics obtained from the oscillating magnetron and thus facilitates the interpretation of all the data. The second part of Chap. 18 explains the technique of taking operating data and gives instructions for operating both pulsed and c-w magnetrons.

Chapter 19, "Typical Magnetrons," is a record of practical accomplishments of the many laboratories that were involved in the development of microwave magnetrons. Essential dimensions and operating characteristics for representative magnetrons of proved design are given.



## CHAPTER 17

### CONSTRUCTION

BY J. R. FELDMER

Wartime research has greatly advanced the art of fabricating electronic tubes that do not depend on glass envelopes for their vacuum. Most of this advance resulted from klystron and magnetron construction, in which it has been necessary to build high- $Q$  resonant cavities into the vacuum chamber. In the case of the magnetron, the necessity for working copper into intricate shapes to form several parallel-resonant cavities about a cylindrical anode has resulted in techniques that will be of use in the construction of a great number of other devices. In addition to recording these new techniques this chapter will give information by detail or reference on all steps of magnetron construction, so that an experimenter new to the field of microwave magnetrons will be able to build tubes.

To those not already acquainted with tube making, a word of caution is in order. To construct a successful hermetically sealed electron tube is not easy. To build experimental tubes at the rate of only one per week requires the use of a laboratory having equipment readily available to perform every operation. The number of individual operations that go into the construction of a typical magnetron is surprisingly large, usually amounting to about 150. Most of these operations are on component parts that can be readily inspected and errors corrected, but there are about 25 operations of a very critical nature that will lead to a bad tube unless great care is exercised and defects are detected early. Thus care, inspection, and cleanliness cannot be overemphasized. With these facts in mind and from the point of view of the experimenter rather than the manufacturer, the material of this chapter was selected.

It should be emphasized also that this chapter will not be an exhaustive treatment of tube construction but in most cases will give examples of typical procedure that the experimenter will want to modify. It is hoped that the descriptions will suggest modifications appropriate to the special problems.

**17-1. Fabrication of Anode Blocks.**—The anode block includes the resonant system and therefore not only must be a collector capable of power dissipation but must have a high unloaded  $Q$ ; thus a material of high conductivity is required. Copper has been used for the block

material for all present microwave magnetrons (although some effort has gone into the development of tantalum and tungsten blocks to reduce the change in magnetron frequency with temperature at some sacrifice of unloaded  $Q$ ). With the exception of the technique used by RCA in making the 2J41 (see Chap. 19), the copper is also used to form the vacuum seal. To satisfy these requirements of high- $Q$  and good vacuum qualities, OFHC (oxygen-free high conductivity) copper has generally been used. Selenium copper has also been successfully employed here and in England. The advantage of selenium copper over OFHC lies in its superior machining qualities, but the reliability of its vacuum qualities has been questioned.

The methods of fabrication that have been used for magnetron blocks are summarized in Table 17-1 along with examples that are described in Chap. 19.

TABLE 17-1.—FABRICATION METHODS FOR ANODE BLOCKS

Methods of fabrication	Examples
Machining.....	WE 725A
Lamination.....	Raytheon 2J30-34
Jig assembly.....	2J42, RL HP10V
Hobbing.....	3J31
Vacuum casting.....	Machlett HP10V
Sintering.....	Special BM50 anodes

*Machining.*—For making experimental blocks in the 10- and 3-cm wavelength bands, the precision boring, slotting, broaching, milling, or turning of copper is quite successful;<sup>1</sup> and although difficult, tubes at the 1.25-cm band have been made by precision machining methods. For making a few experimental tubes, there is little choice between this method and jig assembly, a process of fabrication that will be described in detail.

*Lamination.*—The lamination method consists of punching disks from thin sheets of copper, stacking them with alternate pieces of solder foil similarly punched, and passing the assembled stack through a brazing furnace to form an anode block. The method has been used successfully for 10-cm magnetrons, but the mechanical irregularities existing among the brazed laminated parts become serious at shorter wavelengths. This method is suitable for large-scale production.

*Jig Assembly.*—The jig assembly method employs precision brazing to form blocks by holding component anode-block parts in a fixture that can be removed after the parts are joined. It has proved to be one of the most effective methods of block fabrication and accordingly will be described here in detail by following the procedure used in con-

<sup>1</sup> E. Oberg and F. D. Jones, *Machinist's Handbook*, Industrial Press, New York, 1945.



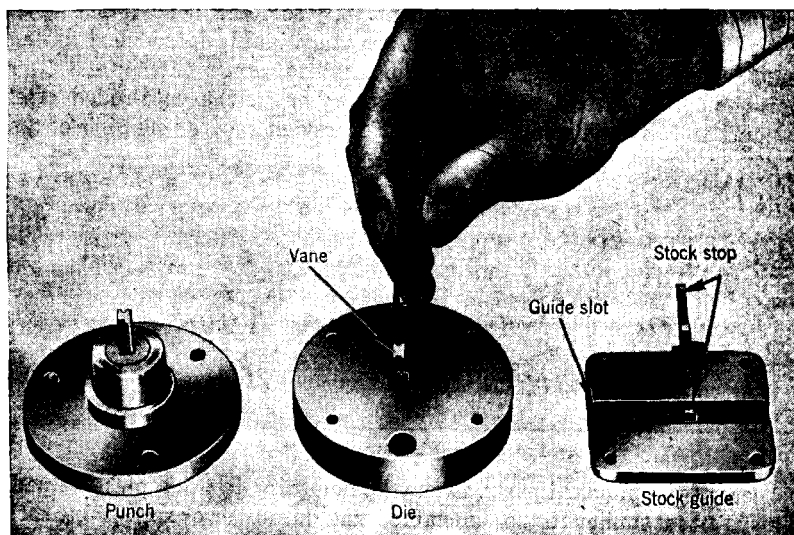


FIG. 17-1.—Vane-punching tools.

structing a specific anode block, namely, the 2J42, a 3-cm pulsed magnetron (see Chap. 19).

The first step in the construction of the 2J42 block is the preparation of the vane and strapping-ring stock, accomplished by rolling OFHC copper strips to a thickness of  $0.020 \pm 0.0005$  in. From this material the block vanes and rings are punched with the aid of the tools<sup>1</sup> shown in Figs. 17-1 to 17-4. The cutting tools are made from Halcomb's Ketos<sup>2</sup> tool steel hardened to a Rockwell C of about 63 and supported in cold-rolled steel holders. In machining the vane punch shown in Figs. 17-1 and 17-2, the strap grooves are milled to size, but the outside surfaces of the tool are left 1 or 2 mils oversize to permit grinding to



FIG. 17-2.—Assembly of vane-punching tools.

<sup>1</sup> For detailed information see F. A. Stanley, *Punches and Dies*, McGraw-Hill, New York, 1943; C. W. Hinman, *Die Engineering Layouts and Formulas*, McGraw-Hill, New York, 1943.

<sup>2</sup> Obtainable from Halcomb Steel Division, Crucible Steel Co. of America, Syracuse, N.Y.

size after the hardening heat treatment. By so doing, some dimensional distortions can be eliminated which are unavoidably introduced during the hardening process. The vane die is milled in two halves; and after hardening, the halves are mounted together in the cold-rolled steel support to form the completed die. To prevent severe rounding of the

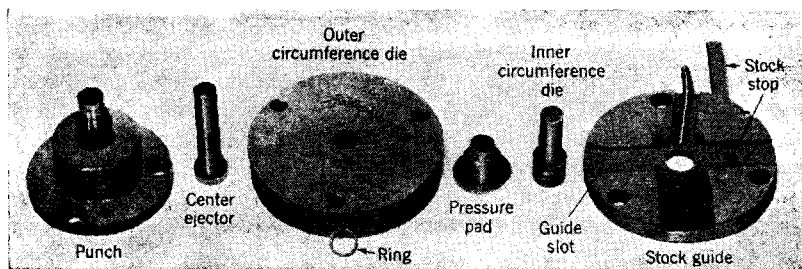


FIG. 17-3.—Ring-punching tools.

corners of the punched parts, it may be necessary to use a pressure pad. This is a tool similar to the punch mounted on rubber or springs beneath the die, so that the copper is always pushed against some backing. In the case of the die in Figs. 17-1 and 17-2 the depth of the die tool is great enough to store several vanes which act as a pressure pad. For larger vanes a pressure pad would probably be necessary. The tools for punching the rings are shown in Figs. 17-3 and 17-4. A pressure pad is necessary in this case. The small pipe on the stock guide is for admitting compressed air to eject the finished rings.

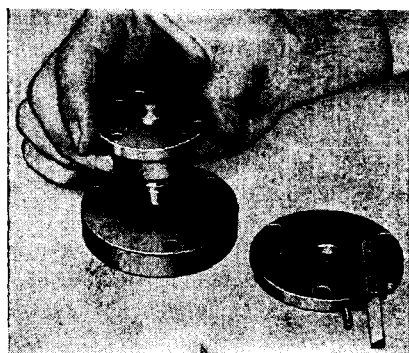


FIG. 17-4.—Assembly of ring-punching tools.

A copper shell (Fig. 17-5) is needed to form the complete anode block; the one shown was turned from round copper stock. The part of the shell that is to be joined to the vanes is reamed to within 0.0005 in. of the specified dimension. All block parts are deburred to obtain proper fitting in the jig, and this can be done by using a scraping tool on individual pieces; or if one has a very large number of parts, they can be successfully deburred by rolling them in a bottle on a ball mill.

The jig for assembling these component parts is made from low-sulfur content stainless steel designated by Industrial No. 18-8 and Type No. 302, 304, or 308, which, when oxidized, will not be wet by the brazing

material. Because the jig must hold in intimate contact the component parts to be soldered, they must be machined to a high degree of accuracy. For a block the size of the 2J42, the tolerance situation is eased somewhat by the fact that the small copper parts can be squeezed into contact without a disturbing amount of distortion. A complication arises from the fact that stainless steel "grows" slightly upon initial heating. As a result, the practice has been to machine the parts to very close

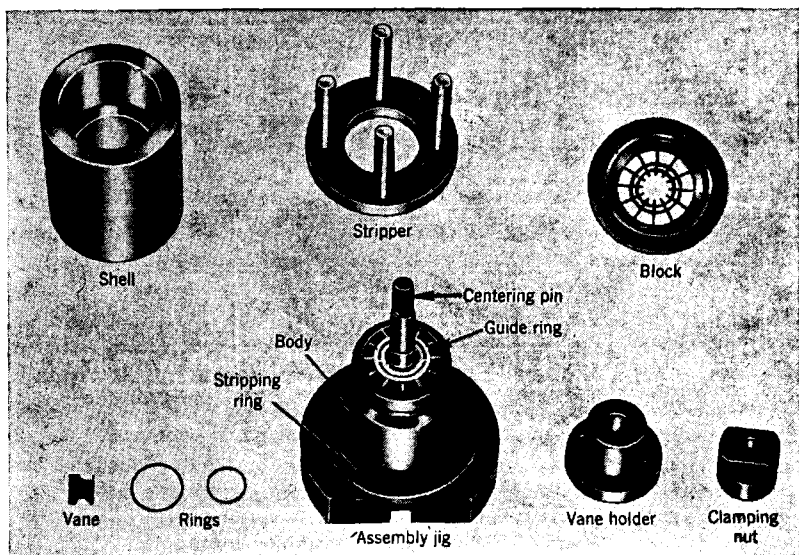


FIG. 17-5.—2J42 anode-block parts, assembly jig, and finished anode block.

tolerances and then make trial-and-error corrections in the jig by observing its brazing accuracy.

The anode block parts are assembled in the following manner:

1. The stripping ring is placed on the jig body.
2. The rings with "strap breaks" are placed in grooves in the jig body (not shown in Fig. 17-5). This lower set of rings has strap breaks that are brought to their proper places by pins in the strap grooves.
3. The center pin is placed in the jig body.
4. The vanes are assembled into the jig slots and into the lower rings.
5. The guide ring is slipped over the vanes to force them against the center pin.
6. The top rings are placed in the vane grooves.
7. The shell is pushed over the assembled vanes, forcing the guide ring down and out of the way.

8. The vane holder is dropped over the center pin.
9. The clamping nut is placed on the center pin and screwed into place, thus holding the assembled structure together ready for brazing (see Sec. 17-3).

After brazing the anode block is removed by

1. Removing the clamping nut and vane holder.
2. Forcing the block off the jig by putting a stripper through holes in the bottom of the jig body and pushing against the stripping ring.

It is necessary to keep the center pin smooth and free from the slightest burr so that the vanes are not distorted while being removed from the jig.

Some 2J42 blocks have been made with a modified jig that is simpler in some respects. The simplification is introduced by broaching slots (0.020 in. deep) into the anode shell; these slots are used to hold and position the vanes during brazing, thus removing the necessity for the accuracy in holding and positioning the vanes that must otherwise be built into the jig. This broaching operation saves considerable time when done with a tool that broaches all 12 slots simultaneously.

For 3-cm wavelength tubes in which the vanes are about 0.020 in. thick, punching is quite satisfactory. For greater thickness, as for 10-cm wavelength tubes, punching may not be practical, but one can mill the vanes from stock material. The HP10V magnetron (see Chap. 19) is made by this method.

With OFHC copper, a ratio of vane thickness to length of 0.08 approximates a lower limit for jig-assembled tubes. With the mechanically stronger metal, Chase alloy No. 58, thinner vanes can be assembled, reaching a corresponding ratio of about 0.05. At room temperature the electrical conductivity of Chase alloy No. 58 is about half that of OFHC copper. At 200°C, however, the conductivities are equal; and hence if the vanes are at this temperature during operation, the unloaded  $Q$  will be unaffected by the use of this alloy.

In the cases where it is necessary to taper the ends of the vanes, as in the BM50 and 2J41 (see Chap. 19), the jig assembly method has a distinct advantage over other methods of construction.

*Hobbing.*—Hobbing is the process of driving a hardened tool (the hob) into a block of metal to produce a desired configuration. In magnetron construction the hob can be so formed that upon the removal of the tool one has a completed copper anode block, except for facing off the ends and for the straps, if they are included in the design. The hobbing method is particularly useful in the construction of small anode blocks and especially advantageous in designs without strapping, like

rising-sun blocks. Hobbing is also adaptable to making other tube parts that have inside shapes which cannot be readily machined, such as the tapered sections of waveguide outputs.

Figure 17-6 shows a typical set of hobbing tools. The hob, bottom plate, driver, shell, and removal tool are all made of tool steel hardened to a Rockwell C of 58 to 60. Among the Carpenter matched tool steels,<sup>1</sup> Hampden oil-hardened steel has proved satisfactory. The shell shown in Fig. 17-6 is 8-in. OD. It is made in two parts in order to ease the hardening problem associated with pieces of such large volume and to

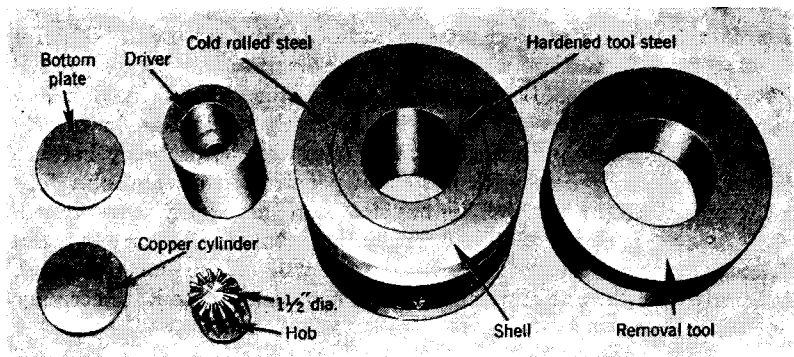


FIG. 17-6.—Hobbing tools.

give radial strength to the tool. For smaller tools the outer cold-rolled steel shell is not necessary.

The hobbing process is performed in the following manner:

1. The bottom plate is placed in the shell.
2. A copper cylinder is placed in the shell and rests on the bottom plate.
3. The hob is placed in the driver.
4. The combined hob and driver are inverted from the position shown in Fig. 17-6 and are placed in the shell, the hob resting on the copper cylinder.
5. The parts thus assembled are placed in a press between hardened steel plates, and the hob driven into the copper cylinder.

A press made by the Watson-Stillman Company of Roselle, N.J., can deliver a force up to 100 tons and has been satisfactory for this job. The best speed for hobbing has not been studied thoroughly. At the Columbia University Radiation Laboratory, the practice has been to hob by a slow, even succession of thrusts. It is a common practice to use castor oil as a lubricant to help reduce the forces required. Aquadag

<sup>1</sup> Frank R. Palmer, *Tool Steel Simplified*, Carpenter Steel Co., Reading, Pa. 1937; *Carpenter Matched Tool Steel Manual*, Carpenter Steel Co., Reading, Pa., 1944.

would probably be effective, but it has been found difficult to cover all portions of an anode-block hob with it. The hobbing force on large blocks can be reduced considerably by boring a hole through the center of the steel bottom plate, thus providing space for the displaced copper. The hole should be about 0.010 in. smaller in diameter than the anode-block diameter to prevent the thin copper vanes from dragging down. Chromium plating the hobs will further reduce the force necessary for driving the tool into the copper, but this technique is not applicable to anode-block hobs, as it is difficult to get the plate to cover the intricately shaped tool evenly. Waveguide hobs, however, are usually chromium plated. Considerable saving in hobbing force can be had if the copper slug is held at an elevated temperature; this process, called "hot hobbing," keeps the copper annealed throughout the hobbing operation. There does not seem to be much advantage in merely annealing the copper previous to the hobbing thrust, probably because the copper work hardens with but small penetration of the hob. The best temperature for hot hobbing has not been thoroughly investigated, but it probably is close to 550°C. This temperature is a balance between softening of the cylinder copper and softening of the hob-tool steel. At these temperatures Hampden steel will not stand up, so it is necessary

TABLE 17-2.—ANODE-BLOCK HOBGING DATA

No. of vanes	Anode diameter, in.	$d_s$ ,* in.	$d_e$ ,* in.	Thickness of Cu fin, in.	Depth of hobbing, in.	Total force required, lb
18	0.413	0.752	0.984	0.0430	0.800	$120 \times 10^4$
18	0.170	0.312	0.502	0.0170	0.530	37
18	0.162	0.291	0.410	0.0150	0.375	39
18	0.148	0.286	.....	0.0100	0.250	20
18	0.093	0.168	0.227	0.0100	0.187	8
26	0.210	0.327	0.478	0.0135	0.375	30
26	0.158	0.256	0.396	0.0100	0.275	27
26	0.137	0.220	0.340	0.0090	0.275	27
26	0.138	0.274	.....	0.0080	.....	3
38	0.337	0.490	0.645	0.0170	0.625	35
38	0.339	0.479	0.726	0.0140	0.450	15
38	0.097	0.122	0.170	0.0040	0.125	4
38	0.093	0.133	0.145	0.0040	0.125	2
50	0.140	0.162	0.222	0.0040	0.125	4

\* See Chap. 19.

to use a steel like Carpenter's Star Zenith,<sup>1</sup> hardened to a Rockwell C of about 59. In making this change one must tolerate hardening distortion in the hob. For hot hobbing, the temperature of the hobbing assembly can be conveniently controlled by r-f induction heating. It has been found that finer structures can be formed successfully if hot hobbing is employed.

The many conflicting factors make it extremely difficult to calculate the force necessary for hobbing. For this reason Tables 17-2 and 17-3 are given<sup>2</sup> to convey an idea of the magnitude of the required forces. In Table 17-2, the 18-vane blocks, the first three 26-vane blocks, and the first 38-vane block were cold hobbled. All others were hot hobbled, and the decrease in total force required to hob these blocks is apparent.

TABLE 17-3.—WAVEGUIDE-OUTPUT HOBGING DATA

Width of waveguide, in.	Height of waveguide, in.	Depth of hobbing, in.	Total force required, lb
1.125	0.500	1	$155 \times 10^3$
0.900	0.400	$2\frac{1}{4}$	100
0.420	0.170	$1\frac{1}{8}$	24
0.112	0.050	$\frac{7}{16}$	4

The first and second 38-vane blocks indicate a lower limit on cold hobbing, because the second 38-vane block could not be successfully cold hobbled. The difference in hobbing force between the third and fourth 38-vane blocks is attributed to the quality of the surface on the hob. The fourth 38-vane block was made with a hob having a smoother surface, since this hob was made by grinding a hardened piece of steel rather than by milling and then hardening. (See later discussion on making the hob.)

After the hob has been driven into the copper cylinder, the copper is separated from the hobbing tools. To do this, the removal tool shown in Fig. 17-6 is placed under the shell. The press is used to drive the copper and hob through the shell until it drops into the central space of the removal tool. If a hole has been made in the bottom plate to reduce the required hobbing force, it will be necessary to drill out the copper pushed into this hole in order to separate the bottom plate from the copper slug. The combined copper and hob are now free from the hobbing tools and ready for separation.

The copper and hob are separated by the use of the stripping tools shown in Fig. 17-7, arranged as in Fig. 17-8. By placing this arrangement in the press and pushing on the cylinder *D*, the hob is pulled out of the copper by a force that is always parallel to the force originally

<sup>1</sup> *Ibid.*<sup>2</sup> Data from S. Sonkin, Columbia University Radiation Laboratory, New York.

used to drive the hob. In stripping, the most important precaution is to use care in making the initial contact of the press-driving piston with the stripping cylinder *D*, as too sudden contact may break the hob off in the copper.

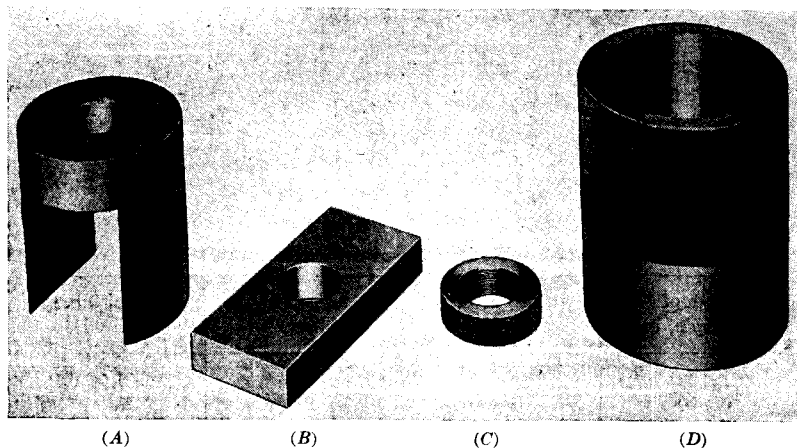


FIG. 17-7.—Stripping tools.

After the copper slug has been stripped from the hob, it is slipped on a mandrel which makes a tight fit in the block hole, and the lower end of the slug is turned off to within a few mils of the farthest penetration

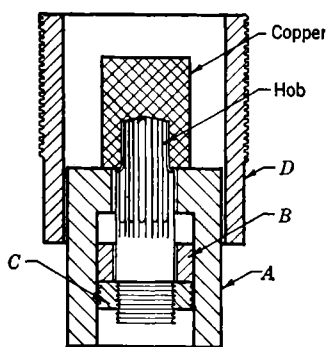


FIG. 17-8.—Assembly of stripping tools.

of the hob, and the anode-block OD turned to size. The block is then removed from the mandrel and placed in a wheel chuck, and the remainder of the cutting is done to arrive at the desired block height. During these machining operations, if the vanes are too thin to support the slug on the mandrel or to resist bending during cutting, a filler must be used that can be leached out after the machining is finished. Lucite is satisfactory for this purpose. It can be put in the copper slug in powdered form and solidified under slight pressure at 150°C.

It can then be leached out with chloroform and leaves no harmful residue.

The hob itself is the most critical of the hobbing tools, and additional information on its construction will be helpful. Figure 17-9 shows the stages of construction of a milled hob used in making 3J31 anode blocks.



Part *A* is turned from Halcomb's Ketos steel. The end of the cylinder to be slotted is left a few mils oversize, so that it can be ground to size after hardening to remove some of the distortion introduced by the hardening process. The threaded portion is for use in the stripping process. The threaded end must be faced off perpendicular to the cylinder axis because the hob is driven by pushing against this surface. Part *B* shows the hob after milling and hardening. "Climb milling"

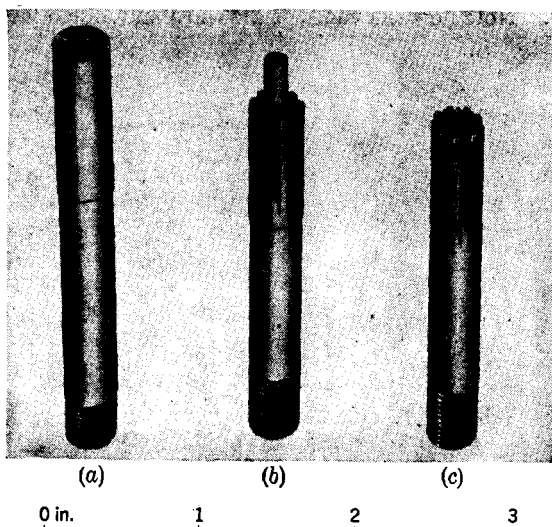


Fig. 17-9.—Stages in the construction of an anode-block hob. (Courtesy of Columbia University Radiation Laboratory.)

in which the cutting part of the milling saw moves in the same direction as the table is used. Table 17-4<sup>1</sup> is given as a guide to the proper cutting speed.

TABLE 17-4.—MILLING SPEEDS

Slot width, in.	Cutter diameter, in.	Cutter speed, rpm	Feed speed, in./min
0.004-0.006	1.75	250	0.020
0.013-0.016	1.75	220	0.070
0.035-0.040	3.00	175	0.060

For the small slot widths, it has often been necessary to improve the concentricity of milling saws over the accuracy supplied by the manufacturer by regrinding and resharpener the saws. After these milling operations are performed, the hob is hardened to a Rockwell C

<sup>1</sup> Data from S. Sonkin.

of about 58. After the hob is hardened, the centering pin is ground off and the hob OD is ground to the proper size. Other surfaces of the hob may be polished to help reduce the required hobbing force. For tube vanes under 0.012 in. thick, polished surfaces are particularly important to avoid dragging down the copper vanes during hobbing. The finished hob is labeled C.

A set of anode-block hobs and some corresponding blocks are shown in Fig. 17-10. Note how the vanes of the third and fourth largest blocks

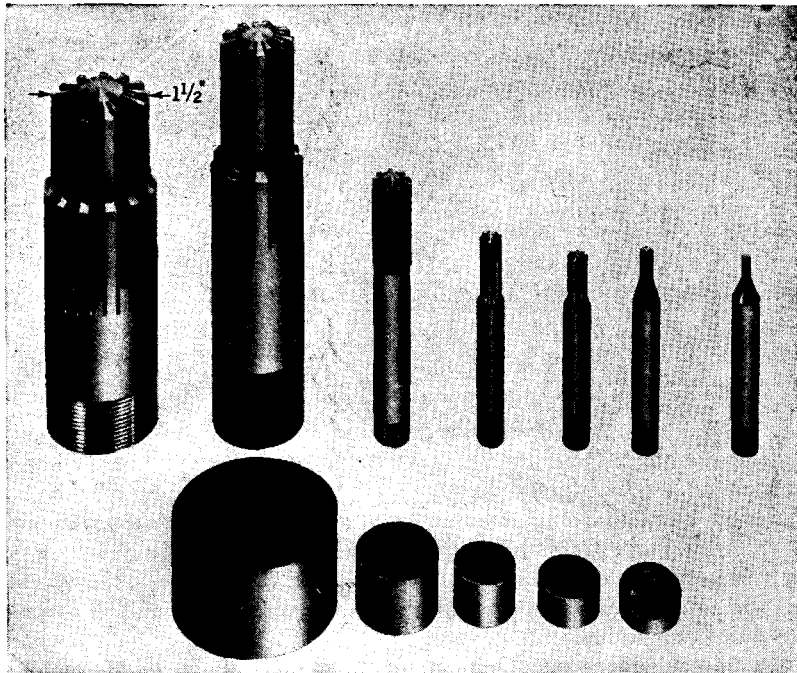


Fig. 17-10.—Set of anode-block hobs and anode blocks. (Courtesy of Columbia University Radiation Laboratory.)

have dragged down as compared with the largest block. The dragging in these blocks is a result of annealing the copper before hobbing (as previously stated, the advantage of annealing before hobbing is questionable). No dragging is evident in the second largest block, because it has been faced off after hobbing.

Figure 17-11 is given to show hobs used for making waveguide outputs for 3- and 1.25-cm wavelength bands. The chamfers improve the breakdown strength of the outputs. The rectangular block on the 3-cm-wavelength chamfer cutter guides the cutter with respect to the rectangular cavity. The relative advantages of blunt hobs as compared

with tapered hobs is not definitely known, but larger hobs are usually tapered to reduce the hobbing force. Waveguide hobs differ from anode-block hobs in that they are hardened to a Rockwell C of about 65 and are usually chromium plated.

Instead of milling the hobs it is possible to grind a hardened cylinder to the desired size and shape. The advantages of ground hobs are no trouble from distortion introduced by hardening; a more uniformly

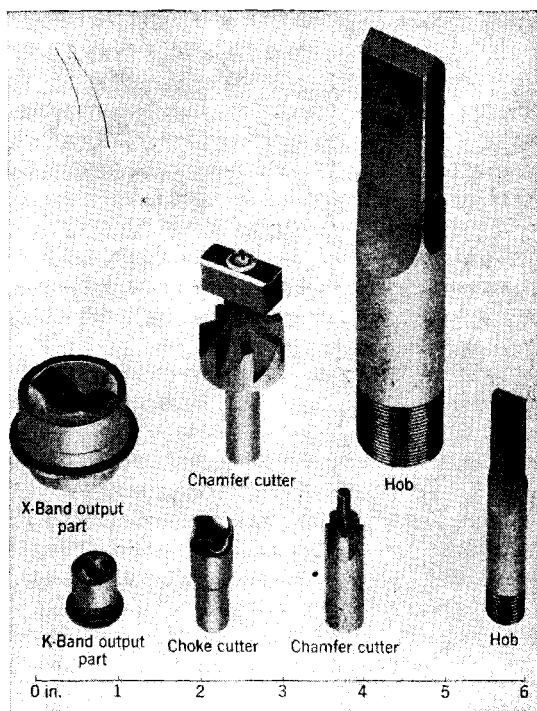


FIG. 17-11.—Waveguide-output parts and associated tools. (Courtesy of Columbia University Radiation Laboratory.)

hardened tool, because a solid cylinder is hardened rather than an intricately shaped tool like an anode block; and smoother surfaces and therefore less hobbing force. (Note the third and fourth 38-vane blocks listed in Table 17-2; the fourth was hobbled with a ground tool.)

**Vacuum Casting.**—Vacuum casting is performed by melting copper in a vacuum chamber and allowing it to flow into a carbon mold that forms the anode block.

Vacuum casting is adaptable to the larger tubes, such as the HP10V (see Chap. 19), but has no great advantage over the jig-assembly method

unless it is desired to have some irregular external shell shape that cannot be conveniently machined. The fact that some precision parts of the carbon mold for vacuum casting must be duplicated for each block represents a disadvantage compared with jig-assembly or lamination methods.

*Sintering.*—Sintering employs the technique<sup>1</sup> of pressing finely powdered metal into the desired shape and then heating this compress at a temperature great enough to cause bonding of the powder.

Sintered copper blocks are useful for small tubes that are difficult to machine, but the method has not been fully tested. For blocks of nonmachinable metals, such as tantalum or tungsten, the method holds promise. Sintering has been employed successfully in making other irregularly shaped objects, such as waveguide-output parts.

*Combination of Methods.*—The different methods of fabrication listed in Table 17-1 have been applied to cases that essentially exemplify one method. The fabrication of some anode blocks, however, might best be done by a combination of these methods. For example, the combination of sintering and jig assembly seems to be the most promising for making blocks out of nonmachinable metals, such as tungsten (the advantage of a tungsten block is that it would be less frequency-sensitive to temperature). The vanes, shell, and straps might be sintered from powdered tungsten, and then these component parts brazed together by the jig-assembly method.

**17-2. Brazing and Soldering.**—Brazing was one of several new metal-working techniques developed to meet requirements associated with magnetron construction. In large measure these techniques are distinctly different from those emphasized in standard references.<sup>2</sup> This aspect of brazing may be classified as high-vacuum precision brazing. The first differentiation from usual brazing is the shift in emphasis from sheer strength to vacuum perfection. A good vacuum requires a solder of low vapor pressure that will alloy with the base metal to give a reliable seal. In the case of purely mechanical joints, the low vapor pressure requirement usually still exists, because most joints are exposed to the tube interior; and although it is best to have alloying between the solder and base metal, sufficient mechanical strength can often be obtained without alloying. In order to accomplish a precision braze it is necessary to localize the flow of solder into well-defined boundaries. Electroplating fixed amounts of solder at the desired places provides a means of limiting the solder flow and gives fairly sharp boundaries. Another method is to use a solder "stop-off" over which the solder will not flow. Chromium

<sup>1</sup> John Wulff, ed., *Powder Metallurgy*, American Society for Metals, Cleveland, Ohio, 1942.

<sup>2</sup> *Welding Handbook*, American Welding Society, New York, 1942.

plate or carbon film serves as useful stop-offs. In either case, liquid or paste fluxes must be avoided in precision brazing, and this has, in general, required the use of hydrogen atmospheres for brazing.

*Preparation of Surfaces for Brazing.*—Cleanliness is of great importance. Parts must be thoroughly cleaned of oxide scale or film, either mechanically or by chemical means as outlined in Sec. 17-4. Immediately preceding the brazing operation all surfaces should be chemically degreased.

The nature of one of the metal surfaces may be such as to inhibit good wetting action of the solder in spite of ideal cleanliness. This condition may be remedied by electroplating the surface with some metal that can be wetted by the solder. The deposited metal may serve other purposes, such as preventing or minimizing intergranular penetration of the solder into the base metal, and improving the fit between parts to be joined.

*Mechanical Preparation of Joints.*—For solder that is applied by electroplating there must be intimate contact between the parts. When solder wire or sheet is applied or placed within the joint, the fit is not so critical because the solder will provide filling for the gaps. If the part is set up to take advantage of gravity flow, the gap may be greater than if flow depends upon capillary action.

Parts brazed in a hydrogen atmosphere are usually supported by oxidized stainless-steel fixtures, and provision for the relative expansion of the assembled parts must be made in order to avoid slippage or warping of the parts.

*Selection of Solder.*—In choosing a particular solder or brazing alloy the following factors should be considered. The solder should have a melting point at least 100°C below that of the metals to be joined unless precise brazing-temperature control is maintained. In the case of those metals where excessive brittleness or phase changes occur at elevated temperatures it is necessary to reduce the soldering temperature further. Joints must not give way below 500°C if the tubes are to be subjected to "bake out" (see Sec. 17-7).

If a low-melting eutectic results through the combination of solder and base metal, care must be exercised by temperature control or control of the amount of solder to avoid undue corroding around the joint. The vapor pressure of a solder exposed to the interior of the tube should be less than  $10^{-6}$  mm Hg at 450°C and less than  $10^{-7}$  mm Hg at room temperature. For this reason, solders containing lead, cadmium, or zinc should be used with caution. Metals having a high vapor pressure can be tolerated in alloys only when their partial pressures are considerably reduced because of compound formation or interstitial adsorption. Excess amounts of low-conductivity solder must be avoided at points of high current density in the case of high- $Q$  oscillators. The choice of

TABLE 17-5.—SOLDERING AND BRAZING ALLOYS AND FLUXES

Melt point		Flow point		Name of solder	Composition	Flux	Comments
°C	°F	°C	°F				
60	140	65.5	150	Wood's metal	Bi 50 Cd 12.5 Pb 25 Sn 12.5	A	Weak, brittle
181	358	181.0	358	Eutectic soft solder	Pb 36 Sn 64	A	.....
188	370	225.0	437	50-50 soft solder	Pb 50 Sn 50	A	Works easily, weak
200	390	260.0	500	20-80 soft solder	Pb 80 Sn 20	A, B	Weak
232	450	231.9	450	Tin	Sn 100	A, B	Shrinks
288	550	.....	....	Alumaweld	Sn 40 Pb 39.9 Zn 20.1	C, F	For castings and all metals except tantalum
304	579	304.0	579	.....	Ag 5-6 Pb 95-94	A, B	.....
304	579	380.0	715	.....	Ag 2.5 Pb 97.5	A, B	.....
327	621	327.0	621	Lead	Pb 100	B	.....
338	640	393.0	740	"TEC" Handy and Harmon	Ag 5 Cd 95	A	Note high cadmium content
400	752	.....	....	Intermediate solder	Ag 20 Cu 3 Zn 2 Sn 75	A	From J. Strong, <i>Procedures in Experimental Physics</i> , Prentice-Hall, New York, 1942
600	1110	630.0	1162	Low-melting hard solder	Ag 45 Cu 35 Sn 25	H <sub>2</sub>	From F. C. Hull, Westinghouse Res. Lab. Very hard, brittle, low vapor pres.
627	1160	635.0	1175	"Easy Flo" Handy and Harmon	Ag 50 Cu 15.5 Zn 16.5 Cd 18	D	For ferrous and nonferrous use, yellow color, mechanically strong
641	1185	704.0	1300	"Sil Fos" Handy and Harmon	Ag 15 Cu 80 P 5	None	For nonferrous work, self-fluxing, yellow color, mechanically strong
646	1195	688.0	1270	"Easy Flo" No. 3 Handy and Harmon	Ag 50 Cu 15.5 Zn 15.5 Cd 16 Ni 3	D	For ferrous and nonferrous use where fillets are required, yellow, strong

670	1238	700.0	1290	Low-melting hard	Ag 53 Cu 32 Sn 15	H <sub>2</sub>	From F. C. Hull, Westinghouse Res. Lab. Very hard, brittle, low vapor pressure
671	1240	779.0	1435	"SS" Handy and Harmon	Ag 40 Cu 30 Zn 28 Ni 2	D	Pale yellow color
677	1250	727.0	1340	"ET" Handy and Harmon	Ag 50 Cu 28 Zn 22	D	Yellow-white color
677	1250	743.0	137	"DE" Handy and Harmon	Ag 45 Cu 30 Zn 25	D	Yellow-white color, ASTM Spec. B-73-29 No. 4
682	1260	718.0	1325	"RT" Handy and Harmon	Ag 60 Cu 25 Zn 15	D, H <sub>2</sub>	Silver-white color
693	1280	718.0	1325	"Easy" Handy and Harmon	Ag 65 Cu 20 Zn 15	D	ASTM Spec. B-73-29 No. 6 silver-white color. For sterling silver
693	1280	774.0	1425	"ETX" Handy and Harmon	Ag 50 Cu 34 Zn 16	D	Yellow-white color. ASTM Spec. B-73-29 No. 5
704	1300	729.0	1345	"TR No. 1" Handy and Harmon	Ag 75 Zn 25	D	.....
707	1304	750.0	1382	Phos-copper Westinghouse	Cu 93 P 7	None	For nonferrous work, self-fluxing
720	1328	740.0	1360	Low-melting hard solder	Ag 59 Cu 31 Sn 10	H <sub>2</sub>	From F. C. Hull, Westinghouse Res. Lab. Very hard (but can be swaged) low vapor pressure
721	1330	779.0	1345	"DT" Handy and Harmon	Ag 40 Cu 30 Zn 28 Ni	D	Pale yellow color
724	1335	754.0	1390	"Medium" Handy and Harmon	Ag 70 Cu 20 Zn 10	D	ASTM Spec. B-73-29 No. 7 for sterling silver. Silver-white color
732	1350	774.0	1425	Hard No. 1 Handy and Harmon	Ag 75 Cu 20 Zn 5	D	.....
738	1360	793.0	1460	"IT" Handy and Harmon	Ag 80 Cu 16 Zn 4	D	White color. ASTM Spec. B-73-29 No. 8
741	1365	788.0	1450	"Hard" Handy and Harmon	Ag 75 Cu 22 Zn 3	D	Silver-white color. For sterling silver
743	1370	766.0	1410	"NT" Handy and Harmon	Ag 30 Cu 38 Zn 32	D	Pale yellow color

TABLE 17-5.—SOLDERING AND BRAZING ALLOYS AND FLUXES.—(Continued)

Melt point		Flow point		Name of solder	Composition	Flux	Comments
°C	°F	°C	°F				
752	1385	785.0	1445	"RE-MN" Handy and Harmon	Ag 65 Cu 28 Mn 5 Ni 2	D	.....
777	1430	816.0	1500	"AT" Handy and Harmon	Ag 20 Cu 45 Zn 35 Cd 0.5 Max.	D	Brass-yellow color. ASTM Spec. B-73-29 No. 2
777	1430	816.0	1500	"ATT" Handy and Harmon	Ag 20 Cu 45 Zn 30 Cd 5	D	Brass-yellow color. ASTM Spec. B-73-29 No. 3
779	1435	779.0	1435	"BT" Handy and Harmon	Ag 72 Cu 28	D, H <sub>2</sub>	Silver-copper eutectic. White color. Excellent for copper
816	1500	857.0	1575	"NE" Handy and Harmon	Ag 25 Cu 52.5 Zn 22.5	D	.....
821	1510	871.0	1600	"TL" Handy and Harmon	Ag 10 Cu 52 Zn 38 Cd 0.5 Max.	D	Brass-yellow color. ASTM Spec. B-73-29 No. 1
857	1575	871.0	1600	"TE" Handy and Harmon	Ag 5 Cu 58 Zn 37	D	.....
875	1607	.....	.....	Brazing compound	Cu 54 Zn 46	E	From J. Strong, <i>Procedures in Experimental Physics</i> , Prentice-Hall, New York, 1942
890	1634	890.0	1634	.....	Au 80 Cu 20	E, H <sub>2</sub>	Lowest-melting gold-copper alloy
950	1742	950.0	1742	.....	Au 82.5 Ni 17.5	E, H <sub>2</sub>	Lowest-melting gold-nickel alloy
950	1742	980.0	1796	.....	Au 94 Cu 6	E, H <sub>2</sub>	.....
960	1760	960.0	1760	Silver	Ag 100	E, H <sub>2</sub>	.....
1063	1945	1063.0	1945	Gold	Au 100	E, H <sub>2</sub>	.....
1082	1980	1082.0	1980	Copper (OFHC)	Cu 100	H <sub>2</sub>	.....
1160	2120	.....	.....	Platinum solder	Ag 73 Pt 27	H <sub>2</sub>	Wets tungsten
1205	2201	.....	.....	Nickel coinage (prewar U.S.A.)	Cu 75 Ni 25	H <sub>2</sub>	Wets tungsten
1450	2642	1450.0	2642	Nickel	Ni + Co 99-99.5, traces C, Mn, Si	H	Wets tungsten and moly



**Flux A**—(a) Liquid: 40 Zn Cl<sub>2</sub>, 20 NH<sub>4</sub> Cl, 40 H<sub>2</sub>O  
(b) Paste: 90 Petrolatum, NH<sub>4</sub> Cl

(c) Solution of resin in alcohol

B—Lloyd's No. 6

C—Lloyd's alumaweld all metal flux (thin paste)

#### Suppliers\*

"Lloyd's, Lloyd S. Johnson Co., 2241 Indiana Ave., Chicago, Ill.

"Handy," Handy and Harmon Co., 82 Fulton St., New York, N. Y.

Lead and tin, Kester Solder Co., 4201 Wrightwood Ave., Chicago, Ill.

Lead and silver, Belmont Smelting and Refining Works, Inc., 330 Belmont Ave., Brooklyn, N. Y.

Phos-copper, Westinghouse Electric Corp., East Pittsburgh, Pa.

\* For purposes of brevity, only one supplier is listed.

D—Handy Flux, Lloyd's No. 7

E—(a) Thin paste (10 parts powdered borax, 1 part boric acid)

(b) Borax applied dry

F—Lloyd's stainless steel liquid flux

H<sub>2</sub>—Hydrogen

solder may be limited by the presence of previous joints, glass seals, or the cathode. By the use of heat shields in certain brazing methods, the solder need not necessarily be restricted to having a flow point less than the melting point of glass or the melting point of some other joint. If the brazing is done in a hydrogen atmosphere in the presence of glass, the glass itself may be damaged by the hydrogen, or the metal oxides involved in the glass-to-metal seals may be reduced and the seal rendered porous. The use of forming gas (80 per cent H<sub>2</sub> and 20 per cent N) instead of hydrogen reduces troubles of this nature, but greater care must then be exercised to remove oxide films chemically from the surfaces to be joined.

The properties of available solders and fluxes are summarized in Table 17-5.<sup>1</sup> It is noted that in the flow-point range of 630° to 1082°C there are 35 solders while in the range of 400° to 629°C there are none. Because tubes are generally baked at 450°C during processing, a solder that flows below this temperature is of little use in magnetron construction. However, the lack of a satisfactory solder in the flow range of 450° to 550°C eliminates the possibility of brazing in a uniform temperature furnace in the presence of glassware.

*Methods of Heating Parts to Be Brazed.*—The methods<sup>2</sup> of heating parts to be brazed are listed in Table 17-6.

Gas-torch heating has the disadvantage of being limited to open-air brazing and therefore requires some chemical flux. This

<sup>1</sup> Original compilation by R. O. McIntosh, Westinghouse Research Laboratories, East Pittsburgh, Pa.

<sup>2</sup> For general information on brazing methods, see *Welding Handbook*, American Welding Society, New York, 1942; J. Strong, *Procedures in Experimental Physics*, Prentice-Hall, New York, 1941.

TABLE 17-6.—METHODS OF HEATING FOR BRAZING  
Heating Method                      Atmosphere\*

Gas torch.....	Air
Electrical resistance heating...	Air, hydrogen bottle
R-f induction.....	Air, hydrogen bottle; vacuum bottle
Radiating filaments.....	Air, hydrogen bottle, hydrogen furnace

\* It is possible to substitute an inert gas atmosphere for hydrogen, but hydrogen is usually used in precision brazing.

objection is not serious with tube parts, i.e., input and output parts, that can be chemically cleaned before being assembled into the tube. However, if the method has been used extensively in the case of final brazing in the presence of glass, flux may creep into the tube and where it cannot be removed. Close-fitting parts tend to minimize this trouble. In torch heating, better temperature control can be had if the flames are not played directly on the tube but are played on copper blocks which serve both for support and for heat conduction. In order to avoid brazing the copper blocks to the tube, they are separated by thin disks of oxidized stainless steel. When using this method it is important to prevent oxidation of the tube interior. This is commonly done by passing CO<sub>2</sub> containing alcohol vapor through the tube during the brazing process. The mixture prevents oxidation by replacing the oxygen of the air, and in addition, the alcohol cleans away by chemical action with copper oxide any oxide films that may have been formed. If CO<sub>2</sub> contains an excessive amount of water vapor and oxygen, it is necessary to pass the CO<sub>2</sub> through a desiccator and through hot copper wool.

Electrical-resistance heating may be used in place of the gas torch with the advantage of improved temperature control. In addition this makes it possible to perform the operation in an inert or reducing atmosphere. The tube may be mounted between carbon blocks supported by heavy copper leads and connected to the secondary winding of a welding transformer (capable of 5- to 10-kw output at approximately 6 volts). Good electrical connections must be made throughout the secondary circuit so that essentially all of the power is dissipated in the carbon supports. In order to get uniform heating in the supports it is necessary to have the carbon under uniform pressure. By Variac control the temperature of the supports and therefore the tube can be closely controlled; and furthermore, the heating time can be much less than in the torch-brazing method.

For speed and temperature control, the r-f heating method<sup>1</sup> is superior to both torch and electric-resistance heating. The method is adaptable to open air, gaseous atmospheres, or vacuum. For heating over a small area it is often desirable to have only a single loop in the working coil,

<sup>1</sup>G. H. Brown, C. N. Hoyler, and R. A. Bierwirth, *Theory and Application of Radio-Frequency Heating*, Van Nostrand, New York, 1947.

in which case an appropriate matching transformer may be required between the output circuit of the r-f generator and the single loop. Because of the heat localization that is possible with a single-coil bombarder, brazing can be done in a hydrogen bottle in the presence of glass and without special protection for glass even though it is close to the joint.

For work demanding uniform temperature over a volume of as much as 300 cu in., a hydrogen-atmosphere furnace heated by radiating filaments is convenient. These furnaces are readily available on the market and are extremely useful in vacuum-tube construction because they provide a clean uniform-temperature chamber for metal cleaning and annealing as well as brazing.

For work that does not demand a uniform temperature chamber and especially for laboratory work, the "hydrogen bottle" is very useful. A typical bottle arrangement is shown in Fig. 17-12. Its advantages are simplicity, flexibility, and convenience in watching the brazing process. Induction and electric-resistance heating can be adapted to the hydrogen bottle, instead of heating by tungsten or molybdenum filaments; the advantage of the substitution depends on the job at hand.

The sequence of steps in operating a bottle is as follows. Adjust the work on a platform using jigs and clamps to hold the parts in place during the heating and subsequent cooling.

Arrange the heating unit to supply heat to the desired parts, shielding other parts with nickel sheet. When radiating filaments are used, a shield should surround the assembly to prevent overheating the glass bottle.

After lowering the bottle over the work, turn on the hydrogen. Sufficient time should be allowed before turning on the heat to be sure that the bottle is full of hydrogen. During brazing, allow the hydrogen to continue to flow at a safe rate to keep the bottle full, and collect the overflow by a ventilating hood. Hydrogen flowing out the bottom of the bottle can be observed as a cooling sensation on the hand. If the bottle is well filled and air pockets are avoided, an explosion can be caused only by circulating drafts at the bottom of the bottle; therefore, all air currents in the vicinity of the bottle should be avoided. In any

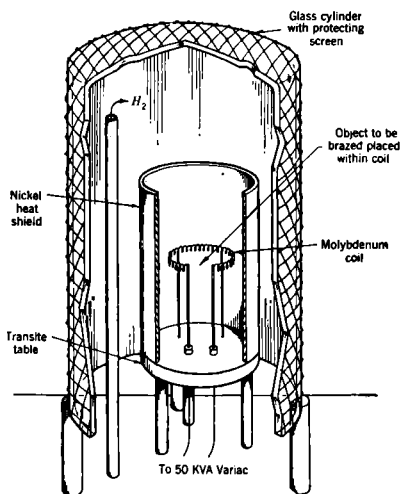


FIG. 17-12.—Hydrogen-bottle arrangement.

event, an explosion caused by drafts is usually mild because the bottom of the bottle is open and the bottle is free to rise.

Turn on the heat source (at least 5 kw of power are necessary), and watch the operation through the glass. After the solder has flowed, a little time should be allowed for adequate penetration of the melt.

The work should be allowed to cool in the hydrogen atmosphere until its temperature is 350°C or below.

**17-3. Selected Brazing Problems.**—The best method for making a particular braze will depend largely on the specific object, the conditions to which it must be subjected later, and the experimenter's available brazing equipment. For these reasons no more general brazing informa-

tion will be given. Solutions to some specific brazing problems may be helpful to the experimenter, however, as typical procedure that can be modified for the individual cases.

*Precision Brazing of Jig-assembled Anode Blocks.*—The method for making component anode-block parts and jig assembling these parts has been discussed in detail for the 2J42 block in Sec. 17-1. It now remains to braze these parts in a precise manner. In order to accomplish a precision braze it is necessary to have a uniform distribution and a controlled amount of soldering material at the points to be joined. In tubes as small as the 2J42, electroplating has been employed successfully for this purpose. Figure 17-5 shows the component parts of the block ready for the brazing of the strapping rings to the vanes and the vanes



FIG. 17-13.—HP10V anode block ready for brazing.

to the block shell. To assure good solder flow and to obtain clean copper surfaces, all parts must be degreased (see Sec. 17-4) before being assembled. The strapping rings and block shell are silver plated (see Sec. 17-4) to a thickness of 0.0004 in. The parts are then assembled as described in Sec. 17-1, and the assembly heated in a hydrogen-atmosphere furnace for 5 min at 850°C. The plated silver melts at this temperature, although the melting point of solid silver is 960°C. The melting begins near the copper-silver eutectic point (779°C), probably because a eutectic

solution of the silver in the copper results. However, since the brazing process is performed at  $850^{\circ}\text{C}$ , the resulting silver-copper alloy will have a melting temperature of  $850^{\circ}\text{C}$ . One can then safely use eutectic solder in subsequent brazing operations.

The success of applying solder to small tubes by plating is partly due to the fact that the component parts can be squeezed into intimate contact by the jig without undue distortion. In larger tubes this may be impossible, and a better method may be to place pieces of Ag-Cu eutectic solder at the points to be joined so that the solder, when melted, flows over the joint, filling places that are not mechanically touching. Such an arrangement is shown in Fig. 17-13 where the anode block is

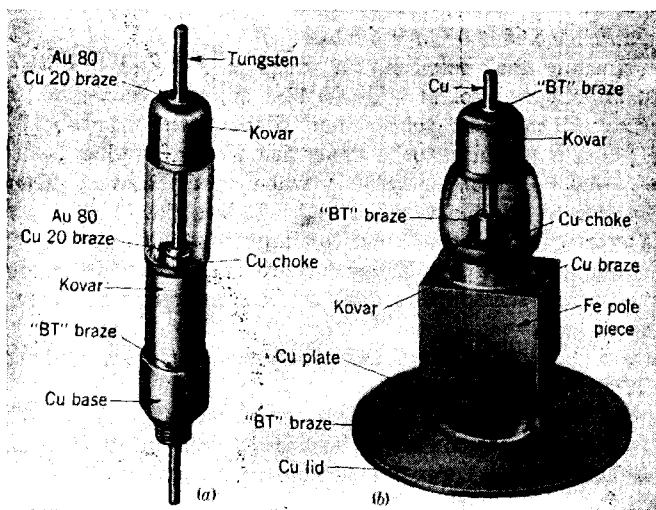


FIG. 17-14.—Voltage connectors. (a) Cathode support; (b) electron-beam collector.

large enough so that manually placing the solder strips is not difficult and the percentage change in dimensions by the melted solder is small.

*Construction of Cathode Supports.*—Figure 17-14 shows two types of stems or pipes whose fabrication presents typical magnetron brazing problems. In the construction shown in Fig. 17-14a a number of brazes are made.

The copper base is joined to the Kovar sleeve with "BT" solder (Ag72-Cu28). The two parts are held perpendicular with an oxidized stainless-steel jig, and one loop of "BT" wire is placed on the Cu base shoulder. The assembly is placed in the hydrogen furnace at  $830^{\circ}\text{C}$  for 5 min and then in the hydrogen cooling chamber for 30 min. For this braze involving Kovar and a silver alloy the Kovar must be annealed in a hydrogen atmosphere at  $900^{\circ}\text{C}$  for 30 min (or at temperatures up to

1100°C for shorter time intervals) before brazing in order to minimize intergranular penetration of the silver alloy into the Kovar. If this is not done, the intergranular penetration may cause Kovar cracks which result in vacuum leaks. Care should be taken in the arrangement of parts so that the Kovar is not subjected to tensional stress during heating, as this may accelerate intergranular penetration. As further insurance, the Kovar may be copper-plated before brazing.

The joint between the copper r-f choke and the tungsten center conductor is for mechanical purposes only, and therefore one need not use an alloying solder if sufficient bonding strength can be had by mere flow of the solder over the tungsten. Gold-copper (80-20) solder is found to give a sufficiently good mechanical joint; the braze is made in a hydrogen furnace at 920°C for 5 min.

The vacuum seal between the tungsten rod and the Kovar cup requires an alloying solder. Table 17-5 suggests platinum solder as the lowest-melting-point solder that alloys with tungsten, but this melting point is too high to be used with Kovar. It has been found, however, that gold-copper (80-20) when used between Kovar and tungsten gives a reliable vacuum seal. It is believed that the nickel in the Kovar enters into the braze to alloy with the tungsten. Because both the copper choke and Kovar cup are brazed to the tungsten with the same solder, these operations can be done simultaneously in the hydrogen furnace.

The two parts of the pipe thus constructed are then glassed according to Sec. 17-5.

The pipe *b* in Fig. 17-14 demonstrates another typical set of brazing problems. The center conductor is made of copper, and the iron pole piece fit through the copper lid. The brazes are made in the order described.

Pure copper is used to braze the iron pole piece to the Kovar sleeve. This is a recommended braze for Kovar because there is no intergranular penetration and the Kovar is raised to a temperature that is sufficient to anneal it during the braze. This braze is made in a hydrogen furnace at 1100°C for 5 min.

For the formation of the vacuum seal between the copper lid and the iron pole piece the iron pole tip is copper plated (see Sec. 17-4) and the braze is made with "BT" solder in a hydrogen furnace at 840°C for 5 min.

The Kovar cup is brazed to the copper center conductor in the same way as the first braze of pipe *a*, and the bonding of the copper r-f choke to the copper center conductor is also a "BT" braze.

*Assembly of Tube Parts and the Final Vacuum Seal.*—The sealing together of the various pipes, covers, or other parts to form the completed

magnetron is the most difficult of the brazing operations. The cathode, the inside copper surfaces, and the glassware must be protected against damage, and the choice of the brazing alloy is limited by solders used in previous brazes and by the softening point of the glass parts.

If a low-vapor-pressure solder existed in the flow range of 450° to 500°C so that the brazing temperature would be low enough to do no damage to the glassware and high enough so that the braze would hold up under the 450°C tube bakeout (see Sec. 17-7), this final braze would

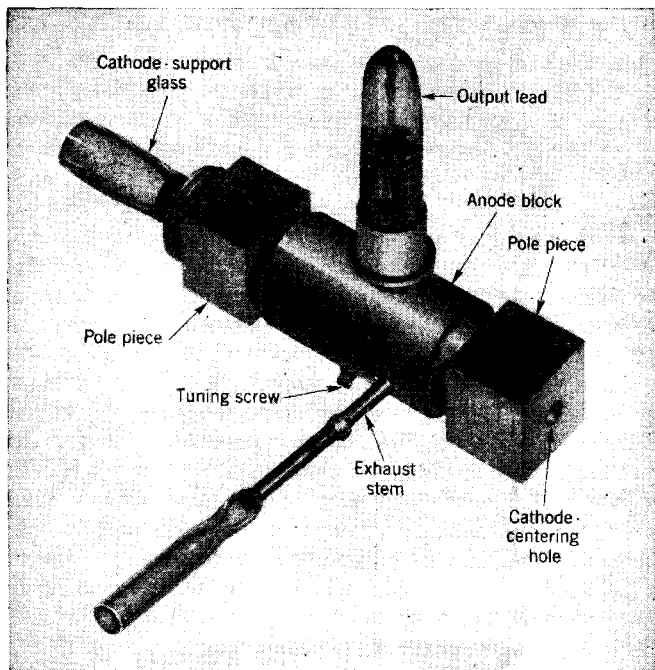


FIG. 17-15.—2J42 ready for cathode mounting.

be considerably simplified. In the absence of such a solder, the covers and pipes are in many cases brazed to the anode block in one brazing operation using either the gas-torch heating method or the electric-resistance method. This braze is in many cases done with Handy and Harmon "Easy Flo" in air, using a flow of alcohol-saturated CO<sub>2</sub> through the tube to protect the cathode and the inside copper surfaces. The objections to this braze are the following: "Easy Flo" solder contains zinc and cadmium, the vapor pressures of which are high enough at the brazing temperature to contaminate the cathode during the braze; the flux used during the braze may enter the tube and cause cathode

contamination; and the flux may cover places where the solder has flowed poorly and that become evident only after the brazing operation is completed and the flux removed.

Some of the above difficulties have been avoided in special cases by doing all brazing in a hydrogen atmosphere and making all joints except the final vacuum seal in the absence of the cathode. The 2J42 is assembled in this manner (see Fig. 17-15). The output lead is placed in the anode block and peened to give some mechanical support. One loop of 0.030-in. "RT" wire solder is placed around the base of the lead. The heating is done in a hydrogen bottle with a molybdenum heating coil placed near the lead base with the glass protected by an asbestos shield. The output lead is soldered into place before the pole pieces are soldered in order that the loop height may be adjusted after the output-soldering operation. The pole pieces, tuning screw, and exhaust stem are next assembled. Solder washers of 0.010-in. "RT" sheet are placed between the pole pieces and block. Four turns of 0.025-in. "RT" wire solder are placed around the tuning screw, and two turns of the same solder placed around the exhaust stem. The heating is again done in an  $H_2$  atmosphere, with molybdenum coils mounted on ceramic coils which fit around the pole pieces. The glass is again protected with asbestos shields, and the temperature is raised only slightly above the flow point in order not to disturb the output-lead braze. The assembly is now ready for mounting the cathode, which is centered through the hole in the pole piece opposite the cathode support. The final braze now consists only of soldering a plug into the cathode-centering hole. This is again done in the  $H_2$  bottle with an "RT" solder washer under the copper plug. The heating this time, however, is done by the electric-resistance method. A carbon rod is pushed against the copper plug, and the other electrical connection is made by a clamp around the same pole piece. Before making this braze, the inside of the tube is flushed free of trapped air. By this system of brazes the copper is never heated except in a hydrogen atmosphere, and the final braze in the presence of the cathode does not raise the temperature of the cathode above  $100^\circ C$ . The only disadvantage of this method is the use of the zinc-bearing solder "RT" which has a questionable vapor pressure.

**17-4. Chemical Processes.**—The importance of cleanliness in tube construction cannot be overemphasized. While it is often impossible to find the reason for the impaired quality of certain tubes, the average tube quality is certainly dependent upon the cleanliness that one exercises during construction. For this reason chemical cleaning is the most frequently used process in tube making. Practically every part that goes into a tube will experience three or four cleanings during the tube fabrication. Electroplating is employed to deposit solder for brazing, to



improve the surface conductivity of certain tube parts, and to provide a base for glass sealing.

The choice of a cleaning or plating process for specific uses is somewhat controversial largely because the technique is as important as the process. The following processes are given, therefore, merely to illustrate ones that have been successfully used in tube construction.

*Cleaning.*—Trichlorethylene is widely used as a general degreasing agent. It is nonflammable and an excellent grease solvent. The degreasing process consists of agitation in trichlorethylene followed by immersion in methyl alcohol and rapid drying in warm air.

Acetone is a milder degreasing agent and one that may be used if a solvent free of chlorine or sulfur is preferred. The acetone washing should also be followed by rinsing in clear methyl alcohol.

Great care should be exercised with cathode nickel to limit the possibilities of contamination. The following cleaning method has been used successfully. Agitate in acetone. Boil for 5 min in a solution composed of 40 g of  $\text{Na}_2\text{CO}_3$ , 13 g of  $\text{NaOH}$ , and 13 g of  $\text{NaCN}$  in 1 liter of distilled  $\text{H}_2\text{O}$ . Rinse thoroughly in boiling distilled water. Boil in second bath of distilled water for 5 min. Rinse in warm 5 per cent acetic acid solution. Agitate in boiling distilled water. Agitate in second bath of distilled water. Rinse in clean methyl alcohol and in warm-air blast.

A 50 per cent solution of inhibited hydrochloric acid at a temperature of about  $70^\circ\text{C}$  will remove the oxides formed on Kovar, copper, and iron parts. The inhibitor is  $\frac{1}{4}$  per cent by volume of Rodine No. 50,<sup>1</sup> used to decrease the attack on the base metal and to prevent immersion copper plating onto the Kovar in the case of copper and Kovar assemblies. The concentration of acid and the immersion time may be modified depending upon the degree of oxidation of the parts.

Heavy oxide coating (or tool marks) on tungsten and molybdenum can be removed by a-c electrolysis at about 7.5 volts in a 20 per cent potassium hydroxide solution using a carbon electrode. The solution may be used repeatedly.

Before being coated, tungsten and molybdenum heaters are boiled in a 20 per cent potassium hydroxide solution for about 5 min and then rinsed in distilled water. Large molybdenum heaters, in addition to the above treatment, should be immersed in warm concentrated sulfuric acid for several minutes.

Heavy oxide on nickel lead stems may be removed first by mechanical abrasion and then by electrolysis in a solution composed of 1 liter of distilled water, 667 cc of concentrated sulfuric acid, and 125 g of nickel sulfate. With the nickel part as anode, voltages of 6 to 12 volts are

<sup>1</sup> Obtainable from the American Chemical Paint Co., Ambler, Pa.

used, depending upon the density of oxide. Highly polished surfaces can be obtained on nickel if the current density is elevated sufficiently.

In addition to the dichromate cleaning solution suggested in the *Handbook of Chemistry and Physics*,<sup>1</sup> the following method of cleaning glass for high-vacuum use is recommended.<sup>2</sup> Prior to storage, degrease in acetone, clean in hot 10 per cent sodium carbonate solution, rinse in hot distilled water, drain dry, and store in cellophane containers. Just prior to use, rinse thoroughly in hot distilled water, wash in 5 per cent acetic acid solution, rinse in warm distilled water, rinse in clean methyl alcohol, and drain dry.

**Plating.**—For general information on plating techniques the reader is referred to the publications listed below.<sup>3</sup> Plating solutions, partially prepared, can be obtained from the Electroplating Division of E. I. duPont de Nemours Company, Wilmington 98, Del.

One of the most common plating processes in metal tube making is silver plating for precision brazing. The following procedure for this process has been used successfully: Degrease the parts in trichlorethylene; rinse them in methyl alcohol; boil 5 min in the solution given previously; rinse well in distilled water; let dry after a methyl alcohol dip; paint parts to be protected from plating with "stop-off" lacquer,<sup>4</sup> and allow to dry; silver plate to desired thickness; rinse well in cold water, and peel off lacquer; wash well in acetone to remove particles of lacquer; rinse in clean methyl alcohol; and let dry.

**17-5. Metal-to-glass Seals.**—To obtain a vacuum seal between glass and metal two major conditions must be satisfied: The thermal expansions of the glass and metal must match or be accounted for in the design, and the glass must wet the metal surface. Two ways of satisfying these conditions have come into use. The copper-to-glass seal developed by Housekeeper<sup>5</sup> is one that satisfies the first condition by mechanical distortion of the metal. In this case the glass is sealed to a copper tube machined to a thin "feather edge," which is easily distorted when the seal is subjected to a change in temperature and thereby prevents the

<sup>1</sup> *Handbook of Chemistry and Physics*, 27th ed., Chemical Rubber Publishing Co., Cleveland, Ohio, 1943.

<sup>2</sup> E. A. Coomes, J. G. Buck, A. S. Eisenstein, and A. Fineman, "Alkaline Earth Oxide Cathodes for Pulsed Tubes," App. II, NDRC 14-933, OEM sr-262, Mar. 30, 1946.

<sup>3</sup> *Modern Electroplating*, The Electrochemical Society, Columbia University, New York, 1942; N. Hall and G. B. Hogaboom, Jr., ed., *Plating and Finishing Guidebook*, Metal Industry Publishing Co., New York, 1943; W. Blum and G. B. Hogaboom, *Principles of Electroplating and Electroforming*, McGraw-Hill, New York, 1930.

<sup>4</sup> Purchasable from Wyandotte Paint Products Co., Wyandotte, Mich.

<sup>5</sup> W. G. Housekeeper, *Jour. Am. Inst. Elec. Eng.*, **42**, 954 (1923).

glass from fracturing. The Kovar<sup>1</sup> (or Fernico<sup>2</sup>) seal satisfies the first condition by virtue of the fact that the metal and Kovar cooling curves are closely matched below the glass-annealing point. Both of these sealing methods satisfy the second requirement because a copper or Kovar oxide is formed during the sealing process that partially dissolves into the glass, thus forming a hermetic seal. The success of the seals in either method lies mainly in the technique of wetting the oxide with glass in the plastic state. The method of copper-to-glass seals is well outlined in Strong<sup>3</sup> and will not be discussed here, except to emphasize that the quality of the copper used in such seals is extremely important. Oxide inclusions in the copper must be avoided to minimize porosity and lessen leak trouble in the feather edge. For this reason OFHC copper is almost a necessity.<sup>4</sup> The technique of making the Kovar seal is described following a discussion of the properties of Kovar and common glasses used in the laboratory.

*Properties of Kovar.*<sup>5</sup>—Kovar, a cobalt-nickel-iron alloy, was specifically developed for making vacuum seals to hard glass. It machines readily at slow speeds (much like stainless steel), when high-speed cutting tools are used with lard oil as a lubricant. It can be deep drawn as described in Table 17-7.<sup>6</sup>

TABLE 17-7.<sup>5</sup>—RECOMMENDED RULE FOR DRAWING KOVAR

	Maximum reduction in diameter, %
First draw.....	40
Redraw.....	25 (30 after reanneal)
Subsequent redraws.....	20 (25 after reanneal)

<sup>1</sup> H. Scott, *Am. Inst. Mining Metal. Eng. Tech. Pub.* 318, 1930; *Jour. Franklin Inst.*, **220**, 733 (1935). Kovar is obtainable from the Stupakoff Ceramic and Manufacturing Co., Latrobe, Pa.

<sup>2</sup> E. E. Burger, *Gen. Elec. Rev.*, **37**, 93 (1934); A. W. Hull and E. E. Burger, *Physics*, **5**, 384 (1934). Fernico is obtainable from the General Electric Co., Schenectady, N.Y. From here on the text will refer only to Kovar, but the remarks are, in general, applicable to Fernico as well.

<sup>3</sup> Strong, *op. cit.*

<sup>4</sup> J. E. Clark, *OFHC Copper for Use in Vacuum Tubes*, BTL Memorandum MM-40-140-42, Sept. 6, 1940.

<sup>5</sup> See "Sealing Glass to Kovar," *Bull.* 145, Stupakoff Ceramic and Manufacturing Co., Latrobe, Pa., 1945.

<sup>6</sup> Subsequent annealing is required only when the length of the cup equals or exceeds the diameter. Using the above rule for drawing, an anneal should be made after the first redraw. When drawing long cups, anneals should follow the third redraw, fifth redraw, etc. For the anneal, the Kovar should be heated in a hydrogen- or inert-atmosphere furnace at a temperature of 1100°C for 15 min or at lower temperatures for longer times down to 800°C for 2 hr.

Table 17-8<sup>1</sup> contains data on the physical properties of Kovar. It is important to realize that the average coefficient of expansion does not alone determine the strength of a seal and deviations of the Kovar from the glass cooling curves must be considered.

TABLE 17-8.1—PROPERTIES OF KOVAR\*

## Specific Properties of Kovar

Composition.....	29% nickel, 17% cobalt, 0.3% manganese, balance iron
Melting point.....	1450°C (approximate)
Density.....	0.302 lb per cu in.
Hardness, annealed.....	760°C—140–160 BHN
Hardness, unannealed.....	200–250 BHN depending on degree of cold work
Specific electrical resistance..	49 microhm cm—294 ohms per cir. mil. foot
Thermal conductivity.....	0.046 calories/cm/sec°C (approximate as measured at room temperature)
Curie point.....	435°C approximate

Physical Properties of 0.030 Thick Sheet Tested Parallel to the Direction of Rolling  
PSI

Yield point.....	50,500
Proportional limit.....	32,300
Tensile strength.....	89,700
Modulus of elasticity.....	$20 \times 10^6$

Thermal Expansion: After annealing in hydrogen for 1 hr at 900°C and for 15 min at 1100°C. The average coefficient of thermal expansion of Kovar falls within the following limits:

30°–200°C	$4.33\text{--}5.30 \times 10^6$ per °C
30°–300°C	$4.41\text{--}5.17 \times 10^6$ per °C
30°–400°C	$4.54\text{--}5.08 \times 10^6$ per °C
30°–450°C	$5.03\text{--}5.37 \times 10^6$ per °C
30°–500°C	$5.71\text{--}6.21 \times 10^6$ per °C

## Magnetic Permeability

Magnetic permeability	Flux density, gauss
1000	500
2000	2,000
3700	7,000 (max. value)
2280	12,000
213	17,000

## Magnetic Losses, Watts per Lb

Thickness	10 kilogauss 60 cycles/sec	10 kilogauss 840 cycles/sec	2 kilogauss 5000 cycles/sec	2 kilogauss 10,000 cycles/sec
0.010	1.05	23.4	16.6	41.0
0.030	1.51	....	....	....
0.050	2.77	....	....	....

\* Tensile strength of Kovar glass seals is 600 lb/sq in. All of the above are typical values.

<sup>1</sup> See "Sealing Glass to Kovar," *Bull.* 145, Stupakoff Ceramic and Manufacturing Co., Latrobe, Pa., 1945.

TABLE 17-9.—PROPERTIES OF LABORATORY GLASSES

Corning Code No.*	Corning laboratory No.*	Thermal coef. of expansion* $\times 10^{-7}$ °C	Softening point,* °C	Annealing point,* °C	Strain point,* °C	Approx. working point,* °C	Volume resistivity at 250°C, † ohm $\times$ cm	Dielectric properties at { room temp. ‡ { $3 \times 10^6$ c/sec		Seals to ‡
								$\epsilon'/\epsilon$	$\tan \delta$	
001	G-1	91	626	428	397	970	$1.19 \times 10^9$	5.95	0.00600	008, 010, 012, Pt. Dumet §
008	G-8	92	696	510	475	1000	$2.26 \times 10^8$	6.71	0.01260	001, 010, 012, Pt. Dumet
012	G-12	89	630	433	400	975	$1.19 \times 10^{10}$	6.64	0.00410	001, 008, 010, Pt. Dumet
171	G-172-RM	41	920	715	675	....	$4.90 \times 10^{11}$	5.95	0.00560	705, 707, 772, 775, 3320, W
704	G-705-BA	47	702	484	450	1080	$5.31 \times 10^9$	4.67	0.00440	705, 7052, 706, 775, Kovar, Mo
705	G-705-AJ	46	703	496	461	....	$2.04 \times 10^9$	4.72	0.00520	704, 7052, 706, 707, 3320, { Kovar 772, 775, 171 { Mo W
7052	G-705-FN	46	708	480	442	1115	$1.00 \times 10^9$	5.04	0.00580	704, 705, 706, 775, Kovar, Mo
706	G-705-AO	50	690	495	463	....	$6.68 \times 10^7$	4.70	0.00540	704, 705, 7052, 775, Kovar, Mo
707	G-707-DG	32	746	490	455	1100	$1.50 \times 10^{11}$	4.00	0.00190	705, 772, 774, 775, 3320, 171
772	G-702-P	36	755	518	484	1110	$6.53 \times 10^8$	4.59	0.00380	705, 707, 774, 775, 171, 3320, W
774	G-726-MX	33	820	553	510	1220	$1.41 \times 10^8$	4.89	0.00890	707, 772
775	G-705-R	41	704	467	431	....	$2.88 \times 10^9$	4.38	0.00430	704, 705, 7052, 706, 707, { Kovar 3320, 171 { W
790	G-790-H	8	1500	910	820	....	$5.19 \times 10^8$	3.84	0.00068	723, SiO <sub>2</sub>
3320	G-371-BN	40	780	535	497	....	$4.17 \times 10^8$	4.72	0.00620	705, 707, 772, 794, 775, 171, W
1990	G-189-IY	127	496	359	334	....	$9.33 \times 10^9$	7.99	0.00200	Steel (SAE 1010) Ag-plated
1991	G-184-ET	128	539	363	366	....	$3.76 \times 10^9$	7.84	0.00380	Fe
....	General	128 ‡	340 ‡	395 ‡	....	....	$3.55 \times 10^9$	7.65	0.00240	1990, 1991, Fe (Cu or Ag plated)
	Electric- R3 ‡									

\* From Bull. ER-S-1, Electronic Sales Dept., Corning Glass Works, Corning, N.Y., Mar. 15, 1945.

† A GE glass.

‡ From "Tables of Dielectric Materials": Report V, NDRC 14-237, February 1944, p. 52; Report VIII, NDRC 14-425, June 1945, p. 63.

§ A copper-clad nickel-copper alloy having a thermal expansion of about  $90 \times 10^{-7}$  per °C.

*Properties of Laboratory Glasses.*—Data on the properties of various glasses are given in Table 17-9. Such information has proved useful in the experimental laboratory and provides necessary information for making Kovar-to-glass seals. The first column of Table 17-9 defines the glass by code number. The second column is included because the laboratory numbers often continue in popular use even after a code number has been assigned. The thermal coefficient of expansion is the average coefficient of expansion from a range of temperatures between 0° and 300°C. The softening point, annealing point, strain point, and working point are merely four arbitrary points on a smooth temperature-viscosity curve. The working point given in Table 17-9 does not constitute a recommendation of the proper temperature for sealing, but it corresponds to the approximate temperature at which seals are usually made. The volume resistivity values (Column 8) are, in general, not true material constants but subject to the experimental conditions as outlined in "Tables of Dielectric Materials."<sup>1</sup> The values will have considerable practical importance, however, in estimating leakage currents and in making comparisons between materials. The dielectric properties are also taken from this reference and defined according to the following:

- $\epsilon'$  = dielectric constant,
- $\epsilon_0$  = dielectric constant of vacuum =  $8.854 \times 10^{-12}$  (farad/meter),
- $\epsilon'/\epsilon_0$  = specific dielectric constant,
- $\epsilon^*$  = complex dielectric constant =  $\epsilon' - j\epsilon''$ ,
- $\epsilon''$  = loss factor,
- $\tan \delta$  = loss tangent =  $\epsilon''/\epsilon'$ .

Properties of glass, such as aging, reactions with gases, and chemical reaction of one glass upon another, are difficult to take into account, and in these cases experience is the best guide.

*Preparation of the Glass and Kovar for Sealing.*—The cutting of the glass tubing or cane to the required lengths can be done with a bonded abrasive wheel. A wheel of approximately No. 200 grit with a surface speed of 8000 ft/min is satisfactory. Care should be taken to avoid forcing the cut because this will produce abrasive inclusions in the glass and result in cloudy seals.

After the Kovar is machined or drawn to size, it should be polished free from any tool marks or scratches, particularly those which run from the inside to the outside of the proposed seal. Deep scratches can be removed with an aloxite cloth of approximately No. 120 grit, but for finishing polish a No. 250 grit cloth should be used. In addition to

<sup>1</sup> A. von Hippel, "Tables of Dielectric Materials," Report VIII, NDRC 14-425, p. 63.

polishing, any sharp edges in contact with the seal should be rounded with a forming tool.

After the machining and polishing, the Kovar should be degreased as described in Sec. 17-4 and then annealed in a hydrogen atmosphere. If the Kovar is not hydrogen fired, the finished seal may contain bubbles which weaken the glass mechanically and increase the probability of vacuum leaks. If the Kovar is not properly annealed, cracks may occur during subsequent brazing operations. This heat treatment in the hydrogen furnace is the same as given in the note to Table 17-7. The seals should be made within a few hours after this hydrogen-atmosphere firing.

*Glass-to-Kovar Seals.*—The best method to be employed for sealing glass to Kovar depends upon many factors, including the size and shape of the glass and metal parts. Some general remarks on sealing can be obtained from the Kovar manufacturer<sup>1</sup> and need not be repeated here. Instead, the technique of sealing glass to Kovar for a specific case will be described in detail as typical sealing procedure. The following description applies to pipe *a* in Fig. 17-14. It is here assumed that the component parts of the base and central lead have been machined and brazed together and the Kovar parts polished, chemically cleaned, degassed, and annealed according to previous sections of this chapter; therefore, the base assembly and the central lead are ready to be glassed. In this case the No. 7052 glass is cut to a length  $\frac{1}{4}$ -in. greater than the desired distance between the Kovar pieces, and a diameter is chosen such that it fits loosely over the Kovar.

The following operations are performed to make the seal to the two Kovar pieces.

The base of the cathode-support lead is placed in a stainless-steel jig which will be used to center the central lead and to position the two Kovar parts at the proper separation. The jig and base are mounted in the headstock of a glass lathe.<sup>2</sup>

The central lead is placed in the tailstock of the lathe.

With the cross fires of illuminating gas and oxygen set to be slightly oxidizing, the Kovar pieces are oxidized by raising their temperatures to a dull red and immediately allowing them to cool. They must not be overoxidized; a heavy black oxide is inclined to result in a leaky seal.

The glass is slid over the Kovar, and the tailstock moved forward until the central lead hits the step in the jig and thus establishes the proper spacing between the two Kovar pieces.

One end is glassed at a time. The fires are placed in a manner to heat the Kovar more than the glass. When the glass reaches the working

<sup>1</sup> "Sealing Glass to Kovar," *op. cit.*

<sup>2</sup> Litton Engineering Laboratories, Redwood City, Calif.

temperatures, it is pushed onto the Kovar with a carbon paddle. When contact has been made between the Kovar and glass all around the circumference, the paddle is removed, but heating is continued until the glass thoroughly wets the Kovar and the glass edges become rounded.

After both seals have been made, the glass can be worked to a uniform diameter.

The glass must be worked at the seals so that it wets the edges of the Kovar. It is advisable to have the edges of the glass always meet the Kovar at a large angle.

The joints are flame-annealed with a bunsen burner.

They are then oven-annealed at 490°C for 20 min, and the oven is allowed to cool to room temperature at the rate of approximately 2°C/min. The color of the seal should be a smoky grey.

*Waveguide Windows.*—An important part of the design of a waveguide output is the waveguide window which serves as a vacuum seal across the guide with minimum power absorption in the dielectric window material.

Waveguide windows such as these can be made on a lathe by sealing to the edges of the opening glass tubing having a diameter approximately equal to the circular opening in the Kovar cup. The tubing is then buttoned-off close to the Kovar, and the remaining glass paddled and worked into the opening. After annealing, excess glass in the windows is ground flat on an abrasive grinding wheel. This method is satisfactory for a few experimental windows, but the quality and speed of construction may be improved by the use of glass disks.

Such disks of different glasses can be purchased from the glass manufacturer or cut with the aid of a diamond-cutting wheel (approximately 300 grit) from glass cane. The disks thus rough-cut can be polished to the exact thickness by conventional optical polishing techniques. During the disk-polishing process, abrasive material may be forced into the glass and cause bubbling when the seal is made. Abrasive inclusions are encouraged if excessive pressure is applied to force cutting. The disk-sealing method of making windows is explained with the aid of Fig. 17-16.<sup>1</sup> The opening in the Kovar is beveled to a 45° angle, and the diameter of the glass is such that it rests on the Kovar opening as shown. The upper stainless-steel tool is used to push the glass disk down as the edges become soft. The lower tool holds the glass in its final position with respect to the Kovar. The fires from the gas-oxygen burners are played on the Kovar cup as shown in Fig. 17-16a and b while the assembly is being rotated in a vertical sealer. (Only two burners are shown, but more may be used.) The flame is not played on the glass,

<sup>1</sup> E. J. Walsh, "Method of Making Glass to Metal Window Seals," BTL Memorandum MM-43-140-48, Oct. 5, 1943.



but melting occurs because of heat conduction from the Kovar to the glass. After the seal is made, the upper tool is removed and the edges of the glass are further melted to avoid small angle contact between the glass and Kovar. The final seal resembles the sketch of Fig. 17-16c. Immediately after being sealed, the window is placed in an annealing oven for about 15 min and then allowed to cool at approximately  $2^{\circ}\text{C}/\text{min}$ .

For sealing to Kovar, the low-loss Corning No. 707 glass is usually not recommended because its coefficient of expansion is considerably less than that for Kovar (see Table 17-9). It has been found, however, that successful seals can be made on the above waveguide window using this glass. It is believed that the success of this seal is related to the fact that the glass is left under compressional stress upon cooling and that this glass can stand a greater stress in compression than in tension. A Kovar cup is used so that when the Kovar is brazed to the copper portion of the tube, the window is relatively free from strains.

Another technique for sealing glass disks to Kovar employs the use of induction heating. Figure 17-17 shows the arrangement of an r-f coil and waveguide window preparatory to sealing. The single-turn r-f coil is connected to the output of an r-f generator through an appropriate matching transformer.<sup>1</sup> The Kovar is held in a Lavite support. The induction heating method provides uniform heating of the Kovar and excellent control of the Kovar temperature, and as a result very flat and uniform windows can be made without the holding tools that are necessary in the method previously described.

<sup>1</sup> *Ibid.*

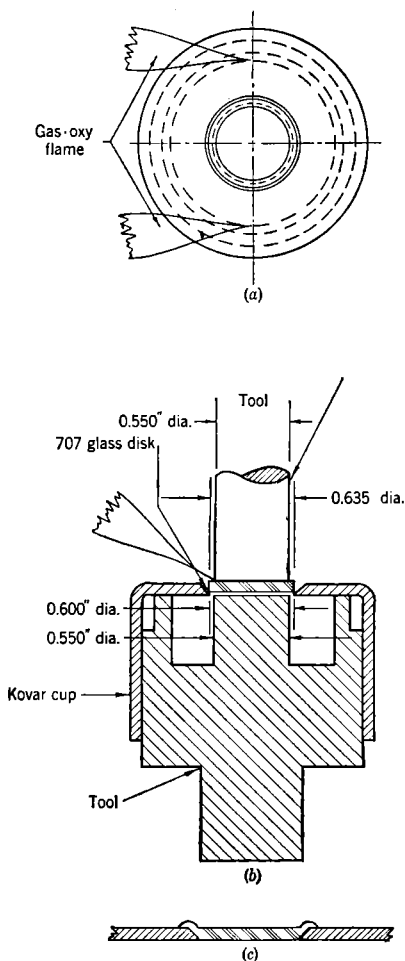


FIG. 17-16.—Sealing glass into a waveguide window. (Courtesy of Bell Telephone Laboratories.)

**Mica Windows.**—The low-loss 707 glass used in the above windows is limited in its average power-handling capacity to about 500 watts transmission of 3-cm radiation. For higher-power outputs mica windows may be used, as losses are about 15 per cent lower than those in 707 glass.

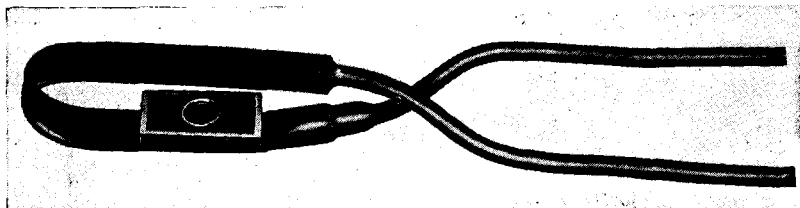


FIG. 17-17.—Coil for r-f heating of waveguide windows.

A technique of making mica windows for waveguide output<sup>1</sup> has been based on a method for sealing mica to metal.<sup>2</sup> The metal cup is made of Allegheny No. 4 Alloy (52 per cent Fe, 42 per cent Ni, 6 per cent Cr) which has a coefficient of expansion of about  $95 \times 10^{-7}$  per degree centigrade and nearly matches the expansion properties of India mica. A lead-borosilicate glass effects a seal between the mica and the metal cup. Such a mica window is shown in Fig. 17-18.

In constructing such a window, the No. 4 alloy cup is fired in a dry hydrogen atmosphere for 15 min at 1100°C to remove the original oxide.

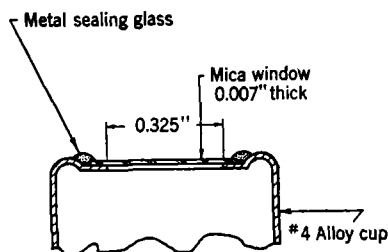


FIG. 17-18.<sup>1</sup>—Mica window for waveguide output.

In the absence of a hydrogen furnace free of oxygen and water vapor, the oxide can be removed by mechanical polishing. The cup is fired in a regular tank hydrogen furnace for 10 to 15 min at 1100°C to form a thin uniform layer of oxide. This chromium oxide is necessary so that the glass will wet the metal and form a hermetic seal. A paste is made of powdered

glass with water. This paste is painted with a small brush around the mica disk placed over the opening in the cup. A lavite slug, slightly smaller in diameter than the mica, is placed over the mica disk, and the lavite, mica, and cup are held together with a supporting jig. The lavite slug not only holds the mica in position but also prevents the glass from flowing over the whole mica surface. This combination

<sup>1</sup> L. Malter, R. L. Jepson, and L. R. Bloom, "Mica Windows for Waveguide Output Magnetrons," NDRC 14-366, Dec. 5, 1944.

<sup>2</sup> J. S. Donal, Jr., "Sealing Mica to Glass or Metal to Form a Vacuum Tight Joint," *Rev. Sci. Instruments*, **13**, 266 (1942).

is fired in an air oven for 15 min at 600°C; the seal between the metal and glass should then have a light green color. To braze the cup to the copper part of the waveguide, the cup must be nickel-plated after the oxide has been removed by polishing. The cup-to-copper waveguide joint can now be made with silver alloys "BT" or "RT" in a hydrogen bottle if the window is protected by blowing nitrogen over its surface during the brazing operation. It is possible with this window to repair a leak in the seal even after the tube is completely assembled. Protection in the form of a section of waveguide extending beyond the mica is desirable, as this type of window is mechanically weak.

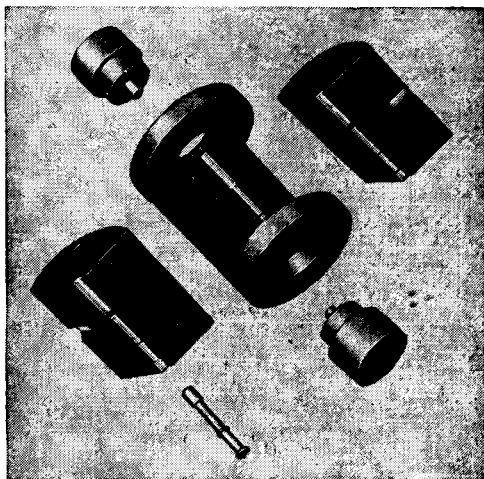


FIG. 17-19.—Cathode-forming die.

**17-6. Cathode and Heater Construction.**—The properties of the alkaline-earth oxide-coated cathode are given in Chap. 12. This section will describe the construction of cathodes for magnetron use. Although the oxide material used in making magnetron cathodes has remained essentially unchanged for several years, there have been important improvements in the construction of the base for the oxide layer. The screen and the porous matrix of nickel<sup>1</sup> are outstanding examples. Methods of making these cathodes will be discussed along with methods of fabricating the plain nickel-sleeve cathode. Finally, the construction of thorium oxide cathodes for high-power application will be considered.

**Cathode-sleeve Construction.**—Plain nickel sleeves can be made by cutting tubing to the proper length with a sharp knife. If seamless Grade A nickel tubing cannot be obtained in the desired size, it can be

<sup>1</sup> R. L. Slobod, "Development of Magnetron Cathodes," BTL Memorandum MM-44-120-73, June 11, 1944.

drawn to size. If the desired seamless tubing is not available, the cylindrical sleeve may be formed from nickel sheet.

For small cathodes it is advisable to machine the sleeve to size from a nickel rod or heavy-walled tubing, as is done for the 725A magnetron cathode, shown in Fig. 17-20, or to press a nickel rod to the desired diameter and shape in a steel-forming die, as is done for the 2J42 magnetron. The parts of such a forming die are shown in Fig. 17-19. These parts are made from Ketos tool steel hardened to a Rockwell C of about 60. Nickel rod of a diameter approximately equal to the cathode diameter is cut to a length sufficient to supply the volume of nickel needed in the finished structure. The best length may be found by trial and error.

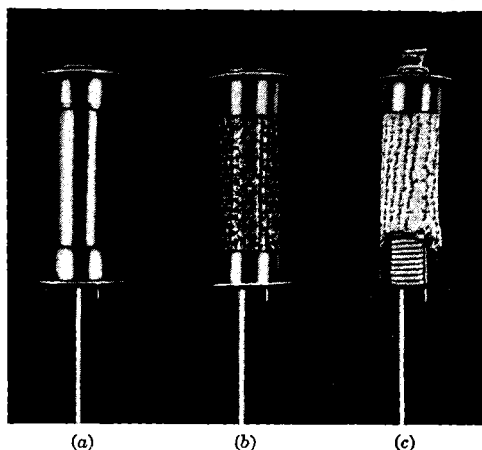


FIG. 17-20.—725A cathode. (a) Plain sleeve; (b) screen sleeve; (c) coated screen cathode. (Courtesy of Bell Telephone Laboratories.)

Before being pressed the nickel rod is annealed in the hydrogen-atmosphere furnace at 900°C for 30 min. It is then placed in the forming die with the pie-shaped sides and end pieces put in place. The outside diameter of the assembled parts has a slight taper so that the assembly can be forced into a hardened cylinder which prevents the pie-shaped parts from moving radially during pressing. The assembly is then placed in a press, and a force is applied between the two end pins. By this technique the cathode sleeve, end shields, and support rod are formed, and all that remains to be done is drilling the central hole through the rod to admit the heater. If the end shields are difficult to form by pressing, punched nickel washers may be put on the initial nickel rod and pressed into place by the forming die.

The screen cathode is formed by applying a nickel mesh to the plain cathode sleeve (see Fig. 17-20a). For the larger cathodes the mesh is spot-welded to the nickel sleeve by conventional spotwelding techniques.

For the smaller cathodes the screen may be sintered onto the sleeve in the following manner. The nickel screen (150 by 150 mesh for the 2J42 size of cathode) is degreased, annealed in a hydrogen furnace at  $900^{\circ}\text{C}$  for  $\frac{1}{2}$  hr, and cut to the proper size to cover the cathode sleeve. The screen is placed around the cathode and held in a K-Monel jig such as the one shown in Fig. 17-21. The grooves in the jig prevent bending of the cathode end shields. The two parts of the jig are then screwed together tightly and passed through the hydrogen furnace at  $1125^{\circ}\text{C}$  for 15 min. In order to get good bonding of the mesh to the nickel sleeve the jig must exert a large and uniform pressure over the whole cathode area, and therefore the screen sintering should be done before drilling the heater hole. In cases where this is impossible, it may be necessary to place a mandrel in the heater hole during the sintering operation.

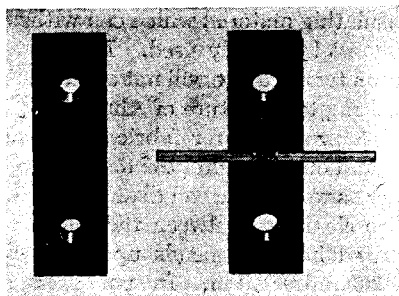


FIG. 17-21.—Screen-cathode sintering jig.

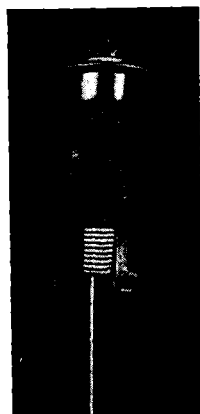


FIG. 17-22.—Porous-nickel-matrix cathode. (Courtesy of Bell Telephone Laboratories.)

The porous-nickel-matrix cathode<sup>1</sup> was developed in an effort to increase the thermal conductivity of the emitting layer of the cathode. To form the porous matrix, nickel powder either is painted onto the plain sleeve in the form of a suspension in amyl acetate with pyroxylin as a binder or is molded onto the sleeve with the aid of a stainless-steel fixture. In the painting method the nickel powder ( $-200 + 325$  mesh) is built up to a thickness of approximately 10 mils and then fired for 15 min in a hydrogen atmosphere at  $1200^{\circ}\text{C}$ . In the molding method the metal powder is introduced into the space between an oxidized stainless-steel mold and the cathode sleeve, and the assembly is fired at  $900^{\circ}\text{C}$  for 10 min to fix the powder into place. The mold is then removed, and the sleeve plus powder refired at  $1200^{\circ}\text{C}$  for 15 min to form a highly porous mass rigidly attached to the base metal as shown in Fig. 17-22.

**Heater Construction.**—The heater conventionally consists of a tungsten or molybdenum wire (or ribbon) inserted into the cathode sleeve, as seen in Fig. 17-23. Because there must be little or no electrical leakage

<sup>1</sup> *Ibid.*

between the heater and the cathode or between adjoining parts of the heater, they are usually coated with some nonconducting nonemissive material. The coating must be hard and tough enough to withstand insertion into the cathode sleeve. Alundum, a nonemissive electrical insulating material which can withstand high temperatures and abrasion, is most frequently used. Heaters must be designed so that their maximum temperature will not exceed  $1400^{\circ}\text{C}$  in order to stay safely below the melting temperature of Alundum.

A procedure for fabricating heater coils is as follows. The wire is wound on a mandrel the diameter of which depends upon the wire diameter as well as the coil diameter and is best determined by trial and error. The clearance between the inside of the sleeve and the outside of the coated heater depends upon the cathode size but is usually between 0.003 and 0.010 in. In some cases, such as a heater to be wound bifilar, it is advisable to wind the wire on a stainless-steel mandrel that has screw threads of the proper pitch cut into it. After winding, the ends of the wire are securely fastened, and the heater coil and mandrel are hydrogen-fired at  $1000^{\circ}\text{C}$  for 5 min. At this temperature, strains are removed from tungsten or molybdenum wire without embrittling the metal. The coil may then be removed from the mandrel by unscrewing. The ends of the coil are then formed to the shape necessary for welding them to the input connectors. The coil is chemically cleaned by boiling it in 20 per cent KOH solution for 5 min, rinsed in distilled water, and dried in a hot-air blast. The heater is next sprayed with a suspension of Alundum. The spraying can be done with a De Vilbiss type CV spray gun, the compressed air being supplied through a De Vilbiss type HB air transformer. The air pressure, the gun fluid screw, and the gun spreader valve should be adjusted to produce a cloud of uniform density. When a small number of tubes are made in an experimental laboratory, the heater coating (which is a suspension of Alundum in an appropriate binder such as amyl acetate) can best be obtained from a commercial radio-tube manufacturer. The suspension must be well agitated before it is used by being rolled on a "ball mill" for  $\frac{1}{2}$  hr at 100 rpm. The thickness of coating should be built up slowly and uniformly to about 0.003 in. by several passes of the gun at several different angles around the axis of the heater. The coil is then baked in a low-temperature oven in air at  $100^{\circ}\text{C}$  for  $\frac{1}{2}$  hr to evaporate the Alundum binder. The coil is then placed in a molybdenum tray and fired in a high-temperature hydrogen-atmosphere furnace at  $1620^{\circ}\text{C}$  for 5 min. If the temperature is too high, the coating will become excessively hard and will be inclined to chip when the heater is bent. If the temperature is too low, a soft coating will result.

*Assembly of Cathode Parts.*—The procedure for assembling the cathode parts will depend upon many factors, especially the method that is chosen

for mounting the cathode in the tube. For magnetrons with unattached magnets the cathode is usually mounted by two radial supports which serve also to complete the heater circuit. For "packaged tubes" it is common to use a single support through a hole in the pole piece; the support is hollow; and the heater circuit is completed by a coaxial wire. These methods of assembly will be described by reference to typical examples.

The cathode for the 725A magnetron (shown in Fig. 17-23) is selected as an example of the radial mount. The details of brazing, cleaning, glassing, etc., have been discussed previously; the assembly of the different cathode parts will merely be listed without discussing the details of these operations. Some detail of making the heater insulator must be

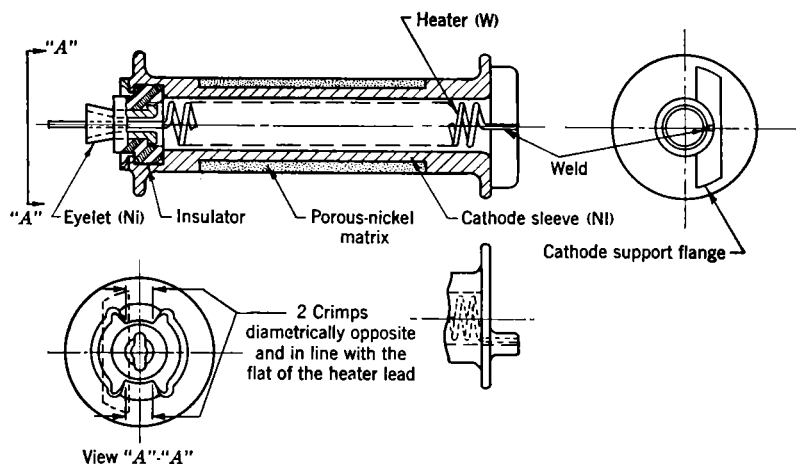


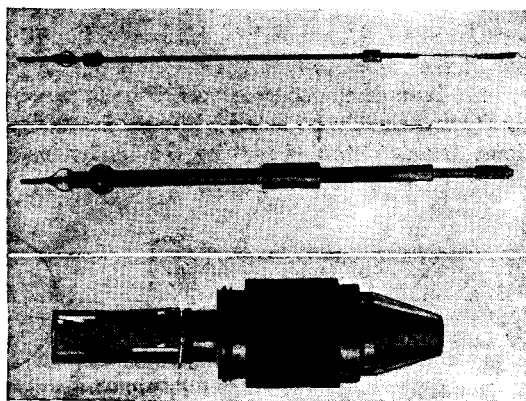
FIG. 17-23.—Construction of 725A cathode. (Courtesy of Bell Telephone Laboratories.)

given, however. Lavite<sup>1</sup> is a convenient material for this purpose. It can be machined to size in the raw state and then hardened in the following manner. Place insulators in nickel tray covered with Alundum sand. Place tray in air oven, and heat at about 500°C for 5 min. Increase over temperature to 1000°C, and heat for  $\frac{3}{4}$  hr. Allow oven to cool to about 200°C before removing insulators. (This procedure is for an oven with an annealing chamber.) The different parts of the cathode (Fig. 17-23) are then assembled by the following process.

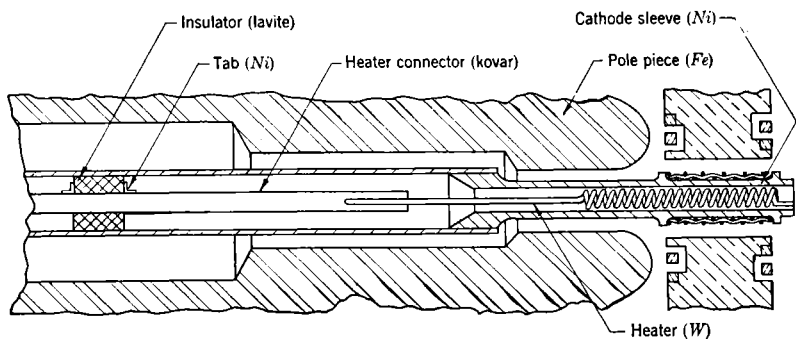
The heater, insulator, and eyelet are arranged as shown. The nickel eyelet is flattened to clamp the heater. The insulator is held in place by crimping the nickel shoulder at the end of the cathode. The heater is spot-welded at one end to the cathode-support flange and at the other

<sup>1</sup> Obtainable from the American Lava Corp., Chattanooga 5, Tenn.

end to the flattened eyelet. The protruding heater wire is cut off flush with the end of the eyelet. The assembled cathode and heater are then ready for mounting in the magnetron. Nickel support wires are welded to the tungsten leads, which are brought through the glass seals, and there support wires are welded to the cathode. The main support for the cathode is the weld to the cathode-support flange. The weld to the



(a)



(b)

FIG. 17-24.—(a) and (b) Construction of 2J42 axial-mounted cathode.

eyelet supplies some support but is essentially to make connection to the heater.

The axially mounted cathode structure for the 2J42 magnetron shown in Fig. 17-24 is typical. As with the radially mounted cathode, the order of assembly of parts will be given without the details of the individual operations for making the parts.

1. The Kovar "heater connector" rod is cut to the proper length and drilled to accept the heater.



2. The heater connector is beaded with 7052 glass in preparation for sealing to the "cathode support."
3. The hardened lavite insulators are slipped onto the rod and spot-welded into place with nickel tabs.
4. The heater is put into the drilled hole of the Kovar rod and spot-welded in place.
5. The screened cathode is copper-brazed to the cathode support.
6. The r-f choke (copper) is "BT" brazed to the cathode support.
7. The assembled heater and heater connector are slipped into the assembled cathode sleeve and cathode support, and the glass seal is made by flowing the 7052 glass bead onto the Kovar tube. At the same time the Kovar tube is beaded in preparation for the seal to the pole piece.
8. The heater is then spot-welded to the projection.
9. The cathode is sprayed and made ready for mounting into the magnetron.
10. At this point, one of two courses can be followed, depending upon the final magnetron braze. One is to glass-seal the cathode structure into the pole piece and mount this assembly into the magnetron. Another is first to braze the pole piece to the block and then make the glass seal between the pole piece and the beaded cathode support. This latter method of mounting is the one described in Sec. 17-3.

*Cleaning and Coating the Cathode Sleeve.*—After the machining or brazing operations are completed upon the cathode sleeve, it is cleaned by the process outlined in Sec. 17-4; and from this time until the tube is completed, the cathode sleeve is handled with great care to prevent contamination that might inhibit cathode emission. It might be necessary, for some tubes, to rearrange the order of events or omit certain operations, but the following method of cleaning and coating the cathode sleeve is typical.

After the sleeve has been cleaned by the process described in Sec. 17-4, it is hydrogen-fired in a covered nickel tray at 900°C for  $\frac{1}{2}$  hr. The sleeve, the heater, and the supports are then assembled, with care to keep the sleeve free from contaminants. (If there is any question about cleanliness, the sleeve should now be rinsed in acetone and in clean methyl alcohol and then dried in clean warm air.) The cathode sleeve is then vacuum fired for 15 min at 1000°C. This can be done by using the heater to control the cathode-sleeve temperature or by r-f induction heating. (This step is sometimes omitted.)

The cathode should be coated immediately after the vacuum firing. For plain-nickel-sleeve cathodes the coating is generally done by spraying. A De Vilbiss type CH spray gun serves this purpose very well. As in

the case of heater spraying the air pressure (controlled by a De Vilbiss type HB air transformer), the fluid screw, and the spreader valve should be adjusted to give a cone-shaped cloud of uniform density. The coating should be sprayed onto the sleeve in thin uniform layers while the cathode sleeve is being rotated, until the desired weight of coating is deposited (usually 9 to 12 mg/cm<sup>2</sup>). During the spraying process the other cathode parts, particularly the end shields, must be protected from the spray.

A recommended BaSr(CO<sub>3</sub>)<sub>2</sub> mixture is the J. T. Baker Manufacturing Company Radio Mixture No. 3 suspended in amyl acetate with a pyroxylin binder. Experimental laboratories may find it convenient to purchase small quantities of cathode-coating material from a commercial radio-tube manufacturer. The coating suspension should be rolled at a speed of 100 rpm for about  $\frac{1}{2}$  hr to prepare it for use. The spray gun and auxiliary equipment should be cleaned frequently with acetone and distilled water.

For screen cathodes or porous matrix of nickel cathodes, the coating is applied with a camel-hair brush which has previously been cleaned with acetone and distilled water. The first coat is applied as a very thin continuous film which barely covers the surface of the nickel. This is allowed to dry thoroughly, and successive layers of coating are applied in the same manner until the screen or porous matrix is filled with coating material as shown in Fig. 17-20. The cathode is finally mounted in the tube and processed according to instructions given in Sec. 17-7.

*Thorium Oxide Cathode.*—Barium strontium oxide cathodes frequently limit the average power of magnetrons because the back bombardment in these tubes overheats the cathode structure. Attempts have been made to develop emitting surfaces that will have satisfactory life at high temperature. Thorium oxide cathodes<sup>1</sup> show promise for high-power magnetron operation. The poor adhesion of thoria to a metallic base<sup>2</sup> or sintered metal surface<sup>3</sup> is overcome by preparing a sintered cylinder of thoria. The preparation of sintered thoria cylinders is outlined.<sup>4</sup>

A uniform density of thoria powder is prepared by converting mantle-grade thorium nitrate into thorium oxide by heating in an air oven at 600°C, fusing the resulting fluffy material in an electric arc, and finally crushing the fused thoria into a 200-mesh powder. The thoria powder is then mixed with thorium chloride to form a paste that can be molded

<sup>1</sup> Martin A. Pomerantz, "Thorium Oxide Cathodes," NDRC 14-517, Bartol Research Foundation, Swarthmore, Pa., Oct. 31, 1945.

<sup>2</sup> S. Dushman, *Rev. Mod. Phys.*, **2**, 423 (1930).

<sup>3</sup> S. V. Forgue, RCA Engineering Memorandum PEM-4C, 1943.

<sup>4</sup> For detailed information on this process see C. D. Prater, "The Fabrication of Thoria Cathodes," NDRC Report, Bartol Research Foundation, Swarthmore, Pa., (June 1946).

into the desired shape. The thorium chloride in the molded ceramic is then converted into the hydroxide by placing it in an atmosphere of ammonium hydroxide for several hours. After removal from the ammonium hydroxide atmosphere and drying at room temperature, the ceramic is fired at about 1900°C in an argon atmosphere which converts the hydroxide to the oxide forming the bond between the grains of thorium oxide. Such thorium oxide cathodes give copious emission at 1700°C (see Chap. 12).

**17-7. Tube Evacuation and Processing.**—The interval between the final hydrogen firing of the tube parts and the evacuation of the tube should be as short as possible, in order to minimize oxidation and adsorption of gases by the internal parts. Tube processing remains to some extent an art and for this reason is less standardized than any of the previous procedures discussed. The following schedule is given merely as a typical one that has proved satisfactory.

After the tube has been sealed onto the vacuum system, the mechanical pump is used to reduce the pressure to about  $10^{-3}$  mm Hg before the diffusion pump<sup>1</sup> (a three-stage oil-diffusion type) is turned on. This pressure can be estimated by the appearance of fluorescence on the glass when touched with a spark coil. When the pressure of the system as read by the ionization gauge reaches 5 by  $10^{-6}$  mm Hg, a bakeout oven is lowered and turned on. As the tube begins to rise in temperature, the pressure will start to increase owing to the release of water vapor and gases from the various tube parts. When the bakeout-oven temperature reaches 450°C, it should be stabilized. The exhaust system should now be carefully torched. The bakeout-oven temperature is maintained at 450°C until the pressure falls to 5 by  $10^{-6}$  mm Hg. When this pressure is reached, the tube should be allowed to cool. The pressure should decrease as the tube cools, reaching about 5 by  $10^{-7}$  mm Hg when the tube returns to room temperature.

The tube is now ready for cathode processing. The cathode-binder residue is removed by increasing the heater power until the cathode temperature is about 600°C. The cathode temperature is raised in one step to 900° or 1000°C and held at this temperature until conversion of the coating is complete. Caution should be exercised in two ways at this point: (1) The cathode temperature should not rise above 1100°C, because the coating will start to evaporate from the sleeve. (2) If the heater voltage for conversion is higher than the CO<sub>2</sub> ionization potential (about 15 volts), a ballast should be inserted in the heater circuit to prevent arcs that would burn out the heater. During the conversion of large cathodes, the pressure may rise so high that it may be necessary to turn off the ionization gauge; in fact, the force pump may sound as

<sup>1</sup> Distillation Products, Inc., Vacuum Equipment Division, Rochester 13, N.Y.

though it has just been turned on. If the conversion from carbonates to oxides is done properly, the pressure should fall rapidly at the end of the process, and at this point the heater power should be reduced until the cathode temperature is about 850°C.

When the pressure has returned to 5 by  $10^{-6}$  mm Hg, activation of the cathode is begun by drawing a small amount of d-c current from the cathode. A burst of gas may be observed when d-c current is drawn; this gas may come from the cathode but is more apt to be ejected from the anode block by electron bombardment. The d-c plate voltage is raised slowly until the tube draws 25 ma/cm<sup>2</sup> and the pressure falls below 5 by  $10^{-7}$  mm Hg. At no time during the activation process should the pressure be allowed to rise above 5 by  $10^{-6}$  mm Hg.

When there is little change in pressure with changes in d-c plate voltage and the pressure remains below 5 by  $10^{-7}$  mm Hg, the tube is ready to be operated. The electromagnet is moved into place; the field is set for low-voltage operation; and the voltage (pulsed or c-w) is applied. The voltage is increased slowly to avoid excessive sparking and to allow time to pump off the gas expelled from the anode block because of high-energy-electron bombardment. Oscillation of the magnetron should be continued until the tube operates stably up to the desired operating input voltages.

When the processing and outgassing are complete, the tube should be allowed to cool to room temperature. The pressure at seal-off should be about 2 by  $10^{-7}$  mm Hg.

**17-8. Examination of Metals.**—In vacuum-tube construction, one error or defect unless detected at an early stage usually results in a worthless piece of metal and glass. A major source of trouble is impurifications in the basic materials. For this reason systematic and careful examination of these materials is almost a necessity to successful tube production.

Some common faults found in the metals used in tube construction should be mentioned. The copper may contain grains of Cu<sub>2</sub>O which often results in porosity after reducing and oxidizing heat cycles. Tungsten and molybdenum may be brittle or contain cracks that cause vacuum leaks or broken heaters. Certain batches of Kovar are also prone to develop cracks. Careful inspection of these metals is thus a necessity if excessive shrinkage is to be avoided.

Although copper may be labeled OFHC (oxygen-free high-conductivity) because it has been put through a deoxidizing process, it may in fact not be oxygen-free by the time it reaches the tube maker. This O<sub>2</sub> taken up may result from the drawing operation that is done after the deoxidizing process and during which copper-oxide scale is drawn into the copper bar. In this case the bar may be satisfactory on one

end and unsatisfactory on the other. Because the copper surface may oxidize while standing, the outer layer of a bar should always be turned off.

Non-OFHC copper can often be detected by its appearance after a "BT" soldering operation in an  $H_2$  atmosphere. One sign, although not definite, is that the "BT" solder is usually almost completely absorbed by the copper, and any fillets of solder that may occur are also copper-colored. Another indication is a peculiar orange color and granular structure of the copper, although this sometimes is also noticed on OFHC copper, especially when it is overfired. One of the most obvious traits of nonoxygen-free copper is that it expands under heat and does not resume its original size upon cooling. After  $H_2$  firing at  $800^\circ C$ , non-OFHC copper shells  $2\frac{1}{2}$  in. OD measure from 0.010 to 0.018 in. greater in diameter than before firing. OFHC copper, on the other hand, returns to within 0.001 in. of its original measurements.

The "bend test" is often employed to distinguish between "good" and "bad" copper. After  $H_2$  firing at  $800^\circ C$ , wire or thin strips of "bad" copper are very brittle and will break at the first attempt to bend them through  $90^\circ$ . "Good" OFHC copper will take at least four  $90^\circ$  bends in alternate directions after this treatment. This test is rather definite but cannot be used on heavy stock.

Most cracks and splints in wires and rods of tungsten and molybdenum can readily be seen under low magnification. Brittleness, especially after firing, is an inherent fault of these metals, but there are wide variations of degree. Tungsten rod that has been heated by a torch in air is much more brittle than the same rod fired in an  $H_2$  oven. Also, tests made on 0.080-in. tungsten rod showed that after  $H_2$  firing, wide differences existed as to brittleness among rods of the same lot of metal.

Cracks in Kovar result when unannealed pieces of the metal are soldered with a silver alloy in an  $H_2$  oven. They appear to be caused by the solder entering the grain boundaries of the Kovar as the stresses in the latter are relieved by heat. The cracks may be seen under a low-power microscope and in most cases even by the naked eye. In order to prevent these cracks, all Kovar should be annealed before it is soldered into assemblies.

The most definitive test for copper containing  $Cu_2O$  is microscopic examination of a polished and etched sample. One can detect the presence of  $Cu_2O$  not only by looking for the  $Cu_2O$  inclusions but also by studying the crystalline size, for the presence of  $Cu_2O$  will inhibit crystal growth.

Samples can be prepared in the following manner: A small piece of the copper under suspicion is cut from the billet. If the examination is concerned with grain structure, the sample is then annealed in an  $H_2$ ,



(a)



(b)

FIG. 17-25.—Photomicrographs of copper taken to detect inclusions of  $\text{Cu}_2\text{O}$ . (a) "Good" copper, magnification 250x; (b) "bad" copper, magnification 405x.

oven at 800°C. The copper is not annealed if detection of  $\text{Cu}_2\text{O}$  grains is desired. The metal is mounted in a molded bakelite<sup>1</sup> cylinder to facilitate holding it during the polishing operations, which must be carried out with some care. Beginning with a coarse abrasive such as No. 320 Aloxite cloth, progressively finer ones are used until the final polishing is done with a very fine alumina solution on Miracloth. These polishings should be done on a slowly rotating wheel, and care should be taken not to carry over any abrasive from one stage to the next. Polishing should continue until no scratches are visible at a magnification of 200 diameters.

If one wishes to study the grain structure, it is necessary to etch the surface of the copper after the polishing has been completed. If one is looking only for  $\text{Cu}_2\text{O}$  inclusions, etching is not necessary or desirable, because the reagent may destroy the inclusions. Under microscopic powers of 200 to 500 $\times$   $\text{Cu}_2\text{O}$  appears as small particles with a distinct bluish color. Their presence indicates that the copper will become porous when fired in an  $\text{H}_2$  atmosphere. To develop the grain structure of the copper, an etch of equal parts of  $\text{NH}_4\text{OH}$  and  $\text{H}_2\text{O}_2$  is applied to the specimen with a soft cloth. Only fresh solutions of this reagent will etch satisfactorily. Because the polishing process usually alters superficially the grain structure of the metal, it is good practice to etch lightly, then polish off this etch on the last wheel, and repeat this process until one has taken off the altered surface. Two etching and polishing cycles are usually sufficient to do this.

A specimen of OFHC copper that has been  $\text{H}_2$  annealed and etched is shown in Fig. 17-25a. Note the very large, rather regular grains with boundaries sharp and free from pits or inclusions. Figure 17-25b shows a sample of nonoxygen-free copper after  $\text{H}_2$  annealing. Note the small irregular grains with boundaries badly pitted and literally blown apart by the decomposition of the  $\text{Cu}_2\text{O}$  by  $\text{H}_2$ . These "blasted" grain boundaries cause the porosity in nonoxygen-free copper.

<sup>1</sup> Molding presses can be obtained from Adolphe I. Buehler Metallurgical Apparatus, Wicker Drive, Chicago 1, Ill.

## CHAPTER 18

### MEASUREMENTS

BY M. A. HERLIN AND A. G. SMITH

#### MEASUREMENTS OF THE RESONANT SYSTEM

BY M. A. HERLIN

Two classes of measurements are made on magnetrons, both of which are essential to the completion of a practical design and as a basis for the understanding of the operation of these tubes. Measurements performed on the nonoperating magnetrons and involving the use of signal generators constitute one class and are here referred to as "cold measurements." These are considered in the first part of this chapter. The second class, here referred to as "operating measurements," is concerned with techniques for obtaining data from operating magnetrons and is the subject of the second part of this chapter.

**18-1. Test Equipment Components.**—Cold-resonance experiments are performed with a number of basic pieces of equipment which may be combined in a variety of ways to yield information. These pieces are (1) a source of microwave power tunable over a wide frequency range and of moderate power output (of the order of milliwatts), (2) a wave-meter to measure the frequency of the power used, and (3) various probes and detectors designed for sampling and indicating the distribution and intensity of r-f energy in the components under test.

*Microwave Signal Generators.*—The most convenient microwave signal generators are reflex klystrons. The power output is supplied either into a coaxial line or a waveguide as desired. Once the generator is set up, the only adjustments to be made are frequency and reflector voltage. The reflector voltage is a partial control on the frequency and can be used to tune the oscillator over a narrow frequency range by electronic sweeping. Special wide-range cavities are available where large mechanical tuning ranges are needed, but in general these cavities are inconvenient to operate. A comprehensive discussion of these tubes is found in Vol. 7, Radiation Laboratory Series.

*Wavemeters.*—Wavelength measurements are made with some form of tunable resonant cavity in which the mechanical motion of the tuner is calibrated in terms of wavelength or frequency. Two methods of resonance indication are available. In the absorption method, a single



coupling loop or other probe is connected to the power source, and a dip in the power output as seen on a meter indicates resonance of the wave-meter cavity. In the transmission method, two coupling loops or other types of probe are coupled into the cavity to form a filter that transmits power only at the resonant frequency of the wavemeter cavity, and this power is indicated on a meter. A coaxial wavemeter and hollow-cavity

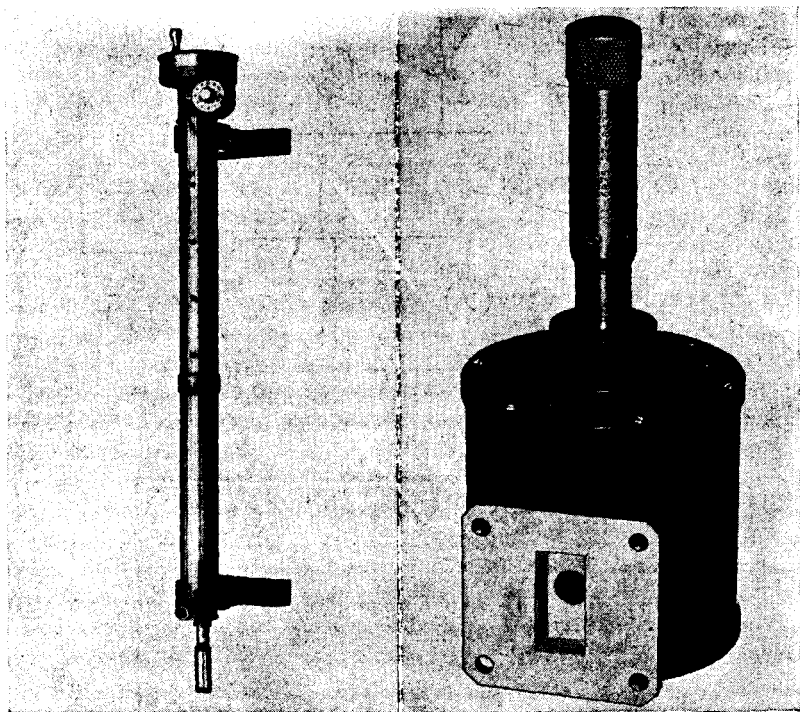


FIG. 18-1.—Microwave wavemeters. (a) S-band; (b) X-band.

wavemeter are shown in Fig. 18-1. A qualitative indication of power is obtained by means of a crystal detector connected to a microammeter. A precaution to be observed here is to provide a d-c return path for the crystal current in addition to the r-f connection to the power source.

*Probes and Detectors.*—At the longer wavelengths the coupling loop is most often employed to sample power from a cavity. A typical coupling loop is shown in Fig. 18-3a. The threaded length of tubing provides a convenient mechanical means of fastening the loop into the metal wall of the cavity, and a connector on the opposite end provides for transmission of the power into a coaxial line. The coupling loop is so

arranged in the cavity that lines of magnetic flux thread the loop. Figure 18-3*b* shows two capacitive probes. They are placed so that lines of the electric field terminate on the probe. For short-wavelength devices, such as the X-band wavemeter illustrated in Fig. 18-1*b*, the coupling into the

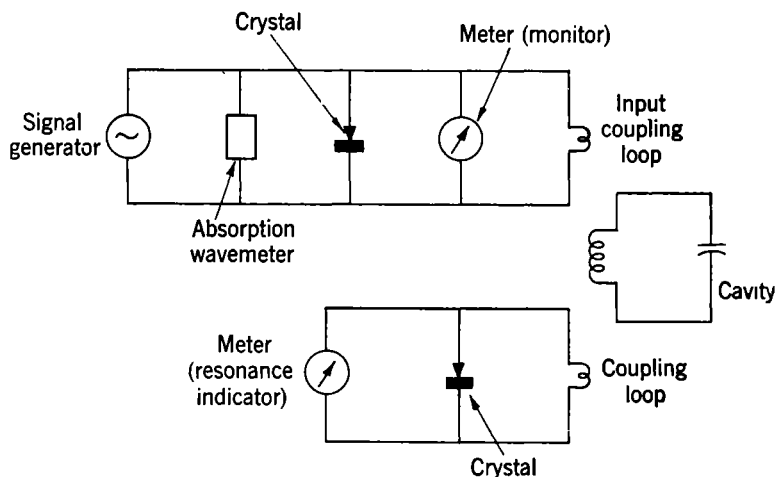


FIG. 18-2.—Schematic drawing of transmission method for resonant-wavelength measurement.

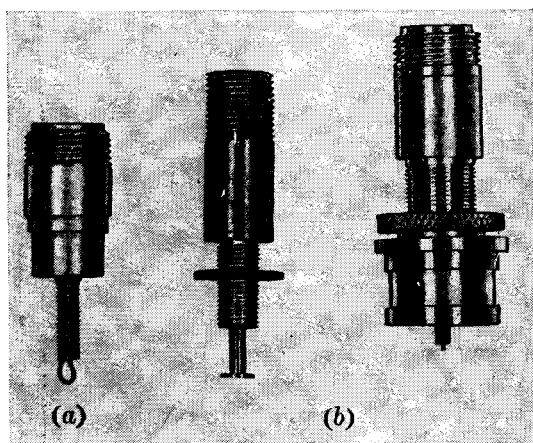


FIG. 18-3*a* and *b*.—Cavity coupling loop and probes.

waveguide may be made through a small coupling iris. In selecting the correct size of any of these coupling devices, the prime consideration is to reach the proper compromise between keeping the perturbation small so that the operating conditions are not changed appreciably

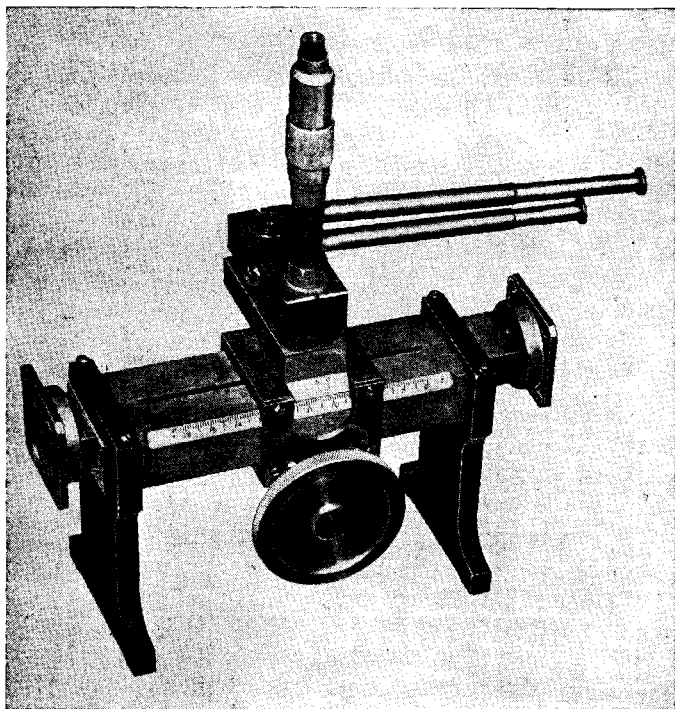


FIG. 18-4a.—Waveguide standing-wave detector.

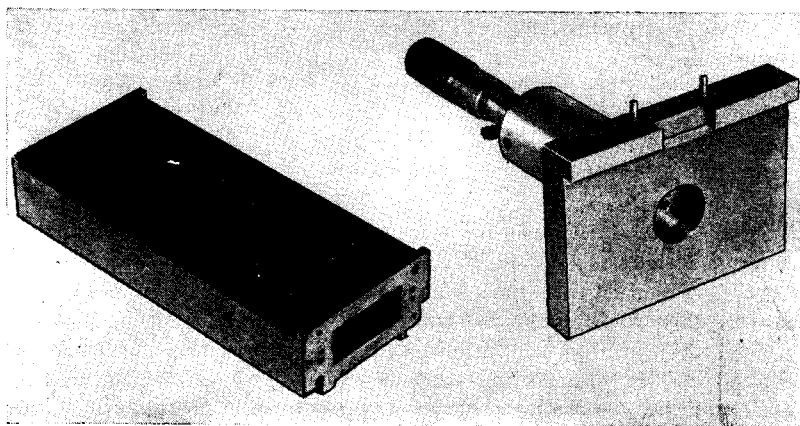


FIG. 18-4b.—K-band standing-wave detector.

during the measurement and coupling out sufficient power to give a positive reading.

A special instrument for measuring the properties of standing waves is the standing-wave detector. The type of detector shown in Fig. 18-4a is used at wavelengths of about 3 cm. A length of the slotted section is fitted with a small capacitive probe, and the power coupled out by this probe is then run into a crystal, spectrum analyzer, or other device for detecting it. The mounting of the probe is movable, so that variations in the power may be observed along the length of the slot. The one shown in Fig. 18-4b is for precise measurements at wavelengths of about 1.25 cm and has an iris pickup. Together with the indicating device, the standing-wave detector provides a measurement of the standing-wave ratio in the transmission line and the position of the voltage minimum. These two quantities can then be used to calculate the impedance terminating the line, as will be shown in Sec. 18-3.

The spectrum analyzer has proved to be a satisfactory indicator for use with the standing-wave detector in cold-measurement work where high standing-wave ratios are to be measured. The data are presented on the screen of a cathode-ray tube. The horizontal sweep provides a baseline along which the frequency is varied several megacycles, and the vertical reading shows power being fed into the analyzer at a given frequency. Inserted in the input line is an attenuator calibrated in decibels by which the relative intensities of two signals may be measured. A wavemeter is also attached to the analyzer connections. For a more detailed discussion of the equipment mentioned above see Vol. 14, Radiation Laboratory Series.

**18-2. Cavity-wavelength Measurements.**—Of particular concern here is the determination of the resonant wavelengths of the resonant system of a magnetron anode block. Magnetron work, however, involves the use of a variety of cavity resonators for various applications, and the method here described may be applied easily to these other cases.

*Transmission Method.*—In the transmission method of measuring resonant wavelength, two probes are placed in the cavity at appropriate points. In the magnetron the magnetic flux threads through the backs of the individual oscillators along the length of the tube, and coupling loops may therefore be placed in a plane perpendicular to the axis of the magnetron, as illustrated in Fig. 18-5. Because of the various configurations of electromagnetic field encountered with the different resonant modes of the magnetron, it is desirable to place the loops in oscillators that are diametrically opposite. This provides coupling to most of the modes and particularly to the more important ones. If all modes are being measured, it is well to run through the experiment with two different positions of one coupling loop.

Resonance is indicated in the same way as it is in a transmission wavemeter (see Sec. 18-1). One loop feeds into a crystal and meter, while the other receives power from the signal generator. When the signal generator is tuned to the resonant frequency of the cavity, power is transmitted through to the crystal and produces a deflection of the meter.

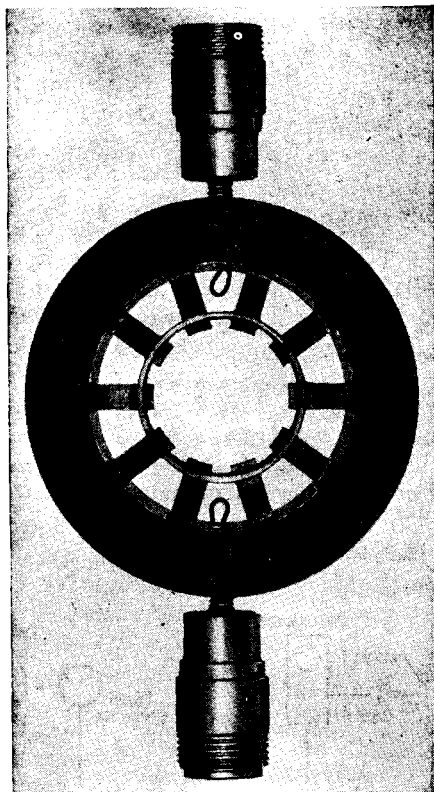


FIG. 18-5.—Anode block showing coupling loops suitable for resonance-wavelength measurement.

Connected to the input coupling loop are also a monitoring crystal and meter and an absorption wavemeter. The monitoring meter gives a continuous check on the signal generator output and also shows the power dip when the wavemeter is used. This arrangement is shown diagrammatically in Fig. 18-2.

The procedure is to tune the signal generator through the desired frequency range while watching the monitoring meter and the resonance-

indication meter. When resonance is reached, the wavelength is measured.

*Absorption Method.*—In the absorption method, use is made of a magic T or directional coupler and the electronic frequency sweep available with velocity-modulated microwave oscillators. This method has the advantage of fast presentation of data and needs only a single coupling loop or probe.

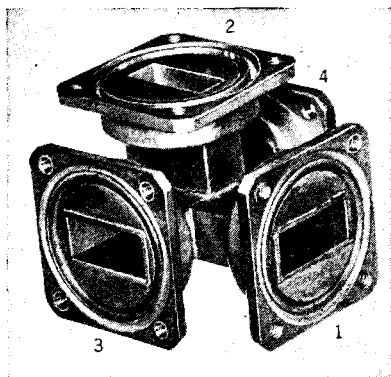


FIG. 18-6.—Magic T.

In the explanation of the use of the magic T for this purpose, reference is made to Fig. 18-6. Arms 1 and 2 are tapped respectively into the  $E$  and  $H$  plane of a waveguide. From symmetry considerations, it may be seen that a wave incident from one of these arms (for example, 1) divides and travels in both directions down the guides (3 and 4) while no disturbance is transmitted to Arm 2. However, if the guide in one direction is not matched, a reflected wave will return and part of it will enter Arm 2. The arrangement of the equipment is shown in Fig. 18-7a. One end of the guide is terminated in a match, and the other

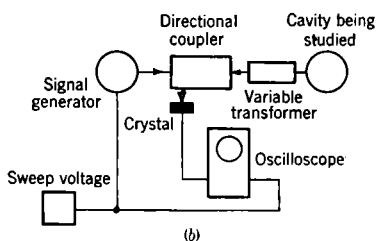
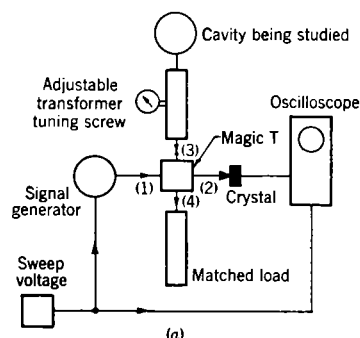


FIG. 18-7.—Resonance indicator setups. (a) Magic T; (b) directional coupler.

is connected to the magnetron or other resonant cavity to be studied. A large signal is then reflected from the cavity off-resonance; but when resonance is reached, some of the energy is absorbed in the cavity and the signal is reduced. If the signal frequency is swept in synchronism with the horizontal sweep voltage of an oscilloscope while the crystal current detected in Arm 2 is applied to the vertical amplifier, an absorp-

tion dip will be seen on the screen as the frequency is swept over a band including the resonant frequency.

A directional coupler may be used similarly. Reference to Figs. 18-7b and 18-8 shows that a wave incident on the cavity divides at the two side openings separated by a distance equal to  $\lambda_g/4$ , and a small

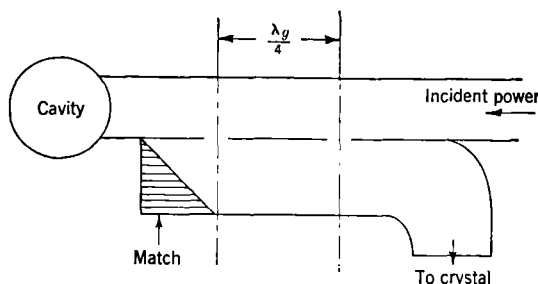


FIG. 18-8.—Directional coupler.

amount is sampled at each and passes into the side chamber. There the energy again divides at each opening, and half travels in each direction. The half going in the direction of the incident power adds and is dissipated in the matched load; that in the opposite direction cancels so that there is no crystal current. The opposite is true, however, for the wave reflected from the cavity; no energy from this wave goes toward the match, but a wave is transmitted to the crystal. The directional coupler therefore behaves in the same way as the magic T in this application, and they may be used interchangeably.

The magic T or directional-coupler setup may be used to measure standing-wave ratio with the aid of a variable transformer, as will be described in the next section.

A circuit diagram showing typical connections for sweeping the reflector voltage of the signal generator is shown in Fig. 18-9. Adjustment of the reflector voltage moves the trace to the right or left, and adjustment of the magnitude of the sweep voltage varies the amount of sweep.

**18-3. Measurement of Standing Waves.**—For cold measurements on magnetrons, standing-wave technique is of great value. The usefulness of this technique consists in the fact that it affords a method of measuring impedances at microwave frequencies where voltmeters and ammeters are out of the question. Use is made of the following property of the transmission line, namely, that the terminal impedance completely determines the standing-wave pattern in the line, which in turn is

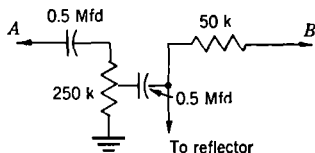


FIG. 18-9.—Reflector sweep circuit. (A) To plate of gas discharge sweep voltage generator tube in oscilloscope. (B) To reflector voltage supply.

characterized by two easily measured quantities: the standing-wave ratio and the position of the minimum voltage point.

Transmission-line theory gives the relationship between the two quantities specifying the complex impedance, and the two quantities specifying the character of the standing wave. These relationships are available in convenient form as circle contour charts giving the transformation from minimum position and standing-wave ratio to resistance and reactance or from resistance and reactance to minimum position and standing-wave ratio.

The transformation from standing-wave measurements to terminal impedance is made with the aid of the complex reflection coefficient  $q$ . Ordinarily the transmission line propagates only one mode, so that the field in the line is given by the linear superposition of two waves traveling in opposite directions. Their relative size and phase are such that the voltage-to-current ratio of the sums corresponds to the terminal impedance. If a voltage wave is given by the expression

$$Ve^{j\omega t} = V_0[e^{j(\omega t - \beta x)} + qe^{j(\omega t + \beta x)}],$$

the corresponding current wave is

$$Ie^{j\omega t} = \frac{V_0}{Z_0}[e^{j(\omega t - \beta x)} - qe^{j(\omega t + \beta x)}],$$

where  $V_0$  is the amplitude of the incident wave;  $\beta = 2\pi/\lambda_0 = \omega/c$  is the imaginary part of the propagation constant, which is purely imaginary because the line is considered lossless;  $x$  is the distance measured from the point where the impedance is considered to be located, and  $Z_0$  is the characteristic impedance of the line. The ratio  $V/I$ , evaluated at  $x = 0$ , is the terminal impedance  $Z_t$ ; hence

$$\frac{Z_t}{Z_0} = z_t = \frac{1 + q}{1 - q},$$

where  $z_t$  is the so-called "normalized" terminal impedance. Solving for  $q$ ,

$$q = \frac{z_t - 1}{z_t + 1}. \quad (1)$$

The impedance at any point in the line is given by the expression

$$z = \frac{1 + qe^{j2\beta x}}{1 - qe^{j2\beta x}}. \quad (2)$$

Here  $qe^{j2\beta x}$  may be regarded as the reflection coefficient of the length  $x$  of line terminated in the impedance  $z_t$ . There is, then, a 1-to-1 correspondence between reflection coefficient and impedance, and the



reflection coefficient merely changes in angle through the factor  $e^{i2\beta x}$  with movement away from the load along the line.

The complex transformation in Eq. (1) may be plotted on the complex  $q$ -plane in polar coordinates. The result is known as the "Smith chart" on which contours of constant resistance and reactance are circles.

The standing-wave ratio, the measurement of which is described below, is defined as the ratio of the maximum to the minimum voltage (or current) in the line. Along the line the maximum voltage will occur at the point where the reflected wave is in phase with the incident wave, and the minimum voltage occurs where they are out of phase. Thus the standing-wave ratio  $\rho$  is given in terms of the magnitude of the reflection coefficient as

$$\rho = \frac{1 + |q|}{1 - |q|} \quad (3)$$

Thus, the magnitude of the reflection coefficient is obtained from the measurable standing-wave ratio.

The angle of  $q$  is obtained from the position of the standing wave in the line. As the minimum-voltage position is sharp, it provides the most accurate measure of the position, or phase, of the standing wave. The minimum position occurs at the point  $x$  in the line where the impedance is real and minimum. From Eq. (2) this will occur when  $e^{i2\beta x} e^{i\theta} = -1$ , where  $\theta$  is the angle of the reflection coefficient, or

$$\theta = \pi - 2\beta x_{\min} \pm 2n\pi, \quad (4)$$

where  $n$  is an integer or zero and  $x_{\min}$  is the minimum position.

The dual relations giving  $y_l$ , the normalized terminal admittance, are given by noting that when  $z_l = 1/y_l$  is placed in Eq. (4), then

$$q = \frac{1 - y_l}{1 + y_l} \quad (5)$$

Thus, a point on an impedance chart rotated through  $\pi$  radians yields the admittance point. The above relations may then be used for admittances if this substitution is made.

*Standing-wave Measurement with Standing-wave Detector.*—The apparatus necessary for standing-wave measurement consists of the following pieces of equipment connected in tandem: a signal generator, a padding attenuator, a standing-wave detector, and a terminating load whose properties it is desired to study. A wavemeter is also connected somewhere between the signal generator and standing-wave detector unless wavelength measurements are made on the spectrum analyzer. From the standing-wave detector the signal is fed through a flexible coaxial line to the spectrum analyzer. Two or three tuning screws in the line near the attenuator provide a means of clearing up bad opera-

tion by changing the load into which the signal generator feeds. A stub tuner in the cable leading from the probe to the spectrum analyzer may be used to maximize the signal strength.

In operation, the traveling probe is set at the point where minimum signal is shown by the pip height on the spectrum-analyzer screen. The scale reading on the standing-wave detector is then noted. The probe is then moved to the point where maximum signal is seen, and the attenuator on the spectrum analyzer is turned until the pip height is the same as it was on the minimum reading. The standing-wave ratio is obtained from the two attenuator settings. This operation is usually repeated over the band of frequencies of interest in the particular measurement, the frequency or wavelength being noted at each point with the aid of the wavemeter attached to the spectrum-analyzer connections.

The spectrum-analyzer attenuator may be calibrated if necessary by comparing its reading with the known variation of field in a short-circuited transmission line and utilizing the fact that a sinusoidal pattern results which has minima separated by half a guide wavelength.

*Standing-wave Measurement with Absorption Resonance Indicator.*—The magic T or directional coupler arranged as a resonance indicator (Sec. 18-2) may also be used to determine the SWVR at resonance. If the standing-wave ratio at resonance is unity, the reflected wave from the cavity will be absent resulting in a zero reading at resonance on the trace. Quantitative measurements of the standing-wave ratio at resonance are possible by introducing a calibrated transformer of variable transformation ratio and variable phase into the line coming from the magnetron. Such a transformer is shown in Fig. 18-10. It takes the form of a tuning screw on a slotted section mounted in the same manner as the traveling probe of the standing-wave detector described earlier. The depth of the tuning screw is read on the dial indicator. Choke joints on the screw and on the traveling section prevent power losses from contacts and from coupling power out of the waveguide into the outside space. The screw introduces a transformer action, the transformation constant being the voltage standing-wave ratio or its reciprocal (depending on the phase) which would be set up by the screw in a matched line. This constant can be measured for various readings of the dial indicator by means of the standing-wave-detector setup described above and in Sec. 18-5. When used in this way the transformer is adjusted in phase and transformer constant until a match is indicated on the oscilloscope trace. The value of the standing-wave ratio at resonance can then be obtained from a previous calibration of the dial indicator. Standing-wave ratios off-resonance also may be measured in this way, but the value at resonance is usually of greatest interest.

It may be noted here that the standing-wave ratio at resonance is

the only quantity needed to compute the circuit efficiency of the ordinary resonant circuit, and the absorption-resonance indicator with the adjustable transformer thus provides a rapid method of measuring circuit efficiency.

Another application of the standing-wave measurement described above is to the preloading of loop-coupled magnetrons. The difficulty of adjusting the load on a magnetron within close tolerances in production

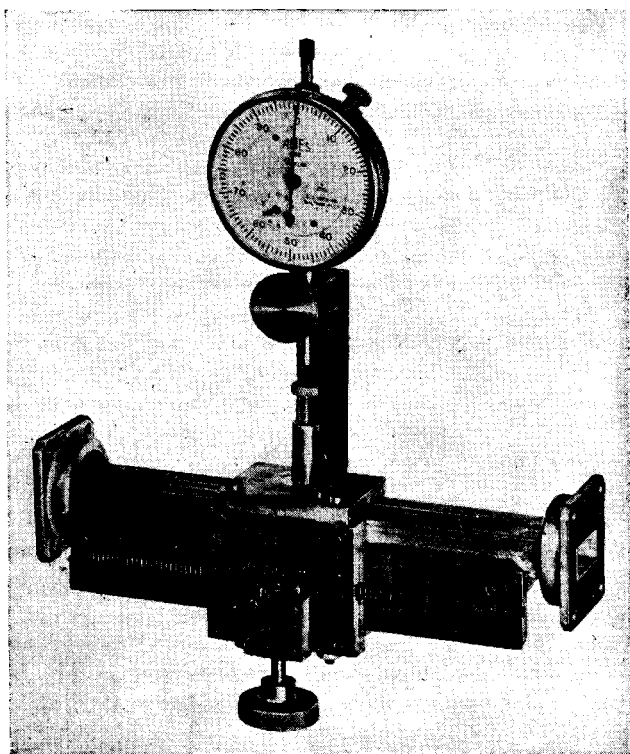


FIG. 18-10.—Adjustable transformer.

is overcome by this procedure, and small-scale laboratory use is also helpful. As will be shown later in the discussion of  $Q$ -measurements the standing-wave ratio at resonance, which may be measured rapidly as described above, is simply the ratio of the unloaded  $Q$  to the external  $Q$  of the cavity. If the unloaded  $Q$  can be controlled within sufficiently close tolerances, then the external  $Q$  may be monitored directly from the resonance standing-wave ratio. Adjustment to the correct value is made easily with the continuous visual presentation of data on the screen

of the oscilloscope. The unaltered unloaded  $Q$  of the cavity, which in practice ordinarily falls within a 10 per cent scatter range, may then be used as a standard load for comparison with the external load, or lossy material may temporarily be introduced into the cavity in a controlled way. If the unloaded  $Q$  is reduced to the desired value of the external  $Q$ , the variable transformer on the indicator setup may be eliminated with considerable simplification of the procedure.

**18-4. Field-pattern Measurements.**—The measurement of the field pattern of a magnetron-resonator system may be conveniently accomplished with the use of a rotary probe.<sup>1</sup> Such pattern measurements are useful for mode identification and for studies of the effect of asymmetries in a magnetron on the field pattern seen by the electrons.

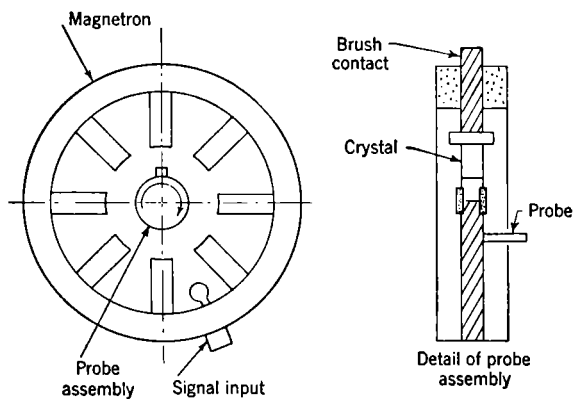


FIG. 18-11.—Rotary-probe assembly.

The rotary probe consists of a small capacitive probe mounted on a cylinder that occupies the space in the magnetron normally filled by the cathode. As the cylinder rotates, the variation of the probe current with angle provides a picture of the electric-field intensity at various angles. The field strength is shown in terms of a crystal current read on an oscilloscope whose horizontal-sweep voltage is synchronized with the rotation of the probe. The arrangement is shown schematically in Fig. 18-11. Interpretation of the pattern should take into account the fact that the crystal current is a function of the absolute value of the field only. Therefore, in the pattern of the  $\pi$ -mode, the alternate positive and negative fields appear as positive currents. In Fig. 18-12a is shown the actual field pattern of an eight-oscillator magnetron oscillating in the  $\pi$ -mode, and in Fig. 18-12b the corresponding current pattern seen on the oscilloscope is given. For this number of oscillators the  $\pi$ -mode

<sup>1</sup> This method was first suggested to the Radiation Laboratory by the Westinghouse Research Laboratories at Pittsburgh, Pa.

corresponds to  $n = 4$ , and the number of peaks is seen to be equal to  $2n$ . This relationship holds for all the modes.

A special phenomenon is observed with longitudinal variation of the probe position in strapped tubes. The presence of one strap nearer to the interaction space than the other at the end of the tube causes the field of the alternate metal tips to which that strap is attached to predominate. The actual field is then altered as in Fig. 18-12c, the corresponding crystal current being given in Fig. 18-12d. The degree to which the alternate tips are raised or lowered for off-center positions

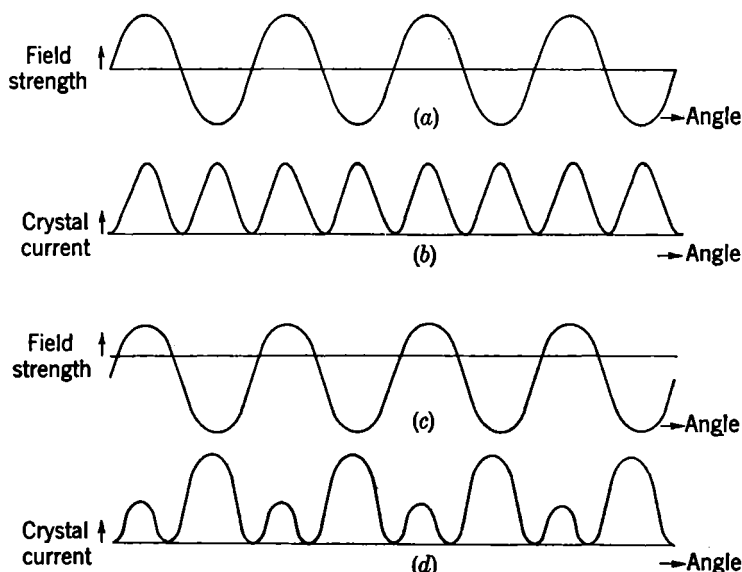


FIG. 18-12.—Field patterns and their presentation by a rotary probe. (a) Ideal field pattern; (b) oscilloscope pattern corresponding to (a); (c) field pattern distorted by strap; (d) oscilloscope pattern corresponding to (c).

of the probe is an indication of the degree of field distortion due to strapping.

It frequently occurs that two modes are so closely spaced that they are both excited at the same time. The resulting pattern is then a combination of the two patterns and may be difficult to interpret.

Details of the equipment are shown in Fig. 18-13. A variable-speed motor rotates the probe. The motor should be run by direct current so that hum picked up from a-c fields will not decrease the sensitivity of the electrical system. Attached to the probe shaft is a small magnet which with each rotation passes by a fixed coil on a yoke and thus induces a synchronizing signal which is connected to the external synchronization

post on the oscilloscope. The probe is removable so that various sizes may be used according to the requirements of the problem. The crystal is contained inside the probe barrel, and the current is taken off the top of the probe by means of a brush. The platform to which the magnetron is clamped is movable vertically so that longitudinal studies of the pattern can be made.

The signal from the brush must be amplified about one hundred times before it is strong enough to show on an oscilloscope of ordinary sensitivity. The amplifier must be capable of good low-frequency response, since slow rotational speeds are necessary to minimize brush

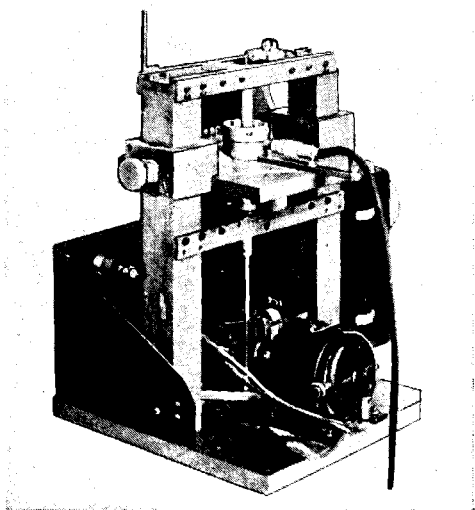


FIG. 18-13.—Rotary-probe setup.

noise. A high-frequency response of about 600 cps is sufficient to show the individual peaks. Phase as well as amplitude distortion in the pass band should be low.

The magnetron may be excited by means of a single coupling loop fed from a signal generator. If the mode spacing is wide, a large loop may be used; but if not, the overlap of modes must be minimized by keeping the loop small. Extremely large loops should not be used because they tend to distort the pattern. If the signal strength is too small, it is frequently necessary to insert a double-stub tuner at the coupling loop so that maximum power may be coupled into the tube.

A variation of the method of handling the signal, developed at Westinghouse, makes use of a modulated oscillator. The r-f signal

exciting the magnetron is modulated with a square-wave modulator of fundamental frequency  $F$ , and the highest frequency of the pattern under study is  $f$ . The sideband frequencies are then  $F \pm f$ , and a bandpass filter containing these would provide an envelope pattern corresponding to the line pattern given by the other arrangement and yet would eliminate considerable brush noise.

**18-5. Measurement of  $Q$ .**—The adjustment of the r-f load of the magnetron is based upon the measurement of  $Q$ 's, as is the determination of internal copper losses through which problems relating to circuit efficiency are solved. The usual definition of  $Q$  is adopted here, that is, the ratio of the stored energy to the energy dissipated per radian. It has been found convenient, however, to divide the dissipated energy into two categories: energy dissipated in the external load and energy dissipated as internal copper losses of the resonant cavity. The  $Q$  accounting for the former is called the "external"  $Q$  and for the latter the "unloaded"  $Q$ . In addition, reference is made to the  $Q$  accounting for the entire loading of the cavity, the "loaded"  $Q$ . From the definitions, the following relationship is written between these quantities:

$$\frac{1}{Q_U} + \frac{1}{Q_E} = \frac{1}{Q_L},$$

where  $Q_U$  is the unloaded  $Q$ ,  $Q_E$  is the external  $Q$ , and  $Q_L$  is the loaded  $Q$ . The problem now is to measure these quantities.

*The Lawson Method.*—An accepted procedure for measuring these  $Q$ 's is the Lawson method. The detailed discussion of this procedure is introduced by a brief review of the theory.

Reference will be made to a simple parallel-resonant circuit, the equivalence of which to the cavity near one of its resonant modes has been justified both theoretically and experimentally for rather general conditions. It has been shown (Sec. 18-3) that the impedance or admittance terminating a transmission line may be measured in terms of the position of the voltage minimum and the standing-wave ratio of the wave in the line. In order to utilize admittance measurements to measure  $Q$ , use is made of the facts that energy storage in a resonant circuit is proportional to the slope of the susceptance curve vs. frequency and that the energy dissipated is obtained from a knowledge of the conductance representing the copper losses.

In terms of the equivalent circuit, a voltage  $\tilde{V}e^{j\omega t}$  can be applied to the terminals, where  $\omega_0$  is the resonant radian frequency; that is  $\omega_0 = 1/\sqrt{LC}$ . The energy stored at resonance is constant throughout the cycle so that it may be evaluated at the time when the voltage is instantaneously maximum and the current through the inductance is zero. The stored energy is then  $\frac{1}{2}C\tilde{V}^2$ . But  $C$  is given by  $\frac{1}{2}(dB/d\omega)_0$ ,

where the subscript denotes resonance. The stored energy is therefore

$$U = \frac{\tilde{V}^2}{4} \left( \frac{dB}{d\omega} \right)_0. \quad (6)$$

It is possible to show directly from Maxwell's equations that this relation holds for most microwave resonant cavities near a single resonant mode even though the lumped constants  $L$  and  $C$  lose their direct physical significance. The  $Q$  of the cavity is then given by the expression

$$Q = \frac{\frac{\tilde{V}^2}{4} \left( \frac{dB}{d\omega} \right)_0}{\frac{1}{2} \tilde{V}^2 \frac{G}{\omega_0}} = \frac{\omega_0}{2G} \left( \frac{dB}{d\omega} \right)_0 = \frac{\omega_0}{2g} \left( \frac{db}{d\omega} \right)_0,$$

where  $g$  and  $b$  are the normalized values of  $G$  and  $B$ . If  $g_0$  represents internal losses, the separate  $Q$ 's are

$$Q_U = \frac{\omega_0}{2g_0} \left( \frac{db}{d\omega} \right)_0; \quad Q_E = \frac{\omega_0}{2} \left( \frac{db}{d\omega} \right)_0; \quad Q_L = \frac{\omega_0}{2(1+g_0)} \left( \frac{db}{d\omega} \right)_0. \quad (7)$$

It is seen that measurement of the  $Q$ 's resolves itself into measurement of  $\omega_0$ ,  $g_0$ , and  $(db/d\omega)_0$ . The quantity  $\omega_0$  is easily determined as previously described; but as it comes from the data required for the other two quantities, a separate determination of the cavity resonant frequency is not necessary.

The measurement of the slope  $(db/d\omega)_0$  is ordinarily made in terms of the half-power points, the frequencies at which  $|b| = g_0 + 1$ , or the susceptance is equal in magnitude to the total conductance connected to the cavity, including the matched transmission line. If these radian frequencies are denoted by  $\omega_1$  and  $\omega_2$ ,

$$Q_L = \frac{\omega_0}{|\omega_1 - \omega_2|} = \frac{\lambda_0}{|\lambda_1 - \lambda_2|}, \quad (8)$$

since  $db = 2(1+g)$  for  $d\omega = |\omega_1 - \omega_2|$ .

The problem is now to measure  $\omega_1$  and  $\omega_2$  and  $g_0$ . These may be obtained from curves of measured standing-wave ratio and minimum position plotted against wavelength. Two cases arise which will be discussed separately.

CASE 1.  $g_0 < 1$ .—If the loading due to internal losses is less than the loading by the transmission line, curves of the shape indicated in Fig. 18-14 result. Using Eqs. (3) and (5), the standing-wave ratio at resonance is  $\rho_0 = 1/g_0$ , whereas at the half-power points, where



$$y_i = g_0 \pm j(g_0 + 1),$$

$$\rho_{1,2} = \frac{\sqrt{2} + \sqrt{\left(\frac{1-g_0}{1+g_0}\right)^2 + 1}}{\sqrt{2} - \sqrt{\left(\frac{1-g_0}{1+g_0}\right)^2 + 1}}. \quad (9a)$$

Replacing  $g_0$  by  $1/\rho_0$ ,

$$\rho_{1,2} = \frac{\sqrt{2} + \sqrt{\left(\frac{\rho_0 - 1}{\rho_0 + 1}\right)^2 + 1}}{\sqrt{2} - \sqrt{\left(\frac{\rho_0 - 1}{\rho_0 + 1}\right)^2 + 1}}. \quad (9b)$$

Because Eq. (9) expresses  $\rho_{1,2}$  in terms of  $\rho_0$  only,  $\lambda_1$  and  $\lambda_2$  may be determined from the standing-wave ratio curve alone, as is  $g_0$ . The process is illustrated in Fig. 18-14. Equation (8) is plotted in Fig. 18-15.  $Q_L$  is determined from Eq. (7), and the other  $Q$ 's are given by

$$Q_U = Q_L(1 + \rho_0),$$

$$Q_E = \frac{Q_U}{\rho_0}. \quad (10)$$

Although it is possible to determine the  $Q$ 's as described above from

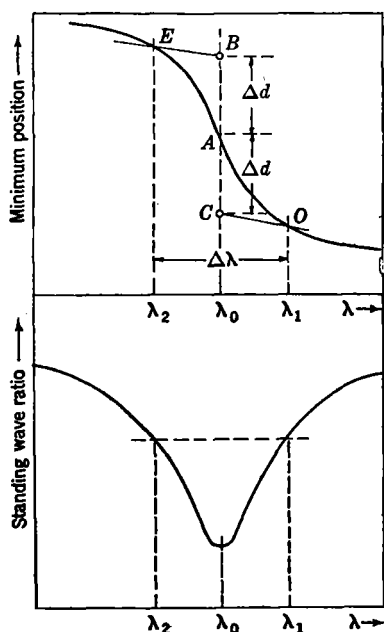


FIG. 18-14.— $Q$ -curves for nonlossy case ( $g_0 < 1$ ).

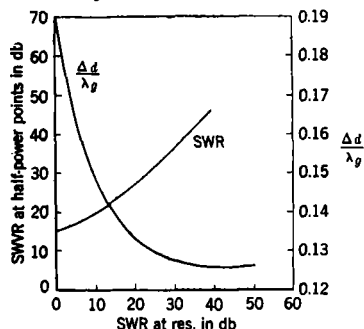


FIG. 18-15.—Lawson curves.

the standing-wave ratio curve alone, it is frequently more accurate to make use of the minimum-position curve. The value of  $g_0$  must still be determined from the standing-wave ratio at resonance as before, but the half-power wavelengths are taken from the minimum-position curve. Since the minimum position is determined by the angle of the

reflection coefficient, the problem is to compute the angular shift in  $q$  or  $\theta$ , from resonance to the half-power points. At resonance  $\theta = 0$  because the load admittance  $y_l = g_0 < 1$ . At the half-power points where  $b = \pm(1 + g_0)$ ,

$$\theta = \Delta\theta = \mp \tan^{-1} \frac{1 + g_0}{1 - g_0} \mp \tan^{-1} \frac{1 + g_0}{1 + g_0} = \mp \left( \tan^{-1} \frac{1 + g_0}{1 - g_0} + \frac{\pi}{4} \right).$$

From Eq. (4),  $\Delta\theta = -2\beta\Delta d = -4\pi(\Delta d/\lambda_0)$ , where  $\Delta d$  is the minimum-position shift from resonance to the half-power frequency. Substituting the value for  $\Delta\theta$  and  $\rho_0 = 1/g_0$ ,

$$\frac{\Delta d}{\lambda_0} = \pm \left( \frac{1}{4\pi} \tan^{-1} \frac{\rho_0 + 1}{\rho_0 - 1} + \frac{1}{16} \right). \quad (11)$$

The positive sign corresponds to the high-frequency side of resonance for by Eq. (6) the slope of the  $b$  against  $\omega$ -curve is positive ( $U$  being positive), and the positive sign corresponds to positive  $b$ . It should be noted that the minimum position shifts toward the load with increasing frequency when  $g_0 < 1$ , a fact that will be used to identify this case when it is subsequently shown that the opposite is true when  $g_0 > 1$ .

Equation (11) is plotted along with  $\rho_{1,2}$  against  $\rho_0$  in Fig. 18-15.

CASE 2,  $g_0 > 1$ .—This case occurs less frequently, except at low wavelengths where small cavity dimensions lead to high losses, because the condition  $g_0 > 1$  implies that the internal losses are greater than the power delivered to the matched transmission line. The standing-wave ratio at resonance is  $\rho_0 = g_0$  instead of  $1/g_0$  as before. Equation (9a) was derived by putting  $y_l = g_0 \pm j(g_0 + 1)$  in Eq. (5), then putting  $|q|$  in Eq. (3). Thus, Eq. (9a) holds for the present case as well, and it will be seen that replacing  $g_0$  by  $1/g_0$  leaves Eq. (9a) unchanged, and therefore Eq. (9b) also holds.

The minimum-position shift is slightly more complicated. At resonance,  $y_l = g_0$  is greater than 1, and hence from Eq. (4)  $\theta = \pi$ . Then Eq. (11) subtracted from  $\pi/4\pi = \frac{1}{4}$ , with  $\rho_0$  replaced by  $1/\rho_0$ , reverts to the same Eq. (11) with the sign reversed and  $\frac{1}{16}$  replaced by  $\frac{3}{16}$ . As the positive sign then corresponds to the low-frequency side of resonance, this case is identified by a minimum-position shift away from the load with increasing frequency. The Lawson curves for half-power point standing-wave ratio and minimum-position shift therefore are applicable to both cases. This latter case is shown in Fig. 18-16.

Equations (10) are altered by replacing  $\rho_0$  by  $1/\rho_0$ .

Referring to Fig. 18-14, the resonant wavelength may be taken from either curve, as it is the center of symmetry in either case. When the resonant properties are only approximated by the simple circuit, the center of symmetry of the curves will be slightly off the resonant wave-

length; in this case the resonant frequency is taken from the minimum-position curve, for it is from this curve that the final  $Q$  readings are taken. The minimum position at resonance, which is the point in the line where the cavity appears series-resonant and which is a quarter wavelength from the point at which the cavity appears parallel-resonant, is obtained at the same time.

The effect of a length of line between the cavity and the measuring device is shown in the  $Q$  curves of Fig. 18-14 in the slope of the minimum-position curve off-resonance. This slope is due to the change in electrical length of line caused by the change in wavelength across the curve. Its effect is to give the plot on oblique coordinates not at right angles to each other; that is, the curves are considered to be plotted on a vertical minimum-position axis but on a wavelength axis differing from the horizontal by an angle depending on the length of line between the measuring equipment and the cavity and on other frequency-sensitive elements in the lead. By thus considering the plot, all the corrections necessary to take this effect into account in the measurement are automatically made. Points  $\Delta d$  above and below the resonance minimum position are projected at this angle instead of horizontally to the intersection with the curve. Incidentally, the value of the slope taken from the curve provides an experimental check on the equivalent length of line to the cavity, which in many cases may not be computed from the geometry because of the complicated structure of the line from the cavity.

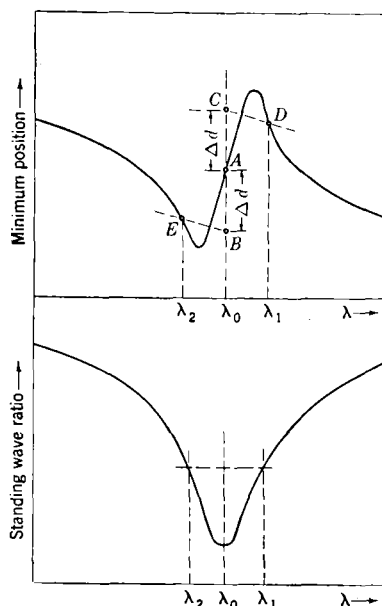


FIG. 18-16.— $Q$ -curves for lossy case ( $g_0 > 1$ ).

The circuit efficiency, or the ratio of the power delivered to a matched line to the total power dissipated in the matched line and cavity, is given by the expression

$$\eta = \frac{g_0}{g_0 + 1}$$

The circuit efficiency is seen to depend only on the standing-wave ratio at resonance.

Another piece of information to be obtained from a Lawson-method  $Q$ -measurement is the loss introduced into the circuit by the output lead. The standing-wave ratio far off-resonance is a measure of this loss. The effect of this loss on the circuit efficiency may be deduced from the approximate equivalent circuit of Fig. 18-17. The value of the resistor representing the lead loss may be taken from the standing-wave ratio off-resonance; thus,  $g_1 = \rho$ .

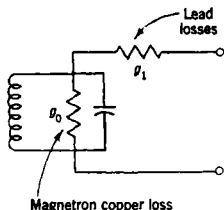


FIG. 18-17.—Equivalent circuit of cavity with lead losses.

Ordinarily the lead losses are so small that they do not affect the  $Q$ -measurement; but if the off-resonance standing-wave ratio is low enough (of the order of 20 db), a correction must be made in the  $Q$ -measurement process. This correction is not given here but may be derived from the circuit of Fig. 18-17 in those cases which require it.

An alternative approximate way of handling lead losses is to consider the transmission line to the cavity as having a complex propagation constant, the magnitude of the loss being again given by the off-resonant standing-wave ratio.

*Modifications of the Lawson Method.*—One modification applicable only to tunable cavities and using the same equipment as the previous method has the advantage of being fast at the cost of some loss in accuracy. The signal generator is set to the wavelength where it is desired to measure the  $Q$ . With the cavity tuned far off-resonance, the standing-wave detector is set at a voltage maximum point; this may best be done by reading the minimum-voltage point and setting it a quarter wavelength from this point (in either direction). The cavity is then tuned until the height of the pip on the spectrum-analyzer screen goes through a minimum, indicating that the minimum position has shifted one quarter wavelength. The resonant frequency of the cavity is then close to the signal-generator setting. Deviation from this condition may be due to variation of signal-generator output with load variation. The signal generator is next set as nearly as possible to resonance by measuring the standing-wave ratio at a few points on either side of the original wavelength. The standing-wave detector is then set to each of the half-power minimum positions (see Fig. 18-15), and the signal generator adjusted until the pip goes through a minimum at each point. The difference in wavelength of these two points may then be used to compute the  $Q$ 's as before. Although this method is fast, it does not take into account the variation of electrical line length with wavelength as described above, and the readings are somewhat inaccurate. It may be used for obtaining variation in  $Q$  over the tuning range of a tunable cavity where the large number of  $Q$  values to be taken requires a faster method of

getting the data. Here the absolute value of the  $Q$  may not be so important as its variation, and the absence of the line-length correction will then not be serious.

A second variation of the Lawson method makes use of the standing-wave-ratio measurement obtained with the absorption-resonance indicator. As discussed in Sec. 18-2, the standing-wave ratio at resonance may be measured with this device, and from the Lawson curve of Fig. 18-15 the standing-wave ratio at the half-power points is obtained. The adjustable transformer screw (see Fig. 18-7) is set to this value, the two wavelengths at which balance of the bridge is obtained being the half-power wavelengths. This process may be carried through rapidly. From the result the  $Q$ 's may be computed. The errors of this method are large also, the principal source of error being the inaccuracy with which the standing-wave ratio determines the frequency. The value of the circuit efficiency, because it is obtained only from the standing-wave ratio at resonance, is usually good, but the half-power wavelengths for the measurement of the  $Q$ 's cannot be measured so accurately and introduce errors in the  $Q$ 's.

It should be noted that the two possible types of resonance illustrated in Figs. 18-14 and 18-16 may be distinguished by making use of the fact that the direction of the minimum shift is different in the two cases. In Case 1,  $g_0 < 1$ , the dip on the screen of the oscilloscope increases in wavelength when the adjustable transformer screw is moved toward the T if it is set near the correct value for measuring the standing-wave ratio at resonance. The opposite is true of Case 2 ( $g_0 > 1$ ).

The Lawson method gives good results until the  $Q$  falls below about 50, when it is often desirable to modify the method somewhat. Then it is convenient to use the slope of the minimum-position curve rather than to locate the half-power points; data need then be taken over only a large enough range to get an accurate value of the slope. At the same time the error due to line length is much more pronounced and must be carefully taken into account.

The external  $Q = Q_E$  may be determined from the slope of the minimum-position curve. The result depends, however, on the standing-wave ratio at resonance, as does the minimum shift to the half-power points. This complication can be neglected when  $Q_E$  is low because, as a result of the heavy loading, the standing-wave ratio at resonance is always very high. The standing-wave ratio at resonance is given by  $Q_U/Q_E$ , and with reasonable  $Q_U$  (typical value being about 2000 at S-band or 1000 at X-band) and low  $Q_E$  there exists essentially a lossless circuit. For the lossless case then,

$$Q_E = \pi \frac{\lambda}{\lambda_g} \frac{dm}{d\lambda},$$

where  $m$  is the minimum position given in the same units as  $\lambda$  and  $\lambda_g$  is the guide wavelength. The loaded  $Q$  is essentially the same as the external  $Q$  under the present conditions. The unloaded  $Q$  may be obtained by measuring the standing-wave ratio at resonance and making use of Eq. (5). Often, however, the unloaded  $Q$  is not needed.

The correction for electrical-line-length change with wavelength may be made most easily by regarding the length of line as an additional resonant circuit whose external  $Q$  adds to that of the cavity being measured. A direct measurement is possible by placing a short circuit across the line or waveguide at the coupling point with the cavity. The slope of the minimum-position curve is measured and its effective  $Q_E$  computed by Eq. (7) and subtracted from the  $Q_E$  of the cavity plus line-length combination. When the geometry of the coupling is simple, the line  $Q_E$  may be computed from the equation

$$Q_E = \frac{\pi}{2} n',$$

where  $n'$  is the equivalent number of half wavelengths of line. In the case of coaxial line,  $n'$  becomes  $n$ , the physical number of half wavelengths, whereas  $n' = (\lambda_g/\lambda)^2 n$  in the waveguide case.

There exists an alternative method of obtaining the minimum-position curve vs. wavelength that may be convenient under certain conditions. If a certain wavelength is being fed into the cavity-plus-line system and the minimum position is noted, a short circuit may be placed at the minimum position to obtain a system resonant at the wavelength in question. Use is made of this fact to get the minimum-position curve by measuring the resonant wavelength of the system as a function of plunger motion when a movable plunger is varied along the output line. The resonant-wavelength measurement may be performed by any of the methods previously given, and from the data obtained and from Eq. (7) one may compute external  $Q$  looking into the output that is being tuned by the plunger.

The unloaded  $Q$  may also be found by a transmission method. Power is fed into one small loop and detected in another small loop in a cavity. Transmitted power as a function of wavelength may be used to obtain the unloaded  $Q$  directly from the half-power points. Refinements of this method for high  $Q$ 's may be made using a sweep presentation on the screen of an oscilloscope so that the operation may be done rapidly.

*Location of Resonant-circuit Terminals.*—The properties of a resonant circuit are ordinarily given when the  $Q$ 's and resonant wavelength are specified, but in the case of a transmission line at microwave frequencies there is an additional parameter that is needed to specify the resonant circuit completely. This parameter is the location of the terminals of the

resonant circuit in the line. There is an ambiguity which may be removed by specifying the character of the resonant circuit as either series or parallel resonance. A series circuit is transformed into a parallel circuit by an addition of a quarter wavelength of line, and the subtraction of a quarter wavelength of line reverses the procedure. Reference will be made in the following discussion to parallel resonance with the understanding that the terms may be changed to apply to those of series resonance if desired.

The location of the resonant circuit in the line is accomplished to a certain degree of accuracy when the Lawson method of  $Q$ -measurement is employed. The point  $A$  of Figs. 18-14 and 18-16 is the point in the line where the circuit is series resonant, and therefore the parallel-resonance point is one quarter wavelength from this point in either direction.

For some purposes it is necessary to measure the position of the terminals very accurately. A method is described below in which the location of this point may be obtained as a correction to a previous determination. The method was first developed for attaching a stabilizing cavity to a magnetron in the output line where the distance between the resonant circuits had to be very closely an integral number of half wavelengths.

In Fig. 18-18 are shown two parallel-resonant circuits connected by a length of transmission line. The two resonant circuits are taken to be of the same resonant wavelength  $\lambda_0$ . Reference to other wavelengths will be made in terms of their percentage difference from  $\lambda_0$ , or by the relation

$$\delta = \frac{\lambda - \lambda_0}{\lambda_0}.$$

The results of solving the circuit of Fig. 18-18 for its modes, or resonances, are

$$\frac{\delta_a + \delta_b}{2} = \frac{\Delta l}{\lambda_0 n'}, \quad (12)$$

$$\frac{\delta_a - \delta_b}{2} = \sqrt{\left(\frac{\Delta l}{\lambda_0 n'}\right)^2 + \frac{1}{2\pi n' y_c'}} \quad (13)$$

where the subscripts  $a$  and  $b$  refer to the long- and short-wavelength modes respectively,  $l$  is the physical length of transmission line that is to be made equivalent to an integral number of electrical half wavelengths at the resonant wavelength of the parallel-resonant circuits after the correction  $-\Delta l$  is made,  $\lambda_0$  is the guide wavelength if the transmission

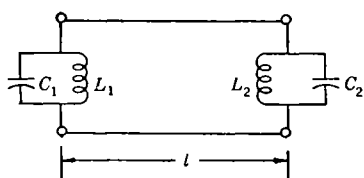


FIG. 18-18.—Two resonant circuits connected by transmission line.

$$y_{c1} = \sqrt{\frac{C_1}{L_1}} \frac{1}{Y_0}, \quad y_{c2} = \sqrt{\frac{C_2}{L_2}} \frac{1}{Y_0}$$

line is waveguide or the space wavelength in a coaxial line, and  $y'_c$  is the characteristic series admittance for  $y_{c1}$  and  $y_{c2}$ ; that is  $z'_c = z_{c1} + z_{c2}$ . The quantities  $y_{c1}$  and  $y_{c2}$  are numerically equal to the corresponding external  $Q$ 's. The resonance whose wavelength is very near to  $\lambda_0$  has been omitted as unimportant in the present discussion.

Equations (12) and (13) form the basis of measuring the line-length error  $\Delta l$ ; and  $\lambda_p$  being known at the point where the correction is made, all that is required for  $\Delta l$  is a knowledge of  $n'$  in Eq. (12). The value of  $\Delta l/\lambda_0 n'$  from Eq. (12) is substituted in Eq. (13) along with the value of  $y'_c$ , which may be obtained from  $Q$ -measurements, and the equation solved for  $n'$ . This value put back in Eq. (12) gives the value of  $\Delta l$ .

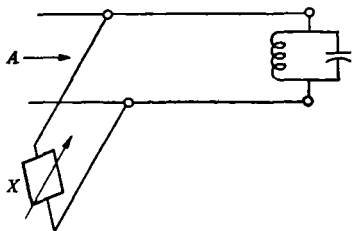


FIG. 18-19.—Resonant circuit and T connected by transmission line.

The above equations have been developed on the basis of two resonant circuits. One of these may be omitted from the equations simply by making  $y'_c$  equal to  $y_c$ , the normalized characteristic admittance of the remaining circuit. Use of both forms of the equations will be made.

For the measurement of  $\delta_a$  and  $\delta_b$ , two cases will be discussed, one in which there are two resonant circuits or cavities separated by a length of line (Fig. 18-18) and the other in which there is one resonant circuit with a length of line terminated in a T as shown in Fig. 18-19. The first step in either case is setting up the first approximation to the correct length of line. The  $Q$ 's of the two cavities or of the one cavity (as the case may be) are measured by the Lawson method, giving the external  $Q$  and the minimum position at resonance. In the two-cavity system, the two circuits are connected so that their minimum positions at resonance occur at the same point in the line. In the T system, the T is placed so that a parallel connection of the three arms is made at a quarter wavelength from the minimum position at resonance or so that a series connection is made at the minimum position at resonance. Within the accuracy of the  $Q$ -run data, then, the connecting line will be of the correct length. Then the mode wavelengths are measured, and from these the correction to the tentative line length set by the  $Q$ -run data is computed.

In the two-cavity case, there is usually a T of some sort for coupling the system to a load. If not, a probe may be installed for the purpose of measuring the wavelengths of resonance. The mode wavelengths are measured directly by any of the means previously described; the data put into the equations given above; and the correction to the line length computed. The line length is the total separation of the cavities.



A variation of the two-cavity system is one in which one cavity is replaced by a short circuit. It will be noted that a short circuit is a resonant circuit in which  $y_c = \infty$ .

In the T case, use is made of a special technique for determining the mode wavelengths. Figure 18-19 shows the T connected to the length of line terminated in the resonant circuit. A variable reactance is connected to one pair of terminals. The resonances seen looking in the terminals *A* will be the resonances of the system of the resonant circuit, the line length, and the variable reactance. The resonance of importance here is the one corresponding to a short circuit at the T terminals. Since for this condition the system is short-circuited from the terminals *A*, the resonance will not be visible on the resonance indicator. As the reactance is varied about this point, the resonance dip on the indicator will progress as shown in Fig. 18-20, a deep resonance dip appearing first, becoming smaller, disappearing completely, and then reappearing, while the wavelength of the dip changes continuously. The disappearance or

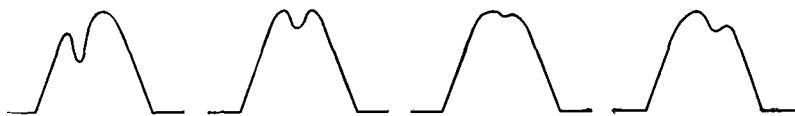


FIG. 18-20.—Measurement of wavelength by null method.

null wavelength is then the mode wavelength to be measured. There will be two such modes: one below the cavity frequency and one above. The wavelength measurement may be made very precisely because the indication is sharp; it is thus possible to obtain great accuracy in the line-length error measurement.

The exact nature of the variable reactance depends on the individual problem. A plunger in waveguide in one of the T arms is suitable. Furthermore, another cavity may be used, the variation in reactance being accomplished by tuning the cavity. The two methods of getting mode wavelengths described here may be combined. Two cavities connected by a length of line and tapped into by means of a T may be adjusted for correct line lengths by measuring the over-all correction as in the first case and the cavity-to-T correction by the second method. The correct relationship between the two cavities and the T may then be easily adjusted.

**18-6. The Stabilization Factor.**—The concept of stabilization was developed as the result of an effort to provide additional r-f energy storage in the resonant system of the magnetron for the purpose of stabilizing its operating frequency. Design of stabilizing equipment is discussed in Chap. 16. The measurement of the degree of stabilization by cold-

measurement techniques is described here, and the results extended to other uses.

The concept of stabilization may be used wherever there exists a resonant system that may be divided into parts for convenience in analysis. Stabilization by means of an external cavity is a problem of this nature. The magnetron contains a resonant system of its own, and the addition of another resonant cavity to the entire resonant system simply adds to the r-f energy storage. The stabilization factor is defined as the ratio of the total r-f energy stored in the entire system to the energy stored in the part of the system used as a basis for reference. Thus, the stabilization factor of the stabilized magnetron system is the ratio of the total energy stored to the energy stored in the magnetron alone. This definition will now be related to practical methods of measurement.

The measurement of stabilization factor rests on the same basis as the measurement of  $Q$ ; that is, the energy storage in a resonant system is proportional to the rate of change of reactance with respect to frequency in a series-resonant system (a system in which resonance is defined as zero susceptance). Since reference to a specific energy level which depends on driving current or voltage is to be avoided, a ratio of energies is taken as in the case of the  $Q$ .

A description is first given of a method for measuring stabilization factors that makes use of the  $Q$ -measurement methods already developed. Stabilization may be measured through the medium of  $Q$ -measurement in at least two different ways. One of these is based directly on the definition of stabilization. If the external  $Q$  of a system is measured looking into a certain output where the measurement is made, a value is obtained that is proportional to the energy stored in the system. If all but the part of the system to which the stabilization factor is referred is shunted out of the system and the external  $Q$  measured again, the stabilization factor will be the ratio of the first to the second  $Q$  taken. In shunting out the remainder of the resonant system the fields at the division surface must be replaced by identical fields that are not frequency sensitive, or in other words that are not associated with energy storage. It is apparent that this process may be very difficult, and for this reason it can usually be done only when the division surface is a surface of zero electric field. Then it is necessary only to replace this surface with a metal surface, thus providing a short circuit. For example, a cavity that is iris-coupled to a magnetron makes up a stabilizing system whose stabilization factor is the ratio of the external  $Q$  looking into the regular output under normal conditions to the external  $Q$  looking in the same way but with the iris filled with a wedge of copper. It is necessary for the field configuration to be kept the same for the two  $Q$ -measurements so that the external

coupling will not be changed. If the coupling were different in the two cases, the proportionality factor of the energy storage would change and the result would be in error.

The second method making use of  $Q$ -measurements may be used when the coupling between the cavities is made in standard transmission line. Then the external  $Q$ 's looking into each cavity separately may be measured, the stabilization factor being 1 plus the ratio of the stabilizing cavity  $Q$  to the magnetron  $Q$ , using the stabilized magnetron case as an example.

A third method of measuring stabilization factor makes use of relative tuning rates. A tunable cavity, when stabilized, tunes less for a given motion of the tuner; that is, as implied by the term "stabilization," the frequency constancy is increased. The quantitative aspects of this behavior are derived from Fig. 18-21, which shows two curves of reactance vs. radian frequency, one for each circuit. Curve  $A$  is assumed to be the reactance curve of the tunable stabilizing cavity, and  $B$  that of the reference cavity. Resonance exists where the sum of the curves is zero. When the two curves both pass through zero reactance at the same point, their resonant frequencies are identical and equal to  $\omega_0$ . Shifting the frequency of  $A$  to  $\omega_1$ , corresponding to the curve  $A'$ , results in making the resonant frequency of the combination  $\omega'_0$ . If  $\Delta_A\omega$  represents  $\omega_1 - \omega_0$  and  $\Delta_T\omega$  represents  $\omega'_0 - \omega_0$ , it may be derived from the geometry of Fig. 18-21 that

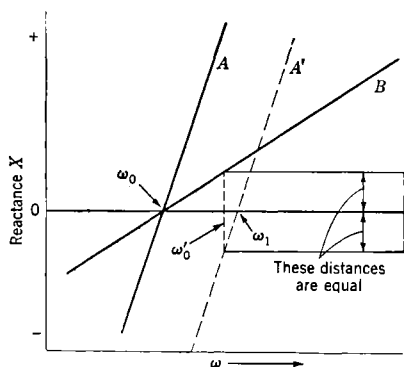


FIG. 18-21.—Effect of tuning the stabilizing cavity.

$$S_{A,B} = \frac{\frac{dX_A}{d\omega} + \frac{dX_B}{d\omega}}{\frac{dX_B}{d\omega}} = \frac{1}{1 - \frac{\Delta_T\omega}{\Delta_A\omega}} \quad (14)$$

Here,  $S_{A,B}$  is the stabilization factor of  $A$  with respect to  $B$  ( $B$  is the reference cavity) and  $\Delta_T\omega/\Delta_A\omega$  is the percentage tuning rate, the factor by which the tuning rate of the stabilizing cavity is reduced by using it for stabilization. The problem now becomes the measurement of the percentage tuning rate. This measurement may be made easily by means of the usual wavelength-measurement methods, the tuning rates being

made on the entire system and on the stabilizing cavity alone with the reference cavity blocked off.

If it is more convenient to tune the reference cavity, the data may be changed to the desired form by means of the relationship

$$S_{A,B} = 1 + \frac{1}{S_{B,A} - 1} = \frac{S_{B,A}}{S_{B,A} - 1}. \quad (15)$$

The stabilization factor, then, may be measured by means of  $Q$ -measurements or by relative tuning rates. In practice,  $Q$ -measurements with and without stabilizing cavity are more accurate for high-stabilization factors, relative tuning rates for low-stabilization factors, and independent  $Q$ -measurements in the connecting line for either. However, a high-stabilization case may be changed into a low-stabilization case by reversal of the sense of stabilization; that is, a cavity stabilizing a magnetron with a high-stabilization factor is itself stabilized by the magnetron with a low-stabilization factor. This fact is shown by Eq. (15).

The concept of stabilization may be used for other purposes, such as the measurement of  $L/C$  ratio of a magnetron oscillator. This problem turns out to be that of measuring either  $L$  or  $C$ , because the other may be computed from the knowledge of the resonant frequency of the cavity.

The problem of determining the value of  $C$  as seen by the electrons in a magnetron will be considered. It is assumed that a hole-and-slot magnetron is being measured; the vane magnetron is more difficult to measure, but the same method may be used. In the region of the slot the capacitance may be computed from the usual formula for a parallel-plate condenser. It is then recognized that the equivalent capacitance of the cavity is greater than that due to fringing fields and displacement currents in the inductive region of the oscillator. The problem then becomes one of measuring the stabilization factor of the extra equivalent capacitance with respect to the computed capacitance. (Energy storage in a parallel-resonant circuit is proportional to capacity.) This is done by inserting a slab of nonconducting material of known dielectric constant into the space whose capacitance may be computed and noting the shift in resonant frequency. The shift to be expected if the total capacitance were lumped into this space may be computed from the dielectric constant, and this value may be compared with the experimental value, the stabilization factor being computed from Eq. (14). The effective capacitance may then be computed by multiplying the computed capacity by the measured stabilization factor.

**18-7. Magnetron-mode Identification.**—Much of the technique of mode identification has been discussed already in connection with the description of the rotary probe; a few remarks about the use of the

rotary probe are given here in addition to two elementary methods of mode identification. The electromagnetic-field configuration for the various modes is assumed to be known (see Secs. 1·4, 2·9, and 3·2).

The use of a hand-operated rotary probe of the kind described in Sec. 18·4 is appropriate when the amount of data to be taken does not justify the use of the more expensive motor-driven device. The same data may be taken point by point with the aid of this simple equipment. The probe itself should be constructed in about the same way as the motor-driven one, but it is not necessary to provide brush contact; a wire connected directly to the crystal output may be run to the meter. This probe is mounted in a rigid frame so that it may be rotated by hand, a pointer indicating the angle against which the meter readings are plotted.

Mode identification is straightforward in the light of the discussion in Sec. 18·4. The modes encountered in a symmetrical magnetron are easily recognizable, the  $\pi$ -mode in particular being nearly always symmetrical. A magnetron employing strap breaks often presents a confusing picture on the lower modes, but the patterns observed on the screen can usually be interpreted. Long anodes should be searched for longitudinal modes. These appear with the same patterns as the standard modes, but they vary in intensity with longitudinal variation of the probe position, the most common one becoming zero at the center of the anode.

The identification of the modes can be made from wavelength measurements if the spectrum of the magnetron is known. For example, a strapped magnetron has modes whose resonant wavelengths decrease with decreasing mode number, and the wavelengths of the modes plotted against number are points through which a smooth curve may be drawn. The series of wavelengths may then be measured and the various modes selected on this basis without the added complication of the probe measurements. A very simple test may then be made to verify these results.

This test consists of inserting a screwdriver, pencil, or other similar object into each oscillator while the magnetron is excited at one of its modes and noting the detuning effect. On the  $\pi$ -mode the detuning effect is the same for all oscillators. On the other modes the detuning effect varies according to the energy stored in each oscillator. There will be two oscillators in which there will be no detuning for the  $\left(\frac{N}{2} - 1\right)$ -mode, where  $N$  is the number of oscillators (ordinarily an even number); four for the  $\left(\frac{N}{2} - 2\right)$ -mode, provided  $N/4$  is an integer; and so forth.

The greatest use of the rotary probe is in the investigation of field intensities in new types of magnetrons or other similar devices.

**18.8. Cathode-lead Loss.**—It is frequently necessary in magnetron design to install chokes in the cathode leads to prevent r-f leakage and radiation which would decrease the efficiency of the device. The first problem in this connection is to determine whether or not such leakage is present to an undesirable degree. Leakage can be detected on the spectrum analyzer during a standard  $Q$ -measurement. The signal generator is tuned to the resonant wavelength of the magnetron, as evidenced by the minimum standing-wave ratio. Then the movement of any conducting material in the neighborhood of cathode leads that couple out power will be reflected in a variation of the size of the signal seen on the spectrum analyzer. Touching the leads with the fingers is a very sensitive test for leakage. The degree of coupling may be estimated from the changes in the standing-wave ratio produced by placing reflecting objects near the cathode leads.

A more convenient method of detecting cathode-lead leakage makes use of the magic T or directional-coupler resonance indicator. The detuning effect of variation in external conditions is easily observed because the data are presented over a band of frequencies and the very convenient form in which the data are presented allows the leakage check to be performed quickly.

The usual remedy for cathode-lead r-f leakage is a quarter-wave coaxial-line choke soldered in each lead that comes out of the magnetron. It is possible, however, that a lead resonance may be set up if the place-

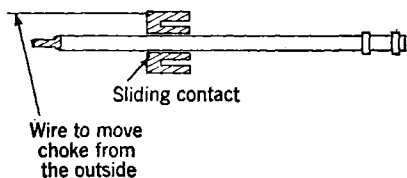


FIG. 18-22.—Movable cathode choke.

ment of this choke is accidentally in the appropriate position. Because this resonance is usually lossy in character, the unloaded  $Q$  of the magnetron is affected adversely with corresponding decrease in the circuit efficiency.

Furthermore, there may be a split in the mode spectrum so that the operation of the magnetron is erratic. There arises, therefore, the special problem to be attacked by cold-measurement methods in locating the cathode choke so that this resonance is avoided.

The 2J42 magnetron is used for an example. This tube has an end-mount cathode so that there is a single cathode lead coming out of the pole piece on one side. The problem to be solved is the location of the places where the choke should not be placed. Figure 18-22 shows the movable cathode choke that was made especially for this experiment. As there is no current flow at the mouth of the quarter-wave choke, the fixed choke may be replaced by the movable one with practically no change in the operating conditions. The sliding movement thus pro-

vided makes possible a continuous motion whose effect may be observed continuously on the screen of a resonance indicator. Figure 18-23 shows a plot of the results observed on the magic T indicator.

The cathode-choke movement  $x$  is plotted horizontally, and the effect on the resonant circuit is plotted vertically. The latter is measured by the height of the minimum point of the trace seen on the screen. The coupling loop loads the magnetron so heavily that the standing-wave ratio at resonance is high. As the loss due to the cathode-choke resonance enters a resonance region, the SWVR drops. The cathode-choke experiment may be generalized to include a wide variety of experiments in insertion loss.

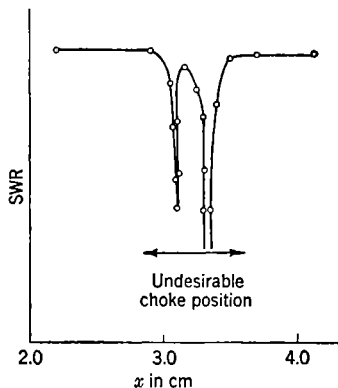


FIG. 18-23.—Effect of cathode-choke position on SWR.

**18-9. Tube-model Techniques.**—An anode block that is similar to but not identical with a proposed design and is constructed especially for the purpose of cold-testing is called a “tube model.” Models have proved to be extremely useful for the investigation of the resonant properties of a magnetron under development. Their principal advantage is that they are easier to construct than actual magnetrons and give a great deal of information on which the design of an actual magnetron may be based. Models may be made for any frequency where the conditions of construction and testing are most advantageous, because wavelength data scale reliably as the first power of the geometrical size. Thus a proposed magnetron that requires special construction techniques to be worked out before it can be constructed may have its properties investigated by means of a model which can easily be built at a longer wavelength. The resonances can be located; mode separation and patterns noted; and the data then scaled to apply to a magnetron at the desired frequency. Unloaded  $Q$  may also be scaled because for any given shape of cavity it is proportional to the square root of the wavelength.

In selecting the wavelength at which to construct a model, the availability of good test equipment is a real consideration. Of importance are signal generators with good power outputs and wide tuning range, spectrum analyzers, calibrated attenuators, and slotted sections. As an illustration, most models at the Radiation Laboratory were constructed largely at 10-cm wavelength because of the general superiority of equipment at this wavelength.

Model tubes can be modified as a result of the cold resonance obtained,

and for this purpose the model may be constructed of brass and bolted together to facilitate changes in form. Wavelength and mode data can be obtained in this way; but if unloaded  $Q$  data are to be taken, it is necessary to hard-solder the model and construct it from the final material. This added expense should not be incurred until such things as resonant wavelength are determined and found to be satisfactory. A typical procedure for the design of a magnetron is first to make a model of brass with various parts bolted or soft-soldered together. The size of certain parts such as the straps and vanes is varied, and the wavelength data taken for each variation. The wavelength-vs.-variation curve then provides the basis for the selection of the correct dimensions. Other quantities, of course, such as stabilization factor, may be adjusted as well. When the final dimensions are selected, a copper model may be constructed for the purpose of measuring the unloaded  $Q$ .

### OPERATING MEASUREMENTS

By A. G. SMITH

Accurate quantitative measurements of the operating conditions of a magnetron are useful as aids to design, as production controls, and

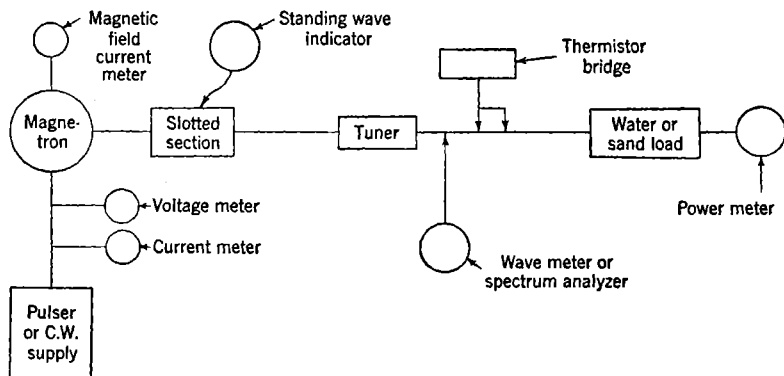


FIG. 18-24.—Arrangement of test bench components.

as guides to intelligent operation. In addition, a magnetron is frequently employed in the testing of other microwave components, and in this application a knowledge of its output power, frequency, and stability is essential.

Although the proper use of scaling principles and cold-measurement techniques may save needless effort in the designing of a magnetron, an operating model must finally be constructed and tested in order to determine quantities that can at present be predicted only approximately. The quantities to be determined are the range of currents and voltages



over which operation is stable, the electronic efficiency, tuning range, cathode-heating effects, electronic leakage current, and the power-handling capabilities of the input and output circuits.

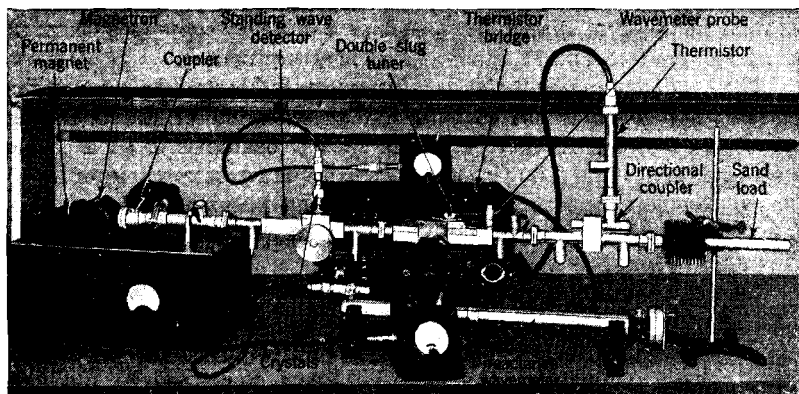


FIG. 18-25.—Low-power coaxial-line magnetron test bench.

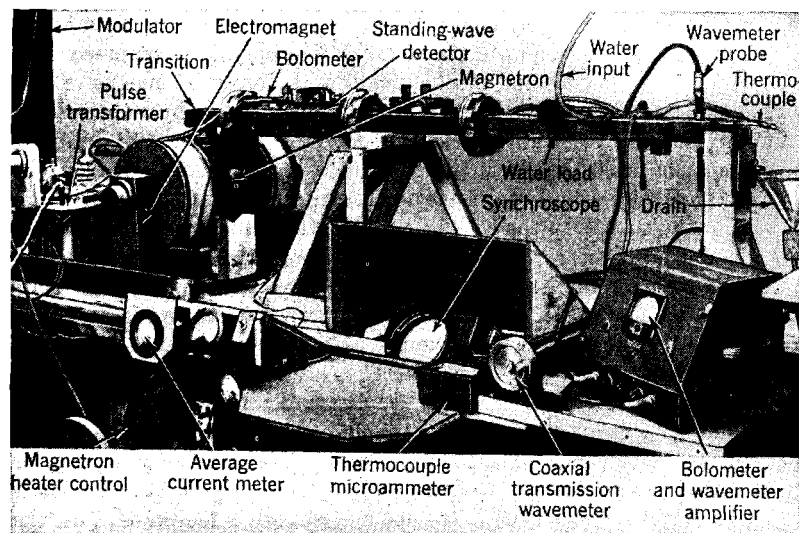


FIG. 18-26.—High-power waveguide magnetron test bench.

Figure 18-24 shows in schematic form the components necessary for testing an operating magnetron and their arrangement on a typical test bench. Either coaxial line or waveguide components can be used; and although the construction of some of the components differs for c-w and pulsed testing, their arrangement remains essentially as shown.

Figures 18-25 and 18-26 are photographs of typical coaxial-line and waveguide test benches, comparable to the schematic view in Fig. 18-24.

The components shown in Fig. 18-24 provide a rather complete set of data on operating magnetrons, but not included are certain pieces of equipment useful in special cases, such as V-I oscilloscopes (see Chap. 8) or r-f viewers (see Vol. 11, Radiation Laboratory Series).

**18-10. Measuring Techniques.** *Performance Charts.*—In general, the performance chart is the most useful presentation of the operating characteristics of a magnetron. (For specific examples of such charts see Chap. 19.) The following measurements must be made in order to plot a complete performance chart, including pushing-coefficient contours:<sup>1</sup> magnetic field, (average) current, (pulse) voltage, (duty ratio), (average) output power, and frequency.

A large amount of data is generally required, and a systematic procedure should be followed in obtaining it. The technique described here has been found satisfactory for most types of testing. It is convenient to begin work at the lowest magnetic field that is to be used; for if a high field is selected first, each time that it is reduced the magnet must be demagnetized in order to preserve its calibration. After the magnet current has been set to the desired value, plate voltage is applied to the magnetron and increased until stable oscillation begins. The presence of r-f output may be detected most quickly and simply by means of a  $\frac{1}{4}$ -watt neon bulb which is excited by inserting its leads into the r-f line through the slot of a standing-wave detector or tuner. Stability of operation can be judged from the steadiness of the neon glow, from the current and voltage pulses on a synchroscope, or from the image on a spectrum analyzer. In the case of a pulsed tube, the spectrum analyzer is a valuable adjunct, for the spectrum of a magnetron frequently deteriorates badly near the limits of its stable range. Having set the plate current at the lowest value at which satisfactory operation is obtained, the operator then records the voltage, current, power output, and frequency. If a water load is being used to measure power, the rate of flow must be determined and checked at reasonable intervals. The plate current is next increased somewhat, and the readings repeated. This process is continued until a limit is set by mode-shifting, arcing, or overheating of the cathode. When one of these occurs, the current is reduced to the starting value, the magnetic field is increased, and the process repeated. The performance chart may be extended in voltage until the magnet saturates or until arcing occurs in the magnetron even at low currents.

The plotting of c-w performance data is relatively simple, requiring only the calculation of plate efficiency. Pulsed data require the con-

<sup>1</sup> The quantities in parentheses apply only to pulsed operation.

version of average-current and average-power readings to the pulse values through division by the duty ratio, which must be determined from a calibration of the apparatus. Performance charts are almost always taken into a matched line, and therefore a tuner and standing-wave detector are not needed, although the latter is a convenience in checking the match of the load.

*Rieke Diagrams.*—The Rieke diagram is of great value in determining the effects of loading on the performance of a magnetron. Many examples of these plots will be found in Chap. 19 of this book. The information that is needed in the preparation of a complete Rieke dia-

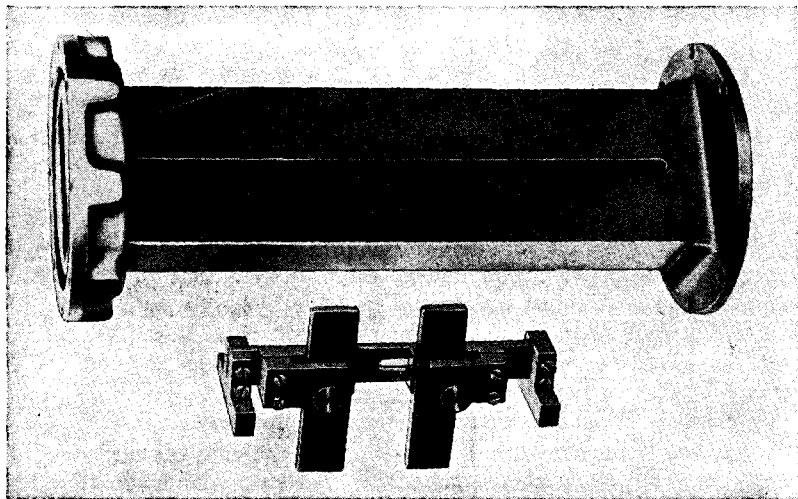


FIG. 18-27.—Waveguide double-slug tuner with Mycalex slugs.

gram is<sup>1</sup> (average) current, (pulse) voltage, (duty ratio), (average) power output, frequency, magnitude of standing wave, and phase of standing wave. The following procedure has, in general, proved to be a satisfactory method of obtaining such data.

In measuring the Rieke diagram the magnetic field and the plate current are held constant, while a standing wave of variable phase and magnitude is presented to the magnetron. This standing wave is set up by means of a double-slug tuner (see Fig. 18-27) and measured by using a standing-wave detector (see Fig. 18-4) placed between the tuner and the magnetron. In the case of high-power magnetrons, it may be necessary to take the Rieke diagram at a power output well below the usual operating point because of breakdown in the slugs or magnetron output or arcing inside the tube itself when a high standing wave is set up.

<sup>1</sup> The quantities in parentheses apply only to pulsed operation.

With the magnetic field set at the proper value, the magnetron is put into oscillation and the distance between the slugs is adjusted until the standing-wave detector indicates that a match has been obtained. The magnetron plate current is then brought to the value that has been decided upon, and the voltage, power output, and frequency are recorded, giving a point that when plotted will lie at the center of the diagram. The separation of the slugs is next changed slightly until a standing wave of small amplitude is set up, and the plate current is reset to its previous value—if, indeed, it has varied at all. The magnitude and relative phase<sup>1</sup> of this standing wave are recorded, the phase being measured from a scale on the standing-wave detector. Leaving the separation of the slugs unchanged, the tuner is now moved a fraction of a wavelength, and all of the readings are repeated. It will be found that although the phase of the standing wave has changed, its magnitude is virtually unaltered, with the result that it will appear on the diagram at the same radius as the second point and removed from it by an angle equal to the difference in electrical degrees between the phases of the two points. In this manner, the operator proceeds around a full circle on the diagram, corresponding to a half-wavelength movement of the slugs and a half-wavelength change in phase. The tuner is then readjusted to set up a higher standing wave, and another circle is completed. The process is continued until r-f breakdown occurs in the line, the magnetron becomes unstable, or the tuner reaches the maximum standing-wave ratio of which it is capable.

Although the phase thus far is referred to a purely arbitrary origin, that is, the zero of the scale, it may be made more specific by referring it to a suitable plane at the magnetron output. This translation, of course, merely involves the measurement in electrical degrees of the distance between the selected plane and the zero point of the scale. It is conventional to plot motion of the phase toward the magnetron in a counterclockwise direction. The radial scale may be marked in SWVR, SWPR, or reflection coefficient.

*Pulling Figure.*—The pulling figure of a magnetron is defined as the maximum change in frequency that occurs as a standing wave with a voltage ratio of 1.5 is presented to the tube and the phase is varied through 360°. Although the pulling may be determined from a Rieke diagram, this technique is needlessly laborious unless the other information contained in such a plot is desired. A more direct method consists simply in placing a tuner in the line, setting up a standing wave of 1.5 in voltage, and determining the frequency limits as the phase is varied. By far the most satisfactory indication of the frequency deviation is obtained with a spectrum analyzer; on the screen of this instrument the

<sup>1</sup> Always measured from the minimum of the standing-wave pattern.

spectrum moves back and forth along the baseline as the phase of the standing wave changes, and the amplitude of the motion is readily measured by means of any of the frequency-measurement techniques discussed in connection with the spectrum analyzer in Vol. 14. It is sound procedure to check the standing-wave ratio at each of the two points at which frequency measurements are made. Even though the separation of the slugs remains constant, slight changes in the impedance of the line or the superposition of a reflection from the load may alter the ratio enough to impair the accuracy of the pulling figure that is obtained. The magnetron should be thoroughly warmed up before pulling-figure measurements are attempted, or thermal frequency drift will enter into the results, although this source of error is more likely to occur in pulling figures obtained from Rieke diagrams.

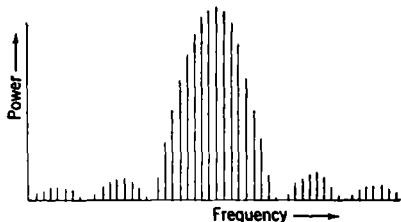


FIG. 18-28.—Spectrum of a pulsed magnetron as seen on a spectrum analyzer.

*Spectrum.*—Much can be learned about the operation of a pulsed magnetron from a study of the r-f spectrum. The theoretical form of this spectrum is shown in Fig. 18-28.<sup>1</sup> Certain deviations from this shape are attributes of the voltage pulse that is applied to the magnetron, and others result from the action of the tube itself. A voltage pulse with an excessively sloped or rounded top will produce a frequency modulation that may broaden the spectrum appreciably, and a frequent concomitant of this condition is a marked difference in the heights of the secondary maxima on one side of the spectrum as compared with those on the other side. Another common phenomenon is the random, intermittent disappearance of one or more of the vertical lines that make up the spectrum; this is an indication that at the moment at which that line should have been formed, the magnetron had shifted modes or was arcing. In certain regions of the performance chart, usually at very low currents, the spectrum may be observed to broaden as the region is entered and finally to break up completely into a distribution resembling noise. A similar deterioration is frequently noticed when a heavily loaded magnetron enters the unstable portion of a Rieke diagram.

The spectrum of a c-w magnetron is of less significance to the operation of the tube. The spectrum analyzer is still very useful, as it provides an effective means of observing small frequency shifts.

**18-11. Operating Technique.**—Before putting a magnetron into operation, it is a reasonable precaution to test it with a spark coil and ohm-

<sup>1</sup> See also Vol. 11, Chap. 12, of this series.

meter to prevent possible damage to the pulse generator or power supply and the associated metering equipment. An ohmmeter will indicate whether or not the heater circuit is continuous and whether or not a short circuit exists between the cathode and the anode.

The magnetron should be mounted so that it is well centered between the pole pieces of the magnet. In some cases the manufacturer indicates a preferred polarity of magnetic field. The output connections should fit well; if they are loose, r-f breakdown is likely; and if they are too tight, the tube may be damaged. Most trouble is caused by the center conductors of tubes with coaxial outputs.

The lead that carries the plate current from the power supply or pulse generator is connected to the cathode lead of the magnetron; if it is connected to the heater lead, all the plate current will flow through the heater, and the transients brought on by arcing may burn it out. Full heater power should always be supplied for at least 60 sec before plate voltage is applied. In pulsed operation, the leads between the pulse generator and the magnetron should be kept short, since the reactance of long leads may distort the pulse waveform and introduce oscillations. Where forced-air cooling is indicated, it should be sufficient to maintain the temperature of the block below 100°C.

The magnetron may be grounded through the r-f line, which should be part of a common ground system embracing the magnet, the power supply or pulse generator, the pulse transformer, and the chassis of the associated amplifiers, spectrum analyzers, etc. If the r-f line is accidentally left ungrounded, the operator may discover that it has become charged to full cathode potential.

*Gassy Tube.*—When plate voltage is applied, a gassy magnetron will draw a large current and the synchroscope or voltmeter will indicate little or no voltage across the tube. A gas discharge may be seen inside the magnetron by looking into the input or output pipes. All magnetrons evolve a little gas when they are left idle for long periods, but this normal outgassing will not produce the condition just described. A spark coil test will confirm the diagnosis.

*Cathode-anode Short Circuit.*—Again, current will be drawn with zero voltage indicated, but there will be no gas discharge. An ohmmeter may be used to settle the matter.

*No Magnetic Field.*—A high current will be drawn at very low voltage. Removal of the magnetic field during operation may result in the destruction of the magnetron; precautions should therefore be taken when an electromagnet is used to prevent failure of the d-c power supply.

*Open Heater.*—The magnetron will fail to start normally when plate voltage is applied and probably will spark. No plate current will be drawn. The usual glow of the cathode, visible in the input pipes of

many magnetrons, will be absent. An ohmmeter test is the final check. A magnetron in this condition may usually be started by continued application of plate voltage at a relatively low magnetic field, although care must be taken not to damage the associated equipment; once oscillating, back bombardment may provide sufficient cathode heating for normal operation. This type of starting cannot be repeated many times without destroying the cathode. A great many heater failures are due to transients accompanying arcing and may be prevented by placing a  $\frac{1}{2}$ - $\mu$ f condenser in shunt with the heater to bypass such surges.

*Arcing.*—Arcing, or sparking, is commonly encountered in magnetron operation, especially at high powers. It may be due to traces of gas, to mode shifting, to high gradients caused by sharp surfaces, or to overworking of the cathode. A magnetron will withstand a surprising amount of arcing over a short period of time without apparent damage, but even intermittent sparking during continuous operation will affect its life adversely. Arcing appears as flashes in the input pipes, unsteadiness of the current meter, missing pulses on the spectrum analyzer, and transient traces on the synchroscope (Fig. 18-29). The evolution of gas occurring during long periods of quiescence may make it necessary to reseason a tube to "clean up" the gas; this should require no more than 15 or 20 min of continuous attention.

The operator should slowly increase the voltage until arcing becomes rather violent, occurring perhaps several times a second; as soon as the sparking has died down, the voltage may again be raised, and so on until the desired operating level has been attained. Should an unusually intense burst of sparks occur, resembling a continuous

arc, the voltage must quickly be backed off to permit the tube to recover. Arcing is frequently associated with mode instability, and it is difficult to determine which is the cause and which the effect.

*Mode Instability.*—This is a phenomenon which occurs in certain regions of the performance charts of all magnetrons, usually at very high or very low currents or at low magnetic fields. A c-w magnetron changes modes abruptly, showing a marked decrease in output power, and may not return to the operating mode until the plate voltage has been shut off and the tube restarted in a more favorable region. Pulsed magnetrons change modes more gradually, passing through a region of operation partly in one mode and partly in another, as evidenced by double voltage, current, and *VI* traces on the synchroscope (Fig. 18-29) and by missing lines in the spectrum; operation in this region is likely to be accompanied

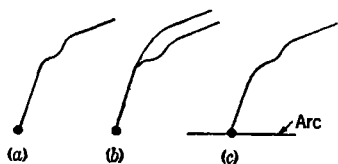


FIG. 18-29.—Appearance of *VI* trace under various conditions of operation, showing (a) stable operation, (b) mode shift, and (c) arcing.

by sparking and by falling output power. The tube will, however, resume normal oscillation as soon as the voltage is changed to bring it back to a region of stable performance. The location of the boundaries where mode changes occur is influenced by cathode quality and temperature, pulse shape, and loading (see Chap. 8). Mode-changing may become more troublesome as a magnetron ages and the cathode emission fails. Although a tube may be oscillating in a lower mode, it is not always possible to detect the wavelength of that mode in the r-f line, since conditions in the magnetron may be such that it does not couple to the output loop. Operation in lower modes is frequently accompanied by serious overheating of the cathode.

*Overheated Cathode.*—Operation of the cathode at temperatures in excess of the normal value (about 850°C) shortens tube life. The heater transformer should be checked for proper voltage; and when operating instructions call for reduction of the heater voltage during oscillation, they should always be followed. In many tubes the cathode glow may be seen directly or by reflection in the input pipes; if the operator familiarizes himself with the appearance of this glow at normal heater input, he will be able to judge for himself when the temperature becomes excessive. Continuous-wave magnetrons are especially likely to suffer from overheating of the cathode.

*Breakdown in the R-f Line.*—This is usually announced by crackling or spitting noises. Coaxial tuners are very likely to break down, and magnetron couplers and transitions are also serious offenders. All components should be clean and well-polished inside; the joints should fit snugly and be tightly clamped. Ignition sealing compound (a heavy grease) may be applied in cases of localized breakdown. For laboratory use, carbon tetrachloride sprayed into the line through a slotted section is surprisingly effective in stopping breakdown, although the application must, of course, be repeated every few minutes. Pressurization, although troublesome, will greatly extend the power-handling capacity of any line, 4 mw having been transmitted successfully by a 1½-in. coaxial line pressurized to 35 lb per sq in. gauge.



# CHAPTER 19

## TYPICAL MAGNETRONS

BY A. G. SMITH

This chapter presents specific data on the performance characteristics and dimensions as well as the over-all design of the principal types of microwave magnetrons in the frequency range of 1000 to 24,000 Mc/sec and output-power range of 25 watts to 2.5 mw. The magnetrons included here were selected as being representative of various wavelength and

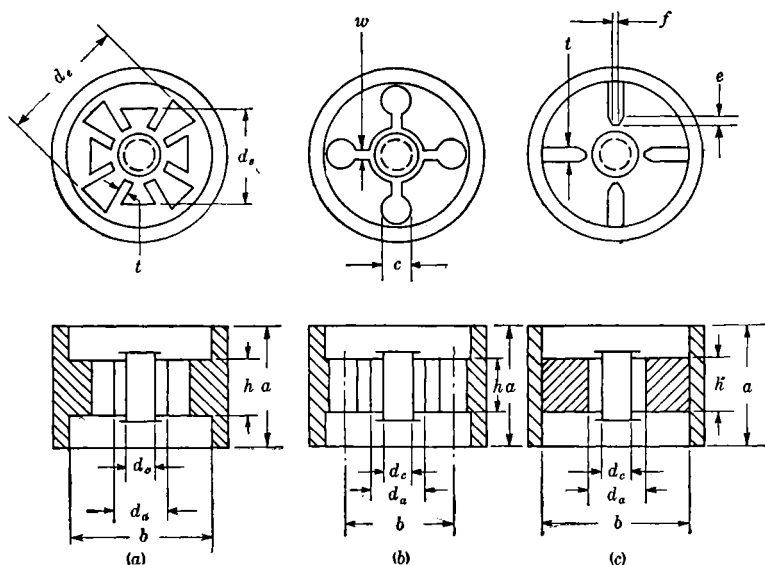


FIG. 19-1.—Generalized figures for anode-block dimensions. (a) Rising-sun; (b) hole and slot; (c) vane. The dimension (a) is the distance between the pole tips or between the lids, whichever is smaller.

output-power ranges and to illustrate particular design features. No attempt was made to make the list complete. Wherever possible, magnetrons that are available for purchase as a consequence of being in production were selected for inclusion, and these are designated by the RMA numbers. Several important magnetron designs that were developed but did not reach the production stage are also included, and

these are referred to by the symbol assigned in the laboratory in which they were developed. Tubes in this category are probably not available for purchase.

For each tube type there is a discussion that covers its general performance and limitations, frequency or frequency range, type of construction, and special features. A performance chart and usually a Rieke diagram provide complete information on the operating characteristics. A plan view and photograph together with a table of dimensions give the construction details. The meaning of the symbols in this

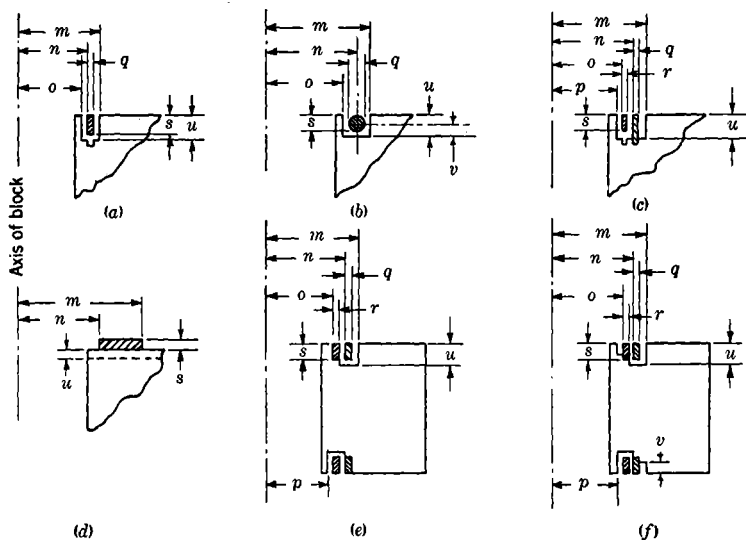


FIG. 19-2.—Generalized figures for magnetron strapping dimensions.

construction table may be determined by referring to Figs. 19-1 and 19-2. A table of characteristic scale factors is given as an aid to magnetron designers. The definitions of the symbols in this table are found in Sec. 10-5. Table 19-1 lists the magnetrons described in this chapter.

**19-1. The LCW L-band C-w Magnetron.**—The LCW is an experimental c-w magnetron, capable of output powers up to 2000 watts at a fixed frequency of 900 Mc/sec. A radially mounted cathode and separate magnet are used.

Operation is satisfactory between 2000 and 4000 volts and from 0.1 to 1 amp. This region of operation, shown in Fig. 19-3, provides useful output powers ranging from 100 to 2000 watts; it is limited at high powers by overheating of the cathode and at low powers by deterioration of the spectrum. The pulling figure is 4 Mc/sec, and the pushing figure

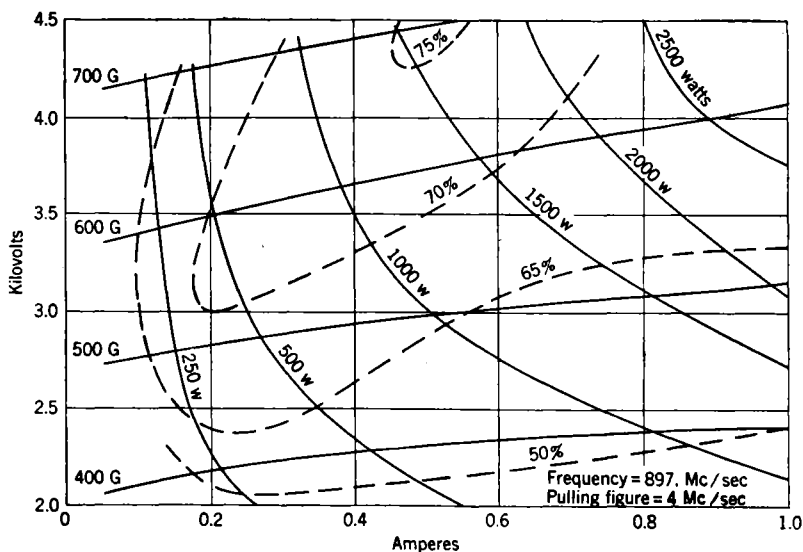
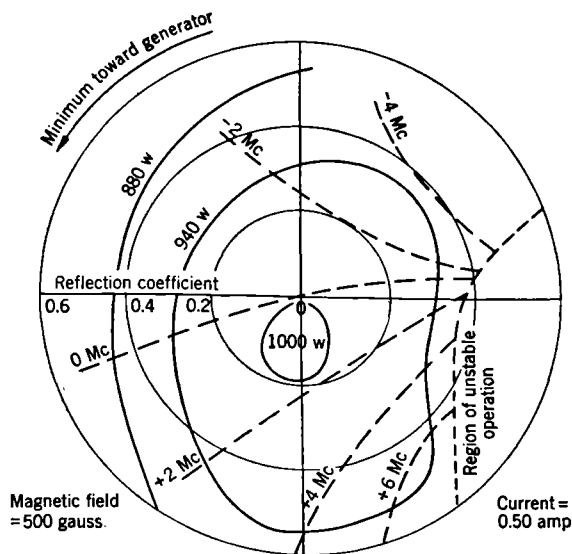


FIG. 19-3.—Performance chart for LCW magnetron.



Frequency of 0 Mc contour = 896.5 Mc/sec

FIG. 19-4.—Rieke diagram for LCW magnetron.

TABLE 19-1.—INDEX OF MAGNETRONS

Frequency, Mc/sec	Power output	Type of operation	Tube No.	Chapter Sec.
900	100-2000 watts	C-w fixed freq.	LCW	19-1
2,830-3,240	5-150 watts	C-w tunable	CM16B	19-2
3,245-3,333	2.5-10 kw	Pulsed fixed freq.	2J38 } series	19-3
			2J39 }	
2,700-3,333	2.5-300 kw	Pulsed fixed freq.	2J22 } series	19-4
			2J34 }	
2,700-3,700	300-1000 kw	Pulsed tunable	4J70 } series	19-5
			4J77 }	
2,800	500-2500 kw	Pulsed fixed freq.	HP10V	19-6
9,375	10-100 watts	C-w, pulsed, fixed freq	BM50	19-7
9,290-9,330	200-1250 watts	Pulsed tunable	2J41	19-8
9,345-9,405	5-20 kw	Pulsed fixed freq.	2J42 series	19-9
9,345-9,405	10-70 kw	Pulsed fixed freq.	725A series	19-10
8,500-9,600	100 kw	Pulsed tunable	2J51	19-11
9,345-9,405	50-300 kw	Pulsed fixed freq.	4J50 series	19-12
9,500	2-1000 kw	Pulsed fixed freq.	AX9	19-13
24,000	50 kw	Pulsed fixed freq.	3J21 } series	19-14
			3J31 }	
24,000	50 kw	Pulsed fixed freq.	22-cavity rising-sun magnetron	19-15
24,000	50 kw	Pulsed fixed freq.	Closed-end 38-cavity rising-sun magnetron	19-16
11,500	500 watts	C-w fixed freq.	High-power 2.6-cm C-w magnetron	19-17

at an operating point of 3000 volts and 0.5 amp is 3 Mc/sec per amp. It is evident from Fig. 19-4 that nothing is to be gained by loading the tube more heavily.

A screened, oxide-coated cathode is used. The heater, which draws 5.2 amp at 6.3 volts, is turned off after the magnetron has been started. Figure 19-5 shows the 16-vane anode block, double-ring-strapped on one end only to allow the addition of a projected electronic tuning device. Characteristic scale factors and dimensions for this block are listed in Tables 19-2 and 19-3.

TABLE 19-2.—CHARACTERISTIC SCALE FACTORS FOR LCW MAGNETRON

$\lambda$ , cm	$\mathcal{B}$ , gauss	$s$ , amp	$\mathcal{V}$ , kv	$\mathcal{P}$ , kw	$\mathcal{G}$ , mhos	$Q_u$	$\eta_c$ , %	$\frac{C}{L}$
33.5	125	0.761	0.423	0.322	$1.80 \times 10^{-3}$	1050	92	0.012

Because the block is short relative to its large diameter, the LCW requires a magnet with a gap of only  $2\frac{1}{4}$  in. and a pole-face diameter of  $2\frac{1}{2}$  in. Experimentally, the tube has been water cooled (Fig. 19-6), but because of its high efficiency air cooling should be feasible.

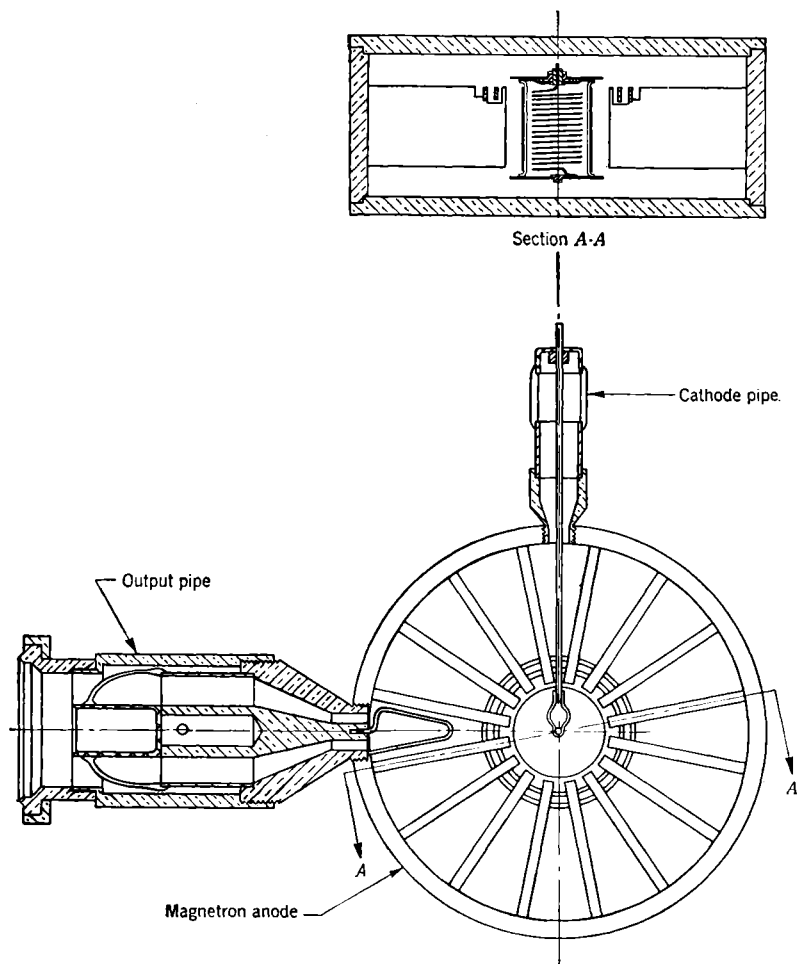


FIG. 19-5.—Cross sections of LCW magnetron.

Further details of the construction, operation, and projected tuning schemes of the LCW may be obtained from Radiation Laboratory Report No. 1005, "LCT, 900-Mc/sec F-m—C-w Magnetron."

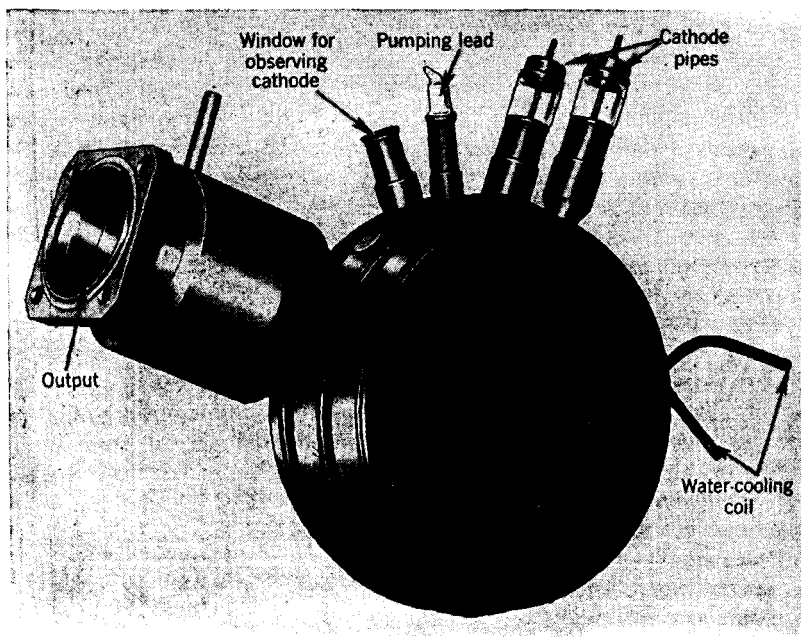


Fig. 19-6.—LCW magnetron.

TABLE 19-3.—DIMENSIONS IN INCHES OF LCW MAGNETRON  
a. Anode-block Dimensions: See Fig. 19-1c

<i>a</i>	<i>b</i>	<i>d<sub>a</sub></i>	<i>d<sub>c</sub></i>	<i>h</i>	<i>t</i>
1.800	5.025	1.370	0.829	1.000	0.150

b. Strapping Dimensions: See Fig. 19-2f

<i>m</i>	<i>n</i>	<i>o</i>	<i>p</i>	<i>q</i>	<i>r</i>	<i>s</i>	<i>u</i>	<i>v</i>
1.075	0.935	0.815	0.735	0.120	0.120	0.188	0.219	0.156

**19-2. The CM16B S-band C-w Magnetron.**<sup>1</sup>—The CM16B magnetron is an experimental c-w oscillator, tunable over the band from 2830 to 3240 Mc/sec at power-output levels up to 150 watts. An axially mounted cathode and attached magnet are used, and the coaxial output shown in Fig. 19-7 fits standard  $\frac{7}{8}$ -in. line components.

Operation is stable between 500 and 2000 volts, and from 25 to 200 ma, with corresponding output powers ranging from 5 to 150 watts.

<sup>1</sup> Data for Sec. 19-2 submitted by A. M. Clogston.

The performance chart of Fig. 19.8 shows the useful region of operation, which is restricted at high currents by mode instability and overheating of the cathode and at low currents by poor spectrum and high pushing.

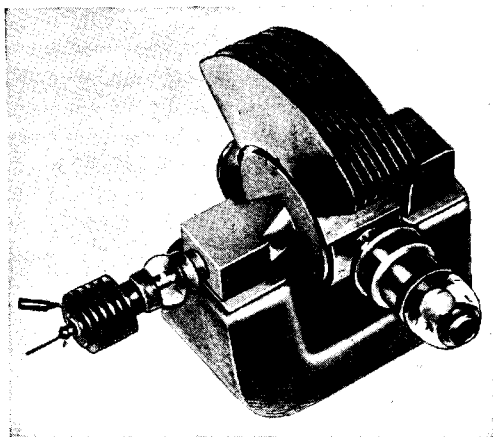


FIG. 19-7.—CM16B magnetron.

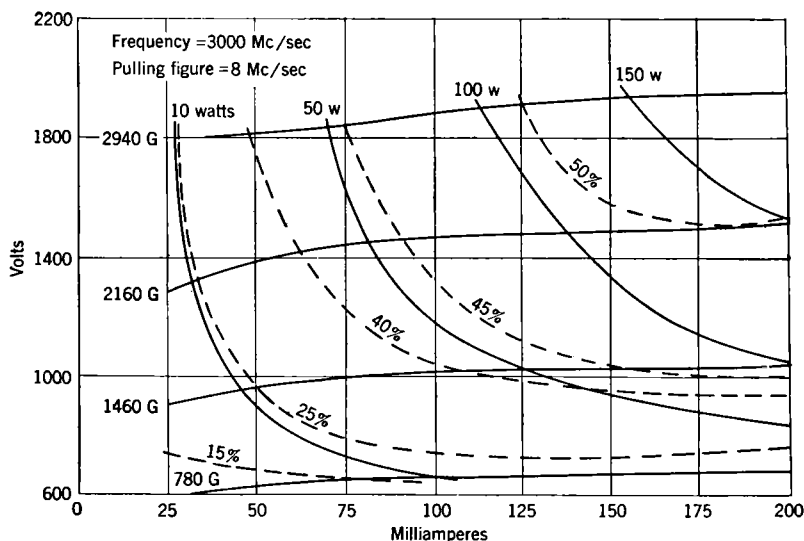


FIG. 19-8.—Performance chart for CM16B magnetron.

Figure 19-9 illustrates the variation of output power with tuning; the reliable tuning range is limited by a tendency to shift modes beyond the extremes of the band shown. The pulling figure is 8 Mc/sec, and

the pushing figure at an operating point of 100 ma and 1400 volts is 20 Mc/sec per amp.

The screened, oxide-coated cathode is capable of dissipating the back-bombardment heating that accompanies up to 600 watts input power.

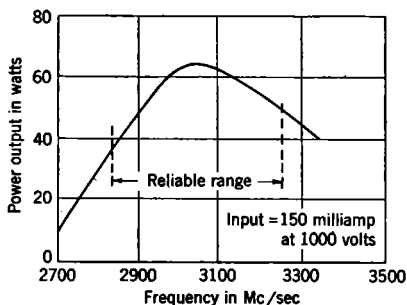


Fig. 19-9.—Frequency characteristic of CM16B magnetron.

The heater rating is 3.5 amp at 6.3 volts; this consumption is reduced during operation at input powers in excess of 150 watts. Characteristic scale factors and dimensions for the 16-vane doublering-strapped anode block are listed in Tables 19-4 and 19-5.

Tuning is accomplished by moving a shorting choke in a coaxial line coupled to the straps on one end of the block. As may be seen from Fig. 19-10, the vacuum is retained by a glass seal near the anode block, so that the portion of the line in which the choke moves is at atmospheric

TABLE 19-4.—CHARACTERISTIC SCALE FACTORS FOR CM16B MAGNETRON

$\lambda$ , cm	$\beta$ , gauss	$s$ , amp	$\mathcal{U}$ , kv	$\phi$ , kw	$\mathcal{S}$ , mhos	$Q_u$	$\eta_c$ , %	$\frac{C}{L}$
10.0	412	0.301	0.132	0.0397	$2.28 \times 10^{-3}$	600	80	0.032

TABLE 19-5.—DIMENSIONS IN INCHES OF CM16B MAGNETRON  
a. Anode-block Dimensions: See Fig. 19-1c

$a$	$b$	$d_a$	$d_c$	$h$	$t$
0.752* 0.577†	1.330	0.230	0.136	0.400	0.023

\* Between lids.

† Between pole tips.

b. Strapping Dimensions: See Fig. 19-2e

$m$	$n$	$o$	$p$	$q$	$r$	$s$	$u$
0.234	0.194	0.154	0.134	0.020	0.020	0.040	0.060

pressure. Every effort has been made to reduce the frequency sensitivity of the tuner through keeping its length at a minimum, for such frequency sensitivity introduces mode-shifting tendencies that markedly restrict the reliable tuning range. A 4-cm motion of the shorting choke is



required to cover the band of Fig. 19-9. Without changing its construction, the CM16B has been made electronically tunable by the substitution of an ET10 reactance tube for the mechanical tuner, and it has been stabilized by a factor of 10 by replacing the tuner with a cavity.

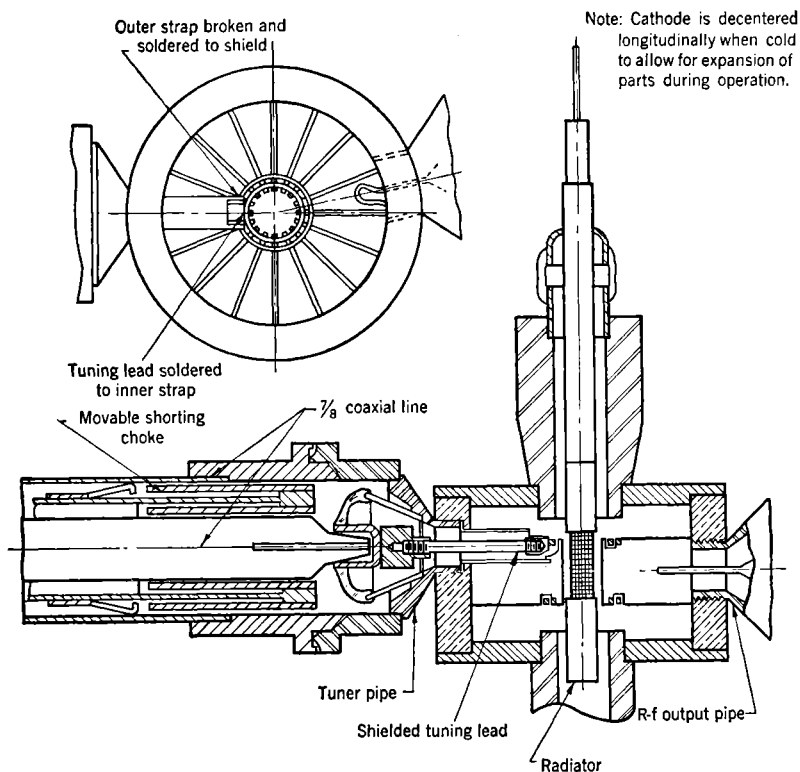


FIG. 19-10.—Cross sections of CM16B magnetron.

**19-3. 2J38-2J39 Low-voltage S-band Magnetrons.**<sup>1</sup>—The 2J38 and 2J39 are fixed-frequency pulsed oscillators designed for operation at pulse-power output levels ranging from 2.5 to 10 kw. The frequency of the 2J38 lies in the band from 3245 to 3267 Mc/sec; that of the 2J39 lies between 3267 and 3333 Mc/sec. Coaxial outputs that fit standard  $\frac{7}{8}$ -in. coaxial-line components are provided; the cathodes are mounted radially, and the magnets are attached to the tubes.

Reliable operation may be expected with pulse current and voltage inputs ranging from 2.5 to 7.5 amp and from 3 to 10 kv. At currents

<sup>1</sup> Data for Sec. 19-3 submitted by J. R. Feldmeier.

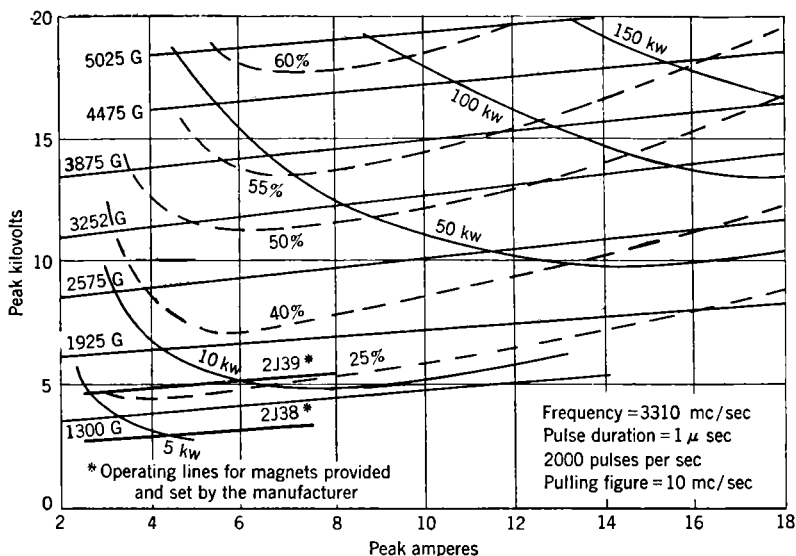


FIG. 19-11.—Performance chart for 2J38 and 2J39 magnetrons.

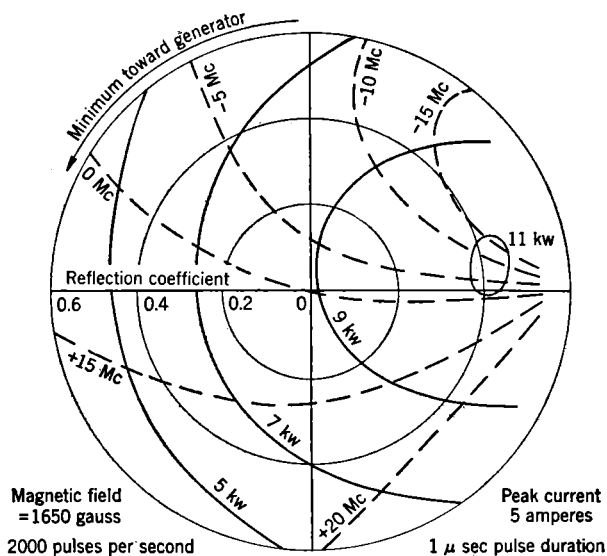


FIG. 19-12.—Rieke diagram for 2J38 and 2J39 magnetrons.

above 7.5 amp mode instability may be encountered, and below 2.5 amp the spectrum becomes poor. Occasional tubes may be seasoned to cover the extensive region shown in Fig. 19-11. The operating lines for the magnets provided and set by the manufacturer are shown in this figure; it may be seen that the pulse-power output ranges available under this condition are 2.5 to 8 kw for the 2J38 and 5 to 12.5 kw for the 2J39. These low levels of operation were established to reduce magnet weight and input power and to ensure stability. A maximum of 200 watts average power, at a maximum pulse duration of 2  $\mu$ sec, may be put into either type. The pulling figures are 13 Mc/sec maximum for the 2J39 and 7 Mc/sec minimum<sup>1</sup> for the 2J38. Figure 19-12 is a Rieke diagram for these tube types.

An unscreened, oxide-coated cathode with a heater rating of 1.3 amp at 6.3 volts is used; at average input powers in excess of 55 watts the heater consumption should be reduced, and above 160 watts the heater should be turned off. Characteristic scale factors and dimensions for the eight-oscillator vane-type block are listed in Tables 19-6 and 19-7.

TABLE 19-6.—CHARACTERISTIC SCALE FACTORS FOR 2J38 AND 2J39 MAGNETRONS

$\lambda$ , cm	$\mathcal{B}$ , gauss	$s$ , amp	$\mathcal{V}$ , kv	$\Phi$ , kw	$\mathcal{G}$ , mhos	$Q_u$	$\eta_c$ , %	$\frac{C}{L}$
9.1	682	2.52	1.22	3.07	$2.07 \times 10^{-3}$	1500	90	0.0020

TABLE 19-7.—DIMENSIONS IN INCHES FOR 2J38 AND 2J39 MAGNETRONS

a. Anode Dimensions; See Fig. 19-1c

$a$	$b$	$d_a$	$d_c$	$h$	$t$
0.750* 0.550†	1.330	0.316	0.120	0.475	0.060

\* Between lids.

† Between pole tips.

b. Strapping Dimensions; See Fig. 19-2b

$m$	$n$	$o$	$q$	$u$	$v$
0.242	0.211	0.180	0.020	0.050	0.039

An unusual feature of the construction is the octagonal wire strap shown in Fig. 19-13. Separation of the frequencies into the two bands is achieved by adjustment of this strap.

<sup>1</sup> The unusual practice of specifying a minimum pulling figure was adopted in order to ensure that these tubes could be "pulled" to a precise beacon frequency.

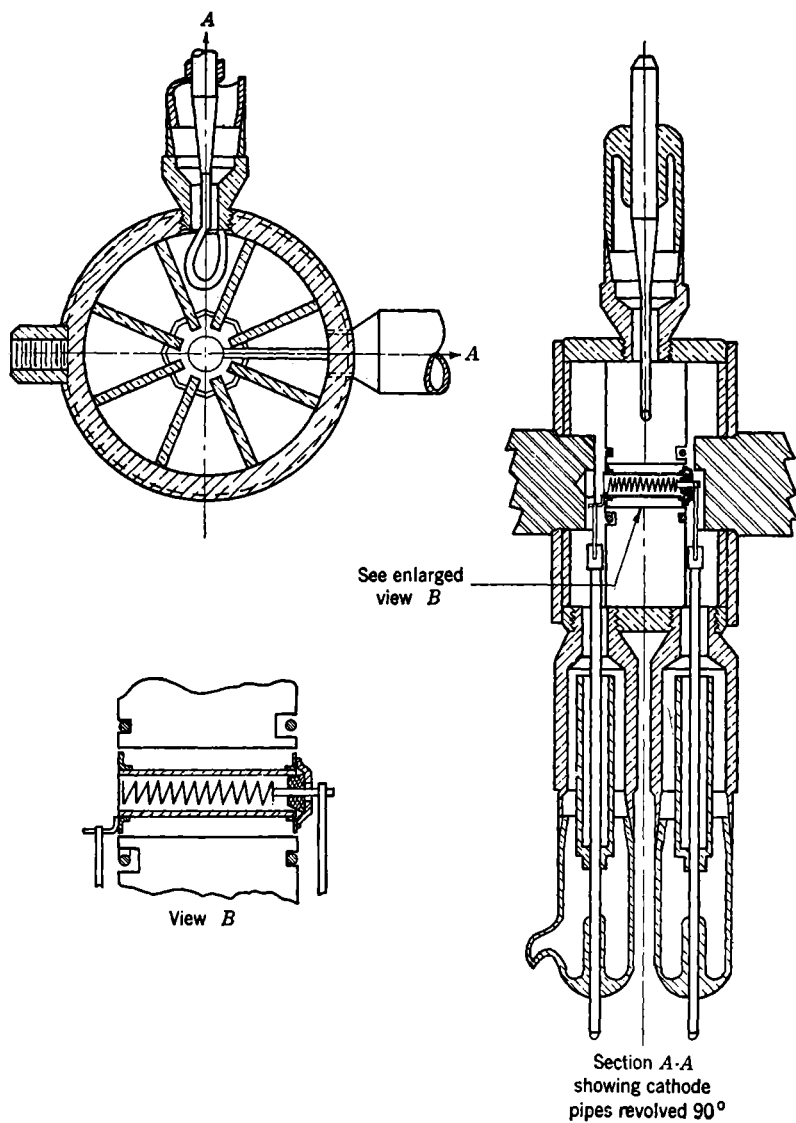


FIG. 19-13.—Cross sections of 2J38 and 2J39 magnetrons.

Although identical internally, the 2J38 and 2J39 differ in their external features. The 2J38 shown in Fig. 19-14 is provided with a larger radiator and with a bracket in which a thermostat may be mounted; these additions permit close control of the block temperature as a means of preventing thermal frequency drift. Figure 19-15 shows the simpler exterior of the 2J39. Forced-air cooling is required by either type.

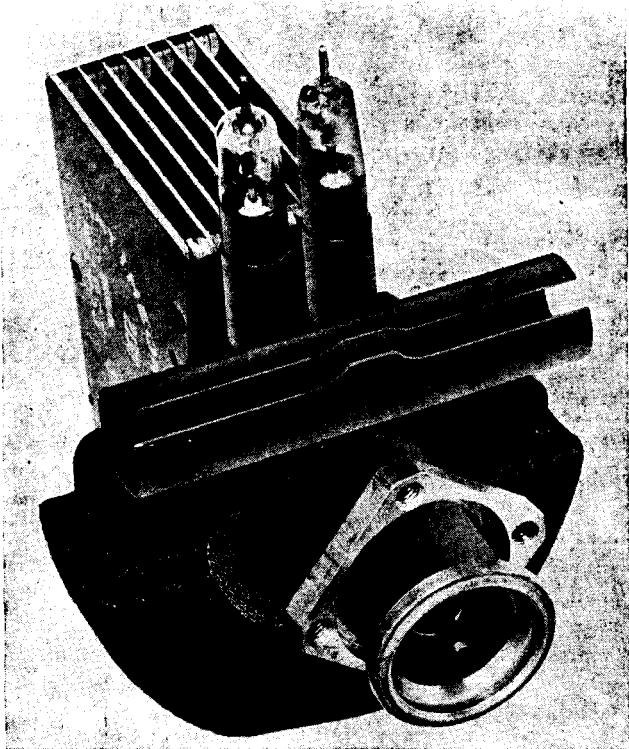


FIG. 19-14.—2J38 magnetron.

Both magnetrons may be mounted from the output, and the 2J39 may in addition be mounted from a flange at the base of the input pipes. The total weight of the magnetron and magnet is 2 lb 10 oz for the 2J38 and 2 lb for the 2J39.

Further information on the operation of these tubes may be obtained from the manufacturer's technical-information sheet.

**19-4. Type 2J22-2J34 10-cm Pulsed Magnetrons.**<sup>1</sup>—The 13 magnetrons of this series are fixed-frequency pulsed oscillators, designed for

<sup>1</sup> Data for Sec. 19-4 submitted by F. F. Rieke.

operation at pulse-power output levels ranging from 25 to 300 kw. Three basic anode-block designs are employed: one for the 2J22 (3267 to 3333 Mc/sec), a second for types 2J23 to 2J29 (2913 to 3100 Mc/sec), and a third for types 2J30 to 2J34 (2700 to 2900 Mc/sec); within each group different frequencies are obtained by varying the strap capacitances. Externally the tubes are alike, and they are mechanically interchangeable.

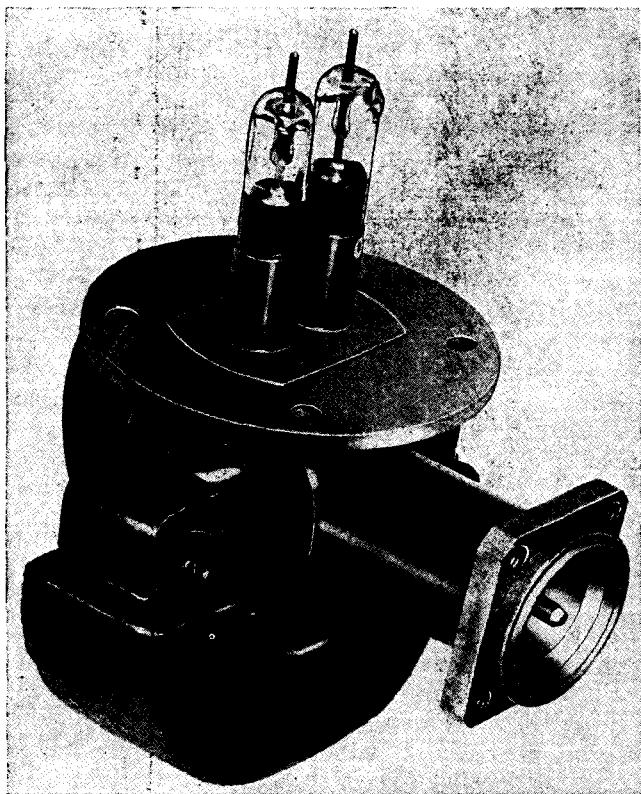


FIG. 19-15.—2J39 magnetron.

Separate magnets are used. The cathodes are mounted radially, and the outputs are coaxial.

Operation is reliable over a range of pulse current and voltage inputs extending from 8 to 30 amp and from 10 to 22 kv (Fig. 19-16). Low-power operation is limited by mode changing and deterioration of the spectrum, and high-power operation by arcing. With specially designed output connections it is possible to select and season tubes to perform satisfactorily at 2800 gauss, 31 kv, and 35 pulse amp, with a pulse-power

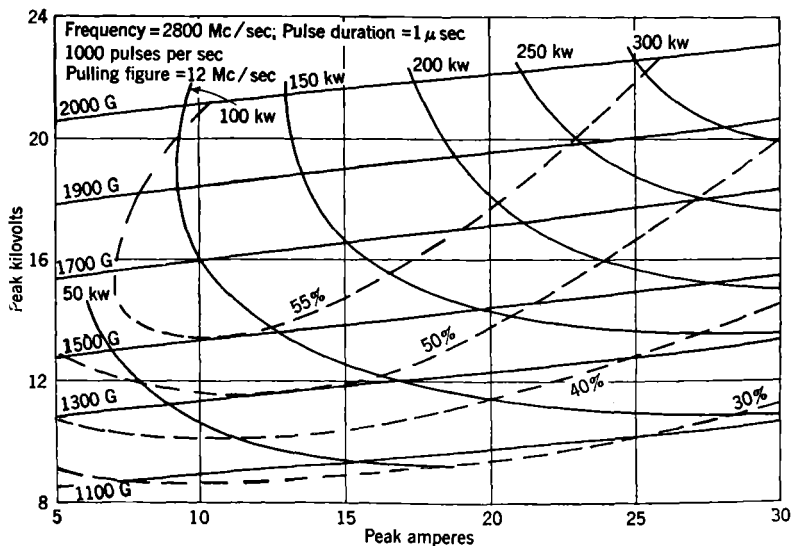


FIG. 19-16.—Performance chart for 2J32 magnetron.

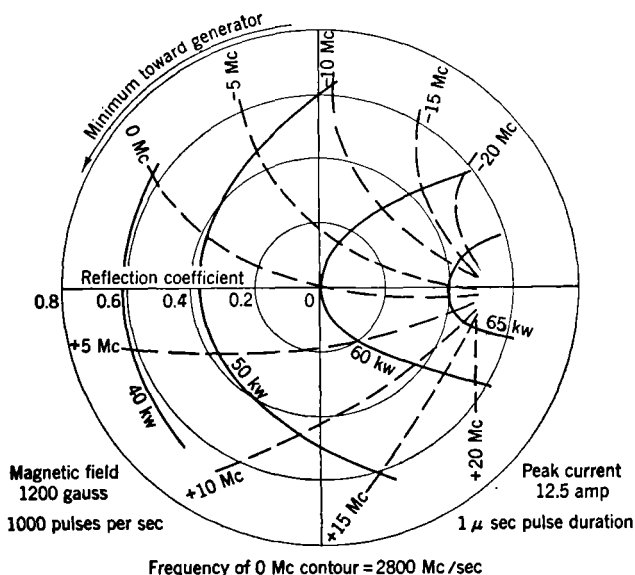


FIG. 19-17.—Rieke diagram for 2J32 magnetron.

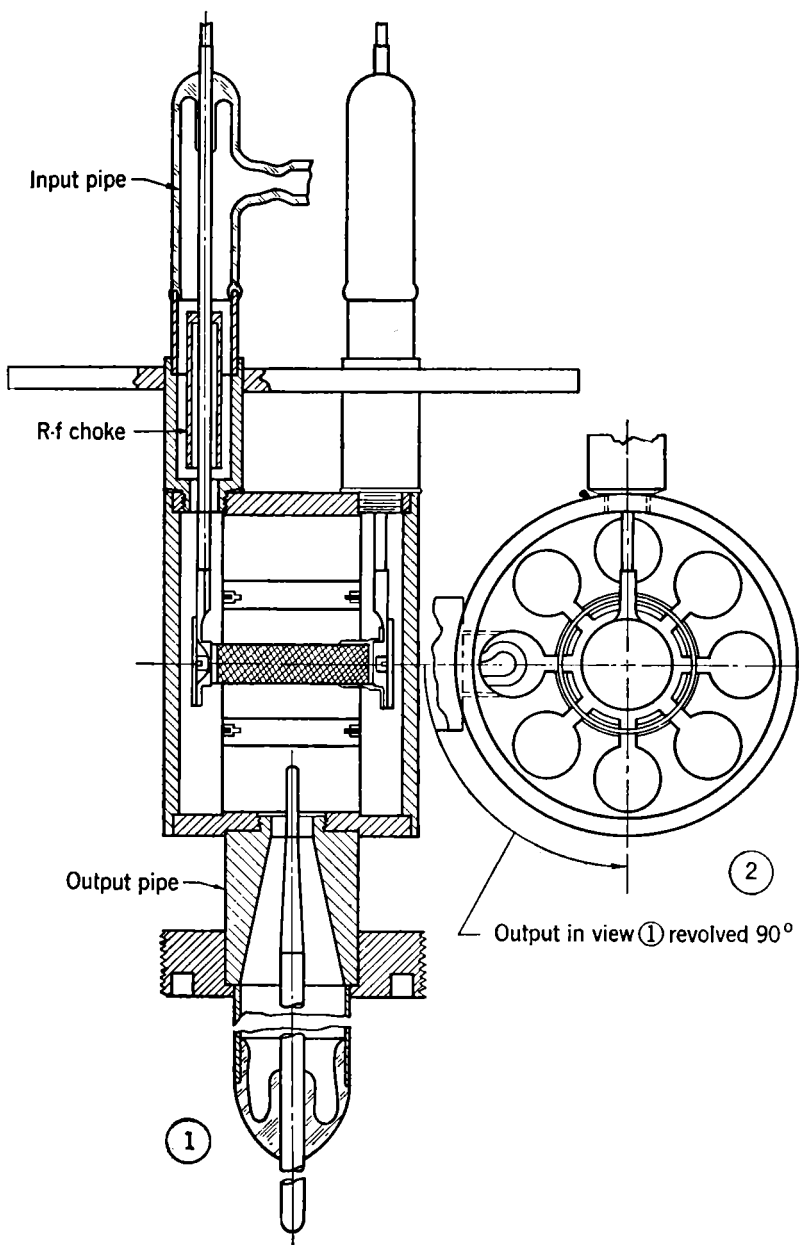


FIG. 19-18.—Cross sections of 2J22 to 2J34 magnetrons.



output of about 750 kw. A maximum average input power of 600 watts may be employed; the maximum specified pulse duration is 2.5  $\mu$ sec. The pushing figure averages 0.3 Mc/sec per amp, and the pulling figure is corrected to a value not exceeding 15 Mc/sec by means of a transformer incorporated in the output coupling; the Rieke diagram of Fig. 19-17 applies to operation with the recommended transformer.

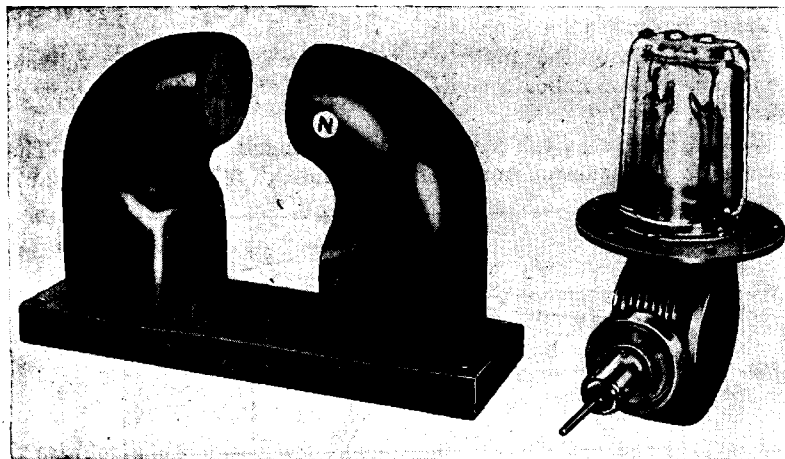


FIG. 19-19.—2J22 to 2J34 type magnetrons.

The cathodes are oxide-coated, with heater ratings of 1.5 amp at 6.3 volts. Characteristic scale factors and dimensions for the 2J32 are given in Tables 19-8 and 19-9. The eight-oscillator hole-and-slot

TABLE 19-8.—CHARACTERISTIC SCALE FACTORS FOR 2J32 MAGNETRON

$\lambda$ , cm	$\mathfrak{B}$ , gauss	$\mathcal{I}$ , amp	$\mathcal{V}$ , kv	$\mathcal{P}$ , kw	$\mathcal{G}$ , mhos	$Q_u$	$\eta_c$ , %	$\frac{C}{L}$
10.7	577	12.0	3.47	41.6	$3.46 \times 10^{-3}$	1600	96	0.012

TABLE 19-9.—DIMENSIONS IN INCHES OF 2J32 MAGNETRON

a. Anode-block Dimensions: See Fig. 19-1b

$a$	$b$	$c$	$d_a$	$d_c$	$h$	$w$
1.279	1.310	0.398	0.635	0.235	0.777	0.090

b. Strapping Dimensions: See Fig. 19-2a

$m$	$n$	$o$	$q$	$s$	$u$
0.415	0.368	0.345	0.020	0.022	0.060

anode block of this tube is shown in Fig. 19-18; the magnetrons of the other two groups differ only in the oscillator dimensions and in the strapping details.

A magnet with  $1\frac{1}{2}$ -in.-diameter pole faces and a gap of  $1\frac{1}{2}$  in. is required. The magnetron is mounted from the circular flange at the base of the input pipes, and forced-air cooling must be provided. Figure 19-19 shows the external appearance of a tube of this series. The weight of the magnetron is 2 lb 4 oz.

Further data on the 2J32 are contained in Chap. 7 of this volume. See also Radiation Laboratory Report No. 451, "Analysis of Magnetron Operation, Part 2."

**19-5. 4J70-4J77 High-power S-band Tunable Magnetrons.**—The series of eight magnetrons numbered 4J70 through 4J77 provides tunable

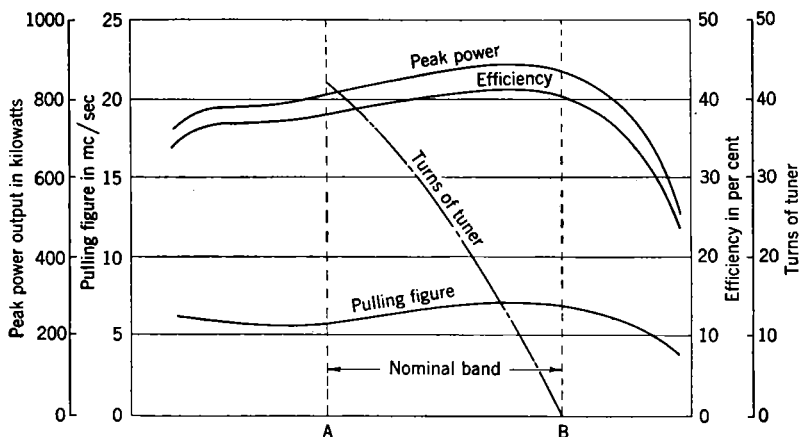


FIG. 19-20.—Typical characteristics of 4J70 to 4J77 magnetrons.

Magnetic field = 2700 gauss  
Pulse duration = 0.8  $\mu$ sec

Peak current = 70 amp  
400 pulses per sec

coverage of the region of the spectrum between 2700 and 3700 Mc/sec. Individual tubes of the series tune approximately 5 per cent (Fig. 19-20) by means of the attached cavity and operate as pulsed oscillators at pulse-power levels ranging up to 1 mw. From 4J70 through 4J73 the output circuits are terminated in  $1\frac{1}{2}$ - by 3-in. waveguides, while the remaining types are equipped with  $1\frac{1}{8}$ -in. coaxial outputs. The cathodes are mounted radially, and a single model of detached magnet serves the entire series.

The useful range of pulse voltage and current inputs (Fig. 19-21) lies between 15 and 30 kv and between 20 and 80 amp, with corresponding pulse-power outputs from 300 to 1000 kw. At voltages or currents higher than those indicated, excessive sparking may occur; operation

in the low-power region is limited by mode instability. At a fixed operating point, the power output varies less than  $\frac{1}{2}$  db as the magnetron is tuned over a 5 per cent band. The rated maximum average input

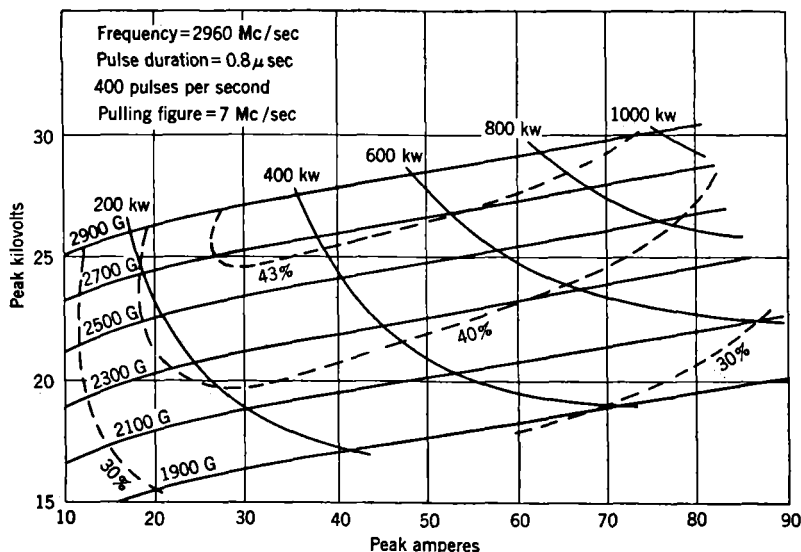


FIG. 19-21.—Performance chart for 4J75 magnetron.

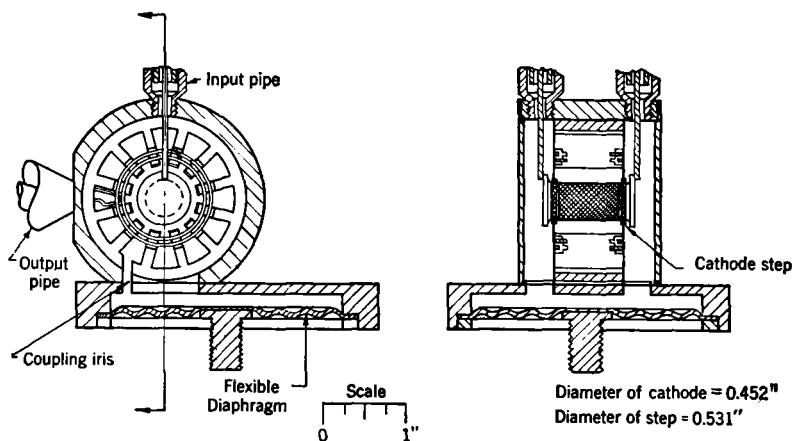


FIG. 19-22.—Cross sections of cavity-tunable magnetron.

power is 1200 watts. Pulse durations up to  $2.5 \mu$ sec may be employed. A maximum pulling figure of 10 Mc/sec is specified, and pushing does not exceed 0.1 Mc/sec per amp.

The screened, oxide-coated cathodes are provided with "steps" to improve operating stability (see Chap. 12). Heater consumption is 3 amp at 16 volts; when the block input power exceeds 200 watts, it is desirable to reduce the heater voltage during operation. Vane-type construction and double-ring strapping are used in the 12-oscillator anode block (Fig. 19-22). Characteristic scale factors for the tubes at either limit of the series are listed in Table 19-10, and tube dimensions are given in Table 19-11.

TABLE 19-10.—CHARACTERISTIC SCALE FACTORS FOR CAVITY TUNABLE MAGNETRONS

Type No.	$\lambda$ , cm	$\mathcal{B}$ , gauss	$g$ , amp	$\mathcal{U}$ , kv	$\mathcal{P}$ , kw	$g$ , mhos	$Q_u$	$\eta_c$ , %	$\frac{C}{L}$
4J77	10.7	502	12.8	2.42	31.0	$5.29 \times 10^{-3}$	2000	92	0.019
4J70	8.5	633	25.4	3.84	97.6	$6.61 \times 10^{-3}$	1500	89	0.031

TABLE 19-11.—DIMENSIONS IN INCHES OF 4J70 AND 4J77 MAGNETRONS

a. Anode-block Dimensions: See Fig. 19-1c

Type No.	$a$	$b^*$	$d_a$	$d_c$	$h$	$t$
4J70	1.561	1.476	0.788	0.452	0.788	0.138
4J77	1.561	1.748	0.788	0.452	0.788	0.138

\* Diameter across flats.

b. Strapping Dimensions: See Fig. 19-2c

Type No.	$m$	$n$	$o$	$p$	$q$	$r$	$s$	$u$
4J70	0.558	0.499	0.448	0.417	0.030	0.020	0.050 (outer) 0.056 (inner)	0.075
4J77	0.558	0.499	0.448	0.417	0.030	0.020	0.050	0.075

Tuning is accomplished by the "cavity-tuning" principle described in Chap. 14. Figures 19-22 and 19-23 illustrate how the shallow, cylindrical cavity is coupled electrically to the anode block by means of an iris. This cavity, in addition to its tuning function, stabilizes the magnetron by a factor of 1.6. The tuning diaphragm is actuated by a mechanism terminated in a standard fitting to which may be attached a length of flexible shafting to permit remote control of the frequency. The rate of tuning is approximately 3 Mc/sec per revolution of the shaft, and the tuning range is limited by stops to the band shown in Table 19-12. Because the diaphragm is flexed beyond its elastic limit, mechanical hysteresis occurs, and a frequency difference of several megacycles per second may be observed at a given tuner setting when

TABLE 19-12.—FREQUENCY BANDS OF MAGNETRONS OF THE 4J70 TO 4J77 SERIES  
See Fig. 19-20

Type No.	Frequency at A, Mc/sec	Frequency at B, Mc/sec
4J70	3540	3710
4J71	3390	3560
4J72	3240	3410
4J73	3090	3260
4J74	2990	3110
4J75	2890	3010
4J76	2790	2910
4J77	2690	2810

that setting is approached from different directions. The life expectancy of the diaphragm is 10,000 cycles.

Either the output or the mounting flange at the base of the input pipes may be used to mount the magnetron. The latter mounting is

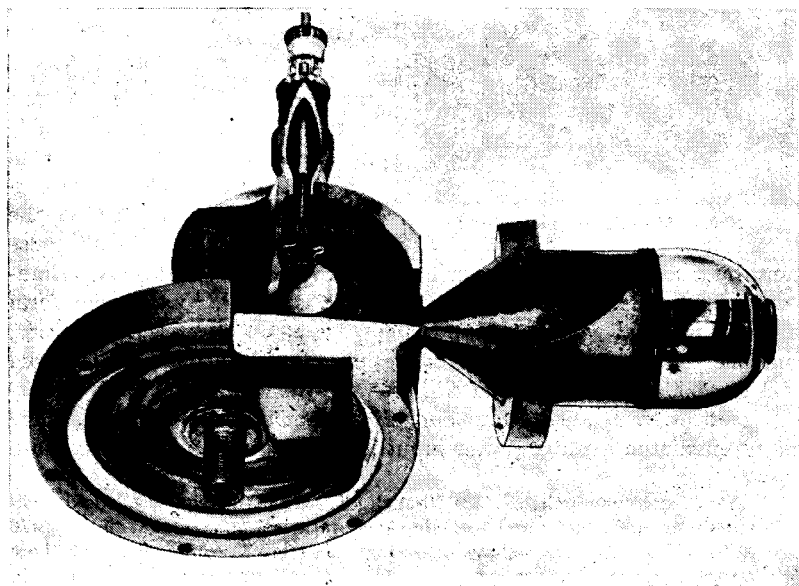


FIG. 19-23.—Cutaway view of 4J77 magnetron.

most useful where it is desired to pressurize the high-voltage components. A magnet with a 1.770-in. gap and  $1\frac{5}{8}$ -in.-diameter pole faces is required. The weight of the magnetron and its associated magnet is approximately 40 lb.

A more complete description of the theory and construction of this series of magnetrons may be found in Radiation Laboratory Report No. 1006, "The 4J70-4J77 Series of Tunable Magnetrons."<sup>1</sup>

**19-6. The HP10V High-power S-band Magnetron.**<sup>2</sup>—The HP10V is a high-power pulsed magnetron, operating at a fixed frequency in the 2800 Mc/sec band. Pulse-power outputs ranging up to 2500 kw are available. The cathode is mounted radially, and the high-voltage input is in the form of a moulded bakelite bushing designed to plug into a receptacle on the pulse transformer (Figs. 19-24 and 19-25). The coaxial output fits standard 1½-in. magnetron couplings, which must be pressurized for high-power operation (above 1000 to 1500 kw). A detached magnet is used.

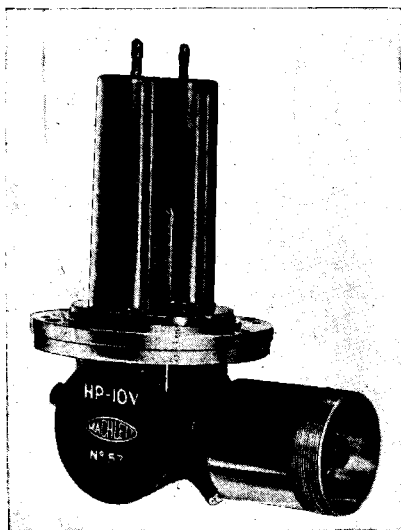


FIG. 19-24.—HP10V magnetron.

Useful pulse voltage inputs range from 30 to 50 kv. At the lower voltage, operation is stable between 60 and 200 pulse amp, while at the 50-kv level the current range is restricted to the region between 100 and 140 pulse

amp by excessive internal sparking at the upper limit and by deterioration of the spectrum at the lower (owing, possibly, to the poor form of the impressed voltage pulse). Operation below 30 kv is satisfactory, but the efficiency is low. Reliable pulse-power outputs extend from 500 to 2500 kw as shown in Fig. 19-26, with a recommended operating point of 1850 gauss, 48 kv, and 130 amp at the 2500-kw level. The rated maximum average power input is 2500 watts, and the maximum

<sup>1</sup> The magnetrons numbered 4J31 through 4J35 are fixed-frequency pulsed oscillators with an anode-block and cathode structure identical with that of the 4J76 and 4J77. These magnetrons have operating characteristics quite similar to those of the tunable series, and they are mechanically interchangeable with types 4J74 to 4J77. The frequencies lie in the range 2700 to 2900 Mc/sec, with the different types separated by changes in strap capacitance.

The group of tubes from 4J36 through 4J41 has an anode-block and cathode structure identical with that of the 4J70 and 4J71; these types are mechanically and electrically interchangeable with the 4J70 to 4J73 group. The frequencies are fixed and lie between 3400 and 3700 Mc/sec.

<sup>2</sup> Data for Sec. 19-6 submitted by R. T. Young, Jr.

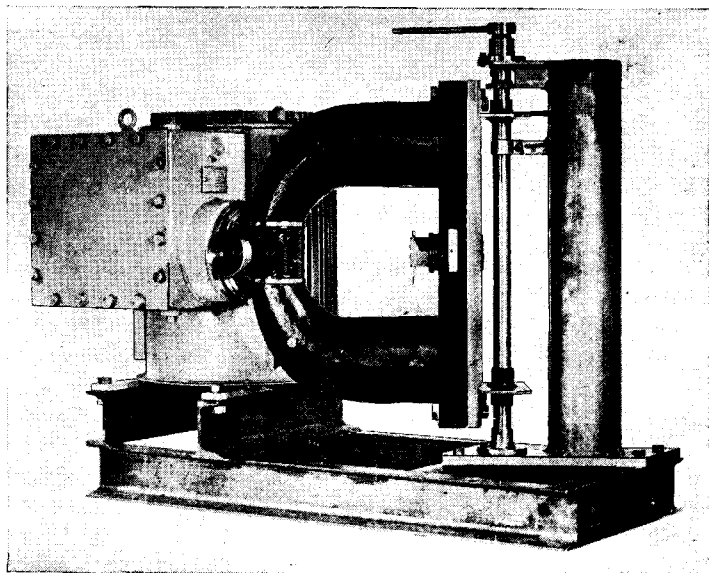


FIG. 19-25.—Mounted HP10V magnetron.

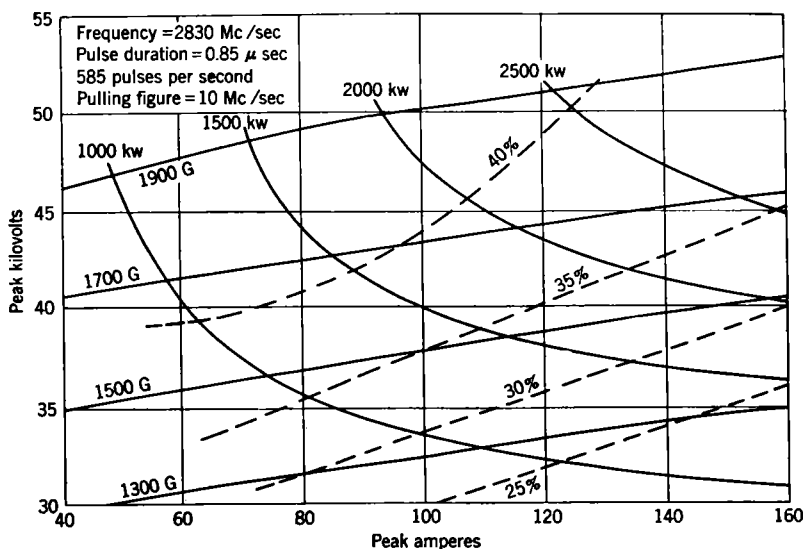
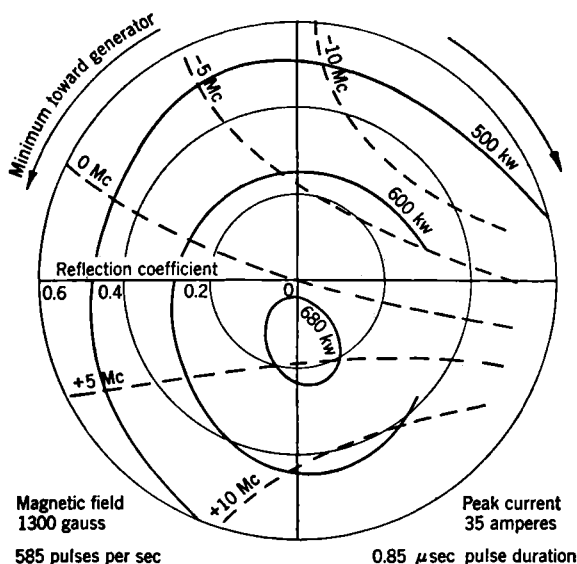


FIG. 19-26.—Performance chart for HP10V magnetron.

pulse duration is 1  $\mu$ sec. Pulling figures for average tubes fall between 8 and 13 Mc/sec, and it is evident from Fig. 19-27 that nothing is to be gained by increasing this loading.

The screened and oxide-coated cathode is provided with end shields which, to inhibit sparking, present only flat or rounded surfaces to the anode block, while for the same reason the supporting leads are designed for the minimum field gradients consistent with available clearances. A current of 8.5 amp at 13 volts is drawn by the heater when the magnetron is started; during operation the heater should be turned off. Localized



Frequency of 0 Mc contour = 2820 Mc/sec  
FIG. 19-27.—Rieke diagram for HP10V magnetron.

deterioration of the central portion of the cathode during operation is attributed to excessive back bombardment in this region because of axial nonuniformity of the magnetic field and/or of the r-f voltage. The unusually long 10-oscillator anode block is of vane-type construction, with a single ring strap, as shown in Fig. 19-28. Attempts to increase the 3 per cent mode separation of this design by a heavier strapping introduced a mode change at high currents. Violent 50- to 300-Mc/sec oscillations of the current and voltage are observed in isolated regions of the performance chart; it is thought that an electronic instability, characteristic of the long anode block, may cause an excitation of an oscillatory circuit in the pulse generator or input leads. All sharp edges in the anode block and in the straps are broken. Characteristic scale



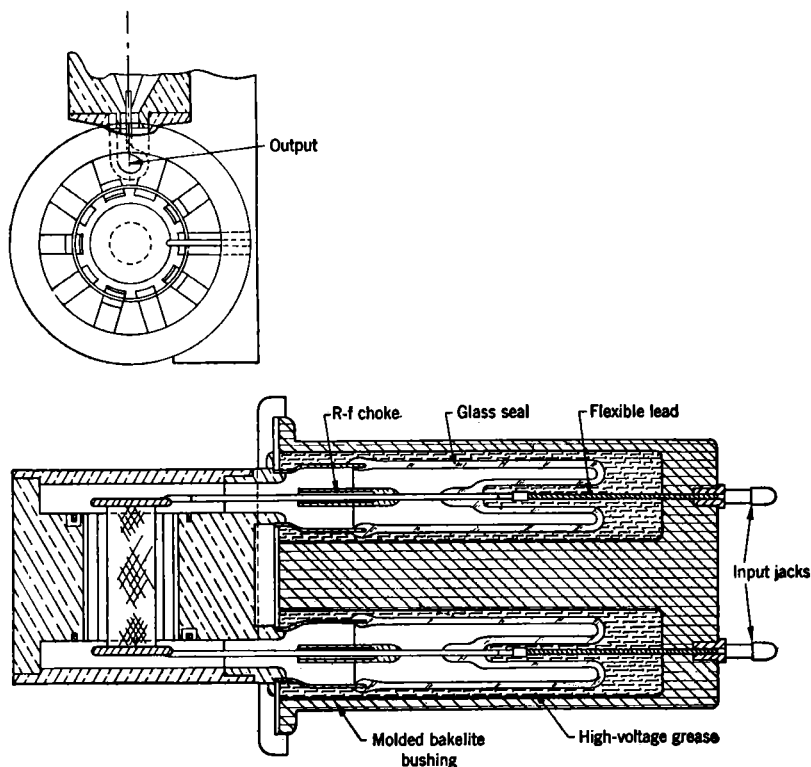


FIG. 19-28.—Cross sections of HP10V magnetron.

FIG. 19-13.—CHARACTERISTIC SCALE FACTORS FOR THE HP10V MAGNETRON

$\lambda$ , cm	$\beta$ , gauss	$s$ , amp	$V$ , kv	$\phi$ , kw	$g$ , mhos	$Q_u$	$\eta_e$ , %	$\frac{C}{L}$
10.6	533	70.8	8.03	568	$8.82 \times 10^{-3}$	1500	93	0.033

TABLE 19-14.—DIMENSIONS IN INCHES OF HP10V MAGNETRON

a. Anode-block Dimensions: See Fig. 19-1c

$a$	$b$	$d_a$	$d_c$	$h$	$t$
2.440	2.255	1.181	0.596	1.575	0.236

b. Strapping Dimensions: See Fig. 19-2a

$m$	$n$	$o$	$q$	$s$	$u$
0.801	0.680	0.621	0.060	0.100	160

factors and block dimensions for the HP10V are listed in Tables 19-13 and 19-14.

The magnetron is mounted by means of the input bushing. A magnet with a gap of  $2\frac{3}{4}$  in. and with pole faces of  $2\frac{3}{4}$ -in. diameter is required; the combined weight of the magnet and the magnetron is approximately 100 lb. A water jacket which is an integral part of the block provides the means of cooling the tube.

Further details of the construction and operation of the HP10V may be found in the following reports: Radiation Laboratory Report No. 793, "Present Status of High Power at S-Band"; Radiation Laboratory Report No. 682-6, "Line Type Modulator and HP10V Magnetron Operation at 6 Megawatts"; and NDRC 14-423, "Final Report Concerning Development Work Done on Contract OEMsr-1146."

**19-7. The BM50 Very Low Power X-band Magnetron.**<sup>1</sup>—Of interest because it is designed to operate at a pulse-power output of only 50 watts,

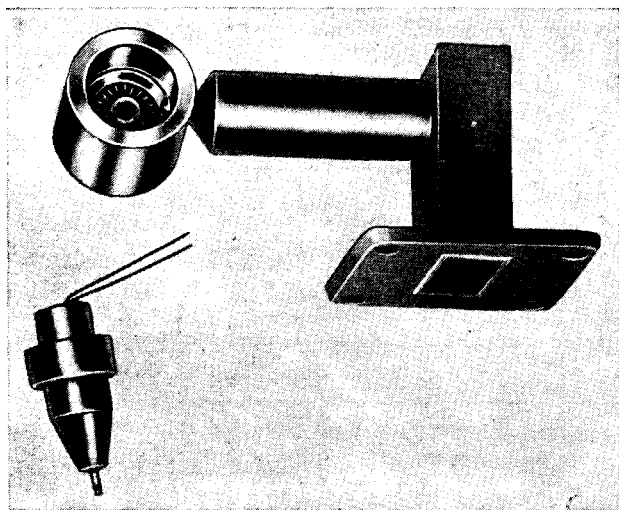


FIG. 19-29.—Anode block and cathode of BM50 magnetron.

the BM50 is an experimental magnetron with a fixed frequency of 9375 Mc/sec. It has been tested under c-w as well as pulsed conditions of operation. The cathode is axially mounted, and the output circuit is of the coaxial-to-waveguide transition type, as shown in Fig. 19-29. An attached magnet has been used.

As a pulsed oscillator, the BM50 operates stably over a range of pulse-input currents and voltages from 75 to 300 ma and from 600 to 1600 volts. Reference to Fig. 19-30 indicates that the corresponding

<sup>1</sup> Data for Sec. 19-7 submitted by J. R. Feldmeier.

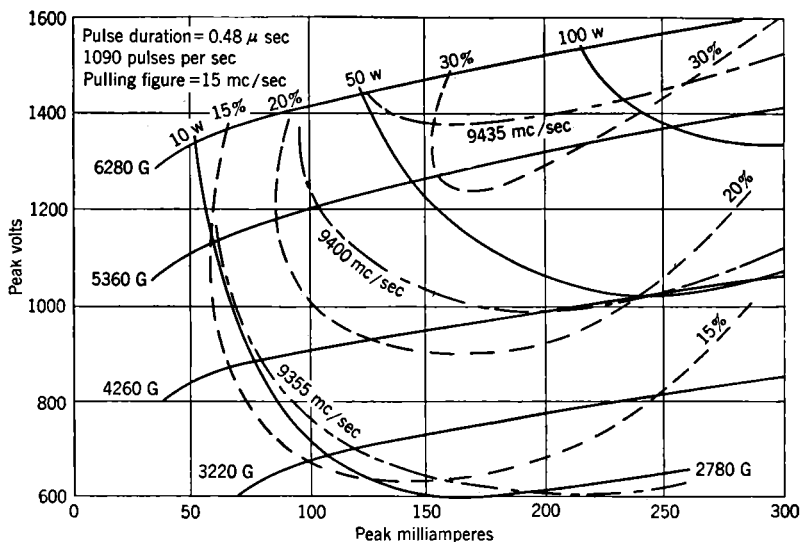


FIG. 19-30.—Performance chart for BM50 magnetron.

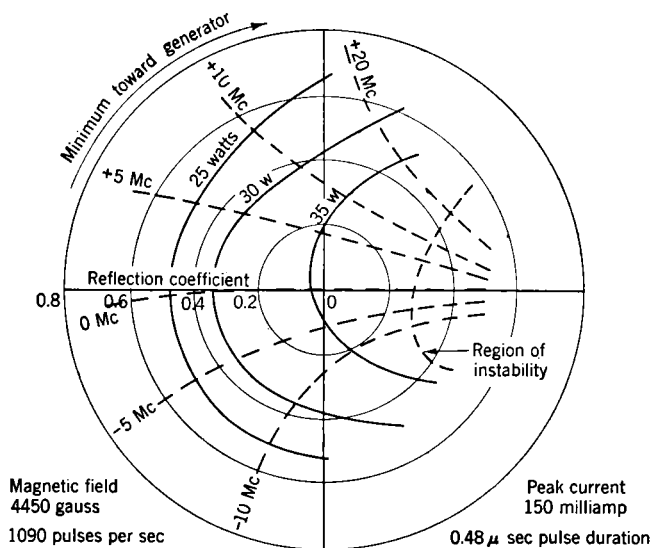


FIG. 19-31.—Rieke diagram for BM50 magnetron.

pulse-power output ranges from 10 to 100 watts. At currents in excess of 300 ma mode instability is encountered, whereas below 75 ma the efficiency is very low. Because of the heavy internal loading introduced by copper losses, operation is unstable at pulling figures in excess of 15 Mc/sec (see Fig. 19-31). From the pushing contours included in Fig. 19-30, it may be seen that pushing is moderate at currents above 150 ma.

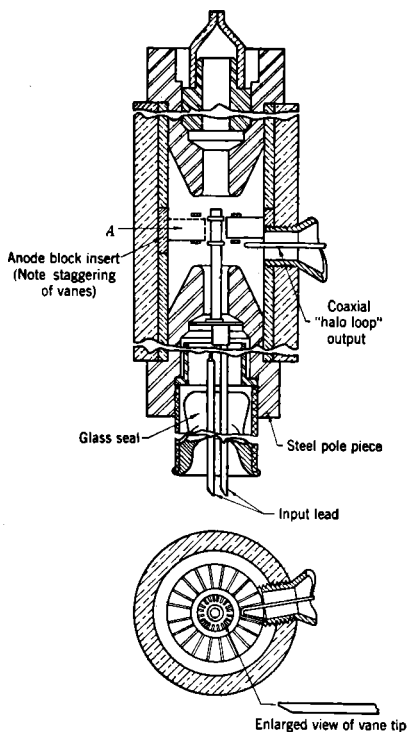


FIG. 19-32.—Cross sections of BM50 magnetron. The vertical position of the vane marked *A* is that of a vane adjacent to the one in the plane of the drawing. This is done to illustrate their staggered arrangement.

The screened, oxide-coated cathode has a heater rating of 0.33 amp at 6.0 volts. Limited by this cathode, which was designed for pulsed operation, the BM50 has been oscillated under c-w conditions at input powers up to 130 ma at 840 volts. Figure 19-32 illustrates the novel method used in strapping the 20-vane anode block; to avoid the necessity for grooving the tiny vanes, they are staggered axially, so that the single ring strap at either end of the anode rests only on alternate vanes. Characteristic scale factors and dimensions for this block are listed in Tables 19-15 and 19-16. More detailed information may be obtained from Radiation Laboratory Report No. 1007.

#### 19-8. 2J41 Low-power Stabilized X-band Magnetron.<sup>1</sup>—The

2J41 magnetron is a pulsed oscillator, tunable over the range from 9290 to 9330 Mc/sec. Pulse-power outputs up to 1.25 kw may be obtained, with a frequency stability of 1 Mc/sec over a wide range of load, temperature, and input conditions. An X-band-waveguide coupling terminates the output circuit, and the magnet is an attached type.

Operation of the 2J41 is satisfactory between 0.25 and 2.0 pulse amp and between 1.25 and 3.0 kv. At currents higher or lower than those indicated, mode instability is encountered. As may be seen from Fig. 19-33, the useful pulse-power output ranges from 200 to 1250 watts;

<sup>1</sup> Data for Sec. 19-8 submitted by M. A. Herlin.

the maximum average power input is 10 watts, and the maximum pulse duration is 0.5  $\mu$ sec. The pulling figure is 1.5 Mc/sec (see Fig. 19-34), and the pushing figure is approximately 2 Mc/sec per amp.

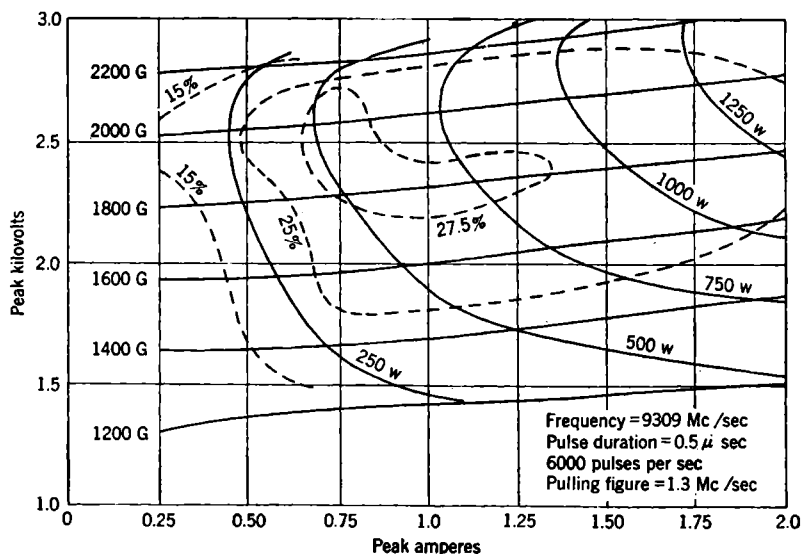


FIG. 19-33.—Performance chart for 2J41 magnetron.

An unscreened, oxide-coated cathode with a heater rating of 0.36 amp at 5.0 volts is used. Characteristic scale factors for the 12-oscil-

TABLE 19-15.—CHARACTERISTIC SCALE FACTORS FOR BM50 MAGNETRONS

$\lambda$ , cm	$\beta$ , gauss	$\phi$ , amp	$V$ , kv	$P$ , kw	$S$ , mhos	$Q_u$	$\eta_c$ , %	$\frac{C}{L}$
3.20	1045	0.227	0.160	0.0363	$1.42 \times 10^{-3}$	600	71	0.047

TABLE 19-16.—DIMENSIONS IN INCHES OF BM50 MAGNETRON

a. Anode Dimensions: See Fig. 19-1c

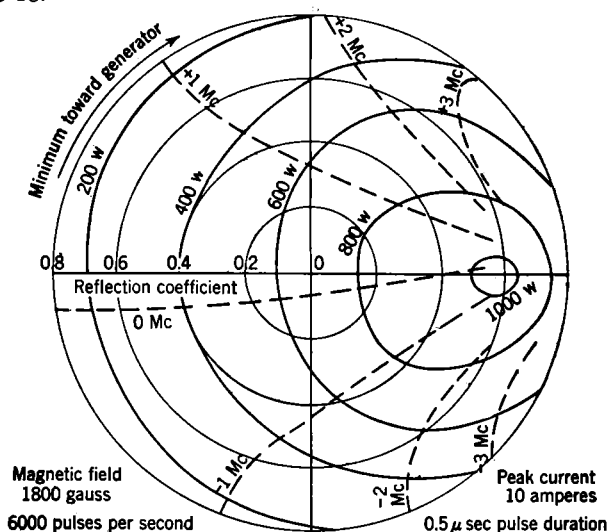
$a$	$b$	$d_a$	$d_c$	$e$	$f$	$h$	$t$
0.264	0.458	0.101	0.065	0.022	0.008	0.095*	0.015

\* Vane length.

b. Strapping Dimensions: See Fig. 19-2d

$m$	$n$	$s$	$u$
0.110	0.070	0.005	0.005

lator double-ring-strapped anode block, shown in Fig. 19-35, are given in Table 19-17, and the dimensions of this vane-type block are listed in Table 19-18.



Frequency of 0 Mc contour = 9310 Mc/sec  
Fig. 19-34.—Rieke diagram for 2J41 magnetron.

TABLE 19-17.—CHARACTERISTIC SCALE FACTORS FOR 2J41 MAGNETRON

$\lambda$ , cm	$\beta$ , gauss	$s$ , amp	$\mathcal{U}$ , kv	$\phi$ , kw	$\mathcal{G}$ , mhos	$Q_u$	$\eta_c$ , %	$\frac{C}{L}$
3.22	1450	1.19	0.382	0.455	$3.12 \times 10^{-3}$	750* 5000†	62	0.033

\* Anode block only.

† Anode block and stabilizer combined.

TABLE 19-18.—DIMENSIONS IN INCHES OF 2J41 MAGNETRON

a. Anode Dimensions: See Fig. 19-1c

$a$	$b$	$d_a$	$d_c$	$e$	$f$	$h$	$l$
0.250	0.435	0.095	0.040	0.015	0.007	0.202	0.0225

b. Strapping Dimensions: See Fig. 19-2e

$m$	$n$	$o$	$p$	$q$	$r$	$s$	$u$
0.153	0.118	0.078	0.063	0.020	0.020	0.015	0.030

The magnetron is tuned by means of a plate suspended above one end of the block. This plate, which appears in Fig. 19-35, is perforated with a circular hole concentric with the anode block, so that only the rear portions of the oscillators are covered. Adjustment of a screw raises or lowers the tuning plate, the frequency being increased as the plate approaches the block. A stabilization of approximately 10 is obtained by coupling a high- $Q$ , temperature-compensated, invar cavity to the output line; at this high value of stabilization it is necessary to introduce heavy mode damping by the insertion of polyiron posts in the waveguide at null-voltage points for the operating mode. The 40-Mc/sec tuning range shown in Fig. 19-36 is covered by tuning the stabilizer only; by tuning both the magnetron and the stabilizer a range of 100 Mc/sec can be achieved without excessive drop in power or increase in pulling figure.

Figure 19-37 shows the unusual construction used in the 2J41. A stainless-steel envelope, acting as the vacuum seal, surrounds the block, pole pieces, and tuner mechanism. The pole pieces, while bolted to the block, are electrically insulated and are operated at cathode potential, so that they serve as end shields. The

assembly of magnetron, magnet, and stabilizer, weighing 6 lb, is attached rigidly to the output flange, from which the tube is to be mounted. This is shown in Fig. 19-38. Forced-air cooling is not required.

Further details of the theory and performance of the 2J41 may be obtained from the following Radiation Laboratory Reports: 52—5/10/45, "Magnetron Frequency Stabilization with Application to the 2J41 Magnetron"; and 52—9/3/45, "Performance Characteristics of the 2J41 Stabilized Magnetron and the Effects of Parameter Variation."

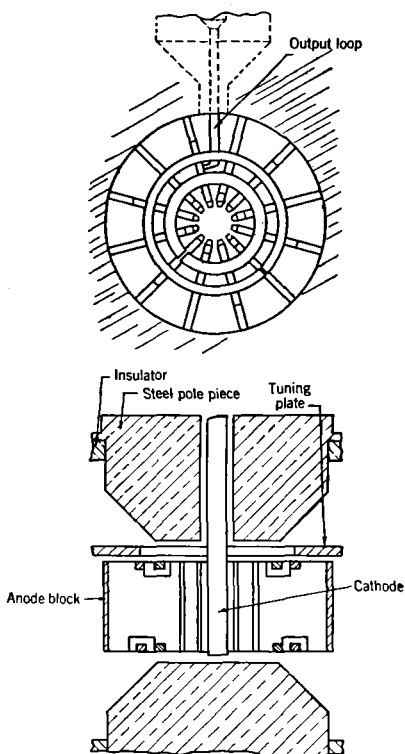
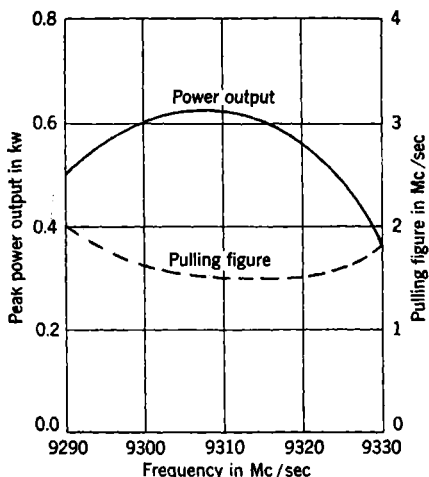


FIG. 19-35.—Cross sections of 2J41 magnetron.

**19-9. The 2J42 Low-voltage X-band Magnetron.**<sup>1</sup>—The 2J42 magnetrons operate as pulsed oscillators with fixed frequencies located in the band from 9345 to 9405 Mc/sec. Pulse-power outputs ranging up to 20 kw are available, and later models of the tube are stabilized by a factor of 2. The cathode is mounted axially; and as manufactured, the



Peak voltage = 2.5 kv; Peak current = 0.9 amp

FIG. 19-36.—Tuning curve for 2J41 magnetron.

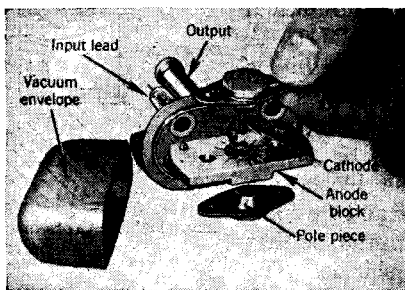


FIG. 19-37.—Exploded view of 2J41 magnetron.

magnet is attached to the tube. The output is of the coaxial-to-waveguide transition type, terminating in an X-band-waveguide coupler.

The useful range of pulse voltage and current inputs lies between 4 and 8 kv and between 2.5 and 6.5 amp, with corresponding pulse-power outputs from 5 to 20 kw. To make use of the full range an electromagnet must be substituted for the standard permanent magnet. At voltages

<sup>1</sup> Data for Sec. 19-9 submitted by J. R. Feldmeier.



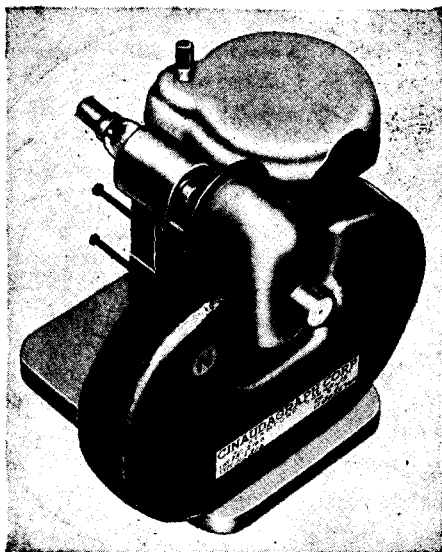
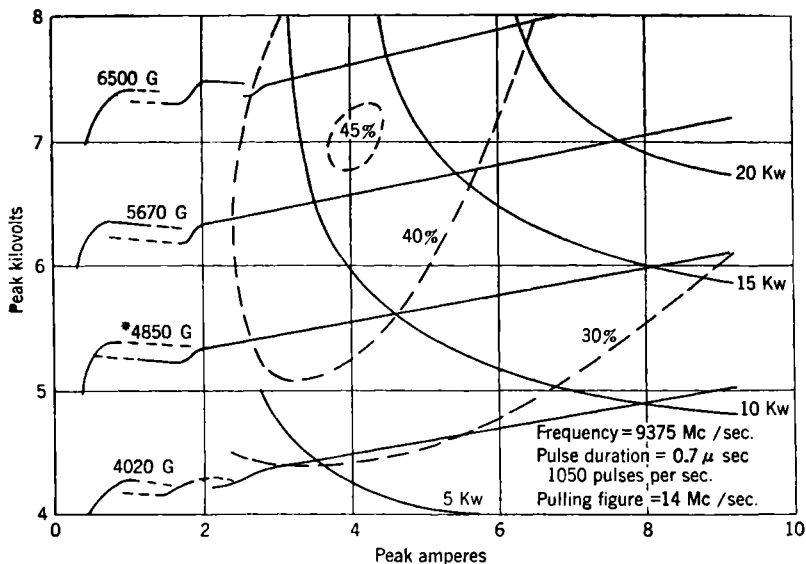
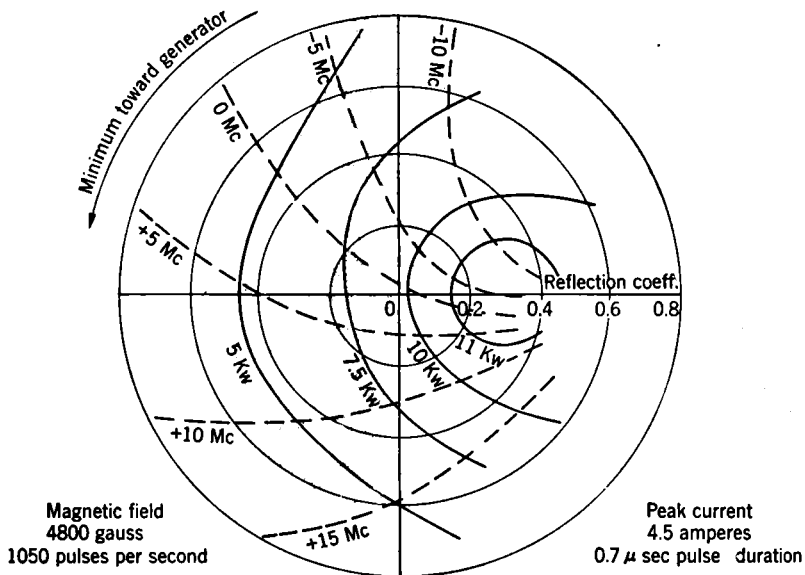


FIG. 19-38.—2J41 magnetron and magnet.



\*Operating line for standard attached magnet

FIG. 19-39.—Performance chart for 2J42 magnetron.



Frequency of 0 mc contour = 9375 mc/sec

FIG. 19-40.—Rieke diagram for 2J42 magnetron.

TABLE 19-19.—CHARACTERISTIC SCALE FACTORS FOR 2J42 MAGNETRON

$\lambda$ , cm	$\mathcal{B}$ , gauss	$s$ , amp	$\mathcal{V}$ , kv	$\mathcal{P}$ , kw	$\mathcal{G}$ , mhos	$Q_u$	$\eta_c$ , %	$\frac{C}{L}$
3.20	1550	3.90	1.064	4.15	$3.66 \times 10^{-3}$	900	75	0.019

TABLE 19-20.—DIMENSIONS IN INCHES FOR 2J42 MAGNETRON

a. Anode Dimensions: See Fig. 19-1c

$a$	$b$	$d_a$	$d_c$	$h$	$t$
0.276	0.478	0.155	0.083	0.206	0.0205

b. Strapping Dimensions: See Fig. 19-2e

$m$	$n$	$o$	$p$	$q$	$r$	$s$	$u$
0.183	0.148	0.108	0.093	0.020	0.020	0.020	0.035

greater than 8 kv, excessive sparking may occur; while at currents below 2.5 amp or above 6.5 amp, mode instability is encountered as illustrated by Fig. 19-39. Up to 80 watts of average power may be put into the magnetron, and pulse durations up to 2.5  $\mu$ sec are permissible. A maximum pulling figure of 15 Mc/sec is specified (Fig. 19-40). For currents greater than 4 amp the pushing figure is usually less than 1 Mc/sec per amp.

A screened, nickel-sleeve cathode with oxide coating is used. During operation at average input powers in excess of 30 watts, the normal heater power consumption of 0.48 amp at 6.3 volts should be reduced. The 12-oscillator double-ring-strapped anode block shown in Fig. 19-41 is of vane-type construction. Characteristic scale factors for this block are listed in Table 19-19, and tube dimensions are given in Table 19-20.

Later models of the 2J42 are stabilized by including in the output circuit a special waveguide section containing a half-wavelength resonant cavity formed by two cylindrical posts extending across the guide. When tuned to the magnetron frequency, this cavity provides a stabilization of 2, which has been used to increase the power output at the 15 Mc/sec pulling figure rather than to reduce the pulling figure. By making the cavity adjustable, it would be possible to obtain a 1 per cent tuning range.

The 27-oz Alnico V magnet supplied with the tube provides a field of 5300 gauss at saturation; this field is reduced during the factory processing until the operating voltage at 4.5-amp pulse current lies between 5.3 and 5.7 kv (see Fig. 19-39). Figure 19-42 shows how the magnet and the block are rigidly attached to the mounting plate, which

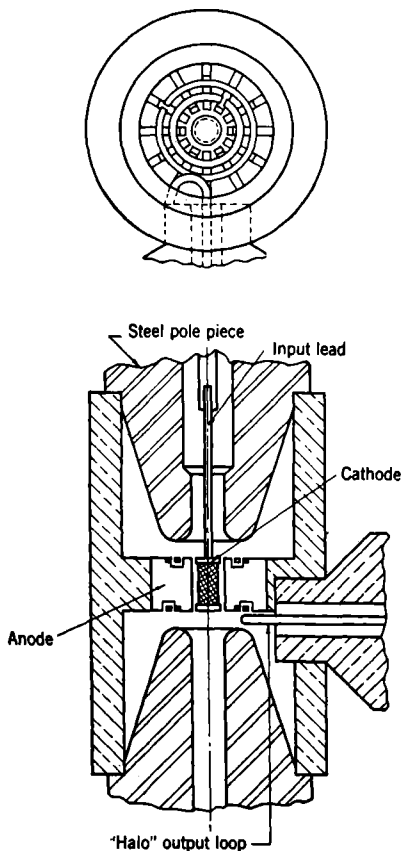


FIG. 19-41.—Cross sections of 2J42 magnetron.

serves also as the output flange. Two struts connecting the block to the mounting plate are used as cooling radiators, and a small current of air should be directed over these during operation. The weight of the entire assembly is 3 lb.

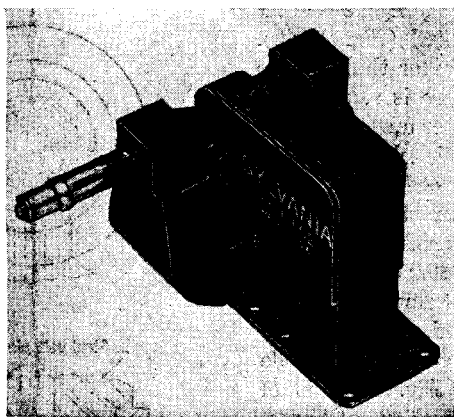


FIG. 19-42.—2J42 magnetron and magnet.

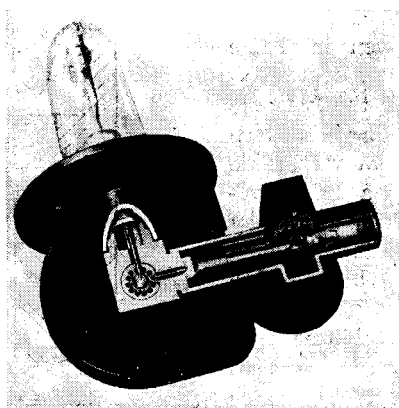


FIG. 19-43.—Cutaway view of 725A magnetron.

**19-10. The 725A Magnetron.**<sup>1</sup>—This magnetron is a fixed-frequency pulsed oscillator operating at pulse-power levels up to 70 kw in the frequency band from 9405 to 9345 Mc/sec. The cathode is radially mounted, and a separate magnet must be used. A standard X-band-waveguide coupler terminates the output circuit, which is of the coaxial-line-to-waveguide transition type as seen in Fig. 19-43.

<sup>1</sup> Data for Sec. 19-10 submitted by L. R. Walker.

The useful range of pulse voltage and current inputs lies between 7 and 16 kv and between 4 and 16 amp. As may be seen from Fig. 19-44, the corresponding range of pulse-output powers extends from 10 to 70 kw. Low-power operation is limited by decreasing efficiency, while the high-power boundary is determined by arcing and overheating of the cathode. No mode shift is observed within the operating region set by these conditions. The maximum average power input at a pulse duration of 1  $\mu$ sec. and a repetition rate of 1000 pps is 150 watts. A maximum

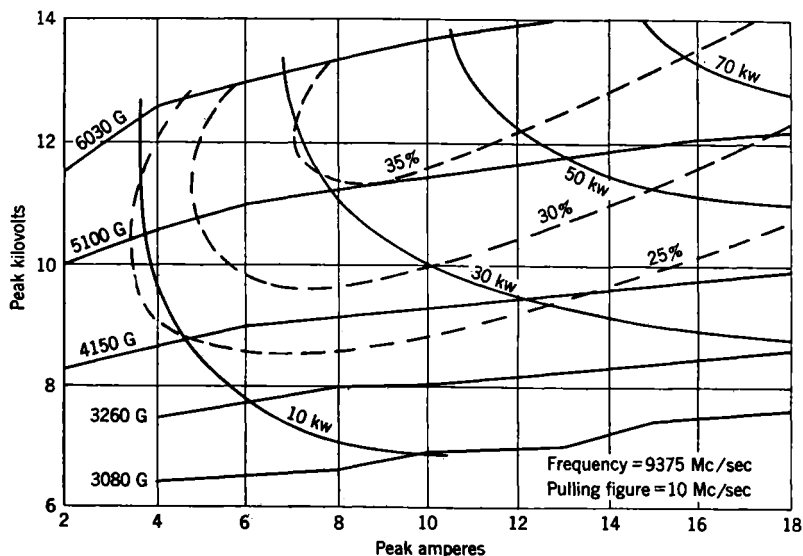


FIG. 19-44.—Performance chart for 725A magnetron.

pulse duration of 2  $\mu$ sec is permissible. Figure 19-45 shows a Rieke diagram for the 725A; the nominal pulling figure is 15 Mc/sec.

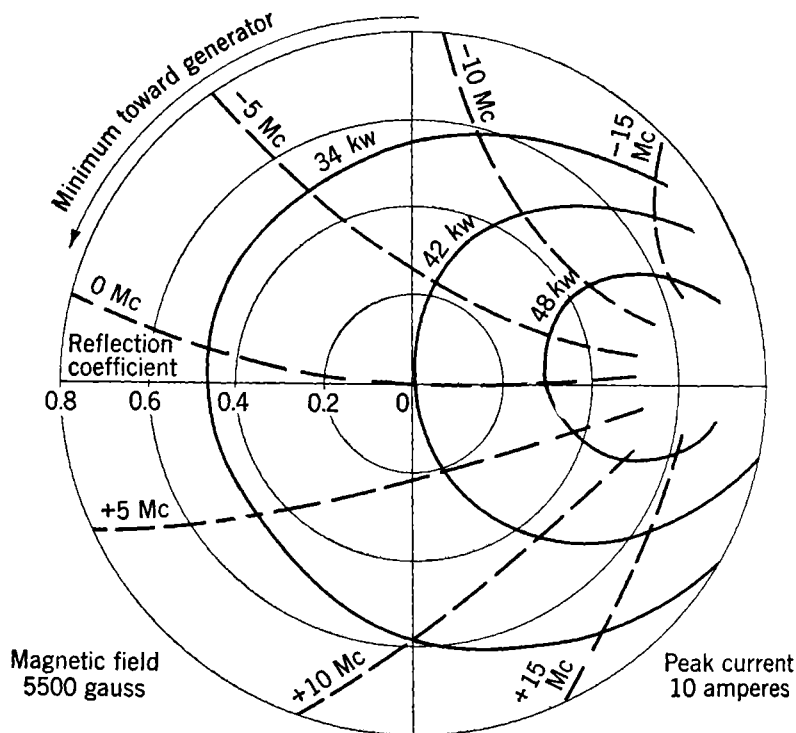
The cathode consists of an oxide-impregnated nickel mesh, formed by sintering nickel powder to a heavy-walled nickel sleeve. The heater rating is 1 amp at 6.3 volts; during operation this heater power should

TABLE 19-21.—CHARACTERISTIC SCALE FACTORS FOR 725A MAGNETRON

$\lambda$ , cm	$\beta$ , gauss	$s$ , amp	$V$ , kv	$P$ , kw	$G$ , mhos	$Q_u$	$\eta_e$ , %	$\frac{C}{L}$
3.20	1480	7.05	1.82	12.8	$3.87 \times 10^{-3}$	650* 1000†	75* 82†	0.107* 0.026†

\* Hole-and-slot version.

† Vane type.



Frequency of 0 Mc contour = 9375 Mc/sec

FIG. 19-45.—Rieke diagram for 725A magnetron.

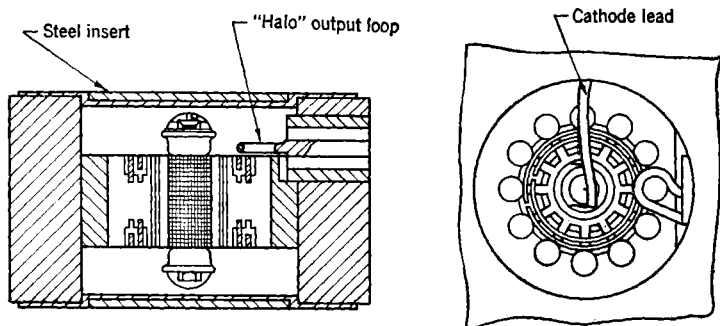


FIG. 19-46.—Cross sections of 725A magnetron.

be reduced. Both vane-type and hole-and-slot anode blocks have been manufactured, each with 12 oscillators. Characteristic scale factors for these blocks are listed in Table 19-21, and Table 19-22 gives the dimensions of both models. The hole-and-slot construction is illustrated by Fig. 19-46.

TABLE 19-22.—DIMENSIONS IN INCHES FOR 725A MAGNETRON  
a. Anode Dimensions, Hole-and-slot Version: See Fig. 19-1b

<i>a</i>	<i>b</i>	<i>c</i>	<i>d<sub>a</sub></i>	<i>d<sub>c</sub></i>	<i>h</i>	<i>w</i>
0.537	0.391	0.079	0.204	0.102	0.250	0.021

b. Strapping Dimensions, Hole-and-slot Version: See Fig. 19-2c

<i>m</i>	<i>n</i>	<i>o</i>	<i>p</i>	<i>q</i>	<i>r</i>	<i>s</i>	<i>u</i>
0.173	0.152	0.130	0.117	0.010	0.010	0.035	0.047

c. Anode Dimensions, Vane Type: See Fig. 19-1c

<i>a</i>	<i>b</i>	<i>d<sub>a</sub></i>	<i>d<sub>c</sub></i>	<i>h</i>	<i>t</i>
0.545	0.524	0.204	0.102	0.250	0.030

d. Strapping Dimensions, Vane Type: See Fig. 19-2e

<i>m</i>	<i>n</i>	<i>o</i>	<i>p</i>	<i>q</i>	<i>r</i>	<i>s</i>	<i>u</i>
0.178	0.153	0.123	0.114	0.014	0.014	0.015	0.025

A magnet with a gap of 0.635 in. and a pole-tip diameter of  $\frac{3}{4}$  in. is required. The tube is mounted by means of a circular flange to which the anode block and radiators are rigidly attached. Forced-air cooling must be provided. The weight of the magnetron is  $1\frac{1}{2}$  lb, while a magnet suitable for operating the tube at 12 kv weighs 8 lb.

Several variations of the 725A have been produced. Type 730A is identical except for the positioning of the input leads, which are located  $180^\circ$  from the output circuit. The 2J49 and 2J50 differ from the 725A only in frequency, the r-f output of the former lying between 9003 and 9168 Mc/sec and that of the latter between 8740 and 8890 Mc/sec. The 2J53, with the same frequency as the 725A, has a special cathode structure designed for operation at high levels and at 5- $\mu$ sec pulse duration: at 1  $\mu$ sec and 1000 pps the average power input can be as high as 230 watts; whereas at 5  $\mu$ sec and 200 pps, 200 watts may be put into the tube.

**19-11. The 2J51 Magnetron.**<sup>1</sup>—The 2J51 is a mechanically tunable magnetron with an attached magnet, and it is designed for pulsed operation in the frequency range from 8500 to 9600 Mc/sec.

Basically, the tube is an adaptation of the Western Electric 725 to permit mechanical tuning. The anode block in the tube is a simple variation of the block in the 725 (see Fig. 19-47a). Operation is at 14 kv and 14-amp pulse current at the magnetic field supplied by the attached magnets. The output circuit used for the 725 has been modified in dimensional details so that the tube, when loaded by a matched wave-

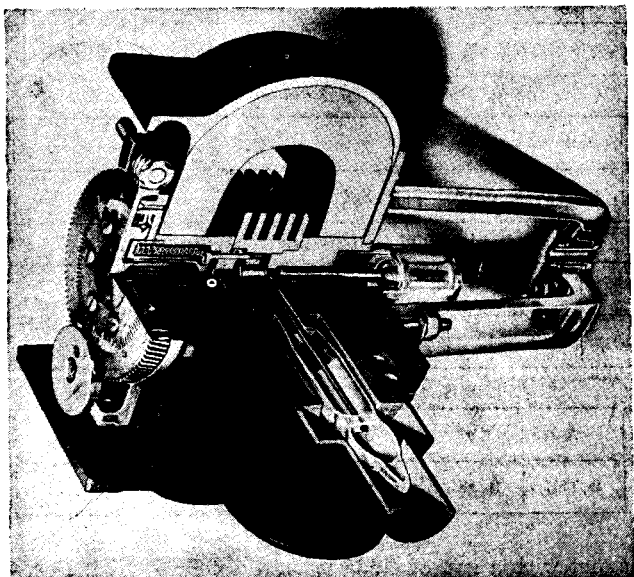


FIG. 19-47a.—Cutaway view of 2J51 magnetron.

guide, will operate at a fairly uniform level of power output and pulling figure over the frequency band.

The cathode is mounted axially through one pole piece of the tube. The tuning mechanism is mounted through the other pole piece. Tuning is accomplished by means of 12 copper pins which may be inserted to a variable depth in the 12 holes of the anode block. The pins are attached to a plunger which is actuated by an external mechanism through a monel-metal bellows. The external drive consists of a worm gear which may be turned from a remote point by means of a flexible shaft.

A schematic cross section of the block region of the 2J51 is shown in Fig. 19-47b. Note that the end space between the anode block and the pole face has been modified at the tuning end of the tube. This

<sup>1</sup> Data for Sec. 19-11 submitted by P. Kusch.



modification ensures that the resonances of the pin system lie at higher frequencies than any of the normal operating frequencies of the tube.

The magnets are adjusted to permit operation at 14 kv and 14-amp pulse current at midband. Four magnetic shunts are provided to adjust

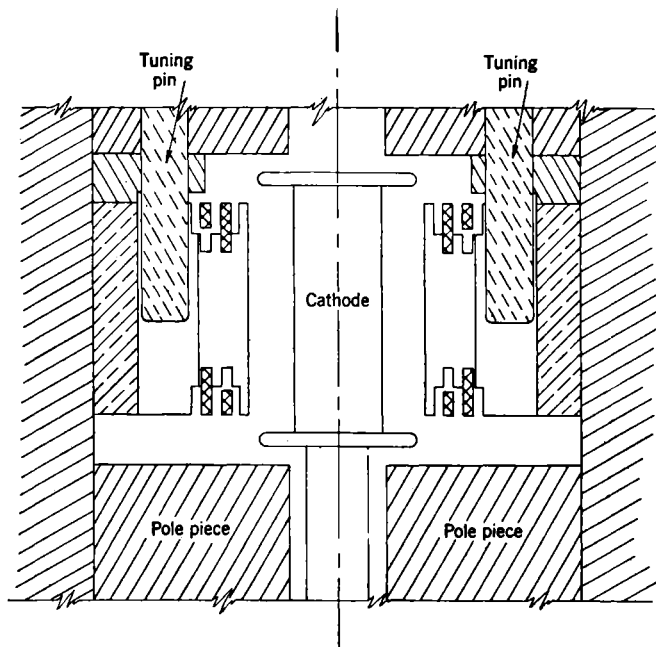


FIG. 19-47b.—Cross section of 2J51 magnetron showing tuning pins.

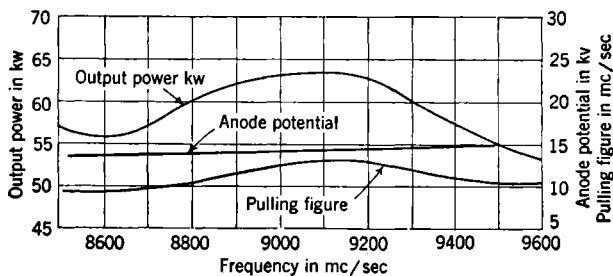


FIG. 19-48.—Tuning characteristics of 2J51 magnetron.

the field downwards. Operation at 10 kv and 10-amp pulse current is possible.

The power output, operating voltage, and pulling figure for a typical tube are shown in Fig. 19.48. The performance chart, the Rieke diagram,

and characteristic scale factors for the 2J51 at any frequency are essentially similar to those obtained for the 725 (see Sec. 19-10).

**19-12. 4J50 (4J52, 4J78) High-power 3-cm Magnetron.**<sup>1</sup>—The 4J50 magnetron is a pulsed oscillator with a fixed frequency lying in the band between 9345 and 9405 Mc/sec. It is capable of a pulse-power output of 400 kw. The cathode is axially mounted, and an attached magnet is used. Radio-frequency power is extracted through a true waveguide output, which terminates in a standard 3-cm waveguide coupler.

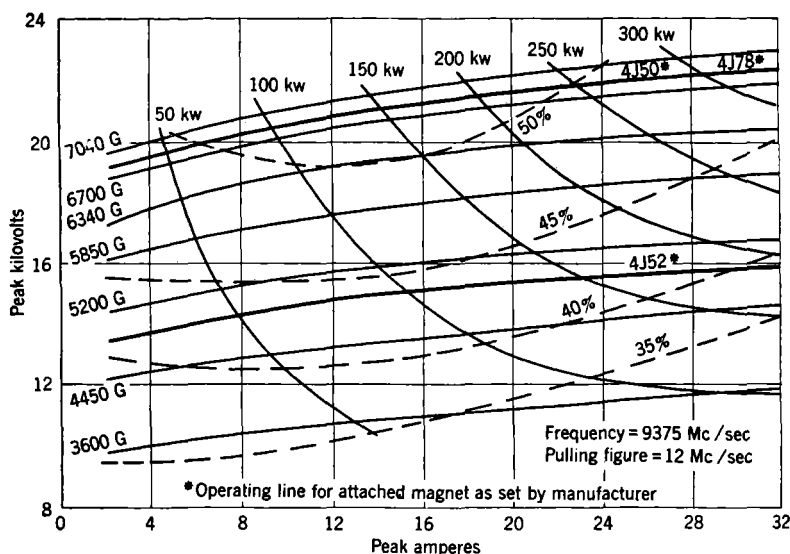


FIG. 19-49.—Performance chart for 4J50 (4J52, 4J78) magnetron.

Useful pulse voltage and current inputs range from 12 to 25 kv and from 8 to 35 amp. Operation is limited at high powers by arcing and at low powers by excessive pushing, although the tube will operate stably at currents as low as 2 amp. The reliable range of pulse powers, indicated in Fig. 19-49, extends from 50 to 300 kw. Figure 19-49 shows the operating line for the attached magnet as supplied and set by the manufacturer. The maximum average input power varies from 1200 watts at  $\frac{1}{2}$   $\mu$ sec to 500 watts at 5  $\mu$ sec. At currents in excess of 15 amp; the pushing figure averages 0.2 Mc/sec per amp; the pulling figure is 12 Mc/sec.

The cathode structure, which appears in Fig. 19-50, is carefully designed for mechanical ruggedness and high heat dissipation. A

<sup>1</sup> Data for Sec. 19-12 submitted by L. R. Walker.

nickel mesh, prepared by sintering nickel powder on a heavy nickel or molybdenum sleeve, forms the base for the oxide coating. Permendur end shields on either end of this sleeve serve also to reduce the magnet gap and to shape the magnetic field. An oxide-blackened molybdenum cylinder extends the cathode structure into the opposite pole piece and

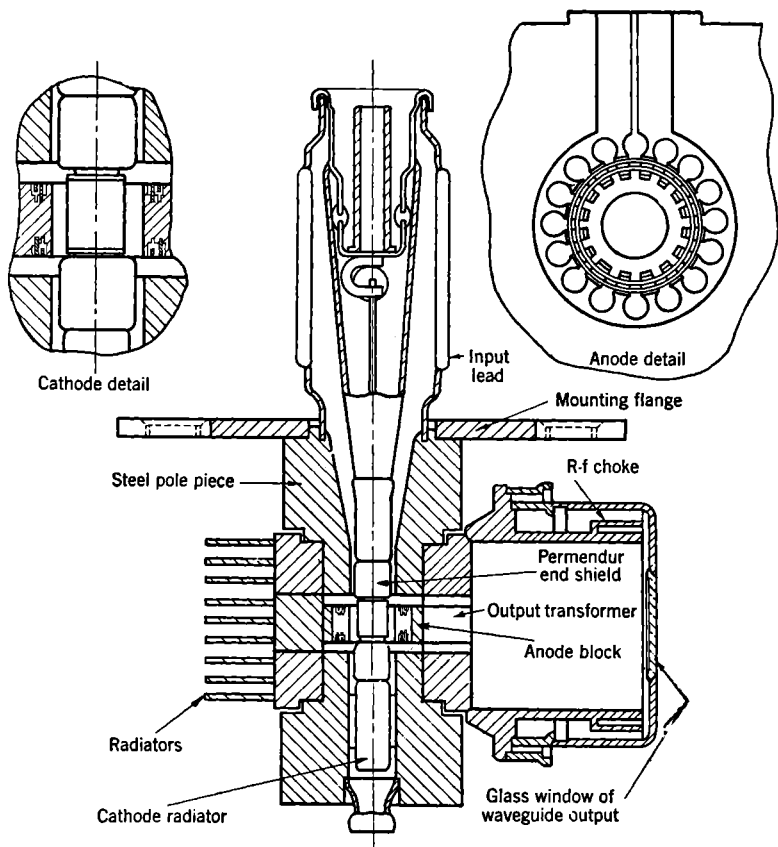


FIG. 19-50.—Cross sections of 4J50 magnetron. (Cathode is decentered longitudinally when cold to allow for expansion of support in operation.)

acts as a radiator to increase the dissipation of heat. The heater is rated at 5 amp and 12.6 volts; at 600 watts input (1- $\mu$ sec pulse duration) this power is reduced 50 per cent, and at higher inputs it is still further decreased. Tables 19-23 and 19-24 list the characteristic scale factors and dimensions of the 16-oscillator anode block, which is of hole-and-slot construction with double-ring strapping.

TABLE 19-23.—CHARACTERISTIC SCALE FACTORS FOR 4J50 AND 4J52 MAGNETRONS

$\lambda$ , cm	$\mathcal{B}$ , gauss	$s$ , amp	$V$ , kv	$\mathcal{P}$ , kw	$S$ , mhos	$Q_u$	$\eta_e$ , %	$\frac{C}{L}$
3.20	1470	15.6	2.50	39.0	$6.25 \times 10^{-3}$	900	70	0.116

TABLE 19-24.—DIMENSIONS IN INCHES OF 4J50 AND 4J52 MAGNETRONS

a. Anode Dimensions: See Fig. 19-1b

$a$	$b$	$c$	$d_a$	$d_c$	$h$	$w$
0.380	0.538	0.087	0.319	0.209	0.250	0.033

b. Strapping Dimensions: See Fig. 19-2c

$m$	$n$	$o$	$p$	$q$	$r$	$s$	$u$
0.225	0.205	0.185	0.175	0.010	0.010	0.018	0.028

The loading characteristics of the waveguide output are shown in the Rieke diagram of Fig. 19-51, and details of its construction appear

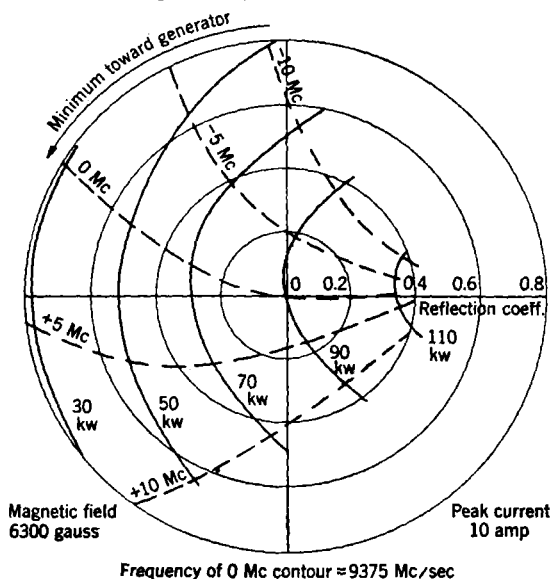


FIG. 19-51.—Rieke diagram for 4J50 (4J52, 4J78) magnetron.

in Fig. 19-52. At atmospheric pressure electrical breakdown occurs across the glass window of the output when the r-f power exceeds 375 kw, but this may be prevented by pressurization of the line.

A four-hole mounting plate, shown in Fig. 19-53, is used to support the magnetron in operation. The magnet is protected by a cast-aluminum sheathing. Forced-air cooling is required. Total weight of the 4J50 is 9 lb.

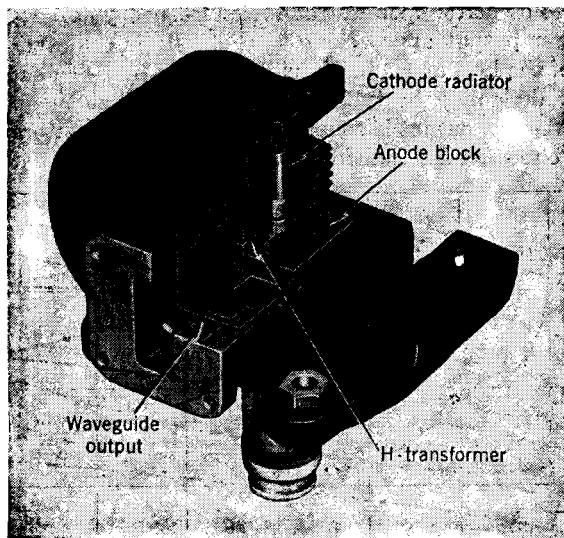


FIG. 19-52.—Cutaway view of 4J52 magnetron.

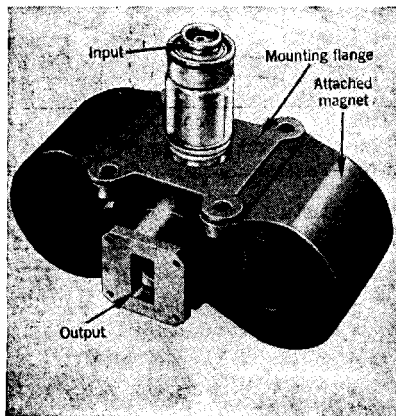


FIG. 19-53.—4J50 magnetron.

The 4J78 differs from the 4J50 only in its specified frequency, which lies between 9003 and 9168 Mc/sec. The 4J52, although identical with the 4J50 in anode-block structure and frequency, is assembled with a lighter magnet and a less massive cathode structure. Figure 19-49

shows the operating line for this magnet, as set by the manufacturer; the maximum average input power is limited to 500 watts, and the total weight of the tube is  $5\frac{7}{8}$  lb. The 4J52 is illustrated in Fig. 19-52.

**19-13. The AX9 Rising-sun Magnetron.**<sup>1</sup>—The AX9 is an experimental pulsed oscillator operating at a fixed frequency near 9500 Mc/sec. A pulse-power output approaching 1 megawatt is achieved by taking advantage of the long anode block made possible by rising-sun construction and by designing the tube for operation at high magnetic fields. A direct waveguide output is coupled to one of the resonators through a quarter-wave rectangular transformer. The cathode is mounted axially.

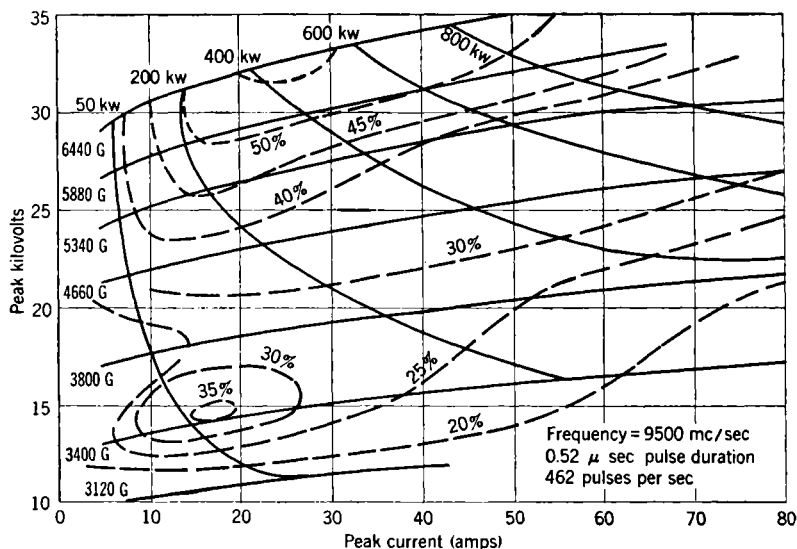


Fig. 19-54.—Performance chart for AX9 magnetron.

Performance characteristics for an AX9 magnetron are shown in Fig. 19-54; note the anomalous efficiencies in the neighborhood of 3500 gauss. The tube is intended for operation at magnetic fields greater than 5000 gauss and at currents above 30 amp. The decrease in efficiency at high magnetic fields is less pronounced than is usual in the rising-sun design because of the relatively low ratio of the cavity depths in this tube. At high pulse-power levels the AX9 must be operated at low duty ratios in order to avoid excessive cathode heating; the maximum average input power is 800 watts. When the output power exceeds 500 kw, the r-f line is pressurized to prevent breakdown, which occurs particularly near the window of the magnetron output. A Rieke dia-

<sup>1</sup> Data for Secs. 19-13 through 19-17 submitted by S. Millman.

gram for the tube is shown in Fig. 19-55. The pulling figure is approximately 16 Mc/sec.

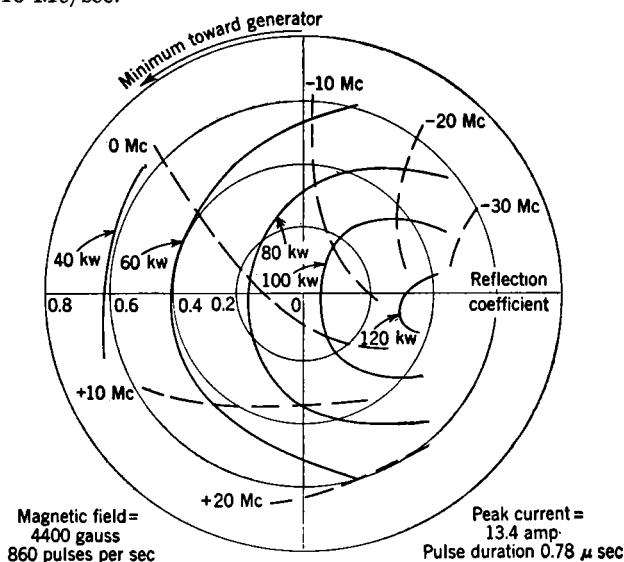


FIG. 19-55.—Rieke diagram for AX9 magnetron.

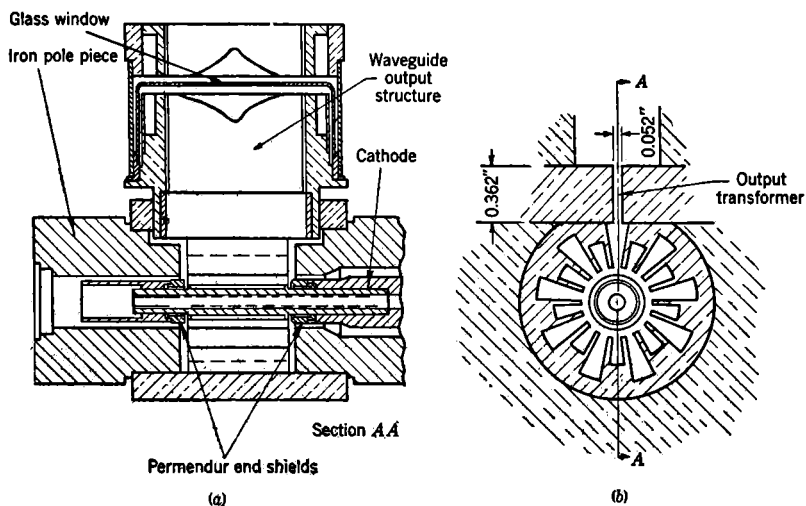


FIG. 19-56.—Cross sections of AX9 magnetron.

Figure 19-56 illustrates the essential features of the AX9 design. The depth ratio  $r_1$  of the resonators is about 1.6, which is appreciably less

than that of the 3J31 magnetron (Sec. 19-14). The mode separation between the operating or ( $n = 9$ )-mode and the ( $n = 8$ )-mode is only 4 per cent as compared with 7 per cent for the 3J31. Permendur end shields similar to those of the 4J50 (Sec. 19-12) are used on the cathode. Characteristic scale factors and dimensions are listed in Tables 19-25 and 19-26.

The long anode block of the AX9 results in a gap of 0.920 in. between the inserted magnet pole pieces and requires the use of a magnet unusually heavy for tubes operating in this frequency region. A magnet capable of supplying 6000 gauss would weigh approximately 40 lb.

TABLE 19-25.—CHARACTERISTIC SCALE FACTORS FOR AX9 MAGNETRON

$\lambda$ , cm	$\mathcal{B}$ , gauss	$\mathcal{V}$ , kv	$Q_u$	$Q_E$	$\eta_c$ , %
3.16	1220	3.45	1250	300	80

This design has not reached production (1946), and only a small number of experimental magnetrons have been studied. No life data are available.

TABLE 19-26.—DIMENSIONS IN INCHES FOR AX9 MAGNETRON  
See Fig. 19-1a

$a$	$d_a$	$d_c$	$d_s$	$d_e$	$h$	$t$
0.920	0.415	0.257	0.757	0.957	0.800	0.043

**19-14. The 3J31 and 3J21 Rising-sun Magnetrons.**—The 3J31 is a pulsed magnetron with a pulse-power output of about 50 kw at a fixed frequency of 24,000 Mc/sec. A direct waveguide output is coupled to one of the anode-block cavity resonators through a quarter-wave rectangular transformer. The cathode is mounted radially, and the magnet is separate from the tube.

Figure 19-57 shows the performance chart of a representative tube. The useful range of peak voltage and current inputs lies between 11 and 16 kv and between 6 and 18 amp, with corresponding pulse-power outputs ranging from 20 to 50 kw. Low-current operation is limited by high pushing, poor spectrum, and mode instability, while the high-current limit is set by excessive sparking. At magnetic fields less than 6800 gauss the efficiency becomes low and there is a possibility of interference from the ( $n = 8$ )-mode. Operation at fields greater than 8400 gauss is inadvisable because of the loss of efficiency that occurs in the  $\lambda H$  region from 10,500 to 15,000 gauss-cm; this phenomenon is typical of rising-sun magnetrons.



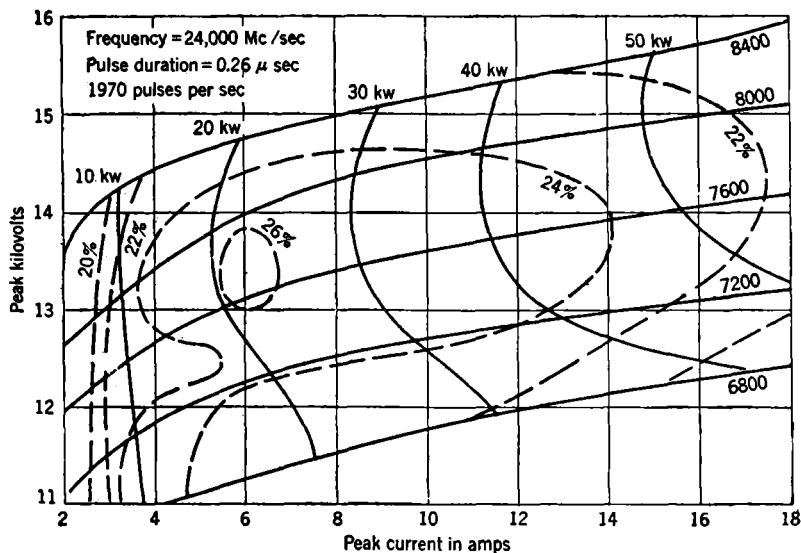


FIG. 19-57.—Performance chart for 3J31 magnetron.

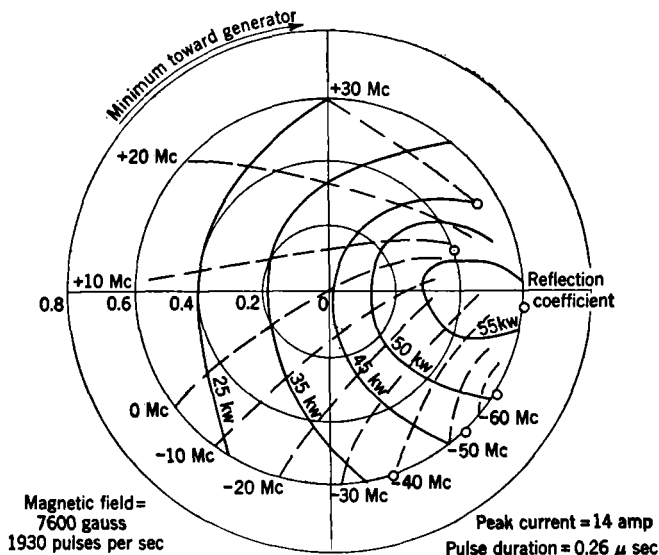


FIG. 19-58.—Rieke diagram for 3J31 magnetron.

The nickel cathode is screened and oxide-coated. In starting the tube the heater draws 1.7 amp at 6 volts. The usual operating point is at 7600 gauss, 14 amp, and 14 kv, with a pulse duration of  $0.5 \mu\text{sec}$  and a duty ratio of 0.0005. Under these conditions the heater may be turned off, and the magnetron will have a useful life of over 200 hr.

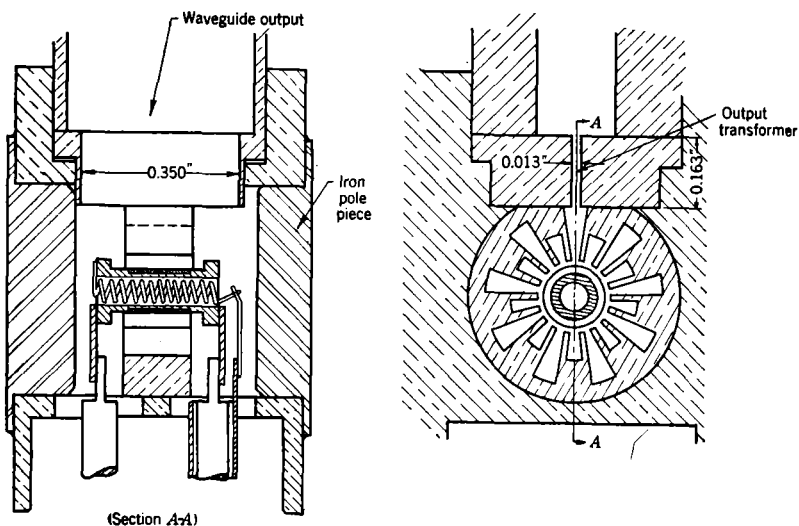


FIG. 19-59.—Cross sections of 3J31 magnetron.

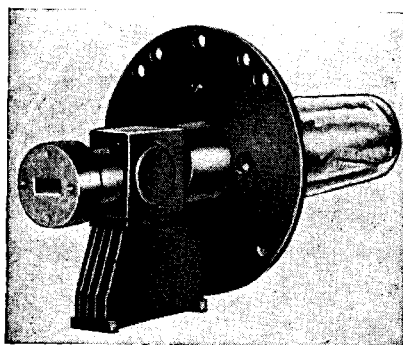


FIG. 19-60.—3J31 magnetron.

The nominal pulling figure is 25 Mc/sec (see Fig. 19-58), while pushing averages 0.5 Mc/sec per amp in the normal operating region.

Rising-sun construction is used in the anode block, which has 18 sector-shaped resonators of the open-cavity type, with a depth ratio  $r_1$  of 1.8. Characteristic scale factors and dimensions are tabulated in

Tables 19-27 and 19-28. Details of the design of the 3J31 are shown in Fig. 19-59. The lids contain iron inserts, leaving an internal air gap of 0.410 in. The magnet that is applied to these pole pieces has a gap of 0.710 in. and a pole-face diameter of  $\frac{3}{4}$  in. The weight of the tube, together with the magnet which is normally supplied, is 15 lb. Forced-

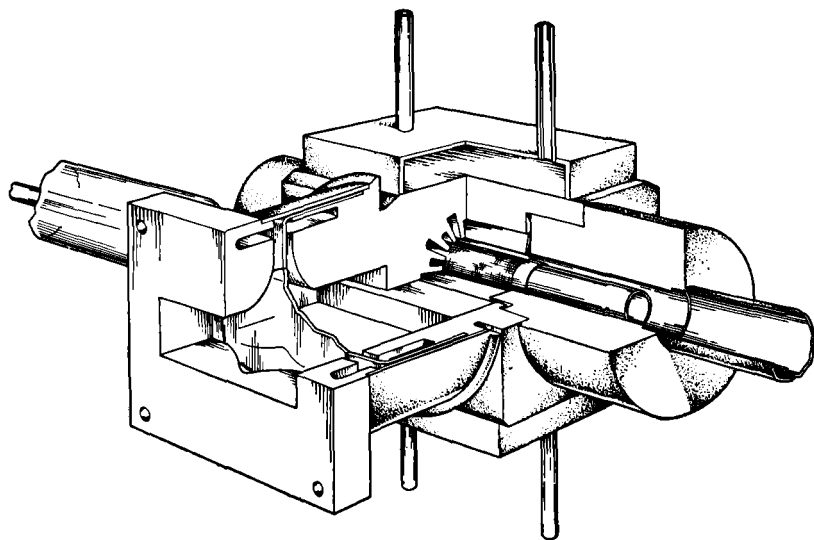


FIG. 19-61.—Cutaway view of 3J21 magnetron.

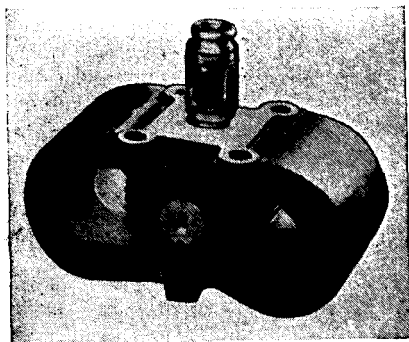


FIG. 19-62.—3J21 magnetron.

air cooling is required. Figure 19-60 shows the external appearance of the 3J31; a more complete description of its operation may be found in a technical report of the Columbia University Radiation Laboratory.

The 3J21 magnetron (Figs. 19-61 and 19-62) is a modification of the 3J31. In addition to an axially-mounted cathode and attached magnet,

it has a stabilizing cavity incorporated in the waveguide output. The cavity stabilizes the magnetron by a factor of 2 and increases the power output and efficiency 15 per cent. The usual operating point is 15 amp and 15 kv at a pulse duration of 0.5  $\mu$ sec and a duty ratio of 0.0005; this duty ratio may be nearly doubled if the heater is turned off during operation.

The 3J31 has also been used as the basis for scaling 18-vane open-cavity rising-sun magnetrons to wavelengths ranging from 0.9 to 4.0 cm.

Tables 19-27 and 19-28 give the characteristic scale factors and some of the 3J31 tube dimensions.

TABLE 19-27.—CHARACTERISTIC SCALE FACTORS OF THE 3J31 MAGNETRON

$\lambda$ , cm	$\mathcal{B}$ , gauss	$\mathcal{V}$ , kv	$\mathcal{P}$ , kw	$Q_u$	$Q_E$	$\eta_c$ , %
1.25	3000	3.3	45	800	400	65

TABLE 19-28.—TUBE DIMENSIONS IN INCHES OF 3J31 MAGNETRONS  
See Fig. 19-1a

$b$	$d_a$	$d_c$	$d_s$	$d_e$	$h$	$t$
0.469	0.160	0.096	0.288	0.390	0.150	0.017

**19-15. 22-cavity Rising-sun Magnetron.**—This rising-sun magnetron is very similar in construction to the 3J31 tube. It is designed for about the same wavelength and operating conditions as the 3J31, differing from it only in that the number of cavity resonators in the block is 22 instead of 18. This is the largest number of resonators used in a successful rising-sun magnetron having open cavities and block design parameters that are not particularly critical. (A sealed version of this tube at 6 mm is currently under development at the Columbia University Radiation Laboratory. A pulsed output power as high as 40 kw has been observed.)

The important tube dimensions are listed in Table 19-30. No photographs or cross-sectional views are given for this tube, as these would be practically identical with those shown in Figs. 19-59 and 19-60 for the 3J31 tube. The anode-block dimensions in Table 19-30 correspond to a cavity depth ratio of about 1.75 and give a wavelength separation between the  $\pi$ -mode ( $n = 11$ ) and the ( $n = 10$ )-mode of about 5 per cent.

The performance characteristics of a 22-cavity magnetron are shown in Fig. 19-63. These are so similar to those of the 18-vane 3J31 magnetron that they will not be further discussed. This applies also to the

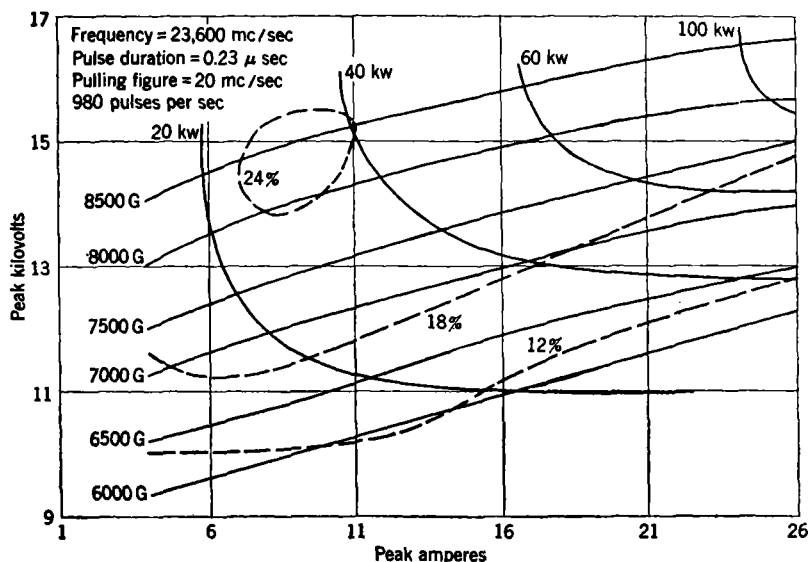


FIG. 19-63.—Performance chart of 22-cavity rising-sun magnetron.

operating conditions and life of the tube. Only a relatively small number of these tubes have been constructed and tested.

TABLE 19-29.—CHARACTERISTIC SCALE FACTORS FOR 22-CAVITY RISING-SUN MAGNETRON

Tube	$\lambda$ , cm	$\mathcal{B}$ , gauss	$\mathcal{V}$ , kv	$\mathcal{P}$ , kw	$Q_u$	$Q_g$	$\eta_c$ , %	$N$
P2	1.21	2700	3.0	50	800	500	60	22

 TABLE 19-30.—DIMENSIONS FOR 22-CAVITY RISING-SUN MAGNETRON  
 See Fig. 19-1a

$d_a$	$d_c$	$d_s$	$d_r$	$h$	$t$
0.181	0.116	0.311	0.410	0.170	0.0145

**19-16. The Closed-end 38-cavity Rising-sun Magnetron.**—This is an experimental pulsed magnetron with a rising-sun anode block of the closed-end type. The magnetron was designed for frequencies near 24,000 Mc/sec for the purpose of developing a tube that could readily be scaled to higher frequencies. As in the 3J31 magnetron, an axially mounted cathode and direct waveguide output are used.

A description of the essential features of the 38-vane magnetron is given in the sectional view (Fig. 19-64) and in Fig. 19-65. For constructional reasons, cylindrical holes are used in the large cavities of the block, producing a modification of the straight sector-shaped cavities commonly found in a rising-sun oscillating system. If the holes were replaced by equivalent sector-shaped cavities, the value  $r_1$  for the resulting ratio of cavity depths would be about 2.7. The height  $h$  of the closed-end block is  $0.65\lambda$ .

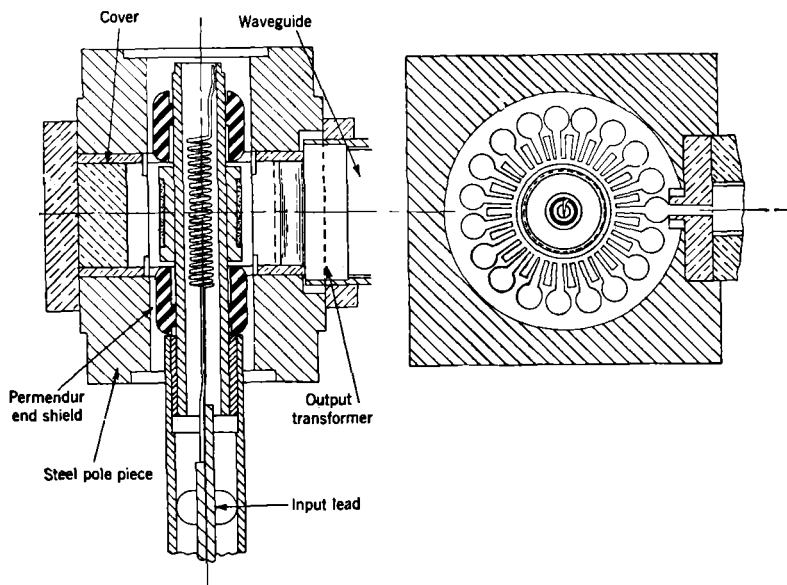


FIG. 19-64.—Cross sections of closed-end 38-cavity rising-sun magnetron.

The large values of the cathode and anode diameters are particularly noteworthy in this magnetron. The anode diameter is about two-thirds of a wavelength. This represents the highest ratio of  $d_a/\lambda$  that has been used in a successful magnetron.

The performance characteristics of a typical tube are shown in Fig. 19-66. The advantage of the large number of resonators is made evident by comparing the magnetic field values at the optimum efficiency region with those for the 3J31 magnetron. The relatively high currents appearing on the performance chart are another result of the use of a large number of resonators. The increased heat dissipation made possible by the large cathode size is not evident from the data supplied in the performance chart, because experiments with the tube were limited to a study of the possibilities of the oscillating circuit. The operation of

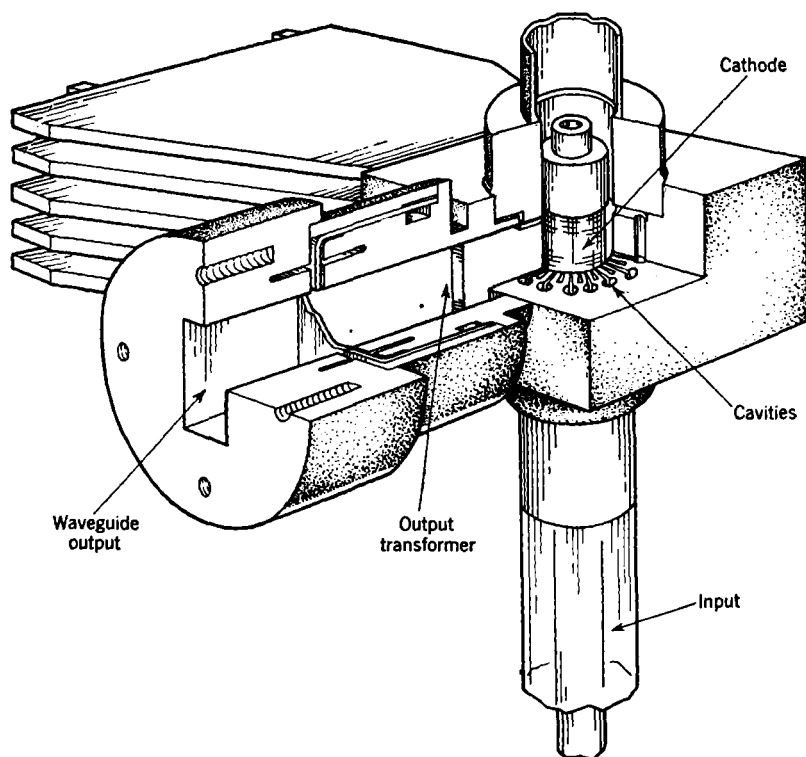


FIG. 19-65.—Cutaway view of 38-cavity rising-sun magnetron.

the magnetron is relatively free from troubles due to mode changes, despite the fact that the wavelength separation between the  $\pi$ -mode ( $n = 19$ ) and the ( $n = 18$ )-mode is only about 1 per cent. Tables 19-31 and 19-32 give the characteristic scale factors and some of the tube

TABLE 19-31.—CHARACTERISTIC SCALE FACTORS FOR 38-CAVITY MAGNETRON

Tube type	$\lambda$ , cm	$\mathcal{G}$ , gauss	$\mathcal{V}$ , kv	$Q_U$	$Q_E$	$\eta_c$ , %
Closed-end 38-vane.....	1.30	2060	3.05	1000	800	56
Closed-end 26-vane.....	1.26	2630	3.35	860	1030	46

TABLE 19-32.—DIMENSIONS FOR 38-CAVITY MAGNETRON  
See Fig. 19-1a and b

$d_a$	$d_c$	$d_s$	$h$	$t$	$c$
0.339	0.257	0.479	0.350	0.015	0.079

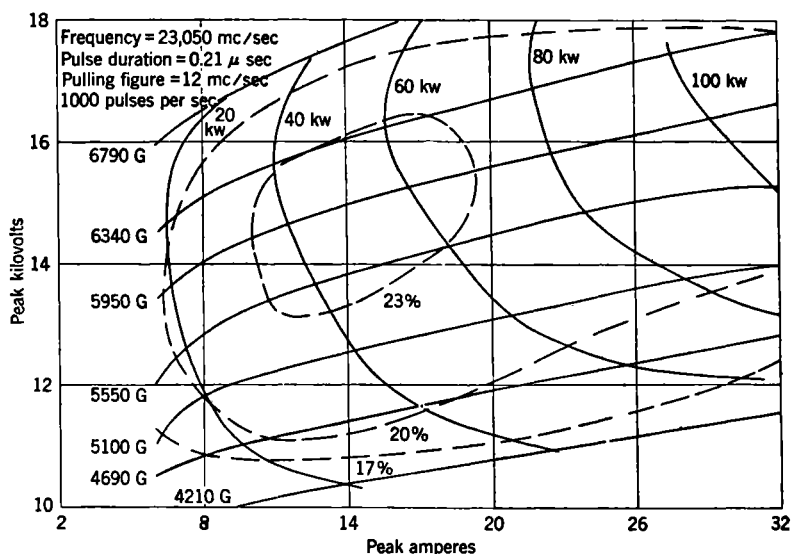


FIG. 19-66.—Performance chart for 38-cavity rising-sun magnetron.

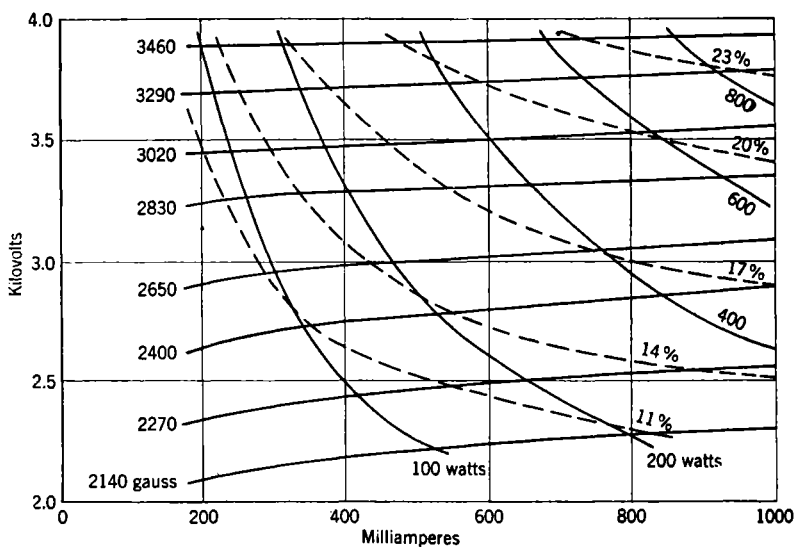


FIG. 19-67.—Performance chart for XCR magnetron.



dimensions. Characteristic scale factors are also listed for a similar design having but 26 resonators.

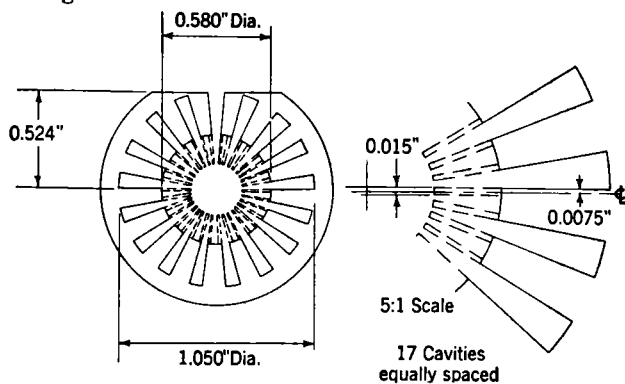


FIG. 19-68.—Transverse cross sections of XCR magnetron.

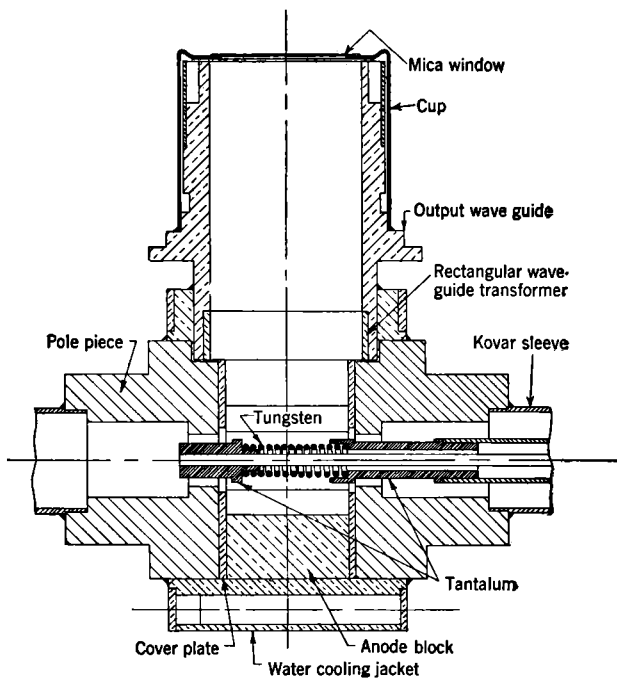


FIG. 19-69.—Longitudinal cross section of XCR magnetron.

**19-17. The XCR High-power 2.6-cm C-w Magnetron.**—This magnetron is a 34-vane experimental tube that utilizes a rising-sun anode block of the closed-end type. The tube is in an early stage of develop-

ment at the Columbia University Radiation Laboratory, and its description is intended principally as an indication of the output power possibilities of c-w magnetrons at short wavelengths. At an operating frequency of about 11,500 Mc/sec, an r-f output of 900 watts has been observed. The performance of the best of the few magnetrons that have been constructed up to the time of the present writing is shown in Fig. 19-67; complete test information is not available for this magnetron. Because of the absence of data on the  $Q$ 's, the circuit efficiency is not known. There is good ground for believing, however, that the electronic efficiencies are not substantially different from those of pulsed rising-sun magnetrons operating at corresponding values of  $H/H_0$ .

The essential constructional features of the 34-cavity magnetron are shown in the two section drawings (Figs. 19-68 and 19-69). The anode block is completely closed. The dimensions correspond to a block height of  $0.78\lambda$ , a cavity-depth ratio of 2.63, an  $H_0$  of 980 gauss, and a  $V$  of 700 volts. The axially mounted helical cathode is made of 0.040-in. tungsten wire, requiring about 45 amp at 3.3 volts for the starting of the magnetron. Only a fraction of this power, however, need be supplied when the tube is operating with high input power. The waveguide design for the tube includes a rectangular guide transformer and a mica window.<sup>1</sup>

<sup>1</sup> Professor W. E. Lamb, Jr., has kindly permitted the publication of the preliminary results that he has obtained with this tube.

# Index

---

## A

Absorption method, 704  
Action function, 226  
Adiabatic theory, 357  
Admittance, 50, 292, 293, 300  
    of annular-sector resonator, 62  
    characteristic, 113, 461  
    computation of, 77  
    of cylindrical side resonator, 59  
    of electron stream, 214  
    electronic, 293, 312  
    of interaction space, 63, 84  
    of rectangular-slot side resonator, 57  
    of side resonators, 56  
Aleksereff, N. T., 7  
Alnico V, 542, 547, 548  
American Chemical Paint Company, 675  
American Lava Corporation, 689  
Anode, double-ring-strapped, 460  
    strapped, circuit constants for, 465  
Anode block, 11, 49, 406  
    closed-end, 69  
    fabrication of, 649-662  
    hole-and-slot, 14  
    rising-sun, 437  
Anode-block height, 473  
Anode diameter, 472  
    ratio of, to cathode diameter, 105  
    to II-mode wave-length, 104  
Anode height, 439  
Anode-segment width, ratio of, to gap width, 107  
Arcing, 737  
Arnold Engineering Company, 542, 551, 552  
Ashkin, A., 500  
Automatic-frequency control, 623  
AX9 magnetron, 429, 784-786

## B

Back-bombardment power, 411, 437, 520, 525, 529  
    as function of total slot conductance  $G$ , 527  
Bandwidth, 390  
Baños, A., Jr., 594, 599  
Bartol Research Foundation, 692  
Bell Telephone Laboratories, 564, 683, 686, 687, 689  
Belmont Smelting and Refining Works, Inc., 667  
Bierwirth, R. A., 668  
Bloom, L. R., 684  
Blow-in, 489  
Blum, W., 676  
BM50 magnetron, 429, 764-766  
Boot, H. A. H., 10  
Boundary conditions, 414  
    cathode, 257  
Brazing, 662-670  
    precision, 670  
    problems in, 670  
Brazing alloys, 664-667  
Breakdown, 641  
    in r-f line, 738  
Breakdown temperature, 529  
Brillouin steady state, 245  
British cavity magnetron, 8  
Brown, G. H., 668  
Buck, J. G., 676  
Buildup, 357, 372  
     $Q$  for, 365, 374  
Bullet, 482  
Bunemann, O., 253  
    (See also Small-amplitude theory)  
Bureau of Ships, 553  
Burger, E. E., 677

## C

- Capacitance, fringing, 464
- Capacity, equivalent, 108
- Cathode, 11, 23, 378, 411
  - back bombardment of, 285
  - construction of, 685-687
  - end-mounted, 411, 530
  - helical-shape, 796
  - localized deterioration of, 762
  - ohmic loss in, 524
  - overheated, 738
  - pulsed, thermal behavior of, 520
  - radial-mounted, 411, 529
  - secondary-emission, 411
  - size of, 23
  - thorium oxide, 534, 692
- Cathode-anode short circuit, 736
- Cathode boundary conditions, 257
- Cathode-current density, 440
- Cathode diameter, ratio of, to anode diameter, 105
- Cathode end shields, 537
- Cathode-lead loss, 728, 729
- Cathode radiator, 781
- Cathode radius, 440
- Cathode sparking, 413
- Cathode steps, 758
- Cathode temperature, range in, 412
- Cathode-temperature characteristics for 2J42 magnetron, 528
- Cavities, side, 49
- Cavity resonators, 290
- Cavity stabilization, 747, 758, 769, 773, 790
- Cavity tuning, 583, 758, 773
- Charge distribution, 17
- Chemical processes used in construction, 674-676
- Chemistry and Physics, Handbook of*, 676
- Choke joint, 483
- Circuit, center-loop, 191
  - equivalent (*see* Equivalent circuit)
  - halo-loop, 191
- Circuit constants for strapped anodes, 465
- Circuit efficiency, 36, 181, 185, 421, 626, 717
  - $\eta_c$ , 407
- Circuit element, electron stream as, 291-297
- Circuit parameters, of hole-and-slot resonator, 463
  - of vane-type resonator, 462
- Clark, J. E., 677
- Cleaning, 675
- CM16B c-w magnetron, 744-747
- Coaxial coupling section, 483
- Coaxial-line chokes, 11
- Coaxial-line tuning, 746
- Coaxial-output circuit, 169, 191
- Coaxial outputs, 482
- Coaxial-to-waveguide transitions, 485
- Columbia University Radiation Laboratory, 655, 657, 659-661
- Components, 340
- Computation of admittances, 77
- Condon, E. U., 567
- Conductance, characteristic, 416
  - electronic, 391
  - $G_L$ , at slots, 422
- Conductance map, 338, 358, 361
- Constant  $b$ , contours of, 447
- Constant  $D$ , lines of, 454
- Construction, chemical processes used in, 674-676
  - tube, 649-697
- Contours, 317, 319, 331
  - efficiency, 443
  - of constant  $b$ , 447
- Cooling by radiation, 524
- Coomes, E. A., 676
- Corning Glass Works, 679
- Coupling, loop-, 169
  - segment-fed, 170, 194
  - strap-fed, 170
- Coupling circuits, strap-fed, 193
- Coupling devices, low- $Q$ , 578
- Coupling loop, 11
- Critical field, 437
- Crout, Prescott D., 554
- Crucible Steel Company of America,
  - Halcomb Steel Division, 651
- Current, characteristic, 416
- Current amplitude, 291
- Current density, reduced linear, 235
- Cutoff, 3, 340, 342, 369
- Cutoff (Hull) voltage, 238
- Cyclotron frequency, 599
- Cyclotron-frequency oscillations, 3

## D

- Demagnetization curve, 542
- Density, cathode-current, 440
  - low-current, 440
- Design formulas, 455
  - general, 454
- "Dielectric Materials, Tables of," 679, 680
- Distillation Products, Inc., 693
- Donal, J. S., Jr., 684
- Doorknob transition, 485
- Double-ring strapped systems, 119
- Dushman, S., 692
- Duty ratios, 8

## E

- Efficiency, 35, 401, 450
  - electronic (*see* Electronic efficiency)
  - of operation, 409
- Efficiency contours, 443, 452
  - adjusted, 445
- Efficiency lines, 447
- Efficiency minimum, 437
- Eisenstein, A. S., 676
- Electromagnets, 540
- Electron emission, 352
- Electron emitters, 411
- Electron gas, 598
- Electron leakage, 537
- Electron stream, admittance of, 214
  - as circuit element, 291-297
- Electronic admittance, 293, 312
- Electronic conductance, 391
- Electronic efficiency, 36, 333
- Electronic susceptance, 410
- Electrons, thermal velocities of, 211
- Electroplating, Modern*, 676
- Emission, 353, 379
  - electron, 352
  - primary, 413
- Emitters, electron, 411
  - metallic, high-temperature, 413
- End plates, insulated, 538
- End shield, 12, 530
  - cathode, 537
  - Permendur, 781
- End space, 11, 91, 498
- End-space effects, 69, 418
- End-space resonances, 74

- Energy loss function, 241
- Energy product, 541
- Equivalent circuit, 289, 293, 297-299, 311, 330
  - of single resonator, 461, 466
- Equivalent ratio  $r_{eq}$ , 108
- ET10 reactance tube, 747
- Everhart, E., 620

## F

- Field distribution for modes, 17
- Field equations, 217-222
- Field fluctuations, 222-228
- Field-pattern measurements, 710-713
- Field theory, spectrum by, 66
- Field uniformity, 552
- Fineman, A., 676
- Fisk, J. B., 582
- Flux leakage, 545
- Flux plotting methods, 72
- Fluxes, 664-667
- Forgue, S. V., 692
- 4J31 magnetron, 760
- 4J33 magnetron, 427
- 4J35 magnetron, 760
- 4J36 magnetron, 760
- 4J39 magnetron, 427
- 4J41 magnetron, 760
- 4J50 magnetron, 428, 780-784
- 4J52 magnetron, 783
- 4J70 tunable magnetron, 756-760
- 4J77 tunable magnetron, 756-760
- 4J78 magnetron, 783
- Fourier analysis, 340
- Frequency, 401
  - complex, 300, 306, 357
- Frequency sensitivity, 482, 582
  - of output circuits, 189
- Frequency sink, 328
- Frequency stability, 35, 408, 409
- Frequency stabilization, 402

## G

- Gap width, ratio of, to anode-segment width, 107
- Gas, residual, 395
- Gassy tube, 736
- General Electric Company, 563, 573, 621, 677

General Electric Research Laboratories,  
554

GK13-1 magnetron, 430

Glass, No. 704, 483

Corning, No. 707, 483, 487

Glass seal, 482

Kovar-to-, 483

Glasses, laboratory, 679, 680

Guide, chamfered, 488

H-section, 199

lumped, 198

## H

H-section transformer, 498

H-shaped cross section, transformer of,  
493

Habann-type oscillations, 4

Haefl, A. V., 601

Halcomb Steel Division, Crucible Steel  
Company of America, 651

Hall, N., 676

Handy and Harmon Company, 667

Hartman, P. L., 582

Hartree, 30

Hartree diagram, 30, 341

Hartree's condition, 340

Heat balance, 412, 519

Heater, open, 736

Heater construction, 687-693

Heater power, 402, 411

rated, 528

Hinman, C. W., 651

Hobbing, 654

Hogaboom, G. B., 676

Hogaboom, G. B., Jr., 676

Hollow pole pieces, 411

Housekeeper, W. G., 676

HP10V magnetron, 426, 760-764

Hull, A. W., 1, 615, 677

Hull, F. C., 664, 665

Hydrogen bottle, 669

## I

Impedance, 290, 705

cold, 329

oscillator, 36

static input, 401

Indiana Steel Products Company, 542

Inductance, equivalent, 114

Inductance-tuned system, multicavity,  
mode spectrum of, 165

Instability, 345, 349, 355

Instability voltage, 264

Interaction field, 74, 92-98

Interaction space, 11, 84, 403

admittance of, 63, 84

equivalent network for, 52

trial design of, 403

Interactions, 380

Ions, 395

Iris coupling, 194

Iris output, stabilized, 498, 499

Iris transformer, 494

Iris windows, 203

## J

James, H. M., 582

Jepson, R. L., 684

Jig assembly, 650

Johnson Company, Lloyd S., 667

Jones, F. D., 650

## K

Kester Solder Company, 667

Kilgore, G. R., 4

Klystron, 597

Kolin, A., 554

Kovar, 677, 678, 695

Kovar-to-glass seal, 483, 677*n*

Kusch, P., 565

## L

Laboratory glasses (*see* Glasses, labora-  
tory)

Lamb, W. E., 471, 617

Lamination, 650

Large-signal conditions, 619

Laws, F. A., 553

Lawson method, 713

*L/C* ratio of magnetron oscillator, 726

LCW magnetron, c-w, 740-744

single, 428

Lead loss, 718

Leakage, flux, 545

of II-mode radiation, 501

Litton Engineering Laboratories, 573, 681

LL3 magnetron, 352, 367

"Lloyd's," Lloyd S. Johnson Company,  
667

Load curves, 444  
 Load  $g$ , reduced, 443  
 Load instability, 42  
 Loaded  $Q$ , 188  
 Loading, 563  
   effect of, on mode spectrum, 141-147  
 Long-line effect, 322  
 Loop-coupling, 169  
 Loops, 297, 305, 310  
   center, 169  
   halo, 169  
 Lord, H. W., 549  
 Lumped guides, 198

## M

*Machinist's Handbook*, 650  
 Machlett X-ray Corp., 650  
 McIntosh, R. O., 667  
 Magnet, 402  
   permanent, 13  
   design of, 540  
 Magnet charging, 548  
 Magnet weight, 414  
 Magnetic circuit, 414, 540-557  
*Magnetic Circuits and Transformers*, 543  
 Magnetic field, 436  
   characteristic, 416  
 Magnetic material, 414  
 Magnetic stabilization, 550  
 Magnetron, AX9, 429, 784-786  
   BM50, 429, 764  
   British cavity, 8  
   c-w, CM16B, 744-747  
     LCW, 740-744  
     XCR, 795, 796  
   early types of, 1  
   family of, 416  
   4J31, 760  
   4J33, 427  
   4J35, 760  
   4J36, 760  
   4J39, 427  
   4J41, 760  
   4J50, 428, 780-784  
   4J52, 783  
   4J78, 783  
   GK13-1, 430  
   HP10V, 426, 760-764  
   index of, 742  
   linear, 233  
     basic equations for, 233

Magnetron, LL3, 352  
   low-voltage, 440  
   microwave, 1  
   packaged, 13  
   performance of, 316  
   pulsed, 42  
     characteristics of, 45  
   QK61, 428  
   RD11-2, 430  
   rising-sun (*see* Rising-sun magnetron)  
   SCWC, 430  
   scaling of, 236  
   725A, 428, 774-777  
   730A, 777  
   single LCW, 428  
   split-anode, 4  
   stabilized, 2J41, 766-769  
   3J21, 789  
   3J31, 429, 786-790  
   tunable, 320  
     4J70, 756-760  
     4J77, 756-760  
     2J51, 778-780  
   2J22, 751-756  
   2J32, 426  
   2J34, 751-756  
   2J38, 747-751  
   2J39, 426, 747-751  
   2J42, 770-774  
   2J49, 777  
   2J50, 777  
   2J53, 777  
 Magnetron design, 403  
 Magnetron diode tuning, 615  
 Magnetron efficiency, limiting, 240  
 Magnetron fields, boundary conditions  
   for, 234  
 Magnetron Modulation Coordinating  
   Committee, minutes of, 620  
 Magnetron oscillator,  $L/C$  ratio of, 726  
 Malearoff, D. E., 7  
 Malter, L., 684  
 Marion Electrical Instrument Company,  
   553  
 Massachusetts Institute of Technology,  
   543  
 Measurements, 553  
 Mica windows, 489, 684  
 Misfiring, 43, 346, 350, 354  
 Mode changes, 343, 345, 376  
 Mode changing, 43

- Mode competition, 100, 474
- Mode damping, 769
- Mode degeneracy, 17
- Mode identification, 726, 727
- Mode instability, 737
- Mode jumps, 355
- Mode number, 29
- Mode number  $n$ , 33
- Mode selection, 339, 348, 575, 586
- Mode separation, 468
- Mode shift, 345, 351
- Mode-shifting, 562
- Mode skip, 345, 348, 350
- Mode spectrum, 474
  - of double-ring-strapped systems, 133-138
  - effect of loading and strap breaks on, 141-157
  - of multicavity inductance-tuned system, 165
  - of multicavity segment-tuned system, 161
  - of multicavity strap-tuned system, 159
  - of single-cavity-tuned strapped system, 157
  - of single-ring-strapped systems, 138
- Mode stability, 538
- Modes, 339
  - component, 32
  - degenerate, 75
  - field distribution for, 17
  - frequencies of, 19
  - of oscillation, 627
  - zero, 472
- Modulation, amplitude, 592
  - frequency of, 592
  - phase, 597
- Morton, G. A., 554
- Motion, equations of, 222-228
  - nonrelativistic, 231-243
- Myers, L. M., 554
- Noise, 365, 367, 388-398
  - origins of, 395-398
- Noise fluctuations, 418
- Nonlinearity, 381
  - of space charge, 313
- Nonoscillating states, 342, 362, 367
- Nordisiek, A., 494, 565

## O

- Oberg, E., 650
- Ohmic loss in cathode, 524
- Operating characteristics, 613, 614
- Operating constants, 405
- Operating curve, 296, 297, 307, 315, 332, 338
- Operating data, reduced, 419
- Operating point, relative, 403, 435, 455
- Operation, efficiency of, 409
- Oscillations, buildup of, 43
  - cyclotron frequency, 3
  - Habann-type, 4
  - modes of, 309
  - negative-resistance, 4
  - $\pi$ -mode, 16
  - spurious, 418
  - traveling-wave, 5
- Oscillator impedance, 36
- Oscillograph, 373
- Oscilloscope, 346
- Output circuits, 11
  - coaxial-, 169, 191
  - functions of, 187
  - high-impedance level, 190
  - low-impedance level, 190
- Output transformers, quarter-wave-length, 195
- Outputs, 481
  - coaxial, 482
  - waveguide, 486
- Oxygen-free high-conductivity (OFHC) copper, 650, 694, 695

## N

- Network, equivalent, for interaction
  - space, 52
  - for side resonators, 52
  - spectrum by, 54
  - rings of, 123-130
- Neutrode, 423

## P

- $\Pi$ -mode, 461, 467, 470, 472, 474, 479
- $\Pi$ -mode field, distortion of, 97
- $\Pi$ -mode operation, 98
  - (See also Zero component contamination)
- $\Pi$ -mode oscillations, 16



$\Pi$ -mode radiation, leakage of, 501  
 $\Pi$ -mode wavelength, ratio of, to anode-block diameter, 104  
 Palmer, Frank R., 655  
 Parallel-resonant circuit, 301, 310  
 Parameter operation, 37  
 Parameters, primary design, 401, 455  
     secondary design, 405, 435  
 Pattern distortion, 141, 144, 151, 189, 576  
 Performance charts, 38, 317, 334, 732  
     reduced, 436, 441  
     universal, 448, 450  
     variation of, with load, 441  
 Permendur end shields, 781  
 Phase coherence, 388  
 Phillips, M., 617  
 Plating, 676  
 Pomerantz, Martin A., 692  
 Posthumus, K., 6  
 Power, back-bombardment (*see* Back-bombardment power)  
     characteristic, 416  
 Power output, 401  
     average, 402  
 Power transmission, average, 484, 489  
 Prater, C. D., 692  
 Probe transition, 486  
 Pseudo scaling, 450  
 Pulling figure, 182, 186, 188, 326, 734  
 Pulse durations, 402  
 Pulser, 343, 380  
     hard-tube, 343  
     line-type, 344

## Q

Q, 301  
     for buildup, 365, 374  
     external, 181  
     loaded, 188  
     measurement of, 713-723  
     unloaded (*see* Unloaded Q)  
 Q-circle, 178-187  
 Q-measurements, 180  
 $Q_L$ , 303  
 QK61 magnetron, 428

## R

Radial cathode supports, 13  
 Radiation, cooling by, 524  
 Radio Corporation of America (RCA), 613, 650

Randall, J. T., 10  
 Raytheon Manufacturing Co., 650  
 RD11-2 magnetron, 430  
 Reflection coefficient, 706  
 Relativistic corrections, 211  
 Relativistic effects, 228  
 Relaxation method, 71  
 Resistance, equivalent, 114  
     internal, 343, 356, 363, 371  
 Resonance indicator, 704  
 Resonances, end-space, 74  
     tuner, 575  
 Resonant cavity, 773  
 Resonant circuit, internal, 7  
 Resonant-circuit terminals, 720  
 Resonant load, mismatched transmission line as, 320-329  
 Resonant systems, 11, 13-23, 297-304, 406, 460  
     components of, 406  
     strapped, 461  
     unstrapped, 49  
     various, 22  
 Resonator depths, ratio of, 102, 478  
 Resonator shape, 108  
 Resonators, 11  
     annular-sector, 62  
     cavity, 290  
     closed-end, 471, 477  
     hole-and-slot, circuit parameters of, 463  
     number of, 472  
     effect of, 107  
     open, 471, 477  
     side, 49  
     admittance of, 56  
     of composite shape, 62  
     cylindrical, 59  
     equivalent network for, 52  
     rectangular-slot, 57  
     single, equivalent circuit of, 461, 466  
     vane-type, circuit parameters of, 462  
 R-f components, 32  
 R-f line, breakdown in, 738  
 R-f output, detection of, 732  
 R-f patterns, 470  
 Rieke diagram, 40, 178-187, 317, 327, 733  
 Rising-sun magnetron, 21, 283, 528  
     22-cavity, 790, 791  
     38-cavity, 791-794  
 Rising-sun resonant system, 470

- Rising-sun systems, 83-117
    - closed-end, 110-113
    - partially closed-end, 113
  - Rotary probe, 710
  - Rotating-wave hypothesis, 219, 282-287
- S
- S-curve method, 177
  - Sanford, R. L., 540, 553
  - Saxon, D. S., 594, 599
  - Scale factors, 448
    - characteristic, 416, 441
  - Scaling, 417, 450, 610
    - pseudo, 450
  - Scaling laws, 414
  - Scott, H., 677
  - SCWC magnetron, 430
  - Seals, glass-to-Kovar, 677, 681
    - metal-to-glass, 676
  - Segment-tuned system, multicavity,
    - mode spectrum of, 161
  - Self-consistent fields, 265-274, 279
    - 704 glass, 483
    - 707 Corning glass, 483, 487
    - 725A magnetron, 428, 774-777
    - 730A magnetron, 777
  - Shape factors, 403, 435, 455
  - Short-line effects, 322
  - Shot effect, 396
  - Shulman, C., 597, 608
  - Signal Corps, 553
  - Signal-to-noise ratio, 388, 394
  - Single-ring strapped systems, 119
  - Single-stream states, conditions for, 251
  - Sintering, 662
  - Slater, J. C., 467, 582
  - Slobod, R. L., 685
  - Slot conductance  $G_L$ , 407
  - Slot width, relative, 442
  - Small-amplitude theory, 253-265
  - Small-signal theory, 616
  - Smith, L. P., 597, 608
  - Smith, P. H., 40
  - Smith chart, 318, 707
  - Solder, 663
  - Soldering, 662-670
  - Sonkin, S., 657, 659
  - Space charge, 24, 340, 391
    - as circuit element, 288-338
    - nonlinearity of, 313
  - Space-charge configuration, 27
  - Space-charge limitation, 211, 412, 418
  - Space-charge properties, 316, 329-338
  - Sparking, 24
  - Spectrum, 83, 325, 345, 389, 735
    - by equivalent network, 54
    - by field theory, 66
  - Sprocket tuning, 565
  - Stability, 305, 313, 328, 362
    - frequency (*see* Frequency stability)
  - Stabilization, 408, 576, 586, 622-645
    - cavity (*see* Cavity stabilization)
    - frequency, 402
    - magnetic, 550
  - Stabilization factor, 625, 723-726
  - Stabilizer, 406, 494, 622
  - Standing-wave measurements, 705-710
  - Standing-wave ratio, 707
  - Stanley, F. A., 651
  - Start, false, 372
  - Starting, 357, 367, 376
    - speed of, 365, 632
  - Starting time, 365, 388
  - Starting voltage, 370
  - Strap breaks, 147-157, 470
    - effect of, on mode spectrum, 147-154
  - Strap-tuned system, multicavity, mode
    - spectrum of, 159
  - Strapped systems, double-ring, 119
    - mode spectrum of, 133-138
    - single-cavity-tuned, mode spectrum of, 157
    - single-ring, 119
    - mode spectrum of, 138
  - Strapping, 118, 384
    - by staggering of vanes, 766
  - Straps, 11
    - definition of, 118
    - effect of, 19
  - Stratton, J. A., 598
  - Strong, J., 664, 666, 667, 677
  - Stupakoff Ceramic and Manufacturing Company, 677
  - Symmetrical states, 243-253
- T
- Temperature, fluctuation in, 521, 523
  - Terminals, 292, 298, 319
  - Test bench, 731
  - Testing, 553

- Thermal behavior of pulsed cathode, 520
- Thermal expansion, 407
- Thorium oxide cathode, 534
- 3J21 magnetron, 789
- 3J31 magnetron, 429, 786-790
- Threshold (Hartree) voltage, 237
- Tibbs, S. R., 266
- Transducer, 298, 299, 319
  - 4-terminal, 171-177
- Transducer constants, 177
- Transformation formulas, 62
- Transformations, bilinear, 174
- Transformer, 489
  - H-section, 498
  - of H-shaped cross section, 493
  - iris, 494
  - quarter-wave, 482
  - rectangular, 491
  - waveguide, 491
- Transformer constant, principal, 177
- Transient behavior, 339-387
- Transients, 315, 357, 359, 366
- Transmission line, mismatched, 309
  - as resonant load, 320-329
- Transmission method, 702
- Tube, gassy, 736
  - reactance, ET10, 747
  - reseasoning of, 737
- Tube construction, 649-697
- Tube evacuation, 693, 694
- Tube model, 729
- Tube processing, 693, 694
- Tuner, multicavity inductance, 165
  - multicavity segment, 161
  - multicavity strap, 159
  - single-cavity, 157
- Tuner resonances, 575
- Tuning, 622
  - capacitive, 570
  - cavity (*see* Cavity tuning)
  - coaxial, 588
  - coaxial-line, 746
  - cookie cutter, 570
  - coupled-circuit, 576
  - double-output, 576
  - electron-beam, 592
  - electronic, 592-621
  - inductive, 565
  - iris-coupled, 583
  - magnetron diode, 615
  - mechanical, 561-591
  - Tuning, by perforated plate, 769
    - by pins in oscillators, 778
    - ring, 572
    - single-stub, 589
    - sprocket, 565
  - Tuning curve, 320, 324
  - Tuning hysteresis, 562
  - Tuning ranges, 402, 407, 408, 643
  - Tuner resonances, 575
  - 2J22 magnetron, 751
  - 2J32 magnetron, 426
  - 2J34 magnetron, 751
  - 2J38 magnetron, 747
  - 2J39 magnetron, 426, 747
  - 2J41 stabilized magnetron, 766-769
  - 2J42 magnetron, 770-774
    - cathode-temperature characteristics for, 528
  - 2J49 magnetron, 777
  - 2J50 magnetron, 777
  - 2J51 tunable magnetron, 778-780
  - 2J53 magnetron, 777
- U
- Underhill, E. M., 544, 548
- Unloaded  $Q$ , 108, 113, 184, 466, 467, 561, 575
- V
- Vacuum casting, 661
- Vane equivalent, 108
- Vane thickness, ratio of, to space between vanes, 473
- Variables, dependent, 294
  - dimensionless, 415
  - independent, 294, 316
  - reduced, 232, 365, 416
- ( $V, I$ )-characteristics, 343, 450
- ( $V, I$ )-diagrams, 341
- ( $V, I$ )-plot, 346
- ( $V, I$ )-scope, 347
- ( $V, I$ )-trace, 347, 348, 358, 368, 372
- Vitter, A. L., Jr., 614
- Voltage, 291
  - characteristic, 416
  - instability, 264
  - reduced, 233
- Voltage breakdown, 484, 488
- Voltage position, minimum-, 707

Voltage range, 401  
 Von Hippel, A., 680

## W

Walsh, E. J., 682  
 Waveguide circuits, directly coupled, 195  
 Waveguide-output circuits, 194-203  
 Waveguide outputs, 170, 486, 497, 782  
 Waveguide transformers, 491  
 Waveguide window, 488  
 Wavelength, 461  
   shift of, with current, 410  
    $\Delta\lambda$ , shift of, 407  
 Wavelength calculations, 479  
 Wavelength measurements, 702-705  
*Welding Handbook*, 662, 667  
 Westinghouse Electric Corporation, 588,  
   667

Westinghouse Research Laboratories,  
   664, 665, 667

Windows, 487  
   iris, 203  
   mica, 489, 684  
   waveguide, 682

Wright, F. I., 266  
 Wulff, John, 662

## X

XCR c-w magnetron, 795, 796

## Z

Zero component contamination, 97, 98  
 Zero mode, 472  
 Zworkin, V. K., 554



